19991123 146

Creep and Fracture of Engineering Materials and Structures

Editors:

T. Sakuma and K. Yagi

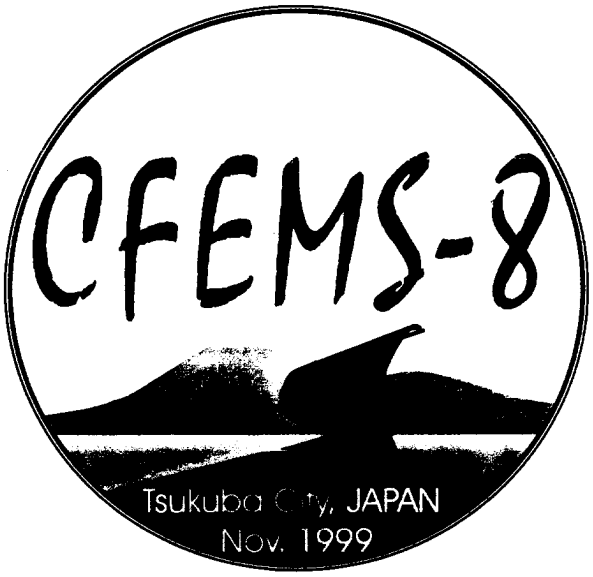

9th IKETANI CONFERENCE

Supported by Iketani Science and Technology Foundation

TRANS TECH PUBLICATIONS

DISTRIBUTION STATEMENT A
Approved for Public Release
Distribution Unlimited

Key Engineering Materials

ISSN 1013-9826

Specializing in the Field of Basic and Applied Aspects of Advanced Ceramic Materials and Composites

Editors:

Erian Armanios
Georgia Institute of Technology
School of Aerospace Engineering
Atlanta, GA 30332, USA
Fax +1 (404) 894 9313
e-mail: erian.armanios@aerospace.gatech.edu

Yiu-Wing Mai
The University of Sydney
Centre for Advanced Materials Technology
Sydney NSW 2006, Australia
Fax +61 (2) 351 2290
e-mail: mai@tiny.me.su.oz.au

Golam M. Newaz
Wayne State University
Department of Mechanical Engineering
Detroit, Michigan 48202, USA
Fax +1 (313) 577 8789
e-mail: gnewaz@me1.eng.wayne.edu

Fred H. Wöhlbier
Trans Tech Publications Ltd
Brandrain 6
CH-8707 Zuerich-Uetikon, Switzerland
Fax +41 (1) 922 10 33
e-mail: f.wohlbier@ttp.net

Editorial Advisory Board:

Australia
C.H.J. Davies (Clayton)
B.H. O'Connor (Perth)
L. Ye (Sydney)

Austria
R. Danzer (Leoben)

Canada
Z. Wang (Toronto)

China P.R.
D.L. Jiang (Shanghai)
J.K. Kim (Kowloon)
Z.G. Wang (Shenyang)
A. Xing (Jinan)

Denmark
B.F. Sorensen (Roskilde)

Egypt
M.A. Taha (Cairo)

France
F. Thevenot (Saint-Etienne)
M. Ignat (Saint Martin d'Hères)

Germany
G. Grathwohl (Bremen)
H. Schmidt (Saarbruecken)
H. Schneider (Köln)
G. Tomandl (Freiberg)
W. Weppner (Kiel)

India
D. Chakravorty (Calcutta)
K. Chattopadhyay (Bangalore)
B.V. Radhakrishna Bhat (Hyderabad)
S. Ray (Roorkee)
B.K. Sarkar (Calcutta)
G.S. Upadhyaya (Kanpur)

Ireland
P. McHugh (Galway)

Israel
R. Fischer (Haifa)

Japan
M. Iwasa (Osaka)
H. Hamada (Kyoto)
M. Mitomo (Ibaraki)
O. Nakamura (Osaka)
H. Sekine (Sendai)
K. Uematsu (Nagaoka)

Korea
S. Baik (Pohang)
C.P. Hong (Seoul)
S.H. Hong (Taejon)

Portugal
R.M. Almeida (Lisboa)

Russia
S.M. Barinov (Moscow)

Singapore
C.Y. Yue (Nanyang)

Slovakia
P. Sajgalik (Bratislava)

Spain
L. Esquivias (Cadiz)
A. Ureña-Fernandez (Madrid)

The Netherlands
R. Fordham (Petten)

UK
A. Hendry (Glasgow)
F.L. Riley (Leeds)
R. Taylor (Manchester)

USA
R. Abbaschian (Gainesville)
D.H. Allen (College Station)
I. Dutta (Monterey)
W.W. Gerberich (Minneapolis)
E.J. Lavernia (Irvine)
S. Mall (Wright-Patterson AFB)
R.O. Ritchie (Berkeley)
J.A. Sekhar (Cincinnati)
J.F. Shackelford (Davis)
J.E. Shelby (Alfred)
A. Shukla (Kingston)
W.O. Soboyejo (Columbus)
R. Solecki (Storrs)
G.J. Weng (New Brunswick)
J.-M. Yang (Los Angeles)

Yugoslavia
D. Uskokovic (Beograd)

Publication Manager:
Marion Joss, Trans Tech Publications Ltd, Brandrain 6, CH-8707 Uetikon-Zuerich, Switzerland
Fax +41 (1) 922 10 33, e-mail: m.joss@ttp.net

Internet:
The table of contents of each volume is freely available on the Internet through Trans Tech Publications' Preview Service (preview@ttp.net) as well as on the World Wide Web at http://www.ttp.net.

Subscription Information:
Key Engineering Materials is published in 18 volumes per year. In 1999, volumes 153-170 are scheduled to be published. The subscription rate is Us $ 78.00 per volume or US $ 1404.00 per year.

Trans Tech Publications Ltd
Brandrain 6 • CH-8707 Uetikon-Zuerich • Switzerland
Fax +41 (1) 922 10 33 • e-mail: ttp@ttp.net
http://www.ttp.net

REPORT DOCUMENTATION PAGE

Form Approved
OMB No. 0704-0188

The public reporting burden for this collection of information is estimated to average 1 hour per response, including the time for reviewing instructions, searching existing data sources, gathering and maintaining the data needed, and completing and reviewing the collection of information. Send comments regarding this burden estimate or any other aspect of this collection of information, including suggestions for reducing the burden, to Department of Defense, Washington Headquarters Services, Directorate for Information Operations and Reports (0704-0188), 1215 Jefferson Davis Highway, Suite 1204, Arlington, VA 22202-4302. Respondents should be aware that notwithstanding any other provision of law, no person shall be subject to any penalty for failing to comply with a collection of information if it does not display a currently valid OMB control number.

PLEASE DO NOT RETURN YOUR FORM TO THE ABOVE ADDRESS.

1. REPORT DATE *(DD-MM-YYYY)*	2. REPORT TYPE	3. DATES COVERED *(From - To)*
15/11/99	Proceedings	1-5 Nov 99, Tsukuba, Japan

4. TITLE AND SUBTITLE
"Creep and Fracture of Engineering Materials and Structures", Proceedings of the 8th International Conference on Creep and Fracture of Engineering Materials and Structures, held in Tsukuba, Japan, November 1-5, 1999

5a. CONTRACT NUMBER
F6256299M9224

5b. GRANT NUMBER

5c. PROGRAM ELEMENT NUMBER

6. AUTHOR(S)
T. Sakuma and K. Yagi

5d. PROJECT NUMBER

5e. TASK NUMBER

5f. WORK UNIT NUMBER

7. PERFORMING ORGANIZATION NAME(S) AND ADDRESS(ES)
The University of Tokyo
7-3-1- Hongo, Nunkyo-ku
Tokyo, Japan

National Research Institute for Metals

8. PERFORMING ORGANIZATION REPORT NUMBER
N/A

9. SPONSORING/MONITORING AGENCY NAME(S) AND ADDRESS(ES)
AOARD
UNIT 45002
APO AP 96337-5002

10. SPONSOR/MONITOR'S ACRONYM(S)

11. SPONSOR/MONITOR'S REPORT NUMBER(S)
CSP-99-12

12. DISTRIBUTION/AVAILABILITY STATEMENT
Approved for public release; distribution is unlimited.

13. SUPPLEMENTARY NOTES
N/A

14. ABSTRACT
Sampling of proceedings includes the following:
"Recent Developments in the Analysis of Creep Rupture Data"
"Creep Crack Growth in Nearly Fully-Lamellar Gamma TiA1 Alloys"
"Research of Welding Effect on Creep Damage of High Temperature Furnace Tubes"
"The Reversibility of Creep Strain at Low Stresses and Low Temperatures"
"Deformation Behavior of 7475 Aluminum Alloy at High Temperatures"
"Creep of Reinforced and Unreinforced AZ91 Magnesium Alloy"

15. SUBJECT TERMS
Creep Rupture, Creep Growth, Creep Gamage, Creep Strain

16. SECURITY CLASSIFICATION OF:			17. LIMITATION OF ABSTRACT	18. NUMBER OF PAGES	19a. NAME OF RESPONSIBLE PERSON
a. REPORT	b. ABSTRACT	c. THIS PAGE			Dr. Koto White
UNCL	UNCL	UNCL	UL	871	19b. TELEPHONE NUMBER *(Include area code)* 81-3-5410-4409 (Tokyo, Japan)

Creep and Fracture of Engineering Materials and Structures

Preceding Pages Blank

Creep and Fracture of Engineering Materials and Structures

Proceedings of the 8th International Conference on Creep and Fracture of Engineering Materials and Structures, held in Tsukuba, Japan, November 1-5, 1999

Editors:

T. Sakuma and K. Yagi

TRANS TECH PUBLICATIONS LTD
Switzerland • Germany • UK • USA

DTIC QUALITY INSPECTED 4

Copyright © 2000 Trans Tech Publications Ltd, Switzerland
ISBN 0-87849-842-7

Volumes 171-174 of
Key Engineering Materials
ISSN 1013-9826

***Distributed** in the Americas by*

Trans Tech Publications Inc
PO Box 699, May Street
Enfield, New Hampshire 03748
USA
Phone: (603) 632-7377
Fax: (603) 632-5611
e-mail: ttp@ttp.net
Web: http://www.ttp.net

and worldwide by

Trans Tech Publications Ltd
Brandrain 6
CH-8707 Uetikon-Zuerich
Switzerland
Fax: +41 (1) 922 10 33
e-mail: ttp@ttp.net
Web: http://www.ttp.net

Printed in the United Kingdom
by Hobbs the Printers Ltd,
Totton, Hampshire SO40 3WX

Organizing Committee

Sakuma, T. (The University of Tokyo), Conference Chairman
Yokobori, T. (Teikyou University), Senior Adviser
Oikawa, H. (College of Industrial Technology), Senior Adviser
Abe, F. (National Research Institute for Metals)
Endo, T. (Yokohama National University)
Higashi, K. (Osaka Prefecture University)
Ikuhara, Y. (The University of Tokyo)
Kikuchi, M. (Nippon Steel Co., Ltd.)
Maruyama, K. (Tohoku University)
Masuyama, F. (Mitsubishi Heavy Industries, Ltd.)
Matsuo, T. (Tokyo Institute of Technology)
Nakashima, H. (Kyushu University)
Nonaka, I. (Ishikawajima-Harima Heavy Industries Co., Ltd.)
Sawaragi, Y. (Sumitomo Metal Industries, Ltd.)
Yagi, K. (National Research Institute for Metals)
Yokobori, A. T. Jr. (Tohoku University)

Iketani Science and Technology Foundation

The objective of this foundation is to promote science and technology and to contribute to the progress and the economy of society. The foundation supports the research of materials science and its related technologies. The foundation also sponsors international Conference attendance in order to facilitate closer research collaboration.

Under the joint auspices of
Japan Institute of Metals
The Japan Society of Mechanical Engineers
The Iron and Steel Institute of Japan
The Society of Materials Science Japan
The Japan Society for Strength and Fracture
The Ceramics Society of Japan
Japan Welding Society

PREFACE

The series of International Conferences on "Creep and Fracture of Engineering Materials and Structures" was initiated at University College Swansea, Wales, thanks to the special efforts of Professors B. Wilshire and R. W. Evans. The Conferences have earned a world-wide reputation in the field of high-temperature creep of materials. I think that the success of the Conferences owes much to the organizational skills of these two professors. The Conferences were intended to be of moderate size so as to preserve the single-session style. The latter works well in encouraging stimulating discussions and in cultivating a friendly atmosphere at all of the Conferences. In addition, all of the participants must have enjoyed the congenial and refined atmosphere of the Conference site, Clyne Castle, and the highly elegant arrangements of the social events, including the formal dinner. It was a good chance for us to taste the sophisticated Welsh life-style.

The seventh Conference was held in August 1997 at the University of California, Irvine, under the chairmanship of Professor J. Earthman. Personally, I was most impressed by the up-to-date presentations and fruitful discussions held in the beautiful campus of Irvine, although the climate and atmosphere in California were very different from those in Wales.

On the request of Professor Wilshire, we organized the eighth Conference at the National Research Institute for Metals (NRIM) in Tsukuba city, Japan. Tsukuba city is not an historical site, but a technopolis established about 30 years ago, and its atmosphere is totally different from that of Swansea or Irvine, but we paid a lot of attention to maintain the original style and policy of the Conferences. The Conference was organized with the assistance of the local organizing committee, and the staff of the NRIM. I would like to acknowledge the financial support of the Iketani Science and Technology Foundation, and also the support of the NRIM. Finally, I wish to express my sincere thanks to all of the authors and participants to whom the success of the conference must be credited.

T. Sakuma

The University of Tokyo, November 1999

Table of Contents

Committee v
Preface vi

I. CREEP DATA ANALYSIS AND CREEP FRACTURE

I-1. Creep Damage, Rupture and Life Assessment

Recent Developments in the Analysis of Creep Rupture Data
S.R. Holdsworth 1

Recent Developments in Stress Relaxation Methodologies within Europe
P.R. McCarthy, D.G. Robertson, J. Orr and A. Strang 9

Recent Results of Long-Term Creep Rupture Test
H. Irie, F. Abe and K. Yagi 17

Experimental and Numerical Investigations on Creep Damage Evolution
A. Klenk, A. Kussmaul, K. Maile and P. Lenk 25

Predicting the Creep Life and Failure Location of Weldments
J.M. Brear, A. Fairman, C.J. Middleton and L. Polding 35

Characterization of Creep Fracture for Weld Fusion Line Cracks
K.B. Yoon and J.S. Lee 43

The Influence of Material Mismatch of Weld on the Evaluation of Time-Dependent Fracture Mechanics Parameters
S.-T. Tu, K.-B. Yoon and J.-M. Gong 51

Rationalisation of the Multiaxial Stress Rupture Behaviour of Components
J.M. Church, J.M. Brear and D.R. Humphrey 61

Secondary Creep in a Damage Tolerant Niobium Aluminide Intermetallic
R.P. Hayes and W.O. Soboyejo 69

Comparison of the Creep and Fracture Behavior of Non-Hardened and Oxide Dispersion Hardened Platinum Base Alloys at Temperatures Between 1200 °C and 1700 °C
R. Völkl, D. Freund, B. Fischer and D. Gohlke 77

Creep and Creep Fatigue Crack Behavior of 1Cr- and 9Cr-Steels
K. Maile, A. Klenk, J. Granacher, G. Schellenberg and M. Tramer 85

Creep Rupture Behavior of Advanced 9-12%Cr Steel Weldment
F. Masuyama, M. Matsui and N. Komai 99

Creep Life Assessment of High Chromium Ferritic Steels by Recovery of Martensitic Lath Structure
K. Sawada, K. Maruyama, Y. Hasegawa and T. Muraki 109

Creep Rupture Properties of Helium Implanted Low Activation Martensitic Steel for Nuclear Fusion Application
N. Yamamoto, J. Nagakawa and K. Shiba 115

I-2. Creep Crack Growth and Fatigue

A Change in the Mechanism of Creep Crack Growth in a Dissimilar Metal Weld at 540 °C
B. Nath 121

Mechanical Behavior and Strengthening Mechanism of W containing 9-12% Cr Steels Under Creep Condition for a Cracked Specimen
A.T. Yokobori Jr., S. Takmori, T. Yokobori, Y. Hasegawa, K. Kubota and K. Hidaka 131

Creep Crack Growth in a High Strength Low Alloy Steel at 360 °C
R. Wu, F. Seitisleam and R. Sandström 139

Creep Crack Growth in Nearly Fully-Lamellar Gamma TiAl Alloys
K.V. Jata and Y.-W. Kim 147

Modelling of High Temperature Multi-Axial Creep Rupture Behaviour of γ-Titanium Aluminide
R. Dempers, K. Nikbin and G.A. Webster 153

Effect of Fiber Orientation on Fatigue and Fracture Properties of Fiber Eutectic Al-Al_3Ni Composite Alloy
S. Goto, S. Aso and Y. Komatsu 161

I-3. Plant Conduct Assessment

On-Plant Test of TÜV HCM12 and ASME T23 Alloys for Use as Water Wall Materials
A. Karlsson, F. Rasmussen and M. Montgomery 169

Evaluation of Long-Term Creep Rupture Strength of Tungsten-Strengthened Advanced 9-12%Cr Steels
F. Masuyama and N. Komai 179

Research of Welding Effect on Creep Damage of High Temperature Furnace Tubes
J.-M. Gong, S.-T. Tu and X. Ling 189

II. HIGH-TEMPERATURE DEFORMATION

II-1. Deformation Mechanisms

The Reversibility of Creep Strain at Low Stresses and Low Temperatures
G.W. Greenwood and Y. Gencer 197

The Significance of Diffusion Creep and Harper-Dorn Creep at Low Stresses
T.G. Langdon 205

Deformation Behavior of Fe-3%Si Steel at High Temperatures
R. Kaibyshev and I. Kazakulov 213

A Critical Reassessment of the Ravotnov-Kachanov Equations
A. Göcmen 219

Lattice-Diffusion Creep Mechanism Not Based on Stress Heterogeneity (1)
G. Itoh and A. Nojima 231

A New Era of Grain Boundary Design and Control for High Temperature Materials
T. Watanabe 237

Modelling the High Temperature Creep Behaviour of a New Single Crystal Nickel Base Superalloy
M. Maldini and V. Lupinc 245

Orientation Dependent Creep Behavior and Dislocation Structure of Nickel Solid Solution Single Crystals
D. Siebörger and U. Glatzel 253

Threshold Stress for High-Temperature Deformation of Dispersion-Strengthened Alloys with Incoherent Dispersoids
F. Yoshida and H. Nakashima 261

High-Temperature Deformation of Cu-SiO_2 Bicrystals with [011] Twist Boundaries
H. Miura, K. Saijo and T. Sakai 269

Kinetic Modelling of the Influence of Particles on Creep Strength
J. Eliasson, Å. Gustafson and R. Sandström 277

Dislocation Activity in Plastically-Accommodated Creep in an Inclusion Bearing Material
E. Sato and K. Kuribayashi 285

Lattice-Diffusion Creep Mechanism Not Based on Stress Heterogeneity (2)
G. Itoh and A. Nojima 291

Effect of Dislocation Substructure on Creep Behavior of Steels Strengthened by Fine Carbides
N. Nishimura, M. Ozaki and F. Masuyama 297

Study on Evaluation Procedure of Multiaxial Creep Strength of Low Alloy Steel
Y. Chuman, M. Yamauchi and T. Hiroe 305

Theoretical and Experimental on the Significant Creep Deformation of SUS 316 Induced by Irradiation at 60°C
J. Nagakawa, Y. Murase, N. Yamamoto and T. Fukuzawa 313

High Temperature Deformation with Interfacial and Plastic Accommodation in Spherical-Al_2O_3-Particle-Dispersed Al-Matrix-Composite
K. Kawabata, E. Sato and K. Kuribayashi 321

II-2. Superplasticity

The Size Effect of Particulate SiC on Activation Energy for High-Strain-Rate Superplastic Flow in Powder-Metallurgy Processed 2124 Al Composites
W.J. Kim and J.H. Yeon 329

Experimental Study of the Mechanical Properties at Elevated Temperatures in Commercial Mg-Al-Zn Alloys for Superplastic Forming
T. Mukai, H. Tsutsui, H. Watanabe, K. Ishikawa, Y. Okanda, M. Kohzu, S. Tanabe and K. Higashi 337

Superplasticity in GeO_2-Nd_2O_3 Doped Y-TZP
M. Nakano, K. Shimura, J. Mimurada, K. Sasaki, Y. Ikuhara and T. Sakuma 343

Low Temperature Superplasticity in Fe_3Al Alloys
A. Shan and D. Lin 349

Deformation Behavior of 7475 Aluminum Alloy at High Temperatures
R. Kaibyshev, O. Sitdikov, A. Goloborodko and T. Sakai 355

Superplasticity at Low Temperatures in a ZK61 Magnesium Alloy Produced by Powder Metallurgy
H. Watanabe, T. Mukai, K. Ishikawa, Y. Okanda, M. Mabuchi and K. Higashi 363

High Strain Rate Superplasticity of a ß-Si_3N_4 Whisker Reinforced Pure Aluminum Composite
I. Tochigi, T. Imai, L. Geng and J. Mao 369

The Effect of Alumina Doping on the Superplastic Characteristics of 3 Y-TZP
K. Sasaki, K. Shimura, J. Mimurada, Y. Ikuhara and T. Sakuma 377

Grain Boundary Analysis and Superplastic Characteristics in GeO_2-Doped TZP
J. Mimurada, K. Sasaki, Y. Ikuhara and T. Sakuma 383

III. MATERIALS FOR HIGH-TEMPERATURE SERVICE

III-1. Structural Steels

Characterization and Mechanical Properties of a δ/γ Duplex Stainless Steel
J.A. Jiménez, M. Carsi, G. Frommeyer and O.A. Ruano 389

Contribution of Tungsten to Microstructure Stabilization and Improvement of Creep Resistance in Simple 9Cr-W Steels
F. Abe 395

Effect of Heat Treatments on Room Temperature Creep Strain of a High Strength Steel
C. Liu, Z. Zhao and D.O. Northwood 403

Strengthening of Heat Resistant Martensitic Steel by Cu Addition
T. Tsuchiyama, Y. Futamura and S. Takaki 411

Creep Resistance and Structural Stability of Low-Alloy CrMo and CrMoV Steels
J. Purmenský, V. Foldyna and Z. Kubon 419

Optimum Tungsten Content in High Strength 9 to 12% Chromium Containing Creep Resistant Steels
Y. Hasegawa, T. Muraki, M. Ohgami and H. Mimura 427

Transient Creep Behaviour of Forged Thick Section 9Cr-1Mo Ferritic Steel
B.K. Choudhary, C. Phaniraj, K. Bhanu Sankara Rao and S.L. Mannan 437

Effect of Soluble Nitrogen on the Creep Strength of an Austenitic 25Cr-20Ni Steel
I. Park, F. Masuyama and T. Endo 445

Microstructural Aspects on the Creep Behaviour of Advanced Power Plant Steels
H. Cerjak, P. Hofer and B. Schaffernak 453

Effect of M-C (M=Mo, Mn, and Cr) Atomic Pairs on Creep Properties of Fe-M-C Ternary Alloys
T. Abe, H. Onodera, K. Kimura and H. Kushima 461

Acceleration of Fe2W Precipitation and Its Effect on Creep Deformation Behavior of 8.5Cr-2W-VNb Steels with Si
N. Fujitsuna, M. Igarashi and F. Abe 469

Strengthening Mechanisms in Heat-Resistant Martensitic 9Cr Steels
K. Iwanaga, T. Tsuchiyama and S. Takaki 477

Heterogeneous Changes in Microstructure and Degradation Behaviour of 9Cr-1Mo-V-Nb Steel During Long Term Creep
K. Kimura, H. Kushima and F. Abe 483

Creep Characteristics of Precipitation Hardened Carbon Free Martensitic Alloys
S. Muneki, M. Igarashi and F. Abe 491

Creep Strengthening Mechanism of Mo and W in 9% Cr Heat Resistant Steels
T. Muraki, Y. Hasegawa and M. Ohgami 499

Creep Properties of Advanced Heat-Resistant Martensitic Steels Strengthened by $L1_0$ Type Ordered Intermetallic Phase
M. Igarashi, S. Muneki and F. Abe 505

Microstructural Evolution in SUS304H Steel during Long-Term Creep Over 10^5 h
M. Murata , H. Tanaka, F. Abe and H. Irie 513

Mechanical Properties of 11Cr-0.4Mo-2W-CuVNb Steel Welded Joints at Elevated Temperatures
M. Tabuchi, T. Watanabe, K. Kubo, J. Kinugawa and F. Abe 521

III-2. Nickel-Base Superalloys

Design of New Creep-Resistant Nickel-Base Superalloys for Power-Plant Applications
F. Tancret, H.K.D.H. Bhadeshia and D.J.C. MacKay 529

Recovery of Creep Properties of Alloy 625 After Long Term Service
M.D. Mathew, K. Bhanu Sankara Rao, S.L. Mannan, K. Paknikar and R. Singh 537

Extension of an Anisotropic Model of Creep in Single Crystal Superalloys to Variable Loading and Multiaxial Loading
H. Basoalto, M. Ardakani, R.N. Ghosh, B.A. Shollock and M. McLean 545

Creep in Single Crystals of γ Single Phase Ni-20Cr Alloy and Evolution of Dynamic Recrystallization
T. Matsuo, S. Takahashi, Y. Ishiwari and Y. Terada 553

Influencing Factors of Stress Rupture at 750 °C Temperature for Cast Nickel Base Superalloy K403
Y. Zheng and Y. Han 561

Study on Creep Properties and Microstructural Relation in Directionally Solidified Nickel Base Superalloy
A. Nomoto, M. Yaguchi and T. Ogata 569

Creep and Evolution of Dynamic Recrystallization in γ Single Phase Single Crystals Located at Poles in Standard Stereo-Triangle
H. Miyazawa, R. Takaku, D. Kawaguchi, Y. Terada and T. Matsuo 577

Stress Dependence of Evolution of Dynamic Recrystallization in γ Single Phase Single Crystal
Y. Terada, Y. Ishiwari and T. Matsuo 585

III-3. Non-Ferrous Alloys

Creep of Reinforced and Unreinforced AZ91 Magnesium Alloy
V. Sklenička, M. Pahutová, K. Kuchařová, M. Svoboda and T.G. Langdon 593

Creep Strength of Binary Magnesium Alloys up to 0.6*T*m
H. Sato, M. Suzuki, K. Maruyama and H. Oikawa 601

Microstructural Evolution during Creep of the Mg-Al-Alloy AZ91hp
P. Zhang, B. Watzinger, Q.P. Kong and W. Blum 609

Effect of Liquid Phase on Creep and Fracture Behavior of Al-5%Mg
H. Iwasaki, T. Mori, M. Mabuchi and K. Higashi 617

High Temperature Strengths of Ir-Based Refractory Superalloys
Y. Yamabe-Mitarai, X. Yu, Y. Gu, Y. Ro, S. Nakazawa, T. Maruko and H. Harada 625

Creep Behavior of Aluminum Alloy Foils for Microelectronic Circuits
Q. Zhou and G. Itoh 633

Creep and Evolution of Dynamic Recrystallization in Single Crystals of Ti-48at%Al with Different Orientation between Stress Axis and γ Lamellar Plate
N. Shiratori, S. Hirata, T. Asai, M. Takeyama and T. Matsuo 639

Anomalous Creep Curve of Cu-30 Mass%Zn Alloy
A. Muto, S. Goto and M. Tagami 647

Deformation Mechanisms in Tin and Tin-Based Electronic Solder Alloys
M.D. Mathew, S. Movva and K.L. Murty 655

Effect of Microalloying on the Creep Strength and Microstructure of Eutectic Sn-Pb Solders
N. Wade, T. Akuzawa, J. Kunii and K. Miyahara 663

Microstructures and Fracture Behaviours of Ir-Nb Two-Phase Refractory Superalloys Containing Various Amounts of Nb, Ni, Mo, C and B
Y.F. Gu, Y. Yamabe-Mitarai, Y. Ro and H. Harada 669

Investigation on Microstructure and Fracture of Quaternary Ir-Based Alloys
X.H. Yu, Y. Yamabe-Mitarai, Y. Ro and H. Harada 677

III-4. Intermetallics

Role of Interfacial Dislocations on Creep of a Fully Lamellar TiAl
T.G. Nieh and L.M. Hsiung 685

Microstructural Evolution Associated with Creep Rate Minima in Pure- and Near-γ TiAl Intermetallics
A. Dlouhý, K. Kuchařová and T. Horkel 693

A New Microstructural View of Creep in Near-γ TiAl-Alloys
B. Skrotzki 701

Creep Deformation of Polysynthetically Twinned (PST) Ti-48mol%Al
G. Wegmann, T. Suda and K. Maruyama 709

Effect of Lamellar Spacing on Creep Strength of Ti-42mol%Al Alloy with Fully Lamellar Structure
R. Yamamoto, K. Mizoguchi and K. Maruyama 717

III-5. Ceramics

Alternative Approaches to Creep Data Analyses for Ceramic-Fibre-Reinforced Ceramic-Matrix Composites
B. Wilshire and F. Carreño 725

Elasticity, Stress Relaxation and Creep in SiC Particle Reinforced Oxynitride Glass
T. Rouxel, J.-C. Sanglebœuf, P. Verdier and Y. Laurent 733

Improvement of High Temperature Strength and Creep of α-Sialon by Grain Boundary Crystallization
T. Nishimura, M. Mitomo, A. Ishida and H. Gu 741

Creep Processes in the Advanced Silicon Nitride Ceramics
F. Lofaj, A. Okada, Y. Ikeda and H. Kawamoto 747

Creep Deformation and Fracture of SiC/SiC Composites
S. Zhu, M. Mizuno, Y. Kagawa and Y. Ochi 755

Cavitation Failure in a Superplastic Alumina with Zirconia-Particle Dispersion
K. Hiraga, Y. Sakka, T.S. Suzuki and K. Nakano 763

Tensile Deformation of Both ZrO_2/TiC Composite and Al_2O_3/TiC Composite at High Temperature
H. Miyazaki, K. Kubobuchi, K. Yamaguchi, T. Iseki and T. Yano 771

Is there Diffusion Creep in Alumina?
R.S. Kottada and A.H. Chokshi 779

High Temperature Mechanical Behavior of YSZ Nanocrystals
F. Gutiérrez-Mora, M. Jiménez-Melendo, A. Domínguez-Rodríguez and R. Chaim 787

Yttrium in Polycrystalline α-Alumina
M.A. Gülgün and M. Rühle 793

Slip Systems in Erbia Single Crystals
A.A. Sharif, A. Misra, J.J. Petrovic and T.E. Mitchell 801

A Critical Factor to Determine the High-Temperature Creep Resistance in Cation-Doped Polycrystalline Al_2O_3
H. Yoshida, Y. Ikuhara and T. Sakuma 809

Compressive Creep and Stress Relaxation Kinetics in a High Purity Silicon Nitride Ceramics in the 1400-1650 °C Range
S. Testu, J.L. Besson, T. Rouxel and G.B Granger 817

Dislocation Structure and Activated Slip Systems in ß-Silicon Nitride during High Temperature Deformation
K. Kawahara, S. Tsurekawa and H. Nakashima 825

Transmission Electron Microscope Observation of Creep-Deformed Al_2O_3, SiC and Si_3N_4 Ceramics
T. Yano and A.T. Yokobori Jr. 833

Lifetime Prediction and Confirmation of Long Term Creep Resistance in Advanced Silicon Nitride Ceramics
Y. Takigawa, J.-W. Cao, Y. Ikeda and H. Kawamoto 841

Creep Behavior of a Fine-Grained Tetragonal Zirconia
K. Morita, K. Hiraga and Y. Sakka 847

High-Temperature Deformation in Unidirectionally Solidified Eutectic Al_2O_3-YAG Single Crystal
H. Yoshida, K. Shimura, S. Suginohara, Y. Ikuhara, T. Sakuma, N. Nakagawa and Y. Waku 855

Author Index 863

Keyword Index 867

Key Engineering Materials Vols. 171-174 (2000) pp. 1-8
© 2000 Trans Tech Publications, Switzerland

Recent Developments in the Analysis of Creep Rupture Data

S.R. Holdsworth

ALSTOM Energy Steam Turbines, Rugby CV21 2NH, UK

Keywords: Creep-Rupture, Data Assessment, Post Assessment Tests (PATs)

Abstract

Recent developments in the analysis of creep rupture data for design and product standards are reviewed. These include the successful implementation of the ECCC[1] post assessment tests for full-size datasets, their integration into a new advanced creep rupture data assessment procedure and their application to the analysis of sub-size datasets.

Introduction

At elevated temperatures, metallic structures deform with time under the influence of applied stress. In the limit, the accumulation of such deformation leads to fracture by a creep rupture mechanism. The consideration of this damage process is a key part of the design assessment of critical components for high temperature applications, with the necessary engineering calculations requiring a knowledge of the creep rupture strength of the material from which the structure is manufactured.

Recent developments in the analysis of creep rupture data for the prediction of long time strength values have been directed towards the statistical assessment of both large (full-size) population datasets as well as those containing relatively small numbers of experimental observations (referred to as 'sub-size' datasets in the following paper).

In ideal circumstances, creep rupture strength values for design purposes are determined from an assessment of the results of sufficient tests on a variety of casts of the material in question to ensure that its true property variance has been fully characterised for an appropriate range of stresses and temperatures (*e.g.* [1]). Such full-size datasets for traditional materials may comprise up to ~1,000 observations for ~100 casts covering several temperatures with test durations up to >100,000h (*e.g.* Fig. 1).

The large international creep rupture datasets originated from an era when national groups from the main industrial nations had the resources to independently generate the long term results required to adequately characterise the behaviour of their strategic alloys to design life durations. Today, new alloys are typically developed as a consequence of focused international collaboration and there is greater pressure than ever before for their introduction into service at the earliest opportunity. Current developments are therefore directed towards the assessment of sub-size datasets and the qualification of strength values which are the result of extended extrapolation.

Post Assessment Tests

In the early 1990s, the drive to greater integration in Europe led to the specification of unified (rather then independent national) design and product standards. ECCC[1] was founded in 1992 to

[1] European Creep Collaborative Committee

provide the means for European industry to have a greater influence over the creep strength values incorporated into these standards [2]. The brief of ECCC's technical working group, WG1, was to devise common rules for the material specialist WG3.x working groups to follow. The outcome was a series of five volumes covering common terminology and the generation, collation/exchange and assessment of creep data [3].

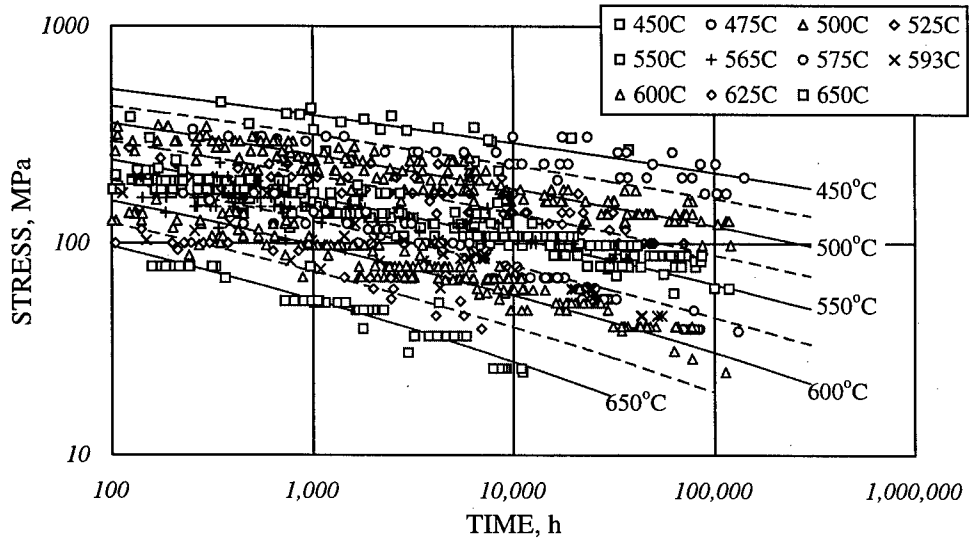

Fig. 1 Large multi-temperature, multi-cast, multi-source creep rupture dataset for 2¼CrMo

A number of well established creep rupture data assessment (CRDA) procedures were employed by the various national specialists involved in ECCC. These provided the mechanism for representing a variety of material rupture characteristics, either by an appropriate model description (*e.g.* [4]) or by means of a graphical method [5]. Such was the reliance by specialist analysts on the experience gained with individual techniques that, in the short term, it was not possible to agree a single European methodology. ECCC-WG1 therefore devised a series of post assessment tests (PATs) to independently test *i)* the physical realism, *ii)* the within-data-range goodness-of-fit, and *iii)* the extrapolation repeatability/stability of a model determined by any procedure (*e.g.* Fig. 2 to Fig. 4).

The effectiveness of the PATs was demonstrated in an inter-analyst assessment comparison exercise [6]. This involved the assessment of large, multi-cast, multi-temperature, multi-source creep rupture datasets for four commonly used engineering alloys, *i.e.* 2¼CrMo (Fig. 1), 12CrMoVNb, 18Cr11Ni and 31Ni20CrAlTi. The datasets were typical of those used for the determination of creep rupture strength values for national and international design and product standards. A total of 48 assessments were performed by 10 European CRDA specialists using a variety of procedures (*e.g.* [4,5,10]), thereby enabling the extent of inter-analyst variability for the same and different assessment methodologies to be evaluated [3e,6].

For a given alloy, the variability in predicted strength values achieved without invoking the PATs was typically >20% at the edge of the data population (*i.e.* at $t_r = t_{r,max}$) increasing to >50% at three times the maximum test duration (*i.e.* $t_r = 3.t_{r,max}$) [2]. Using only those assessment results meeting the requirements of the PATs, the variability in predicted strength values was reduced to <10% at the limit of the data and <20% at $3.t_{r,max}$ [3e,6].

Implementation of the PATs requires significant additional effort, in particular for graphical methods of creep rupture data assessment. The justification for their use is that the uncertainty

[2] A list of Annotations is given at the end of the paper

associated with the consequent predicted strength values is significantly reduced [3e,6]. The extra effort is more than justified when the results of the assessment are likely to be used for critical components and in national and international design and product standards.

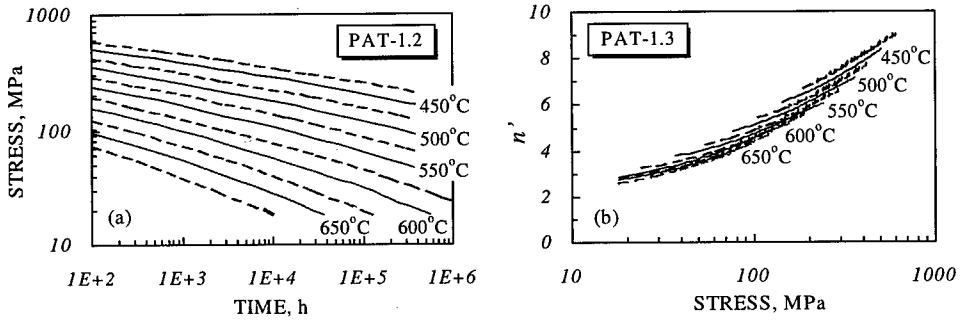

Fig. 2 Examples of 'physical realism' post assessment test results for 2¼CrMo dataset

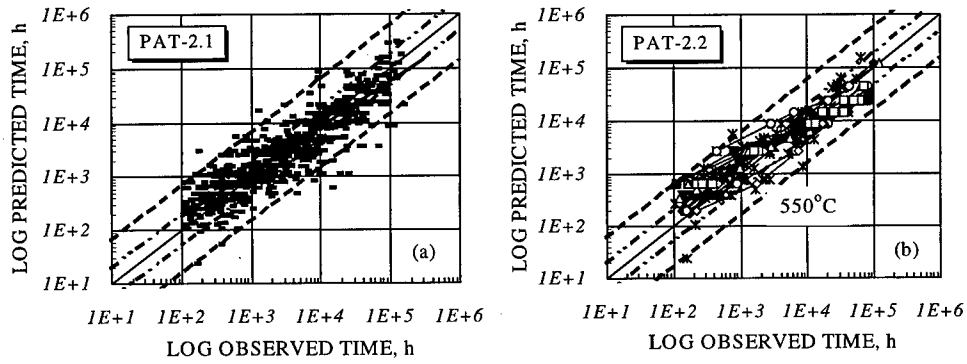

Fig. 3 Examples of 'within-data-range model-fitting' PAT results for 2¼CrMo dataset

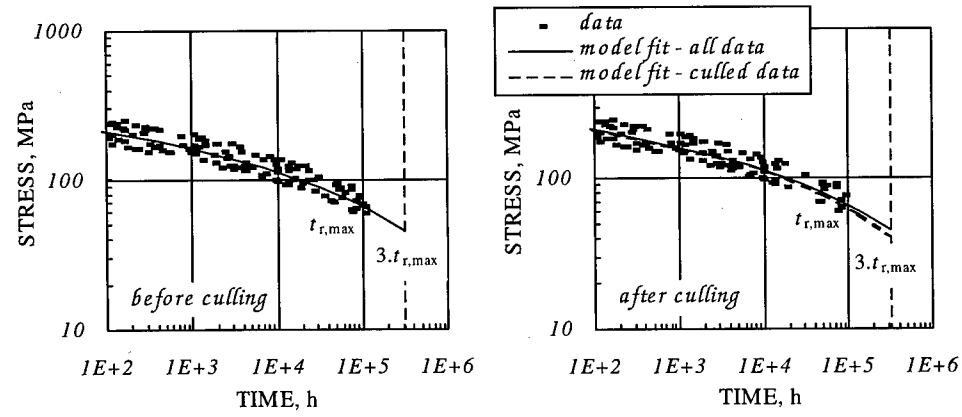

Fig. 4 Comparison of $R_{t/T/3tr,max}$ strength values before and after culling 50% of the data between $0.1.t_{r,max}$ and $t_{r,max}$ in the 'extrapolation repeatability' post assessment test

New Assessment Procedure

In this paper, a clear distinction is drawn between the arbitrary application of a single 'model', *e.g.* Larson-Miller [8], and a formal 'procedure' involving pre-assessment and selection of the most appropriate model to suit the characteristics of the material under consideration (*e.g.* Fig. 5).

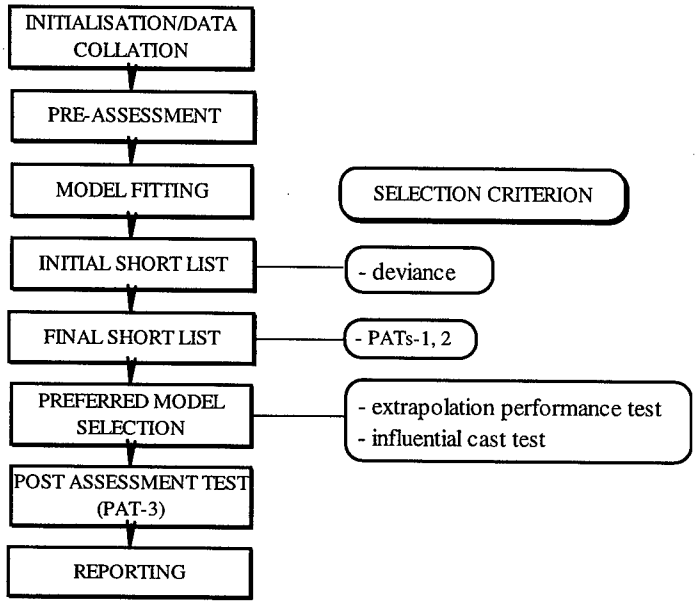

Fig. 5 Flow diagram showing steps in PD6605 assessment procedure

Table 1 Creep rupture model equations

MODEL	*TREND EQUATION*	*REF*
TIME-TEMPERATURE-PARAMETRIC EQUATIONS		
MRM*n*	$t_r^* = \exp[\{\sum_{k=0}^{n}\beta_k\ (\log[\sigma_o])^k\}.(T - T_o)^r/\sigma_o^{-q} + \beta_5]$	[7]
MR*n*‡	$t_r^* = \exp[\{\sum_{k=0}^{n}\beta_k\ (\log[\sigma_o])^k\}/(T - T_o) + \beta_5]$	[7]
LM*n*‡	$t_r^* = \exp[\{\sum_{k=0}^{n}\beta_k\ (\log[\sigma_o])^k\}/T + \beta_5]$	[8]
MH*n*‡	$t_r^* = \exp[\{\sum_{k=0}^{n}\beta_k\ (\log[\sigma_o])^k\}.(T - T_o) + \beta_5]$	[9]
MH0*n*‡	$t_r^* = \exp[\{\sum_{k=0}^{n}\beta_k\ (\log[\sigma_o])^k\}.T + \beta_5]$	[9]
OSD*n*	$t_r^* = \exp[\sum_{k=0}^{n}\beta_k\ (\log[\sigma_o])^k + \beta_5/T]$	[13]
ALGEBRAIC EQUATIONS		
SM1	$t_r^* = \exp[\beta_0 + \beta_1.\log[T] + \beta_2.\log[\sigma_o] + \beta_3/T + \beta_4.\sigma_o/T]$	[14]
SM2	$t_r^* = \exp[\beta_0 + \beta_1.\log[T] + \beta_2.\log[\sigma_o]/T + \beta_3/T + \beta_4.\sigma_o/T]$	[14]
MC	$t_r^* = \exp[\beta_0 + \beta_1.\log[\sigma_o] + \beta_2.\sigma_o + \beta_3.\sigma_o^2 + \beta_4.T + \beta_5/T]$	[15]

‡ *models which may be derived from the MRM equation [7]*

Until recently, the two most widely used CRDA procedures in Europe were the ISO procedure

[4] and the graphical averaging and cross-plotting method [5]. The ISO procedure employs the MRM time-temperature-parameter [7] to model selected $(\log[\sigma_o],\log(t_r])_T$ data co-ordinates from best fit isothermal $\log[\sigma_o](\log[t_r])$ lines derived for all-data at the main test temperatures of the dataset. The MRM model equation set provides a degree of flexibility in its ability to cover a range of material characteristics through adjustment of the constants r, q, and T_o (see Table 1). Indeed, a number of the better-known time-temperature-parameters derive from the MRM expression (*e.g.* Larson-Miller [8], Manson-Haferd [9], Table 1). The so-called German graphical method [5] involves a number of averaging/smoothing iterations between graphically constructed isothermal $\log[\sigma_o](\log(t_r)$ plots and isochronous $\log[\sigma_o](T)$ plots [5].

There have been actions in Germany, and most recently in the UK, to automate and advance the CRDA methodology, in particular using the power of desk top computing. These have resulted in the DESA [10] and PD6605 [11,12] procedures.

The basis of PD6605 is a set of creep rupture models comprising six TTP expressions [7-9,13] and, in addition, three algebraic equations which do not rely on high order polynomials and are thereby potentially more stable in extrapolation [14,15] (Table 1). Moreover, the user may define other models out of preference or when none of the selection provided adequately represents the $t_r(T,\sigma_o)$ data.

During the development of PD6605, a number of two-parameter probability distributions were investigated for their ability to represent the random component of creep rupture data for a range of ferritic and austenitic high temperature steels. The software accompanying the published procedure employs either the Weibull or log-logistic distributions which consistently provided the best representation of the error distribution for the range of alloys investigated.

Maximum likelihood statistics are used to simultaneously estimate the parameters for the systematic and random components of the model using all the $\log[t_r](T,\log[\sigma_o])$ data. The likelihood function for the model has the important characteristic that it comprises probability densities covering *i)* the rupture times for failed specimens and *ii)* the survival times for unfailed specimens. The routine consideration of unfailed tests is a main feature of the PD6605 analysis [11] (*e.g.* Fig. 6). Confidence intervals for the estimated time to rupture are obtained directly from the survival function.

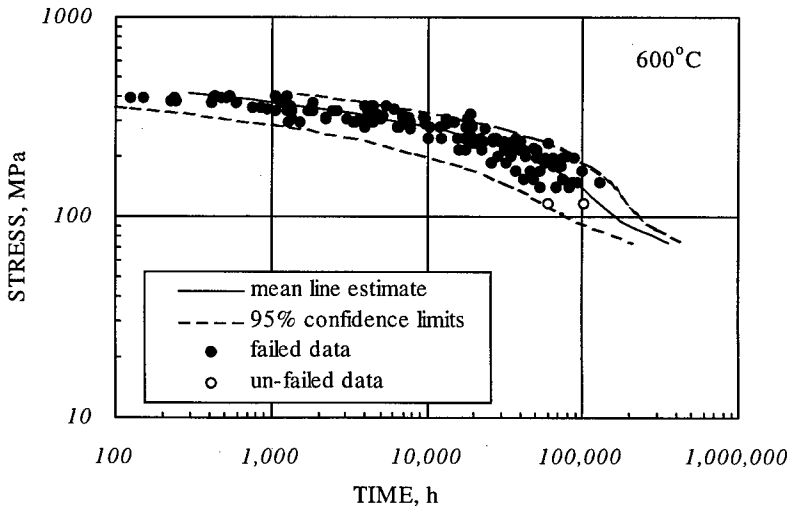

Fig. 6 Model fitting to 12Cr blading steel using PD6605 assessment procedure

The PD6605 analysis also accounts for the variance heterogeneity inherent in many creep rupture

datasets [11]. The trend is apparent in Fig. 3b.

Metallurgical credibility is maintained by a rigorous formal pre-assessment, based largely on the guidance formulated by ECCC [3e], and integration of the post assessment tests (Fig. 2 to Fig. 4) into the model selection procedure (Fig. 5). PD6605 also formally introduces pre-assessment.

Pre-assessment is an important step in the analysis of creep rupture data, involving *i)* characterisation of the data in terms of its pedigree, distribution and scatter, and *ii)* data reorganisation (if deemed necessary by the findings of *i)*). The main objective is to provide an error free, fully characterised dataset for evaluation in the main assessment. Pre-assessment is not a new concept [3e] but its formal inclusion and definition in a standard procedure is unique.

A significant effort has been directed to the assessment of large (full-size) datasets, and major advances have been made. The outstanding challenge is the prediction of design life strength values from sub-size datasets, in particular those for new materials required for market exploitation.

Assessment of Sub-Size Datasets

The focus of this paper is on the assessment of creep rupture data to provide strength values for design and product standards. In this context, use of the term 'sub-size' refers to samples typically of ~20-150 $t_r(T,\sigma_o)$ data.

Uncertainties in strength value predictions for times of up to design life magnitude arise from several sources, and the ways to minimise these for full-size datasets are now well defined (Table 2). The situation for sub-size datasets is not so clear, and significant effort is currently being directed to the qualification of predicted strength values resulting from such sources. In particular, attention is being focused on datasets for which the scope of data is limited, in terms of *i)* the number of casts needed to adequately characterise the specified material, and *ii)* the temperature/ stress conditions on which the required long time strength predictions have to be based.

Table 2 Sources of uncertainty in CRDA predicted strength values

UNCERTAINTY SOURCE	*FULL-SIZE DATASETS*	*SUB-SIZE DATASETS*
QUALITY OF DATA - Material pedigree - Testing practice	Minimised by data satisfying requirements of [3c].	As for full-size datasets.
SCOPE OF DATA - Material characteristics	Minimised by dataset satisfying cast number requirements of [3e,4].	*Validated qualification factor needed for when cast number is less than requirements of [3e,4].*
SCOPE OF DATA - Temperature/stress conditions	Minimised when dataset satisfies extended time/stress extrapolation requirements defined in [1,3e,4,12].	*Validated qualification factor(s) needed for strengths resulting from extended extrapolations (statistical/ empirical)*
MODEL ACCEPTABILITY - Physical realism - Within-data-range fit - Extrapolation credibility	Minimised by dataset satisfying ECCC PAT requirements [3e].	As for full-size datasets for physical realism and within-data-range fit, when sample adequately populated with results from sufficient number of representative casts. Further development required for extrapolation credibility

Whether determined by statistical or empirical analysis, small cast number qualification factors make use of the experience that the scatter about the mean of well specified materials is typically ±20-25% of $R_{r/T/t}$.

An attractive basis for the qualification of mean strength predictions arising from extended

extrapolation is an appropriate statistically derived lower confidence interval. This is a feasible solution for materials whose $t_r(T,\sigma_o)$ data is distributed normally (or log-normally) about the mean $t_r^*(T,\sigma_o)$ line. However, for many materials, the distribution is not normal (see previous section) and the derivation of confidence on mean line estimates is a complex analytical task. More importantly for such materials, lower confidence intervals derived assuming a normal distribution can become increasingly over-conservative as the degree of extrapolation is increased beyond $3.t_{r,max}$. The factors determined by such analyses can penalise the potential of new materials and their early introduction into service.

As a pragmatic alternative solution, empirical factors are being established on the basis of assessments of sub-size datasets which have been reduced (by random culling) from existing full-size datasets (*e.g.* Fig. 7). By this means, it is possible to compare extended-extrapolation strength predictions, assessed from sub-size datasets, with 'actual' strength values determined from long term test results. The main difficulty is with metallurgically active steels, for which extended-extrapolation strength predictions may be significantly over-estimated [16] or under-estimated (*e.g.* Fig. 7), depending on sub-size dataset characteristics. Both of these sub-size dataset assessments passed the requirements of PATs-1,2 (*e.g.* Fig. 2, Fig. 3). Even for relatively stable materials (*e.g.* Fig. 1), the PATs do not appear to provide a reliable indication of mean strength when the sub-size $t_r(T,\sigma_o)$ sample is not adequately populated with results from a sufficient number of representative casts (*e.g.* to give a scatter of ~±20-25% of $R_{r/T/t}$. The effort to overcome these difficulties, and thereby enable the earliest exploitation of new materials at minimum risk, is continuing.

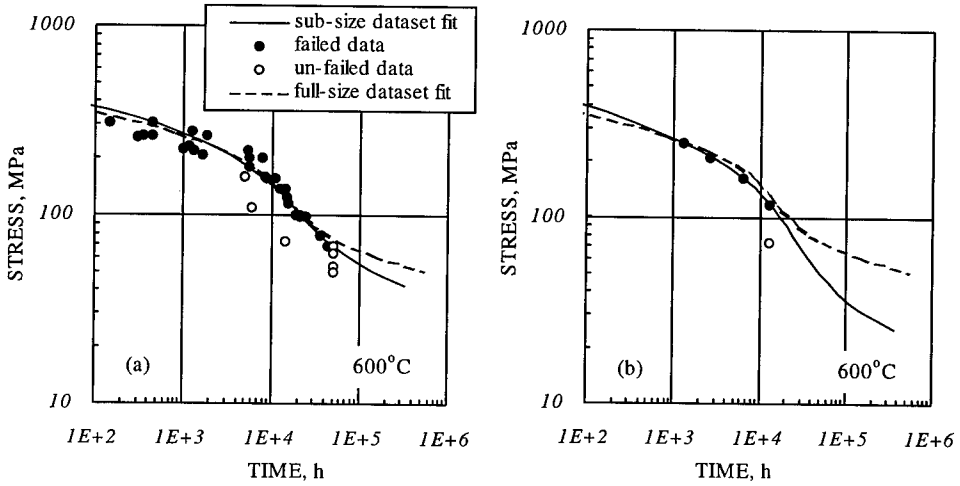

Fig. 7 Comparison of mean line fits to sub-size datasets reduced from full-size dataset for 12Cr blading steel (315 data, 6 temps, 45 casts, 129kh $t_{r,max}$) – (a) 83/6/9/49kh, (b) 18/4/2/22kh

Concluding Remarks

Recent developments in the assessment of creep rupture data have been reviewed. Perhaps the most influential of these are the post assessment tests conceived by the European Creep Collaborative Committee which have been shown to be responsible for a significant reduction in the variability in long time predicted strength values determined by different CRDA specialists using the same and different assessment procedures.

In addition to being influential in their own right, the ECCC PATs have been integrated into a newly developed state-of-the-art creep rupture data assessment procedure. In this role, the PATs provide the means of exerting a strong metallurgical influence on the results of an advanced

statistical modelling analysis which gives the opportunity for unfailed test data to be included in the assessment and for the derivation of confidence intervals.

Despite their effectiveness in qualifying the acceptability of creep rupture strength predictions determined using full-size datasets, further development is required for sub-size datasets.

References

[1] PD6525: 1992, 'Elevated temperature properties for steels for pressure purposes', British Standards Institution.

[2] D.V. Thornton, Proc. Conf. on Life Assessment of Industrial Components and Structures, ERA/VALUE, Churchill College, Cambridge, October (1993), p. 2.9.1.

[3] ECCC-WG1 Recommendations, Ed. S.R. Holdsworth, J. Orr, J. Granacher, C.K. Bullough & G. Merckling, Publ. ERA, Leatherhead, October (1996), (a) Vol.1, Overview, (b) Vol.2, Terminology, (c) Vol.3, Data acceptability criteria, Data generation, (d) Vol.4, Data exchange/ collation, (e) Vol.5, Data assessment.

[4] ISO6303, Annex: 'Method of extrapolation used in analyses of creep rupture data', (1981).

[5] W. Bendick, K. Haarmann & G. Wellnitz, Proc. ECSC Information Day on Manufacture and Properties of Steel 91 for Power Plant and Process Industries, Dusseldorf, November (1992).

[6] S.R. Holdsworth, Proc. 6th Intern. Conf. on Creep & Fatigue – Design and Life Assessment at High Temperatures, IMechE, London, April (1996), p. 101.

[7] A. Mendelson, E. Roberts & S.S. Manson, NASA-TN-D-2975, August (1965).

[8] F.R. Larson & J. Miller, Trans ASME, 74 (1952), p. 765.

[9] S.S. Manson & A.M. Haferd, NASA-TN-2890, (1953).

[10] J. Granacher et al, Proc. SMiRT Post Conf. Seminar on Intelligent Software Systems in Inspection and Life Management of Power and Process Plants, Paris, August (1997), p.179.

[11] S.R. Holdsworth & R.B. Davies, *ibid.*, p.197.

[12] PD6605: 1998, 'Guidance on methodology for the assessment of stress rupture data', British Standards Institution.

[13] R.L. Orr, O.D. Sherby & J.E. Dorn, Trans ASM, 46 (1954), p. 113.

[14] I.I. Trunin, N.G. Golobova & E.A. Loginov, Proc. 4th Int. Symp. on Heat-Resistant Metallic Materials, Mala Fatra, CSSR, (1971), p. 168.

[15] S.S. Manson & U. Muraldihan, Res. Proj. 638-1, EPRI CS-3171, July (1981).

[16] P. Greenfield, COST Status Review, Ed. J.B. Marriott & K. Pithan, EUR 11887 EN, (1988).

Annotations

n	order of stress polynomial in TTP model equations (to max of k, see Table 1)
n'	reciprocal slope of $\log[\sigma_o]$ vs $\log[t_r^*]$, ie. $-\partial(\log[t_r^*])/\partial(\log[\sigma_o])$ (see Fig. 2b)
q	stress exponent in MRM model equation (see Table 1)
$R_{r/T/t}$	rupture strength for a given temperature and time
r	temperature exponent in MRMn model equation (see Table 1)
T	temperature
t_r, $t_{r,max}$	observed time to rupture, maximum observed time to rupture
t_r^*	predicted time to rupture
β_0, β_1, β_3, β_4, β_5	parameters in model equations (see Table 1)
σ_o	initial stress

Key Engineering Materials Vols. 171-174 (2000) pp. 9-16
© 2000 Trans Tech Publications, Switzerland

Recent Developments in Stress Relaxation Methodologies within Europe

P.R. McCarthy[1], D.G. Robertson[1], J. Orr[2] and A. Strang[3]

[1] ERA Technology Ltd, Cleeve Road, Leatherhead, Surrey, KT22 7SA, U.K.

[2] British Steel Swinden Technology Centre, Moorgate, Rotherham, S60 3AR, U.K.

[3] ALSTOM Energy plc, Newbold Road, Rugby, CV21 2NH, U.K.

Keywords: Testing Standards, Extensometry, Test Data, Modeling of Stress Relaxation

Abstract

This paper sets out some of the findings arising from a recent programme of work investigating stress relaxation testing. It reviews current standards and examines the equipment capabilities necessary for successful testing. Inter and intra laboratory variability of data is examined, as is the impact of influences such as loading methods. A means of re-starting previously tested testpieces is described and validated. The need for modulus determinations is explored and a model is used to assess extensometer performance requirements. Recommendations are made as to improvements to the stress relaxation test; these will form the basis of a new Euronorm to address stress relaxation testing.

1. Introduction

The work reported in this paper forms part of a large European programme addressing Stress Relaxation Standards and Testing. It was initiated as a consequence of work performed by the European Creep Collaborative Committee (ECCC) which highlighted an urgent need for the preparation of a new European standard for Stress Relaxation testing [1]. Application was made to the European Commission for support and work was initiated in 1995 under the aegis of the Standards, Measurements and Testing programme of the European Commission. The participants comprised companies from the UK (British Steel, ALSTOM Energy, ERA Technology), Germany (IfW, Darmstadt, MPA Stuttgart, ALSTOM Energie), Italy (Insituto Scientifico Breda) and Portugal (ISQ).

The material selected for this work was steel grade X19 (11%CrMoNbVN), widely used in Europe as a bolting material in steam turbines.

The programme of work addressed three categories of stress relaxation testing, namely uniaxial tests (either sliding weight or servo type machines) and model bolt tests. This paper focuses upon the results from the sliding weight machine category.

2. Purpose of the work

The aims of this programme of work were fivefold, namely :-

(i) to identify weaknesses within existing standards,
(ii) to generate a code of practice to address these weaknesses,
(iii)to generate test data for validation purposes,
(iv)to perform tests against the new code of practice, and
(v) to make recommendations to CEN regarding a new Euronorm to address stress relaxation.

The standards reviewed were ASTM E328-96 [2], JIS Z 2276 [3] and BS3500: Part 6: 1969 [4]. In addition compatibility with Euronorms in the associated fields of creep and tensile testing were also examined. In general terms the existing standards were found to have performed well. However, inconsistencies have appeared when, for example, extensometer performance requirements have moved from strain based requirement to a direct displacement assessment. [5,6]

At the conception of the programme it was evident that the testing needed to be performed on an industrially relevant material, as both industrial and research participants were investing considerable resources into these investigations. It was also important that sufficient long term data be generated to complement existing data sources and allow data extrapolation methods to be validated as part of the programme.

3. Equipment Considerations

The programme of work was designed around three major modules. These modules were related to long term data generation using sliding weight machines, shorter term tests using servo-controlled machines, and model bolt testing. This paper focuses upon the work of the sliding weight data generation working group.

The test machines used by the participating laboratories were of the double lever sliding weight type, designed by the National Physical Laboratory in the early 1950's and manufactured by the Denison company up to the early 1970's. The applied load is adjusted by moving a poise weight along a calibrated steelyard, allowing continuous load adjustment from 0.7kN to 50kN.

Extensometry was of the double sided type, with transducers measuring displacement on either side of the testpiece and subsequently averaging the outputs. Transducers were high precision capacitance or LVDT types. The extensometer was clamped onto ridges machined on the testpiece, thereby providing a very precise and consistent gaugelength for subsequent measurement. Due to the exacting performance requirements defined in BS3500: Part 6 the extensometry needed to meet Class B performance from the old extensometer standard BS 3846. This document, superseded by BS EN 10002:4 in 1995, was used since the Euronorm extensometry grading philosophy is incompatible with BS3500 : Part 6 – a matter to be resolved by the new stress relaxation standard.

Control of test temperature, and minimisation of temperature variations, both in time and along the testpiece itself, were recognised as being of critical importance. All laboratories used three thermocouples along the testpiece gaugelength to measure both test temperature and thermal gradients. Temperature controllers with discriminations of at least 1 ^{o}C were used, with supervisory laboratory logging systems of 0.1 ^{o}C discrimination. Thermocouples were calibrated in accordance with best industry practice and Type R (Pt – Pt 13%Rh) were used for greatest stability and long term performance.

4. Data and Analysis

4.1 Intra-laboratory Variability

In order to assess the intra-laboratory variability of results, each laboratory performed two 500h tests at 550°C for two different loading strains, namely 0.15% and 0.20%. The initial and final values of relaxed stress from these tests are presented in Table 1. In general, the repeatability of results was good within each laboratory, although the 0.15% strain tests of lab 1 exhibited a difference in relaxed stress values of 15 MPa. The latter was consistent with the large difference in initial stress values (~30 MPa), which was attributed to a significant difference in loading rate. There were only small differences in the initial stress values of the tests performed by lab 2 and lab 3, and the stresses relaxed during the tests such that the differences were not significant after 500h.

4.2 Inter-laboratory Variability

Table 1 shows that, in general, the repeatability of results between laboratories was good for the 0.15% strain tests, while there appeared to be more scatter in the data from the 0.20% strain tests. The inter-laboratory variability was further examined through a programme of tests of longer duration (up to 10,000 hours) at different temperatures (450, 500, 550, 600°C) and loading strains (0.10, 0.15, 0.20%). It was found that, in general, the repeatability of results between laboratories was good across the whole temperature range. Using the available data at 550°C, mean values for the relaxed stress at times of 500h, 1000h, and 3000h were calculated for each loading strain, and the standard deviation was estimated, as shown in Table 2. There was no consistent variation of the standard deviation with loading strain or test time, but the overall average of these deviations was ~±7.2%.

4.3 Extrapolation Assessment

Data from selected tests of less than 3000h duration were used to predict 10,000 hour relaxed stress values for comparison with the actual data from long-term 550°C/0.15% tests. The data were culled so that there were reasonably similar numbers of data points for each test, in order to control the bias to any particular test(s). Four methods were used for extrapolation: (i) simple polynomial curve-fitting of linear stress - log time data; (ii) time-temperature parametric correlation; (iii) a simple stress relaxation model; and (iv) the Feltham equation. In the case of (iii), the following relaxation model was applied:

$$\sigma^{1-n} - \sigma_0^{1-n} = -A E (n-1) t^m \qquad \text{Eq.1}$$

where σ = stress, σ_0 = initial stress, E = elastic modulus, t = time, and A, n and m (<1) are material constants. In the case of (iv), the following approximation was used:

$$(\sigma_0 - \sigma) = a \ln(1+t) \qquad \text{Eq.2}$$

where a is a constant. This equation implies that a plot of $(\sigma_0 - \sigma)$ versus $\ln(1+t)$ should be a straight line. However, it was found that the relationship was not linear at short times, and therefore the short-time data were disregarded.

The mean of the actual 10kh relaxed stress measurements from the long-term 550°C/0.15% tests was 89.6 MPa, with a standard deviation of ~±5.8%. Table 3 shows the predicted values and the deviation of the prediction from the mean of the actual measurements. It can be seen that all four approaches give reasonable predictions. Although some methods may give more accurate predictions than others, it would be inappropriate to identify one particular method as the 'optimum'

Laboratory	Loading Strain, %	Initial Stress, MPa		Relaxed Stress after 500 h	
		1st test	2nd test	1st test	2nd test
1	0.15	214	184	125	110
2	0.15	208	211	120	117
3	0.15	216	207	125	122
1	0.20	286	-	154	-
2	0.20	267	265	138	128
3	0.20	297	281	148	142

Table 1. 500 hour relaxed stress data from three laboratories

Strain, %	Time, h	Mean Relaxed Stress, MPa	Estimated Standard Deviation (%)
0.10	500	92	9.1
0.10	1000	86	11.5
0.10	3000	76	5.2
0.15	500	119	5.8
0.15	1000	110	5.8
0.15	3000	99	8.5
0.20	500	145	9.3
0.20	1000	141	2.5
0.20	3000	124	8.3

Table 2. Inter Laboratory Variability Data

methodology for extrapolation because the investigation has been limited to selected data for a single cast of material only.

5. Experimental Observations

5.1 Test initiation

Examination of the data generated by the three laboratories revealed consistent behaviour, the main variable being the stress achieved during loading. Thereafter the stress relaxation rate data formed a coherent data set. Variations of the initial stress on loading were found to be dependent upon the rate at which the load was applied. Due to the nature of the equipment used, i.e. manual, step-wise load adjustments, opportunities can arise for the testpiece to shed load during the loading process itself. To investigate this aspect trials were undertaken where two different loading approaches were used. The first involved loading to the required strain in eight approximately equal increments of load, the second by applying five increments to approximately half load, then loading to a final stress derived from the stress-strain data from a separate tensile test at test temperature. This experiment revealed an initial stress for the second approach some 10% higher than that obtained from the equal increments method; however after ~10 hours the two relaxation curves had converged and thereafter showed similar relaxation behaviour.

Curve fit method	Predicted Stress (MPa)	Deviation from mean, (%)
Stress-log time, 2nd order polynomial	82.2	8.3
Stress-log time, 3rd order polynomial	90.7	1.2
Stress-log time, 4th order polynomial	83.5	6.8
Parametric, 2nd order	81.2	8.4
Relaxation model	91.1	1.7
Feltham Equation	89.3	0.3

Table 3. Comparison of the extrapolation methods

5.3 Test Re-loading

One of the aims of the programme was to establish a validated method for the re-loading of stress relaxation tests. Previous work by the authors indicated that the following protocol was appropriate:-

a) Cool the relaxation test under load to ambient temperature, recording all pertinent information and generating an unloading modulus,

b) Dismantle the test from the test machine,

c) Re-assemble and perform an ambient temperature modulus determination,

d) Check the moduli data and, if consistent, proceed,

e) Apply 50% of the test load from a) above,

f) Heat to the test temperature,

g) When at test temperature apply the remainder of the load. Wait 5 minutes and then record the extensometer output. Use this value as the control value for all subsequent testing.

This process was undertaken on tests running at 550 °C and 0.10%, 0.15% and 0.20% strain. In all three instances the post re-loading behaviour matched that shown by uninterrupted tests performed under identical conditions.

6. Modeling

6.1 Stress Relaxation test control

In order to better understand the impact of variations in operational practice upon the subsequent quality of data a model describing the performance of stress relaxation testing was developed. It used a representation of stress relaxation behaviour based upon a log stress relaxation rate vs. log stress relationship of the following form :

$$\text{Log relxn rate} = -24.7723 + 58.04913 \log \sigma - 45.0346(\log \sigma)^2 + 10.79471(\log \sigma)^3 \qquad \text{Eq.3}$$

This relationship was derived using test data generated by the programme of testing at 550 °C, 0.15% strain.

The model was based upon an iterative process to generate a stress relaxation curve, using a pre-determined strain control level to initiate a stress change. The "virtual test" commenced with the input of an initial stress, modulus at temperature, the required strain and the percentage of the required strain to be used for control purposes. Taking the initial stress and the material relaxation rate relationship a time increment was derived, over which the virtual testpiece relaxed and the total strain increased to a level of (initial strain plus control increment). At this point the model calculated the stress change necessary to bring the testpiece strain back to the required strain, decremented the

test stress and derived a new relaxation rate for that stress. The model then looped back and calculated the next time increment.

Using this model the effect of different control levels upon subsequent stress relaxation properties was examined and an assessment made as to the sensitivity of stress relaxation properties to the applied control level. Three control levels were selected; 0.5% of the applied strain (representing tight test control), 1% of the applied strain (the level called for by BS3500 Pt 6) and 2% of the applied strain (a poorly controlled test). The corresponding data derived from the model are presented in Figure 1. As can be seen the predictions reveal differences in predicted behaviour from the very start of the test. The wider the control band the faster the stress decreases; this is consistent with the testpiece experiencing longer durations at higher stresses and hence there being a greater opportunity for the material to relax. The separation of the predictions continues throughout the test. By the time the "virtual tests" have reached 10000 hours duration the difference between the 0.5% control level and the 2.0% control levels equates to ~30MPa.

An understanding of the consequences of the behaviour predicted by the model are crucial. It is clear that, irrespective of open or closed loop control methods, the level at which load adjustments are made has a direct impact upon the subsequently generated stress relaxation properties. It is therefore vital that the control method, and the control tolerance applied, are known to users of the data and hence these parameters must be recorded as part of the test metadata.

6.2 Extensometry performance and selection

The impact of the strain control band width upon the subsequent data generated by the test highlights the crucial nature of the extensometry used to control the applied strain. BS3500: Part 6 and the ASTM E83-96 both call for extensometry performance to be defined in terms of a percentage of the applied strain. This leads directly to the required performance of the extensometer being defined by the gauge length of the testpiece used (figure 2). As can be clearly seen the required performance characteristics of the extensometry are very exacting, rising as the gauge length reduces. The laboratories partaking in the sliding weight part of this project used an 100mm gauge length which, in order to comply with the testing standard, required extensometry with a bias of $\pm$2.5um and a resolution of 0.6um. This is readily achievable using high quality LVDT and capacitive transducers, indeed the extensometry used by the three laboratories had typical bias levels

Figure 1. Predicted Stress Relaxation Behaviour

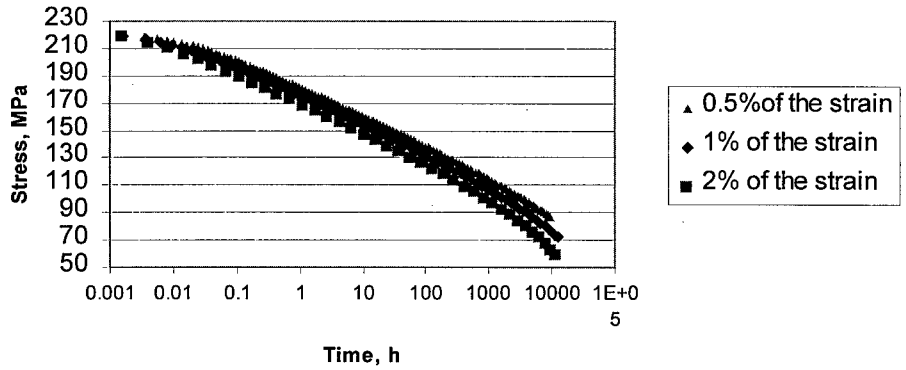

of ±1um, and discriminations of better than 0.1um. However should the gauge length be reduced to 10mm then extensometry performance must be enhanced to compensate. A 10mm gauge length, typical for side contact extensometry, requires performance characteristics compatible with EN10002-4 Grade 0.2 or ASTM E83-96 Class A. Such performance is extremely difficult to achieve, typically being associated with reference standards and laser interferometer systems. Hence, short gauge lengths and high precision stress relaxation tests are mutually incompatible.

6.3 Temperature Control

A concern of the participating laboratories was the effect of temperature variations upon the subsequent data. Fluctuations can arise either within the test furnace, or in the surrounding laboratory. These thermal changes can be translated into variations in the indicated strain from the extensometer. A 1 °C temperature fluctuation can equate to a significant proportion of the strain control band, hence action is needed to address this matter.

Variations of temperature along the gaugelength need to be minimised; a target of less than 2 °C was adopted by the participating laboratories.

6.4 Extensometry stability

Extensometer stability is crucial to the success of stress relaxation testing, with tests often having durations of 30000 hours or more. Examination of archive data at ERA Technology has demonstrated that the necessary level of stability can be achieved, with drift levels of less than 0.7% over a seven year period being the norm.

7. Recommendations

The recommendations arising from this work were as follows:-

a) All tests should include both an ambient and elevated temperature determination of modulus in order to check for the correct functioning of the extensometry. The measured value should be within 10% of the expected value.

Figure 2. A comparison of extensometry performance requirements

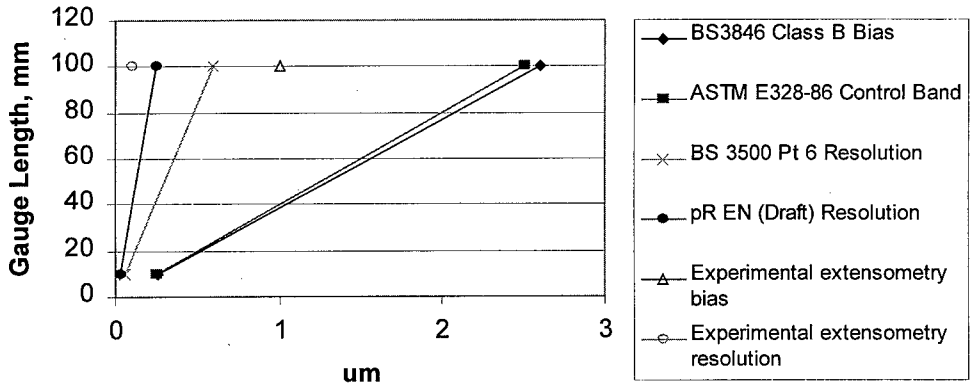

b) The extensometry bias and resolution capabilities to be defined in the new Euronorm standard need to be based upon strain, not displacement.

c) When long term stress relaxation data is to be generated the preferred route would be via testpieces with gauge lengths of at least 100mm. Use of shorter gauge lengths may be allowed providing compensating increases in extensometer performance are available.

d) The loading practice should be based around the application of between eight and ten roughly equal increments over a ten minute period.

e) Test temperature control is crucial and variations should be minimised. In critical applications consideration should be given to limiting stress changes to times when the testpiece experiences the same temperature as that at the start of the test, or alternatively a correction be made for temperature fluctuations, using a correlation derived from the testpiece under test.

f) All reasonable steps should be taken to minimise thermal gradients along the testpiece, variations should be limited to less than 2 °C.

g) An operational philosophy based around stress adjustments using decrements only should be adopted.

h) When tests are completed the determination of an unloading modulus is recommended.

i) Where tests need to be re-loaded, for example when data beyond that currently available is required, the re-loading practice presented in this paper should be adopted.

8. Acknowledgments

The authors would like to thank the directors of ERA Technology Ltd, ALSTOM Energy and British Steel Swinden Technology Centre for their permission to publish this work. The support of the European Commission, who provided partial funding for the programme of work, is also acknowledged. Finally, the help and assistance of the staff of all three laboratories in undertaking the testing is recognised and commended.

9. References

[1] ECCC – WG1 Recommendations – Volume 3 [Issue 3]. Acceptability Criteria for Creep, Creep Rupture, Stress Rupture and Stress Relaxation Data. Reference 5524/MC/30 [Issue 3], 4/10/96

[2] ASTM E328-86 (reapproved 1996). Standard Test Methods for Stress Relaxation for Materials and Structures.

[3] JIS Z 2276 – 1975. Japanese Industrial Standard, Method of Relaxation Test for Metallic Materials.

[4] BS 3500 : Part 6 : 1969. Methods for Creep and Rupture of Metals . Part 6. Tensile Stress Relaxation Testing.

[5] BS 3846 : 1970. Methods for Calibration and Grading of Extensometers for Testing of Metals.

[6] BS EN 10002 – 4 : 1995. Tensile Testing of Metallic Materials – Part 4. Verification of Extensometers used in Uniaxial Testing.

[7] ASTM E83-96. Standard Practice for Verification and Classification of Extensometers.

Further Correspondence regarding this paper should be addressed to:- Mr. Paul McCarthy, Manager, Materials Testing Department, ERA Technology Ltd., Cleeve Road, Leatherhead, Surrey, KT22 7SA, U.K. or by fax to +44 1372 367040, or by e-mail to paul.mccarthy@era.co.uk.

Key Engineering Materials Vols. 171-174 (2000) pp. 17-24
© 2000 Trans Tech Publications, Switzerland

Recent Results of Long-Term Creep Rupture Test

H. Irie[1], F. Abe[2] and K. Yagi[3]

[1] Mechanical Properties Division, National Research Institute for Metals,
1-2-1 Sengen, Tsukuba, Ibaraki 305-0047, Japan

[2]Frontier Research Center for Structural Materials, National Research Institute for Metals,
1-2-1 Sengen, Tsukuba, Ibaraki 305-0047, Japan

[3] The 2nd Research Group, National Research Institute for Metals,
1-2-1 Sengen, Tsukuba, Ibaraki 305-0047, Japan

Keywords: Data Sheet, Creep Rupture Strength, Stress Relaxation, Micro-Structure, Heat Resisting Materials, Ferritic Steels, Austenitic Steels, Superalloys

ABSTRACT

National Research Institute for Metats(NRIM) has been promoting Creep Data Sheet Project since 1966, conducting long-term creep, creep rupture and stress relaxation tests for various commercial heat resisting steels and alloys and publishing more than 110 NRIM creep data sheets. On the bases of those accumulated fact data, a lot of fundamental researches on long-term creep behaviors such as creep and creep rupture properties, creep life prediction, analysis of stress relaxation, creep deformation behavior of heat resisting steels and alloys with micro-structural observations have been actively conducted.

1. INTRODUCTION

As high temperature plants such as power plant, chemical plant and so far are usually designed on the concept of long life, materials to be used should have excellent long-term mechanical properties. Especially for heat resisting steels and alloys, accumulated of reliable data and knowledge of long-term creep rupture strength and properties had been urgently required because of shortage of long-term creep behavior. From this social and academic background, National Research Institute for Metals started NRIM Creep Data Sheet Project in 1966, in which long-term creep data production and publication in form of fact data base have systematically conducted with more than 1000 creep testing facilities. The main purpose of this project is to obtain the more than 100,000 h creep properties and creep rupture strength for commercial heat resisting steels and alloys. In addition to data production, we have actively researched on long-term creep behavior of those materials.

2. SYSTEM OF CREEP TEST

2.1 Sampling of test specimen

Creep tests are carried out for commercial home made steels and alloys which are discussed and decided in a committee, member of which consists of engineers and researchers of Japanese typical steel making and fabricating companies including NRIM staffs, in order that the data produced are useful for practical plants. The creep test specimen is sampled from multi-heats commercial materials for high quality and reliable data sheet, considering scattering of creep

rupture strength properties in commercial productions. Although the creep tests are conducted for materials made by Japanese companies, their fundamental properties such as chemical compositions, heat treated conditions, short time mechanical properties at the creep testing temperature and so on are precisely described in the data sheet so that the data sheet may be useful world-widely.

2.2 Testing

Creep tests are carefully and systematically carried out using precisely calibrated thermocouples according to standards[1,2] and the testing program using more than 1000 creep testing facilities. Not only creep rupture data but also creep deformation data are produced. In addition of creep and creep rupture test, stress relaxation tests also have been conducted for some steels.

2.3 Production of data sheets and publication

Creep data are published in form of NRIM Creep Data Sheet, in which fact data are described in tables and plotted in figures with short time tensile strength at each testing temperature and some typical microstructures. The creep rupture strength data are also statistically treated, including analyses by calculations of master curve of a regression equation and of some typical time-temperature parameters such as Larson-Miller and Manson-Haferd. By these calculations, the estimation of creep rupture strength properties of each heat can be obtained for longer time with standard error.

Creep data sheets for a kind of steel or alloy are published three times. The first edition is published when the data of more than 10,000 h creep test can be analyzed statistically, the second edition when the data of from 50,000 to 70,000 h, the final(third) edition when the data of more than 100,000 h.

3. RESULTS OF CREEP TESTS

3.1 Summary of data sheets

Until now, NRIM Creep Data Sheet Project has conducted creep rupture test and stress relaxation tests for a lot of specimens of steels and alloys. In Table 1, the numbers of specimen are summarized according to testing time.

Table 1 Number of specimen in NRIM Creep Data Sheets

Testing time/h	>100,000	>200,000	Total
Number	550	20	>10,000

About 550 specimen tested for more than 100,000 h and some of them were interrupted to be tested, while about 20 specimen continued to be tested for more than 200,000 h. Total specimen of creep test are more than 10,000 . Until now, carbon steels, low alloyed steels such as 1Cr-0.5Mo and 2.25Cr-1Mo ferritic steels, high alloyed steels such as 9Cr-1Mo ferritic steel and various austenitic stainless steels, super alloys of Fe base, Ni base and Co base have been creep rupture tested as shown in Table 2. At the same time stress relaxation tests of bolt steels

Table 2 Materials being examined in NRIM Creep Data Sheet Project

Materials	Number of Materials	Chemical Composition(mass %)
Carbon steels	3	0.3C, 0.2C, 0.2C-1.3Mn
Low alloy steels	14	0.5Mn, 0.5Cr-0.5Mo, 1Cr-0.5Mo(tube), 1Cr-0.5Mo(plate), 1.25Cr-0.5Mo-Si(tube), 1.25Cr-0.5Mo-Si(plate), 2.25Cr-1Mo(tube), 2.25Cr-1Mo (NT plate), 2.25Cr-1Mo(QT plate), 1.3Mn-0.5Mo-0.5Ni,0.15C-0.5Si-1.3Mn,1Cr-1Mo-0.25V(cast), 1Cr-1Mo-0.25V(forged), 5Cr-0.5Mo
High alloy steels	20	9Cr-1Mo, 9Cr-1Mo-V-Nb, 9Cr-2Mo, 12Cr, 12Cr-1Mo-1W-0.3V, 18Cr-8Ni(tube), 18Cr-8Ni(plate, welded joint), 18Cr-12Ni-Mo(tube), 18Cr-12Ni-Mo(plate), 18Cr-12Ni-Mo(bar), 18Cr-12Ni-Mo-N, 18Cr-10Ni-Ti, 18Cr-12Ni-Nb, 21Cr-32Ni-Ti-Al(tube), 21Cr-32Ni-Ti-Al(plate), 25Cr-12Ni-0. 4C,25Cr-20Ni-0.4C, 25Cr-35Ni-0.4C, 9Cr-0.5Mo- 1.8W-V-Nb, 11Cr-0.4Mo-2W-1Cu-V-Nb
Super alloys	10	Fe-15Cr-26Ni-Mo-Ti-V,Ni-15.5Cr-2.5Ti-0.7Al-Nb-7Fe, Fe-20Cr-20Ni-20Co-W-Mo-Nb-Ta, Fe-21Cr- 20Ni-20Co-3Mo-2.5W-Nb-Ta-N, Ni-13Cr-4.5Mo-0.75Ti-6Al-Nb-Ta-Zr-B, Ni-15Cr-28Co-MoTiAl, Ni-19Cr-18Co-4Mo-3Ti-3Al-B,Co-25Cr-10Ni-7.5W- B, Ni-15.5Cr-8Fe, Ni-16Cr-8.5Co-Mo-W-Ti- Al-Nb-Zr-B

Table 3 Publications of NRIM Creep Data Sheets

Material	Nos.of Material	Nos. of Heat	Publications			
			1st edition	2nd edition	3rd edition	Total
Carbon Steel	3	19	3	2	2	7
Low alloyed Steel	14	141	15	14	14	40
High alloyed Steel	20	164	18	15	10	43
Super alloy	10	48	9	7	7	23

1st edition; Creep Data Sheet up to about 10,000 h

2nd edition; Creep Data Sheet up to about 30,000~50,000 h including 1st edition

3rd edition; Creep Data Sheet up to more than 100,000 h including 2nd edition

and stainless steels have been carried out.

As concerns creep rupture strength of welded joint, only welded joints of SUS304 austenitic stainless steel plate made by submerged arc welding and electron beam welding methods. In case of creep properties of welded joint, all of chemical compositions of weld metal and welding variables were analyzed and described[3]. All of the results have been published in form of NRIM Creep Data Sheet and the summary of publication is listed in Table 3.

3.2 Recent results of NRIM Creep Data Sheet

Typical creep rupture data are shown in Figs. 1 and 2, for 2.25Cr-1Mo and 9Cr-1Mo steels respectively[4,5]. Figure 1 shows the creep rupture data of 2.25Cr-1Mo normalized and tempered steel plates(JIS SCMV 4 NT) of 6 heats tested at the temperature range from 450 to 650℃. Figure 2 also shows the creep rupture data of 9Cr-1Mo steel tubes(JIS STBA 26) of 6 heats tested at the temperature range from 550 to 700℃.

Figure 3 shows the typical stress relaxation data up to 10,000 h of bolting material of 1Cr-0.5Mo-0.25V steel at 500℃[6].

Recently the NRIM Creep Data Sheet Project are aiming to produce new data in addition to creep rupture strength one, in order to supply strong tools for diagnostics and/or life prediction of high temperature plant under operation. One of them is the production of micro-structural atlas of material under creep stress. The 1st issue was completed and published for SUS304 austenitic stainless steel tube(JIS SUS304H TB). Figure 4 shows one of the results of micro-structural change in gauge(stressed) portion[7]. In this data sheet, not only micro-structure but also precipitations of carbide and σ phase and other micro-structural information were analyzed quantitatively.

4. NEW MATERIALS FOR CREEP DATA SHEET

Recent development of power plant and/or high temperature plant requires that it will be operated at higher temperature and higher pressure, directly for higher heat efficiency, in directly for ecology such as saving raw materials and saving fuel in Japan. According to this drequirement, the materials for super-critical and ultra-super-critical have been developed and begun to be used. From this background, creep rupture tests have also done for commercial Cr-Mo-W steels and Ni-based alloys in NRIM Creep Data Sheet Project as shown in high alloy steels and super alloys in Table 2.

5. RESEARCH ACTIVITIES USING NRIM DATA SHEET

Since the main objectives of Creep Data Sheet Project are to produce and supply long-term creep fact data, many fundamental researches have been conducting using those data. It is very difficult to introduce all of them, some example of researches would be described.

5.1 Long-term creep and creep rupture behavior of carbon and Cr-Mo ferritic steels

When the long-term creep data up to more than 100,000hr of carbon and Cr-Mo ferritic steels as shown in Table 2 was summarized by Larson-Miller Parameter $T(20+\log t_R)$, T is testing temperature in K and t_R is rupture time in h, steels of higher rupture stress in small parameter for example 16000 to 20000, do not necessarily show higher one at large parameter such as 22000 or more. In the middle range of the parameter, the stress remarkably goes down due to

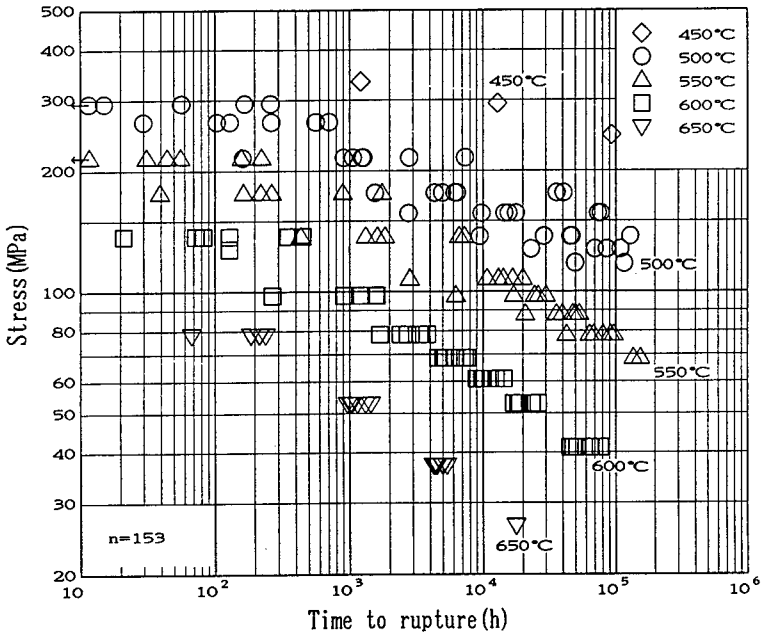

Fig.1 An example of long-term creep rupture data sheet of normalized and tempered 2.25Cr-1Mo steel plates tested at 450,500, 550, 600 and 650℃.

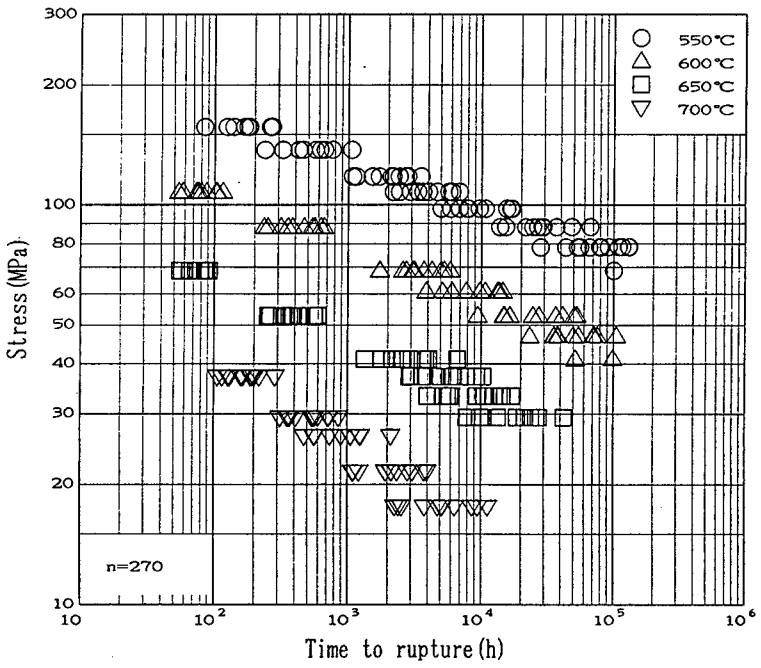

Fig.2 An example of long-term creep data rupture sheet of 9Cr-1Mo steel plates tested at 550, 600, 650 and 700℃.

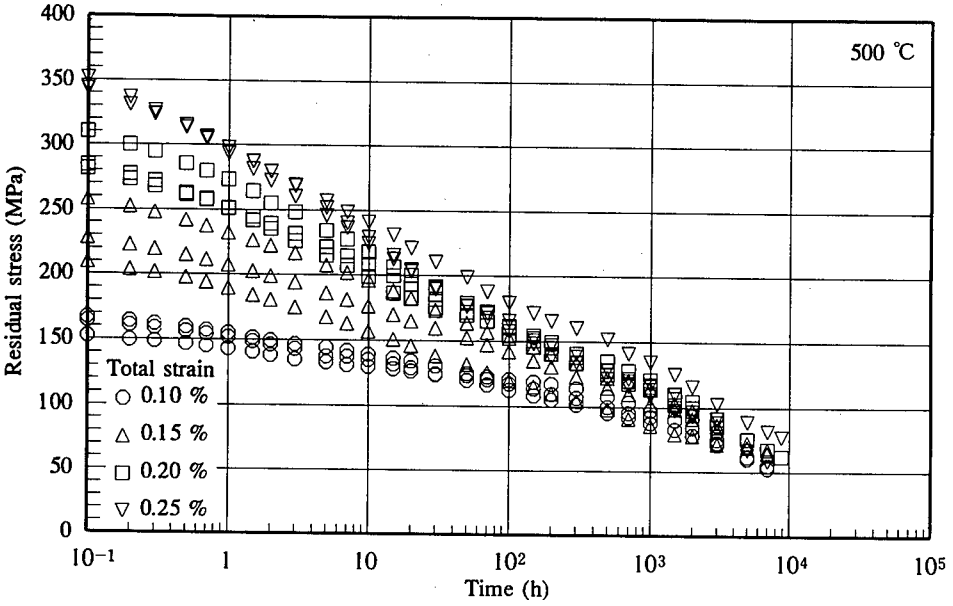

Fig.3 An example of long-term stress relaxation data sheet at 500℃ for 1Cr-0.5Mo-0.25V bolting material

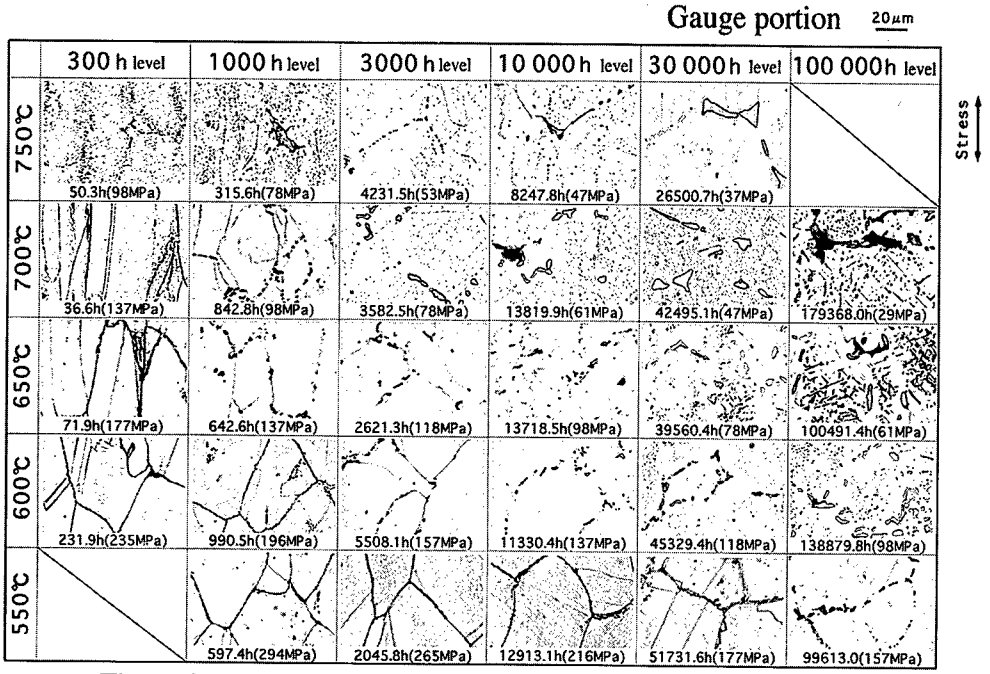

Fig. 4 An example of mirographic atlas of long-term crept SUS 304H stainless steels sampled at gauge portion

micro-structure evolution. From this fact, a concept of 'Inherent Creep Strength' was proposed. Owing to this concept, the gradients of stress with L-M parameter in both regions of small and high parameter values agree with each other and creep rupture property in much longer time could be estimated[8,9].

In addition to the creep rupture behavior, long-term deformation phenomena have been studied using 1Cr-0.5Mo, 2.25Cr-1Mo and other ferritic steels. To the deformation analyses, the modified θ method[10,11] and the Iso-stress method[12] are applied with the micro-structural observation of crept materials. Some results will be presented in this conference.

5.2 Stress relaxation

The results of stress relaxation test have also been analyzed in addition to the publication of data sheets. In the stress relaxation behavior with Cr-Mo ferritic steels and austenitic stainless steel up to 10,000 h, in general the residual stress monotonously decreases with time as shown in Fig. 3. However, in some steel, for instance SUS316 stainless steel, the residual stress behavior is very complicated, especially at more than 1000h. If the total strain is set to 0.2% in this steel, the residual stress rapidly decreased at longer time in certain conditions. These phenomena have close relationships with evolution in mirco-structure[13].

5.3 Micro-structure and fracture mode observations.

A series of creep testing of austenitic stainless steels, SUS304H, 316H, 321H and 347H micro-structure and fracture mode have been observed and analyzed[14]. In these steels, fracture mode is typically classified, by the transgranular fracture, fracture with creep cavity at grain boundaries, fracture from surface cracking, fractures with precipitation of type $M_{23}C_6$ carbide and σ phase at grain boundaries. The relationship between fracture mode and micro-structural evolution under creep testing has been systematically studied and some results will be also presented in this conference.

5.4 Creep phenomena of new steels for USC

Recent development of new steels for USC, the data accumulation of creep properties of these steels are urgently required to apply them to higher temperature power plant safely. For this purpose, NRIM Data Sheet Project began to test new steels, other properties of which are already confirmed including short-time creep properties and commercially produced. The typical new steels under testing are listed in Table 2. In this examination, Mo-Cr ferritic and martensitic steels with various W content have been studied from the point of fundamental creep properties. In this research, the relationship between creep and creep rupture behavior with micro structure evolution with time has been studied[15]. Some results will be also presented in this conference.

Since 1997, NRIM started a new big national project 'Frontier Research Project for Structural Materials', joining NRIM scientists and research scientists of Japanese typical steel making and fabricating companies. One of research item is the development of new strong steels for USC. The fruits of NRIM Creep Data Sheet Project including the new steels above mentioned will be also effectively used.

6. FUTURE PROSPECT OF NRIM CREEP DATA SHEET PROJECT

In the present plan of project, we have many materials to be creep rupture tested, at least for the coming 10 years. In addition to the publication of conventional creep rupture data sheet for safe and rational design of high temperature plant, the data for diagnostic and life prediction of plant under operation such as the micro structural atlas under creep load and the deformation date will be produced and published.

ACKNOWLEDGEMENT

The authors wish to express many thanks to the member on NRIM Creep Data Sheet Project for their efforts of the long-term creep tests

REFERENCES

[1] JIS Z 2271-1978 Method of tensile creep test for metallic materials

[2] JIS Z 2272-1978 Method of creep rupture test for metallic materials

[3] NRIM CREEP DATA SHEET No.32A, DATA SGEETS ON THE ELEVATED TEMPERATURE PROPERTIES FOR BASE METALS, WELD METALS AND WELDED JOINTS OF 18Cr-8Ni STAINLESS STEEL PLATES (SUS 304HP), 1995

[4] *ibid.,* No.11B, DATA SHEETS ON THE ELEVATED TEMPERATURE PROPERTIES OF NORMALIZED AND TEMPERED 2.25Cr-1Mo STEEL PLATES FOR BOILERS AND PRESSURE VESSELS(SCMV 4 NT),1997, p.9

[5] *ibid.,* No. 19B, DATA SHEETS ON THE ELEVATED TEMPERATURE PROPERTIES OF 9Cr-1Mo STEEL TUBES FOR BOILERS AND HEAT EXCHNGERS(STBA 26), 1997, p.10

[6] *ibid.,* No. 44, DATA SHEET ON THE ELEVATED-TEMPERATURE STRESS RELAXATION PROPERTIES OF 1Cr-0.5Mo.-0.25V STEEL AND 12Cr-1Mo-1W-0.25V STEEL BOLTING MATERIALS FOR HIGH TEMPERATURE SERVICE, 1997, p.12

[7] *ibid.,* No. M-1, MICROGRAPHS AND MICROSTRUCTURAL CHARACTERISTICS OF CREPT SPECIMENS OF 18Cr-8Ni STAINLESS STEEL FOR BOILER AND HEAT EXCHANGER SEAMLESS TUBES(SUS 304H TB), 1999, p. 44

[8] K. Kimura, H. Kushima, and K. Yagi, Proc. 7th Int. Conf. Creep and Fracture of Engineering Materials and Structures, (1997), p.89

[9] K. Kimura, H. Kushima, F. Abe, K. Yagi and H. Irie, Proc. 4th Int. Charles Parsons Turbine Conference, (1997) ,p.257

[10] H. Kushima, K. Kimura, K. Yagi, C. Tanaka and K. Maruyama, Proc. Aspects of High Temperature Deformation and Fracture in Crystalline Materials, The Japan Inst. Metals, 1993, p.609

[11] K. Maruyama, H. Kushima, and T. Watanabe, ISIJ Int., 30(1990), p.817

[12] O. Kanemaru, M. Shimizu, T. Ohba, H. Miyazaki, F. Abe and K. Yagi, Materials Science Research Int., 3(1997) ,p.31

[13] T. Ohba, O. Kanemaru, K. Yagi, and C. Tanaka, Materials Science Research Int., 3(1997) p.10

[14] H. Tanaka, M. Murata, F. Abe and K. Yagi, Material Science and Engineering A234-236(1997) p.1049

[15] F. Abe, Materials Sci. and Eng., A234-236(1997) ,p.1045

Key Engineering Materials Vols. 171-174 (2000) pp. 25-34
© 2000 Trans Tech Publications, Switzerland

Experimental and Numerical Investigations on Creep Damage Evolution

A. Klenk[1], A. Kussmaul[1], K. Maile[1] and P. Lenk[2]

[1] Staatliche Materialpruefungsanstalt (MPA), University of Stuttgart, Pfaffenwaldring 32, DE-70569 Stuttgart, Germany

[2] Technical University of Chemnitz, DE-09107 Chemnitz, Germany

Keywords: Cavity Formation, Cavity Growth, Creep Damage, Multiaxiality, Inelastic Strain, Stress State

Abstract

New approaches for life time assessment of high temperature components are based on the description of changes in the microstructure of materials e.g. the formation and growth of cavities. In order to get reliable results using such approaches it is important to obtain a quantitative relationship between parameters like cavity density describing damage situation and stress and deformation state. If life time consumption of components is considered, it is necessary to take into account the actual stress state. It is well known that there is a reduction in deformation capability of a material, but there is little knowledge of the influence of the stress state on the time dependent evolution of creep damage.

For MoV-steel, 2 1/4 Cr -steel and 9 Cr steel tests under uniaxial and multiaxial stress states have been carried out. Hollow cylinders were subjected to combined loading of internal pressure and axial tensile or compressive load. From microstructural investigations cavity size and density are determined. By means of finite element analyses the actual stresses and deformations are calculated taking into account time dependent behavior. As a result there could be found a relationship describing the damage evolution in dependence of inelastic strain and multiaxiality.

Introduction

Over the last 60 years a variety of empirical creep laws e.g. Norton-Bailey, Garofalo, Graham and Walles etc. have been developed to describe the relation between stress, strain and time. To describe damage phenomena, which are known to occur at the end of the secondary creep range, material models and constitutive equations have been developped. Most of them are based on descriptions of macroscopic material behavior determined by uniaxial tests. Some approaches are based on microstructure. In the case of uniaxial creep tests effective stress is equal to the uniaxial stress. In loaded components however, multiaxial stress states occur. In this case , usually the von Mises stress or a combination of the maximum stress and the von Mises stress [1, 2, 3] is used as an equivalent stress. It has been proposed that not only the amount of stress but also the multiaxiality of the stress state has a large influence on the strain and as a consequence also on the creep damage evolution and material failure [4, 5]. This is the reason why damage evolution and hence life time consumption in components is different from that in uniaxially loaded testpieces.

To overcome these difficulties in transferring uniaxial data to components the quantification of this relationship is necessary. This is getting more important since it is possible to determine local stresses and strains for components by means of finite element techniques.

This work is focussed on the characterisation and quantification of damage evolution as a function of inelastic strain and multiaxiality of stress state. To this aim the damage evolution on the surface and along the wall thickness of plane and notched hollow cylinders is investigated. This testpieces are used in order to represent stress state situation in power plant components. Special emphasis was put on the influence of multiaxiality and local strain on the cavity density.
The multiaxiality factor h used in this work is defined by the quotient of the mean stress (hydrostatic pressure) divided by the von Mises stress:

$$h = \frac{\sigma_h}{\sigma_{eq,Mises}} \qquad \text{(Eq. 1)}$$

Materials under investigation

In this study three in power plant technology widely used steels have been investigated. Cavity formation of these steels is quite different. With regard to the service temperature of components the MoV-steel and the 2¼ Cr steel were tested at 550 °C, and 9 Cr steel at a temperature 600 °C. Table 1 shows the chemical composition of the materials.

Mat.	German Standard	C	Si	Mn	P	S	Cr	Cu	Mo	Nb	Ni	V	Al	N
MoV	14MoV6-3	0.15	0.25	0.41	0.009	0.008	0.41	–	0.55	–	0.06	0.29	0.03	–
2¼ Cr	10CrMo9-10	0.12	0.22	0.49	0.008	0.003	2.21	0.13	0.97	–	–	–		–
9 Cr	X10 CrNiMoNb 9 1	0.10	0.30	0.50	0.018	0.01	8.66	0.015	1.02	0.064	0.12	0.24	0.023	0.049

Table 1: Chemical composition of the casts investigated (mass%)

Experiments

Basic creep tests were carried out to determine the creep behaviour of the materials under uniaxial loading. In order to study the influence of multiaxial stress states on the creep behaviour of typical power plant components notched and plane hollow cylinders have been used. The testpieces have been subjected to combined loading of internal pressure and axial tensile or compressive load. The specimen used is shown in Fig. 1.

Determination of materials parameters
For each steel, uniaxial creep tests were carried out applying different stress levels. Based on these results, the parameters of the creep law according to Graham and Walles [4], i.e.

$$\varepsilon_c = A \cdot t^{\frac{1}{3}} + B \cdot t + C \cdot t^m \qquad \text{(Eq. 2)}$$

with $A = a_0 \cdot \exp(a_1\sigma + \ldots + a_n\sigma^n)$, $B = b_0 \cdot \exp(b_1\sigma + \ldots + b_n\sigma^n)$, $C = c_0 \cdot \exp(c_1\sigma + \ldots + c_n\sigma^n)$
were determined using a mathematical optimisation routine. For the MoV steel m = 3,75 was used. For 2¼ Cr-steel and the 9 Cr-steel the tertiary exponent m was calculated by a stress dependent term since this modification allows better approximation of the experimental data:

$$m = \exp(0{,}018 \cdot \sigma) \qquad \text{(Eq. 3)}$$

Multiaxial creep tests
Hollow cylinders were subjected to internal pressure and axial tensile or compressive load. Different combinations of external loading were applied in order to vary stress state and multiaxiality. For the straight cylinders circumferential strain and for notched cylinders axial strain were recorded using capacitive high temperature strain gauges. In notched testpieces high local gradients of multiaxiality and strain occur resulting in high gradients of cavity density in the notch area.

Microstructural investigations
Cavity size and density as well as cavity distribution along the wall thickness of the straight and notched cylinders were determined by metallographic methods including also the replica technique. For the notched hollow cylinders four positions were examined in detail, Fig. 2, in order to study the influence of stress concentrations and inhomogenity of stress fields in this area. The state of damage was characterised by the cavity density in the metallographic plane or the cross-sections examined.

a)

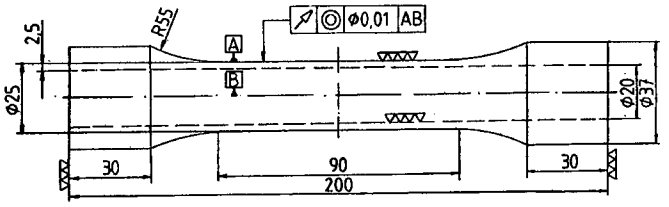

b)

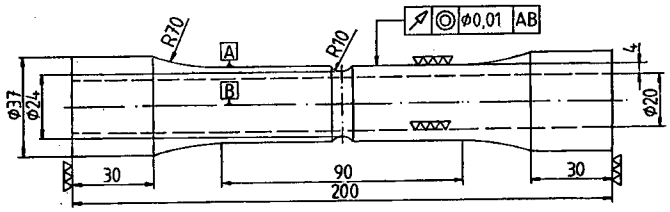

Fig. 1: a) straight and b) notched hollow cylinder specimen.

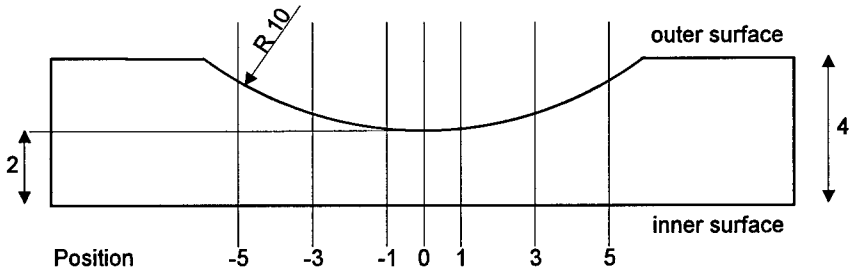

Fig. 2: Examined positions in the notch (all dimensions in mm)

Numerical Simulation of Experiments with Hollow Cylinders

The Graham-Walles creep law was implemented in a user subroutine CREEP. The Finite Element package ABAQUS was used to calculate creep strains, stress distributions and the multiaxiality quotient for the testpieces under different loading conditions.

Straight Hollow Cylinders

As shown in Fig. 3 a good agreement between numerical and experimental results could be achieved. A comparison of measured and calculated deformation is shown in Fig. 4. The agreement is obvious.

According to the identical specimen geometry, the numerical results for all materials subjected to internal pressure reveal very similar stress distributions at the end of the tests. The stress level differs according to variable pressure loads. Fig. 5 shows that for all materials the multiaxiality along the wall thickness of a plane hollow cylinder is identical for long creep times.

The axial stress at the beginning of the loading is constant along the wall thickness, Fig. 6. With increasing creep time the level at the inner surface decreases while at the outer surface the stress increases. The circumferential stress is similar, showing an increase at the outer surface and a decrease at the inner surface with increasing time. The von-Mises stress has a steep gradient (a high value at the inner and a low value at the outer surface) at the beginning. It changes as expected to a constant value along the wall thickness for long creep times.

Multiaxiality h shows only small changes with creep time, Fig. 7. The value at the inner surface slightly decreases from the elastic limit at short times (h=0.37) to the plastic limit for long creep times (h=0.33). At the outer surface the multiaxiality is constant (h=0,57) and not time dependent.

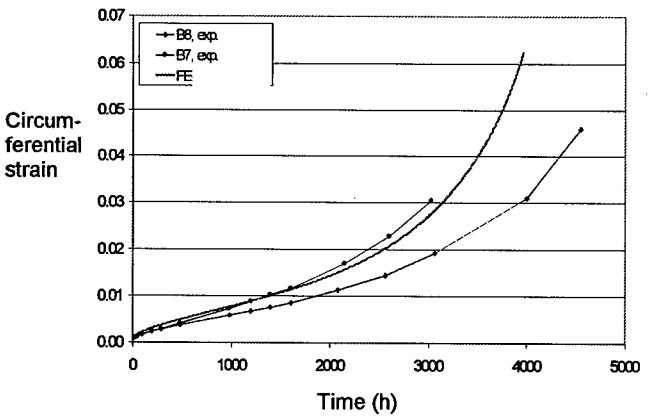

Fig. 3: Experimentally and numerically determined circumferential strain, straight hollow cylinder under internal pressure, MoV steel

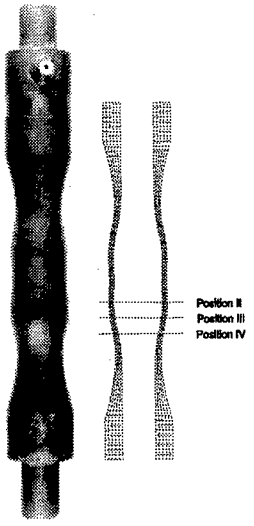

Fig. 4: Specimen after 4730 h test duration and calculated deformation, internal pressure and compression force, MoV-steel

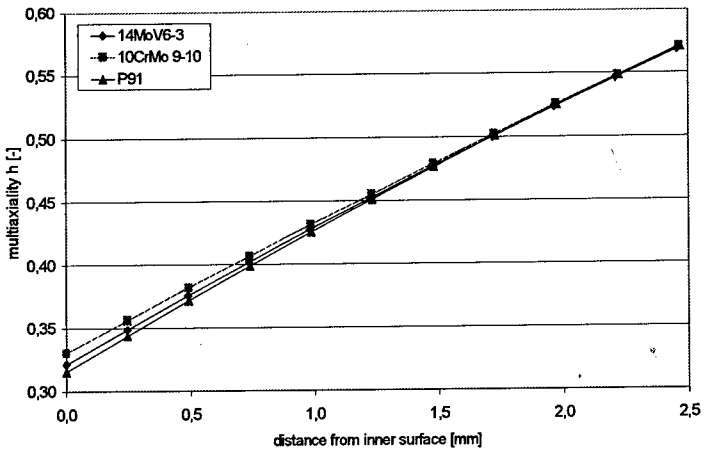

Fig. 5: Multiaxiality h along the wall thickness at the end of the tests, straight hollow cylinder under internal pressure

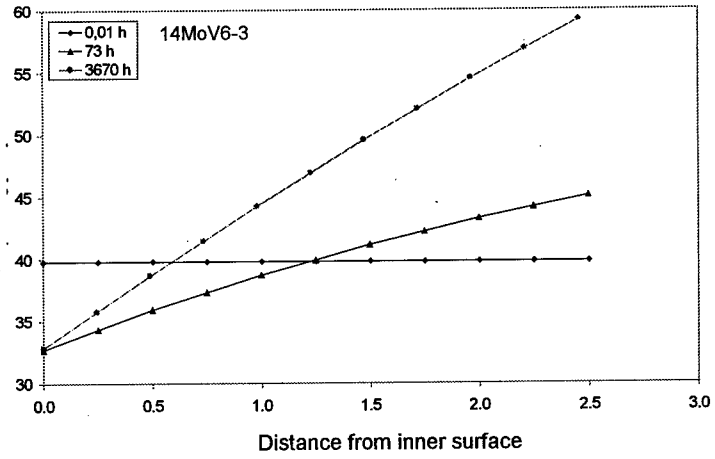

Fig. 6: Axial stress along the wall thickness, straight hollow cylinder under internal pressure, MoV-steel

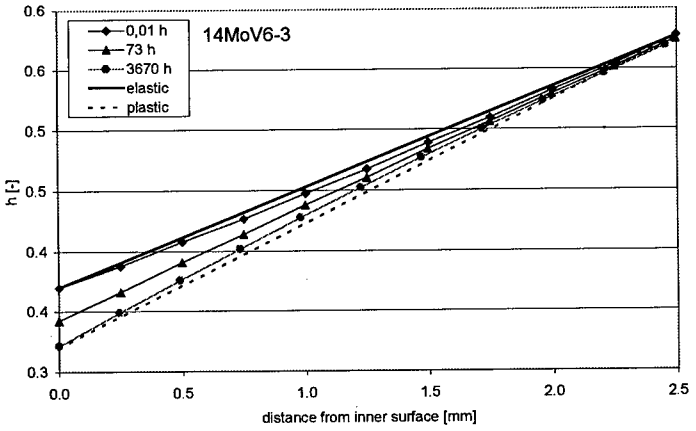

Fig. 7: Multiaxiality h along the wall thickness, straight hollow cylinder under internal pressure, MoV steel

Notched hollow cylinders

The stress and strain field in notched hollow cylinders prooved to be rather non homogenious, gradients in multiaxiality could be observed. Due to the identical geometry no strong differences between the various materials investigated are observed. Comparing the change of stresses with increasing time at different positions, a faster redistribution of stresses at the notch root could be found. The multiaxiality along the wall thickness at the smallest diameter changes from a pure deviatoric stress state in the specimen center to a maximum of h = 0,67at the outer surface, Fig. 8.

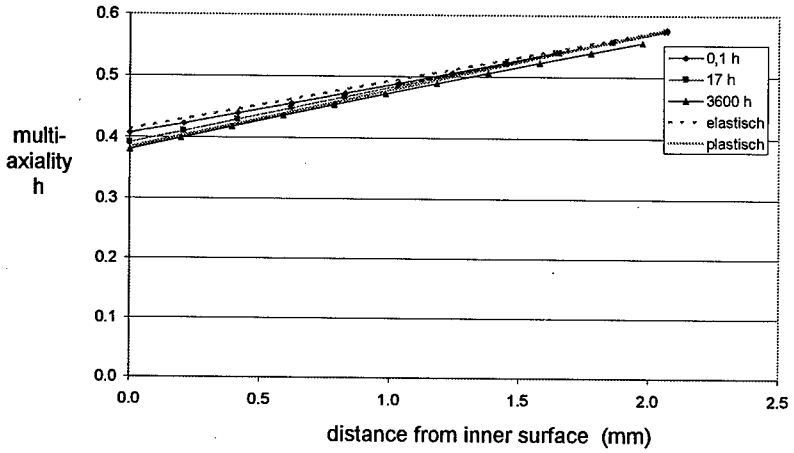

Fig. 8: Multiaxiality quotient h along the wall thickness, notched hollow cylinder under internal pressure

Comparison of metallographic and numerical results

Exemplarily the metallographic results (cavity density) and the numerical results (axial strain and multiaxiality h) for a notched hollow cylinder of MoV-steel under internal pressure and axial tensile load are compared.
For the position at the notch root (Pos. 0 in Fig.2) the axial strain and, consequently, the cavity density are close to zero at the inner surface while the multiaxiality is 0.4, Fig. 9. Thus, for small strains the multiaxiality has less influence on cavity formation than a strain increase. At a position 3 mm from the notch root the axial strain decreases from the inner to the outer surface while the cavity density first increases like the course of multiaxiality, Fig. 10. For larger strains a small change in multiaxiality has more influence on the cavity density than a relatively greater change in strain level.

All available data were used for evaluation, and an analytical expression describing the cavity density N_A as a function of local maximum strain φ and multiaxiality h

$$N_A = f(\varphi, h, \text{material}) \qquad \text{(Eq. 4)}$$

was derived. Fig. 11 shows the graphical representation of this function. The highest values of cavity density occur for high strain and high multiaxiality. The mutual influence of strain and multiaxiality on cavity density is visible more clearly in Fig. 12. The 3D surface in Fig. 11 is

projected on the h-φ plane. Lines with constant cavity density are included. It is obvious that for small strains and high multiaxiality the cavity density is more influenced by strain than by a change in the multiaxiality while for large strains and low multiaxiality a change in multiaxiality has a larger effect on the cavity density.

This analytical expression was implemented in the user defined subroutine of the Finite-Element program. The cavity distribution can be determined dependent on calculated stresses and strains. The evolution of the cavity density at the inner and outer surface of a straight hollow cylinder of MoV-steel is represented as a function of time in Fig.13.

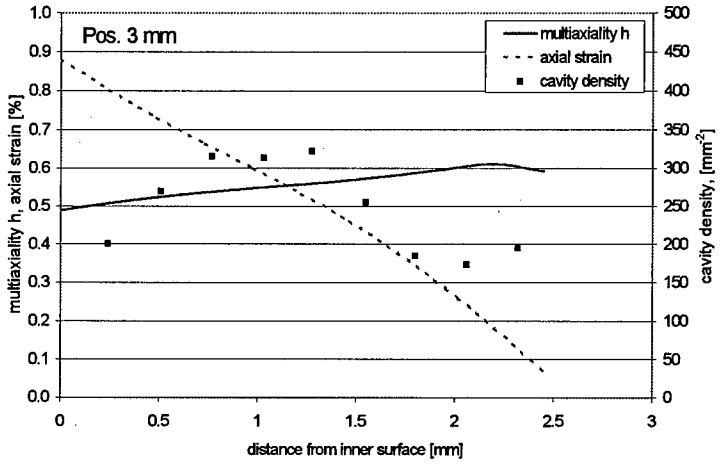

Fig. 9: Multiaxiality h, axial strain and cavity density along the wall thickness at the notch root of a notched hollow cylinder under internal pressure and axial tensile load after 1600 h test duration, MoV-steel

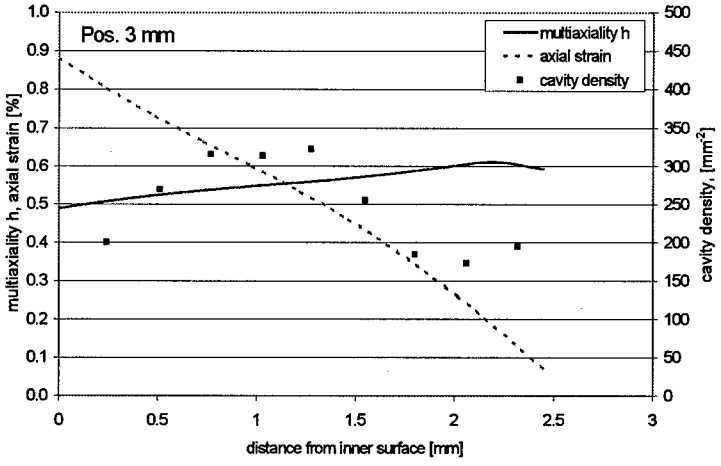

Fig. 10: Multiaxiality, axial strain and cavity density along the wall thickness at a position 3 mm from the notch root of a notched hollow cylinder, under internal pressure and axial tensile load after 1600 h, MoV-steel

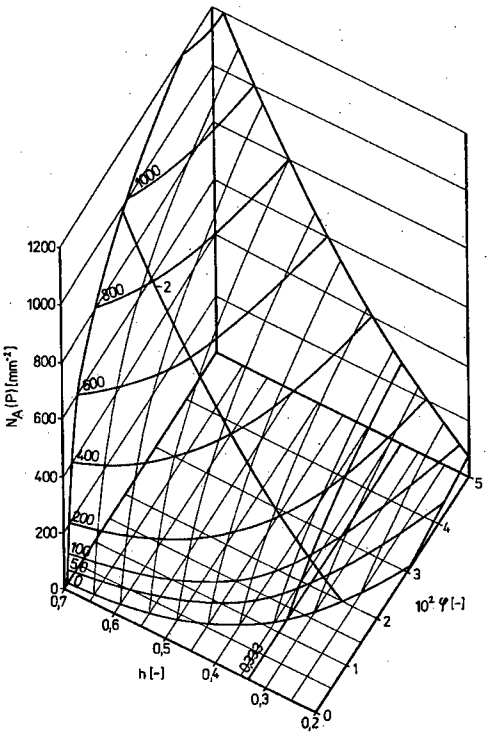

Fig. 11: 3D surface describing the relation between cavity density (N_A), multiaxiality (h) and strain (φ) for MoV-steel.

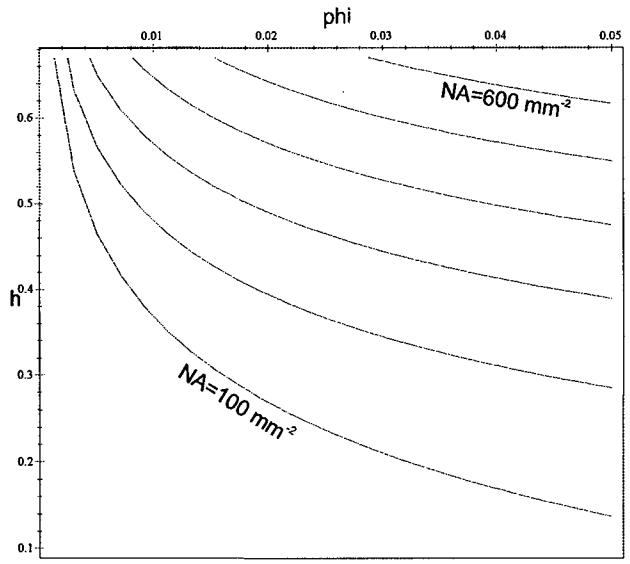

Fig. 12: Projection of the surface of on the h-φ plane showing lines with constant cavity density for MoV-steel

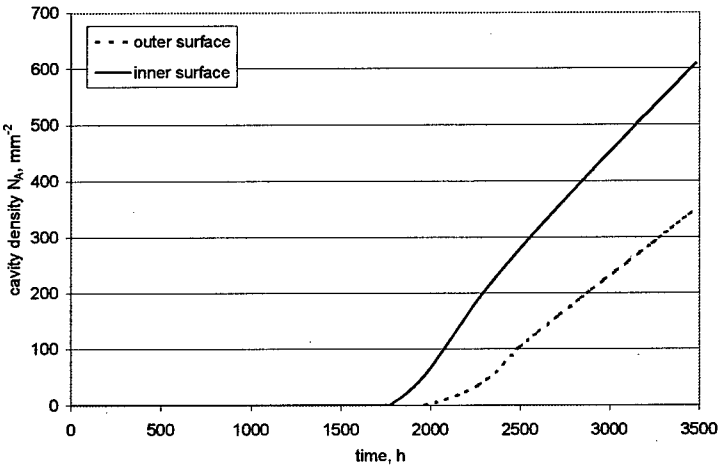

Fig. 13: Cavity density on the inner and outer surface of of a straight hollow cylinder under internal pressure, MoV-steel

Conclusions

Creep Tests with 10 000 h to 15 000 h duration, microstructural investigations to determine cavity density and numerical simulations to calculate stresses, strains and multiaxiality of stress state have been carried out for hollow cylinder specimens made of MoV-, 1 Cr and 9 Cr steel in order to determine the relationship between creep damage evolution, strain and multiaxiality.

For MoV steel an analytical formulation relating cavity density, multiaxiality and local strain has been derived. This relation allows the numerical calculation and the graphical representation of the cavity density for any geometry. An increasing cavity density for increasing strain and multiaxiality and a nearly time independent multiaxiality distribution could be stated. In general maximum strain influences the absolute value of cavity density, multiaxiality influences the gradient of cavity density. Maximum cavity density was found at the outer surface.

For 2¼ Cr-steel less cavities formed during the tests. Therefore the experimental information especially on cavity density was to small to derive an analytical expression like for MoV steel .

For 9 Cr-steel no cavities were found in the testpieces. Investigations of different casts indicate an influence of the copper content on the rupture properties and on the cavity formation. For high Cu concentrations (~ 0,1 %) a strong decrease of the rupture time and an increased tendency of cavity formation has been observed while casts with low copper contents (~ 0,01 - 0,03 %) showed a more ductile behaviour and no cavity formation. Nevertheless the relationship between microstructure and strain resp. multiaxiality demands for experiments with longer test duration which are still going on.

These investigations have been aimed in developing an evaluation method for creep damage in components based on micrographical investigation on the surface of components. It could be shown that for known stress situations an evaluation of creep damage is possible. For materials with a tendency to form cavities like MoV steel cavity density as a function of material,

multiaxiality, maximum strain, temperature and loading duration may be used as a parameter to describe damage and calculate life time consumption. For materials with low tendency to form cavities e.g. new 9-12 Cr steels to this aim another microstructural parameter as a function of material, multiaxiality, maximum strain, temperature and loading duration may be used.

A solid data base for the relationship between cavity density resp. microstructural parameter and multiaxiality and strain allows for including the calculation of a damage parameter based on cavity formation, size and density into finite element calculations. To this aim new approaches to describe the interaction or creep and cavitation have already been put forward [7]. This approach is a combination of Robinsons model of inelastic deformation [8] and the formulation of the cavity damage by Rodin and Parks [9].

Acknowledgement

Thanks are due to the "Arbeitsgemeinschaftsgemeinschaft warmfeste Staehle" and the "Forschungsvereinigung der Arbeitsgemeinschaft der Eisen und Metall verarbeitenden Industrie (AVIF) for their support of this work.

Literature

[1] D. R. Hayhurst, F. A. Leckie and C. J. Morrison: Creep Rupture of Notched Bars, Proc. R. Soc. Lond. A. 360 (1978), pp. 243-264

[2] R. L. Huddleston: An Improved Multiaxial Creep-Rupture Strength Criterion, Journ. Press. Vess. Techn. 107 (1985), pp. 421-429.

[3] S. Sheng: Anwendung von Festigkeitshypothesen im Kriechbereich bei mehrachsigen Spannungs-Formänderungszuständen. Dissertation at the Univerisity of Stuttgart, Techn.-wiss. Ber. MPA Stuttgart (1992) Heft 92-04.

[4] K. Kußmaul, K. Maile, und S. Sheng: Beurteilung von mehrachsigen Spannungs-Dehnungszuständen im Langzeitkriechbereich auf der Basis von Festigkeitshypothesen, Mat.-wiss. u. Werkstofftechn., 25 (1994) 71-78

[5] K. Maile: experimentelle und theoretische Ermittlung des Versagens von Rohrbogen im Zeitstandbereich, 3R International, 32(9) (1993) 500-507

[6] Graham, A. and Walles, K. F. A.: Relations between long and short time properties of a commercial alloy, J. Iron and Steel Inst. (1955) 179.

[7] W. Gaudig, K. Kussmaul, K. Maile, M. Tramer, J. Granacher and K.-H. Kloos: A microstructural model to predict the multiaxial creep and damage in 12 Cr steel grade at 550 °C. In: „Microstructure and mechanical properties of metallic high-temperature materials", Deutsche Forschungsgemeinschaft, Eds. H. Mughrabi, G. Gottstein, H. Mecking, H. Riedel and J. Tobolski, Wiley-VCH, 1999.

[8] D.N. Robinson: Constitutive Relationships for Anisotropic High-Temperature Alloys, Nuclear Engineering and Design 83 (1984) 389-396

[9] G.J. Rodin and D.M. Parks: A self consistent Analysis of a Creeping Matrix with aligned Cracks, J. Mech. Phys. Solids Vol. 36, No. (1988) 237-249.

Corresponding author:
Dr.-Ing. Andreas Klenk, Staatliche Materialpruefungsanstalt (MPA), University of Stuttgart, Pfaffenwaldring 32, D 70569 STUTTGART,
Fax: +49 711 685 3053, e-mail: andreas.klenk@mpa.uni-stuttgart.de

Key Engineering Materials Vols. 171-174 (2000) pp. 35-42
© 2000 Trans Tech Publications, Switzerland

Predicting the Creep Life and Failure Location of Weldments

J.M. Brear[1], A. Fairman[1], C.J. Middleton[2] and L. Polding[3]

[1] ERA Technology, Cleeve Road, Leatherhead, Surrey, KT22 7SA, UK

[2] ERA Inc., Suite 140, 19424 Park Row, Houston, Texas 77084, USA

[3] ERA Asia Pte Ltd. 03-02A The Curie, Singapore Science Park, Singapore

Keywords: Welds, ½ Cr ½ Mo ¼ V, 1CrMo, 2 ¼ CrMo, Grade 91 (9CrMoVNb), Type IV, Type IIIa, Hardness, Continuum Damage Mechanics

Abstract

The creep life of components is frequently dominated by the behaviour of the welds. The association of microstructural complexity with the interaction between local and global stresses makes life prediction more difficult than for regions of the component where the material is homogeneous and the geometry simpler. Preliminary calculation based on inverse use of design codes normally allows for welds by use of a straightforward efficiency factor. Inspection based methods rely on evaluation of damage accumulation and microstructural degradation. Both these approaches have their weaknesses, safety factors assume trends in long term rupture behaviour which may not hold beyond design life and condition based methods require knowledge of the controlling parameters and accessibility to the most critical areas for inspection.

This paper reviews and consolidates experience gained through a number of research projects and practical plant assessments in predicting the life, the likely failure mode and the failure location in alloy steel weldments. The approach adopted begins with the recognition that the relative strength differences between the microstructural regions is a key factor controlling both life and failure location. Practical methods based on hardness measurements and adaptable to differing weld geometries are presented and evidence for correlations between hardness ratio, damage accumulation and strain development is discussed. Data on ½Cr½Mo¼V, 1CrMo, 2¼CrMo and Grade 91 steels are presented.

Predictor diagrams relating weld life and failure location to the service conditions and the hardness of the individual microstructural constituents are suggested and comments are given on the implications for identifying the circumstances in which Type IV cracking is to be expected.

1 Introduction

In previous work [1] a mechanistic model for predicting creep life was presented which took account of both microstructural coarsening and creep cavitation. The cavitation was incorporated using a Continuum Damage Mechanics approach whilst microstructural degradation was modelled in terms of interparticle spacing. As this combined model is quite complex, subsequent developments have tended to treat damage and degradation individually. This present paper majors on the effects of precipitate strengthening effects, quantified indirectly through hardness measurements.

A second line of work [2] specifically addressed Type IV failures in double-V preparation seam welded pipework. Here, a clear relationship was observed between the hardness difference between weld and parent metals and the susceptibility to creep cavity nucleation in the cusp region at the centre of the pipe section. Reasonable success was obtained in using surface hardness measurements to predict relative sub-surface damage levels and thus prioritise pipe spools for further inspection. Core samples could then be taken from

critical positions to allow small specimen cross-weld tests to predict life. However, when attempts were made to extend this approach to other weld geometries - single-V, U and parallel sided - it was found to be unsuccessful. In these situations, the cavity nucleation rate was not dominated by local strength mismatch, but by larger scale stress controlling factors such as pipe ovality and system loads. For practical assessment purposes, full section cross-weld tests at mildly accelerated temperatures are used, with local strain gauges fitted and periodic, automated cavity density measurements.

Further work attempted to reconcile these approaches and to develop an integrated methodology for weld life prediction. The original creep model approach [1] was extended to treat welds [3,4,7], and this yielded some success at predicting weld life and failure location, including the onset of Type IV cracking, in 2¼CrMo steels. The present paper extends this line of research to a wider range of alloys.

2 Modelling

2.1 Development of the model

The model is based on a Norton creep law, with a threshold stress term, σ_0, which has its physical origin in the interaction between moving dislocations and precipitate particles:

$$\dot{\varepsilon} = A.\exp(-Q/RT).(\sigma - \sigma_0)^n \qquad \text{Eq.1}$$

where σ is the applied stress, $\dot{\varepsilon}$ the creep rate and A, Q and n are constants [1,5]. The threshold stress is inversely proportional to the interparticle spacing, λ, but since this is problematic to measure directly, a relationship between threshold stress and hardness, H, is commonly accepted:

$$\sigma_0 = \alpha'\mu b/\lambda = K\alpha'(H - H_{SS}) \qquad \text{Eq.2}$$

where α' is a geometric term, μ the shear modulus and b the Burgers vector.

H_{SS} is the contribution to the hardness due to solid solution strengthening and K defines the (well-established) relationship between hardness and tensile strength. As the precipitates coarsen with time, t, at temperature, the hardness and threshold stress decrease in a manner which may be approximated, in the continuum limit, by the Lifschitz-Slyozov-Wagner-Greenwood kinetic [1,3]:

$$\sigma_0 \sim (H - H_{SS}) \sim 1/\lambda \sim t^{-1/3} \qquad \text{Eq.3}$$

Subsequently the model was extended, for parent material, to yield an expression for the creep rate that included the effects of primary hardening - both kinematic and isotropic - and tertiary softening through both thermal and strain based mechanisms. If the applied stress, σ, is taken as the stress acting on a grain, instead of that on the specimen or component, then the normal Kachanov-Rabotnov type relationships for creep cavitation can be included [6], as can increases in stress due to overall changes in geometry consequent on deformation. Good agreement between the model predictions and experimental data has been demonstrated [3,4].

It would be possible, and informative, to calibrate the model separately for weld metal, the various regions of the heat affected zone and the parent material and use it within a finite element program to model weld behaviour in detail. This would, however, be prohibitively expensive as a routine assessment method and some practical simplification is required. The following approach has been adopted [3,4].

Assuming a Monkman-Grant relationship:

$$\dot{\varepsilon}_m . t_r = \varepsilon_s \qquad \text{Eq.4}$$

and making some bold but realistic assumptions as to the minimum value, $\dot{\varepsilon}_m$, of the creep rate, the rupture life can be approximated by:

$$t_r \approx (\varepsilon_s / \dot{\varepsilon}_0).(\sigma / KH)^{-n} \qquad \text{Eq.5}$$

where H is the initial hardness. This simplified treatment thus generates a relationship between rupture life (which may be temperature compensated) and the ratio of stress to strength. It is, in effect, a modification of the conventional stress rupture plot with the data points normalised according to the hardness of the individual heats of material.

2.2 Experimental validation

Various heats of virgin, laboratory aged and ex-service material were procured for this work so as to allow testing of welds in the virgin condition, ex-service welds and 'repair' welds in ex-service material. Some of the virgin welds were laboratory aged to simulate service. In all cases current welding practices were used. The majority of welds studied had been sub-critically stress relieved. A few renormalised welds were included among the ex-service samples.

All materials were fully characterised metallographically. Tensile and creep testing of parent and weld metals was performed and cross-weld creep tests were carried out on both small (10-15 mm diameter) and large (30-60 mm square) specimens, the latter being equipped with local strain gauges. Small specimens were tested under vacuum and the large cross-weld tests were interrupted periodically to allow replication. All hardness measurements reported were obtained using a conventional Vickers indenter, on surfaces prepared to replication standard finish.

3 Results and Discussion

3.1 Rupture life and creep rate - 2¼CrMo steel

Figure 1 shows data from a variety of parent, intercritical and coarse-grained heat affected zone and weld metal specimens of 2¼CrMo steel, over the ranges 20-125 MPa, 575-720°C and 50-27000 hours, plotted according to equation 5 (with temperature compensation of the rupture lives). A two-slope Kachanov-Rabotnov model fit to the parent material data is shown; the different slopes correspond to the flow controlled and damage controlled regimes. Stress sensitivities of 7 and 4 respectively and a common apparent activation energy of 440900 J/K/mol are in accordance with previous work. They imply a true creep rate stress dependence of 4, a true activation energy of 25200 J/K/mol and a primary hardening coefficient of 1.75 [6].

The rupture data for the constituent microstructures of weldments were obtained from simple tests on weld metal, coarse grained or intercritical heat affected zone material and from small cross-weld specimens showing weld metal failure. They thus represent the behaviour of the individual microstructures, uninfluenced by interactions or constraint effects. The results fall into two groups. For sub-critically heat treated welds, there is no discernible difference between weld metal and coarse grained heat affected zone material; the data from these seem adequately represented by a simple transposition of the parent material lines. Rupture lives of intercritical heat affected zone material lie on the parent material line. Examination of the data reveals that, throughout the range of available information, equal rupture strengths for weld and parent metals are achieved

at a hardness ratio of weld to parent equal to 1.423. By contrast, data for renormalised weld metal and renormalised coarse-grained heat affected zone material fall on the parent material line, implying equal strengths at equal hardnesses.

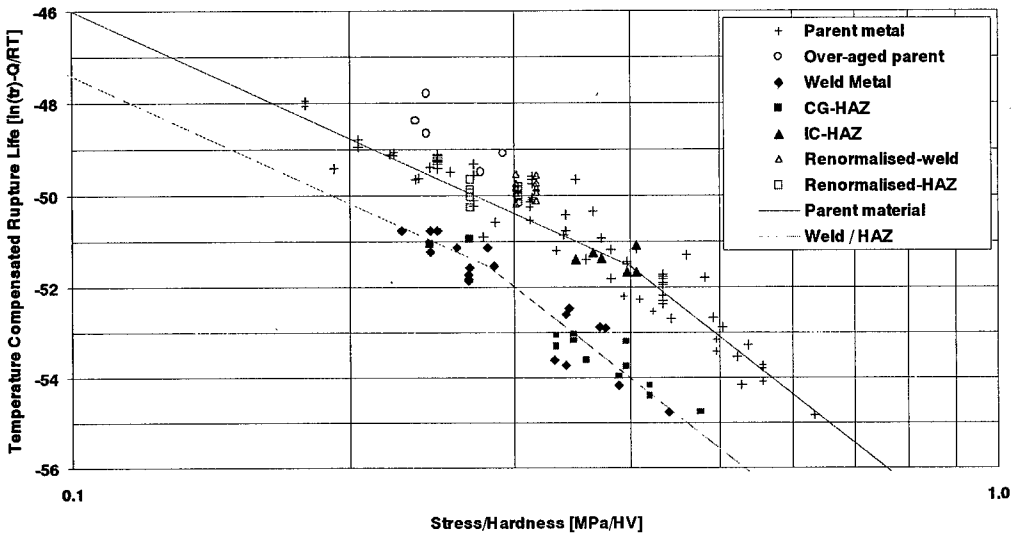

Fig. 1 Hardness compensated creep rupture data for 2¼CrMo steels tested in vacuum.

Having demonstrated the difference in hardness ratio for equal creep strength between the two post weld heat treatment conditions, the remainder of this paper addresses sub-critically heat-treated welds only.

3.2 Failure location - 2¼CrMo steel

From the separation between the parent and weld metal rupture lines in Fig. 1, it is possible to construct a weld predictor diagram, Fig. 2, showing the equal strength condition as a diagonal line on a weld versus parent hardness plot. On either side of this line, the relatively weaker component is predicted to fail first. Points defining an individual weldment may be plotted on this graph and from their position the failure location may be predicted. A weldment is shown as a vertical line, representing the weld metal and coarse-grained heat affected zone hardnesses (vertical axis) plotted against the parent material hardness (horizontal axis). Points above the line indicate that the weld metal is stronger than the parent metal and therefore failure in the parent material is to be expected. The converse applies below the line. Where the weld metal and coarse grained heat affected zone differ significantly in hardness, or show marked internal variation, it is the relatively weakest region that dominates.

All the cross-weld data from specimens that show clear parent, coarse grained heat affected zone or weld metal failure have been plotted on this diagram and it is seen that (with one borderline exception) all failures have occurred in the region predicted. The graph as shown is stress and temperature independent. At a specific pair of conditions, rupture life contours can be added to enable both life and failure location prediction for a given weldment.

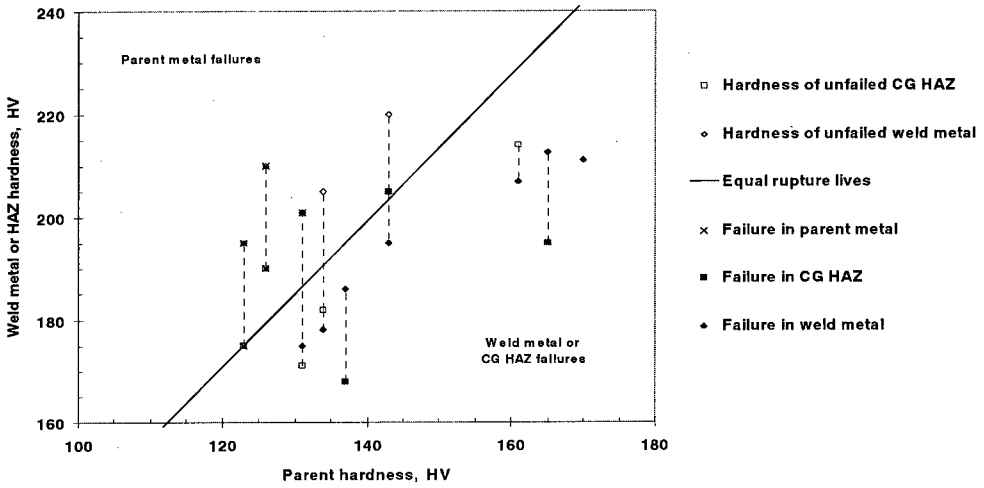

Fig. 2 Weld failure location predictor diagram, for tests that fail before the onset of Type IV cracking, for 2¼CrMo steel.

At longer times, the situation is complicated by the occurrence of Type IV cracking (in the intercritical region of the heat affected zone). By its long-term nature, this failure mode is difficult to achieve in laboratory testing; however a mix of research and plant assessment work has generated some results at 600 and 620°C. Even in programmes where this failure mode has not been directly observed, the tests performed have, nevertheless, enabled some progress to be made in estimating the temperature dependence of its onset. It is interesting that the implied value of the activation energy for the onset of Type IV failures is almost exactly Q/4, where Q is the same as that required for rupture in equation 5 and Fig. 1. The significance of this factor of 4 in the temperature dependence of Type IV failures is not understood.

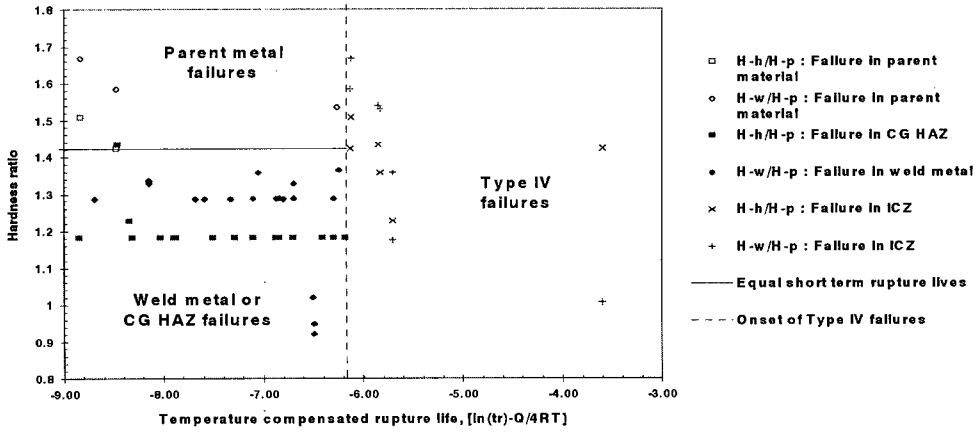

Fig. 3 Weld failure location predictor diagram, including the Type IV cracking regime, for 2¼CrMo steel.

A second type of weld failure predictor diagram can now be constructed; it is shown in Fig. 3. Here, the vertical axis represents the weld to parent metal hardness ratio. Thus the diagonal equal strength line of Fig. 2 becomes a horizontal line. The abscissa is the time-temperature parameter derived for the onset of Type IV failures. Three regions are generated. At shorter times, the failure location varies from parent to weld metal (or coarse grained heat affected zone), dependent solely on the relative hardnesses. At longer times Type IV failures occur, independent of hardness ratio. In all three regions, stress (at least in the range studied) controls life, but not failure location. There are insufficient results at present to construct a rupture life plot for the Type IV failures.

3.3 Other steels

Given the reasonable success obtained with 2¼CrMo steel welds, work has commenced on other materials - 1CrMo, Grade 91(9CrMoVNb) and ½Cr½Mo¼V. Similar patterns emerge, though as yet the full picture has yet to be obtained.

For 1CrMo, short-term tests indicate similar behaviour to 2¼CrMo, with a weld to parent metal hardness ratio of 1.2. There is not yet sufficient long-term laboratory data to establish the criteria for the onset of Type IV failures in this material.

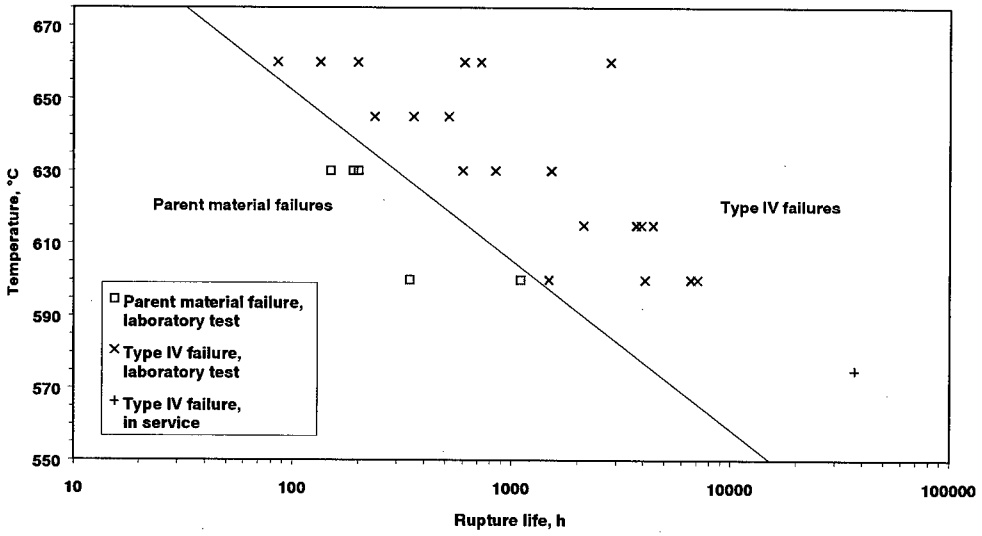

Fig. 4 Weld failure location predictor diagram, for Grade 91 steel.

The behaviour of Grade 91 welds is interesting, in that Type IV failures occur relatively early. It appears that the increase in parent material strength over that of conventional 9CrMo steels is not maintained by the intercritical region of the heat affected zone - to the extent that normal design-code weld factors may not be conservative. Work to date indicates that, as with 2¼CrMo, a time-temperature parameter is sufficient to define the boundary of the Type IV failure regime. This is shown in Fig. 4. In this case, the activation energy is approximately one fifth of that for rupture. The high hardness of the weld metal and coarse grained heat affected zone, compared to the parent, seems to preclude failures in these regions within the timescales studied.

In British practice, it is usual to weld ½Cr½Mo¼V steel with 2¼CrMo weld metal. This makes the situation more complicated than that observed on the other three steels referred to here, where matching electrodes are used. The ½Cr½Mo¼V parent material is much stronger than the 2¼CrMo weld metal, precluding parent material failures in both laboratory tests and service weldments. However, Type IV failures occur, as does another type, peculiar to welds of this nature. Type IIIa cracking occurs in the fully refined regions of the heat affected zone, close to the fusion boundary, and results from strength loss due to carbon depletion, driven by the difference in carbon potential between the weld and parent materials [8]. Data available at present indicate that, in the short-term, Type IV failures occur when the coarse-grained heat affected zone and weld metal are above a critical hardness. Below this hardness limit, weld metal failures are seen. At longer times, Type IIIa failures occur; this is consistent with the diffusion process that underlies the Type IIIa mechanism. There is some evidence that the critical time for Type IIIa failure onset is influenced by the hardness of the weld metal. This is reasonable since, as with Type IV, the failure mode involves the presence of a narrow, soft zone adjacent to a wider, hard region. In practice, geometric factors often lead to mixed mode failures, involving both Type IIIa and Type IV regions of the weldment. Accordingly, no attempt has been made to draw a boundary between these regimes in the failure location diagram, presented in Fig. 5. At this stage, the exact boundary between weld metal and Type IIIa/IV failures is also not fully defined, but estimated on available evidence. Service experience of Type IIIa failure is consistent with the laboratory work, as shown in Fig. 5.

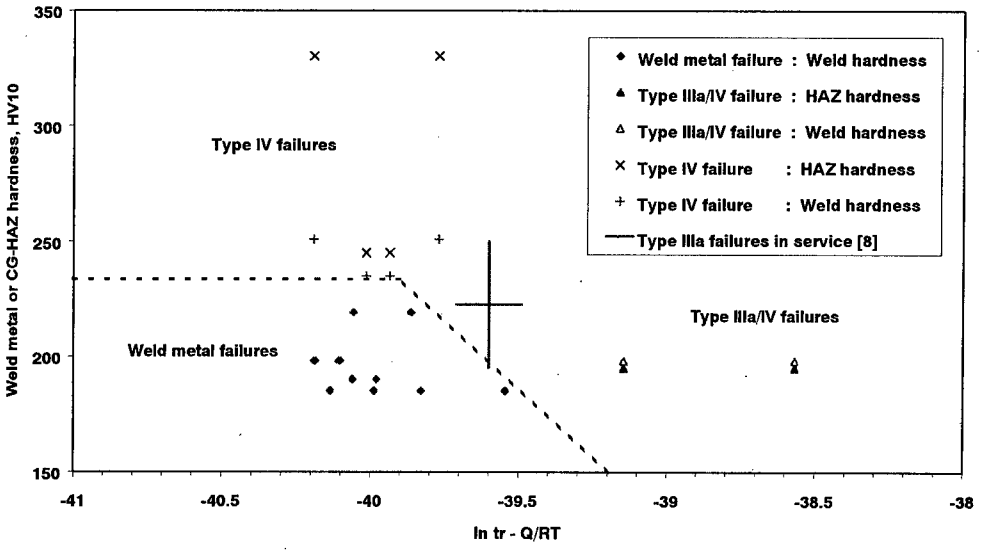

Fig. 5 Weld failure location predictor diagram, for ½Cr½Mo¼V steel welded with 2¼CrMo.

4 Conclusions

The findings of the present work confirm the validity of the hardness based creep model and the application of a simplified version to weldments. The role of relative strength difference in controlling short-term failure location can now be considered well established and appropriate use can safely be made of the predictor diagram.

So far as Type IV failures are concerned, the strong time-temperature dependence and lack of hardness ratio effects for most weld geometries seem clear, but require further validation and a fuller understanding of the details needs to be developed. It is also necessary to explore the boundary between the behaviour observed in the present work and the role of hardness previously reported in the more highly constrained double-V welds.

On current evidence, the general behaviour of 1CrMo, 2¼CrMo and Grade 91 steels is similar, differing only in detail. That of ½Cr½Mo¼V steel welded with 2¼CrMo is somewhat different, as the mismatch of material generates a wider strength difference and also gives rise to an additional failure mechanism. Further work on mismatched and transition welds is clearly required.

5 Acknowledgements

This paper is published with the permission of ERA Technology Ltd. Thanks are due to numerous colleagues, at ERA and several collaborating organisations, for stimulating discussions and for access to test material and data.

6 References

1) Cane, B.J., Aplin, P.F. and Brear, J.M., 4th Int Conf on 'Creep', JSME, IMechE, ASME, ASTM, Tokyo, April 14-18, 1986, p447

2) Bissell, A.M., Cane, B.J. and Delong, J.F., Int Conf 'Life assessment and Extension' VGB, KEMA, CRIEPI, EPRI, The Hague, June 1988

3) Tack, A.J., Brear, J.M. and Seco, F.J., Fifth Int Conf 'Creep of Materials', Orlando, Florida, May 1992

4) Brear, J.M., D'Angelo, D., Seco, F.J. and Tack, A.J., ERA European Conf ''Life Assessment of Industrial Components and Structures'. Cambridge, October 1993, Paper 4.3

5) Cane, B.J., Brear, J.M and Aplin, P.F., Third Int Conf 'Creep and Fracture of Engineering Materials and Structures', Swansea, April 1987, Published Inst Metals, London 1987, pp 853-868

6) Brear, J.M. and Aplin, P.F., Proc. Fifth Int Conf 'Creep and Fracture of Engineering Materials and Structures'. Swansea, April 1993, Published Inst Metals, London 1993, pp 73-79

7) Brear, J.M., Middleton, C.J. and Aplin, P.F., Baltica IV, 'Plant Maintenance for Managing Life and Performance'. Helsinki, Sept 1998, VTT Symposium 184, pp 213-224

8) Brett, S.J. and Smith, P.A., Baltica IV, 'Plant Maintenance for Managing Life and Performance'. Helsinki, Sept 1998, VTT Symposium 184, pp 225-237

Contacts: e-mail: info@era.co.uk

Web site: http://www.era.co.uk/

FAX: +44 1372 367070

Key Engineering Materials Vols. 171-174 (2000) pp. 43-50
© 2000 Trans Tech Publications, Switzerland

Characterization of Creep Fracture for Weld Fusion Line Cracks

K.B. Yoon[1] and J.S. Lee[2]

[1] Associate professor, Department of Mechanical Engineering, Chung-Ang University, 221 Huksuk Dongjak, Seoul 156-756, Korea

[2] Graduate Research Assistant, Graduate School Chung-Ang University, 221 Huksuk Dongjak, Seoul 156-756, Korea

Keywords: Crack, Creep, Weld, Fusion Line, High Temperature, C_t, C^*-Integral

Abstract : Long-term service cracking problems of the most high temperature components occur mainly at welded locations. These cracks are formed due to accumulated creep damage near fusion lines or at heat affected zones(HAZ) of the weld. In this study, creep crack growth test conditions with a crack along the weld fusion line are simulated by the finite element method. Since a new C_t-estimation scheme for a weld fusion line crack is required for characterizing the experimental creep crack growth data, computational studies on the C_t parameter for the fusion line crack are carried out. In performing the finite element analysis, crack tip plasticity as well as secondary creep behavior of the materials are considered. The obtained C_t versus elapsed time curves for various material property combinations are normalized by a steady state C_t value, (C^* for homogeneous specimen) and a transition time t_T, respectively. After normalization a unique C_t versus time curve was obtained. Using this curve, a new C_t-estimation scheme for the weld fusion line crack is proposed.

1. Introduction

When cracks are found at high temperature components such as boiler headers, steam pipes, chemical reactors and turbine casings, it has been usual practice to remove the cracks immediately by weld repair. However, sometimes such weld repair does not seem to be practical. Limited accessibility to internal ligament cracks around the header bore holes or frequent recurrence of cracking in turbine casings after weld repair are well-known such reasons that make the weld repair difficult. In these cases, it may be inevitable to use the components without removing the cracks until the next overhaul or until replacement. Hence, accurate residual crack growth life assessment is necessary to ensure the safety of the components. Very often these cracks (Type IV crack) are usually generated and grow along the narrow band of heat affected zones or along the weld fusion lines formed between base metal and weld metal [1]. For this type of weld interface cracks, proper fracture parameters for characterizing the creep crack growth behavior should be studied for accurate residual life assessment. For elastic-secondary creeping material, a proper fracture parameter under extensive creep condition is C^*-integral [2]. And, under transient creep, C_t-parameter has been used as a proper fracture parameter for characterizing creep crack growth rate [3]. Applicability of C_t to various conditions also has been studied extensively [4-6]. However, applicability of C_t needs further study for a crack located between two materials such as a weld interface crack between weld metal and base metal or other types of interface cracks. Previous estimation equations for C_t have been derived for a crack in homogeneous body. Therefore, they cannot be used for weld fusion line crack problems.

In this study, finite element analyses were performed for a compact tension specimen model with an interface crack along the crack plane. It was assumed that the C(T) was under constant loading condition of Mode I for elastic-secondary creeping materials and elastic-plastic-secondary creeping materials. For various creep and plastic constant combinations for weld and base metals, C_t variation trends with elapsed time were obtained. From the results, effects of creep and plastic constants on C_t variations were studied.

2. Background

If a material shows elastic-plastic-secondary creeping behavior, the constitutive law is expressed as shown in Eq. 1.

$$\dot{\varepsilon} = \frac{\dot{\sigma}}{E} + \dot{\varepsilon}_p + A\sigma^n \tag{1}$$

Where, A is creep coefficient, n is creep exponent, E is elastic modulus and dotted symbols are time derivatives of strain, stress and plastic strain, respectively. C_t under small scale creep condition [7] is expressed as shown in Eq. 2 in terms of measurable load line deflection rate, $\dot{V}_c$.

$$C_t = \left(\frac{F'}{F}\right)\frac{P\dot{V}_c}{BW} \tag{2}$$

Under the steady state creep condition, C_t becomes equivalent to C^* of Eq. 3.

$$C^* = \eta\frac{P\dot{V}_c}{BW} \tag{3}$$

Where, η (a/W) of Eq. 3 is defined in reference [2,7]. During the transition creep condition, C_t is expressed as shown in Eq. 4 by combining Eqs. 2 and Eq. 3.

$$C_t = \frac{P\dot{V}_c}{BW}\frac{F'}{F} - C^*\left(\frac{F'}{F}\frac{1}{\eta} - 1\right) \tag{4}$$

For elastic-secondary creeping materials, C_t can also be calculated from material creep constants, crack size and loading conditions using Eq. 5 without measuring the load line deflection rate [3].

$$C_t = \frac{4\alpha\beta\tilde{r}_c(\theta,n)}{E(n+1)}(1-\nu^2)\frac{K^4}{W}\frac{F'}{F}(EA)^{\frac{2}{n-1}}t^{\frac{n-3}{n-1}} + C^* \tag{5}$$

Symbols for Eq. 5 are same as defined in ref [3]. If crack tip plasticity is considered, Eq. 5 should be modified. When the load is applied, crack tip stress field is relaxed due to instantaneous plastic deformation at the crack tip from the beginning of load hold period. Hence, the initial crack tip stress singularity is much weaker than that of elastic-creeping material and C_t value is also decreased. t_{pl} was defined to consider this effect [8]. t_{pl} was defined as shown in Eq. 6.

$$t_{pl} = \frac{1}{EA}\left[\xi\left(\frac{m-1}{m+1}\right)\left(\frac{1}{2\sigma_{ys}}\right)^2\frac{1}{\alpha\tilde{r}_c(90°,n)}\right]^{\frac{n-1}{2}} \tag{6}$$

In Eq. 6, m is plastic exponent, σ_{ys} is yield strength and ξ is material property depending on m and n values. Equation of C_t for elastic-plastic-secondary creeping materials was derived from Eq. 5 by substituting t with $t+t_{pl}$ [8] as shown in Eq. 7.

$$C_t = \frac{4\alpha\beta\tilde{r}_c(\theta,n)}{E(n+1)}(1-\nu^2)\frac{K^4}{W}\frac{F'}{F}(EA)^{\frac{2}{n-1}}(t+t_{pl})^{\frac{n-3}{n-1}} + C^* \tag{7}$$

Eq. 4 and Eq. 7 are used under overall creep conditions from the small scale creep condition to the extensive creep condition for a cracked homogeneous body. Hence, these equations cannot be used for weld fusion line cracks. These expressions of C_t such as Eqs. 4 and 7 derived under the assumption of homogeneous material should be modified for weld fusion line cracks [9].

3. Finite Element Analysis

A compact tension, C(T), specimen geometry under plane strain condition was analyzed for constant loading conditions. Dimension of the C(T) specimen previously employed for experimental[1] and computational[10] study was used for modeling. Width of the C(T) was 30 *mm*, thickness was 13 *mm*, and crack ratio was 0.5. Static load of 3920 *N* was applied at the nodes of upper half of the pin hole as shown in Fig. 1. The node at the end of extension of the crack plane is fixed as a boundary condition. Figure 1 shows modeling of the crack along weld fusion line in the C(T) specimen. C_t values were determined from the load line deflection rate data, $\dot{V}_c$, obtained from a nodal point at the load line. This is similar to the case when C_t

values were determined by experimentally measure load line deflection rate data. Material properties used in the analysis were the experimentally measured 1Cr-0.5Mo steel data[1] for the base metal and the reported 1.25Cr-0.5Mo steel weld data [11] for the weld metal. Variations of the material property data were made in the scope of real property range. In order to compare C_t variations of the welded C(T) specimen with those of the homogeneous C(T) specimen, both of the welded specimen and the homogeneous specimen were modeled and analyzed. For the homogeneous specimens, analysis with the weld metal properties as well as one with the base metal properties were performed. Material properties such as tensile and creep properties used in these analyses are summarized in Table 1.

Six different cases with various creep and plasticity properties were analyzed for welded specimen and accompanying twelve homogeneous specimen analyses were performed. Material property combinations used for the analyses are summarized in Table 2. In order to avoid problems caused by material incompressibility, 8-node reduced integration elements (ABAQUS Library(3) Element Type CPE8R) were used [12]. Number of elements was 918 and number of nodes was 2941 in the model.

Table 1 Tensile and creep properties of base and weld metals.

Material	Temp. (℃)	E (GPa)	ν	Yield Strength (MPa)	Tensile Strength (MPa)	D (MPa^{-m})	m	A ($MPa^{-n}hr^{-1}$)	n
Base	25	205	0.3	282.0	494.5	2.54E-13	4.68	-	-
Weld				198	382	2.65E-10	3.24	-	-
Base	538	175	0.3	258.8	308	4.95E-34	12.75	1.83E-24	9.03
Weld				136	235	4.03E-17	6.11	6.36E-23	9.36

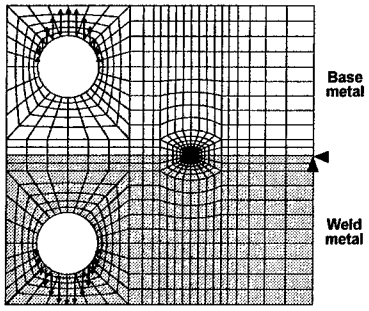

Fig. 1 Finite element mesh for welded specimen analysis.(white: base metal, gray: weld metal)

4. Results and Discussion

4.1 Plastic zone and creep zone evolution of the welded specimen

In Fig.2(a), results of elastic-secondary creep analyses (EL-SC) are compared with those of elastic-plastic-secondary creep analyses (EL-PL-SC). In the analyses, creep constants used for base metal were A=1.27E-23 $MPa^{-n}\cdot hr^{-1}$, n=9.36, those for weld metal were A=1.27E-23 $MPa^{-n}\cdot hr^{-1}$, n=9.36 and plasticity constants for both of the base and weld metals were D=4.95E-34 MPa^{-m}, m=12.75. This figure shows that the trend of C_t variation of elastic-plastic-creep analysis approaches to and becomes identical to that of elastic-creep analysis after a certain period of elapsed time. In Fig.2(b)-(e) evolution of creep zone near the crack tip is illustrated in case of elastic-plastic-secondary creep analysis at the time marked in Fig.2(a). Black region in the figure indicates the creep zone where accumulated creep strain becomes larger than elastic strain. In the white region, the creep strain is less than the half of the elastic strain. When the elapsed time is relatively short, creep zone evolution is negligible as shown in Fig.2(b). As the elapsed time is increasing, the specimen is under the small scale creep condition as shown in Fig.2(c). Fig. 2(d) shows the

creep zone in the vicinity of the transition time from the small scale creep condition to the extensive creep condition. As shown in these figures creep zone size in the weld metal becomes much larger than that in the base metal because the base metal is more creep resistant than the weld metal. Under the extensive creep condition, the creep zones of the both metals extend to the whole uncracked ligament as shown in Fig.2(e). In Fig. 3 sum of creep strain and plastic strain($\varepsilon_c+\varepsilon_{pl}$) is considered as accumulated creep strain and illustrated at the same elapsed time scale as shown in Fig.2. Again, black region in the figure indicates the region where sum of creep strain and plastic strain becomes larger than elastic strain. Compared Fig.3(a) with Fig.2(b), plastic zone grew at the crack tip from the beginning of load application. Hence, initial load line displacement rate was retarded than that of elastic-creeping materials. As time elapsed, creep strain become dominant and initial plastic strain can be neglected. Consequently, shape of Fig.3(c),(d) are almost equivalent with Fig.2(d),(e).

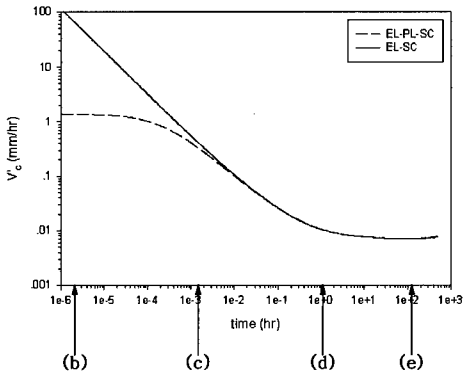

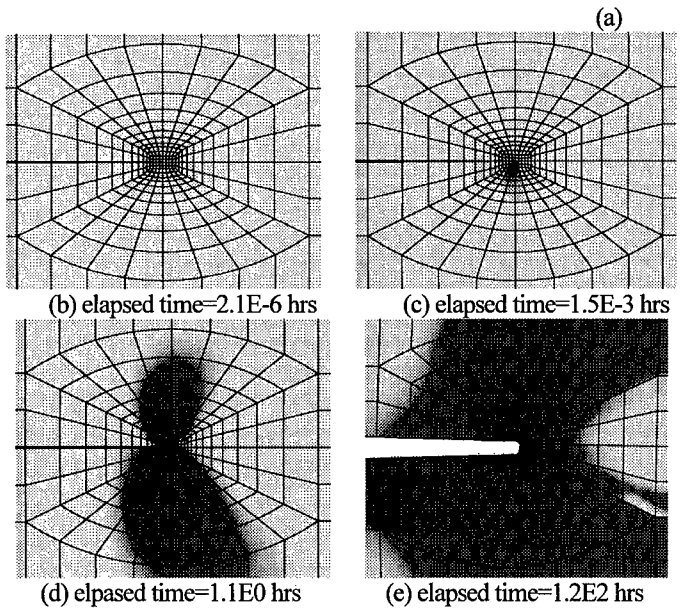

Fig.2 Contour plots of creep zone evolution. (black resion : $\varepsilon_c/\varepsilon_e \geq 1$, white region : $\varepsilon_c/\varepsilon_e \leq 0.5$)

4.2 Dependence of C_t variations of welded specimen on creep and plastic constants

In order to investigate dependence of C_t variations on the material creep constants and plastic constants for the welded specimen, analyses were performed for various combinations of creep and plastic constants for each of the base and weld metal.

Table 2. Material properties for welded specimen analyses

Analysis		D (MPa^{-m})	m	A ($MPa^{-n} \cdot hr^{-1}$)	N
EL-SC	Weld	-	-	6.36E-23	9.36
	Base	-	-	1.27E-23	9.36
		-	-	6.36E-23	9.03
EL-PL-SC	Weld	4.95E-34	12.75	6.36E-23	9.36
	Base	4.95E-34	12.75	1.27E-23	9.36
		4.95E-34	12.75	6.36E-23	9.03
	Weld	4.95E-34	12.75	6.36E-24	9.36
	Base	4.95E-32	12.75	6.36E-24	9.36
		4.95E-34	12.00	6.36E-24	9.36

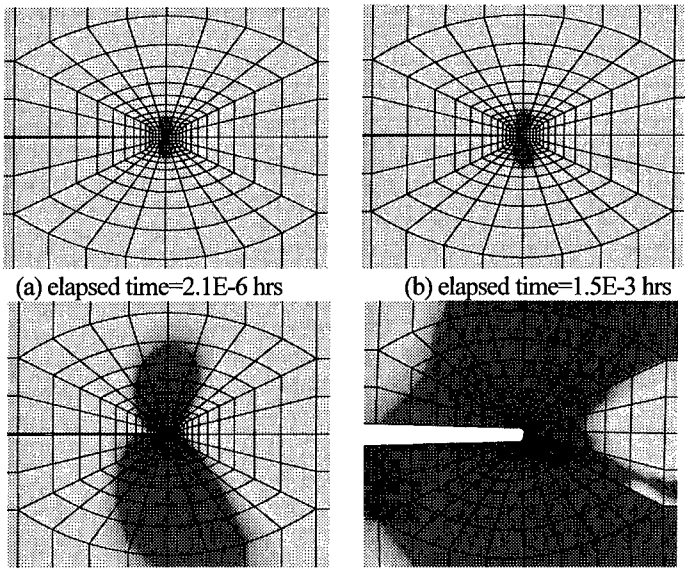

(a) elapsed time=2.1E-6 hrs (b) elapsed time=1.5E-3 hrs

(c) elpased time=1.1E0 hrs (d) elapsed time=1.2E2 hrs

Fig.3 Contour plots of plastic-creep zone evolution. (black : $(\varepsilon_c+\varepsilon_p)/\varepsilon_e \geq 1$, white: $(\varepsilon_c+\varepsilon_p)/\varepsilon_e \leq 0.5$)

As shown in Table 2, three sets of analysis were performed. In the first set, effect of creep constants(A, n) on C_t was investigated for elastic- creeping material. Creep coefficient(A) and creep exponent(n) of the weld metal were fixed as 6.36E-23 $MPa^{-n}hr^{-1}$ and 9.36 and those of the base metal were varied. For one analysis, creep coefficient of the base metal was changed to 1.27E-23 $MPa^{-n}hr^{-1}$ and for the other analysis creep exponent was changed to 9.03. In the second set, the similar analysis with the first set was performed for elastic-plastic-creeping materials. In this case the plastic coefficient(D) and plastic exponent(m) of weld and base metal were fixed as 4.95E-34 MPa^{-m} and 12.75, respectively and creep constants were changed. In the third set, for investigating the effect of plastic constants(D, m) on C_t behavior, plastic coefficient of the base metal was changed to 4.95E-32 MPa^{-m} and plastic exponent was changed to 12. Creep properties of base metal and weld metal were fixed as A=6.36E-24 $MPa^{-n} \cdot hr^{-1}$ and n=9.36 and plastic properties of weld metal were fixed as D=4.95E-34 MPa^{-m} and m=12.75.

In Figures 4~6, the C_t variation of the welded specimen of these analyses are shown together with the C_t variations obtained for homogeneous specimens. For C_t variation of the homogeneous specimen with the base metal, a dashed line(---) is used and for that of the homogeneous specimen with the weld metal, a solid line(——) is used. A dash-dotted line(– · –) is used for the welded specimen in the same figure.

In evaluating the C_t values, load line deflection rate data were inserted into Eq. 2. In reducing the data of

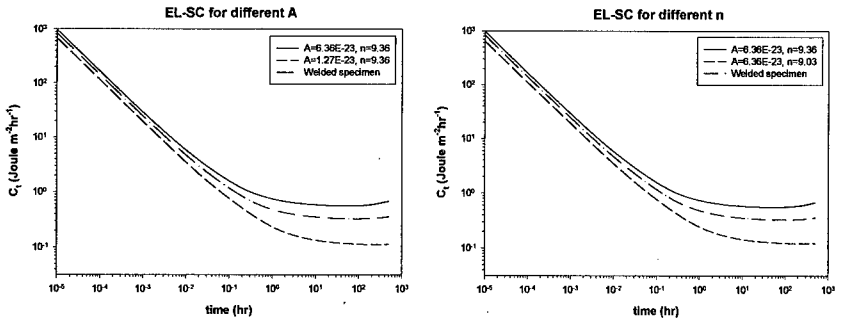

Fig.4 Variations of C_t for EL-SC analyses with different creep properties.

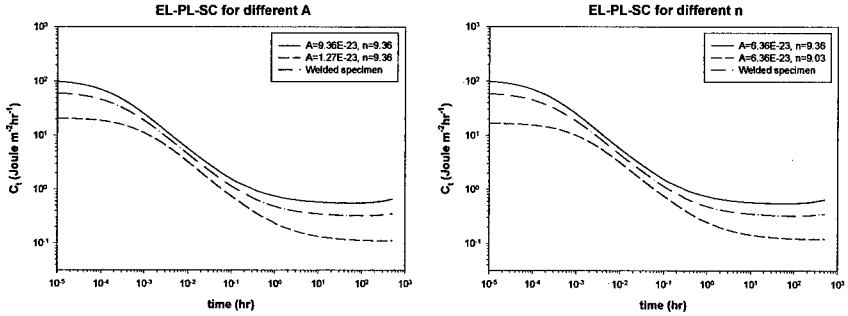

Fig.5 Variations of C_t for EL-PL-SC analyses with different creep properties.

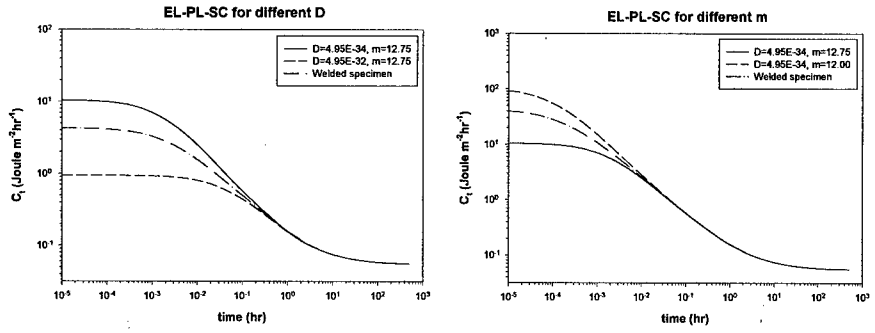

Fig.6 Variations of C_t for EL-PL-SC analyses with different plastic properties.

the welded specimen analysis, load line deflection rate obtained from the base metal part (upper half of the model shown in Fig. 1) and that of the weld metal part (lower half of the model) were not separately determined. This is because the quantity that we can measure experimentally is not the load line deflection rate of each part but the total load line deflection rate which is addition of both rates. Therefore, in this paper the total load line deflection rate values obtained by the analysis were used in determining the C_t values. Even though Eq. 4 is known to be more accurate than Eq. 2 for evaluating C_t in the whole ranges of creep conditions including conditions from the small scale creep condition to extensive creep condition, Eq. 4 could not be used since C^* values of the welded specimen is not defined analytically. Hence, by using Eq. 2 approximate values of C_t were estimated.

For the case of elastic-creeping material shown in Fig. 4, initially high C_t values under small scale creep condition decrease with the elapsed time and reach to the steady state value under the extensive creep condition. The steady state value is equivalent to the C^* value for the homogeneous specimens. Magnitude of the steady state C_t value for the welded specimen is smaller than that of the homogeneous specimen with

weld metal properties and larger than that of the homogeneous specimen with base metal properties. For the case of elastic-plastic-creeping materials, retardation of C_t at the beginning of the load hold period is observed, which disappears after a certain period of elapsed time. From Fig. 4 and Fig. 5, we can see that the homogeneous specimen of the weld metal reaches the steady state condition earlier than the base metal and that the steady state C_t value is higher. This is because the values of A and n of the weld metal is higher than those of the base metal.

For the welded specimen, it was shown from the figure of creep zone evolution(Fig. 2) that the weld metal half reaches extensive creep much faster than the base metal half. Accordingly, apparent C_t variation of the welded specimen which is composed of the weld metal half and the base metal half is much affected by the creep properties of the weld metal rather than that of the base metal. This explains why the dash-dotted line representing the C_t variation of the welded specimen is closer to the dashed line than to the solid line as shown in Fig. 4. For the same reason, transition time of the welded specimen is closer to that of the homogeneous weld metal specimen than to the homogeneous base metal specimen. Same trends were also observed in Fig.5. Figure 6 shows C_t variation when plasticity constants were varied. Generally same trends explained for Fig. 4 and Fig. 5 were observed.

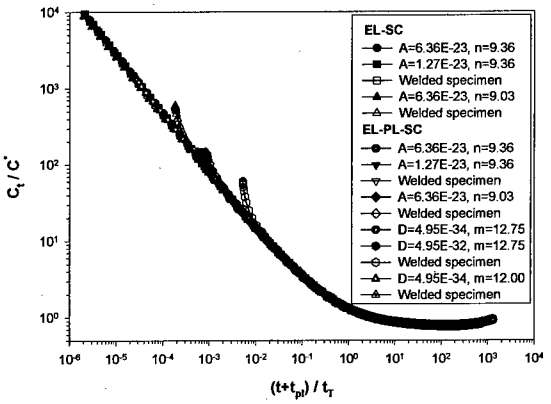

Fig.7 Normalized C_t curve for all of the welded specimen and homogeneous specimen analyses with various creep and plastic properties.

4.3 Normalization of C_t variations

As discussed previously, values of C_t for the welded specimen vary between those for the homogeneous specimen of the base metal and the weld metal. For comparing the trend of C_t variations with each other, the elapsed time t was normalized by the transition time, t_T, and the C_t values at time t was normalized by the steady state value of C_t, $(C_t)_{ss}$ of each case. For the homogeneous specimens, $(C_t)_{ss}$ is equivalent to C^*. For the welded specimens, the $(C_t)_{ss}$ values obtained by the analysis of this study is used. The transition time was determined by Eq. 8.

$$t_T = \frac{K_I^2(1-\nu^2)}{(n+1)E(C_t)_{ss}} \tag{8}$$

Also, in normalizing the elastic-plastic-secondary creep analysis, retardation of C_t is recovered using the concept of t_{pl} whose magnitude is determined by Eq. 6. Since t_{pl} was originally defined[8] to consider retardation of C_t due to instantaneous crack tip plasticity, if we add the retardation level of C_t estimated using the Eq. 6 to the C_t values obtained by elastic-plastic-secondary creep analyses as shown in Figs. 5 and 6, C_t trends of elastic-secondary creeping materials can be predicted. At this time, t_{pl} of the welded specimen was determined as a mean value of the weld and base metals. All of the normalized plots are depicted in Fig. 7. As shown in this figure, the normalized C_t curves of all the homogeneous specimens of the weld metal are coincide with those of the base metal. And these curves are also in good agreement with the normalized C_t curve of the welded specimen. Hence, a unique normalized C_t curve was obtained regardless of the material

properties such as creep properties and plasticity properties.

Indebted to this unique normalized curve, we can easily obtain C_t values of the welded components from Eqs 5-7. Procedures are as follows: For homogeneous materials, C_t vs. time curves can be estimated from Eq. 5 for elastic-creeping material and from Eq. 7 for elastic-plastic-creeping materials. Also, t_{pl} can be estimated from Eq. 6. If these C_t vs. time curves are normalized using C^* and t_T, which are also able to be estimated from known equations, we become to have a normalized unique C_t vs. time curve. Hence, what we need to predict the C_t vs. time curves of the crack in welded structures are only material properties of the base and weld metals of the welded parts.

5. Conclusions

In order to study applicability of the C_t-parameter to a weld fusion line crack problem under high temperature creep conditions, finite element analyses were performed with a compact tension specimen model under various material property conditions. Plasticity constants and creep constants were varied in the analyses.

Apparent C_t variation of the welded specimen which is composed of the weld metal half and the base metal half is much affected by the creep properties of the weld metal rather than the base metal because values of the creep coefficient and the creep exponent of the weld metal is larger than those of the base metal. For comparing the trend of C_t variations of the welded specimen with the homogeneous specimen, the elapsed time, t, is normalized by the transition time, t_T, considering t_{pl} for retardation due to instantaneous crack tip plasticity and the C_t value is normalized by the steady state C_t value, $(C_t)_{ss}$. A unique normalized C_t versus normalized time curve is obtained not only when creep coefficient and creep exponent are varied but also when plasticity coefficient and plasticity exponent are varied for the weld metal and/or the base metal. Discussion is made for application of this result to crack growth life prediction.

Acknowledgement

The authors wish to acknowledge the financial support of the Korea Research Foundation made in the program year of 1998 (Project Number 1998-018-E00091).

References

[1] K.B. Yoon, U.B. Baek and F. Shen *31st ASTM Symposium on Fatigue and Fracture Mechanics, June 21 Cleveland OH USA* (1999)
[2] J.D. Landes and J.A. Begley, *Mechanics of Crack Growth*, ASTM STP 590 (1976), p.695-700.
[3] A. Saxena, *Fracture Mechanics: Seventeenth Volume*, ASTM STP 905 (1986), p.185.
[4] K.B. Yoon, A. Saxena, and P.K. Liaw, *Int. J. of Fracture* 59(2) (1993), p. 95.
[5] K.B. Yoon, U.B. Baek and C.M. Suh, *Elevated Temperature Effects on Fatigue and Fracture,* ASTM STP 1297 (1997), p. 102.
[6] K.B. Yoon, *Proceeding of the KSME Material and Fracture Division* (1997), p. 10.
[7] H. Riedel and J.R. Rice, ASTM STP 700 (1980), p. 112.
[8] K.B. Yoon, A. Saxena and D.L. McDowell, *Fracture Mechanics: Twenty-Second Symposium (Volume I),* ASTM STP 1131 (1992), p. 367.
[9] D.E. Hall, B.C. Hamilton, D.L. McDowell and A. Saxena, *Elevated Temperature Effects on Fatigue and Fracture*, ASTM STP 1297 (1997), p. 19.
[10] K.B. Yoon and K.Y. Kim, *Theoretical and Applied Fracture. Mech.* to be published (1999)
[11] P.K. Liaw, G.V. Rao and M.G. Burke, *Materials Science and Engineering*, A131 (1991), p. 187.
[12] *ABAQUS User's Manual*, Version 5.6, Hibbit, Karlsson & Sorensen, Inc. (1996)

Corresponding Author: Kee Bong Yoon, Fax) +82-2-812-6474, E-mail) kbyoon@cau.ac.kr

Key Engineering Materials Vols. 171-174 (2000) pp. 51-60
© 2000 Trans Tech Publications, Switzerland

The Influence of Material Mismatch of Weld on the Evaluation of Time-Dependent Fracture Mechanics Parameters

S.-T. Tu[1], K.-B. Yoon[2] and J.-M. Gong[1]

[1] Department of Mechanical Engineering, Nanjing University of Chemical Technology, Nanjing 210009, China

[2] Department of Mechanical Engineering, Chung Ang University, Seoul 156-756, Korea

Keywords: Material Mismatch, Time-Dependent Fracture, Weld, Creep Crack Growth, Testing Standard

Abstract The influence of material mismatch on the stress field of uniaxial specimens and the time-dependent fracture mechanics parameters is studied in the present work. It is found that under the extensive creep condition C^* value of hard weld /soft parent metal specimen can be significantly higher than that of single weld metal specimen, and the material mismatch has little influence on $C(t)$ in small scale creep in the studied cases. It is proposed that the C^* formula based on the load-line displacement recommended by ASTM E1457 needs to be modified to interpret the CCG behavior of welded specimens. Candidate modification factors have been proposed. A creep crack growth rate test on SENT specimens has been carried out. The CCG data interpretation in terms of the modified formula illustrates the errors by use of the conventional method.

1 Introduction

In engineering practice, premature failures of weldments due to creep crack growth are a common occurrence. This indicates the detrimental effect of welding on structural integrity and has thus been a problem entangling engineers and researchers since it was introduced into industry. Many fatigue strength data of weldments have been well documented for normal temperatures since the 1950s[1]. In contrast, at elevated temperatures there are only limited studies, that can aid in design and life assessment of the weldments. Over the past 30 years, considerable progress has been made on the creep tests[2 – 4] and theoretical calibration of damage development in the weldments[5 – 7]. However, creep crack growth (CCG) studies seemingly have mostly concentrated on homogeneous materials where the crack growth rate is correlated with $C^*(t)$ in the extensive creep regimes according to ASTM E1457[8], and with C_t in the transition regime from small scale creep to extensive creep[9]. Many available creep crack growth tests on weldments were correlated with $C^*(t)$ or C_t which is generally suitable for homogeneous materials[10,11]. Some recent studies have found that the time-dependent fracture parameters can be significantly influenced by material mismatch indicating that the direct use of the parameters may not be possible[12, 13]. Hence a rigorous mechanics examination of the parameters is needed for predictions of CCG behavior in weldments where the base metal and weld metal have dissimilar creep deformation rates.

In order to provide some mechanics basis for the interpretation of creep crack growth rates, finite element method is used to study the influence of material mismatch on the stress field of a uniaxial specimen and thus on the time-dependent fracture mechanics in the present work. The applicability of conventional C^* equation based on the load line displacement is examined.

2 The Influence of Material Mismatch on the Stress Distribution in Uniaxial Specimen

There have been many examples showing the stress redistributions of a welded pipe subjected to internal pressure[2, 14]. In fact, as long as there is a material mismatch, the stress redistribution is inevitable as creep and damage develop in the materials. Even in a uniaxial cross-weld specimen of a uniform loading section area, the stress redistribution can be significant. In order to have a basic idea of creep stress distribution in the specimens, computations by using finite element method[15] are performed on two types of uniaxial cross-weld specimen. In all the computations the materials are assumed to follow the following constitutive equation:

$$\dot{\varepsilon} = \frac{\dot{\sigma}}{E} + B\sigma^n \tag{1}$$

where σ and ε are the stress and strain respectively, and the dots designate their respective derivatives with time; E is the elastic modulus and B and n are regression constants. The first term on the right-hand side of eqn (1) represents the elastic strain rate that is only pertinent when stress redistribution is occurring. The second term represents the secondary creep portions of the creep deformation behaviour.

A corresponding material mismatch factor is defined as:

$$M = B_p / B_w$$

where B_p and B_w are material constants in eqn (1) with subscripts p and w denote parent metal and weld metal respectively. If $M < 1$, the weld is referred to as creep-soft weld while if $M > 1$, creep-hard weld.

The studied case is a plate specimen of a complete weld profile. The specimen has a width of 12 mm and a length of 40 mm and is loaded in tension at a stress of 100 MPa. Two-material model is used, with $B = 1.772 \times 10^{-14}$, $n = 3.87$ for weld and $B = 1.772 \times 10^{-13}$, $n = 3.87$ for parent metal. The weld metal has a creep strain rate 10 times lower than the parent metal and is a creep–hard weld. Plane strain condition is assumed. Half of the specimen is modelled with 8-node bi-quadratic elements (CPE8R). Computation is carried out until a stationary stress state is reached. In the case of normal temperature, no creep occurs. It is expected that the stress must remain uniform and constant with time. In the high temperature creep case, however, stress redistribution is inevitable. Fig. 1 illustrates the von Mises stress contours in the specimen. Fig. 2 shows the stress along the specimen.

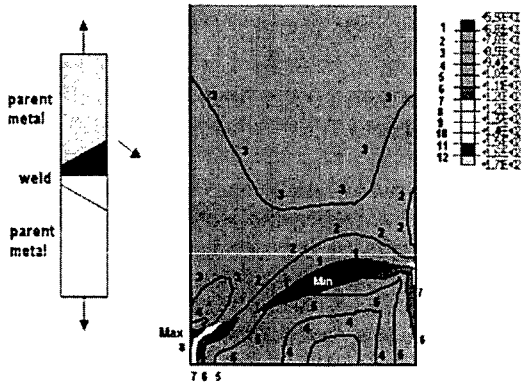

Fig. 1 Von Mises stress contours

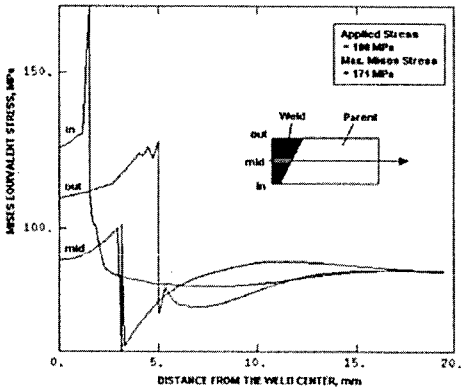

Fig. 2 Mises stress variation along plate specimen

It is seen that the stress distribution is not uniform in the welded specimen. The stress in weld metal is increased while the stress in parent metal is decreased. At the weld root the stress increases to about 1.7 times the applied stress. This is due to deformation compatibility that requires higher stress for the material of smaller creep rate. It can thus be understood that the creep-hard material will generally experience an on-loaded process while the creep-soft material of high creep strain rate an off-loaded process.

The stress redistribution feature due to the mismatch of the material properties suggests that the time dependent fracture parameters in a solid of material mismatch can be very much different from those in a homogenous solid depending on the location of the crack tip.

3 The Influence of Material Mismatch on Time-Dependent Fracture Parameters

It has been shown that the elastic strain rates become negligible compared with creep rates as the crack tip is approached and the near tip stress and strain rate fields are thus of HRR type[16, 17]. The near tip stress and strain fields are expressed as:

$$\sigma_{ij} = \left(\frac{C(t)}{I_n B r}\right)^{1/(n+1)} \tilde{\sigma}_{ij}(\theta, n) \tag{2}$$

$$\dot{\varepsilon}_{ij} = \left(\frac{C(t)}{I_n B r}\right)^{1/(n+1)} \tilde{\varepsilon}_{ij}(\theta, n) \tag{3}$$

where I_n is a factor accounting for stress state and $\tilde{\sigma}_{ij}(\theta,n)$, $\tilde{\varepsilon}_{ij}(\theta,n)$ are non-dimensional functions[18]. $C(t)$ represents the intensity of the stress singularity and is defined as a contour integral. Analogue to the plastic analysis, a creep zone can also be defined by assuming the stress field outside the zone is essentially the same as elastic stress field and its size can be estimated as:

$$r_c(\theta,t) = \beta_c(n,\theta)\left(\frac{K^2}{2\pi}\right)^{\frac{n+1}{n-1}}\left[\frac{I_n}{BC(t)}\right]^{\frac{2}{n-1}} \tag{4}$$

where r_c is the creep zone size, K is the elastic stress intensity factor and $\beta_c(n,\theta)$ a non-dimensional angular function. In the long term, as the creep zone grows and extensive creep condition is achieved, the $C(t)$ approaches a constant value C^*. It had been shown that over the entire transition regime $C(t)$ can be represented as follows within an error of 5%.

$$C(t) \cong \left(1+\frac{t_T}{t}\right)C^* \tag{5}$$

with

$$t_T = \frac{K^2(1-\upsilon^2)}{(n+1)EC^*} \tag{6}$$

As it is demonstrated in the previous section, the creep stress field in a uniaxial cross weld specimen can be quite non-uniform. It is easy to understand that the change in the primary stress field due to material mismatch will certainly influence the evaluation of fracture mechanics parameters. The local crack tip HRR stress field and the primary stress field may also have interacting effect. In order to evaluate the effect of material mismatch, a number of finite element computations are carried out for compact tension (CT) and single edge notched tension (SENT) specimens with and without material mismatch. The finite element models are shown in Fig. 3. The

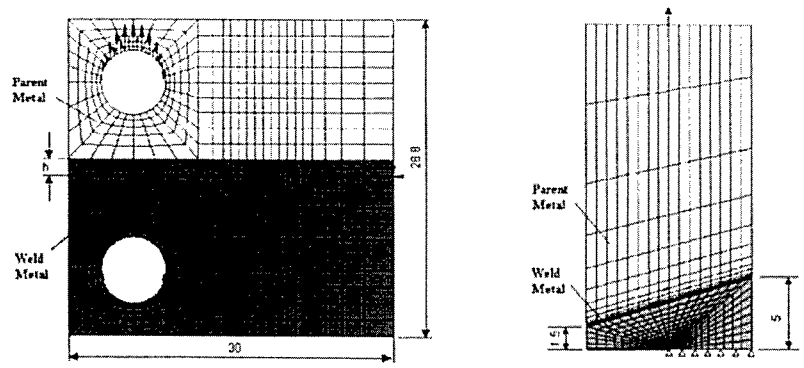

(a) (b)

Fig. 3 Finite element model (a) CT specimen, a/w=0.5, h=1.5 mm: 918 elements, 2941 nodes; (b) SENT specimen, a/w=0.5: 704 elements, 2233 nodes

CT specimen has been widely used and recommended in ASTM E1457. The SENT specimen is generally used for life assessment of welded pipes in-service since it simulates better the constraint and prior damage ahead of a circumferential crack in the weld. 8-node bi-quadratic reduced integration elements (CPE8R) are used in the modelling. The meshes are refined until a converged C^* solution is obtained.

Let us first look into the CT specimen. The specimen has a width of 30 mm and a thickness of 13 mm The material constants are B = 1.772 x 10^{-14}, n = 3.87 for weld metal. The B value is assigned to parent metal according to material mismatch factor while n is kept unchanged. The crack in the model is located at h =1.5mm (the distance between the crack line and the interface). The applied load is 3920 N. For comparison purpose, single weld metal specimens are firstly calculated (M=1). According to eqn (6), the transition time is 219.6 hours.

Fig. 4 shows the development of creep zone in the case M=10. As compared to the single weld material case, in the first 12 hours the shape of the creep zone is almost symmetrical and no evident influence of material mismatch is observed. After 12 hours, however, part of the parent metal also enters the creep region as the result of higher creep strain rate. Two separated creep zones are thus formed. An unbalance development of the creep zone in the crack tip is found. The zone close to the interface is slightly larger than the other due to higher creep stress level created by on-load effect of weld metal. The zones are then connected to each other. Fig. 5 shows the evolution of $C(t)$

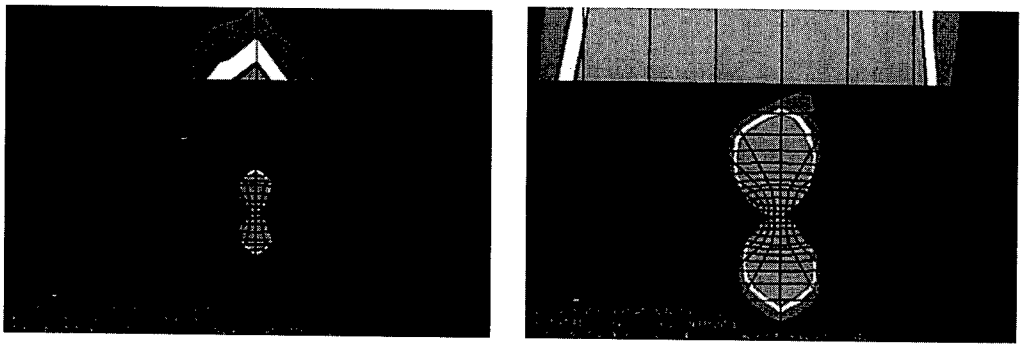

(a) t = 12 hours (b) t = 41.9 hours

Fig. 4 Development of creep zone in specimen M=10

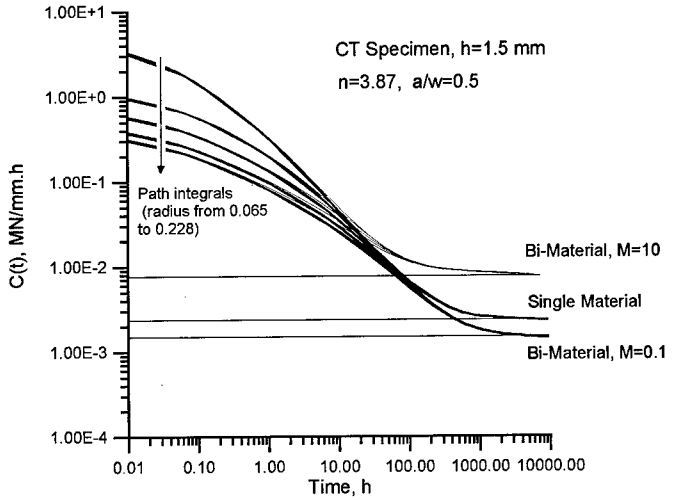

Fig. 5 Evolution of $C(t)$ values with time in CT specimen

values with time. Values from different contour integrals are illustrated in the figure at the same time. Both creep-soft and creep hard welds are calculated. It is obvious that in the small scale creep region the $C(t)$ is a path-dependent variable and curves for specimens of different properties overlap each other indicating that the material mismatch has little influence on $C(t)$ in the small scale creep. After the transition time is finished, all path integrals fall in a same curve showing the path independent feature of $C^*(t)$. When the material mismatch takes effect, i.e. the stress redistribution due to material mismatch plays its role, the $C(t)$ curves deviates from those of the single material specimen. It is seen the transition completes earlier for creep hard weld and later for creep soft weld. Under the extensive creep condition, C^* value of hard weld /soft parent metal specimen is 3.24 times the value of single weld metal specimen, while the value of soft weld/ hard parent metal specimen is about 2/3 of the value of single weld metal specimen.

For the SENT specimen, similar computations are carried out. The specimen has a width of 12 mm, a thickness of 5 mm and a half-length of 20 mm. The same material properties as CT specimen are used. The applied load is a tension stress of 60 MPa on the top of the specimen. For the single weld metal specimen, the transition time given by eqn (6) is 52.87 hours.

Fig. 6 gives a comparison of creep zones between the weld/parent metal specimen and the single weld metal specimen at the same time. No obvious difference is found when the creep is in a small scale. It is seen, however, that in the longer time the creep zone in the weld/parent metal specimen is enlarged due to stress enhancement in the weld. Creep zones are developed both in the weld and parent metals and are connected in the later time.

Figure 7 shows the evolution of $C(t)$ values with time in the SENT specimen. The same trend as the CT specimen is observed. However, the influence of material mismatch is not as significant as that in the CT specimen. This is mainly due to the specimen geometry and the distance between the crack tip and the interface of the two materials. When a welded specimen of a very soft parent metal is encountered (M=100), the C^* is about 3 times that of the single weld metal specimen. However, for a welded specimen of a very hard parent metal (M = 0.01), the decrease of the C^* is not dramatic which is not more than 20%.

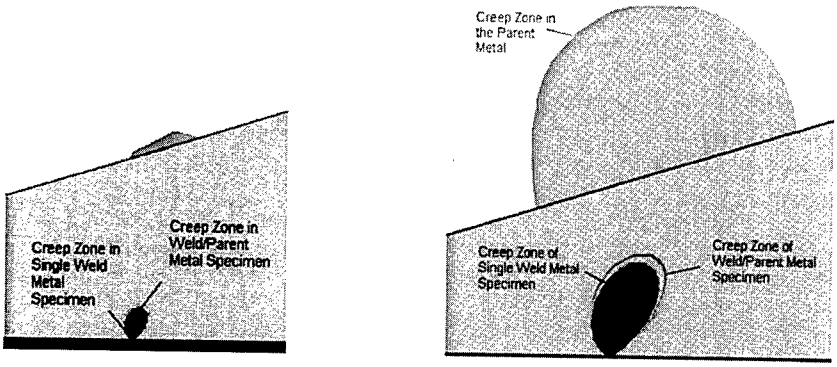

(a) $t = 20.6$ hours (b) $t = 77$ hours

Fig. 6 Comparison of creep zones between the weld/parent metal specimen and the single weld metal specimen

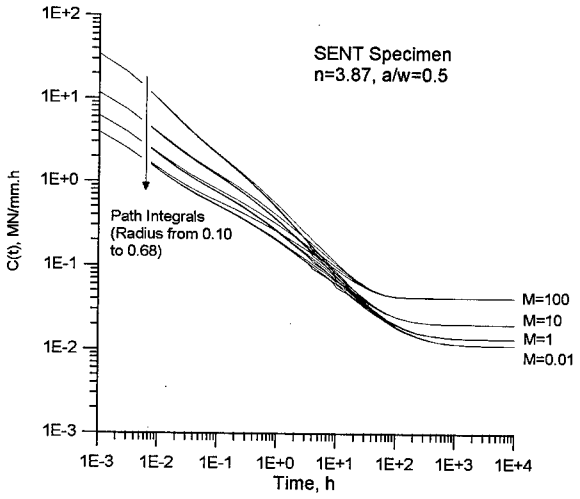

Fig. 7 Evolution of $C(t)$ values with time in SENT specimen

Tentative conclusions can therefore be drawn from the computations: the material mismatch can significantly influence the time-dependent fracture parameters in the extensive creep condition; a higher parent metal creep strain rate will increase the C^* value while a lower parent metal creep strain rate decrease the C^* value.

4 The Applicability of Measured $C^*(t)$ for Two-material Specimen

In the CCG experiments, C^* or C_t are generally calculated in terms of measured load line displacement rather than time-consuming finite element computations. Under steady state creep condition, C^* can be expressed as:

$$C^* = \eta(a/w,n)\frac{P\dot{V}_C}{BW} \tag{7}$$

where η is a function of a/w and n, V_c the load line displacement, P the applied load, B the

thickness and W the width of the specimen. It is apparent that this formula is established without considering the material mismatch. As V_c is also directly measured from the welded specimen, it may reflect partially the influence of material mismatch. But the problem is to what extent that the formula can describe the influence of the material mismatch and how to modify it for welded specimens. A material mismatch coefficient can thus be introduced to modify eqn (7):

$$C_W^* = g(M, a/w, h)\eta(a/w, n)\frac{P\dot{V}_{wC}}{BW} \tag{8}$$

where $g(M, a/W, h)$ describes the material mismatch effect which can be the function of M, a/w, and h. C_W^* is C^*-integral for welded specimen, V_{wc} is the load line displacement.

A division of eqn (8) by eqn (7) results in:

$$g(M, a/w, h) = f(n, a/w, P/BW)\frac{C_W^*}{\dot{V}_{wC}} \tag{9}$$

where $f(n, a/w, P/BM) = \dot{V}_C / C^*$, is determined from a single material specimen.

To quantify the g value, a number of finite element computations are carried out for different n values and also a/w values. The previous CT and SENT finite element models are used.

In order to obtain the f value, the finite element computation is first carried out for a single weld specimen. Based upon the calculated C^* and V_c value, the f value is determined. Then computations are carried out for a number of welded specimens of the same geometry with material mismatches.

Fig. 8 is the variation of g versus material mismatch factor, M for CT specimen. It is seen that $0 < g \leq 1$ for $M \geq 1$ and $g > 1$ for $M < 1$ which implies that the eqn (7) may overestimate C^* for creep-hard weld but slightly underestimate it for creep-soft weld. The n value has a significant influence on the g value. For a same M value, the smaller the n value, the larger of the deviation of g. The distance between the crack tip and the interface line is also a major factor. It seems that reducing the distance may reduce the deviation.

Fig. 9 is the variation of g for SENT specimen when n =3.87. More significant deviation of g is found as compared with CT specimen. For M =10 and a/w = 0.42, the value of g is 0.48 which implies that eqn (7) may overestimate the C^* value of the welded specimen by one time. Eqn (7) may underestimate the C^* value for $M < 1$. A factor of 1.58 is required to modify the eqn (7) in case that M=0.1 and a/w=0.42.

Fig. 10 is the variation of g for SENT specimen when n =11.475. It is obvious that longer crack require less modification due to less interaction between the crack tip and the material interface. As compared with lower n value case in Fig. 9, the deviation of g is less significant.

In order to quantify the possible errors in interpretation of CCGR by use of conventional C^*, creep crack growth tests were carried out on SENT specimens machined from a retired HK40 furnace tube. The test temperature was 850 °C. Two load levels, 20MPa and 21.8MPa were applied. Under the test stresses, the mismatch factor, M equals to 15.13 (21.8MPa) and 19.87 (20MPa) respectively. The modification factor, g can accordingly be found in Fig. 10. Fig. 11 illustrates the correlation between C^* and C^*_W. It is seen a higher CCGR is obtained by use of modified g factor. This implies that the conventional C* that ignores the material mismatch effect leads to a reduced CCGR, which may result in a non-conservative estimation of creep crack growth life.

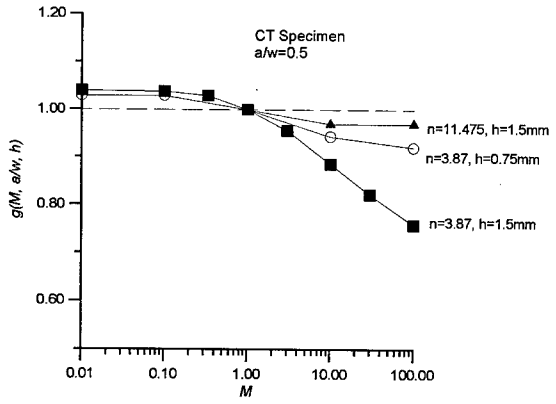

Fig. 8 g value vs. mismatch factor, M for CT specimen

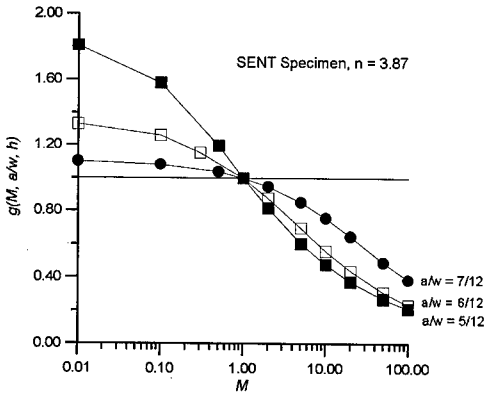

Fig. 9 g value vs. mismatch factor, M for SENT specimen, $n = 3.87$

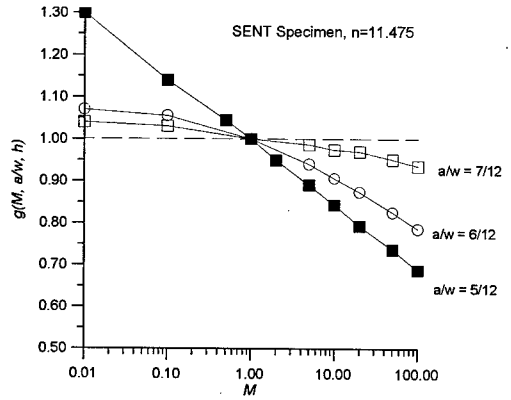

Fig. 10 g value vs. mismatch factor, M for SENT specimen, $n = 11.475$

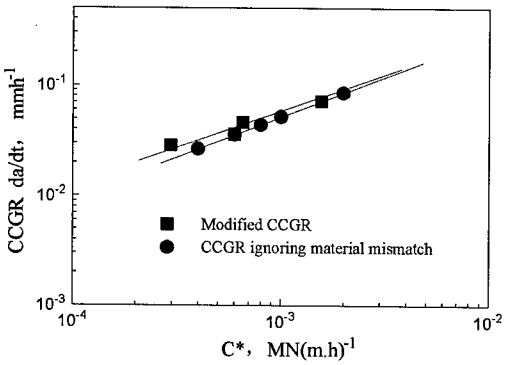

Fig.11 Creep crack growth rates in relation with C^*

5 Conclusions

In order to provide some mechanics basis for the interpretation of creep crack growth rates in the weld, finite element method is used to study the influence of material mismatch on the stress field of uniaxial specimens and the time-dependent fracture mechanics parameters in the present work. The applicability of conventional C^* equation based on the load line displacement is re-examined. Some conclusions have been drawn from the study:

(1) Even in a uniaxial tension specimen, the stress redistribution can be very significant as long as material mismatch exists in the high temperature components.

(2) Under the extensive creep condition, C^* value of hard weld /soft parent metal specimen can be more than 3 times the value of single weld metal specimen, while the value of soft weld/ hard parent metal specimen can be less than 15% of the value of single weld metal specimen. The material mismatch has little influence on $C(t)$ in small scale creep in the cases studied.

(3) The C^* formula based on the load line displacement recommended by ASTM E1457 need to be modified to interpret the CCG behavior of welded specimens. A modification factor, g is introduced. It is found that $0 < g \leq 1$ for $M \geq 1$ and $g > 1$ for $M < 1$, which implies that the recommended formula may overestimate C^* for creep-hard weld but underestimate it for

creep-soft weld.

(4) Creep crack growth tests conducted with SENT specimens from a retired HK40 furnace tube reveals that the conventional C^* that ignores the material mismatch effect leads to a reduced CCGR, which may result in a non-conservative life assessment.

Acknowledgements The supports provided by the China Natural Science Foundation (59875039) and Korean Science and Engineering Foundation (1997 Brain Pool Program) are gratefully acknowledged.

References

[1] S.J. Maddox, *Fatigue Strength of Welded Structures*, Abington Publishing, 1985
[2] M.C. Coleman, J.D. Parker and D.J.Walters, *Int. J. Pres. Ves. & Piping*, **18** (1985) 277-310
[3] M. DeWitte, and G. Cossement, VGB-Conf. "Residual Service Life 1992", Mannheim, 6-7 July 1992, 38. 1-38. 28.
[4] M.Prager, *Serviceability of Petroleum, Process and Power Equipment, PVP-Vol.239,* ASME, New York, 1992, 253-265
[5] S.-T. Tu, R. Wu and R.Sandstrom, *Int. J. Pres. Ves & Piping,* **58** (1994) 345-354.
[6] F.R. Hall and D.R. Hayhurst, *Proc. R. Soc. Lond*, **A, 433** (1991) 383-403
[7] S.-T. Tu and R.Sandstrom, *Proc. 5th Int. Conf. on Creep and Fracture of Engineering Materials and Structures*, B. Wilshire and R. W. Evans eds., Institute of Materials, 1993, 695-704.
[8] ASTM Standard E1457, Standard test method for measurement of creep crack growth rates in metals, 1992
[9] A. Saxena, and P.K. Liaw, EPRI-CS 4688, Electric Power Research Institute, Palo Alto, Ca., 1986
[10] A.Saxena, J.Han and K.Banerji, EPRI Report on Project 2253-10, Electric Power Research Institute, Palo Alto, CA. Apr. 1987
[11] P.R.McCarthy, I.A.Shibli and D.Raynor, *Proc. Int. HIDA Conference: Creep and Fatigue Crack Growth in High Temperature Plant,* 15-17 Apr. 1998, Paris France, S2-12
[12] P. Segle, P. Andersson and L.Samuelson , *Proc. Int. HIDA Conference: Creep and Fatigue Crack Growth in High Temperature Plant,* 15-17 Apr. 1998, Paris France, s2-17
[13] S.T. Tu and K.B.Yoon, Invited Lecture of 1998 Annual Meeting of Korean Welding Society, KWS, October 11-24, 1998
[14] S.-T. Tu and R.Sandstrom, *Int. J. Pres. Ves. & Piping*, **57** (1994) 335-344
[15] ABAQUS, Version 5.7, Hibbit, Karlsson and Sorensen, Inc., 1997
[16] R. Riedel and J.R.Rice, 12th Conf., ASTM STP 700, 1980, 112-130
[17] K. Ohji and S. Kubo, *High Temperature Creep-Fatigue,* eds R. Ohtani, M. Ohnami and T. Inoue, Elsevier, London, 1988, pp.91-113.
[18] Shih, C.F., *Tables of Hutchinson-Rice-Rosengren Singular Field Quantities.* Material Research Laboratories, Brown Univ, MRL E-147, 1983

Key Engineering Materials Vols. 171-174 (2000) pp. 61-68
© 2000 Trans Tech Publications, Switzerland

Rationalisation of the Multiaxial Stress Rupture Behaviour of Components

J.M. Church, J.M. Brear and D.R. Humphrey

ERA Technology, Cleeve Road, Leatherhead, Surrey, KT22 7SA, UK

Keywords: Continuum Damage Mechanics, Stress Rupture, Multiaxial, Stress Rupture Criterion, Stress State, Mechanical Testing, Component Geometry

ABSTRACT

High temperature industrial components invariably experience complex thermal and mechanical loading histories. With regard to degradation and failure as a result of creep deformation and rupture mechanisms, design and remaining life procedures rely extensively on conventional uniaxial creep tests as a source of material and temperature specific property data. Plant assessment often proceeds based upon relatively simple calculations that invariably incorporate distinct levels of conservatism to compensate for inherent uncertainties within the design route. An improved understanding of the influences of component geometry and stress-state upon component creep rupture behaviour will reduce unnecessary conservatisms and potentially extend service lifetime.

In the present paper these concepts are developed to reconcile observed multiaxial stress rupture criteria inferred from tests utilising a range of testpiece geometries. Component rupture under complex loading conditions is seen to depend upon both the materials response and the mechanical interaction between the structure and the loading. These mechanical factors include the component geometry and the evolution of stress during creep life, in addition to the more commonly preferred descriptors of applied stress and stress state. Consideration of these additional elements during the presentation of material stress rupture response enables the true position of component creep rupture results to be determined in relation to uniaxial baseline data.

1. Theoretical Background to Multiaxial Rupture Behaviour

1.1 Historical Approaches to Modelling Rupture Life

The earliest approaches to modelling creep rupture considered the failure of a rod in uniaxial tension. Under constant load conditions, the stress increases with strain, leading to an accelerating creep rate and failure in finite time, with theoretically infinite extension [1]. Though this theoretical ideal cannot be achieved in practice, the rapid evolution of stress in the final stages makes it a reasonably good approximation for a ductile material. It was later realised that neither brittleness nor failure under constant stress conditions could be described in this way. The solution put forward was the concept of damage evolution [2]. In this model, damage evolves as a materials state variable, from zero for virgin material towards unity at failure. This may happen in isolation, or in synergy with strain evolution. This approach, designated *Continuum Damage Mechanics*, continues to be a key element of creep modelling.

Creep life thus depends upon both deformation and fracture mechanisms, and each of these is influenced by both materials and structural factors. Under multiaxial stress conditions, both materials and structural response must be expected to change. The multiaxial stress rupture criterion (MSRC) is intended to accommodate the stress dependencies of the various failure mechanisms and to provide a unifying parameter between uniaxial and multiaxial creep rupture data. In the absence of damage, rupture is controlled by flow processes which, it is generally accepted, are governed by the effective (shear) stress (σ_e). For damage controlled rupture, there is basic justification for the traditional approach of considering rupture as being governed by both effective stress and normal (principal) tensile stress (σ_1). For example, McLean [3] suggests that grain boundary sliding, governed by shear, is the important action in nucleating grain boundary vacancies of a critical size, after which growth is encouraged by diffusion, governed by maximum tensile stress.

Thus the fracture mechanism can be either maximum principal or equivalent stress controlled, or described by a mixed criterion incorporating contributions from both component stresses. A number of workers have described the multiaxial creep rupture behaviour of a range of materials using empirically determined relationships for the MSRC. A review of these criteria is outside the scope of the current work; however, the range is exemplified by the following selection:

$$\sigma_{MSRC} = \lambda\sigma_1 + (1-\lambda)\sigma_e \qquad \text{Sdobyrev} \quad [4]$$

$$\sigma_{MSRC} = \alpha\sigma_1 + \beta I_1 + \gamma I_2^{1/2} \qquad \text{Hayhurst} \quad [5]$$

$$\sigma_{MSRC} = \sigma_1^{v/m} \cdot \sigma_e^{(m-v)/m} \qquad \text{Cane} \quad [6]$$

$$\sigma_{MSRC} = 2.24\sigma_1 - 0.62(\sigma_2 + \sigma_3) \qquad \text{Nix et al} \quad [7]$$

$$\sigma_{MSRC} = \frac{3}{2} S_1 \left(\frac{2\sigma_e}{3S_1}\right)^a \exp\left[b\left(\frac{I_1}{S_s} - 1\right)\right] \quad ; \quad S_s = \left(\sigma_1^2 + \sigma_2^2 + \sigma_3^2\right)^{1/2} \qquad \text{Huddleston} \quad [8]$$

(I_1 and I_2 being the first and second stress invariants)

1.2 Structural Factors

Industrial components rarely experience constant stressing conditions. More typically, the applied load is maintained constant, such that stress increases monotonically with strain. For the relatively common, and simple, case of tubular components subjected to pressure-tension loading, Taira et al [9] have described the changing stress and strain evolution as deformation proceeds, which in the case of thin wall assumptions requires descriptors for the diametral and axial stresses as,

$$\sigma_\theta = \sigma_{\theta o} \exp(\varepsilon_\theta - \varepsilon_r) \qquad \sigma_z = \sigma_{zo} \exp(\varepsilon_z) + \frac{\sigma_\theta}{2}$$

where ε_θ, ε_z and ε_r denote true strains in the hoop, axial and radial directions respectively, $\sigma_{\theta o}$ is the initial diametral stress and σ_{zo} is the initial axial stress generated by the imposition of a tensile load. It is interesting to note that solution of the above for the general pressure-tension loading case predicts both evolving stress levels and evolving stress state.

This evolution of stress state comes about through the non-proportionate interaction between the stresses and strains. That this occurs in such a simple mechanical system immediately implies that it must be taken into consideration in developing any universally accurate MSRC. Just as the evolution of stress with strain can control rupture in a uniaxial bar, so the evolution of stress state with strain can control rupture under multiaxial loading.

It must further be recognized that in many situations, the stress level or stress state are not uniform through the component or test-piece. Stress redistribution in such cases will also contribute to stress state evolution.

1.3 Materials Factors

Figure 1 shows a typical deformation mechanism map for a high temperature engineering steel. In the high stress limit, materials response is governed by instantaneous elastic collapse. However, for practical purposes, instability will be limited by the glide stress, at which time-independent plasticity occurs. Below this limit, regimes of time dependent (creep) flow and brittle intergranular cavitation response will occur – the relative contributions of each, and their interactions, being dependent upon material composition, microstructure and temperature. Material (creep) response below the glide limit has been reconciled through the application of continuum damage mechanics, which allows for the interactive effects of creep strain and damage accumulation [10, 11]. It is unreasonable to expect the MSRC for a given material to remain constant over a change in deformation or fracture mechanism.

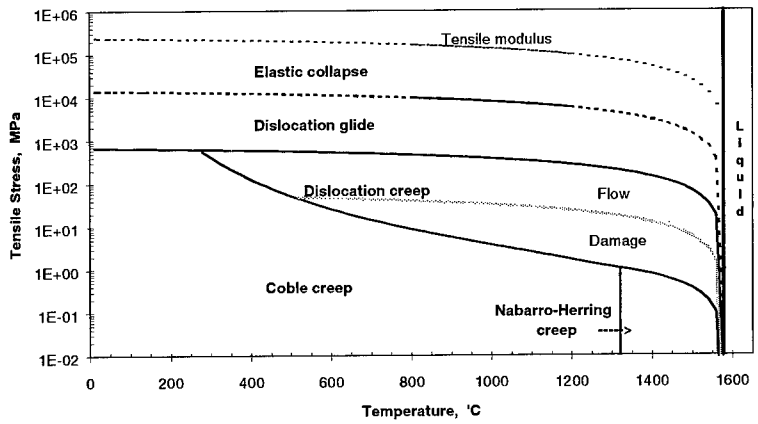

Figure 1: Typical deformation mechanism map in stress-temperature co-ordinates

1.4 Simplifying Assumptions

The above discussion, and indeed the whole of the present paper, considers a very simple situation. The material is assumed to be homogeneous, isotropic and stable - no thermal degradation or embrittlement is allowed. Similarly, all deformation is assumed uniform, the effects of necking or similar instability are neglected. Also, only forward creep is considered; behaviour under displacement control and cyclic effects are not addressed. Each of these factors must be expected to complicate the MSRC further.

2. Multiaxial Mechanical Testing

For a given material, practical determination of the MSRC (which may be temperature dependent) requires testing under multiaxial stressing conditions in addition to baseline uniaxial creep rupture data. Given the influence of both materials and structural factors, it is necessary to classify the different types of test in order to determine what information each can and cannot generate, and how they may be combined.

Table 1 provides a mechanical classification of test type according to the nature of the applied stress, the applied stress-state and the homogeneity of the imposed stress distribution. Under simple uniaxial loading, constant stress and constant load tests provide an illustration of the combined effects of materials and structural factors on rupture behaviour. Figure 2 shows a typical stress rupture curve for conditions that span the glide, flow and damage regimes of Fig. 1. For both test types, the high stress limit is controlled by glide and the low stress behaviour by damage accumulation. In the intermediate

range, under constant load conditions, strain development increases the stress, leading to a flow controlled rupture regime. Under constant stress conditions, this cannot happen and damage controlled rupture persists up to the glide limit. Clearly, a reliable MSRC cannot be obtained from a set of tests that spans such a change in behaviour, without careful analysis.

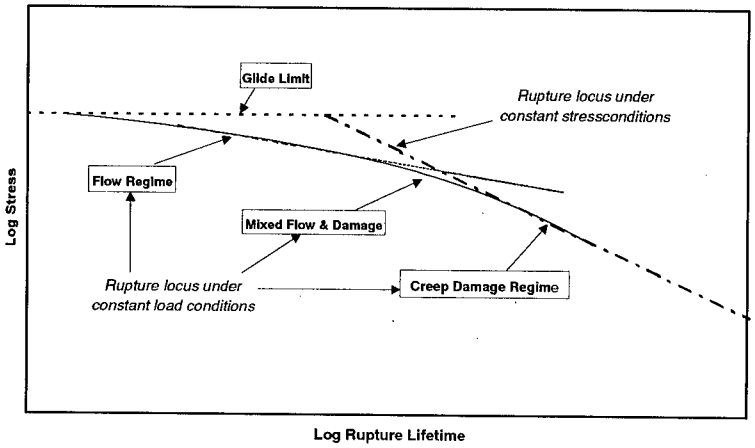

Figure 2: Schematic uniaxial stress rupture response at constant temperature, identifying mechanistic regimes and showing behaviour under constant stress and constant load conditions.

For pure shear, torsion tests on thin-walled tubes and double-shear tests form a similar pair. More general biaxiality can be generated using tubes with internal or external pressure plus an axial end load (though buckling problems limit the practical possibilities in compression). In this case, it must be realised that the stress state evolves, as well as the stress, with strain. This further complicates interpretation. Theoretically, cruciform specimens can also be used to explore biaxial and even triaxial behaviour, though the practical difficulties are immense. It must be realised that the stress state evolution in a cruciform biaxial specimen is different from that in a tube under pressure and end load, for the same starting condition.

The most commonly used triaxial laboratory test is that on a notched bar. Here a further level of difficulty is introduced, since not only do the stress and stress state evolve with strain, but both vary through the cross-section of the specimen. Similar considerations apply to thick-walled tubes and to biaxial disc and bend tests.

This classification is extended in Table 2 to a consideration of the rupture life and ductility to be expected in each test type for different deformation mechanisms. (Clearly, combinations of stress evolution and zero ductility mechanisms are not possible.)

3. Practical Development and Use of a Multiaxial Stress Rupture Criterion

It is clear from the above that a MSRC cannot be generated from a random selection of tests, considering only the initial stress and stress state. However a judicious selection, of developing complexity, can be designed to establish the basic materials behaviour, the response under evolving uniaxial stress and then the effects of stress state and its evolution. For practical purposes, uniaxial tension and tube tests under pressure and end load provide the most flexible and achievable mix. Once a model has been developed which accounts for all structural and materials factors, it can be validated on the more complex bend and notched bar specimens. Usually numerical methods, such as finite element analysis, will be required to achieve this. The validated model can then be applied to real components with confidence. In developing the model, care must be taken to identify and quantify

individual effects within a homogeneous range of materials and structural behaviour, as summarised in these tables.

For simplicity of routine application, it is now common and accepted practice to develop local, approximate solutions to the model for particular, common geometries - such as notched bars and T-piece intersections. These generally take the form of 'reference stress' solutions, where the geometric and loading characteristics are reduced, by an empirical fit to the local solution of the full model, to a single stress that may be directly referred to the uniaxial database.

For the purposes of practical plant life assessment it is often argued that operating stresses are low such that failure will occur at low ductility, which enables constant stress and stress state conditions to be assumed. By contrast, Figure 3 illustrates experimental and predicted creep rupture response of thin walled pressure-tension tubes, of 2¼Cr-1Mo, material under a range of applied stressing ratios (hoop/axial) which range from tensile only loading to pressure only loading [12]. The test series reflects response under identical conditions of initial equivalent stress. The predictions, made using a primary modified continuum model of the Rabotnov-Kachanov type, take account of monotonic stress increase and stress state evolution and reflect the limiting cases of the MSRC. The tests are of short duration and reflect creep under conditions of ductile flow. However, in this particular case the onset of failure was strongly influenced by the high inclusion content in the material - hence the maximum principal stress rupture response. If, for the purposes of the example, the MSRC is considered constant over the range of lifetimes considered, then the observed changes in lifetime directly reflect the roles of monotonic stress increase and evolving stress-state.

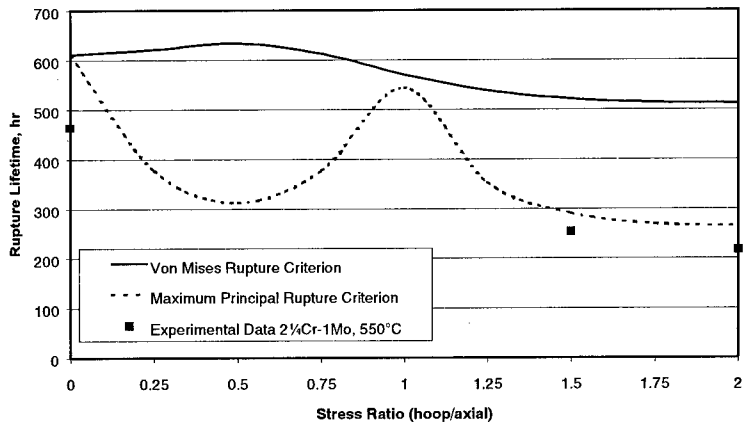

Figure 3: Rupture lifetime as a function of stress ratio (hoop/axial) for tubular 2¼Cr-1Mo components at 550°C [12]

High temperature design codes are necessarily conservative. For pressurised vessels, a basic starting point for calculation is often the mean diameter hoop stress. In the context of Figure 3 this approach is analogous to the more conservative prediction based upon a maximum principal stress rupture criterion. For materials where the equivalent stress contributes significantly to the MSRC, significant additional service life may be available having reached the nominal design life.

4. Concluding Remarks

- Rupture life and ductility are governed by materials and structural factors.
- In developing a model of multiaxial behaviour, stress and stress state evolution must be correctly considered.
- Correct application of such a model to components may also need to take stress distribution into account.
- Multiaxial tests should be performed using testpieces for which the changes in stress and stress state are fully understood. In practice, a combination of uniaxial tests and tubes under pressure and end load has many advantages.
- Practical application of a mutiaxial model may be simplified by the use of a validated reference stress approach.
- Full characterisation of the MSRC and the role of component geometry may facilitate plant life extension.

5. Acknowledgements

This paper is published with the permission of ERA Technology Ltd. Thanks are due to colleagues for their discussions on the subject material.

6. References

1. N.J. Hoff, J. Appl . Mech., 20 p1055, 1953
2. L.M.Kachanov, Izv. Akad.Navk. SSSR, Otd. Tekh. Nauk., 8 p. 26, 1958
3. D. McLean, Mech. Prop. Of Metals, John Wiley and Sons, 1962
4. V.P. Sdobyrev, Izv. Akad.Navk. SSSR, Otd. Tekh. Nauk., 4 p. 92, 1958
5. D.R. Hayhurst, J. Mech. Phys. Solids, 20 pp. 381-390, 1972
6. B.J. Cane, Proc. 5th Int. Conf. On Fracture, Ed. François, Cannes, France, pp. 1285-1292, 1981
7. W.D. Nix, J.C. Earthman, G. Eggeler, B. Ilschner, Acta Metall., 37(4), pp.1067-1077, 1989
8. R.L. Huddleston, J. Press. Vess. Tech., 107, pp. 421-429, 1985
9. J.M. Brear, P.F. Aplin, R. Timmins, ESIS/SIRIUS Int. Conf. 'Behaviour of Defects at High Temperatures', Sheffield, April 1992. ESIS Publication 15, Eds. Ainsworth and Skelton, Mech. Eng. Press, London, pp 401-422, 1993.
10. S. Taira, R. Ohtani, A. Ishisaka, Proc. Japan Congr. Test. Mater., 11, pp. 76-81, 1968
11. B.F. Dyson Met Sci., 10 pp. 349-353, 1976
12. J.M. Church, R.C. Hurst, A.S. McAllister, Proc. BALTICA II, Plant Life, Oct 1992.

Contacts: e-mail: info@era.co.uk
Web site: http://www.era.co.uk/
FAX: +44 1372 367070

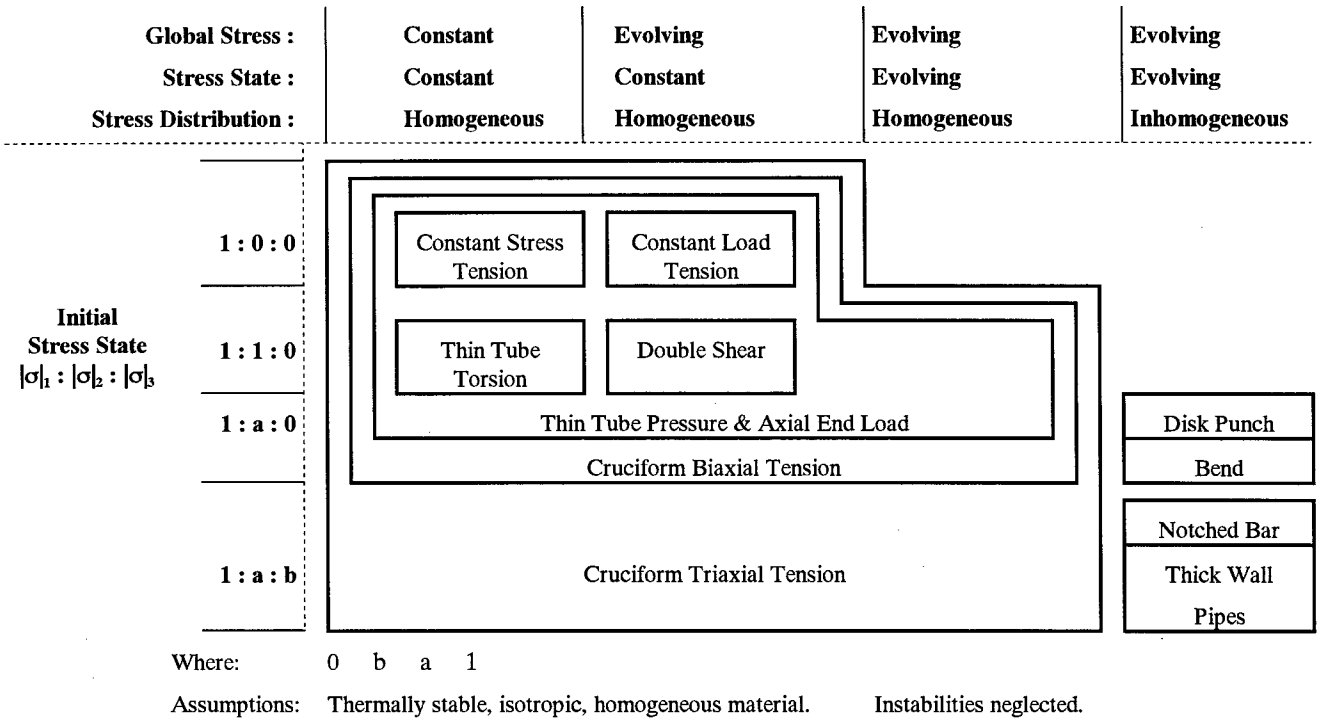

Table 1: Classification of mechanical test types according to nature of stress, stress-state and stress distribution.

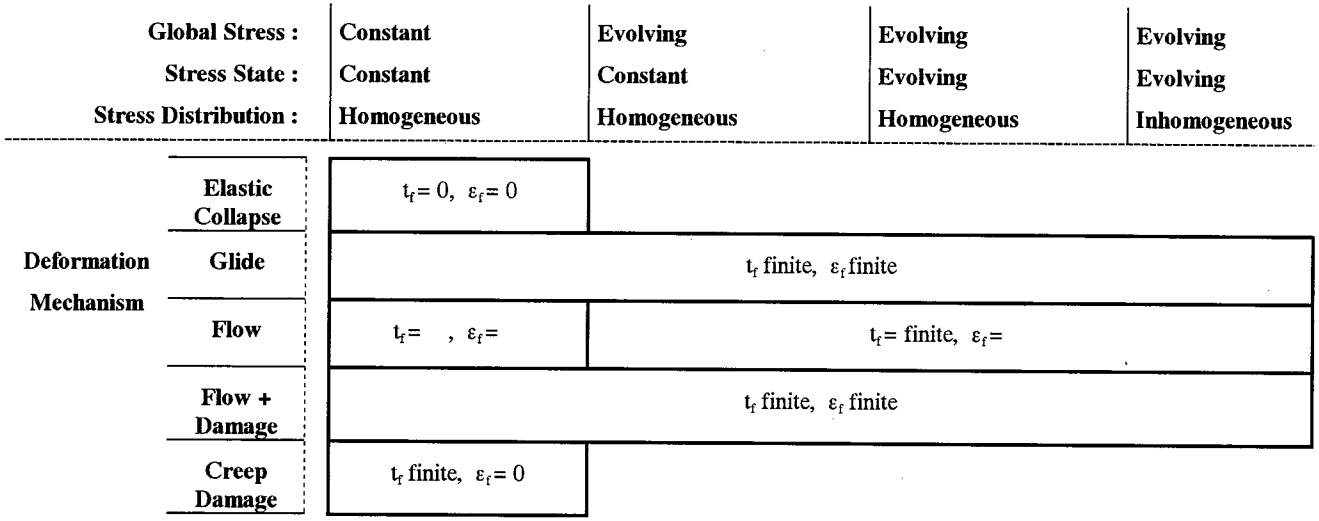

Table 2: **Classification of physical response according to nature of stress, stress-state, stress distribution and deformation mechanism.**

Key Engineering Materials Vols. 171-174 (2000) pp. 69-76
© 2000 Trans Tech Publications, Switzerland

Secondary Creep in a Damage Tolerant Niobium Aluminide Intermetallic

R.P. Hayes[1] and W.O. Soboyejo[2]

[1] Metals Technology, Inc., 19801 Nordhoff Street, Northridge, CA 91324, USA

[2] Department of Mechanical and Aerospace Engineering and the Princeton Materials Institute, Princeton University, 70 Prospect Street, Princeton, NJ 08544, USA

Keywords: Forged Niobium Aluminide Alloy, Creep Resistance, Steady State Creep

Abstract

This paper presents the preliminary results of a recent study of secondary creep in a damage tolerant orthorhombic + B2 niobium aluminide alloy (Nb-11Al-41Ti-1.5Mo-1.5Cr). Tensile creep data are presented for the longitudinal and transverse orientations in the intermediate-temperature regime between 650 and 760°C. The alloy is shown to exhibit creep resistance than orthorhombic titanium aluminide intermetallics. The micromechanisms of creep deformation are also elucidated within the context of measured activation energies and creep exponents.

Introduction

In recent years, a new class of damage tolerant niobium aluminide (Nb_3Al-xTi-base) intermetallics has emerged for potential structural applications in the intermediate-temperature regime (650-750 Nb_3Al-xTi-base intermetallics) [1-8]. The damage tolerance in these alloys was promoted largely by alloying of the Nb_3Al-xTi-base, which has an A15 crystal structure, with Ti to form a partially ordered B2 structure [1]. The early work by Fraser et al. [1] on cast alloys showed that alloying with 40 atomic% Ti resulted in predominantly B2 structures with room-temperature ductilities of 30 %.

Subsequent work by Soboyejo and co-workers [3,4,8] later showed that the microstructures of forged Nb_3Al-xTi-base alloys consist of both orthorhombic and B2 phases when the titanium alloying levels are close to 40 atomic %. The forged orthorhombic + B2 alloys were also shown to have attractive combinations of room-temperature tensile ductility (approx. 5-30%), fracture toughness (approx. 40-110 $MPa\sqrt{m}$) and comparable fatigue crack growth resistance to IN 718 and Ti-6Al-4V [3-8].

There have also been significant efforts to improve the isothermal and cyclic oxidation resistance of Nb_3Al-xTi-base intermetallics via alloying with Cr, or by the use of protective coatings [9,10]. The initial studies showed that the potential service-temperature limit for Nb_3Al-xTi-base intermetallics may be increased from approx. 750 to 800°C by alloying with approx. 5 atomic% Cr [10]. However, the improvements in oxidation resistance were achieved at the expense of room-temperature ductility.

Subsequent work by Soboyejo et al. [4,9] later showed that a good balance of room-temperature ductility (approx. 5% plastic elongation) and oxidation resistance can be

achieved in alloys containing approx. 1.5 atomic % Cr. Preliminary studies of creep rupture lives of Nb_3Al-xTi-base alloys [5] have also showed that their creep resistance can be improved significantly by alloying with approx. 1.5 atomic% Mo. However, there have been no published reports of the secondary creep behavior of Nb_3Al-xTi-base alloys containing both Mo and Cr, although the fatigue and fracture behavior of such alloys has received some attention in a recent paper [6].

The current paper presents the results of a study of the secondary creep behavior of a forged Nb_3Al-xTi-base alloy containing Mo and Cr. The orthorhombic + B2 alloy, Nb-11Al-41Ti-1.5Cr-1.5Mo (compositions quoted in atomic % unless stated otherwise), was engineered to have good combinations of creep and fracture resistance. Following a brief description of the microstructure and basic mechanical properties, secondary creep data are presented for the direct aged alloy in the longitudinal and transverse orientations. The secondary creep rates and creep exponents are compared with those of titanium orthorhombic titanium aluminide intermetallics in the temperature regime between 650 and 760°C. The micromechanisms of creep deformation are then inferred from measured activation energies and creep exponents.

Material

The Nb-11Al-41Ti-1.5Cr-1.5Mo alloy that was examined in this study was produced by triple vacuum-arc-remelting at Pittsburgh Specialty Materials, Pittsburgh, PA. The ingot material was upset forged into a billet at the U.S. Bureau of Mines in Albany, OR. After forging, electro-discharge machined specimens were heat treated in evacuated (10^{-4} Pa) quartz capsules at 750°C for 25 hours (direct aged). The direct aging heat treatment (DA) was used to stabilize the microstructure in the potential service temperature regime.

The direct aged alloy was etched in a solution of 25% lactic acid, 25% concentrated (30%) hydrogen peroxide, 25% hydrofluoric acid and 25% nitric acid was used to etch the specimens. The etch attacked the direct aged specimens much more aggressively, etching the specimens in 1/20th the time required for the as-forged condition.

The etched specimens had similar average grains sizes (~55 microns for the direct aged, and ~52 microns the for the as-forged condition). Figures 1a - 1c show the microstructures of both specimens. The stabilized microstructure of the direct aged specimens clearly shows a second phase precipitating out near the grain boundaries (Figure 1c). The matrix material in both the as-forged and directed-aged specimens has a semi-ordered body centered cubic crystal structure. The second phase platelets in the direct-aged matrix have an orthorhombic crystal structure [6].

The Nb-11Al-41Ti-1.5Mo-1.5Cr alloy has an average modulus of ~ 810 GPa and a 0.2% offset yield strength ~788 MPa in the as-forged condition. The equivalent properties for the direct-aged alloy (750/25hrs) were ~974 GPa and ~995 MPa, respectively. Stress-strain curves obtained from as-forged and direct-aged (750°C/25hrs) Nb-11Al-41Ti-1.5Mo-1.5Cr are presented in Figure 2. This alloy exhibits strain softening in the as-

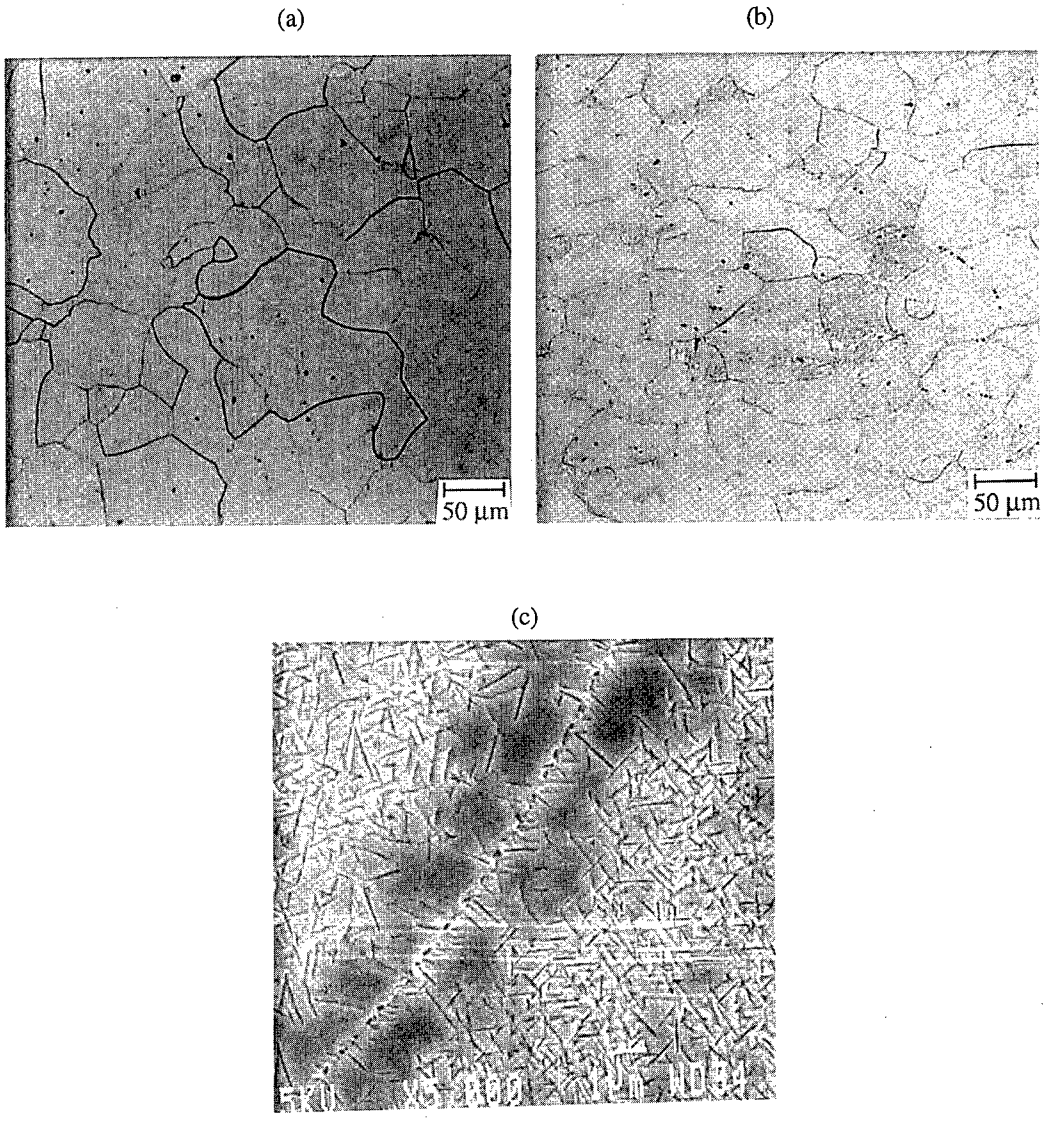

Figure 1: (a) Microstructual profile of the as-forged sample (b) Mircostructual profile of the sample in the direct-aged condition; and (c) Needle-like Orthorhombic Platelets in a Matrix of B2 in the microstructure of the Direct Aged Material. Note the precipitate free zone in the vicinity of the B2 grain boundary.

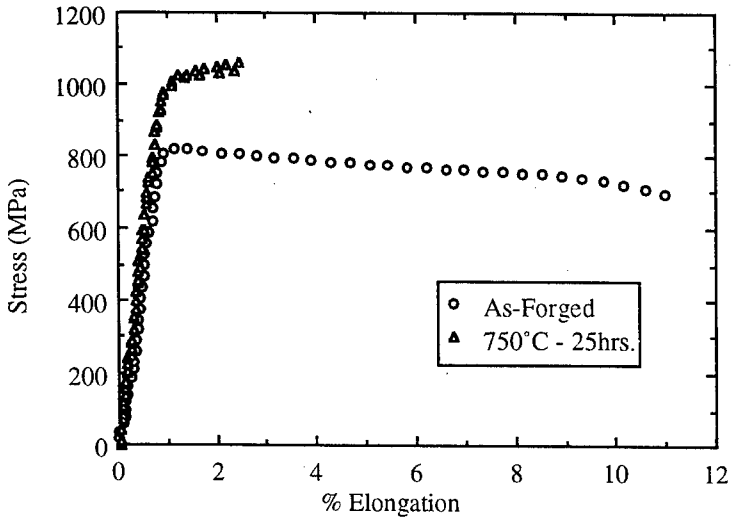

Figure 2: Stress-Strain Behavior of Nb-11Al-41Ti-1.5Mo-1.5Cr Alloy

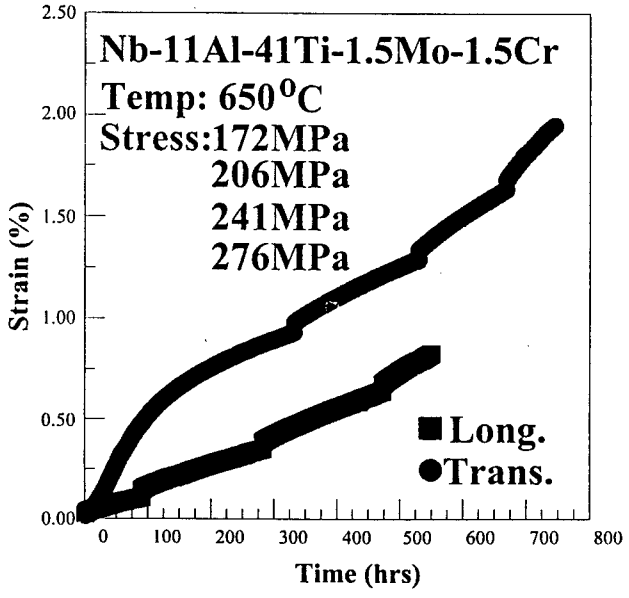

Figure 3: Typical Plots of Stress Versus Time Obtained For The Longitudinal and Transverse Orientations at 650°C

forged condition. The as-forged alloy also has a flow strength of ~788 MPa (Figure 2). However, it exhibits a significant increase in strength and strain hardening after direct aging at 750°C which tends to increase the volume fraction of orthorhombic phase. Furthermore, the ductility is degraded from ~11% to 2.5% after direct aging at 750°C. Also, the as-forged alloy has a fracture toughness of ~83 MPa$\sqrt{m}$ in the L-S orientation. This decreased to ~ 46 MPa$\sqrt{m}$ after direct aging. The fracture toughness level in the L-T orientation also decreased to ~32 MPa$\sqrt{m}$ after direct aging.

Creep Deformation

The creep deformation mechanisms were studied using specimens with similar dimensions and geometries to those that were used in the tensile tests. The specimens were subjected to direct aging at 750°C for 25 hours to stabilize the microstructures prior to creep testing. The creep tests were performed in lab air using a dead load creep machine that was operated under computer control. The tests were conducted at 650, 704 and 760°C in an effort to develop a fundamental understanding of creep deformation behavior in the potential service temperature regime.

Since the forging microstructure was anisotropic (Figures 1a - 1c), the creep behavior was studied in the longitudinal and transverse orientations. At each temperature, multiple creep data were obtained from single specimens that were tested under constant mean stresses until steady-state conditions were reached. The stresses were then increased in incremental stages until subsequent steady state conditions were reached. In this way, multiple steady-state creep rate data were obtained from a limited number of specimens.

Plots of strain versus time obtained from the creep tests at 650°C are presented in Figure 3 for materials that were tested in the longitudinal and transverse orientations at mean stress levels of 172, 206, 241 and 276 MPa. In all cases, the creep strain rates were slower in the longitudinal orientation (elongated grains) than in the transverse (more equiaxed) orientation. The measured creep exponents where also lower in the longitudinal orientation compared to those in the transverse orientation.

The measured secondary creep rates are presented in Figures 4a and 4b for the longitudinal and transverse orientations, respectively. The plots of log of strain rate versus log of stress show that exhibit the usual linear dependence that is expected in the secondary creep regime. The slopes, n, of the plots are approx. 2.2-2.3 for the longitudinal orientation versus 3.1-3.3 for the transverse orientation. The slopes are in the range expected for dislocation glide-controlled creep [11]. However, the slopes of 2.2-2.3 obtained in the longitudinal orientation are also in Harper-Dorn creep regime [11].

Arrhenius plots of the log of strain rate versus the inverse of the absolute temperature are presented in Figure 5 for both the longitudinal and transverse orientations. These were obtained for a common mean stress level of 172 MPa. An activation energy of 322.6 kJ/mole was obtained in the transverse orientation compared with a value of 285.3 kJ/mole in longitudinal orientation. However, it is not yet clear what is responsible for

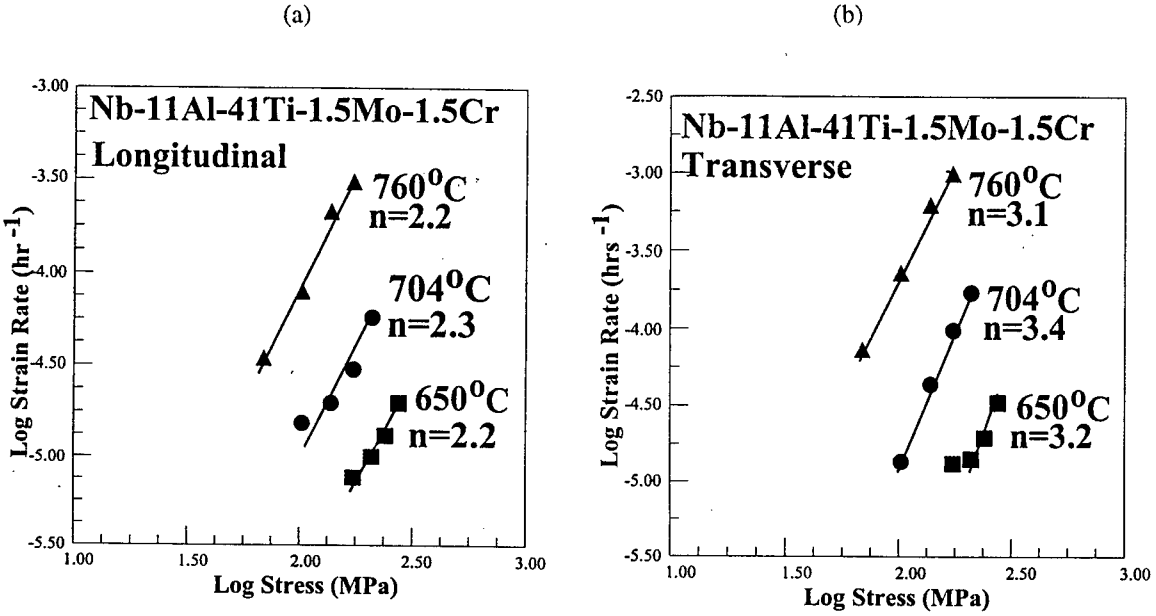

Figure 4: Secondary Creep Data Obtained For (a) Longitudinal and (b) Transverse Orientations

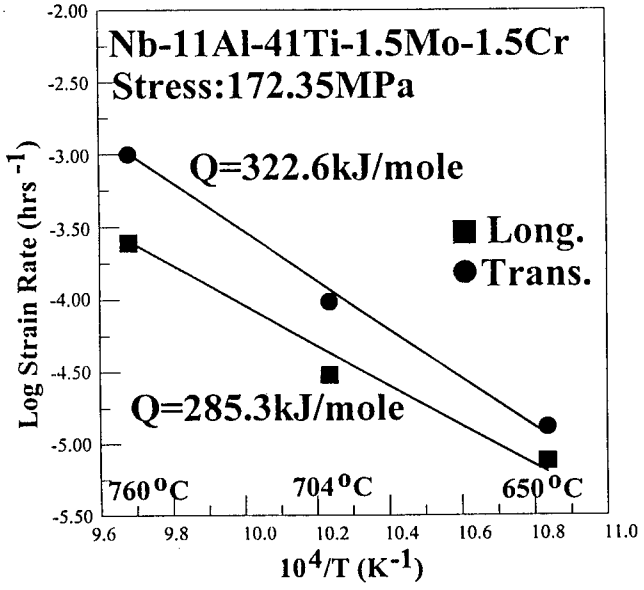

Figure 5: Arrhenius Plot Obtained For The Longitudinal and Transverse Orientations at a Constant Mean Stress of 172.35 MPa

the differences between the activation energies in the different orientations. Nevertheless, it is of interest to compare the activation energies with activation energies in titanium orthorhombic alloys [12], Ti-15Al [13] and Nb-Al-Ti alloys [14] .

The activation energies obtained in the current study are close reported values of approx. 260-270 kJ/mole for the diffusion of Al in Ti-15Al [13]. They are also close to the activation energy of approx. 300 kJ/mole reported for inter-diffusion in Nb-Al-Ti alloys by Ruiz-Aparico and Ebrahimi [14]. The activation energies are also close to creep activation energies of approx. 256 kJ/mole reported for the titanium orthorhombic intermetallic alloy (Ti-22Al-26Nb) by Boehlert at a mean stress of 123 MPa [12].

Finally it is important to note that the orthorhombic + B2 Nb-Al-Ti-base intermetallic (Nb-11Al-41Ti-1.5Mo-1.5Cr) that was examined in this study exhibits somewhat different creep exponents and steady state creep rates from the orthorhombic titanium intermetallic alloy (Ti-22Al-26Nb) that was studied by Boehlert [12]. This is shown in Table 1 in which the steady state creep rate data and creep exponents are summarized for the three test temperatures (650, 704 and 760°C) and a mean stress level of 172.4 MPa (25 ksi). In all cases, the creep exponents are lower, and the steady state creep rates are slower in the case of the orthorhombic + B2 Nb-Al-Ti-base intermetallic alloy.

	Nb-11Al-41Ti-1.5Mo-1.5Cr		Ti-22Al-26Nb (Ref. 12)	
Temperature (°C)	Creep Exponent	Steady State Creep Rate (hr^{-1})	Creep Exponent	Steady State Creep Rate (hr^{-1})
650	2.2	$7.5X10^{-6}$	4.2	$9.76X10^{-6}$
704	2.3	$3.0X10^{-5}$	4.2	$5.3X10^{-5}$
760	2.2	$2.5X10^{-4}$	3.2	$4.4X10^{-4}$

Table 1 - Comparison of Steady State Creep Data For Nb-11Al-41Ti-1.5Mo-1.5Cr and Ti-22Al-26Nb (Ref. 12)

Summary and Concluding Remarks

The secondary creep behavior of the forged and direct aged Nb-11Al-41Ti-1.5Mo-1.5Cr alloy is greater in the longitudinal orientation than in the transverse orientation. The secondary creep exponents are approx. 2.2-2.3 in the potential service temperature regime between 650 and 760°C, and the respective activation energies are approx. 285.3 and 322.6 kJ/mole in the longitudinal and transverse orientations. The forged and direct aged Nb-11Al-41Ti-1.5Mo-1.5Cr alloy exhibits superior creep resistance to the titanium orthorhombic alloy (Ti-22Al-26Nb) over the range of temperatures that was examined.

Acknowledgements

The research was supported by the Division of Materials Research of The National Science Foundation (Grant No. DMR 9458018) with Dr. Bruce MacDonald as Program Monitor. Appreciation is also extended to Prof. Bob Rapp, Prof. Fereshteh Ebrahimi, Mr. Ed Loria, Dr. Craig Wocjik and Dr. Carl Boehlert for useful discussions.

References

1. D. H. Hou, J. Shyue, S. S. Yang and H. L. Fraser, in *Alloy Modeling and Design*, G. M. Stocks and P. Z. A. Turch, Editors, TMS, Warrendale, PA, 1994, pp. 291-298.
2. F. Ye, C. Mercer and W. O. Soboyejo, Metallurgical and Materials Transactions, Vol. 29A, pp. 2361-2374, 1998.
3. W. O. Soboyejo, J. DiPasquale, F. Ye and T. S. Srivatsan, An Investigation of Fatigue and Fracture in a Damage Tolerant Nb-12.5Al-44Ti-1.5Mo Alloy, Metallurgical and Materials Transactions, Vol. 1999.
4. J. DiPasquale, D. Gahutu, D. Konitzer and W. O. Soboyejo, in High Temperature Ordered Intermetallic Materials VI, J. A. Horton, S. Hanada, I. Baker, R. D. Noebe and D.S. Schwartz, Editors, MRS, Pittsburgh, PA, 1994, pp. 1347-1352.
5. C. M. Austin, J. R. Dobbs, H. L. Fraser and D. Konitzer, Rapidly Solidified Oxidation Resistant Niobium Base Alloys, Report No. WL-TR-93-4059, Wright Laboratories, Wright Patterson Air-Force Base, 1992.
6. W. O. Soboyejo, F. Ye, J. DiPasquale and P. Pine, Journal of Materials Science, 1999 (in press).
7. F. Ye, D. Farkas and W. O. Soboyejo, Materials Science and Engineering, Vol. A264, pp. 81-93, 1999.
8. W. O. Soboyejo, J. DiPasquale, F. Ye, C. Mercer and D. G. Konitzer, Metallurgical and Materials Transactions, Vol. 30A, pp. 1025-1038, 1999.
9. Y. Li, W. O. Soboyejo and R. A. Rapp, Metallurgical and Materials Transactions, Vol. 30B, pp. 495-504, 1999.
10. B. V. Cockerman, H. J. Schmutzler, J. Shyue, K. Hoshino, S. Meng, R. Wheeler and H. L. Fraser, Materials Research Society, Pittsburgh, PA, 1994, pp. 1327-1332.
11. A. K. Mukherjee, Treatise on Materials Science and Technology, R. J. Arsenault, Editor, Vol. 6, p. 163, 1975.
12. C. Boehlert, Materials Science and Engineering A, Microstructure, Creep and Tensile Behavior of a Ti-12Al-38Nb (Atomic%) Beta Orthorhombic Alloy, 1999 (in press).
13. P. Shewmon, Diffusion in Solids, TMS, Warrendale, OH, 1992.
14. J. G. L. Ruiz-Abaricio and F. Ebrahimi, Journal of Alloys and Compounds, Vol. 202, pp. 117-123, 1993.

Key Engineering Materials Vols. 171-174 (2000) pp. 77-84
© 2000 Trans Tech Publications, Switzerland

Comparison of the Creep and Fracture Behavior of Non-Hardened and Oxide Dispersion Hardened Platinum Base Alloys at Temperatures Between 1200 °C and 1700 °C

R. Völkl[1], D. Freund[1], B. Fischer[1] and D. Gohlke[2]

[1] Fachhochschule Jena - University of Applied Science Jena, Tatzendpromenade 1b, DE-07745 Jena, Germany

[2] SCHOTT GLAS, Hattenbergstr. 10, DE-55122 Mainz, Germany

Keywords: Creep Test Machine, Strain Measurement, Platinum, Rhodium, ODS, Glass Industry, High Temperature, Fracture Strain, Creep Deformation

Abstract

The paper reports from an ongoing project which is intended to help the design engineers at SCHOTT GLAS to choose the right platinum base alloy for any particular application in the production of special glasses and high-quality glass fibers. In order to investigate the creep and fracture properties at very high temperatures special test facilities were designed and built. The specimens are heated directly by alternating current. The temperature is measured by an infrared thermometer. Strain is measured with the aid of a high resolution camera and the image processing system SuperCreep. Creep tests have been carried out on the solid solution alloys Pt 10 wt.% Rh and Pt 20 wt.% Rh and four oxide dispersion hardened alloys (ODS alloys) with nominal compositions of 90 wt.% Pt and 10 wt.% Rh. The hardening effect in Pt-10 wt.% Rh ODS alloys is due to finely dispersed zirconium and yttrium oxides. The measurements confirm much better creep rupture strength and lower stationary creep rates at high temperatures for oxide dispersion hardened Pt-10 wt.% Rh alloys compared to the conventional alloys Pt-10 wt.% Rh and Pt-20 wt.% Rh.

Introduction

The requirements on structural materials in glass melting technology and for hot parts of the propulsion of aircraft and spacecraft are extremely demanding. High temperatures, high mechanical stresses, an oxidizing and corrosive environment often act together in a complex way. Well known materials for high temperature applications are nickel base superalloys and refractory metals. Considerable efforts were made in the last two decades to develop ceramics and intermetallics for use at very high temperatures. Materials often forgotten in the discussion of materials for high temperature applications are platinum and platinum base alloys.

Platinum base alloys can be used at temperatures up to 2000 K. Despite their high prices, their exceptional chemical stability, resistance to oxidation, high melting points, ductility, thermal shock resistance and electrical and thermal conductivity make them interesting for structural applications in the glass industry and for some aerospace applications [1-4]. High high-quality optical glasses and high-quality glass fibers require the use of platinum-tank furnaces, stirrers and feeders.

Pure platinum has only low mechanical strength at high temperatures. Therefore platinum is usually alloyed with iridium or rhodium [1, 5, 6]. Alloying platinum with up to 20 wt. % rhodium or up to 30 wt. % iridium increases the stress rupture strength considerably. These solid solution alloys have good ductility at high temperatures and can be welded to themselves or similar alloys. The common Pt-10 wt.% Rh and Pt-20 wt.% Rh alloys are oxidation resistant even at temperature above 1300 K. Platinum-iridium alloys show small weight losses at long exposure to high temperatures due to evaporation of the alloying element iridium in the form of volatile oxide.

Several manufacturers have developed platinum base alloys with improved high temperature properties. ODS platinum base alloys [1-4, 15-21] were developed for the most demanding applications. In these alloys small amounts of stable zirconium oxide or yttrium oxide are finely distributed throughout the alloy matrix. The creep and stress-rupture strength at temperatures of 0.8-0.9 T_m are strongly increased due to reduced dislocation mobility and stabilization of the grain boundary structure even for long exposure times. Most ODS platinum base alloys are produced by complicated and expensive powder metallurgical processes (PM) [15-19]. The oxidation and corrosion resistance of the ODS materials is as good as that of the equivalent conventional solid solution alloys.

Experimental

The high prices of precious metals and extremely high test temperatures prevent the use of ordinary creep test facilities. In a suitable creep test machine several problems have to be solved:

- Size and geometry of the specimens
- Application of the load
- Heating of the specimens
- Strain measurement at extremely high temperatures

For investigations on high purity platinum Hamada et al [7] used a tension geometry with gauge dimensions of 38 mm × 6.3 mm × 1 mm. The specimen together with the clamps are introduced into a high temperature furnace which is heated up to 1773 K. The clamps suffer the same high temperatures as the specimen so that they also have to be made of an ODS platinum alloy. The load is applied outside the furnace via a bar linkage. The elongation of the specimen is measured at the bar linkage with the aid of a laser extensometer.

B. Reppich et al [8] and H. Schmidt [9] used Al_2O_3 clamps and a Al_2O_3 bar linkage for creep tests on platinum base alloys. In view of high material costs a small tension geometry of 75 mm × 13 mm × 1 mm was chosen. Strain was measured directly on the specimens with thin Al_2O_3 bars and an inductive linear position transducer. Like Hamada et al they heated the specimen together with the clamps and the alumina bar linkage in a high temperature furnace.

At the University of Applied Science Jena specially designed equipment [10-12] is used for mechanical testing of platinum base alloys and refractory metal alloys at very high temperatures. The equipment permits tests at constant load either in air or under protective gas atmosphere. Creep test on pure rhenium were successfully performed at temperatures up to 3300 K [13]. A schematic diagram of the equipment is given in Fig. 1. The specimen is gripped in clamps and heated directly by an electric current. Lower temperatures at the clamps than in the center of the specimen allow the use of cheap copper clamps. The temperature is monitored by an infrared thermometer focussed on the center of the sample. The thermometer adjusts the heating current to maintain a constant temperature via the controller software LabView and a thyristor regulator. The load is applied to the sample by means of calibrated weights. The specimens have the form of strips with dimensions of 120 mm × 4 mm × 1 mm.

It is important to bear in mind that the deformation is limited to the hottest part of the specimen, i.e. the central zone. The temperature in a zone 30 mm around the specimen center is nearly constant (Fig. 1). In order to measure strain the specimens have four small shoulders in this zone (Fig. 2 and 7). The heated specimens are observed by a high resolution camera which is itself controlled by the program SuperCreep developed at the University of Applied Science for strain measurements by means of digital image analysis. SuperCreep continuously determines the distance between the shoulders with an accuracy better than 0.1 % (Fig. 2). Notched tension specimens are

used in order to investigate the effect of three dimensional stress states and stress concentrations. 1 mm deep and 0.3 mm wide notches are cut with a diamond wire saw (Fig. 7).

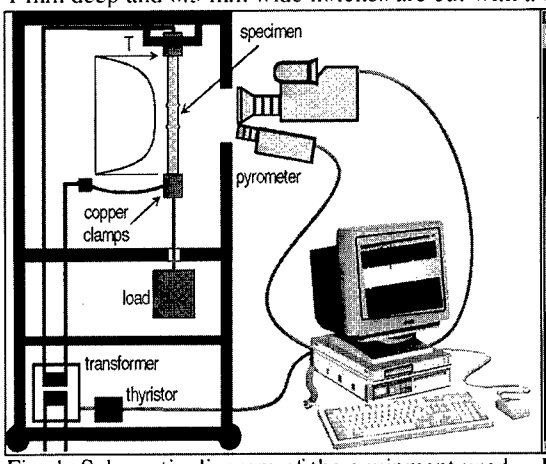

Fig. 1: Schematic diagram of the equipment used to measure stress rupture strength and creep parameters of metals at temperatures up to 3300 K.

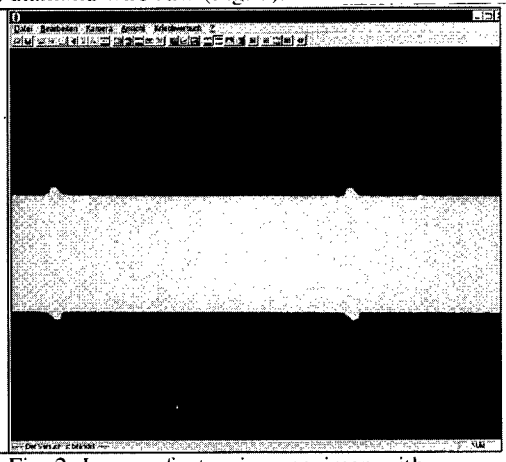

Fig. 2: Image of a tension specimen with shoulders recorded by SuperCreep.

Overall the test equipment described has proven good reliability. The simplicity of the equipment offers the advantages of low costs and easily attainable high temperatures of up to 3300 K. There is no need to use special materials for parts exposed to high temperatures. The free sight to the specimen makes it possible to measure the deformation by means of digital image processing, which also allows not only longitudinal strain but also transverse strain and crack propagation to be measured.

Six different platinum base alloys were investigated. The solid solution alloys Pt-10 wt.% Rh and Pt-20 wt.% Rh are produced by SCHOTT GLAS, these alloys will be named Pt-10% Rh respectively Pt-20% Rh. The other four ODS alloys, named ODS^1, ODS^2, ODS^3 and ODS^4 throughout the paper, had have the nominal composition of 90 wt.% Pt and 10 wt.% Rh. The ODS alloys are commercially available from four international platinum producers. Unfortunately we are not allowed to reveal the names of the producers because of contractual agreements. The alloys Pt-10% Rh and Pt-20% Rh were annealed in air at 1273 K for 100 h in order to get a stable grain structure. The ODS alloys were tested without an additional anneal because the oxide particles stabilize the grain structure.

Creep properties

Fig. 3 shows creep curves of the six alloys at 1723 K and a nominal stress of 10 MPa. The creep curves are typical of all alloys in the chosen temperature range and stress range. No incubation period like that found by Hamada et al [7] was observed for pure platinum. In the creep curves of the alloys ODS^1, ODS^2 and ODS^4 the primary creep stage is missing. After a long secondary creep stage with a constant creep rate a very short tertiary creep stage follows. The alloys Pt-10% Rh, Pt-20% Rh and ODS^3 have creep curves with a short primary creep, a long secondary creep and a well pronounced tertiary creep stage. Most interesting is the different behavior of the alloy ODS^3 compared to the other ODS alloys. The difference can also be seen in much higher fracture strains of alloy ODS^3 compared to the other ODS alloys (Fig. 4). Although the solid solution alloys have even higher fracture strains, the alloy ODS^3 shows high fracture strains in the temperature range from 1473 K up to 1973 K. The fracture strains of the alloys Pt-10% Rh, Pt-20% Rh and ODS^3

increase with increasing temperature. The alloy ODS[3] reaches a maximum fracture stain of 50 % at 1973 K. The other three ODS alloys show low-ductility behavior with mean fracture strains of 4.5 % for ODS[1], 6.0 % for ODS[2] and 8.5 % for ODS[4] (Fig. 4).

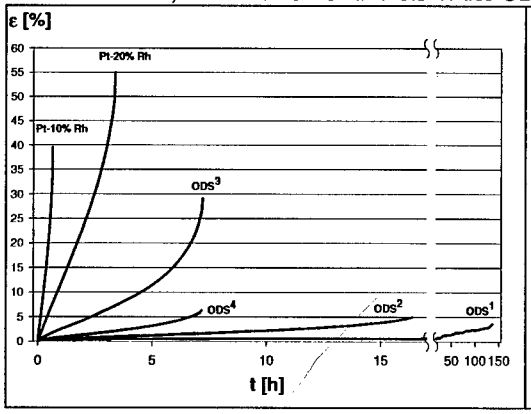

Fig. 3: Creep curves of six platinum base alloys at 1723 K and 10 MPa.

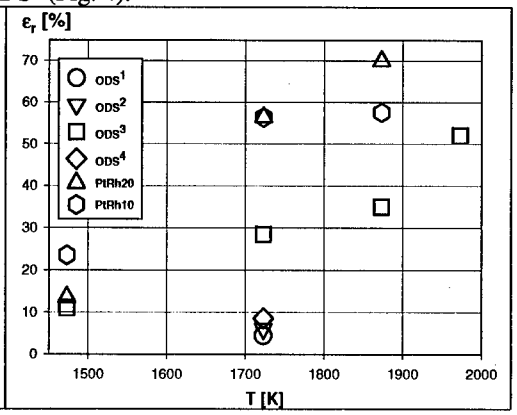

Fig. 4: Mean fracture strain of six platinum base alloys at temperatures between 1473 K and 1973 K.

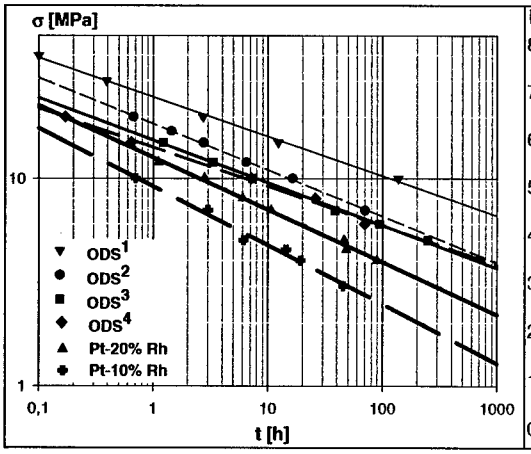

Fig. 5: Stress rupture strength of six platinum base alloys at 1723 K.

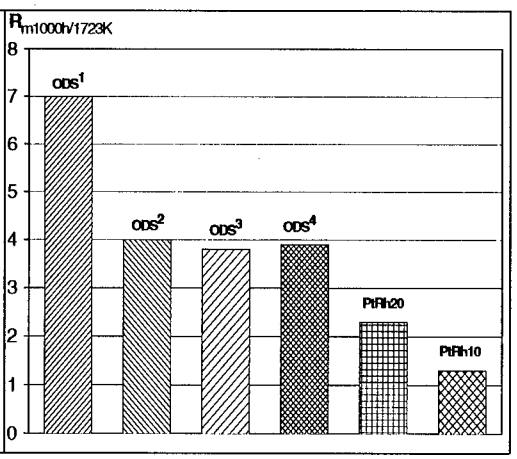

Fig. 6: 1000 h stress rupture strength of six platinum base alloys at 1723 K.

The rupture times of all alloys lay well on straight lines in the double logarithmic plot of the stress rupture diagram shown in Fig. 5, and therefore extrapolation to low stresses and long lifetimes respectively can be made. In contrast to it's fracture strain behavior, the alloy ODS[1] has by far the highest stress rupture strength of all alloys at 1723 K. The 1000 h stress rupture strength is 7 MPa compared to about 4 MPa for the other three ODS alloys and 2.3 MPa and 1.4 MPa respectively for Pt-20% Rh and Pt-10% Rh (Fig. 6). The stress rupture strengths of all four ODS alloys are higher than for the solid solution alloys. The advantage becomes still larger at low stresses and long lifetimes (Fig. 5).

Figure 8 shows a double logarithmic Norton plot for the stationary creep rates of all investigated alloys at 1723 K. ODS[1] has the lowest creep rates followed by ODS[2], ODS[4], ODS[3], Pt-20% Rh and Pt-10% Rh. The Norton exponents are 5.2 for ODS[1], 4.3 for ODS[2], 4.8 for ODS[3], 5.1 for ODS[4], 3.6 for Pt-20% Rh and 2.2 for Pt-10% Rh.

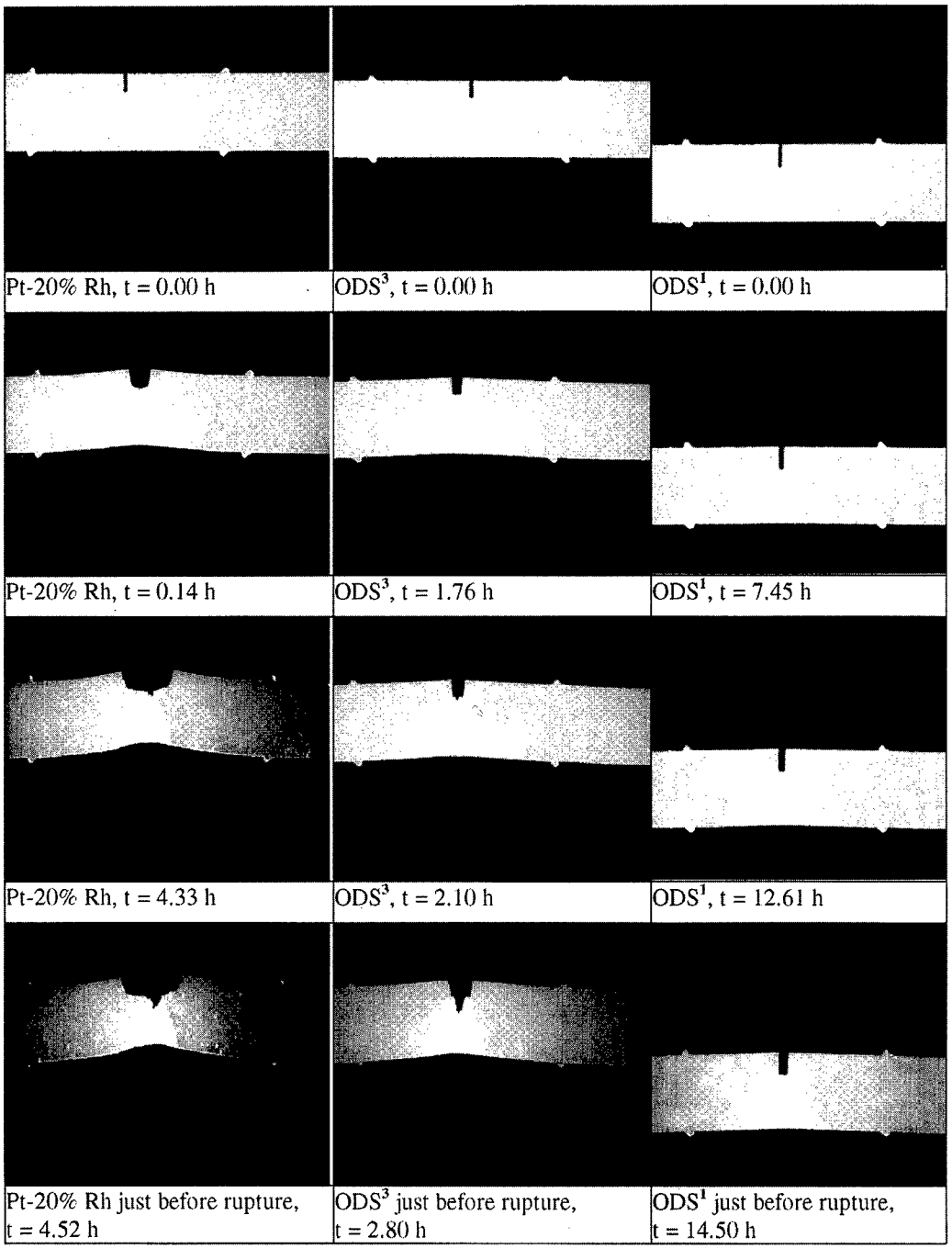

Figure 7: Three image series of creep tests on notched specimens at 1723 K and 10 MPa showing different fracture behavior.

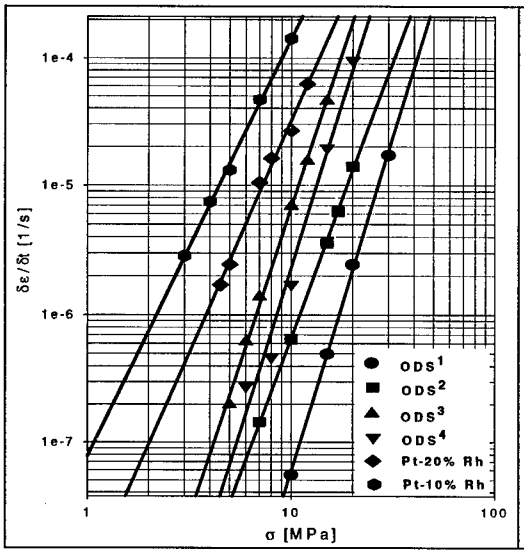

Fig. 8: Stationary creep rates of six platinum base alloys at 1723 K.

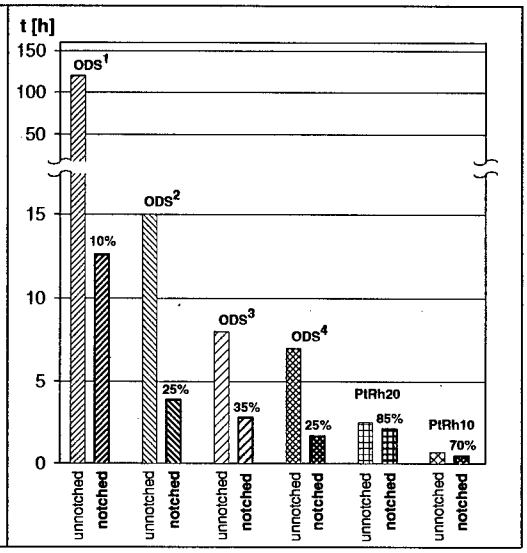

Fig. 9: Lifetimes for notched specimens compared to unnotched specimens of the same alloy at 1723 K and 10 MPa stress.

Notch sensitivity - Fracture behavior

Three series of images taken during creep tests on notched specimens from alloys Pt-20% Rh, ODS[3] and ODS[1] are shown in Fig. 7. The creep tests were performed at 1723 K and a tension stress of 10 MPa.

Image series a) in Fig. 7 is typical for the creep tests on the solid solution alloys Pt-10% Rh and Pt-20% Rh. Good ductility of these alloys leads to a large widening of the notch and pronounced necking. Damage at grain boundaries can be observed after a small fraction of the overall lifetime, but only at the very end of the creep test does a macroscopic crack become visible on the video screen. The notch has only a weak effect on the creep lifetime of the alloys Pt-10% Rh and Pt-20% Rh, whereas all ODS alloys undergo a sharp decline in lifetime (Fig. 9).

The alloy ODS[3] shows a somewhat different behavior compared to all other alloys. The widening of the notch is smaller than for the solid solution alloys but larger than for the other ODS alloys. A macroscopic crack can be observed after about 75 % of the overall lifetime. Crack propagation take place in the way that, in a first step, voids are formed ahead of the main crack tip. In a second step the crack propagates rapidly until crack tip blunting occurs and the formation of voids starts again (Fig. 7 image series b)). Due to the notch the lifetime drops down to 35 % compared to the unnotched case (Fig. 9).

The ODS alloys ODS[1], ODS[2] and ODS[4] undergo very little creep deformation and therefore nearly no widening of the notch can be observed (Fig. 7 image series c)). After a small fraction of the overall lifetime oriented cavities and microcracks are observed in the damage zone ahead of the notch tip. When the damage zone stretches over the whole cross section area rupture takes place immediately. Due to the notches the lifetimes drop down to 10 % for alloy ODS[1], to 25 % for alloy ODS[2] and to 25 % for alloy ODS[4] compared to the unnotched alloys (Fig. 9)

Discussion - Conclusion

The introduction of oxide dispersion strengthened platinum base alloys in the late 1970s was received very enthusiastically in the glass industry. It was considered that much higher creep rup-

ture strengths compared to conventional alloys would lead to longer component lifetimes and / or savings in expensive precious metals. Nevertheless ODS platinum base alloys are nowadays limited to few application in the glass industry. Brittleness and difficulties in welding ODS platinum base alloys have been shown to be the most important points dictating against their practical use.

Our investigations have shown that ODS platinum base alloys with similar chemical compositions can have very different creep and fracture behavior. The alloy ODS[3] has good ductility at high temperatures comparable to conventional solid solution alloys and a creep rupture strength similar to the alloys ODS[2] and ODS[4]. The highest strength shown by the alloy ODS[1] is achieved at the price of low fracture strain, i.e. low ductility at high temperatures.

For most applications in the glass industry the platinum base alloy has to be able to undergo a certain amount of creep deformation. In practice the platinum base alloys are used in combination with ceramic components. Different thermal expansion coefficients together with unavoidable manufacturing tolerances can lead to very high thermal stresses which only a ductile metal can release by creep deformation. From this point of view the progress towards maximum strength in ODS platinum base alloys has lead up to a dead end.

In this paper we could only give a phenomenological description of the creep and fracture behavior of several platinum base alloys. Detailed investigation of the microstructures are in progress. We hope to present microstructural explanations for the creep and fracture behavior of ODS platinum base alloys at the 9th International Conference on Creep and Fracture of Engineering Materials and Structures.

References

[1] D. Lupton, Advanced Materials (May 1990), pp. 29-30
[2] M. V. Whalen, Platinum Metals Rev., 32, (1) (1988), pp. 2-10
[3] H. A. Jansen, F. A. Thompson, Glastech. Ber. 65 Nr. 4 (1992), pp. 99-102
[4] J. Stokes, Platinum Metals Rev., 31, (2) (1987), pp. 54-62
[5] D. Freund, B. Fischer, D. Lupton, Proc. 21st IPMC (1997), San Francisco, USA, pp. 307-322
[6] B. Fischer, A, Behrends, D. Freund, D. Lupton, J. Merker, Proc. TMS Annual Meeting (1999), San Diego, USA, pp. 321-331
[7] T. Hamada, S. Hitomi, Y. Ikematsu, S. Nasu, Materials Transactions, JIM, Vol. 37, No. 3 (1996), pp. 353-358
[8] B. Reppich, F. Brungs, G. Hümmer, H. Schmidt, Proc. CFEMS-4 (1992), pp. 141-158
[9] H. Schmidt, Doctoral Thesis, Universität Erlangen-Nürnberg (1986), Germany
[10] B. Fischer; H. Töpfer; R. Helmich, Patent specification DD WP G 0 1 N / 245 576 A3 (1987)
[11] B. Fischer, D. Freund, D. Lupton, Werkstoffprüfung (1997), Bad Nauheim, Germany
[12] R. Völkl, D. Freund, B. Fischer, D. Gohlke, Werkstoffprüfung (1998), Bad Nauheim, Germany, pp. 211-218
[13] B. Fischer, D. Freund, D. Lupton, Proc. TMS Annual Meeting (1997), Orlando, USA, pp. 311-320
[14] F. A. Thompson, GLASS (July 1990), pp. 279-280
[15] Patent specification 1 340 076 (1973), Johnson Matthey, GB
[16] Patent application WO 81 / 00977 (1981), Owens-Corning Fiberglass Corporation, USA
[17] Patent application DE 30 30 751 A1 (1982), Degussa AG, Germany
[18] Patent specification DE 31 02 342 C2 (1988), Johnson Matthey, GB
[19] Patent specification DE 44 17 495 C1 (1995), SCHOTT GLAS, Germany
[20] Patent specification DE 195 31 242 C1 (1996), Degussa AG, Germany
[21] Patent application DE 197 14 365 A1 (1998), W.C. Heraeus GmbH, Germany

Key Engineering Materials Vols. 171-174 (2000) pp. 85-98
© 2000 Trans Tech Publications, Switzerland

Creep and Creep Fatigue Crack Behavior of 1Cr- and 9Cr-Steels

K. Maile[1], A. Klenk[1], J. Granacher[2], G. Schellenberg[1] and M. Tramer[2]

[1] Staatliche Materialprüfungsanstalt (MPA), University of Stuttgart,
Pfaffenwaldring 32, DE-70569 Stuttgart, Germany

[2] Institute for Materials Technology (IfW), Technical University of Darmstadt,
Grafenstraße 2, DE-64283 Darmstadt, Germany

Keywords: Fracture Mechanics, Creep Crack Growth, Creep Fatigue Crack Growth, Crack Initiation Behavior, Large Scale Specimens, Martensitic Steel, Dwell Times

ABSTRACT

A large database for creep crack initiation and propagation under constant load conditions is available on conventional power plant steels of types 1%Cr and 12%Cr. Modern plants are often used in the medium and peak load regime, thus the dominant loading situation in high temperature components is creep fatigue. For life assessment data about crack initiation and growth under creep fatigue loading are required. These characteristics can not be substituted by pure fatigue or creep crack data. Therefore, a comprehensive test programme was started to investigate the creep fatigue crack behaviour of a 1%CrMoNiV turbine rotor steel (30CrMoNiV 4 11) at 550 °C and a new 9%CrMoVNb pipe steel (type P 9 1) at 600 °C. DENT-specimen with 15 and 60 mm thickness as well as side grooved CT-specimen with 25 and 50 mm thickness have been tested to determine possible influences of geometry and thus to check the transferability of the data to components.

The creep fatigue crack growth results of tests with dwell times between t_H = 0,32h and 10 h lie in the scatterbands given by creep crack growth results. Nevertheless a higher crack growth rate under creep fatigue conditions can be stated. An increase in crack growth rate due to creep fatigue is clearly visible. Loading situations with frequencies higher than $1 \cdot 10^{-4}$ Hz should be not assessed with pure creep crack results or sufficient safety margins have to be applied.

TEST MATERIALS

As test materials the bainitic 1%Cr turbine rotor steel 30 CrMoNiV 4 11 which is mainly used for heavy forgings like rotors and discs for temperatures up to 540 °C and the martensitic 9%Cr pipe steel X 10 CrMoVNb 9 1 (P91) for pipework with steam temperatures up to 600 °C have been used. The chemical composition of both steels are given in Tab. I. The product forms and heat treatments are given in Tab. II

	C	Si	Mn	P	S	Al	Cr	Ni	Mo	V	Nb	N
	Weight %											
1%Cr (30 CrMoNiV 4 11)	0.3	0.24	0.73	0.009	0.018		1.04	0.58	1.05	0.30		
9%Cr (X 10 CrMoVNb 9 1)	0.1	0.30	0.46	0.015	0.003	0.019	8.30	0.17	0.94	0.21	0.066	0.049

Table I. Chemical composition of the test materials

	Product, dimension		Heat treatment
1% Cr (30 CrMoNiV 4 11)	Turbine shaft	$\varnothing_{max}$ = 790 mm Length l = 5800 mm	950 °C / 7 h/ Air 700 °C /15 h/Furnace
9%Cr (X 10 CrMoVNb 9 1)	Pipe	$\varnothing_a$ = 492 mm $\varnothing_i$ = 332 mm	1050 °C / 10 min/ Air 750 °C / 70 min Air

Table II. Product forms and heat treatments

EXPERIMENTAL PROCEDURE

In this study Compact Tension (CT) specimens with side grooves (25 and 50 mm thickness) as well as Double Edge Notch Tension-specimen (DENT, 15 and 60 mm thickness) were used, Fig. 1. Most specimens were spark eroded with a notch tip radius of 0.1 mm as initial crack. A few Cs25 specimens have been fatigue cracked to study the influence of crack starter notch.

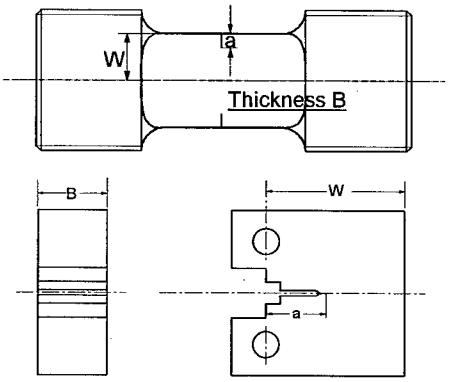

	Cs25	Cs50	D15	D60
B (mm)	25	50	15	60
W (mm)	50	100	10	50
a_0/W	0.55	0.55	0.2	0.2

Fig. 1 Specimen geometry

Different specimen sizes with a variety of cross sections from nearly 240 mm^2 up to 4 800 mm^2 allow the determination of size and geometry effects on crack initiation and growth behavior. Thus, the applicability of test data on components can be studied.

Most of the small scale specimens were tested at IfW Darmstadt using the interrupted test technique. For each stress level, a series of up to 15 specimens were tested under the same loading conditions in a multiple creep test machine. After reaching a predetermined proportion between 10 % and 80 % of the expected "rupture time" t_r the specimens were unloaded. During this interruption the load line displacement of all specimens was measured and some specimens of the series were fractured at low temperature. The crack length of these specimens were fractographically determined. A high accuracy of data is guaranteed, since scattering of the material characteristics and inhomogenity has been taken into account.

The large scale specimens and some single tests on small specimens were tested at MPA Stuttgart in servo hydraulic test machines. During this tests, an online measurement of the load line displacement was performed by means of capacitive high temperature strain gauge. The crack propagation was measured online by means of electric potential drop (AC) technique. At the end of each test the potential drop signal was calibrated with the final crack length observed in the fractured specimen.

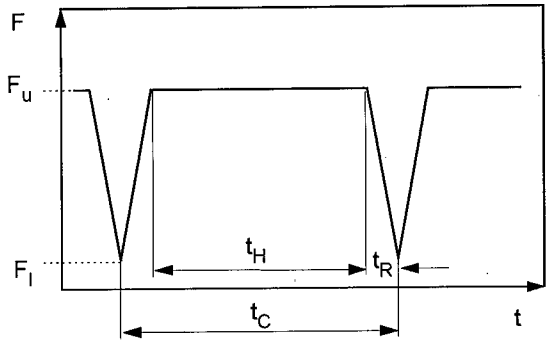

Fig. 2.
Scheme of the applied load cycle

Long term tests up to 8 000 h under cyclic tension load ($R = \sigma_{min}/\sigma_{max} = 0.1$) conditions were performed in the load controlled mode with dwell times at maximum load from 0.1 up to 10 h. With these test durations it is possible to come near to real service conditions of components. In Fig. 2 a scheme of the load cycle is depicted. The low alloyed 1%Cr steel was tested at 550 °C, the martensitic 9%Cr steel at 600 °C.

RESULTS AND DISCUSSION

Creep fatigue crack initiation behavior

Crack initiation is strongly influenced by the interaction between creep and fatigue damage processes. The crack initiation time t_A was defined by a given crack length a_{RA}. This crack length is detectable by electrical potential drop crack length recordings in experiment as well as in large component by non-destructive measurements. To consider different constraints of small and large specimens and differences in stress state along the crack front, the above mentioned initiation crack length is size depending: $a_{RA} = 0.004 \cdot W$ for CT specimens and $a_{RA} = 0.01 \cdot W$ for DENT specimen (W .. specimen width). Results of small and large specimens are depicted in Fig. 3 for 1%CrMoV- and in Fig. 4 for 9%CrMoNbV steel as function of K_I. K_I is in accordance to ASTM E 399-83 for CT-specimen given by

$$K_I = \frac{F}{B \cdot \sqrt{W}} f(a/W) \quad . \tag{1}$$

The use of fictitious stress intensity factor K_I in creep range to describe the conditions at the crack tip is incorrect in physical terms, nevertheless K_I serves as a vehicle to describe the crack tip behavior of a specimen/component [1].

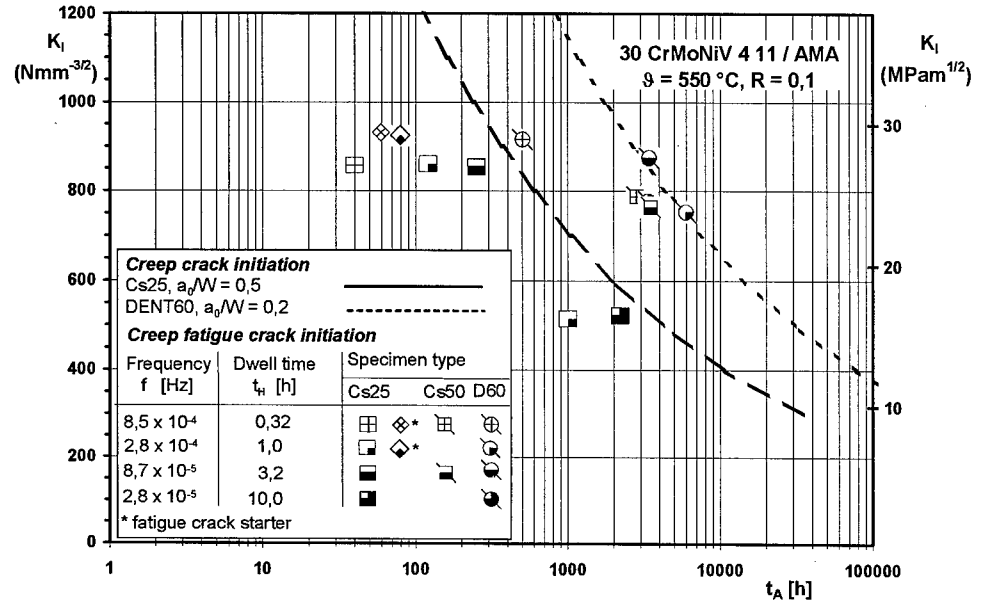

Fig. 3 Stress intensity factor K_I at crack tip vs. creep fatigue crack initiation time t_A, 1%Cr steel

There is a clear relationship between frequency and crack initiation time, regarding only one specimen type, e.g. Cs25 specimen. Even for low frequencies corresponding to tension hold times t_H of 3.2 or 10 h, a decrease of creep fatigue crack initiation time compared with creep crack initiation of the same specimen type (broken line in Fig. 3) has to pointed out. For higher frequencies, the relation between creep fatigue crack initiation and creep crack initiation decreased up to $t_{Ac\text{-}f}/t_A = 0.1$ for $f \approx 1 \cdot 10^{-3}$ Hz. Random based investigations on 1%Cr steel showed no systematic influence of crack starter (fatigue crack at ambient temperature or spark eroded notch).

For large specimen of CT- and DENT-type the same tendency of initiation- and liftetime reduction corresponding to higher cyclic damage at shorter tension loading periods could be observed. Crack initiation occurs in large specimens approx. 10 times later than in small specimens. This behavior under creep fatigue loading conditions corresponds to static creep crack behavior, see dashed line of creep crack initiation results of Cs25- and the dotted line of DENT60-specimen. These differences are not only caused by different initiation crack lengths (a_{RA} = 0,2 mm for Cs25- and a_{RA} = 0,5 mm for DENT60-specimens) but also in differences in constraint and crack-tip/farfield loading situation [1]. In the creep range time dependent changes in stress distribution occur both at the crack tip and in the farfield. This cannot be described by the K_I-parameter. Consequently different farfield loading for differences in failure/specimen geometrie have to be considered.

The fact that this influence is so clearly visible in creep-fatigue behavior indicates a relatively high amount of creep damage for low and higher frequencies, because for pure cyclic loading, no size dependency of crack initiation was observed. Metallographic and fractographic investigations are in coincidence with this, the change from transgranular to intergranular crack growth starts at about $1 \cdot 10^{-3}$ Hz for 1%Cr steel.

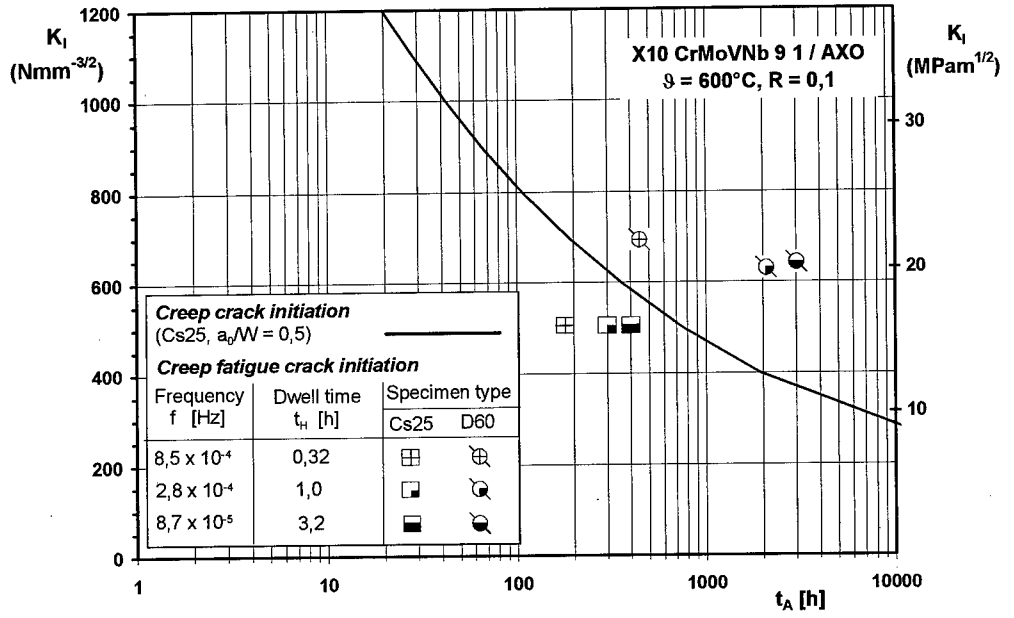

Fig. 4 Creep fatigue crack initiation and comparison with creep crack initiation function, 9%Cr steel

For the creation of a frequency independent failure assessment procedure, a linear life fraction rule was used. For the determination of cyclic life fraction, the number of cycles at creep fatigue crack initiation N_A was related to a cyclic crack initiation mastercurve N_{AM} at the same stress intensity ΔK_I:

$$L_{ERA} = \frac{N_A}{N_{AM}} \tag{2}$$

The N_A mastercurve can be set up by small specimen experiments at higher frequencies. The static life fraction is calculated using the above described creep fatigue initiation times t_A. For a more engineering description it is meaningful to correlate these results with creep crack initiation results of Cs25-specimens $t_{A\text{-}KR}$, because this specimen type shows a relatively strong crack tip damage mode, such experiments are easy to perform and results are wide spread for different types of heat resistant steels. Following this, the static life fraction is given by:

$$L_{KRA} = \frac{t_A}{t_{A-KR}}, \tag{3}$$

t_A is time till crack initiation under creep fatigue loading , $t_{A\text{-}KR}$ is the time under creep load at the same stress intensity. This procedure delivers a strong underestimation of large scale specimen results, Fig. 5, both steels. For small specimens the cumulative life fractions are lower than L = 1, esp. for frequencies in trans-/intergranular transition fracture mode.

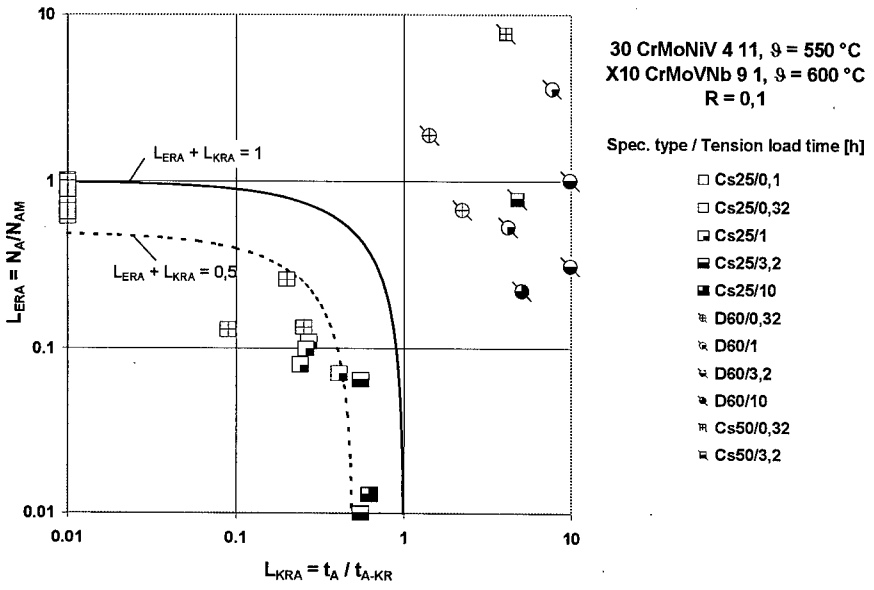

Fig. 5 Results of creep fatigue crack tests and assessment by linear life fraction rule, 1%Cr and 9%Cr steel

Creep crack growth rate

The results of long term creep crack growth (CCG) tests presented in this paper have been partly published [2–5]. These results containing a database of various specimen types, each tested at different sizes up to durations of 30 000 h for some single tests with crack growth rates down to $2 \cdot 10^{-5}$ mm/h. For the evaluation of the test results the linear elastic stress intensity factor K_I, as well as the parameter C* was used. If K_I is used a relatively large scatterband (factor 22) could be seen in Fig. 6.

Within this scatterband the larger specimens show the lower CCG rates but at smaller initial nominal stress values higher CCG rates. The slope of single CCG curves for individual specimens is not parallel to the slope of the overall scatterband. A reduction of the scatterbands could be achived, if the tails of non stationary CCG were neglected.

By using the parameter C* the scatterband for the description of the crack growth rate can be markedly reduced as shown in Fig. 7. For the calculation of the C*-parameter on CT-specimens the following equation in accordance with ASTM E 1457-92 was used:

$$C^* = \dot{v} \cdot \sigma_{net} \cdot g_2(a/w.n.\beta). \tag{4}$$

For plane stress condition C* is approximately

$$C^* \approx 2 \cdot \frac{n}{n+1} \cdot \dot{v} \cdot \sigma_{net} \quad . \tag{5}$$

The slope of the overall scatterband (≈ 0.9) which is similar to a theoretical slope of n/(n+1) is

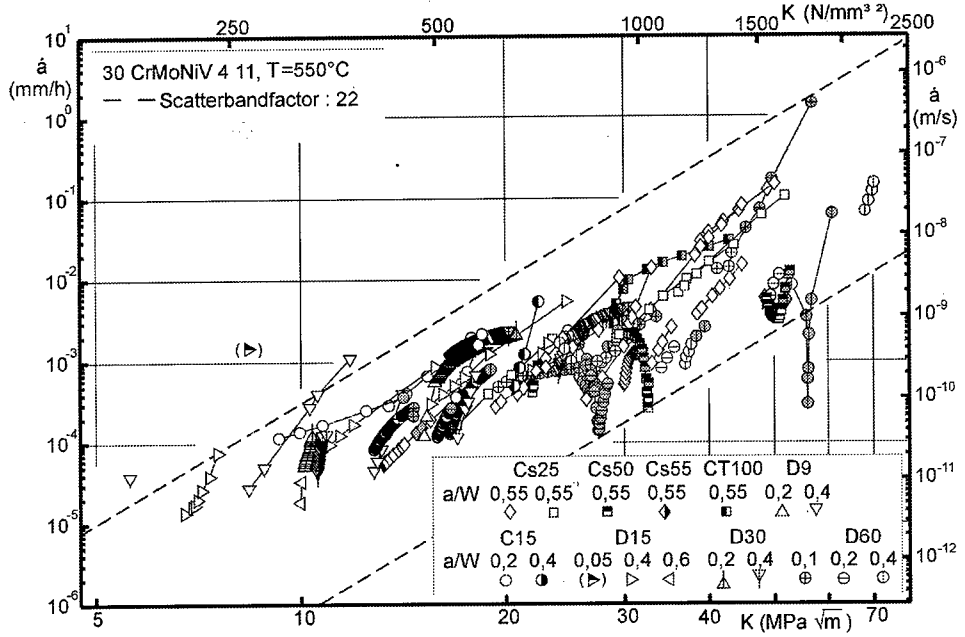

Fig. 6. Creep crack growth rate da/dt versus stress intensity factor K_I, 1%Cr steel, ϑ = 550 °C, [6]

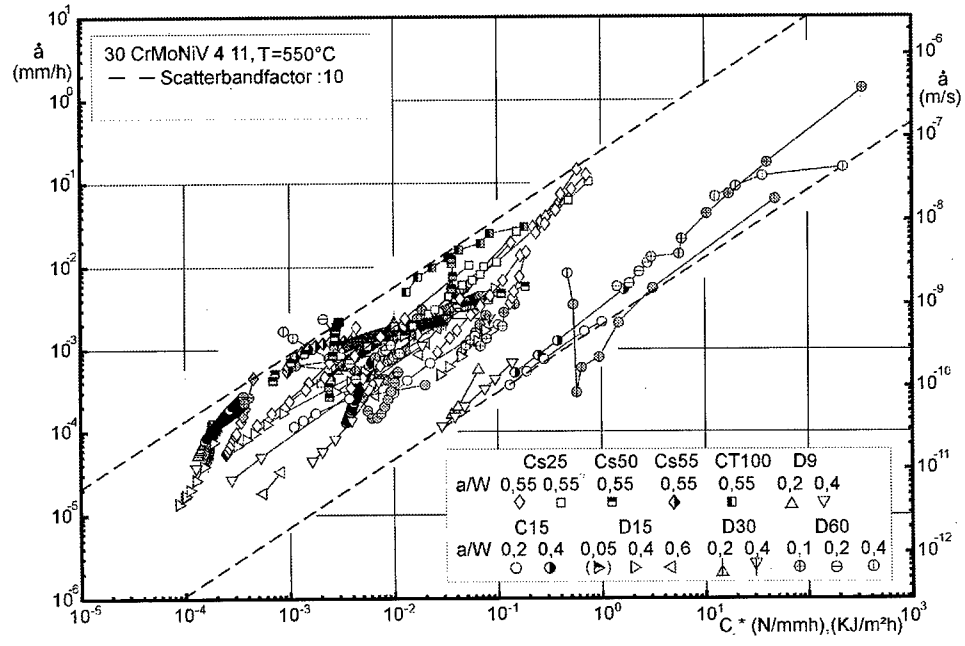

Fig. 7. Creep crack growth rate da/dt versus parameter C*, 1%Cr steel, ϑ = 550 °C, [6]

parallel to the slopes of individual test results. Nearly all curves of the single specimens are parallel to each other. The CCG rate for CT-specimens are within the upper range of the overall scatterband and in the middle and lower region for the DENT-specimen. No significant

influence of the specimen size on the crack propagation behaviour described by C* could be observed.

The CCG scatterbands for the 9% Cr steel are draw from open literature. These results for K_I [7] are valid for specimen of the type Cs25 and Cs50, the C* band includes only results from Cs25 specimen [8].

Creep fatigue crack growth

In Fig. 8 creep fatigue crack growth (CFCG) rates of all tested specimens are depicted for the low alloyed Cr steel as a function of K_I and in Fig. 9 as a function of C* for plain stress conditions. C* and K_I are calculated with applied load F_{max} during dwell times. Additionally, in the figures the scatterbands for CCG rates from Fig. 6 and Fig. 7 have been implemented. The evaluation of all data takes into account data from crack initiation, according to the initiation criteria mentioned above, up to a crack length of $\Delta a = 2$ mm.

With regard to the parameter K_I, all creep fatigue crack results lie inside the scatterband of CCG rates. Small scale specimens tested at higher frequencies show higher crack growth rates than large scale specimens.

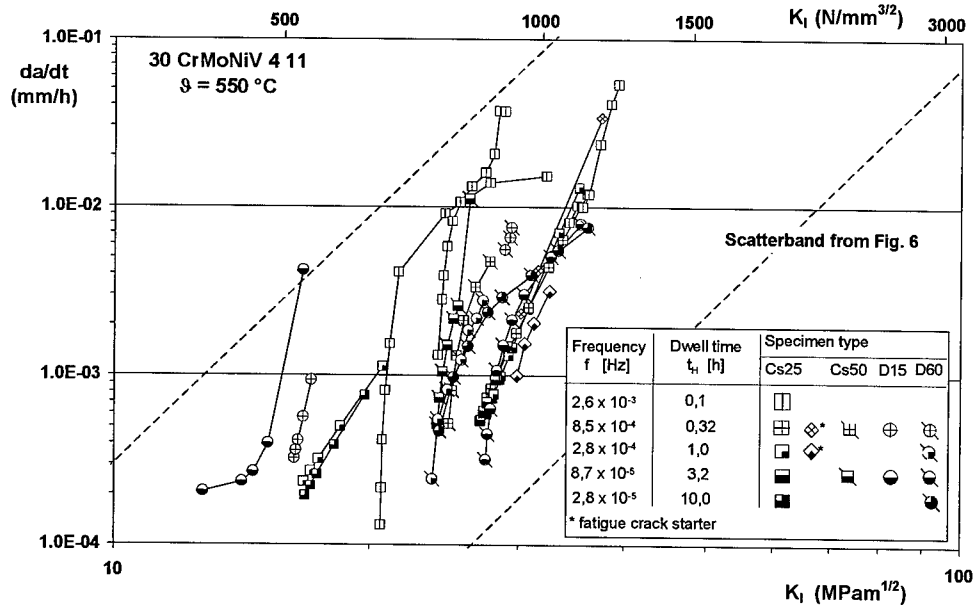

Fig. 8. Comparison of CFCG and CCG data on basis of the stress intensity factor K_I, 1%Cr steel, $\vartheta = 550$ °C

For calculating the C* parameter, plain stress conditions were assumed in accordance to 2- and 3 dimensional FE calculations on CT specimens [9]. For these calculations Norton's parameter for the initial stress in every test was used, since investigations [4] showed a stress dependence of n. Also if CFCG rate is described by C* an influence of dwell time and frequency respectively

is visible. Test with dwell times $t_H > 0.1$ h lie in the upper part of the scatterband, test with t_H = 0,1 h do not fit the scatterband of pure creep crack results. The slope of single specimens are approximately parallel to each other and to the borderlines of the overall scatterbands. No size dependency between small specimens (Cs25, D15) and large ones (Cs50, D60) could be seen. The use of C* as characterizing fracture mechanic parameter is meaningful, like determined by transition time t_1

$$t_1 = \frac{K_I^2}{E' \cdot C^* \cdot (n+1)} \tag{6}$$

with n ... Norton Prameter, E' ... modulus of elasticity with E'=E for plain stress and E'= E/(1-ν^2) for plain strain conditions. For tests with $t << t_1$, the short time or elastic solution by K_I is valid, for tests with $t >> t_1$ C* respectively. For the given creep fatigue results the ratio t/t_1 is between 2 and $\approx$ 100, therefor C* seems to be better qualified to describe the crack growth in tests with dwell times larger than 0.1 h.

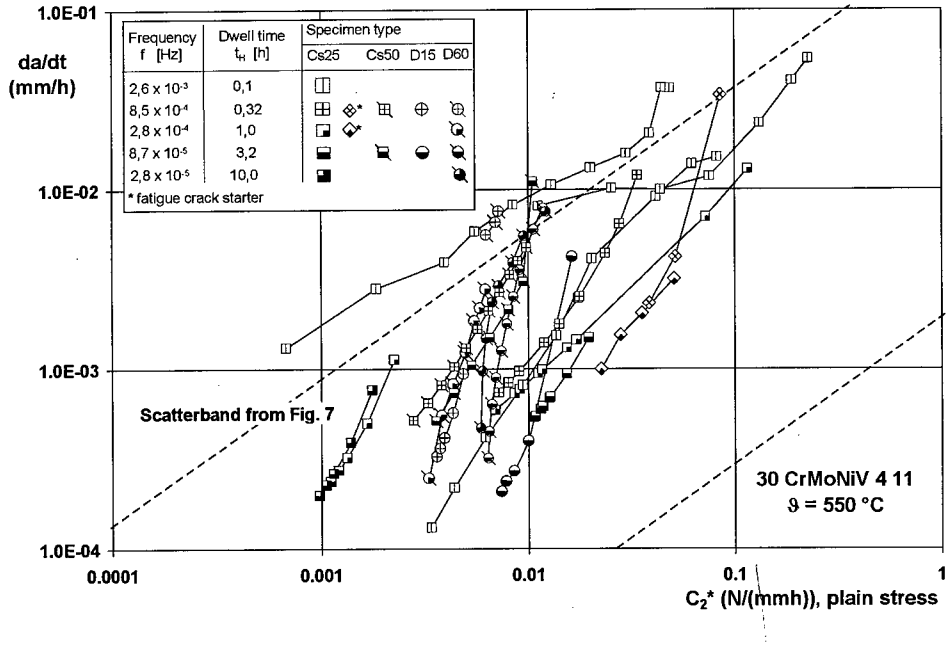

Fig. 9. Comparison of CFCG and CCG data on basis of the parameter C*, 1%Cr steel, ϑ = 550 °C

For the martensitic 9%Cr steel the creep fatigue crack results are depicted in Fig. 10 as a function of K_I and in Fig. 11 as function of C*. The additionally marked scatterbands of CCG results are valid only for a part of the included results, see mentioned above. The frequency dependent increase in crack growth rate is more pronounced for the 9%Cr steel. The validity of the existing C* - CCG scatterband is limited to small scale specimen, that is why the creep fatigue loaded large scale specimens lie on or below the lower borderline respectively. Differences in crack growth rate also appears for the dependence of K_I. This effect illustrates that fracture parameter K_I in creep range is not able to describe crack growth size- and geometry independent. Only if the stress state in the farfield region behind the crack tip is

considered additionally, such a general description of crack growth rates taking into account both size as well as geometry is possible. This is in correspondence to the crack tip/farfild model and the 2 criteria approach for crack initiation [1,11-13].

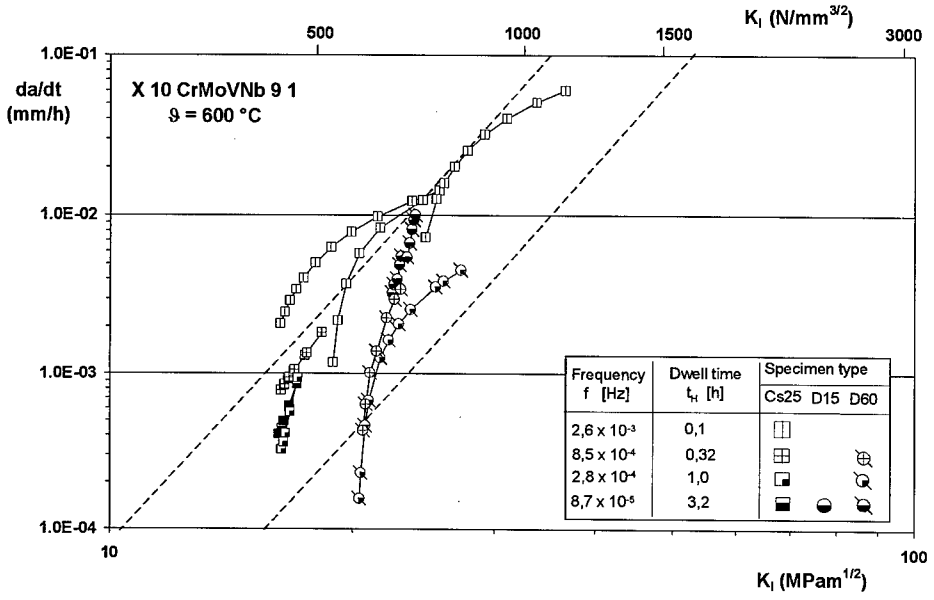

Fig. 10. Comparison of CCG and CFCG data on basis of the stress intensity factor K_I, 9%Cr steel, ϑ = 600 °C

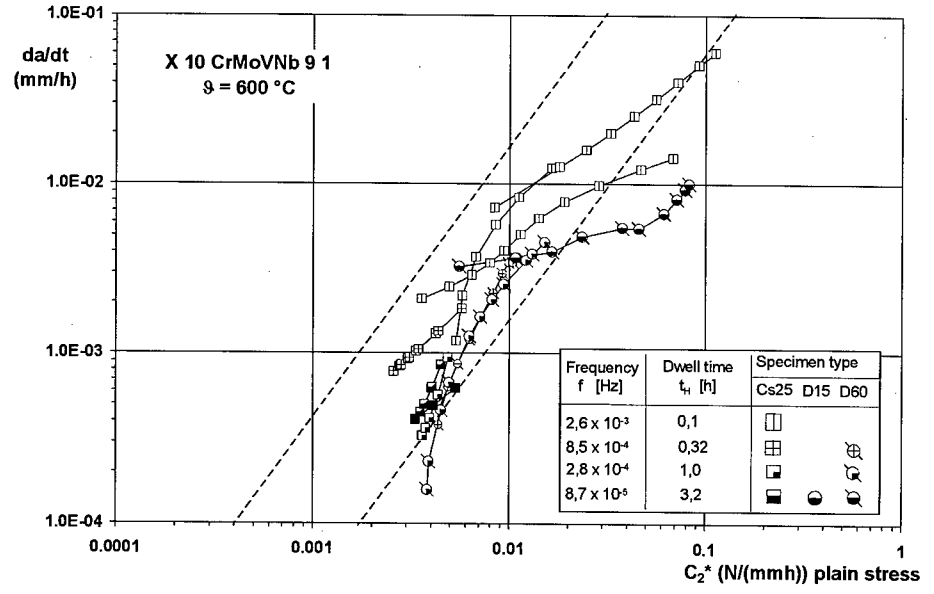

Fig. 11. Comparison of CCG and CFCG data on basis of the parameter C*, 9%Cr steel, ϑ = 600 °C

Damage accumulation

Fatigue processes will dominate the crack growth at high frequencies and creep processes at low frequencies. For intermediate loading conditions a mixture of both processes will occur. For the description of the CFCG it will be helpful to use the widely available data of common CCG and FCG tests on the basis of an accumulation rule. The cyclic crack growth behavior is characterized by the Paris law

$$\frac{da}{dN} = A \cdot (\Delta K_I)^m \tag{8}$$

and the CCG behavior by the equation

$$\frac{da}{dt} = D \cdot (C^*)^{\phi} \tag{9}$$

The CFCG per cycle is then given by combining both equations to an cumulative damage equation

$$\left.\frac{da}{dN}\right|_{CFCG} = A \cdot (\Delta K_I)^m + \frac{D \cdot (C^*)^{\phi}}{f} \tag{10}$$

For the 1%Cr steel the FCG was described with the Paris law coefficients $A = 1.12 \cdot 10^{-6}$ and $m = 1.96$. For the description of the CCG an $\dot{a}$-C*-relation was used, where C* was calculated in [9] by FE-analysis on basis of an modified Garofalo equation.

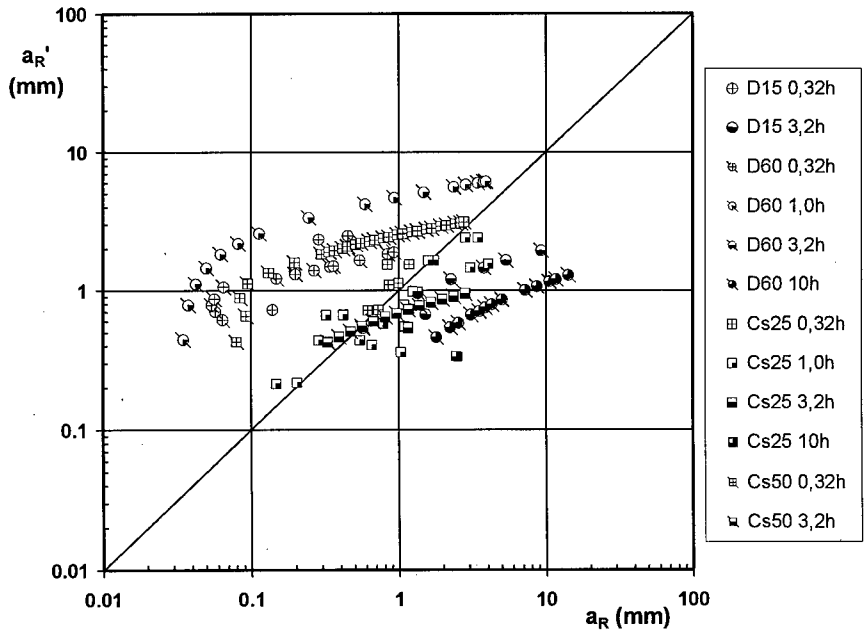

Fig. 12. Comparison between the predicted and experimental CFC length, 1%Cr steel, $\vartheta = 550$ °C

In the specific case of the 1%Cr steel it was also taken into account the incubation period t_i to achieve an creep crack length of 0.004·W in CT specimen and 0.01·W in DENT specimen. This incubation period was calculated in [9] as function of C_{FE}*. The CCG part was then only allowed to cumulate with the FCG part, when the time exceed the creep crack incubation time. For the calculation of the CFCG the mean values of the scatterbands in the $\dot{a}$-C_{FE}*- and t_i-C_{FE}*-relations were used

Comparison between the predicted and experimental CFC length is shown in Fig. 12. It can be seen, that the results are in good accordance. A dependence of the hold time could be seen. Tests with short hold times (0.1 and 0.32 h) lie mostly above the 45° line, tests with 1 h hold time show scattering in the area of the theoretical line and tests with longer hold times are below the line. In most cases the slope of the curves is less than 45° which means, that the calculated CFCG rate is underestimated. These behavior could be explained by following factors. The Paris law doesn't take into account, that there is no fatigue crack growth under an threshold value $\Delta K_{I\,th}$. This causes an overestimation of the fatigue crack growth rate at the beginning. In addition Paris law doesn't consider the accelerated fatigue crack growth rate just before failure. The equation used to predict the CCG rate is also attributed with an uncertainty, because the slope of the individual curves of single tests are different from the used mean curve. Mostly the individual one have an markedly higher slope. This leads to an underestimation of the CCG, even for long periods.

CONCLUSION

For the 1%Cr turbine rotor steel and the martensitic 9%Cr steel for steam pipes a large CCG database have been created covering the influence of size and geometry. In addition, investigations to the influence of creep fatigue loading situations, to determine the start up, shut down and other variable loading conditions in power plant components, have been performed with test durations of 8 000 h up to now.

The existing results of tests with low frequencies, according to dwell times up to 10 h and high frequencies (dwell times t_H = 0,32h) lie in the scatterbands given by CCG results. Nevertheless by comparison with the midline of creep crack growth scatterbands, a higher crack growth rate under creep fatigue conditions can be stated. This applies esp. for the well investigated 1%Cr steel and C* as correlating parameter. An increase in crack growth rate due to creep fatigue is clearly visible. Concerning additionally microstructural and fractographic investigations, a change in fracture mode from trans- to intercristalline crack growth occurs for frequencies of about $1\cdot10^{-3}$ Hz for 1%Cr steel and $5\cdot10^{-3}$ Hz for the 9%Cr steel. Loading situations with frequencies higher than $1\cdot10^{-4}$ Hz should be not assessed with pure creep crack results.

The determination of the transition time demonstrates, that the use of the parameter C* is critical for the short term tests with a short dwell times of 0.1 h. This is presumably a reason of a damage mechanism which is dominated by plastic stress distribution and therefore the description of the creep propagation rate by means of C* or K_I creates problems.

It can be concluded from the above results, that an cumulative damage equation an basis of pure fatigue and CCG allows a satisfactory prediction of CFCG.

ACKNOWLEDGEMENT

Thanks are due to the "Bundesminister für Wirtschaft" (AiF-Nr. 10 395N) and to the "Verein deutscher Eisenhuettenleute" for their support of this work and further to the "Arbeitsgemeinschaft Warmfeste Staehle" for the supply of test material.

LITERATURE

[1] Ewald, J.: Creep crack initiation and growth in terms of K. In: High temperature crack growth in steam turbine materials, ed. by J.B. Marriott, EUR 14678, Petten (1994).

[2] Granacher, J., R. Tscheuschner, K. Maile and W. Eckert: Kriechrißverhalten typischer Kraftwerksbaustähle, Steel research 60 (1989) No. 11, p. 514/521.

[3] Kussmaul, K., K. Maile, J. Bareiss, K.H. Kloos, J. Granacher and R. Tscheuschner: Creep Crack Investigation of Turbine Steels with Specimens of Different Size. ASME-Conference, Denver, July 25-29 (1993).

[4] Granacher, J., R. Tscheuschner, K. Maile: Langzeitiges Kriechrißverhalten kennzeichnender Kraftwerksstähle, Mat.-Wiss. u. Werkstofftechnik 24 (1993) p. 367-376.

[5] Kussmaul, K., K. Maile, J. Bareiss, K.H. Kloos, J. Granacher and R. Tscheuschner: Creep crack investigation of turbine steels with specimens of different size, Proc. of the ASME-Conference, Pressure Vessel and Piping, Denver, USA (July 25-29, 1993) PVP-Vol. 266, Ed. Garud, Y.S., (1993), pp. 119/26.

[6] Berger, C. E. Roos, J. Granacher, K. Maile, M. Tramer, G. Schellenberg: Kriechrißverhalten ausgewählter Kraftwerksbaustähle in erweitertem praxisnahem Parameterbereich. Schlußbericht zum AVIF-FV A78, Institut für Werkstoffkunde, TU Darmstadt und Staatliche Materialprüfungsanstalt, Universität Stuttgart (1999)

[7] Hollstein, T., R. Kienzler: Fracture Mechanics Characterization of Crack Growth under Creep and Fatigue Conditions, Final Report COST 501-Project D 10, Fraunhofer-Institut für Werkstoffmechanik (1987)

[8] Creep and Fatigue Crack Growth in High Temperature Plant, International HIDA Conference Saclay/Paris, France, 15-17. April 1998, ERA Conference Pre-Print (1998)

[9] Granacher, J., R. Tscheuschner, T.S. Mao, K. Maile and J. Bareiß: Numerisch ermittelter Parameter C* zur Beschreibung des Kriechrissverhaltens, Mat.-wiss. u. Werkstofftech. 27 (1996) p. 135-42.

[10] Granacher, J., J. Kostenko, K. Maile, R. Fischer: Kriechrißeinleitung bei warmfesten Stählen, Vortrag auf der 30. Tagung des DVM-Arbeitskreises Bruchvorgänge am 17.02.98 in Dresden (1998)

[11] Ewald, J., K.H. Keienburg, K. Kussmaul: Hinweise auf Mechanismen und Einflußgrößen zur Beurteilung des Bauteilverhaltens im Kriechbereich anhand von Kleinproben, VDI-Bericht Nr. 354 (1979)

[12] Ewald, J., K.H. Keienburg: A two criteria diagram for creep crack initiation, Int. Conf. on Creep, Tokyo, 14-18 April 1986, pp. 173-178,

[13] Ewald, J. und S. Sheng: The two criteria diagram for creep crack initiation and its application to an ip-turbine. International HIDA Conference Saclay/Paris, France, 15-17. April 1998, ERA Conference Pre-Print (1998)

Corresponding author:
A. Klenk, MPA Stuttgart
Fax.: (+49)711-6853053
e-mail: a.klenk@mpa.uni-stuttgart.de

Key Engineering Materials Vols. 171-174 (2000) pp. 99-108
© 2000 Trans Tech Publications, Switzerland

Creep Rupture Behavior of Advanced 9-12%Cr Steel Weldment

F. Masuyama, M. Matsui and N. Komai

Mitsubishi Heavy Industries Ltd., Nagasaki Research and Development Center,
5-717-1, Fukahori-machi, Nagasaki 851-0392, Japan

Keywords: Creep Rupture Strength, 9%Cr Steel, 12%Cr Steel, Weldment, Failure Mode, Creep Strain, Rupture Strain

Abstract

In order to apply advanced 9-12%Cr steel such as Mod.9Cr-1Mo (P91), 9Cr-0.5Mo-1.8W (P92), and 12Cr-0.4Mo-2W (P122) for use in high temperature and high pressure components, creep rupture strength of weldments and failure behavior are very important. The work reported here employed P92 steel and P122 steel to carry out uniaxial creep rupture tests on cross weld samples from SMAW and SAW welded joints of plate and pipe. The creep rupture strength of the weldments of these advanced steels was accordingly determined, with the respective results compared to each other and to base metal strength. The failure mode of the weldment in terms of stress and temperature was also clarified on the basis of the long-term creep rupture data. Furthermore, it is suggested that creep strain measurement for weldments is useful in predicting long-term creep rupture life.

Introduction

The steam conditions of power plants recently constructed have successfully been elevated in consideration of environmental protection and energy savings. The design of header and steam pipings using conventional steel including P91 (Mod.9Cr-1Mo) require the wall thickness to be excessively large for temperatures of 600℃ and above. Thus, stronger materials have been needed in order to achieve reduced wall thickness and diameter. To meet this demand, NF616 (designated as T92/P92, 9Cr-0.5Mo-1.8W-V-Nb) steel and HCM12A (T122/P122, 12Cr-0.4Mo-2W-1Cu-V-Nb) steel, both of which have been recently developed, are the best candidates, as they exhibit superior creep rupture strength of about 130MPa at 600℃ and 100,000 hours. Their weldability, fabricability and material properties have already been found satisfactory for practical use[1]. However, as is well known, high strength steels with tempered martensitic structure are unfortunately characterized by a soft area or Type IV region in the heat affected zone of weldments, and tend to rupture at this portion due to weaker strength in terms of creep than the base metal. High temperature and high pressure components must therefore take into account the creep strength reduction of weldments. In work reported here uniaxial creep rupture tests were carried out on cross weld samples to determine the rupture strength and creep strain as well as weldment failure mode of P92 and P122 steels, although only rupture strength was demonstrated for the P122 steel weldment portion in order to compare its strength with that of P92 steel weldments.

Weld Fabrication and Creep Rupture Test

Table 1 shows the chemical compositions of the materials tested and the Gr.92 weld metals. The dimensions of the tested P92 and P122 pipes were ϕ350mm in outside diameter and ^{t}50mm in wall thickness. The details of the manufacturing processes have been previously reported[2].

In addition to these pipes, a rolled plate of P92 with ^{t}50mm thickness was used to fabricate the

Table 1 Chemical compositions of test materials and weld metals (mass%)

Steel	Materials	C	Si	Mn	P	S	Ni	Cu	Cr	Mo	W	V	Nb	B	N
P92	Plate	0.09	0.06	0.45	0.005	0.002	–	–	9.01	0.50	1.77	0.20	0.050	0.004	0.048
	Pipe	0.11	0.04	0.46	0.008	0.001	–	–	8.96	0.47	1.84	0.20	0.069	0.001	0.051
P122	Pipe	0.12	0.05	0.64	0.016	0.001	0.32	0.86	10.61	0.44	1.87	0.21	0.050	0.002	0.064
Gr.92 Weld Metal	SMAW	0.08	0.49	1.46	0.002	0.001	0.56	–	8.88	0.52	1.68	0.24	0.080	–	0.040
	SAW	0.08	0.32	1.49	0.008	0.001	0.58	–	8.91	0.49	1.60	0.29	0.047	0.003	0.042

weldment. The weldments were fabricated by means of a Shielded Metal Arc Welding (SMAW) process and a Submerged Arc Welding (SAW) process using Gr.92 filler metal with matching composition of P92 for both grades of steels. A Gas Tungsten Arc (GTA) process was also employed for the root pass welding. The welding conditions have been reported as preheat temperature of 200 ℃ and interpass temperature of 150℃ to 300℃, with 7 passes and 10 layers for SMAW and 22 passes and 14 layers for SAW[2]. The weldments were subjected to post weld heat treatment (PWHT) under the condition of 740℃×4hFC. Part of plate weldment was then over-aged at 720℃ for 200h, which is parametrically equivalent to heating at 600℃ for 230,000 hours of service exposure.

The cross weld samples were machined to standard creep rupture specimens in which the fusion line must be placed at the longitudinal center of the specimen in order to include weld metal (WM), heat affected zone (HAZ), and base metal (BM), while the weld metal creep rupture specimens were machined from the center of the weld deposit along the direction of welding. The creep rupture tests were conducted at temperatures of 550℃, 600℃ and 650℃ and at stress ranging from 95 to 255MPa, reaching a maximum of 20,000 hours rupture time.

Weld Metal Strength and Hardness Profile in Weldments

The iso-stress creep rupture tests were carried out on the SMAW and SAW weld metal of the weldment made of Gr.92 filler metal after PWHT at 125MPa and at temperatures ranging from 600℃ to 660℃. Fig. 1 demonstrates the temperature-time to rupture plot for the weld metals in comparison with the P92 pipe base metal. The extrapolated temperatures at a rupture time of 100,000 hours were 583℃ for the SMAW weld metal, 545℃ for the SAW weld metal, 603℃ for the base metal, although the weld metals exhibited similar or greater strength compared with the base metal in the short-term region as shown in the figure. This indicates that SMAW weld metal and SAW weld metal are respectively 3% and 15% weaker than base metal on the basis of 10^5 temperature.

Fig. 2 shows hardness profiles in the P92 weldments of plate by SMAW and pipe by SAW. Hardness was measured at the inside and outside of the wall, as well as at midwall. The over-aged weldment of plate by SMAW was subjected to hardness measurement at the outside and midwall. In both weldments, a softened region was seen in the heat affected zones, while the hardness in the base metal was measured as being Hv 210 for pipe and Hv 215 for plate. The maximum reduction of hardness in the softened zone was determined to be Hv 30 for pipe and Hv 15 for plate, although the softened region of both weldments had almost the same width at any portion along the wall. Over-aging produced a major reduction of hardness on the entire surface of the weldment section. No difference in the hardness of weld metal was seen between the weldments by SMAW or SAW.

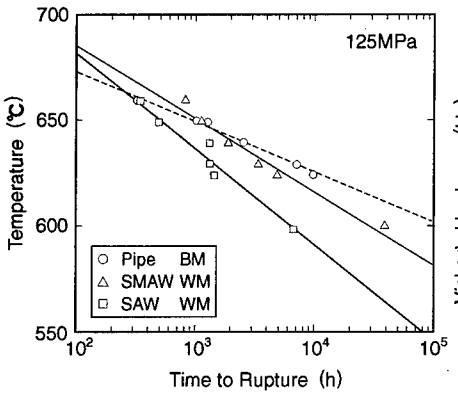

Fig. 1 Iso-stress plots of creep rupture data for Gr.92 weld metal compared with pipe base metal

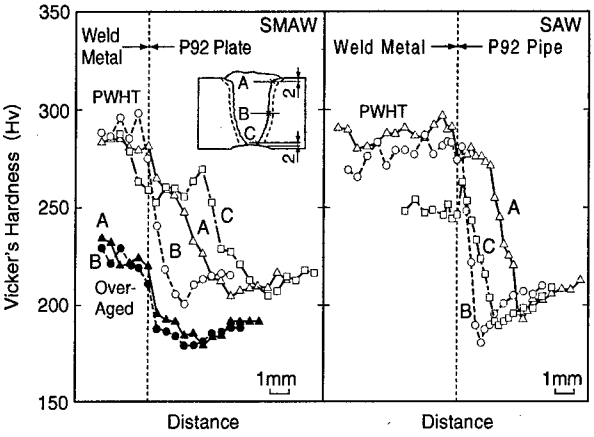

Fig. 2 Hardness profile in P92 weldments

Creep Rupture Properties of Weldments

The cross-weld creep rupture tests revealed the rupture stress, ductility represented by rupture strain or elongation, and failure mode. The location of failure was also determined by the visual examination of ruptured specimens and by the cross-sectional observation of macrostructure. However, it is often difficult to distinguish the failure location, particularly in the heat affected zone and base metal, and criteria were developed as shown in Fig. 3. Figs. 4 and 5 show the stress-time to rupture diagram and Larson-Miller plot of rupture data, which indicate the creep rupture strength of SMAW weldments. In these figures solid lines (P92) and dotted line (P122) show the average strength of the base metal as-manufactured[3][4]. Fig. 4 also illustrates the location of failure using the symbols H (HAZ failure), W (weld metal failure), and no sign (base metal failure) on the data plots. Fig. 5 also includes the data points of P122 for comparison. There is little difference in the creep rupture strengths of the weldments with the exception of the over-aged one, meaning that the differences between plate and pipe, and between P92 and P122, are small. The over-aged weldment has remarkably lower strength due to weld metal failure, that is, the measured strength indicates the properties of the weld metal. The 10^5h creep rupture strengths at 600℃ of SMAW weldments (excepting the over-aged one) were extrapolated from Fig. 5 to be approximately 15% weaker than the base metal. The over-aged one was 25% weaker than the base metal. Fig. 6 shows rupture

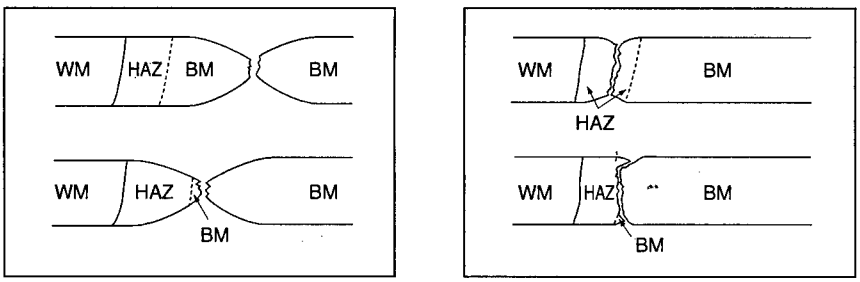

(a) Base Metal Failure (b) HAZ Failure

Fig. 3 Failure location criteria for cross weld creep rupture specimens

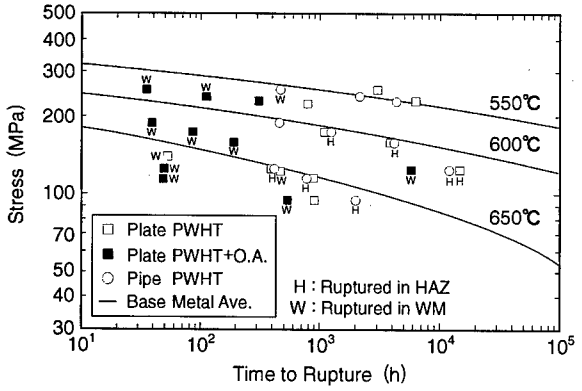

Fig. 4 Isothermal time to rupture diagram for P92 SMAW weldment

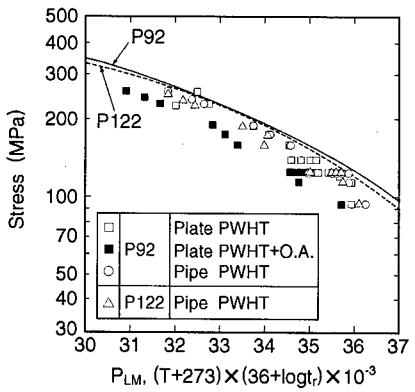

Fig. 5 Larson-Miller plot of creep rupture data for P92 and P122 SMAW weldment

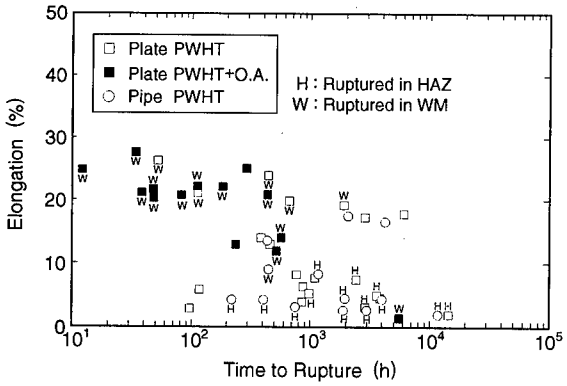

Fig. 6 Creep rupture elongation against time to rupture for P92 SMAW weldment

elongation against time to rupture for the SMAW weldments. The rupture elongation tends to decline with the time to rupture, and the HAZ failure in particular shows lack of ductility.

Figs. 7 and 8 show the stress-time to rupture diagram and Larson-Miller plot for SAW weldments of P92 and P122 pipes The average strength of the base metal are also demonstrated in the figures. Here, in the short-term region, the rupture strengths of the SAW weldments are almost at the same level as the minimum strength of the base metal; in the long-term region, strength declined substantially due to HAZ failure in the pipe weldment and WM failure in the plate weldment. Fig. 8 clearly shows that the difference in rupture strength between plate and pipe and between P92 and P122 is small. The extrapolated 10^5h creep rupture strength at 600℃ for the SAW weldment was approximately 15% lower than the base metal strength. Fig. 9 shows rupture elongation against time to rupture for the the SAW weldment. The tendency toward reduced rupture elongation with the time to rupture of SAW weldment is similar to that of the SMAW weldment.

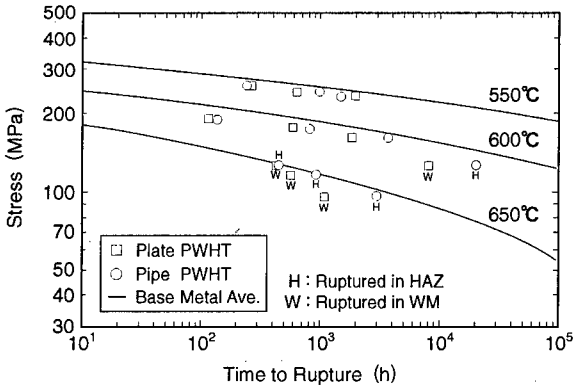

Fig. 7 Isothermal time to rupture diagram for P92 SAW weldment

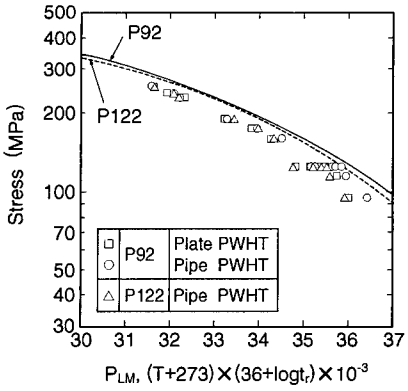

Fig. 8 Larson-Miller plot of creep rupture data for P92 and P122 SAW weldment

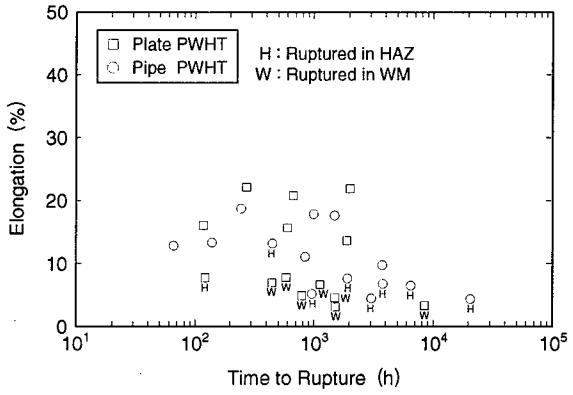

Fig. 9 Creep rupture elongation against time to rupture for P92 SAW weldment

Rupture Strain Behavior and Failure Mode

Cross-weld creep rupture specimens consist of the weld metal, the heat affected zone, and the base metal itself. The heat affected zone is composed of a fine grain region, a coarse grain region, the transitional region, and the intercritical HAZ and tempered region heated at a temperature just under Ac_1. The creep strain behavior of the weldment is therefore easily recognized to be more complicated than in monostructured material.

Fig. 10 gives the relationship between average creep rate and time to rupture which can be expressed by the Monkman-Grant equation[5]

$$\dot{\varepsilon}_{ave} = K_{MG}\, t_r^{-m} \qquad (1)$$

where K_{MG} and m are constants. In this figure the solid line is expressed by use of 7.0 for K_{MG} and 1.3 for m, which is regarded as the average line for all the data. The dotted lines are paralleled to the average line as the maximum and minimum lines for the data band. The Monkman-Grant equation for

the P92 weldment can be approximately expressed as follows,

$$\dot{\varepsilon}_{ave} = 7.0^{+21.2}_{-4.8}\ t_r^{-1.3} \tag{2}$$

Fig. 11 gives the relationship between average creep rate and applied stress, which is expressed by the Norton equation[6]

$$\dot{\varepsilon}_{ave} = A\sigma^n \tag{3}$$

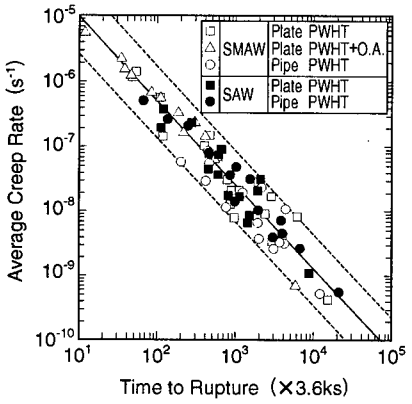

Fig. 10 Monkman-Grant plot of average creep rate against time to rupture for P92 weldment

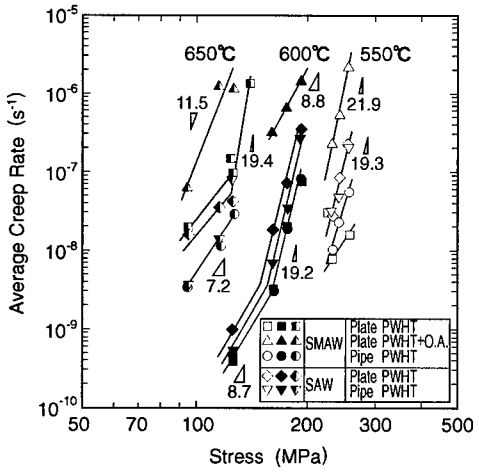

Fig. 11 Stress dependence of average creep rate for P92 weldment

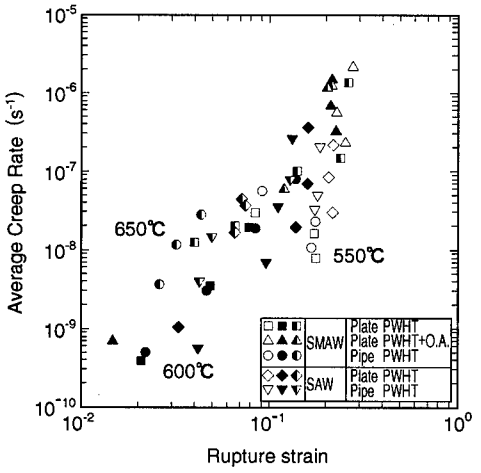

Fig. 12 Relationship between average creep rate and rupture strain for P92 weldment

where A and n are respectively the constant and the Norton stress exponent. The Norton stress exponent is assumed to be as large as approximately 19 in the high stress region and to be reduced to about 7 to 9 in the low stress region. From those findings it can be said that creep strain measurement is useful in predicting long-term creep rupture life. That is, the creep life at a given stress is extrapolated by use of the Monkman-Grant equation as shown in Fig. 10, together with the Norton equation shown in Fig. 11.

Fig. 12 shows the relationship between the average creep rate and rupture strain. The rupture strain appears to be constant with an average value of approximately 20% at the average creep rate above $1\times10^{-7}s^{-1}$, and shifting to decline with a decrease of the average creep rate. Since the average creep rate is taken to be proportional to the minimum creep rate, the minimum creep rate affects rupture elongation.

Figs. 13 and 14 demonstrate the failure mode of the P92 weldments in terms of the stress and temperature of creep rupture tests for the plate weldment and the pipe weldment respectively. In the case of the plate weldment, the failure map is not clear due to weld metal failure at a higher temperature, considered to be caused by the small difference of the hardness between the softened region of the heat affected zone and the base metal. However, the location of failure shifted from weld metal at temperatures below 650℃ to HAZ at 660℃ under stress of 125MPa. This suggests that HAZ failure occurs more easily at higher temperatures. On the other hand, the pipe weldment clearly showed a failure map with two regions, divided into base metal failure and HAZ failure as shown in Fig. 14. From the figure, the HAZ failure took place at higher temperature and lower stress. The present results with respect to P92 pipe weldment indicate that SAW allows base metal failure at a lower stress region than SMAW.

Figs. 15 and 16 show sectional macrostructures of creep rupture specimens from P92 pipe SMAW weldments. The HAZ failure is observed at 160MPa and at 600℃, and at temperatures of 600℃ and above under stress of 125MPa. Figs. 17 and 18 show rupture specimens from P92 pipe SAW weldments. Here, under stress of 125 MPa HAZ failure is demonstrated at temperatures of 600 ℃ to 650℃, and base metal failure takes place at 660℃. This suggests that the stress level of 125MPa is still too high at 660℃ to cause HAZ failure in SAW weldments.

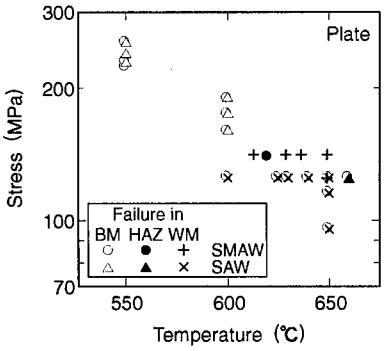

Fig. 13 Creep rupture failure map for P92 plate weldment

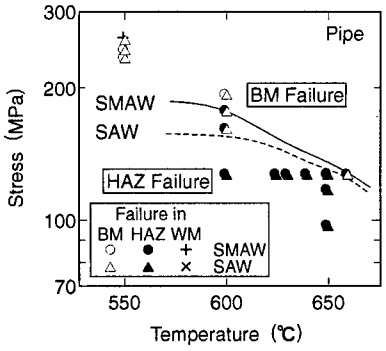

Fig. 14 Creep rupture failure map for P92 pipe weldment

Temp. (℃)	Stress (MPa)	Time to Rupture (h)	Sectional Macrostructure
550	240	2123	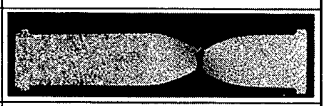
	230	4312	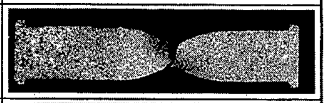
600	175	1206	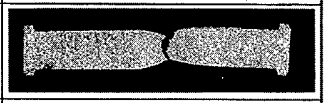
	160	4075	
	125	11808	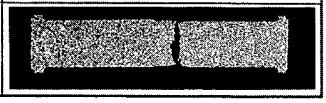

Fig. 15 Sectional macrostructures of cross-weld creep rupture specimens for P92 pipe SMAW weldment in terms of stress dependence at 550℃ and 600℃

Stress (MPa)	Temp. (℃)	Time to Rupture (h)	Sectional Macrostructure
125	625	3686	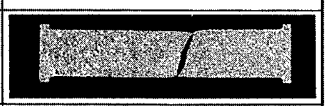
	630	2985	
	640	1916	
	650	413	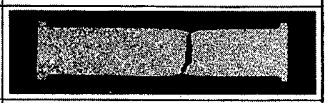
	660	203	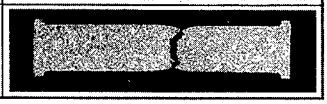

Fig. 16 Sectional macrostructures of cross-weld creep rupture specimens for P92 pipe SMAW weldment in terms of temperature dependence at 125MPa

Temp. (℃)	Stress (MPa)	Time to Rupture (h)	Sectional Macrostructure
550	240	999	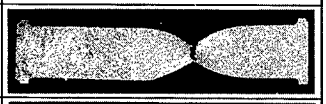
	230	1512	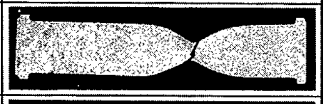
600	175	835	
	160	3737	
	125	20553	

Fig. 17 Sectional macrostructures of cross-weld creep rupture specimens for P92 pipe SAW weldment in terms of stress dependence at 550℃ and 600℃

Stress (MPa)	Temp. (℃)	Time to Rupture (h)	Sectional Macrostructure
125	625	6546	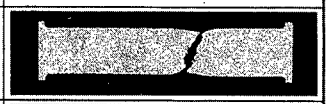
	630	3890	
	640	1909	
	650	449	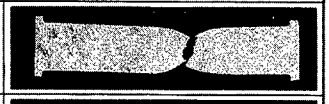
	660	66	

Fig. 18 Sectional macrostructures of cross-weld creep rupture specimens for P92 pipe SAW weldment in terms of temperature dependence at 125MPa

Conclusions

Uniaxial creep rupture tests were carried out on cross weld samples from P92 steel weldments made with SMAW and SAW processes on plate and pipe in order to determine the rupture strength and rupture strain, as well as failure mode in terms of stress and temperature. P122 steel pipe weldments were also subjected to cross weld creep rupture tests in order to compare the strength with that of P92 in a Larson-Miller parametric diagram. The results obtained are as follows,

(1) The creep rupture strength of the weldments was found to be at almost the same level as the minimum strength of the base metal in the short-term region, while the weldments were found to exhibit reduced strength of up to approximately 15% from the base metal average. However, a large reduction in rupture strength was seen in the P92 plate SMAW weldment due to weld metal failure.

(2) Little difference was observed in the creep rupture strength of weldments among the plate and pipe product forms, SMAW and SAW welding processes, or P92 and P122 materials.

(3) Rupture strain tended to decline with the time to rupture. The HAZ failure in particular showed a lack of ductility. The pipe weldment exhibited a failure map with two regions divided into base metal failure and HAZ failure, as the HAZ failure took place at higher temperature and lower stress.

(4) The average creep rate of the weldment was well correlated to the time to rupture as expressed by the Monkman-Grant equation, albeit with some deviation. The relationship between average creep rate and applied stress was also expressed by the Norton equation, which resulted in the success of the prediction of the long-term creep rupture life by measuring the creep strain in the weldment.

References

[1] F. Masuyama and T. Yokoyama: D. Coutsonradis et al. (eds.), Materials for Advanced Power Engineering, Part 2, Kluwer Academic Publishers, Netherland, (1994), 301

[2] F. Masuyama and T. Yokoyama: E. Metcalfe (ed.), New Steels for Advanced Plant Up to 620℃, PicA Publishing, London, UK, (1995), 30

[3] Y. Hasegawa, K. Shibata, H. Dohnomae and Y. Yazaki, Int. Conf. Ecology and Economy in Metal Forming and Cutting, Archen, Germany, June 24-27, (1995)

[4] Y. Sawaragi, A. Iseda, K. Ogawa, F. Masuyama and T. Yokoyama: E. Metcalfe (ed.), New Steels for Advanced Plant Up to 620℃, PicA Publishing, London, UK, (1995), 45

[5] F. C. Monkman and N. J. Grant: ASTM Proceedings, 56 (1956), 593

[6] F. H. Norton: The Creep of Steel at High Temperature, McGraw-Hill, New York, (1929)

Fujimitsu Masuyama, e-mail: masuyama@ngsrdc.mhi.co.jp, fax: +81-95-834-2055

Key Engineering Materials Vols. 171-174 (2000) pp. 109-114
© 2000 Trans Tech Publications, Switzerland

Creep Life Assessment of High Chromium Ferritic Steels by Recovery of Martensitic Lath Structure

K. Sawada[1], K. Maruyama[1], Y. Hasegawa[2] and T. Muraki[2]

[1] Department of Materials Science, Graduate school of Engineering, Tohoku University, Sendai, 980-8579, Japan

[2] Nippon Steel Corporation, Technical Development Bureau, Steel Research Laboratories, Steel Products Research Lab.-II, Shintomi 20-1, Futtsu-shi, Chiba-ken 293-8511, Japan

Keywords: Ferritic Steel, Lath Structure, Creep Damage, Hardness

Abstract

High chromium ferritic steels have a tempered martensitic lath structure. Increase of lath width during creep results in the acceleration of creep rate and eventual failure of the steels. Lath width d increases during creep, and reaches a stationary value d_s determined by creep stress. The growth rate of lath width is faster at a higher stress and temperature. A normalized change in lath width, $\Delta d/\Delta d_s$, was introduced as a measure of the recovery process of martensitic lath structure. $\Delta d/\Delta d_s$ is uniquely related to creep strain ε and the relation is independent of creep stress and temperature. This $\Delta d/\Delta d_s$ - ε relation obtained by an accelerated creep test at a higher temperature or stress is applicable to any creep condition including service conditions of engineering plants. Creep strain can be estimated from the measurement of $\Delta d/\Delta d_s$ based on the $\Delta d/\Delta d_s$ - ε relation.

Introduction

Many of power generating plants in Japan have been operating for more than 100000 hours. When components in the plants have been used at elevated temperatures for longer-term than design life, it is necessary to assess residual life of the components. In order to assess the residual life, creep damage of materials composing the components has to be measured. Plants operating under USC steam conditions of an increased pressure at a higher temperature require boiler and steam turbine components with higher creep rupture strength than those of conventional low Cr ferritic steels. High Cr ferritic steels are used for the components in USC plants. The methods of residual life assessment of low Cr ferritic steels have been proposed, [1,2] however, there is a few study about measuring creep damage of high Cr ferritic steels.[3-5] For example, measurement of hardness is tried to estimate the creep damage of high Cr ferritic steels.[4,5] The hardness of high Cr ferritic steels decreases during long-term annealing and creep deformation.[4,5] The steels have a tempered martensitic lath structure and are strengthened by precipitates. The decrease of hardness is caused by recovery of the lath structure and coarsening of the precipitates during creep.[5,6] The recovery of the lath structure can be strongly related to creep strain because the recovery takes place during creep even if the creep condition is higher stress and short-term.[7] Relationship between hardness and creep time has to be clear under

*Present address : Strength and Life Evaluation Research Station, Frontier Research Center for Structural Materials, National Research Institute for Metals, Sengen, Tsukuba, 305-0047, Japan

various creep conditions in order to assess residual creep life by measuring hardness. It is important to investigate the recovery process of the lath structure during creep since the recovery results in the decrease of the hardness.

The objective of this study is to investigate quantitatively relationship between the recovery of lath structure and creep deformation in high Cr ferritic steels.

Experimental procedure

Chemical compositions of the steels studied are given in Table 1. The materials were normalized and then tempered under the conditions listed in the table. The gauge length and diameter of creep specimens were 50mm and 10mm on ASME-T91 steel, and 30mm and 6mm on ASME-P92 steel respectively. Creep tests were carried out under constant loads in air, and some tests were interrupted to study recovery of lath structure during creep. Several test conditions were selected to investigate effects of stress and temperature on the recovery process of the lath structure.

Lath width and dislocation density in lath interior were measured by TEM observations. The short distance between a pair of lath boundaries was taken as the lath width, and its mean value was evaluated by taking an average of 150～200 lath width. Vickers hardness was measured in crept specimens.

Table 1. Chemical compositions (mass%) and heat treatment procedures of the steels studied.

	C	Si	Mn	P	S	Ni	Cr	Mo	W	V
ASME-T91	0.10	0.40	0.43	0.014	0.001	0.07	8.73	0.96	—	0.22
ASME-P92	0.114	0.30	0.33	0.011	0.001	0.13	9.10	0.36	1.75	0.16

Nb	Al	N	B	Normalizing	Tempering
0.09	0.013	0.051	—	1323K 3.0ks A.C.	1053K 3.6ks A.C.
0.059	<0.002	0.036	0.0012	1343K 14.4ks O.Q.	1033K 16.2ks A.C.

Results and Discussion

Dislocation substructure of ruptured specimens

Figure 1 (a) shows dislocation substructure of T91 steel before creep. The steel has tempered martensitic lath structure without δ -ferrite. The mean lath width is 0.53μm.

Fig.1. Changes of lath structure in T91 steel. (a) Before creep, (b) 873K 137MPa t_r= 12.2Ms(3397.5h), (c) 923K 118MPa t_r = 0.54Ms(149.3h), (d) 923K 73.5MPa t_r= 27.4Ms(7614h).

Screw portion of ruptured specimens was observed by TEM to make clear the change of lath structure during aging without deformation. The lath width was 0.55μm in the specimen ruptured at 923K after 27.4Ms(7614.2h). This value indicates that lath boundary is thermally stable and the lath width does not change without deformation.

Figure 1 (b)~(d) show the lath structure observed in gauge sections of ruptured specimens. The widths obviously increase after creep deformation. The relationship between lath width and creep stress normalized by the shear modulus measured in ruptured specimens is shown in Fig.2. The creep stress is the true stress in the portion of each specimen at which the lath width was measured. The lath width d is represented by the following equation :

$$\frac{d}{b} = A\left(\frac{G}{\sigma}\right) \tag{1}$$

where b is the length of Burgers vector, A is a coefficient, σ is creep stress, and G is the shear modulus.(G(MPa) = $-43T$(K)$+103572$, 823K < T < 923K) In Fig.2, A is 11. The relation defined by eq. (1) has been established between subgrain size and creep stress in single phase materials.[8] The same relation has been reported also on 12Cr steel.[9,10] As seen in Fig.2, this relation is not affected by testing temperature.

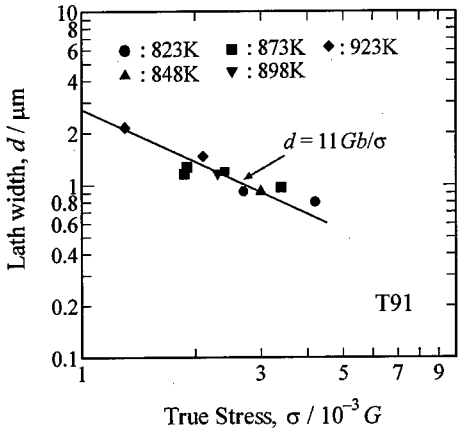

Fig.2. Relationship between lath width and true stress normalized by the shear modulus in T91 steel.

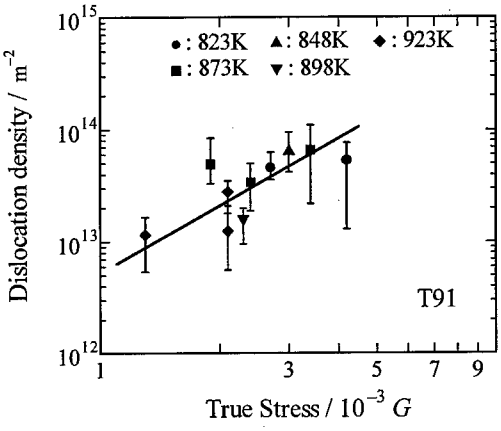

Fig.3. Relationship between dislocation density in lath interior and true stress normalized by the shear modulus in T91 steel.

Dislocation density in lath interior decreases with the progress of creep deformation. Figure 3 shows the relation between the dislocation density ρ in lath interior measured after rupture and creep stress. The results are described by the following well known equation [11] :

$$\rho b^2 = C\left(\frac{\sigma}{G}\right)^2 \tag{2}$$

where C is a coefficient. This relation also does not change with testing temperature.

Consequently, the lath width and dislocation density in lath interior increases and decreases respectively during creep, and finally reach the stationary values given by eqs. (1) and (2). The stationary values depend only on creep stresses. The decreasing process of the dislocation density during creep is not appropriate measure of the recovery process because the dislocation density

has a large scatter in data.

Recovery process of lath structure

Figure 4 demonstrates effects of stress and temperature on the recovery process of the lath structure. Microstructural change of the lath structure during creep under 873K,137MPa is shown in Fig.5. The lath width gradually increases with increasing creep time. In Fig.4, the data points at the longest creep time in each creep condition were observed in ruptured specimens. These data are the stationary values determined by creep stress shown in Fig.2. The lath width increases rapidly at a higher temperature and stress. It is necessary to express the recovery process of the lath structure independent of stress and temperature in order to assess creep life by measuring the lath width.

The increase of the lath width is caused by the migration and unknitting of dislocations forming lath boundaries. These processes suggest that creep strain affects the recovery of lath structure.

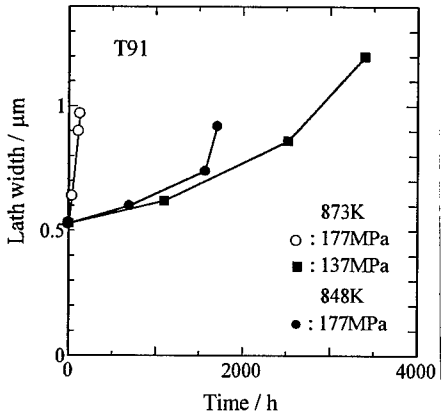

Fig.4. Effects of temperature and stress on recovery process of lath structure in T91 steel.

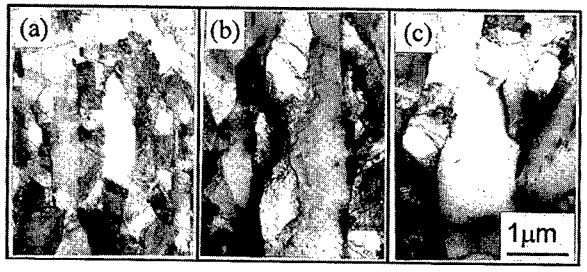

Fig.5. Change of lath structure as a function of time. (a) Before creep, (b) 4.0Ms(1100h) and (c) 9.0Ms (2500h) at 873K 137MPa. (T91)

Creep strain is accumulated more rapidly at a higher temperature and stress. This fact can explain the quick recovery process of lath structure at the higher temperature and stress shown in Fig.4. Figure 6 shows effects of temperature and stress on relationship between the lath width and creep strain. The lath width increases with increasing strain and reaches the stationary value after rupture. The relationship between the lath width and strain does not depend on testing temperature. This fact indicates that creep strain plays an important role in the recovery of lath structure.[12] On the other hand, the increase of lath width per a strain is larger at the

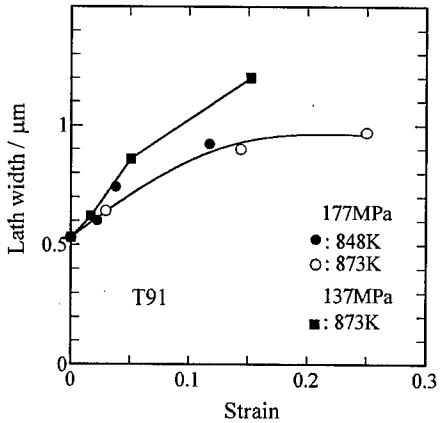

Fig.6. Effects of temperature and stress on relationship between lath width and creep strain in T91 steel.

lower stress.

Normalized recovery of lath width

The relation between lath width and strain changes with stress as shown in Fig.6. The different values of the stationary lath width at each creep stress can affect the recovery process of the lath structure. The difference between the initial lath width and stationary value is larger at a lower stress. When the difference is larger, the lath width increases more quickly with strain. To cancel this effect, a normalized change in the lath width, $\Delta d/\Delta d_s$, was introduced as the measure to explain the effect of stress on the relation between the lath width and strain.

Δd is the change in lath width from initial value d_0. Δd_s is defined by the following equation :

$$\Delta d_s = d_s - d_0 \tag{3}$$

where d_s is the stationary value given by eq. (1). Relationship between $\Delta d/\Delta d_s$ and creep strain under various creep conditions is shown in Fig.7. This figure contains data observed in T91 and P92. There is a almost linear relation between the $\Delta d/\Delta d_s$ and creep strain. The relation does not depend on temperature and stress, and can be obtained by an accelerated creep test at a higher temperature and stress. From this relation one can estimate creep strain by measuring lath width. Creep damage of materials with high ductility is assessed by measuring creep strain because creep strain is closely related to creep life.[12] Thus, combining creep data and the creep strain calculated from the relation in Fig.7, one can assess creep life of the high Cr ferritic steels with martensitic lath structure.

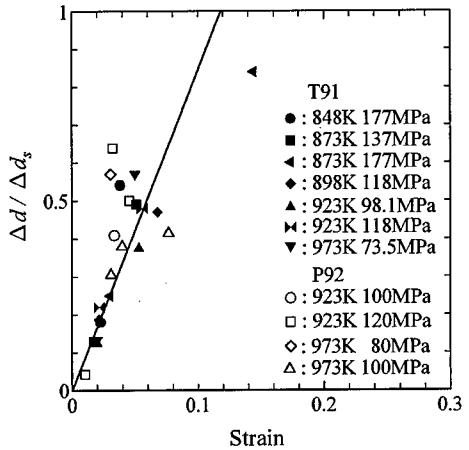

Fig.7. Relation between normalized lath width and creep strain under various creep conditions in the two steels.

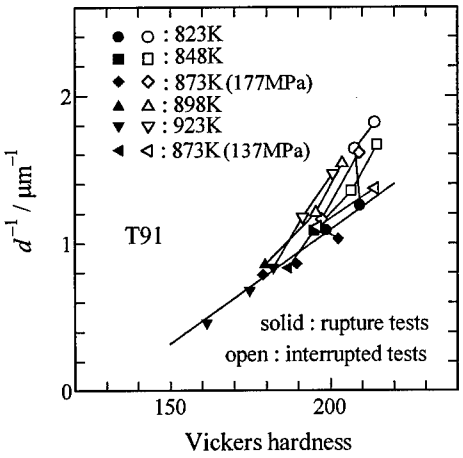

Fig.8. Relationship between lath width and hardness in T91 steel.

Relation between lath width and hardness

Figure 8 shows relationship between the lath width and hardness of ruptured and interrupted specimens. The lath width of ruptured specimens has a linear relation to hardness independent of creep conditions. On the other hand, the hardness of interrupted specimens deviates from the linear relation, and the relation depends on creep conditions. However, the hardness can have a relation to creep strain since there is the close relation between $\Delta d/\Delta d_s$ and creep strain as shown in Fig.7. In order to assess creep life by measuring hardness, it is necessary to make clear

the effects of temperature and stress on the relation between the lath width and hardness of interrupted specimens.

Conclusions

(1) Lath structure in high Cr ferritic steel recovers during creep deformation. Lath width increases and dislocation density in lath interior decreases to the stationary values determined by creep stress.

(2) Growth rate of the lath width is faster at a higher temperature and stress. The lath width has a linear relation to creep strain independent of testing temperature. A relation between a normalized change in lath width, $\Delta d/\Delta d_s$, and creep strain does not depend not only on temperature and stress but also the materials.

(3) There is a relation between hardness and lath width in crept specimens. The hardness can have a relation to creep strain because the $\Delta d/\Delta d_s$ -strain relation is uniquely related to creep strain.

References

[1] F.Masuyama, Materia Jpn., 35 (1996), p.753.
[2] H.Yoshizawa, M.Nakashiro, S.Kihara and H.Umaki, Tetsu-to-Hagané, 82 (1996), p.1011.
[3] Correlation between microstructure and strength of high Temperature Materials, The society of Materials Science Japan, (1997).
[4] F.Masuyama, N.Nishimura and A.Sasada, CAMP-ISIJ, 11 (1998), p.614.
[5] A.Tohyama, Y.Minamai and Y.Masuyama, CAMP-ISIJ, 11 (1998), p.615.
[6] K.Sawada, K.Maruyama, R.Komine and Y.Nagae, Tetsu-to-Hagané, 83 (1997), p.466.
[7] K.Sawada, M.Takeda, K.Maruyama, R.Ishii and M.Yamada, The 6th Liege Conference on Materials for Advanced Power Engineering, 5-7 October, I (1998), p.577.
[8] S.Takeuchi and A.S.Argon, J. Mater. Sci., 11 (1976), p.1542.
[9] W.Blum and S.Straub, Steel Res., 62 (1991), p.72.
[10] Y.Kadoya, B.F.Dyson and M.McLean, The 6th Liege Conference on Materials for Advanced Power Engineering, 5-7 October, I (1998), p.595.
[11] J.Cadek, Creep in Metallic Materials, Elsevier, Amsterdam, (1988).
[12] K.Asakawa, A.Ohtomo and Y.Saiga, Tetsu-to-Hagnaé, 65 (1979), p.869.

Corresponding author
K.Sawada
e-mail : sawada@nrim.go.jp
Fax : +81-298-59-2201

Key Engineering Materials Vols. 171-174 (2000) pp. 115-120
© 2000 Trans Tech Publications, Switzerland

Creep Rupture Properties of Helium Implanted Low Activation Martensitic Steel for Nuclear Fusion Application

N. Yamamoto[1], J. Nagakawa[1] and K. Shiba[2]

[1] National Research Institute for Metals, 1-2-1, Sengen, Tsukuba, Ibaraki 305-0047, Japan

[2] Tokai Establishment, Japan Atomic Energy Research Institute, Tokai, Ibaraki 319-1106, Japan

Keywords: Nuclear Fusion Reactor, Radiation Effect, Nuclear Transmutation, Helium Embrittlement, GB Embrittlement, Mechanical Properties, Ion Irradiation, Helium Implantation

Abstract

We have examined the effect of nuclear-transmutational helium, which is known to often induce grain boundary embrittlement at high temperatures, on creep rupture properties of a candidate low activation martensitic steel, F82H (Fe-8%Cr-2%W-0.2%V-0.04%Ta), for first wall/blanket structural applications in advanced nuclear fusion reactors. Utilizing α-particle irradiation at an accelerator, helium was introduced into creep specimens at 823 K with concentrations up to about 300 appmHe. It has been demonstrated through subsequent creep tests at the same temperature that both creep rupture time and elongation were not degraded by helium. The fracture appearance of ruptured faces remained perfectly transgranular after helium implantation and no indication of grain boundary fracture was detected. These results prove superior helium-embrittlement-resistance of this steel and raise its potential for future fusion use.

Introduction

Neutronic production of radio-active nuclides has been recognized as a main material problem in the field of nuclear fusion technology from the viewpoint of waste management, environmental safety and public acceptance. It is particularly important in case of advanced systems, that is, a prototype reactor and the beyond, because much larger neutron doses should be exerted in these reactors in comparison with an experimental one like ITER (International Thermonuclear Experimental Reactor) of which construction is now under consideration. The activation occurs most extensively in structural materials employed for first wall/blanket structures. Accordingly, a great concern has been paid to reducing the amount of activation in those materials. At the same time they must withstand severe fusion environments, such as heavy irradiation of energetic neutrons, and keep material integrity.

In order to develop the materials which meet the demands stated above, many investigations have been conducted and some candidates were proposed. Amongst them, the family of low activation martensitic steels (Fe-Cr-W-V-Ta) is now evaluated as a most promising one, mainly due to its maturity in industrial standpoints [1].

The propose of this work is to clarify the influence of helium which is generated in materials as a result of (n, α) reactions and often deteriorates high temperature mechanical properties by inducing intercrystalline separation, on creep rupture properties of a representative low activation martensitic steel and, more ultimately, to obtain information useful for feasibility inspection of this kind of steels for advanced fusion applications. Long term tests are especially crucial since detrimental helium effects are more liable to arise in these tests relative to short time examinations like tensile ones, as

formerly established [2-4].

Experimental

The material studied here is the IEA (International Energy Agency) version of F82H (Fe-0.09%C-7.82%Cr-1.98%W-0.19%V-0.04%Ta-0.07%Si-0.1%Mn-0.003%P -0.001%S) [5] which was prepared for an international round-robin test [6] organized by the agency. The 25 mm thick plate stocks of this steel were supplied by NKK Corporation after normalizing (1313 K, 2.4 ks) and tempering (1023 K, 3.6 ks). Creep test samples with dimensions shown in Fig. 1 were fabricate from those plates through spark cutting and mechanical grinding. The unusual small thickness of the samples is due to the projective range of α-particles mentioned below.

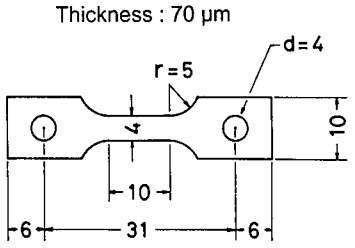

Fig. 1. Dimensions of creep specimen (in mm).

Helium implantation which aims to simulate its transmutational production in the reactor was carried out using a 20 MeV α-beam from the NRIM compact cyclotron. Fig. 2 gives a schematic illustration of the irradiation arrangement of the target chamber utilized in this work. The energy of incident ions was moderated with an energy degrader comprising 32 Al-foils with different thicknesses so as to achieve homogeneous helium deposition all through the specimen depth. In addition, the beam was scanned over irradiation area with two directions. The temperature of specimens during irradiation was measured with two chromel-alumel thermocouples spot-welded on a dummy plate situated in the middle of the irradiated area. To compensate the temperature change due to fluctuation of the beam, a infra-red lamp heater with rapid response was applied for temperature control. The amount of implanted helium was estimated on the basis of measured target current.

Helium was injected to specimens at 823 K, a desired upper temperature limit of this steel for

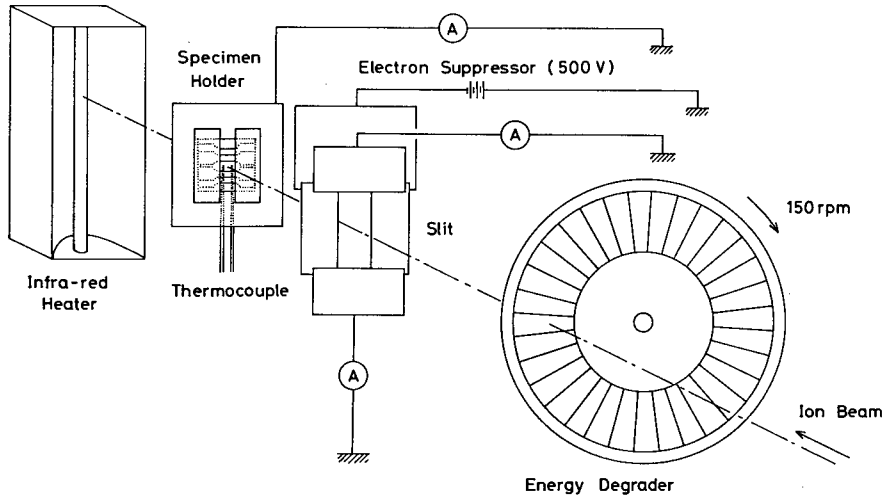

Fig. 2. Schematic illustration of irradiation setup for helium implantation.

fusion use, to contents of about 100 and 300 appm with an implantation rate of around 1×10^{-3} appm/s in a vacuum. Throughout the implantation, temperature change was suppressed within 4 K and the difference of readings between left and right thermocouples (see, Fig. 2) was less than 20 K even in the worst instance.

Creep rupture tests after implantation were performed also at 823 K in a vacuum on electronically controlled rigs illustrated in Fig. 3. In this machine the applied load is always observed with a load cell and a load deviation from the stated value is canceled by cross head motion based on feedback signals. The shifts of load and temperature from nominal values during creep tests were maintained less than ±1 MPa and ±1 K, respectively. The creep strain was monitored in a high accuracy of several μm with two linear variable differential transformers each connected to a rotary encoder. Such creep rupture tests have similarly been done for reference control specimens which were not irradiated but underwent an annealing to neutralize thermal exposure during the implantation. The creep ruptured surface was fractographically examined under SEM (Scanning Electron Microscope) chiefly to determine the type of failure.

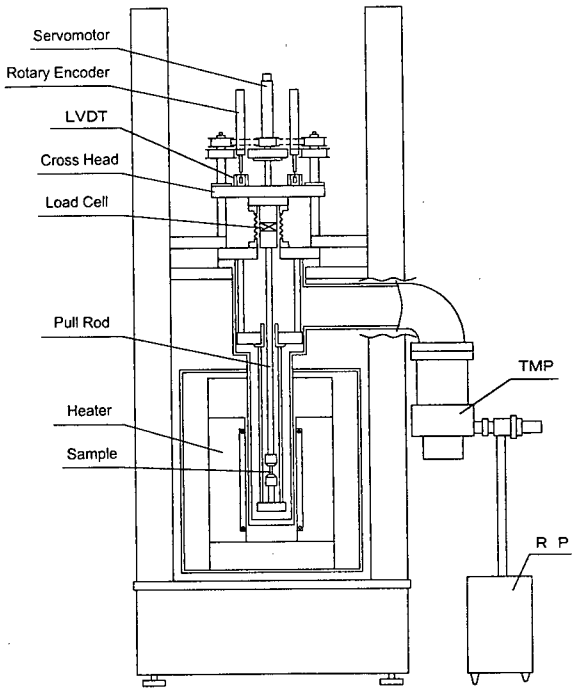

Fig. 3. Creep testing machine.

Results and Discussion

Fig. 4 presents ordinary creep stress versus time to rupture relation on helium implanted and reference specimens for both helium concentrations. As seen in the figure, every set of data revealed very strong stress dependence and data points were thereby somewhat scattered in some cases. Concerning helium effects, there was noticed no meaningful disagreement between rupture strength of irradiated samples and that of corresponding references when helium was introduced at 100 appm. In the meanwhile, samples bearing 300 appmHe exhibited mostly five times longer rupture time compared to that of helium free controls. Though microstructures of ruptured samples have not been observed yet, this extension in the creep life is most probably due to precipitation of small helium bubbles and/or clusters within grains which prevent dislocation motions by pinning.

The rupture elongation is given in Fig. 5, also as a function of creep rupture time. It seems to have lain within the variation of normal experimental errors, regardless of whether helium was present or not. No significant helium effect was hence perceived in respect to creep rupture strain with concentrations up to 300 appmHe. The values of rupture elongation observed in this experiment ranged roughly from 3 to 6 % and these values were much smaller than those of ordinary bulk round-bar samples previously tested [5]. This difference can be attributed to specimen size effects [7], at

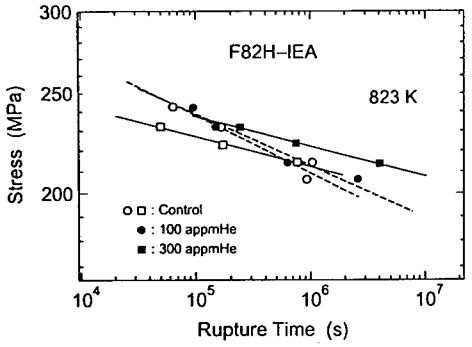

Fig. 4. Creep rupture strength as a function of creep life at 823 K for helium implanted specimens and unimplanted controls of F82H IEA heat material.

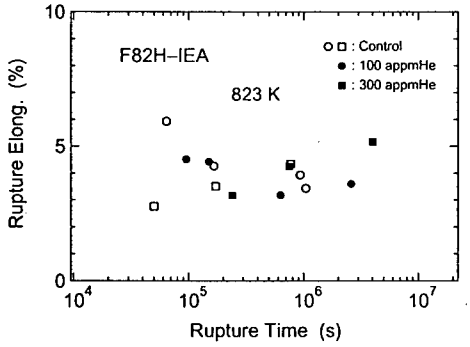

Fig. 5. Creep rupture elongation as a function of creep life at 823 K for helium implanted specimens and unimplanted controls of F82H IEA heat material.

least, to some extent.

Fig. 6 compares representative creep curves of helium implanted and unimplanted specimens which crept at nearly the same stress for both helium contents. The foregoing features of creep behavior are clearly reflected in the figure. The short tertiary creep strain would be responsible for the smaller rupture elongation relative to the bulk material.

The general appearances of rupture surfaces for implanted and unimplanted conditions are exemplified in Fig. 7. All the specimens both with and without helium failed in a perfectly intragranular ductile manner and, alternatively, helium brought about no implication of intergranular decohesion. It has been pointed out in previous literature [8-10] that helium reduces a tendency of necking in ductile fracture faces besides promoting intercrystalline separation. In order to check whether the same is held in this experiment or not, ruptured surfaces were classified to two portions, namely knife-edge fracture regions (far necked parts: Figs. 7a and 7c) and dimple fracture regions (less necked parts: Figs. 7b and 7d), and fractions of each were evaluated on the basis of line analysis. Obtained results are summarized in Fig. 8, as a plot of percentage of dimple fracture versus rupture time. As shown in the figure, there observed no substantial effect of helium on the fraction of dimple fracture. Therefore, the above mentioned helium effect of suppressing necking propensities did not appear in our case.

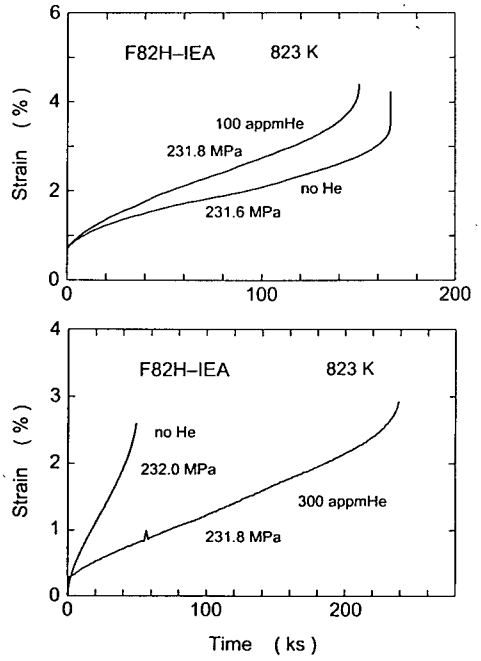

Fig. 6. Comparison of creep curves of F82H IEA heat material in helium free and implanted (C_{He}=100, 300 appm) conditions tested at 823 K, 232 MPa.

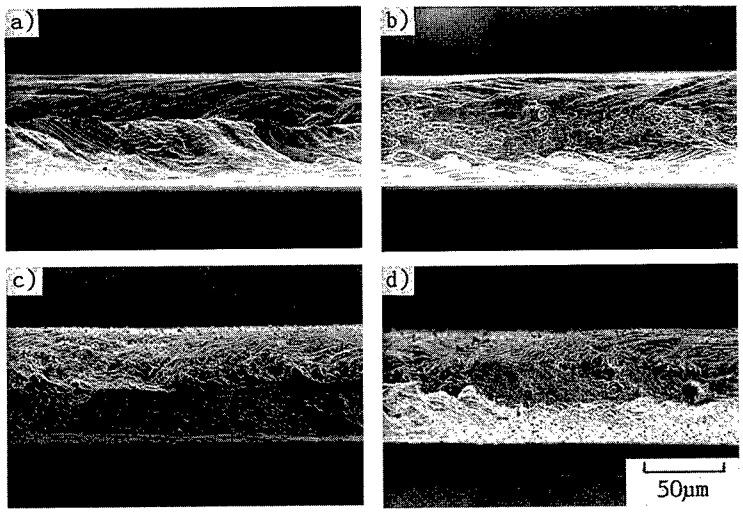

Fig. 7. SEM fractographs showing typical creep-ruptured surfaces of F82H IEA heat material tested at 823 K, 214 MPa; a), b): unimplanted control (t_r=770 ks); c), d): helium implanted sample (C_{He}=300 appm, t_r=4.02 Ms).

Conclusions

Creep rupture tests at 823 K were run on the IEA-heat of low activation martensitic steel, F82H, after hot helium implantation ($T_{impl.}$=823 K, C_{He}=100, 300 appm). The principal conclusions obtained are as follows:

(1) Helium introduction caused no effectual deterioration in terms of both creep rupture strength and elongation. In addition, the increase of the creep life by helium was even discerned in case of 300 appmHe implantation.

(2) SEM fractography showed that all the samples including helium implanted ones fractured in a fully transcrystalline and ductile fashion, and grain boundary separation induced by helium was not appreciated at all.

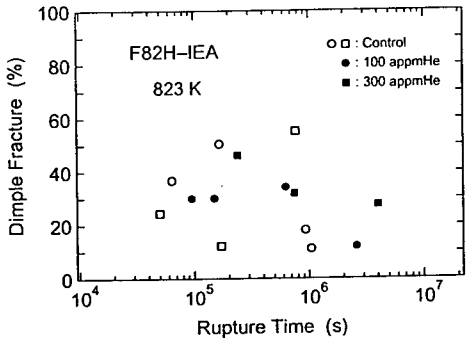

Fig. 8. Percentage of regions decorated with dimples on creep rupture surface as a function of creep life at 823 K for helium implanted specimens and un-implanted controls of F82H IEA heat material.

Thus, F82H demonstrated its fairly good resistance toward helium embrittlement through present creep experiments.

References

[1] A. Kohyama, *et al.*, J. Nucl. Mater. 233-237 (1996), p. 138.

[2] B. van der Schaaf, M.I. de Vries and J.D. Elen, *Proc. Int. Conf. on Radiation Effects in Breeder*

Reactor Structural Materials, eds. M.L. Bleiberg and J.W. Bennett (AIME, New York, 1977) p. 307.
[3] C. Wassilew, K. Ehrlich and H.-J. Bergmann, *Proc. 13th Int. Symp. (Part II) on Influence of Radiation on Material Properties, eds. F.A. Garner, C.H. Henager and N. Igata, ASTM STP 956* (ASTM, Philadelphia, 1987) p. 30.
[4] N. Yamamoto, *et al.*, J. Nucl. Sci. Technol. 28 (1991), p. 1001.
[5] K. Shiba, *et al.*, *JAERI-Tech* 97-038 (1997).
[6] A. Hishinuma, *et al.*, J. Nucl. Mater. 258-263 (1998), p. 193.
[7] N. Yamamoto, J. Nagakawa and K. Shiba, unpublished data.
[8] U. Stamm and H. Schroeder, J. Nucl. Mater. 155-157 (1988), p. 1059.
[9] A. Hasegawa and H. Shiraishi, J. Nucl. Mater. 191-194 (1992), p. 910.
[10] A. Hasegawa, N. Yamamoto and H. Shiraishi, J. Nucl. Mater. 202 (1993), p. 266.

Corresponding author: Norikazu Yamamoto, e-mail; yamamoto@nrim.go.jp, Fax; +81-298-59-2801

Key Engineering Materials Vols. 171-174 (2000) pp. 121-130
© 2000 Trans Tech Publications, Switzerland

A Change in the Mechanism of Creep Crack Growth in a Dissimilar Metal Weld at 540 °C

B. Nath

National Power Plc, Windmill Hill Business Park, Whitehill Way, Swindon SN5 6PB, UK

Keywords: 2¼Cr1Mo, Low Alloys Steels, Ferritic Steels, Transition Joints, Creep Embrittlement, Grain Boundary Segregation, Effect of Composition on Properties

Abstract

Dissimilar metal welds between ferritic and austenitic steels are widely used in power plants, mostly in the creep regime at and above 540°C. Except for some early failures in flash-butt-welds due to poor adhesion, the experience has been satisfactory. An international consensus has emerged that such joints should be welded using nickel-based filler metals.

However, in 1986 a 2¼Cr1Mo\Inco 182/Type 316 weld failed in one of CEGB power plants after only ~8,000 hours operation and numerous other similar joints cracked. The welds were located in the steam line close to the Type 316 secondary superheater outlet header and had operated at probably 480-490°C but certainly below 500°C. The fracture revealed some very unusual microstructural characteristics.

Investigations showed that time-dependent creep crack growth occurs at these temperatures, reproducing the microstructure of in-service cracking. Crack growth rates were fastest at 480-490°C, which coincided with the probable temperature of the failure.

This paper highlights the microstructural differences in cracking above and below 540°C and describes the results of creep crack growth tests. It argues that creep embrittlement due to residuals lead to a change in the mechanism of cracking below 540°C.

Abbreviation

DMW (Dissimilar metal weld)
PAGB (Prior austenite grain boundary)
S-type (DMWs made with Type-300 stainless steel filler)
N-type (DMW fabricated with Ni-based weld metal)
AES (Auger Electron Spectrometer)
CCG (Creep crack growth)

Introduction

Power plant boiler construction utilises ferritic steels because of their low cost, adequate strength and good resistance to stress corrosion cracking. However, at high temperatures austenitic steels are chosen because they possess higher creep strength and oxidation resistance. Therefore, the two grades of steels have to be welded together. In general, the service experience with such DMWs is acceptable, although they fail more frequently than the similar metal welds [1]. This can be attributed to marked changes in the chemical, physical, and mechanical properties at the junction between the two different materials.

Early joints were made using Type-300 austenitic filler metals. However, there is an international consensus now that such welds should be made with Ni-based fillers e.g. Inconel 182 or equivalent.

A very large number of transition joints are in service worldwide. In The Central Electricity Generating Board alone there were more than one quarter of a million welds between 2¼Cr1Mo and austenitic stainless steels. Most of these operated at temperatures of 540°C or above. Consequently, published literature on the service experience and on laboratory tests generally refers to 540°C or above. First failures of 2¼Cr1Mo\Ni-filler/austenitic-steel joints occur after 40,000 hours service at 540°C and above.

However in 1986, steam leaked from a weld between 2¼Cr1Mo and the Type-316 secondary superheater outlet header of a CEGB power plant, after less than 8,000 hours service at a probable temperature of 480-490°C, certainly below 500°C. The weld had been fabricated with the Ni-filler, Inco-182. Subsequent investigations revealed that many more joints had cracked. This led to the wholesale replacement of all 128 welds in two affected plants.

A creep crack growth study was initiated to understand the mechanisms of failures and the results revealed different mechanisms of cracking in the low temperature regime (i.e. below 540°C) from those at higher temperatures. The results are presented in this report.

Cracking at 540°C and Above

Cracks in medium to long term laboratory tests [2] or in service exhibit similar characteristics, which are summarised below.

- Short-term creep failures of both types of welds occur in the parent low alloy steel, away from the weldment. In medium to long term the joints fail in the ferritic HAZ, near the fusion boundary.
- In S-type joints, PAGB cavities form in 2¼Cr1Mo HAZ, at 1-2 grains from the fusion boundary. They coalesce to develop cracks.
- Medium term failures of the N-type joints also occur by PAGB cavitation, at 1-2 grains from the fusion line. However, after long-term exposures a string of carbides develops in 2¼Cr1Mo, at 1-2 μm from the fusion line [3]. These act as preferential sites for the nucleation of cavities and cracks [4].
- The fusion boundary or the weld metals do not generally crack in either joint.
- In laboratory tests and in service, the N-type joints exhibit significantly longer lives than those of the S-type welds.

Service Damage at 480-490°C

Sections of the failed weld showed it to be free of defects and with a microstructure typical of such joints. The microstructural nature of the cracks was different from those which form at 540°C and above in the following respects.

- The crack path was predominantly along the 2¼Cr1Mo fusion boundary. The fracture surface was remarkably smooth, as though little mixing or interdiffusion had occurred during welding and subsequent heat treatment.
- In many cases, the crack path deviated into the weld metal, before returning back to the fusion boundary.

A simplified weld fabrication sequence was as follows: 2¼Cr1Mo was buttered with Inco-182, stress relieved and then welded on site, using the same filler but without any further stress-relief. This resulted in residual stresses of around 400 MPa in the ferritic HAZ, comparable with the as-

welded condition, and twice the 200 MPa measured in a stress-relieved joint. This suggested that the high residual stresses might have led to early failures. However, the following result from a pressure vessel test at the Marchwood Engineering Laboratories shows that other factors may also be important.

The pressure vessel contained four 2¼Cr1Mo\Inco-182/Type-316 welds all subjected to the same pressure and end-loads.

1. The original weld procedure resulting in a residual stress of around 400 MPa. The test temperature was 500°C.
2. Fully stress-relieved joint also tested at 500°C, with 200 MPa residual stresses.
3. An end-cap joint in the as welded condition and at the test temperature of 500°C.
4. The second end-cap weld in the as-welded state at 480-490°C. (It lay outside the uniform hot zone of the furnace.)

The two test welds, 1 and 2 were from one cast of 2¼Cr1Mo and the two end-cap joints from a second cast. Weld 4, which is expected to have the same residual stresses as Welds 1 and 3, failed after 7828 hours, although it was at a lower temperature [5].

Experimental

The following weld pads were made by depositing 26-32mm thick weld metal on 2¼Cr1Mo plate of similar thickness.

1. SR-series (Type-316 weld deposit on a commercial purity 2¼Cr1Mo)
2. SHC-series (Type-316 weld deposit on a high purity 2¼Cr1Mo)
3. NR-series (Inco-182 weld deposit on a commercial purity 2¼Cr1Mo)
4. NHC-series (Inco-182 weld deposit on a high purity 2¼Cr1Mo)

Table 1: Chemical composition of the two 2¼Cr1Mo steels

	C	Cr	Mo	Mn	Si	P	S	As	Sb	Sn
Commercial	0.11	2.06	1.08	0.62	0.23	0.032	0.025	0.037		0.016
High purity	0.12	2.03	0.96	0.55	0.017	0.004	0.004	0.003	<0.005	<0.005

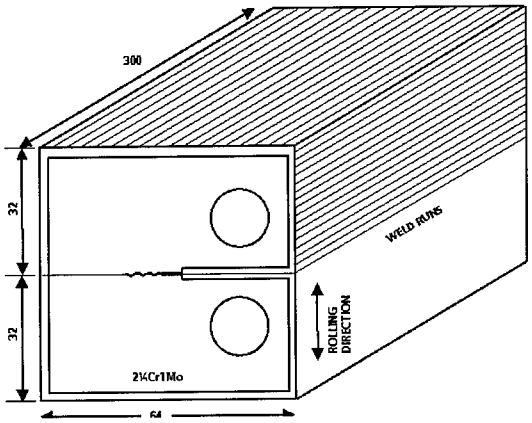

Figure 1 Schematic weld pad and 25mm CT sample location

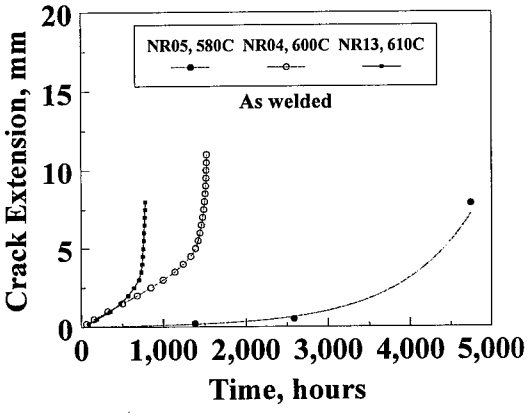

Figure 2 Decreasing life with increasing temperature

The rolling direction of the plate was such any slag inclusions lay parallel to the loading direction. 25mm compact tension samples were extracted from these weld pads so that the fusion surface lay at the centre of the sample, normal to the direction of loading (Fig. 1). Some samples were tested in the 'as-welded' condition while others were stress-relieved at 700°C for 3h prior to testing. This heat treatment can generate a thin, approx. 120 μm wide, C-depleted zone in the 2¼Cr1Mo HAZ in S-type welds but not in the N-type joints [6].

A spark-eroded notch was placed at or very close to the fusion line, with a root radius of 0.2mm. Creep crack growth tests were conducted at different temperatures in the range 450-600°C. Crack growth was monitored by DC potential drop across the crack and the load-line displacement was measured via a pair of extensometers. The SR- and NR-welds were tested at identical test parameters (viz. initial a/W, load and temperature) to ensure that the data could be compared directly.

Experience showed that side grooving was not necessary because the strength mismatch across the fusion line was sufficient to constrain crack growth along the fusion boundary, nominally normal to the load.

Results

High Temperature (540°C and above)

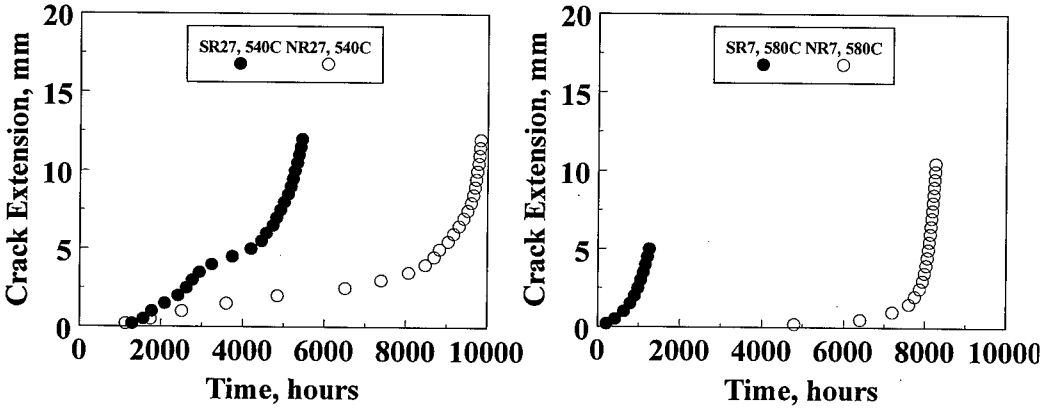

Figure 3 At 540°C and above N-type welds exhibit longer lives than the S-type joints. These samples were tested after 700°C 3h stress relief

The results can be summarised as follows.

- Increasing temperature reduced failure times, as expected in thermally activated damage mechanisms like creep (Fig. 2).
- Under identical test conditions, the lives of NR-samples were significantly longer than those of the SR-specimens (Figs. 3a-3b). Similar relative performance is observed in service at these temperatures.
- Crack growth occurred by cavitation at PAGB ahead of the crack tip and its coalescence.
- Cavitated grain boundaries exposed by low temperature fracture in AES revealed MnS precipitates in cavities of the S-type welds (Figs. 4). Most particles in N-joints were not sulphides (Fig. 5).

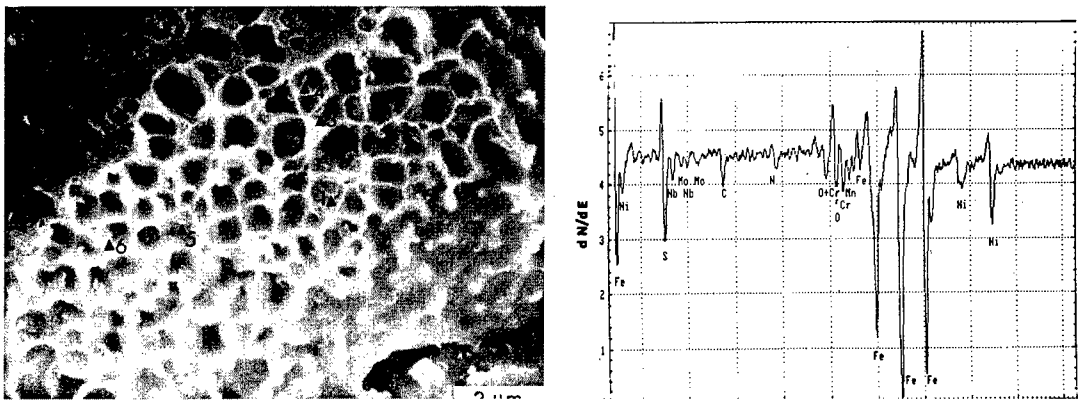

Figure 4 SR-Welds at 580°C: Grain boundary cavities in 2¼Cr1Mo HAZ contain MnS particles

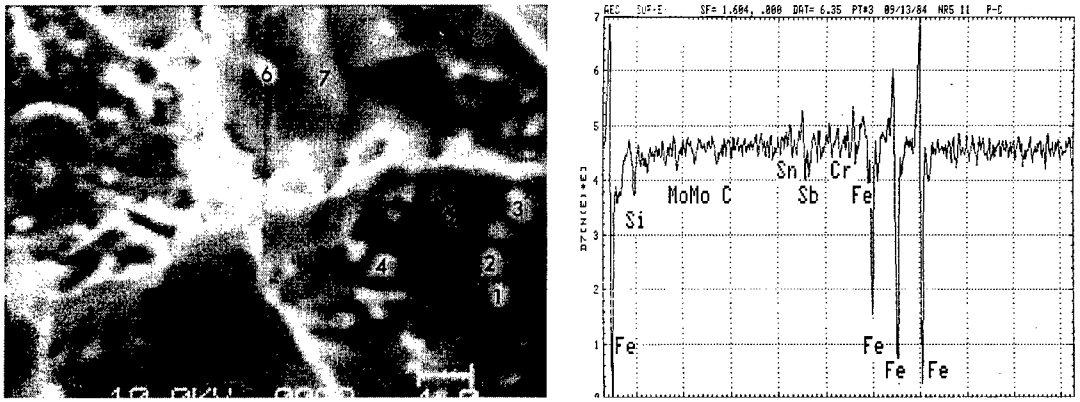

Figure 5 NR-Welds at 580°C: Most precipitates in cavities are not MnS

Table 2: Time for 0.2mm crack extension in commercial grade and the high purity 2¼Cr1Mo steel. Both types of welds were tested in the as-welded condition.

Weld Metal	Test Temperature, °C	a/W	K_I, MPa√m	Initiation time, in commercial 2¼Cr1Mo, hr	Initiation time, in high purity 2¼Cr1Mo, hr
Inco-182	580	0.51	12	371	>11414
	580	0.434	12	1384	>14234
	500	0.434	20	154	933
Type-316	580	0.434	12	31	>14246
	500	0.434	20	354	-

- Crack initiation did not occur in identical tests on SHC- and NHC-samples, made with the high purity 2¼Cr1Mo (Table 2). At significantly higher loads blunt cracks propagated in the 2¼Cr1Mo HAZ (See for example, Fig. 10)

These results are consistent with other laboratory tests (e.g. creep-rupture under uniaxial or multiaxial stresses) and the service experience, which are well documented in the literature

Low Temperature (Below 540°C)

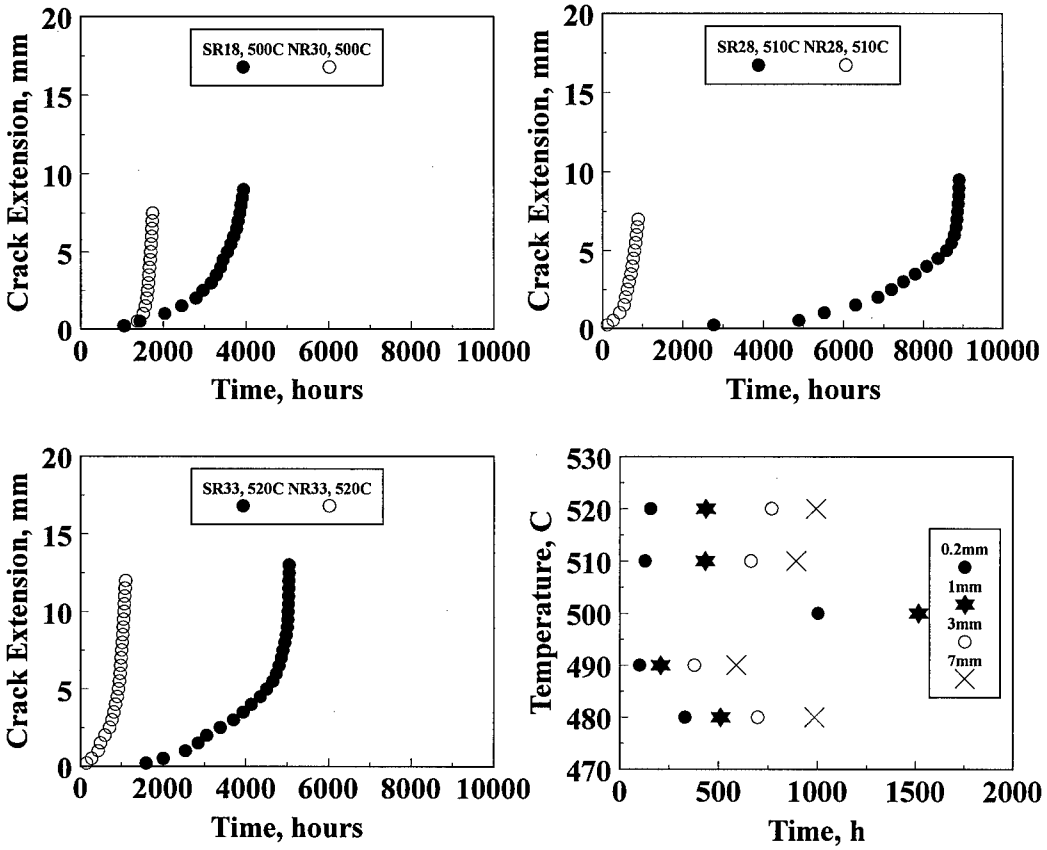

Figure 6 Below 540°C, SR-welds exhibit longer lives than those of the NR-joints. Time for 0.2 to 7mm crack growth show C-curve kinetics. These tests were conducted on stress-relieved joints

The results revealed many differences from the high temperature behaviour.

- The lives of the NR-series of samples were shorter than those of the SR-series under identical loads and temperatures (Fig. 6). This is a highly unusual result because almost all tests and service experience above 540°C show that welds fabricated with Ni-based fillers are superior to those made with austenitic weld metals. It is even more note worthy because of the C-depletion in SR-samples, which is generally perceived to be a weak zone.
- The shortest lives were obtained in NR-samples at 480-490°C (Fig. 6). It should be emphasised that the failure times increased on increasing the temperature to up to 520°C. This is a remarkable result for a thermally activated damage mechanism.

- The temperature of shortest life coincided very well with the estimated temperature of the welds, which failed in service and in the pressure vessel test.
- The crack in NR-specimens propagated along the fusion boundary, occasionally deviating into the weld metal and returning to the fusion line (Fig. 7). The fracture surface was remarkably smooth (Fig. 8) and the energy dispersive analysis revealed that very little mixing or inter-diffusion had occurred. Thus, all microstructural features of the service failure were reproduced in these tests.
- Tramp elements e.g. P, Sn, Sb and As were found on fracture surfaces on N-welds, exposed by low temperature fracture in AES (Fig. 8).
- Crack growth in S-type joints occurred along the 2¼Cr1Mo HAZ (Fig. 9).
- NHC-series joints were significantly more resistant to cracking than the NR-series (Table 2). In fact the ferritic HAZ and the fusion boundary proved so resistant that the crack path lay almost exclusively in the Inconel-182 weld metal (Fig. 10).

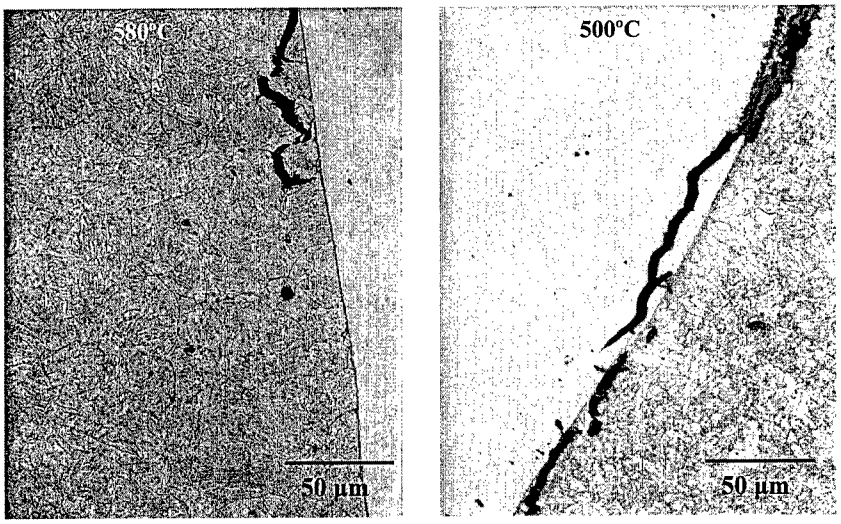

Figure 7 NR-Welds: Cracks at 540°C and above grow in the 2¼Cr1Mo HAZ but at lower temperatures follow the fusion line and deviate into the weld metal

Discussion

Creep crack growth results show two distinct behaviours, not only in terms of the relative performances of the SR- and the NR-welds but also in the microstructural modes of cracking. In both these respects the laboratory tests reflect the service experience in CEGB plants. The observed results can be rationalised on the basis of local ductility in the vicinity of the crack tip.

High Temperature (540°C and above)

During welding, MnS slag stringers dissolve and reprecipitate as small particles at PAGBs in the HAZ of low alloy ferritic steels. Creep cavities nucleate on these particles and grow to form cracks. This happens in S-type welds in the high temperature regime. However, MnS precipitates are not so abundant at PAGBs in N-type joints probably because the heat input used for this filler is not high enough to dissolve many MnS stringers. Consequently, the HAZ is more resistant to cavitation. The difference in the CCG behaviours is attributed to different susceptibilities to

creep cavitation of the two joints. Markedly high resistance of the high purity samples, NHC- and SHC-series, is consistent with this.

Other factors e.g. α-mismatch play a secondary role, if any, in isothermal test described in this paper.

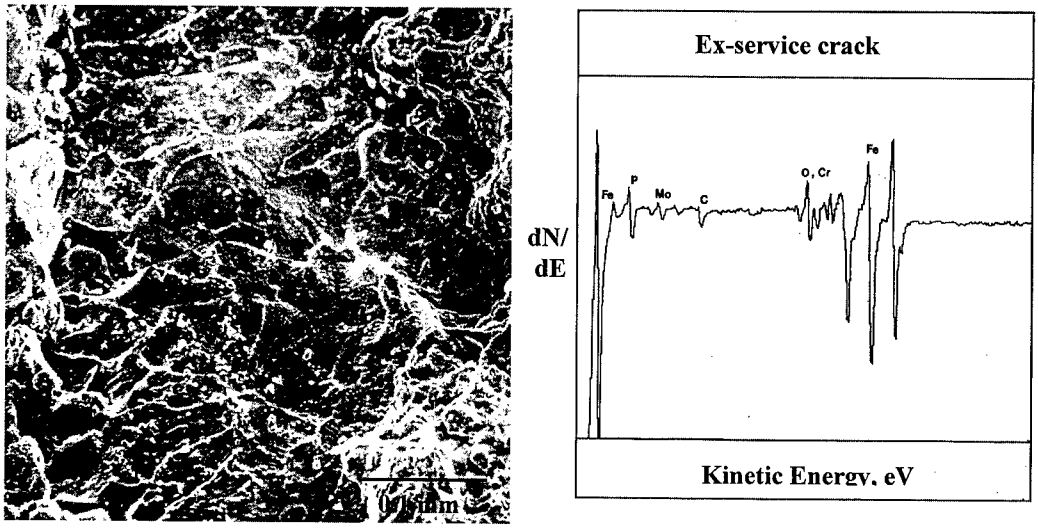

Figure 8 The weld metal half of the fractured joint exhibits smooth nature of the interface crack, typical of service damage with P-segregation

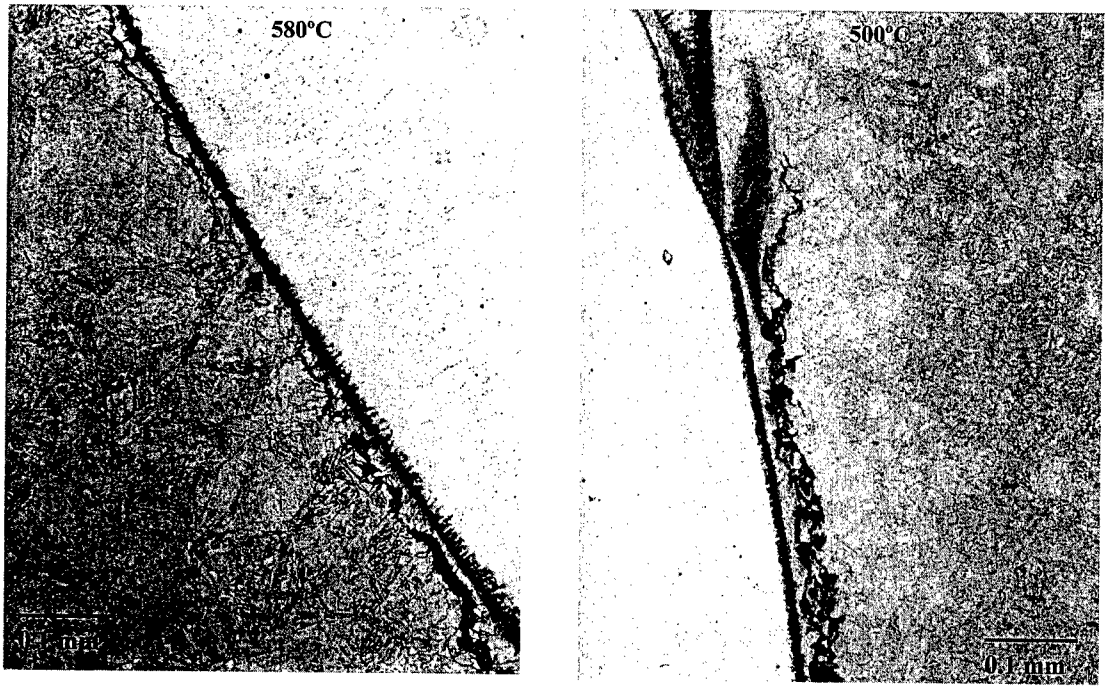

Figure 9 SR-Welds: Cracks in both temperature regimes propagate in the 2¼Cr1Mo HAZ

Low Temperature (Below 540°C)

A different mechanism, akin to temper embrittlement, dominates at these low temperatures. The weld interface in N-joints behaves like a grain boundary. This is believed to be another consequence of the low heat input welding, which does not allow significant, co-melting and inter-diffusion. The smooth nature of the fracture surface and its composition demonstrate lack of inter-diffusion. Consequently, tramp elements segregate to the fusion boundary, in a manner analogous to grain boundaries, and reduce the creep ductility of the interface. It is probable that the impurities in both the 2¼Cr1Mo and the Inconel-182 segregate to the fusion boundary. Whether the fusion boundary behaves like a grain boundary in 2¼Cr1Mo or one in Inconel-182, is not clear. Segregation of Sn, and Sb is known to cause creep embrittlement of 2¼Cr1Mo at 480°C [7]. Similarly, P-segregation leads to embrittlement of the Ni-based Alloy 80A [8].

The S-weld, which forms a thin band of martensite on welding, does not present a similar microstructural feature for segregation. Furthermore, carbon migrates from the ferritic HAZ to the austenitic weld metal during the stress relieving treatment, creating a C-depleted zone, which is expected to be more ductile. Therefore, in comparison with the N-type welds, the creep ductility of the joint is relatively high in the vicinity of the fusion boundary. Consequently, the welds are more resistant to CCG below 540°C.

Welds made with the high purity 2¼Cr1Mo are markedly more resistant to CCG, as expected from the discussions presented above.

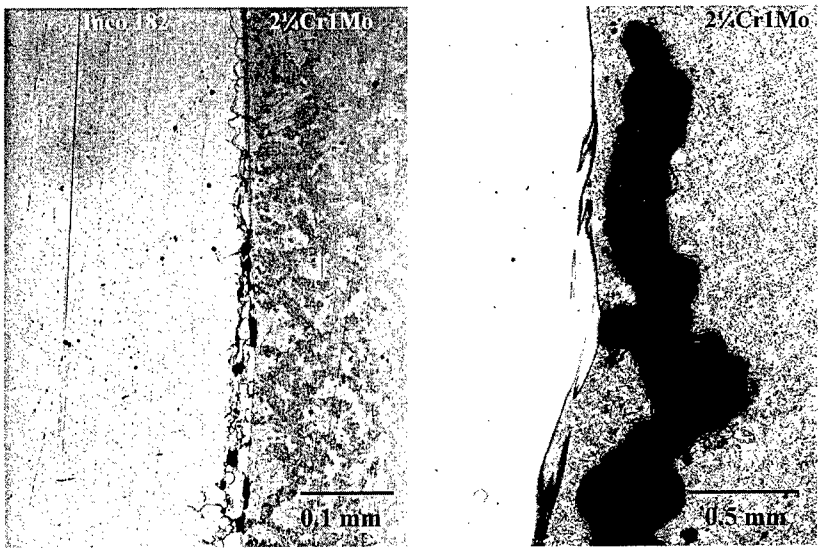

Figure 10 High purity 2¼Cr1Mo: Cracks in N-type welds at 500°C are largely in the weld metal. At 580°C, extensive damage accompanied growth of blunt cracks in the ferritic HAZ

Conclusions

1. There are two different temperature regimes for creep cracking in transition joints, one at 540°C and above and the other at lower temperatures.
2. The differences are attributed to different mechanisms of creep embrittlement. At high temperatures, the N-type joints are more resistant to creep crack growth than the S-type joints because of the abundance of MnS precipitates at PAGBs, which facilitate cavitation in the

latter. In the low temperature regime, the N-joints become less resistant because of the embrittlement of the fusion boundary due to the segregation of the residuals.

3. Creep crack growth tests in both these temperature regimes have been found to be good indicators of the relative service performances of DMWs made with either the austenitic or the Ni-based fillers. They also reproduce all essential microstructural features of cracks in service.

Acknowledgement

This paper is published with the permission of National Power Plc.

References

[1] B. Nath, J. Phillips and J.A. Williams, 1990, Seminar on Life of welds at High Temperature, June 1990, London, IMechE (London)
[2] B. Nath, 1982, Proc Int Conf on Welding Technology for Energy Applications, Gatlinburg, May
[3] D.I. Roberts, C.C. Li and R.D. Nicholson, 1985, EPRI Report CS-4252, Vol.2
[4] R.J. Gray, J.F. King, J.M. Leitnaker and G.M. Slaughter, 1977, "Microstructural Science", Vol. 5, ed. L.D. Brown, Elsevier North, Holland
[5] M.C. Coleman and P.C. Rowlands, 1989, PowerGen Report RD/M/1878/RR89
[6] B. Nath, 1982, 4th Int Conf Welding in Nuclear Engineering, November, Achen, DVS (Düsseldorf)
[7] R. Pilkington, R. Dicken, P. Peura, G.W. Lorimer, G.C. Allen, M. Holt and C.M. Younes, 1995, Trace Element Embrittlement in a 2.25%Cr 1Mo Steel, University of Manchester Report
[8] B. Nath, 1991, "An Assessment of Nickel-based Alloys for High-Temperature Bolting Applications", ed: J.B. Marriott, Publ: CEC (Brussels), ISBN 92-826-3235-0

Fax: +44-1793-89-6391
e-mail: birendra.nath@natpower.com

Key Engineering Materials Vols. 171-174 (2000) pp. 131-138
© 2000 Trans Tech Publications, Switzerland

Mechanical Behavior and Strengthening Mechanism of W containing 9-12% Cr Steels under Creep Condition for a Cracked Specimen

A.T. Yokobori Jr.[1], S. Takmori[1], T. Yokobori[2], Y. Hasegawa[3], K. Kubota[4] and K. Hidaka[5]

[1] Fracture Research Institute, Tohoku University, Aoba Aramaki, Aobaku 01 Sendai-shi, #980-8579, Japan

[2] Faculty of Science and Engineering, Teikyo University, 1-1, Toyosatodai Utsunomiya-shi, #320-0003, Japan

[3] Nippon Steel Corporation, Steel Research Laboratories, 20-1, Shintomi, Futtsu-shi, #293-8551, Japan

[4] Hitachi Metals Ltd., Metallurgical Research Laboratories, Yasugi-cho, Yasugi-shi, #692-001, Japan

[5] Hitachi Ltd., Hitachi Research Laboratories, 1-1, Saiwai-cho 3 chome, Hitachi-shi, #317-0073, Japan

Keywords: 9-12% Cr Steels, Tungsten, Creep Crack, NF616, TAF650, Creep Deformation Curve

Abstract

Tungsten strengthening 9-12% heat resistant steels have been developed for the application of the highly efficient ultra supercritical steam power plant because of the protection of natural environment and the preservation of fossil fuel. For these materials, creep test for a smooth specimen and charpy impact test have been performed to investigate basic mechanical properties. However, mechanical behaviors of creep crack growth and fracture have not yet been clarified. In this paper, using NF616 and TAF650, creep crack growth tests were performed and load line displacement laws under creep condition were derived and compared with those for creep ductile and brittle materials such as Cr-Mo-V steel and IN100 alloy. Furthermore, creep crack growth behavior was investigated and related to the metallurgical structure. From these studies, however, both of NF616 and TAF650 have initial ductility, load line displacement under creep condition was found to be restrained owing to the increase in the resistance to the creep deformation and crack growth due to structural strengthening mechanism. This characteristic is qualitatively similar as that for nickel based γ' precipitated superalloy (IN100).

1. Introduction

Tungsten strengthening 9-12% heat resistant steels (NF616, HR1200 and TAF650) have been developed for the application of the highly efficient ultra supercritical pressure steam (USC) power plant because of the protection of natural environment and preservation of fossil fuel[1-4].

In 12% CrWCoB steels (HR1200 and TAF650), Co is added to suppress the delta ferrite formation which causes brittle fracture[1]. This is aimed the application of 650℃ class USC power plant.

For practical use of these materials as a power plant, it is necessary to determine the period of regular inspection to insure the structural safety on the creep fracture induced by creep crack

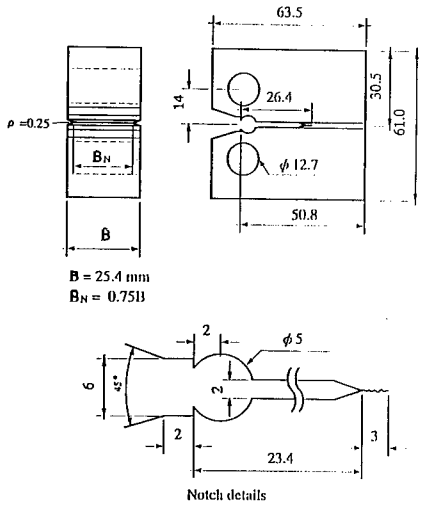

Fig. 1 Geometry and size of the CT specimen.

Table1. Chemical composition of the materials. (mass%)

	C	Si	Mn	P	S
9Cr (NF616)	0.101	0.036	0.466	0.011	0.0011
12Cr-2.62W (TAF650)	0.11	0.04	0.42	0.010	0.004

Al	Cr	Mo	W	Nb	V	Ni	N
0.005	8.96	0.48	1.94	0.065	0.201	0.054	0.0452
0.005	11.08	0.16	2.62	0.05	0.20	0.51	0.016

B	Co
0.0037	—
0.015	2.93

Table2. Mechanical properties of the materials.

	Temp (°C)	UT (MPa)	σ_Y (MPa)	EL (%)
9Cr (NF616)	20	840	716	18.7
	600	475	380	22.8
12Cr-2.62W (TAF650)	20	941	809	17.8
	600	544	449	21.6
	650	456	360	27.1

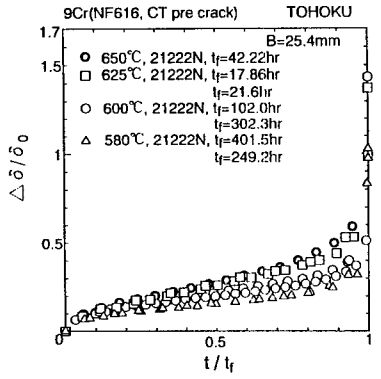

Fig. 2

The characteristics of LLD for NF616 plotted against t/t_f. (t:stress applied time, t_f:creep fracture life)

Table3. The test conditions and symbols.

(B=25.4mm)

	Temp. (℃)	Load (N)	Symbol
9Cr (NF616)	650	21222	○
	625	21222	◒
		18672	◓
	600	24517	●
		21222	◐
		18672	◑
	580	21222	ⓓ
12Cr-2.62W (TAF650)	700	21222	□
	675	21222	◧
	650	23771	■
		21222	⬓
		18672	⬒
	625	21222	◨

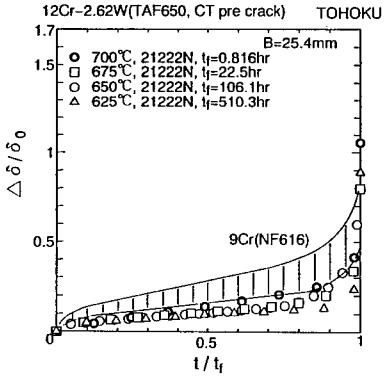

Fig. 3

The characteristics of LLD for TAF650 plotted against t/t_f. (t:stress applied time, t_f:creep fracture life)

growth. To predict this period, it is necessary to construct the laws of creep fracture and remnant lives by clarifying the characteristics of creep crack growth, damage accumulation and deformation.

Parts of authors derived the load line displacement law of a cracked specimen under creep condition, which is concerned with creep crack growth behavior and related it to the characteristics of creep deformation of smooth specimen [5]. On the basis of these results, a prediction method of creep fracture and remnant lives for creep ductile materials such as Cr-Mo-V steel was proposed [5].

In this study, using a precracked CT specimens, the law of load line creep displacement for 9% CrW (NF616) and 12% CrWCoB steel (TAF650) were investigated and compared with those of Cr-Mo-V steel and γ' precipitated Ni-based superalloy (IN100). Furthermore, the strengthening mechanism of these tungsten strengthening 9-12% heat resistant steels were related to the law of load line creep displacement.

2. Materials, specimens and experimental procedure

Materials used are 9% CrW (NF616) and 12% CrWCoB (TAF650) steels [1-4]. NF616 was normalized at 1070℃ for 1 hr and then tempered at 780℃ for 1 hr, whereas, TAF650 was normalized at 1100℃ for 1 hr and then tempered 750℃ for 2 hr. Typical martensitic lath structures are observed in both NF616 and TAF650. The martensitic lath structures, which have the same crystallographical direction, gather and form a block and these blocks form a packet.

The chemical composition and mechanical properties of these materials are shown in Tables 1 and 2. Specimen used is a standardized CT precracked specimen for creep crack growth test [6] as shown in Fig.1. A fatigue precrack was about 3 mm, which was introduced by step decreasing loading condition. Final load level is lower than that of initial stress intensity factor of creep crack growth test.

To perform creep crack growth test, a lever-type creep testing machine was used. The experimental conditions are shown in Table 3. The load line displacement was measured to a precision of below 1 μm [7]. Details of the experimental method were given in our previous paper [7].

Another experiment was carried out to clarify the high temperature creep damage and fracture mechanism. The specimens were cut from the material and machined into the double edge notched specimens. High temperature creep tests have been carried out on these specimens using *in situ* observation technique under 10^{-5} torr vacuum condition [8,9].

3. Experimental results and analyses

3.1 The characteristics of load line displacement (LLD)

Values of load line displacement (LLD) of NF616 and TAF650, $\Delta\delta/\delta_0$ $(\delta_0 = 6\text{mm})$ are plotted by the non-dimensional time of stress application, t/t_f, as shown in Figs. 2 and 3, where t is the time of stress application and t_f is the creep fracture (life) for each specimen. (t/t_f is a

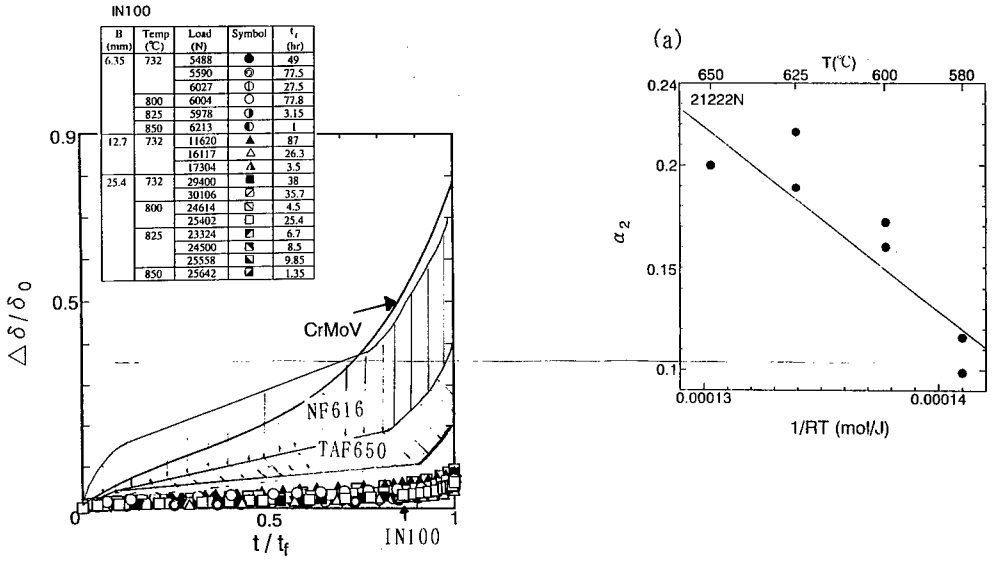

Fig. 4 The comparison of the characteristics of LLD between Cr-Mo-Vsteel, NF616, TAF650 and IN100.

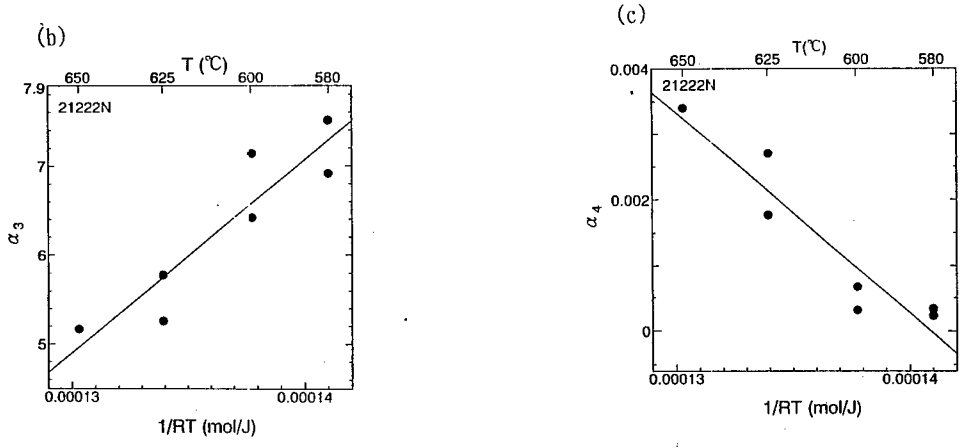

Fig. 5 The relationship between coefficient values of LLD laws and 1/RT for NF616.
(a) The relationship between α_2 and 1/RT
(b) The relationship between α_3 and 1/RT
(c) The relationship between α_4 and 1/RT

value which is controlled by applied stress and temperature.) In NF616, values of $\Delta\delta/\delta_0$ increase regularly with increase in temperature in spite of these data being represented by t/t_f. On the other hand, in TAF650, the LLD curves are independent of temperature and they are represented by a unique master curve. This curve takes lower values of LLD than the minimum value of the characteristics of LLD for NF616.

The characteristics of LLD for NF616 and TAF650 were compared with those for Cr-Mo-V steel and IN100 alloy as shown in Fig. 4. These results show, however, in the region of $t/t_f < 0.1$, both NF616 and TAF650 have same values of $\Delta\delta/\delta_0$ as that of Cr-Mo-V steel which is creep ductile material, in the region of $t/t_f > 0.1$, the time derivative of LLD, $\frac{d}{dt}\left(\frac{\Delta\delta}{\delta_0}\right)$ has a constant value and the LLD has similar qualitative characteristics as that of Ni-based superalloy, IN100. The absolute values of LLD for NF616 in the region for $T \leq 600$℃ and TAF650 are lower than those for Cr-Mo-V steel. Furthermore, values of LLD for NF616 under $T \leq 600$℃ and TAF650 at $t/t_f = 0.8$ are limited to a factor of 2 of those at $t/t_f = 0.1$.

3.2 The law of load line displacement (LLD)

For smooth specimen, θ projection method was proposed to describe a creep deformation law as a function of t[10,11]. We adopted a little different treatment to characterize the LLD law[5]. Using the non-linear least square method, the experimental characteristics of LLD represented by t/t_f were approximated by Eq. (1) and each value of $\alpha_i\ (i=1\sim4)$ were determined, where t_f is a creep fracture life for each specimen.

$$\frac{\Delta\delta}{\delta_0} = \alpha_1 + \alpha_2\left(1 - e^{-\alpha_3(t/t_f)}\right) + \alpha_4\left(e^{\alpha_3(t/t_f)} - 1\right) \qquad (1)$$

The relationship between the value of $\alpha_i\ (i=1\sim4)$ and temperature for NF616 are shown in Figs. 5 (a), (b) and (c). Equation (1) for TAF650 is given by Eq. (2).

$$\frac{\Delta\delta}{\delta_0} = 5.04\times10^{-3} + 8.94\times10^{-2}\left(1-e^{-7.85(t/t_f)}\right) + 1.59\times10^{-4}\left(e^{7.85(t/t_f)}-1\right) \qquad (2)$$

These results show each value of α_i for NF616 has a linear relationship with (1/RT) and the value of α_3 equals to 5.1 and 7.5 respectively for 650℃ and 580℃. The value of α_3 for TAF650 equals to 7.85. In Cr-Mo-V steel, which is a creep ductile material, α_3 has a value of 4.9. On the other hand, in γ' precipitated Ni based superalloy, cast IN100, α_3 has a value of 7.51.

These results show that with decrease in temperature, the LLD law of NF616 changes from that of Cr-Mo-V steel which is a creep ductile material, to that of γ' precipitated Ni based superalloy, IN100 and the LLD law of TAF650 has the similar qualitative characteristics of IN100. Because values of α_3 equal to each value of α_3 for Cr-Mo-Vsteel and IN100.

From these results mentioned above, however, both NF616 and TAF650 have creep ductility in initial LLD law, the structural strengthening mechanism increase the resistance to creep crack growth and deformation and it controls the followed LLD.

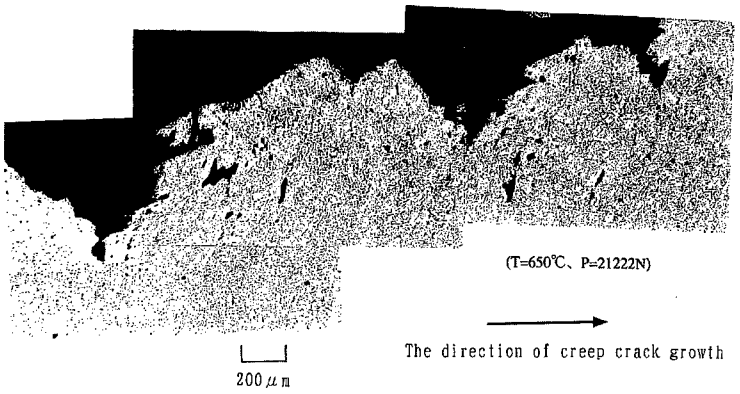

Fig. 6(a) Creep crack growth path of NF616. (T=650° C, P=21222N)

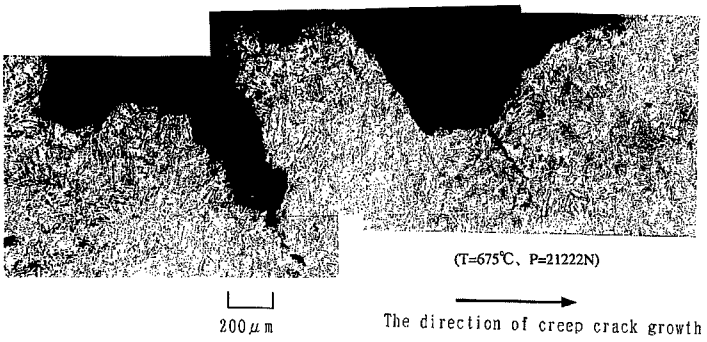

Fig. 6(b) Creep crack growth path of TAF650. (T=675° C, P=21222N)

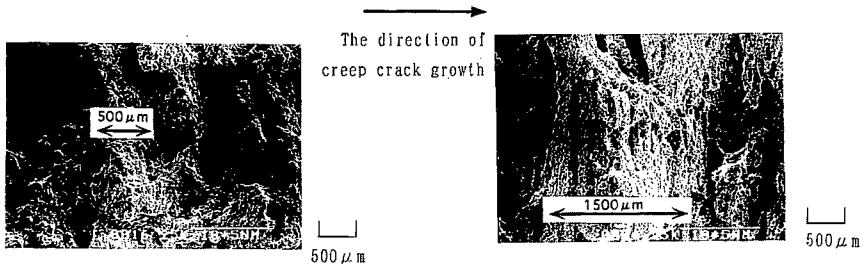

Fig. 7(a)

Creep fracture surface of NF616.
(T=580° C, P=21222N)

Fig. 7(b)

Creep fracture surface of TAF650.
(T=675° C, P=21222N)

3.3 Creep crack growth path and observation on fracture surface

Creep crack growth paths of NF616 and TAF650 are shown in Figs. 6 (a) and (b). Both creep crack growth paths show convex and concave shapes dominated by material structure. Especially, in TAF650, many creep cracks grow along lath boundaries in martensitic structures.

Fracture surfaces of NF616 and TAF650 observed by SEM (HITACHI Ltd. S415) are shown in Figs. 7 (a) and (b). In NF616, colony like micro fracture units which are considered to be induced by subcritical creep crack growth are observed. The average length is about 500 μm. On the other hand, in TAF650, lamellar type long fracture units perpendicular to the creep crack growth direction are observed and the length is about 1500 μm. These results are in good agreement with those in Figs. 6 (a) and (b).

3.4 The effect of material strengthening mechanism on the creep crack growth

Using a double edge specimen, the *in situ* observational result of creep crack growth behavior for NF616 is shown in Figs. 8 and 9 (T=630℃, σ=375.4 MPa, t_f is creep fracture life). This result shows void formation proceedingly occurs (Fig. 8) and two branched creep cracks initiate from a notch tip (Fig. 9). These branched cracks are composed of micro-branched cracks induced by void formation. On the other hand, in TAF650, void formation can not be clearly observed and convex and concave large creep cracks are observed along martensitic lath boundaries (Fig. 6 (b)). This is considered to be induced by the following mechanism. The martensitic lath structures in TAF650 are much more developed as compared with that in NF616. It constrains dislocation glide and void formation [12], which protects the occurrence of grain boundary cracking and causes branch cracks along martensitic lath boundaries. However martensitic lath structures are a little different between NF616 and TAF650, they constrain LLD. Due to this strengthening mechanism, LLD laws in NF616 and TAF650 become similar as those in IN100 and TiAl intermetallic compound with full lamellar microstructure, which are also structural strengthening materials.

4 Conclusion

Tungsten strengthening 9-12% heat resistant steels (NF616 and TAF650) have creep ductility in initial load line displacement (LLD) law. However, the structural strengthening mechanisms increase the resistance to creep crack growth and deformation, and it controls the followed LLD. This characteristic is similar as that of IN100.

Acknowledgements

Thanks should be made for financial aid to the Japan Society for Promotion of Science(JSPS) (Professor Takeo Yokobori, the chairman of 129 committee)of the RFTF Program 97R12101. NF616 and TAF650 were provided by Nippon steel Corporation and Hitachi Metals Ltd.

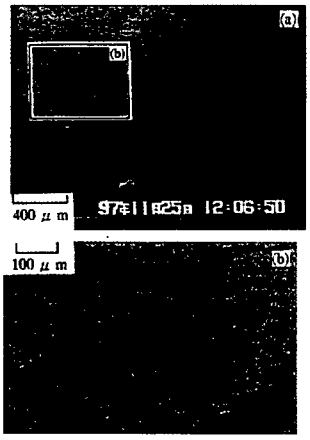

Fig. 8 The result of in situ observation on void formation for NF616 under creep condition. (T=630 C, σ =375. 4MPa, t/t_f=0. 34, t_f=290. 8h)

(a) t/t_f=0.666

(b) t/t_f=0.998

Fig. 9 The result of in situ observation on branched crack growth from a notch tip. (T=630 C, σ =375. 4MPa)

References

[1] T. Fujita, Materials Engineering in Turbines and Compressions Part II, The Institute of Materials, Newcastle, UK (1995) p.493

[2] K. Hidaka, Y. Fukui, R. Kaneko and T. Fujita, IMechE Conference Transactions (1997) p.99

[3] F. Maruyama, The Iron and Steel, 80, 8 (1994) p.7

[4] H. Masumoto, M. Sakakibara and T. Fujita, in Proc. EPRI 1st Int. Conf. on Improved Coal Fired Plants, (1986) p.5-203

[5] A. T. Yokobori, Jr., T. Yokobori and M. Tabuchi, J. of Mater. Sci., 31 (1996) p.4767

[6] ASTM standard E1457 (1992) p.1031

[7] T. Yokobori, C. Tanaka, K. Yagi, M. Kitagawa, A. Fuji, A. T. Yokobori, Jr., and M. Tabuchi, Mater. At High Temp., 10, 2 (1992) p.97

[8] T. Yokobori, H. Sakata and A. T. Yokobori, Jr., Engng. Fract. Mech., 13, 3 (1980) p.533

[9] A. T. Yokobori, Jr., Engng. Fract. Mech., 62 (1999) p.61

[10] R.W. Evans, J. D. Parker and B. Wilshire, in Recent Advances in Creep and Fracture of Engineering Materials and Structures, edited by B. Wilshire and D. R. J. Owen (Pineridge Press, 1982) p.135

[11] R.W. Evans and B. Wilshire, in "Creep and Fracture of Engineering Materials and Structures" edited by B. Wilshire and R.W. Evans (Institute of Metals, London, 1987) p.59

[12] K. Sawada, M. Takeda, K. Maruyama, R. Ishii and M. Yamada, in Proc. of the 6th Liège Conf. Part1, "Materials for Advanced Power Engineering 1998", J. L. Beckers et al., Editors, Univ. de Liège Euro. Commission, (1998) p.575

e-mail yokobori@cc.mech.tohoku.ac.jp

Key Engineering Materials Vols. 171-174 (2000) pp. 139-146
© 2000 Trans Tech Publications, Switzerland

Creep Crack Growth in a High Strength Low Alloy Steel at 360 °C

R. Wu, F. Seitisleam and R. Sandström

Swedish Institute for Metals Research, Drottning Kristinas väg 48, SE-114 28 Stockholm, Sweden

Keywords: High Strength Low Alloy Steel, Uniaxial Creep, Notch, Creep Crack Growth, Simulated Heat Affected Zone, Intergranular Rupture

Abstract: Uniaxial creep, round notched and creep crack growth (CCG) tests at 360°C as well as post test metallography were carried out on a high strength low alloy steel (BS 1501-271). As-received material and simulated coarse grained heat affected zone microstructure across a weldment (simulated HAZ) were tested. It was found that creep crack growth did occur below the limit temperature. The shortest life was seen in the CCG tests with the simulated HAZ. The crack growth rate can be described by creep parameter C*. Some relations between failure time, reference stress and steady crack growth rate were found for the CCG tests. Intergranular crack initiation, growth and fracture were observed in the CCG tests with the simulated HAZ, in particular at longer lives.

1. INTRODUCTION

Over the last two decades, about 125 failures due to creep crack growth (CCG) in high strength low alloy steels are known worldwide. Failures, initially in cold bent feed pipes and more recently in boiler tubing, were found in power generation equipment under steam conditions of 360°C and 168 bar. The failures usually occurred after service lives from 8,000 to 100,000 hours. Examples of investigations into the CCG behaviour are given in [1-3].

Early analyses of the failures showed that laps on the surfaces of the bends [2], or a hammer blow mark or a shallow notch which resulted in stress concentration [4] acted as a crack starter. Subsequent crack growth led to final failure. Two types of brittle failures were reported [4]: leakage before failure and violent failure causing damage to the surrounding structure. Evidence revealed that bends with high hardness and low ductility were more susceptible to violent failure than softer ones [2]. Recent studies [5] revealed that plant failures have also been associated with areas of high residual stress in the cold bent pipes, welds on tubes, etc.

At such low temperature as 360°C, which is below the limit temperature of about 430°C for these steels, design stresses in power generating applications are actually based on tensile properties, and creep is generally considered to be of little importance [6]. Somewhat surprisingly, the mechanism of cracking was eventually identified as being creep [2].

Under steady-state conditions, creep crack growth rates can be correlated to the parameter C*, an energy rate line integral which uniquely characterises the crack tip stress and strain rate field for cracked bodies [7-9]. Recently, C* has been applied to correlate the creep crack growth rates in a low alloy nuclear reactor pressure vessel steel at 360°C - 420°C [10].

The *purposes* of this paper are to study the creep and CCG behaviour in a high strength low alloy steel at 360°C and to examine the effects of microstructure on the CCG and failure.

2. *EXPERIMENTAL*

2.1 Material and Heat Treatment Simulation

A 52 mm thick high strength low alloy plate steel (BS 1501-271) was used in the study. The as-received steel was normalised at 880°C/15 minutes, air cooled, tempered at 670°C/one hour, air cooled. The chemical composition is shown in Table 1. The steel consists of a mixture of bainite and ferrite with a grain size of approximately 7 μm, see Fig. 1(a). Pre-test metallography results including mechanical properties are given in Table 2.

To simulate microstructure in the coarse grained heat affected zone (HAZ) across a weldment, the as received steel was furnace heat treated at 1150°C/30 minutes, boiling water quenched. The steel was then tempered at 630°C/two hours, air cooled, resulting in a mixed tempered bainite and martensite with a grain size of approximately 100 μm, see Table 2 and Fig. 1(b).

Table 1 *Chemical compositions (wt%)*

C	Si	Mn	S	P	Cr	Mo	Ni	V	N	Nb	Ti	Cu	Al
0.14	0.29	1.36	0.003	0.008	0.53	0.17	0.62	<0.07	0.005	≤0.005	0.001	0.14	0.029

Table 2 *Grain size, microstructure, hardness and mechanical properties at 22°C and at 360°C.*

	Microstructure	Grain size, μm	Hardness, HV10	$\sigma_{0.2}$, MPa	σ_B, MPa	A_5 (%)	Transit. Temp. (27 J)
As-received parent material	Ferrite + bainite	7	187	464 (389)	612 (555)	27 (23)	-80°C
Simulated HAZ microstructure	Bainite + martensite	100	292				

$\sigma_{0.2}$ is the yield strength, σ_B the tensile strength, A_5 the elongation at failure. The values in brackets were obtained at 360°C.

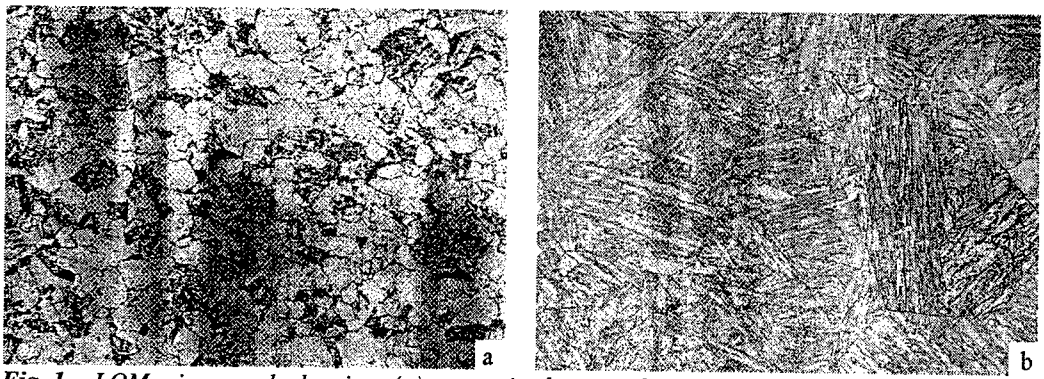

Fig. 1 *LOM micrograph showing (a) as-received material with mixed bainite and ferrite, 400X, and (b) furnace simulated coarse grained HAZ microstructure with mixed bainite and martensite, 400X.*

2.2 Uniaxial Creep, Double Round Notched and Compact Tension Specimens

In total, six series were tested at 360°C in air and intended to progress to rupture. They are two uniaxial creep series (uniaxial), two double round notched series (notched) and two compact tension series for creep crack growth (CCG) tests. For the same type of the series, one was taken from the as received parent material (PM), designated PM-uniaxial, PM-notched and PM-CCG, respectively, and one was taken from the simulated HAZ microstructure, designated SHAZ-uniaxial, SHAZ-notched and SHAZ-CCG, respectively.

The uniaxial specimens were cylindrical with threaded ends with 5 mm diameter and 55.5 mm gauge length. All notched specimens had a gauge length of 51 mm with two equally spaced notches in each specimen with a notch acuity, a/R, of 15. The parameter 'a' is the radius of the specimen at the base of the notch position (2.82 mm in all cases), and R is the notch root radius. The compact tension specimens were manufactured in accordance with ASTM E 1457 [12] for the CCG tests. The spark machined notch had a root radius of 0.15 mm.

2.3 Testing

The uniaxial and notched specimens were tested by using single specimen, uniaxial constant load creep testing machines. For the notched specimens, the net section stress, σ_{net}, was used where σ_{net} is the load divided by initial cross-sectional minimum area at the notch root. For the CT specimens, the reference stress, σ_{ref} in MPa, was calculated according to

$$\sigma_{ref} = \frac{P}{m \cdot B_{eq} \cdot W} \qquad 1$$

where $m = -(1+\gamma(\frac{a}{W})) + \sqrt{(1+\gamma)(\gamma(\frac{a}{W})^2+1)}$, $B_{eq} = B - \frac{(B-B_n)^2}{B}$ and $\gamma = \frac{2}{\sqrt{3}}$.

P is the load in N, W the width of the CT specimen in mm, B the CT specimen thickness in mm, a the crack length in mm and B_n the net thickness between the side grooves in mm. For the estimation of C*, the following expression is now well accepted [11]

$$C^* = \frac{P \cdot \dot{\Delta}_c}{B(W-a)}\left[\frac{n}{n+1}(2+0.522\frac{W-a}{W})\right] \qquad 2$$

where C* is in MPa m/h, $\dot{\Delta}_c$ is the load line displacement rate due to creep in mm/h, n the stress index in Norton's law. The CCG tests followed the instructions described by [12]. The potential drop output and the load line displacement for the CCG tests, the creep strain for the creep and notched specimens as well as temperatures were recorded periodically.

2.4 Post Test Metallography

Some failed uniaxial, notched and CT specimens were metallographically examined using light optical microscope (LOM). In this case, the mid-thickness of the specimens which was perpendicular to the fracture was sectioned, ground and polished to 1 μm before etched in 4% nital. Fractography was performed on some failed notched and CT specimens using scanning electron microscopy (SEM). Prior to examination, the fracture was ultrasonically cleaned.

3. *RESULTS AND DISCUSSIONS*

3.1 Uniaxial, Notched and CCG Tests

Time to rupture t_R versus applied stress σ for uniaxial tests, versus net stress σ_{net} for notched tests, and versus reference stress σ_{ref} for CCG tests are given in Fig. 2. It can be seen that

i) the t_R-σ, t_R-σ_{net} and t_R-σ_{ref} relations are fairly linear in the double logarithmic scales. t_R increases with decreasing σ, σ_{net} or σ_{ref}.

ii) for the uniaxial tests, the simulated HAZ shows longer lives than those of the PM. This is independent of the stresses.

iii) independent of microstructure, notch strengthening is observed, in comparison to the uniaxial tests. The simulated HAZ gives much longer lives than those of the PM at the same σ_{net}.

iv) for the CCG tests, the PM shows longer lives than those of the simulated HAZ.

v) for the PM, t_R for the CCG test is longer than that for the uniaxial test. This case is reversed for the simulated HAZ. For the simulated HAZ, the failures for the CCG tests occur at much short times than those for the uniaxial tests.

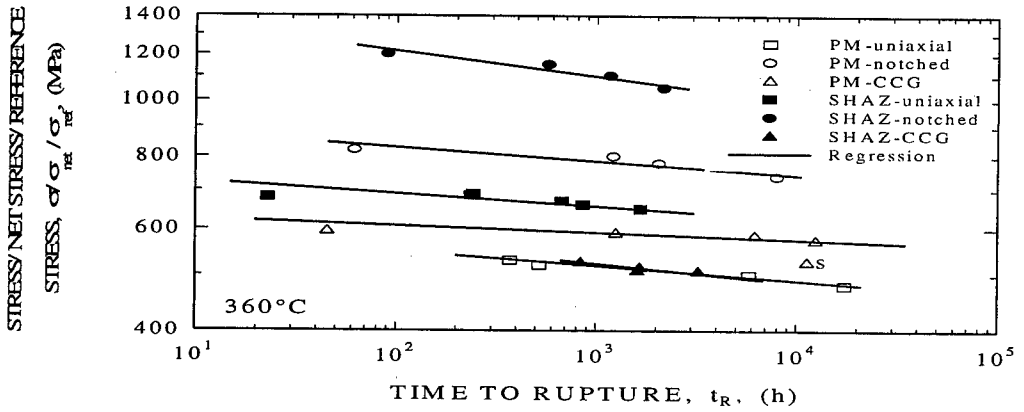

Fig. 2 *Stress σ, net stress σ_{net} and reference stress σ_{ref} versus time to rupture t_R. s means the stopped tests.*

t_R versus elongation at rupture, ε_R, and reduction of area at rupture, A_R, are given in Fig. 3 for the uniaxial tests. Independent of microstructures, ε_R is insensitive to the variation of t_R, whereas A_R decreases slightly with increasing t_R. Comparing to the simulated HAZ, the PM has a better ductility. Minimum creep rate $d\varepsilon/dt_{min}$ versus σ for the uniaxial tests follows Norton's law, see Fig. 4. At the same σ, $d\varepsilon/dt_{min}$ is found to be much larger in the PM in comparison with the simulated HAZ. The stress index n is 38.5 for the PM and 42.5 for the simulated HAZ.

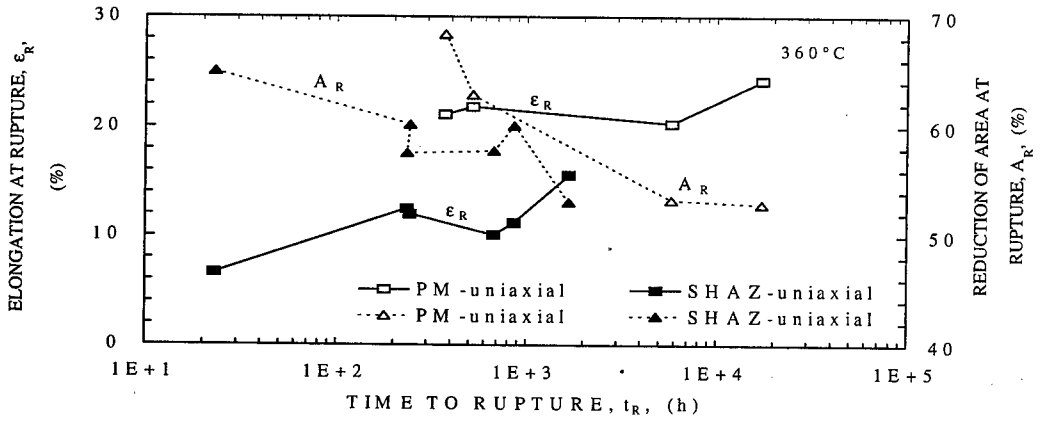

Fig. 3 *Elongation at rupture, ε_R, and reduction of area at rupture, A_R, versus time to rupture t_R for uniaxial tests.*

Crack growth rate, da/dt, versus creep parameter C* is shown in Fig. 5(a) for the PM and in Fig. 5(b) for the simulated HAZ. C* is calculated according to Eq. 2. The load line displacement rate, $\dot{\Delta}_c$, is determined from two adjacent data points on the load line displacement recordings.

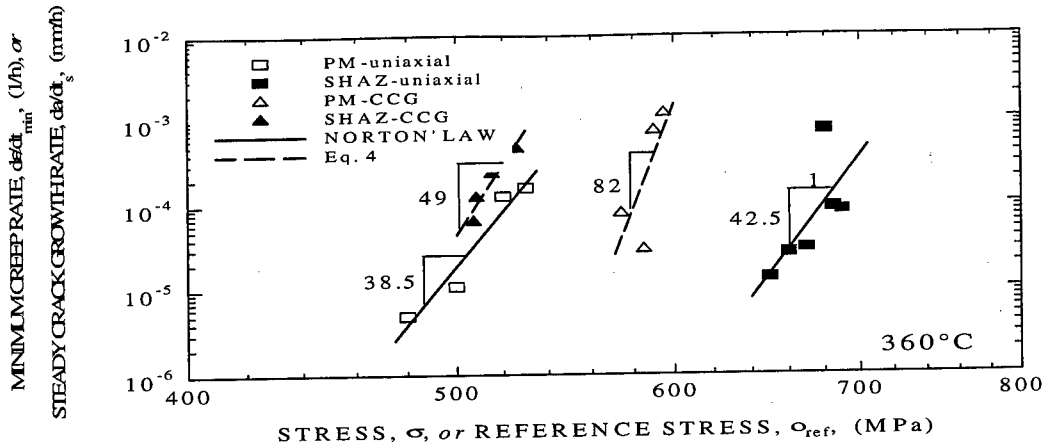

Fig. 4 *Minimum creep rate, $d\varepsilon/dt_{min}$, versus stress σ for uniaxial tests and steady state crack growth rate, da/dt_s, versus reference stress σ_{ref} for CCG tests.*

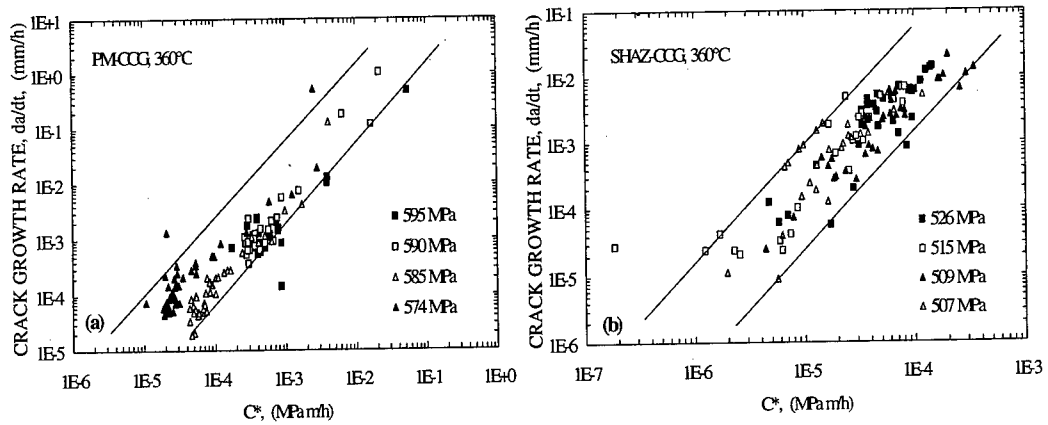

Fig. 5 *Crack growth rate, da/dt, versus C* at given reference stresses for (a) the PM, and (b) the simulated HAZ.*

Independent of reference stress and microstructure, da/dt falls in a narrow band for all the CCG tests. In the double logarithmic scales da/dt increases linearly with increasing C* and this relation can be expressed as

$$\frac{da}{dt} = D_0 (C^*)^{\phi} \qquad 3$$

where D_0 and ϕ are constants. The values of ϕ are between 1 to 1.5.

Steady state crack growth rate, da/dt_s, as a function of reference stress, σ_{ref}, is also given in Fig. 4 for the CCG tests, c.f. series PM-CCG and SHAZ-CCG. da/dt_s is actually the growth rate which is constant within a period. It can be seen that at the same σ_{ref}, da/dt_s in the PM is much lower than that in the simulated HAZ. The steady state crack growth rate follows the power-law relation, which is in the same form as the Norton's law, and can be written as

$$\frac{da}{dt_s} = \nu' (\sigma_{ref})^{\nu} \qquad 4$$

where ν′and ν are coefficient and stress index, respectively. ν is 82 and 49 for the PM and the simulated HAZ, respectively.

da/dt_s is plotted against t_R in Fig. 6 for the CCG tests, c.f. series PM-CCG and SHAZ-CCG. Fig. 6 also includes uniaxial creep tests where t_R is plotted against $d\varepsilon/dt_{min}$, c.f. series PM-uniaxial and SHAZ-uniaxial. It should be mentioned that da/dt_s and $d\varepsilon/dt_{min}$ have different units. In the double logarithmic scales, the da/dt_s-t_R and $d\varepsilon/dt_{min}$-t_R relations are reasonably linear. For the CCG tests, da/dt_s-t_R relation seems to be independent of the microstructure. For the uniaxial tests, $d\varepsilon/dt_{min}$-t_R relation depends somewhat on the microstructure. The power-law da/dt_s-t_R relation for the CCG tests and the power-law $d\varepsilon/dt_{min}$-t_R (Monkman-Grant) relations for the uniaxial tests propose

$$\frac{da}{dt_s} \cdot t_R^{\beta_{CCG}} = C_{CCG} \qquad 5a$$

$$\frac{d\varepsilon}{dt_{min}} \cdot t_R^{\beta_{PM}} = C_{PM} \qquad 5b$$

where C_{CCG}, C_{PM}, β_{CCG} and β_{PM} are constants. β_{CCG} and β_{PM} take the values of 1.09 and 0.93, respectively, which are very close to unity.

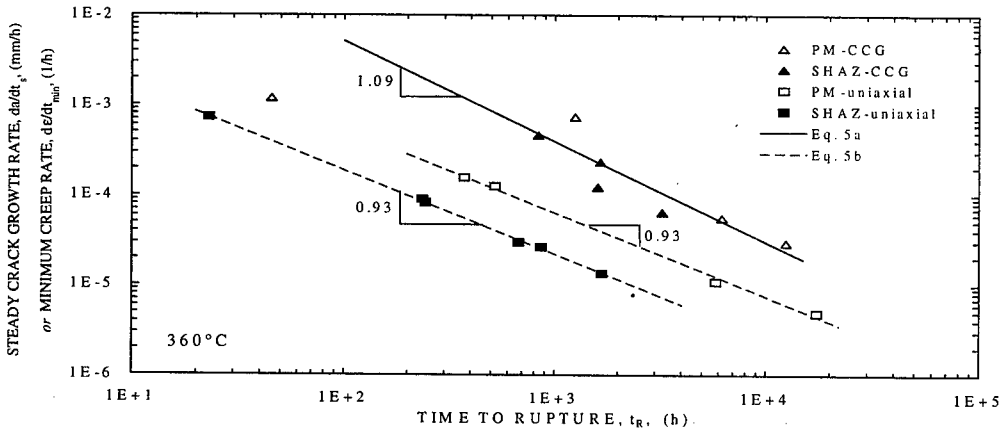

Fig. 6 Steady state crack growth rate, da/dt_s, for CCG tests and minimum creep rate, $d\varepsilon/dt_{min}$, for uniaxial tests versus time to rupture t_R.

3.2 Post Test Metallography

For the uniaxial tests, necking appeared prior to rupture. Grains adjacent to the fracture were elongated along the stress direction and the rupture mode was transgranular. No creep cavitation was observed. These observations were independent of stresses and microstructure.

For the notched tests, transgranular crack initiation and growth were dominant in the PM. Deformed grains and micro-cracks at about 45° to the stress direction were observed at the unfailed notch, see Fig. 7a. For the simulated HAZ, neither cracking, cavity nor deformed grains were observed at the unfailed notch. Transgranular and intergranular crack initiation and growth were dominant at shorter and longer failure times, respectively. The intergranular initiation and growth is shown in Fig. 7b.

For the CCG tests, deformed grains close to the crack and transgranular crack initiation, propagation and final fracture were observed in the PM, being independent of time to failure, see Fig. 7c. For the

simulated HAZ, intergranular crack initiation, growth and final fracture were observed, see Fig. 7d. This was independent of time to failure.

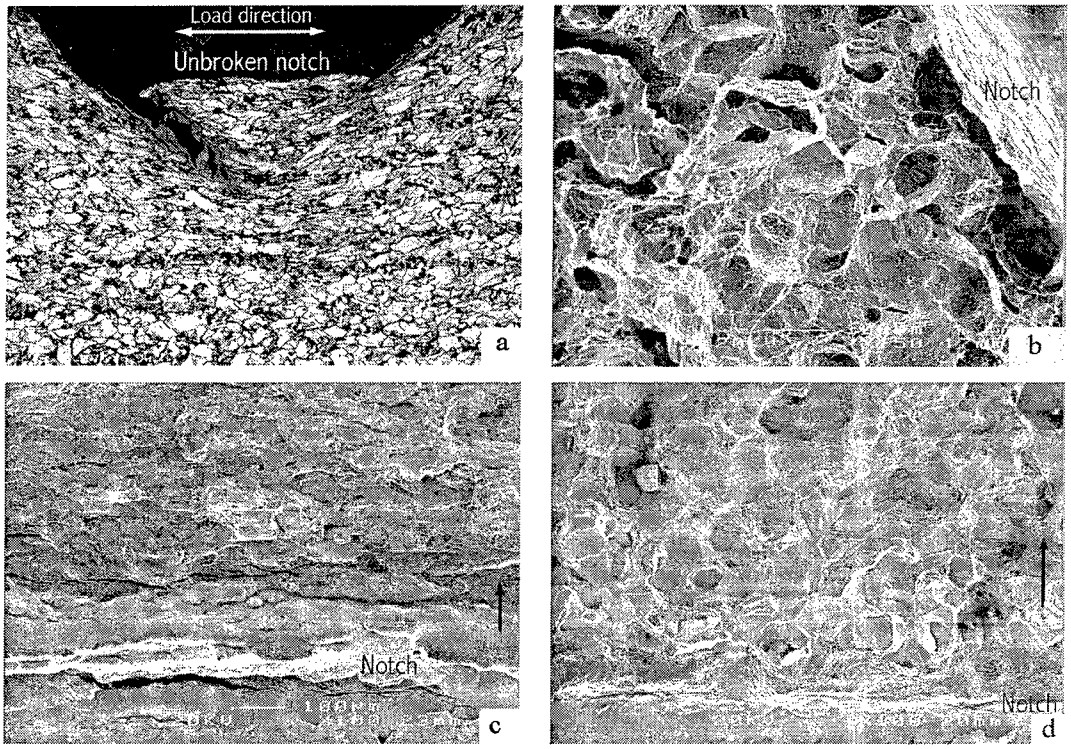

Fig. 7 LOM (a) and SEM (b-d) micrographs: (a) PM-notched, cross section of the unbroken notch on the failed specimen after 2074 hours at 780 MPa, 200X. (b) SHAZ-notched, fracture surface of the failed specimen after 2172 hours at 1050 MPa, 150X. (c) PM-CCG, fracture surface near the notch of the failed specimen after 12457 hours at 574 MPa. Arrow indicates the crack growth direction. 100X. (d) Same as (c), but for the failed specimen from SHAZ-CCG after 3237 hours at 507.4 MPa, 100 X

4 CONCLUSIONS

This study has addressed creep crack growth in the high strength low alloy steel used in the power generating industry below the limited temperature. The following conclusions can be drawn.

1) Creep crack growth (CCG) did occur below the limit temperature where creep is not usually anticipated. CCG can be a main factor restricting the performance of the material.

2) The shortest failure time was found in the CCG tests with the simulated HAZ, especially at lower reference stresses. This shows that the simulated HAZ is quite sensitive to creep crack growth.

3) For the parent metal, the shortest failure time was found in the uniaxial tests, indicating that the parent metal is insensitive to creep crack growth.

4) The CCG behaviour was analysed by means of the creep parameter C*. The crack growth rate correlated well with C* and it fell in a narrow band when plotted against C*.

5) The power-law relations between the failure time and reference stress, between the steady state crack growth rate and reference stress (Norton's law for the uniaxial tests), between the steady state crack growth rate and failure time (Monkman-Grant correlation for the uniaxial tests) were found in the CCG tests. These findings may have a potential application in the estimation of lifetimes where the CCG dominates.

6) For the parent metal, failure was transgranular for the uniaxial tests and crack initiation and growth were transgranular for the notched and CCG tests. These were independent of failure time.

7) For the simulated HAZ, failure was transgranular for the uniaxial tests. For the notched tests, transgranular and intergranular crack initiation and growth dominated at shorter and longer failure time, respectively. For the CCG tests, intergranular crack initiation, growth and final fracture were observed, independent of failure time.

ACKNOWLEDGEMENTS

Stockholm Energi AB, Stockholm, Sweden, is gratefully acknowledged for financial support and for providing test materials. Dr. J. Storesund, SAQ Inspection Ltd, Stockholm, had involved in the initiation of the project. Mr. J. Lindblom, Swedish Institute for Metals Research (SIMR), is thanked for experimental recording set-up and Mr. A Mårtensson, SIMR, for literature collection.

REFERENCE

[1] G. J. Neate, Mat. Sci. and Tech., Vol. 3, No. 1, (1987), p. 14
[2] I. A. Shibli, Mat. Sci. and Tech., Vol. 3, No. 2, (1987), p. 110
[3] D. J. Gooch, Mat. Sci. Eng. Vol. 64, No. 2, (1984), p. 183
[4] R. Sandström and G. Östberg, Swedish Institute For Metals Research, IM-2517, (1989)
[5] Creep Crack Growth in Carbon-Manganese Steels at 300-420°C, Synthesis report for publication, Brite/Euram BE 7463, (1998)
[6] D. J. Gooch, Mat. Sci. Eng. Vol. 83, No. 1, (1986), p. 17
[7] M. P. Happer and E. G. Ellison, J. Strain Analysis, Vol. 12, No. 3, (1977), p. 167
[8] A. Saxena, Mat. At High Temp., Vol. 10, No. 2, (1992), p. 79
[9] D. J. Gooch and S. T. Kimmins, J. Strain Analysis, Vol. 21, No. 4, (1986), p. 231
[10] R. Wu, F. Seitisleam and R. Sandström, Proc. of Int. Conf. on Baltica IV: Plant Maintenance For Managing Life and Performance, Vol. 2, Helsinki – Stockholm – Kirkkonummi, September 7-9, (1998), p. 623
[11] G. A. Webster and R. A. Ainsworth, High Temperature Component Life Assessment, Published by Chapman & Hall, 2-6 Boundary Row, London, (1994)
[12] Standard Test Method For Measurement Of Creep Crack Growth Rates In Metals. Designation E 1457 - 92, Annual Books of ASTM Standards, (1992), p. 925

ruiwu@simr.se; rsand@kth.se; www.simr.se

Key Engineering Materials Vols. 171-174 (2000) pp. 147-152
© 2000 Trans Tech Publications, Switzerland

Creep Crack Growth in Nearly Fully-Lamellar Gamma TiAl Alloys

K.V. Jata[1] and Y.-W. Kim[1,2]

[1] AFRL/MLLM, Materials and Manufacturing Directorate, Air Force Research Laboratory, 2230 Tenth Street, Suite 1 Wright-Patterson AFB, OH 45433, USA

[2] Universal Energy Systems, Dayton, OH, USA

Keywords: Gamma Titanium Aluminide, Creep Crack Growth

Abstract Creep crack growth behavior of gamma titanium aluminide alloys was investigated over 650 to 800°C temperature range under constant load conditions. Alloys were chosen in a nearly fully lamellar microstructural form. Analysis of creep crack growth data obtained from CT specimens suggests that elastic stress intensity factor K best describes the crack growth rate data at the lower test temperatures. At 800°C tests had to be discontinued because of creep blunting. At 650°C and 720°C creep crack extension occurred through formation of microcracks along interlamellar interfaces and their joining to the main crack-tip through translamellar fracture. At 800°C, extensive high temperature deformation and creep accompanied crack extension. Fracture at 800°C is predominantly grain boundary fracture consisting of grain boundary voiding and interlamellar separation. For similar K's, crack extension and growth-rate were greater at 800°C than at 650°C.

Introduction Creep crack growth of flaws is an important phenomenon to understand and arises in situations where structural parts operate at high temperatures under constant load or cyclic load with hold periods. A number of publications in the literature have addressed the fracture mechanics framework and understanding of creep crack growth mechanisms to describe sustained load crack growth rates at high temperatures as a function of crack-tip driving force [1-9]. Although numerous investigations have been done on materials that exhibit considerable creep [1-5], recent emphasis has been on the understanding of creep crack growth in creep-brittle materials [6-9]. For example, the ASTM standard [10] that addresses testing of creep–ductile materials is currently being modified to accommodate test requirements and method for creep-brittle materials. Furthermore, the VAMAS group in collaboration with ASTM has published a special volume on the creep crack growth behavior to include creep-brittle materials [7].

Gamma titanium aluminide alloys based on γ-TiAl phase are emerging as engineering materials especially for high temperature structural applications particularly due to their low density, high-temperature strength and modulus retention. For the last ten years, low-temperature property evaluations have been extensive; however, the increasing need for understanding the high-temperature performance of these alloys has only recently led to a greater attention to investigate high temperature mechanical behavior including creep, high-temperature fatigue and fracture resistance. The objective of this work was to understand the creep crack growth behavior of gamma titanium aluminide alloys with nearly fully lamellar microstructure under sustained loading. Role of microstructure and creep deformation on crack growth is also emphasized.

Experimental Procedures Two gamma TiAl alloys were chosen for this study.

Composition of Alloy A is Ti-46.5Al-2Cr-3Nb-0.2W-0.2Si-0.15O and composition of Alloy B is Ti-47Al-2Cr-2.5Nb-0.2W-0.12B-0.03C (in at %). Both were obtained as forgings and were given the following heat treatment. Alloy A was annealed at 1340°C for 30 min in an air furnace followed by furnace cooling at a rate of 100°C/min to 1200°C and then cooled to RT in air. Material was aged at 900°C for 8 hours to stabilize the microstructure. Alloy B was annealed at 1350°C for 1 hour, furnace cooled to 1250°C and then air-cooled. A 6-hour heat treatment was used to stabilize the microstructure prior to testing.

Creep crack growth testing was performed on compact tension specimens with dimensions of W = 41 mm and B_e (effective thickness) of 5 mm. Specimen surfaces were mechanically polished to a 1μm finish. Specimens were either tested after precracking at RT at a K value between 8-9 $Mpam^{1/2}$ or with only an EDM notch. Data shown in this paper are for specimens that were tested only with an EDM notch (radius equal to 0.05 mm) and without a precrack. Test procedures used were in accordance with the ASTM test standard E1457-92 [10]. Crack length was measured using DCEPD and crack opening displacement was measured at the load-line by a clip gage with extended ceramic arms. Creep crack growth test data shown in this paper is for 720°C tests. Specimen temperature was maintained within 1.1°C. A load equal to 0.225 kN was applied on the specimen during heating.

Some tests were interrupted and stopped to record crack profiles to understand creep crack growth mechanism. Profiles on the surface and interior of the specimen were recorded. In this paper microcracks and unfractured ligament distribution of a specimen tested at 650°C are shown.

Results and Discussion The heat treatment employed for alloys A and B resulted in a nearly fully-lamellar (NFL) microstructure. Microstructure of Alloy A, Figure 1, consists of lamellae with an average grain size (GS) of 500 μm and a minor fraction (<5%) of small (10-30 μm) gamma grains. These gamma grains are distributed in stringer forms throughout the matrix; however, many of them are present along the grain boundaries. The lamellar spacing varied between 0.2 and 0.7 μm with the mean value of 0.3 μm. Alloy B has a finer grain size than alloy A and is fully lamellar and the equiaxed gamma grains have been eliminated. The yield strength and Youngs Modulus of Alloy B at 720°C are 420 MPa and 150 GPa, respectively. The creep stress exponents is a function of stress ranging from 3 for 150 MPa to 8 for higher stresses.

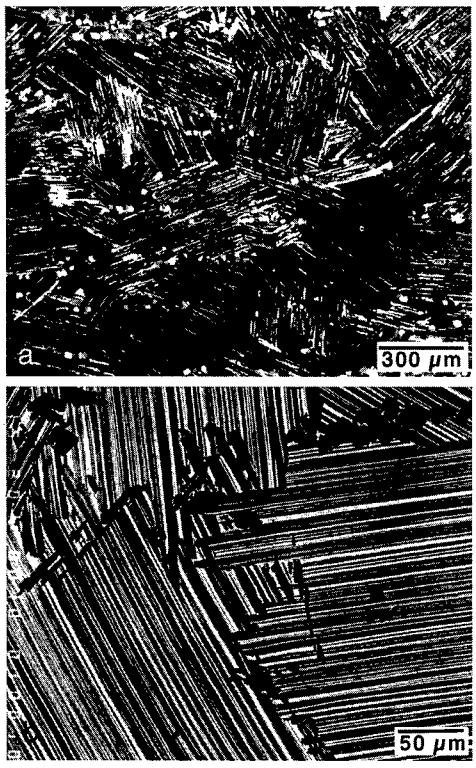

Figure 1. Optical and back scattered electron micrograph showing nearly fully lamellar microstructure and the fine equiaxed gamma grains for the gamma titanium aluminide alloy.

Creep crack growth tests were performed at 650, 720 and 800°C. Figure 2 shows crack extension in alloy B, as a function of time. Data are for a test temperature of 720°C and for two load levels. For the sample loaded at 5.4 kN approximately $(2/10)^{th}$ of the life time is spent in initiation time whereas the specimen loaded to 4.1 kN crack growth appears to be instantaneous. The scatter observed in the data is believed to be due to the deformation anisotropy of the lamellar microstructure of the gamma alloys.

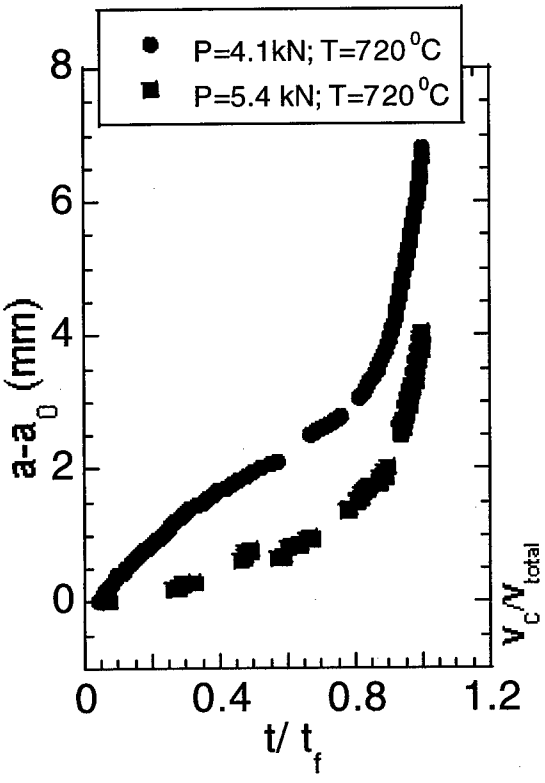

Figure 2. Crack extension as a function of time normalized with respect to time to failure for Alloy B (Ti-47Al-2Cr-2.5Nb-0.2W-0.12B-0.03C) at 720°C.

At all test temperatures, crack extension proceeded by microcrack formation in front of the crack tip. Microcracks formed by interlamellar splitting and they joined the main crack through translamellar fracture of the connecting ligaments. Even in the case of the 800°C test microcracks developed by interlamellar splitting and at this temperature microcracks formed as far as 3.5 mm ahead of the crack tip. At this temperature, however, the ligaments joining the microcracks fractured by "intergranular and interlamellar fracture" (termed as boundary fracture). These features are shown (in the next page) in Figure 3 (a) to (c) for the case of 650°C test.

In order to apply the proper crack tip driving force parameter, further analysis of the data was performed. Shown in Figure 4 is the variation of the displacement rate of the creep component to the total displacement rate for the Alloy B.

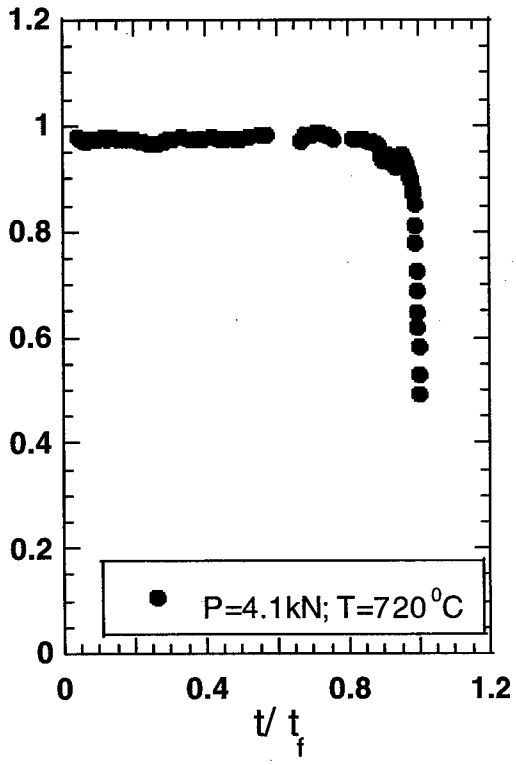

Figure 4. Normalized creep displacement V_c/V_T rate as a function of time for Alloy B.

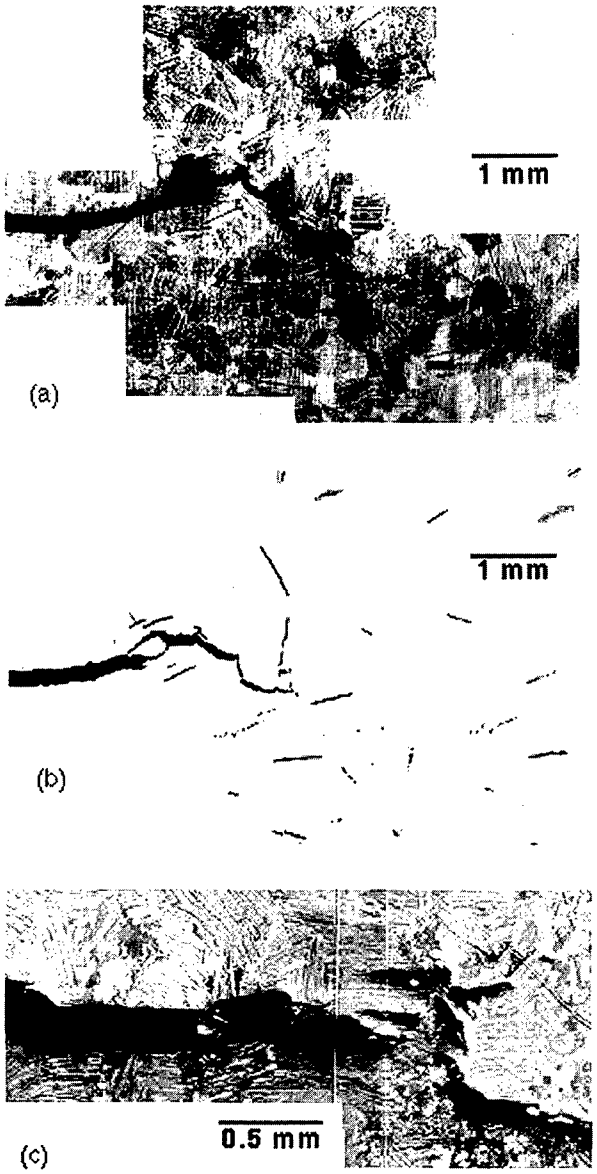

Figure 3. Microcrack distribution and fractured ligaments ahead of the crack tip in the creep crack growth specimen tested at 650^{0}C; (a) on the surface, (b) and (c) in the interior of the specimen. Test was discontinued and crack profiles were recorded

Transition time t_T was then calculated using

$$t_T = (K^2)/((n+1)\,EC^*) \qquad (1)$$

and the maximum value was chosen. E1457 recommends data prior to this transition time be discarded because creep stress distribution is considered non-steady state prior to this transition time. Not only data prior to this transition time should be discarded but also the data prior to a crack extension of 0.5 mm have to satisfy the criterion of V_c/V_{total} to be greater than 0.8, otherwise they too have to be discarded. These criteria are only applicable if the crack tip driving force parameter is C*.

In the case of creep- brittle materials, such as Al 2519 and Ti 6242 [9] it was observed that the above criteria are rather stringent. In fact, not many of the creep crack growth data points were left out for analysis when the condition of crack extension of 0.5 mm and V_c/V_{total} to be greater than 0.8 had to be satisfied. Therefore, it was recommended that these conditions be relaxed to include data after a crack extension of 0.2 mm that satisfy V_c/V_{total} greater than 0.5. These conditions then are found to allow creep crack growth data of creep brittle materials to be represented by C* as well.

For alloy Bthis does not seem to be an issue. Most of the data points show V_c/V_{total} greater than 0.8. These data show that a steady state creep stress distribution has been produced early in the test and remains such for most of the specimen lifetime. Also shown in this Figure 4 are the transition times required for 0.2 mm and 0.5 mm crack extensions. The analysis of the data up to this point suggests that the behavior of the gamma titanium aluminide alloy B at 720°C can be considered as creep-ductile according to the ASTM standard E1457-92. Surprisingly, however, creep crack growth rate data for alloy B did not show a good correlation to the crack tip driving force parameter, C* (da/dt = Constant $C^{*\phi}$ where ϕ is approximately equal to 1). Instead, Figure 5 shows creep crack growth rates plotted as a function of elastic stress intensity factor K. Except for the initial transient data, the rest of the data show a fairly good correlation to the elastic stress intensity factor K. However, it is recognized that the validity of K has to be proven for different specimen geometries.

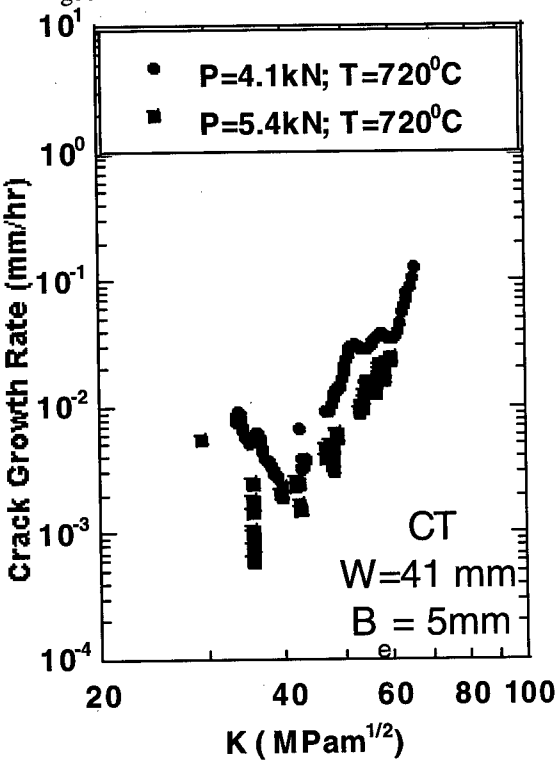

Figure 5. Creep crack growth rates shown as a function of elastic stress intensity factor, K, for Alloy B (Ti-47Al-2Cr-2.5Nb-0.2W-0.12B-0.03C) at 720°C.

It should be pointed out to the reader, however, that gamma titanium aluminide behaves differently at 650, 720 and 800°C. As will be discussed in a different publication, creep crack growth behavior of these alloys is creep-brittle at 650°C and creep-ductile above this temperature.

Conclusion Creep crack growth behavior of gamma TiAl alloys with lamellar

microstructure was investigated at 650, 720 and 800°C under constant load conditions. Analysis of the data at 720°C shows that a steady state creep stress distribution is attained early in the test and remains through the majority of the lifetime. At 720°C all the criteria for a C* crack tip driving force parameter are met, but a good correlation of crack growth rates to the elastic stress intensity factor crack K is also observed. At all test temperatures, microcrack formation is observed to occur at the interlamellar interfaces. At 650° the ligaments between the microcracks fracture in a translamellar fracture mode. At 800°C the ligaments between the interlamellar microcracks fracture by interlamellar cracking and intergranular separation.

Acknowledgment The author would like to acknowledge the metallographic assistance of Ms. Sonya Boone and Mr. Robert Lewis. The assistance of Mrs. Lisa Farmer, in preparing the manuscript is greatly appreciated.

References

1. Saxena, A., "Evaluation of *C** for the Characterization of Creep Crack Growth Behavior in 304 Stainless Steel," Fracture Mechanics: Twelfth Conference, 1980 *ASTM STP 700,* ASTM, pp. 131-151.
2. Saxena, A., "Creep Crack Growth Under Non Steady-State Conditions," Fracture Mechanics: Seventeenth Volume, *ASTM STP* 905, ASTM, Philadelphia, 1986, pp. 185-201.
3. Nikbin, K.M., Webster, G.A., and Turner, C.E., "Relevance of Nonlinear Fracture Mechanics to Creep Cracking," Crack and Fracture, *ASTM STP 601,* ASTM, 1976, pp. 47-62.
4. Sadananda, K. and Jata, K.V., *Metallurgical Transactions*, 1988, Vol. 19A, pp. 847-54.
5. Saxena, A., "Evaluation of Crack Tip Parameters for Characterizing Crack Growth: Results of the ASTM Round-Robin Program," *Materials at High Temperatures*, Vol. 10, 1992, pp 79-91.
6. Dogan, B., Saxena, A., and Schwalbe,K-H., " Creep crack growth behavior of Titanium alloy Ti6242," Materials at High Temperatures, Vol. 10(2), pp.138-143, 1992
7. Hui, C.Y., "Steady-State Crack Growth in Elastic Power Law Creeping Materials," Elastic-Plastic Fracture, Vol. 1, *ASTM STP 803*, ASTM, Philadelphia, 1983, pp 573-593.
8. Saxena, A. and Yokobori, T., editors, "Crack Growth in Creep-Brittle Materials," Special issue of *Engineering Fracture Mechanics*, Vol. 62, No.1, 1999.
9. Kwon, O., Nikbin, K.M., Webster, G.A., and Jata, K.V. "Crack Growth in the Presence of Limited Creep Deformation" Engineering Fracture Mechanics, 1999, Vol. 62, pp 33-46.
10. ASTM E1457-92, Philadelphia, 1992, Vol. 03.01, pp.1031-1043

Key Engineering Materials Vols. 171-174 (2000) pp. 153-160
© 2000 Trans Tech Publications, Switzerland

Modelling of High Temperature Multi-Axial Creep Rupture Behaviour of γ-Titanium Aluminide

R. Dempers, K. Nikbin and G.A. Webster

Department of Mechanical Engineering, Imperial College of Science, Technology and Medicine, Exhibition Road, London, SW7 2BX

Keywords: Intermetallic, Notched Bars, Multi Axial Stress, Creep, Finite-Element Analysis

Abstract The creep behaviour of the intermetallic γ-TiAl under conditions of multi-axial stress is considered. The particular alloy tested is known as 4722XD (Ti-47Al-2Mn-2Nb+0.8%vol.TiB_2) alloy as produced by the Howmet Corporation. Tests on plain and round bar double notched tensile test pieces with different notch sharpness were carried out on this alloy at 750 °C. The creep stress distributions generated across the notch throats were calculated by finite element analysis. For each notch geometry a skeletal point has been identified where the stress state is insensitive to the creep law assumed. Metallographic observations have been made of the creep damage developed in the notch throats. It has been found that the location of this damage can be correlated with the finite element results using models for the influence of state of stress on the creep ductility of materials.

Introduction The evolution of the gas turbine has to a large extent been dependent on the development of new advanced materials capable of withstanding higher temperatures and thus allowing more efficient operation. An entire family of alloys, the so-called superalloys, based primarily on nickel and cobalt has been produced for components such as turbine blades, vanes, discs and combustion cans.

For intermediate temperature applications, considerable research has and indeed is continuing to be performed on intermetallic materials such as γ-TiAl. The low-pressure turbine section, where blade temperatures up to 750°C and blade root temperatures of 500°C are commonplace, is seen as a typical environment for this material. γ-TiAl is particularly attractive because of its low density (approximately half that of nickel-based superalloys), and good creep resistance. However it exhibits only low fracture toughness and limited ductility.

Typical gas turbine components at elevated temperature experience multi-axial stress states and therefore it is important to examine creep failure under these conditions. The aim of this paper is to develop a multi-axial stress rupture criterion for the intermetallic γ-TiAl. The particular alloy that has been investigated is known as 4722XD (Ti-47Al-2Mn-2Nb+0.8%vol.TiB_2) alloy as produced by the Howmet Corporation. This alloy has a fine equiaxed grain structure offering a balance between fatigue and creep properties and more repeated behaviour than earlier alloys which suffered from significant material variability [1,2].

Experiments A tri-axial state of tension is the most damaging for creep failure [3-6]. This state of stress can most conveniently be generated in the throat of axi-symmetrically notched bars [3]. Notched and un-notched bars were machined from γ-TiAl cast rods. Fig. 1 shows the dimensions of the circumferential notches used. Three notch geometries were tested; blunt (B), medium (M) and sharp (S) with notch throat to root radius a/R ratios of 1.5, 5 and 15 respectively.

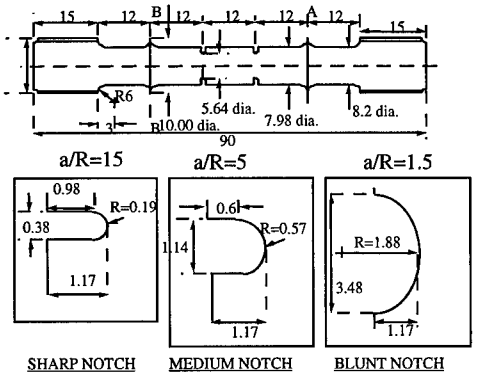

Figure1: Notched Bar Specimen Dimensions

Double notches were employed so that both failed and unbroken notches from the specimens could be examined. In some cases diametral measurements of strain were made as well as the axial elongations. The specimens were tested in dead weight lever arm machines with a lever arm ratio of 10:1. Three-zone electrical resistance furnaces were used to heat the specimens to within ±1°C of the desired temperature of 750°C. The temperature was monitored with two chrome-alumel thermocouples tied to the specimen with heat resistant string. Fig. 2 which shows the normalised creep curves obtained from both plain and medium notched bar tests provides an example of the creep behaviour of this material under both uni-axial and multiaxial stress states. Typical primary, secondary and tertiary regimes are observed for both although it is clear that the secondary region dominates. It has been found that the stress dependence of the secondary regime can be described satisfactorily either by a power law or a hyperbolic sinh law in the form

$$\dot{\varepsilon}_{\min} = A\sigma^n \qquad (1)$$

$$\dot{\varepsilon}_{\min} = A'\sinh\left(\frac{\sigma}{\sigma_0}\right) \qquad (2)$$

where $\dot{\varepsilon}_{\min}$ is the minimum creep rate and A, A', n and σ_0 are material constants. Models are available due to Rice and Tracey [4], Cocks and Ashby [5] and Spindler [6] for predicting the effects of multi-axial stress on the creep ductility of materials. With these models the multi-axial failure strain ε_f^* is given in terms of the uniaxial creep ductility ε_f by Rice and Tracey as

$$\frac{\varepsilon_f^*}{\varepsilon_f} = 1.65\exp\left(\frac{-3\sigma_m}{2\sigma_e}\right) \qquad (3)$$

by Cocks and Ashby as

$$\frac{\varepsilon_f^*}{\varepsilon_f} = \sinh\left[\frac{2}{3}\left(\frac{n-0.5}{n+0.5}\right)\right] \Big/ \sinh\left[2\left(\frac{n-0.5}{n+0.5}\right)\frac{\sigma_m}{\sigma_e}\right] \qquad (4)$$

and Spindler as

$$\frac{\varepsilon_f^*}{\varepsilon_f} = \exp\left(p\left(1-\frac{\sigma_1}{\sigma_e}\right)\right)\exp\left(q\left(\frac{1}{2}-\frac{3\sigma_m}{\sigma_e}\right)\right) \qquad (5)$$

where σ_1 is the principal stress, σ_e is the equivalent stress, σ_m is the mean stress and p and q are constants, with values of 0.15 and 1.25 for stainless steel [6]. These equations will be used to interpret the notched bar data.

Results In Fig 3 the notched bar failure lives are compared with the uni-axial failure lives on a net section stress basis. There is no significant trend with notch geometry. The stress dependence of rupture of the notched bars is similar to that of the plain bars but with a notch strengthening factor of 1.2.

Metallurgical inspection All specimens have been sectioned and subjected to mechanical. polishing and etching with Kroll's reagent. Figs. 4-6 illustrate the typical creep damage found in the unbroken notch of the blunt, medium and sharp notched specimens respectively. It is evident from these figures that cavitation becomes increasingly concentrated towards the notch root with increase in notch sharpness.

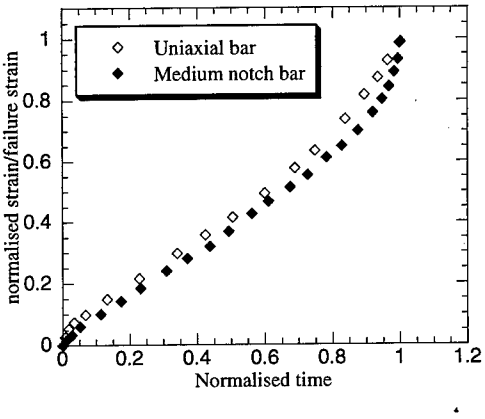

Figure 2: Comparison of Normalised uniaxial and notched bar average strain (measured between A and B as shown in Fig 1) for the γ-Ti ally tested at 750 °C

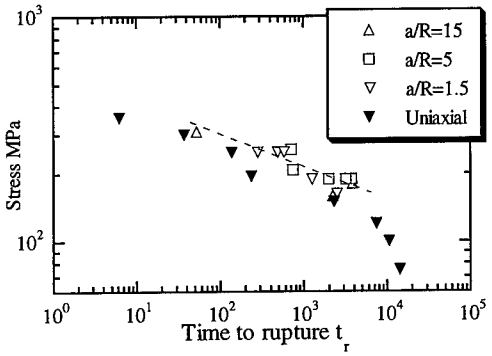

Figure 3: Comparison of net-section stress versus time to rupture for uniaxial and notched bar specimens of different a/R ratios

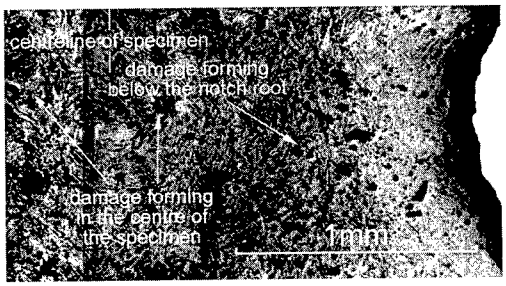

Figure 4: Optical micrograph of the unbroken notch of a/R=1.5 showing large-scale cavitation below the surface of the notch root.

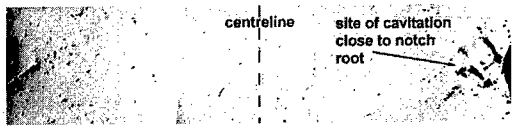

Figure 5: Optical micrograph of the unbroken notch of a/R=5 in the unetched condition.

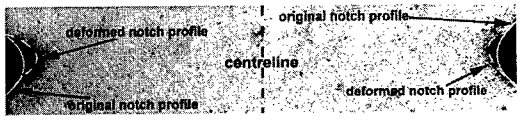

Figure 6: Optical photograph of the unbroken notch of a/R=15 in the unetched condition illustrating the comparative lack of cavitation.

Finite element analysis Numerical analysis was carried out using the ABAQUS finite element package to explain the results. Suitable meshes were produced to represent the notched bar specimens [7-8]. For the creep calculations it has been assumed that creep strain rate can be represented by the Norton creep law or the hyperbolic sinh law (Eq. 1,2). Initially calculations were made for the power law with n=3, 6 and 9 to demonstrate the existence of a skeletal point [7,8] where the stress state is insensitive to the value of n. This is illustrated in Fig 7 for a medium notch where a skeletal point is observed at a normalized radial distance r/a of $r^*/a = 0.825$. This distance is approximately the same for all the normalized stresses σ_e/σ_{net}, σ_1/σ_{net} and σ_m/σ_{net} for this geometry. A complete list of the skeletal points for each notch shape is given in Table 1. It is evident that this point moves closer to the notch root with increase in notch sharpness.

	r*/a	σ_e^*/σ_{net}	r*/a	σ_1^*/σ_{net}	r*/a	σ_m^*/σ_{net}
B1	0.68	0.74	0.725	1.04	0.755	0.54
M1	0.82	0.68	0.825	1.16	0.83	0.74
S1	0.90	0.66	0.895	1.36	0.895	0.96

Table 1: Stress ratios predicted at the skeletal point.

Additional FE calculations have also been made with eqs (1) and (2) for properties specific to γ–TiAl. Comparisons of the stress distributions obtained for a medium notch are shown in Fig 8. It is apparent that a skeletal point is still obtained which corresponds to the same location as determined in Fig 7 although the stress distributions are quite different. A greater range of stress is predicted with the hyperbolic sinh law than when a power law is used.

To predict failure strain across the notch bars calculations were performed using the relevant models given by Eqns (3-5) to produce plots of $\varepsilon_f^*/\varepsilon_f$ (multiaxial ductility versus uni-axial ductility ratio) versus normalised radial distance. These are shown in Figs 9-11 for the blunt, medium and sharp notches. Examination of Fig. 9-11 reveals that the Rice and Tracey model always predicts the highest ductility ratio at all locations, with the Spindler model predicting an intermediate value and the Cocks and Ashby model giving the lowest ratio. The location of the minima in the ductility ratio curves moves progressively towards the root of the notch in a similar manner to the skeletal point as the notch acuity is increased.

Discussion Although the Norton and hyperbolic sinh relationships are both satisfactory for describing the secondary creep properties of γ–TiAl, it has been found from further calculations that significantly different stress distributions can be obtained across the notch throat. The effect is most marked for the blunt notch and least for the sharp notch. The hyperbolic law predicts higher stresses at the notch root than the power law an lower at the centreline for each of the geometries. The predicted stress distributions cross over at the approximate location of the respective skeletal point for each notch providing further proof that the existence of a skeletal point is independent of the form of the creep law assumed.

The trends identified in the stress distributions calculated can be used to explain Figs 9-11. The biggest difference in predictions between the power law and hyperbolic sin h law of $\varepsilon_f^*/\varepsilon_f$ corresponds with where the large differences in stress distributions were calculated. The ductility ratio at the minima decreases with increasing notch acuity thus indicating that less deformation is required to cause failure with increase in notch sharpness. In fact the ductility ratio at all points across a notch throat reduces as notch acuity increases. The ductility ratios calculated by the power and hyperbolic sinh laws exhibit a divergence at low values of r/a for both the blunt and medium notches, however the curves obtained for the sharp notch are almost identical.

Comparison of the $\varepsilon_f^*/\varepsilon_f$ versus normalised radial distance plots with the optical micrographs shown in Figs 4-6 shows evidence of a link between damage location and minimum $\varepsilon_f^*/\varepsilon_f$. The minimum value of $\varepsilon_f^*/\varepsilon_f$ corresponds to the location at which damage would be expected to initiate. Examination of Fig 4 shows a broad band of damage across the unbroken notch below the surface of the notch root. This high level of cavitation suggests that initiation occurred somewhere in this region. This corresponds to the location of the shallow trough in the $\varepsilon_f^*/\varepsilon_f$ curve shown in Fig 9. Comparison of Figs 4-6 with Figs 10-11 shows a similar link for the medium and sharp notches respectively. The cavitation suffered by the sharp-notched test pieces was found to be very localised at the notch root suggesting that failure in this geometry initiates close to the surface. Further evidence of this was provided from other unbroken notches in sharp notched specimens which were found to contain cracks which had grown from the

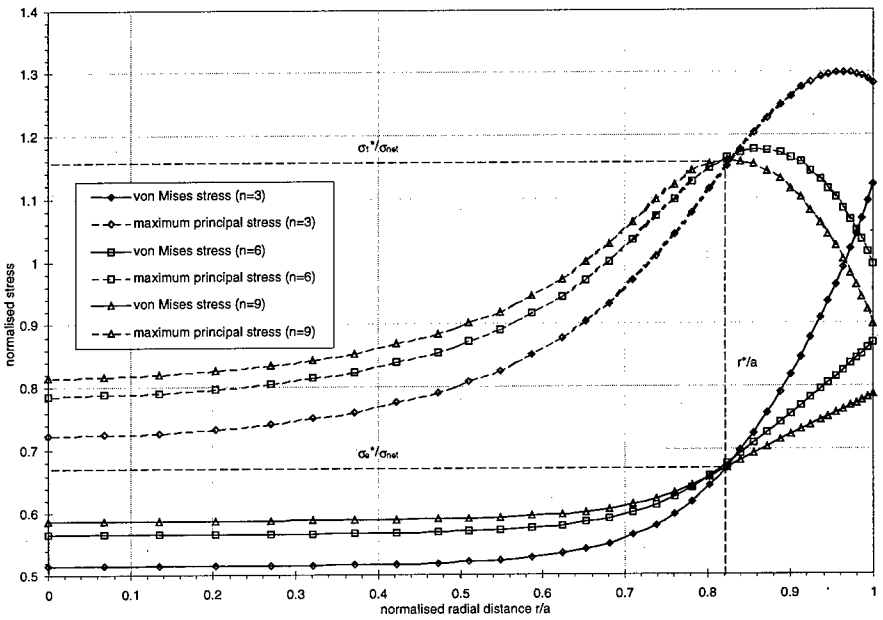

Figure 7: Graph of normalised stresses versus normalised radial distance illustrating the existence of a skeletal point in the medium notch.

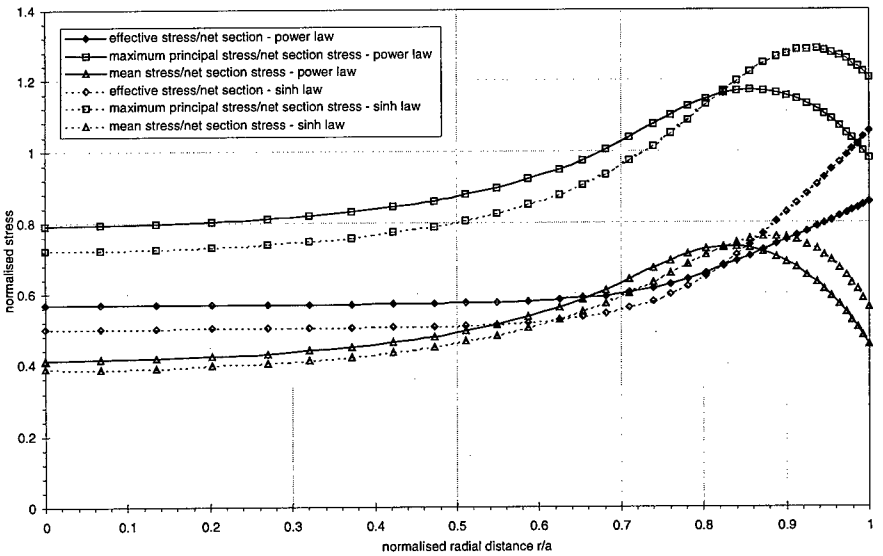

Figure 8: Stress distributions obtained from power law and hyperbolic sinh law for a medium notch. The distance r*/a is the same as figure 7 and table 1.

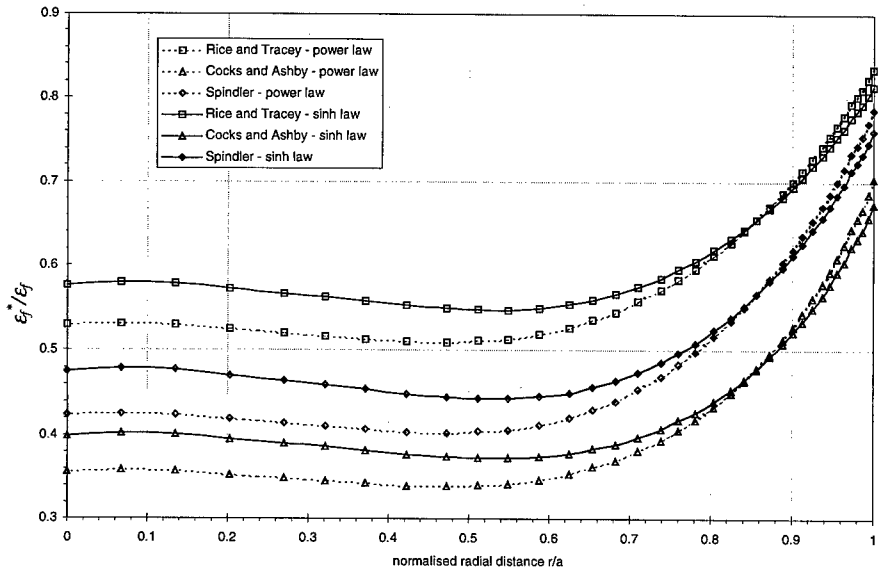

Figure 9: Plots of $\varepsilon_f^*/\varepsilon_f$ using the Rice and Tracey, Cocks and Ashby and Spindler models for a blunt notched bar.

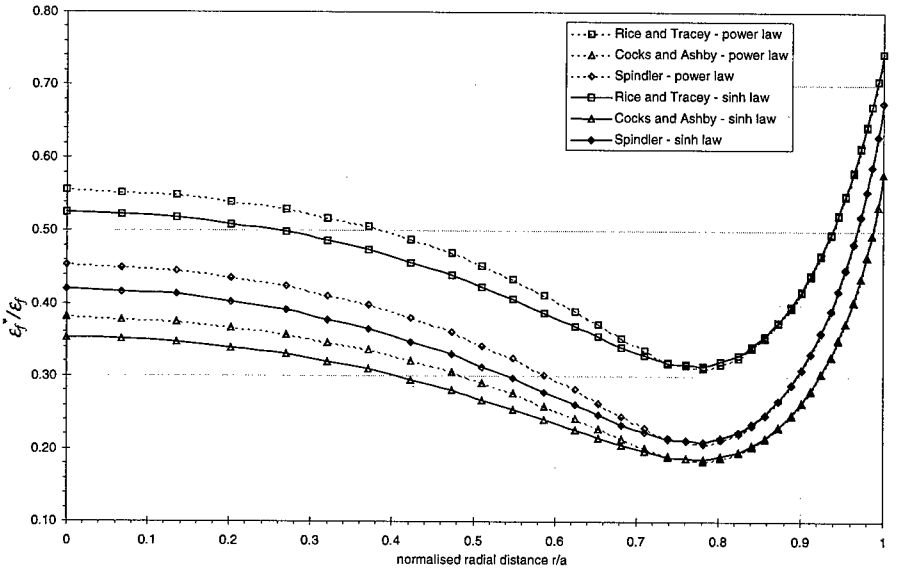

Figure 10: Plots of $\varepsilon_f^*/\varepsilon_f$ using the Rice and Tracey, Cocks and Ashby and Spindler models for a medium notched bar.

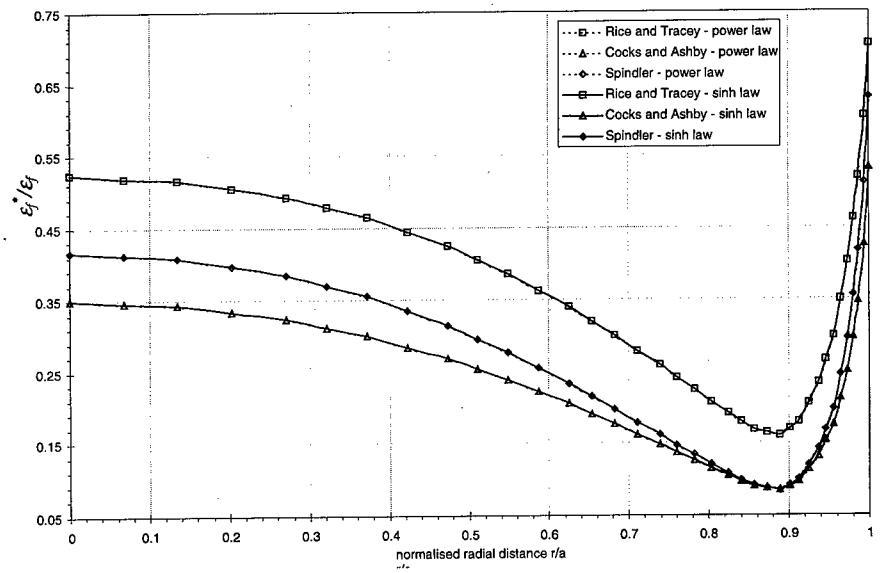

Figure 11: Plots of $\varepsilon_f^*/\varepsilon_f$ using the Rice and Tracey, Cocks and Ashby and Spindler models for a sharp notched bar.

notch root. The normalised stress distributions (σ_e/σ_{net}, σ_1/σ_{net}, σ_m/σ_{net}, σ_1/σ_e, σ_m/σ_e) and ductility exhaustion ($\varepsilon_f^*/\varepsilon_f$) plots all suggest that as notch acuity increases the site of damage initiation becomes more localised and moves towards the root of the notch.

Conclusions The existence and location of skeletal points for the three notched geometries has been verified using both a simple power law and a hyperbolic sinh law. This has enabled skeletal values of the effective, mean and maximum principal stresses to be calculated for each of the geometries.

The stress distributions across the notch throat have been studied in detail using each creep law. These stresses have been used to predict the distribution of multiaxial creep ductility with radial position across each notch throat from void growth models due to Rice and Tracey, Cocks and Ashby and Spindler. It has been found that all the models show similar trends, with the minimum in ductility becoming increasingly localised towards the notch root with increase in notch sharpness. It has been demonstrated that these calculations are consistent with metallurgical observations that cavitation initiates across most of the cross section of blunt notches, below the surface of medium notches and from those to the notch root of sharp notches.

References

1. Kerr, D.C., et al., Effects of State of Stress on the Tensile and Creep Properties of γ-TiAl. 1995.
2. Kerr, D.C., et al. Creep Strain Determinations across the Root of a Notch. in Local Strain and Temperature Measurements in Non-Uniform Fields at Elevated Temperatures. 1996. Berlin: Woodhead Publishing Limited.
3. Hayhurst, D.R., F.A. Leckie, and J.T. Henderson, Design of Notched Bars for Creep-Rupture Testing under Tri-Axial Stresses. International Journal of Mechanical Sciences, 1977. Volume 19: p. 147-159.

4. Rice, J.R. and D.M. Tracey, On the Ductile Enlargement of Voids in Triaxial Stress Fields. Journal of Mechanical Physics of solids, 1969. 17: p. 201-217.
5. Cocks, A.C.F. and M.F. Ashby, Intergranular fracture during power-law creep under multiaxial stresses. Metal Science, 1980: p. 395-402.
6. Spindler, M.W., The Multiaxial Creep of Austenitic Stainless Steels, . 1994, Nuclear Electric.
7. Hayhurst, D.R. and J.T. Henderson, Creep Stress Redistribution in Notched Bars. International Journal of Mechanical Sciences, 1977. Volume 19: p. 133-146.
8. Al-Faddagh, K.D., R.T. Fenner, and G.A. Webster, Steady-State Stress Distributions in Circumferentially Notched Bars Subjected to Creep. Journal of Strain Analysis, 1982. Volume 17(No.3): p. 123-132.

Key Engineering Materials Vols. 171-174 (2000) pp. 161-168
© 2000 Trans Tech Publications, Switzerland

Effect of Fiber Orientation on Fatigue and Fracture Properties of Fiber Eutectic Al-Al_3Ni Composite Alloy

S. Goto, S. Aso and Y. Komatsu

Department of Materials Science and Engineering, Faculty Engineering and Resource Science, Akita University, Tegata Gakuencho, Akita, 010-8502, Japan

Keywords: Fatigue, Bending Fatigue, Al-Al_3Ni, Fiber-Reinforced Composite, Fiber Orientation, Inter-Fiber Spacing, Eutectic Alloy, Unidirectional Solidification, Mechanical Property

Abstract

In order to clarify the relation between tensile and fatigue behaviors of fiber-reinforced composite, four kinds of eutectic Al-Al_3Ni composite materials with different inter-fiber spacings were prepared by unidirectional solidification. They were cut out to make five kinds of specimens with different angles between applied stress and fiber orientations. Their tensile and fatigue properties were compared with each other by means of a tensile test at a strain rate of $7.7 \times 10^{-5} s^{-1}$ and a bending fatigue test at a strain cycle of 7 Hz under stresses from 50 to 150 MPa at room temperature in air. Their fracture surfaces were also comperared with each other.

1. Introduction

There are a significant number of basic studies on the fatigue properties of metal-matrix composite resulting in models whose predictions have been verified by experiments. Harmon and Saff [1] have shown that there are two fatigue failure modes which can initiate and grow in the vicinity of a hole in a panel with unidirectinal reinforcements. When the strength of the matrix is small, cracks grow parallel to the fibers but when the matrix is strong, the cracks grow perpendicular to the fibers. Bridging models have been developed by McMeeking and Evans [2] and Cox and Marshall [3], while Hillberry and Johnson [4] have included both initiation and crack growth considerations when estimating the fatigue life of notched components. The fatigue and strength characteristics of deeply notched specimens have received extensive attention from Walls and Zok [5].

On the other hand, eutectic composites continue to show promise as potential structural materials for high-temperature applications as, for example, gas turbine blades, because the microstructure is very thermally stable and has a greater strengthening effect in addition to composite strengthening effect of two phase alloy [6]. In order to clarify the mechanical properties of the eutectic composites, pretty many investigations [7] have been carried out about the structure effect on the strength of fiber eutectic composite. However, the experimental results do not always agree with another and are not yet conclusive. As possible sources of the discrepancies, differences in the fiber orientation relative to the loading axis and inter-fiber spacing effect have been considered.

By the way, discussions with designers suggests that the primary consideration in fatigue is the avoidance of crack initiation during the life of the structure[8]. Initiation is usually defined by the appearance of a measurable crack in a range. Should cracks initiate for unforeseen circumstances, it is necessary at the design stage, to demonstrate that crack propagation can continue for twice the life of the structure without catastrophic failure. In traditional design procedures, these considerations

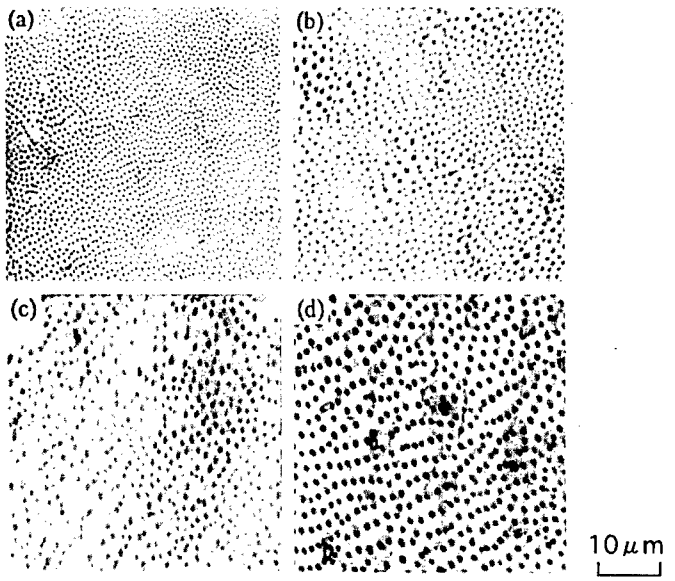

Fig. 1 Microsturucture of transverse section of unidirectionally solidified Al-Al_3Ni alloy materials: (a) F material, (b) M material, (c) L material and (d) C material.

are satisfied by using the so-called S-N curve for initiation and the law of crack growth rate in terms of the range of stress intensity. The advances in the fatigue strength of composites have not yet reached the stage of easy application and the methods are still very much in the domain of the expert. This is especially true in micromechanics based models which require many properties far removed from the interest of the designer.

The aim of this paper is to pesent a knowledge about the relation between tensile properties and fatigue properties of fiber reinforced metal-matrix composites in a form readily applicable to design procedures.

2. Materials and experimental procedure

2-1. Specimen preparation

After casting into a virtical type crucible, an eutectic Al-6.2 mass % Ni alloy was unidirectionally solidified to make ingots of metal matrix composite with reinforcement fibers aligned with the solidification direction. The inter-fiber spacing was controlled by changing the solidification rate in a range from 3.06×10^{-3}mm s^{-1} to 1.11×10^{-1} mm s^{-1}. Four kinds of Al-Al_3Ni alloy ingots with different inter-fiber spacings were prepared. **Figure 1** shows their optical microstructures. Hereafter they will be referred to as F material (the fiber spacing λ is 1.04 μm), M material (λ=1.54 μm), L material (λ=3.23 μm) and C material (λ=6.79 μm) respectively. From these ingots, specimens were cut out by a diamond cutter, so that the fiber orientation relative to the specimen axis may be 0 to $\pi/2$ as shown in **Fig. 2**. They were finished to the size about 4～5 mm x 1.5 mm in cross-section and 28 mm in length by means of the technique reported previously [9]. For comparison, a cast Al-6.2 mass % Ni eutectic alloy specimen with random oriented fibers (λ=1.15 μm) was also prepared. Every specimen was annealed for 1.8 ks at 673 K.

2-2 Mechanical tests

Shimazu Autograph IS-10T was used for the tensile test. The stress-strain curve was measured

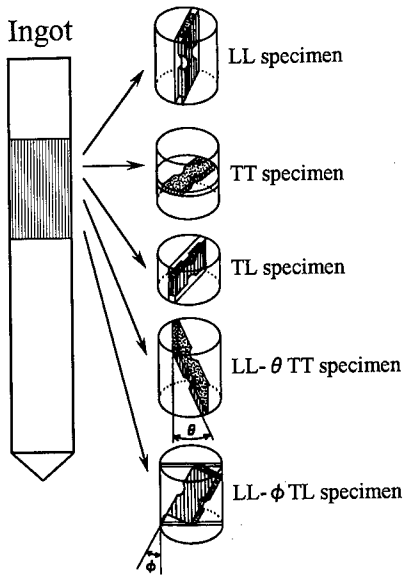

Fig. 2 Different types of the specimens cut out from ingot.

under a strain rate of $7.76 \times 10^{-5} s^{-1}$ at room temperature. In addition to the entire stress-strain curve, the yield stress ($\sigma_{0.2}$), maximum tensile stress (σ_B) and their dependence on fiber spacing and fiber orientation were investigated. Fatigue properties were investigated by using a bending type hand-made fatigue machine. The woheler curve (S-N curve) was measured at a strain cycle of 7 Hz under stresses from 50 to 150 MPa at room temperature in air.

2-3 SEM observation

To reveal the morphology of fracture surface after tensile test or fatigue test, EPMA (JEOL-JXA 733) was used. The effect of fiber orientation on the morphology of fracture surface was analyzed qualitatively.

3. Results and discussion

3-1. Stress-strain curve

Figures 3 and 4 are typical examples of the true stress-true strain curves. Figure 3 shows the stress-strain curves of specimens F, M and C in which the tensile axis was parallel to the fiber orientation (LL) and perpendicular (TT and TL). In either case, the stress level decreases with increasing the inter-fiber spacing λ in the sequence F→M→C. In the sequence LL→TT→TL, the stress level also decreases, while the elongation (strain to fracture) increases. Figure 4 shows the dependence of stress-strain curve on the fiber orientation for the M material. As expected, the stress level decreases with increasing the angles ϕ and θ which are the angle between the fiber orientation and the longitudinal direction of the specimen, as mentioned in the reported paper [10] about the strength of fiber reinforced materials. From above results it is concluded that the tensile properties strongly depend on the inter-fiber spacing and the fiber orientation.

3-2. S-N curve

Figurs 5 and 6 are typical examples of the S-N curves at room temperature. Figure 5 shows the S-N curves of specimens F, M, L and C, in which the bending stress axis was parallel to the fiber orientation (LL) and perpendicular (TT and TL). In either case, the fatigue strength (fatigue

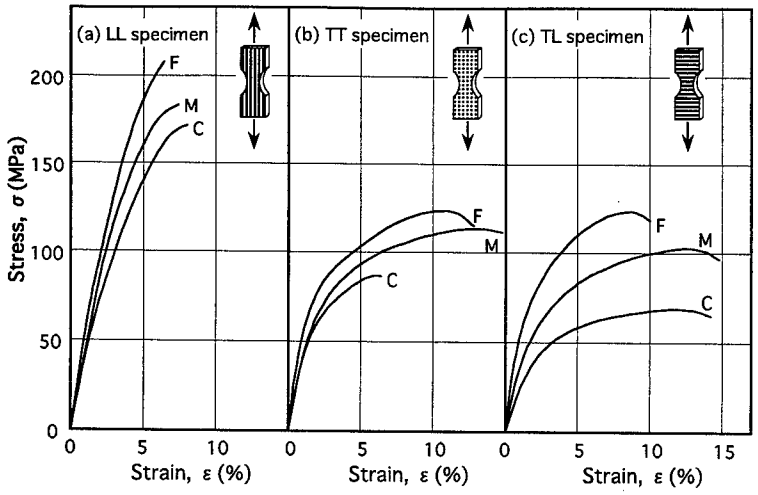

Fig. 3 Stress-strain curves of materials F, M and C : (a) LL specimen, (b) TT specimen and (c) TL specimen.

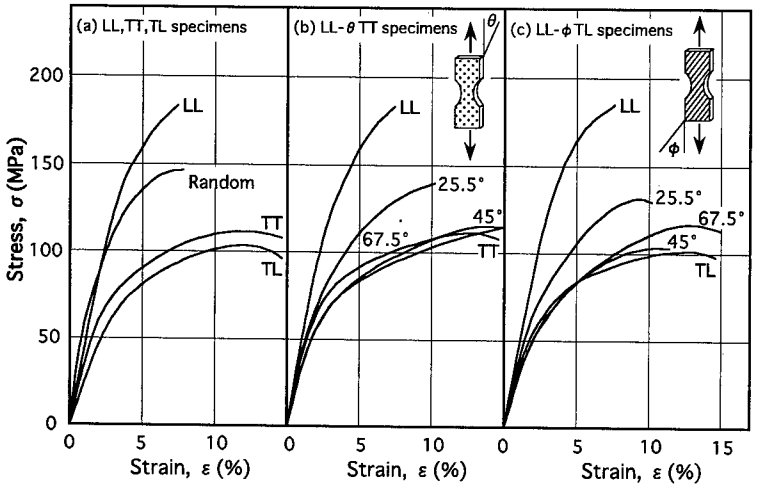

Fig. 4 Stress-strain curves of the M materials: (a) LL, TT and TL specimen, (b) LL-θ TT specimens and (c) LL-ϕ TL specimens.

failure life under cyclic bending) decreases with increasing the inter-fiber spacing λ in the sequence F $\rightarrow$M$\rightarrow$L$\rightarrow$C. In the sequence LL$\rightarrow$TT$\rightarrow$TL, the fatigue failure life decreases and the slope of the S-N curve decreases in the sequence F$\rightarrow$M$\rightarrow$L$\rightarrow$C. Figure 6 shows the dependence of S-N curve on the fiber orientation of the M specimen. As expected, the fatigue strength decreases with increasing the angles ϕ and θ . The fatigue strength of the specimens TT and TL is about one half that of the specimen LL. From above results it is concluded that the fatigue strength strongly depend on the inter-fiber spacing and the fiber orientation.

Figure 7 shows variation of the fatigue ratio (a ratio of the fatigue strength to the ultimate tensile strength) with inter-fiber spacing λ for LL,TT and TL specimens of the M material. The values of fatigue ratio range from 0.4 to 0.5 for fracture life of 1 x 10^5 cycles. That is to say, the fatigue ratio does not depend on the inter-fiber spacing and the fiber orientation. The fatigue strength appears to vary linearly with the tensile strength.

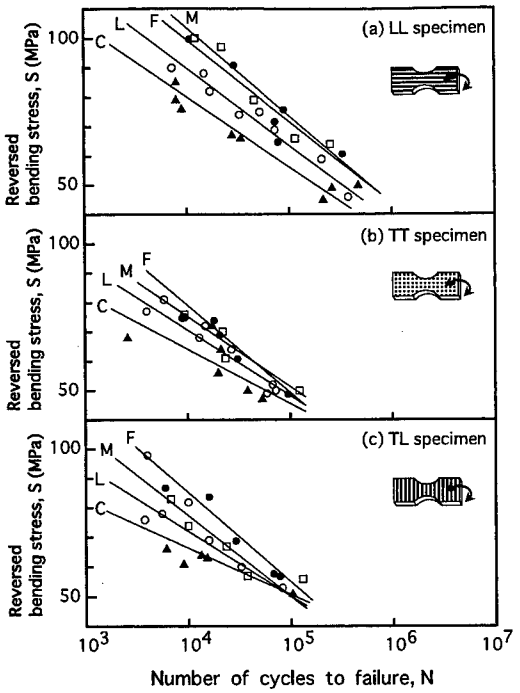

Fig. 5 S-N curves of materials F,M,L and C : (a) LL specimen, (b) TT specimen and (c) TL specimen.

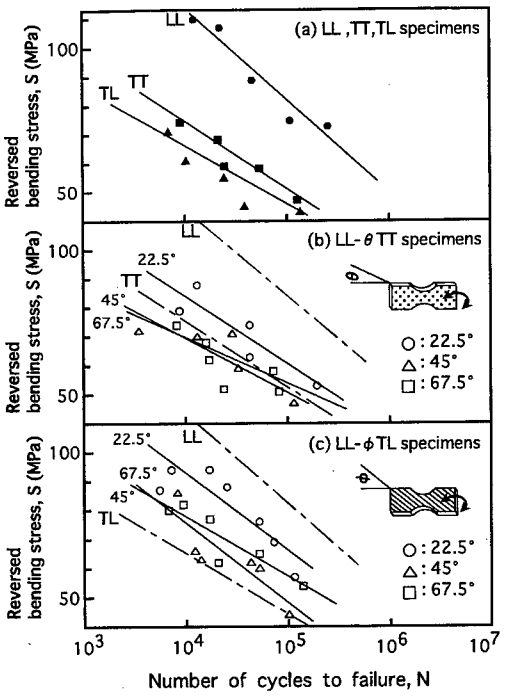

Fig. 6 S-N curves of the M materials: (a) LL,TT and TL specimens, (b) LL-θ TT specimens and (c) LL-ϕ TL specimens.

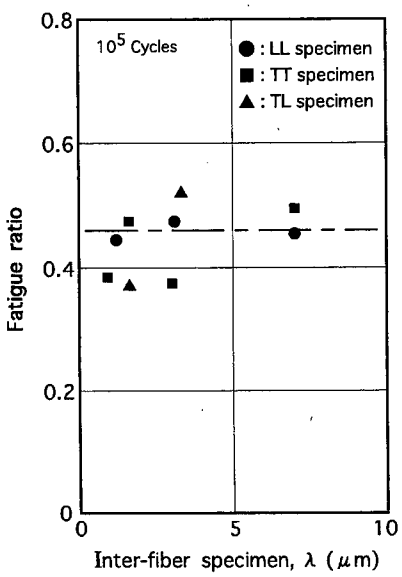

Fig. 7 Variation of fatigue ratio with inter-fiber spacing for LL,TT and TL specimens of M material.

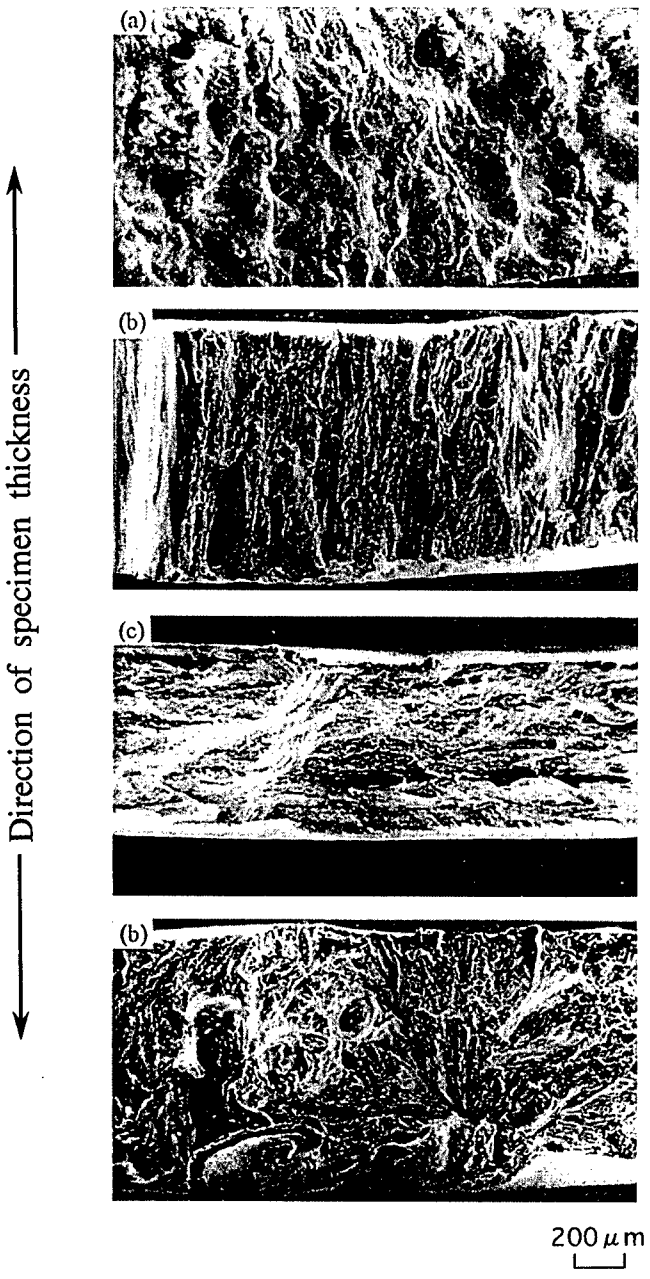

Fig. 8 SEM micrographs showing tensile fracture surface of the M material: (a) LL specimen, (b) TT specimen, (c) TL specimen and (d) Random specimen.

3-3. Fracture surface

Figure 8 shows typical examples of the tensile fracture SEM microstructures of the M material. Figure 8 (a) shows the structure of the LL specimen, having a very fine dimple pattern This microstructure depended on the inter-fiber spacing and the dimple size decreased with

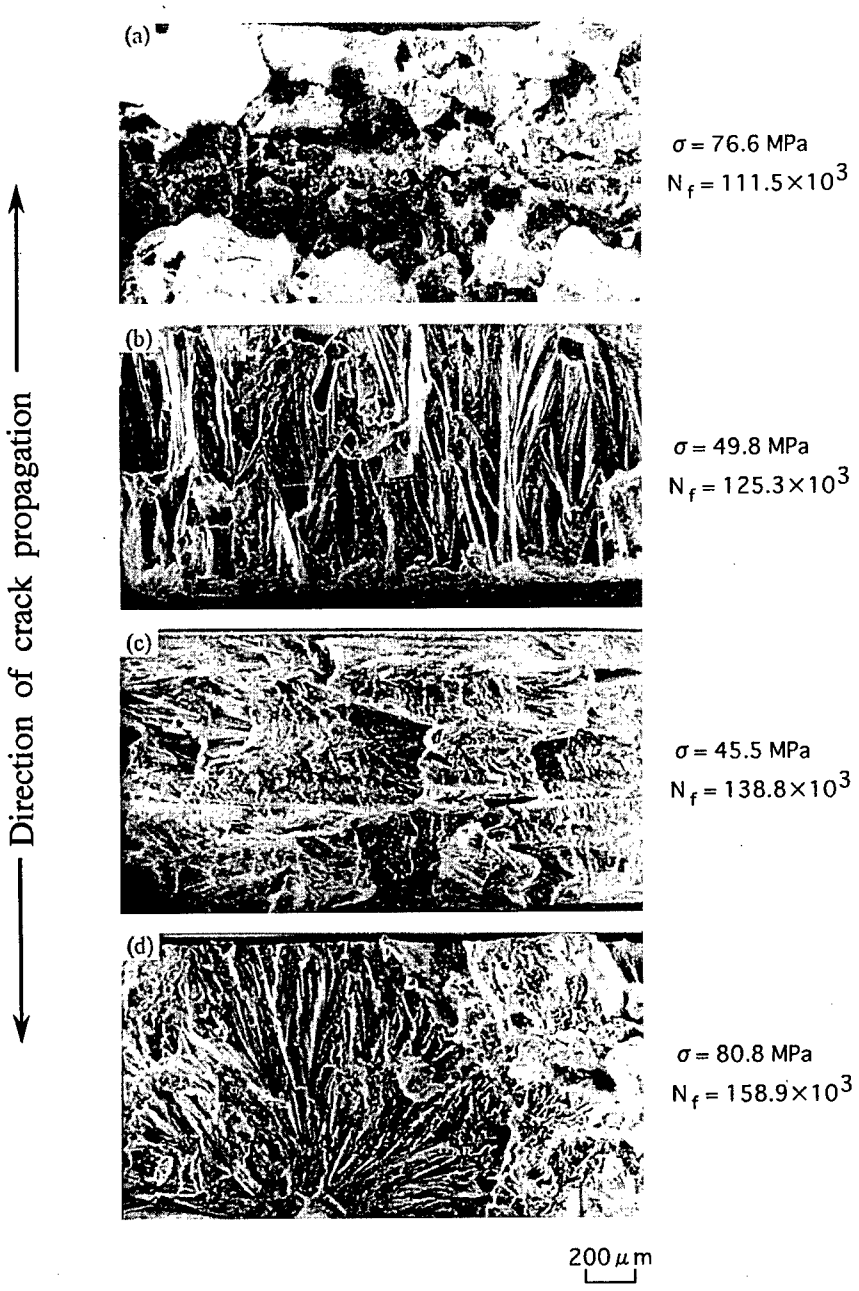

Fig. 9 SEM micrographs showing fatigue fracture surface of the M specimen: (a) LL specimen, (b) TT specimen, (c) TL specimen and (d) Random specimen.

decreasing the inter-fiber spacing. Therefore, fracture region of the fibers seems to be the origin of the dimple structure. Figure 8 (b) shows the structure of the TT specimen, having very fine dimples and large dimples elongated to the thickness direction (fiber orientation) of the specimen. From

these elongated dimples, the interface between the fiber and matrix metal seems to be providing points of cracks and their propagation. However, the dimple size did not depend on the inter-fiber spacing. Figure 8 (c) shows the structure of the TL specimen. Very fine dimples reveal to align in perpendicular to the specimen thickness direction, which is longitudinal direction of the fibers. In this case, the interface between the fiber and matrix metal also seems to be providing points of cracks. Figure 8 (d) shows the structure of the specimen with random fiber orientation, having very complex dimple pattern because of the random orientation of fibers.

Figure 9 shows typical examples of the fatigue fracture SEM microstructures of the M material. Figure 9 (a) shows the structure of the LL specimen, having very deep dimple pattern. An exfoliation at the interface between the fiber and matrix metal attributes to the crack propagation and the deep dimple seems to be formed due to the shear fracture at the interface. In this case, the microstructure did not depend on the inter-spacing of the fiber, though the striation structure was observed in all the cases. Figure 9 (c) shows the structure of the TL specimen, having a relatively planer surface. The fatigue fracture structure of LL, TT, TL and Random specimens are quite similar to their tensile fracture one, respectively. That is, the fatigue fracture structure also depend on the fiber orientation as shown in the structure of tensile fracture.

4. Conclusions

Tensile and fatigue experiments of eutectic Al-Al_3Ni fiber-reinforced composites in conjuction with observations of microstructural details lead to the following conclusions.

(1) The tensile properties strongly depend on the inter-fiber spacing and the fiber orientation. The tensile strength decreases with increasing inter-fiber spacing and angle between applied stress and fiber orientations.

(2) The fatigue properties also strongly depend on the inter-fiber spacing and the fiber orientation. The fatigue life increases with decreasing inter-fiber spacing and angle between applied stress and fiber orientations.

(3) The fatigue ratio (the ratio of fatigue stress to tensile stress) does not so much depend on the inter-fiber spacing and the fiber orientation.

(4) Therefore, the fatigue life is suggested to be predicted from the tensile properties of the material.

References

[1] D.M.Harmon and C.R.Saff, Metal-Matrix Composites, ASTM STP **1032** (1989), p. 237-50.
[2] R.M.McMeeking and A.G.Evans, Mech. of Mtls, **9** (1990), p. 217-37.
[3] B.M.Cox and D.B.Marshall, Acta Metall. Mater., **39**(4) (1991), p. 579-89.
[4] B.M.Hillberry and W.S.Johnson, NASA Langley Tech Memorandum, (1991), p. 104141.
[5] D.P.Walls and F.Zok, Advanced Metal Matrix Composites for Elevated Temperatures, ASM. (1991), p. 101.
[6] M.McLean, Proc. Conf. in situ Composite IV, Elsever Science Publishing Co. (1982), p. 1-18.
[7] S.Goto, Proc. Int. Conf. on Strength of Metals and Alloys, (1988), p. 983.
[8] J.M.Domergue, S.J.Connell and F.A.Leckie, Structral Materials : Engineering Application Through Scientific Insight, The Institute of Materials, (1996), p.191-212.
[9] S.Goto,S.Hachita,S.Aso,Y.Komatsu and E.Fromm, J. Japan Institute of Light Metals,**47**(7) (1997),p. 363.
[10] A. Kelly, Strong Solids, Oxford University Press, (1966), p.175.

Key Engineering Materials Vols. 171-174 (2000) pp. 169-178
© 2000 Trans Tech Publications, Switzerland

On-Plant Test of TÜV HCM12 and ASME T23 Alloys for Use as Water Wall Materials

A. Karlsson[1], F. Rasmussen[2] and M. Montgomery[3]

[1] Elkraft Power Company Ltd., Lautruphoj 5, DK-2750 Ballerup, Denmark

[2] SK Power, Lautruphoj 5, DK-2750 Ballerup, Denmark

[3] Technical University of Denmark, Building 204, DK-2800 Lyngby, Denmark

Keywords: Thermal Fatigue Crack, Thermal Cycling, USC, Panel Wall, On Plant Test

Abstract

The development of Ultra Super Critical power plants has emphasised the need for stronger alloys for use as water walls. For this purpose TÜV HCM12 and T23 have been tested at 2 Danish power plants. TÜV HCM12 and T23 have been tested for their weldability, for thermal fatigue properties and for their oxidation properties under steam conditions 435-520° C, 26-27 MPa. The test included application of different weld methods and testing of the mechanical properties of the weld seams. The weld parameters giving the optimal properties were chosen to manufacture two pieces of water wall (1 times 1.5 meter). The two test pieces each had two separate steam loops, which could be feed by steam having different steam parameters. Each test piece was installed in a coal fired power plant (steam parameters 540° C, 25 MPa) and exposed to alternating steam conditions. In each test piece one loop was subject to constant steam parameters (434° C, 27 MPa) and another loop was subject to alternating steam parameters (switching between 485° C, 25.9 MPa and 434° C, 27 MPa). Steam parameters were switched app. 2000 times. By this exposure each test piece was subject to alternating thermal stress' corresponding to the stress' which appear in the water walls of an USC plant. The exposure was performed in the stress region close to the yield strength limit and cracks appeared in one of the materials. The tests have revealed that TÜV HCM12 is difficult to weld but develops no thermal fatigue crack whereas T23 is easy to weld but develops thermal fatigue cracks.

Introduction

The project was initiated by the fact that very little information is available about thermal fatigue of new steels for ultra super critical power plants. If new steels shall be employed in future advanced power plants knowledge about thermal fatigue properties of these steels shall be present when the plants are being designed. In ultra super critical power plants the materials will be stressed beyond the limits used for today's power plants. Therefore more detailed knowledge most be provided for the new steels to ensure that they have adequate materials properties.

The ageing process due to thermal fatigue is related to the rate of change of temperature, to the temperature gradient in a particular material and to the dimensions of this material. If the rate of change in temperature is small (few degrees per minute) and the temperature gradient is below 10° C/millimetre and the dimension (e.g. wall thickness) is less than 10 millimetres then the effect of thermal fatigue is negligible. However for power plants with peek load operation or in ultra super critical power plants it is likely that the materials will be stressed beyond these limits.

Background

Boiler walls in Danish power plants have up to 1995 been produced without heat treatment of the weldings. The reason is that it is too costly and by choosing the right alloys the heat treatment can be omitted. However the right alloys must have special properties. One requirement is that the residual stress of the welding must be below a certain level. According to a standard design rule this requirement is met if the hardness of the welding is below 350 HV10. Below 350 HV10 the residual stress is so low that cracks induced by thermal fatigue are unlikely to occur.

Concerning manufacturing of boilers it is common practice to produce boiler walls without heat treatment of the weldings in the boiler walls. This practice is based on the simple fact that boiler walls are big constructions, which are impossible to heat treat in one piece. Leaving out the heat treatment of the weldings requires special properties of the steels used. Part of the properties must be that the residual stresses of the weldings must be below a certain level and the German TRD standard design rule says that the hardness of the weldings must be below 350 HV. Below this level the residual stress is so low that it is very unlikely that cracks will be induced by thermal fatigue.

For Danish power stations commissioned till now the traditional material for boiler walls have been 1Cr½Mo or in Germany notation 13CrMo44. It has the sufficient strength for construction of boiler walls up to steam data of 475° C and 30 MPa. However, alternative steels have to be considered if the steam data of the boiler walls are raised to 500° C and 35 MPa. It is primarily a question of creep strength. In this investigation two potential alloys T23 and TÜV HCM12 were tested. Chemical compositions and specifications are given in Table 1a and 1b. 10CrMo910 was used as fin material.

Table 1a: Chemical compositions of test tubes (mass %).

	TÜV HCM12 analysis	T23 analysis
C	0.10	0.06
Si	0.18	0.21
Mn	0.51	0.52
Cr	12.2	2.24
Mo	1.00	0.12
W	0.99	1.54
V	0.24	0.26
Nb	0.05	0.042

Table 1b: Specification of chemical compositions (mass %)

	ASME T23	TÜV HCM12	10CrMo910
C	0.04-0.1	≤ 0.14	0.07 - 0.15
Si	≤ 0.5	≤ 0.5	0.20 - 0.50
Mn	0.10 – 0.60	0.30 – 0.70	0.40 - 0.70
P	≤ 0.030	≤ 0.030	≤ 0.0305
S	≤ 0.010	≤ 0.030	≤ 0.0305
Cr	1.90 – 2.60	11.00 – 13.00	2.0 – 2.5
Mo	0.05 – 0.30	0.80 – 1.20	0.90 - 1.10
W	1.45 – 1.75	0.80 – 1.20	-
V	0.20 - 0.30	0.20- 0.30	-
Nb	0.02 – 0.08	≤ 0.20	-
Others	B 0.0005 – 0.006 N ≤ 0.030 sol. Al ≤ 0.030		Ni ≤ 0.30

Purpose

The purpose of the project

- was to test the thermal fatigue properties of the materials TÜV HCM12 and T23 (as tube materials) welded to 10CrMo910 (as fin material) with weld seams TÜV HCM12/TÜV HCM12 (tube/tube), T23/T23 (tube/tube), TÜV HCM12/10CrMo910 (tube/fin) and T23/10CrMo910 (tube/fin).
- was to constructed two panels of the tube/fin combinations TÜV HCM12/10CrMo910 and T23/10CrMo910 without heat treating the weld seams and test the panels with approximately 2000 temperature cycles. The thermal cycling should be done be switching the inlet steam temperature between the two levels 435° C to 485° C.

From the start of the project it was a primary wish to carry out the test in a power plant where the steam conditions were as close to the desired test conditions as possible. The possibility of performing a test was present at the power plant Amagerværket (live steam 540° C, 25 MPa) in Copenhagen, Denmark. Given these conditions it was estimated that if the test panel wall could endure the thermal fatigue test set up in the purpose then this particular combination of materials had qualified for use in panel walls in power stations with ultra super critical steam data.

Manufacturing of the panel

A test panel was manufactured without heat treatment of the tube/fin weld seams. It was the aim to test if the hardness of the weld seams could be kept below 350 HV. The tubes had the dimensions 31.8mm x 5.6 mm. and the 10CrMo910 fins, 6mm x 28mm. The tube to fin welds were performed as two welds (one from each side of the panel) with a gap in between. The gap had a length of app. 2 mm. The panel was made up of two separate steam circuits a and b which could be fed by steam of two different temperatures (434° C and 485° C) or by steam of one temperature (434° C). The differing temperatures were obtained by switching on and off steam of 485° C supplied through a time controlled on/off motorised valve and a stop/check valve (a one way valve) on string a. The test panel which was manufactured by ABB Kesselanlagen, is shown in Figure 1 and the steam circuit in the panel is shown in Figure 2.

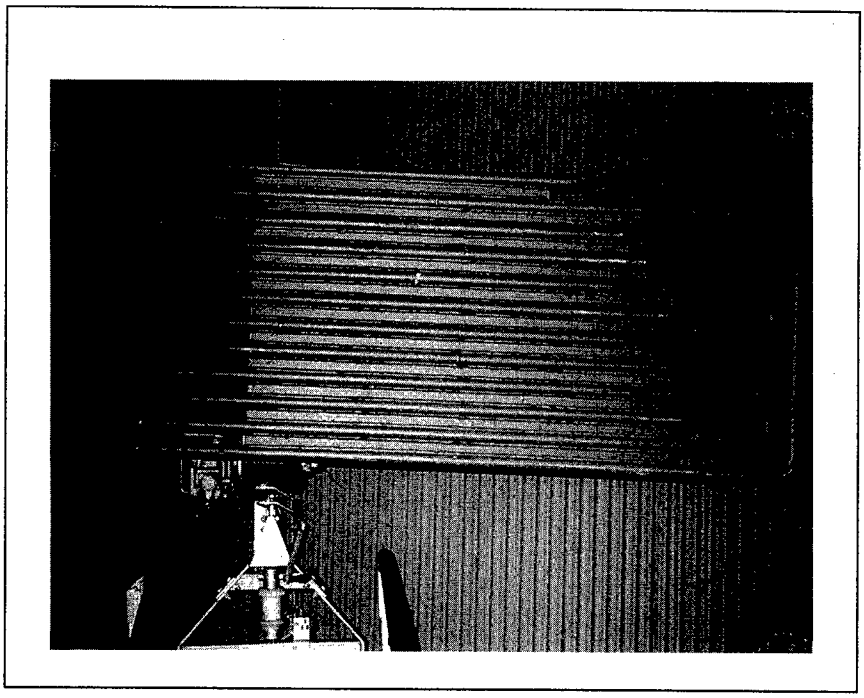

Figure 1: Photograph of the first panel wall test piece after installation.

When the motorised valve, AA002, is closed both string a and b are supplied with 434° C, 25.9 MPa steam. Since the inlet steam temperatures of string a and b are the same the thermal gradient over the fins will be small except for the fin between a1 and a6. The temperature gradient over this fin is 5-10° C.

In case the motorised valve, AA002, is open then the stop/check valve AA004 will be closed and string a is fed with 434° C, 26.9 MPa steam and string b is fed with 485° C, 25.9 MPa steam. In this case a thermal gradient of app. 50° C will arise between substring a1 and substring b1. The thermal gradient between substring a1 and substring a6 will remain 5-10° C. These are the two steam thermal situations between which the panel has been toggled every second hour. The welding materials were in case of TÜV HCM12/10CrMo910: Fluxofil 37 (E80 T5-G) and in the case T23/10CrMo910: Cromocord 2STC (Specification E9018–B3) or Fluxofil 37 STC (specification E 89 T5-G).

Finite element modelling of thermal fatigue stresses

A finite element modelling was done of the test panel design. The modelling was done based on a number of assumptions. The first assumption was that the test panel was subjected by a heat flux equal to 100-120 KW/m^2. The second assumption was that the temperature increase of the steam was between 5-10° C for each of the circuits a and b or 1-2° C for each of the substrings a1-a6 and b1-b6. The third assumption was that the uptake of heat over the length of the strings was assumed to be linear. The fourth assumption was that the tubes and the fins were made of the same material (without joints and without the gab between tube and fin). Data for 4 temperature dependent parameters have been used: Thermal expansion, modulus of elasticity, thermal conductivity, and heat capacity. The two thermal situations described above have been modelled and the model has

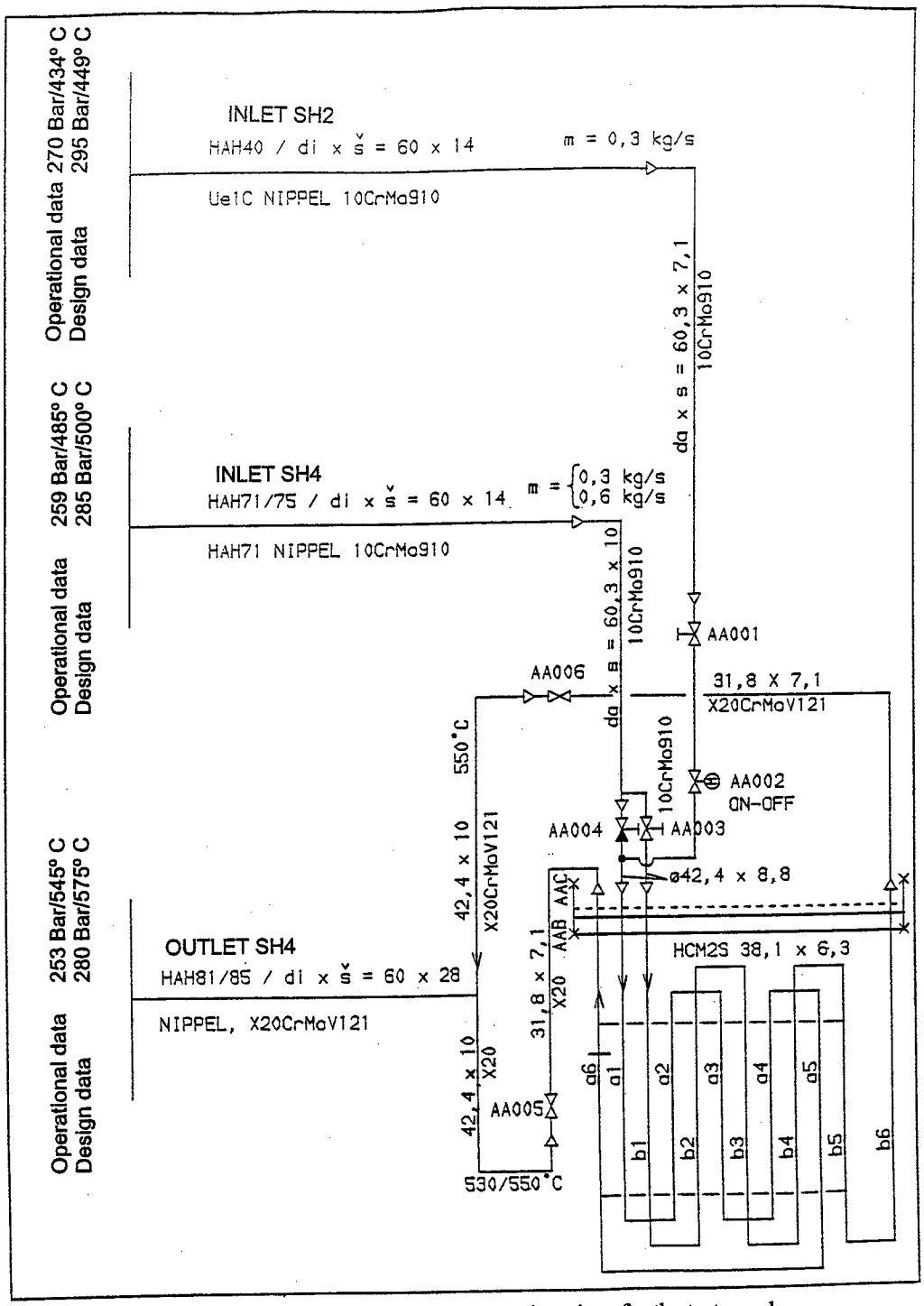

Figure 2: Schematic diagram of steam connection pipes for the test panel.

been recalculated for 2000 thermal cycles. For each cycle the fatigue load was estimated and summed. Final fatigue load estimation was done according the norm CEN TC 54. The summed up fatigue load accounted for only 15% of the fatigue exhaust life thus indicating that no cracks will appear after 2000 cycles.

Installation of panel - description of external steam circuit

Steam with two different sets of steam data (434° C, 26,9 MPa) and (485° C, 25:9 MPa) were bleed from two different headers. The steam was piped through control valves to the test panel, which was installed inside the boiler. The amount of steam fed into the panel was 0.3-0.6 kg/sec.
Each test panel was subjected to approximately 2000 (TÜV HCM12: 2030 cycles and T23 2165 cycles) thermal cycles lasting 2 hours at the lower temperature and 2 hours at the higher temperature. The steam temperature of a6 cycles between 455 and 505°C, which gives a fluctuating thermal gradient over the fin between a6 and a1 of 20° C. To estimate an approximate metal temperature, 40°C can be added to the relevant steam temperatures. The two thermal situations are summarised in Table 2: Temperature a1= temperature b1 and temperature a1< temperature b1.

	a6	a1	b1	b6
a) 2 hours	500-510° C	485°C	485°C	485-520° C
b) 2 hours	434-444°C	434°C	485°C	485-520° C

Table 2: Conditions of steam thermal cycling.

The measured steam temperature of b6 which has not experienced thermal cycling is 520°C . The measured steam temperature from the outlet of a6 was between 434°C and 485 °C.

Test and dismanteling

The TÜV HCM12 panel was tested from August 1994 to July 1995 and the T23 panel was tested from August 1995 to July 1997. The TÜV HCM12 panel piece was exposed to 2030 thermal cycles while the T23 panel piece had 2165 thermal cycles.

Examinations

After dismantling of each of the test panels, sections were cut out of the panels for examination. The highest load was assumed to be at the rim of the panels. The strings examined were a6, a1, b1 and b6 with respect to cracks and to hardness of the tube to fin weldings. Figure 3 and 4 shows a sketch of the part of the panels, which was cut out and examined. The examinations showed a significant difference between the panels.

Hardness measurements

The hardness of the tube to fin welding was measured **before exposure** using a Vickers hardness testing equipment with a 10 kg load. The data for the TÜV HCM12 panel shows that the hardness of the weld seam after welding and without heat treatment reaches a level of 396 to 419 HV10. This level is somewhat higher than the maximum allowed level of 350 HV10 recommended for panel wall weldings.

The hardness of the tube to fin weldseams was measured likewise **after exposure**. All hardness' of the TÜV HCM12 material except one were below the recommended level of 350 HV10 and by comparing with the hardness' before exposure it is obvious that some kind of heat treatment has happened during the thermal fatigue test. The hardness of the tube to fin weld of the T23 was

measured after exposure. The hardness reached a top level of 320-345 HV10 in the heat affected zones.

Microstructure

In the T23 panel it was found that there were cracks in some of the tube to fin welds ½ cm from the beginning of the fins so an area 10 cm from the beginning of the fins was also investigated.

No thermal fatigue cracks were seen in the TÜV HCM12 panel neither at the top of the panel nor 10 cm from the top. Cracks were seen on the T23 panel in string a1 and b1 and b6. Strings b1 and b6 had not been subjected to thermal cycling. Moreover the string where thermal cycling had been greatest a6, showed no cracks. As mentioned all cracks originated from the gap between the weld and the tube and into the HAZ between the tube and weld material. No cracks could be detected on the surface panel wall piece.

The microstructure of the welds is seen in Figure 5 showing the tubeweld zone of T23 panel wall test piece. It shows the tube b1, the fin (below, left) and the gap. The gap seems to act as a notch initiating the crack. The crack is intergranular and contains corrosion products. Cracks were also seen in b6 which had not been thermally cycled. Microsections were also investigated 10 cm from the beginning of the fin weld and at same positions in the TÜV HCM12 panel.

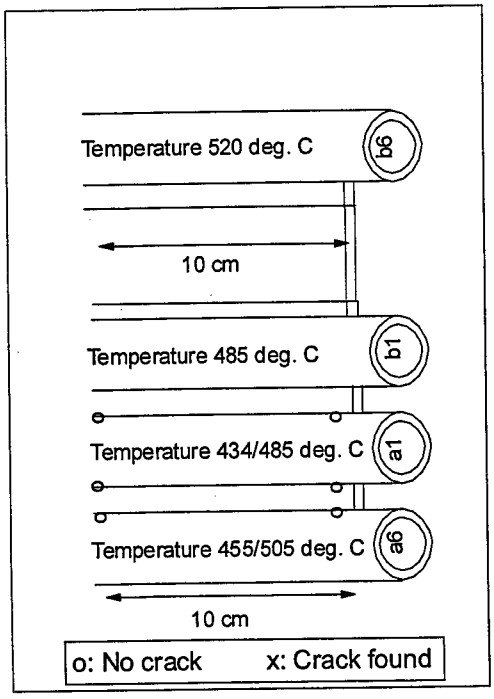

Figure 3. Examined section of TÜV HCM12 panel wall piece.

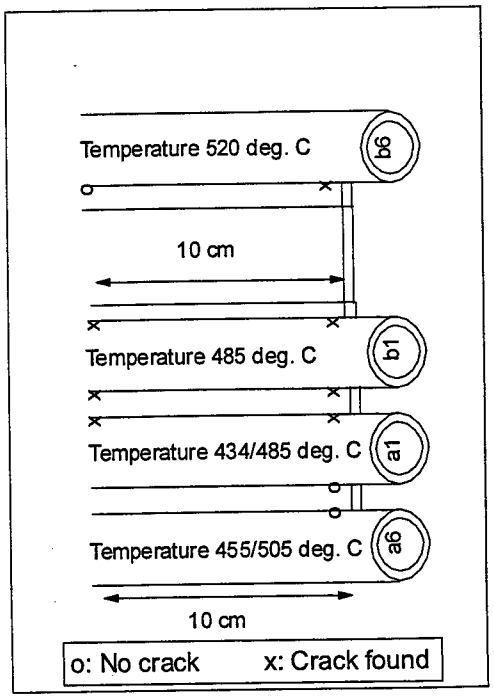

Figure 4. Examined section of T23 panel wall piece.

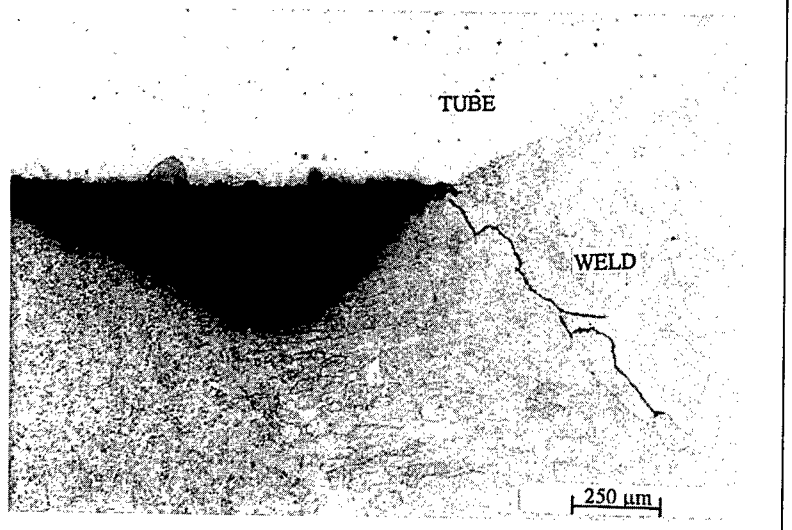

Figure 5: Crack into the weld material between the tube b1 and the fin.

Discussion

The first part of the project was to manufacture two test panel wall pieces: One of TÜV HCM12 tubes and 10CrMo910 fins and one of T23 tubes and 10CrMo910 fins. The second part of the project was to expose each of the panel wall pieces to approximately 2000 thermal cycles. The hardness of the tube to fin weldings turned out to be around 400-419 HV10 in the TÜV HCM12-10CrMo910 case, which highly exceeds the German TRD standard design rule of 350 HV10. For the T23-10CrMo910 tube to fin weld the hardness was lower than 350. The highest hardness was 340 HV10. This hardness was found in the heat affected zone between the tube and the weld. The hardness' are thus within the German TRD design rule.

Cracks were not seen in the TÜV HCM12-10CrMo910 welds but in the T23-10CrMo910 welds. The cracks were seen originating from the weld gab between the tube and the fin and progressed either along the HAZ between the weld and the 10CrMo910 material or along the filler material.

From the investigation of the T23 it is seen that the cracks do not progress into the T23 material. Cracks start from the gab and progress along the HAZ. This is not the case for TÜV HCM12 where no cracks appeared

As the thermal fatigue can only account for 15% of the fatigue exhaust life the observed cracks in the T23/10CrMo910 welds must have other reasons. It is believed that the cracks appear because the gab between the tube and the fin act as a notch. If the gab can be avoided it is believed that no cracks will appear after 2000 thermal cycles. This has been confirmed by later research.

Conclusion

The purposes of the project have been fulfilled except for the hardness of the TÜV HCM12 weldings, which was measured to 419 HV10 after manufacture before load. This far exceeds the permissible level, 350 HV10. This level is based on experience with the German 1Cr½Mo steel 13CrMo44. If a hardness of 419 HV10 can be tolerated in the manufacturing process then the

project has provided a significant contribution to the knowledge needed for the future use of TÜV HCM12 in the manufacture of panel walls. If not then more research is need to workout the allowed level of hardness of TÜV HCM12 welds.

In the case of T23 cracks were seen. However the reason for the crack formation in the tube to weld HAZ region could not be clearly identified. It can be due to the welding procedure or due to the gab between the tube and the fin.

Key Engineering Materials Vols. 171-174 (2000) pp. 179-188
© 2000 Trans Tech Publications, Switzerland

Evaluation of Long-Term Creep Rupture Strength of Tungsten-Strengthened Advanced 9-12%Cr Steels

F. Masuyama and N. Komai

Mitsubishi Heavy Industries, Ltd. Nagasaki Research and Development Center,
5-717-1, Fukahori-machi, Nagasaki 851-0392, Japan

Keywords: Creep Rupture Strength, 9%Cr Steel, 12%Cr Steel, Life Prediction, Creep Strain, Rupture Strain

Abstract

Evaluation and reliability assessment of the long-term creep rupture strength of recently developed tungsten strengthened advanced steels such as P92 and P122 are very important in terms of the use of these steels in actual power boilers. This paper reports the results of standard creep rupture tests reaching a maximum of 50,000 hours, which have been carried out for various material conditions including as-manufactured, fully-processed, over-aged and induction-bent pipes and forgings. Creep strain tests up to 2,000 hours have also been conducted for as-manufactured materials in order to study creep strain behavior and creep life. Based on the data obtained, 10^5h creep rupture strength was predicted, and the relationship was investigated between a) the long-term creep rupture strength extrapolated from short-term creep test results using the parametric and iso-stress methods, and b) actually measured long-term strength. Creep life prediction from the creep strain and rupture time relationship was also carried out, and the accuracy of life prediction is demonstrated.

Introduction

Advanced steam cycles in power boilers achieved by increasing the steam temperature and pressure are accompanied by increased thermal efficiency and consequent lower fuel costs. Demand for these benefits has provided the incentive for the development of high strength 9-12%Cr martensitic steels, aimed at improved creep rupture strength[1]. In the early 1990s tungsten strengthened steels with a general composition of 9-12%Cr, 0.5%Mo and 1-2%W, NF616 (designated as T92/P92)[2] and HCM12A (T122/P122)[3] were developed to deliver improved mechanical properties at elevated temperatures for use in advanced steam cycle power boilers.

In order for these steels to be used in actual plants, allowable tensile stress must be determined on the basis of creep rupture data as well as creep data from tests of a duration beyond 10,000 hours, extrapolating 100,000 hour strength. As these steels have been newly developed, long-term creep rupture and creep data are limited, while the evaluation and reliability of the long-term creep strength of these steels have become important for power plant applications. In the work reported here, standard creep rupture tests reaching a maximum of 50,000 hours have been carried out for various material conditions of P92 and P122 pipes, including as-manufactured, fully-processed (subjected to post weld heat treatment), over-aged, and induction-bent material and forgings. Additionally, as-manufactured pipe material has been subjected to creep strain tests to study the correlation between creep deformation behavior and rupture time.

Using the creep rupture data obtained, the relationship was investigated between a) long-term creep rupture strength extrapolated from short-term creep rupture data using the parametric and direct

methods, and b) actual long-term creep rupture data.

Test Materials and Creep Rupture / Creep Tests

Test materials employed consisted of pipe and forgings of P92 and P122 manufactured on a commercial basis. The chemical compositions of these test materials are listed in Table 1. The dimensions of the tested P92 and P122 pipes were $^{\phi}$350mm in outside diameter and ^{t}50mm in wall thickness; they were manufactured respectively by Nippon Steel and Sumitomo Metals in Japan. The ingots for the pipes were melted in an electric furnace and refined by vacuum ladle and ESR processes, and then forged to square blooms of 315mm in width and height for P92 followed by pipe rolling, whereas P122 was directly rolled into pipes. The heat treatment applied to P92 consisted of normalizing at 1065℃×2h AC and tempering at 770℃×2h AC; for P122, normalizing at 1050℃× 1h AC and tempering at 770℃×7h AC.

The pipes were subjected to the processes described below in order to simulate the material conditions induced by PWHT, long-term service exposure, and induction bending. (Note that the differences in the microstructures were too small to be determined.) The heating condition for PWHT was 740℃×4h AC (referred to as fully-processed), and additional heating at 720℃×200h AC was applied to fully-processed materials (over-aged). 720℃×200h is assumed to correspond to 600℃× 230,000h of service exposure in terms of the Larson-Miller parametric technique. The full size of the pipes was bent by induction heating at an OD surface temperature of 1050℃ and forming at a radius of 4.5D (D is the diameter of pipe), followed by heat treatment under the same conditions for as-manufactured materials.

The forgings were melted in an electric furnace and refined by the AOD process for P92, and using the VOD process for P122. The ingots were forged into Tee junctions with forging ratios of 3.6S for P92 and 4.2S for P122. P92 forgings having dimensions of $^{\phi}$378mm in outside diameter and ^{t}80mm in wall thickness were normalized at 1040℃×3hOQ and tempered at 780℃×5hAC, and P122 forgings with dimensions of $^{\phi}$403mm in outside diameter and ^{t}125mm in wall thickness were heat treated at 1050℃×3hAC and 770℃×8hAC.

Creep rupture specimens were taken from the walls of pipes and forgings, and subjected to testing at 550℃ to 700℃ at intervals of 50℃, with stress ranging from 60MPa to 275MPa. The creep rupture specimens from the pipes included the material conditions of as-manufactured, fully-processed, over-aged, and induction-bent, while creep strain specimens were taken only from as-manufactured pipes.

Analyses of creep rupture data were performed using the Larson-Miller technique (representative of parametric extrapolation methods), while iso-stress creep rupture data were used as a direct extrapolation method to predict temperature at a given stress and at 100,000 hours to rupture. The creep strain data were used in the creep model and to evaluate the accuracy of the estimation of long-term creep rupture life.

Table 1 Chemical compositions of steels tested (mass%)

Steel	Form*	C	Si	Mn	P	S	Ni	Cu	Cr	Mo	W	V	Nb	N	Al	B
P92	P	0.11	0.04	0.46	0.008	0.001	0.06	–	8.96	0.47	1.84	0.20	0.069	0.051	0.007	0.0010
	F	0.10	0.23	0.50	0.008	0.001	0.21	–	9.09	0.43	1.83	0.20	0.064	0.046	0.003	0.0012
P122	P	0.12	0.05	0.64	0.016	0.001	0.32	0.86	10.61	0.44	1.87	0.21	0.050	0.064	0.022	0.0022
	F	0.13	0.27	0.61	0.014	0.001	0.34	0.49	10.15	0.36	1.94	0.20	0.055	0.057	0.017	0.0019

*P : Pipe, F: Forgings

Extrapolation of 10^5h Creep Rupture Strength

Creep rupture data are important in determining design stresses from the point of view of rupture time and the number of data points, but these data are usually provided by steel manufacturers for as-manufactured materials. Figs. 1 and 2 show isothermal time to rupture at temperatures of 550℃ to 700℃ respectively at 50℃ intervals, as well as Larson-Miller plots of rupture data for various material conditions of P92 and P122 steels. The figures include data reaching to about 50,000 hours, and the comparative average line[4][5] for as-manufactured materials was obtained from a sufficient number of data points and test durations beyond 10,000 hours. In the present study, as-manufactured materials were used only for creep strain testing which rupture times were up to 2,000 hours. Among the various material conditions, over-aged material showed slightly lower strength in the medium stress region of 130MPa to 200MPa. Basically, the figures indicate little difference in creep rupture strengths between P92 and P122.

The iso-stress rupture data were obtained for fully-processed, over-aged and induction-bent P92 and P122 steels at temperatures of 600℃ to 660℃, and at 125MPa and 140MPa. The temperature at

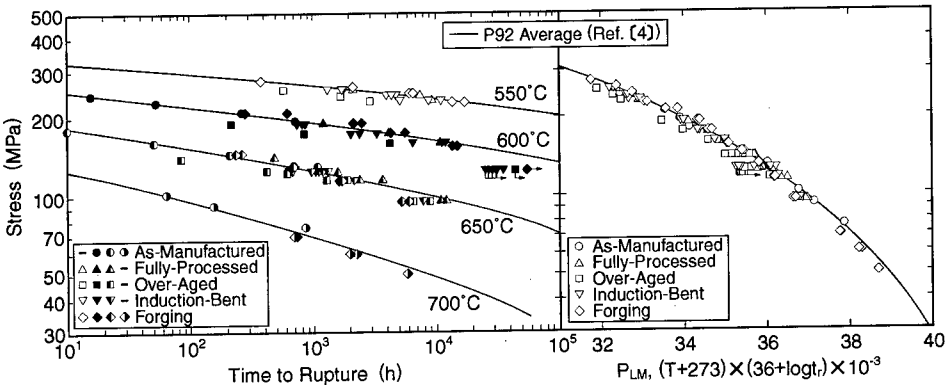

Fig. 1 Isothermal time to rupture diagram and Larson-Miller plot of creep ruptured data for P92 steel

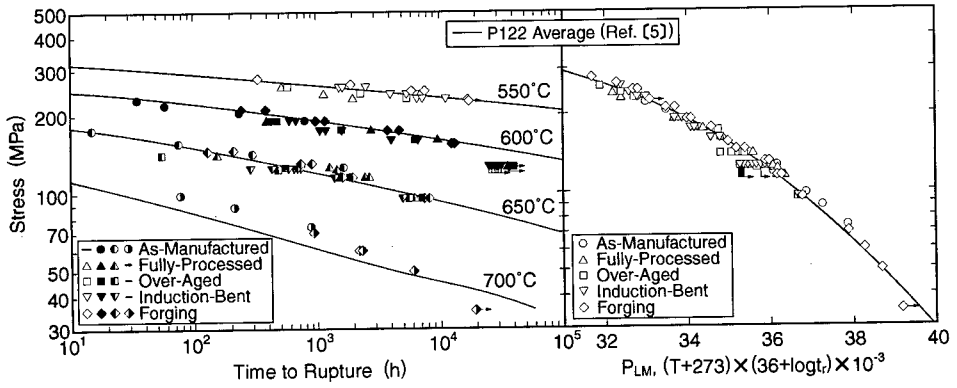

Fig. 2 Isothermal time to rupture diagram and Larson-Miller plot of creep ruptured data for P122 steel

100,000 hours and at a given stress was directly predicted using Fig. 3, while the Larson-Miller diagrams in Figs. 1 and 2 were used for predictions of 10^5h creep rupture strength at temperatures from 550℃ to 675℃ at 25℃ intervals. In the Larson-Miller technique, extrapolation was made using data sets of up to 2,000 hours, over 2,000 hours, and all data in order to compare the effect of data sources on the estimation of 10^5h creep rupture strength.

Fig. 4 gives 10^5h creep rupture strength obtained by means of the Larson-Miller technique[6] and iso-stress technique in terms of temperature. Table 2 lists extrapolated strength from the Larson-Miller technique and temperature from the iso-stress technique. It is obvious that temperatures above and below approximately 600℃ give larger differences in extrapolated strength due to material conditions. The difference in strength between the maximum and minimum values at 550℃ and 675℃ was approximately 25MPa, in contrast differences of less than 10MPa that were seen for both steels at temperatures of 600℃ to 625℃. This indicates that the 10^5h creep rupture strengths were extrapolated within a ±5% scatter band from the average strength for the material conditions, prediction methods, and data sets investigated within the above-stated temperature range, which is typically used in the design of boiler components. Even the data up to 2,000 hours provided accurate

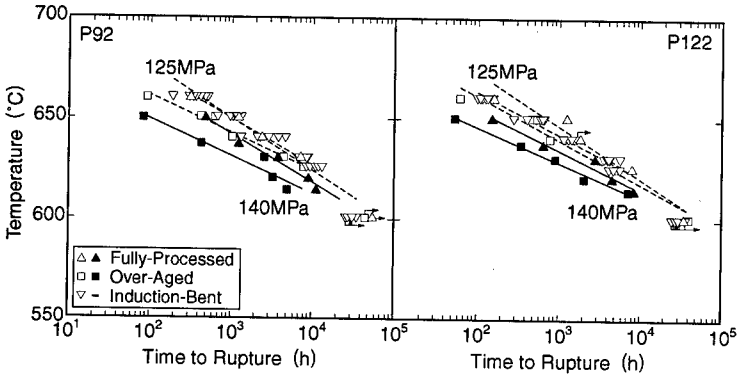

Fig. 3 Iso-stress plot of creep ruptured data for P92 and P122 steels

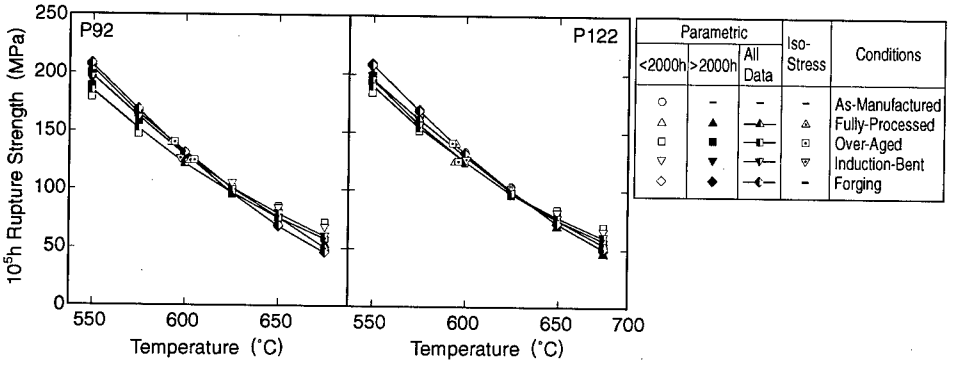

Fig. 4 Comparison of extrapolated 10^5h creep rupture strength by Larson-Miller technique and iso-stress technique

Table 2 Extrapolation results of 10^5h creep rupture strength by Larson-Miller technique and 10^5h temperatures by iso-stress technique

Steel	Material Conditions	Larson-Miller Technique (MPa) Temperature (℃)						Iso-Stress Technique (℃) Stress (MPa)	
		data used	550	575	600	625	650	675	125	140
P92	As-Manufactured	<2000h	200	165	132	102	77	57	–	–
		>2000h	–	–	–	–	–	–		
		all	–	–	–	–	–	–		
	Fully-Processed	<2000h	204	168	134	103	76	54	603	593
		>2000h	206	169	133	101	74	52		
		all	206	169	133	101	74	52		
	Over-Aged	<2000h	180	148	123	102	85	72	605	594
		>2000h	191	158	126	96	71	50		
		all	186	153	123	98	76	58		
	Induction-Bent	<2000h	195	160	130	105	84	67	597	–
		>2000h	198	163	130	101	77	57		
		all	198	162	130	103	80	61		
	Forging	<2000h	209	170	132	98	69	47	–	–
		>2000h	207	167	130	96	69	47		
		all	208	169	131	97	69	47		
P122	As-Manufactured	<2000h	197	164	131	102	76	54	–	–
		>2000h	–	–	–	–	–	–		
		all	–	–	–	–	–	–		
	Fully-Processed	<2000h	194	161	130	102	79	59	595	595
		>2000h	195	162	128	96	68	46		
		all	193	160	128	99	74	53		
	Over-Aged	<2000h	183	150	122	100	81	66	596	594
		>2000h	192	155	122	93	69	50		
		all	187	152	122	95	74	56		
	Induction-Bent	<2000h	190	153	123	98	79	63	601	–
		>2000h	196	157	123	94	70	51		
		all	192	154	123	96	75	58		
	Forging	<2000h	205	166	131	99	73	51	–	–
		>2000h	207	167	129	97	70	48		
		all	206	170	130	97	70	49		

extrapolated values in comparison with long-term actual rupture strength. The prediction results yielded by the iso-stress technique (a typical direct method) were within the range established by the Larson-Miller parametric method, although the temperature-rupture time diagram is marked by stress dependence.

Creep Strain Behavior and Creep Life

The tensile creep strain behaviors of as-manufactured P92 and P122 are given in Figs. 5 and 6 at temperatures of 600℃, 650℃ and 700℃. All specimens subjected to creep testing described here were ruptured at times up to 2,000 hours. The creep curves plotted as creep rate against time consist of primary and tertiary parts, showing the minimum creep rate at stress-dependent times. The lower stresses prolong the time of primary creep to induce a large reduction in the minimum creep rate. There are few differences in the creep curves for P92 and P122 steels, or in the temperature and stress dependencies, although the creep curves at 650℃ differ slightly from those at 600℃ and 700℃, as the reduction of minimum creep rate at 650℃ is rather greater than at other temperatures. According to a study[7] on precipitation evolution in these steels, there exists a peak nose at 650℃ in the C curve for the Laves phase of the time-temperature-precipitation diagram. The greater reduction of minimum creep rate is therefore presumed to be caused by Laves phase precipitation hardening. Fig. 7 gives the relationship between minimum creep rate, $\dot{\varepsilon}_{min}$, and average creep rate, $\dot{\varepsilon}_{ave}$ (the divisor of the rupture strain), ε_r, and time to rupture, t_r. As seen from the figure there is a linear relationship between $\dot{\varepsilon}_{min}$ and $\dot{\varepsilon}_{ave}$, which is expressed by the following equation.

$$\dot{\varepsilon}_{ave} = C\,\dot{\varepsilon}_{min}^{\,r} \qquad (1)$$

where C and r are constants, and C is 5.3, and r is 0.98 for P92 and P122 steels.

It is well known that the minimum creep rate is inversely proportional to rupture time from the Larson-Miller assumption, as well as from further refinements by Monkman and Grant as the Monkman-Grant equation[8]

$$\dot{\varepsilon}_{min} = K_{MG} t_r^{-m} \tag{2}$$

Fig. 8 plots log minimum creep rate and log average creep rate as a function of rupture time for P92 and P122 steels, thereby giving a straight line for $\dot{\varepsilon}_{min}$- t_r up to 2,000 hours from which K_{MG} and m can be determined. K_{MG} and m are 0.9×10^{-1} and 1.1 respectively for P92, and 1.6×10^{-1} and 1.1 for P122. From the figure, the Monkman-Grant relationship can be observed for $\dot{\varepsilon}_{ave}$- t_r over 10,000 hours with a relatively wider scatter band at times beyond 1,000 hours as follows,

$$\dot{\varepsilon}_{ave} = K'_{MG} t_r^{-m'} \tag{3}$$

K'_{MG} and m' are 5.3×10^{-1} and 1.1 respectively for P92, and 9.9×10^{-1} and 1.1 for P122. m and m' are equal to 1.1 in both steels; these are usually in the range 0.8–1.2 for conventional steels.

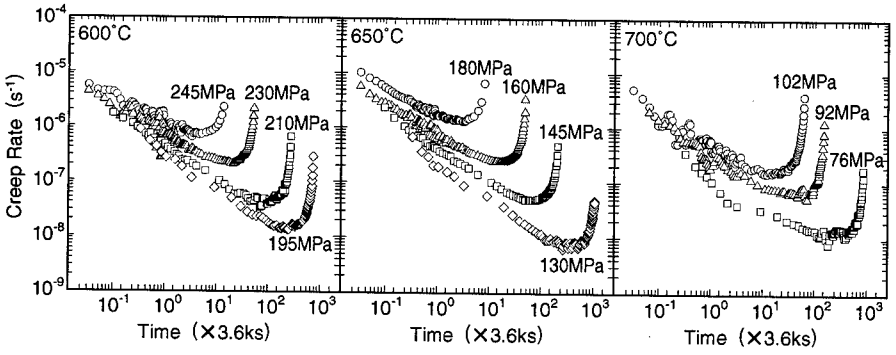

Fig. 5 Relationship between creep strain rate and time for P92 steel

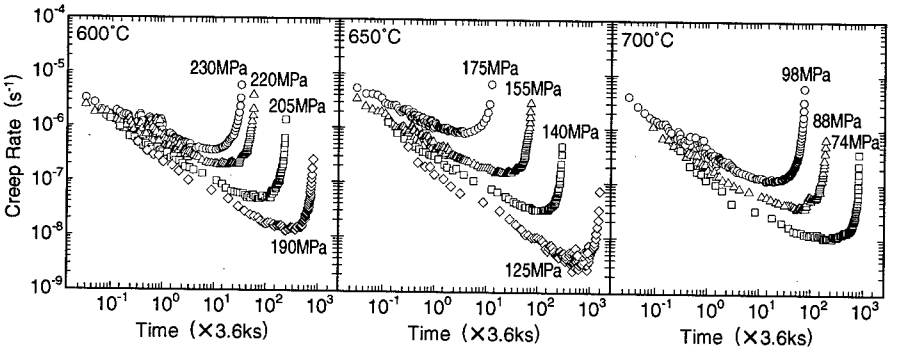

Fig. 6 Relationship between creep strain rate and time for P122 steel

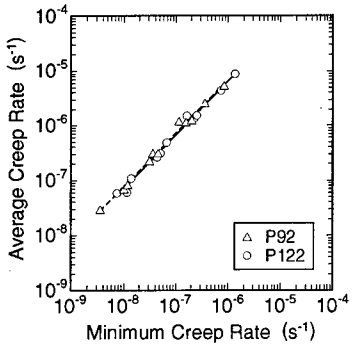

Fig. 7 Relationship between minimum creep rate and average creep rate

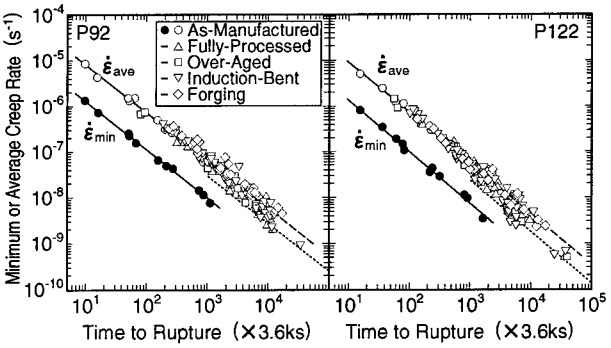

Fig. 8 Monkman-Grant plot of minimum creep rate and average creep rate against time to rupture

The deviation line of the minimum creep rate from the average line toward lower values (which gives an optimistic extrapolation of rupture time using the average line) appears to be parallelly shifted to the minimum line with approximately half values of K'_{MG} as shown in Fig. 8. If we assume the same deviation of the minimum creep rate-time to rupture relationship, half the value of K_{MG} is expected for the Monkman-Grant equation, resulting in the estimation of half the rupture time, or half the minimum creep rate. Creep life at given stress is easily extrapolated using of the Monkman-Grant equation, together with the Norton equation[9]

$$\dot{\varepsilon}_{min} = A\sigma^n \tag{4}$$

where A and n are the constant and Norton stress exponent respectively. The minimum creep rate to given stress can be read from the Norton equation plot, and the creep rupture life for this minimum creep rate can be determined from the Monkman-Grant plot. The stress drop due to the reduction of K_{MG} can also be estimated from the Norton equation plot. Fig. 9 shows the Norton plots for P92 and P122 steels. The reduction of stress at 600℃ and 650℃ is estimated to be approximately 4% provided the minimum creep rate is reduced to half the value of that at a given stress, but an 8% reduction in stress is expected at 700℃. In the case of advanced steels such as P92 and P122, the Norton stress exponent is much higher than for conventional steels as shown in Fig. 9, and changes in stress with the minimum creep rate are rather small as noted above. That is, a 50% reduction of the minimum creep rate corresponds to an approximate 4% reduction of strength at 600℃ and 650℃ for P92 and P122 steels. This 4% maximum reduction of strength agrees well with the scatter band of ± 5% from the average of 10^5h creep rupture strength extrapolated using parametric and direct methods.

The average creep rate deviated with a wider scatter band at the time to rupture beyond 1,000 hours is shown in Fig. 8, with 1,000 hours corresponding to an average creep rate of $5\times10^{-8}s^{-1}$. Fig. 10 shows the relationship between the average creep rate and rupture strain. The rupture strain appears to be constant, with an average value of approximately 30% at an average creep rate above $5 \times 10^{-8}s^{-1}$, and comes to show creep rate dependence. This figure suggests the insight that, at longer creep rupture times beyond 1,000 hours, creep rate affects not only the rupture time but also the rupture strain, while the creep rate up to 1,000 hours does not affect rupture strain.

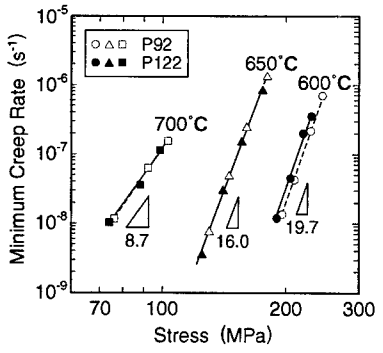

Fig. 9 Stress dependence of minimum creep rate

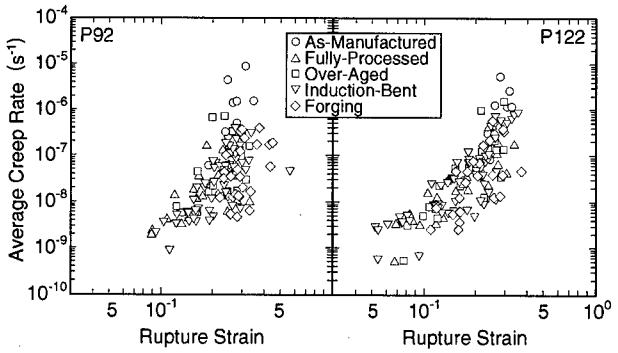

Fig. 10 Relationship between average creep rate and rupture strain

Conclusions

A comparative investigation was carried out on the 10^5h creep rupture strength extrapolated using different data sets including data up to 2,000h, data over 2,000h, and all data for various material conditions of pipes and forgings of P92 and P122 steels. The creep strain behaviors of both steels were also investigated in order to consider the reliability of extrapolated long-term creep strength. Accordingly, the following results have been obtained.

(1) The predicted 10^5h creep rupture strengths of as-manufactured, fully-processed, over-aged, and induction-bent pipes and forgings were within a $\pm 5\%$ scatter band of average strength at temperatures from 600℃ to 625℃, which is the typical design temperature range for these steels.

(2) The data set ruptured up to 2,000 hours accurately predicted the long-term creep rupture strength by means of the parametric method, corresponding to the actual data.

(3) There was found to exist a linear relationship between the minimum creep rate and average creep rate, and the Monkman-Grant equation was found to be applicable not only for the minimum creep rate, but also for the average creep rate for rupture time reaching up to 100,000 hours. Due to the scatter of data beyond 1,000 hours, the minimum line of the Monkman-Grant equation was parallelly shifted from the average line by half the value of the Monkman-Grant constant; this yielded a 50% reduction in creep rupture life, corresponding to a 4% reduction of creep rupture strength from average values for all data points obtained from various material conditions of pipes and forgings.

References

[1] F. Masuyama: J. Lecomte-Becker et al. (eds.), Mateials for Advanced Power Engineering 1998, Part III, Forschungszentrum Jülich, Germany, (1998), 1807

[2] H. Masumoto, H. Naoi, T. Takahashi, S. Araki, T. Ogawa and T. Fujita: 2nd Int. Conf. Improved Coal-Fired Power Plants, Palo Alto, CA., Nov. 2-4, (1988)

[3] A. Iseda, Y. Sawaragi, S. Kato and F. Masuyama: 5th Int. Conf. Creep of Materials, Lake Buena Vista, FL., May 18-21, (1992)

[4] Y. Hasegawa, K. Shibata, H. Dohnomae and Y. Yazaki: Int. Conf. Ecology and Economy in Metal Forming and Cutting, Archen, Germany, June 24-27, (1995)

[5] Y. Sawaragi, A. Iseda, K. Ogawa, F. Masuyama and T. Yokoyama: E. Metcalfe(ed.), New Steels for Advanced Plant Up to 620℃, PicA Publishing, London, UK, (1995), 45
[6] F. R. Larson and J. Miller: Trans. ASME, 74 (1952), 765
[7] J. Hald and S. Straub: J. Lecomte-Beckers et al.(eds.), Materials for Advanced Power Engineering 1998, Part I, Forshungszentrum Jülich, Germany, (1998), 155
[8] F. C. Monkman and N. J. Grant: ASTM Proceedings, 56 (1956), 593
[9] F. H. Norton: The Creep of Steel at High Temperature, McGraw-Hill, New York, (1929)

Fujimitsu Masuyama, e-mail: masuyama@ngsrdc.mhi.co.jp, fax: +81-95-834-2055

Key Engineering Materials Vols. 171-174 (2000) pp. 189-196
© 2000 Trans Tech Publications, Switzerland

Research of Welding Effect on Creep Damage of High Temperature Furnace Tubes

J.-M. Gong, S.-T. Tu and X. Ling

High Temperature Technology Division, Department of Mechanical Engineering, Nanjing University of Chemical Technology, 210009, China

Keywords: Welding, Life Assessment, Creep, Damage Mechanics, Ductility, Multiaxiality, High Temperature, Furnace Tube

Abstract In the present paper, difficulties in material data sampling and lifetime estimation are discussed. A local deformation measuring technique is proposed to determine the creep properties of the weld. A damage mechanics approach is introduced to study the damage development and creep rupture of HK-40 furnace tubes due to the presence of a weld. It has been illustrated that damage is prone to the weld in the later period of service life. Metallographical research also indicates that the weld may have a higher damage rank. It is thus concluded that the weldments may become the weak link in HK-40 furnace tubes.

1. Introduction

Among the failure cases of high temperature components, premature failures of weldments have taken a large percentage that indicates the detrimental effect of welding on structural integrity. The accurate prediction of the high temperature behavior of welded components is thus becoming increasingly important in order to realize an optimized design and maintenance of a plant life.

Reformer furnace tubes are generally fabricated from centrifugally cast creep resistant austenitic steel HK Grade (0.4C, 25Cr, 20Ni) or HP Grade (0.4C, 25Cr, 35Ni). The whole furnace tubes have about 14,000mm length, which is fabricated by welding together four to five short tubes. In long-term service at high temperature, the damage, such as creep cavities and microcracks, occurs inevitably in the tubes, much research has been done during the past two decades[1-4]. However, the works mostly concentrates on damage assessment of the parent metal of the tubes, damage characteristics of the welds in the whole tubes don't be fully understood. The recent researches show that the weld has the highest damage level in the later period of service life, and is one of weakest location in furnace tubes[4].

In the present paper, difficulties in material data sampling and lifetime estimation are discussed. A local deformation measuring technique is proposed to determine the creep properties of the weld. A damage mechanics approach is introduced to study the damage development and creep rupture of HK-40 furnace tubes due to the presence of a weld.

2. Measuring Technique for Local Creep Deformation

For conventional uniaxial tensile creep testing the evaluation of creep deformation and fracture resistance is only an average information within a gauge length equal to five times the diameter of specimens. The gauge length is generally 50mm or 100mm, and 25mm at the least[5]. Assessment of creep behavior of different region of a weldment is required to provide an assessment of overall high temperature performance for weldments. However, it is not possible to measure creep

deformation of the regions in term of the current uniaxial tensile creep test due to narrow regions such as weld metal and HAZ region (less than 10 mm). Thus factors affecting the creep and fracture of welments are not well identified.

A new method based on quartz optical fiber and digital image analysis is proposed to acquire actual creep behavior of a narrow region in a weldment. In order to realize long-term and high precision measurement of local creep deformation, a measuring system is set up (shown in Fig.1). The selected quartz optical fibers have good heat resistance and good light conductivity at high temperature. So they are stuck on a side surface of a test specimen and employed as light marks by irradiating one end of optical fiber with laser and giving out light from the other end at high temperature. Raying ends of quartz optical fibers form dot-shaped marks, and then received by a long distant microscope and imaged on CCD's target. The marks are extracted by a point-dependent image segment technique[6]. On the basis of the extracted marks, the center of a mark can be explicitly obtained by the region-center method, which allows the measuring precision to reach sub-pixel level, displacements of the marks are accordingly acquired.

Under the condition of no loading in high temperature, two measured digital images have fine distinction for images of the light spots sampling at two different times, the distance between light spots has elementary error for the images, the error is called as the zero shift of the system. The zero shift does not exceed 0.05 pixel. Most of zero shifts are generally in the range of 0.02-0.04 pixel. According to the resolution of the used CCD (512×512) and distance between the two marks (about 300 pixel in an image) , measuring sensitivity of the system is about 100$\mu\varepsilon$[6].

The sensitivity basically satisfies the requirement of long-term creep deformation measurement. The use of higher CCD resolution will certainly improve the measuring accuracy.

3. Creep Testing of Weld Metal in HK 40 Reformer Tubes

3.1 Specimen and testing method

A HK-40 reformer tube serviced for 80,000h is selected for creep test. Plate type cross-weld specimens are produced from upper welds of the tube, which has little detectable damage. In order to measuring creep deformation of weld metal, a waisted cross-weld specimen with 3mm thickness is designed. Six quartz optical fibers are stuck onto a side surface in waisted weld region (see Fig. 2).

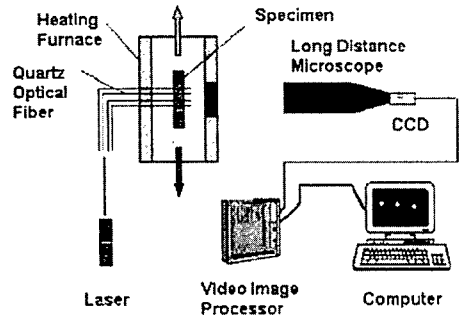

Fig.1 Sketch of measuring system of local creep deformation

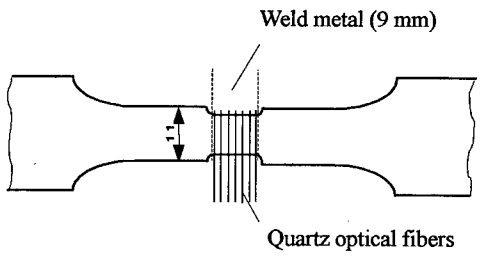

Fig. 2 HK-40 waisted cross-weld specimen and stuck fibers

Because the maximal effective wall temperature is 850°C in the service period of the selected furnace tube, uniaxial creep tests are performed in air at the temperature of 850°C with stresses in the rang of 40-50 MPa , and the temperature difference is maintained within ±3°C. The creep deformation of the weld metal is obtained by measuring local deformation between the optical fiber marks.

3.2 Creep behavior of HK-40 weld metal

Creep strains versus time at three stresses of 40MPa, 45MPa and 50MPa are shown in Fig.3. The steady creep strain and creep rupture time versus stress are shown in Fig.4 and Fig.5 respectively. It should be noted that the rupture occurs in the notch root rather than the middle of the specimen.

Creep behavior of HK-40 parent metal is also needed in order to analyze creep behavior of welds of HK-40 furnace tubes. The creep data of HK 40 parent metal generated in our previous research [7] are used. As the data was obtained at 871°C, they should be transferred to the temperature of 850°C . Based on B. D. Roach's research[8], N. Miyazaki proposed that material constants, B and A in Norton law ($\dot{\varepsilon} = B\sigma^n$) and creep rupture equation ($A\sigma^v t_r = 1$) have the following relation for HK 40 material[9],

$$B = 10^{0.022537\,T - 36.3551} \tag{1}$$

$$A = 10^{0.0135T - 22.7355} \tag{2}$$

Thereby the steady creep strain rate $\dot{\varepsilon}$ and creep rupture time t_r at 871°C can be transferred to that at 850°C. The steady creep strain and creep rupture time versus stress of HK-40 parent metal at 850°C are also shown in Fig.4 and Fig.5 respectively. Fig.4 shows that the weld metal has a lower creep strain rate at low stress levels (less than 45 MPa). Therefore, the HK-40 weldment belongs to a creep-hard weld as defined by Tu *et al.* in the condition of low stresses[10]. For the creep-hard weld, creep rupture time of the weld metal should be longer than that of the parent metal due to lower steady creep strain rate of weld metal. However, Fig.5 shows that creep rupture time of the weld metal is shorter than that of the parent metal, which may be the result of notch effect in the waisted cross-weld specimens. Because the weld metal has lower creep ductility (0.87%, 40MPa) as compared with the HK-40 parent metal (1.5%, 35MPa), stress concentration built up in notch roots does not easily release away due to creep deformation, which will accelerate creep damage and fracture in the roots of the waisted cross-weld specimens. So creep rupture time obtained from creep tests should be further modified to obtain actual creep rupture time for the weld metal.

Although it has been known that the weld of HK-40 tubes is creep-hard material by measuring creep deformation of the weld metal, it does not necessarily mean that failure will first take place in parent metal at high temperature.

4. Creep Damage Analysis of Welds of HK-40 Furnace Tubes by use of The Creep Damage Mechanics Approach

4.1 Constitutive equations describing inhomogeneity in creep damage

In fact, when certain volume of material is subjected to creep, some parts may be well in the tertiary creep while some still in the secondary creep. By constructing a composite element of damaged and undamaged phases, a modified Kachanov-Rabotnov constitute equation which

accounts for inhomogeneity in creep damage is used[11] and is shown below

$$\frac{d\varepsilon_{ij}^{c}}{dt} = \frac{3}{2} B \sigma_e^{n-1} s_{ij} \left[(1-\rho) + \rho (1-D)^{-n} \right] \tag{3}$$

$$\frac{dD}{dt} = g \frac{A}{\phi + 1} \frac{\left[\alpha \sigma_1 + (1-\alpha)\sigma_e \right]^{\nu}}{(1-D)^{\phi}} \tag{4}$$

$$D_{crit} = 1 - (1-g)^{1/(\phi+1)} \tag{5}$$

where ε^{c}_{ij} and s_{ij} are the creep strain tensor and stress deviator tensor, respectively. σ_1 and σ_e are the maximum principal stress and von Mises stress, α is the material constant relating to the multiaxial rupture criterion which ranges from zero to unity. D and D_{crit} are the damage variable and critical damage where the material creep life is assumed to be fully utilized when D/D_{crit} reaches the value one. B, n, A and ν are material constants relating to the steady creep strain rate and rupture behavior, g, ϕ and ρ the constants accounting for the inhomogeneity of the damage where ρ represents the volumetric ratio of the damaged phase.

4.2 Creep rupture analysis of the waisted cross-weld specimens

Based on the described creep damage mechanics approach, creep ruptures of the waisted cross-weld specimens are evaluated by use of finite element damage simulation and modifying the material constants A and ν of creep rupture behavior of HK-40 weld metal. The finite element model of the waisted cross-weld specimen is shown in Fig.6, the weld width is 9mm, radius of weld

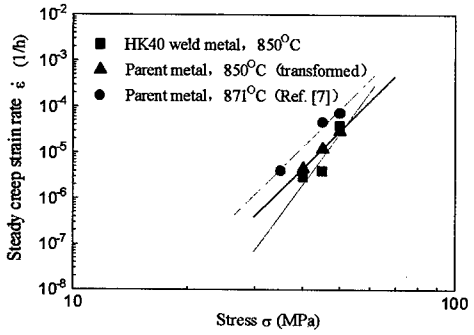

Fig. 3 Creep curves for weld metal of cross-weld specimens

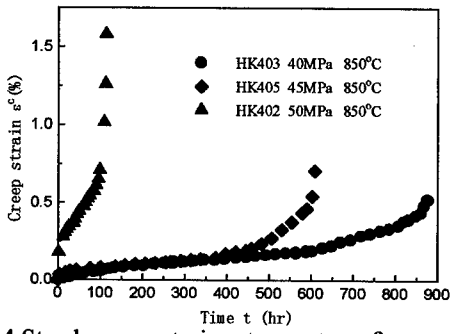

Fig. 4 Steady creep strain rate vs. stress for parent and weld metal of HK-40tubes at 850°C

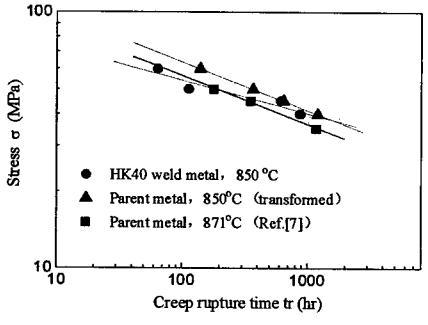

Fig. 5 Creep rupture time vs. Stress for parent and weld metal of HK-40tubes at 850°C

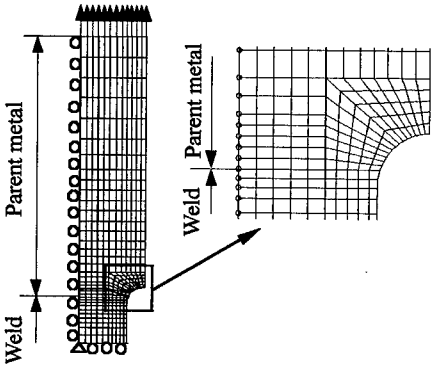

Fig.6 Finite element model for creep rupture analysis of the waisted cross-weld specimens

roots is 1.5 mm. Half of the waisted cross-weld specimen is discretized into 421 rectangular isoparametric elements with 474 nodes. In the present work, a two-materials model (HK-40 parent metal and weld metal) is used, the material constants in the constitutive equations are listed in Table 1. It is common to use the non-linear regression method to obtain material constants g, ϕ and ρ, while a statistical optimization procedure is used which ensures the global minimization of the objective functions[12]. The multiaxial rupture parameter α has been suggested to equals to 0.25 for austenitic stainless steels[13]. For the weld metals, no data for α have been available, it is assumed that they have the same values as the parent metals.

Creep rupture times and locations of the waisted HK-40 cross-weld specimens are determined at 50MPa, 45MPa and 40MPa by use of finite element damage simulation. The material constants A and ν in the creep rupture equation are adjusted time after time in the process of simulating damage and rupture of the waisted HK-40 cross-weld specimens. The results of damage analysis distinctly show that cracking of the waisted cross-weld specimens results from notch roots near fusion lines, and leads to creep rupture. Creep rupture locations predicting by finite element damage simulating is consistent with experimental results (as shown Fig.7). Cracking and rupture take place in the weld side of fusion line at 50MPa (see Fig.7a), and cracking first occurs in the parent metal near fusion line and rupture finally takes place in the weld side of fusion line at 40MPa (see Fig.7b). Creep rupture times predicting by finite element damage analysis are quite close to the results obtained by regressing experimental data (as shown in Fig.8), with maximum relative error 8.11%.

The above cases simulated show that creep rupture life and location of the waisted cross-weld specimens can be accurately predicted on the basis of appropriate creep behavior of HK-40 parent and weld metal. The appropriate creep behaviors of the weld metals can be determined by modifying the material constants relating to creep behaviors for the waisted cross-weld specimens, which is built on the basis of combination of finite element damage analysis and the present method for measuring the long-term local creep deformation.

4.3 Welding effect on creep damage of welds of HK-40 furnace tubes

It was less reported about damage assessment of welds of HK-40 reformer furnace tubes in past decade. Recently, Silveria and May [4] pointed out that the useful life of tubes was controlled by the damage that accumulated in the welds situated in hotter section. Therefore, welding effect on creep damage of welds HK-40 furnace tubes is studied by use of finite element damage simulation based on material constants of parent and weld metal determined from the above analysis.

In the present investigation, the creep damage evaluation in a circumferential V-shaped weldment in HK-40 furnace tubes, see Fig.9. The outer diameter and the wall thickness of the tubes

Table 1 Material constants for parent and weld metals of HK-40 welds (Stress, MPa and time, h)

Constants	Parent metal	Weld metal (tested)	Weld metal (modified)
B	3.247×10^{-19}	8.569×10^{-25}	8.569×10^{-25}
n	8.308	11.475	11.475
A	2.565×10^{-12}	3.234×10^{-16}	5.591×10^{-16}
ν	5.313	7.779	7.507
g	3.100	3.000	3.000
ϕ	0.0984	0.920	0.920
ρ	0.0538	0.043	0.043
D_{crit}	0.635	0.468	0.468
α	0.25	0.25	0.25

are 129mm and 12mm, respectively. The welded tube is subjected to an internal pressures of 4MPa, effective wall temperature is 850°C. The constants in constitutive equations for parent and weld metals are listed in Table 1. The tube with weldment is modeled by four-node axisymmetric element with reduced (2×2) Gaussian integration. In FEM mesh 492 elements with 549 nodes are used.

Fig.10 shows that creep damage develops with time when the tube with the weld is subjected to an internal pressure of 4 MPa, and rupture life resulting from creep damage is 94,680 h Damage localization occurs in welds. The maximum creep damage occurs in internal surface near fusion line at 94,570 h, and separate small cracks occur near fusion line at 94,670 h (see Fig.10a and 10b). After this, the weld metal is heavily damaged as seen Fig.10c, final failure of the HK-40 furnace tube takes place in the weld metal.

Another creep damage evaluation of the HK-40 furnace tube is studied by taking actual operating condition into account. The tube is subjected to an operating pressure of 1.8MPa and has a temperature difference of 28°C between internal and external surfaces. The results of creep damage evaluation are shown in Fig.11. Predicted rupture life is about 120,000 h, the weldment has maximum creep damage and reveals characteristic of localization. Some separate creep cracks occurs in the weld metal at 80,000 h, see Fig.11a. Creep cracks propagate from internal surface to external surface of the wall, which results in rupture of the HK-40 furnace tube, see Fig.11b.

Based on above mentioned creep damage evaluation of the weldment of the HK-40 furnace tube, it can be concluded that the accumulated damage in the weldment is non-uniform and has the

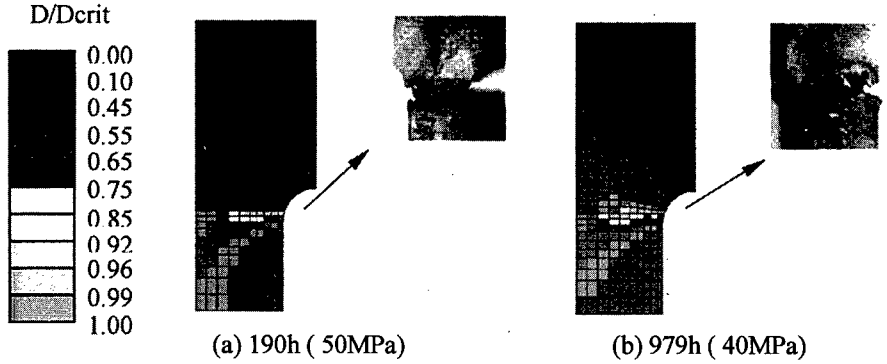

(a) 190h (50MPa) (b) 979h (40MPa)

Fig.7 Creep rupture of a waisted cross-weld specimen

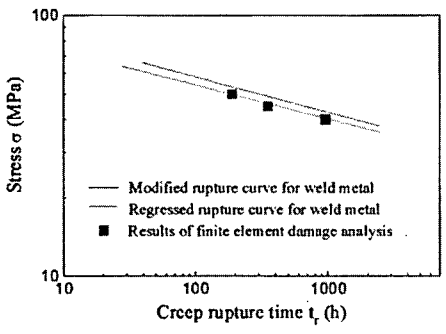

Fig.8 Results of Finite element analysis by modifying creep rupture behavior of weld metal for the waisted cross-weld specimens

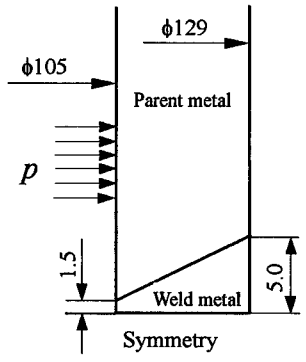

Fig.9 Geometry of HK-40 reformer furnace tube with weldment

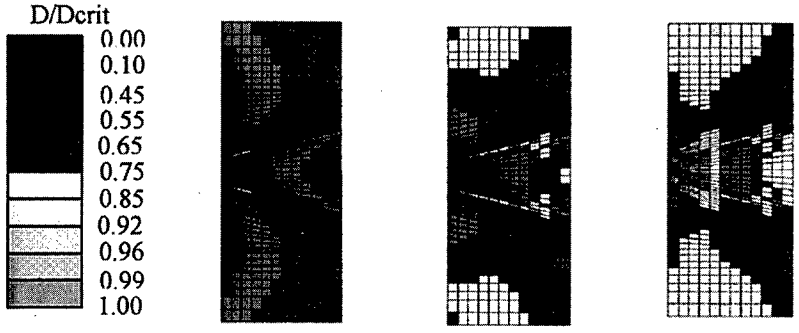

(a) 94,570h (b) 94,677 h (c) 94,679 h

Fig. 10 Creep damage development of the weldment of the HK-40 furnace tube at an internal pressure of 4 MPa

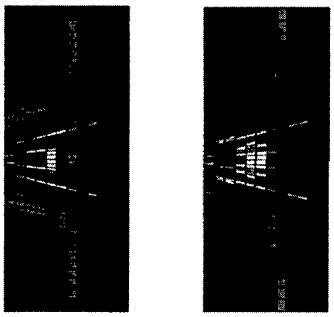

(a) 80,000 h (b) 120,000 h

Fig. 11 Creep damage development of the weldment of the HK-40 furnace tube(an internal pressure of 1.8 MPa and temperature difference of 28°C)

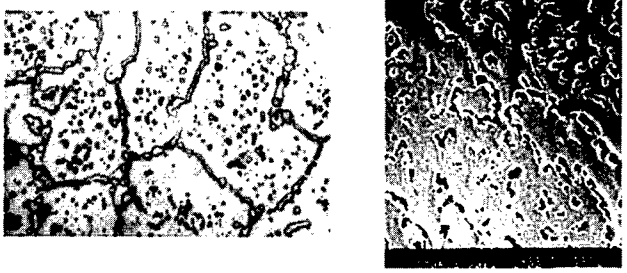

(a) Parent metal (300X) (b) Weld metal (SEM)

Fig.12 Microstructure of the parent metal and the weld metal in the analyzed weldment ((a) carbides morphology, (b) Grain boundary creep voids and microcracks)

characteristic of creep damage localization. It is unanimously indicated that damage in the weld is heavier than that in the parent metal at the end of creep life of the weldment and final failure occurs in the weld, which means that the welds may be the weakest sites in HK-40 furnace tubes.

The states of damage along a HK-40 reformer tube in service for 80,000h are metallographically analyzed [14]. The results show that damage concentrates in the hotter section about 2 m from the bottom end and maximum accumulated damage located in the weld. For the parent metal, primary carbides are linked and blocky while the secondary carbides coalesce obviously and partly dissolved, see Fig.12a. For the weld metal, primary carbides are significantly coarsening and blocky while the secondary carbides coalesce obviously and are partly dissolved. There are strings of cavities and some microcracks from the internal surface to the middle in the weld region, see Fig.12b. The metallographic analysis proves rationality of above-mentioned finite element simulation of welding effect on creep damage of the weldment of HK-40 furnace tubes.

5. Conclusions

(1) A long term and local creep deformation at high temperature can be measured by use of

anew measurement technique, which utilizes particular performance of quartz optical fiber and technique of distant image formation and the CCD digital image analysis. The measuring sensitivity of local deformation at high temperature is below 100με.

(2) Based on the new measuring technique, creep deformation of the weld metal of a HK-40 furnace tube is measured by the waisted cross-weld specimens. Creep behavior of the weld metal is obtained and compared with that of the parent metal.

(3) A modified creep damage mechanics method is introduced to analyze creep rupture of the waisted cross-weld specimens, creep rupture behavior of weld metal is simultaneously modified by taking notch effect into account. On the basis of this, creep rupture time and location of the waisted cross-weld specimens are accurately predicted.

(4) Creep damage of the weldment of the HK-40 furnace tube is evaluated by finite element damage simulation. The simulating results show that the accumulated damage in the weldment is non-uniform and has the characteristic of creep damage localization. At the later service of the weldment, the creep damage in the weld is heavier than that in the parent metal and final failure occurs in the weld. Metallographical research also indicates that the welds may have a higher damage rank and may become the weak link in HK-40 furnace tubes.

Acknowledgements

The authors wish to acknowledge Foo Ying-Tung Education and Research Foundation of China for their financial support of the work.

Reference

[1] K. Kasahara, Paper C235/8, Proc. Int. Conf. Engineering Aspects of Creep, IME 4 (1980), p. 249
[2] D. C. Shipley, Int. J. Press. Ves. And Piping 14 (1983) p.21
[3] Y. Lin, Z. L. Xu and J. R. Huang, J. Chemical Machinery 5 (1986) p.44
[4] I. Le May, T. C. Da Silveria, and C. H. Vianma, Int. Pres. Ves. and Piping 66 (1996) p.233
[5] J. D. Parker and G. C. Stratford, Int. J. Pres. Ves. and Piping 68 (1996) p.135
[6] J. M. Gong, S. T. Tu, J. Xia and X. Ling, Acta Metallurgica Sinica(English Letters) 11 (1998) p. 442
[7] H. G. Yan, Ms. Thesis 1986, Nanjing Institute of Chemical Technology , Nanjing (in China)
[8] D. B. Roach and VanEcho, J. A., ASTM STP 756 (1982) p. 275
[9] N. Miyazaki, Y. Aihara, S. Hagihara and T. Munakata, Computer Aided Innovation of New Materials (eds. M. Doyama, T. Suzuki, J. Kihara and R. Yamamoto), Elsevier Science Publishers, 1991, p. 625
[10] S. T. Tu, P. M. Segle and L. A. Samuelson, PVP Conf. High Temperature Service and Time-Dependent Failure ASME 262 (1993) p.27
[11] Y. Liu, Ph. D. Thesis 1990, Southwesten Jiaotong University, Chengdu (in China)
[12] S. T. Tu and W. B. Yang, Proc. Int. Conf. on Advanced Exper. Mech. , China, 1988 p.142
[13] D. R. Hayhurst, P. R. Dimmer and C. J. Morrison, Phil. Trans. Roy. Soc. Lond. Ser. A 311 (1984) p.103
[14] J. M. Gong, S. T. Tu and K. B. Yoon, Engng. Failure Analysis 6 (1999) p.143

Key Engineering Materials Vols. 171-174 (2000) pp. 197-204
© 2000 Trans Tech Publications, Switzerland

The Reversibility of Creep Strain at Low Stresses and Low Temperatures

G.W. Greenwood and Y. Gencer

Department of Engineering Materials, University of Sheffield, Mappin Street, Sheffield S1 3JD, UK

Keywords: Creep, Diffusion, Dislocations, Anelasticity

Abstract

Small time dependent transient strains may be anticipated under low stresses at temperatures sufficient for dislocations to climb and bow to attain a radius of curvature such that eventually the applied stress is fully resisted. When the stress is too low for dislocation generation or intersection, this mechanism is expected to be fully reversible such that the dislocations straighten when the stress is removed and the transient strain is progressively recovered.

A simplified analysis is presented to evaluate the time dependence of strain and experimental studies are described whereby small stress changes can be made with the consequent strain increments measured down to 10^{-7} without complications through thermal fluctuations. Though additional mechanisms may occur to account for high initial strain rates, the results demonstrate the importance of dislocation density and provide support for the dislocation bowing mechanism with dislocation climb occurring mainly through core diffusion,

Introduction

The phenomenon of anelastic recovery of strain is well known in many polymeric materials when stress is removed. A similar, but much smaller, effect can occur in metals and ceramics at elevated temperatures [1]. With increased precision in manufacturing processes and the need for improved performance of materials in service, however, such small effects require evaluation.

A possible mechanism to account for this behaviour in crystalline materials is in the bowing of dislocations under stress by climb when vacancies are absorbed [2]. This leads to reversibility of small strains for the dislocations will progressively become straight when the stress is removed. An estimate may be made of the amount of strain that is recoverable and the kinetics of the process can be evaluated to assess the strain rate on loading and on stress removal. To examine the validity of this approach an

experimental arrangement is described whereby strain can be measured with high sensitivity and its time dependence recorded.

Theoretical Considerations

The strain produced by dislocation climb by absorption of vacancies is illustrated in the simplified dislocation arrangement in Fig. 1. To avoid geometrical complications, we consider a segment of edge dislocation of length λ able to climb in a plane perpendicular to a tensile stress. Vacancies will diffuse from one dislocation to another depending upon their orientation and, when the temperature is relatively low, their prominent diffusion path will lie along the dislocation cores. To calculate the resultant strain, we consider each dislocation of length λ as the side of a cube. In Fig.1, when a dislocation of Burger's vector b climbs over an area A, the strain γ is given by $(A/\lambda^2)(b/\lambda)$. As climb proceeds, the dislocation gradually decreases its radius of curvature r, until $r < \lambda/2$, when new dislocations will be generated by the Bardeen-Herring mechanism [3]. After this stage the creep strain caused by climb is not reversible and so there is a limit γ_m to the contribution of this mechanism to anelastic strain which is reached when $A = \pi r^2/2 = \pi\lambda^2/8$. Now the shear stress τ_r required to cause bowing to a radius r is given by $\tau_r = Gb/2r = Gb/\lambda$ and so we obtain

$$\gamma_m = \pi\tau_r/8G \qquad (1)$$

It is noted that τ_r/G is the elastic shear strain limit, thus we may expect dislocation bowing to contribute a reversible strain approximately one half of this elastic strain.

The kinetics of the bowing process can also be estimated. Referring again to Fig.1, the absorption of n vacancies results in dislocation climb through an area nb^2 and this creates a shear strain nb^3/λ^3. When the temperature is sufficiently low that dislocation cores provide the dominant route for diffusion, the rate of strain is calculated from the rate of transfer of vacancies across junctions between dislocations of different orientation with respect to the applied stress. There are analogous problems in heat conduction and analytic solutions are available [4], though when significant bowing takes place numerical evaluations are required. It is, however, feasible to provide a meaningful, though less accurate, analysis through a simpler treatment that provides a suitable physical insight into the kinetics of the bowing process at relatively low temperatures and this will next be presented.

Taking the area of the diffusion path along the dislocation cores as b^2 and with the vacancy core diffusion coefficient D_{CV} then the volume b^3n provided by the vacancy flux dn/dt is given from Fick's first law so that

$$b^3\, dn/dt = D_{cv}\, b^2\, dc_v/dx \qquad (2)$$

where dc_v/dx is the vacancy concentration gradient. To estimate this gradient, we note that the vacancies diffuse over a length proportional to λ which can be taken to be $k_1\lambda$. The vacancy concentration depends on the orientation of the dislocations to the applied stress. Where the tensile stress component σ is perpendicular to the plane of

climb, the vacancy concentration at the dislocation is increased above the equilibrium level c_{vo} to a value c_{vd} given by c_{vo} exp ($\sigma b^3/kT$) where k is Boltzmann's constant. Since, in practice, $\sigma b^3 >> kT$, we may write

$$c_{vd} = c_{vo} [1 + (\sigma b^3/kT)] \quad (3)$$

For dislocations donating vacancies, the plus sign becomes a minus sign and hence the limit of vacancy concentration difference is $2c_{vo}(\sigma b^3/kT)$. Since this difference occurs over a distance $k_1\lambda$, the vacancy concentration gradient is

$$dc_v/dx = 2c_{vo}\sigma b^3 / kT\, k_1\lambda \quad (4)$$

Combining equations (2) and (4) and noting that the product $D_{cv}c_{vo} = D_c$ the diffusion coefficient along dislocation cores, then

$$b^3\, dn/dt = 2\, D_c\, \sigma b^5 / kT\, k_1\lambda \quad (5)$$

Recalling that the shear strain $\gamma = nb^3/\lambda^3$ and, if equal tensile and compressive stresses $\pm\sigma$ are applied in perpendicular directions, then $\sigma = \tau$ the shear stress, so that

$$d\gamma/dt = 2\, D_c\, \tau b^5 / k_1\lambda^4\, kT \quad (6)$$

For comparison with experiment, we require some estimate of the constant k_1. In practice, the vacancy concentration gradient is not uniform and alters as bowing takes place. Moreover, such bowing will not produce a uniform curvature over the dislocation length and this introduces further complexity. This problem has already been identified and an approximate value for $2/k_1$ of 64 has been derived [5]. As the dislocation bows, a back stress will reach a value Gb/r_e where r_e is an effective average bowing radius at instant of time t. The bowing will continue until the back stress rises to reach equilibrium with the applied stress, at a level where $\tau = Gb/r_e$.

Taking these features into account, the strain rate is

$$d\gamma/dt \approx 64\, D_c\, [\tau - (Gb/r_e)]\, b^5 / \lambda^4\, kT \quad (7)$$

It is noted that, on removal of stress, the strain rate is reversed so that the initial strain is recovered provided that $r_e > \lambda/2$ so that new dislocations have not been generated and intersections have not occurred. These theoretical considerations can now be related to experiments and an account of these is next presented.

Experimental Procedures

The scale of sensitivity required can be appreciated from equation (1), when written in the form $\gamma_m = \pi b/8\lambda$. For annealed metals, we expect, typically, that $b/\lambda \approx 10^{-4}$ rising to a value approaching 10^{-2} for heavily worked materials . To monitor rates of strain with sufficient sensitivity it is thus desirable to achieve strain measurements down to a level of about 10^{-7}.

For this purpose, specimens were used in the form of helical coils with a coil diameter of about 20 mm, made from drawn wire of about 1m length and approximately 2 mm diameter. Each coil had about 15 turns covering an axial length of about 50 mm but with each end of the wire remaining straight along the coil axis. The coils were mounted vertically with the upper end fixed and loaded by weights attached to the lower end.

The coils were contained within a vacuum furnace, with facilities for load application and removal, in specially constructed equipment described elsewhere [6]. The axial extension and contraction of the coils were continually monitored by displacement transducer with a sensitivity of < 1 μm. With wire diameter d wound in a coil of N turns of diameter D, the maximum shear strain γ at the wire surface, when the axial extension of the coil is h, is given by

$$\gamma = h\, d / \pi\, N\, D^2 \qquad (8)$$

Hence, with d = 2 mm, N = 15 and D = 20 mm, for displacement h = 1 μm, $\gamma = 10^{-7}$.

The maximum shear strain at the wire surface τ was calculated from

$$\tau = 8\, Mg\, D / \pi\, d^3 \qquad (9)$$

so that loading, for example with a mass M = 0.1 kg , gave a value of τ = 6 MPa.

Experimental Results

Experiments were carried out on copper wires both in the annealed and heavily deformed states. There were large differences in behaviour between material in these different states. As anticipated from the theoretical considerations presented, both the extent and the rates of transient creep deformation and of strain recovery were much greater for material in the heavily worked condition in which the dislocation density was high. In this condition, the kinetics of the process were similar to those occurring in the annealed material at a temperature about 300 deg. C higher.

For fully annealed copper, which had average grain size 42 μm, under a shear stress of 5 Mpa at a temperature of 813 K, the measured average strain rate over the first 5 seconds was 9×10^{-7} s^{-1}. For the same material in a heavily worked condition, where grains were narrow, highly elongated with a high dislocation density, under a stress of 5 MPa at 373 K, the measured average strain rate was 9×10^{-8} s^{-1}.

From the bowing theory, the initial strain rate can be estimated if a value can be ascribed to the dislocation core diffusion coefficient for which direct measurements are not available. It has been argued that it should be comparable with the grain boundary self diffusion coefficient, which for Cu at 813 K is expected [7] to be about 1.3×10^{-12} m^2/s. Taking the Burger's vector $b \approx 2 \times 10^{-10}$ m, the initial strain rate at this temperature can be calculated for the same conditions as the experiments. Some

value must also be ascribed to the dislocation density and annealing reduced this to values where 3×10^{-7} m $< \lambda < 10^{-6}$ m. Taking $\lambda \approx 5 \times 10^{-7}$ m, the expected value from equation (7) is thus

$$d\gamma/dt \approx 64 \times 1.3 \times 10^{-12} \times (5 \times 10^{6}) \times (2 \times 10^{-10})^{5} / (5 \times 10^{-7})^{4} \times (1.38 \times 10^{-23}) \times 813$$

giving $d\gamma/dt \approx 2 \times 10^{-7}$ s^{-1}. Noting the very substantial uncertainties in this calculation, the similarity with the measured value of 9×10^{-7} is remarkably close. At the lower temperature of 373 K, the value of the average link length λ is more difficult to evaluate since the dislocation arrangements in the heavily worked materials are more complex. However, taking $\lambda \approx 10^{-8}$ m, we can repeat this calculation for the initial rate of creep at 373 K. where the dislocation core diffusion coefficient D_c is expected to be about 1×10^{-12} m^2/s. For the same stress of 5×10^6 Pa, under these conditions we derive a value $d\gamma/dt \approx 8 \times 10^{-9}$ s^{-1}. This theoretical derivation gives a result about an order of magnitude below the measured value. In view of the uncertainties in the data used, especially in the estimate of pipe diffusion, this difference may not be unreasonable but it must be noted that an average link length of $< 10^{-8}$ m is improbable and so some additional contribution to the high initial strain rate at this temperature seems likely. Some evidence of mechanisms additional to the bowing model to explain the high initial rate of strain at low temperature was also inferred from the observation that rates of strain both on loading and unloading were found to be numerically similar.

Because the radius of curvature of the dislocation at all stages of bowing is not expected to be uniform along their lengths, it is difficult to evaluate the change of strain rate over significant periods of time either in the loading or unloading conditions. By analogy with phenomena of strain recovery in polymeric materials, an exponential decay of strain rate with time has sometimes [1] been assumed. The exponential function is highly convenient for mathematical manipulation and its application to the present analysis might be expected to lead to an effective time constant of given from, equation (7), by λ^4 kT / 64 D_c τ b^5 , for the condition when $(Gb/r) \ll \tau$. Such an approach was considered in the present study but it was invariably found that the rate of change of strain with time could not be described by an exponential relationship.

The variation of strain with time was not identical on loading and on unloading. For the former, an Andrade [8] type equation $\gamma = a\, t^{b}$, where a and b are constants, was applicable. The theoretical basis for such an equation has proved difficult to establish, and recent proposals are based on dislocation obstacle interaction inapplicable to the situation described here. It is, however, an interesting feature of the present work that the Andrade Law of primary creep has been shown to continue to apply down to very low stress and strain levels where, on Deformation Mechanisms Maps [9], a different mode of deformation in the steady state is expected to occur.

In the examination of the rate of strain recovery after load removal, curve fitting procedures suggested that an equation $\gamma = A - B \ln (1 + t)$ provided a reasonably close fit, as shown in Fig. 2 where A and B are constants at a specific temperature and initial creep strain. This was much closer than those provided by power law or exponential functions, . It follows, from differentiation, that the expected rate of strain recovery $d\gamma/dt = - B / (1 + t)$. We noted earlier from equation (7), that the driving force for

recovery was the term (Gb/r_e), though with the problem that its precise evaluation was hampered by the variation of curvature along the dislocation lines. Nevertheless, the rate of strain recovery must decrease as r_e increases and strain is progressively recovered. Similarly, there must be a dependency of r_e on the amount of initial strain induced on loading. If this loading is applied for a time to give a creep strain γ_p, then we may expect a relationship of γ_p with B. This relationship was examined with results illustrated in Fig. 3 which reveals that, approximately, B is proportional to $\gamma_p^{0.5}$. The theory of bowing based on dislocation climb is qualitatively in agreement with this, though more development of the theory is required for a quantitative comparison.

Conclusions

It has been shown that a model of dislocation climb by bowing through the pipe diffusion of vacancies along dislocation cores can account for several features of the time dependent strain that occurs on loading to small stress levels. When the strain is sufficiently small, this process is reversible so that the strain is recovered on unloading.

The most significant feature revealed by the study is the importance of initial dislocation density. It follows that a material with a high degree of initial cold working, though it will have a higher yield strength, will be susceptible to the development of small creep strains when stresses are applied at relatively low temperatures. The kinetics of the process lead to a transient creep law similar to that proposed by Andrade that is known to apply at higher stresses.

At the low stresses and strains explored in the present work, the initial forward and reverse strain rates on loading and on unloading were similar. They were also more rapid than estimated by the theory of bowing by climb at lower temperatures, indicating some inaccuracies in the data used or that some additional mechanisms are involved. On unloading, a logarithmic dependence of recovery strain on time was noted. As suggested from the theory of dislocation bowing, the extent and kinetics of strain recovery were dependent on the creep strain produced by loading,

Acknowledgements

The authors wish to thank Dr. B. Burton for useful discussion and the EPSRC and the University of Sheffield for provision of facilities. One of us (YG) is grateful to the Government of Turkey and the Gebze Institute of Technology for financial support.

References

[1] G. E. Dieter, *Mechanical Metallurgy*, McGraw-Hill, NY. (1988), p.434.

[2] J. Cadek, *Creep in Metallic Materials*, Academia Prague (1988), p.133.

[3] J. Bardeen and C. Herring, *Imperfections in Nearly Perfect Crystals*, John Wiley, NY. (1952), p.261.

[4] H.S.Carslaw and J.C.Jaeger, *Conduction of Heat in Solids,* OUP. (1959).

[5] D. T. Knight, Ph.D. Thesis, University of Sheffield, UK. (1989).

[6] T.W.Eaton, G.W.Greenwood and D.T.Knight, Eur. J. Phys. 14 (1993), p234.

[7] A.M. Brown and M.F. Ashby, Acta Metall., 28 (1980), p1085.

[8] E. N. Andrade, Proc. R. Soc., London A84 (1911), p1.

[9] M. F. Ashby, Acta Metall., 28 (1972), p887.

For correspondence
e-mail g.w.greenwood@sheffield.ac.uk
FAX +44 0114 222 5943

Illustrations

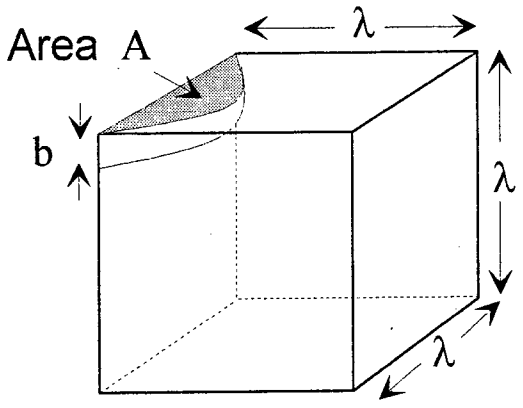

Fig.1. A simplified illustration of the bowing by climb over an area A of a dislocation of Burgers vector b and length λ

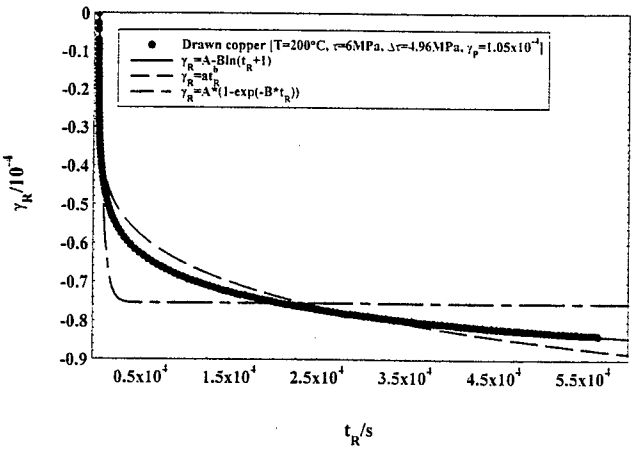

Fig. 2. A typical curve for the time dependence of strain relaxation γ_R showing that the best fit equation is of the form $\gamma_R = A - B \ln(t_R + 1)$.
The curve shown is for the strain relaxation of drawn copper at a temperature of 200° C when a stress of 4.96 MPa has been removed after a prestrain γ_p of 1.05×10^{-4}.

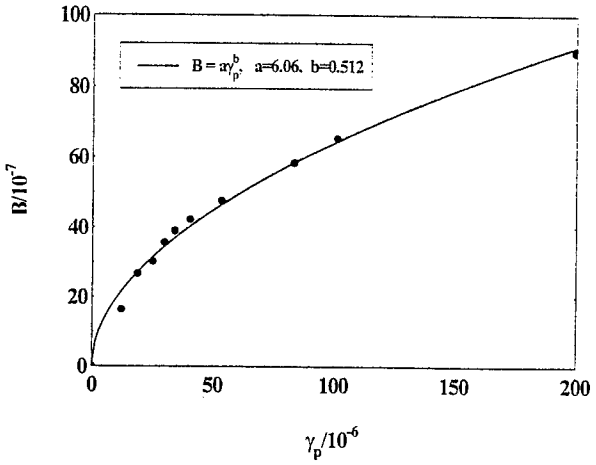

Fig. 3. Illustrating that the parameter B in the formula for strain relaxation is approximately proportional to the square root of the prestrain γ_p.
The data is taken from annealed copper at 540° C prestrained to various levels at 5.13 MPa before stress removal of 4.26 MPa.

Key Engineering Materials Vols. 171-174 (2000) pp. 205-212
© 2000 Trans Tech Publications, Switzerland

The Significance of Diffusion Creep and Harper-Dorn Creep at Low Stresses

T.G. Langdon

Departments of Materials Science and Mechanical Engineering, University of Southern California, Los Angeles, CA 90089-1453, USA

Keywords: Denuded Zones, Diffusion Creep, Grain Boundary Sliding, Harper-Dorn Creep, Newtonian Viscous Flow

ABSTRACT

Diffusion creep and Harper-Dorn creep are two distinct flow mechanisms occurring at low stress levels under conditions where the stress exponent, n, is equal to 1. There is a clear difference between these two processes because diffusion creep leads to offsets in marker lines at the points where the lines impinge on grain boundaries whereas there are no offsets in marker lines in Harper-Dorn creep. It is shown that this difference is consistent with published measurements taken in these two regions of flow.

INTRODUCTION

When creep occurs at elevated temperatures, the steady-state creep rate, $\dot{\varepsilon}$, varies with the applied stress, σ, through a relationship which generally may be expressed in the form

$$\dot{\varepsilon} = \frac{ADGb}{kT}\left(\frac{b}{d}\right)^p\left(\frac{\sigma}{G}\right)^n \qquad (1)$$

where D is the appropriate diffusion coefficient [given by D_o exp (-Q/RT), where D_o is a frequency factor, Q is the activation energy, R is the gas constant and T is the absolute temperature], G is the shear modulus, **b** is the Burgers vector, k is Boltzmann's constant, d is the grain size, p and n are the exponents of the inverse grain size and the stress, respectively, and A is a dimensionless constant.

A standard procedure in experiments on high temperature creep is to measure the values of the steady-state creep rates over a range of applied stresses at a constant testing temperature and then to plot these data logarithmically in the form of $\dot{\varepsilon}$ versus σ. Results of this type usually show a reasonably high value for the stress exponent at intermediate and high levels of the applied stress but with a transition to a region of Newtonian viscous flow with n = 1 at the lowest stress levels. The behavior in this low stress region has been interpreted either as diffusion creep or as an intragranular dislocation mechanism designated Harper-Dorn creep. The purpose of this paper is to examine the experimental evidence for the occurrence of these two creep processes.

CREEP MECHANISMS AT ELEVATED TEMPERATURES

To place this report in perspective, it is convenient to examine the anticipated creep behavior in pure metals over a wide range of applied stresses. Figure 1 shows a schematic illustration of the anticipated variation of the strain rate with stress (in arbitrary units) covering more than 8 orders

of magnitude of strain rate: the solid line relates to data obtained at a constant testing temperature within the diffusion-controlled regime and therefore above $\sim 0.5\ T_m$, where T_m is the absolute melting temperature [1].

Over a range of intermediate stresses, the stress exponent is generally close to ~ 5 and the behavior is attributed to a recovery process such as dislocation climb at high temperatures (H.T.) controlled by the rate of lattice self-diffusion. In practice, the precise value of n recorded in this region tends to vary inversely with the magnitude of the stacking fault energy in f.c.c. metals [2] and there is evidence this additional dependence can be incorporated into eqn. (1) by including a term of the form $(\Gamma/Gb)^3$ where Γ is the stacking fault energy [3]. This creep behavior is termed Class M (Metal type) and it is distinct from Class A (Alloy type) which occurs under some conditions in solid solution alloys [4]. This power-law behavior breaks down at high stresses and the strain rate then increases exponentially with the applied stress. At low stresses, and at strain rates which are often close to the limiting values for experimental measurements, there is generally a transition to a region in which the behavior is Newtonian viscous with $n = 1$. The behavior in this region has been attributed to the occurrence of either diffusion creep or Harper-Dorn creep.

Diffusion creep is well formulated on theoretical grounds and it refers to the stress-directed flow of vacancies which occurs in response to an applied stress. This vacancy flow arises because there is an excess vacancy concentration at the grain boundaries lying approximately perpendicular to the tensile axis and a corresponding depletion of vacancies at the boundaries lying almost parallel to the tensile axis. In practice, the vacancies may flow either through the crystalline lattice in Nabarro-Herring diffusion creep [5,6] or along the grain boundaries in Coble diffusion creep [7] and these two processes both give creep rates which are in agreement with eqn. (1) with $n = 1$ but with $D = D_\ell$ and $p = 2$ in Nabarro-Herring creep and $D = D_{gb}$ and $p = 3$ in Coble creep, where D_ℓ and D_{gb} are the coefficients for lattice self-diffusion and grain boundary diffusion, respectively. By contrast, Harper-Dorn creep is less well formulated but the evidence suggests $n = 1$ with $D = D_\ell$ and $p = 0$. The possible significance of these two processes within the low stress region is illustrated in Fig. 1 where the two larger grain sizes, d_1 and d_2, deform by Harper-Dorn creep where there is no dependence on grain size and the two smaller grain sizes, d_3 and d_4, deform by diffusion creep to give faster creep rates.

The evidence for the occurrence of Harper-Dorn creep is based on experimental results on high purity aluminum first reported by Dorn and co-workers [8,9]. In these experiments, conducted at temperatures very close to the absolute melting temperature, it was found that the measured creep rates were up to three orders of magnitude faster than those predicted by the Nabarro-Herring theory for diffusion creep and, in addition, there was no dependence on grain size so that similar creep rates were recorded both in polycrystalline samples having a grain size of 3.3 mm and in single crystals. These results are illustrated in Fig. 2 where, re-arranging eqn. (1) in terms of the shear strain rate, $\dot{\gamma}$, and the shear stress, τ, the normalized shear strain rate, $\dot{\gamma}kT/D_\ell Gb$, is plotted logarithmically against the normalized shear stress, τ/G. Subsequently, these results were confirmed in two independent sets of experiments by Barrett *et al.* [10] and Mohamed *et al.* [11] and these additional results are also included in Fig. 2. Thus, the experimental data show a very clear transition with increasing stress from $n = 1$ to $n \simeq 4.5$. Also included in Fig. 2 are two lines denoting the predicted normalized strain rates for Nabarro-Herring creep with grains sizes of 3.3 and 9 mm, respectively. As a consequence of the very clear discrepancy between the experimental results illustrated in Fig. 2 and the traditional models for diffusion creep, this behavior became known as Harper-Dorn creep. More recently, results have been presented on several different materials where there appears to be evidence for the occurrence of Harper-Dorn creep at low stress levels [12,13].

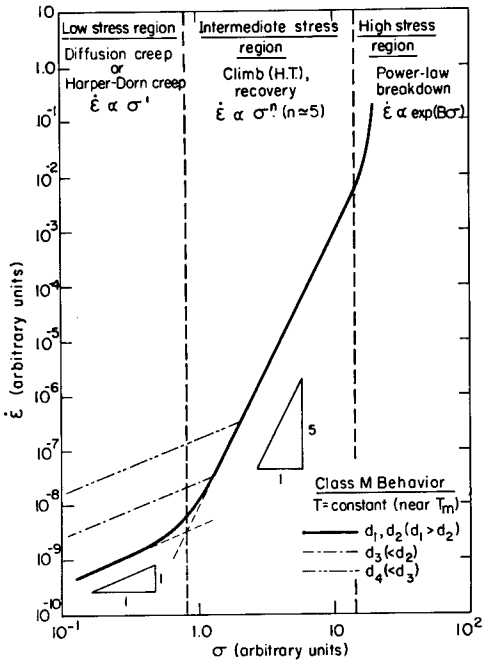

Fig. 1 Schematic illustration of strain rate versus stress for the creep of pure metals.

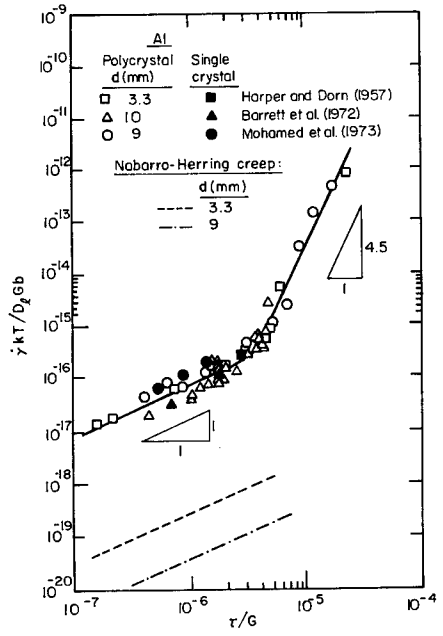

Fig. 2 Normalized shear strain rate versus normalized shear stress for samples of pure Al showing experimental evidence for the occurrence of Harper-Dorn creep [8,10,11] and the theoretical predictions for Nabarro-Herring creep.

It is important to note that, although the direct evidence for Harper-Dorn creep is reasonably strong, close inspection of some of the data which have been interpreted as Harper-Dorn creep suggests that the interpretations may be in error [14,15]. Despite these problems, and suggestions that Harper-Dorn creep may be only an artifact [16,17], there remains a substantial body of evidence, such as the results in Fig. 2, which provide good support for the occurrence of some flow process at low stress levels which is different from that predicted by diffusion creep. It is important, therefore, to seek additional procedures which may be used to unambiguously distinguish between these different flow processes in the $n = 1$ region.

DISTINGUISHING BETWEEN DIFFUSION CREEP AND HARPER-DORN CREEP

An initial difficulty in distinguishing between these two different processes is that the precise flow mechanism in Harper-Dorn creep is not known. In general, Harper-Dorn creep appears to be associated with some form of intragranular creep mechanism and in this respect there are two additional experimental observations associated with Harper-Dorn creep. First, the dislocation density is independent of the applied stress in this flow regime [10,18]. Second, the occurrence of Harper-Dorn creep requires that the initial dislocation density in the material is low [19]. Several different models have been developed to explain Harper-Dorn creep [13,19-27] but there is at the present time no clear consensus on the precise rate-controlling mechanism.

Despite these difficulties, however, it is apparent there are significant microstructural differences between diffusion creep and Harper-Dorn creep. In diffusion creep, the grains become elongated along the stress axis and this occurs, in effect, through the removal of layers of atoms from the grain boundaries lying parallel to the tensile axis and the deposition of equivalent atomic layers at the boundaries lying perpendicular to the tensile axis. This process necessitates the need for a concomitant accommodation mechanism in the form of grain boundary sliding which maintains coherency within the specimen. By contrast, Harper-Dorn creep occurs through some form of intragranular dislocation mechanism so that the grains become elongated but without the requirement for any grain boundary sliding. This difference has led to the proposal of a simple procedure for separately identifying Harper-Dorn creep and diffusion creep [28]. This procedure is illustrated in Figs 3 and 4 where grain configurations are illustrated for a situation where the tensile axis is vertical.

Figure 3(a) shows an array of three grains in a polycrystalline matrix with two surface or internal marker lines labelled AA′ and BB′. The same three grains are illustrated after identical strains in Figs 3(b) and (c) but with the deformation occurring by Harper-Dorn creep or diffusion creep, respectively. Thus, in Harper-Dorn creep the grains become elongated but the marker lines retain their respective positions within each grain and no offsets are produced at the points where these marker lines traverse the horizontal boundaries. In diffusion creep, however, the removal of material at the vertical boundary separating the two upper grains leads to a situation in which the two markers in the upper grains move towards each other and, since there is no corresponding movement of the markers in the lower grain, offsets are developed at the horizontal boundary as indicated in Fig. 3(c). Figure 4 shows a similar effect except only that the initial three grains in Fig. 4(a) are now arranged in a different configuration and the marker lines are horizontal. Again, no marker offsets are created in Harper-Dorn creep as shown in Fig. 4(b) whereas the deposition of material at the horizontal boundary in diffusion creep leads to a movement of these two markers away from each other and the consequent development of offsets at the points where the markers impinge on the vertical boundary as indicated in Fig. 4(c).

There is experimental evidence supporting the difference in behavior illustrated in Figs 3 and 4.

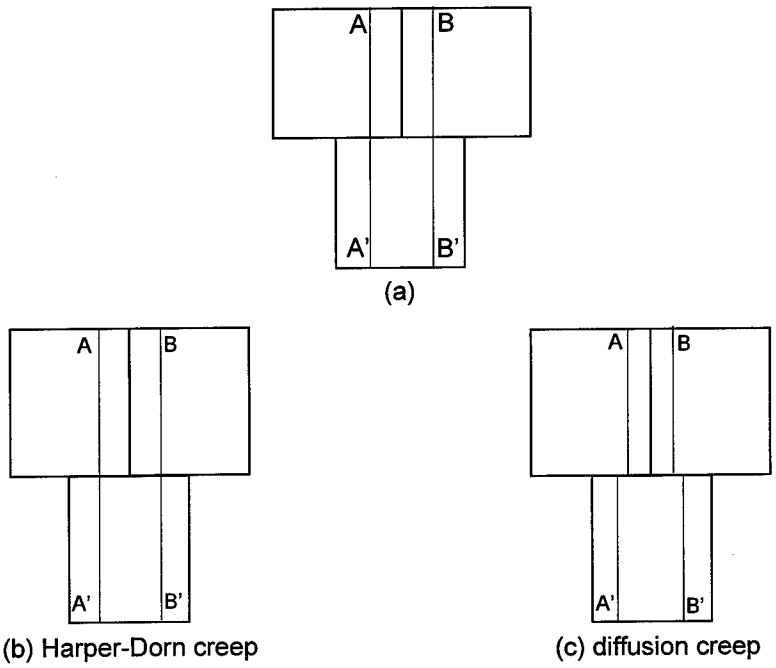

Fig. 3 An array of three grains with marker lines parallel to the tensile axis (a) before creep testing and (b) after Harper-Dorn creep and (c) after diffusion creep, respectively.

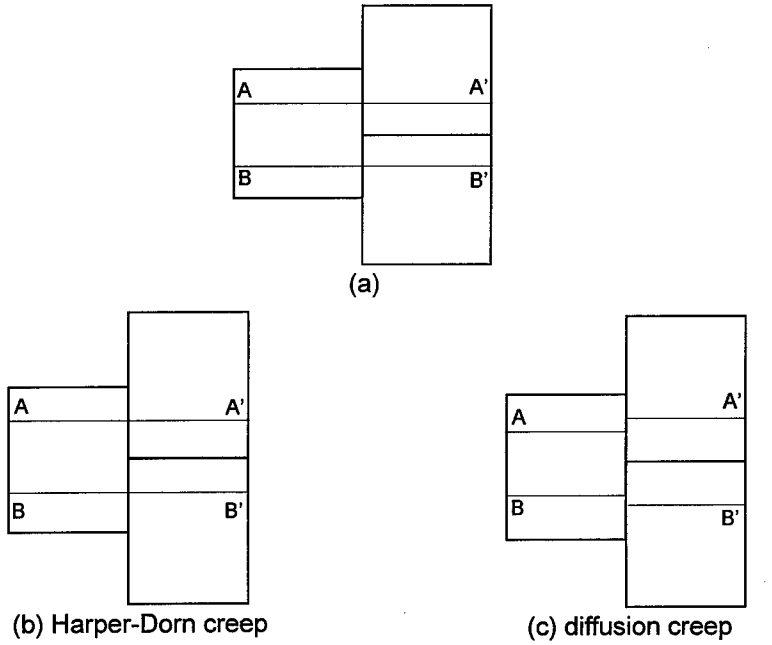

Fig. 4 An array of three grains with marker lines perpendicular to the tensile axis (a) before creep testing and (b) after Harper-Dorn creep and (c) after diffusion creep, respectively.

Harper and Dorn [8] ruled a series of transverse marker lines on the surface of one of their specimens, similar to the lines in Fig. 4(a), and they measured the contribution of sliding to the total strain, ξ, as $\sim 12\%$, where ξ is defined as $\varepsilon_{gbs}/\varepsilon_t$ where ε_{gbs} and ε_t are the strain due to grain boundary sliding and the total strain, respectively. Subsequently, Harper *et al.* [9] used the same procedure to conduct more extensive measurements and obtained a maximum value of $\xi \simeq 14.9\%$. These low values of ξ are therefore consistent with the expectations from Fig. 4(b). Conversely, Gifkins and Langdon [29] examined a Mg-0.55% Zr alloy, termed Magnox ZR55, which was subjected to experimental conditions appropriate for diffusion creep (T = 673 K, σ = 2.0 MPa, L $\simeq$ 80 μm and ε_t = 13.3%, where L is the mean linear intercept grain size). A photomicrograph of the microstructure of this sample is shown in Fig. 5 where the tensile axis is vertical and there is clear evidence both for hydride stringers lying approximately parallel to the tensile axis and the development of zones denuded of precipitates lying along the grain boundaries approximately perpendicular to the stress axis. The results of measurements of offsets in the hydride stringers gave $\xi \simeq 60\%$ and this high value for the sliding contribution is consistent with the behavior illustrated in Fig. 3(c). There is experimental evidence that the procedure of measuring offsets along longitudinal marker lines tends to underestimate the values calculated for ξ [30] so that the effective value for ξ in this sample is extremely high.

Although the differences in the appearance of marker line offsets for the two creep processes of Harper-Dorn creep and diffusion creep are unambiguous, Ruano *et al.* [31] argued that the measurements taken on the ZR55 alloy illustrated in Fig. 5 relate to experimental conditions where grain boundary sliding is the dominant process rather than diffusion creep. To check this possibility, Fig. 6 shows a plot of creep rate against stress for the Magnox ZR55 alloy tested at 673 K using experimental data from Pickles [32] and a single datum point reported by Harris [33] for the same specimen shown in Fig. 5 and used to determine the value of $\xi \simeq 60\%$. Superimposed on Fig. 6 are two broken lines for Nabarro-Herring (NH) creep estimated for the appropriate spatial grain sizes determined from the relationship d = 1.74L. Inspection shows that the experimental rates for the samples used by Pickles [32] are in reasonable agreement with the predictions of the theory, up to and including a stress level of 2.0 MPa as used in the sample where $\xi \simeq 60\%$, but the estimated creep rate for the sample of Harris [33] is lower than the experimental rate by slightly more than one order of magnitude. It should be noted that Harris [33] reported a calculated strain rate for this specimen which was lower than the measured initial rate of $\sim 3 \times 10^{-7}$ s^{-1} by a factor of only ~ 4. The difference is larger in the present calculation for two reasons. First, Harris [33] used an estimated mean linear intercept grain size of ~ 100 μm whereas the line in Fig. 6 was calculated using the spatial grain size. Second, the standard relationship for Nabarro-Herring creep has a strain rate given by $BD_\ell\sigma\Omega/d^2kT$ where Ω is the atomic volume and B is a constant which was taken as 40 by Harris [33] but put equal to 12 in the present calculations. Despite the uncertainties associated with the values of some of the parameters in the model, the information in Fig. 6 suggests reasonable agreement with Nabarro-Herring creep for the sample shown in Fig. 5 but it appears there is probably an additional minor contribution to the strain from grain boundary sliding in the early stages of the test.

In order to unambiguously differentiate between diffusion creep and grain boundary sliding for the ZR55 sample shown in Fig. 5, measurements were taken to determine the average grain aspect ratio along the tensile axis [34]. These measurements show that the grains are elongated with an average measured aspect ratio of ~ 1.25: evidence for this grain elongation is clearly visible in Fig. 5. Since grain elongation is not consistent with flow by grain boundary sliding, it is therefore concluded that the earlier result of $\xi \simeq 60\%$ [29] was obtained within the region where Nabarro-Herring creep was the dominant flow process. Thus, there is good microstructural evidence that Harper-Dorn creep and diffusion creep are viable and distinct creep processes at low stresses.

Fig. 5 The appearance of denuded zones and hydride stringers in a Magnox ZR55 alloy tested under conditions of diffusion creep: the tensile axis is vertical [28].

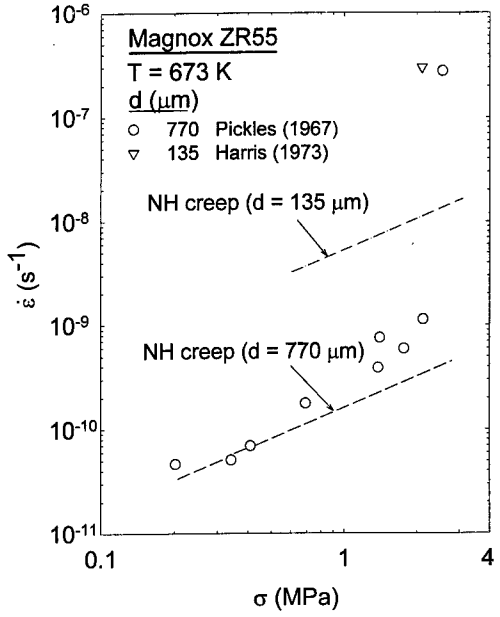

Fig. 6 Strain rate versus stress for the Magnox ZR55 alloy tested at low stress levels, showing experimental data [32,33] and the predictions for Nabarro-Herring (NH) creep.

ACKNOWLEDGEMENT

This work was supported by the United States Department of Energy under Grant No. DE-FG03-92ER45472.

REFERENCES

1. P. Yavari and T.G. Langdon, Acta Metall. **30** (1982) 2181.
2. J.E. Bird, A.K. Mukherjee and J.E. Dorn, *Quantitative Relation Between Properties and Microstructure* (D.G. Brandon and A. Rosen, eds.), p. 255. Israel Universities Press, Jerusalem (1969).
3. F.A. Mohamed and T.G. Langdon, Acta Metall. **22** (1974) 779.
4. P. Yavari, F.A. Mohamed and T.G. Langdon, Acta Metall. **29** (1981) 1495.
5. F.R.N. Nabarro, *Report of a Conference on Strength of Solids*, p. 75. The Physical Society, London (1948).
6. C. Herring, J. Appl. Phys. **21** (1950) 437.
7. R.L. Coble, J. Appl. Phys. **34** (1963) 1679.
8. J. Harper and J.E. Dorn, Acta Metall. **5** (1957) 654.
9. J.G. Harper, L.A. Shepard and J.E. Dorn, Acta Metall. **6** (1958) 509.
10. C.R. Barrett, E.C. Muehleisen and W.D. Nix, Mater. Sci. Engng **10** (1972) 33.
11. F.A. Mohamed, K.L. Murty and J.W. Morris, Metall. Trans. **4** (1973) 935.
12. F.A. Mohamed and J. Wolfenstine, *Hot Deformation of Aluminum Alloys* (T.G. Langdon, H.D. Merchant, J.G. Morris and M.A. Zaidi, eds.), p. 223. The Minerals, Metals and Materials Society, Warrendale, PA (1991).
13. J.N. Wang and T.G. Langdon, Acta Metall. Mater. **42** (1994) 2487.
14. M.Z. Berbon and T.G. Langdon, J. Mater. Sci. Lett. **15** (1996) 1664.
15. M.Z. Berbon, D.M. Owen and T.G. Langdon, *The Johannes Weertman Symposium* (R.J. Arsenault, D. Cole, T. Gross, G. Kostorz, P.K. Liaw, S. Parameswaran and H. Sizek, eds.), p. 145. The Minerals, Metals and Materials Society, Warrendale, PA (1996).
16. J. Weertman and J. Blacic, Geophys. Res. Lett. **11** (1984) 117.
17. W. Blum and W. Maier, Phys. Stat. Sol. (a) **171** (1999) 467.
18. P. Yavari, D.A. Miller and T.G. Langdon, Acta Metall. **30** (1982) 871.
19. F.A. Mohamed and T.J. Ginter, Acta Metall. **30** (1982) 1869.
20. T.G. Langdon and P. Yavari, Acta Metall. **30** (1982) 881.
21. M.Y. Wu and O.D. Sherby, Acta metall. **32** (1984) 1561.
22. O.A. Ruano, J. Wadsworth and O.D. Sherby, Acta Metall. **36** (1988) 1117.
23. A.J. Ardell and S.S. Lee, Acta Metall. **34** (1986) 2411.
24. P. Lin, S.S. Lee and A.J. Ardell, Acta Metall. **37** (1989) 739.
25. F.R.N. Nabarro, Acta Metall. **37** (1989) 2217.
26. J.N. Wang and T.G. Nieh, Acta Metall. Mater. **43** (1995) 1415.
27. A.J. Ardell, Acta Mater. **45** (1997) 2971.
28. T.G. Langdon, Scripta Mater. **35** (1996) 733.
29. R.C. Gifkins and T.G. Langdon, Scripta Metall. **4** (1970) 563.
30. T.G. Langdon, Mater. Sci. Engng **A174** (1994) 225.
31. O.A. Ruano, O.D. Sherby, J. Wadsworth and J. Wolfenstine, Scripta Mater. **38** (1998) 1307.
32. B.W. Pickles, J. Inst. Metals **95** (1967) 333.
33. J.E. Harris, Metal Sci. J. **7** (1973) 1.
34. T.G. Langdon, to be published.

Corresponding author: Terence G. Langdon (e-mail: langdon@usc.edu).

Key Engineering Materials Vols. 171-174 (2000) pp. 213-218
© 2000 Trans Tech Publications, Switzerland

Deformation Behavior of Fe-3%Si Steel at High Temperatures

R. Kaibyshev and I. Kazakulov

Institute for Metals Superplasticity Problems RAS, RU-450001, Khalturina 39, Ufa, Russia

Keywords: Deformation, Threshold Behavior, Activation Energy, Threshold Stress

Abstract

Deformation behavior of a Fe-3%Si steel with ultrafine MnS inhibitors was studied in the temperature range 500-1000°C. The steel exhibits a threshold behavior. Analysis in terms of threshold stress shown that there were two characteristic modes of deformation behavior in the power-law creep regime. At temperatures 500-700°C the value of the stress exponent, n, is equal to 6, and the true activation energy for plastic deformation, Q, linearly increases from 170 kJ/mol to value closed to 239 kJ/mol with temperature rise. At temperatures above 700°C the stress exponent is about 4, and the true activation energy for plastic deformation is about 240 kJ/mol. Two temperature dependencies of normalized threshold stress differed by a value of the energy term, Q_o, were found in these two temperature intervals. The value Q_o is about 55 and 39 kJ/mol in an intermediate and high temperature range, respectively. Operating deformation mechanisms in two temperature regions are discussed.

1. Introduction

The raise of service temperature is very important for some alloys and steels used at high temperatures. Dispersion strengthening is an attractive approach to enhance the creep resistance of these materials due to introducing of ultrafine dispersoids into metallic matrix. It leads to appearance of threshold stress and an improvement of creep resistance at high temperatures. In spite of numerous works dealing with creep of dispersion strengthened materials [1-9], their deformation behavior is insufficiently understood [10-11]. The main limitation of existing threshold models is the fact that there is no prediction of the experimentally observed strong temperature dependence of threshold stress. This dependence could not been attributed to the shear modulus temperature dependence [7,9,10]. At present the origin of such strong temperature dependence of threshold stress is not yet clear. It should be noted that reported experimental data of threshold behavior of dispersion strengthened materials were obtained in rather narrow temperature interval. Complex examination of the temperature dependence of threshold stress in a wide temperature range has not been performed yet.

Thus, the aim of the present study is to report threshold behavior of well-known steel Fe-3%Si at high and intermediate temperatures.

2. Experimental material and procedures

The material of testing was a hot-rolled ferritic Fe-3%Si steel supplied by ChMZ, Chelyabinsk, Russia, having the following chemical composition: 3.1%Si, 0.06%Mn, 0.025%S, 0.025%C,

0.06%N, 0.01%P, 0.03%Cr, 0.06%Ni, 0.06Cu, 0.003%Al, 0.008%As, Fe balance. The average matrix grain size was about 5mm. The material contains several types of dispersion particles. MnS inhibitors are dominant precipitations in this type of Fe-3%Si steel. The number of spherical-shaped particles was approximately 1.7×10^{18} particles/m^3 and their average size was about 80nm.

The specimens with 10 mm in diameter and 15mm in height were machined in perpendicular to the prior rolling direction. Compression test was conducted in temperature interval 500-1000°C at strain rates of 10^{-6} to 10^{-2} s^{-1} using testing machine Schenck-RMS100. For surface examinations the specimens were prepolished by a diamond paste and deformed to the strain ε=15% at $\dot{\varepsilon}=7.0\cdot10^{-4}$ s^{-1}. Surface observations of deformed specimens were performed using a SEM JSM-840.

3. Experimental results

3.1 Mechanical properties

3.1.1 The shape of σ-ε curves. Two temperature intervals differed by a shape of true stress-strain curves were found (Fig.1). In temperature range 800-1000°C the plastic flow attains a stable stage after minor strain. At intermediate temperatures, 500-700°C, three stages of plastic deformation are observed. Minor strain hardening takes place at first stage at $\varepsilon\leq15\%$. The strain hardening coefficient, θ, decreases from 0.9-1.0 at $\varepsilon\leq$1-1.5% to 0.6-0.8 MPa/mm^2 with increasing strain. The second stage is a well-established steady-state region. The duration of the secondary stage is essentially short and does not exceed ε=30-35%. Extensive strain hardening occurs at the third stage where strain hardening coefficient increases from 1-2 at ε=35% up to 5-7 MPa/mm^2 at ε=45%.

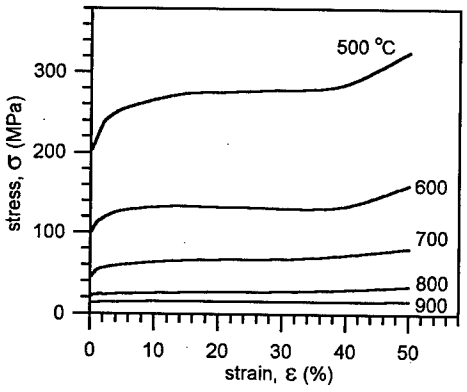

Fig. 1. Typical true stress - strain curves for Fe-3%Si steel in temperature interval 500-900°C at $\dot{\varepsilon}=7.0\cdot10^{-4}$ s^{-1}.

3.1.2 The variation of steady-state stress with strain rate. Figure 2 shows the variation of initial strain rate with flow stress plotted logarithmically. It is seen that deformation behavior of the steel at temperatures above 500°C is described in terms of the power law

$$\dot{\varepsilon} = A\cdot\sigma^n\cdot\exp\left(\frac{-Q}{R\cdot T}\right) \qquad (1)$$

where A is a constant, n is the stress exponent, σ is the steady state flow stress, Q is the activation energy for plastic deformation, R is the gas constant and T is the absolute temperature. In temperature range 600-1000°C the values of stress exponent vary from 6 to 7.8 and do not remarkably depend on temperature and strain rate. At temperatures 500-550C the values n increase up to 9-9.3. Notice that at temperatures less than 500°C the power law breakdown takes place.

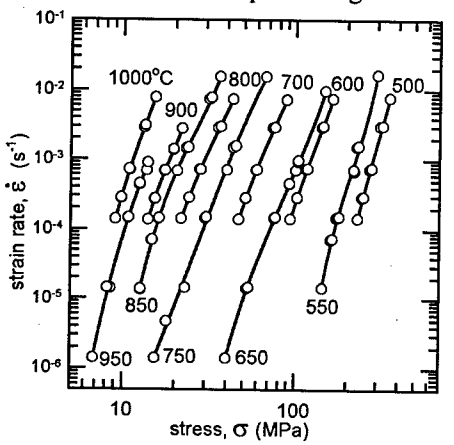

Fig. 2. Double logarithmic plot of the initial strain rate *vs* flow stress for temperatures from 500 to 1000°C.

3.1.3 The activation energy for plastic deformation. Algebraically, Eq.1 can be converted [12] to

$$\ln\sigma = \ln(\dot{\varepsilon}/A)^{1/n} + \frac{Q}{Rn}\cdot\frac{1}{T} \qquad (2)$$

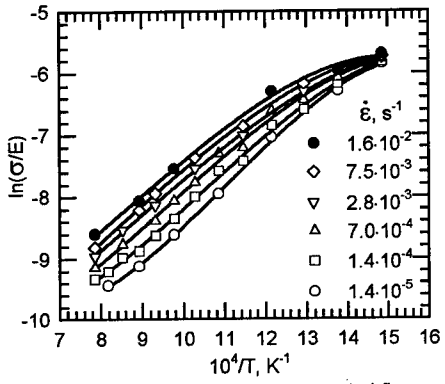

Fig. 3. Elastic modulus-compensated flow stress *vs* inverse of absolute temperature.

The apparent activation energy for plastic deformation, Q_a, was obtained graphically by logarithmic plotting of the normalized stress compensated by non-linear temperature dependence of the elastic modulus [13], σ/E, against the inverse of the absolute temperatures and taking the slope of tangent to be Q/(Rn) (Fig.3) for different strain rates.

It is seen, that calculated values of Q_a, lying in range from 300 to 400 kJ/mol, are much higher than the activation energy for self-diffusion in α-Fe (Q_l=239 kJ/mol) [13].

3.2 Surface observation

The surface metallographic features were found to be dependent on temperature (Fig.4). At all examined temperatures, the slip morphology observed in this investigation could be classified as multiple slip. Wavy slip features indicate that there is extensive cross slip occurrence. Temperature decrease leads to localization of dislocation glide. At high temperatures uniform dislocation sliding takes place and extensive microscopic strain localization is observed at low temperatures.

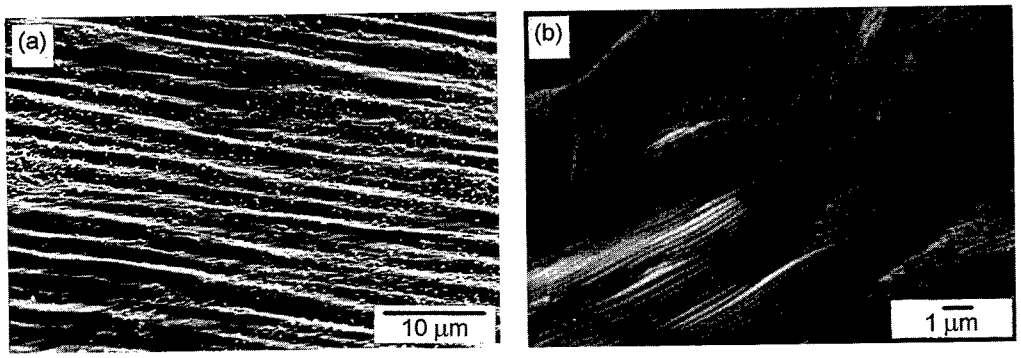

Fig. 4. Deformation relief of Fe-3%Si specimens deformed up to ε=15% at $\dot{\varepsilon}=7.0\cdot10^{-4}$ s^{-1}: a) t=600°C; b) t=900°C.

4. Analysis and Discussion

4.1. An examination of threshold stress. It is obvious that deformation behavior of the Fe-3%Si steel cannot be described over a wide examined range of strain rate and temperature by Eq.1. It is known [7-10] that an increase of the stress exponent with decreasing strain rate and the high values of the activation energy for plastic deformation are attributed to threshold behavior of a material. Therefore, the following phenomenological equation for plastic deformation can be used

$$\dot{\varepsilon} = A\cdot\left(\frac{\sigma-\sigma_o}{E}\right)^n\cdot\exp\left(\frac{-Q}{R\cdot T}\right) \qquad (3)$$

where σ_o is threshold stress.

The standard procedure was used to determine the threshold stress [7,9,10]. In estimating the threshold stress, σ_o, the experimental data were plotted as $\dot{\varepsilon}^{1/n}$ against σ on a double linear scale (Fig.4) at a temperature in the range t=500-900°C. This graphic method can be used if the deformation of a material obeys equation Eq.3 and if σ_o is independent from the strain rate. The datum points in this strain rate interval fit with excellent accuracy to a straight line by varying the stress exponent, as 3,4,5,6,7 and 8. Extrapolation of this line to zero gives the value σ_o. The obtained values of threshold stress at different temperatures are presented in Table 1.

Table 1. Threshold stress at different temperatures.

t, °C	500	550	600	650	700	750	800	850	900
n	6	6	6	6	5	4	4	4	4
σ_o, MPa	133.0	90.4	34.9	24.7	22.2	12.1	9.0	7.4	6.9

The temperature dependence of normalized threshold stress, σ_o/E, can be represented by [6, 7]

$$\frac{\sigma_o}{E} = B_o \exp\left(\frac{Q_o}{RT}\right) \qquad (4)$$

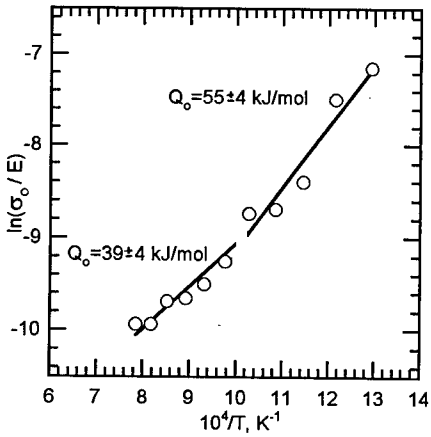

Fig. 5. The temperature dependence of the normalized threshold stress.

where B_o is a constant, and Q_o is an energy term [9]. The value of Q_o can be obtained graphically by plotting $\ln(\sigma_o/E)$ *vs* 1/T (Fig. 5). It is seen that there are two temperature intervals which differ in a value of energy term. At high temperatures (700-900°C) it is 39kJ/mol and at intermediate temperatures (500-700°C) this value is higher, 55kJ/mol. It should be noted that temperature dependence of threshold stress was reported for classic superplastic materials and for aluminum alloys and metal matrix composites on their base, produced via powder metallurgical techniques [7,9]. However, the temperature influence on the energy term in Eq.4 has not been reported yet. It seems that it was caused by the fact that threshold behavior of numerous materials was examined in the narrow temperature interval which did not exceed 100°C. As a result, the transition from one value of energy term to the other was not found.

It is seen that deformation behavior of the Fe-3%Si steel is typical for behavior of dispersion strengthened alloys. It is caused by the presence of ultrafine MnS inhibitors. It is known [14-16] that there is no remarkable temperature dependence of MnS precipitate size and their volume fraction at t<900°C. Consequently, the transition in threshold behavior of the steel is associated with change of interaction mechanism between dislocations and the hard obstacles.

4.2. An examination of the normalized deformation data. The data of the analysis of deformation behavior of the Fe-3%Si steel in terms of threshold stress (Fig.2, Table 1) allow to plot the normalized strain rate, $\dot{\varepsilon}kT/(D_IEb)$, against the normalized effective stress, $(\sigma-\sigma_o)/E$ (Fig.6). There $D_I=2\cdot10^{-4}\exp(-251/(RT))$ is the lattice diffusion coefficient in α-iron.

It is seen that the steel exhibits two characteristic modes of deformation behavior. First, at high temperatures, 700-1000°C, and at low normalized strain rate, $\dot{\varepsilon}kT/(D_IEb)<10^{-8}$, there is a well-defined power-law relationship with n=4.1. Such deformation behavior is associated with dislocation climb controlling by lattice diffusion [17]. This region locates below the Sherby-Burke criterion ($\dot{\varepsilon}kT/(D_IGb)\cong10^{-8}$) which has to represent the breakdown of the power law. At intermediate

temperatures, 500-700°C, the slope of straight line dependence $\dot{\varepsilon}kT/(D_iEb)$ *vs* $(\sigma-\sigma_o)/E$ is equal to 6. Such transition could be interpreted in terms of transition to low temperature climb controlled by pipe-diffusion along the dislocation cores. The classic relationship $n_{lt}=n_{ht}+2$ is observed for transition from high to intermediate temperature. Notice, that the experimental points in that region lie above the Sherby-Burke criterion which exactly matches transition from one interval of power-law creep to another. From this point of view there is an unambiguous of such simple interpretation of presented results.

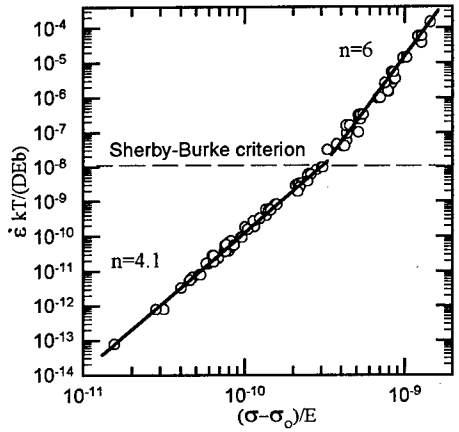

Fig. 6. Normalized strain rate *vs* normalized stress, showing the transition from power-law plastic deformation with n=4.1 (high temperature region) to the creep with n=6 (intermediate temperature region)

The temperature of transition from one region of the power law to another and the temperature which is the inflection point for threshold behavior of the Fe-3%Si steel are similar. The change of rate-controlling deformation processes is accompanied by change of mechanism of interaction between dispersoids and lattice dislocation. Thus, it is possible to presume that there is a connection between mechanism of interaction between dislocations and obstacles and a rate-controlling mechanism of plastic deformation.

4.3. True activation energy for plastic deformation in two intervals of power-law creep. The true activation energy for plastic deformation, Q, in Eq.3 could be determined, as mentioned above, by logarithmic plotting the elastic modulus compensated effective stress *vs* the inverse absolute temperatures (Fig.7). In addition, we should take into account the existence of non-linear temperature dependence of elastic modulus caused by the second order phase transition in Fe-3%Si

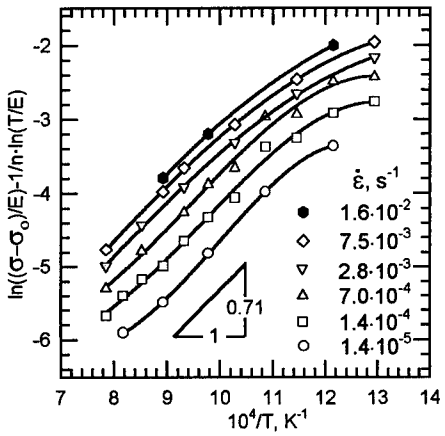

Fig. 7. Normalized effective stress *vs* inverse of absolute temperature.

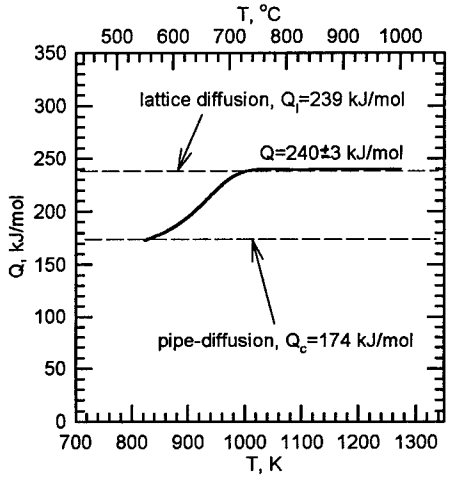

Fig.8. Temperature dependence of the true activation energy.

steel. Therefore the graphical plot $\ln((\sigma-\sigma_o)/E)-1/n\cdot\ln(T/E)$ *vs* 1/T was made. The second term on the ordinate axis is the modulus correction of non-linearity of temperature dependence, in which the value of n was chosen 4.1 in the examined temperature interval. The slopes of the tangent to the curves at t≥700°C are virtually unchanged and are about 7100K. At lower temperatures the value of the slope decreases to 2100-2600K down to 500°C, monotonically.

The true activation energy calculated from the slope Q/(Rn) are presented in Fig.9. Notice that here we used true values of n from Table 1. It is seen that classic temperature dependence [17] of true activation energy is observed. At t≥700°C the value of Q does not change and is 240±3 kJ/mol. It coincides with exellent accuracy with the value of activation energy of lattice self-diffusion in α-iron (Q_l=239 kJ/mol). In temperature interval 500-700°C the true activation energy decreases to 170±10 kJ/mol, approaching asymptotically to activation energy for pipe diffusion, 174 kJ/mol [13].

It may argued from presented results that the transition from one controlling mechanism of plastic deformation to another, with temperature, results in a change of mechanism of an interaction between dislocations and dispersoids. There is a strong connection between the dislocation ability to climb and the dislocation mechanism to surmount an obstacle. At higher temperatures the general dislocation climb is a controlling mechanism of plastic deformation and dislocations overcome obstacles, easily. A decrease of a dislocation climb velocity at intermediate temperatures causes growth of activation term associating with the barrier to dislocation bypass. At present the origin of the temperature dependence is not entirely clear. However, it is obvious that the dependence could not be explained on the base of existing models [1-3,7,12] and new models should be developed.

5. Conclusion

It was shown that deformation behavior of the Fe-3%Si steel at intermediate temperatures 500-700°C and at high temperature 700-1000°C was different.

1. The value of the stress exponent, n, decreases from ~6 at the intermediate temperature to ~4.1 above ~700°C.
2. The true activation energy for deformation, Q, decreases linearly with increasing normalized stress from ~240 kJ/mol at temperatures 700-1000°C to ~170kJ/mol at t=500°C.
3. It is demonstrated that high temperature data having n=4.1 lie below the Sherby-Burke criterion ($\dot{\varepsilon}kT/(D_1Gb)\cong10^{-8}$) and intermediate temperature data having n=n+2 lie above this criterion..
4. Two different temperature dependencies of threshold stress were found. At intermediate temperatures the energy term, Q_o, is ~55 kJ/mol and at high temperature Q_o is equal to ~39 kJ/mol.

6. References

[1] E.Arzt, J.Rösler, Acta Metall. 36 (1988), p.1043.
[2] E.Arzt, J.Rösler, Acta Metall. 36 (1988), p.1052.
[3] E.Arzt, D.S.Wilkinson, Acta Metall. 34 (1986), p.1893.
[4] W.C.Oliver, W.D.Nix, Acta Metall. 30 (1982), p.1335.
[5] R.W.Lund, W.D.Nix, Met. Trans. 6A (1975), p.1329.
[6] K.T.Park, E.Lavernia and F.Mohamed, Acta Metall. 38 (1990), p.2149.
[7] F.A.Mohamed, K.T.Park and E.J.Lavernia, Mater. Sci. Eng. A150 (1992), p.21.
[8] J.Rosler, E.Arzt, Acta Metall.Mater., 38 (1990), p.671.
[9] K.T.Park, E.Lavernia and F. Mohamed, Acta Metall. Mater., 42 (1994), p.667.
[10] J.Cadek, H.Oikawa, V.Sustek, Mater. Sci. Eng. A190 (1995), p.9.
[11] F.Dobes, K.Kucharova, A.Orlova, K.Milicka, J.Cadek, Mater. Sci. Eng. A174 (1994), p.37.
[12] J.R.Pickens, T.J.Langan, R.O.England and M.Liebson, Metall. Trans. 18A (1987), p.303.
[13] H.J.Frost, M.F.Asnby, Deformation-mechanism maps, Pergamon Press (1982).
[14] H.E.Grenoble, J. Appl. Phis. 38 (1967), p.1083.
[15] J.W.Flowers, S.P.Karas, J. Appl. Phys. 38 (1967), p.1085.
[16] W.M.Swift, Metall.Trans. 4 (1973), p.153.
[17] S.V.Raj, T.G.Langdon, Acta Metall. 37 (1989), p.843.

For correspondence: Prof. Rustam Kaibyshev, fax: +7 (3472) 253856, e-mail: ilkaz@anrb.ru

Key Engineering Materials Vols. 171-174 (2000) pp. 219-230
© 2000 Trans Tech Publications, Switzerland

A Critical Reassessment of the Ravotnov-Kachanov Equations

A. Göcmen

ABB Corporate Research Ltd., CH-5405 Baden-Dättwil, Switzerland

Keywords: Damage, Rabotnov-Kachanov, Tertiary Creep, Stress Redistribution, Creep Acceleration Growth, Strain Exhaustion, Life Exhaustion, Remnant Strain, Remnant Life, Creep Modeling

Abstract

The use of state equations, which describe the growth of damage in metals and the effect of this damage on creep strain rates, is discussed. The Rabotnov-Kachanov (R-K) equations, which are characterized by different power laws of a damage parameter ω and of the applied stress, represent a special example of such equations. It is demonstrated, that a more general creep law can be developed from the R-K equations for the growth of creep strain rates and the exhaustion of remnant strain. The creep law, which is represented as a differential equation of a defined and measurable creep acceleration parameter, is shown to provide an opportunity of determining key constants of the R-K equations, without the knowledge about damage evolution and the strain to rupture. The R-K equations can now effectively be applied with use of the new creep law to predict the remnant strain and the remnant life from registration and analysis of the creep acceleration growth. The R-K equations predict a time and strain independent effectiveness of stress redistribution. The newly developed creep law is applied along with the R-K equations for an assessment of temporary stress redistribution, when its effectiveness alters with strain and time. Studies are made for a description of the failure development under conditions of altering stress redistribution.

1. Introduction

A large number of engineering alloys used in power generation operate at temperatures at which creep damage processes limit the lifetime of load-carrying components over time ranges of 10 to 30 years. The appearance of creep damage is experienced by acceleration of creep deformation in creep tests at low and constant stresses and by the occurrence of brittle rupture. As a matter of creep acceleration, the accumulated strain to rupture can be much larger (by a factor λ) than the strain that would accumulate within the same time period at constant minimum creep strain rate (figure 1). This provides a good balance between creep rupture strength and creep ductility and enables reliable operation of alloys subjected to tertiary creep. A detailed knowledge and understanding of the laws describing creep acceleration processes and its effect on failure of components is of fundamental interest for the development and application of materials at high temperatures.

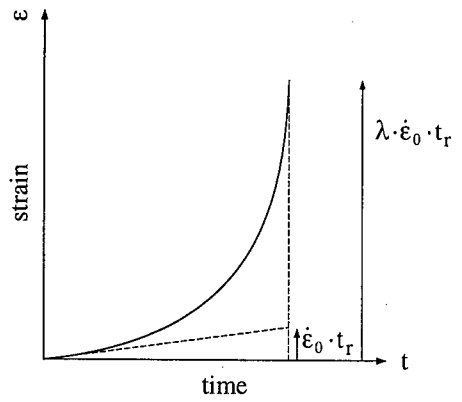

Fig. 1: Determination of the quantity λ

The Rabotnov – Kachanov (R-K) equations represent a phenomenological theory of creep acceleration and of creep rupture [1,2]. The theory accounts for stress redistribution provided by the softening effect of damage on creep strain rates. Two state equations describe the growth of damage and the effect of this damage on creep strain rate by using a single state variable, the so-called damage parameter ω. It is assumed that the growth rates depend on stress as well as on damage giving state equations of the type:

$$\dot{\omega} = f(\sigma,\omega)$$
$$\dot{\varepsilon} = g(\sigma,\omega)$$

Various creep strain growth processes and their effect on the strain to rupture can be described by an appropriate definition of the functions $g(\sigma,\omega)$ and $f(\sigma,\omega)$. However, a more general creep law, which is free of state variables, can sometimes be developed from such state equations to describe the same process. In the case of the R-K equations, the knowledge of a more general creep law of tertiary creep is of fundamental interest from the viewpoint of remanent life assessment and creep failure analysis based on strain rather than damage analysis.

The aim of this paper is to demonstrate that a more general creep law can indeed by developed from the R-K equations. Application of this alternative creep law along with the R-K equations provides new opportunities for life and failure predictions. Main emphasis shall be given to the question of "what can be learned from the R-K equations about damage and failure besides the R-K predictions".

2. Discussion of the Rabotnov – Kachanov Equations

The Rabotnov – Kachanov equations are characterized by power laws of stress and damage. They are represented by the following kinetic equations [2]:

$$\dot{\omega} = \frac{c\sigma^k}{(1-\omega)^r} \qquad (1)$$

$$\dot{\varepsilon} = \frac{a\sigma^n}{(1-\omega)^q} \qquad (2)$$

Integration of the equations (1) and (2) in consideration of the boundary value conditions that the damage parameter ω is zero at time zero and that it is one at the time to rupture leads to relations between damage and consumed strain and life fractions, which are given by

$$\frac{t}{t_r} = 1 - (1 - \omega)^{1+r} \tag{3a}$$

$$\frac{\varepsilon}{\varepsilon_r} = 1 - (1 - \omega)^{r+1-q} \tag{3b}$$

Insertion of the expression within the bracket of equation (3a) into equation (3b) leads to an expression for the strain-time trajectory

$$\varepsilon(t) = \dot{\varepsilon}_0 \, t_r \, \lambda \left\{ 1 - \left(1 - \frac{t}{t_r} \right)^{\frac{1}{\lambda}} \right\} \tag{4}$$

with a material constant λ determined by (figure 1)

$$\lambda = \frac{r+1}{r+1-q} = \frac{\varepsilon_r}{\dot{\varepsilon}_0 \cdot t_r} \tag{5}$$

It follows from the equations (1) to (5) that there is an excess of constants for the representation of creep curves. For example, if the value of λ in equation (5) is fixed, the values of the constants r and q can still be varied without altering the shape of the creep function (4). As a consequence, different damage evolution functions $\omega(t)$ can be fitted to one and the same creep function (4) with different values of the constants r and q.

The equations (3) to (5) suggest, that there is a remnant strain problem. It is not possible to predict the remnant strain and the remnant life only from an analysis of creep strain growth characteristics without the knowledge about the damage evolution $\omega(t)$. In particular, equation (4) suggests that the time to rupture and the strain to rupture had to be known, before the strain-time trajectory can be expressed.

It has been suggested by Goodall and coworkers that the value of λ would give a better measure of the effective ductility than the strain to rupture[3]. This is because it takes into account of the ability of the material to stress redistribution, which can have a beneficial effect on the creep-lifetime of components and of structures in the presence of stress concentrators. Their study brings as a result, that the value of λ should be larger than 10 in order to attain the full beneficial effects of stress redistribution. Leckie and Hayhurst applied the R-K equations to determine the time to rupture in a constant strain rate test and found that the time to rupture increases with increasing value of the constant λ [4]. According to the R-K equations large values of λ are attained, when the relative effect of damage on the creep strain rates given by the difference between the material constants (q-r) is large (equation 5).

Within the frame of the R-K theory the constant λ is a strain and stress independent quantity. It suggests, that the effectiveness of stress redistribution does not alter with strain and time. On the other hand, besides the predictions of the R-K theory, where tertiary creep can no longer be modeled with

only one state parameter, the effectiveness of stress redistribution is likely to alter with time and strain. However, there is no fundamental reason, why the R-K equations could not be applied to characterize temporary stress redistribution, if the value of λ could directly be determined for each state from the exploitation of specific creep growth characteristics.

3. An Analytical Solution of the Remnant Strain Problem

The growth equation for the strain rate (2) suggests that creep will accelerate to infinity, when the damage parameter ω will grow towards a value of one. Consequently, a creep acceleration parameter δ, which id appropriately defined as

$$\delta \equiv -\frac{d\log\dot{\varepsilon}}{d\varepsilon} = -\frac{\ddot{\varepsilon}}{\dot{\varepsilon}^2} \tag{6}$$

is expected to increase to infinity, when the strain grows towards the value of the strain to rupture.

The creep acceleration parameter, which results from the R – K equations can be determined from the first and second time derivatives of the creep strain function (4), which leads to

$$\delta(t) = \frac{(1-\lambda)}{\lambda}\cdot\frac{1}{\dot{\varepsilon}_0\cdot t_r}\cdot\left(1 - \frac{t}{t_r}\right)^{-\frac{1}{\lambda}} \tag{7}$$

Equation (7) confirms that the creep acceleration parameter will indeed grow to infinity towards the time to rupture. Insertion of the expression within the bracket of equation (7) into the same bracket expression of the creep strain function (4) leads to a relation between remnant strain and creep acceleration, which is given by:

$$1 - \lambda = \delta_i\,(\varepsilon_r - \varepsilon_i) \tag{8}$$

In this equation δ_i represents the creep acceleration at an arbitrary strain ε_i and ε_r represents the strain to rupture (figure 2). It follows from equation (8) that the value of λ can be determined by measuring the value of the creep acceleration parameter δ at two different strains. As a result, the remnant strain can be determined through equation (8) and the remnant life through equation (3). This is the analytical solution of the remnant strain problem of the R-K theory.

A generalized differential equation for the coupled strain and life exhaustion processes can now be gained through differentiation of the creep acceleration of equation (8) with respect to strain. It is given by:

$$\frac{d\delta(\varepsilon)}{d\varepsilon}\cdot\frac{1}{\delta^2} = \frac{\delta'}{\delta^2} = C_G = \frac{1}{1-\lambda} \tag{9}$$

Thus, any creep curve, which can be described by means of the R-K state equations can alternatively be described by a differential equation of creep acceleration growth with a single material constant C_G, which is directly related to the material constant λ of the R-K theory.

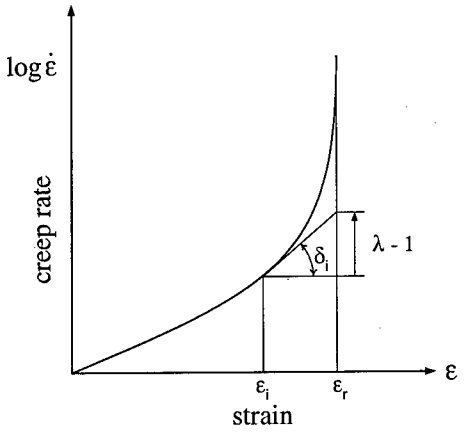

Fig. 2: Relationship between the strain to rupture and the constant λ.

Integration of equation (9) leads to the following expressions for the creep strain rate and creep strain growth:

$$\frac{\dot{\varepsilon}}{\dot{\varepsilon}_0}(\varepsilon) = (1 - C_G\delta_0\varepsilon)^{-1/C_G} \tag{10}$$

$$\varepsilon(t) = \frac{1}{\delta_0 C_G}\left\{1 - \left(1 + \frac{\delta_0\dot{\varepsilon}_0}{1+C_G}\right)^{C_G+1}\right\} \tag{11}$$

The initial creep acceleration δ_0 and the initial creep rate are measurable quantities with different stress dependencies. The creep acceleration growth C_G is a stress and strain independent constant within the frame of the R-K theory and is related to the stress redistribution capability λ through equation (9). The main benefit of equation (9) is the opportunity of determining the value of λ directly from the measurement of the creep acceleration and its strain derivative.

Equation (9) is an alternative mean to the R-K equations to describe the growth of the creep strain rate and the exhaustion of remnant strain (equation 8). The R-K state equation approach is using only one state variable and will therefore not be able to predict the full spectra of possible tertiary creep curves. However, the creep equation (9) can easily be extended by defining an appropriate creep acceleration growth function $C_G(\varepsilon)$.

4. Application of the Creep Acceleration Growth Function $C_G(\varepsilon)$

4.1 Besides the Rabotnov – Kachanov Predictions

Any tertiary creep curve, which is predicted by the R-K equations, is characterized by a constant creep acceleration growth. Thus plotting of the creep acceleration growth C_G as a function of strain would give a straight line parallel to the x-axis. It is interesting to note, that also the strain hardening law for primary creep is characterized by a strain independent value of the creep acceleration growth function $C_G(\varepsilon)$ (figure 3).

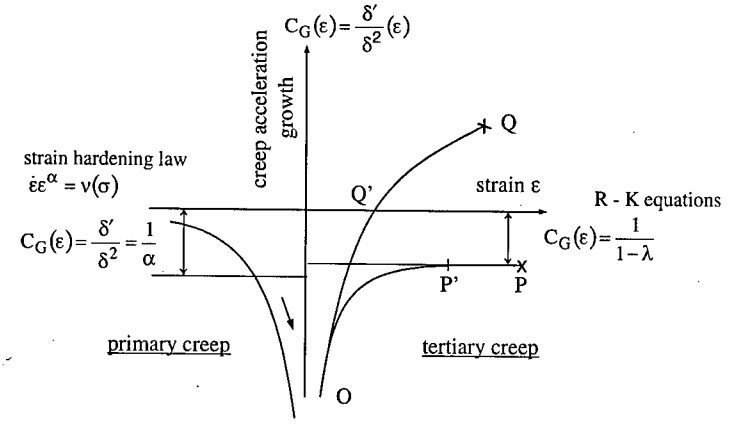

Fig. 3: Representation of the creep acceleration function with $C_G(\varepsilon)$ for various manifestations of creep with negative values of $C_G(\varepsilon)$ below the x-axis and positive values of above the x-axis $C_G(\varepsilon)$.

The R-K equations predict a finite creep acceleration δ at the minimum creep rate (t = 0 in equation 7). Since the minimum creep rate is characterized by zero creep acceleration, a pole is to expect for the creep acceleration growth function $C_G(\varepsilon)$ on the tertiary side of a true minimum creep rate. The fact that a point of minimum creep rate is reached at a finite time and strain of primary creep suggests that there will also be a pole on the primary side of the creep curve.

The deviation from the R-K prediction besides the minimum creep rate is influenced by the effect of plastic deformation on the work hardened state. A creep path, which comes close to the R-K prediction in the end-stages of tertiary creep could be OP'P. On this creep path the effectiveness of stress redistribution, which is quantified by the value of λ, is suggested to increase from the point O to the point P'. This implies that the state of minimum creep rate represents a state of minimum stress redistribution. Within the frame of the R-K theory, the stress redistribution effectiveness λ is determined by the relative values of the constants q and r, which will no longer be constants, when the work hardened state alters. On the path OP' for example, it is near to assume, that the work hardened state degrades (softens) under the influence of damage accumulation, which provides an increasing effect of damage on creep strain rates quantified by the parameter q.

Large deviations from the predictions of the R-K theory are found in creep curves, in which the creep acceleration function $C_G(\varepsilon)$ takes positive values. On the path OQ'Q pictured in the figures 3 the creep acceleration parameter δ initially growths between O and Q' and starts to decrease again above the state point Q' (figure 4). The creep acceleration parameter δ tends to decrease to a value of zero towards the state point Q. In this case large stress redistribution capabilities appear to be generated between O and Q', which however, do not directly affect the remnant strain. The total strain to rupture, and particularly the potential remnant strain at the point Q, will depend on the effect of damage on the creep strain rate influenced by the work hardened state, which has developed towards the point Q.

Failure of the material expresses the end of a creep growth process, which occurs at a finite strain. It is a key property of the creep acceleration function $C_G(\varepsilon)$ that failure paths end up (marked by an x in figure 3 and figure 4). The end points of theses paths can be found by integration of the creep acceleration growth function $C_G(\varepsilon)$, since the creep acceleration parameter will growth to infinity (OP in fig. 3,4) or it will decline towards zero (OQ in fig. 3,4) during integration.

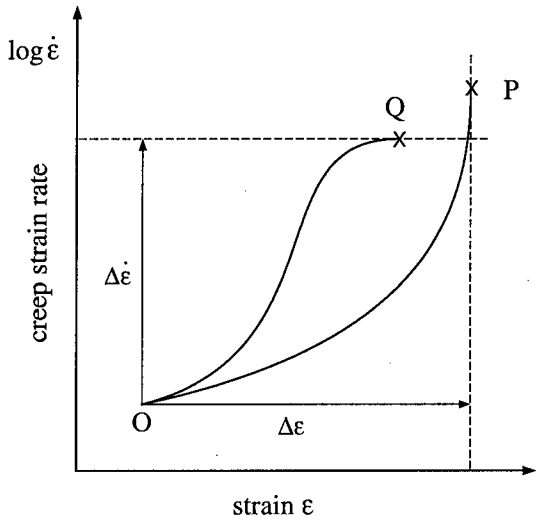

Fig. 4: Exhaustion of remnant strain (OP) and exhaustion of creep strain rate growth (OQ) of fig. 3

Failure predictions base on hypotheses of specific exhaustion processes. The two different failure paths OP and OQ shown in figure 4 will be characterized by application of the creep acceleration function $C_G(\varepsilon)$ and of the R-K equations (1-2) in more detail in the following two sections. In the first case (OP), which is called ductility exhaustion, failure is characterized by the growth of the creep acceleration parameter δ towards infinity and failure is rationalized to be a consequence of the exhaustion of creep strain growth. In the second case (OQ), which is called softening exhaustion, failure is characterized by the decline of the creep acceleration parameter δ towards zero and failure is rationalized to be a consequence of exhaustive growth of the creep strain rate.

4.2 Ductility Exhaustion

In figure 5 different creep acceleration growth paths with negative values of the creep acceleration growth function $C_G(\varepsilon)$ are considered. At point A the creep acceleration parameter δ_A as well as the creep acceleration growth parameter $C_G(A)$ are assumed to be known.

The growth of the creep acceleration parameter δ_A between the creep states A and any other creep state P_i can be calculated by integration of the differential equation (9), which gives

$$\int \frac{1}{\delta^2(\varepsilon)} \cdot \frac{d\delta}{d\varepsilon}(\varepsilon)\, d\varepsilon = \int \frac{1}{\delta^2}(\varepsilon)\, d\delta = -\frac{1}{\delta} + C \qquad (10)$$

For a constant value of the creep acceleration growth $C_G(\varepsilon)$, the remnant strain AB is given by the integral:

$$\int_{\varepsilon_A}^{\varepsilon_r} \frac{\delta'}{\delta^2} d\varepsilon = -\frac{1}{\delta}\Big|_{\delta_A}^{\infty} \tag{11}$$

The value of the creep acceleration parameter δ_A equalizes the reciprocal value of the area A_{OABC} (equation 8).

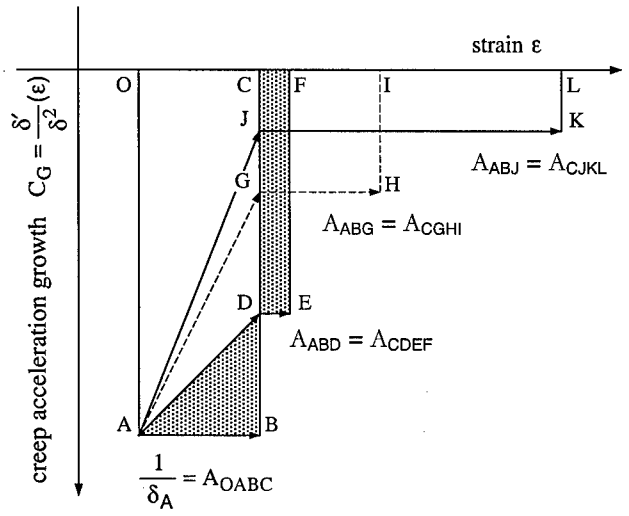

Fig. 5: Representation of the area relations expressed by the integral equations (10) and (11)

The growth of the creep acceleration function $C_G(\varepsilon)$ along the path AG is now considered. The reciprocal value of the creep acceleration parameter δ_G at the point G follows from the integral (11) to be given by the area A_{ABG}. If the creep acceleration function $C_G(\varepsilon)$ would be constant from the point G on, the resulting remnant strain GH would follow from the area condition $A_{ABG} = A_{CGHI}$. In this particular case the remanent strain GH is the same as the remnant strain AB. It appears that the vector AG points to a direction of ductility conservative tertiary creep, which is characterized by the fact that this creep acceleration growth process does not immediately limit the achievable strain to rupture. Moreover, along the path AJ the expectations to the remnant strain even increase.

Besides the predictions of the R-K theory it becomes possible to differentiate between paths of continuous ductility exhaustion and paths of ductility conservation. As long as the creep acceleration growth function $C_G(\varepsilon)$ is not constant, the effectiveness of stress redistribution is suggested to increase starting from the minimum creep rate in both cases. However, the effectiveness of stress redistribution saturates in the case of ductility exhaustive creep. The saturation of λ can be related to an increased susceptibility to crack initiation, since the remnant strains are going to be exhausted through limited stress redistribution. As opposed to that, ductility conservative creep can be characterized by an ever-increasing capability for stress redistribution.

So far, stress redistribution has always been characterized through its relation to remanent strain. One would like to get a more physical picture of stress redistribution, by considering of how it is

determined by damage accumulation. For that purpose, the strain dependence of damage shall be considered. The general relation between the strain fraction and damage is given by equation 3b:

$$\frac{\varepsilon}{\varepsilon_r} = 1-(1-\omega)^{1+r-q} \qquad (12)$$

Since the value of the damage parameter increases with proceeding strain, the relative value of (r-q) has to increase, if the strain fraction shall decrease with proceeding damage accumulation as is the case with ductility conservative creep. According to that, the relative effect of damage on creep will increase. On the other hand, the relative difference (q-r) affects the strain derivative of damage according to:

$$\frac{d\omega}{d\varepsilon} = \omega_0'(1-\omega)^{q-r} \qquad (13)$$

The strain derivative of damage can dependent on the relative values of q and r decrease or increase. However, if the value of q begins to increase over r, the strain dependence of damage will decrease, which reflects spreading out of damage from more strained regions of high stress concentrations into less strained regions.

In order that large values of λ can be measured through the time to rupture, the strain to rupture and the minimum creep rate (figure 1, right side of equation 5), the creep acceleration growth parameter $C_G(\varepsilon)$ will have to start to growth from small values to large values. The apparent creep damage tolerance, which is provided by large values of the so determined λ, can through the registration of the creep acceleration growth $C_G(\varepsilon)$, be experienced by an ever-increasing reassessment of remnant strain during tertiary creep. Application of the R-K theory brings as a new result, that creep damage is probably provided by an augmenting but finally saturating stress redistribution. The state equations can picture stress redistribution as a spreading out process of damage from points of high stress concentrations.

4.3 Softening Exhaustion

In figure 6 the case of an inversion of creep acceleration growth is considered. Moving from a point A, which is characterized by a creep acceleration δ_A and a creep acceleration growth $C_G(A)$, towards a point C will result in a temporary maximum of the creep acceleration parameter δ_C. Above the creep state C, the creep acceleration parameter will decline again.

The integral equation (10) can be applied to determine the strain, when the same initial creep acceleration δ_A is reached again at larger strains. It follows from the integral equation 10 that the same creep acceleration δ_A is re-attained, when the condition of area $A_{ABC}=A_{CEF}$ is fulfilled. Obviously, further growth of the creep acceleration function $C_G(\varepsilon)$ in the direction of the vector CF would finally end up with zero creep acceleration, which would represent a state of pseudo steady state creep.

If the creep acceleration δ would growth again from the point F on, there would be a discontinuance in the creep acceleration function from F to for example A'. It is then interesting to note that an alternative path can be found in order to readjust the same creep acceleration δ_A, like for example the path CG (the area below the function CG is same as the area CEF). Since the creep acceleration declines weaker on the path CG than on the path CF, creep strain rate grows stronger on the path CG than on the path CF. Thereby, the total increase of the creep strain rate is larger on the path

ACG than on the path ACF, whereas the renewed growth of the creep acceleration parameter δ will begin at larger strains.

Similar to the ductility exhaustive and the ductility conservative path of the previous section, on can differentiate between softening exhaustive paths (ACF) and softening conservative paths (ACG), whereas the exhaustive property refers to the limited growth of the creep strain rate during an inversion from negative to positive values of the creep acceleration function $C_G(\varepsilon)$.

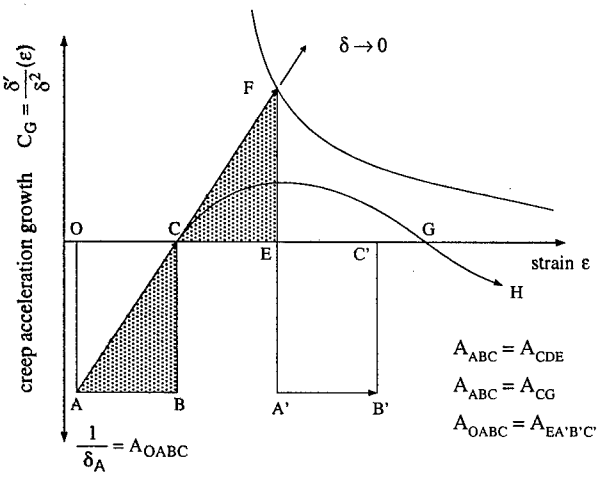

Fig. 6: Representation of the area relations expressed by the integral equations (10) and (11)

Figure 6 suggests that the achievable strain to rupture on the path ACGH is generally larger than the one that can be achieved on the path ACFA'B'. This would be correct for the case that the material provides no large stress redistribution capability at the point A'. The knowledge of the stress redistribution capability at the point A' is important form the viewpoint of a potentially large remnant life (remind that the increase of the creep strain rate from A to F had been limited).

For a rough assessment of the residual stress redistribution capability at point F consider for example the initiation of damage somewhere below the point F. Application of the R-K equations (1-2) results in the following creep acceleration parameter at this point:

$$\delta(\varepsilon) = -q \frac{d\omega}{d\varepsilon} \frac{1}{(1-\omega)} \qquad (14)$$

In order that the creep acceleration parameter δ can further decline either the value of the strain derivative of damage ω' or the effect of damage on creep strain rate (parameter q) should decrease. The strongest decline of the creep acceleration parameter δ occurs, when the parameter q decreases towards the value of r. In this case, the strain derivative of damage ω' will decrease towards the value of zero (equation 13). Consequently, ideal softening exhaustion would be identified with a total exhaustion of the stress redistribution capability. This hypothesis predicts, that no damage characterized by cavities will be observed over a large strain and time fraction of the total rupture time and the rupture strain, since the introduction of cavities will immediately initiate rupture.

A somewhat weaker decline of the creep acceleration parameter δ occurs, when the strain derivative of damage ω' decreases due to an increasing effect of damage on the creep strain rate

(growth of the parameter q). As a result, the creep acceleration δ can weakly decline with a continuously increasing effectiveness of stress redistribution. In this case, the appearance of cavities is suggested to become observable at "smaller" fractions of the total strain to rupture.

5. Summary

The Rabotnov-Kachanov state equations have been studied. A growth law of the creep acceleration has been developed from these state equations. The growth law, which is represented as a differential equation of a defined creep acceleration parameter δ, defines a measurable creep acceleration growth constant C_G, which reflects the effectiveness of the stress redistribution according to the R-K theory. Integration of this differential equation has been demonstrated to be an alternative mean to the R-K equations to describe the growth of creep strain rates and the exhaustion of remnant strain. The solution of this differential equation has been shown to provide a direct assessment of remnant strain and remnant life from registration of the creep strain rate and its strain and time derivatives.

Deviations from the R-K theory have been recognized as an alteration of the creep acceleration growth constant C_G with strain. Deviations from the R-K theory have been characterized by different strain dependences of the creep acceleration growth function $C_G(\varepsilon)$. The R-K theory has been applied to describe the development of the effectiveness of stress redistribution starting from the minimum creep rate. Failure has been discussed in terms of strain exhaustion (ductility exhaustion) and of exhaustion of creep strain rate growth (softening exhaustion). In the former case, initiation of failure has been shown to depend on the saturation of stress redistribution, whereas stress redistribution can be rationalized by the R-K theory being provided by spreading out of damage from points of high stress concentration. In the latter case, initiation of failure has been rationalized to depend on generation and exhaustion of alternative stress redistribution processes, in which the ultimately initiating damage process has no beneficial effect on creep strain rates.

References

1. Kachanov, L.M., 1958, *Izv. Akad. Nauk*, **8**, 26

2. Rabotnov, Y.N., 1969, *Creep Problems in Structural Members*, (Amsterdam: North-Holland)

3. Goodall, I.E. Cockroft, R.D.H. and Chubb, E.J., 1975, *Int. J. mech. Sci*, **17**, 351

4. Leckie, F.A. and Hayhurst, D.R., 1977, *Acta metall. mater.*, 1977, **25**, 1059

Acknowledgments

This study has been made within the frame of a Ph.D. carried out at the Institute of Metallurgy of the Swiss Federal Institute of Technology in Zurich (ETHZ) with the financial support of ABB Management Ltd. The author wishes to thank Prof. M.O. Speidel for the opportunity of making this study. The author further wishes to thank the management of ABB Corporate Research for financial support.

Mailing adress: alkan.goecmen@chcrc.abb.ch

Key Engineering Materials Vols. 171-174 (2000) pp. 231-236
© 2000 Trans Tech Publications, Switzerland

Lattice-Diffusion Creep Mechanism Not Based on Stress Heterogeneity (1)

G. Itoh[1] and A. Nojima[2]

[1,2] Department of Mechanical Engineering, Nagaoka University of Technology, Kami-Tomioka, Nagaoka, Niigata-Pref., 940-2188, Japan

[2] Graduate Student

Keywords: Lattice-Diffusion Creep, Diffusion Creep, Diffusion Mechanism, Creep Rate Expression, Stress State, Vacancy Concentration, Einstein's Equation

Abstract

It has been deduced that there is a serious problem in the assumption of the vacancy concentration gradient based on the stress heterogeneity in the Nabarro-Herring mechanism for lattice-diffusion creep. A new lattice-diffusion creep mechanism which is not dependent on the diffusion mechanism and hence is not based on the vacancy concentration gradient has been proposed. Based on this new mechanism, the correlation of the strain rate with applied stress, atomic volume, diffusivity, grain size and temperature has been described as an equation, in the case of uniaxial tensile creep on a cube-shaped grain. The resultant equation was identical with that in Nabarro-Herring mechanism except the factor that depends on the shape of the grain. In the new mechanism, the diffusion was presumed to be caused by a force which applies each atom in the grain in the direction perpendicular to the tensile axis. This force was thought to arise to keep the grain volume constant during the plastic deformation. Another mechanism proposed by Kimura has been referred to. Both Kimura's and the authors' mechanisms have been considered to be more plausible than the Nabarro-Herring mechanism in that they are not based on stress heterogeneity, although modification by a further study is needed to correlate the elementary process of diffusion, i.e., vacancy mechanism.

Introduction

The mechanism of the lattice-diffusion creep proposed by Nabarro [1] and Herring [2] (this will be abbreviated to N-H mechanism) has been so widely accepted that the lattice-diffusion creep is also called Nabarro-Herring creep in most textbooks, research papers, reviews, etc. In this mechanism, in the case of uniaxial tensile creep, it is assumed that the vacancy concentration at a grain boundary perpendicular to the tensile axis is raised from the equilibrium vacancy concentration without stress because of the tensile stress, and that the concentration at a boundary parallel to the tensile axis is lowered because of the compressive stress. This concentration difference (concentration gradient) causes the diffusion of vacancies, namely the diffusion of atoms in the reverse direction as schematically illustrated in Fig. 1. The creep rate $\dot{\varepsilon}$ was expressed in the following equation as a function of applied tensile stress σ, grain size d, self-diffusion coefficient D, atomic volume Ω and absolute temperature T [1-4]:

$$\dot{\varepsilon} = B\Omega\sigma D / d^2 kT, \qquad (1)$$

where k is the Boltzmann constant and B is another constant. In several recent papers, Ruano et al. [5] have thrown questions to the experimental results that were thought to be the evidence of this N-H mechanism.

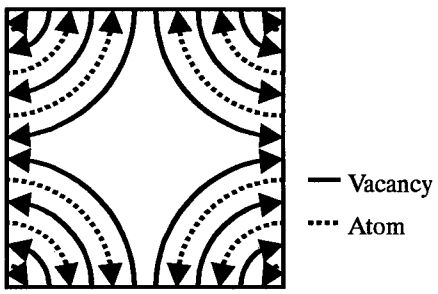

Fig. 1 Schematic drawing showing the diffusional flow based on the Nabarro-Herring mechanism. Flows of vacancy and atom are indicated by solid and dotted arrows, respectively.

On the other hand in the theoretical point of view as well, Mori et al. [6] pointed out that there should be no difference in the vacancy concentration because the stress state is identical at both boundaries perpendicular and parallel to the tensile axis, having no hydrostatic component. Since the N-H mechanism is deeply based on this vacancy concentration gradient, following discussion will no longer make sense if there is no such vacancy concentration gradient. Mori et al. claimed the necessity of grain boundary sliding to bring about the vacancy concentration difference at grain boundary triple junctions, as shown in Fig. 2. However, it will be difficult to interpret many experimental results [1, 4, 7] obtained on the specimens having what is called bamboo structure that has grain boundaries exclusively perpendicular to the tensile axis with no triple junctions as illustrated in Fig. 3. Hence, some other mechanism for the lattice-diffusion creep was needed to understand the experimental results. From this viewpoint, the authors proposed a new theory on the mechanism of lattice-diffusion creep which is not based on the vacancy concentration gradient [8]. Being independent of the authors, Kimura proposed another new theory which is not based on the stress heterogeneity either [9]. In this paper, the two new theories will be re-described and briefly discussed.

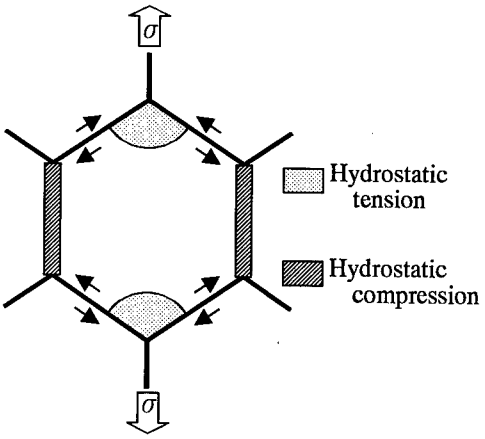

Fig. 2 Formation of heterogeneity in hydrostatic stress arising from grain boundary sliding in a polycrystalline material, according to Mori et al. [6]

Migration of atoms not based on the stress heterogeneity [8]

Assume that a tensile stress σ is applied in z direction of a cubic grain (simple cubic lattice with lattice constant a) of side length d, causing elastic strain ε_{el}. In x and y direction strain $-\nu\,\varepsilon_{el}$ (compression) is produced where ν is the Poisson's ratio, and the increase in elastic energy from unstressed state is $\sigma\,\varepsilon_{el}/2$. If the grain is kept with constraint only in z direction at a temperature where diffusion occurs, like a stress relaxation test, plastic contraction due to diffusion will take place in x and y directions, and the initially elastic strain ε_{el} will be converted to a plastic strain ε_{pl} after sufficiently prolonged time, reducing the energy increment from $\sigma\,\varepsilon_{el}/2$ to zero. This process is schematically illustrated in Fig. 4. Although in this discussion, the diffusion mechanism is not discussed (that is to say, the vacancy concentration difference is not indispensable), the driving force of the diffusion should surely exist, since the energy decreases owing to the diffusion. However, usual Fick's law on diffusion cannot be applied to this situation, because there is no concentration gradient. Instead, if a force F operates in the direction of the migration of atoms, Einstein's equation,

$$V = -M\nabla\mu = MF = DF/kT, \qquad (2)$$

can be used to describe the migration velocity of atoms, where M and μ are the mobility and chemical potential, respectively, and there is a relationship of $M=D/kT$ between D and M.

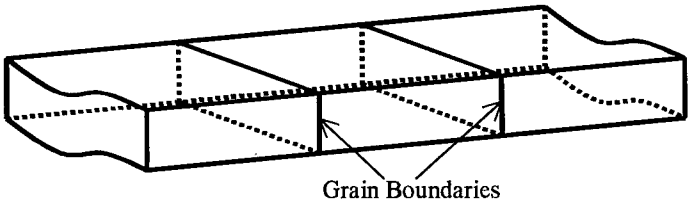

Fig. 3 Schematic drawing of what is called bamboo structure.

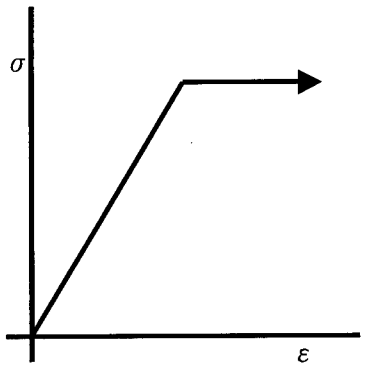

Fig. 5 Stress-strain history of a specimen subjected to a tensile creep test.

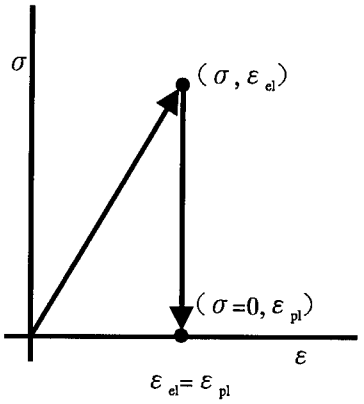

Fig. 4 Stress-strain history of a specimen initially stretched elastically and subsequently kept at fixed ends for very long period at a temperature where diffusion takes place.

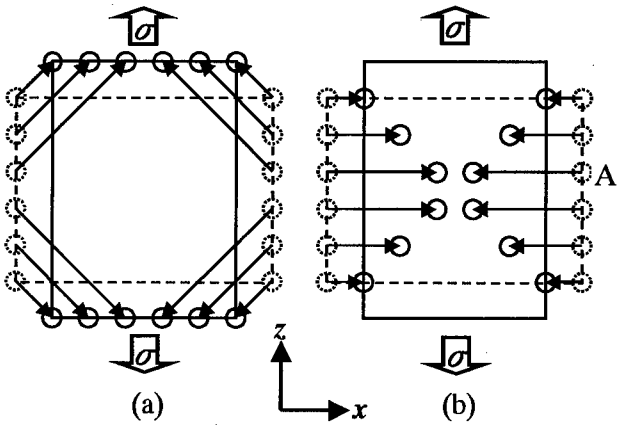

Fig. 6 Schematic diagram showing two kinds of atom diffusion paths. (a): diagonal path from vertical boundary to horizontal one, (b): shorter path from vertical boundary to grain interior.

Description of creep rate [8]

Next, the stress is assumed to be applied continuously like actual creep, as illustrated in Fig. 5. At the first step, consider that monolayer of atoms at the lateral boundaries move to the upper and lower boundaries as in the N-H mechanism as schematically shown in Fig. 6 (a). The final shape of the grain does not depend on whether the atoms move to the upper or lower boundary, and thus the net component of the atomistic force F in z direction should be zero. Actually, there is no need for the atoms at the lateral boundaries to reach the upper or lower boundaries; they can simply enter the interstitial site inside the grain. Therefore, a migration path, as is illustrated in Fig. 6 (b), can be assumed in order to attain uniform plastic strain of two atomic layers in z direction with minimum diffusion distance. Assume that only the atoms at the two y-z boundaries move in x direction, then the number of moving atoms is that of monolayer of atoms of the two lateral boundaries, namely $2(d/a)^2$, and the average migration length is $d/4$, providing the total deformation

distance

$$\Delta X=(d/4)\times 2(d/a)^2 = d^3/2a^2. \quad (3)$$

In the actual deformation, identical strain can be obtained if the atom A in Fig. 6 (b), for example, does not move directly to the grain center but another atom does, by receiving the baton so to speak. Thus, all atoms in the grain may be considered to relate to the deformation. Since the total number of atoms in the grain is $(d/a)^3$, average migration distance Δx for an atom is expressed as

$$\Delta x = \Delta X/(d/a)^3 = a/2. \quad (4)$$

The F has been defined as a force which is the driving force of the diffusion and is applied to an atom, and hence the work w_1 which has been done by this force to an atom in the deformation is given by

$$w_1 = F\Delta x = aF/2. \quad (5)$$

On the other hand in the macroscopic point of view, tensile load of $\sigma \times d^2$ has brought about the deformation amount of $2a$. Therefore, the work per an atom, w_2, which has been done by this tensile load should be,

$$w_2 = \sigma d^2 \times 2a/(d/a)^3 = 2\sigma a^4/d. \quad (6)$$

Since the work given by the force F to an atom must coincide with that per an atom obtained from macroscopic work, that is $w_1 = w_2$,

$$aF/2 = 2\sigma a^4/d$$

$$F = 4a^3\sigma/d = 4\Omega\sigma/d, \quad (7)$$

where Ω, the atomic volume, is equal to a^3. From Einstein's equation (Eq. 2) and Eq. 7,

$$V = FD/kT = 4\Omega\sigma D/dkT. \quad (8)$$

From Eqs. (4) and (8), letting the time for the deformation be t,

$$t = \Delta x/V = (a/2)/(4\Omega\sigma D/dkT) = adkT/8\Omega\sigma D. \quad (9)$$

Since the strain of $2a/d$ is produced within this time, strain rate $\dot{\varepsilon}$ is given by

$$\dot{\varepsilon} = (2a/d)/t = 16\Omega\sigma D/d^2kT. \quad (10)$$

This is the final description of strain rate in the lattice-diffusion creep by the present authors which is not based on stress heterogeneity. As mentioned earlier, the N-H mechanism generally provides the creep rate described in Eq. 1, where the constant B which depends on shapes of the crystal grain etc. was initially 2 [4], and was reported to be 12 after the diffusion path was re-discussed for the cube-shaped grain [8]. It should be noted that both mechanisms result in almost the same final form, although the starting point has been completely different. It must be emphasized again that compressive stress never exists from macroscopic elasticity theory, although it is apparently seen as if the F corresponded to the compressive stress in x direction which is a premise in the N-H mechanism. The F can be regarded as the force which intends to keep the volume of the grain constant in the plastic deformation.

Kimura's theory

As mentioned previously in the introduction, being independent of the present authors, Kimura [9] also lead the same equation as Eq. 10 without using stress heterogeneity very recently. He discussed based on the activation energy for deformation schematically shown in Fig. 7. In this theory, when a stress σ is applied, the activation energy for a process that favors the

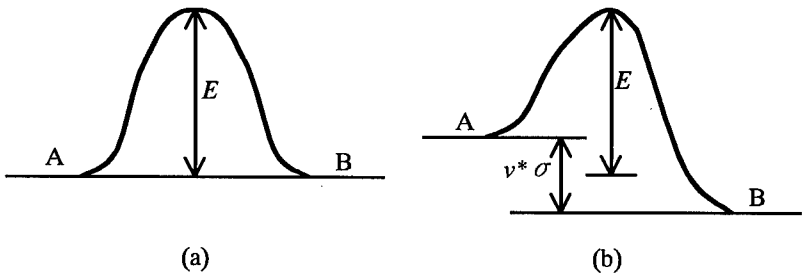

Fig. 7 Activation energy for a jump of an atom in diffusion. (a) without stress, (b) with stress.

deformation is lowered while that for the reverse process is raised compared to that without stress, E. When diffusional deformation by ΔL occurs in a columnar grain with cross section area S and length L, from the macroscopic work done by the tensile stress, $\sigma S \Delta L$, and from the number of atoms moving from the lateral boundary to the upper or lower boundary, $S \Delta L/\Omega$, the work done per an atom (w_2 in the authors' theory) is described as $\sigma \Omega$. Since he considered the diffusion path to be of the distance of $L/2$ only in z direction, energy gradient along the diffusion path became $2\sigma \Omega/L$, giving the energy difference between the sites A and B in Fig. 7 of $v^* \sigma = 2b \sigma \Omega/L$ where b is the jump distance corresponding to a in the authors' theory. In the case of random jump, both jump frequencies in the direction A to B and B to A in Fig. 7 (a) are given by $6D/b^2$. The activation energy E naturally corresponds to that for self-diffusion and has an Arrhenius-type relationship with self-diffusion coefficient D of

$$D = C\exp(-E/kT)$$

where C is a constant. In the stressed state on the other hand, the difference in the jump frequency, Δf, between A to B and B to A is given by

$$\Delta f = \frac{6C}{b^2}\left\{\exp\left(-\frac{E - v^*\sigma}{kT}\right) - \exp\left(-\frac{E + v^*\sigma}{kT}\right)\right\} \tag{11}$$

$$= \frac{6C}{b^2}\exp\left(-\frac{E}{kT}\right)\left\{\exp\left(\frac{v^*\sigma}{kT}\right) - \exp\left(-\frac{v^*\sigma}{kT}\right)\right\}$$

$$= (12/b^2)D \sinh(v^*\sigma/kT) = (12D/b^2) \times (2b\sigma\Omega/kTL)$$

$$= 24\Omega\sigma D/d^2kT, \tag{12}$$

when $v^*\sigma/kT = 2b\sigma\Omega/kTL$ is close to zero. Since, the number of atoms reaching the top or bottom boundary during unit time (1s) is $\Delta f \times (S/b^2)$, and deformation amount is b^3/S when an atom moves by a distance b, the deformation amount in unit time becomes $\Delta f (S/b^2) \times b^3/S = b\Delta f$. Hence, the creep rate is given by

$$\dot{\varepsilon} = b\Delta f/L. \tag{13}$$

From Eqs. 12 and 13, the creep rate is finally expressed as

$$\dot{\varepsilon} = 24\Omega\sigma D/L^2kT, \tag{14}$$

where the final form is again the same except the constant B.

Minor correction may be needed in the above treatment; the $v^*\sigma$ in Eq. 11 should be replaced by $v^*\sigma/2$, and the final form will be

$$\dot{\varepsilon} = 12\Omega\sigma D/L^2kT, \tag{15}$$

since $v^*\sigma$ has been defined as the total difference in the potential energy between the two sites A and B, with an average activation energy of E.

Discussion

Since neither the authors' nor Kimura's theory is based on vacancy concentration gradient or heterogeneity of the stress state in a grain, the two theories might provide a precise premise for the lattice-diffusion creep. The major difference is in the direction of atom migration, that is, the direction of the force applied to the atom, and another difference is that hypothetical motion into the interstitial site is assumed in the authors' theory. The use of energy gradient or activation energy and the use of the force applied to the atom are basically the same. If the energy gradient in z direction actually exists, the process by Kimura using activation energy is strict, and seems to be the origin of the Einstein's equation with chemical potential since the energy gradient becomes chemical potential gradient in a pure metal. However, in his theory migration in x and y direction is not assumed, which is essential in the lattice-

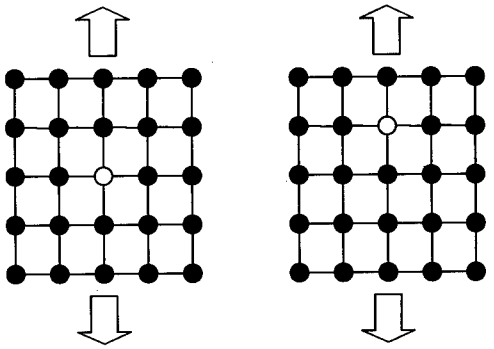

Fig. 8 A jump in z direction of an atom/vacancy pair with no work done by the tensile stress.

diffusion flow. Moreover, no work is done as long as the atom jumps in z direction in the grain interior, as illustrated in Fig. 8, and therefore it may be a problem that no energy gradient in z direction is thought to exist. The author' theory has similar problem when the actual diffusion mechanism, that is, vacancy mechanism is taken into account. The atom on the lateral boundary cannot move into an interstitial site but must move into a vacant lattice site. Consequently, no work will be done either, when the atom jumps in x or y direction. In addition, vacancy should be supplied from the top or bottom boundary, which has not been taken into account in the present paper.

Further study will be carried out in the next paper at this conference, based on energy gradient or chemical potential gradient, as well as the interrelations with vacancy mechanism as the actual diffusion mechanism.

Summary

Although the vacancy-concentration gradient which is an essential premise in the N-H mechanism cannot be interpreted in terms of macroscopic stress field, it has been deduced that the elastic energy in the grain is lowered by the diffusion deformation irrespective of the diffusion mechanism, and that the driving force of the diffusion is the force applied to each atom in the direction perpendicular to the tensile axis. The equation describing the strain rate in the lattice-diffusion creep which is not based on stress heterogeneity has been successfully obtained from this discussion. Both Kimura's and the authors' mechanisms have been considered to be more plausible than the N-H mechanism in that they are not based on stress heterogeneity although modification by further studies is needed to correlate the elementary process of diffusion, i.e., vacancy mechanism.

Acknowledgments

The authors are deeply grateful for the financial support from the Light Metal Educational Foundation and from the Iketani Foundation for the Promotion of Science and Technology. The research was also supported by a Grant-in-Aid for Scientific Research (C) from Ministry of Education, Science Sports and Culture of Japan, which is highly acknowledged.

References

[1] F. R. N. Nabarro : *Report of Conference on Strength of Solids*, Phys. Soc. London, (1948), p. 75.
[2] C. Herring : J. Appl. Phys., **21**(1950), p. 437.
[3] H. Oikawa and S. Karashima : Bul. Japan Inst. Metals, **11**(1972), p. 567.
[4] B. Burton : *Diffusional Creep of Polycrystalline Materials*, Trans. Tech. Publications, (1977), p. 1.
[5] For example, O. A. Ruano, O. D. Sherby, J. Wadsworth and J. Wolfenstine : Mater. Sci. Eng. A, **A211**(1996), p. 66.
[6] T. Mori, S. Onaka and K. Wakashima : J. Appl. Phys., **83**(1998), p. 7547.
[7] H. Jones : Mater. Sci. Eng., **4**(1969), p. 106.
[8] G. Itoh and A. Nojima : J. Japan Inst. Metals, **62**(1998), p. 1206.
[9] H. Kimura : *How to Understand the Strength of Materials*, AGNE Gijutsu Center, (1998), p. 369.
[10] G. B. Gibbs : Mém. Sci. Rev. Métall., **62**(1965), p. 781.

Key Engineering Materials Vols. 171-174 (2000) pp. 237-244
© 2000 Trans Tech Publications, Switzerland

A New Era of Grain Boundary Design and Control for High Temperature Materials

T. Watanabe

Laboratory of Materials Design and Interface Engineering, Department of Machine Intelligence and Systems Engineering, Graduate School of Engineering, Tohoku University, Sendai, 980-8579, Japan

Keywords: Grain Boundary Design and Control, Grain Boundary Character Distribution GBCD, Grain Boundary Structure, Fracture Control, Oxidation, Wetting

Abstract

The background of the grain boundary design and control for high temperature plasticity and fracture is discussed showing important findings of structural effects on the related boundary phenomena which have been effectively utilized for development of high temperature materials. Recent progress in grain boundary engineering has been introduced to demonstrate a high potential of this approach to future development of high temperature materials. Some open problems associated with the thermal stability of grain boundary microstructure which may be affected by grain boundary structural transformation and wetting are also discussed.

1. Introduction

Grain boundaries and interphase boundaries are important microstructural elements in polycrystalline materials. They can affect the bulk properties of polycrystalline materials, differently depending on grain boundary phenomenon associated with a specific bulk property. Grain boundaries can play more significant roles in deformation and fracture as temperature increases because grain boundary phenomena become more significantly involved. We also know that grain boundaries (hereafter including interphase boundaries) can affect beneficial or detrimental effects on high temperature plasticity. Unfortunately, their detrimental effects have been extensively studied because serious problems associated with intergranular creep fracture and brittleness must be solved urgently. However now the time has come when their beneficial effects of grain boundaries should be properly understood and effectively utilized in development of advanced materials. At the first Swansea creep conference of this series held in 1981, I presented a small sprout of the possibility of grain boundary design and control, underlining the importance of structural effects on grain boundary sliding and creep fracture observed on metal bicrystals [1]. Soon after then I proposed the concept of grain boundary design and control for strong and ductile polycrystalline materials [2]. Since then the concept has been successfully applied and now a new era of Grain Boundary Design and Control (Grain Boundary Engineering) has come [3,4]. I believe that the concept can provide a new powerful approach to materials design and development in the coming next century, including functional materials as partly proved recently [5].

2. Structural Effects on Grain Boundary Sliding and Fracture in Bicrystals

There are several key issues associated with high temperature materials. Most of them is concerned with grain boundary phenomena such as sliding, migration, segregation, cavitation and fracture. As the result of recent studies of the relationship between grain boundary structure and properties in bicrystals, much knowledge of structural effects on boundary properties have been obtained which can be used to control creep fracture and to enhance creep strength by utilizing beneficial effect of boundaries in the same material. Let us look at some evidences.

Firstly, grain boundary sliding takes place and contributes to creep deformation in a polycrystal, as one of important deformation mechanisms, particularly to superplasticity [6]. Figs. 1(a) and (b) which were presented at the first Swansea Creep conference to demonstrate how grain boundary sliding is related to creep deformation and fracture, and how the boundary type and misorientation angle can affect sliding and fracture in orientation-controlled zinc and copper bicrystals, respectively. We see a large difference of the contribution of grain boundary sliding to the total creep deformation, $\varepsilon_{gb} / \varepsilon_t$, among the bicrystal samples with different misorientation angles. It was found that the contribution was small at low angle boundary and some special high angle boundaries like $\Sigma 9$ coinci-

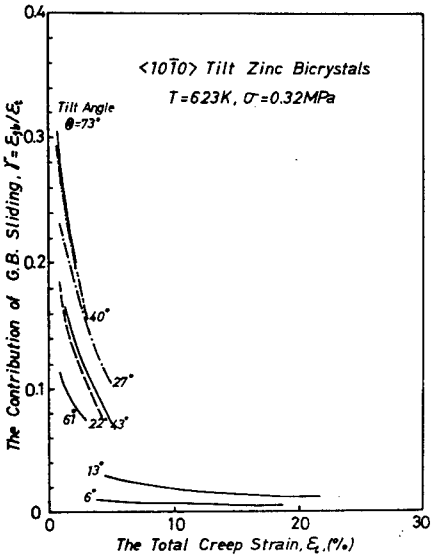

Fig. 1 (a) The contribution of sliding to the total creep deformation of < 10$\bar{1}$0 > tilt zinc bicrystals [1].

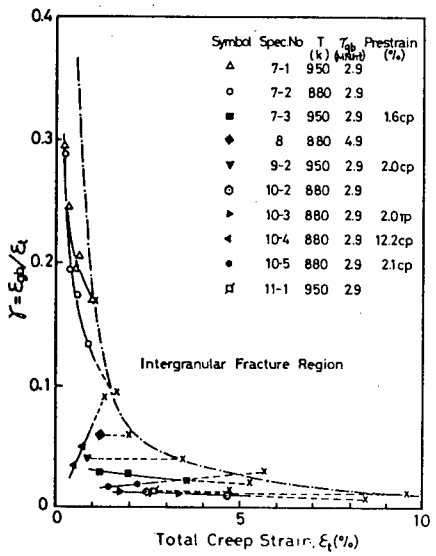

Fig. 1 (b) 'Grain boundary sliding -fracture diagram' for copper bicrystals with different types of boundaries [1].

dence boundary with the misorientation angle of 61°, resulting in slow creep deformation and high resistance to intergranular fracture caused by sliding. This was also confirmed to be valid for grain boundary sliding and fracture in polycrystals[3]. Grain boundary sliding and creep intergranular fracture preferentially took place at random general boundaries, but they were very difficult at low-angle boundary and low Σ coincidence boundaries. Moreover we found that intergranular crack would not propagate into the clustered region of low-angle and special boundaries. Thus we can understand that structural effects are the most important and can be a key factor controlling creep deformation and fracture in polycrystals.

3. The Importance of Grain Boundary Character Distribution (GBCD)

The grain boundary character distribution (GBCD) defining the type and the frequency of grain boundaries and the grain boundary connectivity defining the configuration of different types of boundary, have been found to control creep intergranular fracture in polycrystals. The presence of more random boundaries and their extensive connectivity can promote intergranular fracture and brittleness, as shown earlier [2,3]. Until recently we have been performing experimental and theoretical work for the control of intergranular fracture and brittleness particularly for 'intrinsically brittle' materials by manipulating GBCD. A systematic investigation into GBCD had been made paying particular attention to the evolution of grain boundary microstructure and microscale texture for different types of material produced by different processing methods [7]. It has been found that GBCD can be closely related to the grain size, the type and sharpness of texture. We have proved that the control of GBCD is useful and powerful for the control of brittleness caused by predominant intergranular fracture [3,4,8].

4. Grain Boundary Engineering for High Temperature Materials

4.1 The Control of Intergranular Brittleness in Ni_3Al and Molybdenum

It is well known that intermetallics and ordered alloys have excellent high temperature strength, particularly such as positive temperature dependence of the strength. However severe intergranular brittleness has hindered this type of materials from their development so far. Many attempts have been made to control their intergranular brittleness [8]. The addition of the third element boron was once thought to be a solution of the problem, but later it turned to be not. Recently we have found that intergranular brittleness of polycrystalline Ni_3Al can be controlled by reducing the frequency of weak random boundaries and conversely by increasing the frequency of fracture resistant low Σ boundaries by unidirectional solidification through zone melting even for B-free Ni_3Al [9,10]. As shown in Figs. 2(a) and 2(b), the introduction of a high frequency of low Σ boundaries (Σ1, 3 and 9) could lead to the

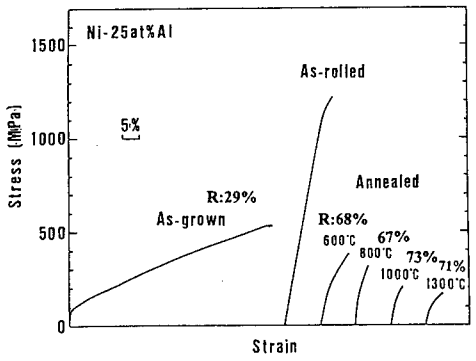

Fig. 2(a) Stress-strain curves of B-free polycrystalline Ni_3Al with grain boundaries differently engineered. Note that the fraction of random weak boundaries control the ductility of this material [11].

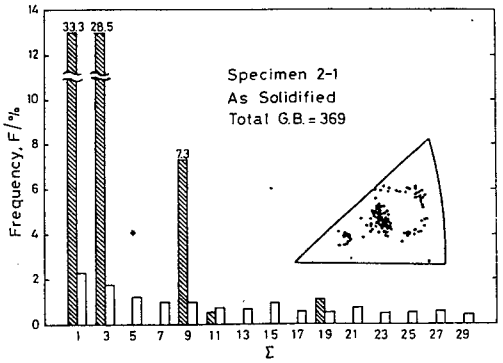

Fig. 2(b) The grain boundary character distribution (GBCD) in as-solidified Ni_3Al with high ductility and sharp texture [11].

development of high ductility in as-grown specimen. But once deformed and annealed, the observed high ductility of the as-grown specimen disappeared and would be never restored. This clearly shows the importance and usefulness of the control of GBCD for the control of intergranular brittleness. The important effect of GBCD on intergranular crack propagation in polycrystalline Ni_3Al was also reported by Lin and Pope [12].

The other example of grain boundary engineering for the control of intergranular brittleness is from a work of polycrystalline molybdenum performed quite recently [13]. Figure 3 shows that the fracture stress systematically increases with increasing the frequency of low Σ boundaries, from the value theoretically predicted for a random polycrystal up to 20% and remains unchanged. This corresponds to a change of fracture mode from dominant intergranular fracture to transgranular cleavage fracture, as previously predicted by modelling of GBCD-dependent fracture and fracture toughness [14]. It is very challenging to test whether grain boundary engineering for the control of intergranular brittleness by manipulation of GBCD is applicable to ceramics. To my knowledge, there has been no literature which reported GBCD-dependent fracture in ceramics, except for a recent work on fracture in piezoelectric ceramic (PZT) performed by the author's group [15,16].

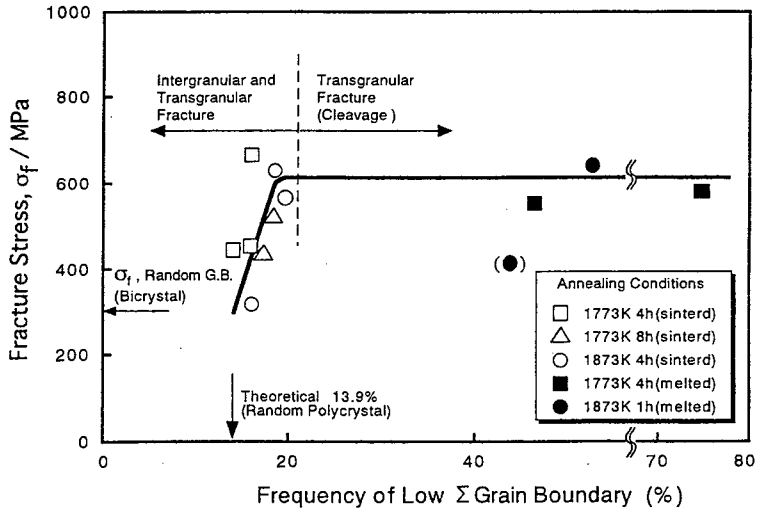

Fig. 3 Fracture stress vs. grain boundary character distribution diagram for polycrystalline molybdenum at 77K [13].

4.2 Enhancement of Creep Strength in Ni-base Alloy

Grain boundaries can be a barrier to the motion of lattice dislocations because of the discontinuity of crystal orientation between neighbouring grains. The absorption of lattice dislocations at grain boundary has been found to be strongly influenced by the boundary type in creep deformation of aluminium [17]. Random boundary can easily absorb them while low Σ coincidence boundary can not. This may affect the effectiveness of grain boundary as barrier to dislocation motion. Figure 4(a) shows creep curves observed on $<10\bar{1}0>$ twist zinc bicrystal specimens with different twist angles [18]. It is evident that creep behaviour of individual specimens strongly depends on the boundary twist angle and surprisingly the presence of a special boundary with the twist angle around 51°~54° (almost corresponding to Σ9/56.6°) can drastically reduce the creep rate. Accordingly this suggests that the introduction of a high frequency of low Σ boundaries would be able to enhance the bulk creep strength of polycrystalline materials because of the difficulty of sliding and of the absorption of lattice dislocations at such low Σ boundaries. In fact this was confirmed recently by Was and coworkers [19]. Figure 4(b) shows that an increase of the frequency of low Σ boundaries from 15% to 30~40% can drastically increase the creep strength, showing a rapid decrease of the steady state creep rate at 360°C by factor of 10 to 30 in ultrahigh-purity Ni-16Cr-9Fe alloy. This is an important finding that high temperature strength of the alloy can be drastically increased by grain boundary engineering without using any conventional strengthening method.

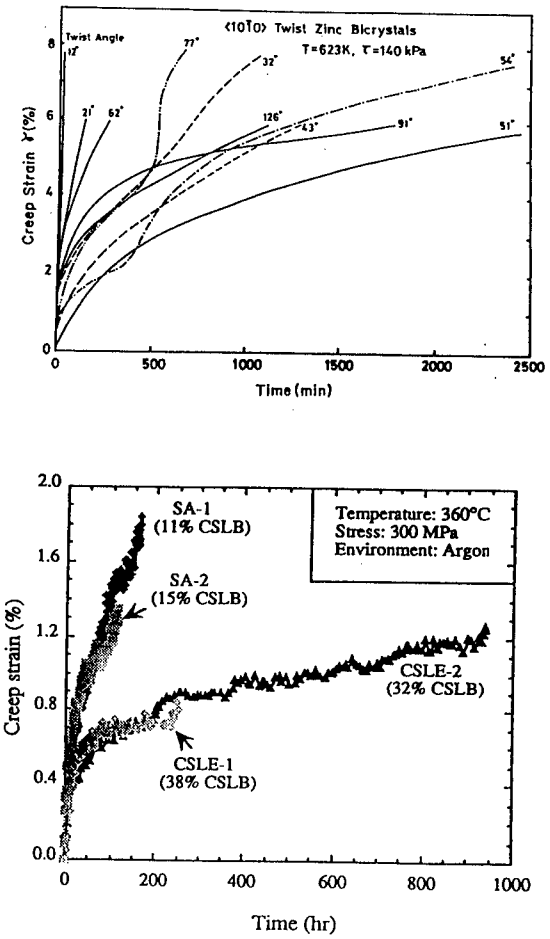

Fig. 4 (a) Creep curves for $<10\bar{1}0>$ twist zinc bicrystals with different twist angles under constant resolved shear stress. Note high creep resistance in the bicrystal with the misorientation angles around 56°/Σ9 coincidence orientation[3], (b) Effect of the frequency of low Σ (CSL) boundaries on creep deformation in Ni-16Cr-9Fe alloy at 360°C, σ=300 MPa[19].

4.3 Optimization of GBCD for Superplasticity in Al-Li Alloy

Recently a new approach to superplasticity has been attempted by grain boundary engineering through the control of the grain boundary character distribution (GBCD) and the grain boundary connectivity [6,20]. In principle, the presence of grain boundaries or interphase boundaries which can easily slide is expected to promote deformation caused by interfacial sliding in single phase or multiphase materials. In single phase material, sliding takes place preferentially at high angle random boundaries when more random boundaries are connected to each other, the plastic strain produced by interfacial sliding become significant. However this situation also leads to predominant intergranular fracture unless the stress concentration at triple junctions or boundary irregularities is relaxed during deformation. Quite recently we have found a salient change of grain boundary microstructure during superplastic deformation in Al-Li based alloy [21]. The change of GBCD observed by using Orientation Imaging Microscope (OIM) are shown along the stress-strain curve in Fig. 5. It was found that the frequency of random boundaries remained almost constant during early stage of deformation up to the peak stress and then increased rapidly showing the reduction of the flow stress producing superplastic deformation characterized by the maximum elongation of 253% (ε=1.3). This finding can well explain the reported early observations on the change of grain boundary microstruc-

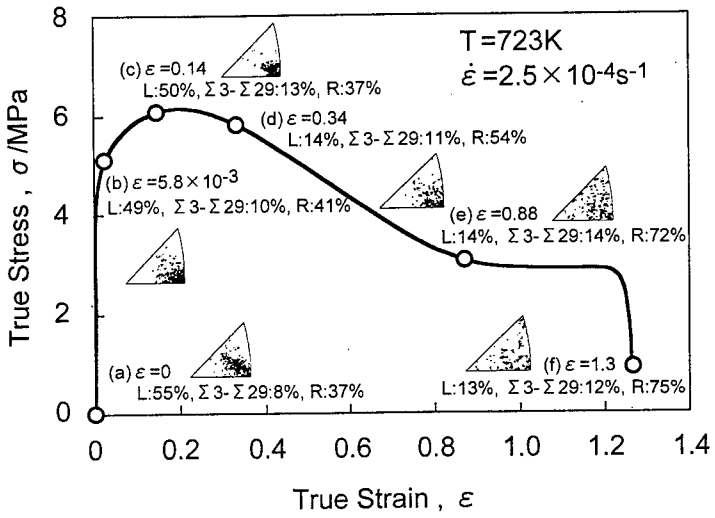

Fig. 5 Changes of the grain boundary character distribution (GBCD) and texture during superplastic deformation in Al-Li-Cu-Mg-Zr alloy[21]. Note that significant changes occurred after the peak stress.

ture that the formation of high angle (random) boundaries results in grain boundary sliding in Al-Li alloy [22] and the change of texture from sharp to random one in Sn-Pb alloy [23], during superplastic deformation. However further consideration of the details of the interaction between GBCD and the grain boundary connectivity and the optimization of GBCD seems necessary because these may be one of key factors controlling superplasticity and post mechanical performance of superplastically deformed material.

4.4 The Control of Oxidation-Induced Brittleness in Ni-Fe Alloy

Oxidation degrades mechanical performance and causes severe brittleness in high temperature materials during their service. The requirements of high temperature strength and formability are not necessarily compatible with oxidation resistance. In particular, selective oxidation along grain boundaries becomes an important source of premature fracture in the materials [24]. This often hinders promising materials from their development. Accordingly the control of oxidation-induced intergranular fracture is one of important issues for development of high temperature materials. As shown in Fig. 6(a) and 6(b), intergranular oxidation does not always occur uniformly but selectively at individual grain boundaries in a polycrystal. It is very likely that the difference of oxidation propensity from boundary to boundary is due to the effect of grain boundary type and structure. However there has been no available literature on structural effect on intergranular oxidation, to the author's knowledge. Quite recently we have studied the effect of grain boundary type on intergranular oxidation and found the possibility of grain boundary engineering for the control of oxidation-induced intergranular brittleness in a Ni-40at%Fe alloy [25] as mentioned below. Figure 7 shows the effect of

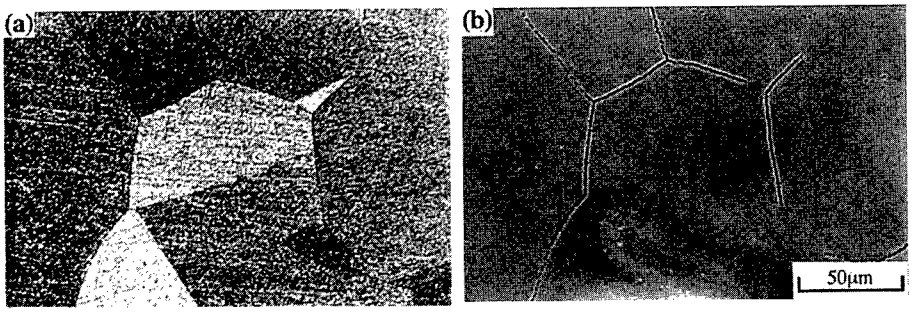

Fig. 6(a), (b) Optical micrographs of the surfaces in Ni-40at.%Fe alloy oxidized at 1273K for 5hr[25]. Note high oxidation resistance at the boundary in the middle of the micrograph (b).

boundary type on intergranular oxidation in dilute oxygen atmosphere (25.9 ppm O_2) at 1273K for 5 hr. Filled circle and triangle indicate heavily oxidized boundary and slightly oxidized boundary, respectively. Open circle indicates non-oxidized boundary. As predicted by Brandon's criterion, $\Delta\theta_C=15°/\Sigma^{1/2}$, low Σ coincidence boundaries which have the deviation angle within $\Delta\theta_C$ tend to be resistant to oxidation while random boundaries are selectively oxidized, as indicated by plots below and above the dotted curve given by Brandon's criterion. Some low Σ boundaries (Σ3, 11, 19, 27 given by the series $\Sigma=8n+3$ ($n\geq0$)) particularly showed high resistance to oxidation. These Σ boundaries are known to be of lower energy than other Σ boundaries. On the basis of structure-dependent intergranular oxidation, a new approach to the control of oxidation-induced intergranular brittleness has been established and tested by experiments on the specimens with grain boundary microstructures systematically controlled by rapid solidification and annealing. As schematically indicated in Fig. 8, the formation of grain boundary microstructure with small grain size and a high frequency of oxidation-resistant special boundaries (thin boundaries) is the requirement for the control of oxidation-induced brittleness.

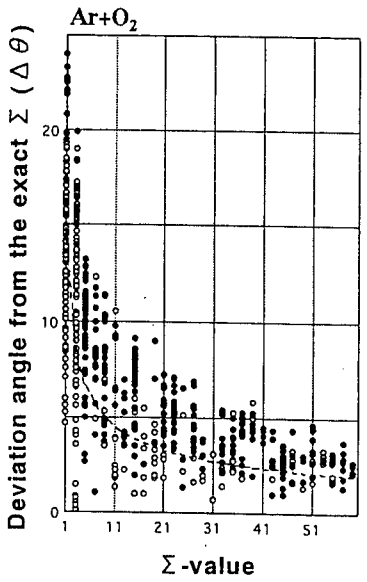

Fig. 7 The propensity to intergranular oxidation as a function of Σ, which is a measure of G.B. structural order, in Ni-40at.% Fe alloy oxidized at 1273K for 5hr[25].

5. How to Enhance Thermal Stability of Grain Boundary Microstructure ?

5.1. Grain Boundary Structural Transformation

High temperature material always requires the thermal stability of microstructure which is the source of property of performance of the material. Since the grain boundaries are preferential sites for most metallurgical phenomena occurring at high temperature, the establishment of thermal stability of grain boundary microstructure may be the most important issue for development of excellent high temperature materials. There is a basic knowledge of grain boundary phenomenon which has not yet fully understood and utilized for materials development. That is grain boundary structural transformation. In fact the atomic structure of grain boundary changes due to the entropy term of the free energy as temperature increases. Temperature dependence of grain boundary phenomena often changes abruptly at certain critical temperature, T_c, which normally ranges from 0.5-0.9T_M (T_M is the melting temperature). Figure 9 shows the temperature dependence of grain boundary sliding rate observed on $<10\bar{1}0>$ tilt zinc

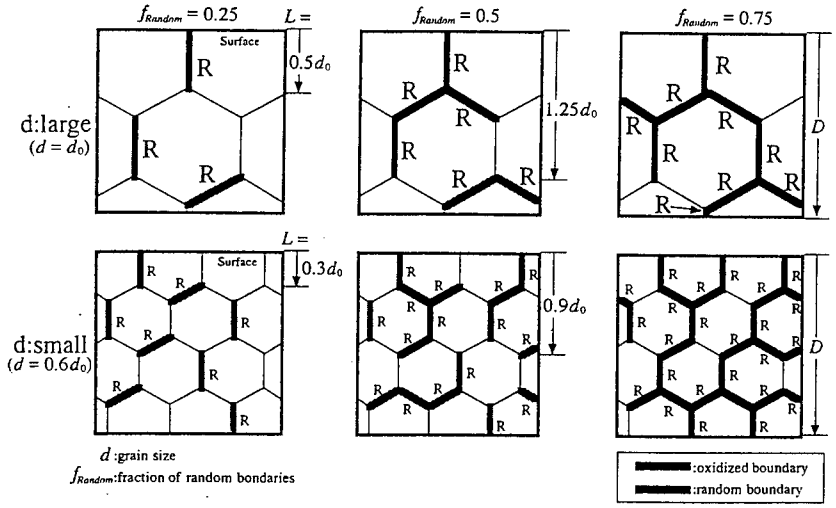

Fig. 8 Schematic representation of oxidation-induced intergranular brittleness in polycrystals with different grain sizes and grain boundary character distribution (GBCD).

bicrystal specimens [26]. We clearly see that the temperature dependence of the sliding rate for high angle boundaries changes at certain critical temperature, T_c, which depends strongly on the misorientation angle. Of particular interest is that the boundary with orientation of $\Sigma 9/54°$ has the highest critical temperature and the 16.5° low-angle boundary did not show any change of temperature dependence while random boundaries showed rather lower critical temperatures. The observed change of the temperature dependence has been explained to be attributed by grain boundary structural transformation. The result implies that the low-angle boundary and the $\Sigma 9/54°$ coincidence boundary have high thermal stability of grain boundary structure so that the structure remained unchanged up to the melting temperature or higher temperature of $0.9T_M$. Similar change of temperature dependence has been reported early for grain boundary migration [27]. It is not unreasonable to expect that temperature dependence of fracture stress and other properties associated with high temperature materials may be affected by similar influence of grain boundary structural transformation. If a polycrystalline material did not have a thermally stable grain boundary microstructure, the related performance would change and cause serious problem during its service. Unfortunately there has been little work which has taken account such effect of grain boundary structural transformation in development of a high temperature material. This still awaits a future challenge.

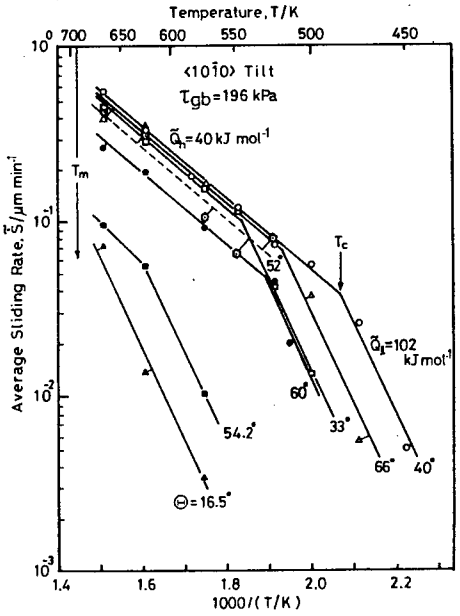

Fig. 9 The effect of grain boundary structural transformation on temperature dependence of sliding[26]. Note higher critical temperature, T_c, and slower sliding rate of 16° low-angle boundary and $\Sigma 9/54°$ boundary.

5.2 Grain Boundary Wetting

One more important grain boundary phenomenon which is closely related to thermal stability of grain boundary microstructure is the wetting of grain boundary by liquid phase. Grain boundary wetting is always involved in sintering of ceramics and refractory metals. Moreover high temperature strength and superplasticity can be affected by grain boundary wetting[28]. Again grain boundary wetting has been found to be affected by the boundary misorientation angle (boundary type and structure) [29], as indicated in Fig. 10. The wetting of zinc boundaries by Sn-rich liquid phase. We know that the critical temperature above which complete wetting takes place depends on the boundary misorientation angle and

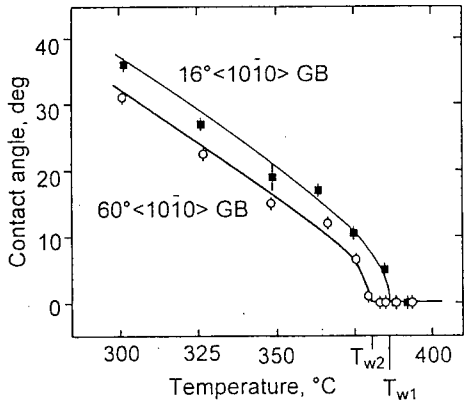

Fig. 10 Temperature dependence of the contact angle, θ, for the 16° low-angle boundary [29]. The wetting temperatures are T_{w1}=386.5 ±1°C, T_{w2}=381±1°C.

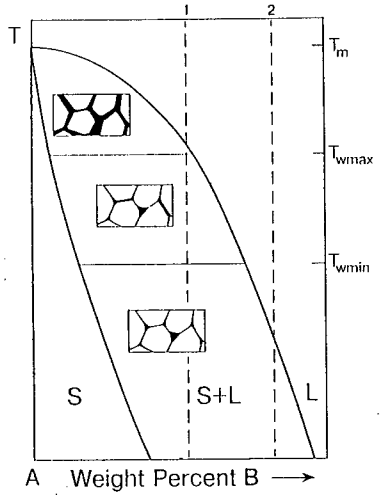

Fig. 11 A schematic phase diagram showing the lines of G.B. wetting phase transitions and the corresponding microstructure of two-phase polycrystals[30].

boundary type, corresponding grain boundary energy. The 16° low-angle boundary shows a higher critical temperature than that of 60° high energy random boundary. Such consideration of structural effect of grain boundary wetting is thought to be extremely important to high temperature deformation and fracture at the presence of liquid phase. More severe intergranular brittleness may occur by complete grain boundary wetting when a high frequency of random boundaries exist, depending on temperature and composition of a specific alloy used [30], as schematically shown in Fig. 11. So the grain boundary character distribution (GBCD) again comes to a key role in deformation, superplasticity and fracture at high temperatures.

6. Conclusion

The potential of the concept of grain boundary design and control has been proved. The control of intergranular fracture and an enhancement of high temperature strength and the fracture toughness can be effectively achieved by manipulating the grain boundary character distribution (GBCD) and the grain boundary connectivity. However the grain boundary engineering for advanced materials has just launched and it still awaits future work to establish basic knowledge associated with unsolved structural effects on such grain boundary related phenomena as grain boundary structural transformation and grain boundary wetting occurring at high temperatures. I hope and believe that basic knowledge of Interface Science will be used more wisely and beneficially for the development of the grain boundary engineering for advanced materials in the 21st century.

Acknowledgements

The author thanks coworkers for their important contributions to the long term project of grain boundary design and control performed in almost two decades. This work was supported partly by a Grant-in-Aid for Basic Research of the Ministry of Education Science and Culture. The author also thanks Dr. K. Kawahara for his help in preparation of the manuscript of this paper.

References

[1] T. Watanabe, Proc. the First Conference on Creep and Fracture of Engineering Materials and Fractures, B. Wilshire and D. R. J. Owen (ed), Pineridge Press, Swansea, (1981), p.263.
[2] T. Watanabe, Res Mechanica, **11**(1984), p.47.
[3] T. Watanabe, Materials Science and Engineering, **A166**(1993), p.11.
[4] G. Palumbo, E. M. Lehockey and P. Lin, J. Metals, **50**(1998), No.2, p.40.
[5] Y. Furuya, N. W. Hagood, H. Kimura and T. Watanabe, Mater. Trans. **JIM**., **39**(1998),p.1248.
[6] T. Watanabe, Mater. Sci. Forum, **233-234**(1997), p.375.
[7] T. Watanabe, Texture and Microstructures, **20**(1993), p.195.
[8] T. Watanabe, Materials Science and Engineering, **A176**(1994), p.39.
[9] C. T. Liu, Mater. Res. Soc. Symp. Proc., **81**(1987), p.355.
[10] T. Hirano, Acta Metall., **38**(1990), p.2667.
[11] T. Watanabe, T. Hirano, T. Ochiai and H. Oikawa, Mater.Sci.Forum, **157-162**(1994), p.1103.
[12] H.Lin and D.P.Pope, Acta Metall.Mater.,41(1993),p.553.
[13] S. Tsurekawa, S. Kokubun and T. Watanabe, Mater. Sci. Forum, **304-306**(1999), p.687.
[14] L. C. Lim and T. Watanabe, Acta Metall., **38**(1989), p.2507.
[15] T. Watanabe, S. Ikeda, T. Matsuzaki and X. Zhao, Proc. Japan-French Seminar on Intelligent Materials and Structures, (1997), p.159.
[16] T. Watanabe and S. Tsurekawa, Acta Mater., in press.
[17] H. Kokawa, T. Watanabe and S. Karashima, Philos. Mag., **44**(1981), p.1239.
[18] T. Watanabe, M. Yamada and S. Karashima, Philos. Mag., **A63**(1991), p.1013.
[19] G. S. Was, V. Thaveeprungsriporn and D. C. Crawford, J. Metals, **50**(1998), p.44.
[20] T.Watanabe, Mater.Sci.Forum,304-309(1999),p.421.
[21] S. Kobayashi, T. Yoshimura, S. Tsurekawa and T. Watanabe, Mater. Sci. Forum, **304-306** (1999), p.591.
[22] L. Qing, H. Xiaoxu, Y. Mei and Y. Jinfeng, Acta Met. Mater., **40**(1992), p.1753.
[23] C. P. Cutler and J. W. Edington, Metal Sci. J., **5**(1971), p.201.
[24] A. Katsman, H. J. Grabke and L. Levin, Oxidation of Metals, **46**(1996), p.313.
[25] S. Yamaura, Y. Igarashi, S. Tsurekawa and T. Watanabe, Acta Mater., **47**(1999), p.1163.
[26] T. Watanabe, S. Kimura and S. Karashima, Philos.Mag., **A49**(1984), p.845.
[27] K. Aust, Prog. in Mater. Sci., Chalmers Anniversary Volume, (1981), p.49.
[28] N. Eustathopoulos, Intern. Metals Rev., **28**(1983), No.4, p.189.
[29] B. B. Straumal, W. Gust and T. Watanabe, Mater. Sci. Forum, **294-296**(1999), p.411.
[30] B. B. Straumal, T. Watanabe and W. Gust, unpublished work.

Key Engineering Materials Vols. 171-174 (2000) pp. 245-252
© 2000 Trans Tech Publications, Switzerland

Modelling the High Temperature Creep Behaviour of a New Single Crystal Nickel Base Superalloy

M. Maldini and V. Lupinc

CNR-TEMPE, Via R. Cozzi 53, IT-20125 Milano, Italy

Keywords: Creep Damage, Single Crystal, SMP14 Alloy

Abstract The creep curves of nickel base superalloys are often characterised by a dominant tertiary creep stage due to the accumulation of internal damage proportional to the creep strain and depending on the values of the applied load/temperature.
A simple procedure is presented to obtain the parameter values of a constitutive equation able to describe the tertiary creep under constant load.

Introduction

The introduction of nickel base single crystal rotating blades in advanced gas turbines has allowed increasing the turbine inlet temperature enhancing their thrust and operating efficiency. While the use of single crystal components in aero-engine gas turbines is well established, nowadays research activities are concentrating on making single-crystal technology widely available also for land-based gas turbines for power generation.
This paper reports the creep behaviour in the temperature range 900-1000°C of SMP14, a new single crystal based superalloy, developed by CSIR Pretoria, RSA, for turbine blade and vane applications [1]. More than on the creep strength [2] the analysis of the results is focused on the shape of the creep curves in order to characterise the large dominant tertiary creep stage.

Material and experimental procedure

The material studied in this work is SMP14, a promising candidate alloy to be utilised in single crystal rotating blades.
The nominal chemical composition of the examined alloy is given in Table 1.
Fully heat treated 9 mm diameter bars have been supplied by Ross & Catherall Ltd, Sheffield U.K. Deviations of <001> crystalline direction from the rod axis were within 6°. The mean size of the cuboidal γ' particles was 0.45 μm. The hardening phase occupied approximately two thirds of the alloy volume [1].
The creep specimens had cylindrical symmetry of 5.6mm gauge diameter with 28mm gauge length. Creep strain was continuously monitored using capacitive transducers connected to extensometers clamped to the shoulders of the specimen. Three thermocouples were placed in the gauge length allowing to control the temperature gradients. The furnace was controlled by the central thermocouple. The creep tests were run at constant load.

Results and discussion

The constant load and temperature tests studied in this work were performed at 900, 950 and 1000°C at stresses between 175 and 425 MPa to produce time to rupture between 200 and 2500 h. The results of the experimental creep tests are reported in Table 2.

The creep curves of SMP14 single crystal alloy exhibit near no or a short and small primary stage and the majority of the single creep curves consists of tertiary creep. The results are consistent with those obtained on CMSX 4 [3] and on other single crystal nickel base superalloys [4-6] for equivalent applied stresses/temperatures.

The experimental creep curves are plotted in Figs. 1 as strain in function of a normalised time, t/t_{10}, where t_{10} is the time to reach 10% of strain, about 90% of the time to fracture. In these figures we note that all the creep curves are similar. In other words, the shape of the creep curves depends only slightly on the test conditions even if the time to rupture spans in a large interval. The curvatures of the SMP 14 creep curves seem continuously increasing with the decreasing of the applied load, and only small temperature dependence is evident. This dependence is better shown in Fig. 2, where the strains of Figs. 1, obtained at $t/t_{10}= 0.8$ are plotted in function of the applied stress.

Equivalent results, for similar test conditions, have been found for SRR 99 [4, 5].

Figs. 3 show, for a large portion of the creep curves, a linear dependence between the strain rate $\dot{\varepsilon}$ and the accumulated strain, ε. On time basis, this linear strain softening takes up most of the creep life. Only for large strain, in the last per cent of the creep life, there is evident further acceleration in part due to the homogeneous reduction of the gauge section of the specimen (the creep tests were at constant load) and to the localised necking [7].

Table 1 Composition of SMP 14 in weight %.

Al	Co	Cr	Mo	Nb	Re	Ta	W	Ni
5.4	8.1	4.8	1.0	1.4	3.9	7.2	7.6	Bal

Table 2 Experimental creep results on SMP14.

Temp. (°C)	Stress (MPa)	Time in h to 2%	Time in h to 10%	Time to rupture (h)	Elong. (%)	Area red. (%)
900	425	254	395	450.1	25.7	27
900	400	331	550	605.2	19.3	31.3
900	375	455	717	806.8	29.2	32.6
900	325	965	1477	1692.5	27.7	35.2
900	300	1460	2190	2433.9	22.9	33.7
950	320	183	246	302.9	25.5	32.3
950	275	394	591	665.1	27.1	34.6
950	220	1100	1627	1798.2	25.8	32.3
950	215	1363	1980	2178.2	24.7	32.3
1000	230	177	256	276.6	22.0	29.4
1000	200	367	579	622.9	21.6	28.7
1000	175	825	1151	1188.7	17.4	30.9

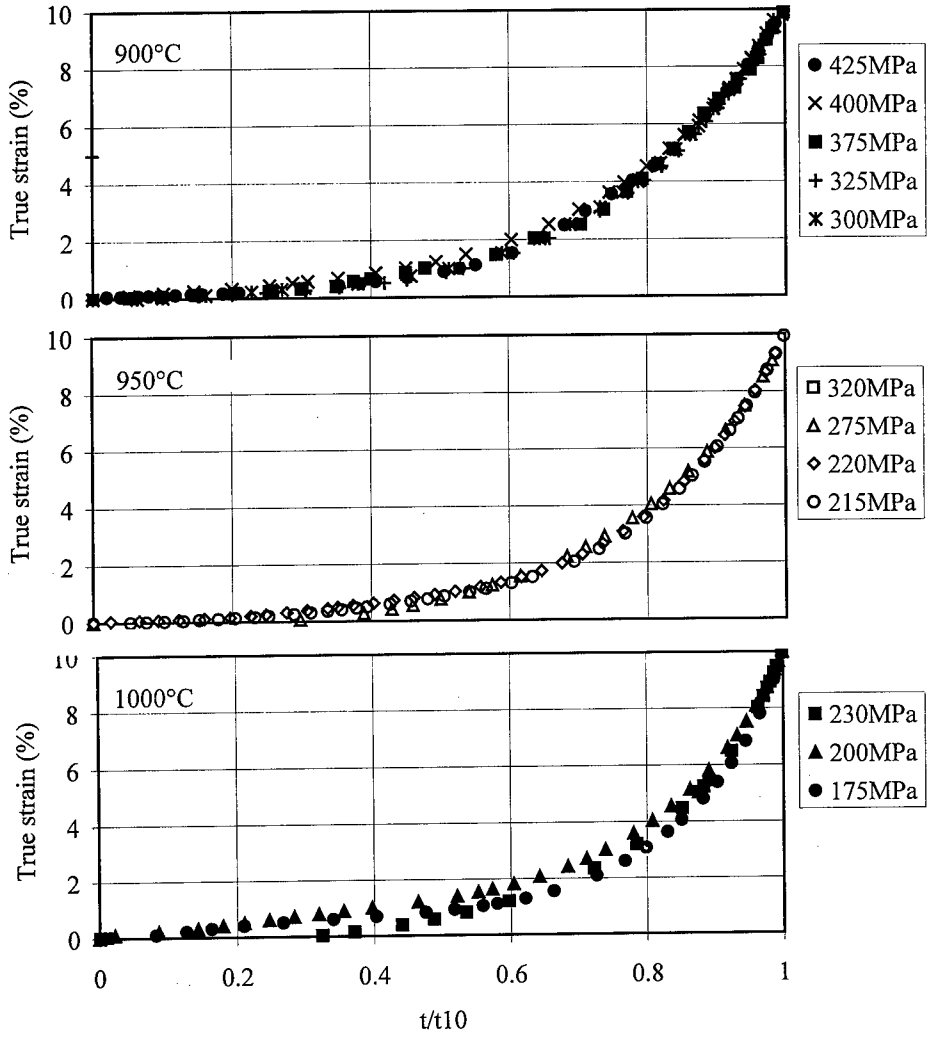

Fig. 1 Creep curves normalised with respect to the time to reach 10% strain

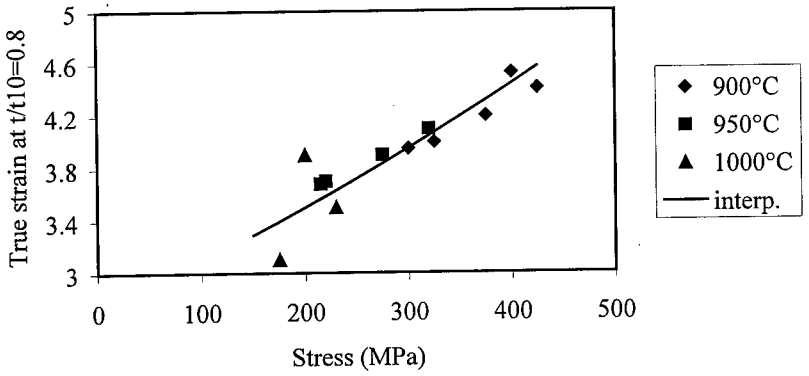

Fig. 2 Strain values of creep curves of Fig. 1 at $t/t_{10} = 0.8$

Modelling

The designing of high temperature components often requires constitutive equations able to describe not only the time to rupture, in function of the test parameters, but also the shape of the creep curves.
The θ-projection concept [8] and the Crispen methodology [9] are among the most recent attempts to describe the shape of complete creep curves.
The single crystal nickel base superalloys, uniaxially loaded in the <001> direction, generally present a short and small primary stage compared to the dominant tertiary stage. Although such a small stage cannot be a priori neglected, its contribution to the creep strain is particularly little in the temperature range around 950°C and stresses of engineering interest. For example, in the alloy here studied, and in CMSX 4 [3] the accelerating tertiary stage can start at the beginning of the test or at a strain < 0.1%. The contribution of primary creep stage to the total creep strain is then always <<0.1%. Moreover small differences in the orientation and chemical composition of the specimens, contributions of not very well understood factors as the "negative creep" that can influence the primary stage and the minimum creep rate, and also experimental errors, like small initial bending in the specimens, can greatly influence the experimental measure of such a small strain producing a relatively large experimental scatter both in the size of the primary and sometime in the value of the minimum creep rate (for example in [3] the minimum strain rate behaves inconsistently and it is not easy to measure its stress dependence). If in one hand to model the primary stage sometimes becomes prohibitive, due to the experimental scatter, on the other hand its engineering importance decreases, and its contribution to the creep strain can be neglected.
Due to the small contribution of the primary stage to the total creep strain, in this model only the dominant tertiary creep contribution will be studied. The following relationship can describe the experimental creep curves shown in Figs. 3:

$$\dot{\varepsilon} = \dot{\varepsilon}^{\circ} (1 + C\varepsilon) \qquad (1)$$

where C is a parameter and $\dot{\varepsilon}^{\circ}$ represents the extrapolated creep strain rate at ε=0 and corresponds to the minimum creep rate if the primary creep mechanisms are not active. Recently various papers have pointed out that such an expression can well describe the tertiary creep behaviour in nickel base superalloys [4, 5, 9, 10] and it has been physically justified in [11].
The Eq. 1 has the following analytical solution:

$$\varepsilon = (\exp(C\dot{\varepsilon}^{\circ}t) - 1)/C \qquad (2)$$

i.e. a relationship identical to the portion of the θ concept function [8] describing the tertiary creep with $\theta_3 = 1/C$ and $\theta_4 = C\dot{\varepsilon}^{\circ}$.
If ε_x is the strain accumulated after an arbitrary time t_x, from Eq. 2:

$$\dot{\varepsilon}^{\circ}t_x = (1/C)\ln(1+C\varepsilon_x) \qquad (3)$$

For $t_x=t_f$, time to fracture, and then $\varepsilon_x= \varepsilon_f$ strain to fracture, the Eq. 3 gives an expression of the Monkman-Grant constant in terms of ε_f and the parameter C.
Combining the previous equations, it leads to the following expression:

$$\varepsilon = (1/C)\,[(C\varepsilon_x +1)\hat{}(t/t_x) -1] \qquad (4)$$

The previous equations can be utilised to study the creep curves up to the arbitrary strain, $\varepsilon=\varepsilon_x$, we are interested in. Of course, to have meaningful parameter values, ε_x and t_x must be in the portion of

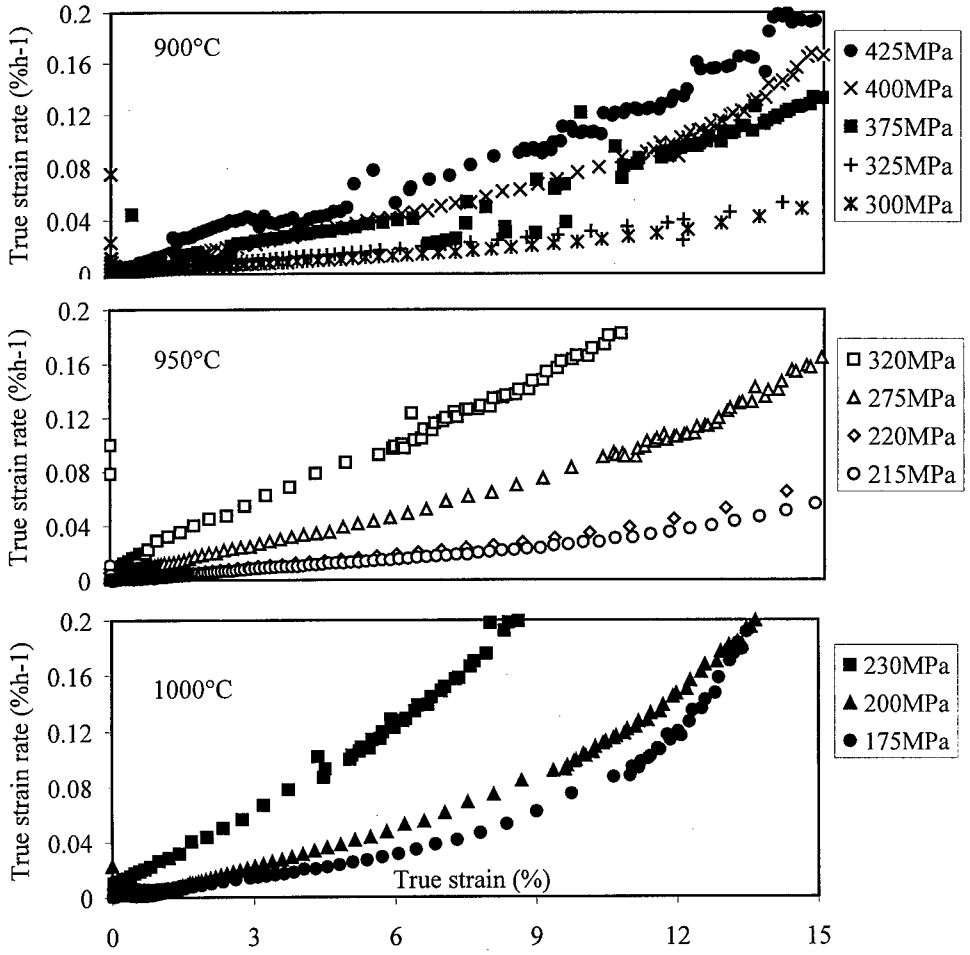

Fig. 3 Strain rate vs strain: linear strain softening appears up to large values of strain.

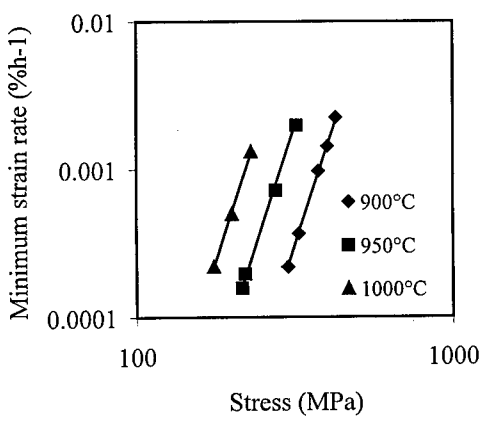

Fig. 4 Stress dependence of the initial creep strain rate

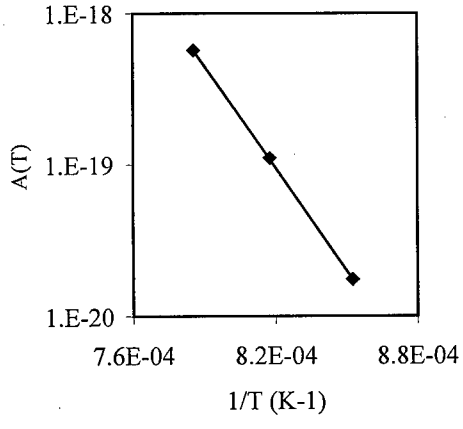

Fig. 5 Temperature dependence of the parameter A(T) of Eq. 5.

the creep curve that can be sufficiently well described by the Eq. 1 and then the strain and the time to rupture could not be used in Eq. 4.
Here, as an example, we consider ε_x=10% and $t_x = t_{10}$, although for the tests at 1000°C a smaller value of ε_x should be utilised.
From Eq. 4 it is evident that the parameter C controls the curvature of the creep curves. The values of the parameter C describing the experimental creep curves can be easily obtained comparing experimental creep curve shapes in Figs. 1 and the curves obtained by Eq. 4, or utilising this relationship and the data shown in Fig. 2.
Following our earlier work [5], an exponential function of stress is used to represent the parameter C and no temperature dependence is considered:

$$C = A_1 \exp(-A_2 \sigma) \qquad (5)$$

The curve in Fig. 2 represents the strain predicted by Eq. 4 with ε_x = 10%, t/t_x = 0.8 and the values of the parameter C(σ) obtained through the Eq. 5 with A_1 = 6453 and A_2 = 6.38e-3 MPa^{-1}.
Combining the Eq. 3 with the Eq. 5, it is now possible to obtain the values of the parameter $\dot{\varepsilon}^\circ$ for the different test conditions (Table 3).
A plot of the parameter $\dot{\varepsilon}^\circ$ in function of the stress (Fig. 4) shows that the parameter $\dot{\varepsilon}^\circ$ varies with the stress according to a Norton type behaviour:

$$\dot{\varepsilon}^\circ = A(T)(\sigma/\sigma^\circ)^n \qquad (6)$$

Since the temperature dependence of A follows the classical Arrhenius relationship: $A = A^\circ \exp(-Q/RT)$, Fig. 5, the values of Eq. 6 parameters are: n = 6.5, Q = 432 kJ/mol and $A^\circ = 0.03137\ h^{-1}$.
The creep curves predicted by the Eq. 2 and the interpolated parameter values are represented in Figs. 6 by the continuous lines together with the experimental curves. From these figures it is apparent that the proposed equation excellently describes the whole experimental creep curves, up to the fracture.

Table 3 Values of the parameters C and $\dot{\varepsilon}^\circ$.

Temperature (°C)	Stress (MPa)	Parameter C*	$\dot{\varepsilon}^\circ$(%h-1)
900	425	428	2.13e-3
900	400	502	1.43e-3
900	375	588	9.42e-4
900	325	810	3.72e-4
900	300	950	2.21e-4
950	320	837	2.11e-3
950	275	1115	7.89e-4
950	220	1584	1.85e-4
950	215	1635	1.59e-4
1000	250	1486	1.28e-3
1000	200	1800	5.16e-4
1000	175	2111	2.17e-4

* Interpolated value (Eq. 5)

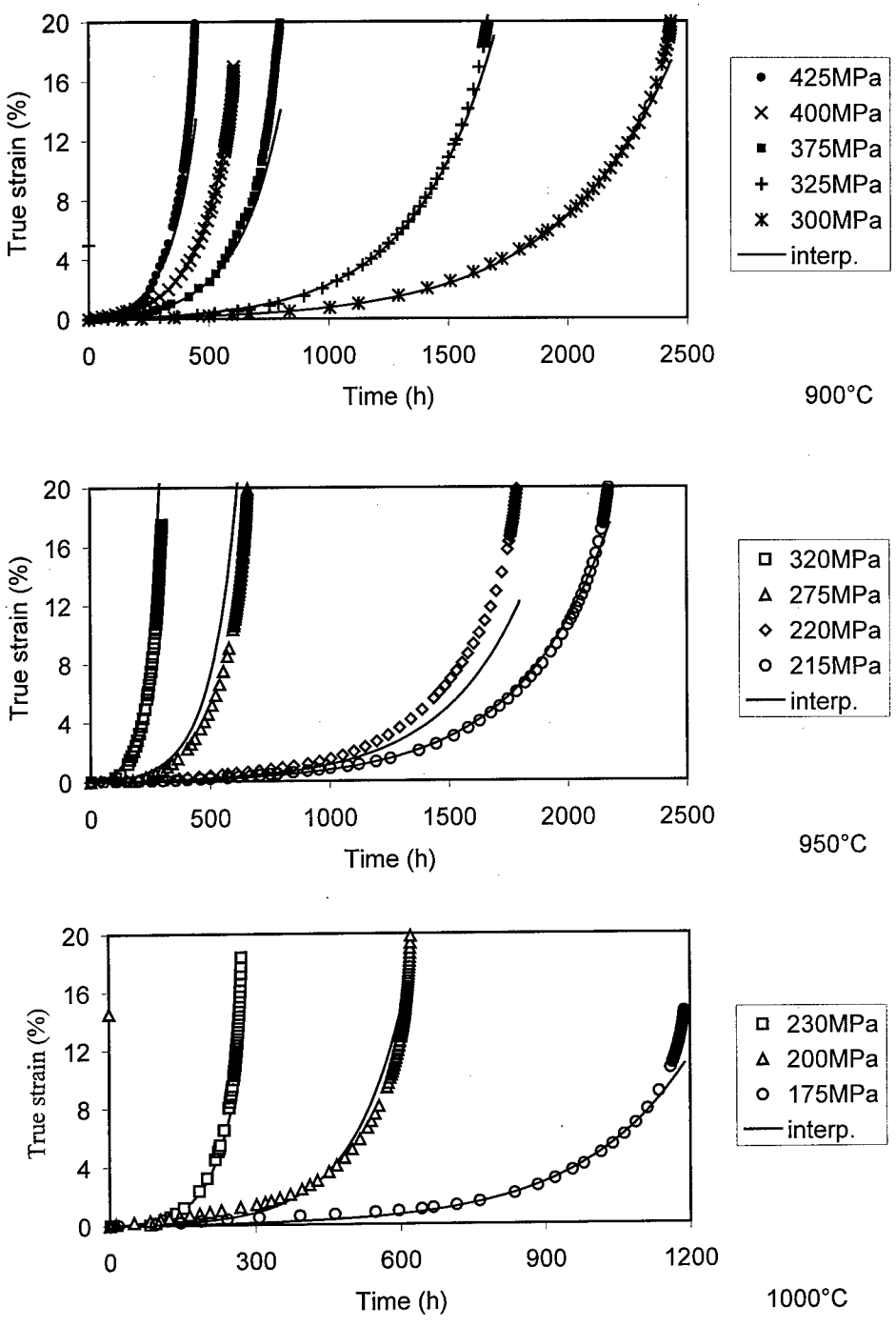

Fig. 6 Comparison between the experimental creep curves and the interpolations obtained by the Eq. 2.

Conclusions

1) The creep curve shape is dominated by tertiary creep: the contribution of the primary creep can be neglected.
2) A linear relationship between the strain rate and the strain dominates the creep curves.
3) The shape of the creep curves depends mainly on the stress in the explored stress/temperature field.
4) A simple model has been presented to describe the creep experimental curves.

Acknowledgements: The authors are grateful to Ross & Catherall LTD, Sheffield U.K. to have supplied the SMP 14 alloy.

References

1. J.M.Benson et al. "SMP 14 advanced high strength single crystal superalloy" report of CSIR, Pretoria, RSA.
2. N. Gravill et al., Proc. Conf. Materials for Advanced Power Engineering 1998, pp. 1025-1034, ed. by Lecomte-Beckers et al., Forschungszentrum Julich (1998).
3. P.J. Henderson and J. Lindblom, Scripta Mater., **37**, p.491 (1997).
4. M. Maldini and V. Lupinc, Materials at High Temp., **14**, p.47 (1997).
5. M. Maldini and V. Lupinc, Scripta Met., **22**, p.1737 (1988).
6. M. Maldini and V. Lupinc, Proc. Conf. Strength of Materials, pp. 697-700, ed. by H. Oikawa et al., Japan Institute of Metals, Sendai (1994).
7. M. Maldini and V. Lupinc, Scripta Mater., **32**, p. 337, (1995).
8. R.W.Evans, J.D.Parker and B. Wilshire, Recent Advances in Creep and Fracture of Engineering Materials and Structure, ed. by B. Wilshire and D.R.J. Owen, p.135. Pineridge Press, U.K. (1982).
9. L.M. Pan, B.A. Shollock and M. McLean, Proc. R. Soc., London, **453**, p. 1689, (1997).
10. B.F.Dyson and M. McLean, Acta Metall., **31**, p.17, (1983).
11. B.F. Dyson, Revue Phys. Appl., **23**, p. 605 (1988).

Author to whom correspondence should be sent:

M. Maldini
Email: maldini@tempe.mi.cnr.it
Fax : +39-02-66173321

Key Engineering Materials Vols. 171-174 (2000) pp. 253-260
© 2000 Trans Tech Publications, Switzerland

Orientation Dependent Creep Behavior and Dislocation Structure of Nickel Solid Solution Single Crystals

D. Siebörger and U. Glatzel

Friedrich-Schiller-Universität Jena, Metallische Werkstoffe,
Löbdergraben 32, DE-07743 Jena, Germany

Keywords: Anisotropic Creep, Dislocation, Superalloy, Nickel, Solid Solution, Single Crystal, Microstructure, Matrix

Abstract

The creep behavior at 1123 K and the microstructure of undeformed and creep deformed single-crystal specimens of two nickel-base solid solution alloys with various orientations has been investigated. One of the alloys, having the composition of the matrix of the superalloy CMSX-4, contains a volume fraction of about 10% γ' phase precipitates. This alloy shows an orientation-dependent ratio of the stationary strain rate at 1123 K and 200 MPa of $\dot{\varepsilon}_{ss}^{[001]}:\dot{\varepsilon}_{ss}^{[011]}:\dot{\varepsilon}_{ss}^{[111]} = 60:50:1$. In comparison, a single-phase solid solution alloy with nearly the same composition, but without the γ' forming elements (Al,Ti,Ta), is found to have the dependence $\dot{\varepsilon}_{ss}^{[001]}:\dot{\varepsilon}_{ss}^{[011]}:\dot{\varepsilon}_{ss}^{[111]} = 2:5:1$.

A way of estimating the stress state of matrix channels in superalloys is presented. The correlation of shear stress and dislocation density is determined for the particle-free matrix alloy giving the parameters of the Taylor relation $\rho=(\tau/(\alpha Gb))^2$. With the dislocation densities found in matrix channels of superalloy CMSX-4 the Taylor relation predicts a resolved shear stress of about 85–150 MPa in the vertical channels and 240–380 MPa in horizontal channels. The predicted stress levels are in good agreement with finite element calculations.

Intensive dislocation analysis has been carried out in order to determine the glide systems of the dislocations. At all observed specimen orientations, octahedral glide is dominating and only a small amount of cube glide is observed. During primary creep the deformation process is mostly due to single octahedral glide, while only few of the possible octahedral glide systems with high Schmid factors and no systems with low Schmid factors are activated. During secondary creep all octahedral glide systems are activated, even those with a Schmid factor close to zero, the fractional density of each glide system corresponding roughly to its Schmid factor. Near screw and 60° dislocations appear to dominate in all specimens. The fraction of 60° dislocations increases with strain.

Introduction

There are many studies of the orientation-dependent creep behavior of the two-phase, nickel-base superalloys, for example see [1–5]. Also the mechanical behavior of the hardening γ' phase [6–8], in most cases approximated by Ni_3Al, has been reported in many studies. For an overview see [7]. Even though the major part of the deformation process of superalloys takes place in the matrix phase, there has been much less research on the solid-solution matrix of second-generation superalloys than for the γ' phase [5,9–12]. An improved understanding of the deformation mechanisms of the matrix phase will hopefully offer insight into the deformation processes in superalloys. Recently, the research on the matrix phase of superalloys has accelerated: Clément et al. [9] observed disordered dislocation structures after creep tests of the γ matrices of MC2 and AM3 at 1173K and a structure with the majority of dislocations localized in planar groups at lower temperatures. They identified the presence of friction in γ phase by short range ordering which leads to dislocation pairing and the pile-up of the first dislocations of a planar group [10]. Nitz and Nembach [11-13] observed that the single phase γ matrix of NIMONIC 105 shows the standard behavior of solid solutions: the critical resolved shear stress is isotropic and decreases with increasing temperature and the matrix obeys the

Schmid law. Shah and Cetel [5] determined the anisotropy of the minimum creep rate in compressive creep tests of the γ alloy Hastelloy-X ($Ni_{48.4}Cr_{22}Co_{1.5}Mo_9W_{0.6}Fe_{18.5}$) at 1255 K and 34MPa to $\dot{\varepsilon}_{min}^{[001]}:\dot{\varepsilon}_{min}^{[011]}:\dot{\varepsilon}_{min}^{[111]} = 7:3:1$ and at 1033K $\dot{\varepsilon}_{min}^{[001]}:\dot{\varepsilon}_{min}^{[111]} = 13:1$, which is in a good agreement with their anisotropic model with the assumption no cube slip.

Observations on Undeformed Samples

Element:	Ni	Cr	Co	W	Mo	Re	Al	Ti	Ta
Matrix with 10 vol-% precipitates	51.6	19.7	18.3	2.7	0.8	2.9	3.5	0.2	0.3
Precipitate free matrix	54.9	20.0	18.6	2.7	0.8	3.0	-	-	-

Table 1: Nominal composition of examined alloys in at-%.

Single Crystals of the alloy compositions shown in Table 1 have been cast by V. Toloraia [8].
The Matrix with precipitates has exactly the same composition as the matrix of CMSX-4 measured by energy dispersive X-ray analysis in the transmission electron microscope (TEM) [14] and verified by atom probe field ion microscopy [15]. This alloy has a volume fraction of 10% γ'-phase precipitates, which can be seen from the TEM overview Fig. 1.

Fig. 1: Matrix with precipitates, [111]-oriented, cross-cut, 2.4% strain

Precipitate free matrix has nearly the same composition (see Table 1), but without the γ'-forming elements Al, Ti and Ta. This alloy remains single-phase even after high temperature exposition for several days, independently of the stress. Fig 2 shows an overview micrograph of this alloy.

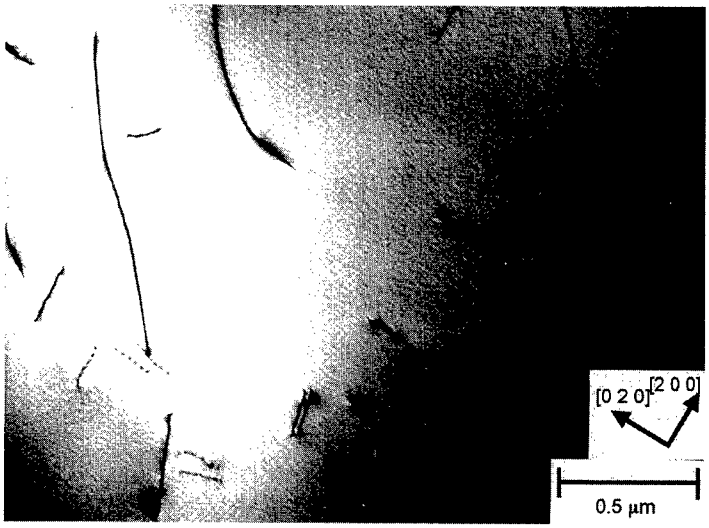

Fig. 2: precipitate free matrix, [137]-oriented, [001]-cut, 2% strain

Creep Experiments

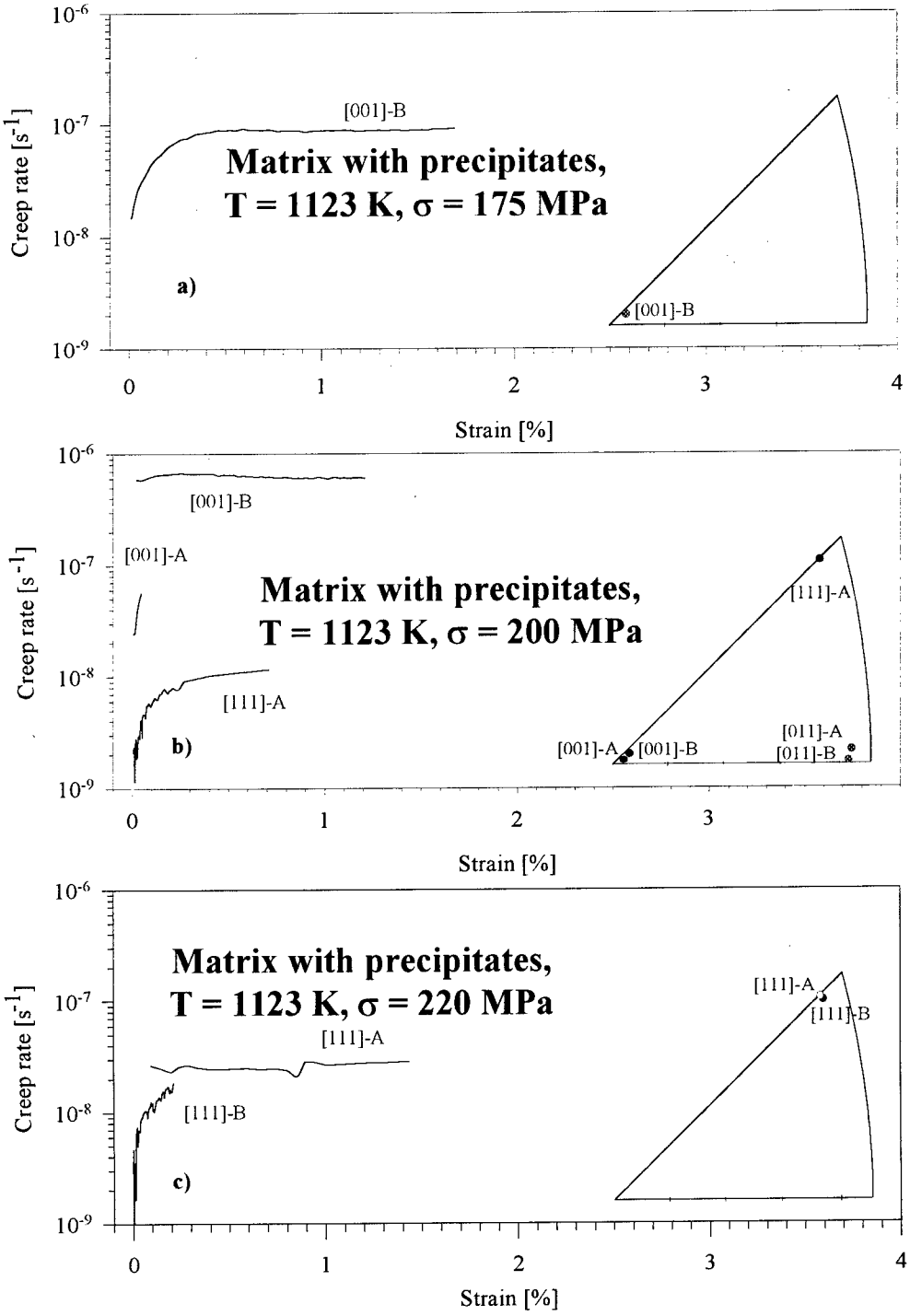

Fig. 3: Creep curves obtained in matrix with precipitates.

Several orientations of single crystals of both alloys have been tested in tensile creep tests. Fig. 3 and 4 show the logarithm of the strain rate versus strain curves together with the orientation in the standard unit triangle. The specimens of matrix with precipitates have a higher deviation from the corners of the orientation triangle than the specimens of the precipitate free alloy.
Some of the specimens can be seen at two stress levels in Fig. 3 because stress-change tests were performed. All creep curves start with an increasing creep rate within the first 0.5% of strain. This is known as inverse primary creep and is similar to Ni_3Al behavior [8,16] but different from superalloy behavior [17,18]. The inverse primary might be explained by the relatively low stress levels [19].

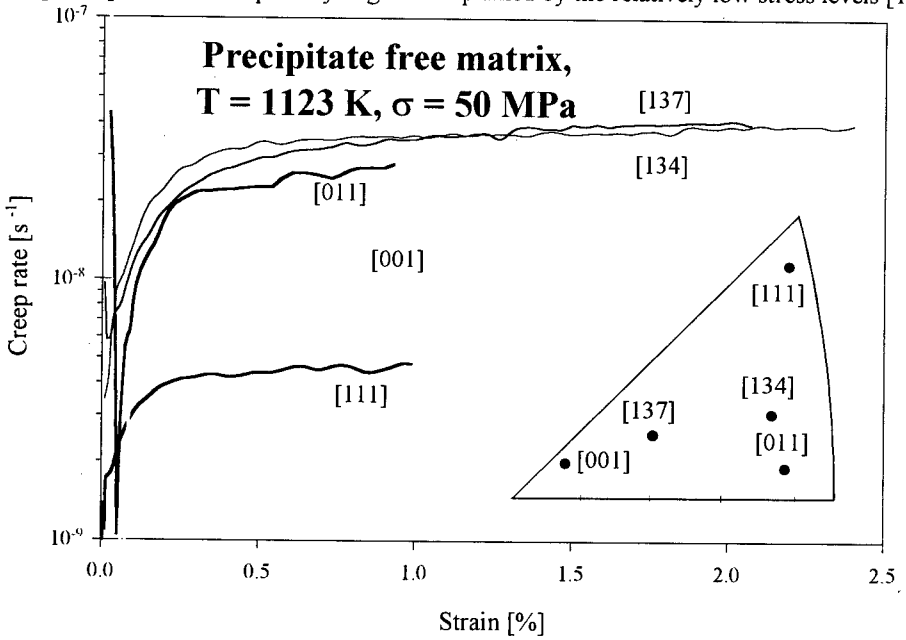

Fig. 4: Creep curves obtained in precipitate free matrix.

Comparing Fig. 3b and Fig. 4, the creep rate of the precipitate-containing matrix phase at 200 MPa stress is roughly as high as the creep rate of the precipitate free matrix at 50 MPa. The strengthening effect of 10% volume fraction of γ' phase leads to a creep strength which is four times higher when compared to the precipitate-free alloy.
Compared to the single-phase matrix, there is a significantly higher anisotropic creep behavior of precipitate free matrix. To first order, the matrix behavior can be explained by the difference of Schmid factors assuming octahedral glide only. [001] and [011] orientations have the same high Schmid factor of 0.41 for octahedral glide, whereas [111] oriented specimens have a Schmid factor of only 0.27. A dislocation-density-based model to describe this behavior is in progress of being developed [20].
To preserve the dislocation structure, the creep tests have been stopped by cooling the specimen under load.

Dislocation Density Measurements

TEM foils have been prepared from the creep test specimens by electropolishing 200 μm thick samples with a perchloric acid-methanol electrolyte. Most of the dislocations are not arranged in ordered arrays but spread randomly. This is in good agreement with the observations of Clément et al. [9,10], who observed a disordered dislocation structure after creep tests of the γ matrices of MC2 and AM3 at 1173 K. At temperatures lower than 1123 K, they have seen a structure with the majority of dis-

locations localized in arrays. Thus, at these higher temperatures, short-range order apparently has a minimal effect of the dislocation dynamics.

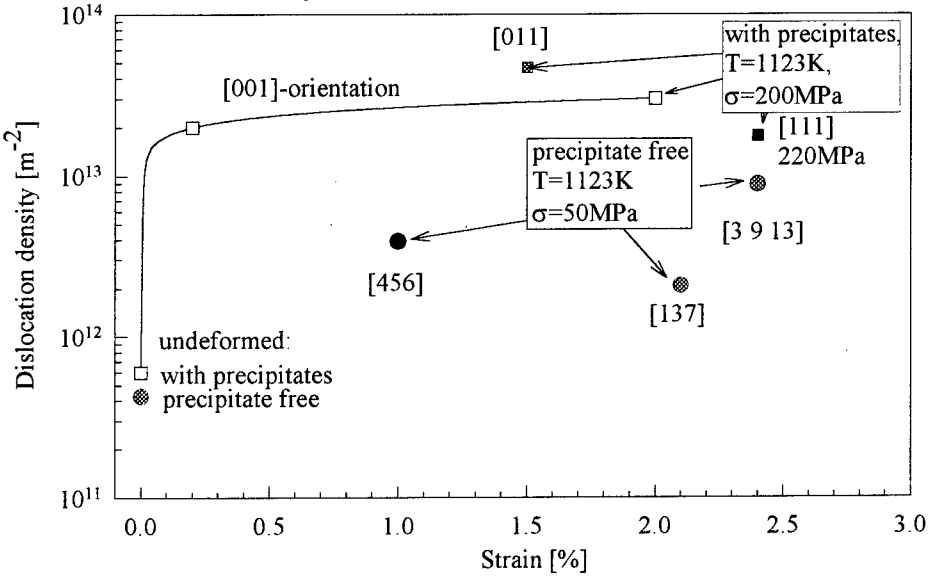

Fig. 5: Overall dislocation density.

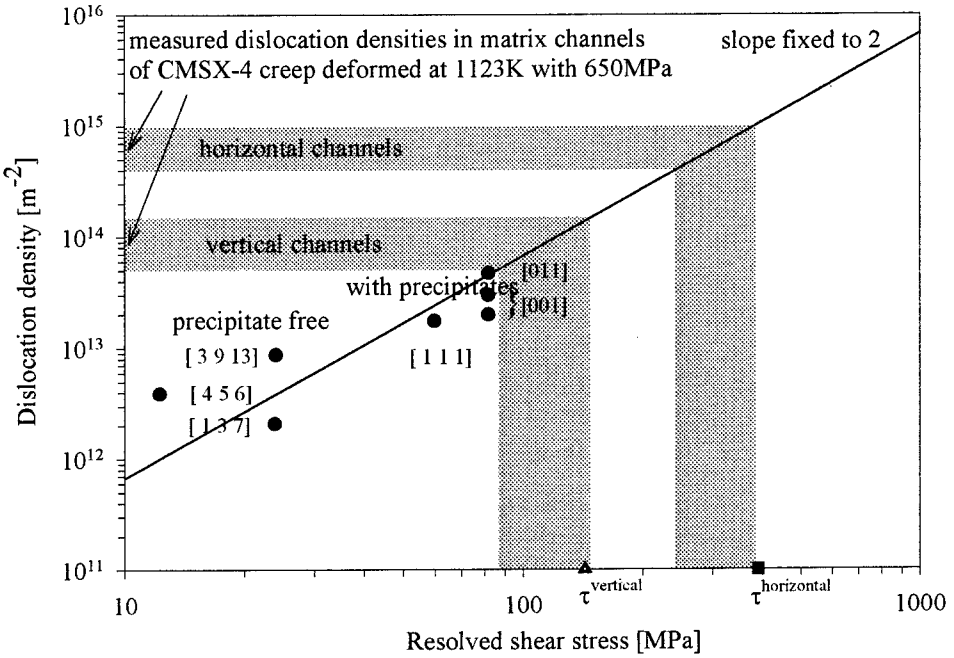

Fig. 6: Dislocation density in stationary creep, T = 1123 K.

Fig. 5 shows the overall dislocation density, given by half of the number of dislocation ends divided by the visible area of the TEM micrograph. Fig. 6 shows a way of approximating the stress levels in the matrix channels of CMSX-4 after creep. The dislocation density in matrix channels of an [001] oriented specimen after a creep test at 1123K and 650 MPa, see for example Fig. 40 and 41 in [14]

or Abb. 5-10 in [17], is determined roughly to be $0.5–1.5 \cdot 10^{14}\,m^{-2}$ in vertical and $4–10 \cdot 10^{14}\,m^{-2}$ in horizontal channels. The slope of the regression line was chosen to be fixed with a value of 2 according to the Taylor relation $\rho=(\tau/(\alpha Gb))^2$. G = 97 GPa is calculated with the data of a Ni-Cr-Co-W matrix [21]. With b = 0.253 nm, the best fit to all data points is achieved with $\alpha = 0.49$. With these parameters a resolved shear stress of about 85–150 MPa in the vertical channels and 240–380 MPa in horizontal channels is extrapolated.

In [22] these results are compared to finite element calculations of stress states within matrix plates. The finite element calculated values are marked with a filled square and a triangle respectively in Fig. 6. These predictions are in good agreement with the values extrapolated from the experimental data.

Observation of Glide Systems

In order to determine the line vector of the dislocations, specimen areas containing 10-15 dislocations are photographed in five different low-index-zone axes, preferably [001] and four <112> zone axes. After digitizing dislocation lines, the line vector is calculated by the length ratio and the projected direction of two zone axes. The line vector is taken by the average of all possible combinations of two zone axes.

The Burgers vector of the dislocations can be determined by checking the invisibility condition $\vec{g} \cdot \vec{b} = 0$ from another set of 6-8 pictures photographed at different two-beam Bragg conditions.

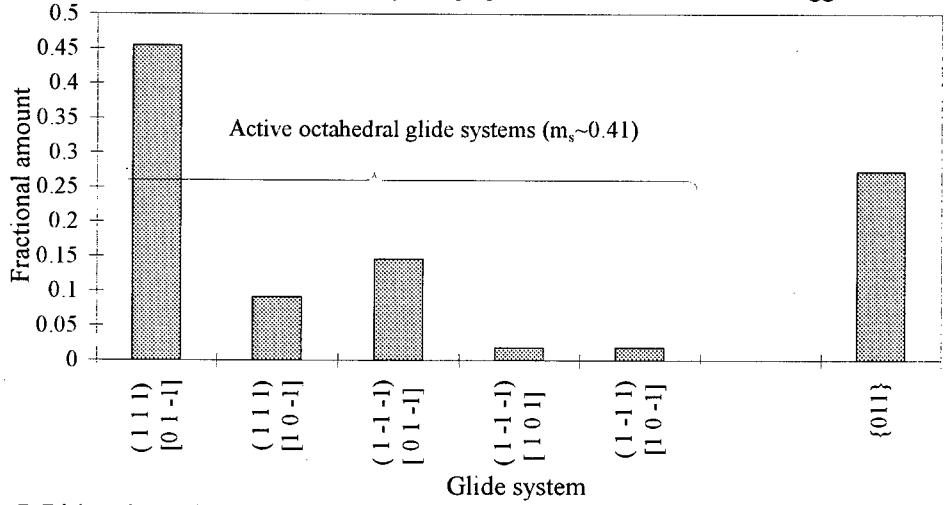

Fig. 7: Dislocations of a 0.06% (200MPa) deformed single-crystal [001]-oriented specimen of matrix with 10% precipitates.

In Fig. 7 the fractional amount of each observed glide system can be seen. In this early state of glide, there is mostly single glide: more than one half of the examined dislocations are gliding on the (111) plane, most of which have the same plane and the same Burgers vector. All observed dislocations have a high Schmid factor (≈ 0.41) but only in 3 out of 8 possible active glide systems more than a negligible number of dislocations was found. The remarkable result is the high amount of dislocations which are on {011} planes. No cube glide planes have been observed, as one would expect from the vanishing Schmid factor.

During secondary creep all glide systems are activated: Fig. 8 shows that 7 out of the 8 possible active glide systems are activated and all 4 passive octahedral glide systems (zero Schmid factor) have been observed. These latter dislocations can be explained by interactions of the type $a/2\,[011] + a/2\,[10\bar{1}] = a/2\,[110]$ (producing a dislocation with zero Schmid factor for (001)-oriented

specimens). A reasonable amount of {011} glide plane activity is still present, but no cube glide planes are observed.

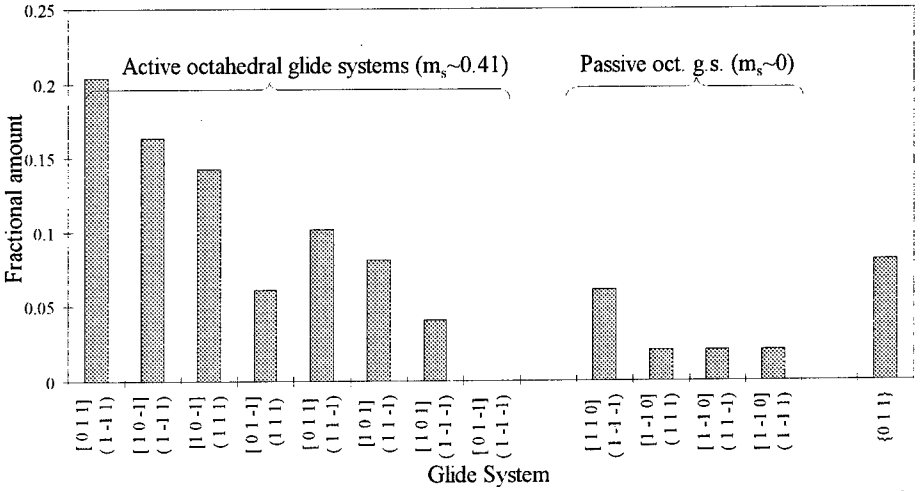

Fig. 8: Dislocations of a 3% (200 MPa) deformed single-crystal [001]-oriented specimen of precipitates containing matrix.

Since the specimens of precipitate free matrix have a greater deviation from the edges of the orientation triangle the glide systems can not simply be divided into active and passive glide systems. The Schmid factor of the individual slip systems with the observed fractional amount of these systems is shown in Fig. 9.

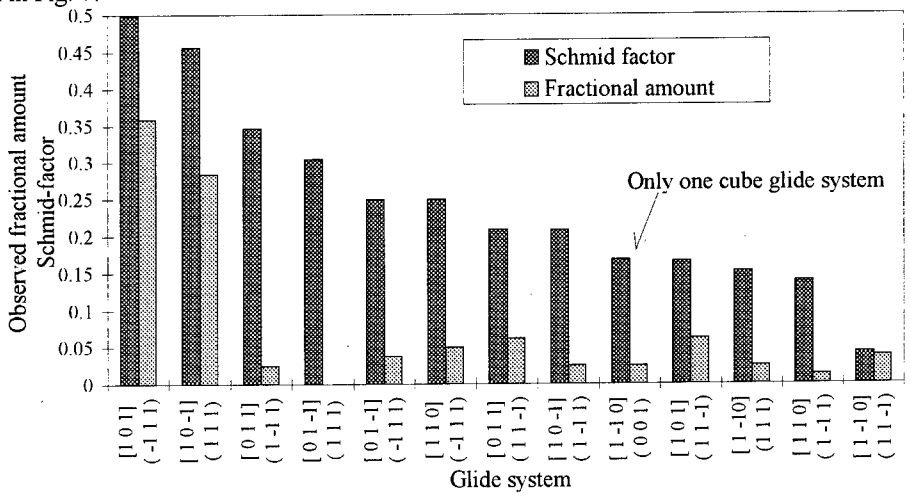

Fig. 9: Comparison of Schmid factor with observed fractional dislocation density in the 2% deformed single-crystal [137]-oriented precipitate free specimen. Creep stress: 50 MPa.

Fig. 9 shows that the two glide systems with the highest Schmid factor contain the largest number of dislocations and that the other glide systems are containing only a low number of dislocations. The fraction of cube glide planes is very low.

Table 2 shows the observed fractional amount of dislocations with a given range of angles between line and Burgers vector after creep. It can be seen that during primary creep (specimen [001]-A) screw and 60° dislocations are dominating. With increasing strain the dislocations have a higher tendency to be closer to edge in character, so the number of screw dislocations decreases and the

amount of dislocations with an angle of 60° or more increases. In precipitate free matrix during secondary creep, there is a more or less even distribution of dislocation characters for all orientations.

	Matrix with γ'-precipitate				Precipitate free matrix		
	[0 0 1]-A 0.06% def.	[0 0 1]-B 3% def.	[0 1 1]-A 1.5% def.	[1 1 1]-A 2.4% def.	[1 3 7] 2.1% def.	[3 9 13] 2.4% def.	[4 5 6] 1.0% def.
0°-15°	0.44	0.23	0.19	0.28	0.25	0.18	0.25
15°-45°	0.01	0	0.11	0.06	0.06	0.17	0.13
45°-75°	0.48	0.68	0.60	0.67	0.59	0.52	0.43
75°-90°	0.07	0.09	0.09	0	0.10	0.14	0.20

Table 2: Fractional amount of dislocation angles after creep.

References

1. P. Caron, T. Khan, Y.G. Nakagawa, Scripta Metall. 20 (1986), p. 499
2. P. Caron, Y. Ohta, Y.G.Nakagawa, T. Khan, in: S. Reichmann et al (Eds.), Superalloys 1988, (1988), p. 215
3. V. Saß, U. Glatzel, M. Feller-Kniepmeier, in: R. Kissinger et al. (Eds.), Superalloys 1996 (1996), p. 283
4. V. Saß, U. Glatzel, M. Feller-Kniepmeier, Acta Met. Mat. 44 (1996), p. 1967
5. D. Shah, A. Cetel, in: R. Kissinger et al (Eds.), Superalloys 1996 (1996), p. 273
6. D. P. Pope, S. S. Ezz, Inten. Mat. Rev. 29 (1984), p. 136
7. N. S. Stoloff, Inten. Mat. Rev. 34, 153 (1989)
8. C. Knobloch, V.N. Toloraia, U. Glatzel, Scripta Mater. 37 (1997), p. 1491
9. N. Clément, A. Coujou, M. Jouiad, P. Caron, H. Kirchner, T. Khan, in: R. Kissinger et al. (Eds.), Superalloys 1996 (1996), p. 239
10. M. Jouiad, N. Clément, A. Coujou, Phil. Mag. A 77 (1998), p. 689
11. A. Nitz, E. Nembach, Mat. Sci. Eng. A 234-236 (1997), p. 684
12. A. Nitz, E. Nembach, Mat. Sci. Eng. A 239-240 (1997), p. 164
13. A. Nitz, E. Nembach, Met. Mat. Trans. A 29 A (1998), p. 799
14. U. Glatzel: "Microstructure and Internal Strains of undeformed and Creep Deformed Samples of a nickel-Base Superalloy" Habilitation thesis, publisher: Köster, Berlin (1994) ISBN 3-929937-91-3
15. N. Wanderka, U. Glatzel, Mat. Sci. Eng. A203 (1995), p. 69
16. K. Hemker, W. Nix, Mat. Res. Symp. Proc. 133 (1989), p. 481
17. V. Saß: "Untersuchungen der Anisotropie im Kriechverhalten der einkristallinen Nickelbasis-Superlegierung CMSX-4" Ph.D. thesis, publisher: Köster, Berlin (1997) ISBN 3-89574-236-8
18. V. Saß, D. Siebörger, K. Knobloch and U. Glatzel, in: J. Earthman et al. (Eds.), Creep and Fracture of Eng. Materials and Structures 1997 (1997), p. 687
19. M. Heilmaier, K. Wetzel, B. Reppich, in: Oikawa H. et al. (Eds.), Strength of Materials (1994), p. 563,
20. H. Brehm, U. Glatzel, Int. J. Plasticity, in press
21. H.A. Kuhn, H.G. Sockel, Phys. Stat. Sol. (a) 119 (1990), p. 93
22. D. Siebörger, U. Glatzel, Acta Metall. 47 (1999), p. 397

Please send any correspondence to:
uwe.glatzel@uni-jena.de
Fax: ++49 3641 947792

Key Engineering Materials Vols. 171-174 (2000) pp. 261-268
© 2000 Trans Tech Publications, Switzerland

Threshold Stress for High-Temperature Deformation of Dispersion-Strengthened Alloys with Incoherent Dispersoids

F. Yoshida and H. Nakashima

Department of Molecular and Material Sciences, Graduate School of Engineering Sciences, Kyushu University, Kasuga 816-8580, Japan

Keywords: Orowan Stress, Void-Hardening Stress, Aluminum-Beryllium Alloy, Aluminum-Manganese Alloy

ABSTRACT

The threshold stress of Al-1.5vol%Be alloy and Al-0.7at%Mn alloy with incoherent dispersoids was measured at 673K and 623K by stress abruptly loading test (SAL test); a new measuring technique for threshold stress. In both alloys, the threshold stress obtained by the SAL test decreased from the Orowan stress to the void-hardening stress as the time elapsed under load at 623K and 673K. The time needed for change from the Orowan stress to the void-hardening stress approximately agrees with the time necessary to the full relaxation of normal traction of dislocation stress field on the surface of the dispersoids.

It is concluded that the originating mechanism of threshold stress is the Srolovitz's one.

1. INTRODUCTION

Dispersion strengthening was found to be effective in increasing the strength not only at room temperature but also at high temperatures. The flow-stress increase expectable from the strengthening is considered to be the stress needed for the dislocations to pass through dispersed particles. This stress is called the threshold stress. Because the threshold stress is closely related to the mechanism of dislocations to pass through the particle, the threshold stress has been measured by several techniques [1 - 4]. Based on the measured values, several mechanisms have been proposed for the threshold stress : Orowan mechanism [5], local climb mechanism [6], general climb mechanism [7, 8] and Srolovitz mechanism [9, 10]. Among these mechanisms, Srolovitz mechanism is the mechanism that was proposed most recently. According to this mechanism [9, 10], when the matrix-particles interface is incoherent, the normal traction of dislocation stress field on the particle surface will be relaxed by the interface sliding and volume diffusion, and the dislocation will be attracted to particles. When the relaxation is fully completed, the particles are felt by dislocations as voids, and the threshold stress should be equal to the void-hardening stress [10].

The authors' group has investigated the dislocation-particle interaction by the transmission electron microscopy (TEM) for Al-1.5vol%Be [11] and Al-0.7at%Mn alloys [12] with hard incoherent dispersoids and found that at high temperature the interaction in both alloys was in fact attractive type, and no dislocation contrast was observed at the interface. As shown in Fig.1, the threshold stresses obtained by the steady-state creep rate[11, 13, 14] agree well with the void-hardening stresses,σ_v , calculated from the

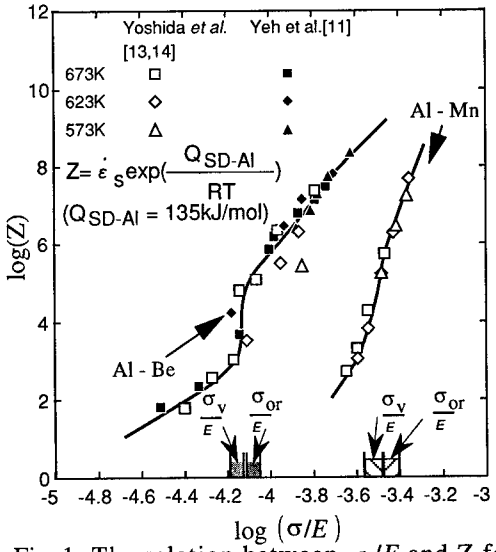

Fig. 1 The relation between σ/E and Z for steady-state creep of Al-1.5vol%Be alloy[11, 13] and Al-0.7at%Mn alloy[14]. The hatched areas respectively represent the ranges of the Orowan stress and the void-hardening stress calculated from dispersion parameters.

dispersion parameters in both alloys. However, the stress, σ_v, is not much different from the Orowan stress, σ_{or}, : the void-hardening stress is lower than the Orowan stress only by about 15% as shown in the next section. Accordingly, it is hard to distinguish between Orowan and Srolovitz mechanisms based on threshold stress measured by the conventional technique.

The diffusion induced relaxation of the normal traction of dislocation stress field on the surface of dispersoid is required if the threshold stress comes from Srolovitz mechanism. Therefore, when the time under load is a short time for which the relaxation is not complete, it is considered that the threshold stress will come from the Orowan mechanism. If this assumption is justified, depending on the time under load, the mechanism that determines the threshold stress changes from Orowan's to Srolovitz's. In addition, the threshold stress changes from the Orowan stress to the void-hardening stress. Therefore, if the transition of the threshold stress is able to be observe depending on the relaxation, the mechanism of the origin of the threshold stress is truly the Srolovitz mechanism.

In this paper, the threshold stresses of Al-1.5vol%Be alloy and Al-0.7at%Mn alloy with incoherent dispersoids measured by the stress abruptly loading (SAL) test and the originating mechanism of threshold stress for high temperature deformation of dispersion-strengthened alloys with incoherent dispersoids will be discussed.

The SAL test is a new method to measure the threshold stress. In this method , the instantaneous strains on applying various creep stress, and creep strains afterwards are precisely measured, and the threshold stress is measured as the critical stress above which the plastic strain is included in the instantaneous strain.

2. EXPERIMENTAL PROCEDURES

2.1 Specimen

For the sample of stress abruptly loading test (SAL test), Al-1.5vol%Be alloy and Al-0.7at%Mn alloy were used.

An alloy ingot of Al-1.03mass%(1.5vol%)Be with a size of 10mm× 100mm× 110mm was prepared by melting and casting from commercial Al-2.55mass%Be mother alloy and 99.99mas% pure aluminum ingots. After peeling the surface by about 1mm, the ingot was cold-rolled and machined to plate specimens of 12mm in length and 4.0mm× 1.2mm in cross section in the gauge part. The specimens were recrystallization-treated at 673K for 3.6ks and stabilization-treated at 873K for 3.6ks and then supplied to the test. The grains were equi-axed and the average grain size was about 40μm in the resultant dispersion-hardened Al-Be alloy specimens. The chemical composition of Be is 1.02mass%. Based on the fact that beryllium is almost insoluble in aluminum, the volume fraction of beryllium particles was calculated to be 1.5vol%.

An Al-0.7at%Mn alloy was melted in air from commercial grade Al-10.1mass% Mn mother alloy and high purity aluminum ingot. Ingots of 160mm in length and 15 mm in diameter were obtained by chill-cast. They were cold-swagged and cold-rolled to sheets of about 0.8 mm in thickness. They were machined to plate specimens of 12 mm in length and 4.0 mm × 0.7 mm in cross section in the gauge part. The specimens were recrystallization-treated at 673K for 3.6ks and stabilization-treated at 773K for 10.8ks, and then supplied to the test. The chemical analysis gave the Mn composition of 0.7at%. The grains were equi-axed and the average grain size was about 75μm. The dispersed particles were confirmed to be Al_6Mn [12]. The volume fraction of Al_6Mn particles was estimated from a solubility[15] at each test temperature. The estimated volume fractions are 4.08vol% (at 673K) and 4.21vol% (at 623K).

2.2 Orowan Stress and Void-Hardening Stress

The Orowan stress, σ_{or}, was evaluated by the following equation proposed by Scattergood and Bacon[16], which takes into account the interaction between the branches of the bowed out dislocation around a particle.

$$\frac{\sigma_{or}}{E} = A\frac{Mb}{4\pi(1+\nu)\bar{\lambda}}\left\{\ln\left(\frac{\bar{D}}{r_0}\right)+B\right\} \qquad \text{Eq.1}$$

$A=1/(1-\nu)$, $B=0.6$: for screw dislocation
$A=1$, $B=0.7$: for edge dislocation.

Here, E is the Young's modulus, ν the Poisson's ratio, M the Taylor factor, b the magnitude of Burgers vector, and r_0 the inner cut off radius of dislocation core. Further, $\bar{\lambda}$ is the average face to face distance between particles on a slip plane and is given as a function of the average particle radius, $\bar{r}_s$, and the average center to center distance, $\bar{l}_s$, (for square distribution) between the particles cut by the slip plane by

$$\bar{\lambda}=1.25\bar{l}_s-2\bar{r}_s, \qquad \text{Eq. 2}$$

where the averages are calculated by considering the size distribution of the particles. The factor 1.25 is the conversion coefficient from regular square distribution to random distribution of the dispersed particles. It has been given by Foreman and Makin[17].

In eq.(1), $\bar{D}$ is the harmonic mean of $2\bar{r}_s$ and $\bar{\lambda}$. By considering the size distribution of the particles, $\bar{l}_s$ and $\bar{r}_s$ are respectively given by

$$\bar{l}_s = \sqrt{\frac{2\pi}{3f}\frac{\overline{r^3}}{\bar{r}}} \qquad \text{Eq. 3}$$

$$\bar{r}_s = \frac{\pi}{4}\frac{\overline{r^2}}{\bar{r}}. \qquad \text{Eq. 4}$$

Here, f is the volume fraction of the dispersed particles, $\bar{r}$ and $\overline{r^2}$ and $\overline{r^3}$ are the averages of r, r^2 and r^3, respectively. The details of this evaluation method are the same as those described in a previous paper[11].

The beryllium particles in the Al-1.5vol%Be alloy and the Al_6Mn particles in the Al-0.7at%Mn alloy were observed by TEM, and the size distribution of the particles was measured. The values of $\bar{r}$, $\overline{r^2}$ and $\overline{r^3}$ determined from the size distribution are shown in Table 1(Al-Be alloy) and 2 (Al-Mn alloy) together with the values of $\bar{\lambda}$, $\bar{l}_s$ and $\bar{r}_s$ calculated using eqs.2, 3 and 4. From these dispersion parameters, the Orowan stress was calculated by eq.1 putting M=3.06[18], ν = 0.34[19] and b = 2.86×10^{-10}m. Further, b or $3b$ was used as r_0. The geometrical mean of the Orowan stresses for screw and edge dislocations was adopted as the Orowan stress which will be compared with the experimental threshold stress. Thus the Orowan stresses determined are shown in Table 3 and 4.

Table 1 Dispersion and related parameters in the Al-1.5vol%Be alloy.

$\bar{r}$/μm	$\overline{r^2}$/μm^2	$\overline{r^3}$/μm^3	$\bar{l}_s$/μm	$\bar{r}_s$/μm	$\bar{\lambda}$/μm
0.39	0.17	0.080	5.34	0.34	6.00

Table 2 Dispersion and related parameters in the Al-0.7at%Mn alloy at 673K and 623K.

T/K	$\bar{r}$/μm	$\overline{r^2}$/μm^2	$\overline{r^3}$/μm^3	$\bar{l}_s$/μm	$\bar{r}_s$/μm	$\bar{\lambda}$/μm	f/%
673	0.117	0.017	0.003	1.14	0.11	1.20	4.08
623	0.117	0.017	0.003	1.12	0.11	1.17	4.21

Table 3 Modulus-compensated Orowan stress and void-hardening stress in the Al-1.5vol%Be alloy

	$r_0=b$	$r_0=3b$
σ_{or}/E	8.9×10^{-5}	7.7×10^{-5}
σ_v/E	7.5×10^{-5}	6.5×10^{-5}

Table 4 Modulus-compensated Orowan stress and void-hardening stress at 673K and 623K in the Al-0.7at%Mn alloy.

T/K	σ_{or}/E		σ_v/E	
	$r_0=b$	$r_0=3b$	$r_0=b$	$r_0=3b$
673	3.83×10^{-4}	3.24×10^{-4}	3.22×10^{-4}	2.73×10^{-4}
623	3.90×10^{-4}	3.30×10^{-4}	3.28×10^{-4}	2.78×10^{-4}

The void-hardening stress, σ_v, is theoretically given by the same form of equation as that of eq. 1, provided that the coefficient A is different. The coefficient A for σ_v is given as follows[19].

$$A=\frac{1+\nu\sin^2\phi}{1-\nu}\cos\phi \quad : \text{for screw dislocation}$$

$$A=\left(1-\frac{\nu}{1-\nu}\sin^2\phi\right)\cos\phi \quad : \text{for edge dislocation.}$$

Here, ϕ is the critical angle at which the dislocation breaks away from the voids. According to Scattergood and Bacon[19], ϕ depends on the Poisson's ratio ν, and in aluminum ($\nu = 0.34$) ϕ is 0.82rad. (47deg.) for screw dislocation andϕ is 0.33rad.(19deg.) for edge dislocation. The geometrical mean of the void-hardening stresses for screw and edge dislocations was adopted as in the case of the Orowan stress and shown in Table 3 and 4. The difference between the theoretical Orowan stress and void-hardening stress is only about 15%.

2.3 Stress Abruptly Loading Test (SAL test)

The stress abruptly loading test (SAL test) to measure the instantaneous strain on applying the creep stress was conducted by using electrically controlled hydraulic machine(Shimazu Servopulser of EHF-2 type) at 673K and 623K . For the stress measurement, a shear type load cell of 1kN in capacity was used, and for the displacement measurement, a L.V.D.T. of ± 0.2mm/V in sensitivity was used. For recording the displacement and load, a digital memory (analyzing recorder : Yokogawa AR1100) was used. The time interval of the measurement was 1ms. The time needed to apply a stress was about 30ms, and the changes of load and displacement could be recorded with a high accuracy using the recorder of 1ms in recording time interval. The time needed to apply a stress is quite shorter than the relaxation time as shown in the next section.

The stress was applied to the specimen which had been prestressed by a low stress (0.84MPa: Al-1.5vol%Be alloy and 2.0MPa :Al-0.7at%Mn Alloy), and the applied stress was increased step by step. An example of the result of Al-1.5vol%Be Alloy is shown in Fig.2[13], where the noise with the electric source frequency was removed by the averaging treatment. The errors of strain and stress measurement arisen by the noise were ± 1.3×10^{-5} and 0.09MPa, respectively. The time shown in Fig.2 is corresponded to the loading time. From this figure, it is seen that the instantaneous strain could be measured accurately.

For heating the specimen, a resistance heating furnace composed of three parts was used, and the temperature was controlled by P.I.D.(Proportional, Integral, Differential). A voltage stabilizer (Toshiba GM2) was used as the electric source of the furnace.

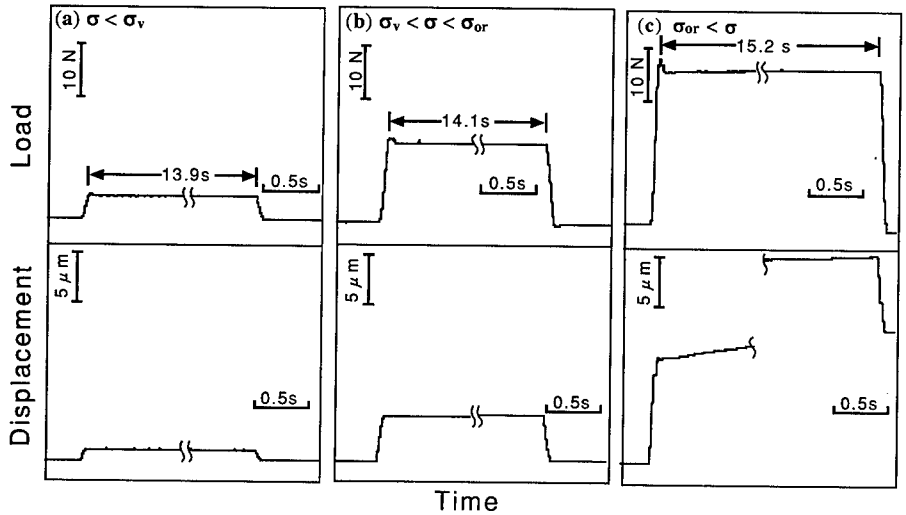

Fig.2 An example of recorded load- and displacement-time curves of Al-1.5vol%Be alloy at 623K[13].

3. EXPERIMENTAL RESULTS AND DISCUSSION

As shown in Fig. 2 an instantaneous strain clearly observed on applying a stress to the specimen. Figure 2 (a) is an example that the applied stress is lower than the void-hardening stress. A creep strain never observe after the instantaneous strain. Figure 2 (b) is an example that the applied stress is presumably lower than the Orowan stress and higher than the void-hardening stress. In a short time

after the instantaneous strain the creep deformation does not occurred, but at about 14 s elapsed, at the time of unloading, the creep deformation is observed, though it is very little. Figure 2 (c) is an example when the applied stress is higher than the Orowan stress, where the creep deformation proceeds from just after the instantaneous strain. Similar results are obtained for Al-0.7at%Mn alloy.

The total strain, ε_a, is plotted against the creep stress, σ, in Fig. 3[13] using the time elapsed after applying the stress as a parameter. Here, this total strain include the elastic and plastic strain. Figure 3(a) is the result obtained at 673K, where the strain at 0.84MPa is made zero, because the stresses were applied to the specimen preloaded by 0.84MPa as described in section 2.3. The dotted line in the figure shows the elastic strain obtained from the stress reduction to the base stress (0.84MPa). The instantaneous strain is denoted by □. Datum points below 4.3MPa lie on a elastic line. This means that below 4.3MPa the instantaneous strain caused by the elastic deformation. On the other hand, the datum points above 4.3MPa do not lie on the elastic line. This fact shows that plastic strains are included in the instantaneous strains. In general, the threshold stress come from the critical stress which caused by the dislocation passing through the particles. Then, the threshold stress correspond to the critical stress measured by the SAL test. As shown in Fig.3, the threshold stress for the instantaneous strain agrees with the Orowan stress. However, as the time elapses, the threshold stress decreases to the void-hardening stress. From these findings, the threshold stress obtained by the SAL test changes as the time elapses after loading.

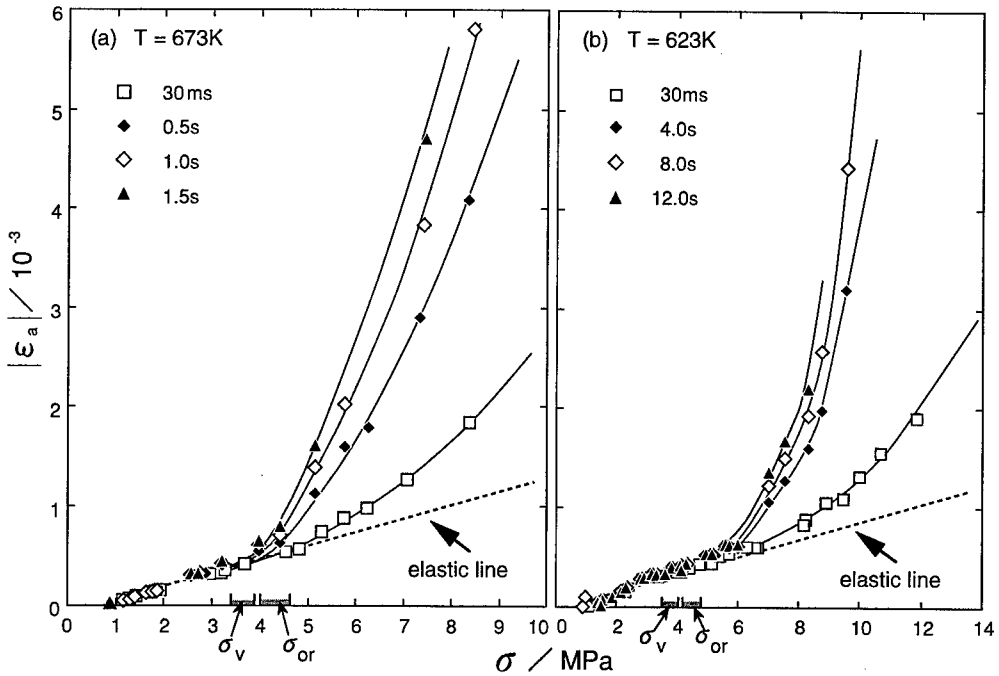

Fig.3 The relation between σ and ε_a obtained by the stress abruptly loading test for Al-1.5vol%Be alloy at (a) 673K and (b) 623K[13]. The hatched area represents the range of the Orowan stress and void-hardening stress shown in Table 3.

Figure 4(a) [14] is shown as the result obtained for Al-0.7at%Mn alloy at 673K. The threshold stress just after loading approximately agrees with the Orowan stress and decreases to the void-hardening stress in time of 1.0 second. Figure 4(b) [14] is the result obtained at 623K. Also at this lower temperature, the threshold stress just after loading approximately agrees with the Orowan stress and approximately decreases to the void-hardening stress in a longer time of 4.0 seconds.

In order to show the threshold stress obtained by SAL test more clearly, the plastic strain component is obtained by subtracting the elastic component from the total strain, and divided by time under load to obtain the average plastic strain rate $\bar{\dot{\varepsilon}}$. Thus , $\bar{\dot{\varepsilon}}$ is plotted against the modulus-compensated stress

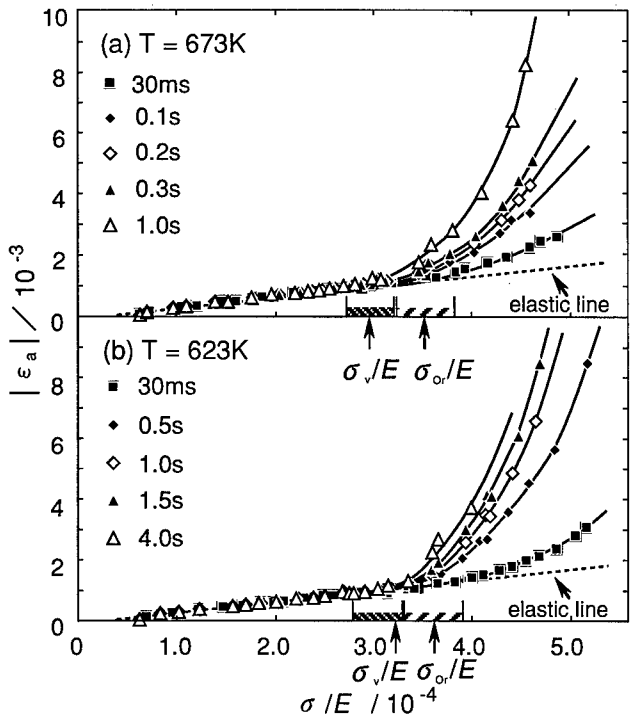

Fig.4 The relation between σ/E and ε_a obtained by the stress abruptly loading test for Al-0.7at%Mn alloy at (a)673K and (b)623K[14]. The hatched areas respectively represent the ranges of the Orowan stress and the void-hardening stress shown in Table 4.

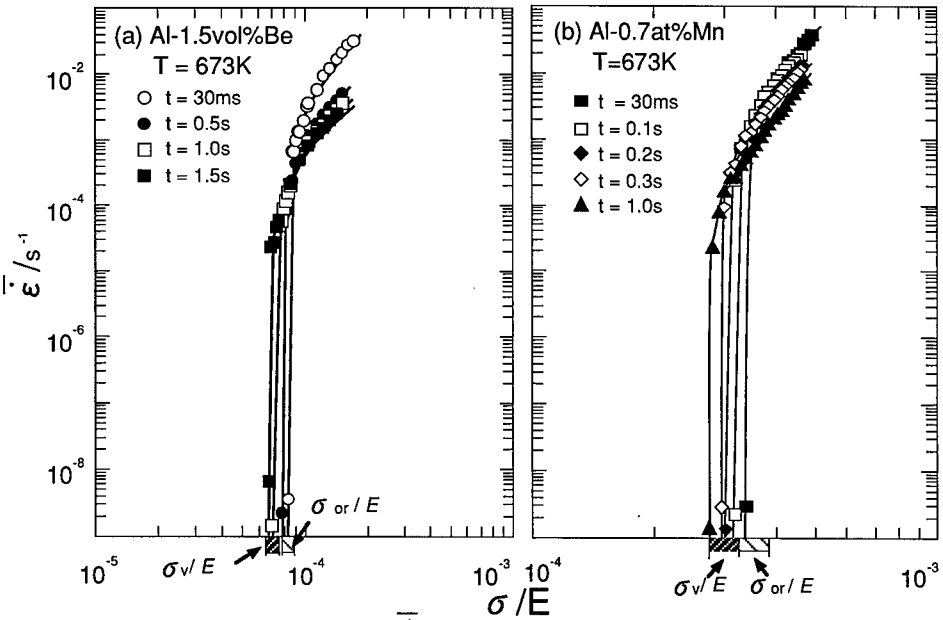

Fig.5 The relation between σ/E and $\dot{\varepsilon}$ obtained from Fig.3(a) and 4(a)[13, 14]. The hatched areas respectively represent the ranges of the Orowan stress and the void-hardening stress shown in Table 3 and 4.

σ / E, in Fig. 5[13, 14], where the strain rate just after loading was obtained by dividing the instantaneous plastic strain with the time of 30ms needed to apply the stress. It is seen that the threshold stress clearly exists and changes form the Orowan stress to the void-hardening stress as the time elapses in

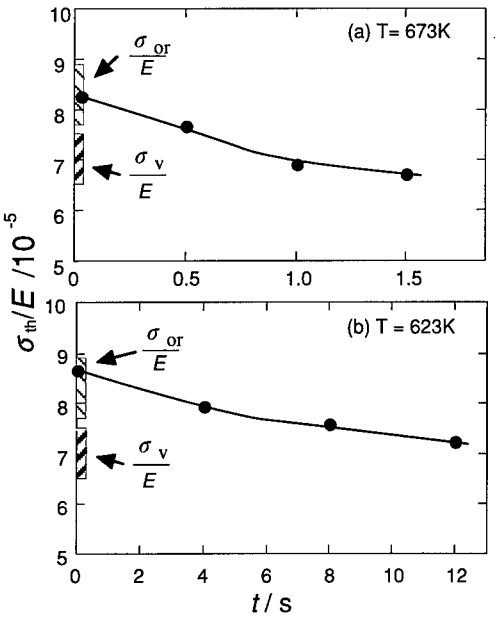

Fig.6 Time dependence of the threshold stress, σ_{th}, obtained by stress abruptly loading test of Al-1.5vol%Be alloy at (a) 673K and (b) 623K[13]. The hatched areas respectively represent the ranges of the Orowan stress and the void-hardening stress shown in Table 3.

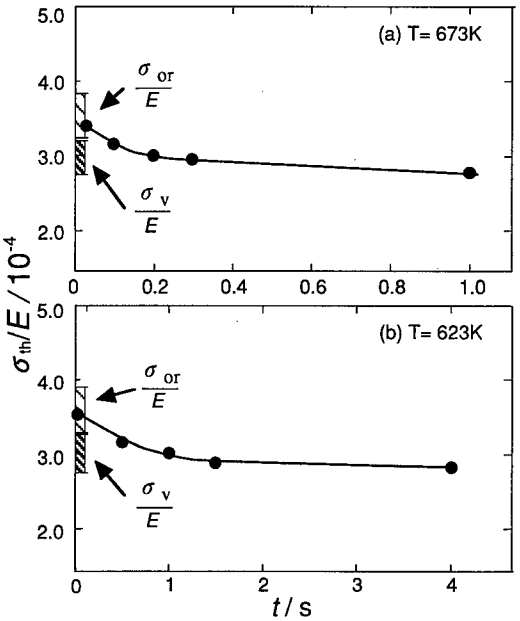

Fig.7 Time dependence of the threshold stress, σ_{th}, obtained by stress abruptly loading test of Al-0.7at%Mn alloy at (a) 673K and (b) 623K[14]. The hatched areas respectively represent the ranges of the Orowan stress and the void-hardening stress shown in Table 4.

both alloys.

Figures 6[13] and 7 [14] are the time dependence of the threshold stress, σ_{th}, obtained from Figs. 3 and 4, showing the change of the threshold stress from the Orowan stress to the void-hardening stress as the time elapsed.

According to Srolovitz et al.[9, 10], the interface sliding and volume diffusion are needed for the full relaxation. In general, the interface diffusion occurs much faster than the volume diffusion. Therefore, the time required for the stress relaxation should be determined by the time needed for the volume diffusion. Srolovitz et al.[10] reported that the time, t_{relax}, necessary to the full relaxation by the volume diffusion is given by

$$t_{relax} = \frac{3(1-\nu)\bar{r}^2 kT}{4(1+\nu)D\Omega G}, \qquad \text{Eq. 5}$$

where kT is usual meaning, D the diffusion coefficient(the lattice self diffusion in pure aluminum), Ω the atomic volume($\Omega = a^3/4 = 1.65\times10^{-29}m^3$, a : lattice constant), G the shear modulus of the matrix. Table 5 shows the relaxation time calculated by using the above equation, where for D and G, the values given in Table 5 were used. Comparing the calculated time with the time needed for the change from the Orowan stress to the void-hardening stress (Figs.6 and 7), it is seen that the times approximately agree with each other.

Table 5 The relaxation times in Al-1.5vol%Be alloy and Al-0.7at%Mn alloy, shear modulus and diffusion constant.

T/K	D/m^2·s^{-1}	G/10^{10}Pa	t_{relax}/s	
			Al-1.5vol%Be	Al-0.7at%Mn
673	6.42×10^{-16}	1.94	2.9	0.2
623	9.33×10^{-17}	2.02	17.9	1.4

From these results, it is concluded that the originating mechanism of threshold stress for high temperature deformation of dispersion- or precipitation hardened alloys with incoherent dispersoids is

truly the Srolovitz's one.

4. CONCLUSIONS

In order to clarify the originating mechanism of threshold stress for high temperature deformation of dispersion-strengthened alloys with incoherent dispersoids, the threshold stress of Al-1.5vol%Be alloy and Al-0.7at%Mn alloy with incoherent dispersoids was measured as the critical stress for the instantaneous plastic strain obtained by the stress abruptly loading test at 673K and 623K. The results obtained are summarized as follows.

1. The critical stress for the instantaneous plastic deformation obtained by the stress abruptly loading (SAL) test almost agreed with the Orowan stress in the whole temperature range tested.

2. In both alloys, the threshold stress obtained by the SAL test changed from the Orowan stress to the void-hardening stress as the time under load elapsed in either temperature of 673K or 623K. The time needed for the change from the Orowan stress to the void-hardening stress almost agrees with the time necessary to the full relaxation of normal traction of dislocation stress field on the surface of the dispersoids.

From these results, it is concluded that the originating mechanism of threshold stress for high temperature deformation of dispersion- or precipitation strengthened alloys with incoherent dispersoids is the Srolovitz's one.

ACKNOWLEDGMENT

We are also grateful to Emeritus Prof. H. Yoshinaga (Kyushu University) and to Prof. H. Abe (Kyushu University) for fruitful advice and discussions. The financial support provided through the Scientific Research Fund from the Japan Light Metal Association for a part of this work is gratefully acknowledged.

REFERENCES

[1] R. S. W. Shewfelt and L. M. Brown, Phil. Mag., **30**(1974), p. 1135.
[2] Y. Miura and H. Nakashima, Proc. 6th Inter. Al-Li conf., DGM, (1991), p. 101.
[3] B. I. Kim and H. Yoshinaga, J. Korean Inst. Met. and Mater., **30**(1992), p .640.
[4] H. Nakashima, K. Iwasaki, S. Goto and H. Yoshinaga, Mater. Trans. JIM, **31**(1990), p. 35.
[5] E. Orowan, *Discussion in the symposium on Internal Stresses in Metals and Alloys*, Institute of Metals, (1948), p. 451.
[6] R. S. W. Shewfelt and L. M. Brown, Phil. Mag., **35**(1977), p. 945.
[7] R. Lagneborg, Scripta Metall., **16**(1973), p. 605.
[8] E. Arzt and M. F. Ashby, Scripta Metall., **16**(1982), p. 1285.
[9] D. J. Srolovitz, R. A. Petkovic-Luton and M. J. Luton, Phil. Mag., **A48**(1983), p. 795.
[10] D. J. Srolovitz, M. J. Luton, R. Petokovic-Luton, D. M. Barnett and W. D. Nix, Acta Met., **32**(1984), p. 1079.
[11] Y. Yeh, H. Nakashima, H. Kurishita, S. Goto and H. Yoshinaga, Mater. Trans. JIM, **31**(1990), p. 284.
[12] Y. Yeh, H. Nakashima, H. Kurishita, S. Goto and H. Yoshianga, Mater. Trans. JIM, **32**(1991), p. 52.
[13] F. Yoshida, J. Sugamoto, H. Nakashima and H. Yoshinaga, J. Japan Inst. Metals, **58**(1994), p. 613.
[14] F. Yoshida, J. Sugamoto, H. Nakashima and H. Yoshinaga, J. Japan Inst. Metals, **59**(1995), p. 1.
[15] L. F. Mondolof, Aluminum Alloy, Butterworth & Co Ltd, London, (1976), p. 324.
[16] R. O. Scattergood and D. J. Bacon, Phil. Mag., **A31**(1975), p. 179.
[17] A. J. E. Forman and M. J. Makin, Phil. Mag., **A14**(1966), p. 911.
[18] G. I. Taylor, J. Inst. Metals, **62**(1938), p. 307.
[19] W. Köster and H.Franz, Met. Rev., **6**(1961), p. 1.
[20] R. O. Scattergood and D. J. Bacon, Acta Metall., **30**(1982), 1665.

Corresponding author; Fuyuki Yoshida, e-mail; yoshida@mm.kyushu-u.ac.jp,
fax; +81-92-575-2318, web site; http://ktj.tj.kyushu-u.ac.jp/index.html

Key Engineering Materials Vols. 171-174 (2000) pp. 269-276
© 2000 Trans Tech Publications, Switzerland

High-Temperature Deformation of Cu-SiO_2 Bicrystals with [011] Twist Boundaries

H. Miura, K. Saijo and T. Sakai

Department of Mechanical Engineering and Intelligent Machines, The University of Electro-Communications, Chofu, Tokyo 182-8585, Japan

Keywords: Cu-SiO_2 Bicrystal, Grain-Boundary Fracture, Grain-Boundary Sliding, Grain-Boundary Energy, High-Temperature Deformation

Abstract Cu-SiO_2 bicrystals having [011] twist boundaries with different misorientation angles were tensile tested at various temperatures from 473 to 1073K and at an initial strain rate of $4.2 \times 10^{-4} s^{-1}$. Most bicrystals fractured intergranularly. As the grain-boundary energy increases, intergranular brittle fracture tended to take place more easily at lower temperatures ; the ductility of bicrystals with higher energy boundaries became lower. The elongation to fracture of the intergranularly fractured bicrystals decreased almost monotonically with increasing temperature. These grain boundary dependent characteristics of deformation and fracture behavior of the bicrystals could be understood reasonably by considering the difference in easy occurrence of grain-boundary sliding. That is, when grain-boundary sliding takes place, grain-boundary SiO_2 particles suppress the sliding, and therefore, stress concentration sites around the particles are formed which promote preferential nucleation sites of voids and cracks. It can be concluded that the easier the saturated grain-boundary sliding occurs, the more brittle the grain boundary becomes.

Introduction It is widely known that ductility of dispersion-hardened alloys decreases at high temperatures, even though the particles are dispersed in metrics and grain boundaries aiming to maintain material strength. The dispersed particles are expected to lower the mobility of dislocations in matrix and to suppress occurrence of grain-boundary sliding (GBS) on grain boundary[1-3]. The loss of ductility is mainly caused by the preferential occurrence of brittle-intergranular fracture [1,2]. Miura et al.[1,2] have explained the mechanism of grain-boundary fracture induced by GBS in the dispersion-hardened alloys from the experiments using orientation-controlled bicrystals. These secondary phase particles on the grain boundaries act as a suppressor of GBS, and provide stress concentration sites to promote the preferential nucleation of voids and cracks. This introduces an earlier grain-boundary fracture, and therefore, loss of ductility. Therefore, strengthening by dispersing second phase particles brings two inconsistent mechanical behaviors, i.e. preservation of strength and loss of ductility at high temperature.

It is also known that the occurrence of grain-boundary fracture at high temperature is strongly dependent on the grain-boundary character [1-3]. Grain-boundary fracture of various dispersion-hardened alloys has been studied extensively using polycrystalline alloys [4-6], and the fracture behavior has been discussed in conjunction with Σ values[6]: Boundaries with higher Σ values are more resistive to the grain-boundary fracture. However, this criterion was found to not be always true. Recently, Miura et al. [1,2] explained the occurrence of such grain-boundary dependent fracture

behavior in Cu-SiO_2 bicrystals by considering grain-boundary related factors, such as grain-boundary viscosity and distribution of grain-boundary particles, etc.. Further, they have also suggested that fracture takes place more easily in higher-energy boundaries.

In the present study, temperature dependence of grain-boundary fracture and strength will be examined by using orientation-controlled bicrystals with [011] twist boundaries. Particular attention will be placed upon the correlation between grain-boundary energy and the occurrence of grain-boundary fracture.

Experimental Cu-0.2mass%Si alloy bicrystals with [011] twist boundaries were grown by the Bridgman method using seed crystals. The misorientation angles were 2°, 7°, 20° and 41°. Hereafter, these bicrystals are referred to as the 2°, 7°, 20° and 41° bicrystals, respectively. Grain-boundary energies of these bicrystals increase in the order of 2°, 7°, 20° and 41° [7]. After confirming by the X-ray Laue technique that the actual misorientation-angles were within 1° of the above nominal angles, these bicrystals were internally oxidized at 1223K for 24h with a powder pack method. Dispersed SiO_2 particles were obtained both in the matrices and on the grain boundaries by this internal oxidation treatment. After degassing in a graphite mold in vacuum, tensile specimens of 14.8mm gage length and 4x1mm^2 cross section were spark cut having the boundaries oriented 45° against the tensile direction (Fig. 1). Grain-boundary and in-matrix particles were observed by transmission electron microscope (TEM). After the mechanical and electritical polishing, the tensile specimens were finally annealed at 1223K for 0.5h in a graphite mold in vacuum. Tensile tests in vacuum were conducted at various temperatures from 473 to 1073K on an Instron-type testing machine at a strain rate of 4.17 x $10^{-4}s^{-1}$. After the tests, fracture surfaces were observed on a scanning electron microscope (SEM).

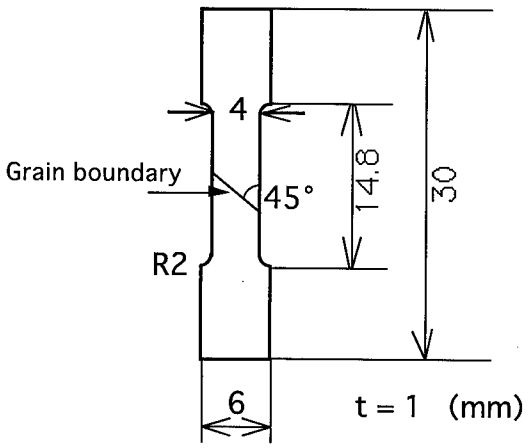

Fig. 1. Schematic illustration of a tensile specimen.

Table 1. Distribution of grain-boundary SiO_2 particles.

Misorientation angle	2°	7°	20°	41°
Particle radius $r/\mu m$	-	0.34	0.41	0.52
Density of grain -boundary particles $\rho/\mu m^{-2}$	-	0.98	0.48	0.33
$r\rho/\mu m^{-1}$	-	0.33	0.20	0.17

Results The distribution of grain-boundary particles depends strongly on the grain-boundary character (Table 1). Mean particle radius viewed from grain-boundary normal increases and density of grain-boundary particles (number of particles per unit grain-boundary area) decreases with increasing misorientation angle or grain-boundary energy in the order of $2° < 7° < 20° < 41°$.

Figure 2 shows TEM photographs of the grain-boundary particles viewed from grain-boundary parallel. It can be seen that particles on 41° boundary (Fig. 2 (b)) is slightly more oblate than those on 20° boundary (Fig. 2(a)). Particles become more oblate with increasing grain-boundary energy[7].

Figure 3 (a) and (b) show the series of true stress (σ) vs. true strain(ε) curves for 7° and 20° bicrystals, respectively. After the clear yielding, all of the flow curves show work hardening with increasing strain and proceed to the fractures with rapid drops in flow stresses. It is notable that the temperature dependence of the strain to fracture differs much depending the bicrystals. Though the fracture strain in the 7° bicrystal is almost constant irrespective of temperature, the fracture strain in the 20° bicrystal decreases rapidly with increase in temperature. Oscillation of flow stress, which characterize the occurrence of dynamic recrystallization (DRX), is not observed. This suggests that no DRX took place in the present experimental condition, even though some testing temperatures were over 0.5Tm. In fact, optical microscopic observation revealed that no DRX took place in all the deformed bicrystals.

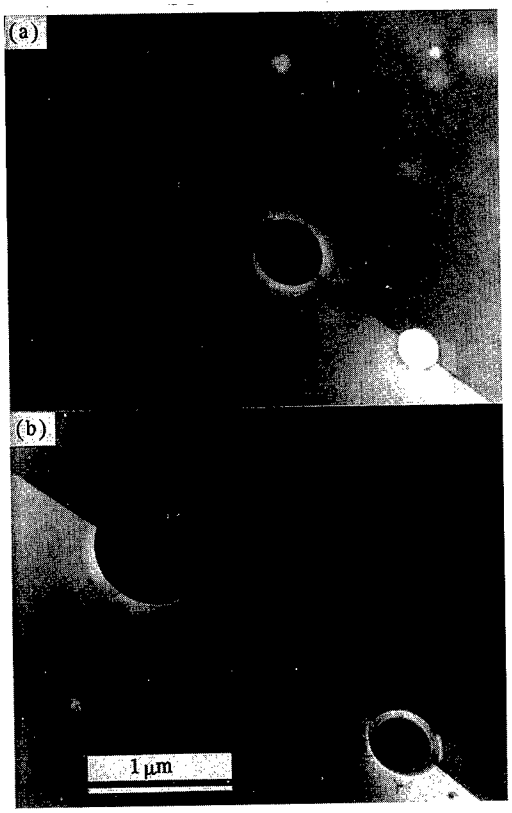

Fig. 2. TEM photographs of grain-boundary SiO_2 particles by edge-on observation for (a) 20° and (b) 41° boundaries, respectively.

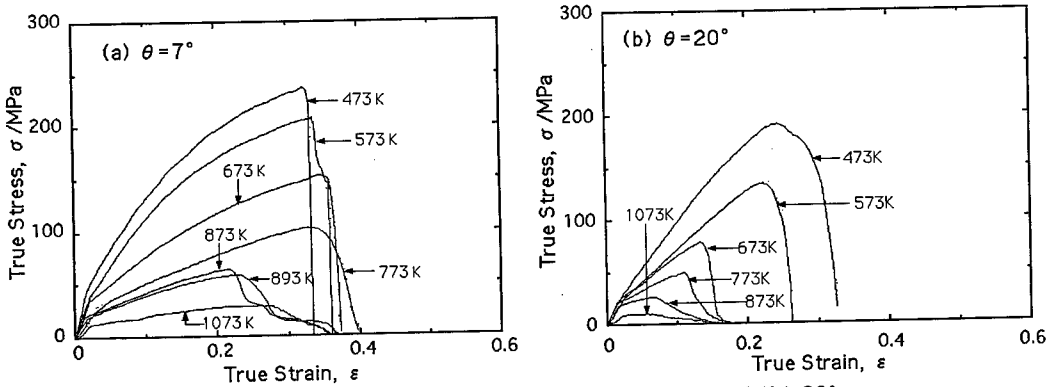

Fig. 3. True stress-true strain curves of (a) 7° and (b) 20° bicrystals deformed at various temperatures.

Figure 4 summarizes the temperature dependence of peak stress, i.e. grain-boundary strength. Open and filled symbols indicate transgranular and intergranular fracture, respectively. And half-filled symbol indicates occurrence of mixed-mode fracture of transgranular and intergranular. Then, the results from transgranularly fractured bicrystals do not indicate grain-boundary strength. Although most of the 2° and 7° bicrystals fractured transgranularly, these results are also plotted in Fig. 4 for convenience sake. Because these grain-boundary strength can be estimated higher than the values plotted in Fig. 4. The fact that the grain-boundary strength of the 7° bicrystal deformed at 773K is just on the strength curve is suggestive that the grain-boundary strength of the 7° bicrystal at the other temperatures is not so different from the expected strength by transgranular fracture. As can be seen in Fig. 4, the grain-boundary strength is a strong function of grain boundary and temperature: 1) The grain-boundary strength decreases monotonically with increase in temperature. 2) The higher is the grain-boundary energy, the lower is the grain-boundary strength. This is also in good accordance with the result of the grain boundary dependence of fracture strain which will be shown in Fig. 5. This is due to the ease of occurrence of GBS, which weakens grain boundary, with increasing temperature and grain-boundary energy, as will be discussed below.

Figure 5 summarizes the experimental results of the fracture strain as a function of temperature. Open, filled and half-filled symbols again indicate transgranular, intergranular and mixed-mode fracture, respectively. The strain to fracture in the 2° and 7° bicrystals looks to be almost constant independent of temperature. On the other hand, the elongation for the 20° and 41° bicrystals rapidly decreases with

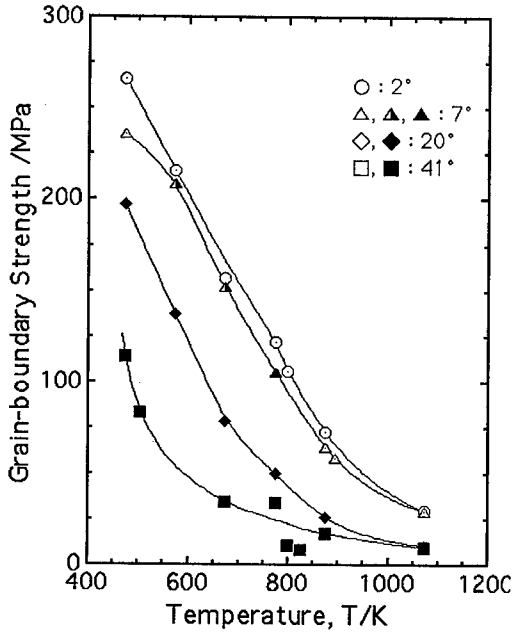

Fig. 4. Temperature dependence of grain-boundary strength. Open, filled and half-filled symbols indicate transgranular, intergranular and mixed-mode fracture, respectively.

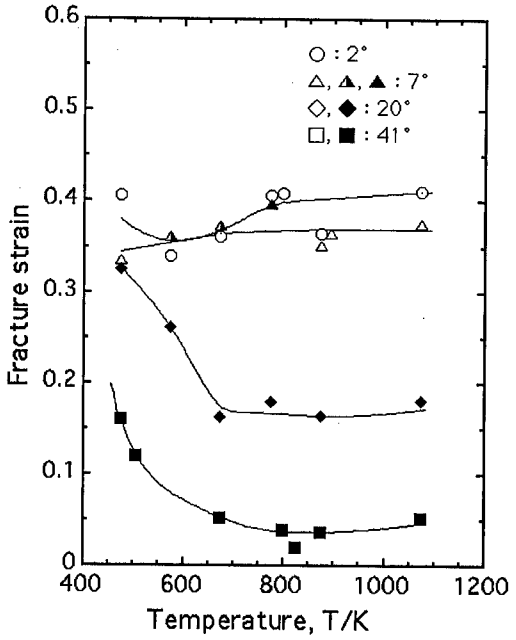

Fig. 5. Temperature dependence of fracture strain. Open, filled and half-filled symbols indicate transgranular, intergranular and mixed-mode fracture, respectively.

increasing temperature accompanied by intergranular fracture. Therefore, the rapid drop of ductility in the 20° and 41° bicrystals can be characterized by the occurrence of intergranular fracture.

At a fixed temperature, the total elongation tends to decrease with increase in grain-boundary energy in the order of 2° > 7° > 20° > 41° boundary. Furthermore, intergranular fracture seems to take place more easily with increase in grain-boundary energy. This is because that the grain boundary becomes more brittle with increase in grain-boundary energy, as will be discussed later.

SEM photographs of grain-boundary fractured surfaces of 20° bicrystals are shown in Fig. 6. At 473K, fine dimples indicative of occurrence of ductile fracture can be seen. Existence of SiO_2 particles in the dimples would indicate that the cracks initiated at the Cu/SiO_2 interface. Grain-boundary fracture surface becomes flatter with increase in temperature. This indicates that grain boundary becomes more brittle and fracture mode changes from ductile intergranular to brittle intergranular with increasing temperature. This temperature-dependent fractography is in good correspondence to the results shown Figs. 4 and 5 that grain-boundary strength and fracture strain become smaller as the temperature increases. What is more notable in Fig.6 (c), parallel-elongated voids appear. They are thought to be formed by dragging of the grain-boundary particles by GBS activated at an increasing tempo at higher temperatures.

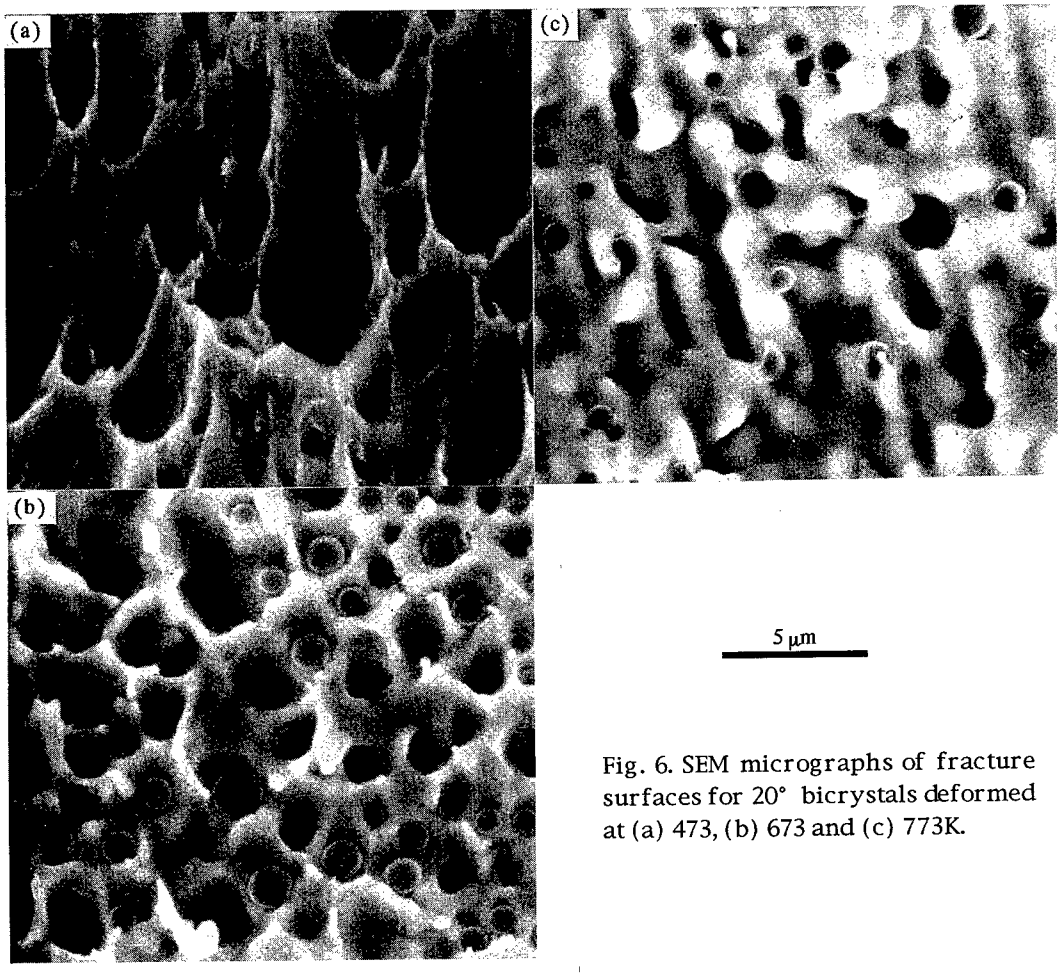

Fig. 6. SEM micrographs of fracture surfaces for 20° bicrystals deformed at (a) 473, (b) 673 and (c) 773K.

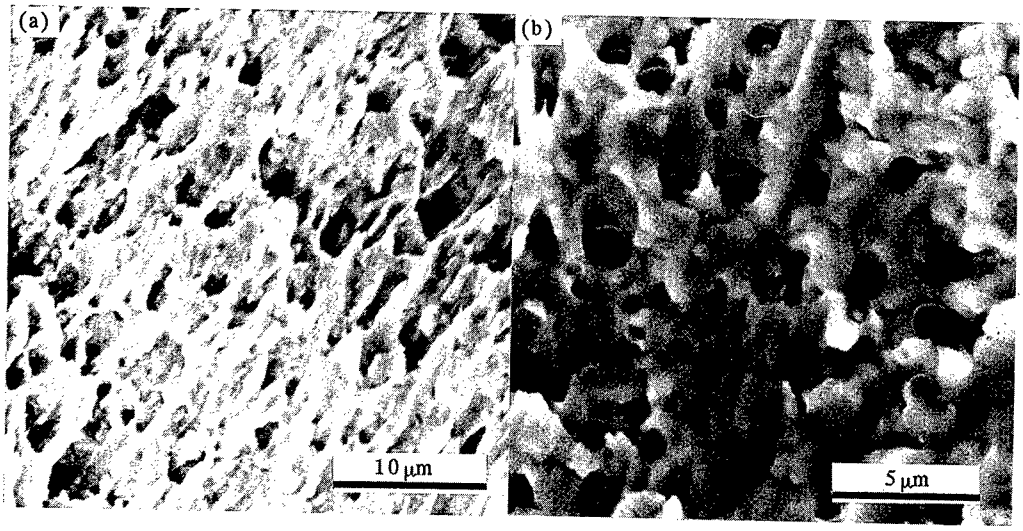

Fig. 7. SEM micrographs of fracture surfaces for (a) 7° and (b) 41° bicrystals deformed at 673K.

Figure 7 shows SEM photographs of the grain-boundary fracture surfaces of the 7° and 41° bicrystals deformed at 673K. The photograph of the fracture surface of 20° bicrystal has already shown in Fig. 6(b). The 2° bicrystal fractured in the transgranular ductile manner. Therefore, its photograph is not shown here. A tendency can be found from the comparison of these photographs; as the grain-boundary energy increases, the appearance of grain-boundary fracture surface becomes flatter, ie. fracture mode changes from ductile intergranular to brittle intergranular. This fact would be suggestive that grain-boundary strength becomes lower as the grain-boundary energy increases.

Discussion The occurrence of grain-boundary fracture seems dominating the total strain to fracture. The observed misorientation and temperature dependence of the fracture strain will be discussed below in relation to the occurrence of GBS.

As the temperature increases, grain-boundary diffusion becomes more operative. Diffusion at grain boundary is strongly dependent on grain-boundary character[8]. If the GBS is assumed to be controlled by grain-boundary diffusion as discussed by several investigator[8,9], therefore, GBS should occur more easily at lower temperatures in bicrystals with higher energy boundaries[10]. When GBS occurs, GBS is suppressed by the grain-boundary particles, and therefore, the amount of sliding will soon be saturated. The blocking develops an internal stress, which acts against the applied shear stress on the particle-free area of the boundary, and eventually stops the sliding. When a shear stress σ_{shear} parallel to the boundary is applied, the characteristic time τ_L for saturated GBS is written as[9]

$$\tau_L=(4/\pi^2)\{(1-\nu)/(2-\nu)\}(\eta/\mu r \rho c) \qquad \text{Eq.1}$$

where ν: Poisson ratio, η: boundary viscosity of GBS, μ: shear modulus, r : particle radius, ρ : number of particles on an unit area of grain boundary and c: half of the boundary thickness. Further, boundary viscosity η is expressed as

$$\eta = \eta_0 T \exp(Q/kT) \qquad \text{Eq.2}$$

with η_0 : inherent boundary viscosity, Q: activation energy for GBS, k : Boltzmann constant and T : temperature.

If GBS is controlled by grain-boundary diffusion, η is inversely proportional to the grain-boundary

diffusivity. Monzen et al. [8,9] have reported that η value at a fixed temperature varies significantly by several orders of magnitude with increase in grain-boundary energy. On the other hand, the values of $r\rho$ in different bicrystals differ only within a factor two (see Table 1). Therefore, GBS is controlled by η, and τ_L value at a fixed temperature abruptly decreases depending strongly on η value with increasing grain-boundary energy.

When GBS takes place, the grain-boundary SiO_2 particles act as an inhibitor of GBS and provide stress-concentration sits to promote the nucleation of voids and cracks. Therefore, it can be naturally expected that the grain boundary becomes more brittle as the GBS takes place easier at a fixed temperature. This explains the rapid drops in ductility and fracture stress at lower temperatures in the bicrystals having higher-energy boundaries. τ_L values for each boundaries at 673K, where the difference of the fracture strain is most obvious, are estimated approximately to be $1x10^{1}$s for 7°, $3x10^{-3}$s for 20° and $7x10^{-4}$s for 41° boundaries by using the values in Table 1, $\mu = 4.6x10^{10}$Pa, $\nu = 0.34$, c= $2.5x10^{-10}$m and results of Q and η_0 derived by Monzen et al. [11]. Because such low-energy boundary like 2° boundary hardly slides [11], τ_L value for 2° boundary should be much larger than that of 7° boundary. After all, it can be recognized that τ_L value decreases in the order of $2° \gg 7° \gg 20° > 40°$ at a fixed temperature, and then, grain-boundary fracture to lower the ductility and fracture stress (and/or strength) would take place easier in the order of 40°, 20°, 7° and 2° boundary, which is the order of decreasing grain-boundary energy.

From the Brandon's criterion [12], the 20° and 41° boundaries are recognized as Σ33A and Σ9 boundaries, respectively. According to coincidence site lattice theory, the grain boundaries having low Σ value would be expected to have more ordered atomic arrangement, and therefore, to show superior mechanical and chemical properties to those having low Σ value. However, the 41° (≃ Σ9) boundary showed lower strength than 20° (Σ33A) boundary in the present experiment. Grain-boundary fracture seems to take place more easily with increasing grain-boundary energy. Therefore, grain-boundary energy would be better parameter to describe the character of grain boundaries rather than the Σ value.

The strain to fracture of 20° and 41° bicrystals in Fig. 5 decreases as temperature increases at lower temperatures. This is because the saturated GBS is achieved with by shorter period of time with increasing temperature. Therefore, with increasing temperature, grain-boundary fracture takes place more easily, and then, fracture strain and strength become smaller.

Stress concentration at the edges of particles σ_{max} generated by applied tensile stress is commonly written as

$$\sigma_{max} = \sigma_{tensile}(1+2(a/\rho)^{1/2}) \qquad \text{Eq.3}$$

with $\sigma_{tensile}$: tensile stress normal to the line of apsis of an ellipse-shaped particle, a : half length of the apsis and ρ : radius of the edge curvature of the particles. If the lenticular-shaped SiO_2 particles are assumed to be ellipse in section, the degree of stress concentration at the particle-edge should qualitatively become higher with increasing grain-boundary energy even under a constant applied tensile stress. It is because the value of a increases and value of ρ looks to decrease with increasing grain-boundary energy. Such particle-shape dependent stress concentration should strongly affect on the nucleation of voids and cracks at the edges, and this effect would emphasize grain-boundary dependent occurrence of fracture and its temperature dependency.

Over the temperature of about 800K, the fracture strain seems to be almost saturated. Miura et al. [1,2] have shown that stress relaxation by Cu/SiO_2 interfacial diffusion attributes to the recovery of ductility at higher temperatures in copper bicrystals with dispersed SiO_2 particles. Occurrence of the stress relaxation vanishes stress concentration around the particles. No dynamic recrystallization, which

can be another cause of ductility recovery, took place in any experimental conditions in present study. Therefore, we assume that influence of the stress relaxation is the cause of the saturation of the fracture strain at higher temperatures over 800K. The reason that clear recovery of ductility at higher temperatures could not be observed should be due to much lower density of grain-boundary particles in these [011] twist boundaries. The density of the particles per unit boundary area in [011] twist boundaries is about ten times lower than that in [001] twist boundaries. The low-density distribution of particles on grain boundary unables effective suppression of GBS and makes the easy void formation possible by particle dragging as already shown in Fig. 6 (c). This void formation by the particle dragging made the clear ductility recovery difficult. The saturated fracture strain over 800K should be the result of balancing of these effects.

Summary The results are summarized as follows.

1. Grain-boundary strength and ductility of bicrystals decreased with increasing grain-boundary energy.
2. Ductility of bicrystals with high-energy boundaries decreased abruptly with increasing temperature accompanied by the occurrence of intergranular fracture, though bicrystals having low-energy boundaries showed almost constant fracture strain.
3. Grain-boundary dependency of fracture behavior could be reasonably understood by the easy occurrence of stress concentration at matrix/particle interfaces induced by grain-boundary sliding.
4. The shape and radius of the grain-boundary particle seemed to also affect the easy occurrence of grain-boundary fracture.

Acknowledgments The authors acknowledge the material supply from Nippon Mining and Metals Co. Ltd, Kurami Works, Japan.

References

[1] H. Miura, T. Sakai, N. Tada, M. Kato and T. Mori, Acta Metall. Mater. 41 (1993), p.1207.
[2] H. Miura, T. Sakai, N. Tada and M. Kato, Phil. Mag. A 73 (1996), p.871.
[3] T. Watanabe, Trans. JIM, suppl., 27 (1986), p.73.
[4] S. Onaka, M. Kato and R. Tanaka, Trans. JIM, 28 (1987), p.32.
[5] W. Pavinich and R. Raj, Metal. Trans. A, 8A (1977), p.1917.
[6] T. Shibayanagi, A. Yoshimoto and S. Hori, Mater. Trans. JIM, 31 (1990), p.1057.
[7] H. Miura, M. Kato and T. Mori, Coll. de. Phys., C1-263 (1990), p.51.
[8] R. Raj and M.F. Ashby, Metall. Trans., 2 (1971), p.1113.
[9] T. Mori, M. Koda, R. Monzen and T. Mura, Acta Metall., 31 (1983), p.275.
[10] R. Monzen, Y. Sumi, K. Kitagawa and T. Mori, Acta Metall. Mater, 38 (1990), p.2553.
[11] R. Monzen, M. Futakuchi and T. Suzuki, Scripta Metall. Mater., 8 (1995), p.1277.
[12] D.G. Brandon, B. Ralph, S. Ranganthan and S. Wald, Acta Metall., 12 (1964), p.813.

Key Engineering Materials Vols. 171-174 (2000) pp. 277-284
© 2000 Trans Tech Publications, Switzerland

Kinetic Modelling of the Influence of Particles on Creep Strength

J. Eliasson[1,3], Å. Gustafson[2,3] and R. Sandström[1,3]

[1] Department of Materials Science and Engineering, Division of Materials Technology, Royal Institute of Technology, S-100 44 Stockholm, Sweden

[2] Department of Materials Science and Engineering, Division of Physical Metallurgy, Royal Institute of Technology, S-100 44 Stockholm, Sweden

[3] Department of Materials Science and Engineering, Brinell Centre, Royal Institute of Technology, S-100 44 Stockholm, Sweden

Keywords: Particle Strengthening, Particle Size Distribution, Climb, Orowan Mechanism, Particle Coarsening, High Temperature, Austenitic Stainless Steel

Abstract

The influence of particles on creep strength is studied for an austenitic stainless steel strengthened with TiC-particles in the temperature interval 550-800 °C. At lower temperatures, when the dislocations cannot climb over the particles, the Orowan mechanism dominates. At higher temperatures, the increase in strength is limited by climb. At intermediate stresses both climb and the Orowan mechanisms are active. By kinetically analysing the time it takes for the particles to be climbed, the role of the two mechanisms can be clarified. Smaller particles will first be overcome with climb, while larger ones have to be surounded with Orowan loops, which considerably contribute to strength. At low stresses, all particles are overcome with climb, and the strengthening contribution is small. Particle coarsening is described with a multi-component model.

Introduction

Alloys with good creep properties earn their strength from precipitation hardening. The particles act as obstacles for the moving dislocations. The particles can be overcome by different mechanisms. At lower temperatures, the dislocations either cut the particles when they are sufficiently small, or Orowan loops are formed around them. At elevated temperatures, the dislocations will have the possibility to crosslip or climb over the particles. The classical models for particle strengthening in creep resistant materials are based on an energy criterion, [1]. If energetically favourable, the dislocations will climb across the particles, otherwise not. The strength contribution is related to the Orowan strength, which is essentially inversely proportional to the interparticle spacing. A climb factor is introduced to reduce the strength contribution when climb is taken into account. If the dislocations are attached to the particles during climb, the strength contribution is larger than when the dislocations will relax and not adhere to the particles, see below. These classical models have a major drawback. They are almost independent of temperature, except from the reduced shear modulus. Experimentally the creep strength decreases exponentially with temperature. The purpose of the present paper is to consider kinetic effects by taking the time it takes for dislocations to climb across particles into account.

Model

The Orowan contribution

The contribution from this mechanism can be estimated according to the following relationship, [1]:

$$\sigma_o = \frac{2MGb}{3.5L_{sq}} \qquad (1)$$

where M is the Schmid factor ≈ 3, b Burgers vector, G the shear modulus and L_{sq} the mean Orowan particle distance. The value of 3.5 is based on an averaging over screw and edge components in the dislocations, [2]. The distance between the particles is given by, [1]:

$$L_{sq} = r\sqrt{\frac{2\pi}{3f}} \tag{2}$$

where r is the average particle radius and f the volume fraction of particles.

Traditional description of creep threshold stresses

At higher temperatures, the dislocations can climb over the particles. There are several factors determining the effectiveness of climb. In local climb, a larger part of the dislocation interacts with the particle than in general climb. The former configuration also gives a larger contribution to the strength. For general climb, the energy required is low. The critical stress allowing the particles to be overcome by climb based on the energy criterion is related to the Orowan stress and given by, [1]:

$$\sigma_{climb} = \frac{(\alpha_{cl})^{3/2}}{2\sqrt{2} + (\alpha_{cl})^{3/2}}\sigma_o \tag{3}$$

The parameter α_{cl} is called climb resistance. It is a description of the rate of increase of the line length as the dislocation segment climbs over the particle. α_{cl} depends on particle shape. In local climb α_{cl} equals 0.77 for spherical particles, [1]. In general climb, this value is only a fraction of this value. It is also dependent on the volume fraction particles to a factor $f^{1/2}$. The α_{cl}-values are then reduced to below 0.1, and can be below 0.01 at small volume fractions. Equation 3 also takes into consideration that there is a statistical distribution of particle spacings. The dislocations can find easy gates through the particle structure. If local climb is active, the influence from particles on creep strength is about $0.2\sigma_o$. If general climb is controlling, a volume fraction between 1-10% would give an influence between $0.004\text{-}0.02\sigma_o$.

For some materials, especially those where there is a large misfit between the matrix and particle, the dislocation is attached to the particle after the passage of it. This is found in oxygen dispersion strengthened materials. In that case, the particles become very effective as strengtheners also at high temperatures, [3, 4].

Influence of creep rate

The Norton relationship has been used in the past to describe the influence on creep strain rate at a temperature for many materials

$$\dot{\varepsilon} = A_0\sigma^n e^{-Q/RT} \tag{4}$$

where A_0 is a constant, σ is the applied stress, Q is usually set to the activation energy for self-diffusion, R=8.314 J/molK, T is the temperature in Kelvin.

For pure metals and one-phase materials, the stress exponent n is typically about 5 in the power law regime and the activation energy Q is close to that for self-diffusion. Solution hardening is generally decreasing the stress exponent at a specific stress. In particle strengthened materials the value of n is often larger. Stress exponents between 20-40 have often been found, [3]. The apparent activation energy is higher than the activation energy for self-diffusion. The high n-value is usually explained by introducing inner stresses, σ_i, from dislocations and particles. The relationship is then transferred to:

$$\dot{\varepsilon} = A_0(\sigma - \sigma_i)^n e^{-Q/RT} \tag{5}$$

$$\sigma_i = \sigma_{disl} + \sigma_{part} \tag{6}$$

where σ_{disl} is the backstress from the dislocations and σ_{part} from the particles respectively. In this way, the stress exponent is reduced to lower values, generally between 4-7. The back stress from the dislocations is related to the dislocation density ρ, [5]:

$$\sigma_{disl} = \alpha M G b \sqrt{\rho}\,, \tag{7}$$

When limited climb takes place σ_{part} is given by the Orowan stress, Eq. 1. When on the other hand climb is very rapid, $\sigma_{part}=\sigma_{climb}$, Eq. 3. The intermediate situation will now be analysed.

The average speed of dislocations is given by:

$$v_\rho = \frac{\dot{\varepsilon} M}{\rho_m b} \tag{8}$$

where ρ_m is the mobile dislocation density. A fraction γ of dislocations is considered mobile. v_ρ will be compared to the dislocation climb speed [6]:

$$v_{climb} = M_s b \sigma \tag{9}$$

where M_s is the mobility of dislocations. The mobility M_s includes the following components, [2]:

$$M_s = \frac{D_s b}{kT} \tag{10}$$

where k is Boltzmanns constant and D_s is the self-diffusion constant at the temperature T.

If the glide time between particles is neglected climb thus yields an effective average dislocation speed which is a factor $L_{sq}/2r$ larger than the climb speed.

$$v_{eff} = v_{climb} \frac{L_{sq}}{2r} \tag{11}$$

If $v_{eff} > v_\rho$, the contribution of climb becomes important. In the equations above, creep strain rate is used. To be able to use standard creep data containing information about creep stress and creep rupture time t_R, the creep rate is calculated using the Monkman-Grant relationship, [7].

$$\dot{\varepsilon} = B \frac{\varepsilon_R}{t_R} \tag{12}$$

where B is a constant, ε_R is the rupture elongation in the creep test.

Influence of particle size distribution on creep strength

It has been verified for ferritic steels that the carbide distribution can be written as, [8]:

$$f(r) = f_0 e^{-\beta(r - r_{res})} \tag{13}$$

where $f(r)$ is the volume fraction of particles which is larger than r. f_0 is the volume fraction particles. r_{res} is the smallest particle size recorded due to the instrumental resolution limit. β is a constant, which is approximately equal to $1/r_{part0}$ where r_{part0} is the average particle size.

If the particles are sufficiently small they will rapidly be crossed by climb and they do not contribute to the Orowan strength. Thus, there is a transfer in mechanism between Orowan and climb. By comparing the dislocation climb speed and the average dislocation speed, the position of this transfer can be estimated. Putting $v_{eff} = v_\rho$ from Eq. 11 and using Eq. 2 give the critical radius r_{crit} when climb starts to be of importance.

$$r_{crit} = r_{part0} \frac{v_{climb}}{v_\rho} \sqrt{\frac{\pi}{6 f_0}} \tag{14}$$

From Eq. 13 the corresponding f_{crit} value can be obtained. A schematic view of the function in Eq. 13 is given in Fig. 1, and the transfer in mechanism is illustrated. When $r_{part0} < r_{crit}$ climb is the dominating mechanism and $\sigma_{part} = \sigma_{climb}$ according to Eq. 3. The dislocations have enough time to climb over all of the particles. In this case $v_{climb} > v_p$. When $r_{part0} > r_{crit}$, the Orowan mechanism is active but only for the particles satisfying $r > r_{crit}$. Inserting $r = r_{crit}$ and $f = f_{crit}$ into Eqs. 1 and 2 then yields the threshold stress at intermediate stresses.

$$\sigma_{crit} = \frac{\sigma_o r_{part0}}{r_{crit}} e^{(-0.5\beta(r_{crit} - r_{res}))} \tag{15}$$

When $r_{part0} >> r_{crit}$ then climb has a negligible influence and $\sigma_{part} = \sigma_o$.

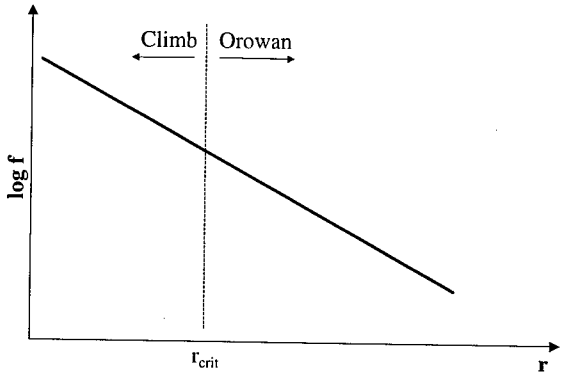

Figure 1. Volume fraction of particles vs. particle radius. r_{crit} is the critical radius below which climb becomes important. It takes higher values at lower stresses, longer times and higher temperatures.

Description of material

15Cr15Ni1MoTi is an austenitic stainless steel which is strengthened with TiC particles. The creep rupture strength is given as a function of time in the temperature range 550-800 °C in Fig. 2., [9]

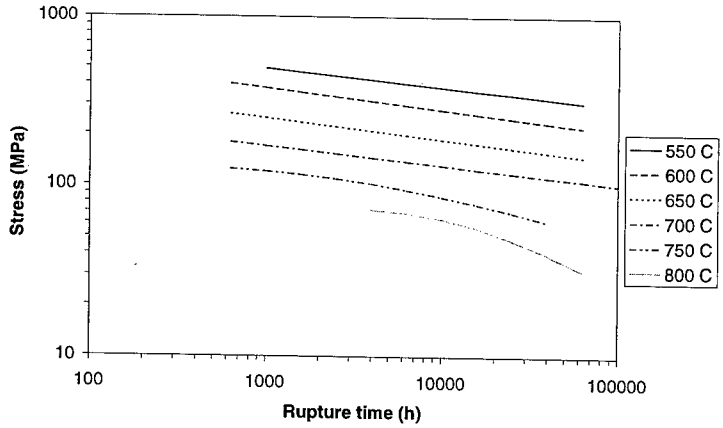

Figure 2. Creep stress vs. rupture time for 15Cr15Ni0.1C0.4Ti between 550-800 °C.

The investigated batch has the composition in (wt%) 15.4 Cr, 15 Ni, 1.38 Mo, 1.84 Mn, 0.38 Si, 0.31 Ti, 0.1 C. It was solid solution treated at 1150 °C, and water quenched. Most of the carbon is bound to titanium to form particles of TiC. The material contains two sets of particles. Coarse primary ones precipitated during cooling after casting, and fine secondary ones precipitated during creep. The secondary particles play a significant role for the creep strength. A fine dispersion of

small size of the precipitates is observed. Compared to 18Cr-10Ni austenitic stainless steels, the creep strength is higher. The strength compared to other materials is maintained in the temperature range. At 750 and 800 °C the reduction in creep strength is accelerated at longer times. One explanation to this is the coarsening of TiC-particles.

Particle coarsening

Simulation of coarsening of TiC in the steel 15Cr15Ni0.1C0.4Ti was performed with the multicomponent coarsening model, [10], in DICTRA, [11]. The model is based on the conclusion from the analysis by Lifshitz and Slyozov, [12, 13], and Wagner, [14], that the size of the largest particle is 1.5 times the average particle size. Since the driving force for coarsening is the difference in surface energy, the larger particle will always grow and smaller ones will shrink. In DICTRA, the model is based on the Gibbs energy difference between particles of different sizes. This difference causes a shift in equilibrium, and as a result material transport from smaller particles to the largest particle occurs. The model has been compared with experimental results, [10], and good agreement has been found.

The model contains only one adjustable parameter, i.e. the surface energy. Here the value 0.4 J/m^2 was chosen in agreement with a previous study by Gustafson, [15]. In the experimental part of that study the size of TiC was measured in the Ti-stabilised austenitic stainless steel 17Cr13NiMoTi for different temperatures and times. The result was also compared with DICTRA-simulations of coarsening and very good agreement between experiments and simulations was found.

However, when the simulations are compared with the experimental data from Engberg and Lagneborg for the steel in the present investigation, [16], a much faster coarsening is observed experimentally than predicted by the simulations, see Figures 3-5. Engberg and Lagneborg made their metallographic examination on creep-tested specimens and it is likely that the continuous deformation processes enhance the transformation kinetics in general and the coarsening in particular.

For the sake of simplicity we shall represent this effect with an enhancement factor e. All diffusion coefficients are then multiplied with e, i.e.

$$D_{kj}^{neff} = eD_{kj}^{n} \tag{16}$$

In general, we expect the enhancement factor to depend on the deformation rate $\dot{\varepsilon}$ and the temperature. This concept will be developed further in coming papers. In the present work, we have simply evaluated the e value to fit the experimental data by Engberg and Lagneborg, [16]. The dashed lines in Fig. 3-5 are calculated using $e = 4$ at 800°C and 18 for 750 and 700°C, respectively. Evidently the enhancement becomes more important at low temperatures when the bulk diffusivities are lower.

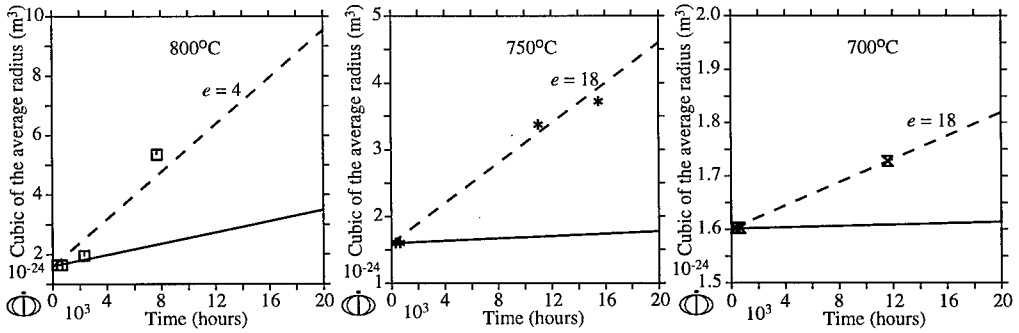

Figures 3-5. Coarsening of TiC in 17Cr13NiMoTi simulation with DICTRA and normal diffusion coefficients (the solid lines) and measurements from Engberg and Lagneborg, [16]. The dashed lines show the coarsening rate with an enhancement factor, see text.

The model used for the coarsening was based on Ostwald ripening where small particles disappear and large ones grow according to the following relationship, [1, 16], in agreement with the computations in Figs. 3-5:

$$r^3 = r_{part0}^3 + k_p(T)t \tag{17}$$

where k_p is a constant and t is the time.

Results of calculations for creep strength

In Table 1, used parameters are listed. The initial β-value used for the particle size distribution is $9.1 \cdot 10^7$. The volume fraction secondary TiC particles is set to $1.5 \cdot 10^{-3}$ and is assumed to be constant during creep. The value was calculated using Thermo-Calc, [17]. The stress exponent n=6. The model is applied in the temperature interval 550-800 °C, here exemplified at 650 and 800 °C. When the dislocations are able to climb over the particles, general climb is assumed. The influence of particle coarsening is included in the analysis. The value on the activation energy, (Q), is higher than the self-diffusion coefficient of iron, which is about 280 kJ/molK in austenite, [18]. This is often found for particle strengthened materials. Some of the increase can be described by solid solution hardening effects.

Table 1. Parameters used in the calculations

Temperature (°C)	A_0	Q (kJ/mol K)	r_{part0} (nm)	γ_{free}	ε_R	G (GPa)
All temperatures	100	318	11	0.1	-	-
600	-	-	-	-	0.4	57.1
700	-	-	-	-	0.4	53.5
800	-	-	-	-	0.2	50

At each temperature, the calculations are compared to experimental values for the material 15Cr15Ni0.1C0.4Ti. Between 550 and 700 °C climb is not the dominating mechanism, not even at longer times. The creep strength is reduced with time, but, the Orowan mechanism still dominates the strength contribution from the particles. The experimental values are in agreement with the calculated ones. This is exemplified at 650 °C in Fig. 6. At 750 °C there is a change in shape of the experimental curve, see Fig. 2. There is a larger reduction in strength at longer times. The dislocations are now to some extent able to climb over the particles. At 800 °C this behaviour is even more pronounced, see Fig. 7.

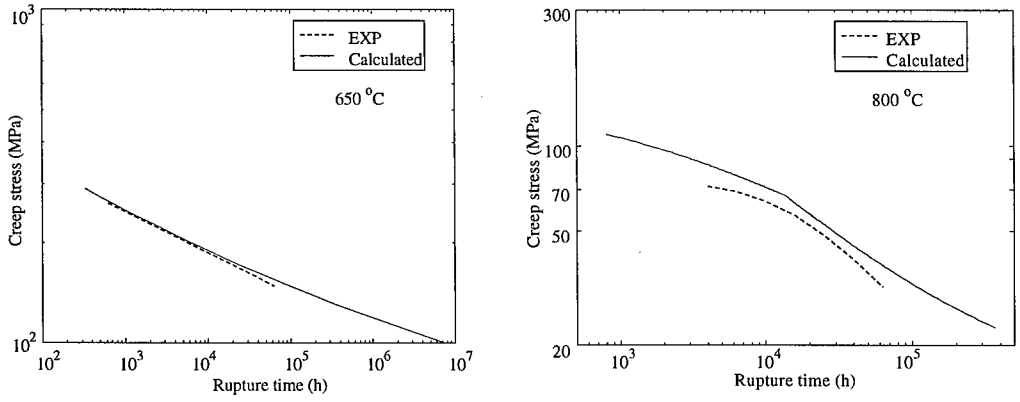

Figures 6-7. Creep stress vs. rupture time at 650 and 800 °C. Experimental and calculated data.

The particles now grow faster, and at longer times, (> 100000 h), practically all particles are overcome with climb. At 800 °C the curve representing the calculated values can be divided into three regions. At shorter times, the Orowan mechanism is active. At intermediate times, there is a mixture between climb and Orowan mechanisms. This is dependent on the particle size distribution. In the third region, at longer times, climb dominates the process. These three stages hence represent a sigmoidal behaviour. The reduction in strength at 800 °C is larger than the model predicts. Some of the decrease can be explained by reduced ductility at low stresses. If instead the creep rate would be analysed, the slope is not reduced to such an extent at lower creep rates.

In Figures 8-9, the influence on strength from dislocations and particles are analysed when compared to the applied stress. In almost the entire stress interval, the Orowan stress is dominating at 650 °C. With the estimated particle size and volume fraction, the value for the Orowan stress is about 58 MPa. The contribution from the dislocations is increasing with applied stress, which is explained with higher dislocation density with higher applied stress. The knees in the back stress for the dislocations are a result of its implicit dependence of the particles. The Orowan stress decreases with the temperature due to particle coarsening and reduction in shear modulus and so is the climb stress, since the model is based on the Orowan stress, see Eq. 3. At 800 °C the Orowan stress is dominating at applied stresses over 100 MPa. Between 40-100 MPa the strength is controlled by the particle size distribution. Below about 40 MPa, climb over the total particle distribution is possible.

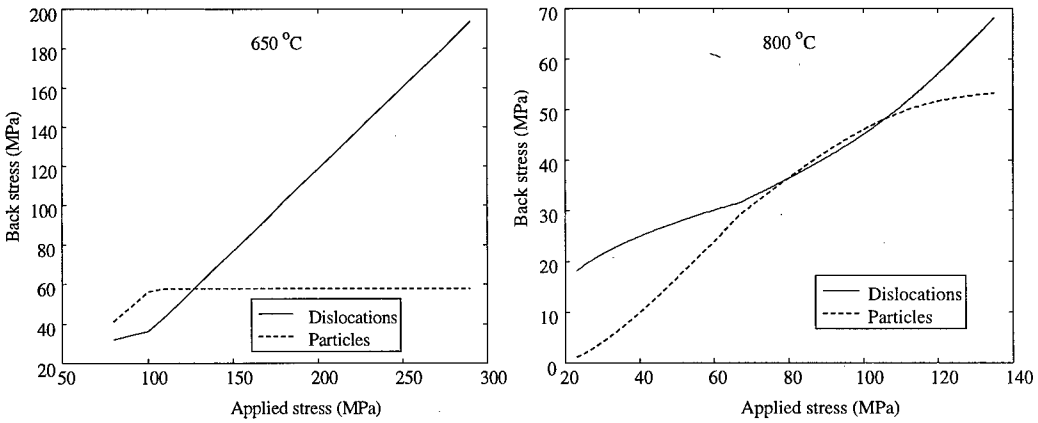

Figures 8-9. Back stress from dislocations and particles vs. applied stress at 650 and 800 °C

Discussion

In the sections above, a new model for particles strengthening was applied and compared to experimental values. Compared to previous models, the particle size distribution is taken into account in accordance with Fig. 1. By doing this, it is possible to kinetically model the strengthening contribution from the particles. A time factor is then introduced when comparing the dislocation climb speed with the dislocation speed in the matrix. The time for the dislocations to pass the particles is analysed. If the particle is large enough, the time is not sufficient for the dislocation to climb over it. The Orowan mechanism then contributes to the strength from the particle. When the applied stress is low and the temperature is high, dislocation climb becomes important. When studying the particle size distribution, the small particles will be climbed first. The fraction of the particles that will be overcome with climb is determined by calculating the critical size according to the definition in Eq. 14. Also see Fig. 1. The particles with larger values than this critical size will not be overcome with climb, and therefore considerably contribute to strength. The critical size increases with lower applied stress and at sufficiently low values, all particles will be overcome with climb, irrespective of particle size. Therefore, at high stresses the Orowan mechanism controls the strength contribution from the particles, and at low stresses climb. In between there is a combination of the two mecha-

nisms. Theoretically this is shown in the calculated curve in the Creep stress-rupture time diagram in Fig. 7. The calculated data is in acceptable agreement with the experimental ones in the temperature interval and supporting the role of the particle size.

Conclusions

1. A kinetic model for particle strengthening during creep has been formulated. It takes into account passage time for climb over a particle.
2. The model can describe the exponential decrease in strength with increasing temperature and has been applied to an austenitic stainless steel.
3. The particle coarsening has been described with a multi-component diffusion model.

Acknowledgements

Financial support from the Foundation for strategic research (SSF) is gratefully acknowledged.

References

[1] W. Blum, B. Reppich, Creep of particle-strengthened alloys, Pineridge press Ltd., Creep behaviour of crystalline solids, (1985), pp. 83-135

[2] R. Sandström, Acta Metall., 25, (1977), pp. 905-911

[3] E. Arzt, Res Mech., 31, 4, (1991), pp. 399-453

[4] B. Reppich, B. Listl, T. Meyer, High temperature alloys for gas turbines and other applications 1986, Conference, Liège, Belgium, 6-9 Oct, (1986), pp. 1023-1035

[5] G. Taylor, Proc. R. Soc., 145A, (1934), pp. 362-404

[6] R. Sandström, Acta Metall., 25, (1977), pp. 897-904

[7] F. C. Monkman, N. J Grant, Proc. ASTM, 56, (1956), pp. 593-597

[8] R. Sandström, G Engberg, B Ivarsson, Materials at high temperature, (UK), 10, 1, (1992), pp. 33-38

[9] R. Sandström, B. Ivarsson, J. Lindblom, Standard Tech. Publ. 1106, ASTM, Philadelphia, (1991), pp. 214-229

[10] Å. Gustafson, L. Höglund, J. Ågren, Conf. proc.: Advanced heat resistant steels for power generation, 27-29 April 1998, San Sebastian, Spain, Institute of Metals communications

[11] J-O. Andersson, L. Höglund, B. Jönsson and J. Ågren: Fundamentals and Applications of Ternary Diffusion, G. R. Purdy, ed., Pergamon Press, New York, NY, (1990), pp. 153-163

[12] I. M. Liftshitz and V. V. Slyozov, Soviet Physics JETP, 35, 8, No. 2, (1959) pp. 331-339

[13] I. M. Liftshitz and V. V. Slyozov, Chem. Solids, 19, Nos. 1/2, pp. 35-50

[14] C. Wagner, Zeitshrift für Elektrochemie, Bd. 65, Nr. 7/8, (1961), pp. 581-591

[15] Å. Gustafson, work to be published, Royal Institute of Technology, SE-100 44 Stockholm, Sweden, (1999)

[16] G. Engberg, R. Lagneborg, Scand. J. Metall., 7, (1978), pp. 282-286

[17] SGTE (Scientific Group Thermodata Europe) solution database of Jan. 1994. Ed. B Sundman, Div. of Computational thermodynamics, Royal Institute of Technology, S-100 44 Stockholm, Sweden

[18] V. Linnenbom, M. Tetenbaum, C. Cheek, J. Appl. Phys., 26, (1955), pp. 932-936

Key Engineering Materials Vols. 171-174 (2000) pp. 285-290
© 2000 Trans Tech Publications, Switzerland

Dislocation Activity in Plastically-Accommodated Creep in an Inclusion Bearing Material

E. Sato and K. Kuribayashi

The Institute of Space and Astronautical Science,
3-1-1 Yoshinodai, Sagamihara, Kanagawa 229-8510, Japan

Keywords: Plastic Accommodation, Dislocation Creep, Metal Matrix Composite, Dislocation Climb

Abstract

Steady-state creep in a dispersion hardening alloy and discontinuous fiber reinforced metal matrix composite without other interfacial relaxation mechanisms than matrix plastic flow has been examined. For a material with an elastic-viscoplastic matrix, the non-uniform strain rate in the steady state is derived using Eshelby's equivalent inclusion method. The obtained creep strain increment is impotent and does not generate any additional internal stress. During this creep deformation, a dislocation comes in from one direction and goes out towards another direction, so that no dislocation nor internal stress but a heterogeneous plastic strain remains in the material. The concrete trajectory of dislocations climbing over a cylindrical inclusion is calculated and illustrated.

1. Introduction

During creep deformation at high temperatures in an inclusion bearing material, i.e. dispersion hardening alloy and discontinuous fiber reinforced metal matrix composite, steady-state creep is achieved only with matrix's heterogeneous creep deformation, when any interfacial accommodation processes, i.e. interfacial diffusion and sliding, do not take place. Although this plastically-accommodated creep has been analyzed using the shear-lag model [1], the potential method [2] and the finite element method [3], the dislocation activity yielding this heterogeneous creep strain has not been discussed in detail.

On the other hand, Mori et al.[4] have recently shown that, when both diffusion and sliding on matrix–inclusion interfaces are inoperative, creep of a composite eventually terminates, through variational principles and FEM analyses. Later we [5] have revealed the mistakes of their understanding that the variational principles do not prove the existence of the creep termination and that FEM analysis brings about an incorrect result of creep termination without the constant dilatation option.

In the present paper, the dislocation activity during the steady-state creep is discussed. We calculate the non-uniform strain rate in the steady state, analyze the nature of an impotent eigenstrain, and then illustrate the concrete trajectory of dislocations climbing over a cylindrical inclusion.

2. Non-uniform strain rate in the steady state

We show a special strain ε^*_{ij}, which can accumulate eternally and can achieve the steady-state creep, for a composite with elastic-viscoplastic matrix with Poisson ratio of 1/2 and a rigid inclusion, as shown in Fig. 1. The elastic strain ε^E_{ij} and the creep strain increment $\dot{\varepsilon}^C_{ij}\,dt$ are expressed by the identical formula against the deviatoric stress σ'_{ij}:

$$\varepsilon^E_{ij} = \frac{3}{2E}\sigma'_{ij} \quad \text{and} \quad \dot{\varepsilon}^C_{ij}\,dt = \frac{3}{2}B\,\sigma'_{ij}\,dt. \tag{1}$$

The calculation of $\varepsilon^E_{ij}=\varepsilon^A_{ij}+\varepsilon^*_{ij}$ caused by an external stress σ^A_{ij} can be obtained by modifying Eshelby's solution of the elastic strain outside an inclusion in an infinite matrix [6] to that in a finite matrix using Eshelby's equivalent inclusion method [7] and Tanaka-Mori's theorem [8]. Here, ε^A_{ij} is an elastic strain of the monolithic material by σ^A_{ij}, ε^*_{ij} is the disturbed strain by the inclusion and C_{ijkl} and $C^*_{ijkl}\,(\to\infty)$ are the elastic moduli of the matrix and inclusion, respectively.

If we consider $\varepsilon^E_{ij}=\varepsilon^A_{ij}+\varepsilon^*_{ij}$ as a plastic strain increment $\dot{\varepsilon}^C_{ij}\,dt$, we can show that it is impotent and generates no additional stress as follows; First, ε^A_{ij} is uniform. Second, ε^*_{ij} satisfies the condition of impotency given by Furuhashi and Mura [9], i.e., the displacement, u^*_i, of ε^*_{ij} on the surface of the material equals nought and ε^*_{ij} is compatible in the material

$$\varepsilon^*_{ij} = \frac{1}{2}(u^*_{i,j}+u^*_{j,i}). \tag{2}$$

Therefore, after loading of σ^A_{ij}, the elastic stress $\sigma_{ij}+\sigma^A_{ij}$ generates an impotent creep strain increment $\dot{\varepsilon}^C_{ij}\,dt$. Since this strain increment yields no disturbance in the stress distribution, it can accumulate infinitely and creep continues infinitely. It must be noted that this creep strain is not uniform. The concrete formula of $\dot{\varepsilon}^C_{ij}\,dt$ is given in §4 for a composite with a cylindrical inclusion.

3. Nature of impotent eigenstrain

3.1. *Impotent eigenstrain and impotent dislocations*

A dislocation density tensor α_{hi} for an eigendistortion β_{ji}, which expresses the x_i-component of the total Burgers vector of dislocations threading the unit surface perpendicular to the x_h-direction, has been introduced by Nye [10] as

$$\alpha_{hi} = -\varepsilon_{hlj}\,\beta_{ji,l}, \tag{3}$$

where ε_{hlj} is a permutation tensor. If the eigenstrain satisfies the impotent condition (eq.(2)), the dislocation density tensor becomes inevitably zero: $\alpha_{hi} = -\varepsilon_{hlj}u^*_{i,jl} = -\varepsilon_{hPQ}u^*_{i,QP} - \varepsilon_{hQP}u^*_{i,PQ} = -u^*_{i,QP} + u^*_{i,PQ} = 0$, where (hPQ) and (hQP) are the even and odd permutations of (123), respectively, and the terms are not summed up for the indices P and Q. It means that an impotent eigenstrain does not remain any dislocations in the material.

On the other hand, Mura [11] proposed impotent dislocations which satisfy

$$\beta^*_{ji} = -\beta^*_{ij}. \tag{4}$$

The displacement and the stress field caused by these dislocations become identically zero, since $\varepsilon^*_{ij}=\frac{1}{2}(\beta^*_{ji}+\beta^*_{ij})=0$ leads to $u_i=\sigma_{ij}=0$. Now it becomes clear that the impotent dislocations remain no

dislocation while the impotent eigenstrain remains no eigenstrain.

3.2. *Dislocation density tensor for impotent eigenstrain*

The dislocation density tensor for a straight positive edge dislocation along x_3 -axis with a Burgers vector parallel to x_1 -axis, as shown in Fig. 2, is given by

$$\alpha_{31} = b\,\delta(x_2)\,\delta(x_1), \tag{5}$$

and this dislocation has an eigendistortion

$$\beta^*_{21} = b\,\delta(x_2)\,H(-x_1) \quad \text{or} \quad \beta^*_{11} = -b\,\delta(x_1)\,H(-x_2), \tag{6}$$

since $\alpha_{31} = -\beta^*_{21,1} = -b\,\delta(x_2)\,\partial H(-x_1)/\partial x_1$ or $\alpha_{31} = \beta^*_{11,2} = -b\,\delta(x_1)\,\partial H(-x_2)/\partial x_2$. The former is caused by a relative slip of b on the half plane (x_2=0, x_1<0) in the x_1 -direction (Fig. 2(a)), and the latter is caused by a relative overlap and removal of b on the half plane (x_1=0, x_2<0) in the x_1 -direction (Fig. 2(b)).

The (31) component (edge component) of a dislocation density tensor of an impotent eigendistortion is given by

$$\alpha_{31} = -\beta^*_{21,1} + \beta^*_{11,2} \quad \text{and} \quad \beta^*_{21,1} = \beta^*_{11,2}, \tag{7}$$

which is satisfied at a point $x=0$ if each eigendistortion is given by

$$\beta^*_{21} = b\,\delta(x_2)\,H(-x_1) \quad \text{or} \quad \beta^*_{11} = -b\,\delta(x_1)\,H(x_2). \tag{8}$$

It means that α_{31} can be caused by a sum of a relative slip on the half plane (x_2=0, x_1<0) in the x_1 -direction and a relative overlap and removal on the half plane (x_1=0, x_2>0) in the x_1 -direction, *i.e.* it is caused by a movement of an edge dislocation along x_3 -axis coming in from $-x_1$ -direction and climbing up towards x_2 -direction, as shown in Fig. 2(c).

In summary, an impotent eigenstrain can be considered as a movement of a dislocation coming in from one direction and going out towards another direction. For an edge component, climbing is indispensable. As a result, no dislocations but a certain heterogeneous plastic strain remains in the material.

4. Trace of dislocations for cylindrical inclusion

We derive a concrete description of the dislocation movement for the plastic accommodation. Here, a composite containing a cylindrical inclusion is loaded with shear stress $\tau_{12} = \tau_{21}$, under which the matrix without inclusions deforms with strain $\varepsilon_{12} = \varepsilon_{21} = \varepsilon^A$. Shear deformation of a matrix material by the shear stress is brought about by a glide motion of edge dislocations along the x_3 -axis with a Burgers vector $b\vec{x}_1$ towards the $\vec{x}_1$ direction and that with $b\vec{x}_2$ towards the $\vec{x}_2$ direction, as shown in Fig.3. The former generates distortion β_{21} and the latter generates β_{12}.

The solution of the creep strain for a composite containing a spherical inclusion of volume fraction f and radius a, loaded with shear stress $\tau_{12} = \tau_{21}$ is given in the form of u_i^C (i=1,2,3):

$$u_1^C = \frac{\varepsilon^A}{1+f}\left[1 - \frac{2a^2}{x^6}\left(a^2(-3x_1^2+x_2^2) + 4x_1^2x^2\right)\right] x_2, \tag{9a}$$

$$u_2^C = \frac{\varepsilon^A}{1+f}\left[1 - \frac{2a^2}{x^6}\left(a^2(-3x_2^2+x_1^2) + 4x_2^2x^2\right)\right] x_1, \tag{9b}$$

and $$u_3 = 0. \tag{9c}$$

A trace of edge dislocations drawn by the above procedure is shown in Fig.4. The deformation of the composite is brought about by the movement and bending of edge dislocations along the x_3 -axis with a Burgers vector $b\vec{x}_1$ (Fig. 4(a)) and of edge dislocations along the x_3 -axis with $b\vec{x}_2$ (Fig. 4(b)). We can infer that the traces on which $b\vec{x}_1$ and $b\vec{x}_2$ dislocations moves satisfy

$$u_2(x_1, x_2, x_3) = \text{constant} \quad \text{and} \quad u_1(x_1, x_2, x_3) = \text{constant}, \tag{10}$$

respectively. Figure 4 clearly reveals that dislocations bypass the inclusion by climbing up or down as the elementary process of plastic accommodation. This dislocation movement generates the inhomogeneous distortion.

The creep strain and dislocation movement in a composite with aligned discontinuous fibers can be directly obtained by the present algorithm. On the other hand, it has the following limit coming from continuum micromechanics. In addition to the traces which pass the matrix from end to end, some dislocations are created near the inclusion, make a small loop and annihilate at the created point, in order to satisfy the volume conservation condition. Since dislocations cannot be created in actual crystalline materials except at a certain sites, such activities might be taken over by vacancy diffusion.

Although the present analysis is for an idealized situation with n=1 and shows the limit of continuum micromechanics, visualizing the dislocation activity promotes the understanding of high-temperature deformation of composites.

Conclusions

At elevated temperatures, dislocations can climb over a particle, generating heterogeneous creep strain which accommodates the strain mismatch between the matrix and the inclusions without yielding additional internal stresses. The non-uniform strain rate in the steady state is derived using Eshelby's method. During this creep deformation, a dislocation comes in from one direction and goes out towards another direction, so that no dislocation nor internal stress but a heterogeneous plastic strain remains in the material. The trace of the dislocations around a cylindrical inclusion in an elastic-viscoplastic matrix has been drawn using the results of the analysis.

References

[1] A.Kelly and K.N.Street, *Proc. Roy. Soc. Lond.,* 1972, **A328**, 283.
[2] B.L.Lee and M.E.Mear, *J. Mech. Phys. Solids,* 1991, **39**, 627.
[3] T.L.Dragone and W.D.Nix, *Acta metall. mater.,* 1990, **38**, 1941.
[4] T.Mori, J.H.Huang and M.Taya, *Acta mater.,* 1997, **45**, 429.
[5] E.Sato, T.Ookawara, K.Kuribayashi, and S.Kodama, *Acta metall. mater.*, 1998, **46**, 4153.
[6] J.D.Eshelby, *Proc. Roy. Soc.*, 1959, **A252**, 561.
[7] J.D.Eshelby, *Proc. Roy. Soc.*, 1957, **A241**, 376.
[8] K.Tanaka and T.Mori, *J. Elasticity,* 1972, **2**, 199.
[9] R.Furuhashi and T.Mura, *J. Elasticity*, 1979, **9**, 263.
[10] J.F.Nye, *Acta metall.*, 1953, **1**, 153.
[11] T.Mura, *Proc. IUTAM Symp. Mechanics of Generalized Continua*, ed. E.Kroner, 1968, p.269.

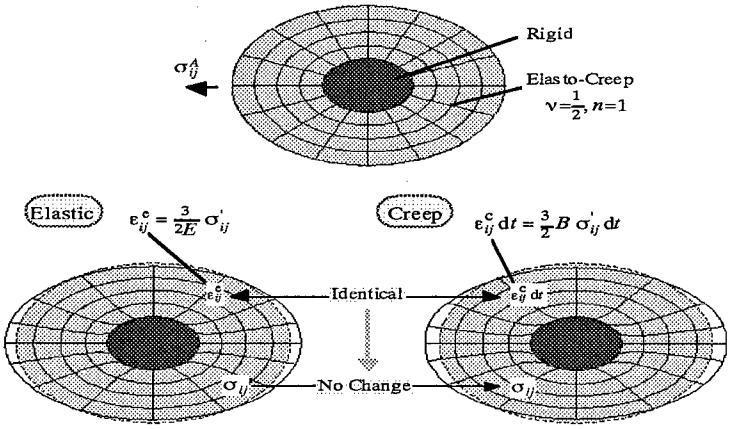

Fig. 1 Schematic of the steady-state creep of a composite, consisting of a rigid inclusion Ω and an elasto–creep matrix $\mathbf{M}$ of ν=1/2 and n=1.

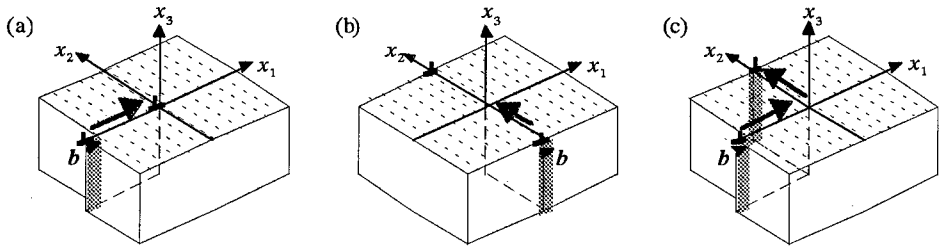

Fig. 2 A straight positive edge dislocation along x_3 -axis with a Burgers vector parallel to x_1 -axis, (a) which is caused by a relative slip of b on the half plane (x_2=0, x_1<0), and (b) which is caused by a relative overlap and removal of b on the half plane (x_1=0, x_2<0). The (31) component (edge component) of a dislocation density tensor of an impotent eigenstrain; It is caused by a sum of a relative slip of b on the half plane (x_2=0, x_1<0) and a relative overlap and removal of b on the half plane (x_1=0, x_2>0).

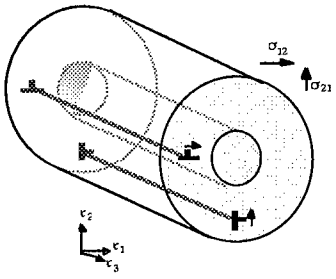

Fig. 3 Configuration of a composite with a cylindrical inclusion is stressed by $\tau_{12}=\tau_{21}$.

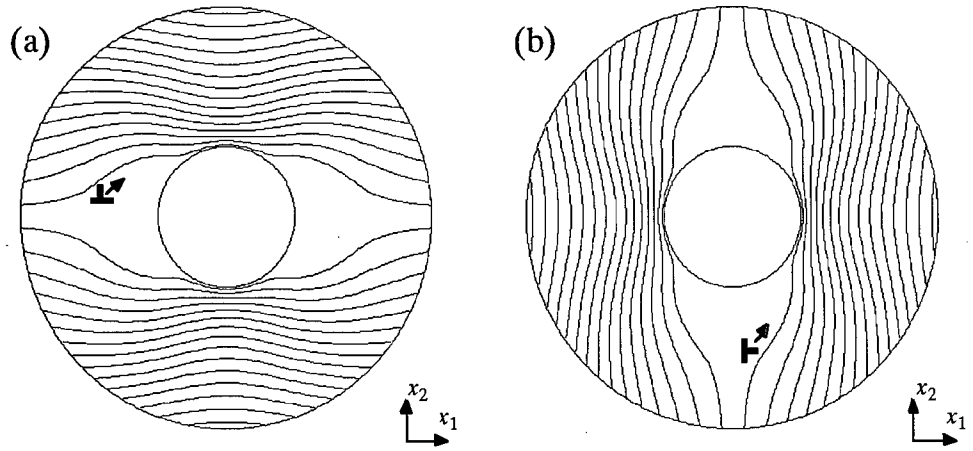

Fig.4 Trace of edge dislocations of $b\vec{x}_1$ (a) and $b\vec{x}_2$ (b) in a composite with a cylindrical inclusions stressed by $\tau_{12} = \tau_{21}$.

Key Engineering Materials Vols. 171-174 (2000) pp. 291-296
© 2000 Trans Tech Publications, Switzerland

Lattice-Diffusion Creep Mechanism Not Based on Stress Heterogeneity (2)

G. Itoh[1] and A. Nojima[2]

[1, 2] Department of Mechanical Engineering, Nagaoka University of Technology, Kami-Tomioka, Nagaoka, Niigata-Pref., 940-2188, Japan

[2] Graduate Student

Keywords: Lattice-Diffusion Creep, Diffusion Creep, Diffusion Mechanism, Vacancy, Vacancy Concentration, Chemical Potential

Abstract

In succession to the previous paper, further theoretical study has been carried out on the mechanism for lattice-diffusion creep again in the case of a cube-shaped grain subjected to a simple uniaxial tensile creep where the stress is in z direction, taking actual diffusion mechanism, that is vacancy mechanism, into account. Firstly, the direction of the flow of atoms was modified from horizontal direction (from lateral boundaries to the interior of the grain) to diagonal direction (from lateral boundaries to top and bottom boundaries). Together with this modification, re-discussion on the driving force of the deformation was also carried out, resulting in the conclusion that the diffusional deformation is caused by a force applied to each atom involved in the flow, and that this force coincides with a energy gradient, more precisely chemical potential gradient. From the latter fact, the mechanism proposed by Kimura is shown to be consistent with the present mechanism, and this consistency corresponds to that in the Einstein's equation on diffusion where negative chemical potential gradient is equal to the force being applied to the diffusing species. Both mechanisms are concluded to be sound in terms of macroscopic stress field, in contrast to the Nabarro-Herring mechanism in which a vacancy concentration gradient based on unreal stress heterogeneity is assumed to be the driving force. Secondly, atomistic process based on the present mechanism was discussed. The whole process was deduced to consist of three elementary processes: (i) creation of a vacancy at the top or bottom boundary that causes not only an energy decrease corresponding the work done by the tensile stress but also an energy increment arising from elastic dilatation, (ii) annihilation of a vacancy at the lateral boundary which counterbalances the energy increment mentioned above, and (iii) restoration of vacancy distribution that has been disturbed by the above two processes.

1. Introduction

In the previous paper [1] in this conference, the authors described a new theory [1, 2] for the mechanism of the lattice-diffusion creep, which is essentially different from that proposed by Nabarro [3] and Herring [4] (this will be abbreviated to N-H mechanism). Although N-H mechanism has been so widely accepted that the lattice-diffusion creep is also called Nabarro-Herring creep in most textbooks [5-7], research papers [8], reviews [9, 10], etc., it contains the premise of vacancy concentration gradient based on stress heterogeneity that was claimed to be unreal in the previous paper as well as by Mori et al. [11] The proposed flows of vacancies and atoms in N-H mechanism are illustrated again in this paper, in Fig. 1, where stress heterogeneity is also indicated in a grain even though a uniaxial tensile stress is applied.

Kimura [12], being independent of the authors, proposed another mechanism that is not based on the vacancy concentration gradient, either. Both mechanisms by Kimura and by the authors are theoretically sound from the viewpoint that they do not assume the vacancy concentration gradient based on unreal stress heterogeneity, although both have some problems. This paper describes these problems and a modified mechanism of the authors'.

Consideration of the direction of migration of atoms

First, all discussion in this paper as in the previous one will be made on the situation of

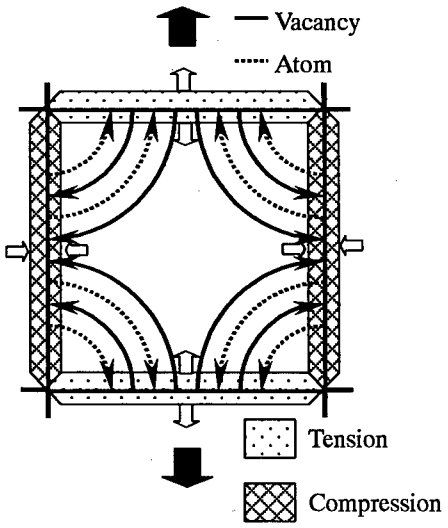

Fig. 1 Schematic drawing showing the diffusional flow (thin arrows) and local stress field (open thick arrows) based on the Nabarro-Herring mechanism. Solid thick arrows indicate macroscopic applied stress.

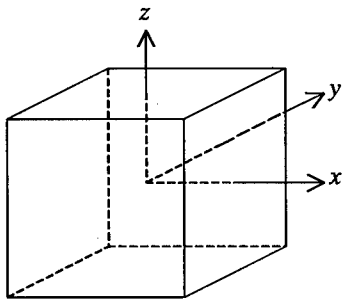

Fig. 2 Geometry of the grain and axes.

uniaxial tensile creep, which is schematically illustrated in Fig. 2. Comparison of the three mechanisms is listed in Table 1. In the authors' previous mechanism, atoms on the lateral grain boundaries have been assumed to move into interstitial site in the grain interior. This assumption is obviously unreal. Similar situation can be produced if edge dislocations with Burgers vector parallel to the tensile axis are readily introduced from the grain boundaries. This situation is illustrated in Fig.3, but also seems to be unreal because dislocation density must be very small at a temperature as high as lattice-diffusion creep takes place. In Kimura's mechanism, only the flow in z direction was described, which will cause an increase in volume when the grain is elongated in z direction. Thus the direction of the movement of the atoms is deduced to be most reasonable in the N-H mechanism: diagonal path from the lateral boundaries to the top and bottom boundaries. However, the modification in the flow direction of atoms is not a serious problem both in Kimura's and the authors' mechanisms, since the direction of the force applied to atoms and that of the energy gradient can be readily changed according to the direction of the flow.

In the authors' mechanism, the direction of the force was initially decided considering the situation where the grain was first subjected to a elastic deformation in z direction and then to

Table 1 Comparison of the three mechanisms for lattice-diffusion creep

Mechanism	N-H	Itoh-Nojima	Kimura
Origin of the diffusion ↓ Process	Tensile stress ↓ Stress heterogeneity ↓ Vacancy concentration gradient ↓ Vacancy flow ↓ Atom flow	Tensile stress ↓ Force applied to atom in x and y directions ↓ Atom flow	Tensile stress ↓ Energy gradient in z direction ↓ Atom flow
Direction of atom migration	y-z boundary to x-y boundary	x and/or y direction	z direction

diffusional flow with the top and bottom boundaries fixed, which should bring about a contraction in x and y directions. In this contraction process, elastic elongation in z direction is converted into plastic elongation, and the atoms on the lateral boundaries must move to the top and bottom boundaries if there is no interstitial site inside the grain. Therefore, the direction of atom flow must be changed even using the previous method for deciding the direction. Once the direction of atom flow is decided, the direction of the force applied to the atoms is automatically decided to be the same by the Einstein's equation,

$$V = MF = DF / kT, \qquad (1)$$

where V, M, F, D, k and T are velocity of an atom, mobility, the force, self-diffusion coefficient, Boltzmann constant and absolute temperature, respectively, and there is a relationship of $M=D/kT$ between D and M.

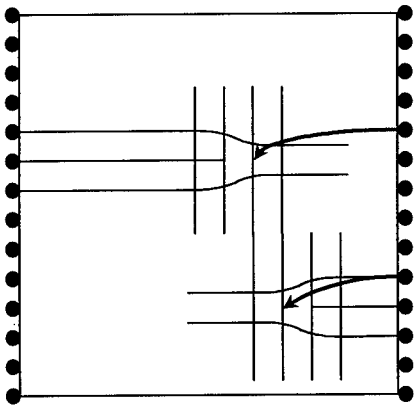

Fig. 3 Schematic drawing showing the migration of atoms on the lateral boundary into edge dislocations.

Assume that only the atoms at the two y-z boundaries in a cube-shaped grain (simple cubic lattice with lattice constant a) of side length d, move linearly to the top or bottom boundaries in diagonal directions, as illustrated in Fig. 4, then the same process and deformation amount as in the previous papers can be led. The number of moving atoms is that of monolayer of atoms of the two lateral boundaries, namely $2(d/a)^2$, and the average migration length is $\sqrt{2}\,d/4$, providing the total deformation distance

$$\Delta X=(\sqrt{2}\,d/4)\times 2(d/a)^2 = \sqrt{2}\,d^3/2a^2. \qquad (2)$$

In the actual deformation, identical strain can be obtained if the atom A in Fig. 4, for example, does not move directly to the top grain boundary but another atom does, by receiving the baton so to speak. Thus, all the atoms in the region swept by the arrows can be considered to relate to the deformation†. Since the number of such atoms is $(d/a)^3/2=d^3/2a^3$, average migration distance Δx for an atom is expressed as

$$\Delta x = \Delta X / (d^3/2a^3) = \sqrt{2}\,a. \qquad (3)$$

The F has been defined as a force, which is the driving force of the diffusion and is applied to an atom, and hence the work w_1 that has been done by this force to an atom in the deformation is given by

$$w_1 = F\Delta x = \sqrt{2}\,aF. \qquad (4)$$

On the other hand in the macroscopic point of view, tensile load of $\sigma \times d^2$ has brought about the deformation amount of $2a$. Therefore, the work per an atom involved, w_2, which has been done by this tensile load should be,

$$w_2 = \sigma d^2 \times 2a / (d^3/2a^3) = 4\,\sigma a^4/d. \qquad (5)$$

Since the work given by the force F to an atom must coincide with that per an atom obtained from macroscopic work, that is $w_1 = w_2$,

$$\sqrt{2}\,aF = 4\,\sigma a^4/d$$

$$F = 2\sqrt{2}\,a^3\,\sigma/d = 2\sqrt{2}\;\Omega\,\sigma/d, \qquad (6)$$

where Ω, the atomic volume, is equal to a^3. From Einstein's equation (Eq. 1) and Eq. 6,

$$V = FD/kT = 2\sqrt{2}\;\Omega\,\sigma D / dkT. \qquad (7)$$

From Eqs. (3) and (7), letting the time for the deformation be t,

$$t = \Delta x/V = \sqrt{2}\,a / (2\sqrt{2}\;\Omega\,\sigma D/dkT) = adkT / 2\Omega\,\sigma D. \qquad (8)$$

The strain of $2a/d$ is produced within this time with respect to the migration from y-z boundaries to

† In the previous papers [1, 2], all the atoms in the grain were considered to relate the deformation, but the number of the atoms involved does not affect the conclusion since it is included both in w_1 and w_2.

x-y boundaries. An identical amount of strain should be produced simultaneously with respect to the migration from x-z boundaries, which was not taken into account in the previous papers. Therefore, strain rate $\dot{\varepsilon}$ is given by

$$\dot{\varepsilon} = 2\times(2a/d)/t = 8\,\Omega\,\sigma D/d^2kT. \qquad (9)$$

This is a modified description of strain rate in the lattice-diffusion creep by the present authors which is not based on stress heterogeneity, although the equation is identical with that in the previous papers, except the factor of 8 instead of 16.

The same conclusion can be drawn in terms of energy gradient or chemical potential gradient instead of F. From the above discussion with respect to Eqs. 4 to 6, F can be represented as $F = w_2/\Delta x$, where w_2 (>0) coincides with energy decrease per atom by the deformation, $-\Delta E$ ($\Delta E < 0$). In this situation on pure metal, chemical potential change $\Delta\mu$ is also coincident with ΔE. Thus,

$$F = -\Delta E/\Delta x = -\Delta\mu/\Delta x, \qquad (10)$$

through which exactly the same equation as Eq. 9 can be derived when energy decrease or chemical potential change by the deformation is taken into account instead of the force F. This is consistent with the fact that the Einstein's equation (Eq. 1) can be described in another form,

$$V = -M\nabla\mu \ (= MF = DF/kT). \qquad (11)$$

In conclusion, both the authors' and Kimura's mechanisms in which the driving force for diffusion was explained in terms of the force F and of the negative energy gradient $-\Delta E$, respectively, are correspondent to each other. In this paper, the two will be referred to as I-N-K mechanism from now on, unless distinction is needed. After the modification in the direction of migration of atoms, it can be again concluded that the two are more plausible in that they do not assume vacancy concentration gradient based on unreal stress heterogeneity in the grain.

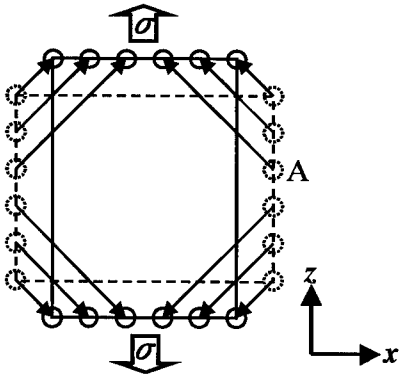

Fig. 4 Schematic diagram showing plausible diffusion path of atoms.

Correlation with the actual elementary process of diffusion: vacancy mechanism

Although the newly established I-N-K mechanism has been concluded to be sound in terms of macroscopic stress field, some interpretation should be needed in relation to the atomistic process of diffusion. Seemingly, potential energy of the grain might not change when a jump of an atom into a vacant site takes place as shown in Fig. 5. However, by considering the energy change of the whole grain, this will be interpreted reasonably. One of the ways of producing a plastic strain of a/d is introduction of monolayer of vacancies at the second layer of the top boundary by jumps of the very top layer of atoms in z direction, as illustrated in Fig. 6. Although this process contributes the energy decrease or the work done by the tensile stress, $\sigma d^2\times a$, it also causes a dilatation $\Delta V = ad^2$, increase in volume, accompanied by a hydrostatic compressive stress $-P$ ($P>0$), resulting in an energy increase of $P\Delta V/2$. Letting the bulk modulus of the material be K, then

$$P = K\Delta V/d^3. \qquad (11)$$

By extrapolating this process into introduction of a single vacancy, ΔV becomes equal to Ω, and energy increase per an vacancy ΔE_V is expressed as

$$\Delta E_V = K\Omega^2/2d^3. \qquad (12)$$

To reduce this energy increase, a vacancy should annihilate somewhere in the grain. The reverse process might take place: the newly created vacancy might annihilate at the top boundary. It is obvious, however, that this reverse process increases the energy, w_3, that has been reduced by creating the vacancy. The amount of w_3 is given by,

$$w_3 = \sigma d^2\times a/(d/a)^2 = \sigma a^3 = \sigma\,\Omega. \qquad (13)$$

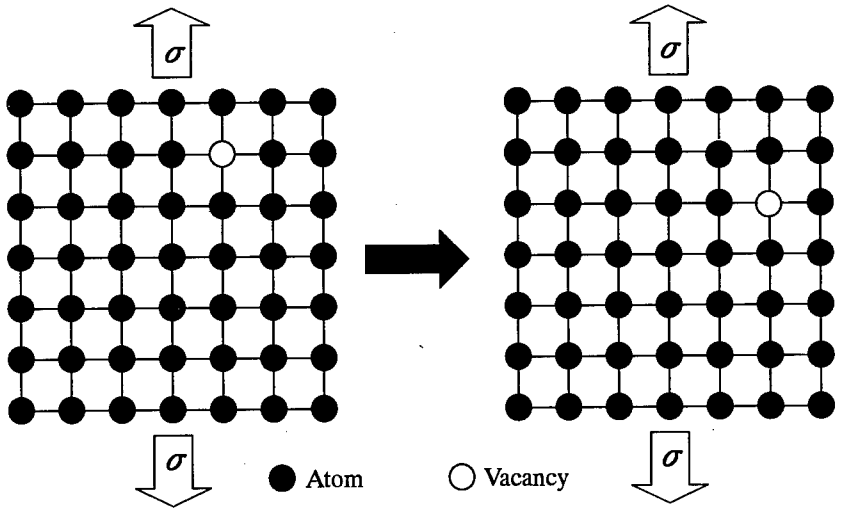

Fig. 5 A jump of an atom following the flow process shown in Fig. 4

Hence, the most probable site of the vacancy annihilation is deduced to be the lateral boundary. The net energy decrease of this set of elementary processes is obviously w_3, being related to the w_2 obtained macroscopically in the previous section. To continue this set of processes, flow of vacancies in the direction which is contrary to that of atoms shown in Fig. 4 is needed. This corresponds to a redistribution of vacancies in the grain where a new vacancy has been created at a top or bottom boundary while one has been annihilated at a lateral boundary. A flow chart indicating the elementary processes in the above discussion is shown in Fig. 7. In the actual deformation, however, all of the elementary processes will take place simultaneously from the statistic point of view, because creation, annihilation and diffusion of vacancies are always taking place in the grain although the creation and annihilation are balanced and the diffusion is random unless the stress is applied. It is natural that the strain rate obtained from the above flow of vacancies should be identical with that obtained macroscopic discussion in the previous section, since the net energy decrease w_2 or w_3 is the same.

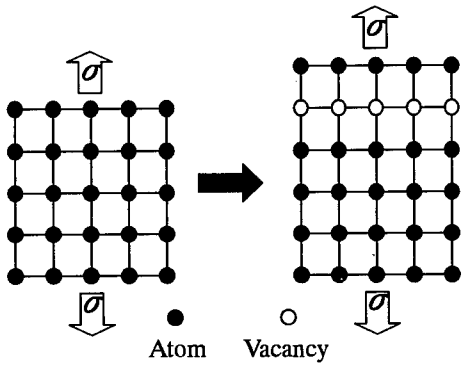

Fig. 6 Creation of mono-layer of vacancies at the second row from the top boundary

In the N-H mechanism, the energy decrease w_3 was thought to decrease the activation energy for vacancy creation at the top and bottom boundaries, leading to an increase in local equilibrium vacancy concentration. Although the energy increase ΔE_v was not taken into account in the N-H mechanism, the concept of vacancy concentration rise is in an indirect agreement with the discussion in the previous paragraph. Nevertheless, it must be emphasized that no such energy decrease accompanied with local vacancy concentration occurs at the lateral boundaries, and hence that the treatment of vacancy flow using Fick's law is not appropriate to interpret the flow of atoms since the other regions of the grain including lateral boundaries have the same vacancy concentration.

Summary

The lattice-diffusion creep mechanism that was originally proposed in the previous paper and not based on unreal stress heterogeneity was successfully modified taking actual diffusion mechanism, that is vacancy mechanism, into account. Firstly, the direction of the flow of atoms was modified from horizontal direction (from lateral boundaries to the interior of the grain) to diagonal direction (from lateral boundaries to top and bottom boundaries). Together with this modification, re-discussion on the driving force of the deformation was also carried out. It was concluded that the diffusional deformation is caused by a force applied to each atom involved in the flow or by an energy gradient, more precisely chemical potential gradient. The equality of the force and the negative chemical potential gradient was reasonable in terms of the Einstein's equation on diffusion, leading to the agreement of the present mechanism with that proposed by Kimura. Both mechanisms are concluded to be sound in terms of macroscopic stress field, in contrast to the Nabarro-Herring mechanism in which a vacancy concentration gradient based on unreal stress heterogeneity is assumed to be the driving force. Secondly, atomistic process based on the present mechanism was discussed, resulting in consistency with the macroscopic feature mentioned above. The set of the elementary processes was deduced to consist of (i) creation of a vacancy at the top or bottom boundary that causes an energy increment arising from elastic dilatation together with an energy decrease corresponding to the work done by the tensile stress, (ii) annihilation of a vacancy at the lateral boundary that cancels the energy increment mentioned above, and (iii) restoration of vacancy distribution that has been disturbed by the above two processes.

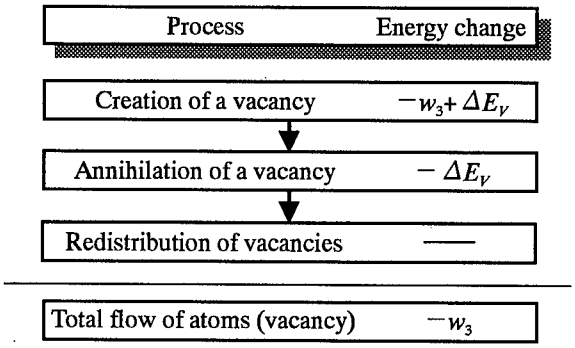

Fig. 7 Flow chart showing elementary processes in the present mechanism for lattice-diffusion creep.

Acknowledgments

The authors are deeply grateful for the financial support from the Light Metal Educational Foundation and from the Iketani Foundation for the Promotion of Science and Technology. The research was also supported by a Grant-in-Aid for Scientific Research (C) from Ministry of Education, Science Sports and Culture of Japan, which is highly acknowledged.

References

[1] G. Itoh and A. Nojima : Appearing in the present proceedings.
[2] G. Itoh and A. Nojima : J. Japan Inst. Metals, **62**(1998), p. 1206., G. Itoh : submitted to Mater., Trans. JIM.
[3] F. R. N. Nabarro : *Report of Conference on Strength of Solids*, Phys. Soc. London, (1948), p. 75.
[4] C. Herring : J. Appl. Phys., **21**(1950), p. 437.
[5] A. S. Argon : *Physical Metallurgy*, ed. by R. W. Cahn and P. Haasen, North Holland, (1996), p. 1958.
[6] B. Burton : *Diffusional Creep of Polycrystalline Materials*, Trans. Tech. Publications, (1977), p. 1.
[7] R. E. Smallman : *Modern Physical Metallurgy* (4th ed.), Butterworths, (1985), p. 445.
[8] R. S. Mishra, H. Jones and G. W. Greenwood : Scripta Metall., **22**(1988), p. 323.
[9] H. Jones : Mater. Sci. Eng., **4**(1969), p. 106.
[10] H. Oikawa and S. Karashima : Bul. Japan Inst. Metals, **11**(1972), p. 567.
[11] T. Mori, S. Onaka and K. Wakashima : J. Appl. Phys., **83**(1998), p. 7547.
[12] H. Kimura : *Understanding of Materials Strength*, AGNE Technology Center, (1998), p. 369.

Key Engineering Materials Vols. 171-174 (2000) pp. 297-304
© 2000 Trans Tech Publications, Switzerland

Effect of Dislocation Substructure on Creep Behavior of Steels Strengthened by Fine Carbides

N. Nishimura, M. Ozaki and F. Masuyama

Mitsubishi Heavy Industries, Ltd. Nagasaki Research and Development Center,
5-717-1, Fukahori-machi, Nagasaki 851-0392, Japan

Keywords: Dislocation Substructure, Martensitic Steel, Bainitic Steel, Heat Resistant Steel, MC Carbide, MX Carbonitride, Back Stress, Dislocation Strengthening, Particle Dispersion Strengthening, Creep Deformation, Recovery Creep, Subgrain, Dislocation

Abstract

Research was conducted to clarify the effect of substructure on the creep properties of advanced ferritic heat resistant steels strengthened by fine carbonitrides. To this end, creep testing and microstructural examination was carried out on Fe-C-Mn-Nb-V systems exhibiting simpler and more stable microstructures with similar dispersion of fine carbonitrides. Several heats of Fe-C-Mn-Nb-V systems with or without small amounts of solution strengthening molybdenum and tungsten were melted in a vacuum induction furnace, forged, rolled, and heat-treated. Constant load creep tests were carried out on these samples and the microstructure was examined before and after creep exposure. While the minimum creep rate of the Fe-0.05C-0.08Nb-0.2V specimen which was composed of a ferrite matrix with low dislocation density and fine (Nb, V)C carbides was more than one order of magnitude lower than an Fe-0.006C specimen which was composed of ferrite matrix, both specimens exhibited similarly shaped creep curves with a relatively long-term steady creep region. Showing bainitic microstructure and similar dispersion of (Nb, V)C carbides, Fe-0.05C-0.08Nb-0.2V specimen with added manganese had a minimum creep rate one order lower than the Fe-0.05C-0.08Nb-0.2V specimen. However, it featured a very different creep curve in which the steady creep region was completely eliminated and a long term accelerated creep region was observed. These creep curve characteristics were related to the results of microstructural examination focused especially on substructure.

Introduction

In recent years, given ecological and economical demands to improve the efficiency and/or reduce the cost of fossil fired power plants, several heat resistant steels[1][2] have been developed with superior properties and applied for high temperature components of power boilers. Among these materials, advanced ferritic steels (ASME Grades 23, 91, 92, 122, etc.) are being used or planned for use in thick wall high temperature components including high temperature steam piping. Because thinner walls and consequent reductions in material costs can be achieved based on the higher allowable design stress of such materials, extensive researches is being conducted to further develop materials with improved high temperature properties.

A number of fundamental research projects have also been carried out to reveal the strengthening mechanisms of these materials, which include around a dozen alloying elements to achieve high strength. Additions of these elements cause several types of precipitates and complex dislocation substructure resulting from martensitic or bainitic transformation. During creep, these precipitates are coarsened or transformed to other types, dynamic recovery annihilates

dislocations and stable subgrains are formed. Owing to the sophisticated microstructural characteristics of these materials, strengthening mechanisms have yet to be sufficiently clarified, especially the effect of dislocation substructure on creep.

Accordingly, the research presented here aimed to elucidate the effect of substructure on the creep properties. Four heats of Fe-C-Mn-Nb-V alloys, including one type of stable precipitates with different dislocation substructures, were melted and the specimens were subjected to creep tests and microstructural examination. The effect of substructure on creep properties was discussed based on the experimental results.

Experimental Details

Test samples

Six ingots, each weighing 50kg, were melted in a vacuum induction furnace, forged into 25mm thick plates, and heat treated. Analyses of chemical compositions are listed in Table 1, along with cooling procedures employed after normalization and observed microstructures. The fundamental characteristics of each sample are as follows:

F : Fe-Mn alloy of ferritic microstructure with no precipitate, resulting from extremely low carbon content,
B : Fe-Mn alloy of bainitic microstructure with large cementite particles resulting from increased carbon content and water quench after solution treatment to induce bainite,
PF : Fe-Mn alloy of ferritic microstructure with fine Nb-V carbides,
PB : Fe-Mn alloy of bainitic microstructure with fine Nb-V carbides,
SPF : Fe-Mn-Mo-W alloy of ferritic microstructure with fine Nb-V carbides, and
SPB : Fe-Mn-Mo-W alloy of bainitic microstructure with fine Nb-V carbides.

Table 1 Chemical composition of test samples

Mark	C	Si	Mn	Mo	W	Nb	V	Cooling Procedure*	Microstructure
F	0.006	0.35	1.61	-	-	-	-	AC	Ferrite
B	0.21	0.26	1.26	-	-	-	-	WQ	Bainite
PF	0.07	0.35	0.41	-	-	0.085	0.193	AC	Ferrite
PB	0.05	0.36	1.61	-	-	0.081	0.195	OQ	Bainite
SPF	0.06	0.37	0.40	0.15	0.63	0.090	0.197	AC	Ferrite
SPB	0.05	0.36	1.61	0.16	0.63	0.088	0.195	OQ	Bainite

WQ: Water Quenching, AC: Air Cooling, OQ: Oil Quenching

The contents of Mo and W were determined using 'Thermo-Calc' software in order to prevent forming any precipitates of these elements from during heat treatment and creep testing. Whole specimens were normalized for 1.2 ks at 1273 K and tempered for 1.8 ks at 1023 K, except for the material 'B'. Material 'B' was normalized at the same temperature but tempered at 873 K due to lower A_{c1} transformation temperature resulting from higher amounts of carbon.

Creep test

The constant load creep test was performed at 873K in an air atmosphere. Some test sessions were interrupted before rupture and specimens were forced air cooled under stress so as to examine the dislocation microstructure during creep.

Microstructural examination

Optical microstructures were examined to characterize the microstructure of specimens after heat treatment. The distribution of precipitates was observed primarily using a Field Emission Scanning Electron Microscope (FE-SEM) with magnification of 20k to 50k. TEM examination of dislocation substructure was conducted on as-heat treated and crept specimens. The TEM specimens were sampled with the specimen disc surface parallel to the stress direction

Results and Discussions

Creep properties

An example of creep curves is shown in Fig. 1. The addition of small amounts of niobium and vanadium ('PF' to 'F' and 'PB' to 'B') increased creep rupture life by more than one order of magnitude. Although the bainitic microstructure improves the creep rupture life to the base materials ('B' to 'F') only slightly, a minor strengthening was achieved in precipitation strengthened materials ('PB' to 'PF') and a significant strengthening was obtained in precipitation and solution strengthened materials ('SPF' to 'SPB'). The bainitic microstructure may therefore be considered not to be an effective strengthening method alone, but to be valuable in combination with other strengthening methods.

Evaluated by the slope of the creep curve, the instantaneous creep rate is plotted against creep strain as shown in Fig. 2, and two types of curve were clearly identified. One, found in ferritic specimens (F, PF and SPF), has a relatively long steady state, and the other observed in bainitic specimens (B, PB and SPG), has no steady state but a long accelerated creep stage. For the bainitic specimens, the steeper slope of the accelerated creep stage in the figure was obtained in

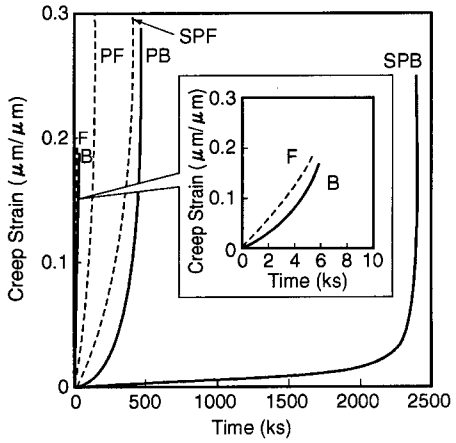

Fig. 1 Example of creep curves of specimens tested at 873K, 98MPa

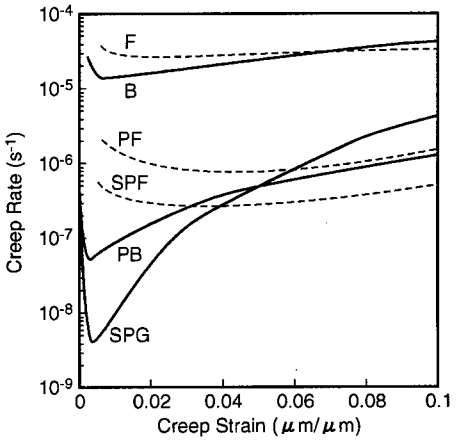

Fig. 2 Spontaneous creep rate against creep strain at 873K, 98MPa

stronger materials. The strongest material 'SPG' exhibits a creep rate at 10% creep strain three orders greater than the minimum creep rate. Thus, the creep rates of bainitic materials are obviously lower at the beginning of the accelerated creep regime, but appear to become similar or greater later in the regime at a creep strain beyond about 5%.

Microstructures

The distribution of precipitates was examined using the FE-SEM, and an example is shown in Fig. 3. The material 'PF' including Nb and V was found to contain fine particles with an average diameter on the order of 30nm which were identified as (Nb, V)C by TEM analysis, while bulky Fe_3C particles were found in the material 'G'. Four materials alloying Nb and V, 'PF', 'PB', 'SPF' and 'SPB', were confirmed to contain fine (Nb, V)C and these were also verified to have similar particle size and spacing. Therefore, neither bainitic microstructure not the addition of small amounts of Mo and W are considered to significantly affect the precipitation of (Nb, V)C. The distribution of precipitates was also examined in crept specimens. Little coarsening of (Nb, V)C was recognized in whole specimens containing (Nb, V)C during creep tests conducted in this study, in which the maximum duration was around 2.4Ms at 873K.

The dislocation substructure was investigated in specimens before and during creep testing. Before creep testing, a relatively low density of dislocations was observed in ferritic specimens without apparent subgrain structure, although numerous dislocations with subgrain structure were identified in bainitic specimens, as shown in Fig. 4. Fig. 5 shows the substructures of the same

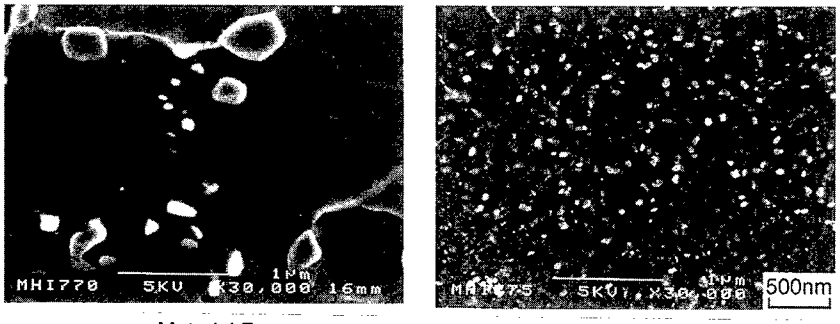

Material F Material PF

Fig. 3 FE-SEM micrographs of materials F and PF

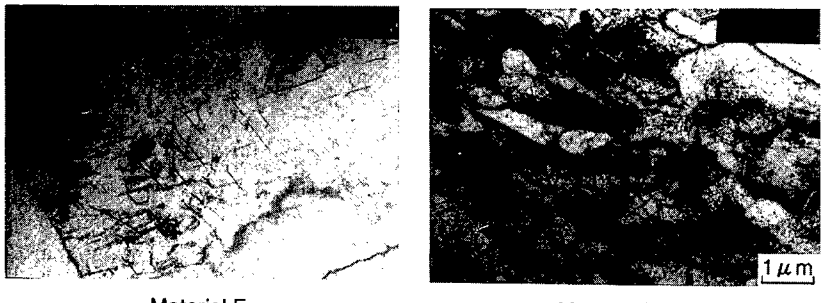

Material F Material SPB

Fig. 4 TEM micrographs of materials F and SPB before creep exposure

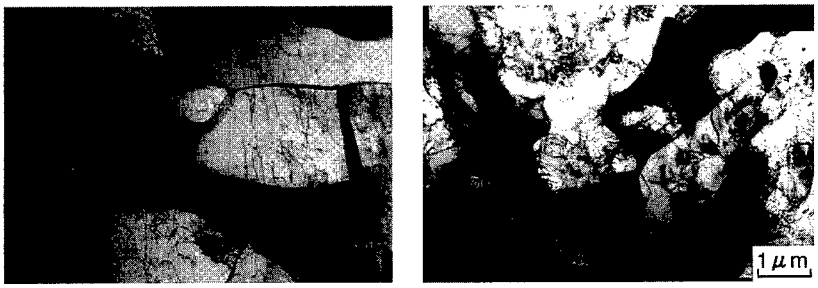

Fig. 5 TEM micrographs of materials F and SPB during creep exposure (873K, 98MPa, $\varepsilon \simeq 5\%$)

materials after creep exposure to creep strain of approximately 5%. During creep, obvious dislocation subgrains were seen to develop in ferritic specimens, while bainitic specimens exhibited extensive reduction in dislocation density and larger subgrains. The dislocation substructures of both ferritic and bainitic specimens were found to be almost equivalent in specimens crept to 5% of creep strain, the point at which the creep rate of bainitic specimens increased to that of ferritic specimens.

Effect of substructure on creep properties

The relation between creep rate and creep strain is shown in Fig. 6. In ferritic specimens, the creep process is mostly composed of steady creep regime. Fine dispersion of precipitates and addition of solution strengthening elements reduce the creep rate over the entire range of the creep process. Therefore the degree of strengthening attributable to particle dispersion and solute atoms is considered to be independent of creep strain and exposure time in ferritic specimens.

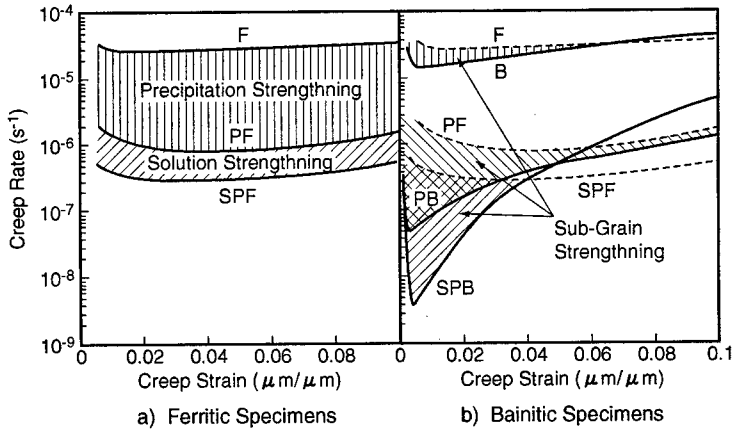

Fig. 6 Relation between creep rate and creep strain of ferritic specimens and bainitic specimens

On the other hand, the creep process in bainitic specimens consists mainly of accelerated creep regime. Although the bainitic specimens exhibit much lower creep rate at the beginning of the accelerated creep regime than corresponding ferritic specimens, the creep rate reaches a similar value at 4 to 10 % of creep strain further along the accelerated creep regime. Accordingly, while the examination of substructure revealed that bainitic materials exhibited harder substructure containing numerous dislocations, the dislocation density of bainitic specimens was found to be greatly reduced to that of ferritic specimens, and the substructure of bainitic specimens was also seen to be similar to that of ferritic specimens. The long term acceleration creep regime in bainitic specimens is therefore considered to be caused by the recovery process, that is, annihilation of excess dislocations formed by the bainitic transformation and growth of subgrains during creep. Thus, the creep strengthening of bainitic substructure is considered to be dependent on creep strain.

Strengthening mechanisms by substructure are illustrated in Fig. 7. In ferritic specimens, dislocation substructure would be formed during primary creep regime, and the back stress induced by the substructure would not be changed during the long steady state. On the other hand, while the excess dislocations in bainitic specimens would induce higher back stress during the early stage of creep, this would be gradually reduced due to the dynamic recovery process during the long accelerated creep regime. The difference in back stress is considered to affect the shape of creep curves as well as creep strength.

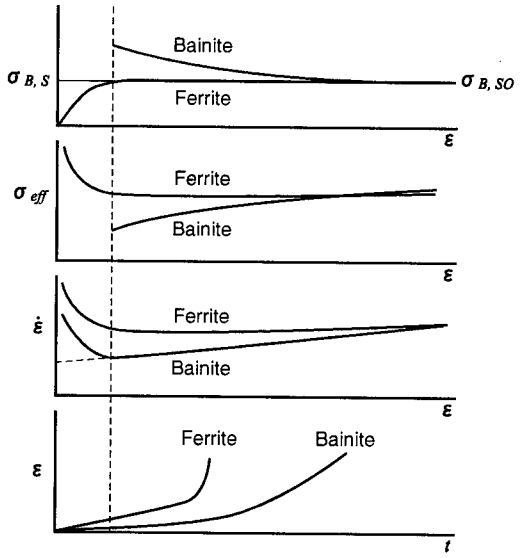

Fig. 7 Strengthening mechanism by sub-structure

Conclusions

Research was conducted on carbon steels alloying small amounts of strengthening elements to simplify the microstructure of advanced ferritic heat resistant steels in order to verify the effect of dislocation substructure on creep properties. The conclusions are as follows:

1) Bainitic structure raised the creep strength of base, particle-strengthened, and solution-strengthened materials.

2) While ferritic specimens possessed creep curves having a long steady state regime, bainitic specimens exhibited creep curves having no steady state but a long accelerated creep regime.
3) Although strengthening by bainite structure resulted in remarkably lower minimum creep rate, the creep rate increased toward similar values of ferritic specimens by 4 to 10% of creep strain.
4) Formed in bainitic steel due to bainite transformation and recovered during creep, the dislocation subgrain structure was not formed in ferritic specimens prior to creep testing but instead developed during creep exposure. Bainitic specimens exhibited a dislocation substructure similar to corresponding ferritic specimens at the creep strain at which a similar creep rate was obtained.
5) Strengthening due to dislocation substructure by bainitic transformation was considered to cause significant reduction in the creep rate at the early stage of creep, but the effect was considered to be eliminated as a result of dynamic recovery during creep at a later stage.

References

[1] F. Masuyama et al., Materials for Advanced Power Engineering, Part I, Ed. D. Coutsouradis , 1994, Kluwer Academic Publishers, Netherlands, p 301
[2] F. Masuyama et al., *ibid.*, p 173

Nobuhiko Nishimura/ e-mail: Nishimur@notesgw.ngsrdc.mhi.co.jp, Fax +81-95-834-2175

Key Engineering Materials Vols. 171-174 (2000) pp. 305-312
© 2000 Trans Tech Publications, Switzerland

Study on Evaluation Procedure of Multiaxial Creep Strength of Low Alloy Steel

Y. Chuman[1], M. Yamauchi[1] and T. Hiroe[2]

[1] Mitsubishi Heavy Industries, Ltd., Nagasaki R&D Center, Fukahori-Machi 5-717-1, Nagasaki 851-0392, Japan

[2] Kumamoto University, Kurokami 2-39-1, Kumamoto 860-8555, Japan

Keywords: Creep Damage, Multiaxial Stress, Maximum Principal Stress, Mises Equivalent Stress, Huddleston Equivalent Stress, Hydrostatic Stress, Ductility Exhaustion Method, 2.25Cr-1Mo Steel

Abstract A creep damage evaluation procedure under a multiaxial stress condition was investigated. Creep tests of 2.25Cr-1Mo steel hollow cylindrical specimens heat-treated to simulate coarse grain in heat affected zone were conducted under the condition of combined axial load and internal pressure. The stress conditions were almost equibiaxial on the outer surface and almost uniaxial on the inner surface in the specimen. After the tests, the distribution of creep cavity density that was considered to represent an amount of creep damage was measured along a radial direction in wall thickness.

The distribution of creep damage in wall thickness was evaluated using maximum principal stress, Mises equivalent stress, Huddleston equivalent stress and ductility exhaustion method to compare with the measured creep cavity density. The tendency of the creep damage distributions evaluated by Mises and Huddleston equivalent stresses was different from the observed creep damage distribution. On the other hand, the results estimated by maximum principal stress and ductility exhaustion method were in good agreement with the measured creep damage distribution. Based on the above results, a new creep damage evaluation procedure under multiaxial stress condition was proposed by taking into account the effect of the hydrostatic stress.

Introduction

Recently, creep cracks, termed Type III in coarse-grained heat affected zone (C.G.HAZ) and Type IV in fine-grained heat-affected zone (F.G.HAZ), have been detected in weldment of low alloy steel in high energy piping of aged fossil-fired power plants. The stress in the weldment is in multiaxial condition, therefore it is necessary to establish the creep damage evaluation procedure under multiaxial stress in order to develop an analytical life assessment method.

In this study, creep tests of 2.25Cr-1Mo steel hollow cylindrical specimens heat-treated to simulated C.G.HAZ were conducted under the condition of combined axial load and internal pressure. After the specimens were ruptured, the distribution of creep cavity density that was considered to represents an amount of creep damage was measured along a radial direction. And then, Creep damage evaluation procedure under multiaxial stress condition was studied by comparing the creep voids density distribution and predicted creep damage distribution.

Multiaxial Creep test

Material and Specimen

Material used in the creep tests was a 2.25Cr-1Mo steel pipe. The chemical composition and the mechanical properties are shown in Table 1 and Table 2, respectively. Before machinery work, the pipe was heat-treated to simulate the thermal history of coarse grain in heat affected zone in the condition shown below:

$$1300℃ \times 15sec+AC$$

After the heat-treatment, the grain size was about 100 μ m.

Figure 1 shows a shape of the specimen. Two types of specimen shown below were used in order to make different stress distribution in wall thickness:

(1) thick hollow cylinder (40mm in outer diameter and 8mm in thickness)

(2) thin hollow cylinder (40mm in outer diameter and 4mm in thickness)

Testing Method and Condition

The creep tests were carried out under the condition of combined axial load and internal pressure. The condition of axial load and internal pressure were determined with steady state creep analysis assuming the Norton's law in order to make an equibiaxial stress condition on the outer surface as follows:

(1) axial load F=18.6kN and internal pressure P=37MPa for thick specimen

(2) axial load F=11.7kN and internal pressure P=14MPa for thin specimen

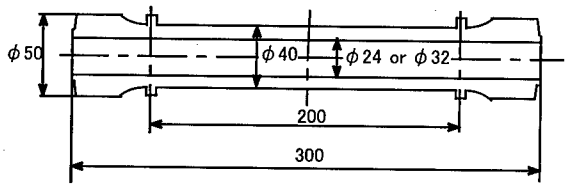

Fig.1 Shape and dimension of specimen

Table1 Chemical composition (wt.%)

C	Si	Mn	P	S	Cr	Mo
0.11	0.26	0.46	0.016	0.007	0.207	0.094

Table 2 Mechanical properties (RT)

0.2% offset yield strength (MPa)	Tensile strength(MPa)	Elongation (%)
324	471	61

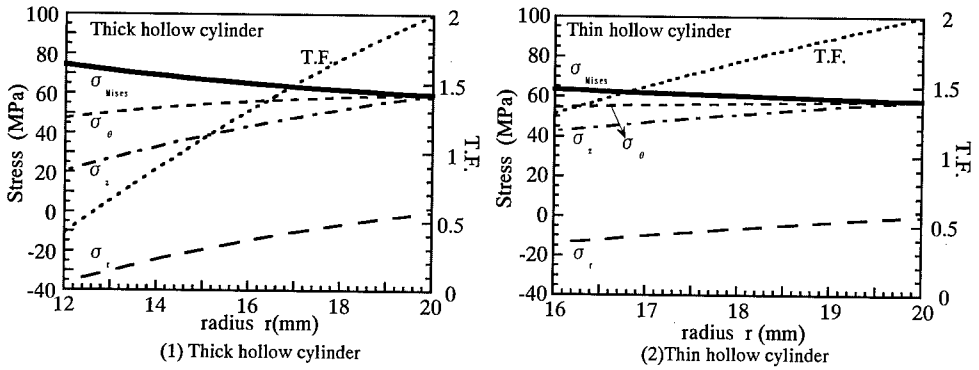

(1) Thick hollow cylinder

(2)Thin hollow cylinder

Fig.2 Distribution of steady stress and triaxiality factor in wall-thickness of the specimen

The steady stress on outer surface was 59MPa and test temperature was 620℃.

Figure 2 shows the distribution of steady stress and the triaxiality factor in wall thickness of the specimen. The triaxiality factor was T.F.=2 on outer surface, and on inner surface T.F=0.4 and T.F.=1.3 for thick and thin specimen, respectively. Here, the triaxiality factor was defined by the following equation:

$$T.F. = \frac{\sigma_1 + \sigma_2 + \sigma_3}{1/\sqrt{2}\left[(\sigma_1 - \sigma_2)^2 + (\sigma_2 - \sigma_3)^2 + (\sigma_3 - \sigma_1)^2\right]^{1/2}}$$

Test Result

The Result of Uniaxial Creep Test

Uniaxial creep tests were conducted to obtain the creep properties of this material by using smooth bar specimen with 6 mm in diameter and 30 mm in gauge length. Figure 3 shows the relationship between the minimum creep rate and stress. From this figure, the exponent in Norton's law was obtained by the data in low stress level corresponded to the test condition.

Figure 4 shows the creep rupture strength of this material.

The Result of Multiaxial Creep Test

From the result of the uniaxial tests and the result of metallurgical life assessment [1] conducted by the interruption of the test, rupture lives of multiaxial creep tests were predicted to be longer than initial predicted ones. Therefore, the applied load conditions were changed at 3140 hours so that the stress in outer surface became 98MPa, as shown below:

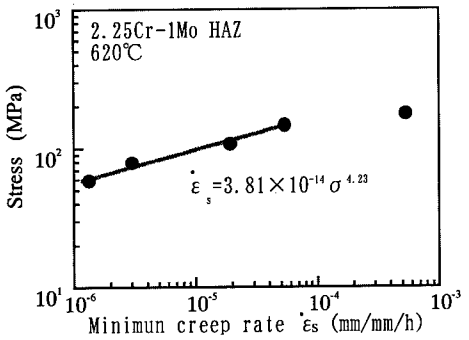

Fig.3 Minimun creep rate of the material tested.

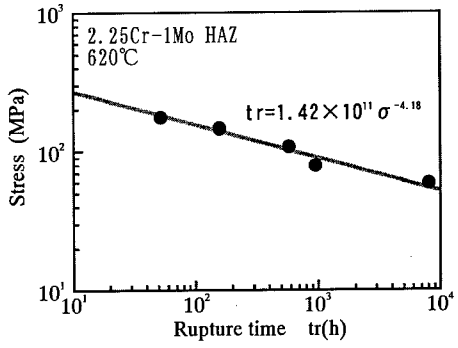

Fig.4 Creep rupture strength of the material tested

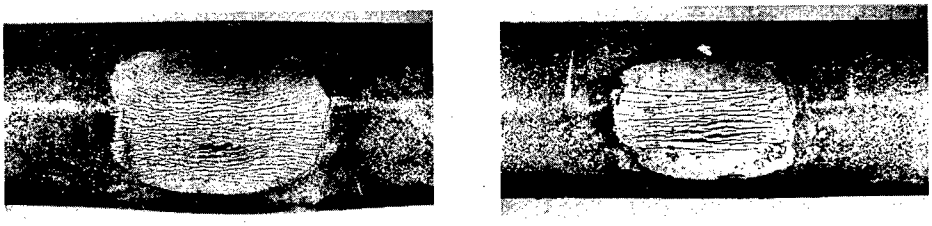

(1) Thick hollow cylinder (2) Thin hollow cylinder

Fig.5 Appearance of crack in specimen after creep rupture test. 10mm

(1) axial load F=30.7kN and internal pressure P=61MPa for thick specimen

(2) axial load F=19.6kN and internal pressure P=24MPa for thin specimen

Total creep rupture lives were as follows:

(1) thick specimen : tr=3279.4 hour

(2) thin specimen : tr=3293.2 hour

Figure 5 shows the appearance of the crack in the specimen after the tests. The cracks were located at the middle part of along axial direction of the specimens. .

Result of Observation of Creep Damage

Figure 6 shows the result of SEM observation of the microstructure of a longitudinal near the outer surface about 10mm distant from the rupture location. Creep voids were observed in the grain boundary. Figure 7 shows the radial distribution of creep voids. The number of creep voids was measured in the area of 0.7mm^2. Both in the thick and the thin specimens, the number of creep voids on the outer surface was more than that in inner surface. The ratio of the number of creep voids on the inner surface to that on the outer surface was about 0.1 for the thick specimen, and was about 0.4 in the thin specimen.

Figure 8 shows the relationship between the number of creep voids and the angles of grain boundary against axial direction of the specimen. The angles of the grain boundaries with creep voids were measured in the area of 1.5mm^2 on the outer and the inner surface. The grain boundary with the angle of 0 degree was vertical to hoop stress, and the grain boundary with the angle of 90 degree was vertical to axial stress. The creep voids at triple points of grain boundary were counted separately. In the outer surface, many creep voids were observed in the grain boundary with the angle of around 0 degree and 90 degree, and fewer voids were detected in the grain boundary with the angle of 45 degree. In the inner surface, many creep voids were observed in the grain boundary with the around angle of 0 degree. This would be caused by the difference in stress state; that is, the stress state was almost equibiaxial in outer surface and the two main principle stresses acted vertically to each grain boundary with the angle of 0 and 90 degree. On the other hand, in the inner surface, the hoop stress mainly governed the stress state.

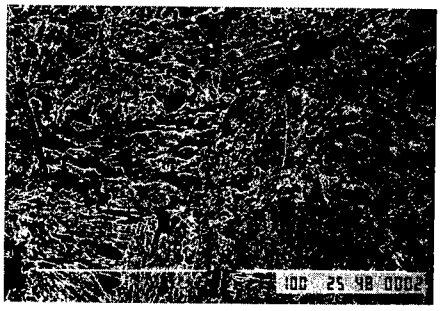

Fig.6 SEM observation result of creep voids

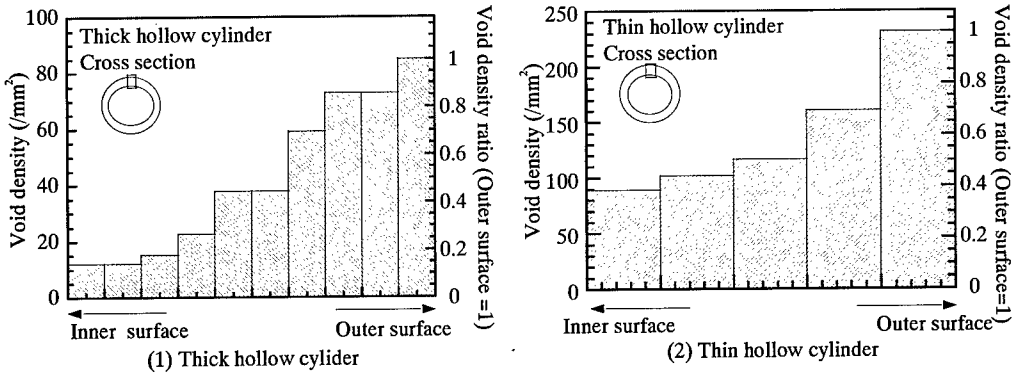

Fig.7 Voids density distribution

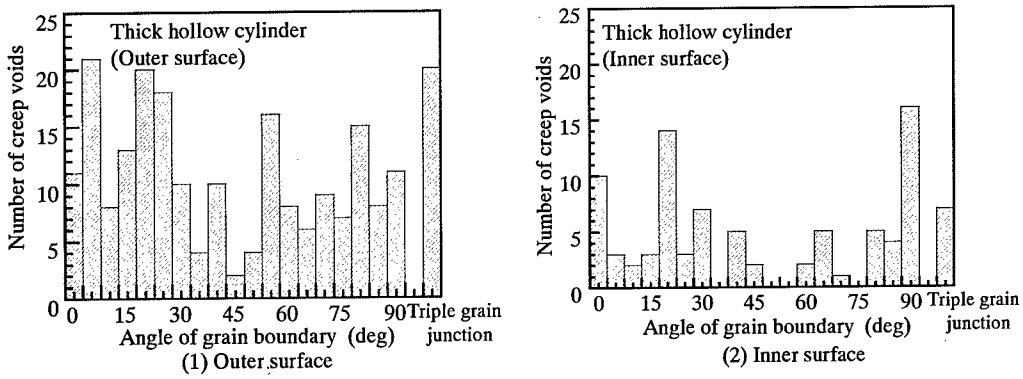

Fig. 8 Relationship between number of creep voids and angle of grain boundary

Evaluation of Creep Damage

Evaluation Procedure

Multiaxial creep tests were evaluated by several multiaxial creep strength evaluation procedures, as shown below:

① Maximum principal stress(MPS)

② Mises equivalent stress

③ Huddleston equivalent stress[3]

$$\sigma_{HU} = \sigma_{Mises} \exp\left[0.24\left(\frac{\sigma_1+\sigma_2+\sigma_3}{\sqrt{\sigma_1^{\,2}+\sigma_2^{\,2}+\sigma_3^{\,2}}}-1\right)\right]$$

④ Hayhurst equivalent stress[4]

$$\sigma_{HA} = \alpha\sigma_1 + (1-\alpha)\sigma_{Mises}, \quad \alpha = 0.48$$

⑤ Ductility exhaustion method [2](DEM)

$$\dot{D}c = \frac{\dot{\varepsilon}_c}{\varepsilon_f} = \frac{\dot{\varepsilon}_c}{\varepsilon_{f0}/T.F.}$$

$\dot{\varepsilon}_c$: equivalent creep strain rate

ε_{f0} : uniaxial creep ductility (minimum creep stain rate×rupture time)

Results of Evaluation

Figure 9 shows the comparison of predicted creep damage distribution by several methods with the measured creep void density ratio for thick specimen. Here, it was assumed that the creep voids distribution of this location were represented that of secondary creep period and the creep void density V was a linear for creep damage Dc during secondary creep period.

$$V = bD_c = b\frac{t}{tr} = \frac{bt}{a\sigma^n} \quad ; \text{here } a, b, n \text{ are constant}$$

Creep void density ratio V/V_o and creep damage ratio Dc/Dc_o based on the outer surface were derived as follows:

$$\frac{V}{V_o} = \left(\frac{\sigma_o}{\sigma}\right)^n, \quad \frac{Dc}{Dc_o} = \left(\frac{\sigma_o}{\sigma}\right)^n \quad ; \text{here suffix } o \text{ shows the outer surface}$$

Therefore, the creep void density ratio was expected to correspond to the creep damage ratio calculated by creep evaluation methods and primary and secondary creep stress distribution.

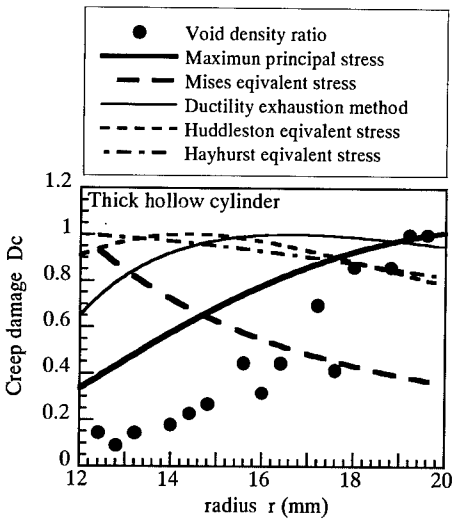

Fig.9 The comparison of predicted creep damage distribution by several method and measured creep voids density ratio

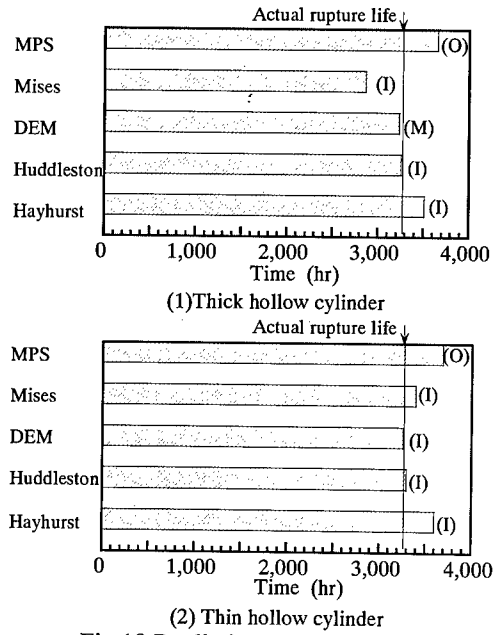

Fig.10 Prediction of creep rupture life

( ) shows the predicted crack initiation site;

O: Outer surface, I: Inner surface

M: Inside of specimen

From Fig.9, the results of the evaluation by the maximum principal stress and the ductility exhaustion method revealed the same tendency as the creep voids density. The results of other evaluation methods have different tendency from the test result.

Figure 10 shows the result of the prediction of creep rupture lives by the multiaxial creep evaluation procedures shown above. All the results were near the actual rupture life, but, except for the maximum principal stress, predicted crack initiation site were at inner surface.

The Study on Multiaxial Creep Equivalent Stress Considering The Hydrostatic Stress.

As shown in Fig.9, it could be seen that all multiaxial creep evaluation methods could not predict the creep damage distribution correctly. The result of maximum principal stress was the nearest to the actual creep damage distribution, but could not predict the quantitative damage ratio of inner and outer surface. Therefore, new equivalent stress for multiaxial creep evaluation was studied based Hayhurst equivalent stress, which was a liner summation of maximum principal stress, Mises equivalent stress and hydrostatic Stress.

Original Hayhurst equivalent stress is expressed next formula.

$$\sigma_{HA} = \alpha\sigma_1 + \beta\sigma_{Mises} + \gamma\sigma_H \ ; \ \alpha+\beta+\gamma = 1, \ \sigma_H = \sigma_1 + \sigma_2 + \sigma_3$$

The values of the constant α, β, γ were obtained to optimize the predicted creep damage distribution for creep void density ratio in thick specimen. As a result, it was obtained that α=0.29, β=0.22, γ=0.49. It suggest that the hydrostatic stress is dominant to evaluate the intergranular creep fracture under the multiaxial stress. Figure 11 shows the comparison of predicted creep damage distribution by this method and creep void density ratio. Predicted creep damage distribution in thick specimen corresponded with the creep voids density naturally, even in thin specimen, it was improved than maximum principal stress.

But, on the other hand, predicted life is 1440hour for thick specimen, which is excessive shorter than actual rupture life. Although it can considered that the predicted life shows crack initiation life

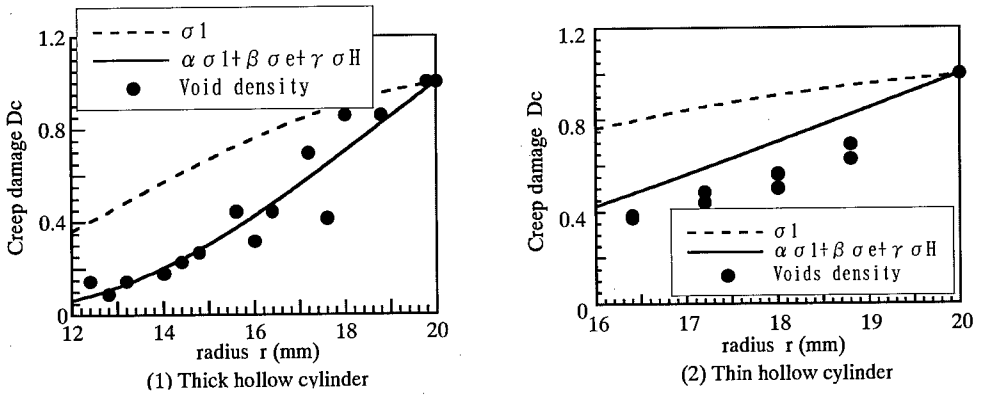

Fig.11 The comparison of predicted creep damage distribution by proposed method and measured creep voids density ratio.

and remain life shows crack propagation life, so as to discuss that, it is necessary to clear the creep crack initiation life under the multiaxial stress state, further.

Conclusion

Creep tests of 2.25Cr-1Mo steel hollow cylindrical specimens heat-treated to simulated coarse grain in heat affected zone were conducted under the condition of combined axial load and internal pressure. And then, Creep damage evaluation procedure under multiaxial stress condition was studied by comparing the creep voids density distribution and predicted creep damage distribution. The results obtained are summarized as follows;

(1) The predicted damage distribution by multiaxial creep evaluation methods such as Mises, Huddleston and Hayhurst equivalent stress have different tendency from the actual creep damage distribution. Only the results of maximum principal stress rule and the ductility exhaustion method considering the effect of the multiaxial stress state have same tendency as the actual creep damage distribution.

(2) Evaluation method by the next equivalent stress could predict the creep damage distribution correctly.

$$\sigma_{HA} = \alpha\sigma_1 + \beta\sigma_{Mises} + \gamma\sigma_H \ , \quad \alpha = 0.29, \beta = 0.22, \gamma = 0.49.$$

This equivalent stress suggests that the hydrostatic stress is dominant to evaluate the intergranular creep fracture under the multiaxial stress.

References

[1] M.Masuyama, N.Nishimura, Bulletin of the Japan Institute of Metals Materia Japan, 27, 287 (1988)

[2] M.Yamauchi, Y.Tanaka, M.Sugasawa, Proceedings of 33rd Symposium on Strength of Material at High Temperatures, pp70 (1995)

[3] R.L.Huddleston, Trans. ASME, Vol.115, pp177 (1993)

[4] D.R.Hayhurst, F.A.Leckie, C.J.Morrison, Proc.R.Soc., A360,pp243 (1978)

Key Engineering Materials Vols. 171-174 (2000) pp. 313-320
© 2000 Trans Tech Publications, Switzerland

Theoretical and Experimental on the Significant Creep Deformation of SUS 316 Induced by Irradiation at 60°C

J. Nagakawa, Y. Murase, N. Yamamoto and T. Fukuzawa

National Research Institute for Metals, 1-2-1 Sengen, Tsukuba, Ibaraki 305-0047, Japan

Keywords: Irradiation Creep, Point Defects, Irradiation Damage, In-Beam Experiment, Simulation

Abstract

Very significant irradiation-induced creep deformation at 60°C in SUS 316 was investigated both theoretically and experimentally. Calculation based on the theoretical modeling of point defect kinetics under stress and the radiation-induced plastic deformation has been performed. This theoretical study revealed the transient nature of the conspicuous radiation-induced creep caused by the high flux of excessive interstitial atoms in the earlier stage of irradiation at 60°C where the diffusivity of vacancies is very low. In order to prove the transient nature, continuous creep measurement under irradiation is inevitable and was carried out using 17 MeV proton beam from the NRIM cyclotron and the in-beam creep/fatigue testing apparatus. Very significant creep strain, much larger than that at 300°C, and continuously decreasing creep rate were observed at 60°C in 20% cold-worked SUS 316 stainless steel just as the calculation predicted. It was concluded that the very significant creep deformation induced by irradiation at 60°C in SUS 316 originates from the overwhelming flux of excess interstitial atoms induced transiently in the matrix due to the large imbalance of diffusivity between interstitial and vacancy at this low temperature.

1. Introduction

Structural materials in the fusion reactor will be subjected to irradiation by energetic particles at temperatures widely ranging from liquid He temperature to above 1000°C. High temperature creep and fatigue strength have been the major concern for these materials. Additional irradiation-induced phenomena such as the irradiation creep, i.e. significant creep deformation which appears only under irradiation as shown for pure Ni in Fig. 1 [1], and the void swelling are considered as important but mainly in the medium temperature range of 300 to 500°C. Accumulation of remarkable creep strain was, however, observed at 60°C recently in the pressurized tube experiments of austenitic stainless steels of both solution-annealed and cold-worked condition irradiated to several dpa (the number of atomic displacement per lattice atom) in the ORR reactor at Oak Ridge National Laboratory [2]. The observed strain was several times larger than the irradiation creep strain at 300 – 400°C, that is already larger by orders of magnitude than that of the thermally activated creep at these temperatures. This significant irradiation creep observed at 60°C is now called "low temperature irradiation creep". Although the major components of the fusion reactors will be irradiated at rather high temperatures, there will be many portions which suffer from atomic displacements and externally applied stress at rather low temperatures around 60°C. Hence, it is quite important to clarify its cause and evaluate its expected strain for the development of fusion reactors.

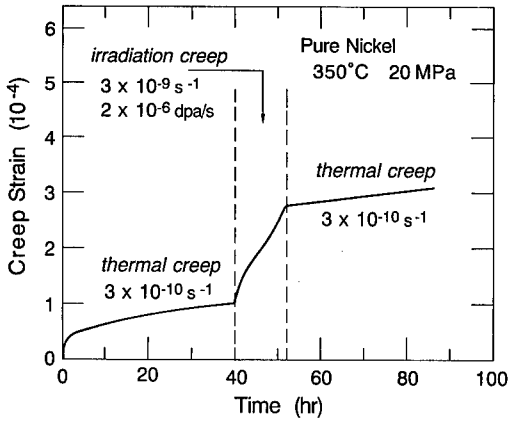

Fig. 1 Irradiation creep and thermal creep in pure Ni at 350°C.

Since the irradiation creep takes place only during the irradiation by energetic particles and the resultant atomic displacement process, it is quite reasonable to search for its cause in the behavior of point defects such as interstitial atoms and vacancies introduced by the irradiation into the crystalline material. In the rather low temperature range around 60°C, vacant lattice sites, which has a high migration energy, can hardly move in SUS 316, while interstitial atoms are able to migrate very actively through the material owing to its low migration energy. Since the radiation-induced deformation is caused mainly by the motion of interstitial atom, which induces a very strong lattice distortion and a consequent intense interaction with the stress field, under the influence of the external stress, the large difference in diffusivity between the two kinds of point defects may introduce a very significant enhancement.

In this study, calculational investigation based on the theoretical modeling of point defect kinetics and radiation-induced deformation has been performed for SUS 316 at both 60 and 300°C. The behavior of interstitial atoms and vacancies under the externally applied stress is simulated by solving the rate equation in the form of simultaneous differential equations of point defects and their agglomerates, taking the stress effect into account. Major radiation-induced deformation mechanisms are also included in the calculation process so that all of them are competing for the point defects and contributing to the deformation. Secondly, continuous measurement of creep strain during 17 MeV proton irradiation was carried out for SUS 316 at both 300°C and 60°C. Since the earlier result of the low temperature irradiation creep at the ORR/ORNL was obtained only for a single dpa value and not as a function of irradiation time, it is not enough for the verification of theoretical conclusion as has been realized in the present study.

2. Modeling and calculation procedure

The present simulation of radiation-induced deformation is based on the stress-affected kinetics of nucleation and growth of defect agglomerates, as well as point defect absorption by network dislocations. Simultaneous differential equations are numerically solved for the following defect concentrations:

(1) single interstitials (C_i),

(2) single vacancies (C_v),

(3) aligned interstitial loop precursors (C_{2iA}),
(4) non-aligned interstitial loop precursors (C_{2iN}),
(5) growing interstitial loops on aligned planes (C_{ilA}),
(6) those on non-aligned planes (C_{ilN}),
(7) accumulated net interstitials in growing aligned loops (C_{ilAi}),
(8) those in growing non-aligned loops (C_{ilNi}),
(9) net interstitials absorbed by aligned network dislocations (C_{dAi}),
(10) those absorbed by non-aligned network dislocations (C_{dNi}).

SUS 316 stainless steel was selected for the sample since the main portion of ITER (International Thermonuclear Experimental Reactor) will be constructed with this steel. Point defect migration energies for SUS 316 were taken from the evaluation by Dimitrov and Dimitrov [3], that is, 0.92 eV for interstitials and 1.15 eV for vacancies. This high migration energy of interstitials in austenitic stainless steels is strongly supported by studies of microstructure evolution [4]. Important parameter values used in the numerical calculation are listed in Table 1.

Table 1. Parameter values used in the calculation

Parameter	Value
Defect migration energy	
interstitial	0.92 eV
vacancy	1.15 eV
Defect migration pre-exponent	
interstitial	8.0×10^{-7} m^2/s
vacancy	1.4×10^{-6} m^2/s
Lattice constant	3.524×10^{-10} m
Atomic volume	1.1×10^{-29} m^3
Strength of Burgers vector	2.1×10^{-10} MPa
Young's modulus	2.6×10^{5} MPa
Shear modulus	1.0×10^{5} MPa
Poisson's ratio	0.3
Dislocation density	
solution annealed	3×10^{12} m/m^3
cold worked	3×10^{15} m/m^3
Defect relocation volume (in atomic volume)	
interstitial	+1.4
vacancy	−0.46
Difference in shear modulus between defect and matrix	
interstitial	-1.0×10^{5} MPa
vacancy	0 MPa

The interstitial absorption bias over vacancy (Z_i) and its stress-induced component (ΔZ_i) for loops and network dislocations were calculated using the equations given by Wolfer and Ashkin [5] and Heald and Speight [6], respectively. As for a vacancy flux, values for Z_v and ΔZ_v given by refs. [5,6] were used in the calculation, but unlike ΔZ_i, ΔZ_v is too small to affect the radiation induced deformation. At each numerical iteration step, the loop size was re-averaged and $Z_{i,v}$ and $\Delta Z_{i,v}$ were re-evaluated. In the interstitial loop nucleation process, a di-interstitial was provided to be a precursor and its formation was considered to be affected by the external stress following the SIPN

model proposed by Brailsford and Bullough [7].

In the present study, SIPN (Stress-Induced Preferential Nucleation of interstitial loops) [7,8] and loop growth driven by SIPA (Stress-Induced Preferred Absorption of point defects) [6,9] are taken into account, as well as PA (SIPA climb) and PAG (glide enabled by SIPA climb) contributions [10] by network dislocations. Also included was TIC (Transient mode of I-Creep [11]; dislocation glide enabled by excess interstitial flux caused during the transient point kinetics) [12,13]. From the calculated derivatives of defect concentrations, plastic strain rate produced by each mechanism was evaluated at every iteration step using the following equations ;

(1) PA (SIPA climb creep by network dislocations) [10]

$$\dot{\varepsilon}_{PA} = \tfrac{2}{3}(dC_{dAi}/dt - dC_{dNi}/dt) \tag{1}$$

(2) PAG (dislocation glide induced by SIPA climb) [10]

$$\dot{\varepsilon}_{PAG} = (4e\sqrt{(\pi L_d)}/3b)(dC_{dAi}/dt - dC_{dNi}/dt) \tag{2}$$

(3) SAIL (SIPA climb creep by growing interstitial loops) [6,9]

$$\dot{\varepsilon}_{SAIL} = \tfrac{2}{3}(dC_{ilAi}/dt - dC_{ilNi}/dt) \tag{3}$$

(4) SIPN (creep by stress-induced preferential loop nucleation) [7,8]

$$\dot{\varepsilon}_{SIPN} = \tfrac{4}{3}(dC_{2iA}/dt - dC_{2iN}/dt) \tag{4}$$

(5) TIC (transient I-creep) [12,13]

$$\dot{\varepsilon}_{TIC} = (e\sqrt{(\pi L_d)}/b)(dC_{dAi}/dt + 2\,dC_{dNi}/dt) \tag{5}$$

where e is the elastic deflection (σ / E ; σ is the external stress, E is Young's modulus), L_d is the network dislocation density, and b is the size of the Burgers vector. The damage efficiency used for the neutron irradiation was 0.3. This value was selected because the in-reactor creep compliance is about 0.3 times that for the light-ion irradiation creep [14]. For the latter case, the efficiency is usually regarded as close to unity and in fact the calculation with the efficiency of 1 showed a very good coincidence with the experimental data including temperature dependence [15]. In the following, a nominal dpa, not the value multiplied by the damage efficiency, is used to describe the damage and the damage rate unless otherwise indicated.

3. Results and discussion

Fig. 2 shows the calculated irradiation creep rate as a function of time at 60°C and 300°C for the displacement rates of 10^{-6} and 10^{-8} dpa/s in the solution-annealed SUS 316 stainless steel. The major mechanism contributing to the irradiation creep at both temperatures is SIPN. As for the cold-worked case, the major mechanism is TIC. Although the prevailing mechanism is different between the two conditions, the resultant creep strain at 2 dpa is almost the same as shown in Fig. 3. This result and the one that irradiation creep strain at 60°C is several times larger than that at 300°C coincide with the ORR/ORNL in-reactor result. The large peaks in Fig. 2 reflect the

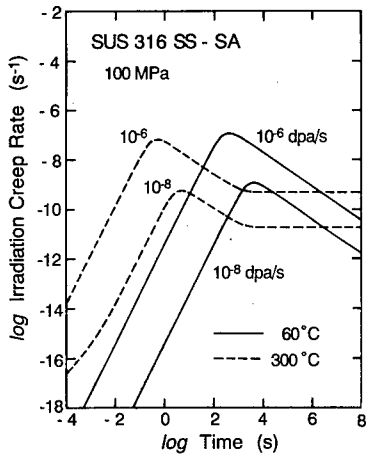

Fig. 2 Calculated transition of irradiation creep rate with time in solution-annealed SUS 316.

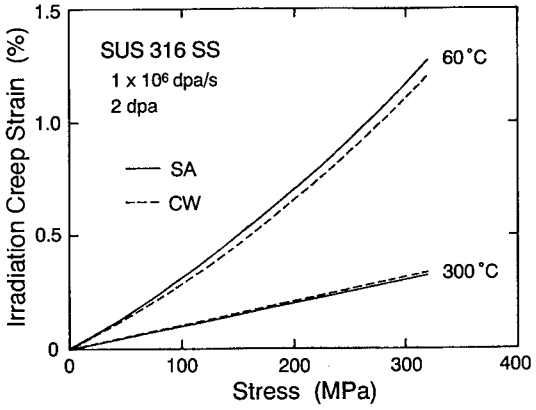

Fig. 3 Calculated creep strain at 60°C and 300°C in SUS 316 irradiated to 2 dpa.

transiently excess interstitial flux which results from the difference in diffusivity between interstitial atom and vacancy. It disappears as the density of vacancies in the matrix increases and the mutual reconbination and the resultant annihilation of both point defects become significant. Ultimately, a steady state creep rate can be attained, as shown in Fig. 2, but it is much delayed at lower temperatures such as 60°C to the order of ten years. The calculation also indicates that the steady state creep rate is higher at 300°C than that at 60°C.

Since the nature of the low temperature irradiation creep is expected to be transitional, the single dpa data of ORR/ORNL [2] is not suitable for its verification. Continuous measurement of creep strain was performed using specially designed in-beam creep/fatigue testing apparatus connected to the NRIM compact cyclotron accelerator [16,17]. In advance of the experiment, the simulation calculation was extended to the same irradiation condition, i.e., 60°C and 300°C, 300 MPa, 1×10^{-7} dpa/s and for 20% cold-worked SUS 316. Fig. 4 shows the calculated irradiation creep rate as a function of irradiation time, in other words accumulated dpa, at both temperatures. Even at 300°C the transient process appears in the early stage but it ceases within the order of ten seconds. In contract, the transiently high creep rate lasts nearly one year at 60°C. The same calculation gives the irradiation creep strain development with the irradiaiton time, shown in Fig. 5. The transient at 300°C is minute and the creep rate is practically constant at 2×10^{-10} s^{-1} from the beginning of irradiation. On the other hand, very clear and significant transient behavior can be recognized at 60°C as a gradually decreasing creep rate. At 60°C the creep rate at $5 - 6 \times 10^4$ s is about 5×10^{-9} s^{-1} which is more than order of magnitude larger than at 300°C.

The tensile creep specimen used for the in-beam experiment was SUS 316 (Cr: 16.79, Ni: 10.30, Mn: 1.17, Mo: 2.16, C: 0.06, Si: 0.68, P: 0.027, S: 0.001, Fe: balance, in wt.%) and in a thin sheet shape with a gauge section of 4 mm wide, 10 mm long and 150 μm thick. The side-notch at the center is given only for the fatigue experiments. The 17 MeV proton beam with intensity of 2 $\mu A/cm^2$ from the NRIM cyclotron produces atomic displacement at a rate of about 1×10^{-7} dpa/s throughout the 150 μm thick specimen as shown in Fig. 6. The temperature of specimen was

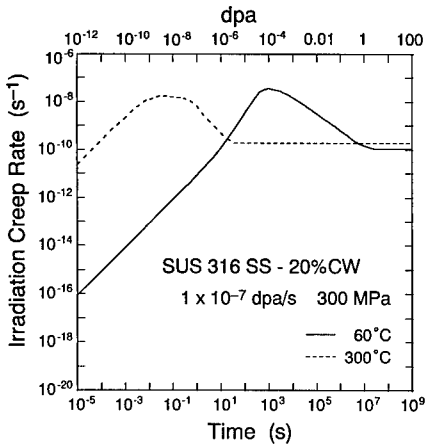

Fig. 4 Calculated irradiation creep rate as a function of time at 60°C and 300°C in 20% cold-worked SUS 316.

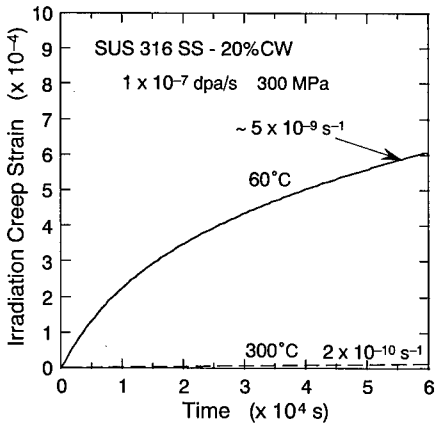

Fig.5 Calculated irradiation creep curves of 20% cold-worked SUS 316 at 60°C and 300°C.

controlled by balancing the beam heating and the He jet cooling for 60°C, while heated He jet was used for 300°C.

Fig. 7 indicates the experimental results in solid line and the calculated ones in broken line for both 60°C and 300°C. At 300°C weak but rather prolonged transient stage was observed in the in-beam experiment. It diminished at about 5×10^4 s and the creep rate became constant and close to the calculated value of 2×10^{-10} s^{-1}. The main cause of this 300°C transient seems to be associated with a thermal recovery, although the exact origin is not clear at this moment. The transient stage at 60°C is far more significant, and the creep rate at 5×10^4 s is an order of magnitude larger than that at 300°C and apparently still decreasing. The correspondence between the experimental and the calculational result at 60°C appears to be fairly good. These continuous creep measurements at 60°C and 300°C clearly indicate the significant irradiation creep at low temperatures around 60°C

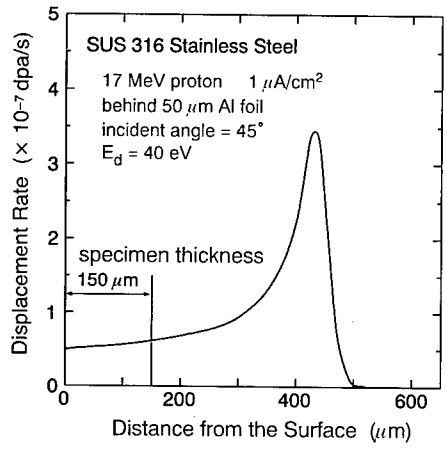

Fig. 6 Atomic displacement rate in SUS 316 irradiated with 17 MeV protons.

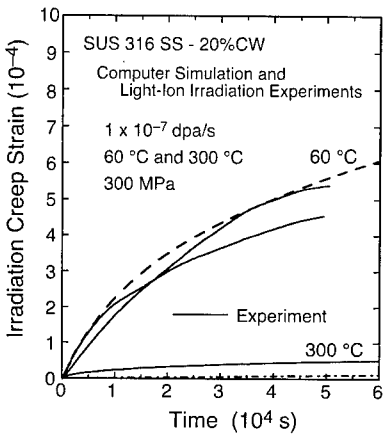

Fig. 7 Experimental irradiation creep curves of SUS 316 irradiatedat 60°C and 300°C.

and its transient nature. The good coincidence between the calculated prediction and the light-ion irradiation experiments strongly suggests that the low temperature irradiation creep at 60°C in SUS 316 originates in the kinetics transient of point defects due to their large imbalance in diffusivity.

4. Conclusions

Very significant irradiation-induced creep deformation at 60°C in SUS 316 was investigated both theoretically and experimentally.

(1) Calculation based on the theoretical modeling of point defect kinetics under stress and the radiation-induced plastic deformation has been performed. This theoretical study revealed that the conspicuous radiation-induced creep at 60°C is a transient phenomenon and it results from the overwhelming flux of excess interstitial atoms in the earlier stage of irradiation at this temperature where the diffusivity of vacancy is far lower than that of interstitial atom.

(2) In order to prove the transient nature, continuous creep measurement under irradiation is inevitable and was carried out using 17 MeV proton bean from the NRIM cyclotron and the in-beam creep/fatigue testing apparatus at 1×10^{-7} dpa/s. Very significant creep strain, much larger than that at 300°C, and continuously decreasing creep rate were observed at 60°C in 20% cold-worked SUS 316 stainless steel just as the calculation predicted.

References

[1] J. Nagakawa, V. K. Sethi and A. P. L. Turner, in: Proc. Symp. on Phase Stability during Irradiation, Pittsburgh, 1980, eds. J. R. Holland, L. K. Mansur and D. I. Potter (TMS-AIME, New York, 1981), p. 445.
[2] M. L. Grossbeck and L. K. Mansur, J. Nucl. Mater. 179-181 (1991), p. 130.
[3] C. Dimitrov and O. Dimitrov, J. Phys. F 14 (1984), p. 793.
[4] N. Yoshida, J. Nucl. Mater. 205 (1993), p. 344.
[5] W. G. Wolfer and M. Ashkin, J. Appl. Phys. 46 (1975), p. 547; 46 (1975), p. 4108.
[6] P. T. Heald and M. V. Speight, Philos. Mag. 29 (1974), p. 1075.
[7] A. D. Brailsford and R. Bullough, Philos. Mag. 27 (1973), p. 49.
[8] R. V. Hesketh, Philos. Mag. 7 (1962), p. 1417.
[9] R. Bullough and J. R. Willis, Philos. Mag. 31 (1975), p. 855.
[10] L. K. Mansur, Philos. Mag. A 39 (1079), p. 497.
[11] J. H. Gittus, Phil. Mag. 25 (1972), p. 345.
[12] R. E. Stoller, M. L. Grossbeck and L. K. Mansur, in: ASTM STP 1125, eds. R. E. Stoller, A. S. Kumar and D. S. Gelles (ASTM, Philadelphia, 1992), p. 517.
[13] J. Nagakawa, J. Nucl. Mater. 225 (1995), p. 1.
[14] P. Jung, J. Nucl. Mater., 113 (1983) 133.
[15] J. Nagakawa, N. Yamamoto and H. Shiraishi, J. Nucl. Mater. 179-181 (1991), p. 986.
[16] J. Nagakawa, Y. Murase and N. Yamamoto, to be published in: Proc. IEA/JUPITER Joint Symp. On Small Specimen Technol. For Fusion Research (1999).
[17] Y. Murase, J. Nagakawa, N. Yamamoto and Y. Fukuzawa, to be published in: ASTM STP 1366, (ASTM, Philadelphia, 1999).

Corresponding author: Johsei Nagakawa, e-mail; johsei@nrim.go.jp, Fax; +81-298-59-2014

Key Engineering Materials Vols. 171-174 (2000) pp. 321-328
© 2000 Trans Tech Publications, Switzerland

High Temperature Deformation with Interfacial and Plastic Accommodation in Spherical-Al_2O_3-Particle-Dispersed Al-Matrix-Composite

K. Kawabata, E. Sato and K. Kuribayashi

The Institute of Space and Astronautical Science,
3-1-1 Yoshinodai, Sagamihara, Kanagawa 229-8510, Japan

Keywords: Metal Matrix Composites, Dispersion Strengthening Alloy, Strain Mismatch, Plastic Accommodation, Interfacial Accommodation

Abstract

Although high temperature deformations of dispersion strengthening alloys and short fiber reinforced metal matrix composites have been studied independently, we should understand them as an unified form of that of inclusion bearing materials, noticing accommodation of misfit strains between matrix and inclusions. The present study reports the experimental examination that spherical-Al_2O_3-particle-dispersed Al-matrix-composite fabricated through pressurized casting shows different deformation modes depending on the strain rate with the respective accommodation processes.

1. Introduction

Dispersing reinforcements into a matrix is one of the methods of strengthening metallic materials at high temperatures. The resultant reinforced materials have been classified into dispersion strengthening alloys (DSAs) [1] and metal matrix composites (MMCs) [2] depending on the size of the reinforcements and on the deformation behaviors at high temperatures. The difference in the deformation behavior arises due to the accommodation processes of strain mismatch between the matrix and the reinforcements, i.e., interfacial accommodation by interfacial sliding and diffusion [3,4] for the former, and plastic accommodation by the heterogeneous flow of the matrix [5-7] for the latter. The deformation processes can be classified into three modes according to the rate of interfacial accommodation by interfacial sliding and diffusion, they are (I) deformation under complete interfacial accommodation, (II) deformation controlled by interfacial accommodation, and (III) deformation controlled by plastic accommodation. In addition, a threshold stress exists through Orowan or void strengthening mechanisms [1]. There has been, however, no report of one material showing deformation behavior with the two accommodation processes.

The conventional materials has not been analyzed from the viewpoint of the accommodation of the strain mismatch because of, for DSAs, fine oxides from the powder metallurgy processes and low volume fraction of the inclusions or, for MMCs, a degradation which is debonding between the matrix and the inclusion of the composites. Both the fine oxides and the degradation results in high value of apparent stress exponents [1, 2].

The present authors reported a quantitative analysis on the three modes of accommodation with an experimental verification using spherical-Al_2O_3-particle-dispersed Al-matrix-composite [8]. In the present study, we propose the entire stress-strain rate relation, whose lower strain rate region corresponds to the deformation behavior of DSAs and higher strain rate region corresponds to that of MMCs.

2. Experimental Procedure

Specimens consisting of a pure Al matrix and spherical Al_2O_3 particles of 10 μm diameter were fabricated by pressurized casting, without the extrusion process which causes a fracture of the reinforcements or the powder metallurgy processes which introduce fined oxides into the material. The stress through the pressurized casting was 150 MPa. Figure 1 is a scanning electron micrograph, which shows the spherical Al_2O_3 particles are not fractured and well dispersed through the pressurized casting. The Specimens of monolithic pure Al were also fabricated by the same processes.

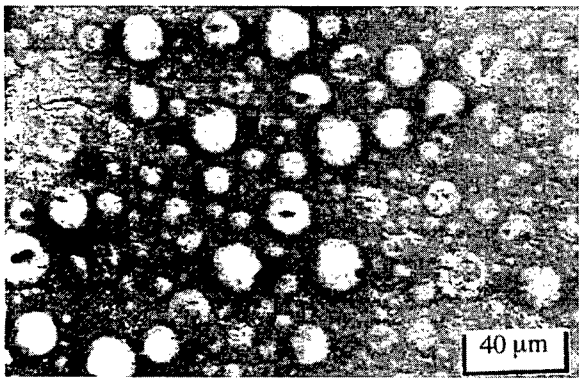

Fig. 1: SEM micrograph of the composite containing spherical Al_2O_3 perticles

The strain rates were measured by compression tests under constant stresses at temperatures more than two-thirds the melting temperature of the matrix. The uniaxial load was applied to the cylinder specimen of 10 mm in length and 6 mm in diameter.

3. Constitutive equations of three modes of deformation

The following is constitutive equations of the deformation behavior of the composites. First, the deformation behavior of the matrix—pure Al—has already been given experimentally

as [9]

$$\dot{\varepsilon}_{Al} = A\frac{D_v}{E^5}\sigma^5 , \qquad \text{Eq. 1}$$

where A, D_v and E are a temperature-independent constant, the volume diffusion coefficient and

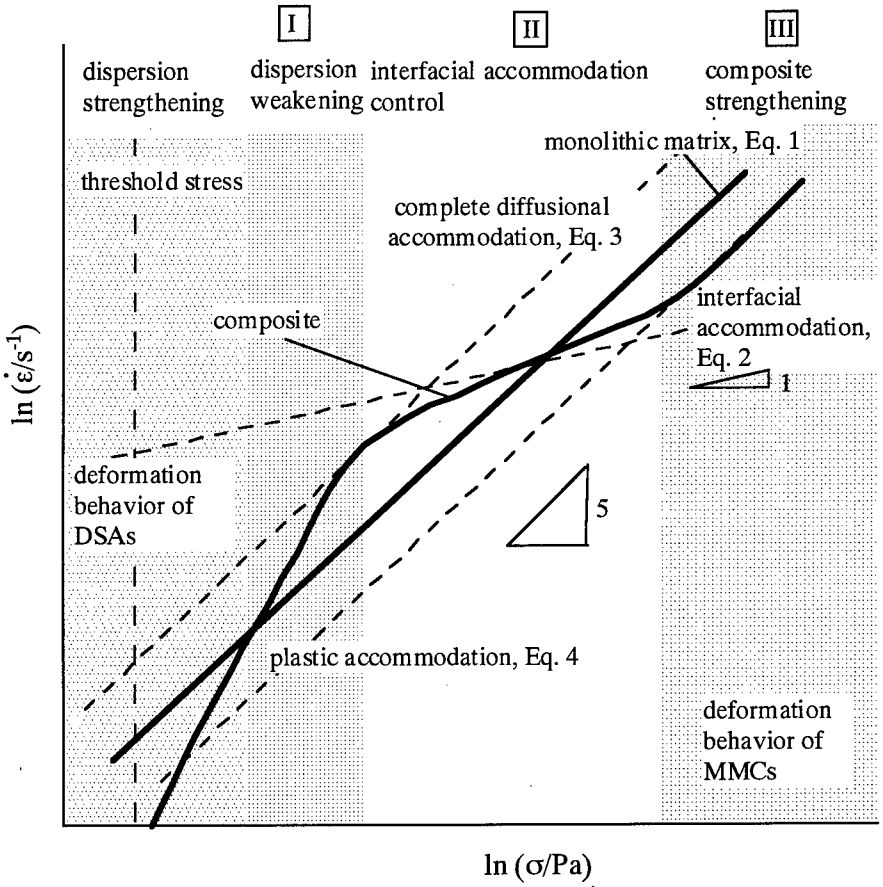

Fig. 2: Schematic drawing of the deformation behavior of the composite in mode I, II, and III, and the threshold stress.

Young's modulus of pure Al, respectively, which are given in appendix. Figure 2 shows a schematic drawing of the deformation behavior of the composite.

The relation between stress and strain rate for interfacial accommodation around a spherical inclusion is given by [10]

$$\dot{\varepsilon}_{dif} = B\frac{D_i}{a^3 T}\sigma , \qquad \text{Eq. 2}$$

where a and T are the radius of the inclusion and the absolute temperature, respectively, and B and D_i are a theoretical constant and the interfacial diffusion coefficient, respectively, which are given in appendix.

When the strain rate of the composite is lower than that for interfacial accommodation (mode I), the strain mismatch is accommodated completely by diffusion, and the inclusions support no external load. It results in a paradoxical phenomenon—dispersion weakening—even in an ideal composite free of material degradation such as interface debonding. The strain rate in this mode is given by [3,4]

$$\dot{\varepsilon}_I = (1- f)^{-5} \dot{\varepsilon}_{Al}, \qquad \text{Eq. 3}$$

where f is the volume fraction of the inclusions.

In the mode where the strain rate is higher than that for interfacial accommodation (mode III), the interfacial accommodation becomes less effective than the plastic accommodation which achieved via a heterogeneous plastic flow of the matrix. In this mode, the inclusions can contribute to strengthening. This deformation behavior was previously roughly analyzed by the shear-lag model [5] and the constitutive potential method [6], and recently analyzed rigorously using micromechanics [7]. The strain rate in mode III is given by [6]

$$\dot{\varepsilon}_{III} = (1- f)^{g} \dot{\varepsilon}_{Al}, \qquad \text{Eq. 4}$$

where g is about 4 for the case of spherical inclusions with the matrix stress exponent of 5.

In the transition between modes I and III (mode II), only a certain portion of the strain mismatch around the inclusions is accommodated completely by the diffusion and the sliding. Defining the portion of complete accommodation as $(1–p)$, we obtain the following simultaneous equations for the strain rate in this mode,

$$\dot{\varepsilon}_p = p\, \dot{\varepsilon}_{dif} = (1- fp)^{-5} \dot{\varepsilon}_{Al}. \qquad \text{Eq. 5}$$

For a given stress, p and $\dot{\varepsilon}_p$ are given by Eq. 5. Since the mechanisms of interfacial and plastic accommodations are independent of each other, the strain rate in mode II is given by

$$\dot{\varepsilon}_{II} = \dot{\varepsilon}_p + \dot{\varepsilon}_{III}, \qquad \text{Eq. 6}$$

and is schematically drawn in Fig. 1 by a bold line. This mode is called that of interfacial accommodation control, since the position of the region is determined by the strain rate for diffusional accommodation.

The threshold stress, σ_{th}, is independent of the above modes, and calculated by the average distance between the inclusions. Though the usual DSAs have the high threshold stress because of the fine oxides produced by the powder metallurgy processes, the present specimens

fabricated by the ingot metallurgy processes is expected to have low threshold stress. Replacing σ by the effective stress, $\sigma_{eff} \equiv .\sigma - \sigma_{th}$, in the above equations, we obtain the stress-strain rate relation of the composite for the entire strain rate region.

4. Result and Discussion

The results obtained at 723 K are shown in Fig. 3 on a double-logarithmic scale of stress σ and strain rate $\dot{\varepsilon}$. Figure 3 shows that under low stresses, the composite is weaker—shows a higher strain rate—than monolithic pure Al even though the reinforcements—Al_2O_3 particles—are dispersed, while under high stresses, the composite is a stronger—shows a lower strain rate—than Al. Equation 1 agrees well with the experimental data in Fig. 3.

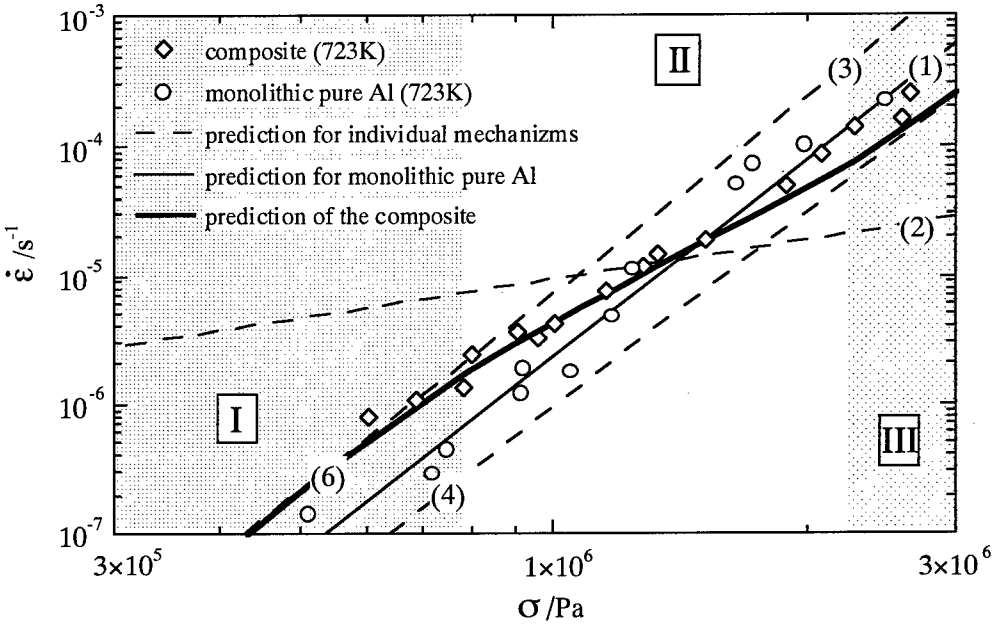

Fig. 3: Deformation behavior of the composite (◊) and the monolithic pure Al (o) at 723 K and theoretical predictions for the individual mechanizms (- -), for monolithic pure Al (—), for the prediction of the composite (—).

Theoretical predictions in § 3 are plotted together with the experimental data at 723 K in Fig. 3. The volume fraction and diameter of the reinforcements are assumed to be 0.2 and 6 μm, respectively, and the other constants are material constants listed in appendix. Figure 3 shows that the composite is weaker than monolithic pure Al in mode I while it is stronger in mode III. The position of the transition—mode II—is determined by the strain rate for interfacial accommodation. In mode II, the data at 723 K agree well with Eq. 6.

The threshold stress observed in dispersion strengthened alloys [1] is not observed in the

present experiment. It would be observed if we were to measure the deformation behavior under significantly lower strain rates. On the other hand, MMCs show high stress exponents during deformation because of the progress of interfacial debonding under applied tensile stresses [2]. In this experiment, we avoid the debonding by using spherical reinforcements and applying a compression load. A similar behavior of plastic accommodation was observed only in a compression test of W-fiber-reinforced Ag-matrix composite [11]. If we can observe the threshold stress expected in lower stress, one composite shows the deformation behavior of both materials in the present study.

5. Conclusion

In this study, we established the experimental condition under which we must consider only the accommodation between the matrix and the reinforcements in an ideal composite free of debonding, and the deformation processes can be classified into three modes according to the rate of interfacial accommodation by interfacial sliding and diffusion.

(I) When the strain rate of the composite is lower than that for interfacial accommodation, the strain mismatch is accommodated completely by diffusion and sliding, and the composite is weaker than monolithic pure Al.

(II) When both interfacial and plastic accommodations work around the inclusions, we showed experimentally that under low stresses, the deformation behavior follows Eq. 6.

(III) When the strain rate of the composite is higher than that for interfacial accommodation, the strain mismatch is accommodated by plastic flow of the matrix, and the composite is stronger than monolithic pure Al.

Appendix

Material constants describing the deformation behavior of monolithic pure Al (Eq. 1) are $A=1.25\times10^{32}$ m^{-2}, $D_v=1.7\times10^{-4}\exp(-Q_v/RT)$ m^{2}s^{-1}, and $E=5.5\times10^{10}$ Pa at 723 K, where Q_v=142 kJmol^{-1} is the activation energy of volume diffusion and R = 8.32 J mol^{-1}K^{-1} is the gas constant.

In the equation of the interfacial accommodation rate around a spherical inclusion (Eq. 2), D_i is given by $1.8\times10^{-4}\exp(-Q_i/RT)$ m^{2}s^{-1}, where Q_i=86 kJmol^{-1} is the activation energy of interfacial diffusion, and B is given by [12]

$$B=\frac{5(1-\nu)}{2G(7-5\nu)}\frac{3\pi^2\delta\Omega}{4k}\left(\frac{G^*G(7-5\nu)}{G(7-5\nu)+G^*(8-10\nu)}\right) \quad \text{K m Pa}^{-1},$$

where G^*, G, ν, δ, Ω, and k are the shear modulus of the inclusions, the shear modulus of the matrix, the poisson ratio of the matrix, the thickness of the interface, the atomic volume, and Boltzmann's constant, respectively, and the following values are adopted: $G^*=163\times10^9$ Pa, $G=22\times10^9$ Pa at 723 K, ν=0.33, $\delta=5.72\times10^{-10}$ m, $\Omega=1.66\times10^{-29}$ m^3 and $k=1.38\times10^{-23}$ JK^{-1}.

Reference

[1] H. Nakashima, F. Yoshida and H. Yoshinaga, Aspects of high temperature deformation and fracture in crystalline materials (eds. Hosoi, Y., Yoshinaga, H., Oikawa, H., & Maruyama, K.) (The Japan Inst. Metals, Sendai, 1993), p. 167.

[2] Y. Li and T. G. Langdon, Metall. Mater. Trans. 30A (1999), p. 315.

[3] R. C. Koeller and R. Raj, Acta Metall. 26 (1978), p. 1551.

[4] T. Mori, Y. Nakashima, M. Taya and K. Wakashima, Phil. Mag. Lett. 75 (1997) p. 359.

[5] A. Kelly and K. N. Street, Proc. Roy. Soc. Lond. A328 (1972) p. 283.

[6] B. J. Lee and M. E. Mear, J. Mech. Phys. Solids. 39 (1991) p. 627.

[7] E. Sato, T. Ookawara, T. Kuribayashi, and S. Kodama, Acta Mater. 46 (1998) p. 4153.

[8] K. Kawabata, E. Sato and K. Kuribayashi, Submitted to Nature.

[9] H. Luthy, A. K. Miller, and O. D. Sherby, Acta Metall. 28 (1980) p. 169.

[10] S. Onaka, T. Okada, and M. Kato, Acta Metall. Mater. 39 (1991) p. 971.

[11] A. Kelly and W. R. Tyson, J. Mech. Solids 14, (1966) p. 177.

[12] T. Mori, M. Okabe, and T. Mura, Acta Metall. 28 (1980) p. 319.

E-mail: kawabata@materials.isas.ac.jp

Fax: (81)42-759-8461

Key Engineering Materials Vols. 171-174 (2000) pp. 329-336
© 2000 Trans Tech Publications, Switzerland

The Size Effect of Particulate SiC on Activation Energy for High-Strain-Rate Superplastic Flow in Powder-Metallurgy Processed 2124 Al Composites

W.J. Kim and J.H. Yeon

Dept. of Metallurgy and Materials Science, Hong-Ik University,
72-1, Sangsung-dong, Mapo-ku, Seoul 121-791, Korea

Keywords: Superplastic, 2124 Al Composite, Activation Energy

Abstract

The true activation energies revealed after the incorporation of threshold stress for plastic flow were compared between the two PM superplastic 20%SiC_p/2124 Al composites with different reinforcement sizes. There was large discrepancy between the activation energy values, though the volume fraction of SiC was same for the two composites. The composite with the finer reinforcement size (3μm) exhibited much larger activation energy value than the other with the relatively coarse SiC particulates (8μm). This difference in the true activation energy was attributed to the difference in the SiC/Al interface area per unit volume of composite.

1. Introduction

High-Strain-Rate Superplasticity (HSRS) in several classes of materials including alloys, metal matrix composites (MMCs) and mechanically-alloyed materials has been realized through recent advance in power-metallurgy technology[1-12]. Among the many HSR superplastic MMCs, 2124 Al composites reinforced by either $SiC_{p\ or\ w}$ or $Si_3N_{4p\ or\ w}$ (p and w denote particulates and whisker respectively) have been most thoroughly studied[1, 3, 4, 11, 12]. As to superplastic deformation mechanism for MMCs, it is well established that grain boundary sliding (GBS) is the rate-controlling process. A consistent problem, however, arises in the analysis of true activation energies for superplastic flow, Q_t, for the 2124 Al composites. That is, the activation energy value is significantly higher than that for grain boundary diffusion or lattice diffusion in pure aluminum even after the incorporation of threshold stress into the analyses of superplastic flow. High Q_t values ranging from 300kJ/mole to as much as ~640kJ/mole have been reported in the HSR superplastic 2124Al composites reinforced by either particulate or whisker form of reinforcement whose sizes are in a range between 0.2 and 3μm[1, 11-13].

The main objective of this study is to investigate the size effect of SiC particulates on the true activation energy for superplastic flow of the PM 20%SiC_p/2124 Al composites. For this purpose, the plastic-flow characteristics of the two 20%SiC_p/composites with different reinforcement sizes (3μm and 8μm) were investigated and compared.

2. Experimental procedures

The chemical composition of the matrix of the composite is 3.5%Cu-1.24%Mg-0.53%Mn-0.14%Fe-0.01%Zn-bal Al by weigh percent. Atomized powders of Al particles have an average size of approximately 20μm. The sizes of SiC particulates are 3μm or 8μm. The Al and SiC powders were mechanically stirred, ultrasonically mixed in an alcoholic solvent and then dried in air. The mixed powders were first cold pressed in an aluminum can, degassed in vacuum and then hot-pressed at 843K with a pressure of 90MPa for 0.2 hour. The consolidated billet was finally extruded at a temperature of 723K with an extrusion ratio of 70:1. Tensile specimens were machined from the as-extruded bar to have a gauge length of 5mm and a gauge diameter of with the tensile axis in parallel to the extrusion direction. The strain-rate-change (SRC) tests were conducted on a screw-driving testing machine controlled by a computer at temperatures between 723-823K and at a nominal strain rates between ~$10^{-4}s^{-1}$ and ~$10^{-1}s^{-1}$. Elongation-to-failure tests were carried out at

808K as a function of strain rate. Microstructures of the material were examined using optical microscopy. DSC tests were conducted on the as-extruded 20%SiC_p(p=3μm)2124 Al composite in a ~50mg specimen during heating at a rate of 10K/min.

3. Results and discussion

Figure 1 shows the optical photographs for the 20%SiC_p(p=3μm)/2124 Al and 20%SiC_p(p=8μm)/2124 Al composites. Examination of each microstructure reveals an uniform distribution of particulate SiC on the equiaxed grains of Al matrix. The linear intercept grain sizes were estimated to be 2.4μm and 4.8 μm for the 20%SiC_p(p=3μm)/2124 Al and 20%SiC_p(p=8μm)/2124 Al composites, respectively. The DSC result for the 20%SiC_p(p=3μm)/2124 Al composite is shown in figure 2. Only a continuous endothermic peak appeared during the heating step. No sign of partial melting exists before the matrix melting. The incipient melting temperature determined from an intercept of two lines indicated on the peak is 877K. The absence of partial melting noted in the present DSC result is in agreement with the DSC study on the 18%SiC_p(p=3μm)/2124 Al [12] but inconsistent with the reports by Mabuchi and Higashi[13, 14] on the 20%Si_3N_4/2124 Al composites reinforced by particulates or whiskers where small and sharp peaks representing partial melting showed up in the temperature range between 784K and 849K before the Al matrix starts to melt. The result of elongation-to-failure tests at 808K is given in figure 3. The optimum superplastic strain rates for the 20%SiC_p(p=3μm)/2124 Al and 20%SiC_p(p=8μm)/2124 Al composites are 10^{-1} and $5x10^{-3}s^{-1}$, respectively, and the maximum tensile elongations associated at these strain rates are 400% and 220%, respectively.

The relationship between flow stress and strain rate is given in figure 4 in double logarithmic coordinates at different temperatures. As can be seen, the apparent stress exponent is not constant but increases with a decrease in strain rate or with a decrease in temperature. The temperature dependence of flow stress investigated at a fixed strain rate are well above the activation energies for grain boundary or lattice diffusion in aluminum, such that existing theories for high-temperature deformation for metallic alloys cannot explain these high activation energies as they stand. When the presence of threshold stress is assumed, the plastic flow occurs under an effective stress, σ-σ_o, where σ_o is threshold stress for plastic flow. In this case, the deformation rate is expressed by a relationship of the form

$$\dot{\varepsilon} = BD\left(\frac{b}{d}\right)^p \left(\frac{\sigma - \sigma_o}{E}\right)^n \qquad (1)$$

where B is the material constant, n is the true stress exponent, E is the Young's modulus, D is the relevant diffusivity, p is the grain-size exponent and d is the grain size. The true n value for each temperature was determined by selecting the value of n giving the best linear fit to the datum points in the plot of $\dot{\varepsilon}^{1/n}$ vs. σ on the double linear axes.

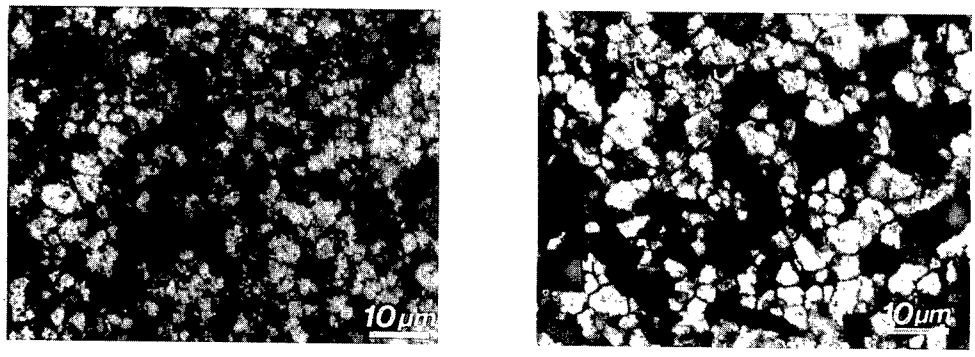

(a) (b)

Figure 1 Optical photographs for (a) 20%SiC_p(p=3μm)/2124 Al and (b) 20%SiC_p(p=8μm)/2124 Al composites.

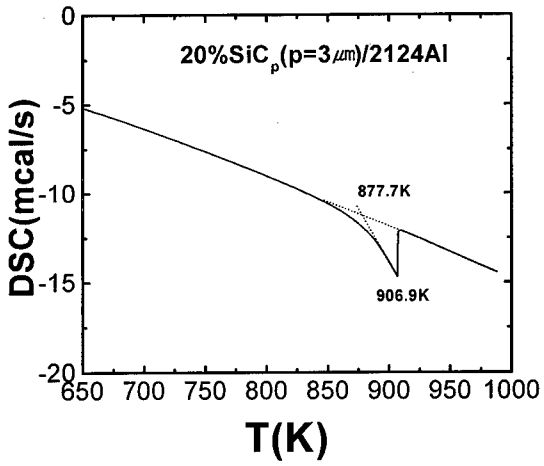

Figure 2. DSC test result for the 20%SiC_p(p=3μm)/2124 Al composite.

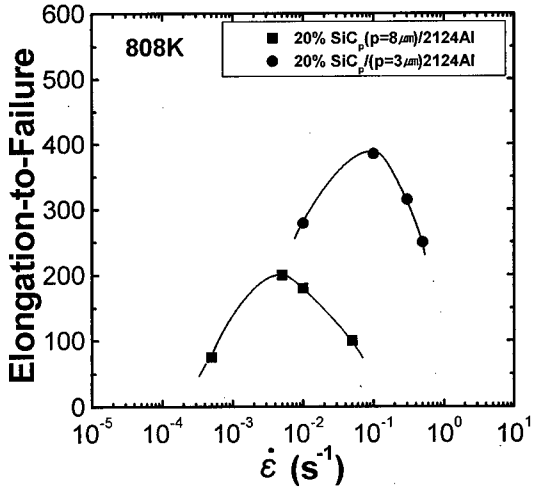

Figure 3. Elongation-to-failure test results given as a function of strain rate at 808K.

The data for both composites yield the best linearity for each temperature when n=2.5 is adopted

except the two highest strain-rate data at 723K for the 20%SiC_p(p=8μm)/2124 Al composite. This is shown in figure 5. The fact that the true exponent is close to 2 or 3 represents that either GBS or solute drag creep controls the plastic flow. One of simple methods to provide guiding information that helps to establish the value of true stress exponent (whether solute drag creep or GBS) is to investigate the dependence of grain size on plastic flow. This is using a well known fact that solute drag creep is independent of grain size whereas GBS is dependent of grain size[15]. Comparison of the strain rate-stress relation [11] indicates that the composite with a larger grain size is stronger than that with a smaller grain size.

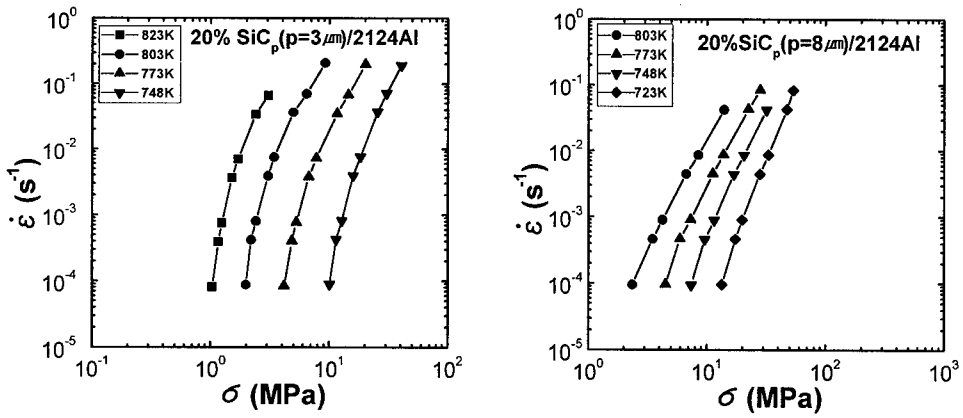

Figure 4. Strain rate-stress relationship at different temperatures (a) 20%SiC_p(p=3μm)/2124 Al composite (b) 20%SiC_p(p=8μm)/2124 Al composite.

This nature of increasing flow stress with increase in grain size is often observed when the plastic flow is controlled by GBS. For this reason, it is believed that the rate-controlling process for the 2124 Al composites is GBS.

True activation energies were estimated by plotting logarithmic $\dot{\varepsilon}$ against the reciprocal of the absolute temperature at a constant value for the modulus-compensated effective stress. The plots given in figure 6. The data for the HSR superplastic 2124 Al alloy[16] are also plotted for comparison. As can be seen, the data for the 2124 Al alloy show $Q_t \approx Q_L$ while those for the composites show the activation energies higher than Q_L. It is interesting to note that the value of Q_t for the 20%SiC_p(p=3μm)/2124 Al composite is significantly higher than that for the 20%SiC_p(p=8μm)/2124 Al composite, even though the volume fraction of reinforcement is identical. This result indicates that the Q_t value for the 2124 Al composites depends on the reinforcement size.

There are several speculations in literatures on the high Q_t for the HSR superplastic composites: (1) load transfer coefficient depending on temperature[17] (2) the presence of liquid phase at the interfaces between SiC and Al phases[13] and (3) superplastic flow controlled by diffusion along the interfaces between SiC and Al phases[18]. For the difference in activation energy to be assessed in

terms of the load transfer effect proposed by Li and Langdon[17], the load transfer coefficient should depend on the size of reinforcement. Li and Langdon[17] explained the Q_t value for the HSR superplastic mechanically alloyed aluminum alloys that is significantly lower than those for the HSR superplastic MMCs, in terms of the load transfer effect becoming ineffective when the reinforcement size becomes extremely fine. This is not, however, for the present case of the 20%SiC_p(p=8μm)/2124 Al composite having the reinforcement size larger than that of the 20%SiC_p(p=3μm)/2124 Al composite. The second and third suggestions may be related to the area of SiC/Al interfaces in a given volume of composite. Consideration of a circumstance that one 8μm sized SiC particle (in a form of perfect sphere) within the matrix is divided into multiple 3μm-sized particles leads to admit that the area for the 20%SiC_p (p=8μm)/2124 Al composite corresponds to 0.37 of that for the 20%SiC_p(p=3μm)/2124 Al composite. This much of area is identical to that can be anticipated from a 7.4%SiC_p(p=3μm)/2124 Al composite. If the Al/SiC interfaces provide the site for partial melting due to the high concentration of solute atoms as argued elsewhere [13, 14], the volume of the liquid phase created upon partial melting would increase with the increase in the area of SiC/Al interfaces. Therefore, it is possible that the abnormally faster increase in strain rate with temperature observed in the 20%SiC_p(p=3μm)/2124 Al composite(see figure 6), when compared with the case for the 20%SiC_p(p=8μm)/2124 Al composite with the lower area of SiC/Al interfaces, is due to the larger increase in the liquid volume upon melting. It should be noted, however, that no sign of partial melting was detected in the DSC trace for the 20%SiC_p(p=3μm)/2124 Al composite(figure 2). Let us think of a final alternative.

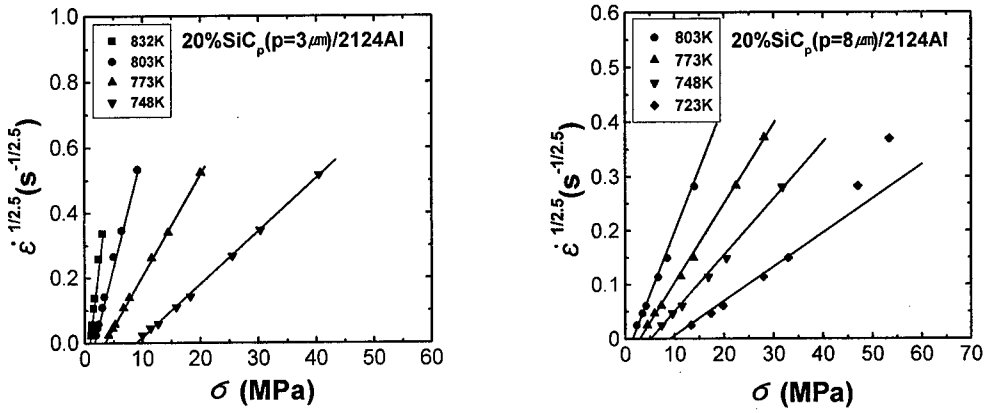

Figure 5. Threshold stress measurement for (a) 20%SiC_p(p=3μm)/2124 Al composite (b) 20%SiC_p(p=8μm)/2124 Al composite.

If the high Q_t is due to the high activation energy for diffusion along the SiC/Al interfaces as argued by Mishra et al.[18], the Q_t value may depend on the area of Al/SiC interfaces. For example, if the interface area is very small or absent, $Q_t \approx Q_L$ will be obtained. If it is sufficiently abundant, on the other hand, $Q_t \approx Q_i$ may be resulted, where Q_i is the activation energy for interface diffusion that is anticipated to be much higher than Q_L. This speculation allows to predict that the composite with the

interface area between these two extremes will have the Q_t value between Q_L and Q_i, which may be the case for the 20%SiC_p(p=8μm)/2124 Al composite.

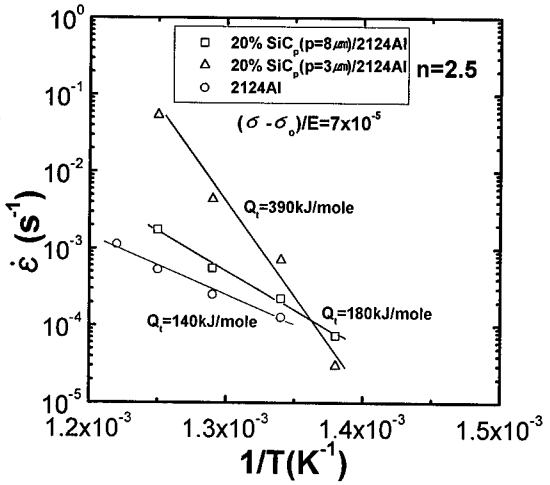

Figure 6. True activation energy measurement for the two 2124 Al composites and unreinforced 2124 alloy.

4. Summary

The superplastic deformation behaviors of the 20%SiC_p(p=3μm)/2124 Al composite 20%SiC_p(p=8μm)/2124 Al composite were investigated. It was found that the true activation energy value for the 20%SiC_p(p=3μm)/2124 Al composite is higher than Q_L (=180kJ/mol) but not so high as that for the 20%SiC_p(p=3μm)/2124 Al composite(=390kJ/mol), though the volume fraction of reinforcement is same. This difference was attributed to the difference in the SiC/Al interface area in a given volume of composite.

Acknowledgment

This work was supported by Korea Research Foundation Grant 98.

References

[1]T.G. Nieh and J. Wadsworth, Mater. Sci. engr., A147, 129 (1991).
[2]T.R. Bieler, T.G. Nieh, J. Wadsworth and A.K. Mukherjee, Scripta metall., 22, 81 (1988).
[3]M. Mabuchi, K. Higashi and T.G. Langdon, Acta metall. Mater., 42, 1793 (1994).
[4]T.R. Bieler and A.K. Mukherjee, Mater. Sci. engr., A128, 171 (1990).
[5]K. Higashi, T. Okada, T. Mukai and S. Tamura, Scripta metall. Mater., 25, 2053 (1991).
[6]M.C. Pandey, J. Wadsworth and A.K. Mukherjee, Mater sci. engr., 80, 169 (1986).
[7]G.S. Murty, M.J. Koczak, Mater. sci. engr., 100, 37 (1988).
[8] W. J. Kim, K. Higashi and J. K. Kim, Mater. Sci. Eng, A260, 170 (1999).
[9]D. W. Kum, W. J. Kim and G. Frommeyer, Scripta mater. 40[2], 223 (1999).
[10]T. Imai, M. Mabuchi, Y. Tozawa and M. Yamada, J. Mater. Sci. Lett., 9, 225

(1990).
[11]W. J. Kim, J. H. Yeon, D. H. Shin and S. H. Hong, Mater. Sci. Eng. in press.
[12]G. H. Zahid, R. I Todd and P. B. Prangnell, Material Science Forum Vol. 304-306, Trans Tech Publications, Switzerland, Editors: T. Sakuma, T. Aizawa and K. Higashi, p. 233 (1999).
[13] M. Mabuchi and K. Higashi, Scripta metall mater. 34[12], (1996) 1893.
[14] K. Higashi and M. Mabuchi, Material Science Forum Vol. 304-306, Trans Tech Publications, Switzerland, Editors: T. Sakuma, T. Aizawa and K. Higashi, p. 209 (1999).
[15] W. R. Cannon and O. D. Sherby, Metall. Trans. 1, (1970) 1030.
[16]W. J. Kim and S. H. Hong, submitted to J. of Mat. Sci. in 1999.
[17]Y. Li and T. G. Langdon, Acta metall. mater. 46[11], (1998) 3937.
[18]R. S. Mishra, T. R. Bieler and A. K. Mukherjee, Acta metall. mater. 45, (1997) 561.

Key Engineering Materials Vols. 171-174 (2000) pp. 337-342
© 2000 Trans Tech Publications, Switzerland

Experimental Study of the Mechanical Properties at Elevated Temperatures in Commercial Mg-Al-Zn Alloys for Superplastic Forming

T. Mukai[1], H. Tsutsui[2], H. Watanabe[1], K. Ishikawa[1], Y. Okanda[1], M. Kohzu[2], S. Tanabe[2] and K. Higashi[2]

[1] Osaka Municipal Technical Research Institute, Morinomiya Joto-ku, Osaka 536-8553, Japan

[2] Mechanical Systems Engineering, College of Engineering, Osaka Prefecture University, Sakai, Osaka 599-8531, Japan

Keywords: Commercial Magnesium Alloy, Grain Size, m-Value, Dislocation Creep, Grain Boundary Sliding, Gas Pressure Forming

Abstract

The mechanical properties in two commercial Mg-Al-Zn alloys were investigated at elevated temperatures. The alloys were examined for tensile tests and then characterized. The deformation mechanism in two alloys varied with their grain sizes. A coarse-grained(>100 μm) alloy exhibited a strain rate sensitivity of ~0.33, and fractured with significant development of necking. On the other hand, finer-grained alloys with grain sizes less than 20 μm exhibited a high strain rate sensitivity ~ 0.5, and failed with brittle fracture corresponding to the cavity growth. The grain size dependence on the tensile properties was discussed to apply these alloys for superplastic forming.

Introduction

A number of magnesium alloys exhibit excellent mechanical properties, such as high specific strength at room temperature and superplasticity at moderate temperatures [1,2]. In addition, there are many potential opportunities for the use of magnesium alloys in motor vehicle components []. This is a consequence not only of magnesium's relatively low density, which can directly and substantially reduce vehicle weight, but also is a result of its good damping characteristics, dimensional stability, machinability, and low casting costs. These desirable attributes enable magnesium to economically replace many zinc and aluminum die castings, as well as cast iron and steel components and assemblies in motor vehicles [3]. Despite of these advantages, however, magnesium alloys normally exhibit limited ductility (~ 7%). In order to exploit the benefits of magnesium alloy, it is important to develop secondary processing which can effectively produce complex engineering components directly from wrought products. Superplastic forming is a viable technique to fabricate a hard-to-form material into complex shapes. Superplasticity in magnesium have been experimentally investigated for extruded bars [1,2,4]. Very limited data are, however, currently available for the superplasticity in a commercial magnesium sheet.

High tensile ductilities associated with superplasticity occur when the grain size is small and typically less than ~10 μm [5]. These fine-grained materials deform principally by a grain boundary sliding mechanism. There is another observation of large tensile elongations in metals. Class I solid solutions are a group of dilute alloys in which the glide segment of the glide/climb dislocation process is rate controlling because solute atoms impede dislocation motion. This group of alloys is of interest in coarse-grained conditions at elevated temperatures because, as a result of the glide-controlled creep mechanism, which have an intrinsically high strain rate sensitivity of about m = 0.33 and therefore should exhibit high elongations of over about 200% [6]. The intrinsic nature of the high strain rate sensitivity is important because it suggests that complex thermomechanical processing, such as that needed

for fine-grained superplastic alloys, is unnecessary in Class I solid solutions. Recent investigations have shown that high ductility can be achieved in coarse-grained solid solution alloys [7-9]. In this study, mechanical properties at elevated temperatures have been investigated for commercial magnesium alloys with various grain sizes. From the experimental results, AZ61 sheet with a fine-grained (~20 μm) structure was experimentally fabricated by gas pressure forming.

Experimental Procedure

The materials used in the present study were commercial Mg-Al-Zn alloys (AZ31 and AZ61). AZ31 was received as-rolled sheet with a thickness of 1.5 mm. AZ61 was received as-extruded in the form of a sheet with a thickness of 2.5 mm. The average grain size, d (= $1.74L$; L is the linear intercept size), of the as-received AZ31 and AZ61 sheet were measured to 130 and 17 μm, respectively. In order to investigate the grain size effect, a finer-grained AZ31 was prepared by a hot extrusion. The grain size of the extruded AZ31 was measured to ~ 5 μm. Inspection of the microstructure by an optical microscope revealed that the grains of all alloys were almost equiaxed.

Tensile specimens, machined directly from the extruded or rolled sheets. To investigate the mechanical properties, tensile tests were carried out at temperatures ranging from 573 to 673 K and constant strain rates from $1\text{x}10^{-5}$ to $1\text{x}10^{-1}$ s^{-1} in air.

Mechanical Properties at Elevated Temperatures

Constitutive equation for describing deformation mechanism at elevated temperatures is generally expressed as [6],

$$\dot{\varepsilon} = A\left(\frac{b}{d}\right)^{p}\left(\frac{\sigma-\sigma_0}{G}\right)^{n} D_0 \exp\left(-\frac{Q}{RT}\right) \qquad (1)$$

where $\dot{\varepsilon}$ is the strain rate, A a constant, D_0 the pre-exponential factor for diffusion, σ the stress, σ_0 the threshold stress, G the shear modulus, n the stress exponent (=$1/m$), d the grain size, b the Burgers vector, p the grain size exponent, R the gas constant, T the absolute temperature and Q the activation energy which is dependent on the rate controlling process. In equation (1), three variables of n, p and Q are noted to be important in order to determine the deformation mechanism. For glide-controlled dislocation creep, $n = 3$, with $p = 0$ and Q is equal to the activation energy for solute diffusion [10]. For grain boundary sliding, $n = 2$, with $p = 2$ when Q is equal to the activation energy for lattice diffusion and with $p = 3$ when Q is equal to the activation energy for grain boundary diffusion [6].

To characterize the plastic flow behavior in AZ31, the true stress as a function of strain rate (at a fixed strain of 0.1) is plotted in Fig. 1 (upper). Data indicate that the flow stress decreases with increasing temperature. The flow stress of the coarse-grained alloy is essentially higher than that of the fine-grained alloy for the same temperature. It is noted that the strain rate sensitivity, m ($m = 1/n$), for the coarse-grained alloy is relatively lower (~0.33) than that for the fine-grained alloy (~0.5).

The elongation-to-failure, ε_f, as a function of strain rate for AZ31 is also shown in Fig. 1 (lower). The coarse-grained alloy exhibits lower values of ε_f with lower strain rate sensitivity corresponding to the dislocation creep. Inspection of the appearance of the fractured specimen revealed that the coarse-grained alloy failed by the development of macroscopic

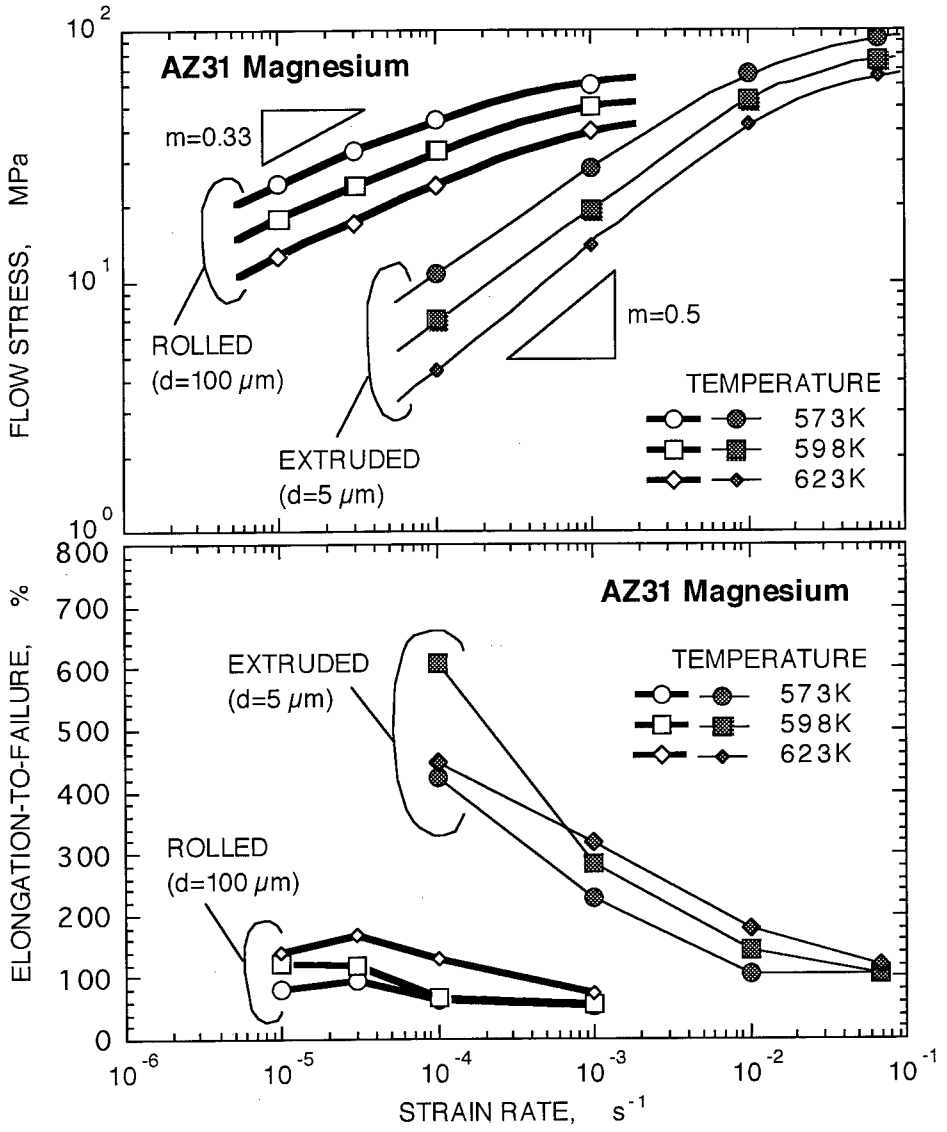

Fig. 1 Flow stress at a fixed strain of 0.1(upper) and elongation-to-failure(lower) as a function of strain rate in a coarse- and fine-grained AZ31 at elevated temperatures.

necking suggesting the transgranular fracture. On the other hand, the finer-grained alloy failed with brittle fracture corresponding to the intergranular fracture.

The flow stress and εf in AZ61 alloy as a function of strain rate is also shown in Fig. 2. The strain rate sensitivity exhibits a higher value of ~ 0.5 corresponding to grain boundary sliding as well as the fine-grained AZ31 shown in Fig. 1. The εf at a temperature of 673 K exhibits ~ 150% which is a possible ductility for superplastic forming at a strain rate of 10^{-3} s^{-1}.

The characteristics at elevated temperatures in the present AZ31 and AZ61 magnesium alloys are summarized in Table 1. The activation energy(Q) in the coarse-grained AZ31 is close to the activation energy of the lattice diffusion in magnesium (Q_L=135 kJ/mol [11]) or Al

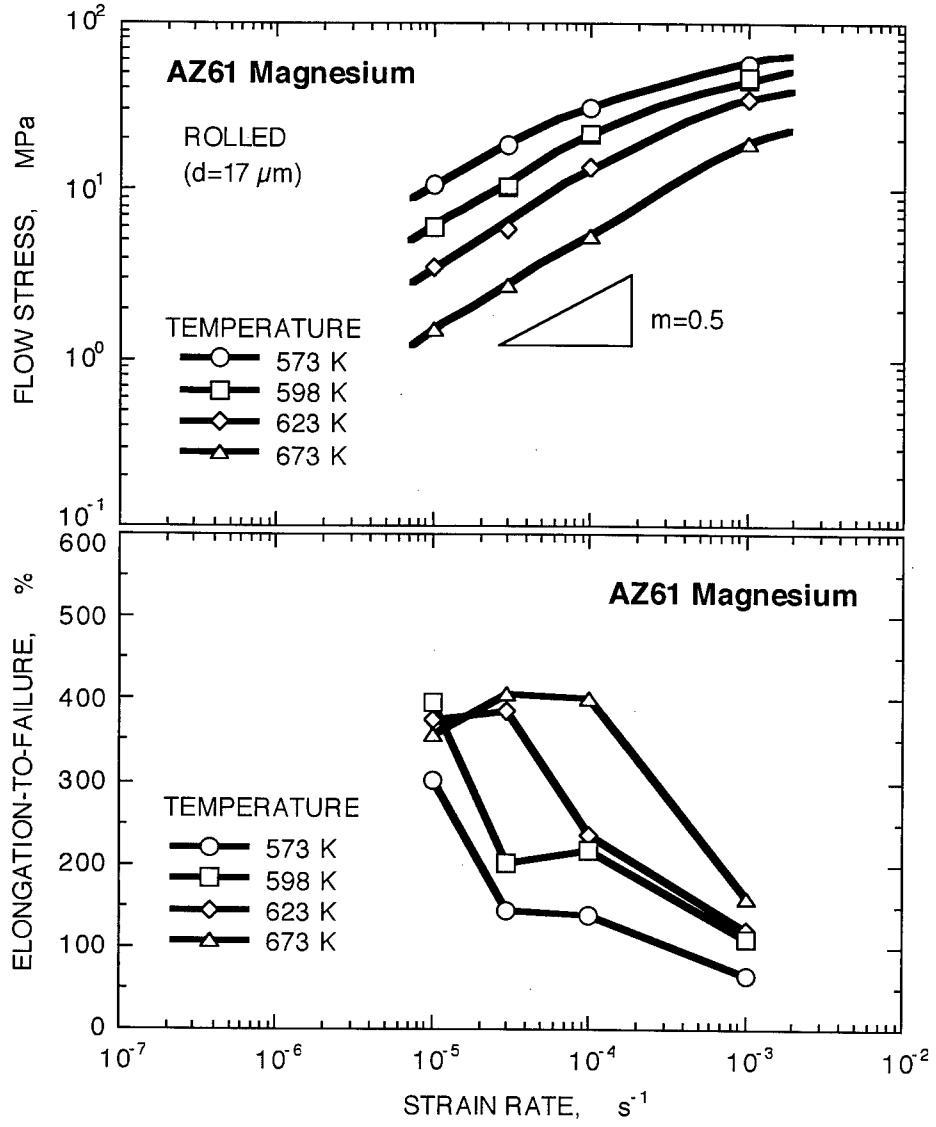

Fig. 2 Flow stress at a fixed strain of 0.1(upper) and elongation-to-failure(lower) as a function of strain rate in a AZ61 at elevated temperatures.

diffusion in Mg (Q_C=143 kJ/mol [12]). From the evidence in the stress exponent(n=3), the grain size exponent(p=0) and the activation energy, the dominant deformation mechanism in the coarse-grained alloy should be glide-controlled dislocation creep. The fine-grained AZ31 alloy exhibits n=2, p=3 and Q=~Q_{gb} (the activation energy of the grain boundary diffusion in magnesium; Q_{gb}=92 kJ/mol [11]), corresponding to the grain boundary sliding accommodated by grain boundary diffusion. The AZ61 alloy exhibits n=2, p=2 and Q=~Q_L corresponding to the grain boundary sliding accommodated by lattice diffusion. Experimental evidence indicates that grain boundary sliding occurs easily for the finer-grained material. It is, however, noted that large elomgation more than 100% can be obtained for the coarse-grained magnesium by dislocation creep mechanism.

Table 1 Characteristics at elevated temperatures in the present AZ31 and AZ61.

Alloys	Grain Size (μm)	Temperature (K)	Strain Rate (s^{-1})	Stress Exponent [n]	Grain Size Exponent [p]	Activation Energy [Q] (kJ/mol)
AZ31 (rolled-sheet)	130	598-673	$10^{-5} \sim 10^{-3}$	3	0	127
AZ61 (extruded-sheet)	17	573-673	$10^{-5} \sim 10^{-3}$	2	2	143
AZ31 (extruded-bar)	5	573-623	$10^{-4} \sim 10^{-1}$	2	3	96

Superplastic Forming

Superplastic forming was performed for a commercial AZ61 sheet. The sheet was formed with N_2 gas pressure of 4 atm at a temperature of 723 K. The sheet was formed in a shape of semi-spherical dome as well as the other conventional superplastic materials as shown in Fig. 3. It was taken about 6 minutes for the forming. The result indicates that the commercial magnesium sheet has a potential for superplastic forming.

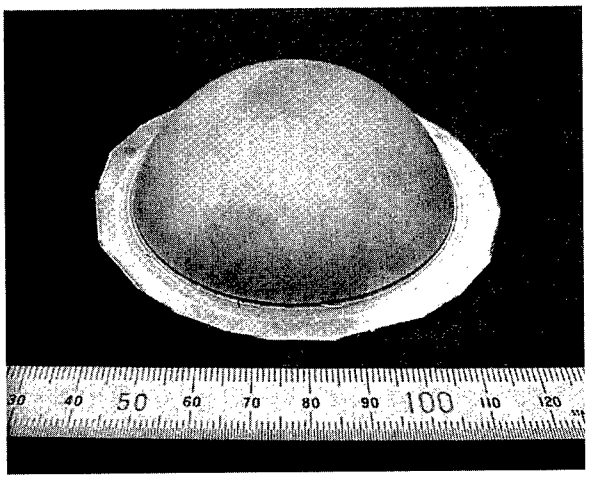

Fig. 3 An example of the semi-spherical dome of AZ61 fabricated with N_2 gas pressure.

Summary

Mechanical properties in commercial Mg-Al-Zn alloys were investigated at elevated temperatures for the secondary processing in a commercial forming. The deformation mechanism in two alloys varied with their grain sizes. A coarse-grained(>100 μm) alloy exhibited a strain rate sensitivity of ~0.33, and fractured with significant development of necking. On the other hand, finer-grained alloys with grain sizes less than 20 μm exhibited a high strain rate sensitivity ~ 0.5, and failed with brittle fracture corresponding to the intergranular fracture. Large elongatio-to-failure(>100%) was, however, obtained for both alloys suggesting the possibility of secondary processing.

References

[1] K. Higashi and J. Wolfenstine: Mater. Lett. 10 (1991), 329.

[2] M. Mabuchi, K. Kubota and K. Higashi: J. Mater. Sci. Lett. 12 (1993), 1831.
[3] J. Davis: 'International Congress and Exposition', SAE Technical Paper #910551, ed. by SAE International (1991).
[4] T.G. Nieh, A.J. Schwartz, and J. Wadsworth: Mater. Sci. Eng. A 208 (1996), 30.
[5] T.G. Langdon, Metall. Trans., 13A (1982) 689.
[6] O.D. Sherby, J. Wadsworth, Prog. Mater. Sci., 33 (1989) 169.
[7] E.M. Taleff, G.A. Henshall, T.G. Nieh, D.R. Lesuer, J. Wadsworth, Metall. Trans., 29A (1998) 1084-1091.
[8] T.R. McNelley, D.J. Michel, A. Salama, in "Advances in Superplasticity and Superplastic Forming", eds., N.Chandra, H. Garmestani, R.E. Goforth, The Minerals, Metals & Materials Society, Warrendale, p. 45 (1993).
[9] J. Saeki, M. Otsuka, in Proceedings of IMSP '97, ed. by T. Aizawa, K. Higashi, M. Tokuda, Mie university press, Tsu, p. 69 (1997).
[10] O.D. Sherbyand M. Burke, Prog. Mater. Sci., 13 (1966) 323.
[11] H.J. Frost and M.F. Ashby, "Deformation Mechanism Maps", Pergamon Press (1982), 44.
[12] S.S. Vagarali, T.G. Langdon, Acta Metall., 30 (1982) 1157.

Corresponding Author: Toshiji Mukai
E-mail: mukai@inet-osaka.or.jp
FAX: +81-6-6963-8145

Key Engineering Materials Vols. 171-174 (2000) pp. 343-348
© 2000 Trans Tech Publications, Switzerland

Superplasticity in GeO_2-Nd_2O_3 Doped Y-TZP

M. Nakano, K. Shimura, J. Mimurada, K. Sasaki, Y. Ikuhara and T. Sakuma

Department of Materials Science, Faculty of Engineering, University of Tokyo,
7-3-1 Hongo Bunkyo-ku, Tokyo 113-8656, Japan
E-Mail: nakano@ceramic.mm.t.u-tokyo.ac.jp

Keywords: Superplasticity, Ductility, TZP, Dopant

Abstract

The effect of dopant addition on the superplastic flow and tensile elongation in TZP was examined. ZrO_2-3mol%Y_2O_3-1.0mol%GeO_2-0.5mol%Nd_2O_3(TZP-1Ge-1Nd) exhibits higher tensile elongations of more than 600% at 1400℃ and lower flow stresses than TZP(ZrO_2-3mol%Y_2O_3). This reduction in flow stress is mainly caused by the codoping of GeO_2 with other elements. The peak temperature for the nominal elongation decrease is shown by TZP-1Ge-1Nd, it is suggested that the reason for the maximum elongation with respect to temperature is caused by the reduction in flow stress of GeO_2 and that of restricted ductility at high temperatures due to Nd_2O_3.

Introduction

Tetragonal zirconia polycrystals (TZP) are known to exhibit superplasticity at high-temperatures[1]. There have been numerous studies on superplastic behavior of TZP, especially yttria-stabilized TZP (Y-TZP). The high tensile ductility in TZP is explained by grain size stability during high temperature deformation [2]. Superplastic properties such as flow stress, strain rate and deformation temperature have been improved for future practical use in industry.

Tsurui et al. reported a unique kind of superplastic characteristics in TiO_2-doped Y-TZP. This material exhibits higher grain growth when compared with Y-TZP, and in spite of this disadvantage, TiO_2-doped Y-TZP shows improved ductility at lower temperatures, together with a stress reduction at all temperatures. Kondo *et al.* developed a new analysis to describe the superplastic behavior of TZP and TiO_2 doped TZP[3]. Their analysis revealed that the tensile ductility in TZP and TiO_2-doped TZP is maximized at an optimum temperature which is dependent on the diffusivity of the material. Recently, Mimurada et.al obtained further improved superplasticity in Ge doped TZP. Ge doped TZP exhibits longer elongation than 2.5Y-TZP throughout the temperature range. The addition of such dopants is thought to affect the diffusion characteristics which improve superplasticity.

In the present study, we studied codoped TZP to investigate the effect of codopants that

have different ionic radii and ionic charges on the superplastic flow of Y-TZP doped with Ge and Nd ions. A novel interpretation about the effect of dopants will be presented for the tensile ductilities in TZPs.

Experimental Procedures

The chemical compositions of the materials prepared in this study were ZrO_2-3mol%Y_2O_3 (3Y-TZP), ZrO_2-2.5mol%Y_2O_3-0.5mol%Nd_2O_3 (TZP-1Nd), and ZrO_2-3mol%Y_2O_3-1mol%GeO_2-0.5 mol%Nd_2O_3 (TZP-1Ge-1Nd). ZrO_2 powders (Tosoh.Inc,TZ-2.5Y and TZ-3Y) were mixed with the suitable amount of GeO_2 and Nd_2O_3 powders (Rare Metallic ,6N for GeO_2, 3N for Nd_2O_3) by a ball-milling method for 24h and dried in Ar atmosphere. Subsequently, the powders were uniaxially pressed under a pressure of 33MPa and then cold-isostatically pressed (CIP) at 100MPa. The green bodies were sintered for 2h in air at 1200℃ for TZP-1Ge, 1300℃ for TZP-1Ge-1Ndand , and 1400℃ for 3Y-TZP and TZP-1Nd. Some of the sintered bodies were further annealed at 1500℃ for a period from 2 to 4h.

Tensile test specimens with a gauge of 13mm and a cross sectional area of 2×2mm were cut and ground from the sintered or annealed bodies. High-temperature tensile tests were conducted for 3Y-TZP, TZP-1Nd, TZP-1Ge-1Nd in air for a temperature at 1300 to 1500℃ at an initial strain rate of $1.3\times10^{-4}s^{-1}$ with a tensile machine (Shimazu AG-5000C). Microstructure analysis was carried out with a scanning electron microscope (SEM, JEOL JSM-5200) for the as sintered and the annealed samples that were polished and thermally etched. The average grain size was measured directly from SEM micrographs by the linear intercept method. Phase identification was made for all the materials by XRD analysis.

Result

(1) High-temperature tensile test

Fig. 1 shows stress strain curves obtained for ZrO_2-2.5mol%Y_2O_3 (2.5Y-TZP) [4], 3Y-TZP, ZrO_2-2.5mol%Y_2O_3-1mol%GeO_2 (TZP-1Ge)[5], TZP-1Nd, TZP-1Ge-1Nd at 1300(a), 1400(b) and 1500℃(c).

In these high-temperature tensile tests, the strain rate decreases with increasing strain because these tests are conducted at constant cross head speed. The flow stress is influenced by the change in strain rate and grain growth during deformation. In Fig. 1(c), at 1500℃, the flow stress for 2.5Y-TZP and 3Y-TZP is almost flat or decreasing with increasing strain. On the other hand, the flow stress for TZP-1Ge and TZP-1Ge-1Nd are increasing with increasing strain. It implies that the grain growth of these materials is enhanced by GeO_2 addition. In Fig. 1 (a)-(c), the stress strain curves of 2.5Y-TZP and 3Y-TZP do not show significant difference in flow stress and elongation to failure showing similar superplastic characteristics.

The results of Fig.1 are rearranged in Fig.2 in terms of elongation to failure as a function of testing temperature. Fig. 2 also shows Ca and, or Ti doped TZP, we discuss about Ca and, or Ti doped TZP as follows. In Fig. 2, the elongation of TZP-1Nd is smaller than that of 2.5Y-TZP, on the contrary, the elongation of TZP-1Ge is higher than 2.5Y-TZP. Therefore GeO_2 addition is preferable and that the addition at Nd_2O_3 is not preferable for superplastic elongation under the tensile test

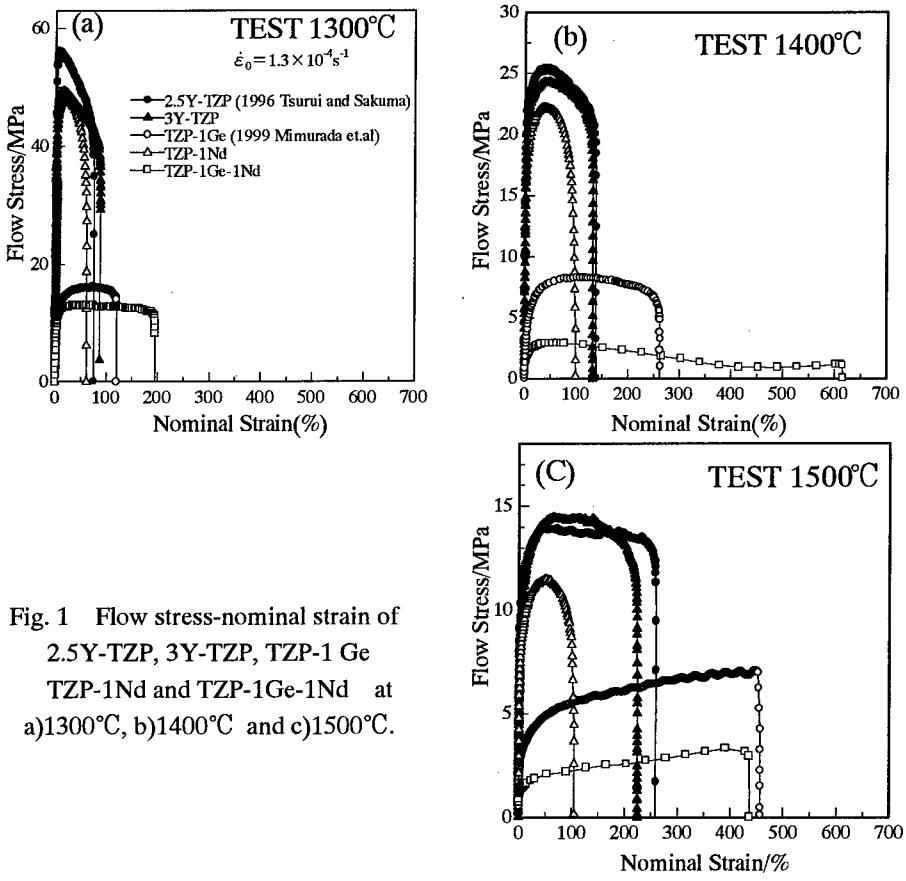

Fig. 1 Flow stress-nominal strain of 2.5Y-TZP, 3Y-TZP, TZP-1 Ge TZP-1Nd and TZP-1Ge-1Nd at a)1300°C, b)1400°C and c)1500°C.

conditions. We also investigated the superplastic behavior of co-doped TZP. The most remarkable characteristic in this material is the temperature dependence of the elongations.

An elongation greater than 600% was obtained at 1400°C, while smaller elongations were observed at 1300°C and 1500°C. We will discuss these points in the later part of this paper.

(2) Flow stress

As can be seen in Fig.3, the flow stress at 10% decreases with increasing temperature in all of the materials examined.

This tendency in flow stress is considered to reflect the fact that the superplastic deformation is controlled by diffusion. The flow stress of TZP-1Nd is not so different

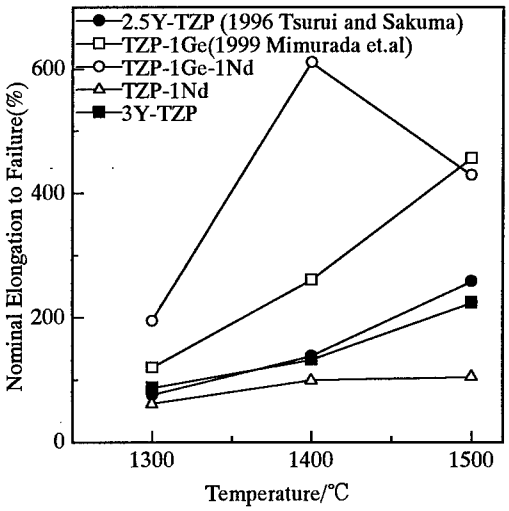

Fig. 2 Temperature dependence of nominal elongation to failure in 2.5Y-TZP, 3Y-TZP, TZP-1Ge, TZP-1Nd and TZP-1Ge-1Nd.

from 2.5Y-TZP and 3Y-TZP. Thus, Nd_2O_3 addition is not so effective in decreasing the flow stress in TZP. On the other hand, the flow stress of TZP-1Ge and TZP-1Ge-1Nd are considerably lower than that of 2.5Y-TZP, 3Y-TZP and TZP-1Nd. In these results, GeO_2 has the effect of decreasing flow stresses in TZP even if doped with Nd_2O_3. However, it is difficult to explain the different tendencies of the temperature dependent elongation characteristics between TZP-1Ge and TZP1Ge-1Nd in terms of flow stress only. There must be other causes that have to be taken into consideration.

(3) Microstructure analysis

XRD analysis was performed to identify the state of GeO_2 and Nd_2O_3 in 2.5Y-TZP. It is important to know this because the presence of secondary phases would influence superplastic behavior. Fig. 4 shows XRD profiles observed in 2.5Y-TZP, TZP-1Nd, TZP-1Ge, and TZP-1Ge-1Nd. The profile of each material suggests that the material consists of a single tetragonal phase. Thus the dopants are thought to be in solution within ZrO_2. This result is consistent with the reported solid solubility of GeO_2 and Nd_2O_3 in ZrO_2[5,6,7]. It is important to know the effect of dopant on grain growth behavior in TZP because the flow stress in TZP is very sensitive to the change in average grain size. Mimurada et al. reported that GeO_2 addition into Y-TZP enhances static grain growth as well as dynamic grain growth[5]. However, there are no reports available for the effect of Nd_2O_3 addition on grain growth in Y-TZP. Therefore, we examined the static grain growth behavior in TZP-1Nd by using SEM observation.

Fig. 5 shows the grain size of the as-sintered specimen and those annealed at 1500°C from 2 to 4 hours. In these results, Nd_2O_3 addition into TZP does not suppress grain growth.

Discussion

As can be seen in Fig. 3, Ge addition into TZP has a drastic effect, decreasing the flow stress[6], while the flow stress of TZP-1Nd is almost the same as that of 2.5Y-TZP and 3Y-TZP. TZP-1Ge

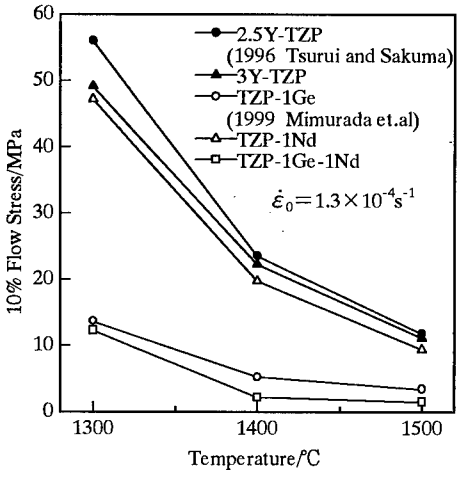

Fig. 3 Temperature dependence of 10% flow stress in 2.5Y-TZP, 3Y-TZP, TZP-1Ge, TZP-1Nd and TZP-1Ge-1Nd.

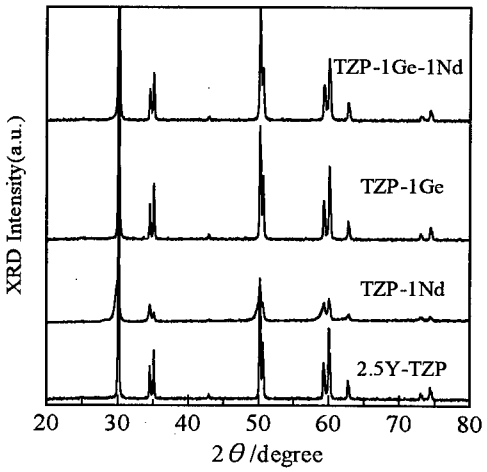

Fig. 4 Intensity profiles of XRD in 2.5Y-TZP, TZP-1Nd, TZP-1Ge and TZP-1Ge-1Nd.

sintered at 1200°C, it is lower than 3Y-TZP and TZP-1Nd. It is suggested that Ge may enhance diffusion, decreasing the flow stress and suppressing cavity creation. The temperature dependence of 10% flow stress of TZP-1Ge-1Nd indicates the fact that Ge has the effect of decreasing the flow stress in TZP even if it was doped with Nd_2O_3. Thus, we conclude that the dopant that makes flow stress lower would be effective when doped with other elements.

As shown in Fig.2, Ge has the effect of improving nominal strain, while Nd deteriorates nominal strain. We doped Ge and Nd to confirm the effect of each dopant on flow stress and elongation. However, TZP-1Ge-1Nd shows improved superplasticity that shows a maximum elongation with respect to temperature.

The characteristics of the temperature dependent elongation in TZP-1Ge-1Nd is that the maximum elongation is at 1400°C followed by a reduction in elongation at higher temperatures. Before arguing the origin of these characteristics, we are going to discuss on the effect of each dopant. The addition of tetravalent elements, Ge^{4+}, into Y-TZP results in improved iductility within the temperature range tested. This would be due to the reduction in flow stress. Nominal elongations in TZP-1Nd that contains Nd^{3+} cations become lower at all temperatures when compared to 2.5Y-TZP or 3Y-TZP. Flow stresses in 2.5Y-TZP and TZP-1Nd are not so different from each other when compared with the specimens of the same grain size in our observation. It indicates that the Nd^{3+} ion is not so effective in altering the diffusion related to deformation. Therefore, the deterioration in elongation would not be from the suppression in the accommodation process but from cavity nucleation and growth.

This may the case for TZP-1Nd, which exhibits lower ductility in spite of its refined grain structure. It is notable that the elongation of TZP-1Nd is more restricted at higher temperatures. It indicates the fact that the effect of Nd^{3+} becomes dominant at higher temperatures in these materials.

Furthermore, these results suggest a novel view for superplastic elongation. If there is only the effect of Nd^{3+} in TZP, the nominal elongation would decrease. If there are both effects of decreasing flow stress by Ge^{4+}, and Nd^{3+}, the elongation would increase further than the material doped with Ge^{4+} only as observed in TZP-1Ge-1Nd at 1400°C. In other words, the presence of

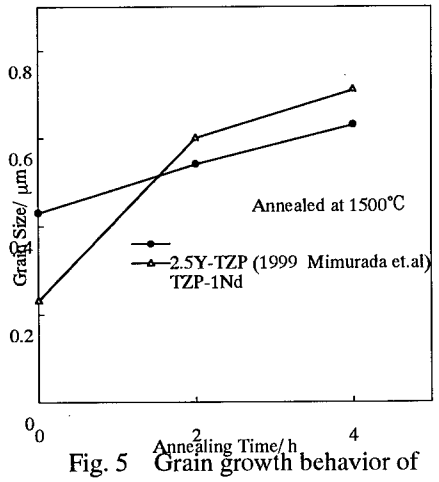

Fig. 5 Grain growth behavior of 2.5Y-TZP and TZP-1Nd.

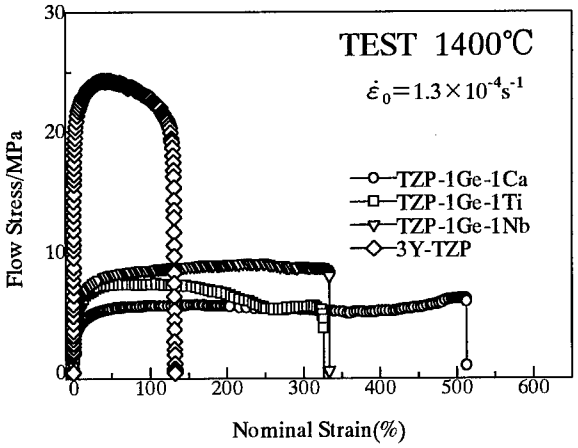

Fig. 6 Flow stress-nominal strain of 3Y-TZP TZP-1Ge-1Ca, TZP-1Ge-1Ti, and TZP-1Ge-1Nb.

Nd^{3+} is favorable for elongations in certain cases.

We discussed about improved superplastic flow caused by the reciplocal action of decreasing flow stress and increasing nominal strain. Fig.6 shows stress-strain curves of 3Y-TZP, ZrO_2-3mol% Y_2O_3-1mol% GeO_2 -1mol%CaO (TZP-1Ge-1Ca), ZrO_2-3mol%Y_2O_3-1mol% GeO_2-1mol%TiO (TZP-1Ge-1Ti), ZrO_2- 3mol%Y_2O_3-1mol% GeO_2-0.5mol%Nb_2O_5(TZP-1Ge-1Nb). Oka et.al also reported the effect of improved superplasticity by codoping for Ca and Ti in 3Y-TZP[8]. As shown in Fig. 6, all of the co-doped TZP show increasing strain and decreasing flow stress greater than 3Y-TZP. In the case of TZP-2Ca-2Ti, Ca and Ti are also known to segragate to the grain boundary[8]. It is suggested that co-doped elements change the grain boundary properties, which influence grain growth or cavity creation. It implies that co-doping itself has the effect of improving superplastic flow.

The mechanism of elongation and the effect of co-doping elements has not been elucidated yet, thus the analysis of cavity, grain boundary and grain growth behavior are necessary in order to understand the effect of codoping. Studying similar and different ionic charged elements in co-doped TZP and further investigation on the state of the grain boundary is required to understand the effect of these co-doping elements.

Conclusion

Superplastic behavior in 3Y-TZP, 2.5Y-TZP-1Nd, 3Y-TZP-1Ge-1Nd was studied by high-temperature tensile tests and X-ray diffraction. The following conclusion are obtained.

1) GeO_2 has the effect of decreasing flow stress for TZP even if it is doped with Nd_2O_3
2) Superplastic elongation of more than 600% was obtained in TZP-1Ge-1Nd at 1400°C.
3) The peak in elongation to failure in TZP-1Ge-1Nd at 1400°C is considered to be caused by Ge which has the effect of decreasing flow stress and Nd that has the effect of decreasing nominal elongation.

Acknowledgement

The authors would like to express their gratitude for the financial support for Scientific Research B 09555208 from the Ministry of Education, Science and Culture, Japan.

Reference

[1] F. Wakai, S. Sakuguchi and Y. Matsuno, Adv. Ceram. Mater., 259(1986).
[2] Y. Yoshizawa and T. Sakuma, Acta Metall. Materm.,**11**, 2943(1992).
[3] T. Kondo, Y. Takigawa and T. Sakuma, Mater. Sci. Eng.,**A231**,163(1997).
[4] K. Tsurui and T. Sakuma, Scripta. Mater.,**34**,443(1996).
[5] J. Mimurada, T. Kondo, Y. Takigawa, Y. Ikuhara and T. Sakuma, Mater. Sci. Forum Vols.304-306,543(1999).
[6] A. Rouanet, Rev. Int. Hautes Temp. Refract.8,161(1971).
[7]S-L Hwang and I-W Chen, J. Am. Ceram. Soc.,**73**[11],3269(1990).
[8] M. Oka, N. Tabuchi and T. Takashi, Mater. Sci. Forum Vols.304-306,451 (1999).

Key Engineering Materials Vols. 171-174 (2000) pp. 349-354
© 2000 Trans Tech Publications, Switzerland

Low Temperature Superplasticity in Fe_3Al Alloys

A. Shan and D. Lin

Department of Materials Science, Open Laboratory of National Education, Ministry of China for High Temperature Materials and Tests, Shanghai Jiao Tong University, Shanghai, 200030, R.P. China

Keywords: Fe_3Al, Low Temperature Superplasticity, Continuous Recrystallization

Abstract Superplasticity was demonstrated in Fe-28Al-2Ti and Fe-28Al-4Ti (in atomic percent) alloys at 600 to 750°C (0.48 to 0.56Tm where Tm is the absolute melting temperature of Fe_3Al). The starting microstructure of the materials contains 30-50 micron grains that are considered as large grains compared to conventional below 10 micron grain sizes for fine grain superplasticity. Optical microscope analysis shows that the grains were elongated after about 100% superplastic deformation. Larger deformation resulted in a DRX microstructure. New and finer grains appeared after large superplastic deformation. Maximum strain rate sensitivity index (m value) was found to be around 0.3, nevertheless large elongation was also observed when m value is lower than 0.2. The superplastic deformation mechanism is suggested to be related with DRX and DRV in such ordered intermetallics.

INTRODUCTION

Superplasticity has been extensively studied in metals and alloys [1]. However, few studies have been carried out in ordered intermetallics [2-5]. It is well known that superplasticity appears in fine-grained metals and alloys. In fine-grained materials grainboundary sliding (GBS) will readily occur at high temperature and low strain rate. This is considered as the main reason for superplasticity in fine-grained materials. Fine grain superplasticity has also been demonstrated in Ni-based[2,3] and Ti-based intermetallics[4,5]. It was found that GBS is the main factor which contribute to the superplasticity, nevertheless intragrain dislocation activity was also observed in Ni_3Al based intermetallics[3]. Superplasticity in a Fe-28Al-2Ti alloy was reported to occur in a temperature range of 800 to 900°C[6]. Maximum elongation was over 600%[7]. Interestingly, superplasticity in this alloy was observed in large grained conditions. Initial grain size was about 100μm, after superplastic deformation, the large grains were broken and finer grains appeared. A continuous recrystallization process was suggested in this alloy upon OM and TEM observation results [7]. It is well known that grain size will greatly affect the tensile properties of a material both at high and room temperatures. So that present research is aimed at the high temperature tensile properties of Fe_3Al based alloys which have finer grain sizes.

EXPERIMENTAL PROCEDURE

Alloys with compositions of Fe-28Al-2Ti and Fe-28Al-4Ti (all in atomic percent) were prepared by arc melting under argon using commercially pure iron, aluminum and titanium. The alloy buttons were remelted three times to improve their homogeneity and were then drop casted into ϕ20 rods. After homogenizing for 24 hours at 1000℃, these rods were hot rolled to about 2.2mm sheets at 900℃~1000℃. To get finer grain sizes, Fe-28Al-2Ti sheets were rolled at 700°C from 2.2mm to 1mm thickness while Fe-28Al-4Ti sheets were rolled at 800°C from 2.2mm to 1mm sheets (For 4Ti alloy, rolling at 700°C was found to be unsuccessful.).Tensile specimens were cut from these sheets using a spark machine. The gauge size of tensile specimens is 4.4×1.0×8mm.

Tensile tests were conducted on a SHIMADZU AG-100 kNA test machine at 600-750℃(0.48-0.54Tm, where Tm is the melting temperature of Fe_3Al) under an initial strain rates of $1.25\times10^{-4}s^{-1}$ and $2.5\times10^{-4}s^{-1}$. Optical microscopic observation was made with a Nephot-II microscope. Samples were etched in a solution of 8parts ethanol + 4parts HNO_3+1part HCl.

RESULTS AND DISCUSSION

1, Flow behavior and tensile properties

Fig. 1 shows the superplastically deformed Fe-28Al-2Ti specimens. At 600°C, deformation seems quite uniform. There are no necks along the specimen including the fracture tip area. With temperature increasing, necking appears. The necks of the specimen deformed at 700°C is sharper than that of deformed at 650°C. Similar phenomenon was also observed in the Fe-28Al-4Ti alloy but in a temperature range of 650°C to 750°C.

Typical true stress-true strain curves of the two alloys were shown in Fig.2 and Fig.3. The flow stresses are sensitively dependent on temperatures. More over, it is worthy to note that the flow stress is much high than that in fine grained materials. For Fe-28Al-2Ti alloy under a initial strain rate of 1.25×10^{-4}/s, strong hardening was observed when deformed at 600°C. At 650°C, hardening was compensated by softening after about 20% deformation. A sound balance of hardening and softening appears when the specimen is deformed at 700°C. Maximum elongation was also observed at 700 °C, which is 362%. For Fe-28Al-4Ti alloys, such phenomenon appears at temperatures of 50 degrees higher.

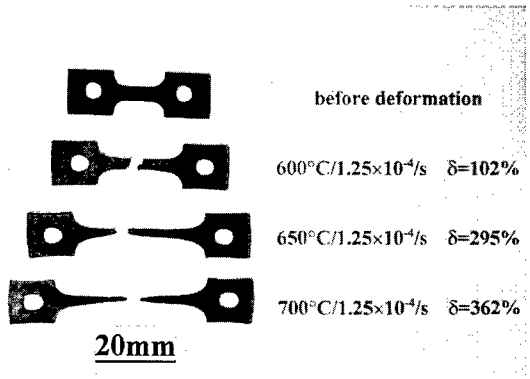

Fig.1 Superplasticity in Fe_3Al alloys at low temperatures.

Tensile properties of the two alloys are shown in Table 1. From this table it is clear that both alloys exhibit superplastic deformation behavior in the studied temperature and strain rate range. The elongation increases with increasing of

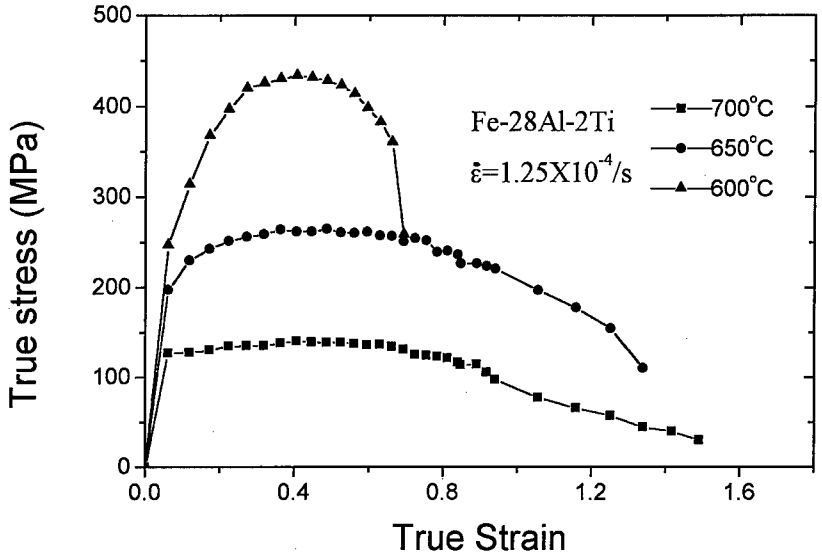

Fig.2 True stress-true strain curves of Fe-28Al-2Ti alloy at different temperatures.

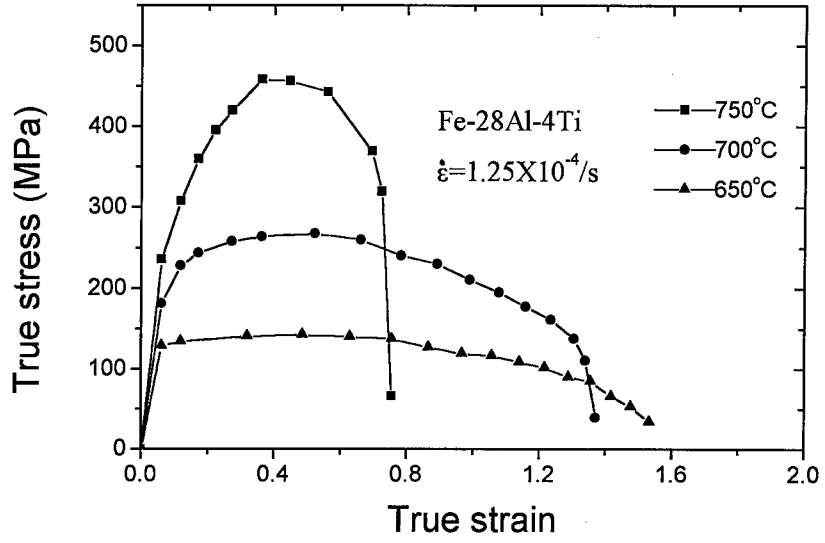

Fig.3 True stress-true strain curves of Fe-28Al-4Ti alloy at different temperatures.

temperature. From the maximum flow stresses, *m* values for Fe-28Al-2Ti are calculated to be 0.188, 0.291, 0.311 for 600°C, 650°C and 700°C respectively. For Fe-28Al-4Ti, *m* values are calculated to be 0.189, 0.279 for 700°C and 750°C respectively.

Take 1813K(1540°C) as the melting temperature of Fe_3Al alloys [8], 600°C-750°C temperature range is about 0.48 to 0.56Tm. Such temperature range was considered as low temperature

range for superplasticity[9-11]. Viscous gliding of dislocations was supposed to be responsible for the superplasticity phenomena [9]. In case of viscous gliding of dislocations, *m* value should be about 0.33. Present results shows that *m* value changes with temperatures and superplastic deformation was observed even when *m* value is lower than 0.2. Therefore, the dislocation viscous gliding mechanism is not enough to explain present results. More research is needed to explain such phenomenon.

Table 1 Tensile properties of Fe-28Al-2Ti and Fe-28Al-4Ti alloys at different temperatures and strain rates

Alloy composition	Temperature (°C)	Strain rate (1/s)	Maximum flow stress (Mpa)	Elongation (%)
Fe-28Al-2Ti	600	1.25×10^{-4}/s	320.3	102
		2.5×10^{-4}/s	365	100
	650	1.25×10^{-4}/s	204.6	295
		2.5×10^{-4}/s	250.3	124
	700	1.25×10^{-4}/s	124.1	362
		2.5×10^{-4}/s	154	263
Fe-28Al-4Ti	650	1.25×10^{-4}/s	316	98
	675	1.25×10^{-4}/s	278.8	100
	700	1.25×10^{-4}/s	217.8	175
		2.5×10^{-4}/s	248.3	156
	725	1.25×10^{-4}/s	171.6	250
	750	1.25×10^{-4}/s	132.9	312.5
		2.5×10^{-4}/s	161.2	316

2, Microstructure

The starting microstructures of these two alloys were shown in Fig.4 (a) and (b). With intercept method the grain sizes of Fe-28Al-2Ti and Fe-28Al-4Ti were measured to be about 32 and 47μm

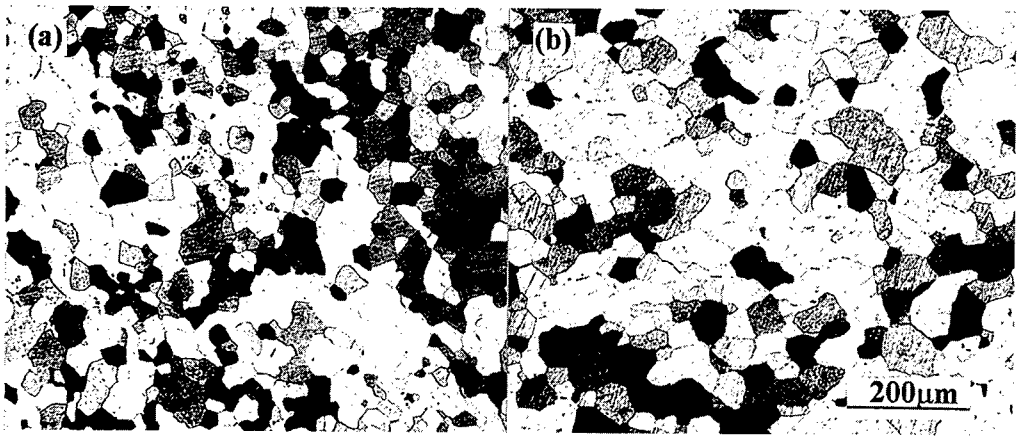

Fig.4 Optical microstructures of Fe-28Al-2Ti (a) and Fe-28Al-4Ti (b) alloys before deformation.

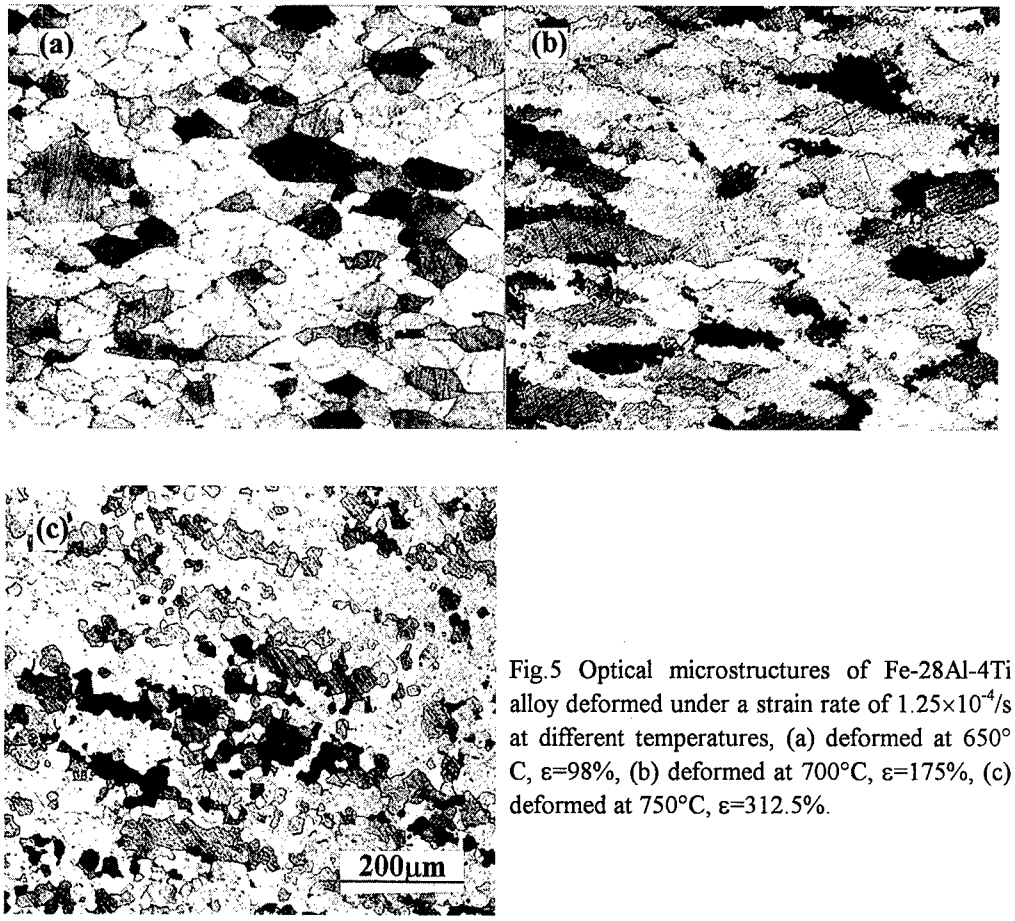

Fig.5 Optical microstructures of Fe-28Al-4Ti alloy deformed under a strain rate of 1.25×10^{-4}/s at different temperatures, (a) deformed at 650° C, ε=98%, (b) deformed at 700°C, ε=175%, (c) deformed at 750°C, ε=312.5%.

respectively. Both microstructures are consisted of eqiaxed grains. These grain sizes are finer than that in earlier report [6,7] but are still much larger than the grain sizes in conventional fine grain superplastic materials where the grain sizes are generally below 10μm. Therefore, GBS model is not applicable in this situation.

Change of microstructure with deformation is shown in Fig.5. From this figure it can be seen that deformation at 650°C resulted in an elongated grain structure. Very small serration appears in the grain boundaries. This phenomena becomes more pronounced when the specimen was deformed at 700°C. Deformation at 750°C resulted in a different microstructure. New and finer grains appeared in the specimen. Measured grain size is about 23μm which is about half of the original grain size. The grain size refinement was also observed in Fe-28AL-2Ti alloy at 850°C when the original grain size is about 100μm[6]. Upon OM and TEM observation, it is suggested that such refinement was introduce by a continuous recovery and recrystallization process. During superlastic deformation an unstable subgrain network forms and these subboundaries absorb gliding dislocations and transform into low and high angle grain boundaries. A dislocation glide and climb process accommodated by subboundary sliding, migrating and rotating, allows the superplastic flow to proceed[7].

For fine grain superplasticity, finer grain structure results in lower temperature and higher stain rate

superplasticity. Low temperature superplasticity has been demonstrated in alloys with extremely fine grain structure (grain size is about 1μm)[9]. In present research it is clear that the starting grain size is much larger than that needed for grain boundary sliding. Considering the initial large grain size and high flow stress as well as finer grain size after deformation, it may be assumed that inner grain dislocation movement has played an important role in the early time of deformation process while DRV and DRX have taken place in the late time of the deformation.

CONCLUSIONS

Low temperature Superplasticity was demonstrated in Fe-28Al-2Ti and Fe-28Al-4Ti alloys at a temperature range of 600-750°C. After superplastic deformation, initial large grains changed to elongated grains or recrystallized grains. The superplastic deformation mechanism is suggested to be related with DRX and DRV in such ordered intermetallics.

ACKNOWLEDGEMENT

This work was supported by the National Natural Science Foundation of China

REFERENCES

[1]J.W. Edington, K.W. Melton, C.P.culter, Prog. Mater. Sci. 21(1976), p.61.
[2] T.G. Nie, and W.C. Oliver, Scripta Metall. 23(1989), p.851.
[3] J.Mukhopadhyay, G. Kaschner, and A.K. Mukherjee, Scripta Metall. 24(1990), p.857.
[4] S.C. Cheng, J.Wolfenstine,and O.D.Shereby, Metall.Trans. 23A(1992), p.1509.
[5] R.M. Imayev, O.A.Kabyshev, and G.A. Salishchev, Acta Metall. Mater. 40(1992), p.581.
[6] D. Lin, A. Shan and D.Li, Scripta Metall., 24(1990), p.857.
[7] D. Lin, A. Shan, and M.Chen, Intermetallics,
[8] C.G. McKamey, J.H. DeVan, P.F. Tortorelli, and V. K. Sikka, J. Mater. Res. 6(1991), p. 1779
[9]M. Mabuchi, H. Iwasaki, K. Yanase and K. Higashi, Scripta Mater. 36(1997), p.681.
[10]T. R. McNelley, E.-W.Lee, and M.E. Mills, Metall.Trans.,17A(1986)1035.
[11] R.Z. Valiev, N.A. Krasilnikov and N.K. Tsenev, Mater. Sci. Eng. A137(1991), p.35.

Corresponding author:
Dr. Aidang Shan,
Fax: +86-21-62820892
Email:adshan@mail1.sjtu.edu.cn

Key Engineering Materials Vols. 171-174 (2000) pp. 355-362
© 2000 Trans Tech Publications, Switzerland

Deformation Behavior of 7475 Aluminum Alloy at High Temperatures

R. Kaibyshev[1], O. Sitdikov[1], A. Goloborodko[1] and T. Sakai[2]

[1] Institute for Metals Superplasticity Problems, Khalturina 39, Ufa RU-450001, Russia

[2] Department of Mechanical and Control Engineering, The University of Electro-Communications, Chofu, Tokyo 182-8585, Japan

Keywords: Hot Deformation, High Strength Aluminum Alloy, Power-Law Regime, Stress Exponent, Threshold Stress, Activation Energy

Abstract

Deformation behavior of the 7475 aluminum alloy was studied in temperature range T=623-793K by compression test. It has been shown that the 7475 alloy exhibits a threshold behavior. Analysis in terms of threshold stress has shown that there are two characteristic modes of deformation behavior in the power-law regime in the examined temperature range. At normalized strain rate $\dot{\varepsilon}RT/D_lGb \leq 1.6 \cdot 10^{13}$ mol^{-1} the value of the stress exponent, n, is equal 4, and at normalized strain rate $\dot{\varepsilon}RT/D_lGb \geq 1.6 \cdot 10^{13}$ mol^{-1} the value of the stress exponent, n, is equal 6. Value of activation energy is close to that for lattice self-diffusion in pure aluminum at temperatures above 763K and close to the value of pipe diffusion at T≤723K. Deformation behavior of the 7475 alloy was interpreted in terms of transition from low temperature climb to high temperature one. Two types of temperature dependence of threshold stress was observed in the examined temperature region. Strong temperature dependence with the energy term, Q_o=130 kJ/mol was revealed at T=743-793K. At T=673-743K the dependence with Q_o= 42 kJ/mol was found. The role of second phase dissolution in threshold behavior of the alloy is considered.

1 Introduction

Deformation behavior of high strength 7XXX Al-alloys was extensively studied in the past in the low temperature range where precipitations of η-phase on aging take place and the high creep resistance of these alloys is caused by the interaction between fine particles and dislocations. By contrast, no investigation has yet been conducted to study the deformation behavior of Al-Zn-Mg alloys with coarse grain structure in high temperature range where dissolution of reinforced phase occurs and a transition in the mechanisms controlling the plastic deformation is expected. Numerous authors [1,2,3] paid a great attention to examination of superplasticity in these aluminum alloys with fine grain structure at high temperatures.

The purpose of this paper is two-fold. Firstly, to report the data of a detailed examination of deformation behavior of modified 7475 aluminum alloy with Zr additives over a wide temperature range. Secondly, careful inspection of these experimental data will be perform to reveal the role of secondary phases in deformation behavior of the alloy and to examine the operating deformation mechanisms.

2 Experimental procedure

The modified 7475 aluminum alloy was used in the present study. The chemical composition (in wt%) of the alloy is 6.4%Zn, 2.46%Mg, 1.77%Cu, 0.23%Cr, 0.16%Zr, 0.03%Si, 0.04%Fe, 0.03%Mn and the balance is Al. The alloy was initially produced by semicontinuous casting by Kaiser Aluminum and was homogenized at 768K for 20h. Initial microstructure of alloy consisted of lamella type grains with size 1 - 10 mm in longitudinal direction and about 50 - 100 μm in transverse direction and bands of essentially equiaxed grains with size from 50 to 100 μm. Both bands and lamellas were located in parallel to the ingot axes. Compression specimens of a diameter 10 mm and a height 12 mm were machined from the ingot. Compression tests were conducted in air at temperatures between 673 K and 793 K at various strain rates from 10^{-5} to 10^{-2} s^{-1} using a screw-driven Schenck machine. In addition, strain rate change tests were performed. The deformation relief was investigated using a JSM-840 SEM. The thin foils were examined with a JEOL-2000EX TEM utilizing a double-tilt stage. Samples for SEM and TEM observation were electropolished in a solution of 30% HNO_3 and 70% methanol at 25V and 243K. Samples for surface observation at high temperatures were plated by platinum. The threshold stress and creep parameters were determined by methods described in detail in [4-10]. Note that the deformation behavior of material was analyzed only in the stable stage (ss) of plastic flow, when $\sigma_{ss}(\varepsilon)$=const. In this case, the deformation under active loading can be treated in the same way as creep [4].

3 Experimental results

3.1 Deformation behavior of 7475 Al alloy

Flow stresses. The typical true stress-strain curves in the temperature range from 623 K to 793 K and strain rates from 10^{-5} s^{-1} to 10^{-2} s^{-1} are presented in Fig.1. Two different temperature regions distinguished by a shape of curves are revealed. At T=763-793K and $\varepsilon=10^{-5}$-10^{-4} s^{-1} the peak stress is observed in the initial stage of plastic deformation (ε_{peak}=2-4%). During subsequent deformation a gradual softening takes place. A decrease in flow stress by at least one and half times is observed after ε_{ss}=40-50%. At lower temperatures (T=673K-723K) the minor peak stress was revealed. The stable stage of plastic flow is reached after strains ε_{ss}=15-25% and values ε_{ss} are diminished with decreasing temperature in this region. Note, that further temperature decrease leads to peak stress disappearance and the stable stage of plastic flow is attained after ε= 3-5%.

The analyze of the effect of the strain rate $\dot{\varepsilon}_{ss}$ and temperature on the flow stress σ_{ss} in the stable stage was performed by the σ-$\dot{\varepsilon}$ plot drown on double logarithmic scale (Fig. 2). It is seen that in both revealed temperature intervals the σ-$\dot{\varepsilon}$ dependence obeys the power law [5-7]:

$$\dot{\varepsilon} = A_1 \cdot \left(\frac{\sigma}{G}\right)^{n_a} \cdot \exp\left(-\frac{Q_a}{RT}\right) \qquad (1)$$

where $\dot{\varepsilon}$ is the strain rate, σ is the flow stress, Q_a is the activation energy for plastic deformation, R is the gas constant per mole and T is the absolute temperature. A and n_a are coefficients. The flow stress exponent n_a=dlog($\dot{\varepsilon}$)/dlog(σ) strongly depends on temperature and increases from n_a~ 4-5 to n_a~ 7-9 with transition from the high temperature interval (T=763-793K) to the lower one (T=673-723K).

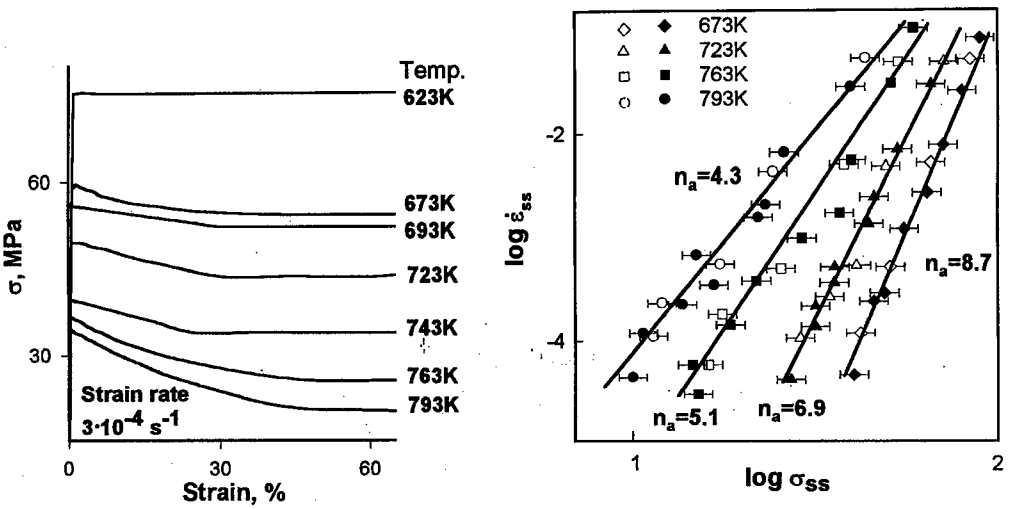

Fig. 1 (left) True stress-strain curves of the AA 7475 at various temperatures.

Fig. 2 (right) The stable state strain rate as function of the stable state stress of the AA 7475. Closed and open symbols indicate the data obtained from the strain rate change test and uninterrupted test, respectively.

Activation energy for plastic deformation. The Eq.1 was used to determine the apparent activation energy for plastic deformation by plotting the stable stage flow stresses vs the reciprocal temperatures in semi-logarithmic scale and taking the slope of tangent to be Q/Rn (Fig. 3). Two temperature intervals could be distinguished in this figure. In range T=723- 793K the slope is equal to 5.5 K^{-1} and values, Q_a, lie in interval 196-233 kJ/mol. These values of Q_a are much higher than the activation energy for lattice self-diffusion in Al (Q_l=142 kJ/mol [8]). At lower temperatures (T=673 to 723K) the slope was found about 2.1 K^{-1}, that led to Q_a=120-152 kJ/mol.

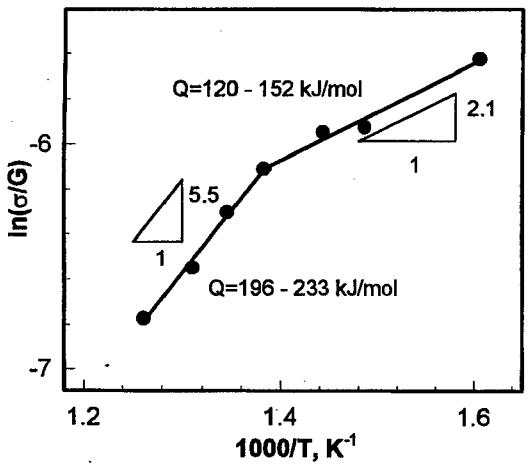

Fig. 3. Shear modulus - compensated stable state flow stress vs inverse of temperature and values of activation energy for deformation.

3.2 Deformation relief

In the temperature region T=673-723K the dislocation sliding is essentially uniform (Fig. 4a). The distribution of slip lines is largely homogeneous within the grain interior. At the same time, slip features vary from one grain to another. In some grains wavy slip lines attributed to the cross-slip are observed and straight slip features are revealed inside other grains. One operating dislocation glide system is in dominant in most grains.

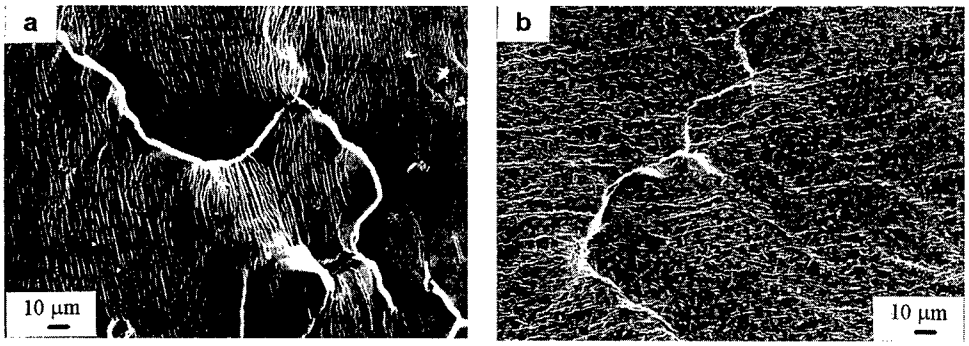

Fig. 4. Deformation relief of the AA 7475 (ε=15%, $\dot{\varepsilon}=10^{-4}$ s^{-1}): (a) T=723K, (b) T=793K.

At higher temperatures (T= 763K- 793K) the dislocation slip is non-homogeneous. The multiple cross-slip is the main deformation mechanism. Slip lines are grouped in slip bands (Fig. 4b).

3.3 TEM observations

The inspection of TEM micrographs reveals the following features and findings.

(a) Strong temperature influence on phase composition of the 7475 alloy was revealed. At T ≤ 723K two types of secondary phase particles are observed (Fig.5.a) both in grain interior and in vicinity of grain boundaries. Distribution of coarse precipitate particles with size 0.4-0.5 μm is not uniform. Clusters of these precipitations are observed in some grains. Dispersoids with size less than 0.1 μm are distributed essentially uniform. Most likely that these particles are intermetallic dispersoids of Al_3Cr and Al_3Zr phases. Temperature increase above 723 K leads to gradual dissolution of coarse precipitate particles and does not significant effect volume fraction of nanoscale particles. At T=763-793K coarse particles of the reinforcement phase does not observed.

(b) An extensive interaction between lattice dislocations and secondary phase particles is observed at all examined temperatures (Fig.5). It is seen, that the dislocations are attached to precipitate particles

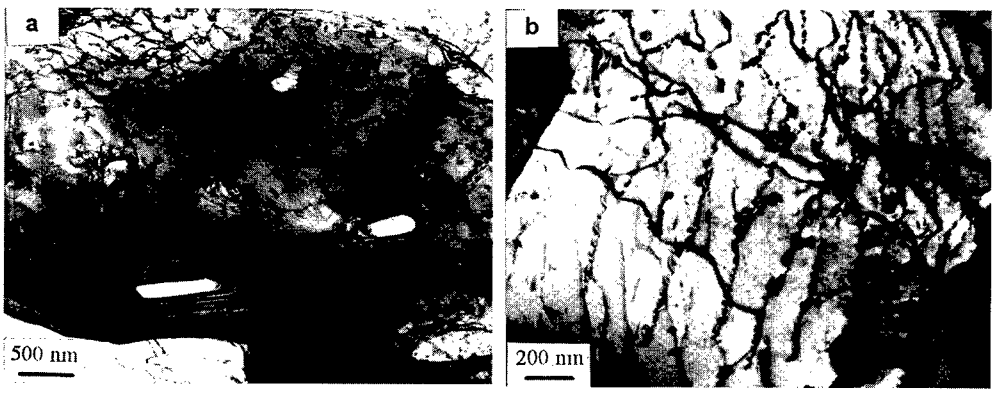

Fig. 5. TEM micrographs of the AA 7475 after deformation: (a) T=723K, $\dot{\varepsilon}=10^{-4}$ s^{-1}, ε=70%, (b) T=763K, $\dot{\varepsilon}=10^{-4}$ s^{-1}, ε=50%.

as well as to dispersoids of transition metals and tangled. Particles play a role of obstacles for dislocation glide. In some areas of grains the lattice dislocations are captured by dispersoids. At T≥763K weak interaction between lattice dislocations and dispersoids takes place. Dissolution of precipitations enhances dislocation mobility and yields more uniform dislocation distribution inside grains.

(c) Extensive occurrence of dislocation climb is evident from observation of helicoidal dislocations [11] at T≥763K (Fig. 5.b).

4 Analysis and Discussion

4.1 Analysis in terms of threshold stress

The deformation behavior of the 7475 aluminum alloy with initial coarse grain structure is very complicated and can not be interpreted in terms of the creep transition from class II (metal class) to class I (alloy class) as deformation behavior of other solid-solution aluminum alloys [4,7,9]. In contrast, the 7475 alloy demonstrates relatively high values of apparent activation energy for plastic deformation at high temperatures and there is a great gap between the stress exponents n=4.3 at T=793K and the value n=8.7 at lower temperature T=673K. It is seen from TEM observations that interaction between dislocations and dispersoids plays an important role in plastic deformation of the 7475 alloy. Threshold stress, σ_{th}, caused by the presence of secondary phase particles may exist and, consequently, deformation behavior of the 7475 Al alloy resembles that of dispersion-strengthened alloys [7,9].

As a result, the deformation is driven by the effective stress $\sigma_{eff}=\sigma-\sigma_{th}$, and not by the applied stress σ. In this case, the deformation behavior can be described by a rate equation in the form [3,6,9]:

$$\dot{\varepsilon} = A_2 \cdot \left(\frac{\sigma - \sigma_{th}}{G}\right)^n \cdot \exp\left(-\frac{Q}{RT}\right). \qquad (2)$$

In examining the possibility of threshold stress in the 7475 Al alloy the data were plotted as $\dot{\varepsilon}^{1/n}$ vs σ on a double linear scale. A value of σ_{th} at each temperature was estimated by extrapolation of this plot to zero: $\sigma_{th} = \sigma$ ($\dot{\varepsilon}^{1/n} \rightarrow 0$) [6,9]. The coefficient n was chosen to obtain the $\dot{\varepsilon}^{1/n}$-σ dependence approximated linearly with the maximum regression coefficient. The results of the best linear fit between $\dot{\varepsilon}^{1/n}$ and σ at some temperatures from lower and high temperature intervals are represented in Fig. 6 a and b, respectively. It is evident that in the temperature interval from 673 to 723K the threshold stresses are relatively high. The values σ_{th} reach 30-50% from applied stresses σ_{ss}.

The temperature dependence of threshold stresses is not monotone (Fig.6c). Values σ_{th} drop sharply from 19 to 1.8 MPa with increasing temperature from 673 to 793K. At T=793K threshold stresses normalized to σ_{ss} hardly exceed 10-15% even at $\dot{\varepsilon}=10^{-5}$ s^{-1}. Such a decrease of threshold stresses cannot be accounted for by the temperature dependence of the shear modulus. As it was demonstrated for dispersion-strengthened alloys, a threshold stress can be described by the relation [3,9]:

$$\frac{\sigma_{th}}{G} = B_0 \exp\left(\frac{Q_0}{RT}\right), \qquad (3)$$

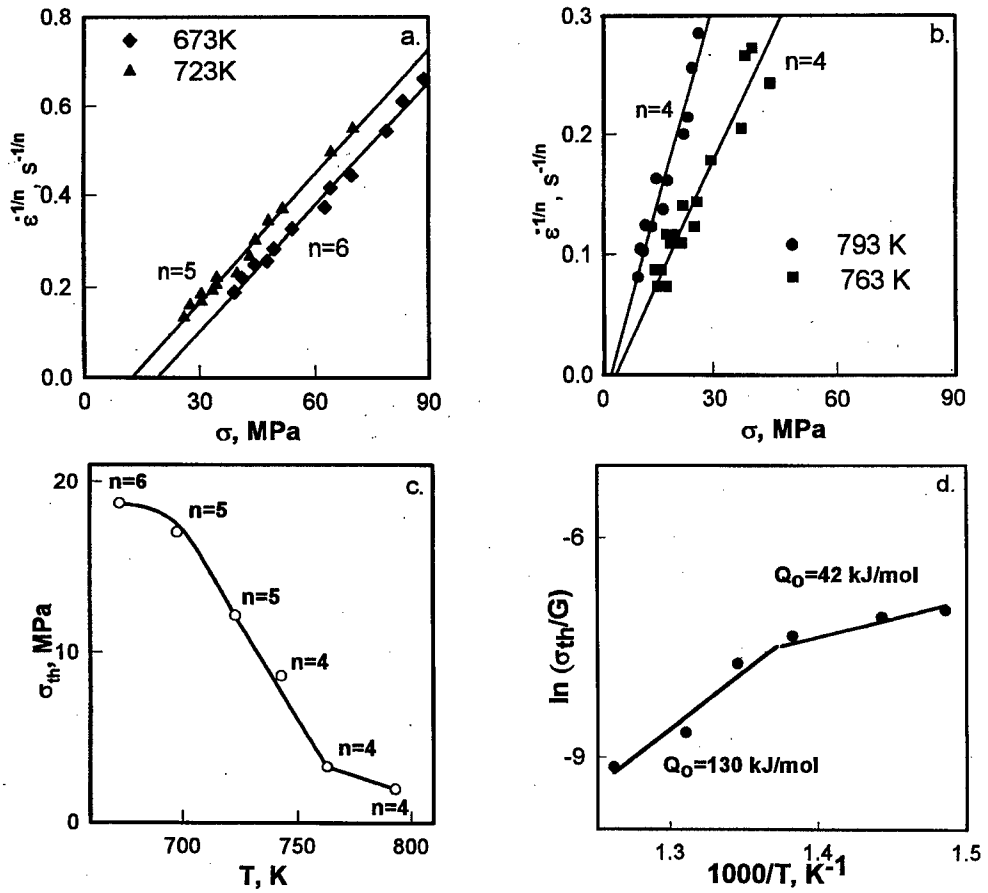

Fig. 6. (a)-(b) plot of $\dot{\varepsilon}^{1/n}$ vs σ_{ss} for determination of σ_{th} at various testing temperatures; (c) temperature dependencies of σ_{th} and n values; (d) plot of σ_{th}/G vs 1000/T showing the temperature dependence of σ_{th}.

where B_o is a constant and Q_o is an energy term. Fig. 6.d in which σ_{th}/G is plotted vs 1/T confirms the validity of Eq. 3. to the results of the present investigation. It is seen, that the strong temperature dependence with the energy term, Q_o= 130 kJ/mol is revealed at T=743-793K. At lower temperatures (T=673-743K) the weak dependence of σ_{th}/G on 1/T with Q_o=42 kJ/mol was obtained.

Also it is important to note that the coefficient n obtained from this plotting is equal to 4 in the high temperature interval and from 5 to 6 at lower temperatures (Fig. 6.a to c).

4.2 Deformation behavior

Using the datum points (Fig. 2.), Fig.7 shows a double logarithmic plot of the normalized strain rate, $\dot{\varepsilon}RT/(D_lGb)$, against the normalized effective stress, $(\sigma-\sigma_{th})/G$. It is seen that deformation behavior of the 7475 alloy obeys the power law and almost all experimental points lie below the Sherby-Burke criterion, representing the breakdown of power law creep [4,10]. At the same time there are two

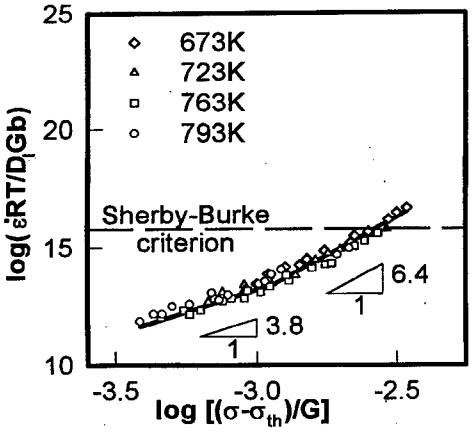

Fig. 7. Dependence of normalized strain rate on normalized effective stress.

different slopes of the dependence. At normalized effective stress bellow $1.2 \cdot 10^{-3}$, there is a line with slope of n=3.8 and at higher stresses n=6.4. These values of stress exponent are closed to n=4 and n=6 which were found by calculation of threshold stresses and, consequently, it is possible to consider the region of lower temperatures where deformation behavior is controlled by pipe-diffusion with increasing stress exponent to (n+2).

Activation analysis supports this approach to description of deformation behavior of the 7475 alloy. The true activation energy was calculated according to the plot represented in Fig. 8 as 146 kJ/mol in temperature interval 763-793 K (Fig. 9).

The activation energy tends to decrease down to 76 kJ/mol with temperature reduction from 673K to 723K. Determined values of Q_c are in a very good agreement with values of activation energies of lattice self-diffusion (Q_l=142 kJ/mol) and pipe diffusion (Q_c=82 kJ/mol) in pure aluminum, respectively [8].

4.3 Interpretation of deformation behavior

Analysis of deformation behavior has shown that the 7475 alloy exhibits two characteristic modes of behavior in the power-law creep regime. First, in the temperature interval 763-793K the values of activation energy and the stress exponent are in consistent with plastic deformation controlling by high temperature climb. Processes of dislocation rearrangement occur at these temperatures, easily. Multiple dislocation cross-slip is a main deformation mechanism. The small values of threshold stresses were found in this region. In addition, the energy term Q_o =130 kJ/mol was determined as a value closed to the activation energy for lattice self-diffusion in Al. It can be explained in terms of the

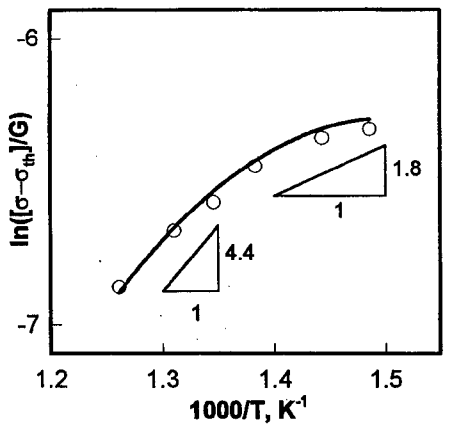

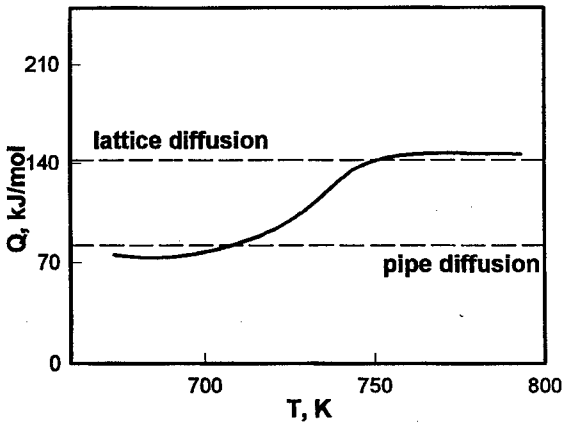

Fig. 8 (left). Shear modulus - compensated effective stress vs inverse of temperature.
Fig. 9 (right). Temperature dependence of activation energy for deformation.

small contact between a dislocation and a particle, when the dislocation overcomes the particle by a manner of general climb [3]. Second, at T=673-763K the transition from high temperature climb to low temperature one takes place with temperature decrease. It reduces dislocation mobility caused by climb. Concurrently single dislocation slip becomes in dominant and cross-slip is hampered. It decreases the ability of lattice dislocations to surmount obstacles by-pass. It is possible to presume that the change of controlling deformation mechanism is the main reason yielding strong increase of threshold stress with temperature decrease at T=673-723K. It means that the characteristics of dislocation climb influence interaction mechanism between lattice dislocations and dispersoids and determine threshold behavior of the material.

Another reason for observing strong temperature dependence of threshold stress in range T=673-763K is associated with dissolution of the secondary η-phase, since solvus of this phase is located near 723K [12]. Strong decrease of dispersoid volume fraction due to disappearance of η-phase at temperatures above the solvus temperature may give a significant contribution to the threshold stress drop.

5 Conclusions

1. The deformation behavior of the modified 7475 aluminum alloy was investigated at temperatures from 673 to 793K and could be described in terms of power law at all examined temperatures.
2. The 7475 alloy demonstrates threshold behavior. Strong temperature dependence with the energy term, Q_o=130 kJ/mol was revealed at T=743-793K. At lower temperatures (T=673-743K) the weak temperature dependence with Q_o= 42 kJ/mol was found.
3. By incorporating a threshold stress into the deformation behavior analysis, it was shown that the value of the stress exponent, n, is 6.4 at normalized effective stresses higher than $1.2 \cdot 10^{-3}$, and n=3.8 at lower normalized effective stresses.
4. The true activation energy for plastic deformation, Q_c, decreases from value ~146 kJ/mol at T=793K to ~76 kJ/mol at T=673K. These values match values of activation energy for lattice self-diffusion (142 kJ/mol) and pipe diffusion (82 kJ/mol) in aluminum with excellent accuracy.
5. The transition from climb controlling by lattice diffusion to climb controlling by pipe diffusion is accompanied by a change in the temperature dependence of threshold stress.

References

[1] D. H. Shin, C. S. Lee, W-J. Kim, Acta Mater, 45 (1997), p.5195.
[2] R.K. Mahidhara, H.S.Yang, A.K. Mukherjee, Z. Metakd. 85 (1994), p. 715.
[3] D. Shin, K.-T. Park, E. Lavernia, Mater. Sci. Eng. A201 (1995), p. 118.
[4] J.-P. Poirier, Plasticite a haute temperature de solides cristallines, Paris: Eyrolles (1976)
[5] S. Vagarali, T. Langdon, Acta Metall. 29 (1981), p. 1969
[6] F. Mohamed, J. Mater. Sci. Lett. 7 (1988), p. 215
[7] J. Cadek, Creep in Metallic Materials, Prague: Academia (1994)
[8] H. Frost, M. Ashby, Deformation-Mechanism Maps, Pergamon Press (1982)
[9] L. Yong, R. Nutt, F. Mohamed, Acta Mater. 45 (1997) p. 2607
[10] S. Raj, T. Langdon, Acta Metall. 37 (1989), p. 843
[11] J. Fridel, Dislocations, Pergamon Press (1964)
[12] G. Kusnezov, A. Barsukov, G. Krivosheeva, Zvetnaja metallurgia 2 (1985) p. 91.

For correspondence: Prof. R. Kaibyshev, fax: +7(3472)253856, e-mail: sitdikov@imsp.da.ru

Key Engineering Materials Vols. 171-174 (2000) pp. 363-368
© 2000 Trans Tech Publications, Switzerland

Superplasticity at Low Temperatures in a ZK61 Magnesium Alloy Produced by Powder Metallurgy

H. Watanabe[1], T. Mukai[1], K. Ishikawa[1], Y. Okanda[1], M. Mabuchi[2] and K. Higashi[3]

[1] Osaka Municipal Technical Research Institute, 1-6-50 Morinomiya, Joto-ku, Osaka 536-8553, Japan

[2] National Industrial Research Institute of Nagoya, 1-1 Hirate-cho, Kita-ku, Nagoya 462-8510, Japan

[3] College of Engineering, Osaka Prefecture University, 1-1 Gakuen-cho, Sakai 599-8531, Japan

Keywords: High-Strain-Rate Superplasticity, Magnesium Alloy, Powder Metallurgy, Strain Rate Sensitivity Exponent, Elongation-to-Failure, Grain Boundary Sliding

Abstract

Superplastic behavior of a fine-grained magnesium alloy, ZK61, was investigated at about half the absolute melting point. The material was produced by powder metallurgy. The tensile test revealed that the material exhibited superplasticity. The maximum elongation of 659% was obtained at 473 K and $1x10^{-3}$ s^{-1}. Furthermore, it was noted that a large elongation of 283% was attained at a high strain rate of $1x10^{-2}$ s^{-1}. The optimum superplastic strain rate in the present alloy was faster than that in some conventional magnesium alloys, that were shown to exhibit superplasticity at low temperatures. It was suggested that the small grain size increased the optimum superplastic flow in the present alloy.

Introduction

Recently there has been a significant increase in the use of magnesium as a structural material. This is a consequence not only of magnesium's relatively low density but also of its good damping characteristics, dimensional stability, machinability and low casting costs. Despite these advantages, however, magnesium alloys normally exhibit low ductility near the room temperature, because of the h.c.p. structure. In order to exploit the benefits of magnesium alloy, it is important to develop secondary processing which can effectively produce complex engineering components. Superplastic forming is a viable technique to fabricate hard-to-form materials into complex shapes.

The conventional superplasticity in pseudo single phase alloys is observed at relatively low strain rates of $<10^{-3}$ s^{-1} and at temperatures of ~0.8 Tm, where T_m is the melting point of the material. Experimental evidence suggests that a reduction in grain size will increase the strain rate and/or decrease the temperature for optimum superplastic flow [1]. It has been demonstrated that a powder metallurgy (P/M) process can give rise to a smaller grain size, compared to an ingot metallurgy (I/M) process [2]. Therefore P/M metals likely show superplastic behavior at higher strain rates and/or lower temperatures than I/M metals. Especially, it is beneficial to exhibit high-strain-rate superplasticity ($\dot{\varepsilon} \geq 1x10^{-2}$ s^{-1}) at low temperatures in magnesium alloys. Since magnesium is susceptible to surface oxidation at high temperatures. Recently, it was demonstrated that the high-strain-rate superplasticity was obtained even at low temperatures in extremely fine-grained alloys [3,4]. However, high-strain-rate superplasticity in magnesium-based materials has been observed only at relatively high temperatures [2, 5-12].

In the present study, superplastic behavior of a pseudo single phase magnesium alloy, ZK61, was investigated at about half the absolute melting point. The material was produced by the P/M route, and had a fine grain size of ~ 500 nm. It is demonstrated that the P/M ZK61 alloy can behave in a superplastic manner at a high strain rate of $1x10^{-2}$ s^{-1} albeit at the low temperature.

Experimental procedure

The material used in the present study was a P/M ZK61 (Mg-6wt.%Zn-0.8wt.%Zr) magnesium alloy. The P/M ZK61 alloy was processed with rapidly solidified powders. The powders were sintered at 523 K at a pressure of 235 MPa in vacuum. The sintered billets were extruded at 523 K with a reduction ratio of 100 : 1. The grain sizes, d (= 1.74L; L is the linear intercept size), were measured from a transmission electron micrograph. Microstructures of the P/M ZK61 are shown in Fig. 1. The grains were equiaxed with a fine grain size of ~500 nm.

Tensile specimens, machined directly from the extruded bars, had tensile axes parallel to the extruded direction. The specimens had a gauge length of 5 mm and a gauge diameter of 2.5 mm. Tensile tests were carried out at temperatures ranging from 448 to 498 K and at constant strain rates from $1x10^{-5}$ to $1x10^{-1}$ s^{-1} in air. The testing temperature is equivalent to the homologous temperatures ranging from 0.49 to 0.55 T_m, where T_m is 908 K for ZK61 [13].

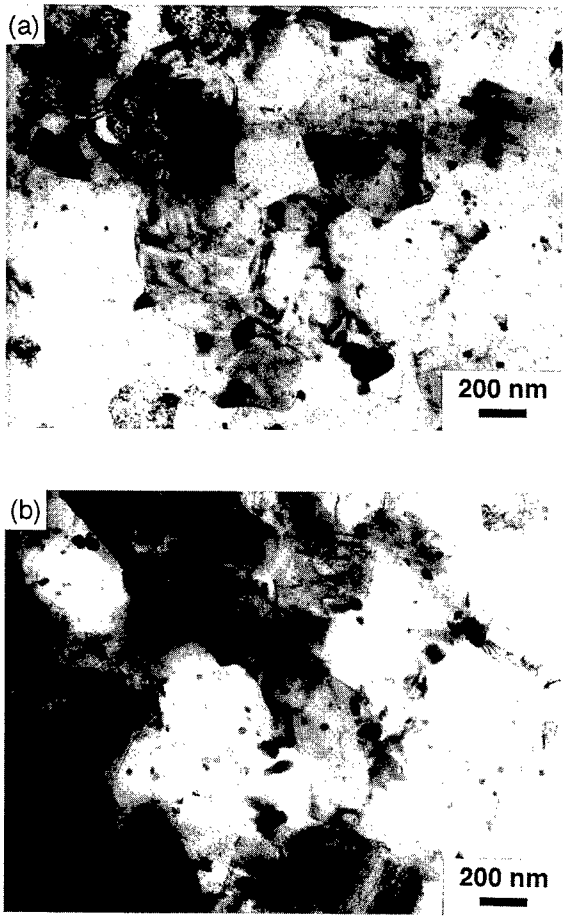

Fig. 1. Typical TEM microstructures of the P/M ZK61 alloy.
(a) The longitudinal section. (b) The transverse section.

Results and Discussion

The variation in flow stress as a function of strain rate is plotted in Fig. 2 for P/M ZK61. The flow stress for each strain rate was determined at a small strain of 0.1. The flow stress decreased with temperature, and increased with strain rate in a typical sigmoidal curve, as has been previously observed for superplastic materials [14,15]. The strain rate sensitivity exponent, m, which was estimated from the slope of the curve, exhibited a maximum value of 0.5 in the intermediate strain rate range. This high m-value of 0.5 is indicative that the dominant deformation process is grain boundary sliding [15]. This was confirmed from an scanning electron microscopic observation of surface appearance, which showed direct evidence for grain boundary sliding as shown in Fig. 3. Low m-value in the low strain rate range is often observed in superplastic materials. Such values have been associated with the existence of a threshold stress [16].

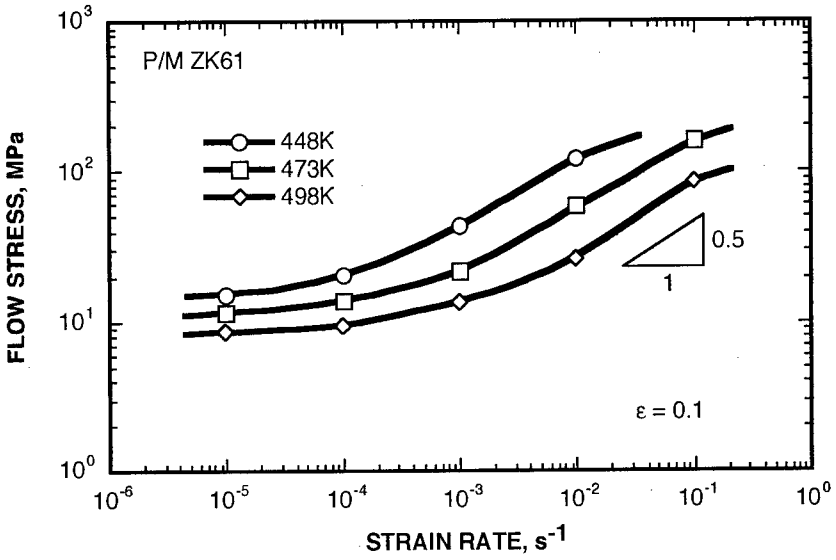

Fig. 2. The variation in flow stress as a function of strain rate in P/M ZK61 alloy.

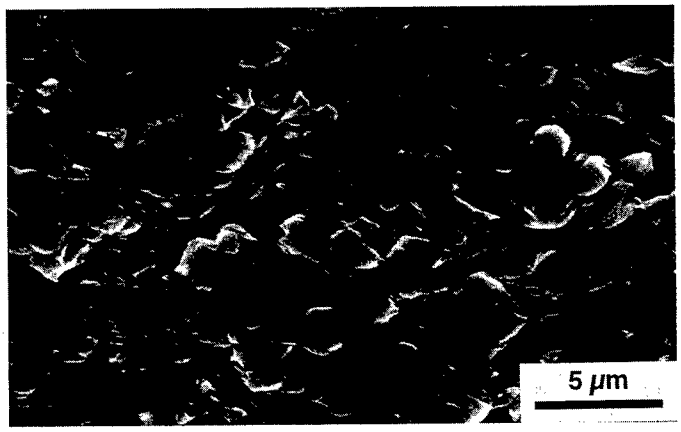

Fig. 3. The surface appearance of deformed specimen fractured at 473 K and $1x10^{-3}$ s^{-1}. Tensile direction is horizontal.

The variation in elongation-to-failure as a function of strain rate is plotted in Fig. 4 for P/M ZK61. The maximum elongation of 659% was obtained at 473 K and $1x10^{-3}$ s^{-1}. However, it is noted that a large elongation of 283% was also attained at 473 K at a high strain rate of $1x10^{-2}$ s^{-1}. It was found that the high-strain-rate superplasticity was attained albeit at low temperatures of ~ 0.5 T_m.

Fractured specimens deformed at 473 K are shown in Figure 5. It is clearly observed that the deformed specimens are fairly uniform with no visible necking over the strain rates of $1x10^{-4}$ s^{-1}.

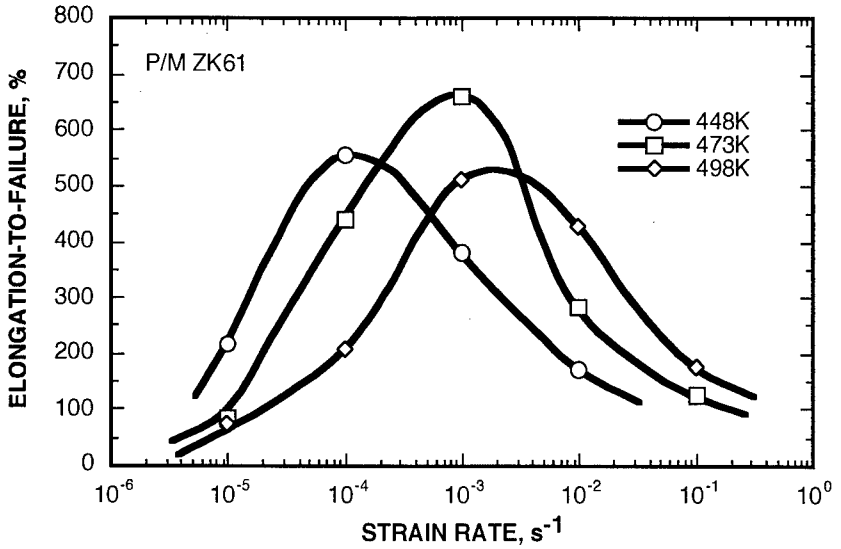

Fig. 4. The variation in elongation-to-failure as a function of strain rate in P/M ZK61.

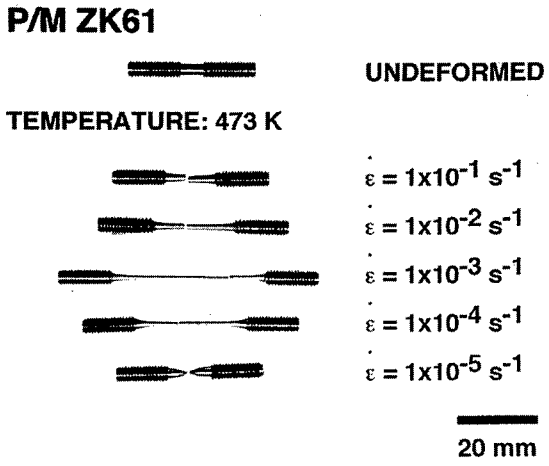

Fig. 5. Fractured specimens deformed at strain rates from $1x10^{-5}$ to $1x10^{-1}$ s^{-1} at 473 K.

The data for superplastic magnesium-based materials at low temperatures of ~ 0.5 T_m [1,17-21] is listed in Table 1. The optimum superplastic strain rate in the present alloy was faster than that in some conventional magnesium-based materials. It appears that the optimum strain rate increases with decreasing grain size. It is suggested that the high-strain-rate superplasticity at low temperatures in the present alloy is attributed to the very small grain size of ~ 500 nm.

Table 1. Superplastic behavior at low temperatures in magnesium-based materials.

Material	e_f, %	T, K	T/T_m	$\dot{\varepsilon}$, s^{-1}	d, μm	Ref.
MA8	>250	453	0.49	$5x10^{-4}$	0.3	[17]
EA55	450	473	0.51	$1x10^{-4}$	-	[18]
AZ91	661	473	0.51	$6x10^{-5}$	1.0	[19]
ZK60	348	473	0.51	$1x10^{-4}$	3.4	[20]
ZK60	444	473	0.51	$2.6x10^{-6}$	6.5	[1]
ZK60/SiC/17_p	350	463	0.50	$4x10^{-3}$	1.7	[21]
ZK61	283	473	0.51	$1x10^{-2}$	0.5	This work
ZK61	659	473	0.51	$1x10^{-3}$	0.5	This work

T_m is 924 K, which is the melting point of pure magnesium [22].

Summary

Superplasticity was found in a fine-grained (~ 500 nm) magnesium alloy ZK61, that was processed by powder metallurgy route, albeit at a low temperature of ~ 0.5 T_m. Although the maximum elongation was obtained at 473 K and $1x10^{-3}$ s^{-1}, large elongation of 283% was also attained at a high strain rate of $1x10^{-2}$ s^{-1}. The optimum superplastic strain rate in the present alloy was faster than that in some conventional magnesium-based materials, that were shown to exhibit superplasticity at ~ 0.5 T_m. This may be attributed to the very small grain size.

References

[1] H. Watanabe, T. Mukai and K. Higashi, Scripta Mater. 40 (1999), p. 477.
[2] M. Mabuchi, T. Asahina, H. Iwasaki and K. Higashi, Mater. Sci. Tech. 13 (1997), p. 825.
[3] P.B. Berbon, N.K. Tsenev, R.Z. Valiev, M. Furukawa, Z. Horita, M. Nemoto and T.G. Langdon, Metall. Mater. Trans. A 29A (1998), p. 2237.
[4] S.X. McFadden, R.S. Mishra, R.Z. Valiev, A.P. Zhilyaev and A.K. Mukherjee, Nature 398 (1999), p. 684.
[5] S. Lim, T. Imai, Y. Nishida and T Choh, Scripta Metall. Mater. 32 (1995), p. 1713.
[6] T.G. Nieh and J. Wadsworth, Scripta Metall. Mater. 32 (1995), p. 1133.
[7] M. Mabuchi, K. Kubota and K. Higashi, Scripta Met. Mater. 33 (1995), p. 331.
[8] T.G. Nieh, A.J. Schwartz and J. Wadsworth, Mater. Sci. Eng. A208 (1996), p. 30.
[9] M. Mabuchi and K. Higashi, Phil. Mag. A 74 (1996), p. 887.
[10] A. Uoya, T. Shibata, K. Higashi, A. Inoue and T. Masumoto, J. Mater. Res. 11 (1996), p. 2731.

[11] T. Imai, S. Lim, D. Jiang and Y. Nishida, Scripta Metall. Mater. 36 (1997), p. 611.
[12] T. Mukai, T.G. Nieh, H. Iwasaki and K. Higashi, Mater. Sci. Tech. 14 (1998), p. 32.
[13] ASM International, ASM Hadbook, Vol. 2, Materials Park, Ohio, (1990), p. 516.
[14] J. Pilling and N. Ridley, Superplasticity in crystalline solids, The Institute of Metals, London (1989), p. 65.
[15] O.D. Sherby and J. Wadsworth, Prog. Mater. Sci. 33 (1989), p. 169.
[16] R.S. Mishra, T.R. Bieler and A.K. Mukherjee, Acta Metall. Mater. 43 (1995), p. 877.
[17] R.Z. Valiev, N.A. Krasilnikov and N.K. Tsenev, Mater. Sci. Eng. A137 (1991), p. 35.
[18] S.K. Das, C.F. Chang, D. Raybould, J.F. King and S. Thistlethwaite, Proc. Magnesium Alloys and Their Applicaitons, Ed. by B.L. Mordike and F. Hehmann, DGM Informationsgesellschaft mbH, Oberursel,(1992), p. 487.
[19] M. Mabuchi, H. Iwasaki, K. Yanase and K. Higashi, Scripta Mater. 36 (1997), p. 681.
[20] H. Watanabe, T. Mukai and K. Higashi, Superplasticity and superplastic forming, Ed. by A.K. Ghosh and T.R. Bieler, The Minerals, Metals and Materials Society, Warrendale, (1998), p. 179.
[21] T. Mukai, H. Watanabe, T.G. Nieh and K. Higashi, The 3rd Pacific Rim Intl. Conf. on Advanced Materials and Processing, Ed. by M.A. Imam, R. DeNale, S. Hanada, Z. Zhong and D.N. Lee, The Minerals, Metals and Materials Society, Warrendale, p. 1891 (1998).
[22] H.J. Frost and M.F. Ashby, Deformation-mechanism maps, Pergamon press, Oxford, (1982), p. 44.

Corresponding author: Hiroyuki Watanabe
E-mail : hwata@omtri.city.osaka.jp
FAX : +81-6-6963-8145

Key Engineering Materials Vols. 171-174 (2000) pp. 369-376
© 2000 Trans Tech Publications, Switzerland

High Strain Rate Superplasticity of a ß-Si_3N_4 Whisker Reinforced Pure Aluminum Composite

I. Tochigi[1], T. Imai[2], L. Geng[3] and J. Mao[3]

[1] Kanagawa High-Technology Foundation, Kanagawa Science Park 3-2-1, Sakato Takatsu-ku, Kawasaki 213, Japan

[2] National Industrial Research Institute of Nagoya, 1 Hirate-cho, Kita-ku, Nagoya 462-8510, Japan

[3] Harbin Institute of Technology, Harbin 15000, P.R. China

Keywords: High Strain Rate Superplasticity, ß-Si_3N_4 Whisker, Pure Aluminum Composites

Abstract: β-Si_3N_4 whisker reinforced aluminum composites was fabricated by squeeze casting and an effect of thermomechanical processing and Mg on the High Strain Rate Superplasticity (HSRS) were investigated, The β-Si_3N_4w/Al-0Mg composite produced about 200% elongation at the strain rate of about 0.1 (1/s) and the m value of 0.47 at 903~913K. Theβ-Si_3N_4w/Al-0Mg has the liquid temperature of 913K so that the HSRS could produce without any liquid phases and melting temperature of the β-Si_3N_4/Al-0Mg alloy composites and the optimum temperature of the composite at which maximum total elongation is obtained decreases according to magnesium content, and TEM observation indicates that Theβ-Si_3N_4w/Al-Mg have a fine grain of about 2~3 μm and that the whisker does no react with Mg at the interfaces in the case of theβ-Si_3N_4w/Al-0Mg and theβ-Si_3N_4w/Al-3Mg.

INTRODUCTION

High strain rate superplasticity (HSRS) in ceramic whisker or particulate reinforced aluminum alloy composites is expected to offer an efficiently near-net shape forming technique to automobile, aerospace, and even semi-conductor industries, since the HSRS composites usually exhibit a total elongation of 250-600% at a high strain rate of about 0.1-10 s^{-1} [1-11].

It is thought that primary deformation mechanism of the HSRS is grain boundary sliding since the composites have the fine grain size of 3~0.8μm. The HSRS of the composites usually manifests at above or just below the solid temperature of the matrix and microanalysis of the composites detects segregation of Mg or Cu at interfaces between the aluminum alloys and reinforcements which decreases melting temperature of the matrix near interfaces. Therefore, it is pointed out that an interfacial sliding with a partially liquid phase might contribute to the HSRS as an accommodation mechanism[12-15]. But, deformation mechanism of the HSRS has not yet been understood entirely.

The purpose of this study is to make clear an effect of thermomechanical processing and magnesium on the a HSRS in a β-Si3N4 whisker reinforced 99.99% pure aluminum composite fabricated by squeeze casting. In addition, superplastic deformation mechanism of the composite are also discussed.

EXPERIMENTAL PROCEDURE

The reinforcement materials used was β-Si3N4 whisker which had a diameter of about 1μm and length of 10~30μm The whisker preform was fabricated by a water absorbed method. The β-Si3N4 whiskers contain N:38wt%, O:0.53wt%, Fe:70ppm, Ca:90ppm, Al:20ppm and Y:0.35wt%. The pure aluminum has a chemical composition of Si:2ppm, Fe:10ppm, Cu:1ppm and Al:99.9987 wt%. Amount of magnesium(99.99% purity) to add into pure aluminum were selected to 0, 3 and 4.5wt%(Al-0Mg, Al-3Mg and Al-4.5Mg are expressed, respectively). The preform and the aluminum-Mg matrix were heated up to 1073 K and the mold was kept at 973 K. Then, the molten 99.99% pure aluminum was infiltrated into the β-Si_3N_4 whisker preform under the pressure of about 1000 Pa . The volume fraction of the β-Si3N4 whisker in the composite became Vf=0.30 after the infiltration.

Thermomechanical processing, including extrusion alone and extrusion-hot rolling, were used to produce a fine microstructure. The β-Si_3N_{4w}/Al-0Mg composite before hot rolling was extruded with the extrusion ratio of 100 at 823 K, although in the case of β-Si_3N_{4w}/Al-0Mg, β-Si3N4/Al-3Mg and β-Si3N4/Al-4.5Mg composites extruded only, extrusion temperature selected at 873K which is a little lower than that in the case of extrusion-rolling. Hot rolling was carried out at 913 K. Thickness reduction per pass was less than 0.1 and the reheating time between rolling passes was 5 minutes. The final thickness of the hot-rolled composite was about 0.35~0.75 mm. Tensile specimens with a 3 mm gage width and a 5.5 mm gage length were made in the case of hot-rolling after extrusion processing and in the case of extrusion, a round specimen of 2.5mm gage diameter and 15mm gage length was used. Specimens were pulled at 873-913K and at strain rates ranging from 1×10^{-3} to 1.5 s^{-1}. The microstructure and fracture surface of the samples were examined by TEM and SEM.

RESULTS AND DISCUSSION

SEM microstructure and DSC results

Fig. 1 show the SEM microstructure of the β-Si3N4w/Al-3Mg and β-Si3N4w/Al-4.5Mg composites extruded after squeeze casting. The whiskers are dispersed homogeneously and oriented to extrusion direction.

DSC results indicates that pure Al alone has the liquid temperature of 932.3K(659.3°C) but the liquid temperature of β-Si_3N_{4w}/Al-0Mg extruded at 873K becomes 920.7K(647.7°C) as β-Si3N4 whisker reacts with aluminum so as to create aluminum solid solution and the liquid temperature of β-Si3N4w/Al-3Mg composite extruded are different from that of as-cast β-Si3N4w/Al composites because β-Si3N4 whisker might react with Mg also during being extruded at 873K.

HSRS of the β-Si3N4w/Al-0Mg composite hot-rolled after extrusion

Flow stress (σ) and true strain rate ($\dot{\varepsilon}$) in a superplastic material are related via the equation where K is a constant, and m is the strain rate sensitivity value. The m value of a superplastic material is normally greater than 0.3 because a high m value is expected to suppress neck formation and leads to high tensile elongation. The relationship between the flow stress and the strain rate of

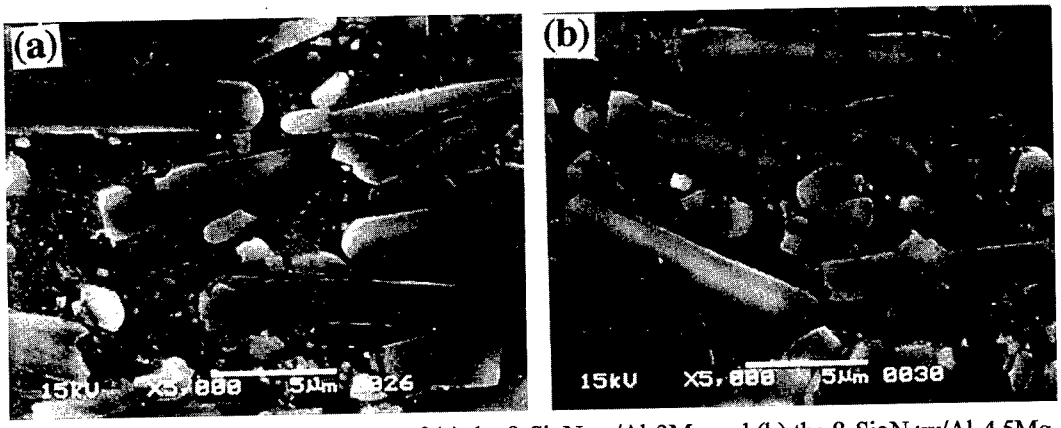

Figs.1 SEM microstructure of (a) the β-Si3N4w/Al-3Mg and (b) the β-Si3N4w/Al-4.5Mg composites extruded only after squeeze casting .

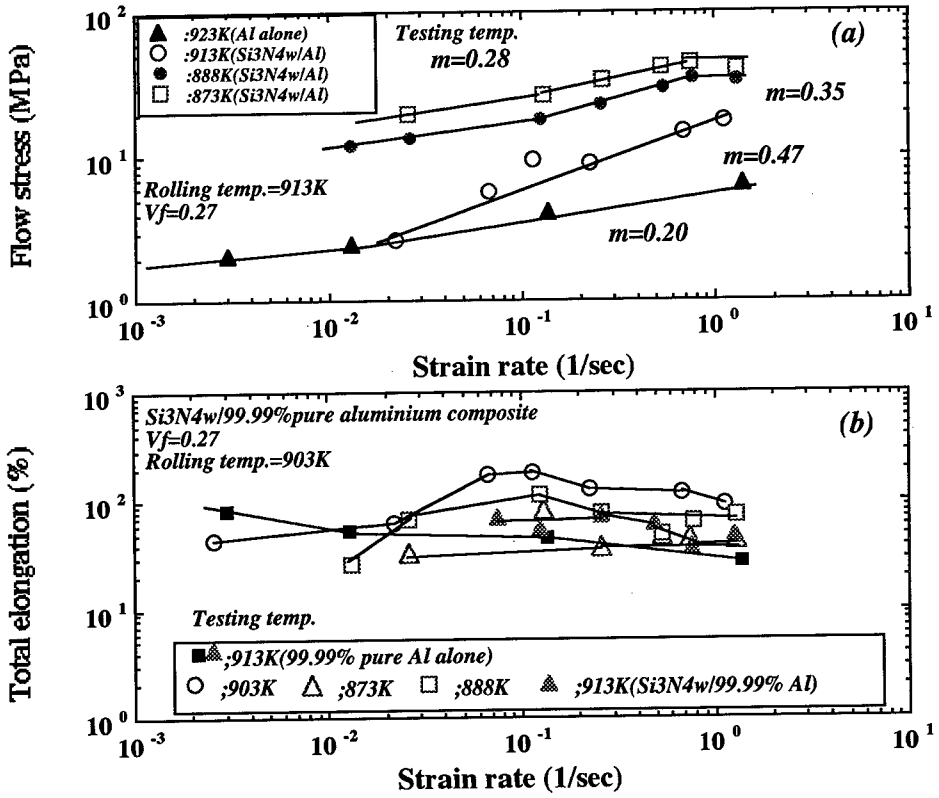

Fig. 2 Superplastic characteristics of the β-Si3N4w/Al-0Mg composite and pure aluminum extruded and hot-rolled

the β-Si3N4w/Al-0Mg composite hot-rolled after extrusion is shown in Fig. 2 as compared with that of pure aluminum alone. Flow stress of the β-Si3N4w/Al-0Mg composite increases with

raising strain rate. The strain rate sensitivity (m value) of the composite pulled at 903K is about 0.47 in strain rate region from 0.02 s^{-1} up to1.5 s^{-1}. And the composite tested at 888K indicates a m value of 0.35 in the strain rate range from 0.1 to 0.8 s^{-1}, but the m value decreases to 0.28 in the same strain rate range in the case of the testing temperature at 873K. On the other hand, a m value of the pure aluminum alone is about 0.2 in the strain rate region from $2x10^{-3}$ up to 1.2 s^{-1}. The results indicate clearly that the β-Si_3N_4w/Al-0Mg composite fabricated by squeeze casting and processed by extrusion and hot-rolling can produce HSRS, although superplasticity does not occur in the pure aluminum alone made by the same processing as that of the composite.

Tensile elongation of the β-Si_3N_4w/Al-0Mg composite and the pure aluminum alone are shown in Fig. 2(b) as a function of strain rate. The maximum tensile elongation of about 200% in the β-Si_3N_4w /Al-0Mg composite was obtained in the strain rate range of $8x10^{-2} \sim 1x10^{-1}$ s^{-1} and at 903K (below liquid temperature). However, when the composite pulled at 888 and 873K, low total elongation of less than 100% is shown. What is important in the β-Si_3N_4w/Al-0Mg composite is that the optimum strain rate at which the maximum total elongation of about 200% is obtained is about 0.1 s^{-1}, which is almost the same as that of β-Si_3N_4w/6061 Al composite [4]. The result indicates that fine grain size is the predominant factor to increase optimum strain rate of superplasticity in the β-Si_3N_4w/Al-0Mg composite. In strain rate range of higher than 0.3 s^{-1}, the elongation value begins to decrease although the m value still keeps more than 0.3 [13]. A total elongation of over 100% is obtained in a wide strain rate region from 0.06 s^{-1} up to 0.7 s^{-1}.

Effect of Mg on HSRS of the β-Si_3N_4w/Al-Mg composites extruded only

Fig 3 shows an effect of testing temperature on total elongations of β-Si_3N_4wAl-0Mg, β-Si_3N_{4w}/Al-3Mg and β-Si_3N_{4w}/Al-4.5Mg composites extruded at 873K. Flow stresses and total elongations of these composites decrease remarkably from solidus temperature of those composites. Fig 4 shows effect of Mg on superplastic characteristics of the β-Si_3N_{4w}/Al-0Mg, β-Si_3N_{4w}/Al-3Mg and β-Si_3N_{4w}/Al-4.5Mg composites. m value of these composites indicates about 0.3 at more than $10^{-2} \sim 10^{-3} s^{-1}$. And total elongation of these composites becomes about 100%, but the β-Si_3N_4w/Al-3Mg shows largest elongation among those composites.

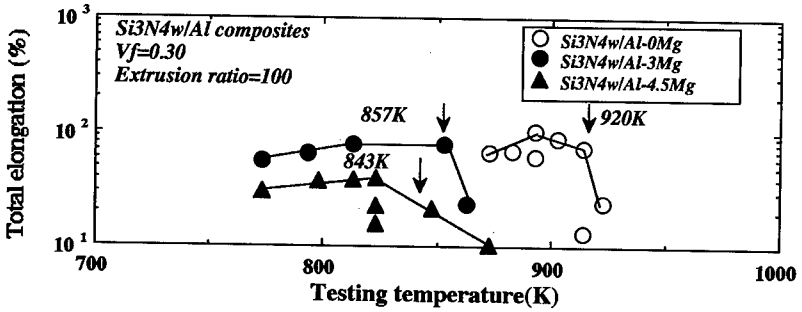

Fig. 3 Relationships between total elongation and strain rate of the β-Si_3N_4w/Al-Mg composites extruded

Several possible deformation processes, including fine grain boundary sliding, interfacial sliding at liquid phase, and dynamic recrystallization, are expected to take place during HSRS. The m value of 0.47 in the composite pulled at 903K indicates that the observed HSRS phenomena occurs predominantly by grain boundary sliding, although 903K is close to the melting temperature of pure aluminium matrix. Melting temperature of the β-Si_3N_{4w}/pure Al composite is 926.3K and that of the pure aluminium alone made by the fabrication processing was 931K. The heat flow of the β-Si_3N_{4w}/pure Al composite decreases at 916.2K. The temperature is called as incipient melting temperature. Incipient melting might indicate that partial liquid phase appears at grain boundaries and at interfaces between pure aluminium matrix and β-Si_3N_4 whiskers. It seems to be possible that β-Si_3N_4 whiskers react with pure aluminium and produce AlN and Al-Si solid solution at interfaces. Al-Si solid solution could decrease melting point at interface of the composite.

Fig.5 shows TEM microstructure of β-Si_3N_{4w}/Al-3Mg(a) and β-Si_3N_{4w}/Al-4.5Mg composites(b). β-Si_3N_{4w} /Al-3Mg has a clean interface by which β-Si_3N_{4w} might not react with Mg. But it is thought that in the case of β-Si_3N_{4w}/Al-4.5Mg, β-Si_3N_4 whisker should react with magnesium during being extruded at 873K so that the total elongation of the composite decrease as compared with those of β-Si_3N_{4w} /Al-0Mg and β-Si_3N_{4w} /Al-3Mg composites.

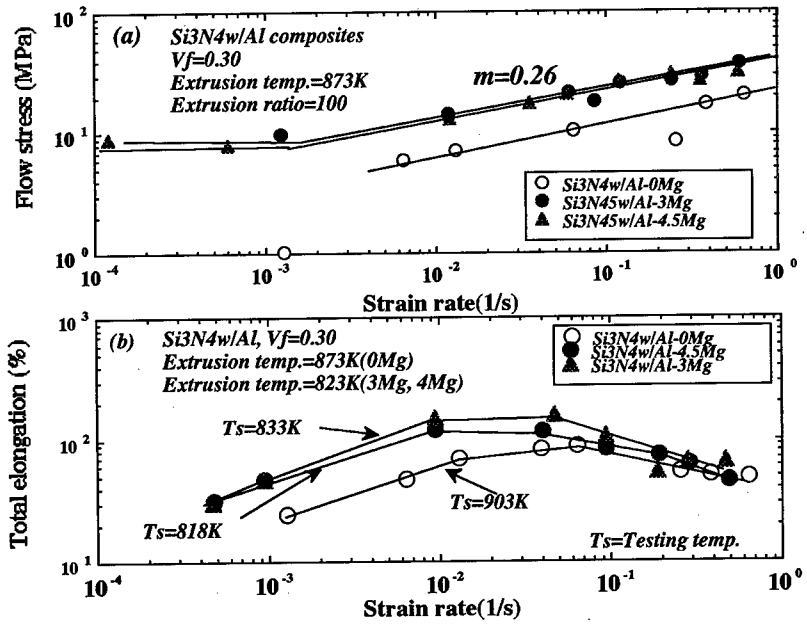

Fig. 4 Superplastic characteristics of the β-Si_3N_{4w}/Al-Mg composites extruded

CONCLUSIONS

Superplastic characteristics of the β-Si_3N_{4w}/Al-0Mg, β-Si_3N_{4w}/Al-3Mg and β-Si_3N_{4w}/Al-4.5Mg composite, fabricated by squeeze casting before hot-rolling after extrusion and extrusion alone, were investigated. The following results were obtained:

(1) The β-Si_3N_{4W}/Al-0Mg composite exhibits a m value (strain rate sensitivity) of about 0.47 and a total elongation of about 200% at the strain rate of 0.1 s^{-1} and at 903K.
(2) The β-Si_3N_{4W} /Al-0Mg composite has a grain size of less than 2 μm
(3) The DSC results indicate that the optimum temperature of 903K at which maximum total elongation of 200% is obtained is below the melting temperature of the β-Si_3N_{4W}/Al-0Mg composite(926.3K).
(4) Τηε β-Si_3N_{4W}/Al-3Mg indicates maximum total elongation as compared with those of the β-Si_3N_4/Al-0Mg and the β-Si_3N_4/Al-4.5Mg composites extruded alone
(5) In the case of β-Si_3N_{4W}/Al-4.5Mg, β-Si_3N_4 whisker reacts with magnesium at the interface so that the composite becomes lowest total elongation less than 100%.

REFERENCES

1. T.G. Nieh, C.A. Henshall and J. Wadsworth, Scripta Metallurgica, 18-12(1984) 1405-1408
2. M.W. Mahoney and A.K. Ghosh, Metall. Trans, 18A (1987) 653-661
3. T. Imai, M.Mabuchi, Y. Tozawa and M. Yamada, J.Materials Science letters, 9 (1990) 255-257
4. M. Mabuchi, T. Imai, K. Kubo, H. Higashi, Y. Okada and T. Tanimura, Materials Letters, 10 (1991) 339-342
5. M. Mabuchi, K. Higashi, Y. Okada, S. Tanimura, T. Imai and K. Kubo, Scripta Metallurgica et Materialia, 25 (1991)2517-2522
6. T. Imai, M. Mabuchi and T. Tozawa, Superplasticity in advanced materials edited by S.Hori,M.Tokizane and N.Furushiro(A Publication of JSRS,1991)373-378
7. T. Tsuzuki and A. Takahashi, Proc. of 1st Japan International SAMPE Symposium (Nov.28-Dec1, 1989)243
8. T.G. Nieh and J. Wadsworth, Superplasticity in Advanced Materials edited by S. Hori, M. Tokizane and N. Furushiro (A Publication of JSRS, 1991), 339-348
9. G. L'Esperance, T. Imai and B.Hong, ibid, 379-384
10. T. Imai, G.L 'Esperance, B. Hong, M. Mabuchi, and Y. Tozawa, Advances in Powder Metallurgy &
Particulate Materials-1992 compiled by J.M. Caus and R.M. German, 9 (1992)181-194
11. T. Imai, G.L 'Esperance & B.D. Hong, Scripta Metall.et Mater., 31-3(1994) 321-326
12. S. Kennerknecht, Fabrication of Particulate Reinforced Metal Composites, Edited by J. Masounave & F.G. Hamel, (1990, Published by ASM International) 87-100.
13. K. Higashi, T. Okada, T. Mukai, S. Tanimura, T.G. Nieh, and J. Wadsworth, in MRS Intl. Meeting on Advanced Materials Vol 7 (IUMRS-ICAM-93, Symp. E, Superplasticity), edited by M. Doyama, S. Somiya, and R.P.H. Chang, Pergamon Press, Netherland (1993). in press
14. T.G. Nieh, J. Wadsworth, and T. Imai, Scripta Metall. Mater., 26 (1992) 551-556.

15. M. Mabuchi, K. Higashi, Y. Okada, S. Tanimura, T. Imai, and K. Kubo, Scripta Metall. Mater. 25 (1991) 2003-2006.

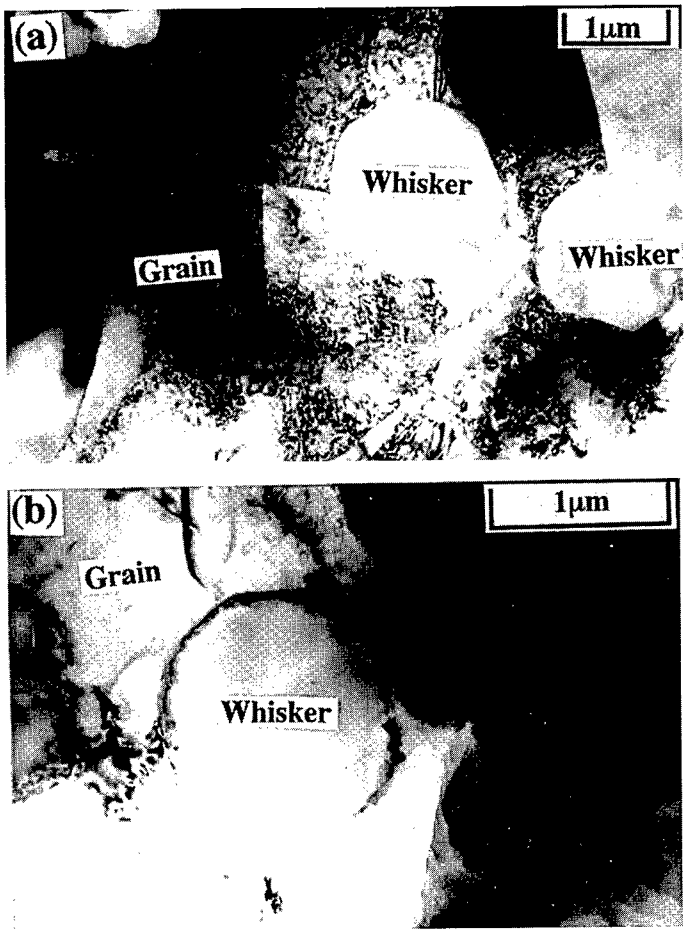

Fig. 5 TEM microstructure of (a)the β-Si_3N_{4w}/Al-3Mg and (b)the β-Si_3N_{4w}/Al-4.5Mg composites

Key Engineering Materials Vols. 171-174 (2000) pp. 377-382
© 2000 Trans Tech Publications, Switzerland

The Effect of Alumina Doping on the Superplastic Characteristics of 3 Y-TZP

K. Sasaki, K. Shimura, J. Mimurada, Y. Ikuhara and T. Sakuma

Department of Materials Science, Faculty of Engineering, University of Tokyo,
7-3-1 Hongo, Bunkyo-ku, Tokyo 113, Japan
E-Mail: sasaki@ceramic.mm.t.u-tokyo.ac.jp

Keywords: Superplasticity, Zirconia, Grain Boundary, Segregation

Abstract

In order to determine the influence of alumina on the superplasticity of yttria stabilized zirconia (YSZ) in the solubility limit of zirconia, 0.4 mol% alumina was doped to 3 mol% yttria stabilized zirconia powders. Improvements for both superplastic flow and elongation to failure were obtained when compared to the undoped samples. TEM analysis, using HREM combined with EDS were carried out on the grain boundary, where no secondary phases were observed at grain boundary triple junctions and on the grain boundary. However both aluminium and yttrium ions were detected at the grain boundary, indicating the segregation of the solute ions over a width of about 6 nm. Aluminium ions were found to segregate to a certain extent to the grain boundary with the rest dissociating in the zirconia matrix.

Introduction

Yttria doped tetragonal zirconia polycrystals (TZP), have the advantage of forming very refined microstructures even at high temperatures, with excellent mechanical properties comparable to metal alloys[1]. It is this refined microstructure that first led to the discovery of superplasticity in yttria doped TZP (Y-TZP) ceramics[2] and has shown elongations of up to 800% at 1550°C in 3 mol % Y-TZP[3]. Control of microstructure and type of dopant addition have since improved the superplastic properties in terms of deformation temperature, flow stress and elongation to failure. Such examples include the addition of 5 wt% silica to 2.5 mol% yttria doped Y-TZP to form a secondary amorphous phase enhancing the strain to failure up to 1038% at 1400°C[4,5]. The addition of 5 wt % TiO_2 to 2.5 Y-TZP[6] and most recently that of 1mol% GeO_2 doped 2.5 Y-TZP[7] gave improved superplastic flow stresses and tensile elongations in single phase zirconias.

The stress-strain rate characteristics of TZP ceramics have been known to be very sensitive to trace impurities, such as silicon and aluminium, present in the powders. Recently Sato et al[8] have analyzed the superplastic properties of 3 Y-TZP and the effect of alumina doping in the range <0.005-0.95 wt% on the stress-strain rate characteristics, which changed quite notably with the alumina content. Sato et al also carried out HREM and EDS analysis, which revealed the absence of any grain boundary phase and the presence of only yttrium segregating at the grain boundary. They concluded that the change in stress exponent was likely caused by the segregation of aluminum ions and the precipitation of alumina after saturation of the grain boundaries. On the other hand Sharif et al[9] have shown the beneficial effects in grain growth repression and reductions in flow stresses in yttria stabilized cubic zirconia by the addition of a secondary alumina phase. These studies have not considered the

possibility of alumina dissolution. Lakiza and Lopato[10] for the alumina-zrconia system the solubility limit of alumina in zirconia is about 3 mol%. It is very likely that addition of alumina within this solubility limit may influence the superplastic characteritics of TZP in a manner similar to germanium and titanium oxide doping. This study focuses on the effect of alumina addition, whether in solution or segregating at the grain boundaries, on the flow stress and elongation. The grain boundary characteristics and composition will also be determined by use of TEM analysis.

Experimental Procedure

3 mol% Y-TZP (3 Y-TZP) powders (average diameter of 25nm), supplied by Tosoh Co. Ltd. and Al_2O_3 powders (average diameter of 0.1μm), supplied by Taimei Chemical Co. Ltd. (TM-DAR) were used as starting materials. 0.4 mol% (0.3 wt%) alumina was added to 3 mol% Y-TZP (3Y-0.4Al) and ball milled in a polyurethane container using ethanol and zirconia balls for 24 hours. The powders were then dried in argon, sieved, pressed into bars at 33 MPa, and then cold isostatically pressed under a pressure of 100 MPa in a rubber tube. The green compacts of both compositions were sintered in air at 1400°C for 2 hours. The density of the sintered bodies was measured by Archimedes method. High temperature tensile tests specimens with an approximate cross section of 2.2×2.2mm^2 and a gage length of 13.4 mm were cut out from the sintered bodies.

The tensile tests (SHIMAZU AG-5000C) were carried out for a temperature range of 1300-1500°C. SEM analysis (JEOL JSM-5200) was undertaken for the as sintered, deformed and failed tensile specimens to find the mean grain size using the linear intercept method. Transmission electron microscope specimens (TEM) were prepared by mechanically grinding the sintered specimens to a thickness of about 0.1 mm. These were further thinned to 50μm using a dimple grinder with 1 μm diamond paste. Further thinning to 10μm for electron transparency was carried out with an ion miller. TEM and high-resolution electron microscopy (HREM) were performed with a Topcon 002BF (200 kV) with a point to point resolution better than 0.18nm. Chemical analysis with EDS (energy dispersive X-ray spectroscopy) was carried out using a Noran Voyager system in the Topcon 002B TEM with a probe size of less than 1nm.

Results

Fig. 1 shows the bright field TEM images of a) 3 Y-TZP and b) 3Y-0.4Al, with average grain sizes of

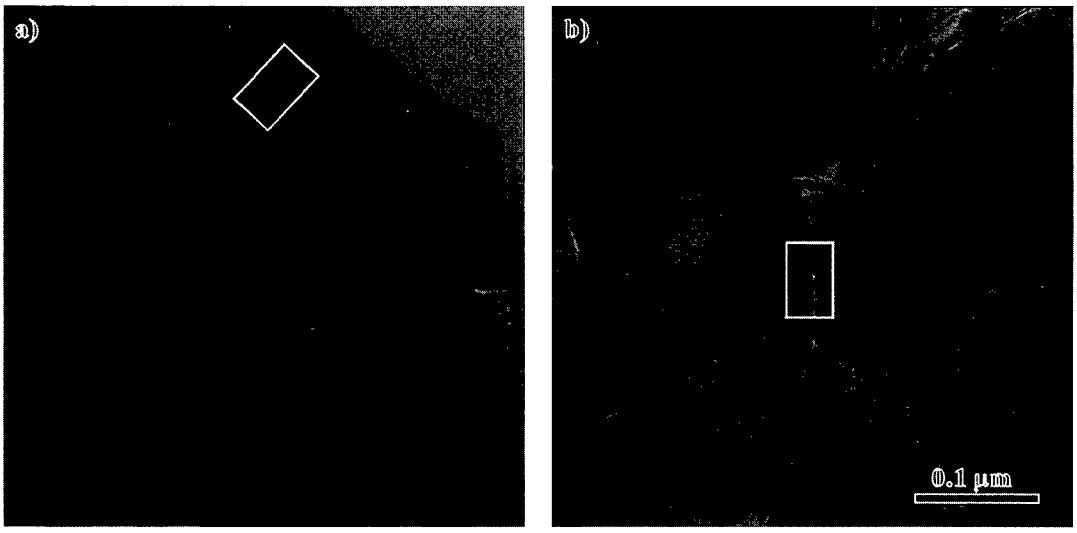

Fig. 1: TEM bright field images of a) 3 mol% Y-TZP and b) 3 mol% Y-TZP doped with 0.4 mol% Al_2O_3

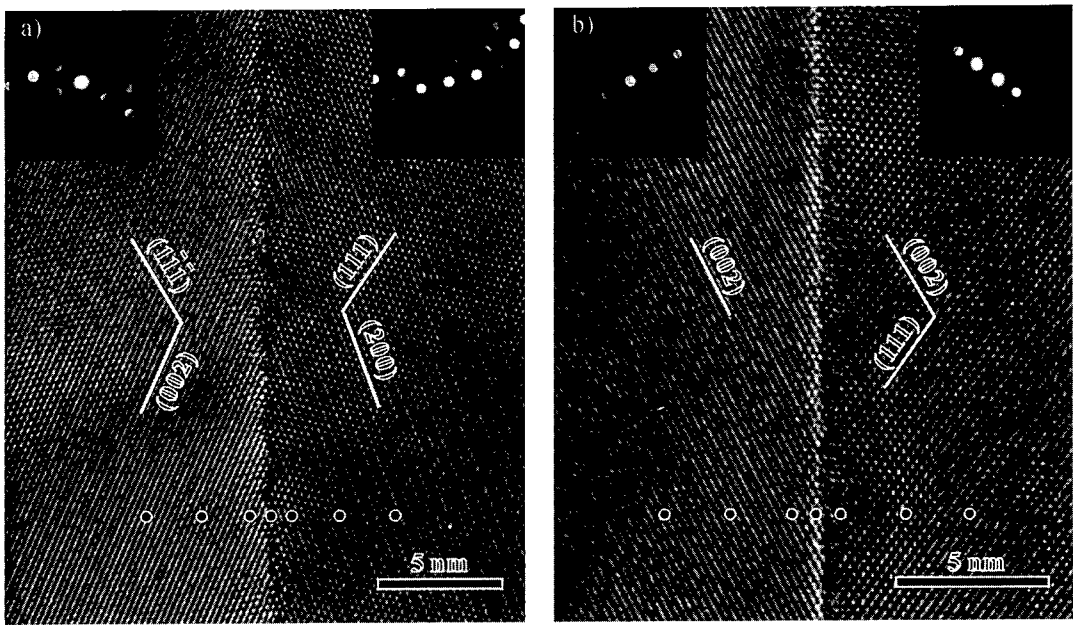

Fig. 2: HREM images of the grain boundaries for a) 3 mol% Y-TZP and b) 3 mol% Y-TZP doped with 0.4 mol% Al_2O_3

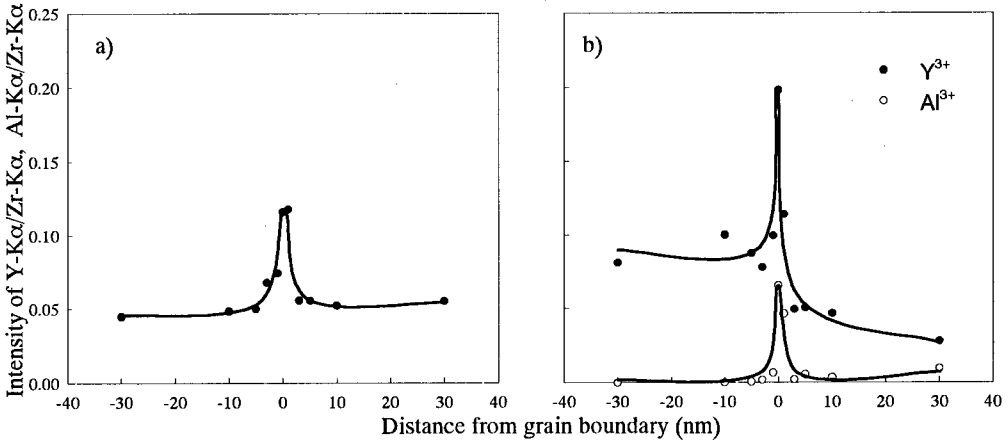

Fig. 3: EDS profiles across the grain boundaries of a) 3 mol% Y-TZP and b) 3 mol% Y-TZP doped with 0.4 mol% Al_2O_3

0.38mm and 0.41mm respectively in the as sintered state. Both compositions were fully dense (>99%) with an equiaxed microstructure and no coarse grains. No secondary phases at grain boundaries and triple junctions were observed. The rectangles depicted in both figures are the areas where HREM and EDS analysis were carried out. Fig. 2 shows the HREM images taken at the grain boundaries for a) 3 Y-TZP and b) 3Y-0.4Al in the as sintered state, together with diffraction patterns of the grains and the areas where EDS analysis was undertaken. No secondary phase is present, clearly showing the intersection of lattice planes at the grain boundary.

EDS spectra were obtained across the grain boundary, along the arrays of circles indicated by Fig. 2.

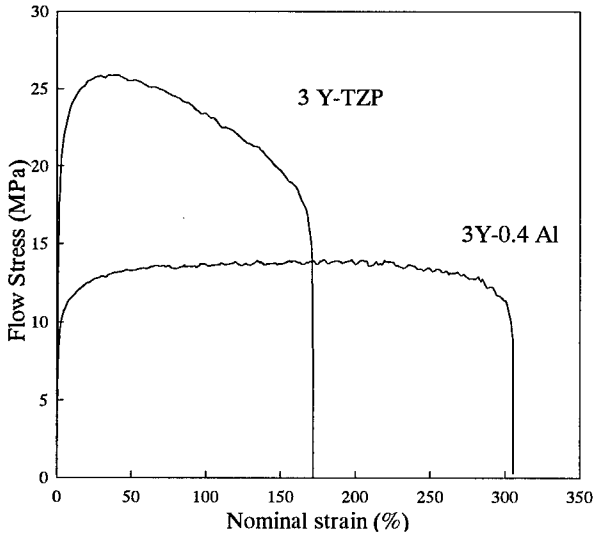

Fig. 4: Stress-strain characteristics of 3 mol% Y-TZP and 3 mol% Y-TZP doped with 0.4 mol% Al_2O_3 at 1400°C (initial strain rate of $1.2\times10^{-4}s^{-1}$)

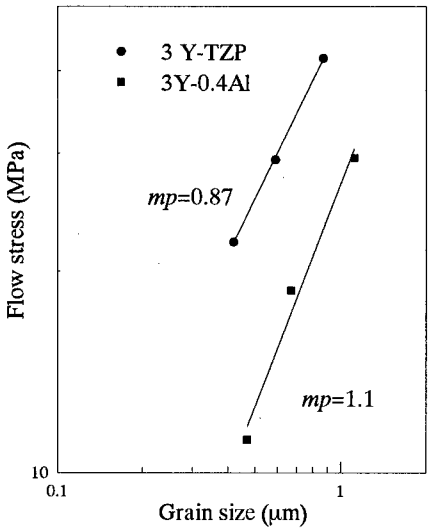

Fig. 5: Flow stress characteristics with respect to grain size (10% true strain) at 1400°C

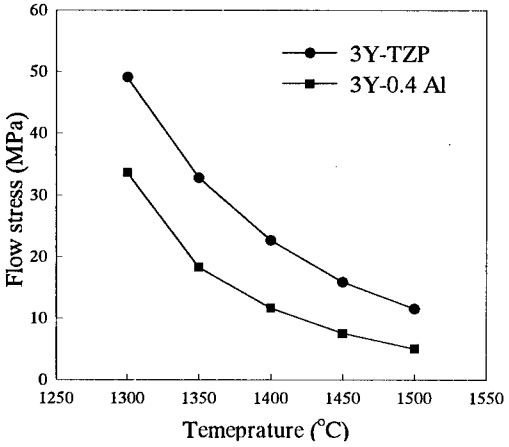

Fig. 6: Flow stresses (10% true strain) with respect to temperature for the two compositions (initial strain rate of $1.2\times10^{-4}s^{-1}$)

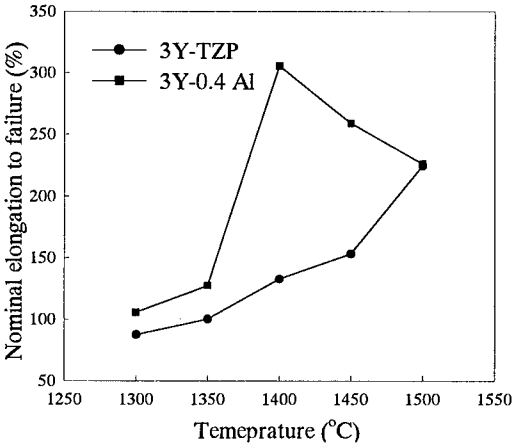

Fig. 7: Elongation to failure with respect to temperature for the two compositions (initial strain rate of $1.2\times10^{-4}s^{-1}$)

using a probe size of 0.5 nm. The intensity ratio profiles across the grain boundary of Y-Kα/Zr-Kα and that of Al-Kα/Zr-Kα are shown in Fig. 3.In both cases the segregation of yttrium ions is evident, spanning a width of 6 nm. In the case of 3Y-0.4Al, aluminium ions also segregate to the grain boundary, again with a thickness of 6 nm.

The stress-strain characteristics of the two compositions with an initial strain rate of $1.2\times10^{-4}s^{-1}$ at 1400°C are shown in Fig. 4. It can be seen that the small addition of alumina was sufficient to reduce the flow stress by more than 10 MPa and more remarkably increases the elongation to failure by more than 150% nominal elongation. The flow stress characteristics with respect to grain size taken at 10%

true strain are shown in Fig. 5. The slopes of the two materials in Fig. 5 are nearly the same, though a reduction in flow stress even for the same grain size is evident.
The flow stresses taken at 10% true strain are presented in Fig. 6 for the two compositions. For both samples the decrease in flow stress with respect to temperature is evident. The sample doped with alumina show lower flow stresses through out the temperature range. Fig. 7 shows the temperature dependence of the elongation to failure for the two compositions. The elongation to failure of 3 Y-TZP increases with temperature up to 225% at 1500°C, while 3Y-0.4Al shows a maximum at 1400°C of 305% after which it decreases with increasing temperature.

Discussion

Improved superplasticity in zirconia has been reported for alumina-composites[8, 11], however the effect of small amounts of alumina, in a single phase tetragonal zirconia has not been fully understood. The solubility and the driving force for segregation of aluminium and yttrium ions in zirconia can be examined in terms of the strain energy caused by solute atoms as proposed by McLean[12]:

$$E_1 = \frac{24\pi KGr_1r_2(r_2 - r_1)^2}{4Gr_1 + 3Kr_2} \quad (1)$$

with K and G the bulk and shear modulus of the matrix respectively and r_1 and r_2 the effective radii of the solvent and solute ions. From the above equation it can be seen that the strain energy is proportional to the square of the misfit value ($\varepsilon = (r_2-r_1)/r_1$). The misfit value of aluminium ions in zirconia is about 0.23 and that of yttrium ions in zirconium is about 0.21. When ε>0.4 segregation will become an important mechanism. For smaller misfit values and if the segregant cation has a valency that is different from the bulk (solvent) cations the formation of charged interfaces becomes an additional force for segregation. It can be seen that in this case both cations will tend to segregate to the grain boundary due to the difference in valency.
Since the detection limit of EDS is about 1 wt % it is very difficult to argue whether aluminium ions are in solution in the zirconia matrix. The average number of atoms per unit volume was estimated from the EDS profiles for a grain boundary thickness of about 6 nm and was found to be 1.73×10^{21} atoms/cm^3 (the cation site density of 3 mol% Y-TZP is 2.97×10^{22} atoms/cm^3). The experimental value can now be compared to the hypothetical case where all the aluminium ions segregate across the grain boundary, 3 nm into the adjacent grains. The grains are treated as simple spheres, having an outer shell with a thickness of 3 nm. The number of atoms present in the grain is found by the following expression:

$$n = \frac{4}{3}\pi\left(\frac{d}{2}\right)^3 \rho_{Y\text{-}TZP}[Al_2O_3]\cdot\frac{N_0}{M} \quad (2)$$

d is the grain size, $\rho_{Y\text{-}TZP}$ the density of 3 mol% Y-TZP, N_0 is Avogadro's constant, $[Al_2O_3]$ the alumina content in weight fraction and M the molecular mass of alumina. Thus the number of atoms per unit volume found near the grain boundary is 5.34×10^{21} atoms/cm^3. These results imply that for this specific grain boundary about a third of the aluminium ions have segregated to the grain boundary over a thickness of 6 nm. The rest of the grain has an aluminium concentration of about 1.63×10^{20} atoms/cm^3, an order of magnitude lower than that found in the grain boundary. Clearly segregation and to a lesser extent dissociation of aluminium ions in zirconia is occurring.
By doping alumina to Y-TZP, elongations to failures were improved when compared to the undoped specimens. This was only achieved at lower temperatures up to 1400°C, where a peak value is observed. Further the decrease in flow stress even for the same grain size indicates an improvement in the diffusive accommodation processes required for superplastic deformation. This trend is consistent with the data reported by Sato et al[9], where an increase in alumina doping resulted in a reduction in stress at the same strain rate. Similar elongation to failure characteristics as a function of temperature have also been reported by Tsurui et al[6] in TZP doped with 5 wt% titania and in 4 and 6 mol% YSZ[11]. Kondo et al[12] phenomenologically interpreted this behavior by considering that the elongation is

determined by the balance between the diffusive accommodation process for grain boundary sliding and grain growth. Thus the type and amount of dopant is thought to influence the diffusive properties which control the accommodation processes and the temperature dependent elongation characteristics (cavity nucleation, growth and fracture).

Small amounts of alumina are known to improve the sinterability of zirconia powders[15] and to affect the ionic conductivity of the grain boundaries, with optimal conditions at 1 wt% alumina[11, 16], for which no major changes are observed in the grain interior. Such results suggest that the diffusivity of oxygen at the grain boundaries is affected by the segregation of aluminium ions, while those of the grain interior are unaffected. The presence of oxygen vacancies is thought to influence the diffusivity of the cations in fluorite structures. From such results it is likely that the grain boundary diffusive (cation) properties may have been altered by the addition of alumina resulting in the improved superplastic properties.

Conclusion

The effect of small amounts of alumina dopants to 3 Y-TZP were examined in terms of its superplastic and grain boundary characteristics:

1. The addition of 0.4 mol% alumina to 3 Y-TZP has improved both flow stresses and elongation to failure for a given temperature range.
2. No amorphous phases at grain boundaries or triple junctions were observed for 3 Y-TZP and 3Y-0.4Al.
3. Both dopant cations were found to segregate to the grain boundaries. Dissociation of yttrium ions is observed, while that of aluminium ions is expected.

Acknowledgemnts

The authors would like to express their gratitude for the financial support of the Ministry of Education, Science and Culture, Japan for Scientific Research B 09555208.

Literature

1. R. C. Garvie, R. H. Hannink and R. T. Pascoe, Nature, vol. 258, 703-704, 1975
2. F. Wakai, S. Sakaguchi and Y. Matsuno, Adv. Ceram. Mater., vol. 1, pp. 259-63, 1986
3. T. G. Nieh and J. Wadsworth, Acta. Metall. Mater., vol. 38, no. 6 pp. 1121-1133, 1990
4. K. Kajihara, Y. Yoshizawa and T. Sakuma, Acta Metall. Mater., vol. 43, no. 3, pp. 1235-1242, 1995
5. Y .Ikuhara, P. Thavorniti and T. Sakuma, Acta Mater., vol. 45, no. 12, pp. 5275-84, 1997
6. K. Tsurui and T. Sakuma, Scripta Mater., vol.4, no. 3, pp. 443-447, 1996
7. J. Mimurada, T. Kondo, Y. Takigawa, Y. Ikuhara and T. Sakuma, Mat. Sci. Forum, vols.304-306, pp. 543-548, 1999
8. A. A. Sharif, P. H. Imamura and M. L. Mecartney, Mater. Sci. Forum, vols. 304-306, 1999, pp. 443-450
9. E. Sato, H. Morioka, K. Kuribayashi and D. Sundaraman, Mater. Sci. Forum, vols. 304-306 (1999), pp. 459-464
10. S. M. Lakiza and L. M. Lopato, J. Am. Ceram. Soc. vol. 80, no. 4, pp. 898-902, 1997
11. K. Yamana, S. Nakamura, T. Yoshimura, K. Ina and W. Weppner, Solid State Ionics, no. 53-56, pp. 763-768, 1992
12. D. McLean, *Grain Boundaries in Metals*, Clarendon Press, Oxford, 1957
13. K. Sasaki, T. Kondo, Y. Ikuhara and T. Sakuma, Proceedings of the Third Pacific Rim Conference on Advanced Materials and Processing (PRICM 3), 12-17 July 1998, pp. 1819-1824
14. T. Kondo, Y. Takigawa and T. Sakuma, Mater. Sci. and Eng., A231 (19997) 163-169
15. M. J. Verkerk, A. J. A. Winnbust and A. J. Burgraaf, J. Mat. Sci., vol 17, 3113-22, 1982
16. M. Mori, M. Yoshikawa, H. Itoh and T. Abe, J. Am. Ceram. Soc., vol. 77, no. 8, pp. 2217-19, 1994

Key Engineering Materials Vols. 171-174 (2000) pp. 383-388
© 2000 Trans Tech Publications, Switzerland

Grain Boundary Analysis and Superplastic Characteristics in GeO_2-Doped TZP

J. Mimurada[1,2], K. Sasaki[1,2], Y. Ikuhara[1] and T. Sakuma[1]

[1] Department of Materials Science, Faculty of Engineering, The University of Tokyo, 7-3-1 Hongo Bunkyo-ku, Tokyo 113-8656 Japan

[2] Graduate student

Keywords: Grain Boundary, EDS, Superplasticity, TZP, Dopant

Abstract

TEM observations in TZP-1Ge were conducted, which has improved superplasticity when compared to 2.5Y-TZP. The TEM analysis consisted of high resolution electron microscopy (HREM) and energy dispersive X-ray spectroscopy (EDS) applied to grain boundaries in TZP-1Ge. HREM image revealed that there are no amorphous phases at multiple junctions or at grain boundaries. EDS profiles taken from the grain boundaries in TZP-1Ge show the segregation of Ge^{4+} at the boundaries. This segregation of Ge^{4+} is considered to be caused by the relaxation in strain energy. Consequently, the flow stress reduction in TZP-1Ge results from the enhanced diffusivity which controls the superplastic deformation by the presence of Ge^{4+} in zirconia. The comparison of the flow stress in Si^{4+}, Ge^{4+} or Ti^{4+} doped Y-TZP suggests that the dopants existing inside zirconia grains affect the flow stress.

Introduction

Superplasticity is obtained in Y-TZP (Yttria-stabilized Tetragonal Zirconia Polycrystals) which has a refined grain structure and grain-size stability at high-temperature tensile test [1-4]. Improvement of superplastic properties is desirable for practical use and many researchers have reported as to improved properties in Y-TZP by means of adding suitable dopants [5-10]. However, the relationship between the properties of dopant and the effects on the superplastic behavior has not been clearly understood yet.

High resolution electron microscopy (HREM) and energy dispersive X-ray spectroscopy (EDS) are the ideal techniques for investigating sub-nanoscale structure and compositional fluctuation[11-13]. The objective of this study is to discuss the relationship between the mechanical properties such as flow stress or ductility and the phenomena on an atomic scale such as diffusion, segregation or bonding state.

Experimental Procedures

The chemical composition of the material prepared in the present study was ZrO_2-2.5 mol%Y_2O_3-1.0 mol% GeO_2 (TZP-1Ge). ZrO_2 powders (Tosoh Inc., TZ-2.5Y) were mixed with the suitable amount of GeO_2 powders (Rare Metallic, 6N) by ball-milling method for 24 hours and dried in Ar atmosphere. Subsequently the powders were uniaxially pressed under a pressure of 33 MPa and then cold-isostatically pressed (CIP) at 100 MPa. The green bodies of TZP-1Ge were sintered for 2 hours in air at 1300℃. This material is thought to be a tetragonal zirconia solid solution under the current sintering condition as reported in our previous study. Specimens for TEM observation were prepared by using standard techniques. Specimens were mechanically ground to a thickness of 0.1 mm, followed by dimpling to a thickness of 10 μm. Consequently, they were thinned to electron transparency by ion milling method at 3-4 kV. The samples were examined by high resolution electron microscopy, HERM, and energy dispersive X-ray spectroscopy, EDS, with a Topcon 002BF (200kV) field emission type high resolution microscope which has a point to point resolution of about 0.17 nm. EDS analyses were performed in the Topcon 002BF by using Noran Voyager system which possesses probe size of about 0.5 nm.

Results

(1) Improvement of superplastic behavior in TZP-1Ge

Superplasticity in TZP is enhanced by the addition of 1 mol% GeO_2 [9]. Figure 1 is the temperature dependence of 10% flow stress and nominal elongation to failure of both materials, 2.5Y TZP [7] and TZP-1Ge. The flow stress of TZP-1Ge is much lower than that of 2.5Y-TZP. This indicates that the 1mol% GeO_2 addition into 2.5Y-TZP effectively reduces the flow stress. Furthermore, Fig. 1 shows the enhanced elongation in TZP-1Ge within the temperature range. To discuss the effect of GeO_2 addition on superplastic behavior, it is necessary to determine the state of GeO_2 by the following investigation.

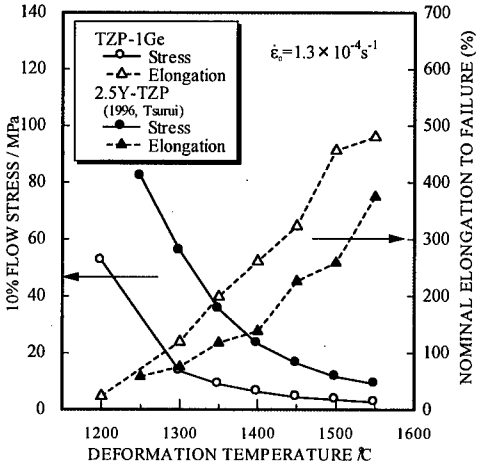

Fig. 1 Temperature dependence of flow stress and elongation to failure in TZP-1Ge and 2.5Y-TZP [7].

(2) Grain boundary structure in TZP-1Ge

Figure 2 is the TEM photograph of TZP-1Ge. The samples observed are in the as-sintered state. This figure has three photographs. The left photograph of the figure, a), shows a typical HREM image of the grain boundary with the lattice planes, diffraction patterns, and where EDS analysis was carried out (the spots correspond to the size of the nano beam). The upper right photograph of the figure is the magnified grain boundary image within an area indicated by the white rectangle in the left HREM image. Lower right photograph is low-magnification bright-field TEM image of the grains and the boundary investigated. The samples were fully dense having more than 99% of relative density and the average grain size is about 0.4μm. As seen in Fig. 2 c), the grains are facetted with straight boundaries and sharp triple junctions indicating that there are no amorphous pools at multiple junctions. Figure 2 a) is the image of the $<1\bar{1}0>\Sigma11$ boundary with a tilt angle of 51° . The magnified image of the boundary in Fig. 2 b) shows coincidence site lattice (CSL) boundary and no amorphous phase was observed in the boundary. TEM analysis was performed on the other boundary and grains directly connected to each other at the boundary without any amorphous phase.

(3) Grain boundary EDS analysis in TZP-1Ge

Figure 3 is the EDS profile of TZP-1Ge that was taken from the boundary with the electron probe size of about 0.5 nm indicated by the white circles in Fig. 2 a). The profile was obtained by normalizing the X-ray intensity for each element using the intensity of Zr-Kα peak. The intensities of Y and Ge taken from grain interior were not so different from the expected values from the composition of Y and Ge as zirconia solid solution. On the other hand, these elements segregate to the grain boundary. The intensity of Ge at the boundary is about 4 times larger than that in grain interior (the enrichment factor of Ge is about 4), whereas the amplitude of the intensity of Y was about 2.5. In addition, we carried out EDS analysis in another boundary and also observed the segregation of Ge at boundary and the enrichment factor was 4.

Table 1 Ionic radii [16] and misfit values of cations

Cation	Zr^{4+}	Y^{3+}	Ge^{4+}
ionic radius (Å)	0.84	1.02	0.68
misfit value, ε	-	0.21	0.19

In oxide ceramics, segregation of solute ions in boundaries has two effects: one is the strain energy relaxation and the other is the electronic charge compensation[14]. McLean has proposed an evaluation of the

strain energy due to the size mismatch between matrix and solute ions[15]. The energy, W, is expressed as follows.

$$W = \frac{24\pi K G r_1 (r_1 - r_2)^2}{[3K + 4G(r_1 / r_2)]}, \quad (1)$$

where K is the bulk modulus of the solute, G is the shear modulus of the solvent, r_1 and r_2 are the ionic radii of solvent and solute ions. The strain energy caused by the solute ions is proportional to the square of the size mismatch or misfit value, ε, expressed as $\varepsilon = (r_1 - r_2)/r_1$. The ionic radii[16] and misfit values of Y^{3+} and Ge^{4+}

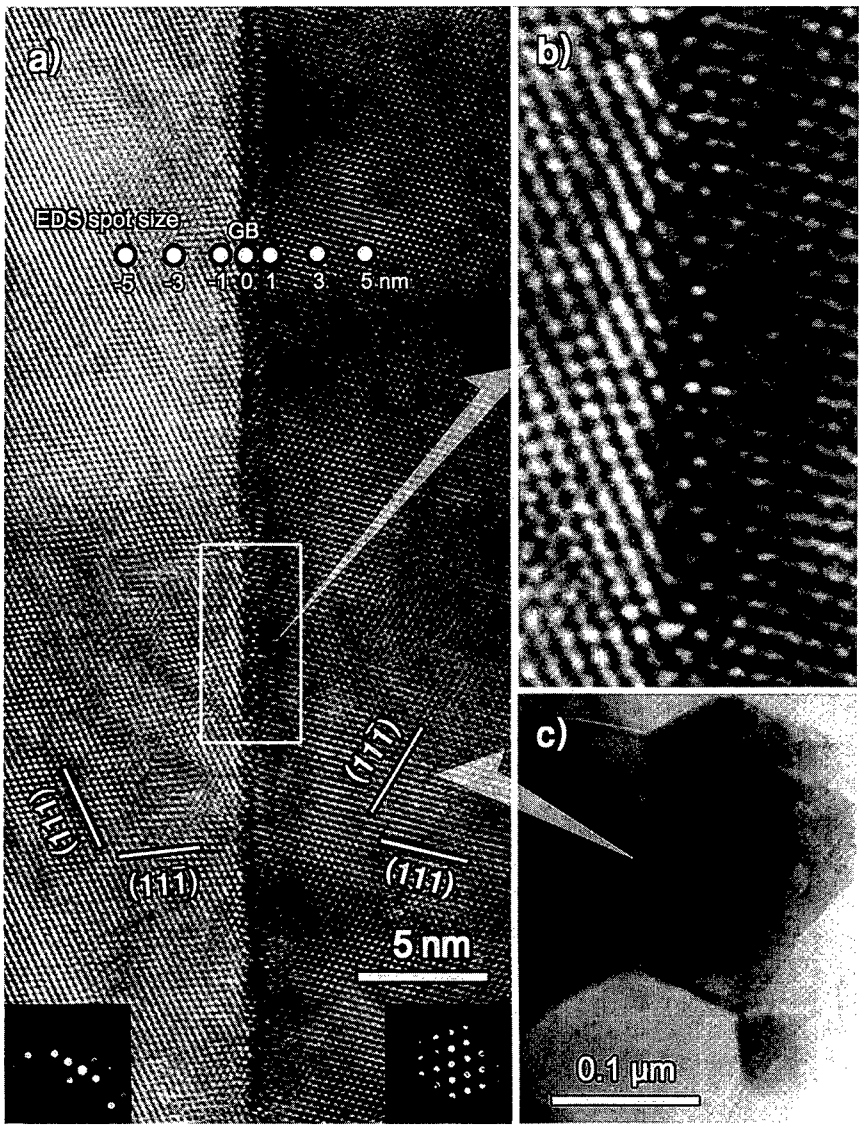

Fig. 2 a) the HREM image of the Σ1 1 boundary in TZP-1Ge, b) the magnified boundary image, c) low magnification TEM image in the vicinity of the boundary.

are summarized in Table 1. When the segregating solute ion has the misfit value of more than 0.4, the strain energy relaxation is dominant and the effect of the electronic charge compensation is negligible. Although Ge^{4+} has a value of 0.19, the strain energy relaxation is the only reason for segregation, because the solvent ion, Zr^{4+}, and Ge^{4+} have same valency. On the other hand, these two effects are taken into account in the case of Y^{3+}. This must be the reason for the difference in the EDS profiles of Ge and Y.

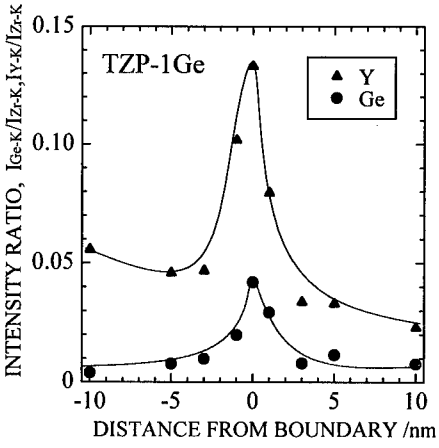

Fig. 3 The EDS intensity profiles of Y and Ge in the boundary.

Discussion

(1) The effect of dopants on the flow stress

Solid solubility of GeO_2 into Y-TZP has been reported to be about 4 mol% [18], and it is adequate to think TZP-1Ge as a t-ZrO_2 solid solution, as reported in our previous study [9]. In this study, we observed the segregation of Ge ions at grain boundaries in TZP-1Ge by EDS analysis. In addition, HREM observation revealed the structures of grain boundaries and multiple junctions. There were no amorphous pools at multiple junctions and amorphous layers in grain boundaries. Hence, we conclude that Ge ions doped into 2.5Y-TZP exist in the ZrO_2 solid solution and also segregate at grain boundaries.

At first, we should compare the superplastic behavior of TZP-1Ge with 2.5Y-TZP because both materials have the same structure without glass pool and amorphous layers at boundaries, and they are thought to deform by a similar mechanism. As illustrated in Fig. 4, the stress in TZP-1Ge is much lower than that in 2.5Y-TZP. Although this reduction must be due to the enhancement of diffusivity that controls the deformation, it is difficult to determine which state of Ge, solid solution or segregation, influences the flow stress by comparing these two materials. Due to these reasons, we are going to take the effect of two more tetravalent dopants, Ti^{4+} and Si^{4+}, into consideration in addition to Ge^{4+}. The amount of additives for each material is TZP-5wt%TiO_2 [7] and TZP-5wt%SiO_2 [5]. The solid solubility of TiO_2 into Y-TZP is about 15mol%, while the solubility of SiO_2 is almost negligible and SiO_2 forms glass pool at multiple junctions as seen in TZP-5wt% SiO_2. Besides, Si segregates at ZrO_2 grain boundaries without forming secondary phase. The profile of Si is shown in Fig. 5. SiO_2 addition is less effective for decreasing the flow stress than TiO_2 and GeO_2 addition when compared with the same grain size as clearly indicated in Fig. 4. On the other hand, 5wt% (7.7mol%) TiO_2 addition attains almost the equal reduction in flow stress to 1mol% GeO_2. TZP-5wt%TiO_2 consists of t-ZrO_2 solid solution and Ti ions segregate at boundaries [19]. Thus, the reduction in TZP-5wt%TiO_2 would be made in the same way as TZP-1Ge by the enhancement of diffusion processes that control deformation. However, GeO_2 is more effective on this process than TiO_2 for the same amount of addition.

The above comparison brings further questions. One is "What is the cause for difference in stress reduction in Ge and Ti addition?", and the other is " Why Si is much less effective?". There are two possible explanations for these questions.

The former is an assumption that the element in ZrO_2 solid solution affects the flow stress. In other words, superplastic

Table 2 Ionic radii [16] and misfit values of cations

Cation	Si^{4+}	Ge^{4+}	Ti^{4+}	Zr^{4+}
ionic radius (Å)	0.40	0.68	0.74	0.84
misfit value, ε	0.52	0.19	0.12	-

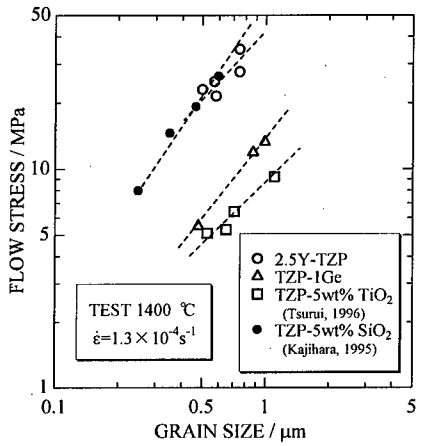

Fig. 4 A log-log plot of 10% flow stress as a function of grain size at 1400℃ at a strain rate of $1.3\times10^{-4}s^{-1}$ in each material[5,7,9].

deformation in Y-TZP is controlled by the lattice diffusion of ions. From this point of view, the poor effect of Si on flow stress is understood by its solubility. Table 2 shows the ionic radii and misfit values of the tetravalent cations. In the table, Ge^{4+} has a larger value of 0.19 than that of 0.12 for Ti^{4+}, which would lead to the difference in their solid solubility into Y-TZP. In terms of the strain energy, *W*, expressed by eq. (1), distortion by the presence of the element becomes large for larger misfit values. This may be connected with the different effect on diffusivity of these elements, Ge^{4+} and Ti^{4+}. It can also explain the poor effect of Si addition from its limit of solubility into ZrO_2.

Besides, another interpretation for the phenomena is also possible. The latter assumption is that the element segregating at grain boundaries does have the effect on the flow stress. From this point of view, the composition of the material is not so significant, but the content at grain boundaries is really important. Though precise quantification of segregants is still difficult for the time being, the contents of Ge and Si ion at grain boundary cannot explain the difference in their effect. Then, it requests the reason for the nature of the element itself, which is difficult just by comparing the ionic radius or valency.

There are some kind of clues that should be taken into account. First is the effect of these elements on the grain growth behavior of Y-TZP. It was reported that GeO_2 or TiO_2 addition enhances the grain growth while TZP-5wt%SiO_2 does not exhibit the enhancement [5,7,9]. The tendency of grain growth is similar to that of stress reduction. Chen and Chen suggested that the small amount of dopant addition such as the case in this study affects the grain growth of ZrO_2 grain by way of Zr lattice diffusion [20]. It may indicate that the diffusion of deformation process and that of grain growth are identical. Tsurui *et al.* reported the decrease in flow stress and activation energy for deformation by TiO_2 addition with increasing the amount of TiO_2 at least until 10wt% (15mol%) TiO_2 that is the largest TiO_2 content examined. These results suggest that the deformation process controlled by lattice diffusion. If the relationship is not proportional between the content of Ti in ZrO_2 grains that is thought to be the same as TiO_2 content within the solubility limit and the content of Ti segregation at boundaries, the origin of stress reduction might be revealed by this comparison because Ti segregation is expected to saturate at a certain amount of TiO_2 addition in contrast to the increase of TiO_2 in ZrO_2 until the solid solubility of 15mol%. It is also expected for GeO_2 addition to decrease the flow stress until about its solubility of about 4%.

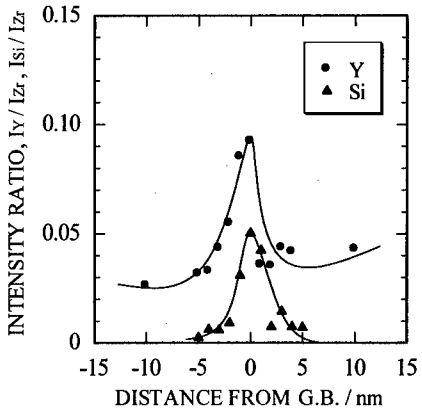

Fig. 5 The EDS intensity profiles of Y and Si in the boundary.

Conclusion

The TEM analysis revealed that the following conclusions.

1. Ge ions segregate in the grain boundaries of zirconia grains. The amount of Ge in the boundaries are estimated to be about 4 times larger than that in zirconia matrix.
2. The stress reduction in TZP-1Ge is attained by the enhanced diffusion by the Ge addtion.
3. The compassion of the dopant effect on flow stress suggests the possibility that the diffusion controlling the deformation process is affected by the dissolved cations into zirconia grains.

Acknowledgement

The authors would like to express their gratitude for Scientific Research B 09555208 from the Ministry of Education, Science and Culture, Japan.

Reference

[1] F. Wakai, S. Sakaguchi and Y. Matsuno, *Adv. Ceram. Mater.*, **1** (1986) 259.

[2] T. Sakuma, *Proc. 1st Pacific Rim. Int. Conf. on Advanced Materials and Processing*, Ed. by C. Shi, H. Li and A. Scott, TMS, Warrendale (1992) 881.

[3] T. G. Nieh, C. M. McNally and J. Wadsworth, *Sci. Metall.*, **22** (1988) 1297.

[4] A. D. Rodriguez, A. B. Leon, J. D. Ye and M. J. Melendo, *Mater. Sci. Eng.*, **A247** (1998) 97.

[5] K. Kajihara, Y. Yoshizawa and T. Sakuma, *Acta Metall Mater.*, **43** (1995) 1235.

[6] Y. Ikuhara, P. Thavorniti and T. Sakuma, *Actya Mater.*, **45** (1997) 5275.

[7] K. Tsurui and T. Sakuma, *Scr. Mater.*, **34** (1996) 443.

[8] T. Kondo, Y. Takigawa ant T. Sakuma, *Mater. Sci. Eng.*, **A231** (1997) 163.

[9] J. Mimurada, T. Kondo, Y. Takigawa, Y. Ikuhara and T. Sakuma, *Mater. Sci. Forum*, **304-306** (1999) 543.

[10] M. Oka, N. Tabuchi and T. Takashi, *Mater. Sci. Forum*, **304-306** (1999) 451.

[11] T. G. Nieh, D. Y. Yaney and J. Wadworth, *Scripta metall.*, **23** (1989) 2007.

[12] M. M. R. Boutz, C. S. Chen, A. J. Winnubst and A.J. Burggraaf, *J. Am. Ceram. Soc.*, **77** (1994) 2634.

[13] S. Primdahl, A. Tholen and T. G. Langdon, *Acta metall. mater.*, **43** (1995) 1211.

[14] A. J. Buggraaf and A. J. Winnubst, in J. Nowotny and L. C. Dufour (eds.), *Surface and Near-Surface Chemistry of Oxide Materials*, Elsevier Science Publishers, (1988) 449.

[15] D. McLean, *Grain boundaries in Metals*, Oxford University Press, 1957.

[16] R. D. Shannon, *Acta Crystallogr.*, **A32** (1974) 754.

[17] W. C. Butterman and W. R. Foster, *Am. Mineralogist*, **52** (1967) 884.

[18] D. J. Kim, J. W. Jang, H. J. Jung, J. W. Huh and I. S. Yang, *J. Mater. Sci. Letters.*, **14** (1995)1007.

[19] G. S. A. M. Theunissen, A. J. A. Winnubst and A. J. Burggraaf, *Mater. Sci. Eng.*, **27** (1992) 5057.

[20] P-L. Chen and I-W. Chen, *J. Am. Ceram. Soc.*, 77 [9] (1994) 2289.

Key Engineering Materials Vols. 171-174 (2000) pp. 389-394
© 2000 Trans Tech Publications, Switzerland

Characterization and Mechanical Properties of a δ/γ Duplex Stainless Steel

J.A. Jiménez[1], M. Carsi[1], G. Frommeyer[2] and O.A. Ruano[1]

[1] Department of Physical Metallurgy, Centro Nacional de Investigaciones Metalúrgicas, C.S.I.C., Avda. de Gregorio del Amo 8, ES-28040 Madrid, Spain

[2] Max Planck Institut für Eisenforschung, Max-Planck Strasse 1, DE-40237 Düsseldorf, Germany

Keywords: High Temperature Creep, Duplex Stainless Steel, Texture, Grain Boundary Sliding

Abstract

The mechanical behavior at high temperature of a duplex stainless steel was investigated by means of strain-rate-change tests in tension. Analysis of the stress-strain rate data revealed a change in the behavior of the material at about 950°C which is attributed to the presence of the σ phase. However, stress exponents of about 5 and 2 were observed at strain rates above and below 10^{-3} s^{-1} respectively, at all testing temperatures. These results suggest a change in the mechanism controlling deformation from slip creep to grain boundary sliding, GBS, as the strain rate decreases. Contribution of GBS to deformation was associated with the fine microstructure developed by recrystallization before testing. This microstructure consisted of colonies of austenite grains of 10 to 15 μm in size surrounded by a ferrite matrix at testing temperatures above 1000°C or by a lamellar microstructure below 950°C. Superplastic behavior of the material at low stresses, where $n \approx 2$, was checked by monotonic strain rate tests at 900 and 1050°C at 10^{-4} s^{-1}. The importance of GBS in this case was corroborated by analysis of the microstructure and the texture in the gage region. The grains of the present phases are intermixed after testing in the superplastic regime. This is due to grain rearrangement occurred during deformation by grain boundary sliding. On the other hand, only minor changes in the texture along the most important fibers (θ-fiber and α-fiber for the ferrite and the ζ-fiber for the austenite) were observed between the undeformed grip region and the gage region.

Introduction

Duplex stainless steels have been used in many diverse fields like ship construction or chemical industry. The large applications of these steels are related to their excellent resistance to corrosion and stress-corrosion, as well as a high strength combined with high toughness [1,2]. The good mechanical properties of these steels are due to the duplex structure of ferrite (δ) and austenite (γ): in one part the ferrite is responsible of the strength, and in the other, the austenite ensures the toughness of the material [3]. However, the embrittlement due to the precipitation of σ phase during the production process is an extremely large problem from the practical point of view [3-4].

The poor workability at low temperature can be avoid using superplastic forming technology. The existence of superplasticity in duplex phase stainless steels has been known for many years [5]. As a fine-grained microstructure is the most important microstructural feature of superplastic materials, it is to be expected that superplastic tendencies would be enhanced by those processing steps which provides the finest microstructures stable at the deformation temperature [6]. Several distinct thermomechanical processing techniques have been used in order to develop a superplastic

microstructure in duplex stainless steels. Such process consists conventionally in hot rolling of the material in the temperature range of 1100-1300°C followed by cold rolling to 50% reduction [7]. Elongations greater than 1000% have been reported in duplex steel after such process for deformation temperatures of 900°C-1100°C [8-11].

This investigation is aimed at determination of deformation conditions under which a commercial duplex stainless shows superplastic behavior. It includes also a detailed microstructural characterization, including texture, of the changes ocurring during deformation to elucidate the mechanisms that take place during deformation.

Experimental procedure

The duplex stainless steel used in this study has the nominal composition (in weight %) Fe- 22.5 Cr-6.0 Ni- 3.0 Mo- 0.6 Si- 1.4 Mn. This material was supplied by Sumitomo Metal Industries Ltd., Japan, as a sheet of 3 mm in thickness prepared by hot forging ingots and further cold rolling deformation of about 50%.

In order to follow the microstructural evolution during deformation, the material was characterized in the as-received condition and after tensile tests in the temperature range 850 to 1100°C. The phases present were identified by X-ray diffraction using Cu K_α radiation. Microstructural observations were conducted using optical microscopy. The microstructure was developed by etching the polished samples with a solution of 15 ml HNO_3 and 30 ml HCl on the δ-ferrite/austenite duplex microstructure and with a solution of 0.5 g of $K_2S_2O_5$, 10 ml of HCl and 50 ml H_2O when the σ phase was present.

Texture measurements were carried out by means of the Schulz reflection method in the as-received material and after deformation at 1050°C. Overlapping of diffraction peaks of the σ phase with some of the peaks of the δ and γ phase did not allow to extend this analysis to the samples tested at temperatures below 950°C. Details of the diffractometer used and the analysis methods are given elsewhere [12]. The orientation distribution function, ODF, not only allows determination of the different texture components, but also calculation of the volume fraction, F_v, associated with each one. In this work, F_v was calculated by a numerical integration method from the ODF intensity data [13]. As integration limits for this calculation, orientations 10° apart from the ideal orientation have been considered to belong to a given fiber.

Mechanical behavior at high temperature was characterized by tensile tests. Tensile samples with a rectangular cross section of 3 x 5 mm and a gage length of 20 mm were machined parallel to the rolling direction. Tensile-strain-rate-change tests were performed at strain rates ranging from 3 x 10^{-6} to 2 x 10^{-3} s^{-1} in the temperature range 850 to 1100°C under a protective argon atmosphere. Superplastic behavior of the material was characterized by monotonic tensile tests at 10^{-4} s^{-1} at 900 and 1050°C.

Results and discussion

Figure 1 shows the result of strain-rate-change tests at high temperatures where the steady state strain rate, $\dot{\varepsilon}$, is plotted against the Young's modulus compensated flow stress, σ/E, in a log-log scale. The values for the Young's modulus at the various temperatures were extrapolated from data measured for a duplex stainless steel with a similar composition [14]. In this plot, the slope of the curves corresponds to the stress exponent, n. At all testing temperatures, Figure 1 shows stress exponents of about 5 and 2 at strain rates above and below 10^{-3} s^{-1} respectively. Furthermore, a change in the behavior of the material can be observed at about 950°C since the data points for this

temperature and at 1000°C almost coincide. This is attributed to the presence of the σ phase, a hard phase, at testing temperatures below 950°C as confirmed by X-ray diffraction.

A stress exponent of about 5 indicates that slip creep is the dominant deformation mechanism at high strain rates. However, low values of n, of about 2-3, are observed at low strain rates. Since the steel is characterized by a fine grain size after recrystallization during heating at testing temperature, the dominant deformation mechanism must correspond to grain boundary sliding, GBS, as is commonly accepted. This is corroborated by the results obtained from two elongation-to-failure tests that were conducted at two temperatures at a strain rate, 10^{-4} s^{-1}, where n was about 2. The temperatures elected, 900 and 1050°C, corresponded to deformation in the three phase and the two phase regions respectively. Elongations to failure of 190 and 275% where obtained at 900 and 1050°C respectively. These high values are typical of superplastic materials where flow is controlled by GBS.

The activation energy for plastic flow, Q_c, was calculated from the data given in Fig. 1. Two different values of Q_c were obtained as a function of the temperature range. At temperatures ranging from 850 to 950°C, Q_c was equal to 290 kJ/mol. At temperatures ranging from 1000 to 1100°C, Q_c was equal to 170 kJ/mol. A value of 290 kJ/mol is close to that obtained for the activation energy for lattice self-diffusion of Fe in Cr-Ni austenitic stainless steels and high alloy steels [15]. On the other hand, an activation energy of 170 kJ/mol is close to the activation energy for grain boundary diffusion for α–iron (174 kJ/mol) and γ–iron (167 kJ/mol) [15]. It is worth noting that comparison with tracer data for lattice and grain boundary diffusion of Fe in a duplex stainless steel with the actual composition is not possible since these data are not available.

Microstructural examination was conducted to gain information about the changes occurring during superplastic deformation. The as-received coarse δ–γ microstructure, with island-like austenitic grains in a more or less continuous matrix of ferrite, recrystallizes during heating at temperatures ranging from 850 to 1100°C. The new microstructure consist of fine ferritic grains and fine austenitic grains of 10 to 15 μm clustered in colonies. For temperatures below 950°C these colonies are surrounded by a laminar microstructure as shown in Fig. 2a for the head (grip section where deformation did not occur) of a sample tested at 900°C. This lamellar structure is constituted by particles of σ phase, not dissolved by the etching used, new austenite grains and some amount of delta ferrite grains, as confirmed by X-ray diffraction. On the other hand, for temperatures above 1000°C a binary microduplex microstructure is obtained consisting of austenite and dark etched ferrite grains as shown in Fig 2(b) for the head of a sample tested at 1050°C.

The grouped colonies of austenitic grains shown in Fig. 2a and b decrease in size after deformation as shown in Figs. 3a and b for the gauge length of samples deformed to failure at 900 and 1050°C respectively. During deformation at 900°C, the lamellar structure present at the beginning of the test evolves to a spherodized structure. On the other hand, the grains of both phases of the sample tested at 1050°C are intermixed making it difficult their identification. This grain rearrangement during deformation is associated with the mechanism of grain boundary sliding.

The texture analysis by means of ODF showed that the rolling texture components were distributed mainly along three fibers: θ-fiber (ND||<100>), α-fiber (RD||<110>), ζ-fiber (ND||<110>), where RD is the rolling direction and ND is the direction parallel to the sheet normal [16]. The volume fraction of crystallites belonging to each fiber was calculated from the ODF and is presented in Table I for a testing temperatures of 1050°C. The overlapping of the diffraction peaks of σ with those of α and γ hinders the study at testing temperatures below 950°C. This table also includes, as reference, the values resulting of the integration of the ODF for a random oriented material between the same limits used for these calculations. The recrystallization occurring during the heating period before testing causes a decrease in the volume fraction of crystallites belonging to mean fibers and an increase in the minor components of both, ferrite and austenite. Therefore, a similar texture is reached in both phases after annealing at 1050°C. Furthermore, only minor

changes in the texture of both phases occurs in the sample which was deformed 290%. These changes consisted mainly in a slight decrease in the volume fraction of the components of each fiber, of 1 to 2 % for the austenite and 1 to 4% for the ferrite. However, a weak texture is still present after such a high elongation as can be inferred by comparison of the actual values with those for a random oriented sample. The presence of this texture points out toward the contribution to deformation of a slip creep mechanism.

Conclusions

1. High n values, of about 5, at all temperatures at strain rates above 10^{-3} s^{-1} were observed. At low strain rates, n values from 2 to 3 at all testing temperatures were observed. A change in the behavior of the steel is observed at about 950°C which is attributed to the presence of the σ phase.
2. At high strain rates the dominant deformation mechanism is slip creep changing to grain boundary sliding, GBS, at strain rates below 10^{-3} s^{-1}.
3. The annealed material above 1000°C has a fine microduplex microstructure consisting of austenite and ferrite grains. After deformation in the superplastic regime the grains of both phases are intermixed as a consequence of the grain rearrangement associated to the mechanism of GBS.
4. Texture analysis by means of the orientation distribution function showed similar texture components for the austenite and the ferrite after annealing at 1050°C. The evolution of these components with deformation at this temperature confirmed the importance of GBS as the dominant deformation mechanism.

Acknowledgments

This work was sponsored by the Comisión Interministerial de Ciencia y Tecnología (CICYT) under Grant MAT 97/0700. The supply of the steel by Sumitomo Metal Industries Ltd., Japan, is gratefully acknowledged.

References

[1] R.G. Gibson, H.W. Hayden and J.H. Brophy, Trans. ASM 61 (1968), p. 85.
[2] J.O. Nilsson, Mater. Sci. Technol. 8 (1992), p. 685.
[3] Y. Maehara, M. Koike, N. Fujino and T. Kunitake, Trans. ISIJ 23 (1983), p. 240.
[4] Y. Maehara, N. Fujino and T. Kunitake, Trans. ISIJ 23 (1983), p. 247.
[5] H.W. Hayden, R.G. Gibson, H. Merrick and J.H. Brophy, Trans. ASM 60 (1967), p. 3.
[6] O.A. Ruano and O.D. Sherby, Rev. Metal. Madrid 19 (1983), p. 261.
[7] M. Kobayashi and M. Miyagawa, Trans. ISIJ 27 (1987), p. 686.
[8] Y. Maehara, Trans. ISIJ 25 (1985), p. 69.
[9] K. Osada, S. Uekoh and K. Ebato, Trans. ISIJ 27 (1987), p. 713.
[10] Y. Maehara and T.G. Langdon, Mater. Sci. Eng. A128 (1990), p. 1.
[11] Y. Maehara, Trans. ISIJ 27 (1987), p. 711.
[12] M.T. Perez-Prado, J. Ibañez, M. Morris, M.C. Cristina, O.A. Ruano and G. Gonzalez-Doncel, Rev. Metal. Madrid 34 (1998), p. 324.
[13] M.J. Cai, W.B. Lee, Mater. Sci. Forum 157-162 (1994), p.327
[14] D. Hernandez, Ph. D. Thesis, MPI-Düsseldorf, Germany, 1995.
[15] H.J. Frost and M.F. Ashby, "Deformation-Mechanism Maps", Pergamon Press, Oxford, 1982, p.60.
[16] J.A. Jiménez, M. Carsí, F. Peñalba and O.A. Ruano, J. Mater. Sci., in press.

TABLE II Volume fraction of crystallites, calculated from ODFs, belonging to the θ-fiber, α-fiber, and ζ-fiber in the as-received material and after testing at 1050°C.

	θ-fiber	α-fiber	ζ-fiber
Ferrite			
As received	35%	25%	12%
Sample's head	20%	19%	17%
Deformed at 10^{-4} s^{-1}	16%	17%	16%
Austenite			
As received	11%	15%	24%
Sample's head	17%	19%	16%
Deformed at10^{-4} s^{-1}	15%	20%	14%
Random oriented	11%	15%	12%

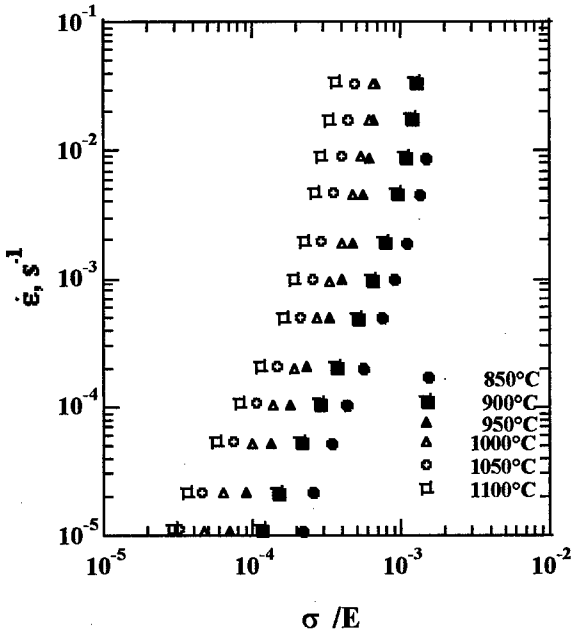

Fig. 1. Logarithm strain-rate *vs.* logarithm Young's modulus-compensated flow stress at various temperatures.

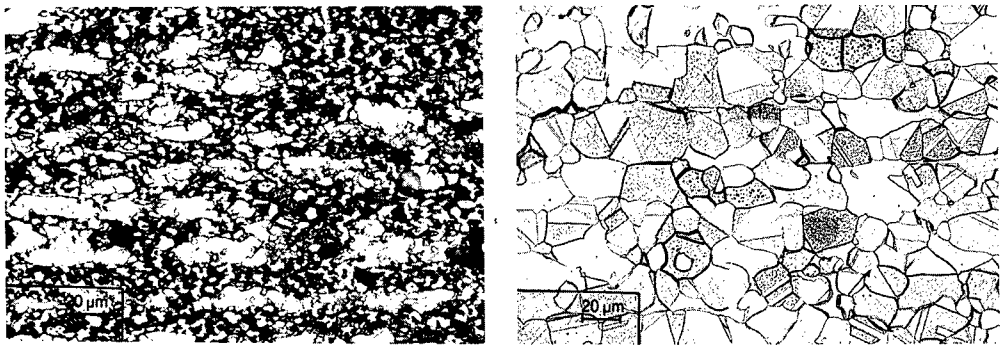

Fig. 2. Microstructure of the head of a sample tested in tension at (a) 900 and (b) 1050°C.

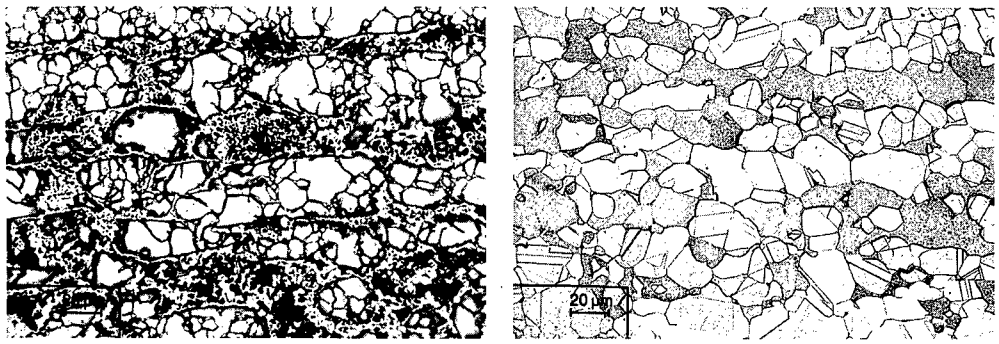

Fig. 3. Microstructure in a region next to the fracture surface after tensile testing at 10^{-4} s^{-1} at (a) 900 and (b) 1050°C.

Key Engineering Materials Vols. 171-174 (2000) pp. 395-402
© 2000 Trans Tech Publications, Switzerland

Contribution of Tungsten to Microstructure Stabilization and Improvement of Creep Resistance in Simple 9Cr-W Steels

F. Abe

National Research Institute for Metals (NRIM), 1-2-1 Sengen, Tsukuba 305-0047, Japan

Keywords: 9Cr Steel, Tungsten, Creep, Minimum Creep Rate, Acceleration of Creep Rate, Fe_2W Laves Phase, $M_{23}C_6$ Carbide, Lath

Abstract

The microstructural evolution during creep and its effect on creep rate have been investigated for tempered martensitic 9Cr-0.1C-(0, 1, 2, 4)W steels. Creep tests were carried out at 550(823), 600(873) and 650 °C (923 K) for up to 15000 h after tempering treatments. During creep, the microstructural evolution such as the recovery of excess dislocations, the coarsening of $M_{23}C_6$ carbides and laths occurs with an aid of creep stress and strain. In the high-W steels containing 2 and 4% W, Fe_2W Laves phase precipitates preferentially at prior austenite grain boundaries and lath boundaries during creep. The coarsening rate of Fe_2W is much larger than that of $M_{23}C_6$. The fine precipitation of Fe_2W contributes to a decrease in creep rate in the transient creep region but the subsequent coarsening of Fe_2W promotes an increase in creep rate in the acceleration creep region, resulting in only a small effect of Fe_2W on the improvement of creep rupture life. It is concluded that W contributes to the improvement of creep rupture strength of 9Cr steels substantially through stabilizing $M_{23}C_6$ carbides and hence stabilizing laths.

1 Introduction

Tempered martensitic 9 - 12 Cr steels strengthened by W have become of much interest as advanced heat resistant steels with sufficient creep rupture strength in application to boiler and turbine of ultra-supercritical electric power plants at temperatures higher than 600 °C (873 K) [1]. These steels are alloyed with many elements, such as C, Cr, W, Mo, V, Nb, N, B, etc., for the improvement of creep rupture strength but the main alloying constituents are C-Cr-W. There are very important differences in the creep deformation behavior of various classes of materials; solid solution alloys, particle-hardened alloys and so on [2]. This implies that different representation of creep and creep rate curves can be applied to different classes of materials, depending on specific mechanisms. The purpose of the present research is to investigate the effect of microstructural evolution during creep on creep rate for tempered martensitic 9Cr steels containing W.

2 Experimental Procedure

Four simple 9Cr-(0, 1, 2, 4)W-0.1C steels were used. The chemical compositions of the steels are given in Table 1. Only the concentration of W was varied from 0 to 4 wt% in the steels. The steel rods were austenitized, quenched and then tempered [3 - 5]. The steels except for the 9Cr-4W steel were 100% tempered martensite, while the 9Cr-4W steel contained 10 volume % δ - ferrite. The tempered martensitic microstructure consisted of laths that contained a high density of dislocations and fine carbides of about 0.07 μ m. The major component of carbides in as tempered condition was $M_{23}C_6$ in each steel. Creep tests were carried out at 550 (823), 600 (873) and 650 °C

(923 K) for up to about 15000 h, using specimens of 6 mm in gage diameter and 30 mm in gage length.

Table 1 Chemical compositions of steels examined (wt%)

	C	Cr	W	Mn	Si	P	S	O	N
9Cr	0.104	8.96	-	0.49	0.30	<0.002	0.003	0.009	0.001
9Cr-1W	0.101	9.01	0.99	0.48	0.29	<0.002	0.004	0.011	0.002
9Cr-2W	0.100	8.92	1.92	0.48	0.28	<0.002	0.003	0.012	0.002
9Cr-4W	0.101	9.09	3.93	0.50	0.29	<0.002	0.002	0.006	0.002

3 Experimental Results and Discussion

3.1 Creep behavior and microstructural evolution during creep

Figure 1 shows the log-log plots of the creep rate-time and creep rate-strain curves for the 9Cr-1W, 9Cr-2W and 9Cr-4W steels at 600 °C and 137 MPa. The creep curves consist of the primary or transient creep region, where the creep rate decreases with time, and of the tertiary or acceleration creep region, where the creep rate increases with time after reaching a minimum creep rate. In the initial stage of creep, the creep rates are not largely different among the steels. In the high-W steels, such as the 9Cr-2W and 9Cr-4W steels, the decrease in creep rate with time becomes more significant at long times above about 10 h in the transient creep region, deviating from the extrapolated lines from the short-time conditions shown by the dotted lines. This causes the longer duration of transient creep and the retardation of the beginning of acceleration creep, resulting in lower minimum creep rate. The significant decrease of creep rate in the transient creep region in the 9Cr-2W and 9Cr-4W steels is also evident from the creep rate-strain curves.

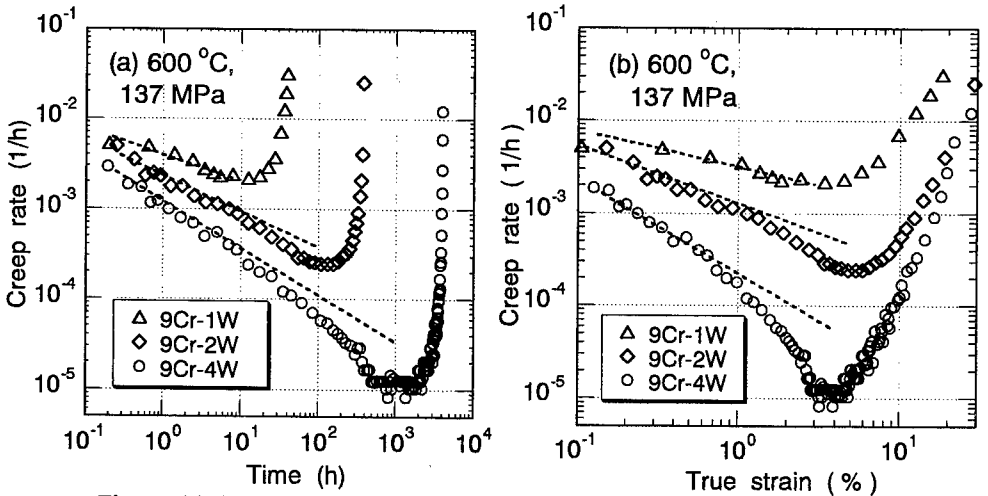

Fig.1 (a) Creep rate-time and (b) creep rate-strain curves in log-log plots for the 9Cr-1W, 9Cr-2W and 9Cr-4W steels at 600 °C and 137 MPa.

During creep, the recovery of excess dislocations, the agglomeration of carbides and the coarsening of martensite laths occurred [3-4]. The precipitation of Fe_2W Laves phase also occurred during creep in the high-W steels, the 9Cr-2W and 9Cr-4W, but not in the low-W steels, the 9Cr and 9Cr-1W. The significant decrease in creep rate at long times above about 10 h in the

9Cr-2W and 9Cr-4W steels (Fig.1) is caused by the fine precipitation of Fe_2W. This suggests that the precipitation strengthening by fine Fe_2W is much larger than the solid solution strengthening by the dissolution of W in the matrix. In austenitic steels, the creep rate decreases significantly in the transient creep region by the precipitation of $M_{23}C_6$ during creep after solution annealing and the Johnson-Mehl equation with the time exponent n = 2/3 provides a reasonable approximation for the kinetics of precipitation [6]. The Vickers hardness of the present 9Cr-W steels decreases substantially in the transient creep region before reaching a minimum creep rate, indicating that excess dislocations present after tempering decreases substantially in the transient creep region [3]. On the other hand, the coarsening of laths occurs mainly in the acceleration creep region after reaching a minimum creep rate. The present results suggest that the transient creep is a consequence of the movement and annihilation of excess dislocations and that the acceleration creep is a consequence of gradual loss of creep strength due to the microstructural evolution, such as the agglomeration of carbides and the coarsening of laths.

3.2 Effect of fine precipitation and subsequent coarsening of Fe_2W on creep rate

Figures 2 and 3 show the semi-log plots of the creep rate-strain curves for the 9Cr and 9Cr-4W steels, respectively. In the 9Cr steel (Fig.2), the creep rate increases linearly with strain for a wide range of strain in the acceleration creep region after reaching a minimum creep rate at about 3% strain, except for the high-temperature and low stress condition (650 °C and 20 MPa) at which the strain to minimum creep rate shifts to a lower value of 2% and the creep rate rapidly increases just after reaching a minimum creep rate. The linear acceleration of creep rate with strain has been reported for several Cr-Mo steels [7-9]. The shape of the creep rate-strain curves of the 9Cr-2W and 9Cr-4W steels, where the precipitation of Fe_2W Laves phase extensively occurs during creep, is quite different from that of the 9Cr and 9Cr-1W steels, where no precipitation of Fe_2W occurs. In the 9Cr-4W steel at 550 °C (Fig.3), the strain to minimum creep rate shifts to higher values and the shape of the creep rate-strain curves changes from a sharp V-shape to a round U-shape with decreasing stress and hence increasing test duration. This is also observed at short times at 600 °C; in the stress range from 186 to 167 MPa. However, further decrease in stress at 600 °C shifts again the strain to minimum creep rate to lower values and changes again the shape of the creep rate-strain curves to a sharp V-shape. At 650 °C, the round U-shaped curve with a minimum creep rate at a large strain, which is observed at the lowest stress and longest test duration at 550 °C, is seen only at the highest stress of 137 MPa and the shortest test duration. Below 137 MPa, the strain to minimum creep rate shifts to lower values and the shape of the creep rate-strain curves changes to a V-shape. With decreasing stress, the $d\ln\dot{\varepsilon}/d\varepsilon$ in the acceleration creep region after reaching a

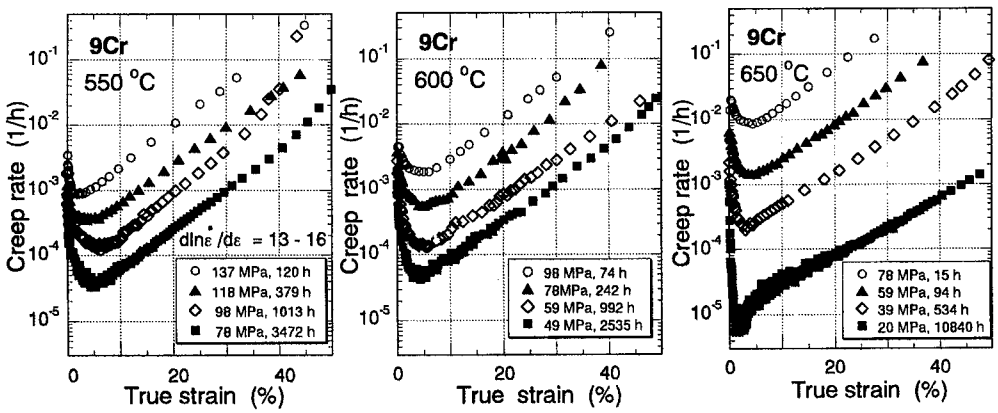

Fig.2 Creep rate-strain curves of the 9Cr steel without W at 550, 600 and 650 °C.

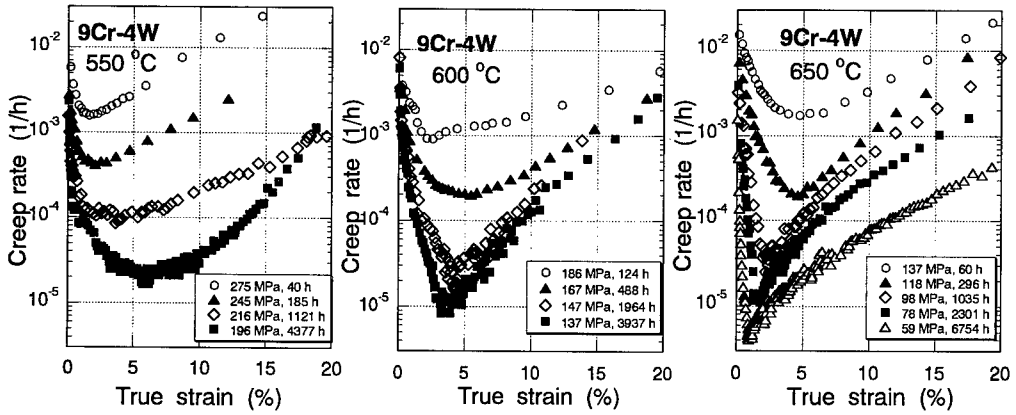

Fig.3 Creep rate-strain curves of the 9Cr-4W steel at 550, 600 and 650 °C.

minimum creep rate at first increases but then decreases again.

The coarsening rate of the Fe_2W Laves phase is much larger than that of $M_{23}C_6$ and the density of Fe_2W is much lower than that of $M_{23}C_6$, suggesting that the $M_{23}C_6$ carbides are more effective obstacles for stabilizing the lath martensitic microstructure than the Fe_2W. The TEM observations show sparse distributions of coarsened precipitates of the Fe_2W Laves phase mainly at prior austenite grain boundaries as shown in Fig.4. The precipitation of Fe_2W has been reported for high-Cr steels containing W by several researchers [10-12].

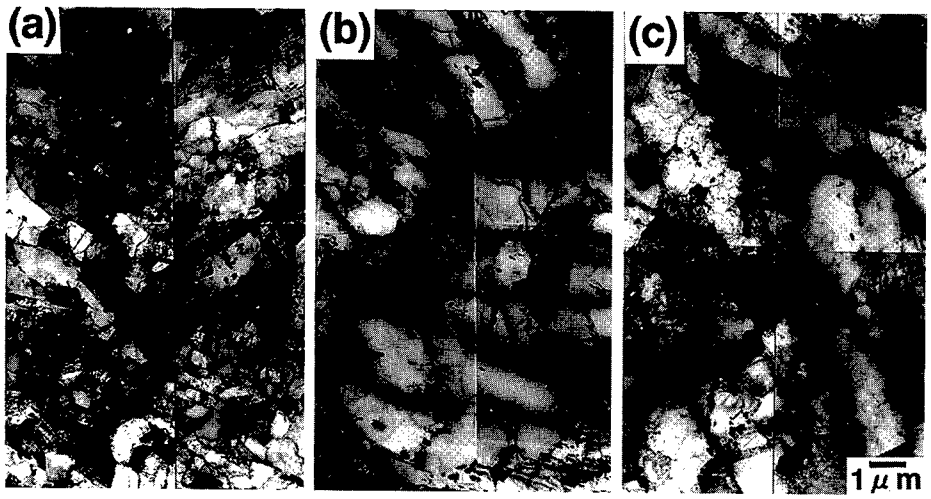

Fig.4 Microstructure of the 9Cr-4W steel; (a) after tempering, (b) after creep ruptured at 600 °C, 147 MPa, 1964 h and (c) after creep ruptured at 600 °C, 137 MPa, 3937 h.

When the agglomeration or the coarsening rate of the Fe_2W is large after completing the precipitation of fine Fe_2W, the creep rate increases due to loss of precipitation strengthening, as shown by the line *B* in Fig.5. The effect of fine precipitation and subsequent coarsening on creep rate shown in Fig.5 is superimposed in the creep rate-strain curves in Fig.6. With decreasing stress and hence with increasing test duration, the strain to minimum creep rate shifts at first to higher values and then to lower values (Fig.3). The round U-shape creep rate-strain curves appears at

high stress and short time conditions at which the significant decrease in creep rate by the fine Fe_2W occurs in the acceleration creep region under no precipitation of Fe_2W (the dotted line), as shown by the line *A* in Fig.6. Both the effect of fine precipitation on the decrease in minimum creep rate and the effect of subsequent coarsening on the acceleration of creep rate are maximized when the maximum decrease in creep rate by fine Fe_2W appears at a minimum creep rate under no precipitation of Fe_2W, as shown by the line *B*. These two effects become reduced at further low stresses where the maximum decrease in creep rate by the fine Fe_2W appears in the transient creep region under no precipitation of Fe_2W, as shown by the line C.

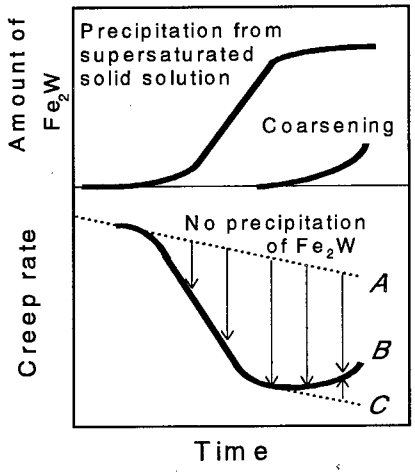

Fig.5 Effects of precipitation and subsequent coarsening of Fe_2W on creep rate.

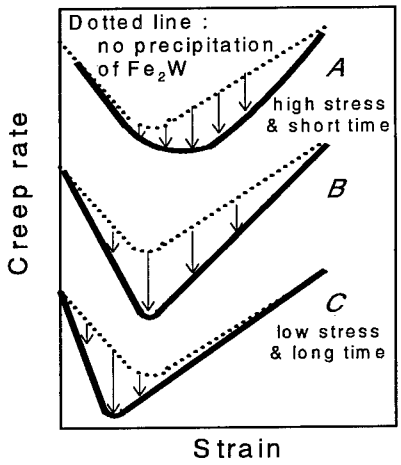

Fig.6 Effects of Fe_2W on creep rate-strain curves.

3.3 Effect of Fe_2W precipitation on stress dependence of minimum creep rate

In the 9Cr and 9Cr-1W steels, the stress dependence of minimum creep rate $\dot{\varepsilon}_{min}$ is approximately described by a power law of

$$\dot{\varepsilon}_{min} = A\,\sigma^{n}. \qquad (1)$$

The value of the stress exponent *n* is evaluated to be about 5 and 7 for the 9Cr and 9Cr-1W steels, respectively, at 550, 600 and 650 °C. On the other hand, the minimum creep rate could not be approximated by the power law with a same value of *n* for the 9Cr-2W and 9Cr-4W steels, as shown in Fig.7 for the 9Cr-4W steel. In the 9Cr-4W steel, the minimum creep rate is described by Eq.1 with $n = 13$ at 550 °C. The *n* is larger at 600 °C ($n = 15$) than at 550 °C. At 650 °C, however, the *n* again exhibits a small value and decreases with decreasing stress. The change in *n* with temperature in the 9Cr-2W and 9Cr-4W steels is also caused by the effect of Fe_2W precipitation on creep rate, as shown in Fig. 8. At low temperature 550 °C, the precipitation rate of Fe_2W is low and hence the decrease in creep rate by the precipitation of Fe_2W is small in the transient creep region. With increasing temperature, the precipitation rate increases and hence the decrease in creep rate by the precipitation of fine Fe_2W is larger at 600 °C than at 550 °C, causing apparently larger *n* at 600 °C than at 550 °C. Further increase in temperature to 650 °C results in the large coarsening rate of Fe_2W and the decrease in creep rate by the precipitation of Fe_2W becomes less pronounced with decreasing stress and increasing test duration, as described in the previous section. This results in the decrease in *n* with decreasing stress in the stress range examined.

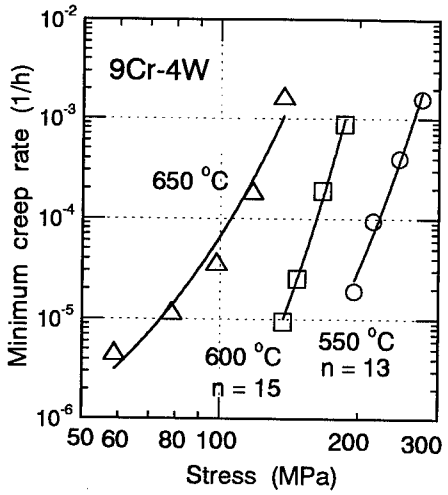

Fig.7 Stress dependence of minimum creep rate for the 9Cr-4W steel.

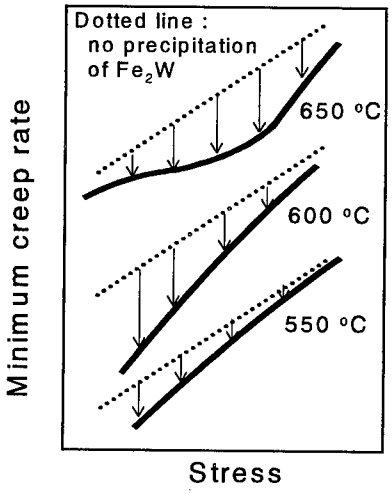

Fig.8 Effect of Fe_2W precipitation on the decrease in minimum creep rate.

3.4 Effect of Fe_2W precipitation on the acceleration of creep rate

The increase in creep rate with strain, $d\ln\dot{\varepsilon}/d\varepsilon$, in the acceleration creep region just after reaching a minimum creep rate was evaluated and is shown in Fig.9 as a function of time to rupture for the 9Cr and 9Cr-4W steels. In the 9Cr steel, the $d\ln\dot{\varepsilon}/d\varepsilon$ is evaluated to be 12 - 15 independent of stress and temperature, except for the high-temperature and low stress condition (650 °C and 20 MPa) at which $d\ln\dot{\varepsilon}/d\varepsilon$ = 19. In the 9Cr-1W, the $d\ln\dot{\varepsilon}/d\varepsilon$ was evaluated to be 20 - 27 for a wide stress range at 550, 600 and 650 °C. Assuming exponential function of strain, the creep rate is described by [7]

$$\dot{\varepsilon} = \dot{\varepsilon}_0 \exp(n\varepsilon)\exp(m\varepsilon)\exp(d\varepsilon) \tag{2}$$

$$d\ln\dot{\varepsilon}/d\varepsilon = n + m + d \tag{3}$$

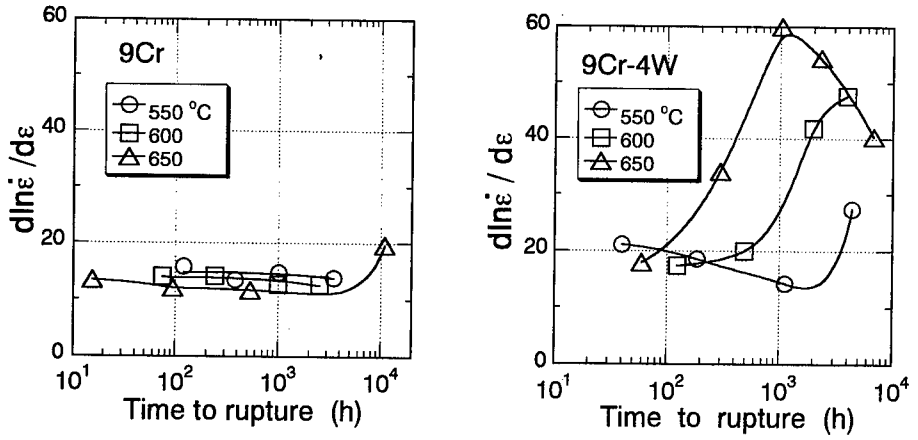

Fig.9 Acceleration of creep rate by strain, $d\ln\dot{\varepsilon}/d\varepsilon$, in the acceleration creep region for the 9Cr and 9Cr-4W steels.

where $\dot{\varepsilon}_0$ is the initial creep rate, n the stress exponent in Eq.1, m the microstructure degradation and d the other parameter associated with damage such creep voids. Because the microstructure observations gave no evidence of any formation of creep voids showing the development of creep damage, the parameter d in Eqs. 2 and 3 is neglected and the acceleration of creep rate results from the parameters n and m. The n and the m correspond to the acceleration of creep rate by the increase in stress due to a decrease in cross section with strain at constant load test and by strength loss due to microstructural evolution, respectively. The value of n was evaluated to be about 5 and 7 for the 9Cr and 9Cr-1W steels, respectively, from the stress dependence of minimum creep rate. Therefore, we obtain m = 7 - 10 and 13 - 20 for the 9Cr and 9Cr-1W steels, respectively. Then, a greater part of the acceleration of creep rate in the acceleration creep region comes from the microstructural evolution.

In the 9Cr-2W and 9Cr-4W steels, the coarsening of Fe_2W also contributes to the acceleration parameter m. This results in larger $d\ln\dot{\varepsilon}/d\varepsilon$ for the 9Cr-2W and 9Cr-4W steels than for the 9Cr and 9Cr-1W steels. In the 9Cr-4W steel, the $d\ln\dot{\varepsilon}/d\varepsilon$ is evaluated to be about 20 or less at short times less than 100 h and it increases with increasing test duration and then decreases after reaching the maximum. The increase in $d\ln\dot{\varepsilon}/d\varepsilon$ with test duration shifts to shorter times with increasing temperature, reflecting the temperature dependence of coarsening rate of Fe_2W.

3.5 Effect of Fe_2W precipitation on the improvement of creep rupture time

The time to rupture was found to depend on the acceleration of creep rate $d\ln\dot{\varepsilon}/d\varepsilon$ in the acceleration creep region as well as the minimum creep rate $\dot{\varepsilon}_{min}$ and is described by

$$tr = 1.5 / (\dot{\varepsilon}_{min} \cdot d\ln\dot{\varepsilon}/d\varepsilon). \quad (4)$$

The same relationship was also observed in austenitic steels [13]. Figure 10 shows the effect of Fe_2W precipitation on the decrease in minimum creep rate, $\dot{\varepsilon}_{min}/(\dot{\varepsilon}_{min})_0$, and on the increase in acceleration of creep rate, $(d\ln\dot{\varepsilon}/d\varepsilon)/(d\ln\dot{\varepsilon}/d\varepsilon)_0$, for the 9Cr-2W and 9Cr-4W steels at 600 °C, where $(\dot{\varepsilon}_{min})_0$ and $(d\ln\dot{\varepsilon}/d\varepsilon)_0$ are the minimum creep rate and the acceleration of creep rate under the condition of no precipitation of Fe_2W. The precipitation of Fe_2W effectively decreases the minimum creep rate due to fine precipitation in the transient creep region but the large coarsening rate of the Fe_2W also promotes the acceleration of creep rate in the acceleration creep region. As a result, the effect of the precipitation of Fe_2W on the extension of time to rupture, tr/tr_0, is rather small less than factor 2 at 600 °C at which the decrease in minimum

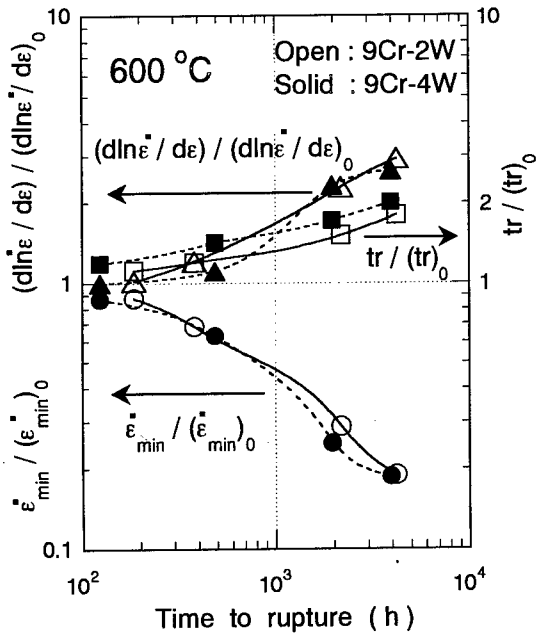

Fig.10 Effect of Fe_2W precipitation on the decrease in $\dot{\varepsilon}_{min}$ and the increase in $d\ln\dot{\varepsilon}/d\varepsilon$ and *tr* for the 9Cr-2W and 9Cr-4W steel at 600 °C.

creep rate by the precipitation of Fe_2W was more pronounced than at 550 and 650 °C.

The increase in time to rupture with increasing W concentration is closely correlated with the less pronounced microstructural evolution during creep with increasing W concentration. The coarsening rate of laths decreases with increasing W concentration of the steels, which is correlated with the reduced coarsening rate of $M_{23}C_6$ carbides. The rate of Ostwald ripening of $M_{23}C_6$ carbides was described by a combination of the rate equations for volume diffusion and boundary diffusion controlled processes [14].

4 Summary

(1) The precipitation of Fe_2W Laves phase occurs at prior austenite grain boundaries and lath boundaries in the high-W steels, the 9Cr-2W and 9Cr-4W, during creep but not in the low-W steels, the 9Cr and 9Cr-1W. The coarsening rate of Fe_2W is much larger than that of $M_{23}C_6$.

(2) In the transient creep region, the decrease in creep rate with time is significant in the 9Cr-2W and 9Cr-4W steels, resulting from the precipitation strengthening by fine Fe_2W. In the acceleration creep region, the creep rate increases linearly with strain for a wide range of strain. The coarsening of Fe_2W increases the $d\ln\dot{\varepsilon}/d\varepsilon$ in the acceleration creep region.

(3) The time to rupture is inversely proportional to the product of $\dot{\varepsilon}_{min}$ by $d\ln\dot{\varepsilon}/d\varepsilon$. The fine precipitation of Fe_2W effectively decreases the $\dot{\varepsilon}_{min}$ but the subsequent coarsening of Fe_2W increases the $d\ln\dot{\varepsilon}/d\varepsilon$ in the acceleration creep region. As a result, the effect of the precipitation of Fe_2W on the extension of time to rupture is rather small less than factor 2.

(4) The increase in time to rupture with increasing W concentration is correlated with the less pronounced microstructural evolution during creep with increasing W concentration. The coarsening rate of laths decreases with increasing W concentration of the steels, which is correlated with the coarsening rate of $M_{23}C_6$ carbides.

References

[1] F. Abe, M. Igarashi, N. Fujitsuna, K. Kimura and S. Muneki, Proc. 6th Liege Conference on Materials for Advanced Power Engineering, Part I, Liege, Belgium (1998), p.259.
[2] B. F. Dyson and M. McLean, ISIJ Intern. 30 (1990), p.802.
[3] F. Abe, S. Nakazawa, H. Araki and T. Noda, Metall. Trans. 23A (1992), p.469.
[4] F. Abe and S. Nakazawa, Metall. Trans. 23A (1992), p.3025.
[5] F. Abe, Mat. Sci. Eng. A234-236 (1997), p.1045.
[6] F. Abe, Metall. Trans. 26A (1995), p.2237.
[7] M. Prager, Pressure Vessel and Piping 288 (1994), p.401.
[8] R. Woo, R. Sandstrom and J. Storesund, Mater. Temp. 12 (1994), p.277.
[9] S. Straub, M. Meier, J. Ostermann and W. Blum, VGB Kraftwerkstechnik 73 (1993), p.646.
[10] F. Abe, H. Araki and T. Noda, Metall. Trans. 22A (1991), p.2225.
[11] H. Naoi, H. Mimura, H. Morimoto, T. Tanaka, Y. Yazaki and T. Fujita, Proc. EPRI/National Power Conf. on New Steels for Advanced Plant Up To 620 °C, London, UK (1995), p.8.
[12] J. Hald, Steel Research 67 (1996), 369.
[13] F. Abe, K. Kimura, E. Baba, O. Kanemaru and K. Yagi, Proc. Intern. Symp. on Materials Ageing and Component Life Extension, Milan, Italy (1995), p.1075.
[14] F. Abe, Proc. 4th Intern. Conf. on Recrystallization and Related Phenomena, Tsukuba, Japan (1999), in press.

e-mail: abe@nrim.go.jp

Key Engineering Materials Vols. 171-174 (2000) pp. 403-410
© 2000 Trans Tech Publications, Switzerland

Effect of Heat Treatments on Room Temperature Creep Strain of a High Strength Steel

C. Liu[1], Z. Zhao[1] and D.O. Northwood[2]

[1] Mechanical & Materials Engineering, University of Windsor, Windsor, Ontario, Canada, N9B 3P4

[2] Faculty of Engineering & Applied Science, Ryerson Polytechnic University Toronto, Ontario, Canada, M5B 2K3

Keywords: Room Temperature Creep, Heat Treatment, High Strength Steel

ABSTRACT Under certain service conditions for some creep resistant metallic materials, creep at ambient temperature rather than high temperature is of concern. The room-temperature creep behavior of a high strength steel has been investigated for five heat treatment schedules. The primary creep behavior obeyed a logarithmic creep law and the creep mechanism was identified as pure dislocation creep. It is demonstrated that for steels of similar yield strength and the hardness after heat treatment, the creep strain was significantly lower in a steel quenched at 210°C in molten salt for 600 minutes and then tempered. The decrease in creep strain is mainly attributed to the absence of ferrite, the refined precipitate distribution, together with the structural uniformity of the tempered martensite. The possible influence of dislocations on the creep strain is discussed.

1. INTRODUCTION

The elevated-temperature creep deformation of engineering materials has been extensively studied for many years [1-4]. Unlike the high temperature case, however, low temperature creep, especially at room temperature (below 0.2 T_m), is not perceived to be a significant technical problem. However, a large number of alloys have been shown to exhibit appreciable amounts of creep at ambient temperatures including titanium [5,6], aluminum [7] and stainless steel [8]. Comprehensive mechanismtic studies of the time dependent deformation of high strength steels at room temperature and at stresses below the yield strength, however, are very limited in number.

It is well known that room temperature creep is strongly dependent on the strength and hardness of the alloy and the applied stress level below the yield strength [9,10]. Creep deformation of an alloy is unlikely to occur in case of a high strength material at low loads. Significant, and desirable, changes in creep properties have often been achieved by different heat treatments. However, further work on the room temperature creep behavior for steels of the similar strength and hardness after heat treatment is needed to determine the creep rate controlling parameters. The purpose of this paper is to present the results of room-temperature creep tests performed on a high strength steel and to outline the possible influence of different heat treatments on the creep deformation behaviour.

2. EXPERIMENTAL PROCEDURES

The SAE 4340 steel in this study was a commercial alloy which has wide industrial applications. The chemical composition is given in Table 1.

Samples, 100mm in diameter, were forged, annealed and cut into 10mm diameter rods for tensile testing or 1.2mm×3.0mm×25mm specimens for room temperature creep testing. The samples were in the rough machined condition when received and were finish machined after full heat treatment. The 5 heat treatment schedules are shown schematically in Fig.1

Table 1. Chemical composition of high strength steel (wt %)

C	Si	Mn	Cr	Ni	Mo	P	S
0.41	0.33	0.62	0.78	1.42	0.22	0.15	0.15

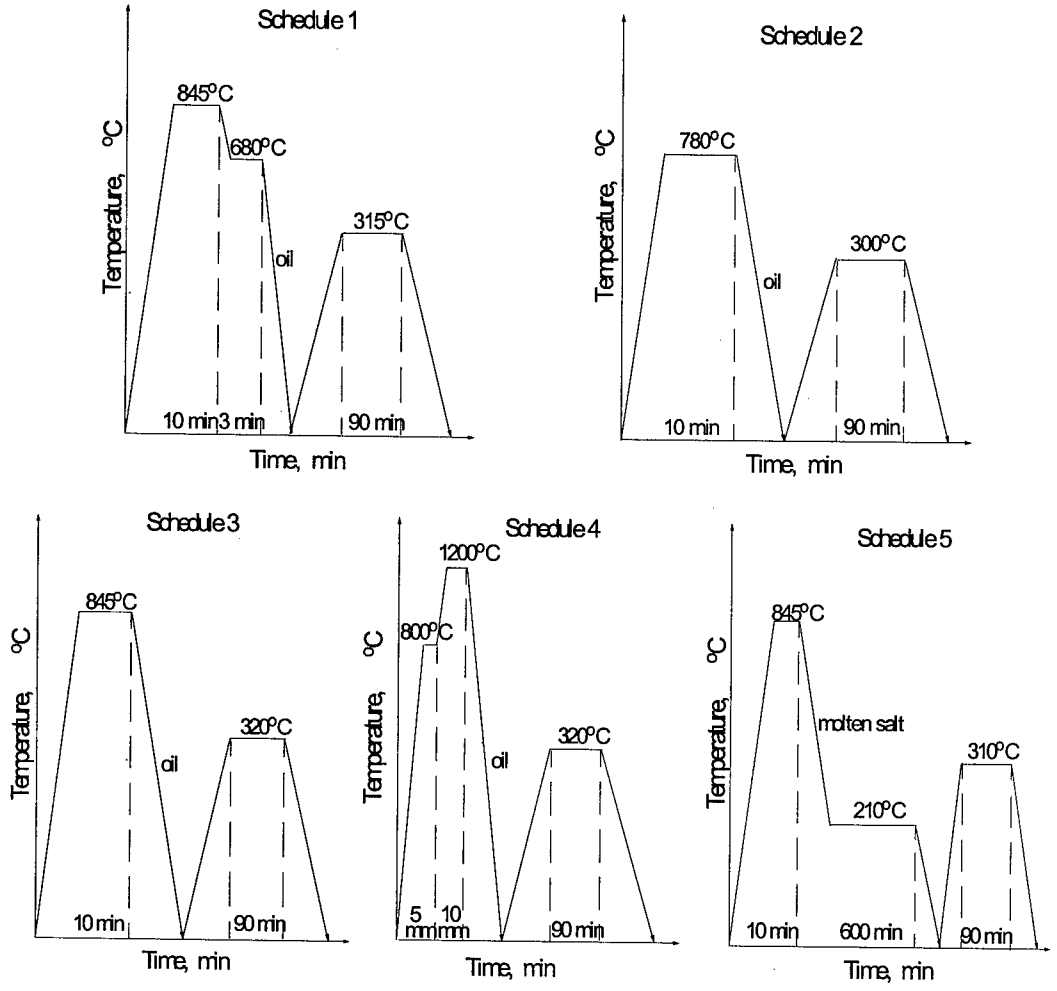

Fig. 1 Schematic diagrams showing the different heat treatment schedules

The room temperature creep testing was conducted on a R-100 creep testing machine equipped with extensometer (The precision of this extensometer is ±0.2μm). The experimental test temperature was 17°C, with a variation of less than 2°C. In the tests, the steel samples were first subjected to 10% of the total load for 5min, then to 100% of the total load ($1/3\sigma_{0.2}$ of the steel) for 15min. This is the starting point for the strain measurements. The microstructures were observed by both optical microscopy and thin foil electron microscopy using an H800 TEM.

3. RESULTS AND DISCUSSION

The room temperature mechanical properties after the 5 heat treatment schedules are summarized in Table 2. Typical creep curves for the different heat treatments are shown in Fig.2. These curves are typical of low temperature creep for high strength steels, where the creep rate is initially rapid and then gradually decreases with the time. However, it is be noted that the effect of heat treatment on the room temperature creep strains is significant even though similar yield strengths and hardnesses are obtained after the different treatments (see Table 2). The best creep resistance at room temperature is for S5.The creep strains for S1 are significantly higher than for the other four heat treatment schedules.

Table 2 Mechanical properties of steel after the different heat treatments

Sample number	S1	S2	S3	S4	S5
Corresponding process in Fig.1	Schedule 1	Schedule 2	Schedule 3	Schedule 4	Schedule 5
Yield strength (MPa)	1270±17	1260±25	1295±8	1280±10	1250±28
Hardness (HRC)	51.0±0.5	51.5±0.4	51.0±0.6	51.5±0.2	51.5±0.2

To determine the rate-controlling process in the primary creep stage of these samples, the slope of the creep curve was determined at given strains for the first 90 min. of the creep test. The curves shown in Fig.3 indicate a linear relationship between the natural logarithm of the creep rate and the creep strain. The room temperature creep rate ε' , decreases with increasing strain ε, according to:

$$\ln \varepsilon' = -A\varepsilon + B \qquad (1)$$

where A=Dh. D=V/kT, V is the activation volume,. Thus, V is constant for a given material and temperature, k is the Boltzmann's constant and h is the working-hardening coefficient [11,12].
B is determined by the applied stress and the D value [12].
Integration of equation (1) yields an equation for the creep strain, ε , and creep time, t, as follows:

$$\varepsilon = BA^{-1} + A^{-1} \ln(At+AC) \qquad (2)$$

where C is the integration parameter from derivation. Thus, the creep strain at room temperature vs creep time relationship obeys a logarithmic law. The creep rate under these conditions is controlled by intersection of glide dislocation with the dislocation forest, or by the movement of jogs [11] Therefore, the creep mechanism governing the time dependent deformation at low temperatures and relatively low stresses is pure dislocation creep [13].As the dislocations move along their glide planes, they overcome local obstacles with the aid of thermal fluctuations. The paramater A depends on the distance between pinning points, the diameter of the obstacle and the Burger's vector according to Seeger's theory [12,14]. For a given material and temperature at a constant stress, a ln ε' vs ε plot is linear with a slope of A. The higher creep deformation in S1 is is considered to be due to an increased mobility of the glide dislocations compared to that for the other heat treatment schedules.

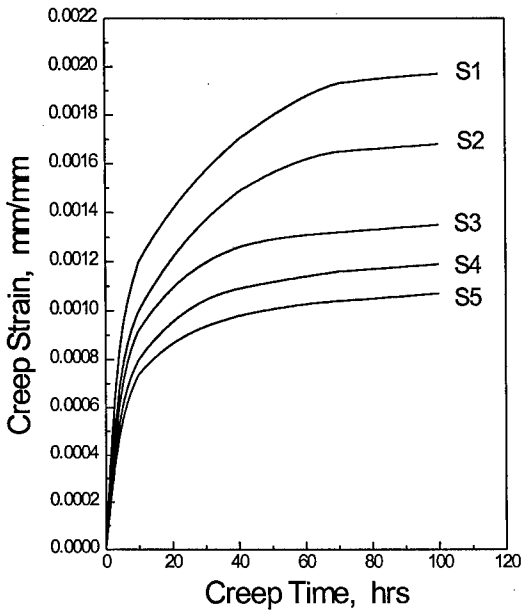

Fig. 2 Room temperature creep curves for different heat treatment schedules and an applied stress of 420MPa

At low temperatures, where no recovery occurs, the creep rate is controlled by dislocation motion and its interaction with the microstructure [15-16]. The microstructures corresponding to the different heat treatment schedules are given in Table 3. When the creep stress is below the yield strength, dislocations with the lowest activation energy are likely to move a certain distance upon the initial loading and they then become immobilized by the interaction with other dislocations, or with obstacles such as grain boundaries or precipitates. Creep can only then be continued by the movement of dislocations of higher activation energy. We will now examine the effects of the different heat treatments on the creep behaviour of this high strength steel. Each heat treatment schedule produced a different microstructure. Both S1 and S2 consist of ferrite with a low yield strength and tempered martensite, which has a high strength. Any microstructure consisting of two phases with large differences in deformability would promote dislocation slip localization which, in itself, gives rise to enhanced creep [17]. Therefore, the creep strains for S1 and S2 are higher than for the other three heat treatment schedules. Ferrite causes softening during the primary stage of creep and increases the mobility of the glide dislocation. However, in S1, 3% lath ferrite is precipited from the austenite by holding at 680°C for 3 min. during the quenching, the 4% massive and undissolved ferrite in S2 is because of the lower austenitizing temperature of 780°C. The slightly higher creep strains for S1 than for S2 are the result of the different ferrite morphologies. There are more grain boundaries between the lath ferrite and tempered martensite than between the massive ferrite and the tempered martensite to cause slip dislocation localization or inhomogeneous slip.

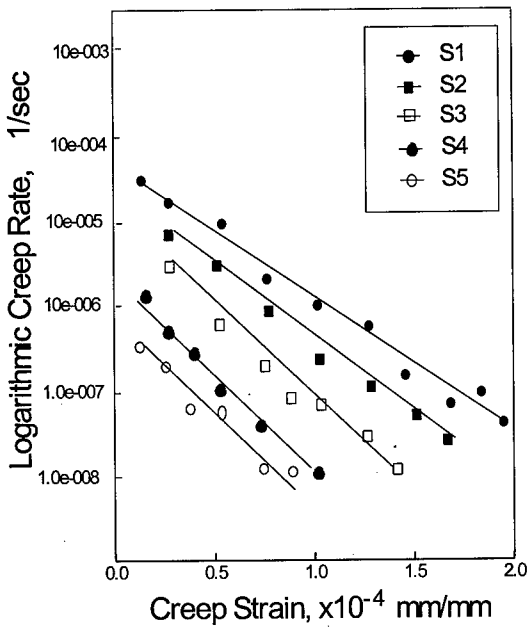

Fig. 3 Relationship between the creep rate (log scale) and creep strain

It can be seen from Table 3 that the single microstructure (i.e.,tempered martensite) for S3 and S4 and the mixed microstructure (the mixture of ferrite and tempered martensite) for S1 and S2 were obtained after different heat treatment schedules. Because the slip homogeneity is more likely in a single phase microstructure than otherwise (such as the mixed microstructure), and the "favorable" contribution of the martensitic structure itself [18], the creep strains of S3 and S4 were lower than that of S1 and S2. However, the creep strains measured for the S4 were lower than that for S3, most likely because of the high slip homogeneity due to the more homogenous microstructure obtained by the homogenizing treatment of preheating at 800°C for 5 min and austenizing at a higher temperature (1200°C) than that for S3 (845°C). The attainment of a more homogenous microstructure with increasing temperature is not surprising and is typically observed, since the diffusion of carbon and alloying elements is enhanced at higher temperatures and eventually a more homogenous composition and microstructure is formed. S5 with a bainite and tempered martensite microstructure, has the lowest creep deformation. Because the deformation characteristics of the tempered martensite and bainite is similar [19] by the treatment at 200°C below the M_S for 600 min. (see schedule 5 in Fig. 1), the slip inhomogeneity caused by the mixture of ferrite and tempered martensite can be avoided in this dual-phase microstructure. Also, the fine carbides precipitated within both the tempered martensite and bainite, can act as obstacles to dislocation slip and thus refine the slip bands through refinement of the substructure of a matrix, i.e. a similar argument to that for the beneficial effect of refining the grain size [17,20,21,22]. As a result, S5 exhibits the optimum creep resistance at room temperature.

Table 3 Microstructures of the samples after the 5 different heat treatment schedules

Sample number	corresponding process in Fig.1	Microstructure
S1	Schedule 1	4% massive ferrite and tempered martensite
S2	Schedule 2	3% lath ferrite and tempered martensite
S3	Schedule 3	tempered martensite
S4	Schedule 4	lath tempered martensite
S5	Schedule 5	30% bainite and tempered martensite

4. CONCLUSIONS

A high strength steel deformed at room temperature exhibited significant creep at stress levels below 1/3 of the yield strength. The transient creep in the high strength steel obeys a logarithmic law, and dislocation creep is identified as the creep mechanism. This room temperature creep behavior has been related to the heat treatment schedule. Despite similar strengths and hardnesses after each heat treatment schedule, the lowest creep strains are obtained in a steel subjected to the following heat treatment: 10min. at 845°C, quenched at 210°C for 600 min. in a molten salt and then tempered at 300°C for 90 min. This creep resistance is due to the fine carbides in both the tempered martensite and the bainite, and the absence of any ferrite which can lead to softening.

REFERENCES

[1] F.S Lin, E.A.Starke, Jr., S.B.Charabortty and A. Gysler, Metall. Tran. A 15A (1984), p.1229.
[2] I. Finnie and W. R. Heller, Creep of Engineering Materials, McGraw-Hill Book Company, London, 1959.
[3] J.S.Zhang, P.E.Li and J.Z.Jin., Acta. Metall. Mater. 39 (1991), p.3063.
[4] L.Bendersky, A.Rosen and A.K.Mukherjee, Int. Metal. Reviews 130 (1985), p.1.
[5] M.A.Imam and C.M.Gilmore, Metall. Tran. A 10A (1979), p.419.
[6] W.H.Miller, Jr., R.T. Chen and E.A. Starke, Metall. Tran. A 18A (1987), p.1451.
[7] O.H.Wyatt, Phy. Soc. Proc. B66 (1953), p.459.
[8] T.H.Alden, Act. Metall. Mater. 35 (1987), p.2621.
[9] A.Oehlert and A. Atrens, Act. Metall. Mater. 42 (1994), p.1493.
[10] G.T.Neate, Mater. Sci. Tech. 3 (1987), p.14.
[11] G. Schoeck, Mechanical Behavior of Materials at Elevated Temperature, John Emil Dorn, ed., McGraw-Hill, New York, NY, 1961.
[12] A. Seeger, Dislocations and Mechanical Properties of Crystals, New York (1957).
[13] J.Gittus, Viscoelasticity and Creep Fracture in Solids.Appl. Sci.,London (1987).
[14] A.W.Thomopson and B.C.Odegard, Metall. Trans. A 4A (1973), p.899.
[15] J.J.Gilman, Micromechanics of Flow in Solids. McGraw-Hill, New York (1969).
[16] C.N.Ahlquist, W.D.Nix and R.Gascaneri, Act. Metall. Mater. 18 (1970), p.663.
[17] E.A.Starke Jr. and G.Lutjering, Fatigue and Microstructure, ASM, Metals Park, OH (1979).
[18] A.Aran and H.Turner, J.Mater. Sci.Lett. 9 (1990), p.1407.

[19] C. Liu, Ph.D. Dissertation, Harbin Institute of Technology, P. R. China, 1998.
[20] C.S.Lee, K.A.Lee, D.M.Li, S.J.Yoo and W.J.Nam, Mater. Sci. Eng. A241(1998), p30.
[21] M.K.Kang, J.L.Sun and Q.M.Yang, J. Northwestern Polytechnical University 26 (1990), p.50.
[22] M.Yalin, M.Bamberger and A.Rose, Metall. Tran. A 26A (1995), p.401.

Key Engineering Materials Vols. 171-174 (2000) pp. 411-418
© 2000 Trans Tech Publications, Switzerland

Strengthening of Heat Resistant Martensitic Steel by Cu Addition

T. Tsuchiyama, Y. Futamura and S. Takaki

Department of Materials Science and Engineering, Graduate School of Engineering, Kyushu University 6-10-1, Hakozaki, Higashi-ku, Fukuoka 812-8581, Japan

Keywords: Heat Resistant Steel, Martensite, Lath Structure, ε-Cu Particle, Recovery, Ostwald Growth, Pinning Force

Abstract

Microstructure and creep deformation behavior were investigated in martensitic 9%Cr-(0~4)%Cu steels, and the strengthening mechanism by Cu was discussed in terms of microstructural change during creep deformation. As-quenched specimens have typical lath-martensitic structure. Cu addition gives no influence on the morphology of martensite-laths, but austenite grains tend to be refined with increasing the Cu content. As a result of creep testing for the quenched specimens with a same grain size, it was found that minimum creep rate is greatly lowered and rupture time are prolonged with increasing the Cu content. TEM observations of a creep-deformed 9%Cr-4%Cu steel revealed that dislocations attractively interact with ε-Cu particles within laths, and also lath boundaries are pinned by the ε-Cu particles. Through these interactions between dislocations or lath boundaries and ε-Cu particles, recovery in martensitic structure is greatly retarded, and dislocation density is kept higher during creep deformation. But once the pinning force by ε-Cu particles falls below the applied stress, the recovery rapidly proceeds and the strain rate is accelerated.

1. Introduction

Recently, many kinds of martensitic heat resistant steels have been developed and applied to power plants in order to improve the power generating efficiency, because these steels have excellent strength properties and small thermal expansion coefficient. In general, these steels are strengthened by the addition of W or Mo with a small amount of carbon. This strengthening is mainly due to the precipitation of carbide particles into martensite matrix. Thus strength of the steels are improved with increasing the amount of carbide. However, the strengthening by carbide is limited, because carbon content can not be increased more than about 0.2% owing to the reduction of ductility which causes quenching crack. On the other hand, Cu addition is very effective for strengthening of martensitic steels. Cu bearing martensitic steels can be greatly strengthened by aging treatment after quenching through precipitation of fine ε-Cu particles within martensite matrix [1], although the as-quenched martensite is not so hardened but possesses enough ductility not to cause quenching crack. In addition, Ostwald growth of ε-Cu particles is much slower than that of carbides such as M_3C and $M_{23}C_6$. This is a comfortable physical nature for high temperature use. For the purpose of strengthening of martensitic heat resistant steels by Cu addition, in this study, microstructure and creep properties of Cu bearing 9Cr steels were investigated, and the effect of ε-Cu particles on creep strength was discussed in terms of microstructural change during the creep deformation.

2. Experimental procedure

Fe-9mass%Cr alloys containing (0 ~ 4)mass%Cu were used. In the base steel (9Cr-0Cu), 2mass%Ni was also added, because the hardenability of Cu free 9Cr steel is insufficient and full martensitic structure can not be obtained even by water-quenching after solution treatment. Chemical compositions of these steels are listed in **Table 1**. Ingots of 1.5kg were produced by induction

melting in Ar gas atmosphere, hot-rolled at 1273K for 18ks, homogenized at 1523K for 18ks, and then subjected to solution treatment at 1273K followed by water-quenching. Since austenite grains in Fe-Cr-Cu steel are refined with increasing of Cu content [2], the different solution treatment condition was adopted for each specimen in order to make the grain size of all specimens equal; 1273K-3.6ks for the base and 1Cu steels, 1273K-7.2ks for 2Cu steel and 1423K-3.6ks for 4Cu steel. Microstructures were examined with optical and transmission electron microscopes. Creep tests were carried out under a condition of 873K-140MPa for cylindric test pieces of $\phi 3 \times 10$ mm gauge dimension.

Table 1 Chemical compositions of steels used. (mass%)

	Cr	Cu	Ni	Si	Mn	P	S	C	N	Fe
Base	8.88	—	2.01	0.02	0.15	0.005	0.014	0.005	0.0097	bal.
9Cr-1Cu	8.93	1.03	—	0.02	0.17	0.006	0.014	0.006	0.0090	bal.
9Cr-2Cu	8.94	2.08	—	0.02	0.16	0.007	0.013	0.006	0.0102	bal.
9Cr-4Cu	8.99	4.19	—	0.02	0.16	0.008	0.013	0.006	0.0118	bal.

3. Results and discussion

3.1 Creep deformation behavior in 9Cr-Cu steels

Fig. 1 represents optical (a) and transmission electron (b) micrographs of 9Cr-4Cu steel which was water-quenched after the solution treatment of 1273K-3.6ks. These photographs reveal that microstructure of the as-quenched specimen is typical lath martensite, and the lath structure is just similar to that in other commercial martensitic steels. There was no difference in morphology of lath structure among the specimens with various Cu content, but as already mentioned, prior-austenite grain size tended to be refined with increasing Cu content. Since creep properties of martensitic steels are influenced by the prior-austenite grain size, it is controlled to about 80μm in all specimens by the different solution treatments. **Fig. 2** shows the creep curves in these specimens with various Cu content under the condition of 873K-140MPa. Creep strength is improved by the Cu addition and the rupture time is prolonged with increasing the Cu content. **Fig. 3** shows the relation between the minimum strain rate and the Cu content for the creep tests. The minimum strain rate is markedly reduced with increasing the Cu content, and the value in 4Cu steel is smaller than that in the base steel by about 4 orders.

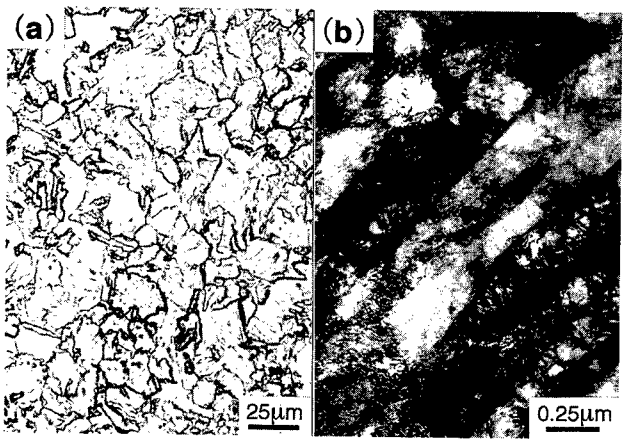

Fig. 1 Optical (a) and transmission electron (b) micrographs of 9Cr-4Cu steel. Water-quenched after solution treatment of 1273-3.6ks.

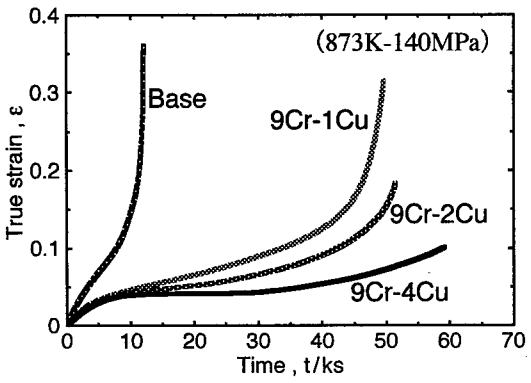

Fig.2 Creep curves in 9Cr steels with various Cu content.

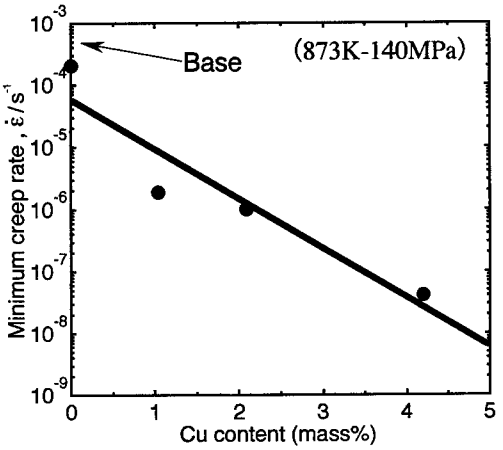

Fig.3 Relation between minimum strain rate and Cu content in 9Cr steels.

3.2 Microstructural change during creep deformation

Fig.4 shows the change in hardness of the specimens during creep deformation. The martensitic 9Cr steels are strengthened mainly through dislocation hardening and precipitation hardening by Cu particles, so the hardness generally corresponds to the dislocation density and the mean free path of dispersed Cu particles. In all specimens, the hardness abruptly drops at the early stage of creep deformation, and then gradually softens after 5.0ks of the creep deformation. With increasing the Cu content, however, the hardness is kept higher, and the softening rate also becomes smaller. This result indicates that, in the high Cu steels, the dislocation density remains higher or the mean free path of dispersed Cu particles remains finer during creep deformation.

Fig.5 shows the microstructural change during creep deformation in the base steel without Cu particles. The lath structure is barely maintained on the transition region, but it is fully collapsed at the steady state creep region and the subgrain structure is formed, where dislocation density is quite low. Once the subgrain structure is formed, the strain rate is accelerated and this leads to a rupture in a short time. On the other hand, the microstructural change in the 4Cu steel is shown in **Fig.6**. Recovery of martensite is greatly retarded and dislocation density remains high in comparison with the case of base steel, and lath structure is maintained even after rupture. This suppression of recovery is due to the dislocation pinning effect by Cu particles precipitated within laths and on lath boundaries. **Fig.7** represents the TEM image of 4Cu steel creep-deformed to 0.1% at 873K showing the interaction between Cu particles and dislocations within a lath. Dislocations vertically sticks to Cu particles and dislocation loops can not be observed around there. This means that the interaction between dislocations and Cu particles is attractive force. Cu particles also attractively interact with lath boundaries, and suppress the migration of them as shown in **Fig.8**. These pinning effects by Cu particles contribute to the retardation of recovery of martensite.

Fig.9 shows the change in the diameter of Cu particles and the mean free path of the Cu particles; λ calculated by the Eq.1 during the creep deformation.

$$\lambda=(1.81 f^{-1/2}-1.63) r \quad \cdots\cdots (1)$$

where f and r denote a volume fraction and a radius of Cu particles, respectively. The value of f was calculated in consideration of the solubility of Cu at the temperature. Cu particles constantly grow on the Ostwald mechanism with no relation to the Cu content. The Ostwald growth of Cu particles results in an extension of λ. However, it should be noted here that, λ is markedly extended in the low Cu

steels, while it does not change so much in the high Cu steels because of their high volume fraction of Cu particles.

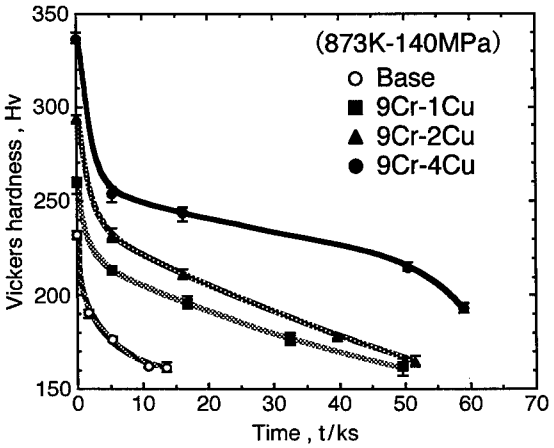

Fig.4 Change in hardness of 9Cr-Cu steels during the creep deformation

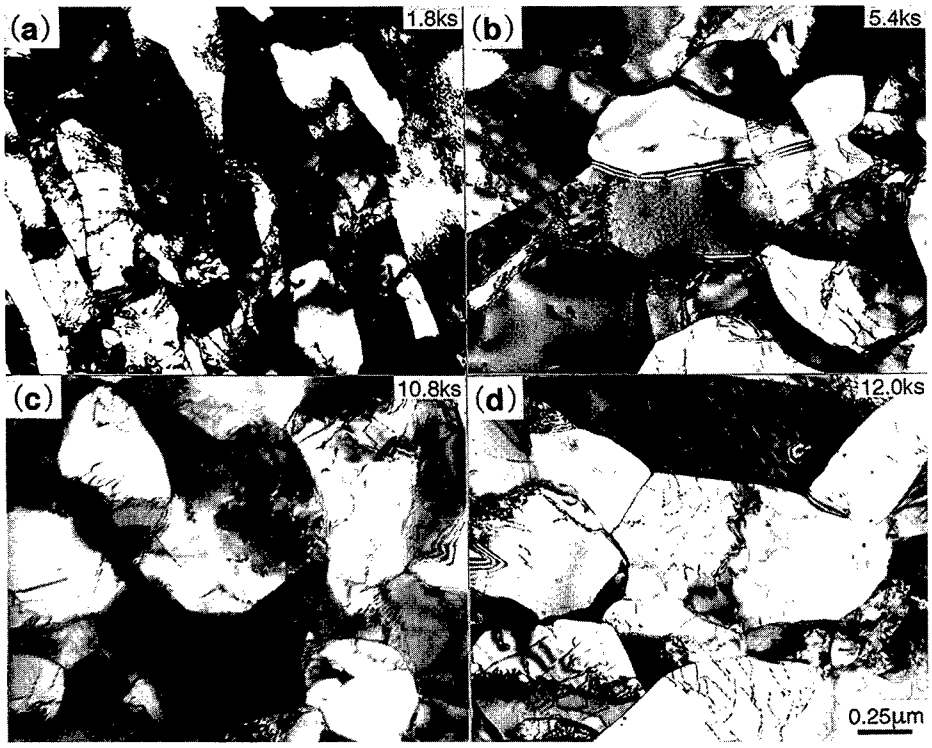

Fig.5 Microstructural change during the creep deformation of 873K-140MPa in the base steel.

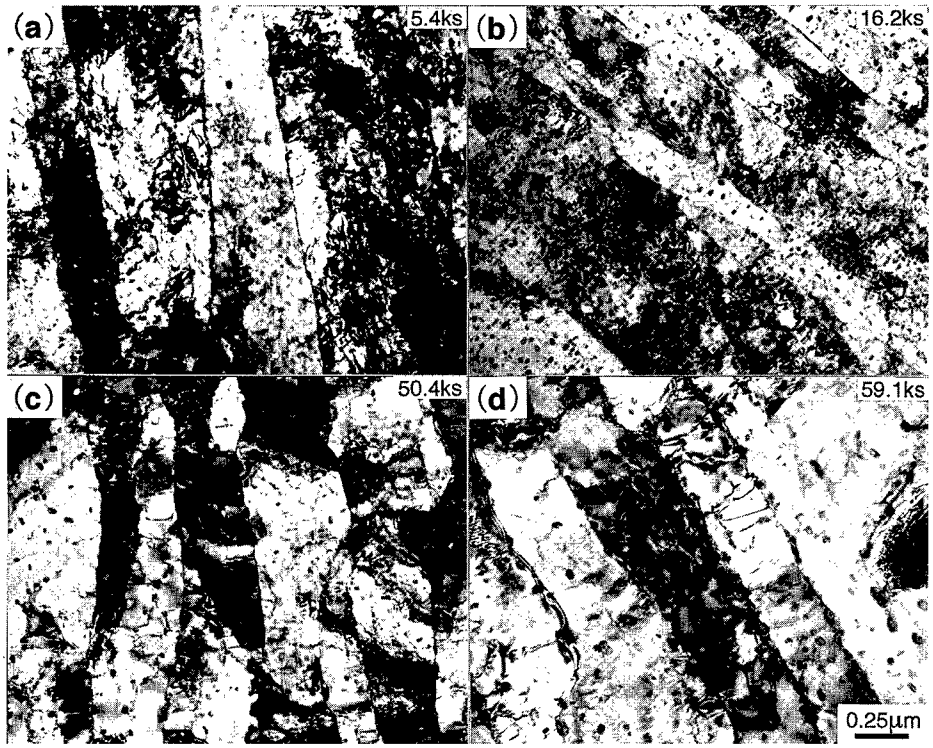

Fig.6 Microstructural change during the creep deformation of 873K-140MPa in the 9Cr-4Cu steel.

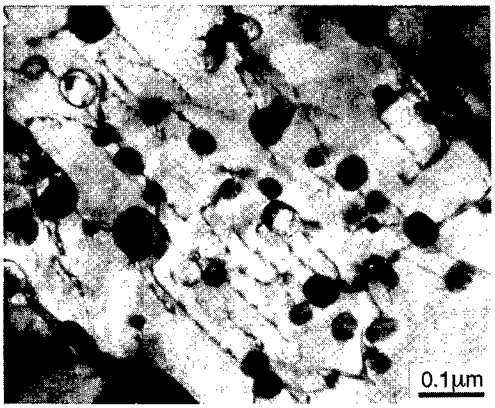

Fig.7 Microstructure of 9Cr-4Cu steel creep-deformed to 0.1% at 873K showing the interaction between Cu particles and dislocations within a lath.

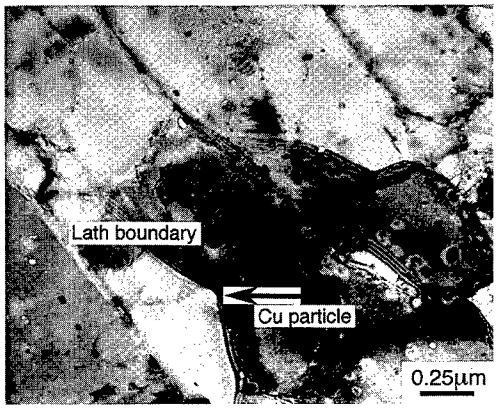

Fig.8 Microstructure of 9Cr-1Cu steel creep-deformed to 0.1% at 873K showing the interaction between a Cu particle and a lath boundary.

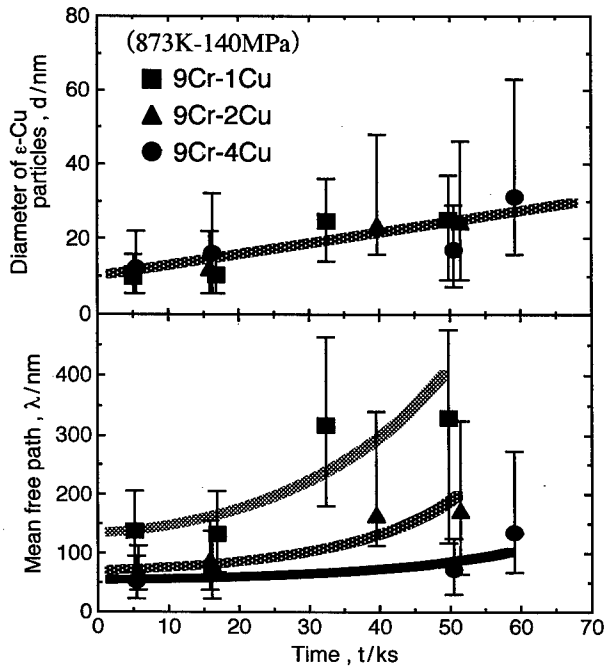

Fig.9 Change in diameter and mean free path of Cu particles during the creep deformation in 9Cr-Cu steels.

3.3 Change in pinning force by Cu particles during creep deformation

When the pinning force by Cu particles is larger than the stress given to a dislocation, the movement of dislocation is suppressed, and the recovery of martensite would be effectively retarded. On the contrary, when the pinning force becomes smaller than the stress, dislocations can move easily, so that the recovery is accelerated. Since the pinning force depends on the mean free path of dispersed particles, creep deformation behavior changes with coarsening of the particles. In general, the pinning force by dispersed particles; $\Delta\tau$ can be estimated from the Eq.2 as a function of the mean free path of the dispersed particles; λ.

$$\Delta\tau = \alpha Gb / \lambda \cdot \cdot \cdot \cdot \cdot (2)$$

The α is a constant (=0.8 [3]). **Fig.10** shows the change in the pinning force by Cu particles with the creep deformation calculated by the Eq.2 using the results of Fig.9. The applied shear stress of the creep tests (τ_0 = 70MPa) are also shown by the gray line. The pinning force is reduced with creep deformation in all specimens owing to the extension of λ through the Ostwald growth of Cu particles. In the 1Cu and 2Cu steels, the pinning forces fall below the applied stress after about 30ks and 40ks deformation, respectively. These times well correspond with the starting times of accelerate creep in each steel shown in Fig.2. On the other hand, in the 4Cu steel where the accelerating creep region could not be observed clearly, the pinning force is larger than the applied stress at all times. That is, strain rate is accelerated by the reduction of pinning force by Cu particles below the applied stress. From these results, it is concluded that the increase of Cu content is effective for strengthening of heat resistant martensitic steels in terms of keeping the mean free path of Cu particles small and making the recovery of martensite retard during creep deformation.

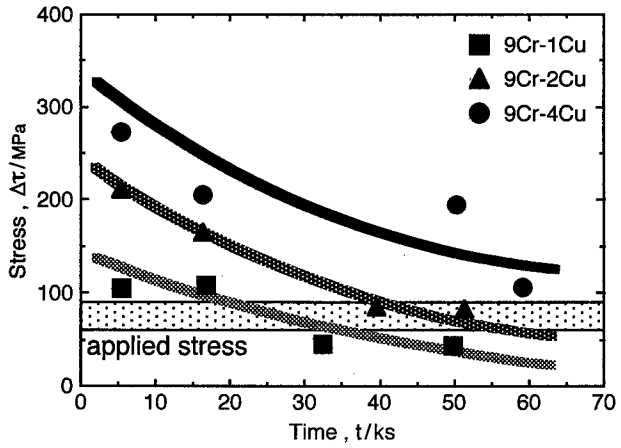

Fig.10 Change in the pinning force by Cu particles with the creep deformation.

4. Conclusion

(1) Creep strength is improved by Cu addition and fracture time is prolonged with increasing Cu content in 9%Cr martensitic steels.

(2) During creep deformation, dislocations attractively interact with ε-Cu particles within laths, and lath boundaries are also pinned by ε-Cu particles. These pinning effects by the ε-Cu particles contribute to the retardation of recovery of martensite.

(3) The pinning force by ε-Cu particles is reduced with creep deformation owing to the extension of mean free path of the particles through the Ostwald growth. But once the pinning force falls below the applied stress, the recovery rapidly proceeds and the strain rate is accelerated.

References

[1] J.Y.Yoo, W.Y.Choo, T.W.Park and Y.W.Kim : *ISIJ International*, **35**(1995), 1034

[2] Y.Futamura, T.Tsuchiyama and S.Takaki : *Tetsu-to-Hagane*, **85**(1999)

[3] K.C.Russell and L.M.Brown : *Acta Metallurgica*, **20**(1972), 969

For correspondence

e-mail: toshi@zaiko.kyushu-u.ac.jp

fax: +81-92-632-0434

Key Engineering Materials Vols. 171-174 (2000) pp. 419-426
© 2000 Trans Tech Publications, Switzerland

Creep Resistance and Structural Stability of Low-Alloy CrMo and CrMoV Steels

J. Purmenský[1], V. Foldyna[2] and Z. Kubon[1]

[1] Vítkovice, a.s., R&D Division, Pohranicní 31, CZ-706 02 Ostrava, Czech Republic

[2] Jinpo Plus, a.s., R&D Division, Kristanova 2, CZ-706 02 Ostrava-Prívoz, Czech Republic

Keywords: Creep Resistance, Low Alloy CrMo and CrMoV Steel, Precipitation Strengthening, Solid Solution Strengthening, Creep Rupture Strength, Steady State Creep Rate, Ostwald Ripening, Coarsening Constant K_d

Abstract: In the 0.5Cr-0.5Mo-0.3V steel a pronounced effect of proof stress at room temperature on the creep rupture strength (CRS) in 10^5 hours is still in evidence at relatively high temperature up to 575°C. In 2.25Cr-1Mo steel such a strong favourable effect is discernible only at lower temperatures up to about 525°C. The beneficial effect of Mo on the CRS of the low alloy CrMoV steels was found only when Mo concentration was up to about 0.5%. Further increasing of CRS is possible by raising vanadium content up to stoichiometric ratio V:C. The precipitation strengthening of CrMoV steels is ruled by V_4C_3 or V(C,N) while in CrMo steels Mo_2C, respectively Mo_2C and Cr_7C_3 are the principal precipitation strengthening particles. The dimensional stability of particles precipitating in CrMoV steel is much higher than those in CrMo steel.

INTRODUCTION

The purposeful development of low alloy steels for elevated temperature started early after the First World War, when some steels with low Mo and Cr contents were developed (1, 2). Before the Second World War the well-known steel 2.25Cr-1Mo was developed, as well (5). The beneficial effect of vanadium on the creep resistance of steels was appreciated later than that of molybdenum (3, 4). The tubes and pipes of the steel 0.5%Mo-0.2%V investigated in NPL in England were firstly installed in power station in 1940 (3-7).

The aim of the presented paper is to outline the fundamental strengthening mechanisms and degradation processes which influence the creep resistance of low alloy steels.

STRENGTHENING MECHANISMS

The most potential strengthening mechanisms operating during high temperature service in low alloy steels are precipitation strengthening (PS) and solid solution strengthening (SS) as the effect of the dislocation strengthening is usually limited to short time.

Precipitation strengthening

When assessing how the dispersion of the secondary phases affects the creep properties of the steel we must take into account not only the dispersion characteristic ascertained immediately after heat treatment, but also their changes caused either by coarsening of the particles or by precipitation of new particles during creep (8, 9, 12).

The best measure of the dispersion of particles has proved to be their mean interparticle spacing ℓ. It is calculated as:

$$\ell = \tfrac{1}{2} \cdot (N_v \cdot d)^{-\frac{1}{2}} - d \cdot \left(\tfrac{2}{3}\right)^{\frac{1}{2}} \qquad (1)$$

where N_v is the number of particles per unit volume, and **d** is the mean particle diameter (8, 9).

Precipitation strengthening in CrMoV steels is predominately effected by vanadium carbide or carbonitride particles.

It was found that when interparticle spacing (IPS) of vanadium carbide decreases, the proof stress at room temperature increases linearly. An increase in IPS of vanadium carbide from 60 to 180 nm reflects in lowering proof stress from 600 to 275 MPa. However, the creep rupture strength at 575°C in 10,000 and 100,000 hours (low stress region) is effected by IPS of vanadium carbide in more complicated way (Fig. 1).

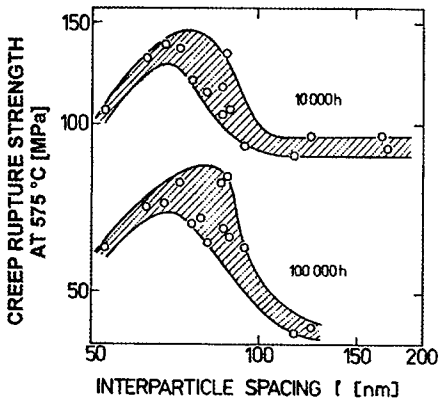

Fig. 1 Dependence of creep rupture strength on the interparticle spacing in (0.5Cr-0.5Mo-0.3V) steel

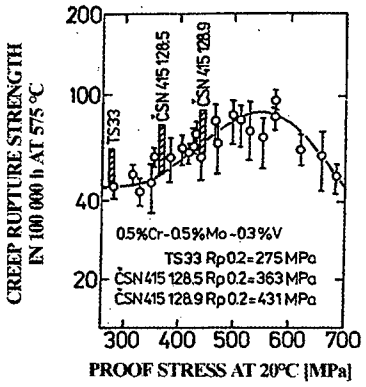

Fig. 2 Dependence of creep rupture strength on room temperature proof stress in low alloy CrMoV steel

The beneficial effect of decreasing the interparticle spacing has been observed in the relatively narrow interval of IPS (from 120 to 70 nm). The relation between CRS at 575°C and room temperature yield stress is very similar (Fig. 2) and for the proof stress raising from about 320 to 550 MPa the substantial increase of CRS is observed (8-13). In accordance with this finding, steel 0.5Cr-0.5Mo-0.3V is produced in two grades with minimum proof stress at room temperature being 363 MPa and 431 MPa, respectively (Fig. 2, Table 1). This steel is delivered in normalized and tempered condition and the higher proof stress should be obtained due to higher cooling rate from the austenizing temperature but not due to lower tempering temperature.

Another way how to improve the CRS of the steel 0.5Cr-0.5Mo-0.3V is to increase vanadium content up to the stoichiometric ratio V:C. The effect of V:C ratio on the time to rupture is shown in Fig. 3. Due to increasing V content, the amount of V(C,N) increases, too and at the same time IPS decreases and cementite practically diminishes at the expense of V(C,N) (8, 10).

The stress and temperature dependence of time to rupture of a commercial heat containing about 0.7 V is shown in Fig. 4 (8, 10).

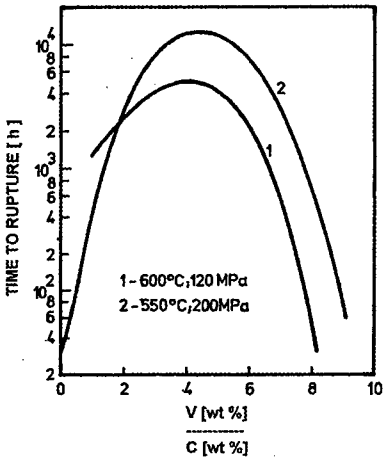

Fig. 3 How time to rupture depends on the ratio V:C at two testing conditions

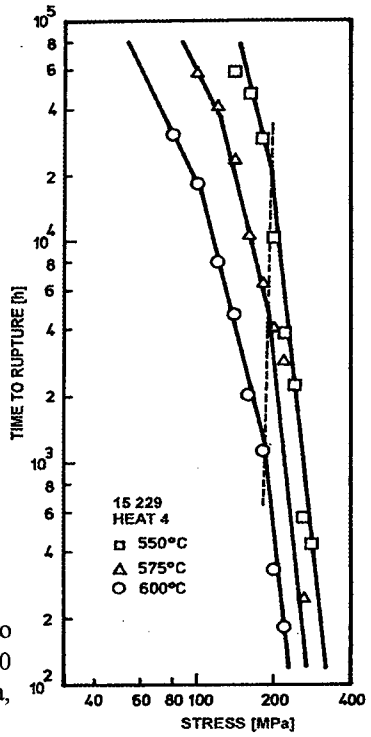

Fig. 4 Stress and temperature dependence of time to rupture (steel 0.12C-0.46Cr-0.51Mo-0.7V, pipe ϕ 580 x120 mm, 1030°C/water+730°C/air, $R_{p0.2}$=390 MPa, R_m=590 MPa, Z=69.7 %, KCU3=25 Jcm^{-2}

Table 1: Comparison of CRS of low alloy CrMo and CrMoV steels

Steel	Proof stress at RT	Creep rupture strength in 10^5 h, MPa					
	MPa	500°C	520°C	540°C	560°C	580°C	600°C
2.25Cr-1Mo	min. 265	137	107	79	59	44	-
0.5Cr-0.5Mo-0.3V	min. 355	169	131	101	78	60	45
0.5Cr-0.5Mo-0.3V	min. 430	197	157	123	93	69	inf. 51
0.7Cr-0.5Mo-0.6V	min. 370	214	166	128	99	75	55

Precipitation strengthening in CrMo steels is chiefly effected by Cr_7C_3 and Mo_2C. The effective IPS ℓ_{eff} should be calculated by means of the relation:

$$\frac{1}{\ell_{eff}} = \frac{1}{\ell_{Cr_7C_3}} + \frac{1}{\ell_{Mo_2C}} \qquad (2)$$

where ℓ_{Cr7C3} and ℓ_{Mo2C} mean IPS of Cr_7C_3 and Mo_2C, respectively.

The data shown in Table 1 confirm that steels alloyed with vanadium exert better creep resistance than chromium-molybdenum steels.

Solid solution strengthening

It is frequently supposed that significant solid solution strengthening (SS) of ferritic steels can be attained due to increasing Mo and/or W contents in the steel. This opinion was based on experimental results performed on binary Fe-Mo alloys (Fig. 5).

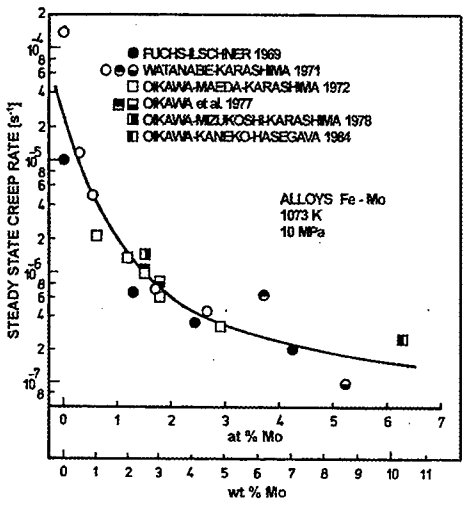

Fig. 5 The effect of Mo content on the creep rate of binary Fe-Mo alloys

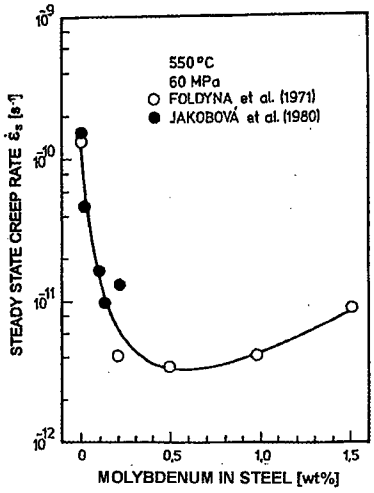

Fig. 6 The effect of Mo content on the creep rate of low alloy steel 0.12C-0.5Cr-0.3V

It was found that in Fe-Mo binary alloy the creep rate decreased with increasing Mo content up to 8 wt. %. In the alloy with 3 wt.% Mo the creep rate decreased about 100 times. The analysis of the effect of Mo on the creep rate of Fe-Mo alloys was performed with respect to different creep rates in ferromagnetic and paramagnetic regions (8) using creep data published in (14-19). It can be expected than after short time creep test (creep rate as slow as 10^{-7} s^{-1}) all Mo content remains in the solid solution. On the contrary, in low alloy CrMoV steels containing about 0.12 %C, 0.5 %Cr and 0.3 %V, the creep resistance raises only up to about 0.5 % Mo (Fig. 6). Creep rate as low as $2 \cdot 10^{-12}$ s^{-1} was observed at temperature 550°C and 60 MPa. In steels with more then 0.5 %Mo slight increasing of creep rate was again observed (23). Low alloy CrMoV steels containing 0.12C, 0.5Cr, 0.3V and from 0 to 1.5 wt.% Mo have been tested in the normalized and tempered condition, as well as in the state N+T and annealed further 600°C/5000h (21). After annealing decline of proof stress as well as CRS was observed but most significant decline was observed in the steel containing highest Mo content (1.5 wt.%). Similarly, creep rupture strength can be markedly improved by increasing Mo content only up to approximately 0.5 wt.%. Higher Mo content causes precipitation of Mo rich phases (Mo_2C and especially M_6C) which depletes the molybdenum content of the solid solution and in this way decreases the CRS. In steel with Mo content about 1.5 wt.% precipitation of M_6C strongly depletes the Mo content of the solid solution and moreover M_6C precipitates on expense of fine particles of vanadium carbides and carbonitrides and leads to the dramatic lowering of precipitation strengthening (21).

Optimum Mo content was found also in CrMoV steels with higher carbon contents (Fig. 7). There is no reason to increase Mo content over 0.5 wt.% also in CrMoV steels with carbon content up to 0.3 wt.% (8, 21, 23, 24).

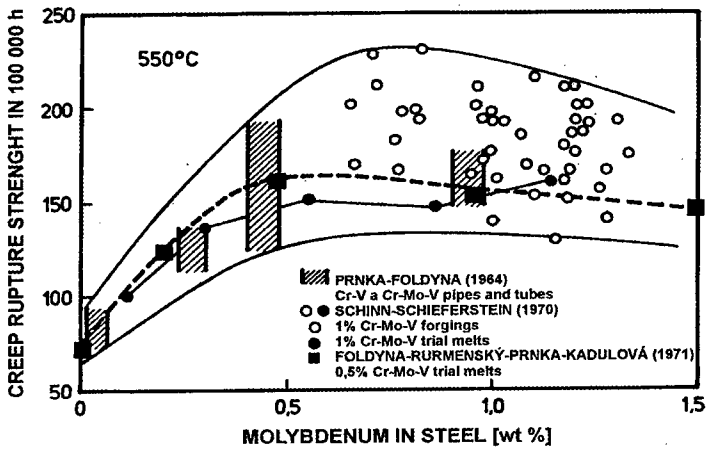

Fig. 7 The effect of Mo content on the creep rupture of CrMoV steels for tubes and pipes (carbon content up to 0.18 wt.%) and forgings (carbon content up to 0.30 wt.%)

The decisive role of molybdenum in the solid solution was pointed out by the experiments performed on the long time annealed material. There the part of Mo content was drawn out of solid solution to precipitate Mo_2C and/or M_6C, with dramatic reducing CRS, especially in steels with higher molybdenum contents. If we realize that M_6C precipitates on expense of fine vanadium carbide particles, lowering of precipitation strengthening is inevitable.

DEGRADATION MECHANISMS

Degradation of mechanical properties as well as creep strength is the consequence of long term high temperature service when microstructural changes lead to decrease of precipitation strengthening and/or solid solution strengthening.

One of the most effective degradation process is coarsening of secondary phases is Qstwald ripening that results in increasing the mean interparticle spacing, lowering number of particles, while the total amount of secondary phases (the volume fraction) remains constant.

The increase of mean particle diameter during coarsening can be expressed by the formula:

$$d^3 - d_0^3 = K_d \cdot t \qquad (3)$$

where d and d_0 are particle diameters after the exposure time t and in the as received state (t=0), K_d is the temperature dependent coarsening constant:

$$K_d = K_0 \cdot \exp(-\frac{Q}{RT}) \qquad (4)$$

where Q is the activation energy of the coarsening process and R, T have their usual meaning.

Figure 8 comprises the coarsening rate of carbides or carbonitrides that precipitate in low alloy steels. The ratio between mentioned K_d values determined experimentally after creep deformation at 600°C was expressed as follows (8, 9, 13, 25):

$$M_7C_3 : Mo_2C : V_4C_3 : VCN(VN) = \quad 2200 : 44 : 18 : 1 \qquad (5)$$

The dimensional stability of carbides precipitating in the 2.25Cr-1Mo steel is much lesser than the dimensional stability of vanadium carbonitride in the 0.5Cr-0.5Mo-0.3V steel. The mean coarsening rate of vanadium carbonitride at 575°C is comparable to that of Mo_2C at 490°C. The coarsening rate of Cr_7C_3 is at comparable temperatures about 50 times higher than K_d of Mo_2C. Described differences in coarsening rate of secondary phases precipitating in CrMo and CrMoV steels is the reason why the effect of proof stress at room temperature of CrMoV steels is still in evidence at

temperature up to 575°C. On the contrary, in CrMo steels this effect is limited by up to about 525°C - see Fig. 9 (8, 11, 12, 26)

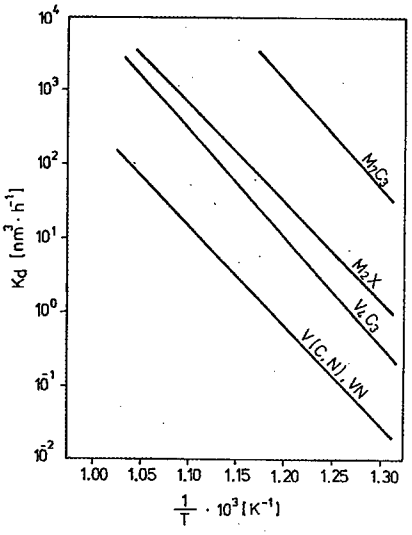

Fig. 8 Temperature dependence of coarsening constants K_d of M_7C_3, Mo_2C, V_4C_3 and VCN(VN)

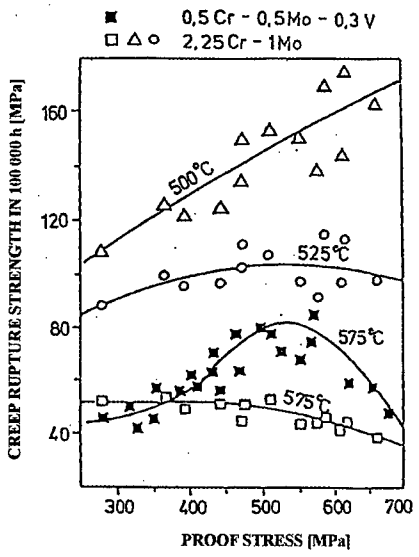

Fig. 9 Creep rupture strength versus proof stress in 0.5Cr-0.5Mo-0.3V and 2.25Cr-1Mo steels

MECHANISMS OF CREEP DEFORMATION AND RUPTURE

Two distinct domains of the stress dependence of creep rate and time to rupture have been frequently observed in the case of precipitation strengthened low alloy and modified Cr steels. The logarithmic plots of creep rate and of time to rupture as functions of stress (Fig. 10) consist of two linear segments, separating the data into low stress and high stress regions. The breakpoints $\sigma_{z(T)}$ in the stress dependence of time to rupture and steady-state creep rate coincide with each other, indicating that the change in mechanism causing the transition in both quantities is the same (8, 11, 12, 26). The creep rupture data have been analyzed by means of the equation:

$$t_r = A \cdot \sigma^{-n_r} \cdot \exp(\frac{Q_r}{RT}) \qquad (6)$$

where t_r is time to rupture [h]; σ means applied stress [MPa]; n_r means stress exponent; Q_r is the apparent activation energy [kJ·mol^{-1}]; A is the constant and R, T have their usual meaning.

This equation can be used for estimation of Q_r and n_r separately for low stress and high stress domains. The stress characterizing the transition between these domains (break point $\sigma_{z(T)}$) was found to be closely related to the critical stress σ_{crit}, which can be expressed as

$$\sigma_{crit} = A^* . \frac{G.b}{\ell} \qquad (7)$$

where constant $A^* \approx 1$; G is the shear modulus; b is the length of Burgers vector and ℓ is the interparticle spacing of secondary phases.

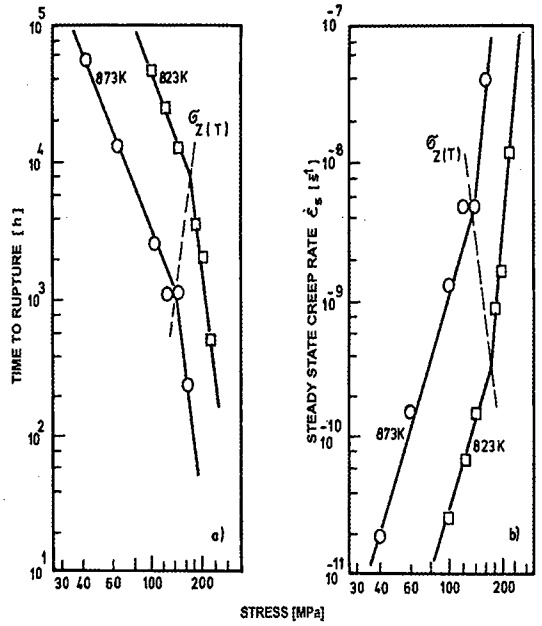

Fig. 10 Stress dependence of time to rupture and steady state creep rate of 0.5Cr-0.5Mo-0.3V steel

The temperature dependence of $\sigma_{z(T)}$ is mainly effected by Ostwald ripening and by additional precipitation of new particles during the creep process. In low alloy CrMoV steel it was observed that at 550°C $\sigma_{z(T)} = 1.0026\sigma_{crit}$, while at 600°C $\sigma_{z(T)} = 0.8713\sigma_{crit}$. It means that at 550°C Ostwald ripening is negligible (up to about 10^4 hours) while at 600°C increasing IPS is more significant. (8). It is supposed that in the high stress region dislocations can overcome particles of secondary phases by Orowan mechanism, while in the low stress domain dislocation should climb over particles (8, 9, 11, 12). The breakpoint thus corresponds to Orowan stress that is necessary for bowing dislocations between particles.

Creep of low alloy steel is characterized by activation energy Q and the stress exponent n. In low stress domain Q about 320 kJmol^{-1} and n about 5 can be expected. In high stress domain both values are higher – Q about 480 kJmol^{-1} and n about 11.

DISCUSSION

The superiority of the creep resistance of CrMoV steels over the 2.25Cr-1Mo steel can be easily demonstrated by the comparison of wall thickness and weight of pipes and tubes. The calculated results for pipeline ϕ245 mm operating at 540°C/13.8 MPa and superheating tubes ϕ35 mm operating at 570°C/16.2 MPa, respectively, are shown in the Table 2.

Table 2: Comparison of wall thickness and weight of pipes and tubes for pipeline and superheaters, using different CrMoV steels and 2.25Cr-1Mo steel.

Steel	Proof stress at RT °C	Tubes and pipes				
		Temperature °C	Pressure MPa	Diameter mm	Wall thickness mm	Weight kg
2.25Cr-1Mo	min. 265	540	13.8	245	36	15728
0.5Cr-0.5Mo-0.3V	min. 355				32	14280
0.5Cr-0.5Mo-0.3V*	min. 430				25	11560
0.7Cr-0.5Mo-0.6V	min. 370				24	11135
2.25Cr-1Mo	min. 265	570	16.2	32	8	34550
0.5Cr-0.5Mo-0.3V	min. 355				7	31492
0.7Cr-0.5Mo-0.6V	min. 370				5.6	26601

* accelerated cooling from austenitization temperature

The weight of pipeline and superheater was calculated on the assumption that the length of pipeline is 85 m and superheater 5400 mm, respectively.

REFERENCE

1. Körber, P. and Pomp, A., Mitteilungen aus dem Kaiser-Wilhelm Institute für Eisenforschung, Vol. 13, 1931, p. 223
2. Prömpel, P. and Pohl, E., Arch. Eisenhüttenw., 1 (1928), p. 785
3. Tapsell, H. J. et al, Proceedings of the Institution of Mechanical Engineers, 146 (1941, p. 208
4. Foldyna, V. and Prnka, T.: Hutnické listy, 24 (1969), p.581 (in Czech)
5. Newell, H. D., Metal Progress, 1936, p. 51
6. Glen, J., JISI, 155 (1947), p. 501
7. Glen, J., JISI, 158 (1948), p. 37
8. Foldyna, V., "Creep of Low Alloy and Modified Chromium Steels", DSc. thesis, IPM-Czechoslovak Academy of Sciences, Brno, January 1988 (in Czech)
9. Purmenský, J. et al, Materials for Advanced Power Engineering", Proceedings of the 5th Int. Conf., 1994, C.R.M. Belgium, October 1994, p. 193
10. Sobotka, J. and Foldyna, V., Hutnické listy, Vol. 37, 1982, p. 338 (in Czech)
11. Sklenicka, V. and Foldyna, V., Acta Technica CSAV (1990), No. 4, p. 495
12. Foldyna, V. and Purmenský J., Czechoslovak Journal of Physics, 39 (1989), p. 1133
13. Purmenský, J., "Structural Stability of Cr-Mo and CrMoV Steels and their Influence on Reliability of Power Plants and Chemical Equipment", DSc. thesis, IPM-Czechoslovak Academy of Sciences, Brno, November 1992 (in Czech
14. Fuchs, A. and Ilschner, B., Acta Met., 17 (1969), p. 109
15. Watanabe, T. and Karashima, S., Met. Trans., 2 (1971), p. 1359
16. Oikawa, H. et al, Scripta Met., 6 (1972), p. 339
17. Oikawa, H. et al, Mat. Sci. Eng., 29 (1977), p. 131
18. Oikawa, H. et al, Met. Trans., 9A (1977), p. 1281
19. Oikawa, H. et al, Scripta Met., 18 (1984), p. 393
20. Jakobová, A. et al, Technické aktuality Vítkovic, No. 3 (1980), p. 43 (in Czech)
21. Foldyna, V. et al, Arch. Eisenhüttenw., 42 (1971), p. 927
22. Jakobová, A. et al, Arch. Eisenhüttenw., 43 (1972), p. 55
23. Schinn, R.and Ruttmann, W., Arch. Eisenhüttenw., 28 (1957), p. 317
24. Diehl, H., Granacher, J. and Wiegand, H., Arch. Eisenhüttenw., 46 (1975), p. 461
25. Purmenský, J. and Foldyna, V., "Creep and Fracture of Engineering Materials and Structures", Proc. 8th Int. Conf., Ed. by J. C. Earthman and F. A. Mohamed, Publication of TMS, Irvine, USA, August 1997, p. 789
26. Foldyna, V., et al., "Creep Strength in Steel and High-Temperature Alloys", Proc. Int. Conf. Sheffield, U.K., September 1972, The Metals Society, London, (1974), p. 230

Key Engineering Materials Vols. 171-174 (2000) pp. 427-436
© 2000 Trans Tech Publications, Switzerland

Optimum Tungsten Content in High Strength 9 to 12% Chromium Containing Creep Resistant Steels

Y. Hasegawa[1], T. Muraki[1], M. Ohgami[2] and H. Mimura[3]

[1] Nippon Steel Corporation, Technical Development Bureau, Steel Research Laboratories, Steel Products Research Lab. II, 20-1 Shintomi, Futsu-shi, Chiba-ken 293-8511, Japan

[2] Nippon Steel Corporation, Technical Development Bureau, Hikari R&D Lab., 3434 Ohaza Shimada, Hikari-shi, Yamaguchi-ken 743-0063, Japan

[3] Nippon Steel Corporation, Head Office, Pipe & Tube Sales Division, Chemical & Boiler Tube Dept., 6-3 Otemachi, 2-chome, Chiyoda-ku, Tokyo 100-8071, Japan

Keywords: Laves Phase, Creep Strain Rate, Transient Creep, Accelerating Creep, ASME-P92

Abstract

Tungsten containing ferritic creep resistant steels are the candidate materials for Ultra-Super-Cretical fossil power plant because of their high creep rupture strength. But the strengthening mechanisms by tungsten addition have not yet been completely studied.

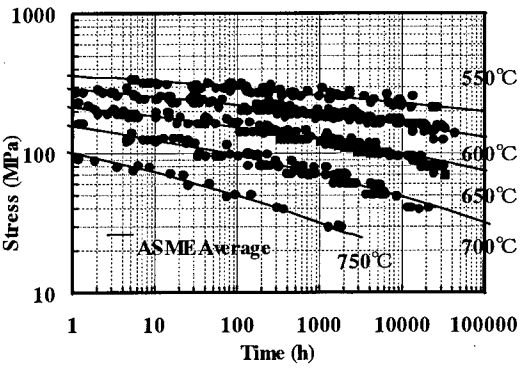

Fig. 1 Creep rupture curve for ASME-P92

In this report, creep rupture time and creep strain rate measurement decided the optimum tungsten content in 9 to 12% chromium ferritic steels. The precipitation behavior of Laves phase and the precise discussion of creep strain rate analyses explain the contribution of Laves phase at the lath boundary and the contribution of tungsten in solid solution. P92 contains the optimum amount of tungsten and chromium, 1.8 mass% and 9 mass% respectively judging from the creep rupture strength point of view.

1. Introduction

One of the high strength 9 % chromium ferritic vreep resistsnt steel, ASME-P92, contains well balanced tungsten and molybdenum, and this optimized amount of tungsten increases the estimated creep rupture strength to 132 MPa at 600 °C for 100,000 hours. Figure 1 shows the stress-rupture plot for ASME-P92.

Nowadys, some advanced research activities try to increase the creep rupture strength and steam oxidation resistance of P92 by tungsten and chromium content increase [1,2]. These

new research activities' alloy designs originate in the chemical composition of ASME-P92 in many cases. Therefore, it is no exaggeration to say that basic concept of the newly investigated steels is possible to follow the alloy design concept for P92.

More than 1 mass% tungsten addition obviously increases the creep rupture strength [3], but the details of the strengthening mechanism by high tungsten content have not yet been completely studied and understood. No experimental evidence indicates the creep rupture strength increase with higher tungsten content than that of P92. Effect of the other chemical composition to the creep properties of the modified steels has not yet been also methodically investigated. Furthermore, no industrial strengthening method has been established to increase the creep rupture strength of ferritic steels other than much tungsten addition. Therefore, precise and quantitative research on the strengthening mechanisms for tungsten containing ferritic steels contributes the development of the new creep resistant steel with higher creep properties at higher application steam conditions than those for P92.

In this report, optimum tungsten content will be decided by the investigation of 9 to 12% chromium steels with various tungsten content and by the discussion of strengthening mechanism by tungsten and analyses of the measurements of creep properties, rupture time and strain rate measurements.

2. Experimental procedure and the specimens.

High frequency induction furnace melted the 8 specimens in vacuum atmosphere and the each molten metal was cast into 50 kg ingot specimen. The parent steel is ASME-P92. From the steel A to F contain up to 3.0 mass% tungsten. Steel G contains 12 mass % chromium instead of 9 mass% of P92 and also contains 0.7 mass% nickel in order to avoid the delta ferrite phase. Steel H contains 11 mass% chromium, 2.5 mass% tungsten and 1.5 mass% cobalt. As a substitution of nickel, cobalt is also effective to obtain the full martensitic structure after quenching without large decrease of Ac1 temperature.

Table 1. Chemical compositions of the specimens in comparison with P92 (mass%).

Name	C	Si	Mn	Cr	Mo	W	Ni	Co	Nb	V	B	N
A	0.099	0.080	0.49	9.0	0.50	0.01	–	–	0.051	0.208	0.001	0.076
B	0.096	0.078	0.48	9.0	0.48	0.95	–	–	0.038	0.205	0.001	0.066
C	0.096	0.077	0.47	9.0	0.49	1.24	–	–	0.042	0.204	0.001	0.069
D	0.096	0.098	0.49	9.2	0.49	2.00	–	–	0.033	0.206	0.001	0.068
E	0.092	0.091	0.48	9.3	0.49	2.45	–	–	0.028	0.206	0.001	0.069
F	0.089	0.091	0.48	9.3	0.49	2.95	–	–	0.025	0.203	–	0.077
G	0.087	0.030	0.46	12	0.50	1.75	0.72	–	0.057	0.200	0.002	0.048
H	0.094	0.019	0.50	11	0.16	2.57	0.41	1.49	0.070	0.200	0.004	0.040
P92	0.090	0.030	0.50	9.0	0.50	1.80	–	–	0.070	0.200	0.002	0.050

Table 1 lists the chemical composition of each specimen. Ingot specimens were normalized at 1200 °C for 1 hour in the electric resistance furnace, and hot rolled into 15 mm thick plate

specimens. The plate specimens were normalized at between 1050 to 1100 °C and quenched in air. Tempering at between 750 to 780 °C for from 1 to 3 hours attained the tempered full matrtensitic structure. Acl and Ac3 transformation temperature confirmation by the Diratometry decided the heat treatment conditions. Creep rupture test specimens and creep strain rate test specimens have the 6mm diameter at the parallel part and their gage lengths are 30 mm. One of the typical austenite phase stabilizing element, nickel, possibly decreases the creep rupture strength, but the large deterioration by 0.7 mass% nickel addition has not yet been reported [4].

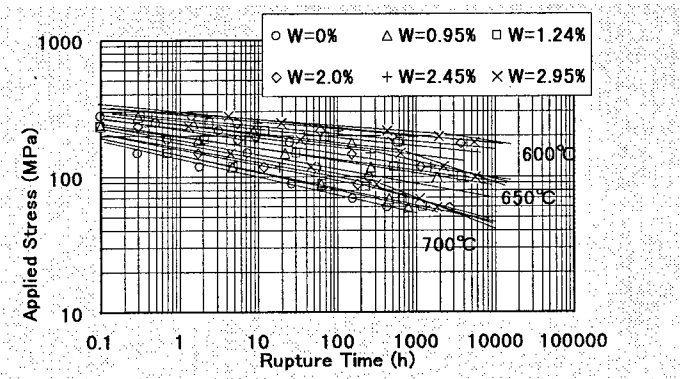

Fig.2 Influence of tungsten on creep rupture strength of P92

3. Experimental results.

3.1 Creep rupture strength dependence of P92 on tungsten and chromium content.

Figure 2 indicates the creep rupture properties for steel A, B, C, D, E and F. Creep rupture strength increases with tungsten content when the creep exposure time and temperature are relatively short and high respectively. But if the tungsten content is higher than 2 mass%, the creep rupture strength doesn't increase as a function of tungsten content any more, and possibly decreases with tungsten content for longer exposure time than thousand hours because of the sudden creep rupture curves' slope change. This tendency is evidently confirmed at 650°C. Therefore, effect of tungsten addition to the creep rupture strength increase saturates with 2 mass% tungsten.

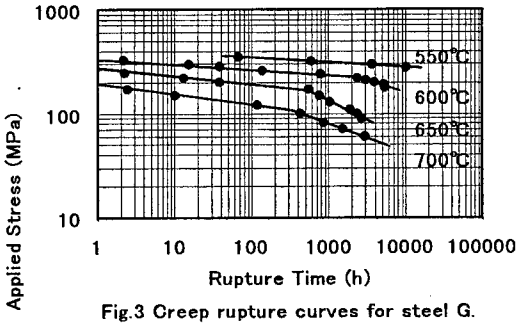

Fig.3 Creep rupture curves for steel G.

Figure 3 is the creep rupture property for steel G. This steel also indicates higher tensile strength than that of P92 at room temperature and it affects the creep rupture strength for short exposure time. But steel G also indicates the creep rupture strength deterioration when the exposure time is relatively long especially at 600 and 650 °C. The increase of tungsten and chromium contents results in the instability of creep rupture properties for long

exposure time.

Steel H contains higher tungsten and at the same time higher chromium than those of P92. Its creep rupture property also indicates the slope change of creep rupture curves at 600 and 650 ℃ as shown in figure 4. Steel H contains 1.5 mass% cobalt instead of nickel in steel G. Therefore effect of nickel addition in steel G can eliminate in the creep property of steel H. Nickel does not affect so severely according to the comparison of creep rupture strength of steel G with steel H. In cases of steel E, F, G and H, increase of tungsten and chromium improves the tensile properties. Therefore the creep rupture strengths of steel E, F, G and H are high for short tome exposure, but they decrease after several thousand hours creep exposure at 600 and 650 ℃, and finally, they possibly indicate almost same strength as P92 indicates if the exposure time is longer than 10,000 hours.

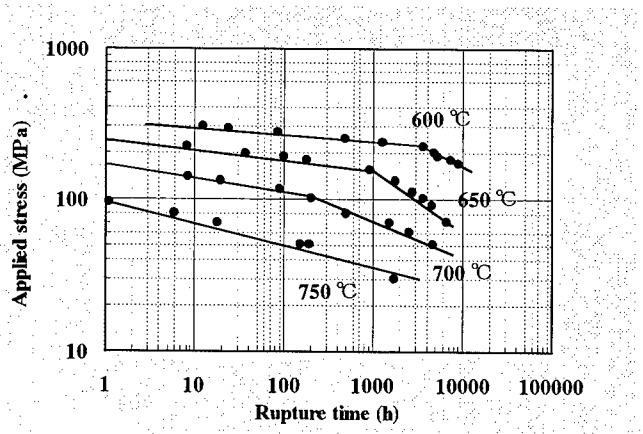

Fig. 4 Creep rupture curves of steel H.

Table 2 shows the tensile properties of steel H in comparison with those of P92.

Table 2. Representative tensile properties of steel H in comparison with those of P92

Steel	Tensilt strength	Yield strength	vE0℃	Elongation	Readuction Area ratio
Steel H	850 MPa	650 MPa	50 J	25 %	70 %
ASME-P92	700 MPa	520 MPa	150 J	25 %	70 %

4. Discussion

4.1 Creep rupture strength detrioration at 600 and 650 ℃ for steel E, F, G and H.

Steel E, F, G and H consist of almost same chemical compositions other than tungsten and chromium. Furthermore, the heat treatment conditions are also not different among four steels. Therefore the creep rupture strength instability derives from the change of strengthening factors from the parent material, P92. MX type carbo-nitrides, (Nb,V)(C,N), affects the creep properties in almost same way in four steels as in P92. Chromium content of the steel affects the constituents of M for $M_{23}C_6$ type carbide. But the stability of $M_{23}C_6$ does not look so strongly influenced by chromium content change of the steel. Chromium content difference affects the tungsten amount dissolved in the $M_{23}C_6$ type carbide. If the chromium atom replace the tungsten atom in $M_{23}C_6$, increase of chromium content in the steel accelerates the Laves phase precipitation. Therefore it is possible to say that chromium content increase in the steel has almost same effect as tungsten content increase.

Tungsten affects the creep rupture strength through solid solution strengthening and lath

structure stabilizing. The former effect depends on the resolved tungsten in supersaturation. The latter effect depends on the precipitated tungsten amount in Laves phase, inter-metallic compound, at the lath boundary. Two strengthening mechnisms strictly depends on the tungsten precipitation behavior, and therefore tungsten content in the steels. Various amount of tungsten in the steels possibly resulted in the stability differences of creep rupture curves.

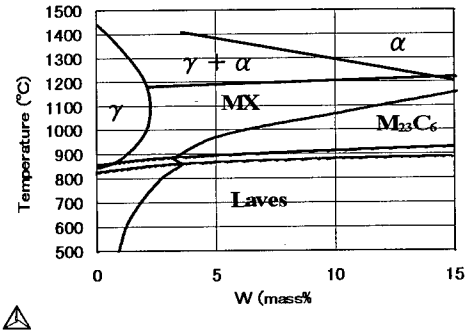

Fig. 5 Experimntal quasi-binary phase diagram of P92-W

Therefore, the precise analyses of tungsten precipitation behavior clarify the reason of unstable creep rupture properties for steel E, F, G and H

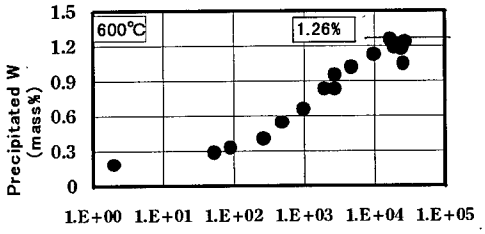

4.2 Precipitation behavior of Laves phase and $M_{23}C_6$ type carbide.

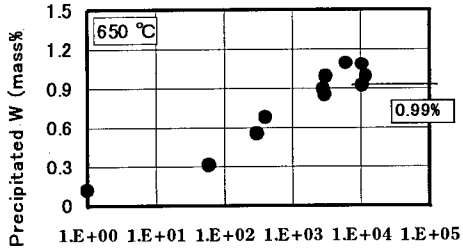

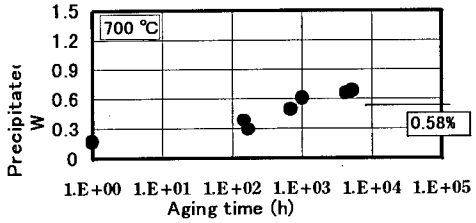

Fig. 6 Tungsten precipitation behavior forP92

$M_{23}C_6$ type carbide resolves into austenite matrix at normalizing temperature, from 1050 to 1100 °C [5], and precipitates mainly during the tempering. On the other hand, Laves phase precipitate only during the creep exposure because of its low resolution temperature, 720 °C in case of P92. Figure 5 is the quasi binary phase diagram between P92 and tungsten with estimated resolution curves for Laves phase which was calculated by Thermo-Calc. Phase stability experiment at austenitizing temperature, from 1000 to 1300 °C, decides the phase boundaries by measurement of delta ferrite phase ratio of various tungsten containing steels[6].

Figure 6 is the amount of tungsten precipitation as a function of aging time at 600, 650 and 700 °C. Quantitative analysis of extracted precipitates from matrix revealed the tungsten precipitation behavior. Laves phase does not precipitate at the beginning of aging. Therefore, initial precipitation amount of tungsten is the resolved tungsten amount in $M_{23}C_6$ type carbide. During the aging, tungsten precipitation amount increases with the time and X-ray

diffraction qualitative analysis identified the Laves phase. Therefore figure 6 implies the Laves phase precipitation with aging time. Laves phase precipitates all the time at 600 °C. It precipitates and saturates after about several 10,000 hours or 1,000 hours at 650 and 700 °C. After saturation of precipitation, Laves phase will coarsen with aging time.

Figure 7 is also the precipitation behavior of tungsten, iron and chromium for steel H from 600 to 700 °C. Creep tests were interrupted at 1, 10, 100, 1000, 3000, 6000, 10000 hours for all temperatures and applied stresses were 170 MPa at 600 °C, 70 MPa at 650 °C and 50 MPa at 700 °C. The precipitates were extracted from within gage length. The acceleration of Laves phase precipitation by stress also affects the precipitation behavior[7], but fur earlier precipitation of tungsten compared with those of P92 was observed in figure 7. Especially, at 650 °C, tungsten precipitation saturated completely after 1,000 hours already. Increase of temperature also accelerates the precipitation, but the equilibrium precipitation amount decreases with the temperature according to the phase diagram, figure 5. Therefore, early precipitation of Laves phase and its saturation in case of creep exposed steel H at 650 °C results in the most severe loss of precipitation strengthening effect by Laves phase and solid solution strengthening effect of supersaturated tungsten in matrix.

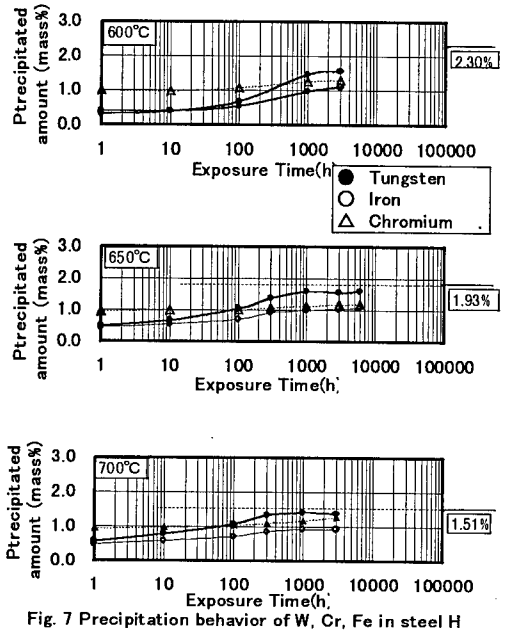

Fig. 7 Precipitation behavior of W, Cr, Fe in steel H

Chromium also precipitates in the same way as tungsten indicates. But its precipitation amount change is small compared with that of tungsten because of its higher resolution temperature. Therefore, tungsten precipitation supposedly affects more largely than chromium affects.

4.3 Analysis of creep strain and strain rate curves for steel H.

Figure 8 is the creep strain rate plot against the normalized strain for steel H at 600 °C. Each curve has the different rupture time. High applied stress test specimen ruptured early time. In case of such high stress test, the creep strain rate deteriorates with the strain during the transient creep stage. The creep strain rate increases with the strain while the accelerating creep stage. The decrease of creep strain rate is 2 orders of magnitude at most. But in case of relative low applied stress test, for 220 and 190 MPa, creep strain rate

decrease more than 5 orders of magnitude during the transient creep stage, and at the same time the strain of transient creep stage against the total creep strain becomes short. This means the creep resistance increased not ordinarily during the transient creep stage.

When the applied stress is 220 and 190 MPa at 600 ℃, the creep rupture strength deteriorate largely. According to the Laves phase precipitation behavior on figure 7, large decrease of creep strain rate is caused by accelerated Laves phase precipitation.

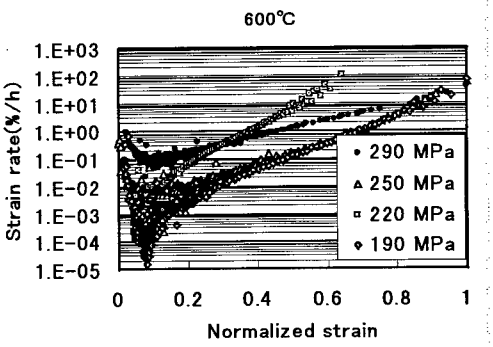

Fig. 8 Creep strain ratye of steel H

Relative low applied stress test also indicate the same mannered creep strain rate behavior at 650 and 700 ℃ in Figure 9 and figure 10 respectively. The keen deterioration of creep strain rate at 650 ℃ reaches about 6 or 7 orders of magnitude. Very early Laves phase precipitation at 650 ℃ decreases the creep strain rate remarkably. All of strain rate curves indicate the large creep strain rate deterioration during the transient creep stage at 700 ℃. But this tendency looks saturate if the applied stress lower than 70 MPa. If the creep strain rate deterioration is large, recover of creep strain rate is also large and the recovering rate seems larger than those of high stress test results. Namely, micro-structural recovering is possibly accelerated during the accelerating creep stage in case of relatively low stress test results. These results imply the effective Laves phase precipitation strengthening at lath boundaries only at the transient creep stage and its loss in early time by coarsening. This precipitation satrengthening is supposedely the restriction of lath structure recovering by pinning of lath boundary movement. The early consumption of supersaturated tungsten in solid solution accelerates the recover of the lath structure during the accelerating creep stage, then the recovering ratio of creep strain curves for low stress creep tests become larger than those of high stress creep tests.

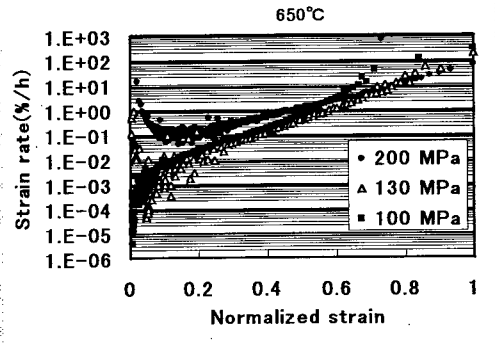

Fig. 9 Creep strain rate of steel H

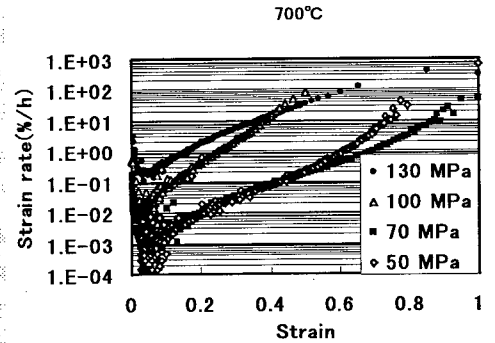

Fig. 10 Creep strain rate of steel H

4.4 Tungsten precipitation behavior and the optimum tungsten content.

Creep rupture strength measurement, creep strain measurement and precipitation behavior explain the instable creep property of modified P92 type steels with higher content of tungsten and chromium content. Tungsten precipitates mainly as inter-metallic compound, Laves Phase, during the creep exposure. Fine Laves phase on the lath boundary restricts the recover of lath structure at the very beginning of the precipitation. But if the tungsten content in the steel exceeds 2 mass%, the Laves phase precipitation will be accelerated and coarsen in short time. This accelerated Laves phase precipitation consumes resolved tungsten in supersaturation, and loses the precipitation strengthening effect at the lath boundary, lath structure recovering restriction. Therefore the recover of the lath structure becomes much faster than P92 and only the solid solution strengthening effect in equilibrium state decides the long time creep properties. The excess chromium, higher than 9 %, affects the tungsten precipitation amount through the change of $M_{23}C_6$ constituent.

The loss of solid solution strengthening effect does not independently explain the creep rupture strength deterioration at 600 and 650 °C for steel G and H.

Judging from the experimental results and discussion above mentioned, optimum chemical composition design is similar to that of ASME-P92 at least the chromium and tungsten content concern, 2 mass% tungsten addition with 9 mass% chromium.

5. Conclusions

5.1 Fe_2W type Laves phase precipitates mainly during the creep exposure. Fine Laves phase on the lath boundary restricts the recover of lath structure at the very beginning of the precipitation.

5.2 Coarsening of Laves phase at lath boundary and consumption of supersaturated tungsten in solid solution lose the strengthening factors and they induces the large decrease of creep rupture strength for the tungsten or chromium content increased specimens, steel G and H.

5.3 High test temperature accelerates the Laves phase precipitation, but the tungsten solution limit is also increased. Therefore, most severe creep rupture strength deterioration can be observed at 650 °C for steel H and G.

5.4 In case of P92, Laves phase precipitation continues 100,000 hours all the time. This continuous precipitation maintains the high creep rupture strength.

5.5 According to the tungsten precipitation behavior, optimum tungsten content is about 1.8 mass%. Higher tungsten content than 2 mass% accelerate the Laves phase precipitation if the chromium content stays 9%.

References

[1] M. Ohgami, Y. Hasegawa, H. Naoi and T. Fujita, IMechE Conference Transactions C522(1997)2, P115

[2] M. Igarashi, M. Muneki and F. Abe, Current Advances in Materials and Processes, Vol.12(1999)P495

[3] H. Mimura, M. Ohgami, H. Naoi and T. Fujita, Proceedings of COST501 Int. Conf., Sep. (1990).

[4] Y. Hasegawa, T. Muraki and M. Ohgami, Japan Society for the promoyion of Sicence, 123rd Committee on Heat Resisting Metals and Alloys, Vol 39, No.3 (1998)P.275

[5] H. Mimura, M. Ohgami, M. Naoi and K. Maruyama, Proceedings of VGB Conference, Mannheim July(1992) P6'1-6'11

[6] Y. Hasegawa, M. Ohgami, Current Advances in Materials and Processes, Vol.12(1999)P489

[7] Y. Hasegawa, M. Ohgami, G. Shigesato, Y. Sato, H. Mimura, Current Advances in Materials and Processes, Vol.11(1999)P1183

Yasushi Hasegawa : e-mail y-hasegawa@lab.re.nsc.co.jp
Fax +81 0439 80 2744

Key Engineering Materials Vols. 171-174 (2000) pp. 437-444
© 2000 Trans Tech Publications, Switzerland

Transient Creep Behaviour of Forged Thick Section 9Cr-1Mo Ferritic Steel

B.K. Choudhary, C. Phaniraj, K. Bhanu Sankara Rao and S.L. Mannan

Materials Development Group, Indira Gandhi Centre for Atomic Research, Kalpakkam-603 102, India

Keywords: 9Cr-1Mo Steel, Transient Creep, First Order Kinetics, Master Creep Curve

Abstract

The results of constant load creep tests on quenched and tempered 9Cr-1Mo ferritic steel in the temperature range 773-873 K and in the stress range 60-275 MPa are analysed in the framework of first order kinetics for transient and steady state creep. The strain-time data was adequately described by the Garofalo relation; $\epsilon = \epsilon_0 + \epsilon_T [(1- \exp(- r.t)] + \dot{\epsilon}_s.t$, where ϵ_0 is the initial strain at time $t = 0$, ϵ_T is the limiting transient creep strain, r is the rate of exhaustion of transient creep and $\dot{\epsilon}_s$ is the steady state creep rate. The stress dependences of $\dot{\epsilon}_s$ and r exhibited two slope behaviour. The results in both the stress regimes obeyed first order kinetics for transient creep, but with different values of $\beta = 15$ and 4.1 for low and high stress regimes respectively, where β is a constant and is the ratio of initial creep rate $\dot{\epsilon}_i$ to $\dot{\epsilon}_s$ (i.e. $\dot{\epsilon}_i = \beta.\dot{\epsilon}_s$). Separate master creep curves relating transient and steady state creep were obtained in the respective stress regimes. Further, analogous to Monkman-Grant and modified Monkman-Grant relationships, the relationship between $\dot{\epsilon}_s$, ϵ_T and time for onset of steady state creep t_{os} of the form $\dot{\epsilon}_s^{\alpha}.t_{os}/\epsilon_T$ = constant was found to be valid; the value of α was equal to unity.

Introduction

9Cr-1Mo ferritic steel is an important candidate material for tubings and thick section tube plates in the steam generator of liquid metal cooled fast breeder reactors (LMFBRs). The detailed investigations on creep, fatigue and creep-fatigue behaviour of this steel are given elsewhere [1]. For the sake of completeness, the results pertaining to the applied stress σ_a and temperature dependences of steady state creep rate $\dot{\epsilon}_s$ of quenched and tempered 9Cr-1Mo steel, tested in the temperature range 773-873 K and in the stress range 60-275 MPa, are summarised in the following. The study [1,2] revealed two stress regimes and they were characterised by different values of stress exponent and apparent activation energy. On incorporating the effective stress in Dorn type universal relationship for ϵ_s, a single slope behaviour with stress exponent of ~4 and true activation energy of ~ 250 kJ mol^{-1} was obtained. Based on these observations, it was concluded that the steady state creep deformation in both stress regimes occurs by climb controlled process. With a view to gaining further insight, the transient creep data obtained in both stress regimes are analysed in the framework of first order kinetic theory [3] first proposed by Webster, Cox and Dorn [4] and subsequently developed by Dorn, Mukherjee and coworkers [5,6].

It is generally observed that upon loading, creep rate ϵ decreases in the transient stage and approaches a steady state value. The major and important substructural change that takes place during transient creep is the rearrangement of dislocations by the diffusion controlled dislocation climb process. Therefore in both transient and steady state, creep is governed by climb controlled first order

kinetic process. This is formulated by the earlier investigators [4-6] as $d(\dot{\epsilon}-\dot{\epsilon}_s)/dt = -(\dot{\epsilon}-\dot{\epsilon}_s)/\tau$, where τ is the relaxation time for rearrangement of dislocations and $1/\tau$ is the rate constant which depends on stress and temperature in same way as does $\dot{\epsilon}_s$ ($1/\tau = K.\dot{\epsilon}_s$, K = constant). It was shown that integrating twice the above formulation leads to the well known Garofalo [7] strain-time relation

$$\epsilon = \epsilon_0 + \epsilon_T [1 - \exp(-r.t)] + \dot{\epsilon}_s.t , \quad (1)$$

where ϵ_0 is the initial strain at time t = 0, ϵ_T is the limiting transient creep strain and r is the rate of exhaustion of transient creep and further r is the same as rate constant $1/\tau$ when transient creep obeys first order kinetics. It may be mentioned that the empirical equation (1) is originally formulated by McVetty [8] and later confirmed by Garofalo [7] and other researchers [9,10]. Another important prediction of the first order kinetic approach is the proportionality between the initial creep rate $\dot{\epsilon}_i$ and $\dot{\epsilon}_s$, i.e. $\dot{\epsilon}_i = \beta.\dot{\epsilon}_s$, where β is a constant > 1. The important outcome of this approach is the universal creep equation of the form

$$\epsilon-\epsilon_0 = (\beta-1)/K [1-\exp(-K.\dot{\epsilon}_s.t)], \quad (2)$$

where $(\beta-1)/K = \epsilon_T$. It is emphasised that ϵ_T is a constant, since β and K are constants. Further, according to the above equation, for conditions obeying first order kinetics and for a constant ϵ_T, the different creep curves obtained for a combination of stress and temperature fall on a single master creep curve when the data is plotted as $(\epsilon - \epsilon_0)$ vs $\dot{\epsilon}_s.t$. In the present paper, the results obtained on 9Cr-1Mo steel in both the stress regimes (i.e. as mentioned earlier) are analysed in the framework of first order kinetics for transient creep. The paper also discusses the influence of stress and temperature on transient creep parameters like ϵ_T, r and K. Further, along with Monkman-Grant [11] and modified Monkman-Grant [12] relationships, the relation involving transient creep parameters [13] is tested for the results obtained in this study.

Analysis of experimental data

9Cr-1Mo steel used in this investigation was supplied in the form of 1000 mm diameter and 300 mm thick forging in the quenched and tempered condition (i.e. 1223 K/5 h, water quenched and 1023 K/8 h, air cooled). Constant load creep tests were conducted on specimens of cylindrical geometry with 50 mm gauge length and 10 mm gauge diameter, in the temperature range 773-873 K and in the stress range 60-275 MPa. The details regarding material, heat treatments, microstructures and creep testing are described elsewhere [1,2,14]. The strain (ϵ) - time (t) data are analysed following Eq. (1). The initial loading strain ϵ_0 and ϵ_T were determined from the normal creep curves. Following Eq. (1), r was evaluated graphically as the slope of $\ln(1-\Delta/\epsilon_T)$ vs t plots, where Δ is the transient creep component of total strain ϵ and $\Delta = \epsilon-\epsilon_0-\dot{\epsilon}_s.t$. Further, $\Delta = 0$ at t = 0 and Δ approaches ϵ_T at $t = t_{os}$, i.e. the time for the onset of steady state creep (since Eq. 1 in principle predicts steady state at $t = \infty$. $\dot{\epsilon}_i$ was calculated as $\dot{\epsilon}_i = \dot{\epsilon}_s + r.\epsilon_T$ which follows from Eq. (1) and β was evaluated from the logarithmic plot between ϵ_i and ϵ_s.

Results and discussion

For test conditions that obey first order kinetics for transient and steady state creep, proportionality is observed between $\dot{\epsilon}_i$ and $\dot{\epsilon}_s$, r and $\dot{\epsilon}_s$, and as a consequence, a constant ϵ_T is obtained. As a corollary, different creep curves with a constant ϵ_T fall on a single master creep curve according to Eq. (2), when data is plotted as $(\epsilon-\epsilon_0)$ vs $\dot{\epsilon}_s.t$. Earlier studies on pure metals and austenitic stainless steels [5,6,13] revealed the constancy of ϵ_T and the unified description in terms of master creep curves. In contrast to this, for high stress results obtained in this study, ϵ_T increased with decreasing stress and accordingly the plots of $(\epsilon-\epsilon_0)$ vs $\dot{\epsilon}_s.t$ (e.g., at 793 K in Fig. 1) resulted in

separate curves. It can be seen from Fig. 1 that with decreasing stress, the data shifted to higher values of $(\epsilon-\epsilon_0)$ in the transient region, whereas in steady state region the plots at different stresses yielded straight and parallel lines. On the other hand, the low stress data at each temperature exhibited a constant ϵ_T and as shown in Fig. 2 could be described by a single master creep curve.

Our attempt to understand the validity of the relationship $\dot{\epsilon}_i = \beta.\dot{\epsilon}_s$ (β = constant) for the results obtained at different temperatures is shown in Fig. 3 as logarithmic plot of $\dot{\epsilon}_i$ and $\dot{\epsilon}_s$. After ignoring the data in the transition stress regime, it is noticed that the results fall into separate regimes and proportionality constant β is obtained as β = 15 and 4.1 for low and high stress regimes respectively. An important observation to make here is that $\dot{\epsilon}_i$ shows the same stress dependences as $\dot{\epsilon}_s$ in both stress regimes at all temperatures. The observed differences in β values reflect the differences in the development of steady state structure from the initial structure in the respective stress regimes. It may be recalled [2] that the two exponent behaviour was observed when $\log\dot{\epsilon}_s$ were plotted against $\log\sigma_a$. In Fig. 4, both $\log\dot{\epsilon}_s$ and logr are plotted against $\log\sigma_a$ for the results obtained at 793 K and it can be seen that in the high stress regime, r shows a higher stress dependence compared to $\dot{\epsilon}_s$. For closer σ_a values in the low stress region, r and $\dot{\epsilon}_s$, show the same stress dependences. It is important to note that unlike smooth transition observed in $\log\dot{\epsilon}_s$ vs $\log\sigma_a$ plot, the variation of r with σ_a exhibited discontinuity in the transition regime. Earlier studies on analysis of first order kinetics for pure metals and austenitic stainless steels [4-6,13] revealed that the results obeyed the relation $r = K.\dot{\epsilon}_s$, where K is a constant. But for the high stress data obtained in this study, $r \neq K.\dot{\epsilon}_s$ (Fig. 4) and K decreased while ϵ_T increased with decrease in σ_a resulting in constant β, since $\beta = 1 + K.\epsilon_T$.

It is already seen in Fig. 1 that Eq. (2) failed to provide the unified description in terms of a master curve, since ϵ_T and K varied with stress and temperature. In this context, it is interesting to recall the relationship

$$(\dot{\epsilon}_s^{\alpha}.t_{os})/\epsilon_T = \text{Constant}, \tag{3}$$

suggested by Phaniraj et al. [13]. It has been shown by them that the value of α is equal to unity for conditions obeying first order kinetics and accordingly Eq. (3) takes the form

$$(\dot{\epsilon}_s.t_{os})/\epsilon_T = \text{Constant} = C_{PC}. \tag{4}$$

Further, for conditions obeying first order kinetics (α = 1), they introduced a parameter $p' = \dot{\epsilon}_s.t/\epsilon_T \geq 0$ ($p' = 0$ at $t = 0$ and $p' = C_{PC}$ at t_{os}) and reformulated the Garofalo relation [i.e. Eq. (1)] in terms of p' as

$$\epsilon-\epsilon_0 = \epsilon_T\,[1-\exp\{-p'(\beta-1)\} + p']. \tag{5}$$

Though they introduced the parameter p', they plotted $(\epsilon-\epsilon_0)$ vs $\dot{\epsilon}_s.t$ for obtaining master creep curves, since ϵ_T was constant for their results. An important implication of Eq. (5) is that when ϵ_T varies and for conditions obeying first order kinetics, i.e. α = 1, a plot of $(\epsilon-\epsilon_o)/\epsilon_T$ vs p' (i.e. $p' = \dot{\epsilon}_s.t/\epsilon_T$) would result in a master creep curve, only if β = constant.

The results at different temperatures in both the stress regimes were found to obey Eq. (4) with α = 1 confirming the validity of first order kinetics and these are presented in the later part of this paper. Our attempts to obtain master creep curves described by Eq. (5) are illustrated in Figs. 5 and 6 for high and low stress regimes respectively. Solid line in these figures corresponds to the theoretical curve according to Eq. (5) with β = 4.1 and 15 for high and low stress regimes respectively. It is seen that irrespective of test temperature, the results yield separate master curves, one for high stress regime (Fig. 5) and another for low stress regime (Fig. 6). Both these master curves following Eq. (5) are shown in Fig. 7. The first observation to make here is that the higher value of β = 15 observed at low

stresses is reflected in higher values of $(\epsilon-\epsilon_0)/\epsilon_T$ in the transient creep region. The second observation is that Eq. (4) is valid (i.e. $\dot{\epsilon}_s.t_{os}/\epsilon_T$ = constant = C_{PC}) for the results with lower value of C_{PC} at low stresses and the onset of steady state is indicated by the vertical arrows in Fig. 7.

The results obtained at different temperatures obeyed Eq. (3), Monkman-Grant (MGR: $\dot{\epsilon}_s^{\,m}.t_r$ = constant) and modified Monkman-Grant (MMGR:$\dot{\epsilon}_s^{\,m'}.t_r/\epsilon_f$ = constant) relationships. The details regarding the values of rupture life t_r and strain to failure ϵ_f are given elsewhere [14]. The validity of Eq. (3) along with MGR and MMGR for the results at 873 K is illustrated typically in Fig. 8; the values of α, m and m' are found to be close to unity. From the value of $\alpha \simeq 1$, we show the validity of Eq. (4) and the first order kinetics for 9Cr-1Mo steel. The results supporting the analogy between Eq. (4), MGR and MMGR are in agreement with those reported by Phaniraj et al. [13]. But the interesting observation to note here is that at various temperatures, the two stress regimes with different stress exponents are manifested as separate set of constant values of transient creep constant C_{PC}, Monkman-Grant constant C_{MG} ($C_{MG} = \dot{\epsilon}_s.t_r$) and modified Monkman-Grant constant C_{MMG} ($C_{MMG} = \dot{\epsilon}_s.t_r/\epsilon_f$) in the respective stress regimes. C_{PC} was found to be 0.35 and 1.35 in the low and high stress regimes respectively (Fig. 8).

It is observed that transient and steady state creep are related by a single master creep curve and are governed by a first order kinetic process. The different stress exponents noticed for the two stress regimes were reflected as separate master creep curves with different values of β and transient creep constant C_{PC}. Further, the differences were also seen in the behaviour of r and ϵ_T in the two stress regimes. These observations suggest that though creep in both stress regimes is governed by dislocation climb controlled first order process, the way the dislocation structure evolves might be different in the respective stress regimes. A low value of $\beta = 4.1$ observed at high stresses suggests that the steady state structure is closer to the initial structure, whereas at low stresses, the steady state and initial structures are farther apart as reflected by a high value of $\beta = 15$. The results imply that in these stress regimes different deformation mechanisms could be operative right from the beginning of the creep test. For AISI 304 stainless steel, Phaniraj et al. [13] observed separate master curves with different K and ϵ_T values in the two stress regimes and was related to the differences in dislocation substructures, i.e. cells at high stresses and subgrains at low stresses. However, it is important to recall that they obtained a single value of β for both the stress regimes. The different β values observed in this study further support the explanation put forward earlier [1,2] for the stress dependence of $\dot{\epsilon}_s$ that the dislocation climb by-pass around particles and Orowan bowing are the dominant deformation mechanisms in the low and high stress regimes respectively. However, at high stresses bowing of dislocations around particles leaves loops that generate back stress and at some stage the back stress will be sufficient to prevent further bowing of dislocations [15]. The rate of creep deformation is then determined by the rate at which the loop nearest to the particle climbs over and gets annihilated. The annihilation of loop allows further dislocation bowing to form another loop [15]. In this case also creep is governed by climb controlled process. Thus creep deformation of 9Cr-1Mo steel in both stress regimes occurs by dislocation climb and the results obey first order kinetics.

Conclusions

The following principal conclusions can be drawn from the present investigation.

1. The results in the temperature range 773-873 K and in the stress range 60-275 MPa reveal two stress regimes and the creep data follows the expression $(\epsilon-\epsilon_0)/\epsilon_T = [1- \exp\{- p'(\beta-1)\} + p']$, where $p' = \dot{\epsilon}_s.t/\epsilon_T \geq 0$ is regarded as a parameter.
2. Results in both the stress regimes obey first order kinetics and $(\epsilon-\epsilon_0)/\epsilon_T$ vs p' results in separate master creep curves, one for low stress regime with $\beta = 15$ and another for high stress regime with $\beta = 4.1$.

3. Similar to Monkman-Grant and modified Monkman-Grant relations, the results obey the relationship between transient and steady state creep of the form $\dot{\epsilon}_s.t_{os}/\epsilon_T$ = constant = C_{PC}, with separate values of C_{PC} in the respective stress regimes.

References

1. B.K. Choudhary, *Tensile, creep and low cycle fatigue behaviour of 9Cr-1Mo ferritic steel*, Ph. D. Thesis, Indian Institute of Technology, Bombay, 1997.
2. B.K. Choudhary, K. Bhanu Sankara Rao and S.L. Mannan, Trans. Indian Inst. Metals, 1999 (in press).
3. C. Phaniraj, *Creep behaviour of AISI 304 stainless steel - Analysis and implications of first order kinetics*, Ph. D. Thesis, Indian Institute of Technology, Bombay, 1997.
4. G.A. Webster, A.P.D. Cox and J.E. Dorn, Metal Sci. J. 3(1969), p. 221.
5. K.E. Amin, A.K. Mukherjee and J.E. Dorn, J. Mech. Phys. Solids 18(1975), p. 413.
6. A. Almadieh and A.K. Mukherjee, Mater. Sci. Eng. 21(1975), p. 115.
7. F. Garofalo, *Fundamentals of Creep and Creep Rupture in Metals*, Mc Millan. New York, 1965.
8. P.G. McVetty, Mech. Eng. 56 (1934), p. 149.
9. J. B. Conway and M.J. Mullikin, Trans. Metall. Soc. AIME 236(1966), p. 1496.
10. W.J. Evans and B. Wilshire, Trans Metall. Soc. AIME 242(1966), p. 1303.
11. F.C. Monkman and N.J. Grant, Proc.Am. Soc. Test. Mater. 56(1956), p. 593.
12. F. Dobes and K. Milicka, Metal Sci. 10(1976), p. 382.
13. C. Phaniraj, M. Nandagopal. S.L. Mannan and P. Rodriguez, Acta metall. mater. 39 (1991), p. 1651.
14. B.K. Choudhary, K. Bhanu Sankara Rao and S.L. Mannan, Metall. Mater. Trans. A, 1999 (in press).
15. G.S. Ansel and J. Weertman, Trans. Metall. Soc. AIME. 236(1959), p. 570.

(Fax: +91-4114-40360/40381/40301/40396, E-mail: bkc@igcar.ernet.in)

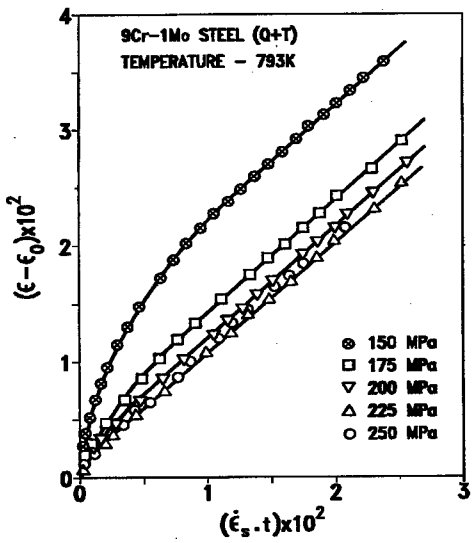

Fig. 1. Plot of $(\epsilon-\epsilon_0)$ vs $\dot{\epsilon}_s.t$ for high stress regime at 793 K.

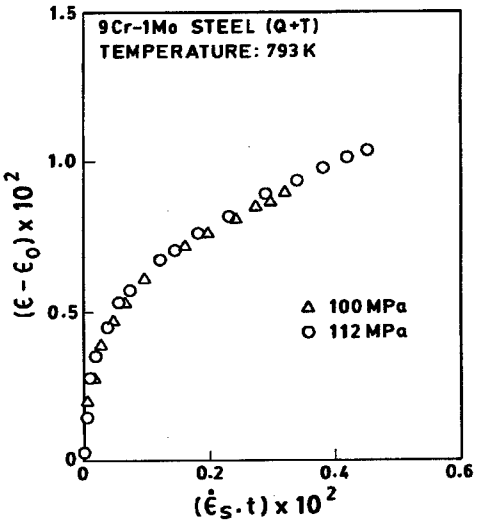

Fig. 2. Plot of $(\epsilon-\epsilon_0)$ vs $\dot{\epsilon}_s.t$ for low stress regime at 793 K yielding a single master curve.

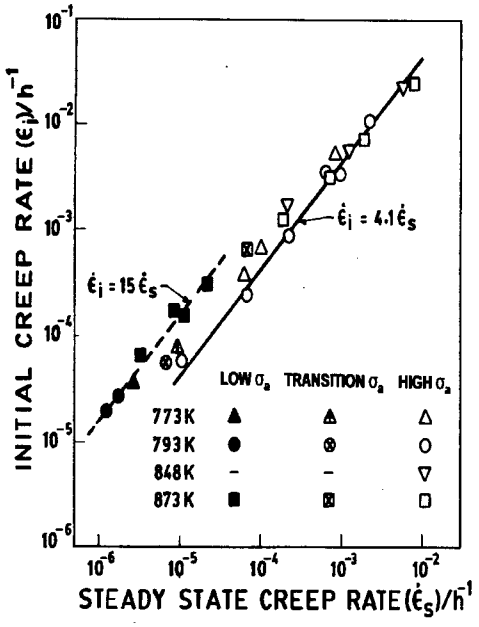

Fig. 3. Plot of initial creep rate $\dot{\epsilon}_i$ against steady state creep rate $\dot{\epsilon}_s$ showing separate β values for low and high stress regimes.

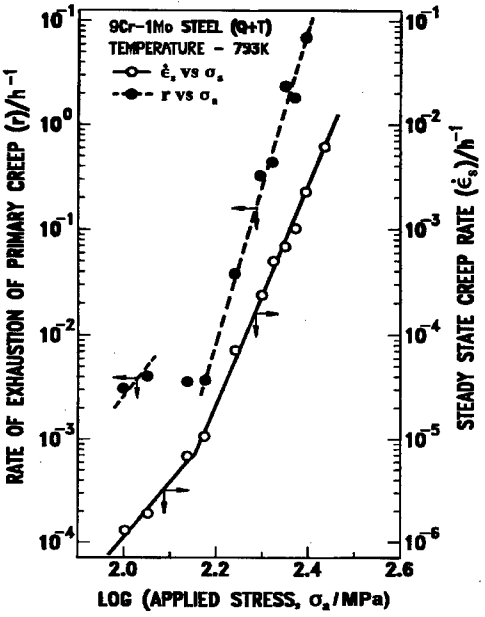

Fig. 4. Stress dependence of rate of exhaustion of transient creep r and steady state creep rate $\dot{\epsilon}_s$ for results at 793 K.

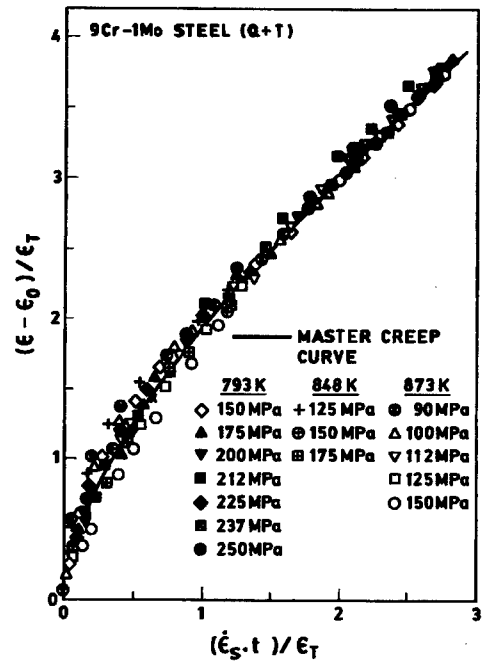

Fig. 5. Master creep curve according to Eq. (5) for high stress regime at various temperatures.

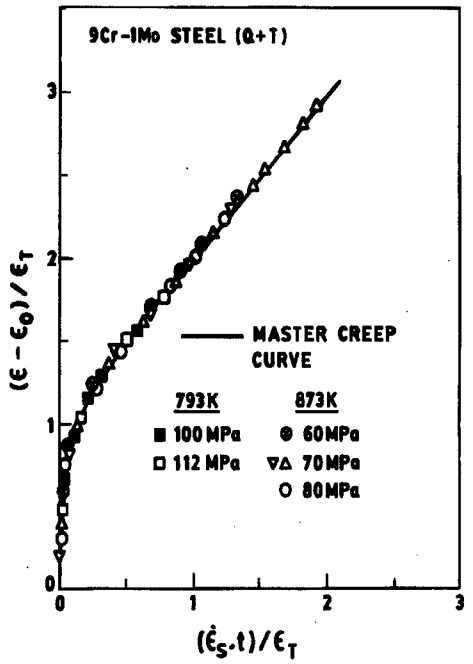

Fig. 6. Master creep curve according to Eq. (5) for low stress regime.

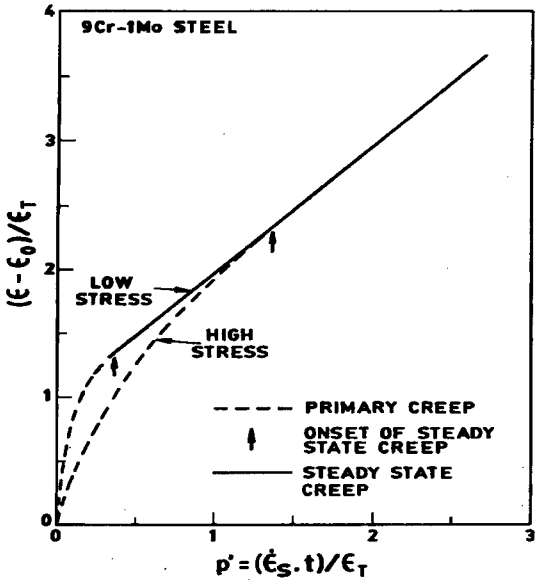

Fig. 7. Separate master creep curves for low and high stress regimes with β = 15 and 4.1 for the respective regimes.

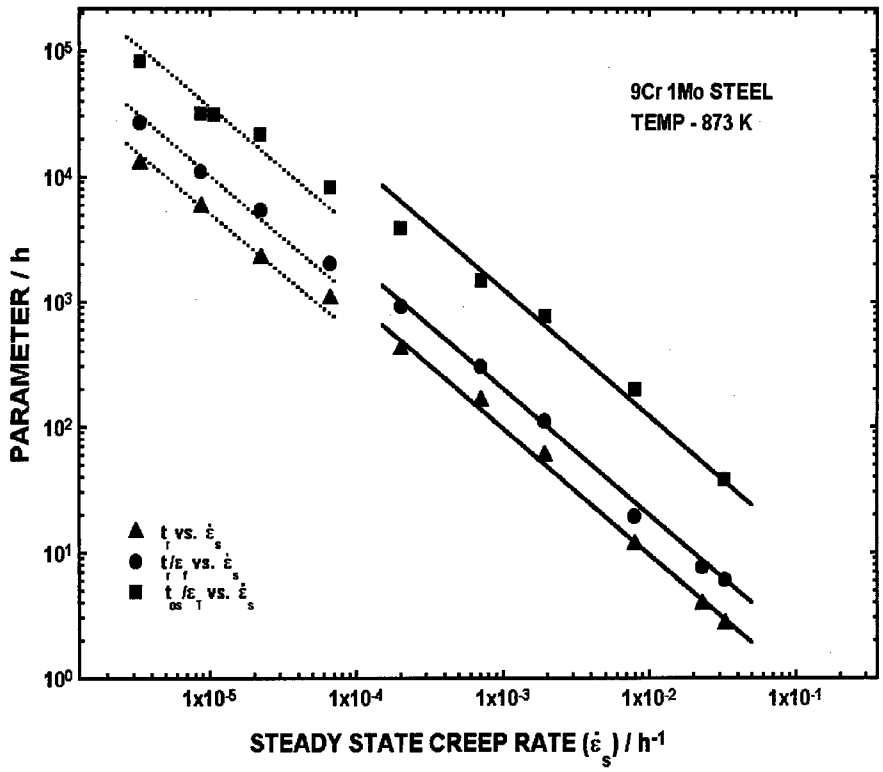

Fig. 8. Analogy of Eq. (4) with MGR and MMGR for tests at 873 K illustrating separate values of C_{PC} = 0.35 and 1.35 for low and high stress regimes respectively.

Key Engineering Materials Vols. 171-174 (2000) pp. 445-452
© 2000 Trans Tech Publications, Switzerland

Effect of Soluble Nitrogen on the Creep Strength of an Austenitic 25Cr-20Ni Steel

I. Park[1], F. Masuyama[2] and T. Endo[3]

[1] Graduate Student, Yokohama National University, Yokohama, 240-8501, Japan

[2] Mitsubishi Heavy Industries, Ltd. 5-717-1, Fukahori-matchi, Nagasaki, 851-0392, Japan

[3] Faculty of Engineering, Yokohama National University,
79-5 Tokiwadai, Hodogaya-ku, Yokohama 240-8501, Japan

Keywords: Stainless Steel, Nitrogen, High Temperature, Creep, I-S Pair, Solid Solution Hardening

Abstract

For the better understanding of the role of nitrogen in a 25Cr-20Ni-0.45Nb-0.2N steel, HR3C, the creep behavior and the response to abrupt stress change were compared with those of a Nb and N free 25Cr-20Ni steel, SUS310S, and the effective stress level of HR3C steel was examined from the stress relaxation curve analysis. It was found that the combined effect of a small amount of N and trace Nb decreased creep rate and increased creep life greatly, and the instantaneous plastic strain was not discernible in HR3C while that of SUS301S was clearly observed. The effective stress in total flow stress was found to be about 15%. From these results, the conclusion was drawn that the solution nitrogen in HR3C steel forms Cr-N clusters and dislocations drag the solute atmosphere composed of Cr-N clusters behind them.

1. Introduction

The 20-25 Cr series steels exhibit higher steam oxidation resistance than that of the 18Cr-8Ni series steels, however, the creep strength of the former is inferior to that of the latter. Based on this background, an attempt has been made to improve creep strength of 20-25Cr series steels. Actually, HR3C steel is an improve version developed from a 25Cr-20Ni series steel of SUS310S. The basic concept adopted here is to bring about the stable austenitic structure by adding 0.2% mass. N instead of decreasing Ni contents as well as in precipitation strengthening by the trace addition of Nb. In practice, except the added N and Nb, the chemical composition of these two steels is much the same, however, creep strength is greatly improved. So far the remarkable increase in creep strength is ascribed mainly to the precipitation strengthening, however, there is a possibility of contribution from chromium-nitrogen clusters to solid solution strengthening, which inevitably increases the "inherent creep strength" governing creep deformation in long term creep region [1]. Present paper will compare the creep characteristic of HR3C with that of SUS301S and throw light on the contribution from chromium-nitrogen clusters to solid solution strengthening in creep of HR3C steel.

2. Materials and Experimental Procedures

The chemical composition of HR3C and SUS310S is shown in Table 1. Flat specimens used for creep tests have four protrusions in both ends of gage section to place an extensometer and they were electrospark machined from as-received tube. The gage section is 40 mm in length, 10 mm in width and 2 mm in thickness. Creep testing was carried out under constant load. The differential tests were conducted using an electro hydraulic universal tester with closed-loop control system. The dimension of test specimens is about the same as those for creep tests. The spring constant of the universal tester was 1.59×10^5 MPa for a 500 kgf load cell. The accuracy of extensometer was better than 1 micrometer. The temperature and stress range adopted in the present study was from 923 K to 973 K and 254.9 to 343.2 MPa for HR3C and 254.9 to 294.1 MPa for SUS310S.

Table 1. Chemical composition of tested materials (mass.%).

	C	Si	Mn	Ni	Cr	Nb	N
HR3C	0.06	0.4	1.2	20.0	25.0	0.45	0.2
SUS310S	0.08	0.4	1.6	20.0	25.0	-	-

3. Experimental Results

3.1. Creep behavior

Figures 1 and 2 are the examples of creep curve obtained at 948 K for HR3C and SUS 301S steels, respectively. All of them exhibit normal primary creep, which is convex upward, and fail to show steady state creep. This is because all creep curves were obtained under constant load. It is worth to note that the creep life of HR3C is about 100 times longer than that of SUS310S steel. The results are not shown here but the rupture strain of the former was about 6% while that of the latter was about 20 %.

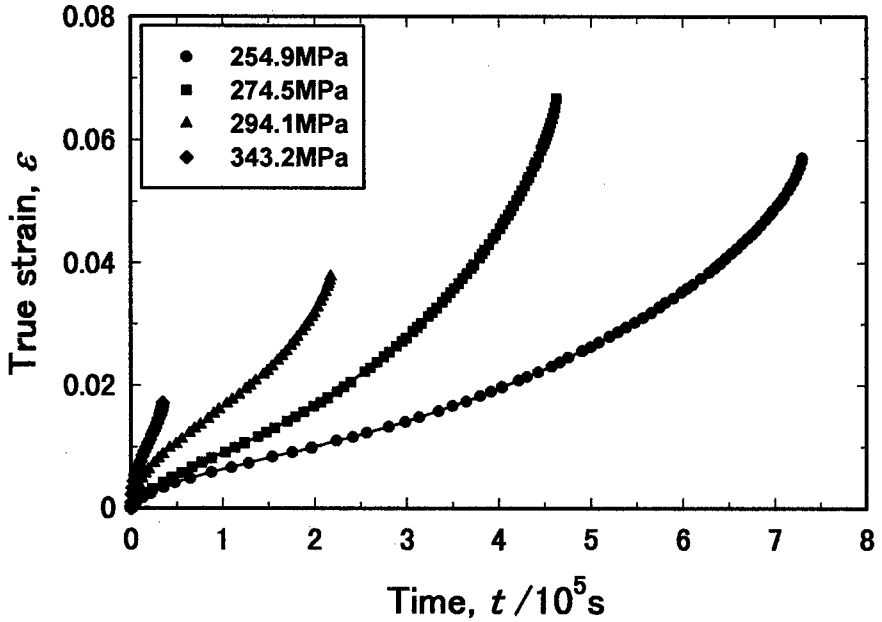

Fig.1 The creep curve of HR3C stainless steel at 948K

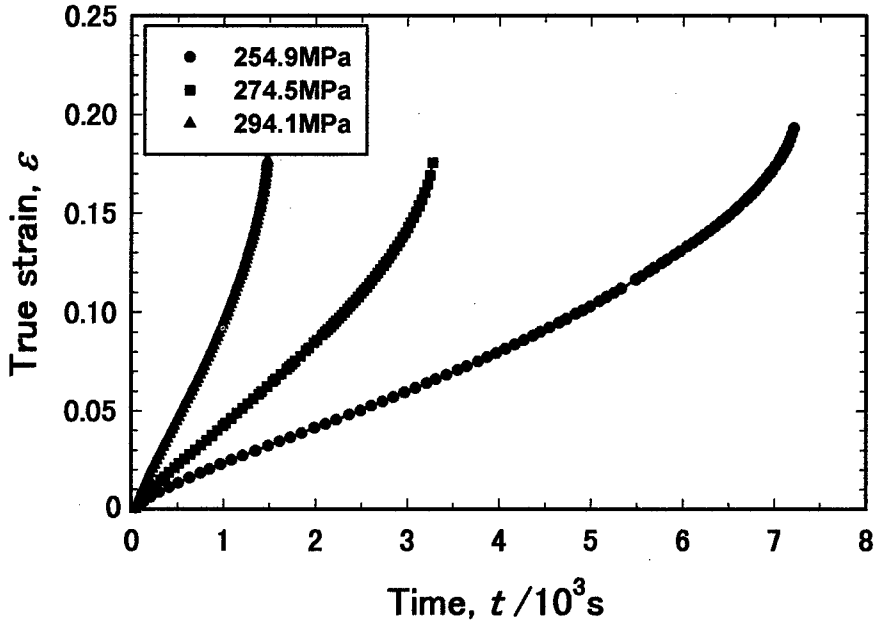

Fig. 2 The creep curve of SUS310S stainless steel at 948K.

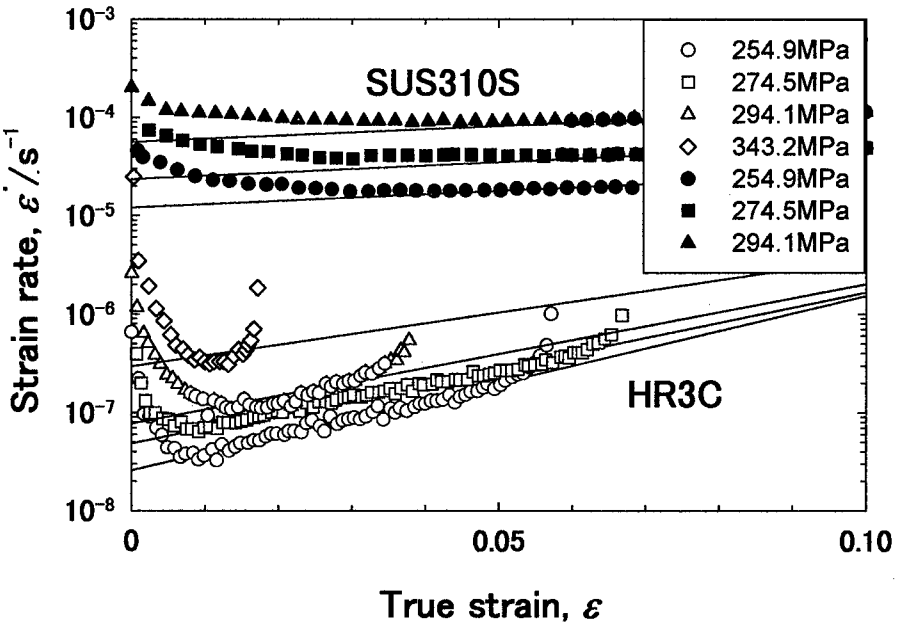

Fig. 3 Relationship between strain rate and true strain at 948K.

Figure 3 shows the relation between logarithm of stain rate and true strain tested at 948 K. The open and solid marks indicate the results of HR3C and SUS310S, respectively. It is seen in Fig.

3 that the relation between logarithm of strain rate and true strain is expressed by Eq.(1) in the region of tertiary creep except a final stage corresponding to the onset of necking.

$$\ln \dot{\varepsilon} = \ln \dot{\varepsilon}_0 + \Omega \varepsilon, \quad (1)$$

where $\dot{\varepsilon}_0$ is the imaginary initial strain rate at zero strain according to Eq.(1) and Ω is the slope of the line in Fig. 3. The magnitude of Ω of HR3C is about 5 times larger than that of SUS301S. The temperature and stress dependence of imaginary strain rate was expressed in the form:

$$\dot{\varepsilon}_0 = A_0 \sigma_0^{n_0} \exp(-Q_0/RT), \quad (2)$$

where n_0 is the stress exponent, A_0 is the constant, σ_0 is the initial stress, and Q_0 is the apparent activation energy. These values are 8.3, 4.64×10^{-10}/s and 330kJ/mol in this order for HR3C, and 12.3, 6.42×10^{-9}/s and 478kJ/mol for SUS310S. In order to examine the validity of the Eq.(1), calculated strain rates from Eq.(1) were compared with the measured values and it was ascertained that the calculated values agreed well wide the measured values. Minimum creep rate is generally employed to express the creep characteristics of materials so that the temperature and stress dependence of minimum creep rates was also formulated similarly. The resultant equation is as follows:

$$\dot{\varepsilon}_m = A_m \sigma_0^{n} \exp(-Q_m/RT), \quad (3)$$

where n is the stress exponent, A_m is the constant, σ_0 is the initial stress, and Q_m is the apparent activation energy. They are 8.7, 1.14×10^{-11}/s and 315 kJ/mol in this order for HR3C, and 12.0, 3.55×10^{-10}/s and 440kJ/mol for SUS310S. Comparison of Eqs. (2) and (3) shows that the stress exponent and activation energy for imaginary initial creep rate are much the same as those for minimum creep rate.

3.2. Abrupt stress change

When dislocations glide viscously, the strain increment with an abrupt stress increase is almost equal to the elastic strain corresponding to the stress increment. On the other hand, when dislocations glide very rapidly until they encounter their glide obstacles (glide in a free flight fashion), the instantaneous strain increment with a small stress increase is larger than that anticipated from elastic strain. Thereby, to examine the response to an abrupt stress change during creep is an effective measure to obtain the information about the mode of dislocation movement.

Figure 4 shows the strain increment as a function of the abrupt stress increment. As shown in Fig.4, the strain increment changes linearly with the stress increment in the case of HR3C while it does not change linearly in the case of SUS301S. Furthermore, the slope of strain against stress coincides with the magnitude anticipated from the combined Young's modulus composed of the machine stiffness and the Young's modulus of the specimen. It is in contrast to this in the case of SUS310S that the slope of strain against stress is larger than that expected from the combined young's modulus, and that the elongation is lager than the magnitude anticipated from the combined Young's modulus. This clearly indicates that the dislocations glide viscously in HR3C while they travel in a free flight manner in SUS310S.

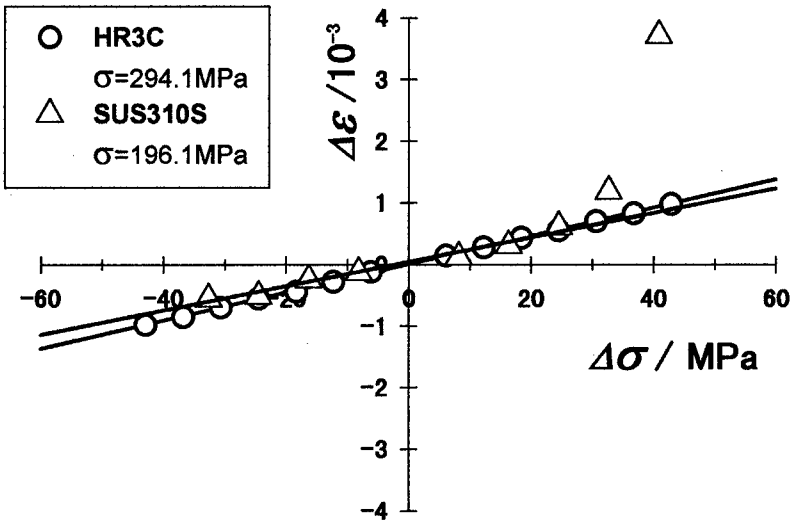

Fig. 4 Relationship between $\Delta\varepsilon$ and $\Delta\sigma$ by stress abruptly loading test.

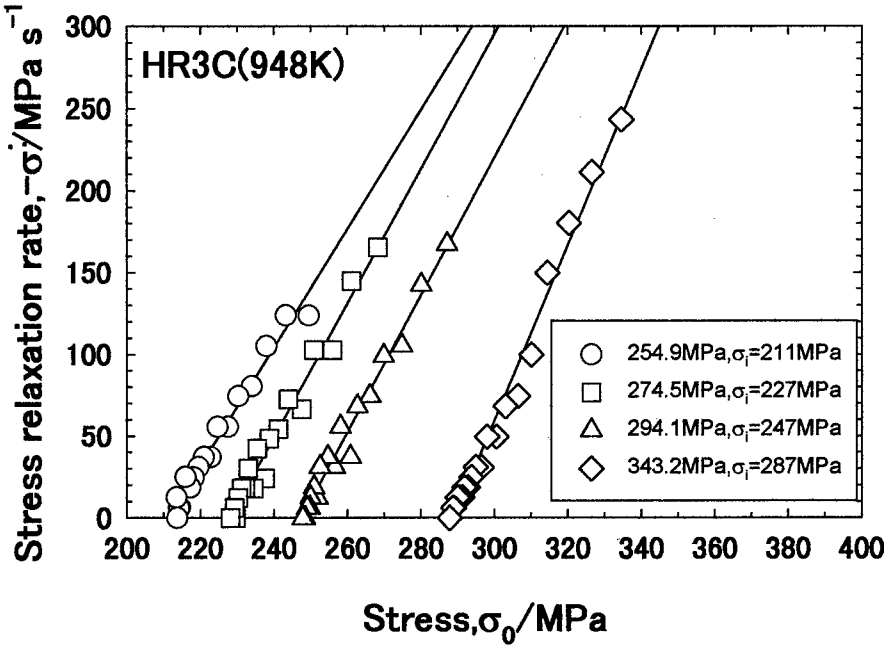

Fig.5 Relationship between stress relation rate and stress in stress relaxation test.

3.3. Stress relaxation

Figure 5 shows the stress rates of HR3C plotted as a function of stress during stress relaxation tested at 948K under various initial stresses. It is seen that the stress rate is approximately linear to stress independently of initial stress levels. As shown in the previous section, the dislocations glide in a Newtonian viscous manner during creep of the HR3C steel. Under this circumstance, the dislocation velocity is proportional to the effective stress. Assuming that the mobile dislocation density and the internal stress remain unchanged during the early stage of relaxation, the stress rate ($-d\sigma/dt$) is expressed as follows[1]:

$$-d\sigma/dt = \phi E_c \rho_m bB(\sigma - \sigma_i), \tag{4}$$

where ϕ is the orientation factor, E_c is the combined Young's modulus, ρ_m is the mobile dislocation density, B is the mobility of dislocations, and σ_i is the internal stress. When the assumption is valid, the internal stress level can be determined from the intercept between horizontal axis and the linear relation. Thus determined internal stress is given in the Fig.5 along with the corresponding initial stress. Using these values, it was found that the fraction of internal stress to total flow stress is about 16.7 percent.

4. Discussion

4.1. Creep life

As Table 1 shows, the chemical composition of both steels is about the same except a small amount of N and Nb added exclusively in HR3C steel. The amount of these trace elements is quite small, however, their effect on creep life is quite large. In practice, the creep life of HR3C is increased by about 100 times as that of SUS310S.

In the case where the change in creep rate during primary creep is small, namely when the creep rate is approximately expressed by Eq.(1) over an entire range of creep, the creep life is expressed by the following Eq. (5).

$$t_r = 1/\Omega \cdot \dot{\varepsilon}_0, \tag{5}$$

According to Eq. (5), the effect of trace elements can be divided into two parts, the effect on imaginary initial strain rate and the effect on the magnitude of Ω. As mentioned previously, the magnitude of Ω of HR3C is about 5 times as large as that of SUS310S. This means that the small amount of trace elements decreases the imaginary initial creep rate by about 500 times as that of SUS310S. Such remarkable decrease in creep rate is due probably to the production of fine precipitates of NbXN in the matrix.

4.2. Stress exponent

The stress exponent of HR3C is about 8 while that of SUS310S is about 12. Among these, the stress exponent of SUS310S is especially larger than the anticipated values for single phase alloys. Actually, Matsuo et al.[2] reported that the stress exponent of 5 for 17mass% Cr-14 mass% Ni stainless steel whose interstitial content is about the same as that of SUS310S in the present study. Furthermore, one naturally anticipates that the stress exponent of HR3C is larger than that of SUS310S because HR3C contains fine precipitates, however, the result on the stress exponent is

reverse. To understand the unexpected results, the strain rate range was examined based on the criterion proposed by Sherby-Burke[3], who have shown that the power law stress region breaks down when the ratio of steady creep rare divided by the appropriate diffusion coefficient reaches 10^{13} /m^2. Above this value, the steady state creep rate becomes greater that those predicted from an extrapolation of intermediate stress range. As the consequence, the stress exponent becomes lager than those of the lower stress range. Applying the criterion for power law breakdown (PLB), it was found that the strain region studied by Matsuo et al. was well below PLB, however, the strain rate region for SUS310S was nearly equal to and that of HR3C was just below PLB. Thus, the reason for the relatively large stress exponent of SUS310S is due probably to the higher stress region than that of Matsuo et al.

4.3. Origin of dragging stress

It was made clear that the dislocations in HR3C glide viscously although they glide in free flight fashion in SUS301S. In this section, the reason for the viscous motion of dislocations in HR3C will be discussed hereafter. For the first of all, the main components of these steels are Fe, Cr and Ni and only a small amount of N and Nb is included exclusively in HR3C. It is well established that foreign atoms with a large atomic size difference to a solvent atom are quite effective for solid solution hardening at elevated temperatures, and W and Mo are typical elements for solution hardening of heat resistant steels. In this sense, no elements effective for solid solution hardening are included as a main component. This is true because dislocations in SUS310S glide surely in a jerky manner. Apart from the substitutional elements, a nitrogen atom has a large atomic size difference to the solvent atom. It is therefore conceivable that nitrogen atoms interact with moving dislocations due to an elastic interaction and extra stress is needed for dislocations to drag nitrogen atmosphere around them. However, single dose of nitrogen can not anticipate so much of the possible hardening effect because of the high diffusivity of nitrogen in steel at elevated temperatures. For these reasons, the precipitation hardening due to dispersed fine particles and/or solution hardening due to substitutional-interstitial atom pair are the candidates to explain the remarkable change in creep rate and creep life.

As mentioned above, the atomic size difference of nickel or chromium atom is so small that the elastic interaction with dislocations can not be expected. However, the chemical affinity of nitrogen to chromium is relatively strong and to nickel is quite small. Therefore, when a chromium atom interacts chemically with nitrogen atom, dislocations have to drag a chromium-nitrogen atom pair (I-S pair) because the nitrogen atom clings to moving dislocations with an elastic interaction. In such a case, the velocity of dislocations dragging I-S pairs is controlled by the diffusivity of substitutional atoms, which is much slower than that of interstitial atom. Thereby the dragging of an I-S atmosphere may contribute to the solid solution hardening at elevated temperatures.

4.4. Contribution of dragging stress to flow stress

Microstructures of many heat resistant steels are strengthened by various mechanisms and

they are not thermally stable. Therefore, heat resistant steels lose their strength as the microstructures become deteriorated during the long-term service and finally they reach the "inherent creep strength" independent of time [1]. From this viewpoint, the solid solution hardening, which is principally independent of time and free from structural degradation, is quite important to improve "inherent creep strength".

In order to measure the effective stress, a part of flow stress originated in solid solution hardening in the present case, the various methods have been proposed so far. These methods all assume that the mobile dislocation density and internal stress or deformation structures remain unchanged during the measurements of effective stress. Therefore, the stress relaxation curve analysis was employed in the present study because the time necessary for the measurements of effective stress is relatively short in comparison with other methods. Actually, the time needed to measure an internal stress level is about 0.5 s in the present case. As shown in section 3.3, the contribution from solid solution strengthening to total flow stress, which was ascribable to the dragging of chromium-nitrogen clusters, was a noticeable fraction of flow stress of about 16.7%. In practice, the numerical calculation [5] shows that the dragging stress depends on dislocation velocity so that the fraction of effective stress is supposed to be smaller in low strain rate ranges, however, the contribution from the solid solution strengthening ascribable to chromium-nitrogen clusters cannot be disregarded.

5. Summary

To make clear the role of nitrogen in the 25Cr-20Ni series of HR3C steel containing N and Nb, creep behavior under constant load, the response to the abrupt stress change and stress relaxation behavior were compared with those of SUS310S, a 20-25Cr-20Ni series steel free from N and Nb. The results obtained are as follows;

(1) Addition of 0.2 mass % N and trace element of Nb increased creep life by a factor of 100 times and decreased the imaginary initial strain rate by about 500 times.

(2) Instantaneous plastic strain was observed on abrupt stress change in SUS310S while it was absent in HR3C. This indicates dislocations travel in a free flight manner in the former and the effective stress of the latter is negligible.

(3) From the analysis of stress relaxation curve, the effective stress to total applied stress was found to be about 16.7 %. The origin of effective stress was ascribable to the stress needed for dislocations to drag the solute atmosphere of Cr-N clusters behind them.

References

[1] K.Kimura, H.Kushima, K.Yagi and C.Tanaka, Institute of Metals,(1993),p.555.

[2] S.Kikuchi,K.Tomita,Y.Motoyama and M.Adachi, J.JILM,Vol.30,No.9(1980),p.480.

[3] T.Matsuo, K.Nakajima, Y.Terada and M.Kikuchi:*Mat. Sci.Eng.*,A146(1991),p.261.

[4] O.D.Sherby and P.M. Burke, Progress in Mat. Sci., vol.13(1966),p.323.

[5] K.Hara and T.Endo, Mat.Sci. & Eng., A234-236(1997),p.234.

Fax number: 045-339-3871, Mail address: endo@post.post.me.ynu.ac.jp

Key Engineering Materials Vols. 171-174 (2000) pp. 453-460
© 2000 Trans Tech Publications, Switzerland

Microstructural Aspects on the Creep Behaviour of Advanced Power Plant Steels

H. Cerjak, P. Hofer and B. Schaffernak

Institute for Materials Science, Welding and Forming, Technical University Graz,
Kopernikusgasse 24, AU-8010 Graz, Austria

Keywords: Ferritic-Martensitic Chromium Steels, Creep Resistance, Microstructural Investigations, TEM, Energy Filtering TEM (EFTEM), Precipitation Sequence, Microstructural Stability

1 Synopsis

There is a world-wide substantial demand to increase the application temperature and design stresses of advanced creep resistant ferritic-martensitic 9-12% Cr steels to increase the efficiency of thermal power plants. These alloys show during service conditions pronounced microstructural changes in the aged as well as in the stressed conditions. Therefore an intensive investigation and modelling of the microstructure of the cast steel material G-X12CrMoVWNbN10-1-1, was applied to understand the mechanisms. Hardness tests, optical microscopy, TEM methods and thermodynamic equilibrium phase diagram calculations were performed. By means of the EFTEM (Energy filtering TEM) method a quantification of the precipitation sequence of $M_{23}C_6$, MX, Laves Phase and Z - Phase could be established at 600°C as a function of exposure time.
A new approach ("Graz Model") was proposed for the improvement of the creep resistant alloys in terms of the α/γ - transformation temperature and diffusion behaviour respectively, which influence the microstructural stability. Both were found as important influencing factors.

2 Introduction

There is a substantial and growing interest in power plants with relatively high process temperature and/or pressures to improve the thermal efficiency and reduce CO_2 emissions. Materials with ferritic/martensitic microstructures (9-12% Cr steels) are preferred because of their favourable physical properties such as good thermal conductivity and low coefficient of thermal expansion coupled with higher resistance to thermal shock.
In Europe mainly in the European research action COST 501 [1] different grades of advanced 9 to 12 % Cr steels containing tungsten and molybdenum were developed for the following grades, E911 designed for tubes and pipes and similar grades for forgings and G-X12 CrMoVNbN 10-1-1 designed for castings.
The intention of this paper is to outline the basic microstructural changes that have the recently developed 9-12% Cr steels in common using the results gained from extensive investigations on a tungsten alloyed modern cast steel G-X12 CrMoWVNbN 10-1-1. The experimental study was performed on broken creep rupture specimens run at 600°C up to 33000 h and a material in the virgin condition with a final heat treatment of 720°C for 9h. The chemical composition of G-X12 CrMoWVNbN 10-1-1 is given in Table 1.

3 Experimental observations during long term exposure

It is well-known that creep resistant materials, mainly type 9 to 12 % chromium steels, show significant changes in different properties and behaviour during exposure at high temperature. In addition these changes may differ whether the material is strained during exposure or merely aged. Although these microstructural changes are hardly detectable with the light microscope, hardness measurements along longitudinal cross sections of creep samples exposed for different times and temperatures show a clear drop in hardness especially in the strained shank sections. From that it can be concluded, that microstructural changes, namely a precipitation and growth of particles and a rearrangement of dislocations yielding the drop in hardness predominately in the strained section of the exposed materials.

3.1 Transmission Electron Microscopy (TEM)

To reveal these microstructural parameters transmission electron microscopic (TEM) investigations had to be performed using materials in the "as received" condition as well as in different exposed or exposed and strained conditions in order to study the microstructural development as a function of exposure parameters. TEM studies were preferably conducted on thin foils to reveal interactions between precipitates and dislocation structure. Further details about technical matters are given in [3]

Figure 1 compares the TEM bright field image of the "as received" condition (quenched and tempered) of G-X12CrMoWVNbN10-1-1 with the aged and crept condition (head and shank portion of creep samples) . This series of TEM images shows clearly that drastic microstructural changes appear in the sub-microstructure of these materials which will be discussed in the following.

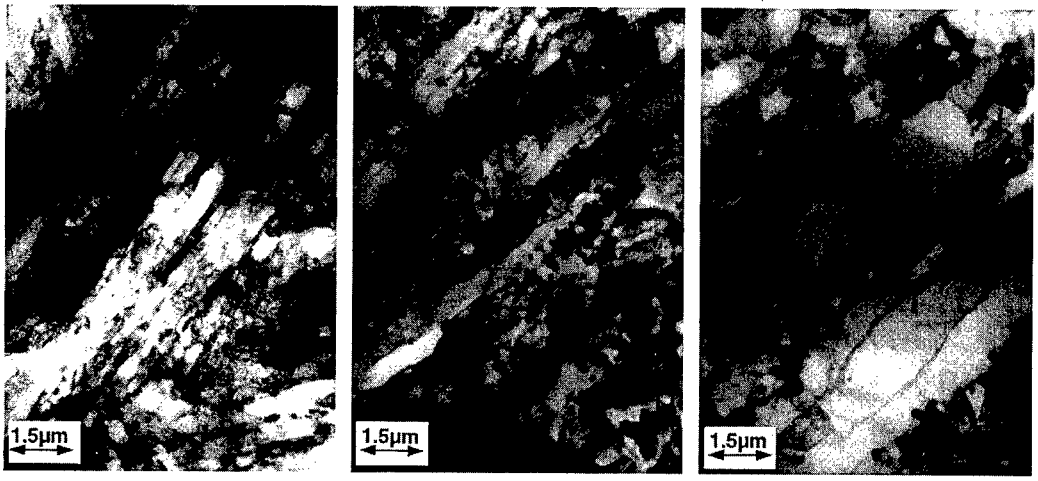

Figure 1: Typical TEM microstructure of material G-X12 CrMoWVNbN 10-1-1, left: "as received" condition; middle: aged at 600°C, 33410h; right: crept at 600°C, 33 410h, 110MPa

In the "as received condition" very fine lath boundaries which showed in the TEM bright field image a high dislocation density and a number of small precipitates relatively continuously distributed over the cross section was detected. Distinct changes in the microstructure can be noticed as a function of ageing and creep exposure. Notable growth of precipitates can be observed as well as recovery of the martensitic lath structure of the "as received" condition to a reordering of subgrains and growth of subgrains as a result of creep conditions (temperature, strain/stress, time). It is also obvious that the aged condition shows less recovery compared to the crept condition.

Special emphasis was given to the description of the state of precipitates. Detailed investigations of precipitates were necessary. In Figure 2 typical examples of most common precipitates occurring in these types of steels are shown. They can be identified i.e. using their EDX-spectra depicted in Figure 2. Figure 2a shows the typical appearance of a $M_{23}C_6$ carbide. From this picture it can also be derived that $M_{23}C_6$ carbides are acting as obstacles for the movement of subgrain boundaries. In Figure 2b a typical Laves Phase particle is shown which appears normally on both lath- and subgrain- boundaries or in the centre of subgrains in the exposed material.

Typical MX precipitates are smaller than $M_{23}C_6$ or Laves phase (Figure 2c) and react with dislocations. In the lower part of Figure 2 EDX-spectra of the investigated particles are shown as well as the composition of the matrix for comparison.

Using the methods discussed above, only single precipitates can be identified definitely. For a better identification of the appearance and statistical distribution of the different types of precipitates other methods must be used.

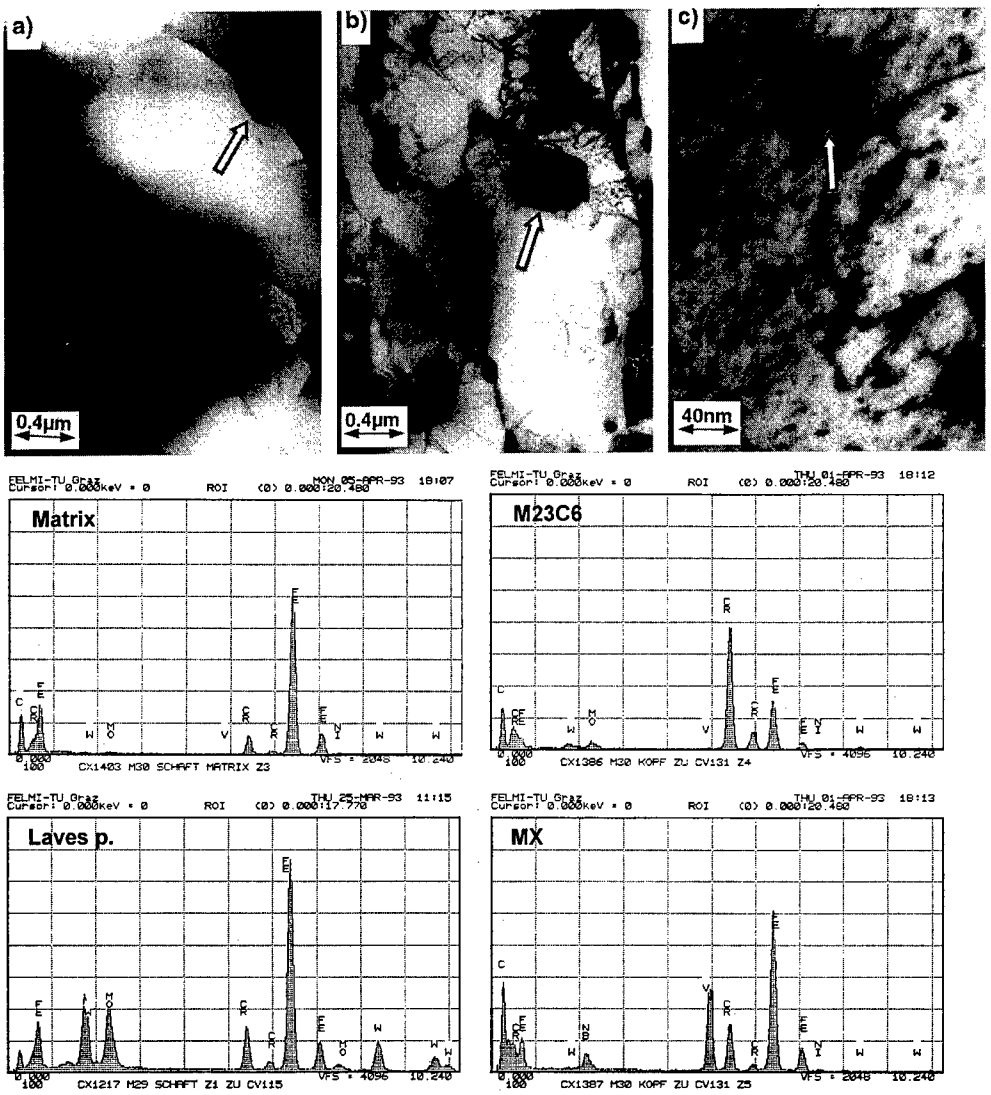

Figure 2: TEM-micrographs and EDX-spectra of investigated particles in G-X12 CrMoWVNbN 10-1-1; a) $M_{23}C_6$ pinning a subgrain boundary, b) Laves Phase, c) fine MX-particles

3.2 The EFTEM method

The energy filter GIF (Gatan imaging filter) analyses the energy spectra of inelastic scattered electrons crossing the sample. It allows the selection of an energy window which can be used to establish images. A special advantage of this energy filter is that a two-dimensional distribution of the chemical elements in small regions of the substrate is represented with very high resolution (about 2 nm) within short time (seconds to minutes). Detailed information about the applicability of EFTEM on steels can be taken from Ref. [2, 3].

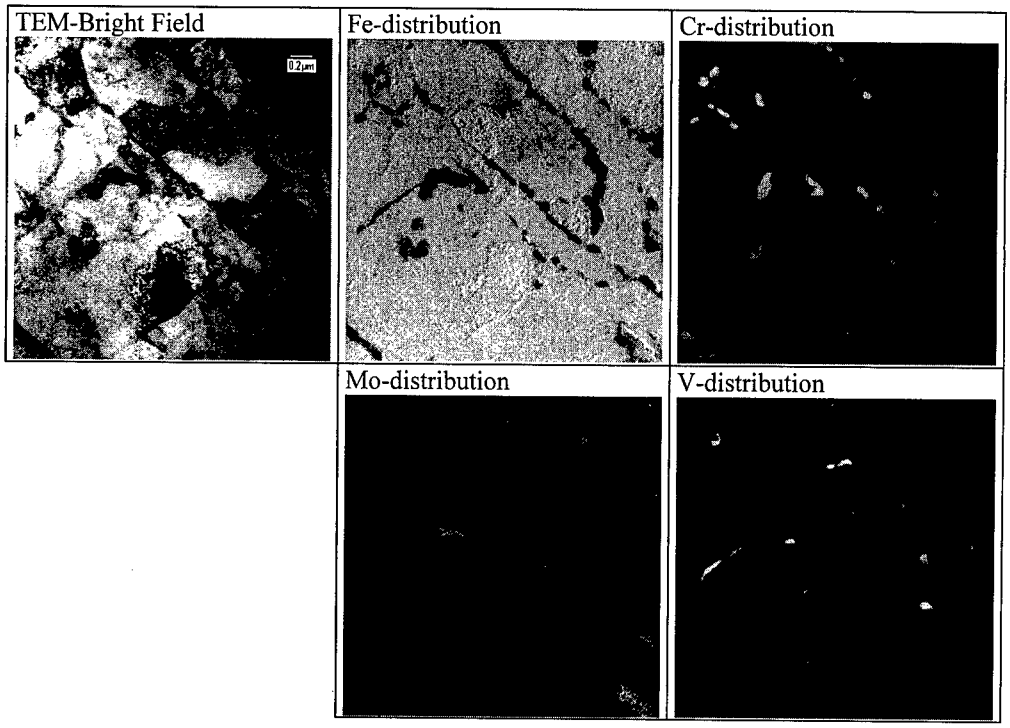

Figure 3: Example for an EFTEM investigation of a test piece made of G-X12 CrMoWVNbN 10-1-1 after 996h ageing at 600°C

Figure 3 shows an example of EFTEM images of a test piece of G-X12 CrMoVNbN 10-1-1 exposed for 996 hours at 600°C. In addition to the well-known bright field image which is displayed in the left-hand corner of Figure 3, EFTEM images including the distribution of iron, chromium, molybdenum and vanadium are depicted. Bright areas represent the respective element. Since these images are a result of the electron energy loss spectroscopy and not gained by optical effects, coherent particles are visible as well as incoherent particles. By selection of chemical elements representative of a precipitate population the actual state of precipitation can be made visible without relying on orientation effects of different particles. In the case shown in Figure 3 the chromium rich particles represent $M_{23}C_6$ carbides, the molybdenum or tungsten rich particles Laves Phase, and the vanadium rich particles the MX (VN) precipitates. Using image analysis the respective distribution image of the elements can be used to quantify the distribution of the particle size of any specific population of precipitates that occur in the investigated material as long as they differ clearly in their chemical composition.

4 Quantification of precipitates

By using the EFTEM method a clear distinction between the different populations of precipitates could be performed.

Detailed investigations of different conditions starting with the "as received" condition and steps of 976, 5014 and 33410 hours exposure time are depicted in Figure 4. Because of the clear EFTEM - distinction between the different types of precipitates, not only the distribution of each single precipitate family could be measured but also the development of the distributions as a function of ageing could be revealed.

Generally it was observed that the measured distributions follow mainly a log normal frequency curve [4].

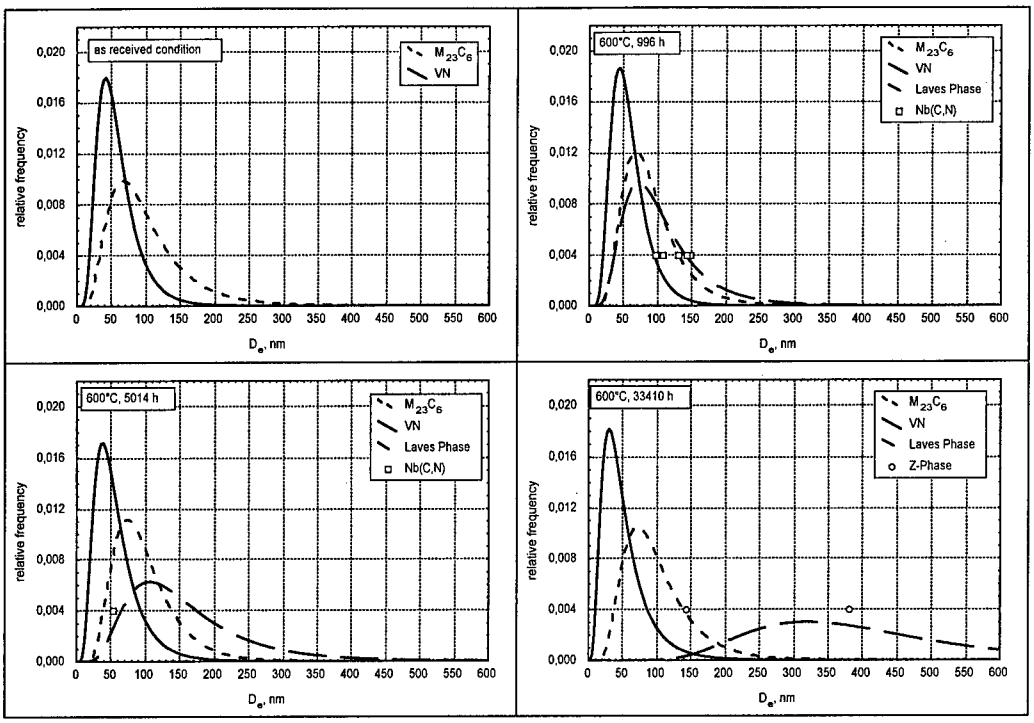

Figure 4: Distributions of $M_{23}C_6$, VN, and Laves phase particles, "as received" condition and aged for 976h, 5014h and 33410 h at 600°C (material G-X12 CrMoWVNbN 10-1-1)

In the "as received" condition only $M_{23}C_6$ and MX (in this case as VN) were seen to be present. After 976 hours exposure two new phases were noted, Laves Phase in a statistical distribution and single measurements of Nb(CN) precipitates. It is clearly seen that the distribution of Laves Phase and $M_{23}C_6$ show more or less the same shape. This means that by using conventional TEM technique these two populations can be easily confused up. After 5.014 hours a limited widening of the distribution of $M_{23}C_6$ could be recognised. More pronounced is the growth of Laves Phase precipitates mainly perceived in the mean value but also in the width of the distribution. Single Laves phase precipitates already reach a size of about 400 nm. After 33.000 hours a logarithmic normal distribution of the three main types of precipitates could be apprehended and the mean size of Laves Phase already reached approximately 300 to 350 nm in diameter.

A relatively new apprehension in the precipitation state of 9-12% Cr steels is the appearance of Z-Phase [5]. The Z-Phase in these types of steels contain high concentrations of chromium and vanadium. The phase occurred in the EFTEM element distribution images both in the Cr- and in the V-distribution. Thus a separation from Cr-rich $M_{23}C_6$ carbides and V-rich MX-particles were easily possible .

The chromium and vanadium rich Z-Phase was first observed after 12118 h creep rupture time in the shank region and after 33.410 hours creep rupture time in the head as well as in the shank region of the sample.

From the results of Figure 4 it can be derived that Laves Phase shows a monotonic growth behaviour. This is depicted in Figure 5: The growth behaviour of Laves Phase can be approximated by a simple cubic growth law $r(t)^3 - r_0^3 = kt$.

However for $M_{23}C_6$ carbides and VN especially at long term exposure no clear growth or enlarging behaviour could be observed. On the contrary, there are some hints that the appearance of Z-Phase might influence the stability of the Cr-rich $M_{23}C_6$ carbides but mainly that of V-rich VN.

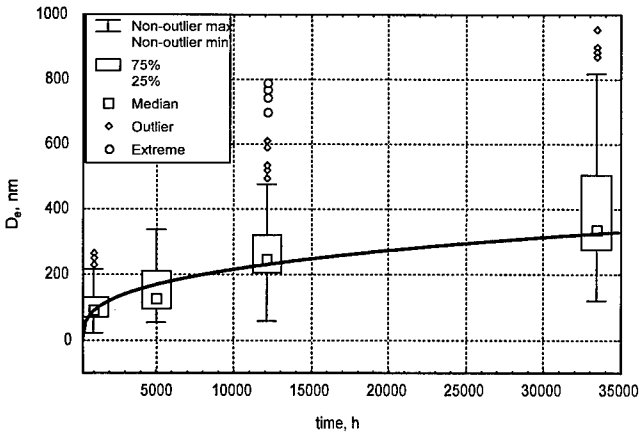

Figure 5: Boxplots of the equivalent particle diameter of Laves phase after different ageing periods at 600°C, comparison with a fit curve based on a cubic growth law (material G-X12 CrMoWVNbN 10-1-1)

5 New approaches for the development of high creep resistant martensitic steels

From the above mentioned observations it can be deduced that the stability of the microstructure might be the main influencing factor for the sustainability of creep strength under long time exposure: The higher the microstructure stability of the alloy under consideration, the higher the creep strength under long term exposure can be foreseen.
Therefor thermodynamic stability calculations of the microstructural behaviour of different alloys were performed by the authors using the computer programs *Thermo Calc* [6] and *Dictra* [7].

5.1 Stability based alloy development "Graz Model"

5.1.1 Influence of Transformation Temperatures

As already mentioned above, the microstructural stability seems to be one of the most important factors influencing the long term creep behaviour of modern 9-12% Cr steels. The experimental observations of test alloys investigated in the European research program COST 501 Round II and Round III showed that the alloy known as B2 [8] (chemical composition see Table 1) showed very good creep resistance even under very long exposure times (> 40.000 h). Microstructural investigations using TEM depicted high dislocation density even in the long term exposed condition.
Through an investigation of the possible reasons or causes for this condition the well known homologous temperature concept was used. The homologous service temperature depicts the distance between the service temperature and the transformation temperature (which describes the stability) of the phase in which the service occur. The body centered cubic (bcc) and ferritic/martensitic phase starts to decompose at A_{c1} and is fully decomposed at A_{c3}. These temperatures were used as a stability criterion. Using this approach the creep strengths at 600 and 650°C of different alloys investigated in the COST Round III and other representative alloys were plotted in relation to the equilibrium transformation temperature A_{c1}. Parameters are the creep strengths at different times from 100 to 100.000 hours, designated as $R_{m/100}$, $R_{m/1000}$ e.c..
Figure 6 shows a good coincidence between creep strengths at 600 and calculated equilibrium transformation temperature [9]. The equilibrium transformation temperature was calculated using *Thermo Calc*. The ranking of this temperature was verified by experimental investigations. The higher the transformation temperature the higher was the observed creep strength. Also it could be observed that the difference in short term creep behaviour caused by different annealing conditions (i.e. alloys D and E) disappear after long term creep exposure.

In a more detailed approach explained in [9] the Curie Temperature was found to be the most important factor influencing the diffusion controlled microstructural stability.

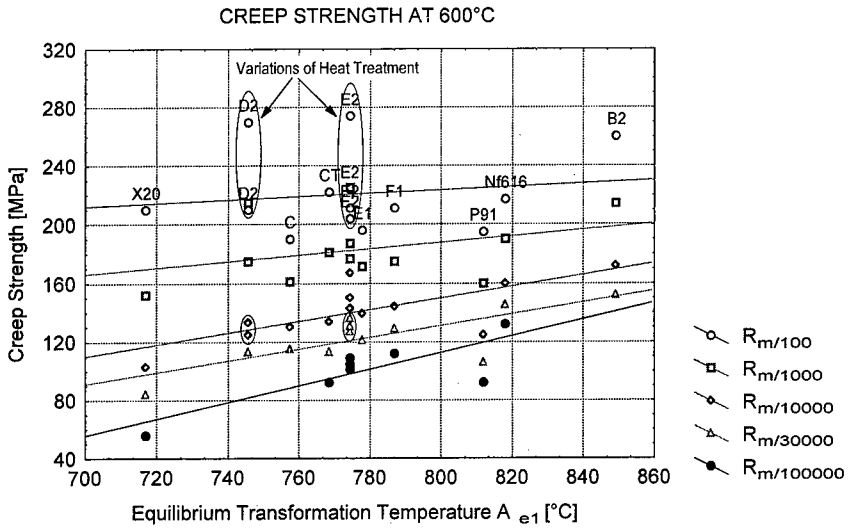

Figure 6: Influence of the equilibrium transformation temperature A_{e1} on the creep strength

Table 1: Chemical composition of the investigated material G-X12CrMoWVNbN10-1-1 and typical values of other 9-12% Cr steels [1]

	C	Cr	Mo	V	W	Nb	B
B2	0.17	9.34	1.55	0.27	0.012	0.063	0.01
E911	0.12	8.7	0.97	0.2	0.96	0.062	
NF616	0.124	9.07	0.46	0.19	1.78	0.063	0.003
P91	0.096	8.41	0.93	0.2		0.065	0.0005
F1	0.13	10.18	1.49	0.2	0.02	0.06	0.003
E1	0.11	11.1	1.13	0.2	0.51	0.06	0.003
E2	0.13	10.2	1.1	0.2	0.9	0.03	
CT (G-X12CrMoWVNbN10-1-1)	0.13	10.5	1.03	0.23	1.01	0.066	
C	0.13	10.6	1.02	0.21		0.07	
D2	0.12	10.25	0.32	0.2	1.81	0.06	
X20	0.2	11	0.85	0.27			

More accurate calculations can be carried out using approaches which verify details like the actual chemical composition including the state of precipitates.
The precipitation, growth and coarsening of precipitates as well as the recovery processes of dislocations are principally diffusion controlled processes. In the case of precipitation we have mass transport of alloying elements as the main influencing factor.

5.1.2 Diffusion parameters

In connection with a mobility data base the computer program *Thermo Calc* allows the calculation of diffusion coefficients (substitutional and interstitial) of different alloys. Figure 7 [10] shows the diffusion coefficients for self diffusion (left) and the diffusion coefficients for chromium in ferrite (right) for three alloys P91, NF616/P92 and B2. As a consequence it can be perceived that, as expected, the diffusion in the high creep resistant alloys is less pronounced than in the lower creep resistant alloys. A clear ranking of the grades P91, NF616/P92 and B2 is apprehended. By using

this approach the recognised higher microstructural stability of the higher creep resistant alloys is supported by the low diffusion rates.

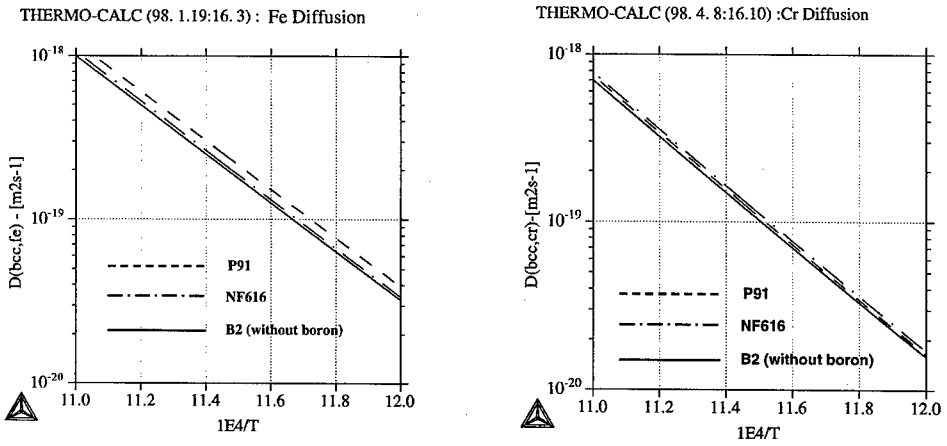

Figure 7: Calculated diffusion coefficients for different steel grades: a) self diffusion, b) diffusion coefficient for chromium in ferrite

6 Conclusions

On the material G-X12CrMoWVNbN-10-1-1 it has been shown using specimens crept up to 33410 h at 600 °C that the main degradation mechanism is the coarsening of the subgrain structure accompanied by the growth and coarsening of different precipitates. The size distributions of $M_{23}C_6$- and VN-precipitates as well as of the Laves phase were established as a function of ageing time. Once these precipitates are nucleated their impact on creep strength strongly depends on their growth and coarsening behaviour.

To retard this for 9-12% Cr steels generic mechanism, a new concept for the development of optimised 9-12% Cr steels were derived from aspects of microstructure stability. Thermodynamic calculations showed that a selection of promising alloy composition leading to the same kind of precipitates should be based on high transformation temperature and low diffusibility of the main alloying elements.

7 References

[1] R. W. Vanstone: Microstructure and Creep Mechanisms in Advanced 9-12% Cr Creep Resisting Steels – a Collaborative Investigation in Cost 501/3 WP11 in: Materials for Advanced Power Engineering 1994, D. Coutsouradis et al., Editors, Kluwer Acadamic Publishers, Dordrecht, Boston, London, Part 1, 465-473

[2] F. Hofer, P. Warbichler and W. Grogger, Ultramicroscopy **59**, (1995), 15-31

[3] P. Warbichler, F. Hofer, P. Hofer and E. Letofsky: Micron Vol.29 (1998) No.1, 63-72.

[4] P. Hofer, H. Cerjak, B. Schaffernak and P. Warbichler: Steel research **69** (1998) No. 8, 343-348

[5] A. Strang, V. Vodarek: Mater. Sci. Technol. (1996) No. 12, 552-556

[6] B. Sundman: Anales de Fisica **36**, 69 (1990)

[7] J.-O. Andersson, L. Höglund, B. Jönsson and J. Ågren: in: Fundamentals and Applications of Ternary Diffusion, G.R. Purdy, Editor, p.153, Pergamon Press, New York (1990)

[8] K. Spiradek K., R. Bauer, and G. Zeiler: Microstructural Changes During the Creep Deformation of 9%Cr-Steel, in: D.Coutsouradis et al. (Editors.), Materials for Power Engineering, Part I, 251-262, 1994, Kluwer Academic Publishers, The Netherlands

[9] H. Cerjak, P. Hofer and B. Schaffernak: VGB Kraftwerkstechnik 77 (1997), Number 9, English issue, 691-698

[10] H. Cerjak, P. Hofer and B. Schaffernak: "Neues Konzept zur Optimierung moderner 9-12% Cr- Stähle", in: Proc. VGB-Konferenz "Werkstoffe und Schweißtechnik im Kraftwerk 1998", Hannover, 14.-15. Oktober 1998, S. 9.1-9.15, submitted and accepted for VGB Kraftwerkstechnik, German and English issue

Key Engineering Materials Vols. 171-174 (2000) pp. 461-468
© 2000 Trans Tech Publications, Switzerland

Effect of M-C (M=Mo, Mn, and Cr) Atomic Pairs on Creep Properties of Fe-M-C Ternary Alloys

T. Abe, H. Onodera, K. Kimura and H. Kushima

National Research Institute for Metals, Sengen, Tsukuba, 305-0047, Japan

Keywords: Atomic Pair, Solid Solution Strengthening, Recovery Rate, Work Hardening Coefficient, Climb Velocity, Thermo-Calc, Central Atoms Model and Co-Segregation

Abstract

Effects of solute elements, Mo, Mn, and Cr, on the creep strength were examined by Fe-M-C (M=Mo, Mn, and Cr) and Fe-C alloys in view of M-C atomic pairs. The largest strengthening effect was obtained by the addition of Mo to the Fe-C alloy, and Mn, and Cr showed almost the same strengthening effects in creep tests at 773K. Measurements of instantaneous elongation and contraction as a function of stress change revealed the existence of instantaneous plastic strain during steady state creep in all alloys. This indicates that the steady state creep is controlled by recovery as in pure metals. For all alloys, the values of about 230GPa were obtained as the coefficient of strain hardening by the method proposed by Ishida and McLean. The recovery rate, r, the coefficient of strain hardening, h, and the steady state creep strain rate, ε, satisfied the Bailey-Orowan relationship in all alloys. These results indicate that the alloying element affects mainly the recovery rate. From analysis by the model proposed by Sandstrom, it is concluded that M-C pair reduces the climb velocity of dislocations due to large interaction energies with dislocations. The magnitude of the reduction can be estimated from the binding energy between M and C atoms and the diffusion coefficient of M atom. The co-segregation of M and C atoms on edge dislocations is predicted by thermodynamic analysis, and it is pointed out that this may result in the apparent reduction of the dislocation climb velocity even in alloys containing very limited amount of alloying elements.

1. Introduction

Kimura et al. [1] have proposed a new concept of inherent creep strength as a determining factor of a long term creep strength of ferritic steels. From the analyses of NRIM Creep Data Sheets, they have found that the creep strength of ferritic steels decreases and converges to the same strength level, inherent creep strength, by losing effects of precipitation hardening, work hardening, and so on. Here, in the long term creep region, the time independent factor such as the solid solution strengthening should play an important role. We have examined the effect of solid solution strengthening due to minute solute elements on the long term creep strength of carbon steels from viewpoint of M-C atomic pairs between a substitutional solute atom, M and an interstitial solute atom, C. We have found [2] a good correlation between the long term creep strength and the concentrations of Mo-C and Mn-C atomic pairs in the ferrite matrix estimated by thermodynamic calculations. This result suggests that the solid solution strengthening due to M-C atomic pairs plays

an important role in the long-term creep tests of ferritic steels. Thus it's necessary to optimize the chemical compositions of alloys with the effect of M-C atomic pairs in order to improve long-term creep properties of ferritic steels.

The strengthening mechanism due to solute atoms depends on the creep mechanism of alloys. In the case of pure metals where the glide motion of dislocations is by the free-flight process, the rate controlling process is a recovery process due to a climb of edge dislocations. On the other hand, in some kinds of solid solution alloys [3], a viscous glide of dislocations is the rate controlling process of creep because of a large dragging stress due to solute atmosphere. In the case of Fe-2.1at%Mo alloy [4], it has been reported that a creep rate controlling process changes from the pure metal type to the alloy type depending on the applied stress.

In the case of ferritic steels containing interstitial solute elements, it has been said that M-C and/or M-N pairs have a strong strengthening effect. Ishida and McLean [5] have reported that Mn-N atomic pair decreases the dislocation climb rate in Fe-Mn-N alloys. However the strengthening mechanisms due to these atomic pairs have not been made clear and the quantitative evaluations have not been done for the strengthening effect of each atomic pair.

In this study, the effect of solute atoms on the creep properties in Fe-M-C (M=Mo, Mn, Cr) ternary systems has been studied from viewpoint of M-C atomic pairs. And the effect of each M-C pair has been evaluated in terms of binding energy of M-C pair and diffusivity of M atom.

2. Experimental procedure

Table 1 Chemical compositions of the alloys (at%) used.

Alloys	C	Cr	Mn	Mo
Fe-C	0.024			
Fe-Cr-C	0.023	0.11		
Fe-Mn-C	0.015		0.11	
Fe-Mo-C	0.030			0.20

S,P<0.0002, N<0.0020

Fe-M-C (M=Mn, Mo, and Cr) alloys and an Fe-C binary alloy were prepared from high purity metals, 99.97%Fe, 99.99%Mo, 99.99%Mn, and 99.99%Cr. Ingots were hot-pressed at 1373K to a reduction of 40%, and cold-rolled to a reduction of 90%. Creep specimens with a gauge length of 30mm and a diameter of 6mm were machined from rods after annealed at 1523K for 5h. An average grain size of specimens was about 0.5mm. Chemical compositions of alloys are shown in **Table 1**. The creep tests were performed at 773K, and 973K under Ar gas atmosphere. Since there was large difference of creep strength among specimens, the applied stress was chosen in the range from 10 to 135MPa so that the steady state creep was reached within 200h. The sudden stress increment test proposed by Oikawa et al. [3] was carried out in order to confirm the rate controlling process. In this method, the initial applied stress was changed by cutting wires holding loads at the both ends of a lever during the steady state creep. The recovery rate was measured by the stress decrement test proposed by Mitra and McLean [6].

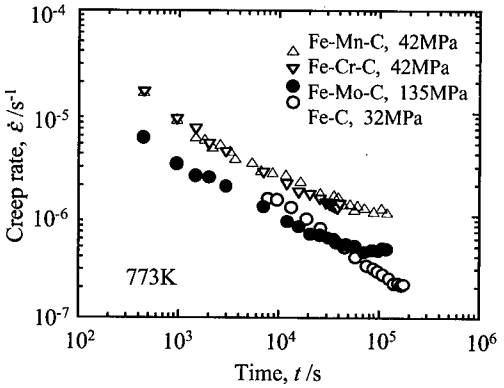

Fig.1 Time dependence of creep strain rates of Fe-C, Fe-Mo-C, Fe-Mn-C and Fe-Cr-C alloys at 773K.

3. Results and Discussion

3.1 Creep curve

Carbides were not observed in optical micrographs of specimens before creep tests. The grain growth was not observed during

creep tests. **Figure 1** shows results of creep tests at 773K. All specimens showed the same type of creep curves. In **Fig.1**, the strain rate (log ε) linearly decreases with creep time (log t) in the transient creep stage, which is a characteristic of pure metal type behavior. Strain rates of Fe-Mn-C and Fe-Cr-C alloys are roughly the same under 42MPa. Although the comparison of creep rate among alloys is impossible because of different applied stresses, Mo is the most effective strengthening element because the steady state creep rate of the Fe-Mo-C alloy under 135MPa is similar to those of Fe-Mn-C and Fe-Cr-C alloys under much lower stress of 42MPa.

3.2 Stress change tests

The rate controlling process of creep deformations can be classified into two types. One is a recovery process due to a climb of edge dislocations, and the other is a viscous glide of dislocations. The effect of solute elements on the creep behavior varies depending on the rate controlling process. Then, at first, it is necessary to confirm the rate controlling process in the creep behavior of each alloy in order to evaluate quantitatively the effect of solute atoms. In this study, the sudden stress increment test was carried out to examine the rate controlling process. **Figure 2** shows an example of the instantaneous elongation (ΔL^+) and contraction (ΔL^-) caused by the sudden stress change by $\Delta\sigma$ in the Fe-Mo-C alloy. **Figure 3** shows the instantaneous elongation and contraction as a function of $\Delta\sigma$ for all alloys. For all alloys, the instantaneous elongation is larger than the instantaneous contraction at the same $\Delta\sigma$, suggesting the existence of instantaneous plastic strain. Thus, it is concluded that the rate controlling process of creep deformations in the present study is the recovery process due to the climb of dislocations in all alloys.

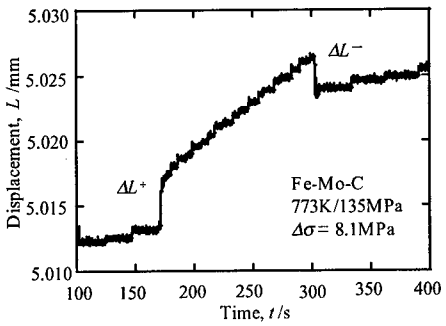

Fig.2 Examples of time-displacement recordings in stress change tests during creep of Fe-0.20at%Mo-0.030at%C alloy under 135MPa at 773K.

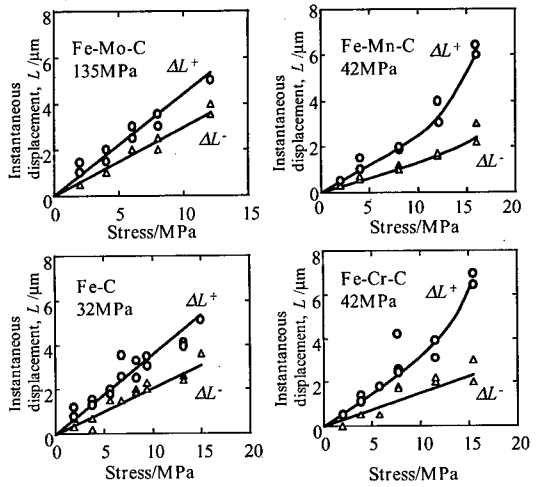

Fig. 3 Apparent instantaneous elongation, ΔL^+, and contraction, ΔL^-, as a function of change in stress during steady-state creep of Fe-C, Fe-Mo-C, Fe-Mn-C and Fe-Cr-C alloys at 773K.

The recovery rate, r, is measured by means of the stress decrement test. When the initial stress is decreased by $\Delta\sigma$, an incubation period (Δt) is observed before the start of deformation with a strain rate slower than the previous one as shown in **Fig.4**. **Figure 5** shows the incubation period in the Fe-Mo-C alloy as a function of $\Delta\sigma$. The recovery rate is determined from this figure according to the method proposed by Mitra et al [6]. The recovery rate in Fe-M-C alloys normalized by that in the Fe-C alloy is shown in **Table 2**. For all alloys, the normalized recovery rate is very close to the steady state creep rate normalized by that of Fe-C alloy. From results of the stress decrement tests, the values of about 230GPa are obtained for

all alloys as the work hardening coefficient, h, by the method proposed by Ishida and McLean [5]. This value is nearly twice as large as that reported by Baird et al [7]. From present analysis, it is clear that ε, r, and h satisfy the Bailey-Orowan equation, ε=r/h. Thus, it is concluded that solute atoms affect the steady state creep rate by decreasing the recovery rate.

4. Discussion

4.1 Effect of substitutional solute elements, M, and M-C atomic pairs on the climb Rate of an edge dislocation

From creep tests at 773K, it is found that Mo addition has the largest strengthening effect and additions of Cr and Mn have similar effects. Since it is known that Cr addition has only a limited strengthening effect in the absence of interstitial solute elements, the observed strengthening in the Fe-Cr-C alloy is due to Cr-C atomic pairs. In the sudden stress increment tests, the instantaneous plastic strain is observed in all alloys, suggesting that the rate controlling process in the creep deformation is the recovery process due to the climb of edge dislocations. Therefore we examine effect of M atoms, and M-C atomic pairs on the recovery rate in terms of diffusivity of M atom and binding energy between the dislocation and M atoms and M-C atomic pairs.

Sandstrom [8] have derived the following equations as the climb rate of an edge dislocation in an alloy containing M element.

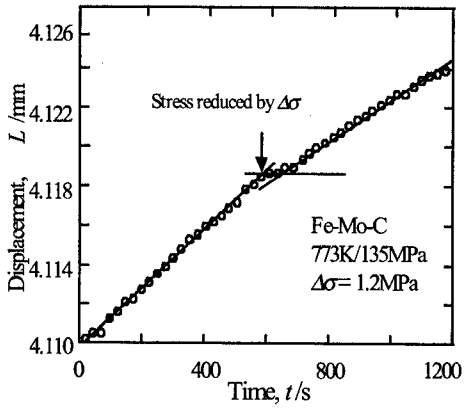

Fig.4 Examples of transient behavior after stress changes during steady-state creep of Fe-0.20at%Mo-0.030at%C alloy under 135MPa at 773K.

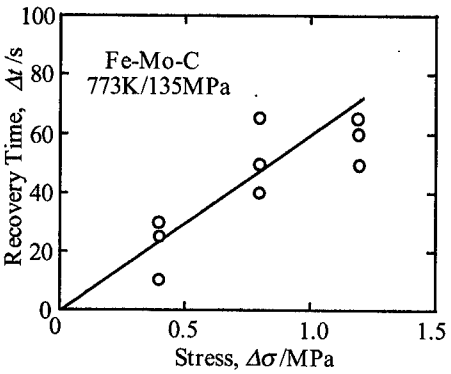

Fig. 5 Recovery time, Δt, as a function of stress decrement, Δσ, in Fe-0.20at%Mo-0.030at%C alloy under 135MPa at 773K.

$$V_{MC} = \frac{D_{Fe} b^2 2\pi\sigma}{k_B T \left[\ln\left(\frac{R_d}{r_1}\right) + \frac{D_v^I}{D_v^2}\ln\left(\frac{r_1}{r_0}\right)\right]}, \tag{1a}$$

$$D_v^I = D_{Fe} V_a C, \tag{1b}$$

$$\frac{1}{D_v^2} = \frac{1}{D_v^I} + \frac{1}{V_a C D_M \exp\left(\frac{-\Delta E}{k_B T}\right)}, \tag{1c}$$

where D_V^2 and D_V^I are vacancy diffusivities in a dislocation core and outside of it. σ, D_{Fe}, b, k_B, T, and Rd are the applied stress, the self-diffusion coefficient of α-Fe, the burger's bector, the Boltzman constant, temperature in kelvin, and an average diffusion length, respectively. And r_0, r_1, V_a, D_M, and ΔE are burger's bector, a radius of the dislocation core, a size of the adjacent area to the

core, the atomic volume of α-Fe, impurity diffusion coefficients of M atoms, and binding energies between an edge dislocation and M atoms or M-C atomic pairs, respectively.

It's well known that the self-diffusion coefficient of α-Fe below the Curie temperature (T_C=1043K) decreases anomalously with decreasing temperature [9]. For the self-diffusion coefficient of α-Fe and the impurity diffusion coefficient of Cr in α-Fe, we evaluated from the equations proposed by Jonsson [10] where the contribution of the magnetic transformation is taken into consideration. For Mo [11] and Mn [12], there are some impurity diffusivity data showing that they are slower than the self-diffusion of α-Fe below Tc, but it is not well established. Thus, we use the self-diffusion coefficient of α-Fe instead of the impurity diffusion coefficients of Mo and Mn, and the results will be compared with the case of fast diffuser, Cr.

The ratio of the climb velocity of dislocations in pure Fe and that in an Fe-M-C alloy is derived as,

$$\frac{V_{Fe}}{V_{MC}} = \frac{\ln(\frac{R_d}{r_1}) + \ln(\frac{r_1}{r_0})[1 + \frac{D_{Fe}}{D_M}\exp(\frac{-\Delta E_{MC}}{k_B T})]}{\ln(\frac{R_d}{r_1}) + 2\ln(\frac{r_1}{r_0})}. \quad (2)$$

The binding energy between an M atom and an edge dislocation is estimated from Eq.3 representing an elastic interaction [13] due to the difference of atomic radii between M and Fe atoms.

$$\Delta E_M = 4 r_{Fe}^3 \mu_{Fe} \frac{|r_M - r_{Fe}|}{r_{Fe}} \frac{1+\nu}{3(1-\nu)}, \quad (3)$$

where υ, μ_{Fe}, r_{Fe} , and r_M are a Poisson's ratio, the shear modulus of Fe, the atomic radius of Fe, and that of M atom, respectively. We adopt the binding energies between M and C atoms as that between M-C pair and an edge dislocation, and the binding energies are estimated from thermodynamic parameters by Eq.4 based on the Fermi-Dirac distribution [14].

$$W_{ij} = \frac{z k_B T}{\beta}[1 - \exp(\frac{\Delta E_{MC}}{k_B T})], \quad (4)$$

where w_{ij}, z, and β are Wagner's interaction parameter between *i* and *j* atoms, a coordination number, and a constant, respectively. Since reported interaction parameters have wide ranges, we calculate the climb velocity with both the maximum and the minimum values of interaction parameters. We use the parameters reported by Wada [15, 16] for Mo-C and Cr-C and the binding energy reported by Abe et al. [17] for Mn-C as the maximum values. The minimum values for are

$$\varepsilon_{ij} = \left.\frac{\partial \ln \gamma_i}{\partial x_j}\right|_{XFe=1}, \quad (5)$$

obtained from data in the SSOL [18-20] database of the Thermo-Calc [21] with Eq.5,
where ε_{ij}, γ_i, and x_j are an interaction coefficient between *i* and *j* elements, an activity coefficient of *i*, and the concentration of *j* in the ferrite phase, respectively. All parameters used are shown in **Table 3**. **Table 4** shows V_{Fe}/V_{MC} and V_{Fe}/V_M for each M-C atomic pair and M atom at 773K estimated from Eq.3. Although V_{Fe}/V_{MC} depends on the interaction parameters between M and C atoms, V_{Fe}/V_{MC} is larger than V_{Fe}/V_M in all alloys. The Mo-C atomic pair shows the strongest effect to reduce the climb velocity. The results of present calculations are consistent with the results of creep tests at 773K, although the direct comparison of creep rate among alloys is difficult because of different applied stresses. The calculations for the same Fe-M-C alloys at 973K explain very well

the effect of alloying element on the steady state creep rate observed in creep tests at 973K under 10MPa [22] (see **Table 5**). Thus, it is found that the Mo-C atomic pair has the largest strengthening effect due to the large binding energy between Mo and C atoms, and the slow diffusivity. From these considerations, it can be concluded that the effect of M-C pair to reduce the climb rate of dislocations originates from the interaction between M-C pairs and dislocations, and the magnitude of the reduction can be estimated from the binding energy between M and C atoms and the diffusivity of M atom.

Table 4 Effects of substitutional solute element, M, and M-C pair on the dislocation climb velocity with respect to the pure Fe calculated by Eq.(3) at 773K for the respective applied stresses.

Substitutional solute element, M	Stress, σ/MPa	Steady-state creep rate in the present tests, $\dot{\varepsilon}_{Fe}/\dot{\varepsilon}_{MC}$	Calculated climbing velocity, V_{Fe}/V_{MC}	V_{Fe}/V_{M}
Cr	42	0.18	4.6-1.5	0.7
Mn	42	0.20	4.1-1.1	1.0
Mo	135	0.44	5.4-1.1	0.8

$\dot{\varepsilon}_{Fe}$: The steady-state creep rate in the Fe-C alloy under 32MPa at 773K.

Table 5 Effects of substitutional solute element, M, and M-C pair on the dislocation climb velocity with respect to the pure Fe calculated by Eq.(3) at 973K under 10MPa.

Substitutional solute element, M	Steady-state creep rate at 973K, 10MPa, $\dot{\varepsilon}_{Fe}/\dot{\varepsilon}_{MC}$	Calculated climbing velocity, V_{Fe}/V_{MC}	V_{Fe}/V_{M}
Cr	2.5	2.7 - 1.4	1.0
Mn	16.7	2.7 - 1.3	1.2
Mo	125.0	8.3 - 3.2	2.7

$\dot{\varepsilon}_{Fe}$: The steady-state creep rate in the Fe-C alloy under 10MPa at 973K.

4.2 Concentration of M-C atomic pairs and M atoms in the ferrite

The maximum C solubility in the ferrite is 0.1at%C (0.02mass%C) at the A1 point (1000K), and it decreases with decreasing temperature. The C solubility decreases drastically with additions of Mo, Mn, and Cr. The C solubility consequently is very limited at the test temperature, 773K, and carbides form in equilibrium with the ferrite matrix. **Table 6** shows the chemical compositions of the ferrite matrix and the volume fraction of carbide at 773K in the present alloys calculated by the Thermo-Calc. The formation of carbides is expected during creep tests from the calculation,. However, it seems impossible to attain the equilibrium state in about 100h [23], which is an average test time in the present study. Thus, the effect of carbide are neglected in the present analyses.

Table 6 Chemical compositions of ferrite matrix and amount of carbides calculated by the Thermo-Calc (at%).

Alloys	C	Cr	Mn	Mo	Carbide(mol%)
Fe-C	0.0059				0.07 (Fe_3C)
Fe-Cr-C	0.0040	0.10			0.07 (Fe_3C+M_7C_3)
Fe-Mn-C	0.0048		0.11		0.04 (Fe_3C)
Fe-Mo-C	0.0001			0.10	0.20 (M_6C)

The assumption in the model proposed by Sandstrom is that atomic pairs are trapped at jogs on edge dislocations. It corresponds to the case that the concentration of M-C atomic pairs is much larger than the jog density. The concentrations of M-C atomic pairs are estimated from the ferrite compositions in **Table 6** by the central atoms model (CAM) [24] which can describe atomic configurations in a solid solution. The calculated concentrations of M-C pairs in the present study ranges from 10^{21} to $10^{23}m^{-3}$, and they are much larger than the jog density, 10^{17}-$10^{19}m^{-3}$, measured by Ishida et al. [5] under similar creep conditions (773K/6-15MPa) in Fe-Mn-N alloys.

The solubilities of alloying elements in the ferrite are very limited. However there should be solute atom segregation on dislocations due to the attractive interaction between them.The co-segregation of C and M atoms on a stationary dislocation can be estimated from the following Langmuir- McLean's equations.

$$\frac{X_C^D}{1-X_C^D} = x_{C0}\exp\left(\frac{\Delta E_C^D + \Delta E_{MC} X_M^D}{k_B T}\right), \quad (6b)$$

$$\frac{X_M^D}{1-X_M^D} = x_{M0}\exp\left(\frac{\Delta E_M^D + \Delta E_{MC} X_C^D}{k_B T}\right), \quad (6a)$$

where X_C^D, X_M^D, x_{C0}, and x_{M0} are C, and M concentrations on the dislocation, average concentrations of C, and M, respectively, and ΔE_{CD}, ΔE_{MD}, and ΔE_{MC} are binding energies between a C atom and an edge dislocation, and between M and C atoms, respectively. **Figures 6, and 7** show M, and C concentrations on the dislocation in Fe-0.1at%M-0.01at%C alloys. The largest co-segregation is observed in the Fe-Mo-C alloy, and the degree of segregation increases with decreasing temperature in all alloys. At 773K, the concentrations of C and Mo amount to 2at% and 4at% on the dislocation, respectively, and they are 200 times and 40 times as large as the average concentrations of C and Mo, respectively. In the alloys Fe-Mn-C and Fe-Cr-C, the co-segregation is also observed, however, the degree of segregation is smaller than that in the Fe-Mo-C alloy because of smaller binding energies between a M atom and a dislocation. The above calculations are performed on the static dislocations, and the degree of segregation is expected to be decreased when the dislocation is moving. However these calculations suggest that an extremely large co-segregation can be induced even in dilute alloys, depending on conditions. Such segregation is expected to accelerate the effect of M-C atomic pairs to reduce the climb velocity of dislocation.

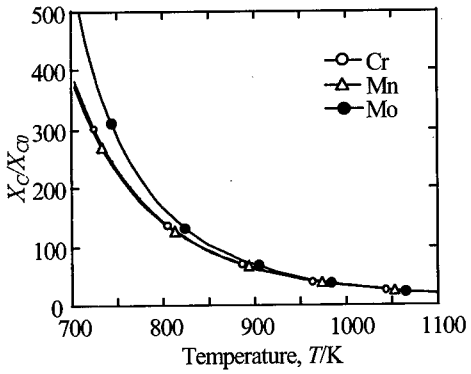

Fig. 6 Temperature dependence of carbon co-segregation on the edge dislocation in the Fe-0.01at%C-0.1at%M (M=Mo, Mn and Cr) alloys.

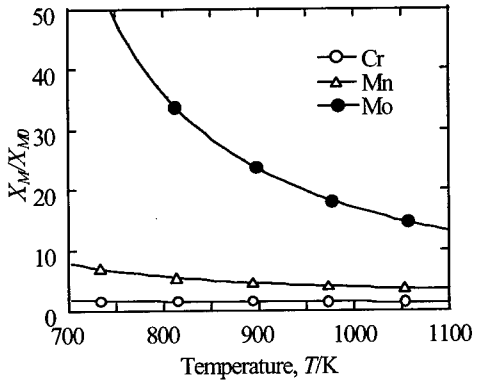

Fig. 7 Temperature dependence of co-segregation of substitutional solute element, M, on the edge dislocation in the Fe-0.01at%C-0.1at%M (M=Mo, Mn and Cr) alloys

4. Conclusion

In order to improve the long-term creep strength of the ferritic steels, the effect of M-C atomic pairs on the creep properties have been examined. The results obtained are as follows,

1. In creep tests at 773K, the Mo addition shows the largest strengthening effect, and additions of Mn and Cr show almost the same effects.
2. The results of the sudden stress increment tests suggest the existence of instantaneous plastic strain in all alloys. Thus, it is concluded that the rate controlling process of creep deformations in the present study is the recovery process due to the climb of dislocations.
3. From the stress decrement tests, it is found that ratios of the climb velocities are similar to the ratios of the steady state creep rate. This suggests that M-C atomic pairs reduce the steady state

creep rate by reducing the climb velocity of dislocations.

4. From analysis by the model proposed by Sandstrom, it is concluded that M-C pair reduces the climb velocity of dislocations due to large interaction energies with dislocations. The magnitude of the reduction can be estimated from the binding energy between M and C atoms and the diffusion coefficient of M atom.
5. The co-segregation of M and C atoms on edge dislocations is predicted by thermodynamic analysis, and it is pointed out that this may result in the apparent reduction of the dislocation climb velocity even in alloys containing very limited amount of alloying elements.

Reference

[1]K.Kimura, H.Kushima, K.Yagi, and C.Tanaka : Trans. ISIJ,81(1995),p.739.
[2]H.Onodera, T.Abe, M.Ohnuma, M.Fujita, and C.Tanaka : Trans. ISIJ,81(1995),p.191.
[3]H.Oikawa and K.Sugawara:Scripta Metall.,12(1978),p.85.
[4]H.Oikawa and S.Nanba:Trans.ISIJ,27(1987),p.402.
[5]Y.Ishida and D.McLean:J.Iron and Steel Inst.,205(1967),p.88.
[6]S.K.Mitra and D.McLean:Proc.Roy.Soc.,A295(1966),p.283.
[7]J.D.Baird and A.Jamieson:J.Iron and Steel Inst.,11(1972),p.847.
[8]R.Sandsrtom:Acta Metall., 25(1977),p.905.
[9]H.Oikawa:Tech.Report Tohoku Univ.,48(1983).
[10]B.Jonsson:Z.Metallkd.,83(1992),p.349.
[11]K.Nohara and K.Hirano : Trans. JIM,10(1976),p.1053.
[12]V.Irmer and M.Feller-Kniepmeier:J.Phys.Chem.Solids, 33(1972),p.2141.
[13]A.H.Cottrell:Dislocation and Plastic Flow in Crystals,(1954).
[14]H.Numakura:Proceedings of the computer aided materials design,ISIJ,(1998),p.17
[15]H.Wada:Metall.Trans.A,16A(1984),p.1479.
[16]H.Wada:Metall.Trans.A,17A(1986),p.391.
[17]H.Abe, T.Suzuki, and S.Okada:Trans.JIM,25(1984),p.215.
[18]W.Huang:Metall.Trans.A,21A(1990),p.2115.
[19]J-O.Andersson:Calphad,11(1987),p.271.
[20]J-O.Andersson:Calphad,12(1988),p.1.
[21]B.Sundman, B.Jansson, and J-O.Andersson:Calphad, 9(1985),p.153.
[22]T.Abe, H.Onodera, M.Ohnuma, K.Kimura, H.Kushima:the Report of the 123 committee,JSPS,37(1996),p.249.
[23]M.Hasebe,H.Ohtani,and T.Nishizawa:Metall.Trans.,16A(1985),p.913.
[24]E-H.Foo and C.H.P.Lupis : Acta Metall.,21(1973),p.1409.

Contact Author:Taichi Abe, Email:taichi@nrim.go.jp, FAX:+81-(0)298-59-2628

Key Engineering Materials Vols. 171-174 (2000) pp. 469-476
© 2000 Trans Tech Publications, Switzerland

Acceleration of Fe2W Precipitation and Its Effect on Creep Deformation Behavior of 8.5Cr-2W-VNb Steels with Si

N. Fujitsuna, M. Igarashi and F. Abe

National Research Institute for Metals (NRIM), 1-2-1 Sengen, Tsukuba 305-0047, Japan

Keywords: High-Cr Ferritic Steels, Si, Laves Phase, Precipitation

Abstract

The effect of Si on the precipitation behavior of $M_{23}C_6$ and Fe_2W Laves phase during creep and on the creep deformation behavior was studied on 8.5Cr-2W-VNb steels at 650℃ for up to 10000h. During creep and aging, Fe_2W Laves phase precipitated and then the amount and the mean particle size of Fe_2W precipitates became larger with increasing Si concentration, while the amount and the mean size of $M_{23}C_6$ was scarcely changed by the addition of Si. It was cleared that Si-addition influence more strongly on the precipitation of Fe_2W than $M_{23}C_6$. The creep rupture strength of the steels increased with increasing Si concentration at high stresses and short rupture times less than 2000h, while it had a maximum at 0.3% Si and then decreased with increasing Si concentration at low stresses and long rupture times longer than 2000h. The decrease of creep rate in the acceleration creep region was more significant by Si-addition, and the minimum creep rate was decreased by Si-addition at all stress conditions. The change in creep deformation behavior by Si-addition resulted mainly from the change in precipitation behavior of Fe_2W, such that the decrease of creep rate in transient creep region is more significant by acceleration of Fe_2W precipitating on the lath boundary to suppress the recovery of the lath structure and that the extreme increase of creep rate after reaching a minimum creep rate and the decrease of duration of acceleration creep region occurred with coarsening of Fe_2W.

1. Introduction

The improvement of energy efficiency in a thermal power plant is indispensable form a viewpoint of the environmental protection and the saving fossil fuel. Nowadays, the plant serviced at 600℃ is practically operated, the study of the 630℃ plant using new steels, NF616 and HCM12A, is performed. In the future, the 650℃ plant should be established.

High-Cr ferritic steels are selected for large parts as if main steam pipes in boiler plants from a viewpoint that thermal fatigue property is better than austenitic steels. It is recognized that the maximum allowable temperature determined by oxidation resistance is 630℃ in case of ferritic steels, so it is necessary to improve oxidation resistance for use at 650℃. Si is the effective to improve oxidation resistance, oxidation rate decrease with Si concentration [1,2]. In relation to the influence of Si-addition on creep properties, it is indicated that there is little influence on creep rupture strength by small amount of Si up to 0.176% [3]. But, in generally, it is recognized that creep rupture strength and toughness decrease by Si-addition [3,4,5,6] because coarsening of carbides and precipitation of Laves phase are accelerated by Si-addition. So, in order to optimize the concentration of Si from a viewpoint of sufficient creep and oxidation resistance in 650 °C USC boilers, the effect of Si on the precipitation

behavior during creep and on the creep deformation behavior was investigated in this study.

2. Experimental Procedure

In this study, 0.14C-8.5Cr-2W-0.2V-0.05Nb steel was selected as the base steel so that there is no δ-ferrite phase in a normalized state up to 1%Si-addition. Amount of Si added was 0.3, 0.5, 0.8%. 17.5kg ingots of these steels were produced by vacuum induction melting. Bars with 20mm in diameter were hot-forged from ingots at heating temperature of 1100℃. All steels were normalized at 1050℃ for 1h followed by air cooling and then tempered at 760℃ for 1h followed by air cooling. Chemical compositions and Vickers hardness of the steel rods after tempering are summarized in Table 1. Creep tests were carried out at 650°C for up to about 10,000 h, using specimens of 6mm gage diameter and 30mm gage length. The longitudinal cross section of the specimens was observed metallographically by SEM and TEM. Thermal aging was also performed at 650 and 750℃ for 3,000h.

Table 1 Chemical composition and Vickers hardness

	C	Si	Cr	W	V	Nb	N	Al	P	S	Mn	Hardness
Base	0.14	0.01	8.49	1.93	0.206	0.047	0.007	0.008	<0.001	0.001	<0.001	215
0.3Si	0.14	0.34	8.47	1.95	0.204	0.046	0.007	0.007	<0.001	0.001	<0.001	218
0.5Si	0.13	0.52	8.49	1.93	0.195	0.045	0.005	0.008	<0.001	0.001	<0.001	223
0.8Si	0.13	0.72	8.42	1.90	0.195	0.046	0.006	<0.001	<0.001	0.001	<0.001	229

3. Results and discussion

3-1 Effect of Si on particle size and amount of $M_{23}C_6$ and Fe_2W in thermal aging

Identification of precipitates was carried out by X-ray diffraction of electrolytically extracted residues of steels aged at 650℃ and 750℃, the result is shown in Table 2. After tempering, $M_{23}C_6$ and MX were present in each steel. In case of 750℃, only $M_{23}C_6$ and MX were observed, there is no change from tempered state. During aging at 650℃, Fe_2W Laves phase precipitate from supersaturated solid solution, it was not observed after aging for 100h. Precipitation of Laves phase was observed only in steels added with Si after aging for 300h, not in the base steel.

Table 2 Result of X-ray diffraction of electrolytically extracted residues of aged steels

Base : 0.14C-8.5Cr-2W-0.2V-0.05Nb

	Base steel		0.3%Si-steel		0.5%Si-steel		0.8%Si-steel	
	650℃	750℃	650℃	750℃	650℃	750℃	650℃	750℃
NT	$M_{23}C_6$, MX							
100h	$M_{23}C_6$, MX							
300h	$M_{23}C_6$ MX	$M_{23}C_6$ MX	$M_{23}C_6$ MX Laves	$M_{23}C_6$ MX	$M_{23}C_6$ MX Laves	$M_{23}C_6$ MX	$M_{23}C_6$ MX Laves	$M_{23}C_6$ MX
1000 h	$M_{23}C_6$ MX Laves							
3000 h								

Laves phase precipitate, there is no influence of Si on particle size of $M_{23}C_6$, while particle size of $M_{23}C_6$ become larger with increasing Si concentration after aging at 750℃ where Laves phase did not precipitate. On the other hand, the particle size of Laves phase becomes larger with increasing Si concentration. The cause of coarsening of Laves phase by addition of Si may be the increase of the precipitation rate and the precipitated amount of Laves phase as shown in Fig.2 because number of Laves phase precipitates is scarcely changed.

3-2 Creep deformation behavior

Fig.4 shows a relationship between stress and time to rupture and Fig.5 shows the effect of Si on time to rupture. The creep rupture strength increased with increasing Si concentration at high stresses and short rupture times less than 1,310 h, while it had a maximum at 0.3% Si and then decreased with increasing Si concentration at low stresses and long rupture times longer than 2,000h. At 60.8MPa, rupture times of steels added with 0.5% and 0.8%-Si become extremely shortened in comparison with the base-steel and the 0.3%Si-steel.

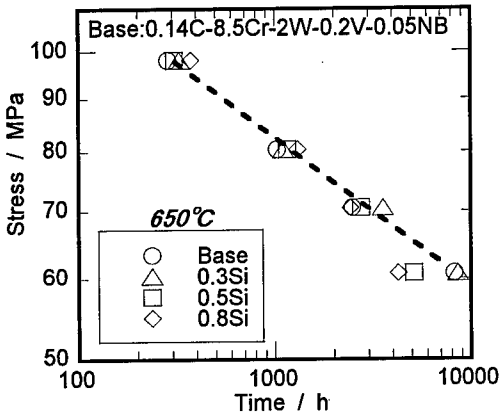

Fig.4 Creep rupture property

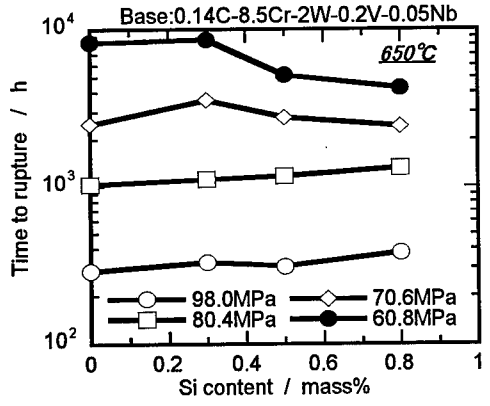

Fig.5 The effect of Si on the rupture time

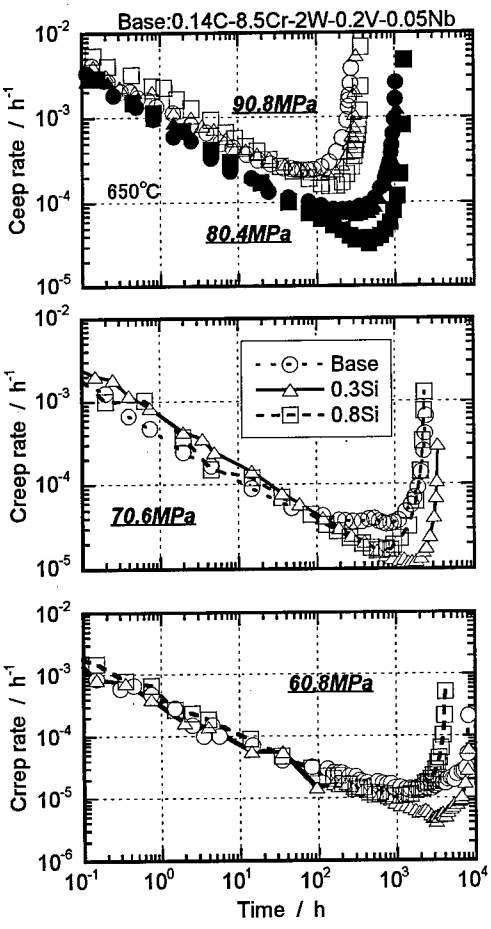

Fig.6 Creep rate vs. time curves at 650℃

In order to determine the amount of Laves phase and $M_{23}C_6$ precipitates after aging at 650℃for 3000h, chemical analysis of extracted residues were performed. There was little change in the amount of $M_{23}C_6$ by Si concentration, while the effect of Si on the amount of Laves phase is significantly recognized. The ratio of precipitated amount determined by chemical analysis to a equilibrium precipitated amount that is calculated using Thermo-calc was determined, this ratio is defined as the precipitation rate in this study. The effect of Si on the amount and the precipitation rate of Laves phase is shown in Fig.1. Both the precipitated amount and the precipitation rate increases with Si concentration. Especially in cases of the steels with 0.5% and 0.8%Si, the precipitation of Laves phase from supersaturated solid solution may be almost finished because the precipitation rate reaches almost 90%. From the above results, it is considered that precipitation of Laves phase is accelerated by Si-addition.

SEM micrographs of the base-steel and the steel added with 0.8%-Si aged at 650℃ for 3,000h are shown in Fig.2. These are secondary electron images (SEI) and backscattered electron images (BSEI) at the same region. High contrast region in the backscattered electron image is inferred to be Laves phase. Precipitation of Laves phase is mainly observed on the grain boundaries, particle size of the 0.8Si-steel is larger than that of the base-steel. Number of Laves phase precipitates may be scarcely changed between the base-steel and 0.8Si-steel.

Fig.3 shows the result of mean particle size of $M_{23}C_6$ and Laves phase after aging for 3,000h. Particle size of $M_{23}C_6$ after aging is larger in comparison with tempered state. However, at 650℃ where both $M_{23}C_6$ and

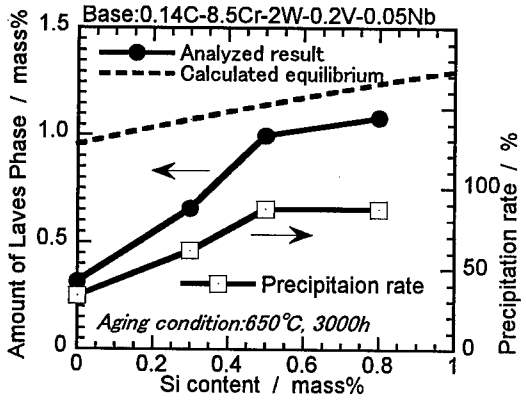

Fig.1 The effect of Si on the amount of Laves phase

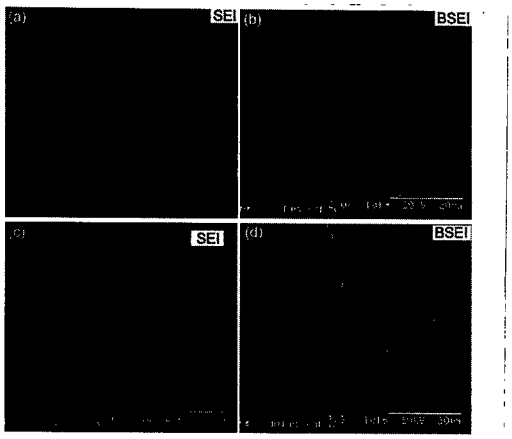

Fig.2 SEM micrographs after aging for 3000h at 650℃
(a),(b):base-steel, (c),(d):0.8%Si-steel
SEI : secondary electron image
BSEI : backscattered electron image

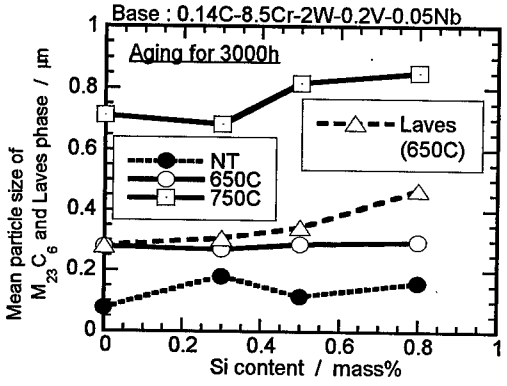

Fig.3 The effect of Si on the particle size of precipitates

Fig.6 shows creep rate vs. time curves of the base-steel, the 0.3%Si-steel and the 0.8%Si-steel. All most of these curves show simple creep deformation such that acceleration creep occurs after reaching a minimum creep rate, complex creep deformation with two minima of creep rate is revognized only in the base steel crept at 70.6MPa. And in all stress conditions, the decrease of creep rate in transient creep region is more significant by Si-addition. At stress condition higher than 80.4MPa, minimum creep rate becomes smaller and duration of transient creep region becomes longer with rupture time become longer. At stress lower than 70.6MPa, in spite of minimum creep rate of the 0.8Si-steel is smaller than that of the base-steel, rupture time of the 0.8Si-steel becomes shorter than the base-steel.

Creep rate vs. strain curves at stress of 70.6MPa is shown in Fig.7. From this, acceleration of creep rate after reaching minimum creep rate becomes larger by Si-addition. This may be the cause that rupture time of the 0.8Si-steel becomes shorter than the base-steel in spite of minimum creep rate of the 0.8Si-steel is smaller than that of the base-steel. Here, it is considered that the duration of acceleration creep region after reaching a minimum creep rate became shortened by Si-addition at low stresses. The relationship between duration of acceleration creep region and concentration of Si is shown in Fig.8. From this, Only a little influence of Si on the duration of acceleration creep region at stress higher than 70.6MPa, while the duration of acceleration creep region significantly become shortened with increasing Si concentration at 60.8MPa.

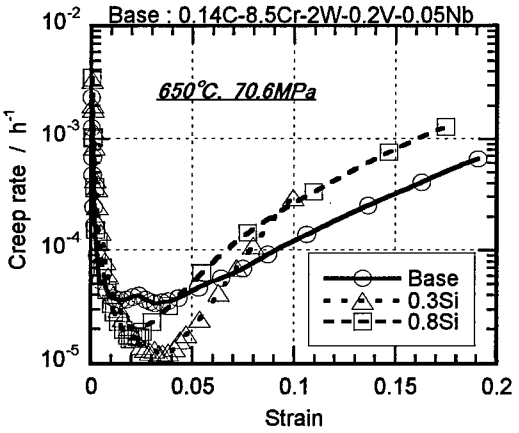

Fig.7 Creep rate vs. strain curves at 650℃ and 70.6MPa

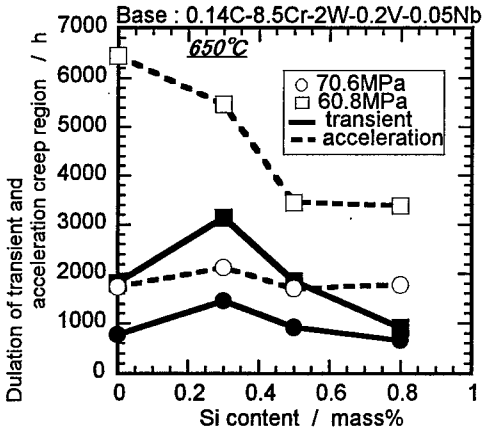

Fig.8 The effect of Si on duration of transient and acceleration creep region

3.3 Precipitation of Laves phase and microstructural change during creep

In order to investigate precipitation behavior and changes of martensitic structure during creep, creep interruption tests were carried out at stress of 70.6MPa where two minima of creep rate was observed in the base-steel. At 650℃, Si-addition affects more strongly precipitation of Laves phase than $M_{23}C_6$ as already shown. Changes in the amount of Laves phase precipitates were determined by the ratio of X-ray intensity between Laves phase and $M_{23}C_6$. The result is shown in Fig.9. It is confirmed that precipitation of Laves phase is accelerated by Si-addition and that amount of Laves

phase precipitates becomes larger with increasing Si concentration as same as thermal aging. Especially, because Laves phase did not precipitate in the base-steel without Si crept for 360h reaching the first minimum of creep rate, it should be noted that precipitation of Laves phase mainly occurs after reaching the first minimum. It is considered that this behavior is the cause that the base steel shows two minima of creep rate. It is indicated that reducing of creep strength in the long-term creep region at lower stress is caused by a depletion of solution hardening elements as if W in the ferrite matrix with precipitation of Laves phase [7]. It is considered that the same thinking is possible after disappearing the precipitation hardening of Laves phase by coarsening of Laves phase precipitates and that extremely shorting of rupture time in the high-Si steels at lower stress is caused by this effect in addition to the weakening by coarsening of precipitates.

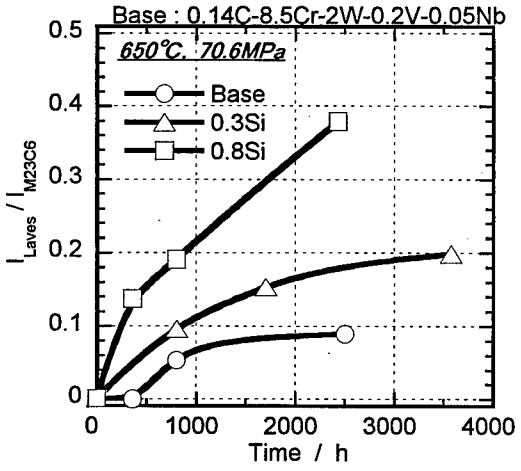

Fig.9 Change in amount of Laves phase precipitates during creep at 650℃ and 70.6Mpa

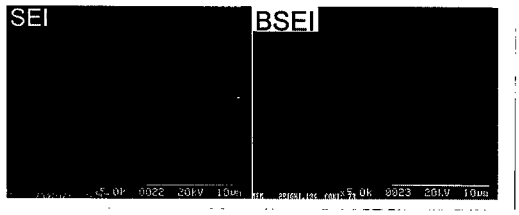

Fig.10 SEM micrographs of the 0.8%Si-steel crept for 800h at 650℃ and 70.6Mpa
SEI:secondary electron image
BSEI:backscattered elctron image

The example of distribution of Laves phase during creep is shown in Fig.10. Laves phase precipitated during creep exit on both grin boundaries and lath boundaries, which is different from thermal aging as shown in Fig.2.

Fig.11 shows changes of martensitic structure during creep at 70.6MPa. The morphology of all steels is tempered martensitic structure with a lot of dislocations at tempered state. After creep for 360h reaching the first minimum of creep rate in the base steel, the recovery of excess dislocations and the coarsening of laths occur in the base steel. On the other hand, in the 0.8Si-steel, much more precipitates of Laves phase precipitate on the lath boundary and the recovery of martensitic structure in the 0.8Si-steel may less pronounced than the base steel. Precipitating of many precipitates recognized as Laves phase on the lath boundary suppress the recovery of martensitic structure and promote the decrease of creep rate in the transient creep region because Laves phase precipitating on the lath boundary has effect of suppressing the recovery of martensitic structure as shown by

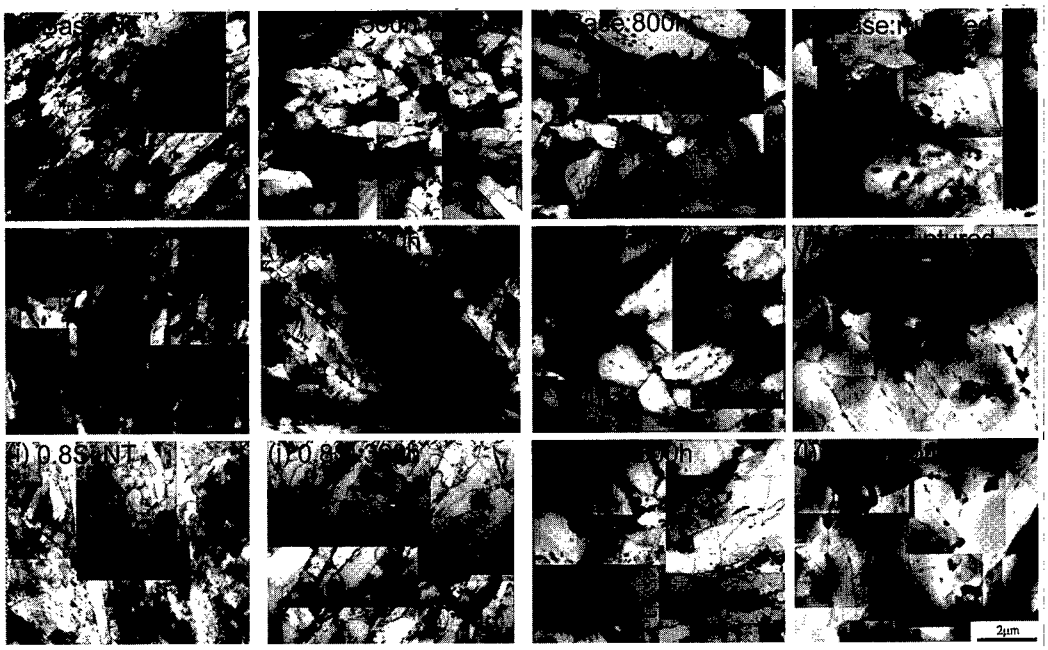

the base steel: a) as-tempered, b) ti=360h, c) ti=800h, d) tr=2501h
the 0.3Si steel: a) as-tempered, b) ti=800h, c) ti=1704h, d) tr=3573h
the 0.8Si steel: a) as-tempered, b) ti=360h, c) ti=800h, d) tr=2434h

Fig.11 TEM micrograps of as-tempered and, after interrupted and ruptured condition

Yoshizawa et al.[8]. After creep for 800h reaching the minimum creep rate in the base steel and the 0.8Si-steel, the recovery of martensitic structure and the coarsening of laths progresses. Coarsening of precipitates which is recognized Laves phase as the above-mentioned significantly occurs in the 0.8Si-steel, it is considered that the effects of Laves phase precipitating on the lath boundary to suppress the recovery of martensitic structure begin disappearing. In the 0.3Si-steel which shows the longest rupture time, the recovery of martensitic structure is much slower than other steels and then the lath structure is maintained after crept for 1704h. In the ruptured state, morphology maybe change into the cell structure in the base steel and 0.8Si-steel, but the lath structure is still maintained in the 0.3Si-steel. From these results, it is noted that the 0.3Si-steel shows the longest rupture time because microstructural stability is the best. And, it is considered that microstructural stability of the 0.3Si-steel become the best because the effect of precipitation hardening of Laves phase and the recovery of microstructure with coarsening of Laves phase precipitates are well balanced in the 0.3Si-steel.

From above results, the change in creep deformation behavior at low stresses and long times by the addition of Si resulted mainly from the change in precipitation behavior of Fe_2W.

4. Conclusion

1) Si-addition accelerated the precipitation of Laves phase and the mean particle size of Laves phase became larger with increasing Si concentration. But the effect of Si on precipitation of $M_{23}C_6$ was not recognized during creep and thermal aging at 650℃ where both Laves phase and $M_{23}C_6$

precipitate.

2) In the range tested in this study up to 10,000h, the creep rupture strength of the steels had a maximum at 0.3% Si at low stresses and long rupture times longer than 2000 h.
3) The extremely decrease of creep rate in the transient creep region of the steels added with Si was caused by the effects of Laves phase precipitating on the lath boundary to suppress the recovery of martensitic structure.
4) Microstructural stability of the 0.3Si-steel became the best because the effect of precipitation hardening of Laves phase and the recovery of microstructure with coarsening of Laves phase precipitates were best balanced in the 0.3Si-steel.
5) The change in creep deformation behavior by Si-addition resulted mainly from the change in precipitation behavior of Fe_2W, such that the decrease of creep rate in transient creep region is more significant by acceleration of Fe_2W precipitating on the lath boundary to suppress the recovery of the lath structure and that the extreme increase of creep rate after reaching a minimum creep rate and the decrease of duration of acceleration creep region occurred with coarsening of Fe_2W.

Reference

1) H.Kutsumi, N.Fujitsuna, T.Itagaki and F.Abe : CAMP-ISIJ, 11(1998), p.1290
2) Y.Fukuda, K.Tamura and K.Suzuki : Pro. Int. Symp. on Plant Aging and Life Predictions of Corrodible Structures, Sapporo(1995), p.835
3) K.Asakura, T.Fujita and Y.Otsuguro : Report of the 123rd Committee on Heat-Resisting Materials and Alloy, 26(1985), p.247
4) Y.Hosoi, N.Wade, S.Kunimitsu and T.Urita : Tetsu-to-Hagane, 76(1990), p.1116
5) "Modified 9Cr-1Mo Steel Technical Program and Data Package for Use in ASME Section I and III Design Analyses", Oak Ridge National Laboratory, (1982), p.195
6) Y.Hasegawa, T.Muraki and M.Ohgami : Report of the 123rd Committee on Heat-Resisting Materials and Alloy, Japan Society for the Promotion of Science, 39(1998), p.275
7) Y.Kadoya, N.Nishimura, B.F.Dyson and M.McLean : Proc. 7th Int. Conf. Creep and Fracture of Engineering Materials and Structures, TMS, Irvine(1997), p.343
8) M.Yoshizawa, K.Miyata, J.Senba and Y.Sawaragi : CAMP-ISIJ, 12(1999), p.294

e-mail:fujituna@nrim.go.jp

Key Engineering Materials Vols. 171-174 (2000) pp. 477-482
© 2000 Trans Tech Publications, Switzerland

Strengthening Mechanisms in Heat-Resistant Martensitic 9Cr Steels

K. Iwanaga[1], T. Tsuchiyama[2] and S. Takaki[2]

[1] Graduate Student, Department of Materials Physics and Chemistry, Kyushu University, 6-10-1 Hakozaki, Higashi-ku, Fukuoka 812-8581, Japan

[2] Graduate School of Engineering, Kyushu University

Keywords: Heat-Resistant Steel, Martensite, Creep Strength, Carbide Forming Element, Solid Solution Strengthening, Carbide Particle, Recovery

Abstract

Strengthening mechanisms of heat-resistant martensitic steels were discussed in terms of microstructural evolution and changes in hardness during creep deformation. In carbon-free 9%Cr steels, it was confirmed that the Mo or W addition improves creep properties of martensite through the solid solution strengthening. On the other hand, creep tests of low-carbon 9%Cr steels revealed the fact that carbide particles precipitated along lath boundaries markedly contribute to the retardation of the recovery of martensite, and this leads to an excellent creep properties. The addition of Mo or W to the low-carbon steels does not give a large effect to the retardation of recovery, but causes a large solid solution strengthening in the materials with the subgrain structure, which has been formed in the latter stage of creep deformation.

1. Introduction

Recently, many kinds of heat-resistant martensitic steels have been developed in terms of alloy design for improving power generating efficiency. In many developed steels, carbide forming elements (Mo, V and W) are added to improve the creep property, but the strengthening mechanism has not been cleared because these elements are shared between martensite matrix and carbide particles to contribute the strengthening through the solid solution [1] and the stabilizing effect to carbide growth [2], respectively. This leads to the difficulty of quantitative evaluation on the improvement of the creep property by the addition of carbide forming elements. On the optimum alloy design, it is important to know the quantitative contribution of alloying elements to the strengthening mechanisms individually.

In this study, the effect of solute Mo and W on creep deformation behavior was previously investigated in carbon-free 9mass% martensitic steels, and then discussed by comparing the deformation behaviors among many kinds of low-carbon 9mass%Cr martensitic steels with or without the alloying elements.

2. Experimental procedure

Fe-9mass%Cr-2mass%Ni alloys (carbon-free steels) and Fe-9mass%Cr-0.1mass%C alloys (low-carbon steels) with or without 0.5at% of Mo or W were used. In the carbon-free steels, 2mass% of Ni was added to obtain martensitic structure. Chemical compositions of the steels used are listed in **Table 1**. Ingots of 1.5kg were molten in vacuum, homogenized at 1473K for 18ks, and then hot-rolled at 1273K to 15mm thick plates (30% reduction in thickness). The steel plates were solution-treated at 1273K for 1.8ks and then oil-quenched to obtain martensitic structure. After this treatment, the specimens were tempered at 923K for 3.6ks (QT specimens). Some of carbon-free martensitic steels were subjected to the recrystallization treatment ; 60% cold rolling followed by annealing at various temperatures, in order to obtain ferritic structure without dislocations(RC specimens). All of heat treatments were performed in Ar gas atmosphere to avoid

the surface decarburization of the steels.

Creep tests were carried out at 873K-138MPa. The tested specimens were subjected to Vickers hardness testing at room temperature under the load of 9.8N and to microstructure observation. Microstructures of specimens were examined with transmission electron microscope (TEM).

Table 1 Chemical compositions of the steels used (mass%).

		C	Cr	Ni	N	additional alloying elements
carbon-free steels	base	0.005	9.09	1.97	0.0042	
	9Cr-0.5at%Mo	0.003	9.48	1.94	0.0046	Mo:0.84(0.49at%)
	9Cr-0.5at%W	0.004	9.40	1.94	0.0060	W :1.58(0.48at%)
low-carbon steels	9Cr-0.1%C	0.11	8.95	—	0.0072	
	9Cr-0.1%C-0.5at%Mo	0.11	8.81	—	0.0096	Mo:0.88(0.51at%)
	9Cr-0.1%C-0.5at%W	0.11	8.94	—	0.0087	W :1.53(0.47at%)

others Si<0.06 Mn<0.40 P<0.012 S<0.014

3. Results and discussion

3.1 Strengthening by solute Mo or W in carbon-free 9Cr martensitic steels

Fig.1 shows creep curves of the carbon-free martensitic steels ; 9Cr (base steel), 9Cr-0.5at%Mo and 9Cr-0.5at%W steels, under the condition of 873K-138MPa. The rupture time is greatly prolonged by Mo or W addition.

Fig.2 shows TEM micrographs of as-tempered specimens (before creep test) and crept specimens to the steady state (ε=0.1) in these steels. In the as-tempered specimens (a)~(c), lath-martensitic structure is kept and the density of dislocations is not reduced so much even after the tempering. In the crept specimens (a')~(c'), however, the recovery of martensite significantly proceeds after the creep deformation, that is, the lath-martensitic structure completely disappears and changes to subgrain structure. There is no large difference in the subgrain size and dislocation density among these specimens ((a')~(c')). These results indicate that the addition of Mo or W does not give a large influence to the microstructural change of martensitic steels which is caused during the creep deformation, but markedly lowers the speed of dislocation movement (Fig.1).

Fig.3 shows the changes in hardness during the creep deformation as a function of the strain subjected to test pieces. In all steels, hardness abruptly drops at the early stage of creep deformation ($\sim\varepsilon$=0.1) due to the microstructural change shown in Fig.2, and then levels off at a constant value, although it is different depending on the kind of steels. The level-off hardness is much higher in Mo or W bearing steels than the base steel, and the difference is kept to the rupture.

Table2 represents Vickers hardness of the test pieces with creep deformation (ε=0.1) and the RC specimens with ferritic structure. The increment of hardness by the addition of 0.5at% Mo or W are also shown in the parenthesis. The hardness increment in the ferritic steels almost correspond to the solid solution strengthening by Mo or W in the test pieces. This suggests that the main creep-strengthening by Mo or W addition can be simply explained by the solid solution strengthening even in the martensitic steels with high density of dislocations.

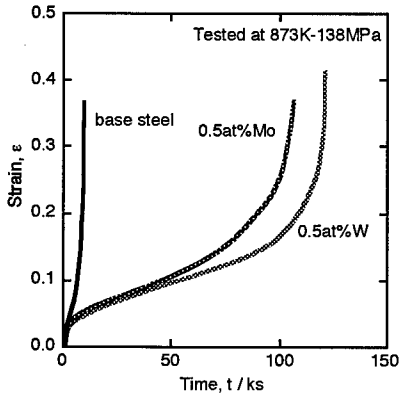

Fig.1 Creep curves of carbon-free martensitic steels; 9%Cr (base steel), 9%Cr-0.5at% Mo and 9%Cr-0.5at%W steels.

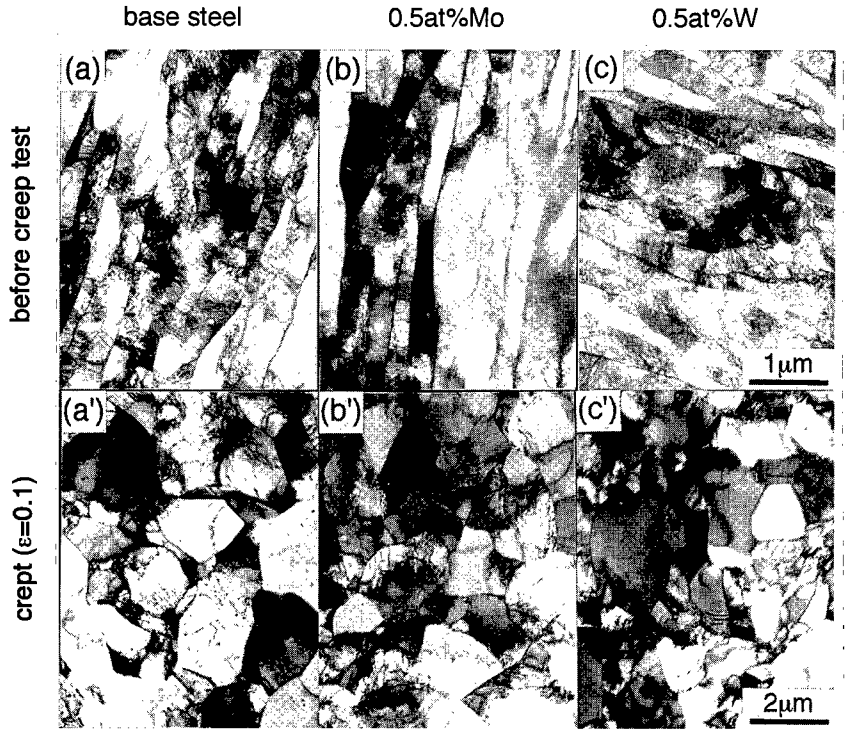

Fig.2 TEM micrographs of as-tempered specimens (before creep test) (a)~(c) and crept specimens to the steady state (ε=0.1) (a')~(c') in carbon-free martensitic steels.

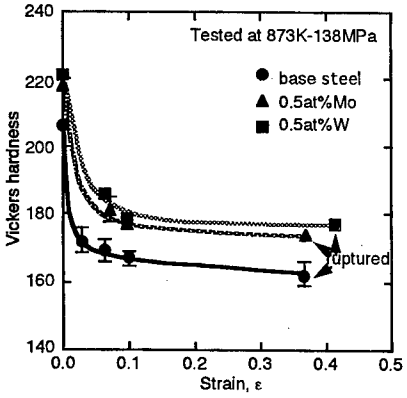

Fig.3 Changes in hardness during creep deformation in carbon-free martensitic steels.

Table2 Vickers hardness of carbon-free martensitic steels with creep deformation (ε=0.1) and recrystallized ferritic steels. The values in the parenthesises are the increment of hardness by the addition of 0.5at% of Mo or W.

specimen	crept martensite	recrystallized ferrite
base steel	167	125
0.5at%Mo	177(+10)	141(+16)
0.5at%W	178(+11)	142(+17)

3.2 Role of carbide particles on creep deformation behavior in martensitic steels

Fig.4 shows creep curves of the low-carbon steel (9Cr-0.1C) and the carbon-free base steel (9Cr) under the condition of 873K-138MPa. Creep strength is markedly improved in the low-carbon steel.

Fig.5 shows TEM micrographs of as-tempered specimens (before creep test) and crept specimens to the early stage of acceleration creep (54ks) in the low-carbon steel. In the as-tempered specimen (a), lath martensitic structure is kept and the morphology of lath is quite similar to that in the carbon-free base steel (Fig.2(a)) except for the existence of carbide particles which precipitate along lath boundaries. Carbide particles were identified as $M_{23}C_6$ and their size is about 80nm. After the creep deformation for 54ks, the morphology of lath tends to be changed to dislocation cell structure. Besides, carbide particles grow and dislocation density is lowered. It should be noted that the recovery of martensite is significantly retarded in comparison with the carbon-free base steel (Fig.2(a')). This means that carbide particles on lath boundaries play an important role for suppressing the recovery of lath-martensitic structure and this leads to holding the dislocation density high[3][4].

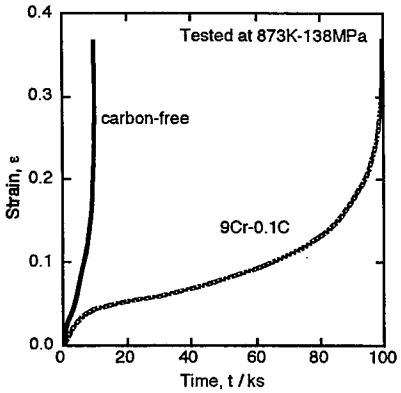

Fig.4 Creep curves of low-carbon martensitic steel (9%Cr-0.1%C) and carbon-free martensitic steel (9%Cr).

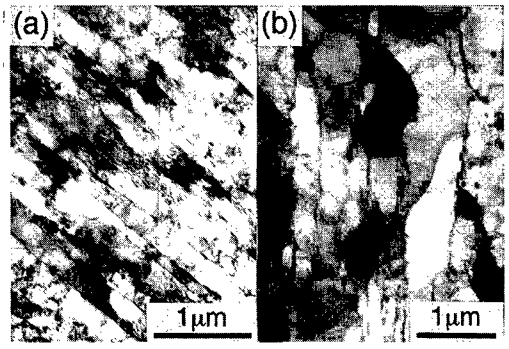

Fig.5 TEM micrographs of as-tempered specimen (before creep) test (a) and crept specimen to the early stage of acceleration creep (54.0ks) (b) in low-carbon martensitic steel.

Fig.6 shows the changes in hardness during creep deformation as a function of strain in the low-carbon steel and the carbon-free base steel. Due to the retardation of recovery by carbide particles, the low-carbon steel undergoes gradual softening ,whereas the carbon-free steel does abrupt softening at the early stage of creep deformation. Here, the comparison of softening behavior between Fig.2 and Fig.6 demonstrates that the contribution of carbide particles to creep strength is substantially different from that of alloying elements (Mo or W). That is, carbide particles contribute to the improvement of creep strength through the retardation of recovery of lath-martensitic structure.

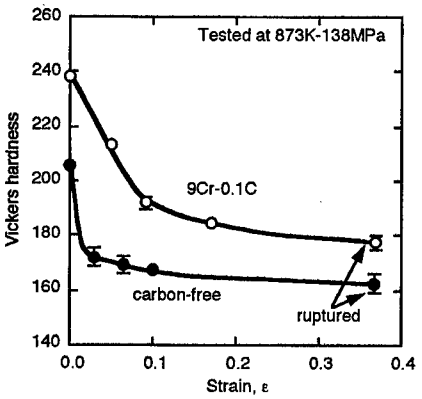

Fig.6 Changes in hardness during creep deformation in low-carbon martensitic steel (9%Cr-0.1%C) and carbon-free martensitic steel (9%Cr).

3.3 Strengthening mechanism in Mo or W bearing low-carbon martensitic steels

Fig.7 shows the changes in hardness during creep deformation under the condition of 873K-138MPa as a function of strain in the low-carbon steels (9Cr-0.1C) with or without 0.5at% of Mo or W. In all over the strain range, the hardness of crept specimens is higher in Mo or W bearing steels than in the plain low-carbon steel (9Cr-0.1C), and the difference is kept to the rupture. Besides, the increment of hardness by Mo or W addition well correspond to the solid solution strengthenings which are represented in Table2. If the carbide particles were stabilized by Mo or W addition, the retardation of recovery should be more intensified in the Mo or W bearing steels. However, the softening behavior was not influenced by Mo or W addition. Hence it is concluded

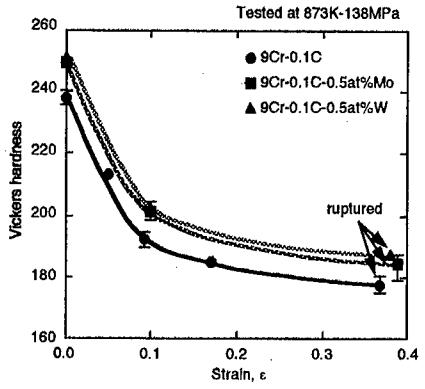

Fig.7 Changes in hardness during creep deformation in low-carbon martensitic steels; 9%Cr-0.1%C, 9%Cr-0.1%C-0.5at%Mo and 9%Cr-0.1%C-0.5at%W steels.

that the addition of Mo or W to the low-carbon steels does not give a effect to the retardation of recovery, but causes a large solid solution strengthening even in low-carbon martensitic steels with a high density of dislocations.

3.4 Strengthening mechanisms for creep deformation in heat-resistant martensitic steels

Fig.8 illustrates the effects of strengthening mechanisms ; solid-solution strengthening and the retardation of recovery produced by carbide particles, in the softening behavior during creep deformation. The solute alloying element (Mo or W) raises hardness by a certain value through the solid solution strengthening (the curve(1)). On the other hand, carbide particles retard the recovery of martensite and hold the dislocation density high, thus the softening curve is shifted to higher strain region (the curve(2)). In the Mo or W bearing low-carbon steels, the addition of Mo or W does not affect the curve(2) but raises the level-off hardness through solid solution strengthening. Therefore, it is concluded that the addition of Mo or W to low-carbon martensitic steels contributes to the strengthening of ferritic matrix itself.

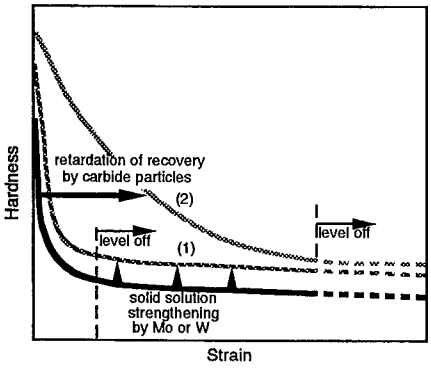

Fig.8 Schematic illustration showing the effects of strengthening mechanisms ; solid-solution strengthening and retardation of recovery, in the softening behavior during creep deformation.

4. Conclusion

(1) In carbon-free steels, Mo or W addition improves creep properties through the solid-solution strengthening.

(2) Carbide particles markedly retard the recovery of lath-matensitic structure during creep deformation, and this leads to a great improvement of creep properties in low-carbon steels.

(3) The addition of Mo or W to the low-carbon steels does not give a large effect to the retardation of recovery, but causes a large solid solution strengthening.

References

[1] T. Motoyoshi, H. Sato and H. Oikawa : Trans. JIM, **57**(1993), p. 890.
[2] T. Fijita : ISIJ int., **32**(1992), p. 175.
[3] S. Takaki, S. Iizuka, K. Tomimura and Y. Tokunaga : Mater. Trans. JIM, **32**(1991), p. 207.
[4] K. Iwanaga, T. Tsuchiyama and S. Takaki, Tetsu-to-Hagane, **84**(1998), p. 896.

Key Engineering Materials Vols. 171-174 (2000) pp. 483-490
© 2000 Trans Tech Publications, Switzerland

Heterogeneous Changes in Microstructure and Degradation Behaviour of 9Cr-1Mo-V-Nb Steel During Long Term Creep

K. Kimura[1], H. Kushima[2] and F. Abe[2]

[1] Materials Creation Research Station, Frontier Research Center for Structural Materials, National Research Institute for Metals, 1-2-1 Sengen, Tsukuba, Ibaraki 305-0047, Japan

[2] Strength and Evaluation Research Station, Frontier Research Center for Structural Materials, National Research Institute for Metals, 1-2-1 Sengen, Tsukuba, Ibaraki 305-0047, Japan

Keywords: 9Cr-1Mo-V-Nb Steel, Creep Strength, Creep Deformation, Microstructural Change, Degradation, Prior Austenite Grain Boundary, Heterogeneous Recovery

ABSTRACT

Creep deformation behaviour and microstructural change have been investigated on 9Cr-1Mo-V-Nb steel (ASME SA-213 T91) in order to understand a degradation mechanism at the elevated temperatures, especially at the long term condition. Remarkable decrease in creep rupture strength at 873K and 923K have been observed at the long term region longer than about 10,000h. Under the higher stress and short term region, homogeneous progress in recovery of tempered martensitic structure, such as increase in lath width and coarsening of subgrain, has been observed. However, remarkable progress in such recovery of the microstructure has been observed only at the vicinity of prior austenite grain boundary under the lower stress and long term region. It has been found that such preferential recovery along a prior austenite grain boundary promotes the beginning of tertiary creep. It has been concluded that preferential recovery at the vicinity of prior austenite grain boundary is a main factor of degradation during long term creep deformation.

INTRODUCTION

From a viewpoint of global environment, especially to suppress a CO_2 emission, there is a strong demand to improve the energy efficiency of electrical power plant. Therefore, a lot of effort have been done to develop a new high strength ferritic creep resistant steel which is used for large components of fossil fired power plant [1],[2]. Because of degradation which should occur during long term services at the elevated temperature as a result of microstructural change [3], improvement of microstructural stability is most important to obtain an excellent long term creep strength. 9Cr-1Mo-V-Nb steel is recently widely used in modern fossil fired power plant and many researches on a correlation between microstructure and creep strength have been reported [4]-[8]. However, most of such researches were conducted on relatively short term creep strength property up to about 10,000h.

The aim of present study is to understand a degradation mechanism of 9Cr-1Mo-V-Nb steel, especially at the long term creep condition. Creep deformation behaviour has been investigated in conjunction with changes in microstructures and a main factor of degradation during long term creep deformation has been discussed.

EXPERIMENTAL PROCEDURE

9Cr-1Mo-V-Nb steel (ASME SA-213 T91) [9] has been used in this study. Chemical composition and heat treatment condition of the steel are shown in Table 1. Creep specimen with 6mm gauge diameter and 30mm gauge length have been taken from boiler and heat exchanger tube with about 8mm wall thickness. Creep tests were conducted over a range of temperatures from 823 to 998K. Creep deformation have been measured using by an extensometer attached to the gauge portion of specimen.

Evaluation of creep strength and prediction of long term creep rupture strength were

performed by analysis of the short term data which less than 1,000h, using by a modified θ projection method [10]. Vickers hardness of as received steel and creep ruptured specimens were measured under load of 98N. Scanning electron microscope and transmission electron microscope were used for the observation of the microstructures.

Table 1. Chemical composition (mass%) and heat treatment of the steel studied.

C	Si	Mn	P	S	Ni	Cr	Mo	Cu	V	Nb	Al	N
0.09	0.29	0.35	0.009	0.002	0.28	8.70	0.90	0.032	0.22	0.072	0.001	0.044

Heat treatment : 1323K/10min. Air cooling + 1038K/30min. Air cooling

RESULTS AND DISCUSSION

Creep strength property

Stress vs. time to rupture curves of the 9Cr-1Mo-V-Nb steel tested over a range of temperatures from 823 to 998K are shown in Fig. 1. Dotted lines are predicted rupture life from the short term data indicated by solid symbols, using by a modified θ projection method [10]. Good correspondence between experimental data and the predicted curves are observed in the short term region less than 10,000h. The differences of predicted curves from the experimental data, however, increase with increase in time to rupture in the long term region more than 10,000h at 873 and 923K, since the stress dependence of creep rupture life decrease abruptly. With decrease in applied stress, creep rupture life decrease to less than half of the predicted one. Such differences between the experimental data and predicted rupture life are observed at the stress regions lower than about 120 and 70MPa at 873 and 923K, respectively.

Rupture elongation is plotted against the time to rupture and shown in Fig. 2. Although the rupture elongation is higher than 25% in the short term region less than about 10,000h over a range of temperatures from 823 to 998K, tendency to decrease with increase in time to rupture is observed in the long term region over 10,000h. Such decrease in rupture elongation at the long term region corresponds to abrupt decrease in stress dependence of the rupture life, as shown in Fig. 1.

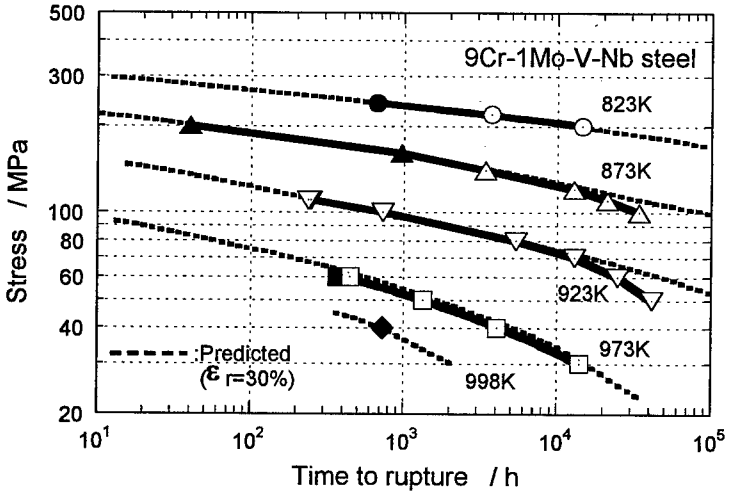

Figure 1. Stress vs. time to rupture curves of the 9Cr-1Mo-V-Nb steel tested over a range of temperatures from 823 to 998K.

Vickers hardness of the as received steel and the specimens creep ruptured at 873, 923 and 973K are plotted against the time to rupture and shown in Fig. 3. Hardness of the as received steel is HV235 and that of the creep ruptured specimens decreases with increase in time to rupture up to about 10,000h. Although the abrupt decreases in creep rupture strength and rupture elongation is observed in the long term region, however, no significant decrease in hardness of the creep ruptured specimens are observed in such long term region, and even a tendency to increase in hardness is observed at 923K.

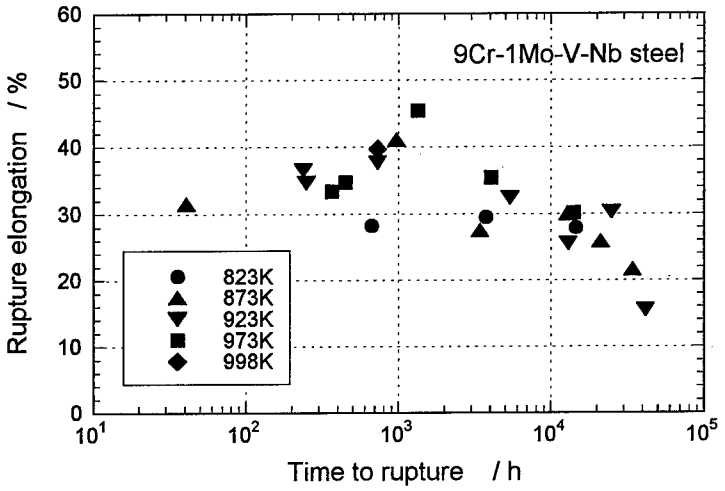

Figure 2. Rupture elongation of the 9Cr-1Mo-V-Nb steel tested over a range of temperatures from 823 to 998K.

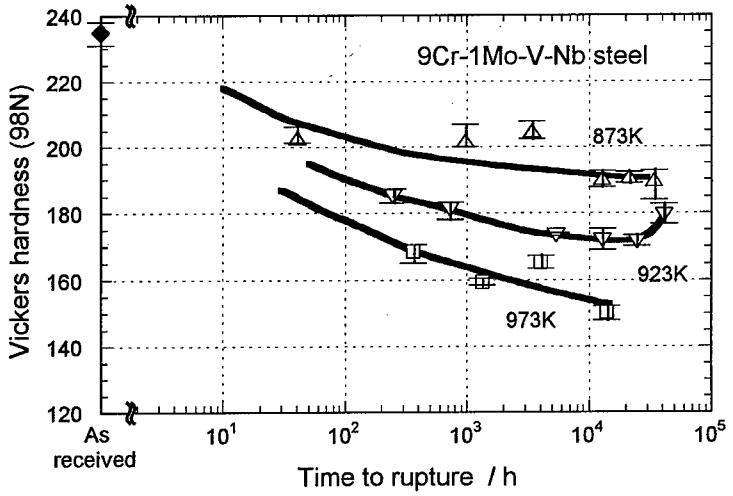

Figure 3. Changes in Vickers hardness of the 9Cr-1Mo-V-Nb steel with increase in time to rupture at 873, 923 and 973K.

Creep deformation behaviour

Creep rate vs. time curves tested over a range of stresses from 100 to 200MPa at 873K are shown in Fig. 4. Creep deformation consists of transient and acceleration creep stages under all stress conditions. Stress dependence of the minimum creep rate is about 4 orders in magnitude. It is significantly larger than that of the creep rate at the beginning of the creep deformation which is about 1 order in magnitude at t=0.1h. On the other hand, stress dependence of the onset time of tertiary creep decreases with decrease in applied stress.

Creep rate vs. true strain curves tested over a range of stresses from 100 to 200MPa at 873K are shown in Fig. 5. Under the higher stress conditions from 140 to 200MPa, minimum creep rate is observed at the strain range from 0.02 to 0.03. Under the stress conditions lower than 120MPa, however, creep rate represent minimum value at the small strain less than 0.01. At the long term creep conditions in which abrupt decrease in creep rupture strength is observed, consequently, creep deformation shift from transient creep stage to tertiary one at the relatively small strain in comparison with that at the higher stress and short term creep condition. Abrupt decrease in creep rupture strength and rupture elongation at the long term creep conditions may attribute to such changes in creep deformation behaviour at the lower stress conditions.

Microstructural change

SEM micrographs of the as received steel and the specimens creep ruptured at 873K-160, 120 and 100MPa are shown in Fig. 6. On the as received steel (a), precipitates whose size is about 0.1 μ m are observed at the prior austenite grain boundaries, and similar precipitates in size and fine precipitates which is less than 0.1 μ m are observed within grain. Coarsening of precipitates at grain boundary is observed on the specimen ruptured at 160MPa (b), and the ratio of the grain boundary covered by the precipitates is larger than that of the as received steel. Increase in size up to about 0.3 μ m and decrease in number of the grain boundary precipitates are observed on the steel ruptured at 120MPa (c), and deformed precipitates free grain boundary is also observed. Significantly coarsened precipitates whose size is about 0.5 μ m are observed at grain boundary of the steel ruptured at 100MPa (d), however, fine precipitates which is less than 0.1 μ m are also still observed within grain.

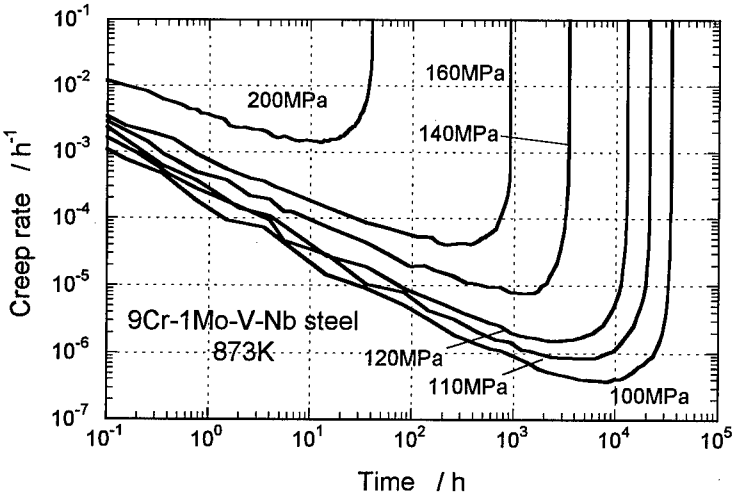

Figure 4. Creep rate vs. time curves of the 9Cr-1Mo-V-Nb steel at 873K-100~200MPa.

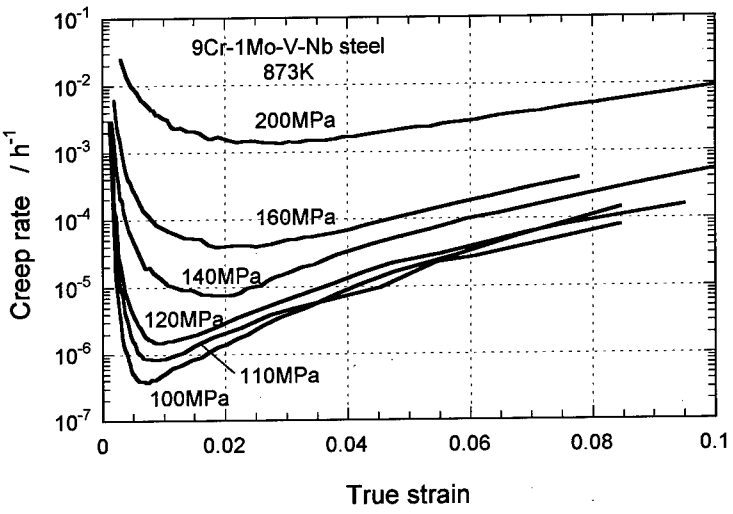

Figure 5. Creep rate vs. true strain curves of the 9Cr-1Mo-V-Nb steel at 873K-100~200MPa.

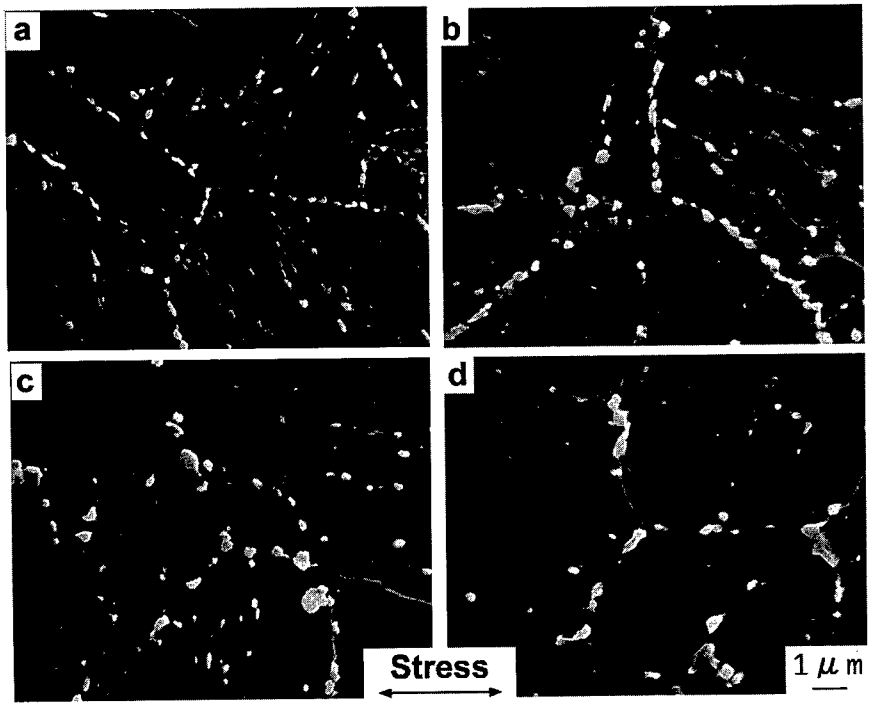

a) As received
b) 873K-160MPa, tr=971.2h
c) 873K-120MPa, tr=12,858.6h
d) 873K-100MPa, tr=34,141.0h

Figure 6. SEM micrographs of the as received steel and the steels ruptured at 873K-160, 120 and 100MPa.

TEM micrographs of the same steels are shown in Fig. 7 as those in Fig. 6. Tempered martensitic microstructure is observed on the as received steel (a). Dislocation density of it is very high and the lath width is about 0.3 μ m. Recovery of tempered martensitic microstructure, such as increases in lath width and subgrain size is observed on the specimen creep ruptured at 160MPa (b). Size of coarsened subgrains is more than 1 μ m. The specimen creep ruptured at 120MPa (c) represents significant progress in recovery of tempered martensitic microtructure. Martensitic lath structure has been annihilated by recovery during creep deformation.

On the other hand, different features of the microtructure from those of the above creep ruptured specimens are observed on the specimen creep ruptured at the lowest stress of 100MPa (d). Significantly recovered region is observed along prior austenite grain boundary, however, microstructure within grain is still fine in comparison with that at the vicinity of grain boundary. Although a time to rupture of the specimen crept at 100MPa (d) is about three times longer than that of the specimen crept at 120MPa (c), subgrain size within grain of the former specimen which is less than 1 μ m is smaller than that of the latter one. Similar heterogeneously recovered microstructure is also observed on the specimen creep ruptured at 923K-50MPa whose time to rupture of 41425.2h is similar to that of the specimen crept at 873K-100MPa. Such heterogeneous progress in recovery of the microstructure is observed only for the specimens creep ruptured at the lower stress conditions in which abrupt decrease in creep rupture strength is observed. It should be a reason why hardness of the creep ruptured specimen does not decrease in the long term region.

Effect of heterogeneous recovery

Recovery of tempered martensitic microstructure, such as increase in lath width and coarsening of subgrain progress homogeneously at the higher stress and short term region. At the lower stress and long term condition, however, such microstructural change proceeds heterogeneously, since remarkable progress in recovery occurs at the vicinity of prior austenite grain boundary. At the higher stress condition, changes in microstructure occur homogeneously with creep deformation and creep rate shows minimum value at relatively high strain range 0.02 to 0.03. On the other hand, preferential recovery at the vicinity of prior austenite grain boundary at the lower stress condition promotes the onset of tertiary creep and, consequently, minimum creep rate is observed at the smaller strain in comparison with that at the higher stress. It has been concluded that degradation at the long term region is caused by a start of tertiary creep at the early stage due to preferential recovery occurred at the vicinity of prior austenite grain boundary. Remarkable decrease in rupture elongation in the long term region is also caused by such heterogeneous recovery, since creep deformation is mainly dependent on a deformation at the vicinity of prior austenite grain boundary.

There are two possible factors which cause a preferential recovery at the vicinity of prior austenite grain boundary during long term creep deformation. First one is changes in precipitates, especially along prior austenite grain boundary. High creep strength of the 9Cr-1Mo-V-Nb steel is obtained by very fine and stable MX type carbonitride particles. Coarsening of grain boundary precipitate may affect the distribution of MX particles at the vicinity of grain boundary. At temperatures less than about 900K, decrease in Mo content in solid solution of ferrit matrix is also caused by a precipitation of Laves phase (Fe_2Mo). Since Mo is effective to increase in creep strength by solid solution strengthening, decrease in Mo content in ferrite matrix is possible to decrease in creep strength.

Second one is an internal stress of the steel itself. A certain extent of internal stress is introduced by martensitic transformation and that is distributed nonuniformly. An extent of internal stress at the vicinity of prior austenite grain boundary is thought to be higher than that of within grain. Stress is important factor to promote recovery of tempered martensitic microstructure. It seems that an effect of higher internal stress at prior austenite grain boundary on microstructural change may be pronounced in the long term region, since applied stress is lower than that in the short term region.

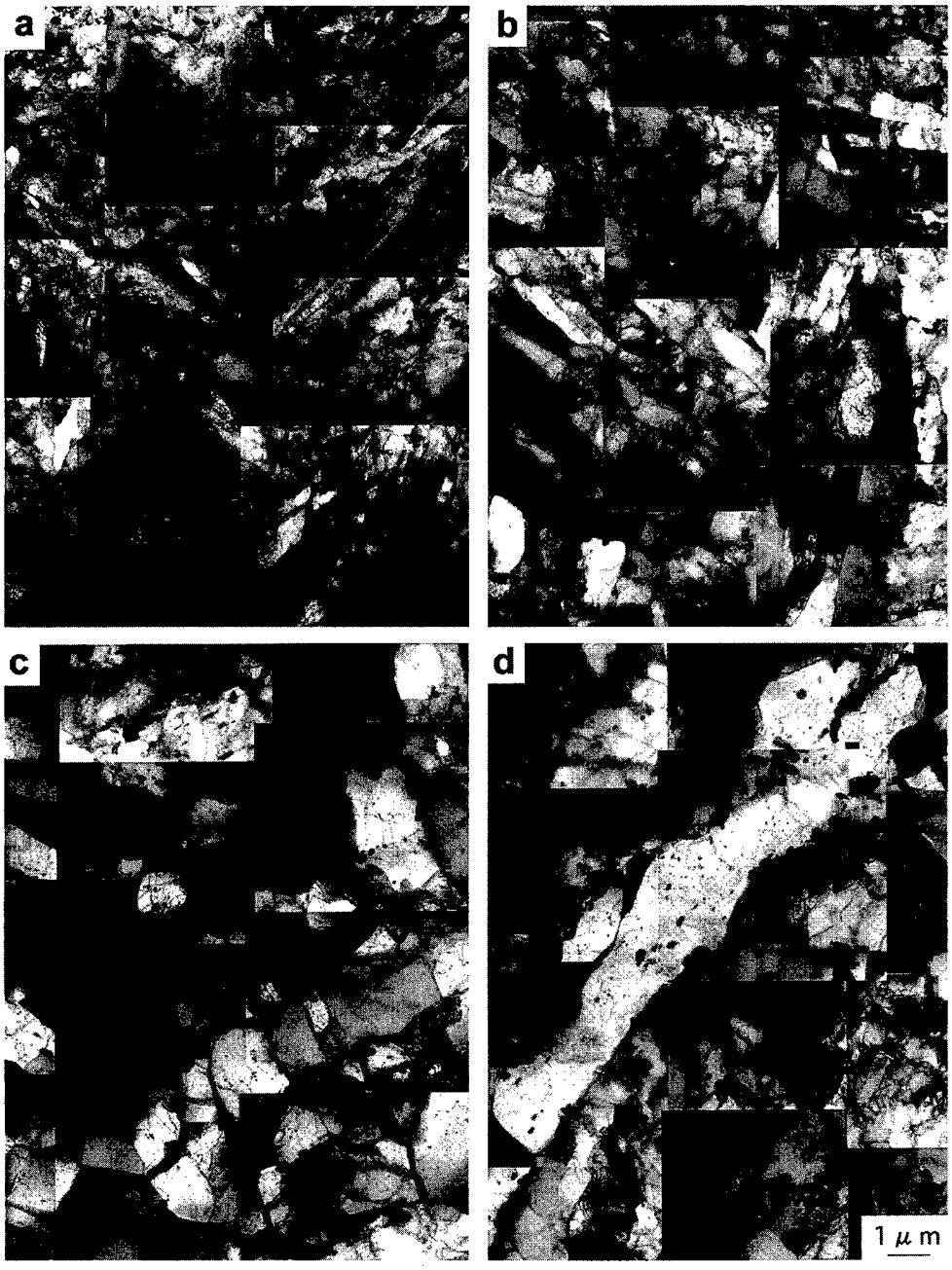

a) As received
b) 873K-160MPa, tr=971.2h
c) 873K-120MPa, tr=12,858.6h
d) 873K-100MPa, tr=34,141.0h

Figure 7. TEM micrographs of the as received steel and the steels ruptured at 873K-160, 120 and 100MPa.

To develop high strength ferritic creep resistant steel, it is important to retard a degradation in the long term region. Consequently, preferential recovery at the vicinity of prior austenite grain boundary should be suppressed and the mechanism of such remarkable recovery should be investigated more detail in the future.

CONCLUSIONS

Long term creep strength properties of the 9Cr-1Mo-V-Nb steel has been investigated in conjunction with both creep deformation and changes in microstructure and the following results have been obtained.

1) At the long term region more than about 10,000h, abrupt decreases in both creep rupture strength and rupture elongation were observed.
2) Under the lower stress condition in which creep rupture strength shows significant decrease, transient creep stage shift to tertiary one at the small strain of less than 0.01, in comparison with those of more than 0.02 at the higher stress condition.
3) Progress in recovery of the tempered martensitic microstructure during creep deformation is homogeneous at the short term region.
4) Under the lower stress condition, recovery of microstructure is significantly heterogeneous, since it proceeds preferentially at the vicinity of prior austenite grain boundary.
5) Degradation in the long term region is caused by a preferential recovery along prior austenite grain boundary which promotes the onset of tertiary creep.
6) It has been concluded that suppression of the preferential recovery at the vicinity of prior austenite grain boundar is important to retard a degradation and to maintain high creep strength during long term creep deformation.

REFERENCES

1. F.Abe, M.Igarashi, N.Fujitsuna, K.Kimura and S.Muneki : Proc. 6th Liege Conf., Materials for Advanced Power Engineering 1998, **1**(1998), p.259.
2. F.Masuyama : ibid. **3**(1998), p.1807.
3. K.Kimura, T.Matsuo, M.Kikuchi and R.Tanaka : Tetsu-to-Hagané (J. Iron Steel Inst. Japan), **72**(1986), p.474.
4. K.Hamada, K.Tokuno and T.Takeda : Nuclear Engineering and Design, **139**(1993), p.277.
5. A.Toyama and Y.Minami : Report of the 123rd Committee on Heat-Resisting Metals and Alloys, **34**(1993), p.23.
6. F.Masuyama and N.Nishimura : Strength of Materials, Edited by H.Oikawa, K.Maruyama, S.Takeuchi and M.Yamaguchi : The Japan Inst. Metals, Sendai, Japan, (1994), p.657.
7. K.Sawada, K.Maruyama, R.Komine and Y.Nagae : Tetsu-to-Hagané (J. Iron Steel Inst. Japan), **83**(1997), p.466.
8. K.Sawada, M.Takeda, K.Maruyama, R.Komine and Y.Nagae : Tetsu-to-Hagané (J. Iron Steel Inst. Japan), **84**(1998), p.580.
9. NRIM Creep Data Sheet, National Research Institute for Metals, Tsukuba, Japan, **43**(1996).
10. K.Maruyama, C.Harada and H.Oikawa : Trans. Iron Steel Inst. Japan, **26**(1986), p.212.

Key Engineering Materials Vols. 171-174 (2000) pp. 491-498
© 2000 Trans Tech Publications, Switzerland

Creep Characteristics of Precipitation Hardened Carbon Free Martensitic Alloys

S. Muneki, M. Igarashi and F. Abe

Frontier Research Center for Structural Materials, National Research Institute for Metals, 1-2-1, Sengen, Tsukuba, Ibaraki 305-0047, Japan

Keywords: Fe-Ni-Co Martensite, Homogeneous Deformation, USC Plant, Boilers, Long Term Stability

ABSTRACT

A new attempt has been demonstrated using carbon free Fe-Ni-Co martensitic alloys strengthened by Laves phase such as Fe_2W or Fe_2Mo to achieve homogeneous creep deformation at high temperatures under low stress levels. Creep behavior of the alloys is found to be completely different from that of the conventional high-Cr ferritic steels. The alloys exhibit gradual change in the creep rate with strain both in the transient and acceleration creep regions, and give a larger strain for the minimum creep rate. In these alloys the creep deformation takes place very homogeneously and no heterogeneous creep deformation is enhanced even at low stress levels. The minimum creep rates of the Fe-Ni-Co alloys at 700°C are found to be much lower than that of the conventional steel, which is due to fine dispersion strengthening useful even at 700°C in these alloys. It is thus concluded that the Fe-Ni-Co martensite strengthened by Laves phase is very useful to increase the creep resistance at elevated temperatures over 650°C.

Introduction

High Cr ferritic steels such as 9Cr-1MoVNb steel (ASME SA335 P91) have successfully been used for large diameter and thick section boiler components such as main steam pipe and header in super critical (SC) boilers in fossil-fired power plants [1]. Recent trend to utilization of clean energy leading to protection of global environment has been accelerating application of ultra super critical (USC) boilers, which are operated with higher efficiency in power generation than in conventional ones and thus release less amount of carbon dioxide etc.[2, 3]. The USC boiler requires heat resistant materials with improved creep rupture strength at elevated temperatures over 600℃, because of increase in operating temperature and pressure of the steam used. The expected goal of the USC boilers is, however, now considered to be 630℃ and 30MPa [3], which might be the applicable limit of the conventional ferritic steels regarding creep strength and steam-oxidation resistance.

The high-Cr ferritic steels for USC power plants are basically used after normalizing and tempering to obtain long-term creep rupture strength with enough toughness. A typical microstructure of the steels consists of lath-martensite matrix and $M_{23}C_6$ (M; Cr, Fe, Mo, W etc.) type carbide along prior austenite grain boundaries and lath boundaries, MX (M; V, Nb, etc. and X; C, N) type carbonitride inside lath-martensite grain. The addition of W to the steels enhances precipitation of intermetallic phases such as Laves and μ phases mainly along prior austenite grain boundaries and lath boundaries, and also inside grain during long-term exposure at high temperatures.

Creep deformation of the ferritic steels is controlled by recovery and softening process of the tempered martensite described above, which strongly depends on the constitution of the microstructure and its change with time [4, 5]. To achieve long term stability of the tempered martensite is considered to be the key to increase the creep resistance of the steels at elevated

temperatures over 600°C. It is also noted that at low stress levels the creep deformation of the tempered martensite proceeds heterogeneously around prior austenite grain boundaries, since excess dislocations inside grain are hard to rearrange via ordinary dislocation motion under such a low stress level and a new dislocation generation is required to enhance creep deformation elsewhere. Coarsening of grain boundary precipitates such as $M_{23}C_6$ carbide also enhances such a heterogeneous creep deformation, since non-coherent interfaces between precipitates and matrices are likely place of dislocation generation above.

In this paper, a new attempt has been demonstrated using carbon free martensitic alloys strengthened by intermetallic phase to achieve homogeneous creep deformation at high temperatures under low stress levels. We choose Fe-Ni-Co martensite as matrix and Laves phase type intermetallic compound such as Fe_2W or Fe_2Mo as precipitate and find that no heterogeneous creep deformation takes place in these alloys.

Experimental procedure

The chemical compositions of the Fe-Ni-Co alloys used in this study are given in Table 1. They were melted as 17.5kg-ingots in a vacuum induction furnace. The ingots were pressed to 40mm square billets, and then hot rolled to 16mm square bars after heating for 1h at 1200°C. They were solution treated for 30min at 1000°C. Some specimens were then aged for 10 to 6000h at temperatures between 500 and 800°C to examine the long-term stability of the microstructure of the alloys. A 9Cr ferritic steel denoted by the base steel in Table 1 was also prepared for comparison. It was normalized for 1 h at 1100°C and tempered for 4 h at 770°C. Creep rupture testing was conducted at the temperatures of 650 and 700°C using a 6mm diameter x 30mm gauge length tensile specimen as solution treated condition. Microstructures of the specimens solution treated and crept were observed by an optical microscope and a transmission electron microscope. Precipitates formed after long-term aging treatments were electrolytically extracted as residue using a 1% tetramethyl ammonium chloride-10% acethyl aceton-methanol solution. The extracted residue was then examined by X-ray diffraction and chemical analyses to identify the precipitates.

Table 1 Chemical composition of the alloys used (mass%).

	C	Si	Mn	Cr	Ni	Co	Mo	W	V
Base	**0.089**	**0.32**	**0.52**	**8.99**				**3.23**	**0.20**
5Mo	**0.0021**	**0.01**	**0.45**		**11.96**	**8.99**	**4.94**		
5W	**0.0015**	**0.01**	**0.45**		**11.63**	**8.62**		**4.90**	
10W	**0.0014**	**0.01**	**0.47**		**12.18**	**9.04**		**10.06**	

	Ti	Al	Nb	B	N	P	S	Fe
Base			**0.047**	**0.0043**	**0.068**	**0.002**	**0.001**	**Bal.**
5Mo	**0.18**	**0.085**		**0.0048**	**0.0011**	**0.001**	**0.001**	**Bal.**
5W	**0.2**	**0.087**		**0.0049**	**0.0014**	**<0.001**	**0.001**	**Bal.**
10W	**0.2**	**0.088**		**0.0050**	**0.0015**	**<0.001**	**0.001**	**Bal.**

RESULTS AND DISCUSSION

Fig.1 shows optical micrographs of Fe-Ni-Co alloys with 5%Mo, 5%W and 10%W after solution treatment for 30min at 1000°C. It is seen that in all the alloys martensitic single phase matrix with neither δ-ferrite nor retained austenite phase has been observed. It is also confirmed that there is no evidence of unexpected precipitation such as Laves phase during the solution treatment. Prior austenite grain size of each alloy measured is about 50μm.

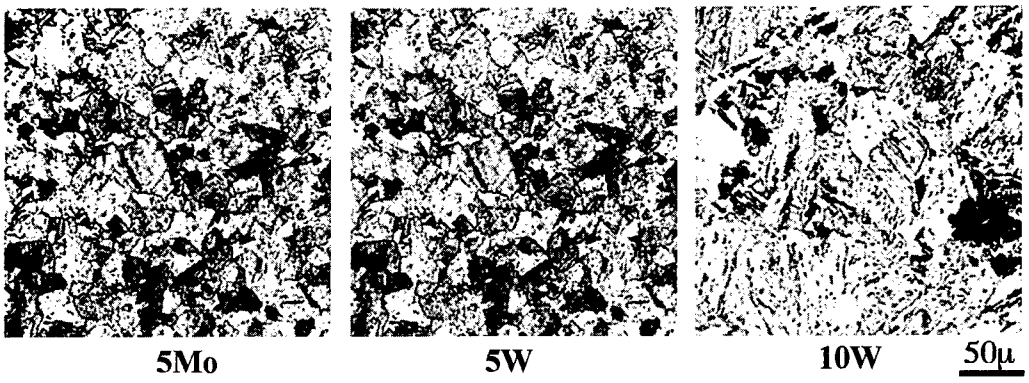

Fig.1 Optical micrographs of Fe-12Ni-9Co alloys with 5%Mo, 5%W and 10%W after solution treatment for 30min at 1000℃.

Fig.2 shows the effect of Mo and W addition on the transformation temperatures of A_{c1}, A_2 and M_s measured by a differential scanning calorimetry (DSC) on heating and cooling with the rates of 10 K/min. It is found that both A_{c1} and A_2 temperatures are not much affected by the kinds and amounts of alloying elements, while the M_s temperature of the alloy with 5%W is about 100°C higher than those of the other alloys. It is considered that the A_{c1} and A_2 temperatures are governed mainly by Co and Ni, and the M_s temperature is by Mo and W which are large in atomic size compared with Fe, Co and Ni.

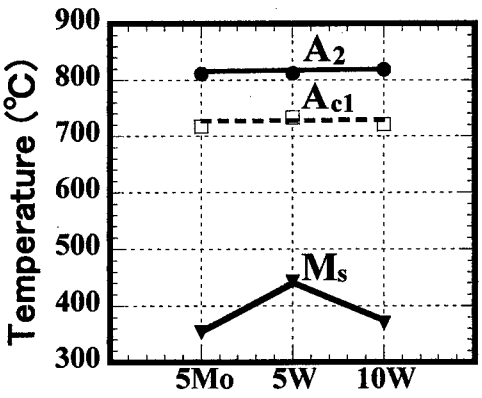

Fig.2 Effect of Mo and W addition on the transformation temperatures of A_2, A_{c1} and M_s.

Fig. 3 shows age-hardening behavior of the alloys with (a) 5% Mo and (b) 10% W on aging at 500 to 800°C for up to 6000h. Initial hardness of both alloys is in a same level of about HV330, which may be due to the similar microstructure and transformation characteristics of these two alloys as shown in Figs. 1 and 2. It is seen that the alloy with 5% Mo is markedly hardened by aging at 500 to 600°C for 1 to 10 h, although the hardness values decrease very rapidly with increasing aging time. This alloy still exhibits a slight increase in hardness by aging at higher temperatures up to 750°C for 1 to 10 h, but a decrease to about HV270 by the longer-term aging. The alloy with 10% W is found to be remarkably hardened by aging at all the temperatures between 500 and 800°C for 1 to 10 h. This alloy is hardened much more than the alloy with 5% Mo even at higher aging temperatures and keeps high hardness value of about HV300 after aging for 6000 h at 650°C. The alloy with 5% W exhibits the similar hardening behavior as observed in the alloy with 10% W, although the initial and maximum values in hardness are much lowered, which may be due to the smaller amount of precipitation.

Fig.4 shows creep curves of the alloys with 5% Mo, 5% W and 10% W crept at 650°C with the applied stresses of 200 and 120MPa. It is seen that the alloy with 10% W exhibits longest creep life among the alloys at 200 MPa, while the alloy with 5% Mo does at 120 MPa. Fig. 5 shows the creep rate vs. time curves of the alloys with 5% Mo and 10% W comparing with the base steel. It is seen that the creep curves of all the specimens consist of a transient creep region and a

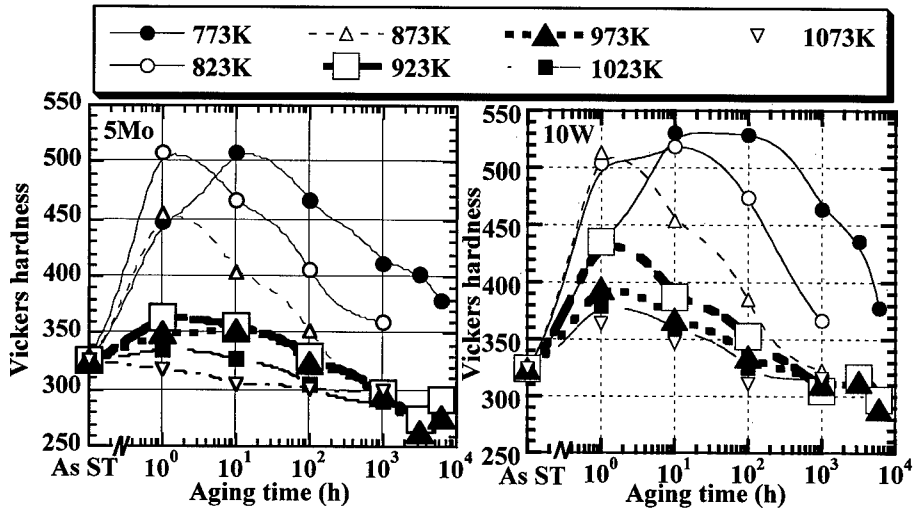

Fig.3 Age-hardening behavior of the alloys with 5%Mo and 10%W on aging at 500 to 800℃ for up to 6000h.

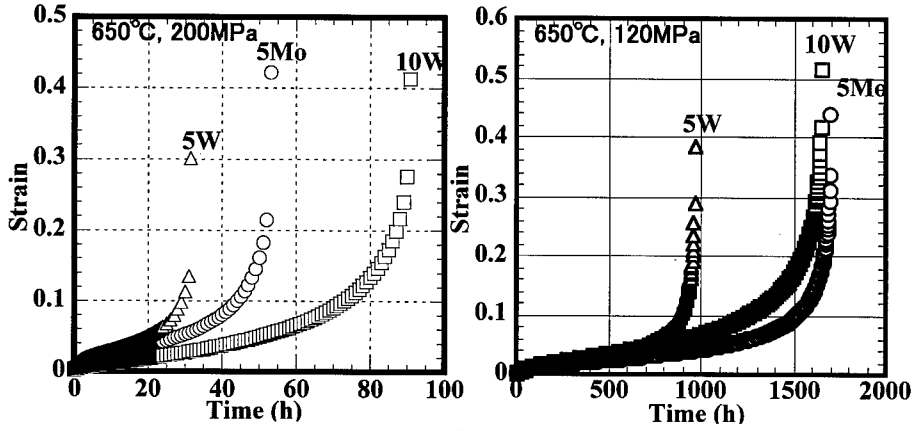

Fig.4 Creep curves of the alloys with 5%Mo, 5%W and 10%W crept at 650℃ with the applied stresses of 200 and 120MPa.

subsequent acceleration creep region, which have been observed in the conventional high Cr ferritic steels [6]. Creep rates of all the specimens decrease gradually in the transient creep region and reached at minimum creep rates, and then turn out to increase with time in the acceleration creep region. It is, however, noted that the creep behavior of the present Fe-Ni-Co alloys strengthened by Laves type phase is completely different from that of the base steel. In the transient creep region, for instance, the creep rate of the alloy with 10% W decreases with time and then tends to stay for a while, before it decreases again until reaching the minimum creep rate. The resultant minimum creep rate of the alloy crept at 120 MPa is much higher than that obtained for the base steel, but the total creep lives of these specimens are in a same level. This is because, in the acceleration creep region, the creep rate of the alloy with 10% W increases with time more slowly

compared with that of the base steel does.

Fig. 6 shows the creep rate vs. strain curves of the same specimens shown in Fig. 5. This type of the figure is very useful to understand the creep deformation mechanism involved. It is seen that the base steel exhibits steeper decrease of the creep rate with strain in the transient creep region and steeper increase of it in the acceleration creep region, giving the smaller strain for the minimum creep rate at which the acceleration creep starts. On the other hand, the Fe-Ni-Co alloys with 5% Mo and 10% W exhibit gradual change in the creep rate with strain both in the transient and acceleration creep regions, and give a larger strain for the minimum creep rate. This suggests that in the Fe-Ni-Co alloys the creep deformation takes place very homogeneously both in the transient and acceleration creep regions and no heterogeneous creep deformation is enhanced even at such a low stress level.

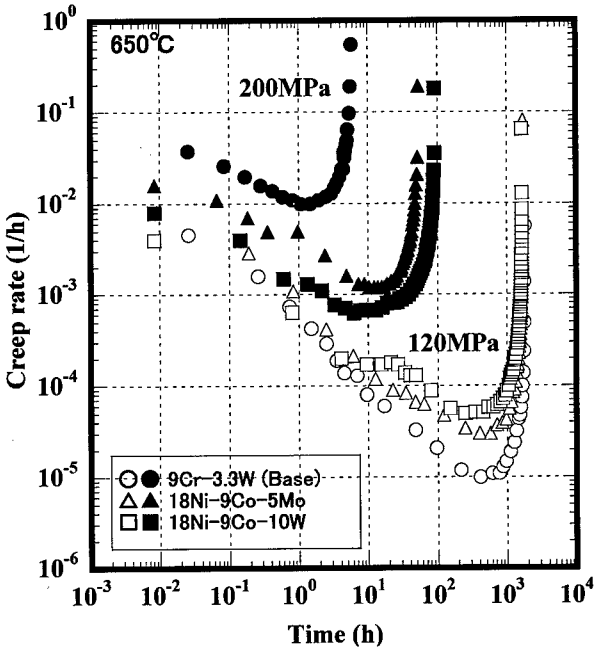

Fig.5 Creep rate vs. time curves of the alloys with 5%Mo and 10%W comparing with the base steel.

Fig. 7 shows extraction replicas taken from the alloys with 5% Mo and 10% W aged for 10 to 1000 h at 650°C. The precipitates identified are Fe_2Mo in the alloy with 5% Mo and Fe_2W in the alloy with 10% W by X-ray diffraction analysis of the extracted residue and by a quantitative EDX spectroscopy in FE-TEM for all the aging conditions. It is seen that fine precipitate of about 10 nm in size inside grain is dominant in both alloys at the early stage of aging. The size of the precipitates in the alloy with 10% W is smaller than that in the alloy with 5% Mo in all the aging conditions. The precipitates along prior austenitic grain boundaries and also block boundaries are coarsened rapidly in the alloy with 5% Mo, while the precipitates inside grain stay fairly small even after aging for 1000 h.

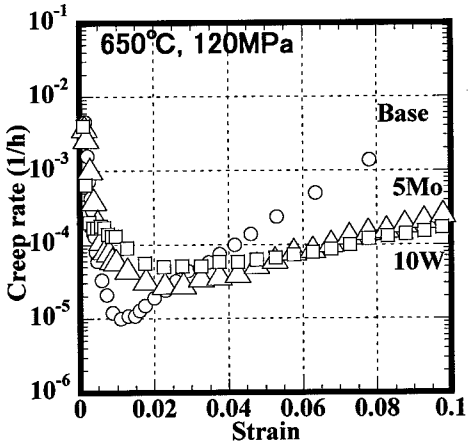

Fig.6 Creep rate vs. strain curves of the base steel and the alloys crept at 650℃ and 120MPa.

Fig. 8 shows amount of the extracted residue taken from the alloy with 10% W aged in the same conditions. The elements identified are W, Fe, Co and Ni, which are all the constituent element for Laves phase. The amount of these elements increases with increasing aging time. Assuming that both Co and Ni substitute for Fe, the composition of the precipitates is determined as $(Fe+Co+Ni)_{0.63\text{-}0.65}$, which is in a good agreement with the composition of the Laves phase, $Fe_{0.67}W_{0.33}$ or $(Fe+Co+Ni)_{0.67}W_{0.33}$.

Fig. 9 shows the temperature dependence of the minimum creep rate of the specimens crept at

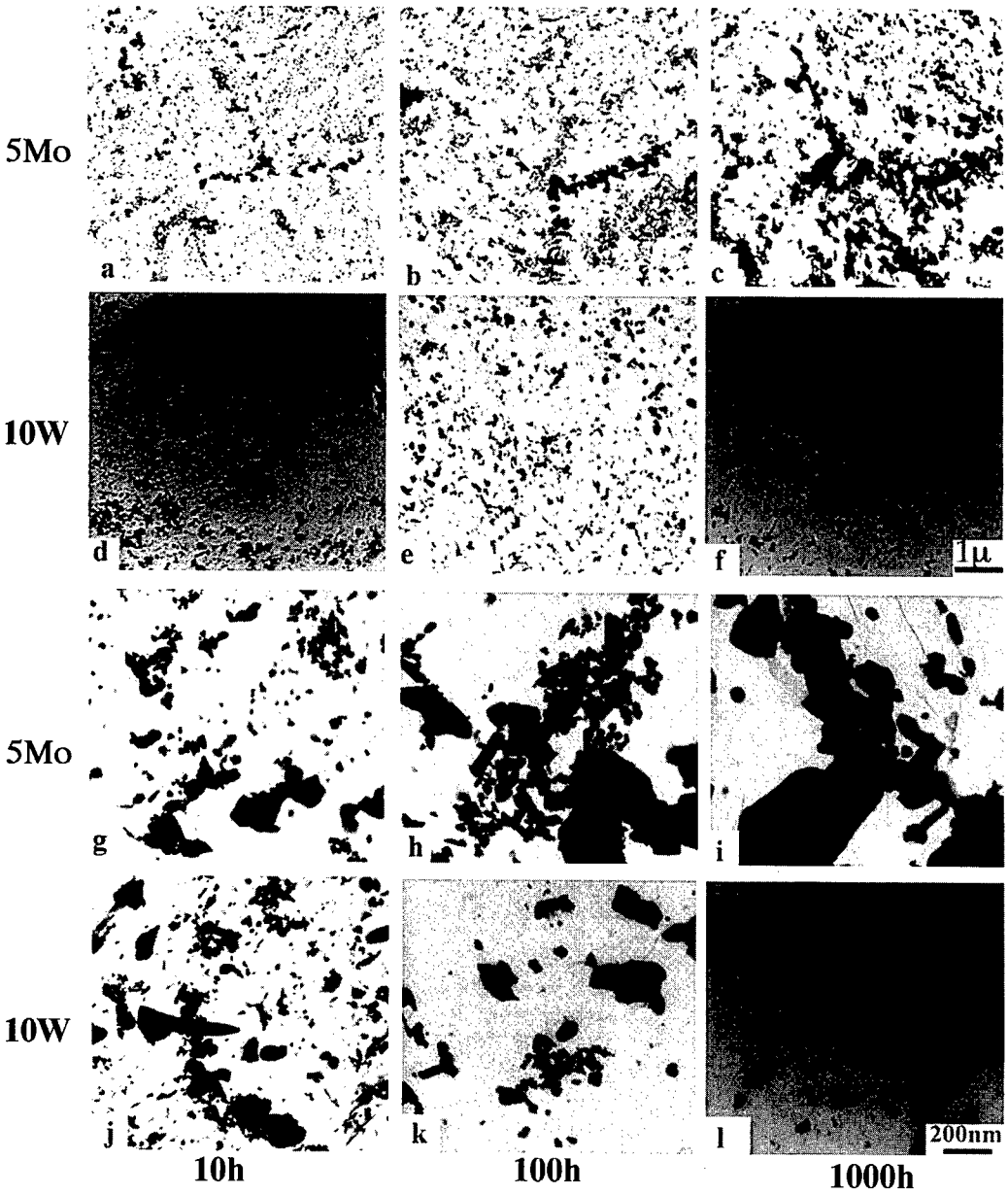

Fig.7 Extraction replicas of the alloys with 5%Mo (a, b, c, g, h and I) and 10%W (d, e, f, j, k and l) aged for 10 to 1000h at 650℃. (g) to (l) are higher magnification of (a) to (f).

650 and 700°C with the applied stress of 120 MPa. The minimum creep rates of the Fe-Ni-Co alloys at 700°C are much lower than that of the base steel, while they are quite higher at 650°C. This means that the creep resistance of the base steel decreases very much at higher temperatures, but those of the Fe-Ni-Co alloys do not.

Fig. 10 shows the amount of the extracted residue taken from the specimens aged at 700°C for 1000 h comparing with the result obtained for 650°C. It is seen that the amount of the

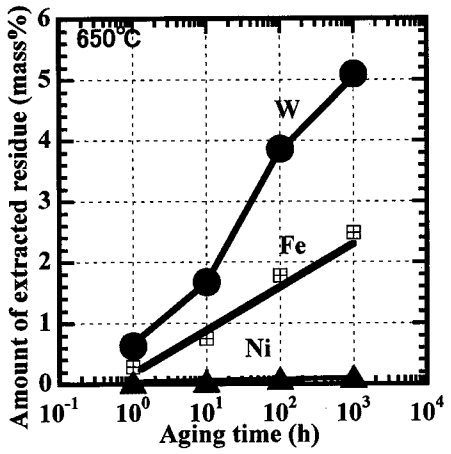

Fig.8 Amount of the extracted residue with aging time of the alloy with 10%W.

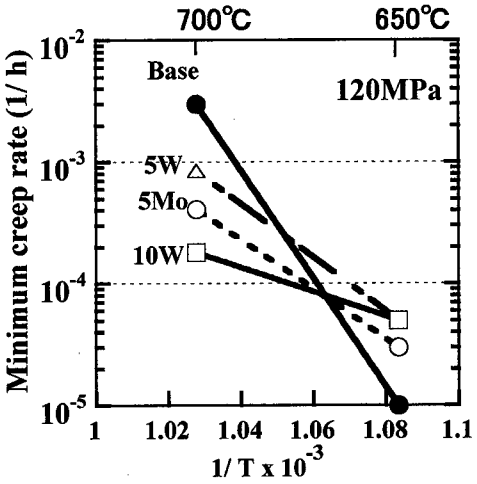

Fig.9 Effect of temperature on the minimum creep rate of the alloys and the base steel.

precipitates of the alloys aged at 700°C is in a same level as observed in the specimens aged at 650°C. This means that the fine dispersion strengthening is useful even at 700°C in these alloys.

It is thus concluded that the Fe-Ni-Co martensite strengthened by Laves phase is very useful to increase the creep resistance at elevated temperatures over 650°C. This is achieved by the homogeneous creep deformation in the Fe-Ni-Co martensite and by the stability of fine dispersed particles at high temperatures. The results obtained in this study involve some important guiding principles to increase the creep resistance of the ferritic steels. Further investigations are necessary to enhance the homogeneous creep deformation in the ferritic steels and to increase the creep resistance of the Fe-Ni-Co alloys at lower temperatures.

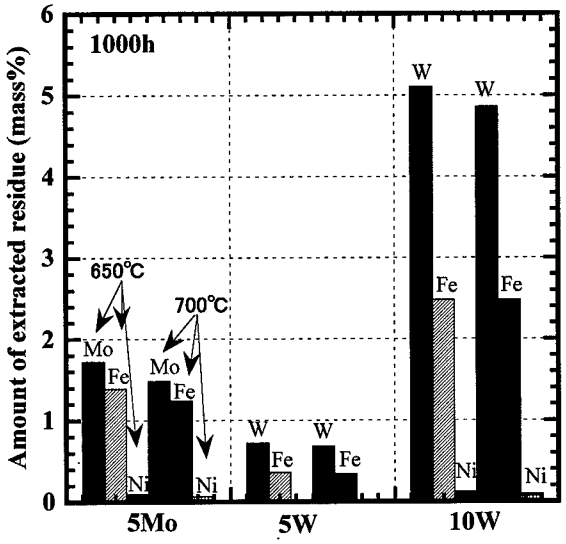

Fig.10 Chemical analysis of the extracted residue taken from the alloys aged for 1000h.

Conclusion

A new attempt has been demonstrated using carbon free Fe-Ni-Co martensitic alloys strengthened by Laves phase such as Fe_2W or Fe_2Mo to achieve homogeneous creep deformation at high temperatures under low stress levels. It is found that the creep behavior of the Fe-Ni-Co alloys is completely different from that of the conventional high-Cr ferritic steels. The Fe-Ni-Co

alloys exhibit gradual change in the creep rate with strain both in the transient and acceleration creep regions, and give a larger strain for the minimum creep rate. This suggests that in the Fe-Ni-Co alloys the creep deformation takes place very homogeneously and no heterogeneous creep deformation is enhanced even at low stress levels. The minimum creep rates of the Fe-Ni-Co alloys at 700°C are much lower than that of the conventional steel. This means that the fine dispersion strengthening is useful even at 700°C in these alloys. It is thus concluded that the Fe-Ni-Co martensite strengthened by Laves phase is very useful to increase the creep resistance at elevated temperatures over 650°C. This is achieved by the homogeneous creep deformation in the Fe-Ni-Co martensite and by the stability of fine dispersed particles at high temperatures.

References

[1] V.K.Sikka, C.T.Ward and K.C.Phomas, in ASM Int. Conf. Production, Fabrication, Properties and Application of Ferritic Steels for High Temperature Applications, Warren, PA. Oct.6-8 (1981).
[2] F.Masuyama, I. Ishihara, T. Yokoyama and M.Fujita, The Thermal and Nuclear Power, **46**, 498 (1995).
[3] K.Muramatsu, in Proc. Advanced Heat Resistant Steels For Power Generation, 27-29 April, Miramar Palace, San Sebastian, Spain, (1998).
[4] F.Abe, M.Igarashi, N.Fujitsuna, K.Kimura and S.Muneki, in Proc. 6th Liege Conf. On Materials for Advanced Power Engineering, 5-7 October, 1998, Liege, Belgium, **I**. 259-268.
[5] M. Igarashi, S. Muneki and F. Abe: ibid., **I**. 637-646.

email : muneki@nrim.go.jp

Key Engineering Materials Vols. 171-174 (2000) pp. 499-504
© 2000 Trans Tech Publications, Switzerland

Creep Strengthening Mechanism of Mo and W in 9% Cr Heat Resistant Steels

T. Muraki[1], Y. Hasegawa[1] and M. Ohgami[2]

[1] Nippon Steel Corporation Technical Development Bureau, 20-1 Shintomi, Futtsu-shi, Chiba, 293-8511, Japan

[2] Nippon Steel Corporation Technical Development Bureau, 3434 Shimada, Hikari-shi, Yamaguchi, 743-8510, Japan

Keywords: Heat Resistant Steel, Ferritic Steel, Molybdenum, Tungsten, Creep Strain, Lath Structure, Solid Solution Strengthening, Precipitation Strengthening

Abstract

In this paper, precise investigation on the 9 mass% chromium ferritic steels with up to 2 mass% molybdenum or 4 mass% tungsten extracts the contribution of molybdenum and tungsten to the strengthening mechanism. The creep rupture strengths of molybdenum containing steels increase with molybdenum content because of the molybdenum in solid solution and stabilized $M_{23}C_6$ by molybdenum. The extended transient creep stage implies the effective precipitation strengthening effect of the stabilized $M_{23}C_6$. Also, estimated creep rupture strength increases with tungsten content increases up to 2 mass%. But in case of tungsten containing steels, precipitation of Laves phase possibly contributes the lath structure stabilization. The resolution temperature difference between Fe_2W type Laves phase and Fe_2Mo type Laves phase explains the difference of precipitation strengthening effects for molybdenum and tungsten containing steels.

1. Introduction

Molybdenum and tungsten in chromium ferritic heat resistant steels improve the creep rupture strength at high temperature. However no established concept describes the mechanism of creep rupture strengthening increase owing to molybdenum and tungsten. High solid solution strengthening effect of molybdenum and tungsten is caused by both the small values of diffusion coefficients and the large misfit of atomic radius between the resolved atoms and that of base matrix. Stabilization of $M_{23}C_6$ by resolved molybdenum or tungsten in the carbide is also one of the explanations for the high creep resistance. Furthermore, Laves phase precipitation strengthening effect at the lath boundary is one of the lately introduced mechanisms for high creep rupture strengths of the steels[1].

In this paper, precise experiments and discussions on the 9 mass% chromium ferritic steels with up to 2 mass% molybdenum or 4 mass% tungsten and without niobium, vanadium and nitrogen tries to elucidate the contribution of molybdenum and tungsten from the both point of views, the precipitation strengthening by $M_{23}C_6$ or Laves phase and the solid solution strengthening effect.

2. Experimental methods

2.1 Test specimens

Test specimens studied in this work were melted in a high frequency induction furnace under a vacuum atmosphere, and cast into 20 kg ingot moulds. Hot-rolling from 1200 ℃ for 2 hours holding in

an electric resistance furnace produced 15 mm thick plate specimens. Heat treatment, normalizing at 1070 °C for 60 minutes followed by quenching in air and tempering at 780 °C for 60 minutes followed by air cooling achieved the tempered full martensitic microstructure. Selected chemical compositions of the steels after heat treatment is listed in table 1. Steel A, B and C contain molybdenum aiming at the extraction of molybdenum effect on the creep rupture strength. Steel D, E and F contain only tungsten. These 6 steels will distinguish the strengthening mechanism of 9% chromium steel with molybdenum and tungsten eliminating the MX type carbo-nitride precipitation effect.

Table 1 Chemical compositions of the steels (mass%)

Steel	C	Si	Mn	Cr	Mo	W	N
A	0.101	0.10	0.49	8.97	0.01	-----	0.0008
B	0.097	0.10	0.49	8.93	0.98	-----	0.0007
C	0.093	0.10	0.49	8.89	2.02	-----	0.0008
D	0.098	0.09	0.49	8.90	-----	1.00	0.0008
E	0.081	0.08	0.48	8.91	-----	1.95	0.0007
F	0.050	0.07	0.46	8.95	-----	3.95	0.0008

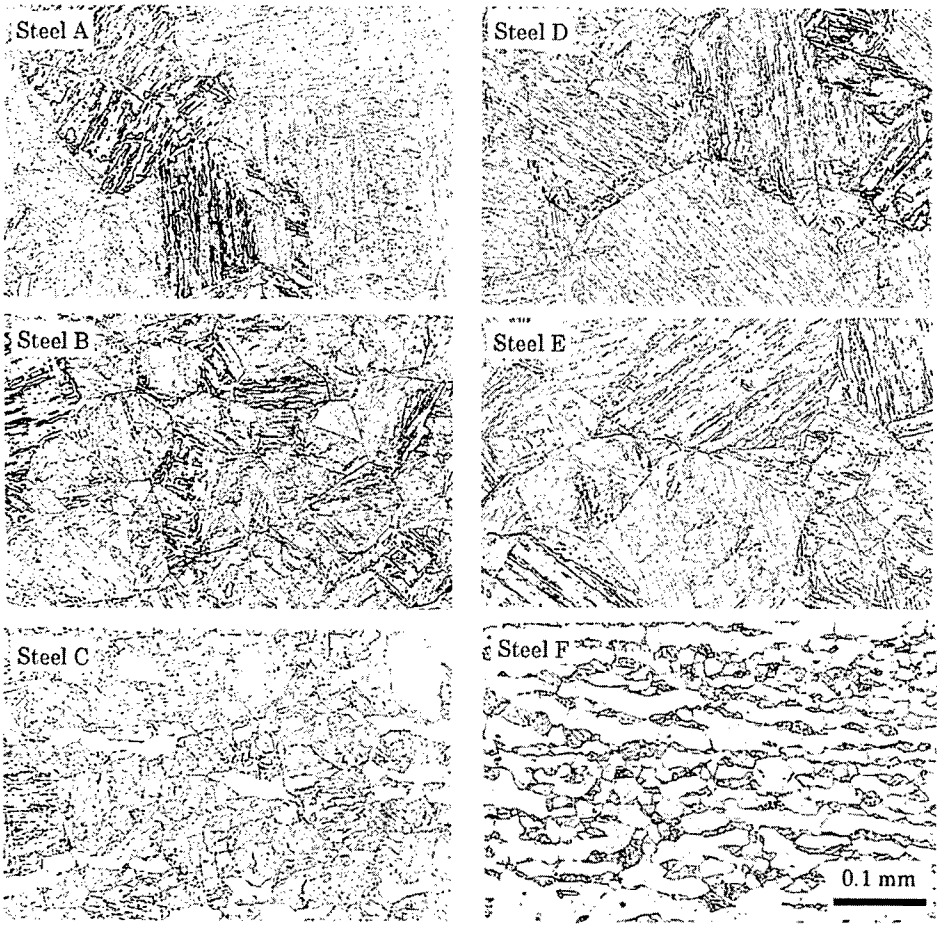

Figure 1 Optical microstructures of test steels after heat treatment.

2.2 Experimental Procedures

Round-bar specimens, 6 mm in parallel-part diameter and 30 mm in gauge length, investigated the creep rupture strength and the strain at 600 °, 650 ° and 700 °C and at constant load from 20 to 150 MPa.

Another type of round-bar specimen, 6 mm in parallel-part diameter and 32 mm in gauge length, investigated the strength from room temperature up to 750 °C.

Optical microscope confirmed the phase structures. TEM observation of extracted replica identified the precipitates in the specimens before aging and aged at from 600 ° to 700 °C for 1000 hours.

3. Results and Discussions

3.1 Microstructure

Figure 1 shows the microstructure of test steel after heat treatment. The specimens microstructures of steel A and B of molybdenum containing steel were tempered full martensite, but that of the steel C was dual phase consists of tempered martensite and delta ferrite. Similarly, the microstructures of steel D and E of tungsten containing steel were tempered full martensite, but that of the steel F was almost delta ferrite. The difference of the microstructure among the test specimens affected the creep rupture strengths of the steels not a little.

3.2 Mechanical properties

Figure 2 and 3 show the tensile properties from room temperature to high temperature for molybdenum and tungsten containing specimens. In case of molybdenum containing steels, tensile properties increase as a function of molybdenum for all test temperature. In the case of tungsten containing steels, tensile properties increase also as a function of tungsten except steel F. The high delta ferrite area ratio decreased the tensile properties of steel F for all temperature.

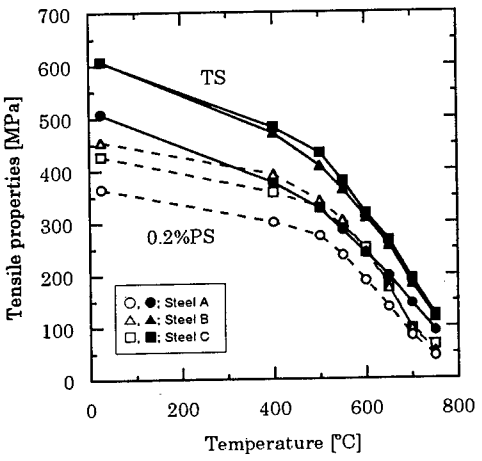

Figure 2 Tensile properties for steel A, B and C.

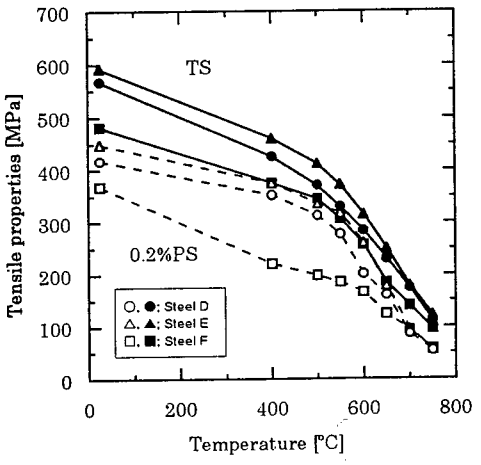

Figure 3 Tensile properties for steel D, E and F.

Figure 4 and 5 show the applied creep stress - rupture time curves for molybdenum and tungsten containing steels. Molybdenum and tungsten increase the creep rupture strength for all temperatures. The creep rupture strengths of the molybdenum containing steels, A, B and C, increase with the function of molybdenum contents of the steels except at 650° and 700 °C for steel C. If the molybdenum content exceeds 1 mass%, the creep rupture strength increase looks to be in saturation.

Tungsten in the steels increases the creep rupture strengths for relative long time creep exposure obviously. The creep rupture strength increase at 600 °C looks to be in saturation.

Tungsten amount in solid solution is supersaturated when the creep exposure time is short. Therefore, the resolved tungsten in early creep exposure is almost the same amount as in starting material. As a result of the mixed influences, the positive effect by much tungsten addition and the negative effect by high delta-ferrite area ratio of the steel F, the same chromium contents of three steels also do not differentiate the $M_{23}C_6$ type carbides precipitation behavior. Consequently, only small creep rupture strength differences are derived from the supersaturated tungsten in the steels. On the other hand, large difference of rupture life among three steels can only be explained by the microstructural changes during the creep exposure, Laves phase precipitation is the sole clear microstructural change in tungsten containing steels.

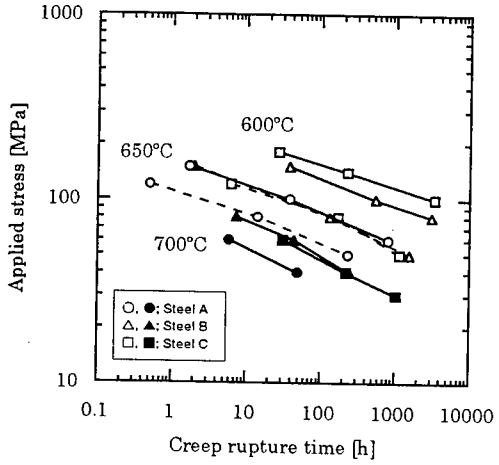

Figure 4 Creep rupture curves for steel A, B and C.

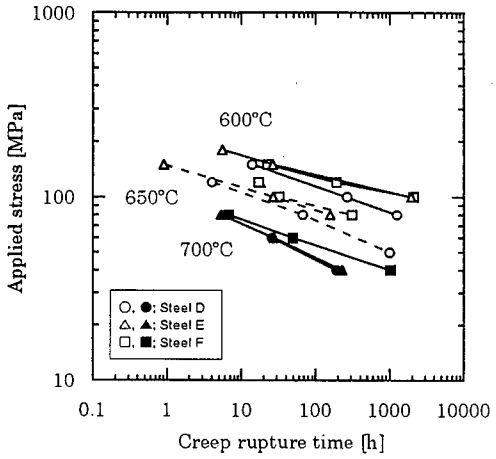

Figure 5 Creep rupture curves for steel D, E and F.

The supersaturated tungsten amount also decreases during the creep, but the effect is negligible from the reason above mentioned. Therefore, in case of tungsten containing steels, Laves phase precipitation at the lath boundary extend the rupture life, and this fact implies evident stabilization of the lath structure. Low area ratio of tempered martensitic structure in the steel F restricted the Laves phase precipitation at the lath boundary, and it decreased the effect of 4 mass% tungsten addition.

Figure 6 shows the creep rupture time - strain curves at 600 °C for molybdenum containing steels. The applied stress is 100 MPa for all the curves. The minimum creep rate decreases as a function of molybdenum.

The increase of molybdenum content extends the transient creep stage, and decreases the

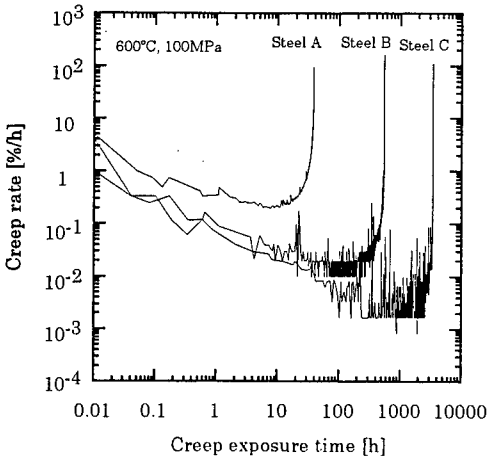

Figure 6 Relationship between creep exposure time and creep rate at 600 °C under 100MPa.

minimum creep rate at the same time. This experimental result implies the increase of the creep resistance, the increase of the precipitation strengthening factor. Laves phase precipitation strengthening in molybdenum containing steels can not be expected as tungsten containing steels indicated[2]. Therefore, molybdenum affected the sole precipitation strengthening factor, $M_{23}C_6$ type carbide precipitation. Molybdenum can be one of the constituents of M in $M_{23}C_6$, therefore molybdenum possibly restricted the coarsening of $M_{23}C_6$ at lath boundary. But the detail of the mechanism must be discussed and clarified experimentally in a further work.

Figure 7 shows the normalized creep strain - creep rate curves at 600 ℃ for molybdenum containing steels. This figure confirms the extension of the transient creep stage by molybdenum.

Figure 8 is the creep rate - normalized creep strain curves for tungsten containing steels at 600 ℃. The applied stress is 100 MPa. Increase of tungsten content extends the transient creep stage. The observed precipitation strengthening is possibly caused by the fine Laves phase.

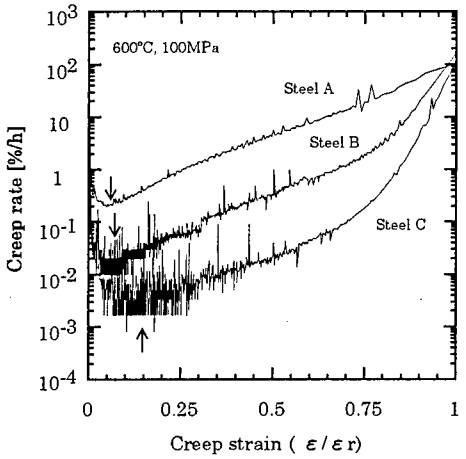

Figure 7 Relationship between creep strain and creep rate for steel A, B and C.

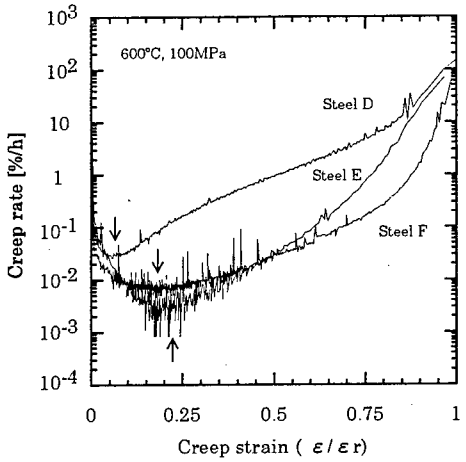

Figure 8 Relationship between creep strain and creep rate for steel D, E and F.

Generally, the creep rupture strength of tungsten containing steels is higher than that of molybdenum containing steels. The comparison of the creep properties of steel B and E whose microstructures are tempered full martensite confirmed the higher creep rupture strength of steel E than that of steel B. Steel B and E contain same amount of molybdenum or tungsten in percent of atomic. Judging from the experimental results in this report, this difference of creep rupture strength is not derived from the difference of the solid solution strengthening effects of supersaturated molybdenum or tungsten, but derived from the different precipitation effects. Molybdenum stabilizes the $M_{23}C_6$ type carbide by molybdenum resolution into $M_{23}C_6$. Tungsten increases the precipitation density through the Laves phase precipitation with $M_{23}C_6$, compared with in case of molybdenum containing steel. Both precipitates stabilize the lath structure by pinning of the lath boundary.

Quantitative comparison of precipitation strengthening effect between molybdenum and tungsten containing steels through the TEM observation of thin foil gives the empirical confirmation to the hypothesis.

4. Conclusions

1) The creep rupture strengths of the molybdenum containing steels increase as a function of

molybdenum content. The increase of molybdenum content extends the transient creep stage and decreases the minimum creep rate. This phenomenon implies the increase of the precipitation strengthening factor. Therefore molybdenum supposedly stabilizes the $M_{23}C_6$ and restricts the coarsening.

2) Tungsten increases the creep rupture strengths of the steels for long time creep exposure. Large difference of rupture life can be assumed by the microstructural changes during the creep exposure, therefore Fe_2W type Laves phase precipitation at the lath boundary. At the same time, we also resolves into $M_{23}C_6$ and stabilizes. Both precipitates stabilize the lath structure together, and resulted in the higher creep rupture strength of tungsten containing steel compared with that of molybdenum steel.

References

[1] R. Ishii, Y. Tsuda and M. Yamada, CAMP-ISIJ, 8 (1995), p.673.
[2] M. Igarashi, Y. Sawaragi, F. Masuyama, CAMP-ISIJ, 7(1994), p.1724

Corresponding author
Taro Muraki
e-mail : t-muraki@lab.re.nsc.co.jp
Fax : 0439-80-2744

Key Engineering Materials Vols. 171-174 (2000) pp. 505-512
© 2000 Trans Tech Publications, Switzerland

Creep Properties of Advanced Heat-Resistant Martensitic Steels Strengthened by $L1_0$ Type Ordered Intermetallic Phase

M. Igarashi, S. Muneki and F. Abe

Frontier Research Center for Structural Materials, National Research Institute for Metals, 1-2-1 Sengen, Tsukuba, Ibaraki 305-0047, Japan

Keywords: FePd, Intermetallic, Dispersion Strengthening, Coherent Precipitation, Lattice Misfit

Abstract

Creep properties of advanced heat-resistant martensitic steels with the compositions of 0.08C-0.3Si-0.5Mn-9Cr-3.3W-(0/3)Pd-0.2V-0.05Nb-0.05N-Fe (in mass%) have been studied to explore the fundamental guiding principles for the development of new steels with improved creep strength at higher temperatures over 650°C. The steel with 3%Pd exhibits higher creep strength than that of the base steel, in particular, at higher temperatures. The microstructure of the steel with Pd is characterized by fine precipitation of a FePd based $L1_0$ type ordered phase, α'' phase. The α'' phase forms in the tempered martensitic matrix, α, along with the existing phases such as MX (M; V, Nb, X; C, N) carbonitride and $M_{23}C_6$ (M; Cr, Fe, W) carbide after normalizing at 1100°C and tempering at 770°C. A detailed TEM observation has shown that the α'' phase precipitates in a plate-shaped with the habit plane parallel to $\{001\}_\alpha$ and with a crystallographic orientation relationship with the matrix, $\{001\}_\alpha // \{001\}_{\alpha''}$ and $<100>_\alpha // <110>_{\alpha''}$. The α'' phase is found to be a most effective precipitate to increase creep resistance of the steel in terms of the inter-particle spacing estimated. The α'' phase is stable even after aging at 700°C and hence is more useful at higher temperatures. It is thus concluded that the creep resistance of the ferritic steels can be increased further by optimizing the combination of fine precipitation such as the α'' phase and MX carbonitride.

Introduction

The heat-resistant ferritic steels developed for USC power plants are basically used after normalizing and tempering to obtain long-term creep rupture strength with enough toughness [1]. A typical microstructure of the steels consists of lath-martensite matrix and $M_{23}C_6$ (M; Cr, Fe, Mo, W etc.) type carbides along prior austenite grain boundaries and lath boundaries, MX (M; V, Nb, etc. and X; C, N) type carbonitrides inside lath-martensite grain [2]. The addition of W to the steels enhances precipitation of intermetallic phases such as Laves and μ phases mainly along prior austenite grain boundaries and lath boundaries, and also inside grain during long-term exposure at high temperatures [2].

Creep deformation of the ferritic steels at elevated temperatures over 600°C is controlled by recovery and softening process of the tempered martensite described above, which strongly depends on the constitution of the microstructure and its change with time [3]. Recently, the addition of Pd to the steels is found to increase long-term creep resistance at elevated temperatures, in particular, over 650°C [4]. This is considered due to fine precipitation of FePd-based $L1_0$ type ordered phase (α'') in martensitic matrix, which is stable even at 700°C.

This paper describes first the effect of Pd on the microstructure and creep properties of the steels. Using a detailed TEM observation the homogeneous precipitation of the α'' phase is confirmed in the specimens after tempering and also after long-term ageing at high temperatures. Fine

dispersion of the α″ phase is found to enhance the creep resistance of the steels, in particular, in the transient creep region. We then discuss about which precipitate is most effective to strengthening of the steel according to evaluation of the dispersion strengthening parameters and find that the α″ phase is most effective.

Experimental

Model steels with a base composition of 0.08C-0.3Si-0.5Mn-9Cr-3.3W-0.2V-0.05Nb-0.05N-Fe (in mass%) and with 1-3% Pd were vacuum induction melted and processed to 15 mm square bars by hot-forging and hot-rolling. They were normalized for 0.5 h at 1100°C followed by air cooling, and tempered for 4 h at 770°C for creep testing. Some of the specimens were aged for 1000 h at 600, 650 and 700°C to examine the long-term stability of the α″ phase. The microstructure of the steels was examined using an optical microscopy and a field emission transmission electron microscopy (FE-TEM; Hitachi HF-2000) operated at 200kV. The creep testing was performed at 650°C and 700°C with stresses of 100, 120, 140 and 200 MPa.

Results and discussion

Fig.1 shows optical micrographs of the steels with the base composition and with 1-3% Pd after normalization at 1100°C. It is seen that in the base steel δ-ferrite remains in a banded appearance along the rolling direction in between martensitic phase matrix. In the steels with 1-3% Pd, however, fine lath-martensitic single phase matrix with no δ-ferrite has been observed. This is confirmed by a differential scanning calorimetric (DSC) measurement of the specimens on cooling after normalization, which gives no indication of the exothermic reaction corresponding to the magnetic transition at the Curie temperature of the δ–ferrite. Pd is thus considered to be one of the effective austenite-forming elements such as Co, Ni and Cu.

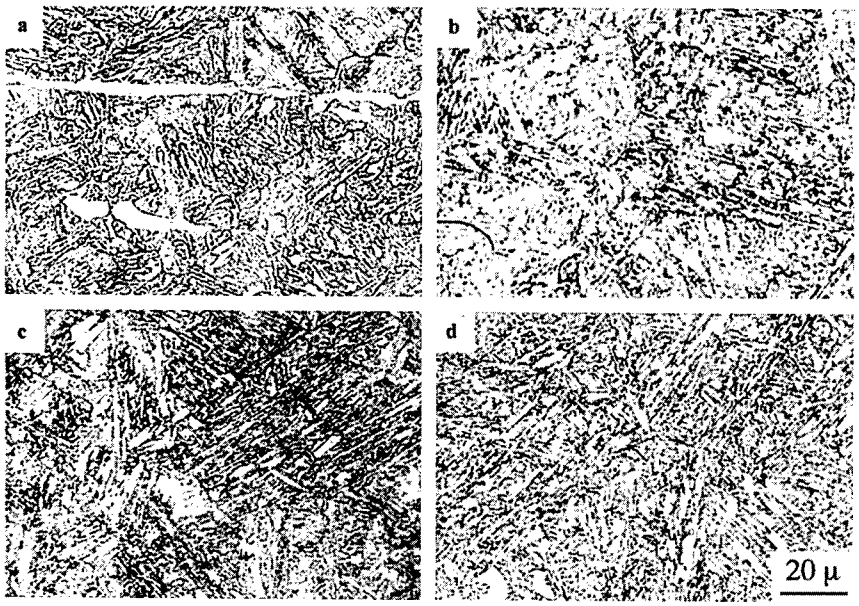

Fig.1 Optical micrographs of the steels with the base composition (a), 1%Pd (b), 2%Pd (c) and 3%Pd (d).

Fig.2 shows creep curves of the steels with the base composition and with 3% Pd crept at 650°C with the stresses of 140 and 100 MPa. It is seen that the steel with 3% Pd exhibits higher creep resistance and longer creep lives in both testing conditions than those of the base steel. Fig.3 shows the corresponding creep rate vs. time curves of the same specimens shown in Fig.2. It is seen that the creep curves of all the specimens consist of a transient creep region and a subsequent acceleration creep region, which have been observed in the conventional high Cr ferritic steels [5]. The initial creep rates of the steel with 3% Pd crept at both stress levels are lower than those of the base steel. The creep rate of the steel with 3% Pd decreases more with time than that of the base steel in the transient creep region, and much lowered minimum creep rates give rise to at longer period of time in both testing conditions. The creep rate then turns out to increase with time in the acceleration creep region after reaching the minimum creep rate. The resultant creep lives of the steel with 3% Pd for both stress levels are much longer than those of the base steel.

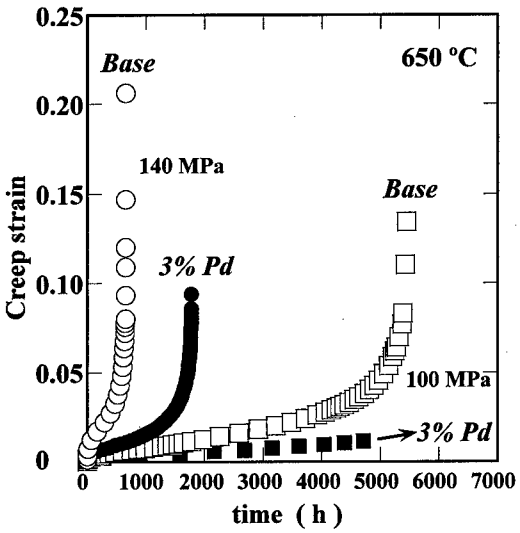

Fig.2 Creep curves of the steels with the base composition and with 3% Pd.

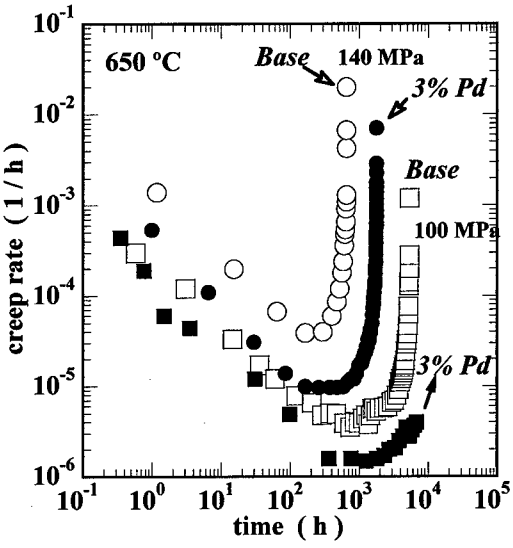

Fig.3 Corresponding creep rate vs. time curves of the steels shown in Fig. 2.

Fig. 4 shows stress dependence of the minimum creep rate obtained for the steels with the base composition and with 1–3% Pd crept at 650°C. It is seen that with increasing Pd content the minimum creep rate decreases at all the stress levels tested. This means that the addition of Pd to the steels is effective to increase the creep resistance of the steels and its effect is significant even for long-term creep testing at low stress levels.

Fig. 5 shows the creep curves of the same steels crept at 650 and 700°C with 120 MPa. The steel with 3%Pd exhibits large decrease in the creep rate in the transient creep region, resulting in the lower minimum creep rate. It is noted that the difference in the minimum creep rate between two steels at 700°C is much larger than that at 650°C. This means that the addition of Pd to the steels

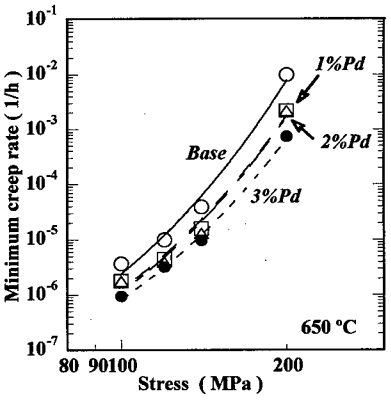

Fig.4 Stress dependence of the minimum creep rate of the steels.

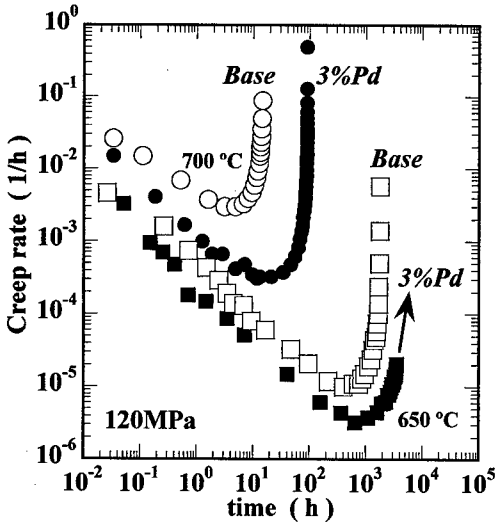

Fig.5 Creep rate vs. time curves of the steels crept at 650 and 700°C with 120 MPa.

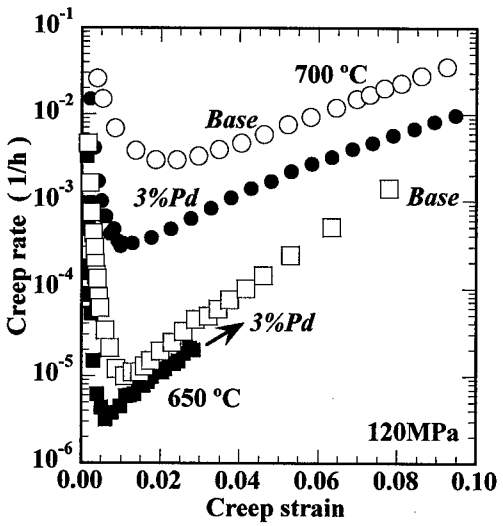

Fig.6 Corresponding creep rate vs. strain curves of the steels shown in Fig. 5.

becomes more useful at higher temperatures to increase the creep resistance of the steel.

Fig. 6 shows the corresponding creep rate vs. creep strain curves of the same steels shown in Fig.5. This type of the figure is sometimes very useful to understand the creep deformation mechanism involved. The parameters to be considered are the slopes of the curve in both transient and acceleration creep regions and the strain giving the minimum creep rate. The steels with 3%Pd exhibits steeper decrease in the creep rate with strain in the transient creep region and gives the smaller strain giving the minimum creep rate. This suggests that fine dispersion of the α″ phase reduces much the creep rate in the transient creep region but enhances to some extent to start the acceleration creep maybe due to the heterogeneous creep deformation. In the acceleration creep, however, increase in the creep rate with strain of the steel with 3%Pd is in the same level as that of the base steel. This clearly means that in the acceleration creep region the homogeneous creep deformation is dominant and no further acceleration takes place as observed in the case of 9Cr-4W steels with a large amount of Fe_2W type Laves phase [6]. The creep deformation of the steel with the α″ phase is therefore considered to be similar to that of the steels with MX [7].

Fig. 7 shows a TEM micrograph of the steel with 3%Pd after normalizing and tempering. The microstructure consists of a typical lath-martensite matrix with $M_{23}C_6$ along prior austenite grain boundaries and lath boundaries, and MX inside lath-martensite grain. A striking feature of this microstructure is frequent appearance of fine precipitates inside lath-martensite grain as shown in Fig. 8(a). These precipitates are found to be a $L1_0$ type ordered phase, the α″ phase which is uniquely confirmed by a dark field image by taking (100) α″ reflection [8]. In this figure the α″ phase forms homogeneously and in a plate-shaped with a crystallographic orientation relationship with matrix, $\{001\}_\alpha$ // $\{001\}_{\alpha''}$ and $<100>_\alpha$ // $<110>_{\alpha''}$. This particular relationship is the same as those observed for V_4C_3 precipitated in 9Cr-1V steel [5].

Fig. 8 shows TEM micrographs of the steels with 3% Pd after tempering and after long-term aging for 1000 h at 600, 650 and 700°C. It is seen that most of the α″ phase precipitate during tempering and remain in the same size and shape even after the exposure for 1000 h at 700°C. A small amount of secondary precipitation of the α″ phase is also identified in all the specimens aged, which has the same crystallographic orientation relationship with matrix above.

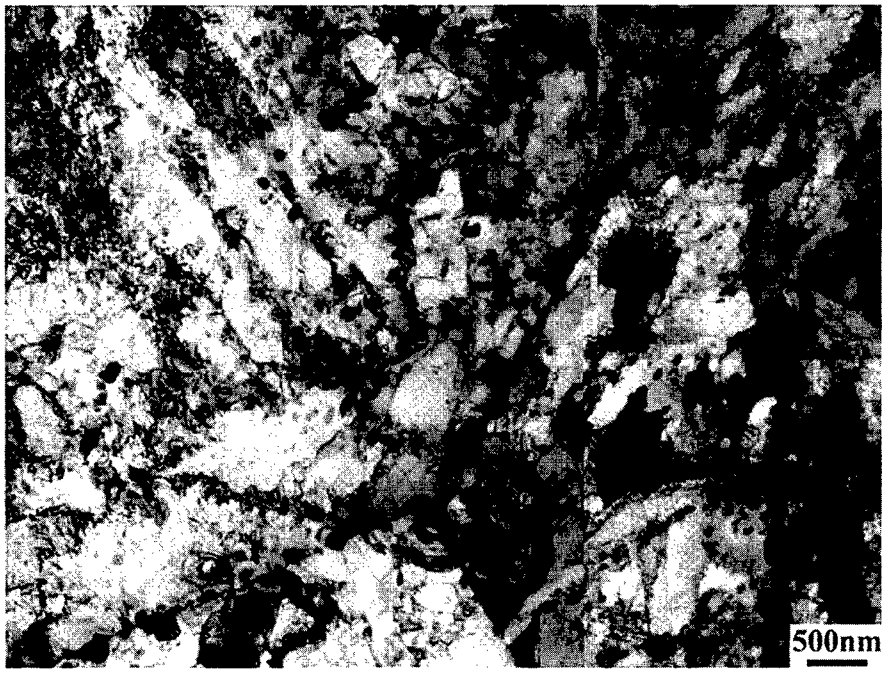

Fig.7 TEM micrograph showing the lath-martensite strucure of the steel with 3% Pd after normalizing and tempering.

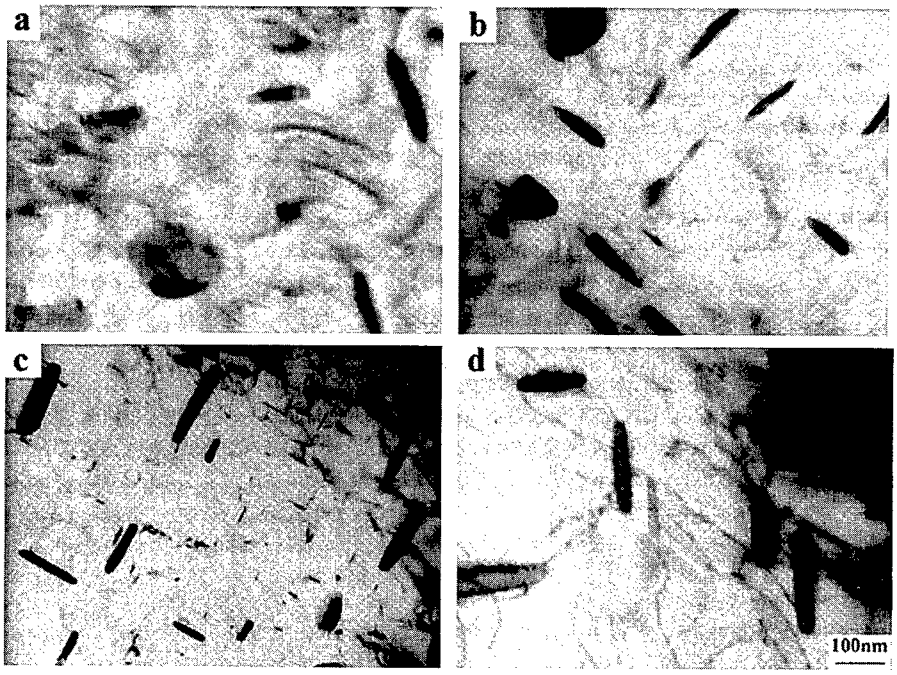

Fig.8 TEM micrographs of the steel with 3% Pd tempered at 770°C (a), and aged for 1000 h at 600°C (b), 650°C (c) and 700°C (d).

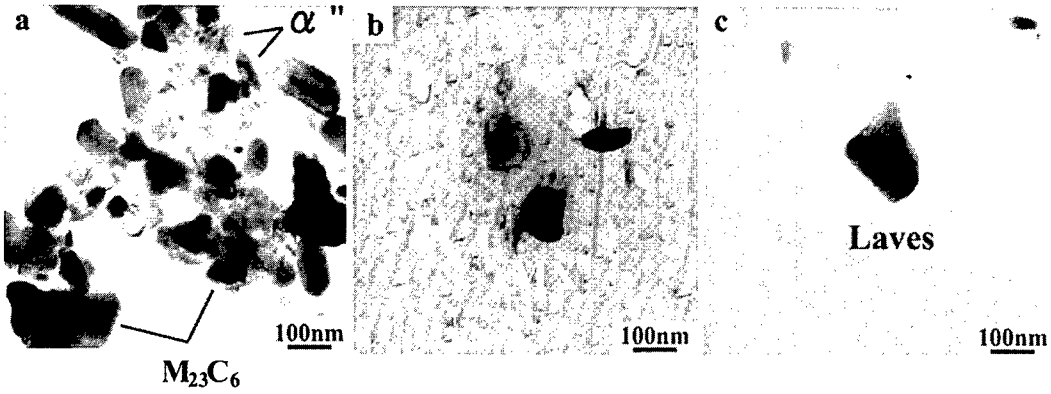

Fig.9 Extraction replicas of the steel with 3% Pd tempered and aged for 1000 h at 650°C showing the α″ phase and $M_{23}C_6$ (a), MX (b) and Laves phase (c).

Fig.9 shows extraction replicas taken from the steel with 3% Pd aged for 1000 h at 650°C. The composition of each precipitate has been determined using a quantitative EDX spectroscopy in FE-TEM. It is seen that the α″ phase is characterized by a thin-plate shape and by an abundant amount. It is also noted that MX seems to be scarce to find and to be rather large in size as compared with the α″ phase. This may be due to a small volume fraction of the MX carbonitride in the steels. $M_{23}C_6$ carbide and Laves phase are found to be in a blocky shape, although some of them are comparably small to the α″ phase.

Fig. 10 shows the result of the chemical analysis of the extracted residue taken from the steels tempered and aged for 1000 h at 600, 650 and 700°C. In this figure the elements such as V and Nb which compose the MX carbonitride are not depicted, since they are all in same levels, that is, about 0.15 % for V and about 0.05% for Nb, nevertheless the steels with or without Pd, and the specimens tempered or aged. The extracted residue from the steel with 3% Pd after tempering consists of W, Cr, Fe, Pd and Mn, while one from the base steel does of W, Cr and Fe, which are the major constituents of $M_{23}C_6$ carbide. This means that the α″ phase forms during tempering and its major constituent elements are Fe, Pd and Mn. It is also noted that after aging only a small amount of secondary precipitation of the α″ phase takes place, which is observed in the TEM micrographs as shown in Fig. 8 (c).

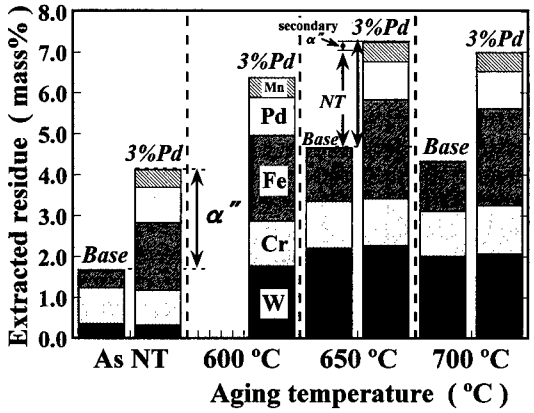

Fig. 10 Chemical analysis of the extracted residue taken from the steels tempered and aged.

Fig. 11 shows a TEM micrograph of creep deformation structure observed in the specimen with 3% Pd interrupted during creep testing at 650°C with 120 MPa at a creep strain of 0.05 which corresponds to the acceleration creep region. It is seen that most of the excess dislocation inside grains disappears and rearrangement of sub grain structures is proceeding. The creep deformation seems to be enhanced by dislocation generation around coarse precipitates such as $M_{23}C_6$ and Laves phase along grain boundary, but to be retarded by the α″ phase inside grains.

To evaluate which precipitate is most effective to increase the creep resistance of the steel, the dispersion strengthening parameters such as particle size, volume fraction and the inter-particle spacing of the precipitates in question have been calculated based on the fine dispersion strengthening of the steels [9]. For simplicity, the precipitates are treated as VN for MX, FePd for α″, $Cr_{23}C_6$ for $M_{23}C_6$ and Fe_2W for Laves phase, respectively. The volume fraction of each precipitate is evaluated from the result obtained for the extracted residue taken from the steel with 3% Pd aged for 1000 h at 650°C using the average particle size estimated from TEM observation. It is seen that the α″ phase is a most effective precipitate in terms of the inter-particle spacing, although the particle size is rather large compared with that of MX. This is due to a large volume fraction of the α″ phase. This is one of the big advantages to use the α″ phase instead of MX, since the volume fraction of the MX cannot be increased much, because increase of V, Nb and C causes MX formation during normalization temperature, resulting in non-coherent precipitation.

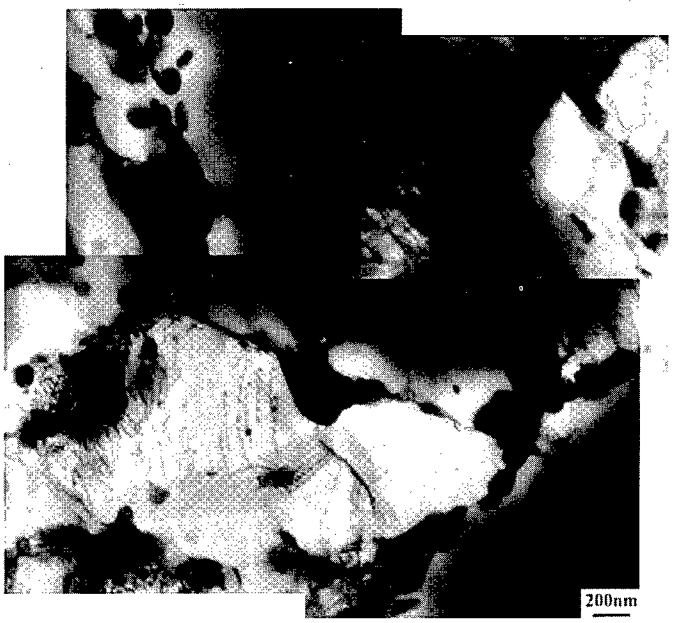

Fig. 11 A TEM micrograph showing creep deformation structure observed in the specimen with 3% Pd crept at 650°C with 120 MPa at a creep strain of 0.05.

Table 1 Summary of the dispersion parameters of the precipitates

Name compo. structure	Misfit param. (%)	Shape & size Coherent size	Site	Volume fraction	Inter- particle spacing	Fine dispersion strengthening
MX VN B1 (fcc)	+ 0.55	plate 50x10nm (eq. sphere 17nm) coherent < 80nm	inside grain homogeneous	0.0038	200nm	good
α″ FePd $L1_0$ (fct)	- 4.9	plate 100x20nm (eq. sphere 33nm) coherent < 10nm	inside grain homogeneous	0.0248	150nm	good
$M_{23}C_6$ $Cr_{23}C_6$ $D8_4$ (fcc)	-	blocky < 50 nm	inside grain homogeneous	0.0182	268nm	moderate
		blocky > 100nm	grain boundary heterogeneous		536nm	none
Laves Fe_2W C14 (hex)	-	blocky < 50 nm	inside grain homogeneous	0.0205	254nm	moderate
		blocky > 200nm	grain boundary heterogeneous		1017nm	none

We thus conclude that the α″ phase is a most effective precipitate to increase the creep resistance of the ferritic steels at elevated temperatures over 650°C. It is also concluded that the creep resistance of the ferritic steels can be increased further by optimizing the combination of fine precipitation such as the α″ phase and MX carbonitride.

Conclusion

Creep properties of advanced heat-resistant martensitic steels with the compositions of 0.08C-0.3Si-0.5Mn-9Cr-3.3W-(0/3)Pd-0.2V-0.05Nb-0.05N-Fe (in mass%) have been studied to explore the fundamental guiding principles for the development of new steels with improved creep strength at higher temperatures over 650°C. The steel with 3%Pd exhibits higher creep strength than that of the base steel, in particular, at higher temperatures. This is mainly due to fine precipitation of a FePd based $L1_0$ type ordered phase, α″ phase. The α″ phase forms in the tempered martensitic matrix, α, along with the existing phases such as MX (M; V, Nb, X; C, N) carbonitride and $M_{23}C_6$ (M; Cr, Fe, W) carbide after normalizing at 1100°C and tempering at 770°C. The α″ phase is found to precipitate in a plate-shaped with the habit plane parallel to $\{001\}_\alpha$ and with a crystallographic orientation relationship with the matrix, $\{001\}_\alpha$ // $\{001\}_{\alpha''}$ and $<100>_\alpha$ // $<110>_{\alpha''}$, which is the same relation as observed for MX in 9Cr ferritic steels. The α″ phase is found to be a most effective precipitate to increase creep resistance of the steel in terms of the inter-particle spacing estimated. The α″ phase is stable even after aging at 700°C and is hence more useful at higher temperatures. It is thus concluded that the creep resistance of the ferritic steels can be increased further by optimizing the combination of fine precipitation such as the α″ phase and MX carbonitride.

Acknowledgment

The authors would like to express their sincere gratitude to Masaru Itoh for his collaboration in experiments.

References

[1] F. Masuyama: in Proc. of the 6th Liege Conf. on Materials for Advanced Power Engineering, 5-7 October, Liege, Belgium, (1998), **III**. 1807-1824.
[2] K. Sawada, M. Takeda, K. Maruyama, R. Ishii and M. Yamada: ibid., **I**.575-583.
[3] M. Igarashi, S. Muneki and F. Abe: ibid., **I**. 637-646.
[4] M. Igarashi, S. Muneki and F. Abe: Report of 123rd Committee on Heat- Resisting Metals and Alloys, Jpn. Soc. for the Promotion of Sci., **39** (1998), 355-362 (*in Japanese*).
[5] F. Abe, T. Noda and M. Okada: J. Nucl. Maters., **195** (1992), 51-67.
[6] F. Abe: Abstracts of the 124th JIM Annual Meeting, 29-31 March, Tokyo, (1999), 434 (*in Japanese*).
[7] F. Abe: J. Maters. Sci. & Eng., **A234-236** (1997), 1045-1048.
[8] M. Igarashi, S. Muneki and F. Abe: in Proc. of Inter. Conf. on Solid-Solid Phase Transformations '99, May 24-28, Kyoto, Japan.
[9] J. W. Martin: 'Micromechanisms in particle-hardened alloys', Cambridge University Press, London, (1980), pp.41.

e-mail: igar@nrim.go.jp

Key Engineering Materials Vols. 171-174 (2000) pp. 513-520
© 2000 Trans Tech Publications, Switzerland

Microstructural Evolution in SUS304H Steel during Long-Term Creep Over 10^5 h

M. Murata[1], H. Tanaka[1], F. Abe[1] and H. Irie[2]

[1] Frontier Research Center for Structural Materials, National Research Institute for Metals, 1-2-1 Sengen, Tsukuba 305-0047, Japan

[2] Mechanical Properties Division, National Research Institute for Metals, 1-2-1 Sengen, Tsukuba 305-0047, Japan

Keywords: SUS304 Steel, Creep, $M_{23}C_6$ Carbide, σ Phase, Creep Void, Precipitate Size, Composition of Precipitate, Hardness

Abstract

The microstructural evolution has comprehensively been investigated for type 304H austenitic stainless steel after creep rupture testing for up to about 180,000 h at temperatures between 550 (823) and 750 °C (1023 K). Fine $M_{23}C_6$ carbides and σ phase precipitated in the specimens during creep. The concentration of Cr in the $M_{23}C_6$ carbides increased during creep, while that of Fe decreased and they reached substantially equilibrium values at long times over 10^5 h. No change was found for the concentrations of Cr, Fe and Ni in the σ phase. The Vickers hardness of the specimen gauge portion decreased with time after reaching a maximum at short times less than about 10^2 h, while it had a tendency of increase again at long times at 600 °C. The creep voids formed at the interface between the precipitates of σ phase on grain boundaries and austenite matrix at low stresses and long times.

1 Introduction

The establishment of reliable methods for evaluating the material degradation and remaining life has earnestly been wished for the high-temperature components being operated for long duration [1, 2]. For the material degradation evaluation based on microstructural examinations, it is necessary to produce precise microstructures by suitable etching and to examine quantitatively the microstructural changes in the structures. The microstructural evolution during thermal aging under no stress was examined by Minami et al. [3] for austenitic stainless steels, 304H, 316H, 321H and 347H steels, for up to $5x10^4$ h at temperatures between 600 (873) and 800 °C (1073 K). At present, little is known on the microstructural evolution during long-term creep for up to 10^5 h or more for the steels. In the present research, the behavior of microstructural evolution during creep has comprehensively been investigated for type 304H austenitic stainless steel after long-term creep rupture tests for up to $1.8x10^5$ h, using specimens tested in the NRIM Creep Data Sheet Project [4]. Type 304H steel is one of the most popular austenitic heat resistant steels. A number of micrographs for type 304H steel were recently published as 'Metallographic Atlas of Long-Term Crept Materials' [5], parallel with the NRIM Creep Data Sheets.

2 Experimental Procedure

The material used for microstructural examinations was the heat ABE of 18Cr-8Ni steel (SUS 304H TB) in the NRIM Creep Data Sheet No.4B [6], where the creep rupture data were presented for nine heats of 18Cr-8Ni steel. The chemical compositions of the steel are given in Table 1. The creep specimens, having a geometry of 6 mm in diameter and 30 mm in gauge length, were taken longitudinally from the middle of wall thickness of the as-received boiler tube. The tube had

a size of 50.8 mm in outer diameter and 8 mm in wall thickness and was already solution annealed. Creep and creep rupture tests were carried out for up to about 180,000 h at temperatures between 550 (823) and 750 °C (1023 K). The longitudinal cross-section of the gauge and head (or grip) portions of the specimens was observed using optical, scanning and transmission electron microscopes. The head portion can be regarded as unstressed portion. The details of the experimental procedure are described elsewhere [4].

Table 1 Chemical compositions of SUS304H steel examined (wt%)

C	Si	Mn	P	S	Ni	Cr	Mo	Cu	Ti	Al	B	N
0.07	0.55	1.46	0.23	0.006	9.57	18.95	0.04	0.07	0.062	0.014	0.0018	0.0278

3 Experimental Results and Discussion

3.1 Microstructural evolution during creep

Figure 1 shows the stress versus time to rupture data for the heat ABE of SUS304H steel, where the solid symbols show the data for the specimens used for microstructural examinations. The solid curves are drawn on the based of the time-temperature parameter method of Manson-Haferd [6]. The creep fracture modes for the SUS304H steel are divided to one transgranular fracture (denoted by T) and three types of intergranular fracture; the wedge-type cracking (W), the creep cavitation associated with $M_{23}C_6$ carbides at grain boundaries (C) and the σ/ matrix interface cracking along grain boundaries (σ). The present results suggest that the creep fracture modes at long times above about 10^4 h are closely connected with the precipitation behavior of $M_{23}C_6$ carbides and σ phase.

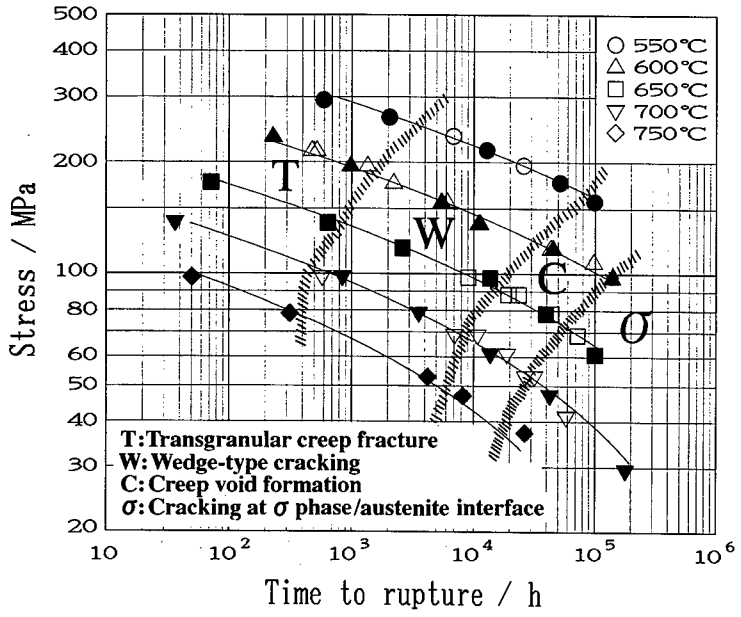

Fig.1 Stress versus time to rupture for the heat ABE of SUS304H steel.

3.2 Change in size of $M_{23}C_6$ carbides and σ phase

Figure 2 shows the optical microstructure of the gauge portion after creep rupture testing, including 10^5 h-microstructures. Combining with the results of time-temperature-precipitation (TTP) diagram shown in Fig.3, it becomes evident that only the $M_{23}C_6$ carbides precipitate in the specimens at short times less than about 10^4 h at 650 °C but that both the $M_{23}C_6$ carbides and σ phase precipitate at long times above about 10^4 h. The distributions of the $M_{23}C_6$ carbides cannot be recognized clearly on the optical micrographs, because of their small size. The TEM micrographs clearly show the distributions of them as shown in Fig.4, where the $M_{23}C_6$ carbides are observed in the form of cube-like particles in Widmanstatten distributions in the matrix and in the form of chain of enlarged particles along grain boundaries. The σ phase is observed in the form of large and irregular shapes on grain boundaries and of needles in the matrix on the optical micrographs (Fig.2), which are more clearly show in the TEM micrographs in Fig.4.

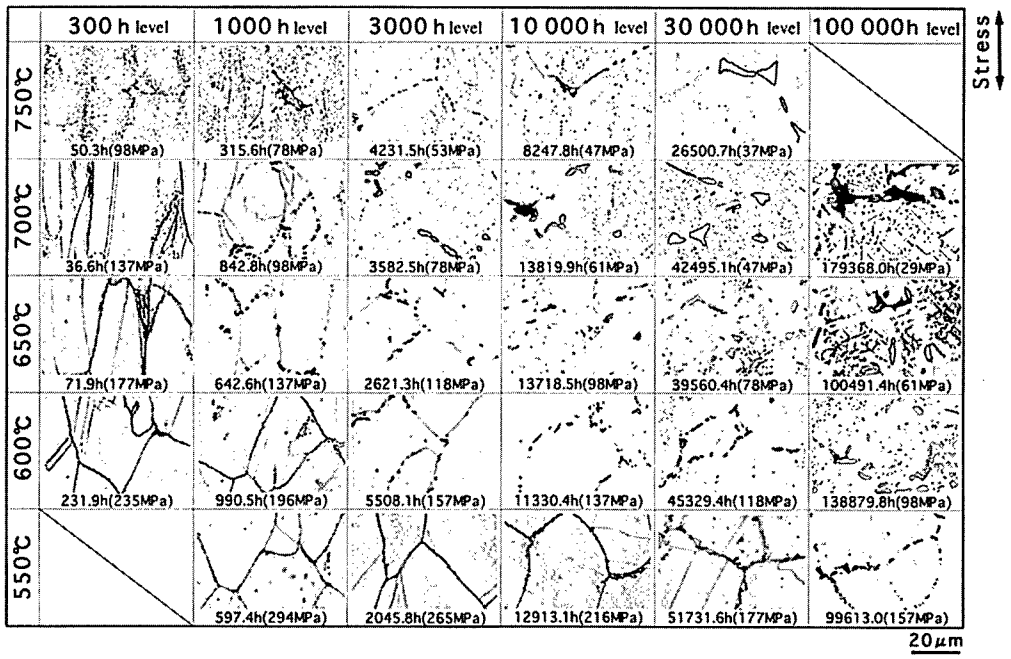

Fig.2 Change in optical microstructure of specimen gauge portion for SUS304H steel during creep.

Based on the TEM micrographs, about 30 precipitate particles of the $M_{23}C_6$ were selected at random in each specimen for the size measurement and the average value of them in the specimen head portion was plotted in Fig.5 as a function of time. The length of long side of the cube-like $M_{23}C_6$ particles was measured as their size in the matrix, while the length in longitudinal direction of the enlarged $M_{23}C_6$ particles along grain boundaries was measured as their size on grain boundaries. In the initial stage of precipitation in the matrix, the size of $M_{23}C_6$ particles is approximately described by $d \propto t^{1/2}$, suggesting diffusion-controlled growth of the $M_{23}C_6$ carbides from supersaturated solid solution [7]. The slope of the size-time curves decreases at long times and the particle size reaches to about 0.05 - 0.07 μm at 10^5 h at 600 - 700 °C. There is no large difference in size of the $M_{23}C_6$ at long times among the different temperatures. For the $M_{23}C_6$ carbides on grain boundaries, the slope of the size-time curves also decreases at long times similar as in the matrix, although the size is much larger than those in the matrix.

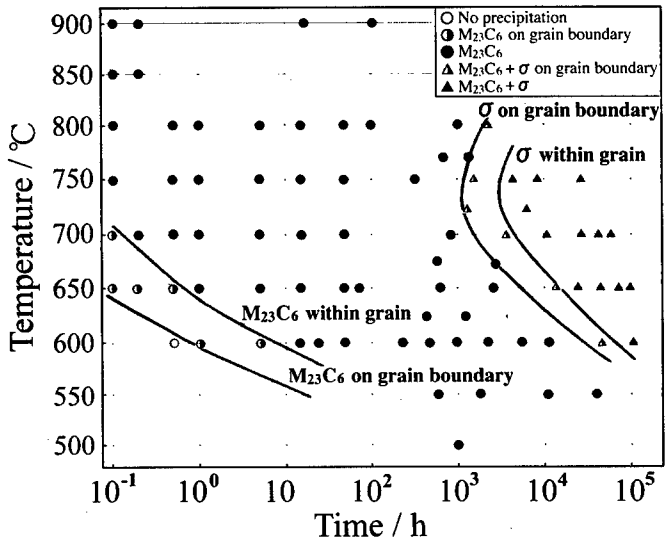

Fig.3 Time-temperature-precipitation (TTP) diagram for specimen head portion of SUS304H steel.

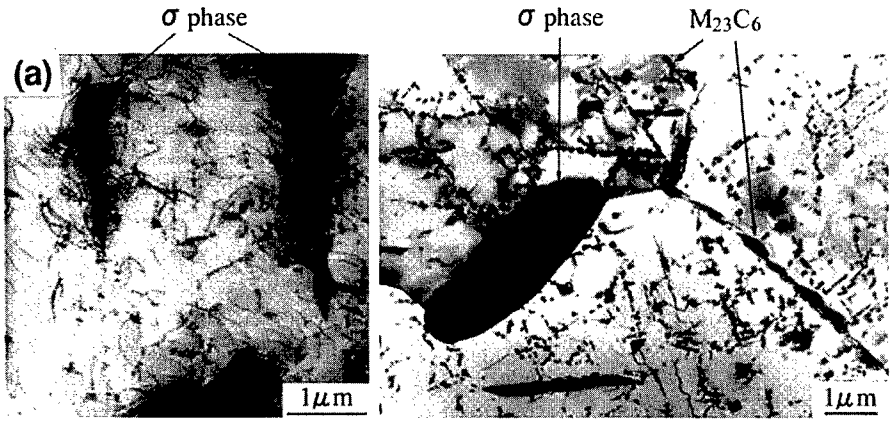

Fig.4 TEM microstructures; (a) matrix in the specimen ruptured after 39560 h at 650 °C and 78 MPa and (b) near grain boundaries in the specimen ruptured after 138880 h at 600 °C and 98 MPa.

The size, area fraction and number density of the σ phase on grain boundaries were measured on the optical micrographs and are shown in Fig.6 as a function of time. Although the σ phase was observed to have irregular shapes, the particle was assumed to be a sphere having the equal volume and the diameter of the sphere was regarded as the size of σ phase. The area fraction, corresponding to the amount of precipitated σ phase, is much larger in the gauge portion than in the head portion, indicating a large acceleration effect of stress and or strain on the σ phase precipitation. In the head portion under no stress, the number of σ phase significantly increases with time, while the size increases only slightly. In the gauge portion under stress, on the other hand, the number of σ phase decreases or is constant with time, while the size significantly

increases with time. These results indicate that the rate-determining process of the precipitation of the σ phase on grain boundaries is mainly the nucleation at new sites in the head portion under no stress. However, in the gauge portion under stress, the nucleation is almost completed in the initial stage of precipitation and the major process of precipitation is the growth. The available nucleation sites are restricted to grain boundaries perpendicular to stress direction in the gauge portion, while all grain boundaries are available for the nucleation in the head portion.

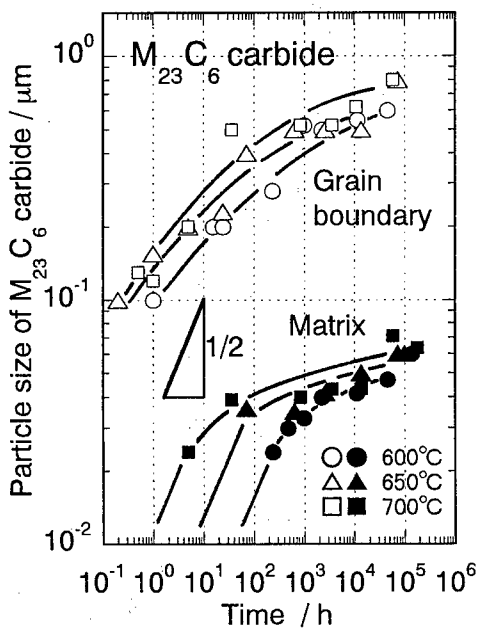

Fig.5 Mean size of $M_{23}C_6$ carbides in specimen head portion, as a function of time.

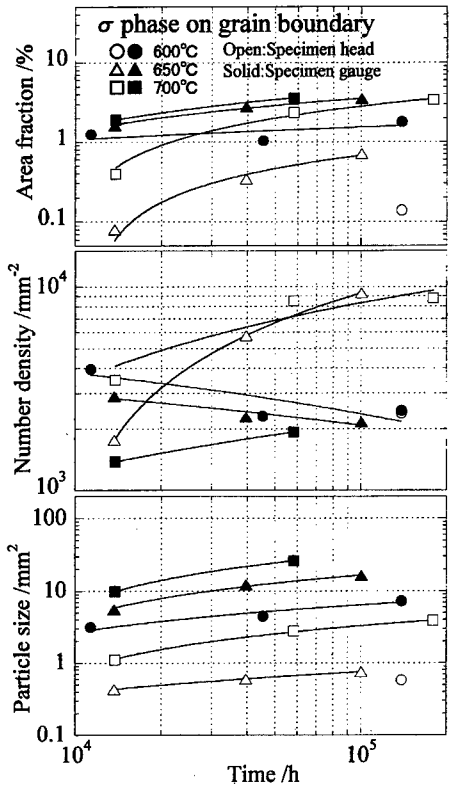

Fig.6 Area fraction, number density and particle size of σ phase on grain boundaries, as a function of time.

3.3 Change in chemical composition of $M_{23}C_6$ carbides and σ phase

The concentration of major components Cr and Fe in the $M_{23}C_6$ carbides were measured on extracted replicas by EDX in SEM. The summation of the concentrations of Cr and Fe is assumed to be 100%. The results are shown in Fig.7 as a function of time. At 650 °C, the concentration of Cr increases from 72% at 10^2 h to 85% at 10^5 h in the specimen head, while that of Fe decreases from 28% at 10^2 h to 15% at 10^5 h. The change in the concentrations of Cr and Fe with time shifts to shorter times with increasing temperature, suggesting diffusion-controlled process. At long times over 10^5 h, the concentrations of Cr and Fe in the $M_{23}C_6$ carbides are roughly the same, about 85%Cr and 15%Fe, among the different temperatures and also between the specimen head and gauge portions, suggesting that these values are substantially equilibrium ones. The change in the concentrations of Cr and Fe with time was also accelerated under stress.

Figure 8 shows the concentrations of Fe, Cr and Ni in the σ phase on grain boundaries as a function of time. The concentrations of Fe, Cr and Ni are evaluated to be 55 - 60, 38 - 42 and 1 - 5%, respectively, from the initial stage of precipitation to long times such 10^5 h in the temperature range between 550 and 750 °C, indicating no change in concentration with time. There was also no difference in concentrations between the specimen head and gauge portions. The present results indicate that the σ phase, having the equilibrium concentrations of Fe, Cr and Ni, precipitate from the initial stage. This is quite different from the remarkable change in concentrations for the $M_{23}C_6$ carbides during creep described above. Because the equilibrium concentration of Cr in the $M_{23}C_6$ carbides is much higher than the concentration of Cr in the matrix at t = 0, it is considered that at first the $M_{23}C_6$ carbides precipitate with Cr concentration much lower than the equilibrium one and then the concentration of Cr gradually increases toward the equilibrium one. The equilibrium concentration of Cr in the σ phase is also higher than the concentration of Cr in the matrix but much lower than that in the $M_{23}C_6$ carbides.

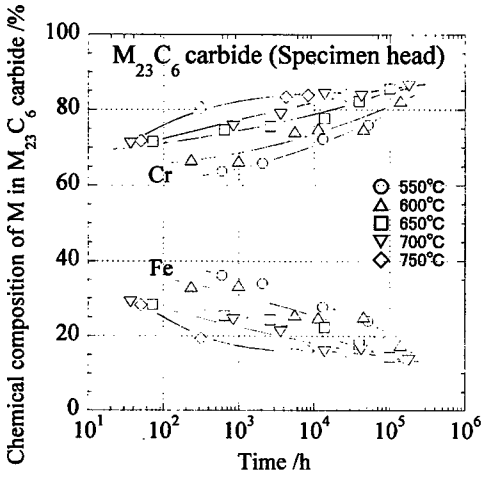

Fig.7 Concentration of Cr and Fe in $M_{23}C_6$ carbides, as a function of time.

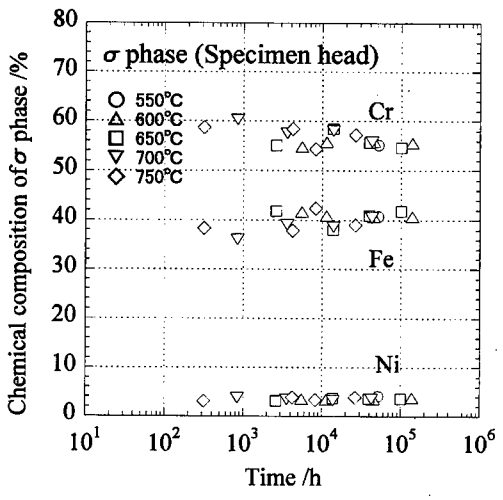

Fig.8 Concentration of Fe, Cr and Ni in σ phase on grain boundaries, as a function of time.

3.4 Change in Vickers hardness

Figure 9 shows the Vickers hardness of the specimen head and gauge portions, as a function of time. The Vickers hardness in as-received condition was 160. In the specimen gauge portion, the Vickers hardness decreases with time after reaching a maximum at short times less than about 10^2 h, while it has a tendency of increase again at long times at low temperature 600 °C. The decrease in Vickers hardness with time results from a recovery of excess dislocations produced by loading at the beginning of creep test. The increase in Vickers hardness at long times at 600 °C results from the age hardening observed in the specimen head portion. The Vickers hardness after the same test duration decreases with increasing test temperature and further decreases below the initial value of 160 at long time above 10^4 h at 700 and 750 °C. Thus the observed change in Vickers hardness with time results from the hardening due to production of excess dislocations by loading, the softening due to recovery of excess dislocations and the age hardening during creep.

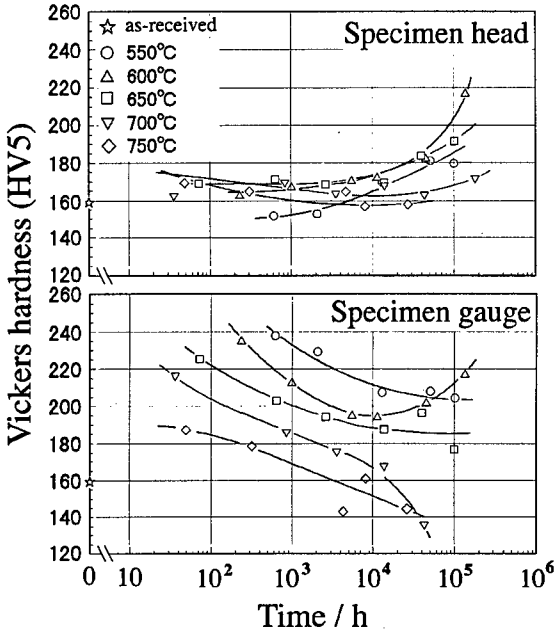

Fig.9 Vickers hardness of specimen head and gauge portions, as a function of time.

3.5 Creep void formation at low stresses and long times

The creep voids were observed to form during creep at low stress and long time conditions. The area fraction and number density of creep voids were measured on the SEM micrographs, after

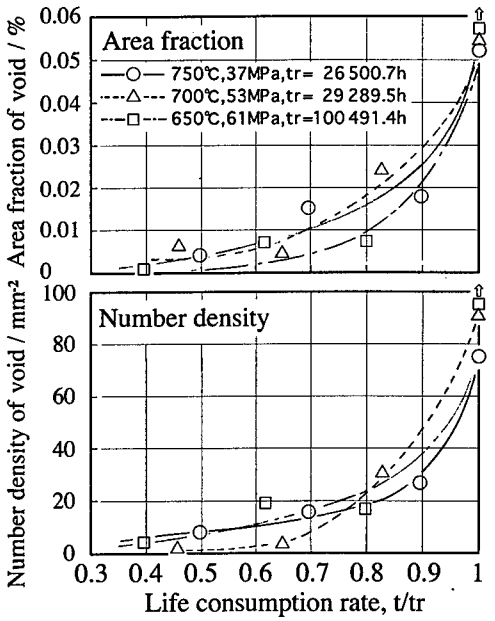

Fig.10 Area fraction and number density of creep voids as a function of t/tr.

interrupted the creep tests at several creep strains. The development of creep voids during creep is shown in Fig.10 as a function of time normalized by time to rupture. The creep voids form at the later stage of creep substantially above t/tr = 0.5 and significantly develop just before creep-rupture above t/tr = 0.9. The creep voids were observed to form at the interface between the precipitates of σ phase on grain boundaries and austenite matrix, reflecting the σ / matrix interface cracking along grain boundaries shown in Fig.1.

4 Summary

(1) In the specimen head portion under no stress, the number of σ phase significantly increased with time, while the size increased only slightly. In the specimen gauge portion under stress, the number of σ phase decreased or constant with time, while the size significantly increased with time.
(2) The concentration of Cr increased while that of Fe decreased in the $M_{23}C_6$ carbides during creep and they reached substantially equilibrium values at long times over 10^5 h. On the other hand, no change was found for the concentration of Cr, Fe and Ni in the σ phase.
(3) The Vickers hardness of the specimen gauge portion decreased with time after reaching a maximum at short times less than about 10^2 h, while it had a tendency of increase again at long times at low temperatures, 550 and 600 °C.
(4) At low stress and long time conditions, the creep voids significantly developed just before creep-rupture above t/tr = 0.9 at the interface between the precipitates of σ phase on grain boundaries and austenite matrix.

References

[1] B. J. Cane and J. A. Williams, Intern. Metals Rev. 32 (1987), p. 241.
[2] H.K.D.H. Bhadeshia, A. Strang and D. J. Gooch, Intern. Metals Rev. 43 (1998), p. 45.
[3] Y. Minami, H. Kimura and Y. Ihara, Mater. Sci. Technol. 2 (1986), p. 795.
[4] F. Abe and K. Yagi, Proc. Fourth Intern. Charles Parsons Turbine Conf., The Institute of Materials, London, (1997), p. 750.
[5] National Research Institute for Metals Creep Data Sheet, Metallographic Atlas of Long-Term Crept Materials, Nat. Res. Inst. for Metals, Tsukuba, No.M-1 (1999).
[6] National Research Institute for Metals Creep Data Sheet, Nat. Res. Inst. for Metals, Tokyo, No.4B (1986).
[7] J. W. Christian, in 'The Theory of Transformation in Metals and Alloys', Pergamon Press, Oxford, First Edition (1965), p.433.

e-mail: murata@nrim.go.jp

Key Engineering Materials Vols. 171-174 (2000) pp. 521-528
© 2000 Trans Tech Publications, Switzerland

Mechanical Properties of 11Cr-0.4Mo-2W-CuVNb Steel Welded Joints at Elevated Temperatures

M. Tabuchi[1], T. Watanabe[2], K. Kubo[1], J. Kinugawa[1] and F. Abe[1]

[1] Frontier Research Center for Structural Materials, National Research Institute for Metals, 1-2-1 Sengen, Tsukuba, 305-0047 Japan

[2] Mechanical Properties Division, National Research Institute for Metals, 1-2-1 Sengen, Tsukuba, 305-0047 Japan

Keywords: W Strengthened High Cr Ferritic Steel, Creep Properties, Simulated HAZ, GTA Welded Joint, EB Welded Joint

Abstract

High Cr ferritic heat resisting steels are now recognized to be the most potential materials for thermal power plants. In view of such trend, the present paper investigates the creep properties of a W strengthened 11Cr-0.4Mo-2W-CuVNb steel welded joints. Joints were prepared by using gas tungsten arc (GTA) welding and electron beam (EB) welding. In order to simulate the microstructure of heat affected zone (HAZ), a technique of furnace heating was adopted with varying peak-temperature. Specimens of the welded joints and simulated HAZ were subjected to creep tests at 923K. Most of the joint specimens were ruptured at their HAZ, and inevitably resulted in certainly shorter creep lives of welded joints than those of the base metals. The comparison of creep properties of simulated HAZ specimens showed that fine grains produced by heating to around Ac_3 were obviously responsible for such degradation of creep strength in welded joints. The creep lives were longer for EB welded joints by about 2 times than for GTA welded joints. For GTA welded joints creep rupture was always located on the higher bevel angle sides. From these results, it is considered that narrower HAZ width with lower bevel angles surely produce higher creep strength of joints. The EB welded joints, however, showed relatively brittle fracture in the fine-grained HAZ after long-term creep tests.

1. Introduction

On an increasing demand to reduce CO_2 emissions, high strength ferritic heat resisting steels of 9-12%Cr, some of which are strengthened by W, have been developed with a view to elevating metal temperatures of thermal power plants. Even for these steels, however, higher metal temperatures accelerate their creep damages especially in welded joints, and sometimes result in serious HAZ cracks [1]. Little has been studied concerning the creep properties of the welded joints for these W strengthened 9-12%Cr steels [2, 3].

National Research Institute for Metals (NRIM) is now conducting a research project to develop new heat resisting steel, which is to be used at 923K for 350MPa [4]. The HAZ cracks are considered to be one of the serious problems for realizing such steel. In the present study, for the first step, creep tests of two kinds of welded joints and simulated HAZ specimens for a W strengthened 11Cr-0.4Mo-2W-CuVNb steel (HCM12A) are conducted. Then some mechanisms for the degradation of creep strength in HAZ are discussed by comparing the obtained properties of creep with corresponding microstructures.

2. Experimental procedures

2.1 Materials

The plate selected for the present study is 27mm thick 11Cr-0.4Mo-2W-CuVNb commercial steel. Its chemical composition is listed in Table I. The normalized condition was 1323K for 100 minutes then air cooled and the tempered condition was 1043K for 6 hours then air cooled.

Table I Chemical composition for the present steel.

C	Si	Mn	P	S	Cu	Cr	Mo	W	V	Nb	B	N
0.12	0.28	0.61	0.018	0.001	0.97	10.5	0.36	2.05	0.21	0.06	0.003	0.069

2.2 Furnace heating to simulate HAZ structures

It is difficult to cut the specimens, the section of which consists of homogenous microstructure, from the HAZ of welded joints. Therefore, in order to simulate the microstructures of HAZ all over the specimens, furnace heating are conducted by varying peak temperature from 1073 to 1473K. After the furnace heating and air cooling, post weld heat treatment (PWHT) at 1013K for 260min was conducted then furnace cooled. The round-bar specimens of 6mm in diameter and 30mm in gage length were machined (Hereafter, they are referred to as "simulated HAZ" specimens.). Figure 1 illustrates the thermal histories of simulated HAZ specimens.

2.3 Welding

In order to get information of the effect of HAZ geometry, the plates were welded by two processes, i.e. multi-layer GTA welding with single bevel groove and EB welding. Procedural data of welding are listed in Table II and Table III for GTA and EB, respectively. The trial filler [5] was fed for GTA welding. The changes of temperatures in HAZ during welding were measured for GTA welding. After welding, the PWHT at 1013K for 260min was conducted then furnace cooled. Figure 2 shows the cross sectional view of GTA and EB welded joints. The width of HAZ was about 2.5mm for GTA and about 0.5mm for EB welded joints.

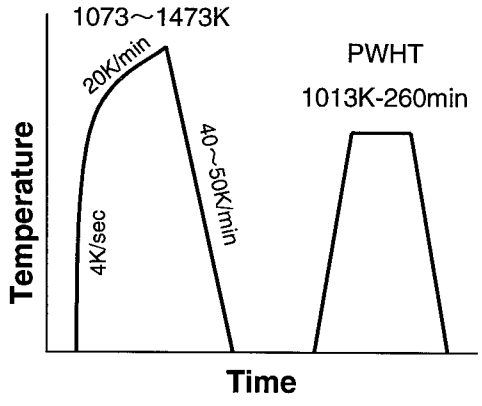

Fig.1 Conditions of heat treatment for simulated HAZ and PWHT.

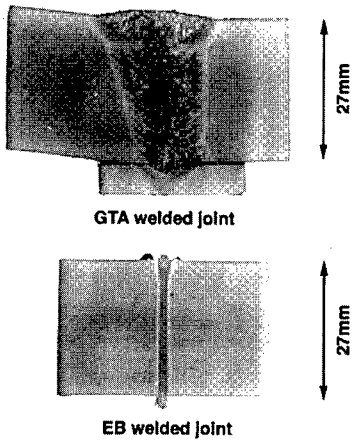

Fig.2 Cross-sectional view of welded joints.

The test specimens with 18 x 5mm cross section as shown in Fig.3 were cut out from these welded joints. These specimens were subjected to creep tests at the target temperature of NRIM project of 923K.

Table II Procedure of GTA welding.

groove	single bevel 20°
welding current	200~250A
arc voltage	10~10.5V
welding speed	70~90mm/min
pre-heating	>373K
multi-layer	33~37 pass

Table III Procedure of EB welding

accelerating voltage	70kV
beam current	400mA
lens current	1.12A
focal length	320mm
welding speed	100cm/min

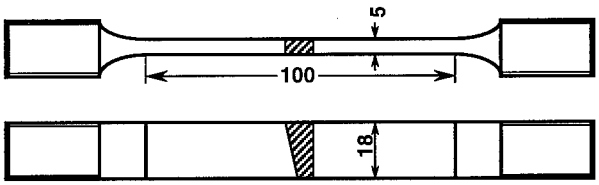

Fig.3. The creep test specimen for welded joints.

3. Results and discussions

3.1 Mechanical properties of simulated HAZ specimens

Most of the welded joint specimens were ruptured at their HAZ as will be mentioned in the following section. Therefore, in order to clarify the relations between creep properties and HAZ microstructures and to obtain the creep constitutive-formula of HAZ, we have conducted the creep tests of simulated HAZ specimens. In the present heat treatment method for simulating HAZ shown in Fig.1, the heating rate was slower than that of actual welding. Figure 4 shows the distribution of Vickers hardness in the GTA welded joint and the measured peak-temperatures at the positions shown by arrows during GTA welding. The Vickers hardness of simulated HAZ specimens were compared with that of GTA welded joints in Fig.4. Because the hardness of simulated HAZ and GTA joints shows nearly the same value, it is considered that the HAZ structure was well simulated by the present method. We measured the temperatures of Ac_1 and Ac_3 at the present heating rate shown in Fig.1 by differential thermal analysis (DSC) method. Those temperatures were about 1093K and 1193K, respectively.

Figure 5 shows the SEM and TEM microstructures before creep tests of the base metal and simulated HAZ specimens heated to nearly Ac_1 and Ac_3. The base metal has the lath structure with high dislocation density. In the simulated HAZ specimen heated to Ac_1, the recovery of sub-structure occurred and the dislocation density was decreased. The coarsening of precipitates were observed in this material. The prior austenite grain size decreased with increasing peak-temperature from Ac_1 up to Ac_3. It showed the minimum value of about 10μm by heating to around Ac_3, while about 35μm for base metal. The simulated HAZ specimen heated to Ac_3 has the fine-grained structure with high dislocation density. The coarsening of precipitates were also observed in this material.

The relationship between creep rupture time and the peak-temperature in simulated HAZ heating are indicated in Fig.6. The Vickers hardness at room temperature of simulated HAZ

specimens before creep tests is also shown in this figure as a function of peak-temperature. The creep rupture time shows its minimum value near the Ac_3 temperature, while the Vickers hardness shows its minimum value near the Ac_1 temperature. The changes in Vickers hardness as a peak-temperature are considered to depend on the dislocation density as explained in Fig.5. The creep rupture time of the specimen heated to Ac_1 was about a half of that for the base metal at 140MPa, while it showed nearly the same value with that for base metal at 100MPa. The heating to Ac_1 brings the recovery of dislocation structure and coarsening of precipitates to the material, however, its creep strength at lower stress becomes nearly the same with the base metal because the recovery

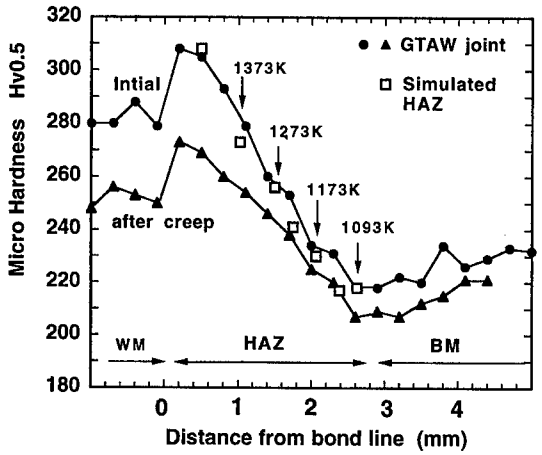

Fig.4. Distribution of Vickers hardness of GTA welded joint and that of simulated HAZ specimens.

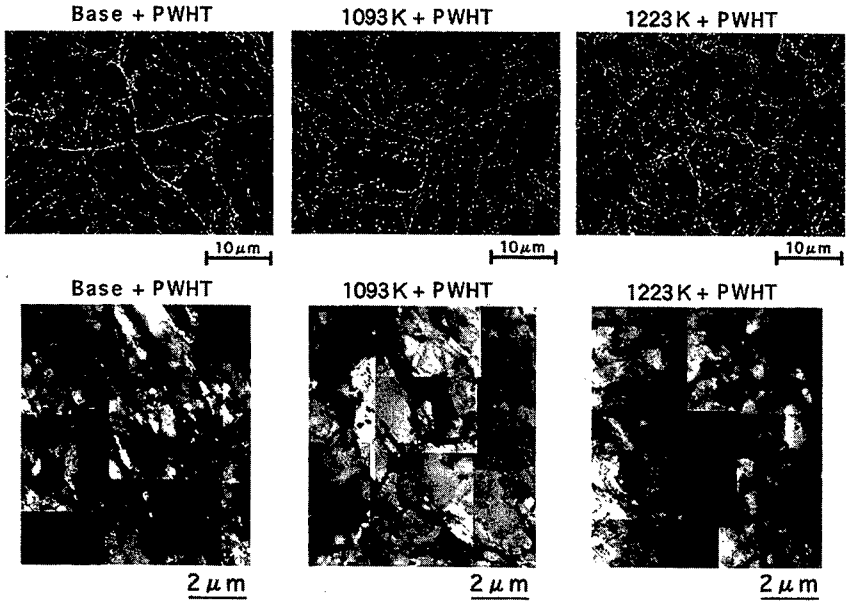

Fig.5. SEM and TEM microstructures of the simulated HAZ specimens for 11Cr-0.4Mo-2W-CuVNb steel.

also occurs in the base metal during creep. The creep rupture time for the specimen heated to around Ac_3 which had fine grains was about one fifth or one sixth of rupture time for the base metal at all stress levels. From the present results, it is considered that the fine grains produced by heating to Ac_3 are responsible for the degradation of creep life in weldments.

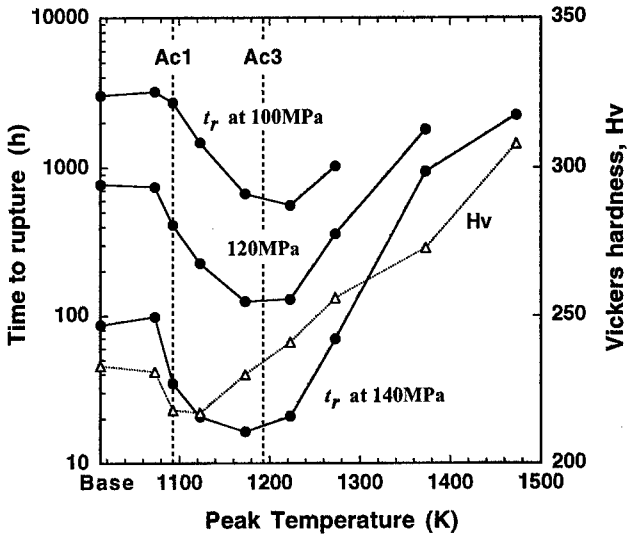

Fig.6. Changes of creep rupture time and hardness in HAZ for 11Cr-0.4Mo-2W-CuVNb steel as a function of peak-temperature.

3.2 Creep fracture of GTA and EB welded joints.

The width and geometry of HAZ are considered to be significant factors to affect the creep lives and fracture modes of welded joints. Figure 7 shows the creep rupture times of the GTA and EB welded joints. The rupture lives of welded joints lie between those of the base metals and those of the simulated HAZ specimens heated to Ac_3. Creep rupture times of the EB welded joints are longer than that of the GTA welded joints by about 2 times.

The macroscopic creep fracture morphology is shown in Fig.8. The GTA welded joints were fractured in HAZ near base metal (Type IV) for 110, 100 and 90MPa at 923K. The single bevel groove is used for the present GTA welded joint, namely, the groove angle of one side was 20 degree and the other side was 0 degree. The bevel angle of creep fractured side was always 20 degree. It is reported that the bevel angle lower than 18 degree was better for creep strength on Mod.9Cr steel [6]. The present results mean that the low bevel angle is better for creep life.

The EB welded joint was fractured in the base metal for 110MPa and the rupture time was nearly the same with base metal, however, it was fractured in HAZ for 90MPa and the rupture time was shorter than that of base metal. The reason why the creep lives of the EB welded joints were longer than those of GTA joints may be due to a mechanical constraint effect. The mechanical constraint in HAZ was larger for the EB welded joints because of the narrower HAZ width. The reduction of area of creep fractured surface was observed for GTA welded joints, however, the EB welded joints were broken under nearly plane strain condition at 90MPa. Some of the present authors have reported that increasing mechanical constraint accelerated the creep crack growth rate [7]. From the present results, it was confirmed that decreasing the width of HAZ compared to the size of specimen or component was effective to prolong the creep life, however the brittle Type IV fracture would be occurred under long-term services.

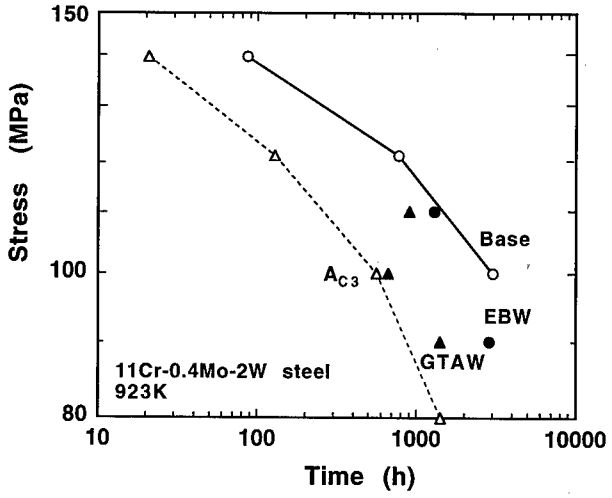

Fig.7. Relationship between creep rupture time vs. stress for simulated HAZ specimens heated to Ac_3, GTA welded joints, EB welded joins and base metals for 11Cr-0.4Mo-2W-CuVNb steel at 923K.

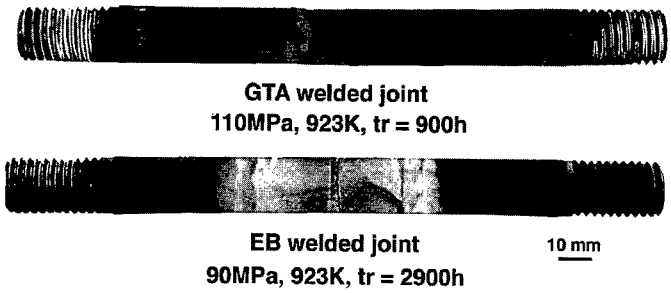

Fig.8. Profiles of the creep fractured specimens for GTA and EB welded joints.

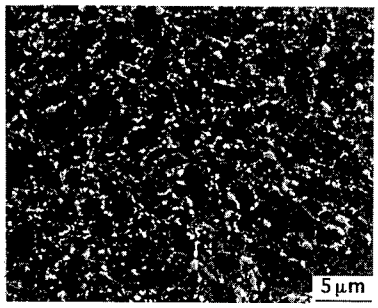

Fig.9. Creep voids observed in the fine-grained HAZ of GTA welded joints crept at 923K for 90MPa.

The hardness distribution of the unbroken side of crept GTA welded joint at 923K for 90MPa was also plotted in Fig.4. We have observed the microstructures near the Vickers marks by SEM. Several creep voids were observed on prior austenite grain boundaries in the fine-grained regions for both welded joints as shown in Fig.9. It is considered that creep fracture of GTA and EB welded joints is accelerated by the formation of creep voids in the fine-grained HAZ heated to around the Ac_3 temperature for the present creep test conditions.

4. Conclusions

In order to clarify the creep properties of welded joints for W strengthened 11Cr-0.4Mo steel, the creep tests up to 3,000 hours were conducted on simulated HAZ specimens, GTA welded joints and EB welded joints. The relation between creep strength and microstructure of HAZ was discussed. The effect of width and angle of HAZ in welded joints were also investigated. The results are summarized as follows;

(1) Hardness showed a minimum value in the simulated HAZ specimen heated to Ac_1 temperature because of extensive recovery of excess dislocations. The long time creep strength of the specimen heated to Ac_1, however, was nearly the same with that of the base metal.

(2) Creep rupture time showed a minimum value at Ac_3 temperature. In the simulated HAZ specimen heated to Ac_3, the grain size was minimized and the creep life was about one-fifth of base metal. It is considered that the fine grains produced by heating to Ac_3 are responsible for the degradation of creep life in weldments.

(3) The GTA welded joints were fractured in fine-grained HAZ. The low bevel angle is considered to be better for creep life.

(4) The EB welded joints that had narrow HAZ indicated the longer creep life than the GTA welded joints by about 2 times. It was effective to decrease the HAZ width for increasing the creep life, however the brittle Type IV fracture was occurred in the EB welded joint for long-term creep test.

References

[1](for example) K. Bell, Elevated temperature midlife weldment cracking (Type IV) –A review, TWI Report, March (1997)

[2]H. Cerjak and E. Letofsky, Proc. of Advanced Heat Resisting Steels for Power Generation, Spain, (1998)

[3]Y. Hasegawa, M. Ohgami and Y. Okamoto, Proc. of Advanced Heat Resisting Steels for Power Generation, Spain, (1998)

[4]F. Abe, M. Igarashi, S. Muneki, K. Kimura, H. Kushima and M. Tabuchi, Proc. of Case Histories on Integrity and Failures in Industry, (1999), (in press)

[5]K. Ogawa, A. Iseda, Y. Sawaragi, S. Matsumoto and F. Masuyama, Sumitomo Metals, **47**(1995), p.39

[6]Y, Tsuchida, H. Sakurai, K. Okamoto and Y. Tokunaga, Quarterly Journal of the Japan Welding Society, **13**(1995),p.579.

[7] M. Tabuchi, K. Kubo and K. Yagi, Eng.Fract.Mech. **40**(1991), p.311.

Key Engineering Materials Vols. 171-174 (2000) pp. 529-536
© 2000 Trans Tech Publications, Switzerland

Design of New Creep-Resistant Nickel-Base Superalloys for Power-Plant Applications

F. Tancret[1], H.K.D.H. Bhadeshia[1] and D.J.C. MacKay[2]

[1] University of Cambridge, Department of Materials Science and Metallurgy, Pembroke Street, Cambridge CB2 3QZ, United Kingdom

[2] University of Cambridge, Department of Physics, Cavendish Laboratory, Madingley Road, Cambridge CB3 0HE, United Kingdom

Keywords: Nickel-Base Superalloys, Creep, Modelling, Gaussian Processes

Abstract: A Gaussian processes computer program has been used to model the mechanical properties of polycrystalline nickel-base superalloys as a function of their chemical composition and heat treatment. The models are able to reproduce well-known metallurgical trends, and to estimate the behaviour of new alloys. On this basis, several new creep-resistant alloys for power plant applications have been proposed. The candidate alloys have been scrutinised further using phase diagram calculations to reveal their equilibrium phase constitutions. This design process has led to a shortlist of alloys on the basis of their expected properties, microstructural stability and cost.

INTRODUCTION

In future, power plant for electricity generation will, for thermodynamic efficiency and ecological reasons, operate with steam temperatures as high as 750 °C. The best steels are currently limited to about 620 °C for such applications and are unlikely to extend in their application to temperatures beyond about 650 °C. On the other hand, many existing polycrystalline nickel-base superalloys of the kind used in the aerospace industry could easily serve the purpose, but they are far too expensive to be used in large scale power plant. The purpose of the present work was to develop novel nickel-base superalloys with good mechanical properties but with greatly reduced cost. The typical design requirements are a creep rupture stress of 100 MPa at 750 °C over 100000 h. To minimise experimental work, we have used a Gaussian processes computer modelling technique [1, 2]. It is an empirical method of representing complex, multidimensional patterns in experimental data in a reliable manner, which is useful in the design of new alloys [3, 4]. This approach has been augmented with phase diagram modelling [5] to help formulate heat treatments and to check the expected long-term microstructure.

MECHANICAL PROPERTY MODELLING ("Tpros" [6])

Modern metallic alloys generally have complex microstructures and may contain a large number of alloying elements. Even if the basic metallurgy is understood, the human brain is unable to explicitly visualise the role of the many interacting variables that contribute to the characteristics of the alloy.

Gaussian processes are statistical tools able to perform, on a database, a multidimensional non-linear regression of an output (in our case a mechanical property) as a function of many different inputs. It can then be used to make predictions on a set of previously unknown inputs. The general theory about Gaussian processes, and examples of their use in metallurgy, can be found in references [1, 2], and [3, 4], respectively. Basically, to make a prediction on a set of inputs, the model calculates the most probable value of the output and its corresponding distribution (through error bars) given the whole data and a set of so-called hyperparameters. These hyperparameters are optimised during the creation of the model, and express the level of noise in the database and the lengthscales on which the output is likely to vary with each input. They allow the definition of smooth-varying models that do not "fit" the noise. The details of the method have been described elsewhere [1 - 4, 6].

The databases we used concerned the yield stress, Y, and the creep rupture stress, CRS, of several tens of different commercial and experimental polycrystalline nickel-base superalloys. Table 1 presents the inputs, as well as the ranges, of the data used.

Input	Range in Y database	Range in CRS database
Cr (wt. %)	5.7 - 30	5.7 - 30
Co (wt. %)	0 - 20	0 - 20.1
Mo (wt. %)	0 - 14.5	0 - 14.5
W (wt. %)	0 - 12	0 - 12
Ta (wt. %)	0 - 9	0 - 9
Nb (wt. %)	0 - 6.5	0 - 6
Al (wt. %)	0 - 6.5	0 - 6.5
Ti (wt. %)	0 - 5	0 - 5
Fe (wt. %)	0 - 57.79	0 - 57.79
Mn (wt. %)	0 - 1.24	0 - 1.25
Si (wt. %)	0 - 2.35	0 - 2.35
C (wt. %)	0.02 - 0.35	0.02 - 0.35
B (wt. %)	0 - 0.16	0 - 0.16
Zr (wt. %)	0 - 0.6	0 - 1
Cu (wt. %)	0 - 0.21	0 - 0.56
N (wt. %)	0 - 0.017	0 - 0.04
S (wt. %)	0 - 0.009	0 - 0.05
P (wt. %)	0 - 0.006	0 - 0.011
V (wt. %)	0 - 1	0 - 1
Forged	0 (no) - 1 (yes)	0 (no) - 1 (yes)
Cold deformed	-	0 (no) - 1 (yes)
t1 (h)	0 - 8	0 - 8
T1 (°C)	0 - 1235	0 - 1235
t2 (h)	0 - 16	0 - 16
T2 (°C)	0 - 1100	0 - 1100
t3 (h)	0 - 50	0 - 50
T3 (°C)	0 - 870	0 - 925
t4 (h)	0 - 24	0 - 24
T4 (°C)	0 - 760	0 - 760
T (°C)	20 - 1093	500 - 1149
log t_r (h)	-	0.6721 - 4.7659
Output	28 - 1310 (Y, MPa)	0.30103 - 3.0149 (log CRS, MPa)

Table 1 : Inputs and outputs ranges in the yield stress and in the creep rupture stress databases.

In Table 1, the heat treatment 1, defined by its duration, t1, and temperature, T1, is the solutionising heat treatment. The heat treatment 2 refers to the new kind of "high temperature" precipitation of coarse cuboidal γ' inclusions (typically around 1000-1100 °C). Heat treatments 3 and 4 refer to a first and second classical "low temperature" γ' precipitation stages (fine and hyperfine inclusions). The inputs "ti" and "Ti" are set to 0 if the heat treatment "i" has not been performed. The cooling conditions following heat treatment have not been included in the analysis because a previous investigation revealed that they are not relevant, largely because they have not been quantitatively reported in the published literature. The yield stress database contained 642 experiments and the creep rupture stress database 1816.

Figure 1 shows that for both the yield stress and the creep rupture stress there is a narrow dispersion of the points around the "x=y" line in the graph reporting the predicted *versus* the measured output for the inputs of the databases. This is a necessary -but not sufficient- indicator of a good model.

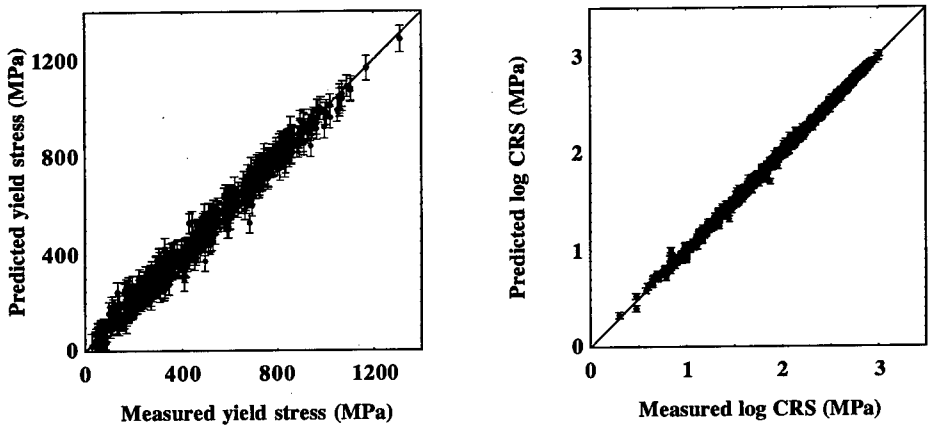

Figure 1: Predicted *versus* measured yield stress and logarithm of creep rupture stress for the inputs of the databases.

The ability of the models to predict and reproduce well-known metallurgical trends in cases *not present* in the databases can be revealing. For this purpose, the predicted influence of solute elements on the mechanical properties has been examined, as illustrated in figure 2.
The 10^5 h creep rupture stress predictions are associated with large error bars because very few measurements of the database exceed 10^4 h. These predictions are consequently extrapolations outside the known domain. Aluminium and titanium strengthen nickel alloys at all temperatures through the precipitation of γ' particles [7, 8]. The larger titanium atom (4% bigger than Al) is found to have a greater effect on the yield strength. This is also consistent with the fact that titanium increases the anti-phase boundary energy of the γ' phase, which makes it more difficult for dislocations to cut into the precipitates [9, 10]. The relative importance of Al and Ti is reversed for the CRS, probably because titanium increases the γ/γ' misfit, which has been reported to be harmful to the creep resistance [11]. However, it is important to note the large error bars associated to the predictions in this domain.

Tungsten partitions in both the γ matrix and the γ' precipitates, and acts as a solid solution strengthener for both phases [12, 13]. It is also known to form carbides that strengthen grain boundaries. It is not surprising that it enhances both the yield stress and the creep rupture stress.

An example where the model is able to predict trends in data that have not been included in its creation are presented on figure 3. The creep model is able to reproduce correctly the experimental data for an Inconel 939 alloy tested at 870 °C (data from [15]). Other trends have been tested (influence of alloying elements, prediction of other published results...), but cannot be all presented here. Most of the expected trends have been confirmed, especially the role of individual solute elements. However, almost all the alloys of the databases are commercial materials for which the heat treatments have already been "optimised". This means that there is a very limited range of heat treatments in the experimental dataset. Thus, the models are not able extrapolate with sufficient certainty to be useful in the study of novel heat treatments. Nevertheless, it has been noticed that including heat treatments as inputs produces better predictions than without them.

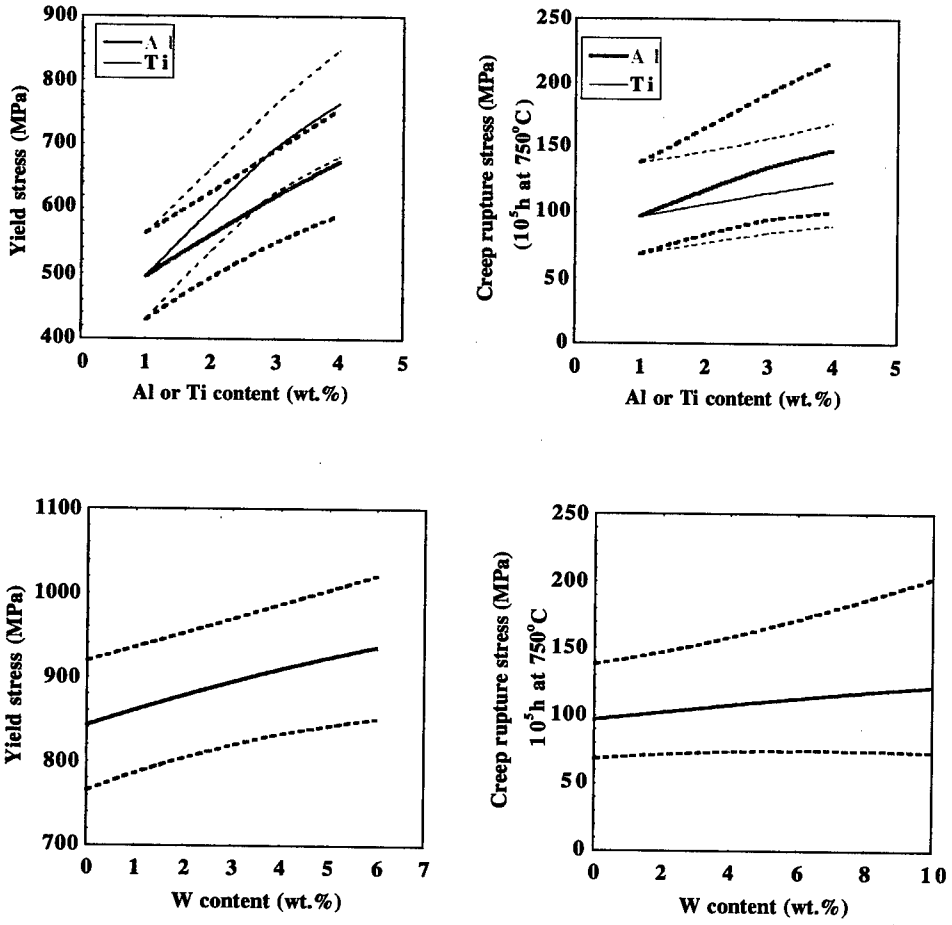

Figure 2: Predicted influence of Al, Ti and W on the room-temperature yield stress and creep rupture stress of a Ni-20Cr-10Co-1Al-1Ti-0.03C wt.% alloy heat-treated 1h at 1175 °C + 8h at 800 °C. Error bounds are indicated by the dotted lines.

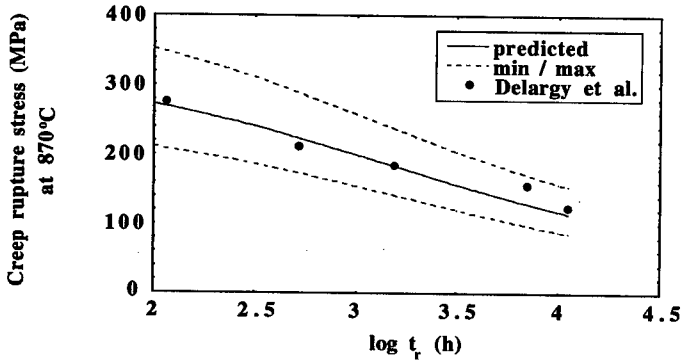

Figure 3: Predicted relation between the creep rupture stress and the lifetime of an Inconel 939 alloy at 870°C. Experimental points from [15].

DESIGN OF NEW ALLOYS

The above models, in combination with a knowledge of physical metallurgy and pricing considerations, have been used to design new creep-resistant nickel-base alloys for power-plant applications. A base alloy containing 15 to 20 wt% Cr is necessary to cope with the corrosive steam atmosphere, cobalt being avoided because of its high price. The main reinforcing elements in nickel-base alloys are Al and Ti (γ' formers)[7, 8], W, Mo, Ta and Nb (γ and γ' strengtheners) [12 - 14]. However, only Al, Ti and W have been chosen, first because of their relatively low price compared to Mo, Ta and Nb, but also because the Gaussian process model didn't infer a positive influence of the latter on the long-term creep rupture stress at 750 °C. Carbon must be included to form carbides which limit grain boundary sliding.
The candidates alloys have been selected on the basis of their predicted mechanical properties, and of their expected microstructure and thermodynamic stability.

1) Mechanical properties

The 750 °C, 10^5 h creep rupture stress of about 2000 alloys with different combinations of Cr, Al, Ti, W and C contents has been predicted. Selection has been made on successive criteria: a predicted minimum CRS above the design requirement of 100 MPa, an error bar smaller than 100 MPa and a relative error bar smaller than 35%. Amongst the remaining alloys, only the ones with the highest CRS/price ratio have been kept, the "price" estimation being based on a list of the relative cost of industrially used raw elements provided by INCO Alloys Ltd..
The predicted relation between the creep rupture stress at 750 °C and the lifetime of one of these alloys* is presented in figure 4.

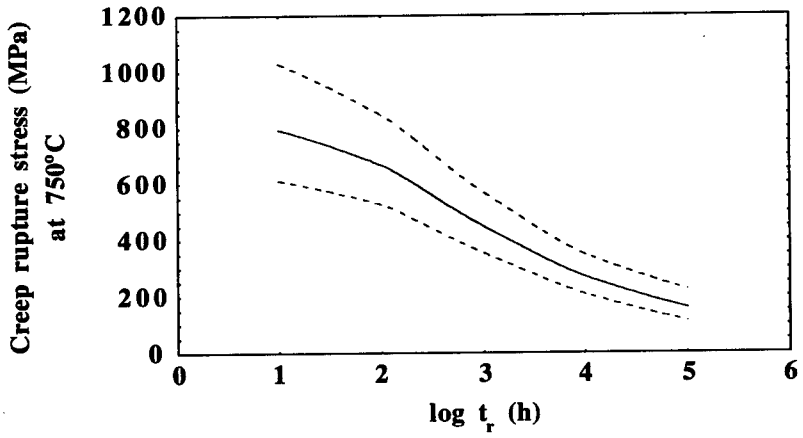

Figure 4: Predicted stress-lifetime relation for one of the candidate alloys at 750 °C.

The evolution of the yield stress of this alloy with temperature has also been predicted, and is presented in figure 5. The shape of this curve is typical of a γ'-strengthened γ matrix. The peak

* This work being part of an industrial project, the exact compositions of the candidate alloys are confidential.

effect results from the competition between the increasing strength of the γ' inclusions up to about 900 °C [16] and the softening of the γ matrix with increasing temperature.

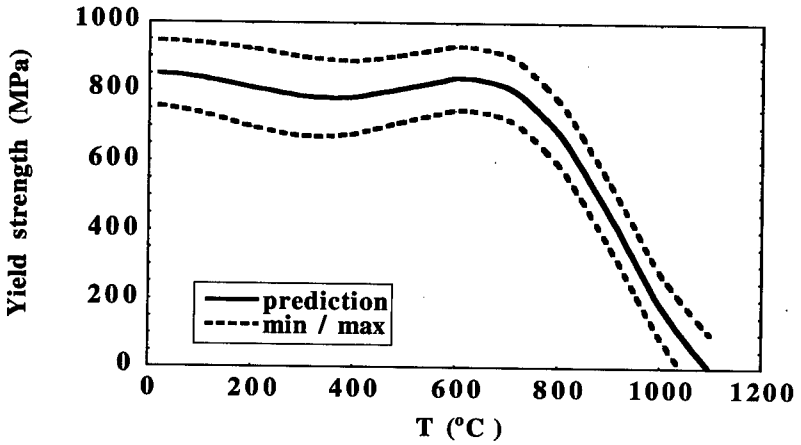

Figure 5: Predicted yield strength of one of the selected alloys as a function of temperature.

2) Thermodynamic simulation ("Thermocalc" [5])

Figure 5 shows the calculated relative amounts of all the phases expected in the temperature range 750 - 1400 °C, for the previously selected alloy (Ni-Cr-W-Al-Ti-C). It can be noted that only γ, γ' and $M_{23}C_6$ carbides are expected at service temperature (750 °C). In particular, no σ, μ, η nor Laves phases, which can be harmful to the creep resistance, are expected.
This graph also gives useful information for the processing of this alloy: it should be melted above 1360 °C, solidified in the range 1360 - 1330 °C, and forged in the range 1330 - 1070 °C, in the γ'-free region, to avoid cracking and a too high flow stress. Then, heat treatment could consist of a solutionising above 1070 °C, and of one or two γ' precipitation ageings below 1070 °C.

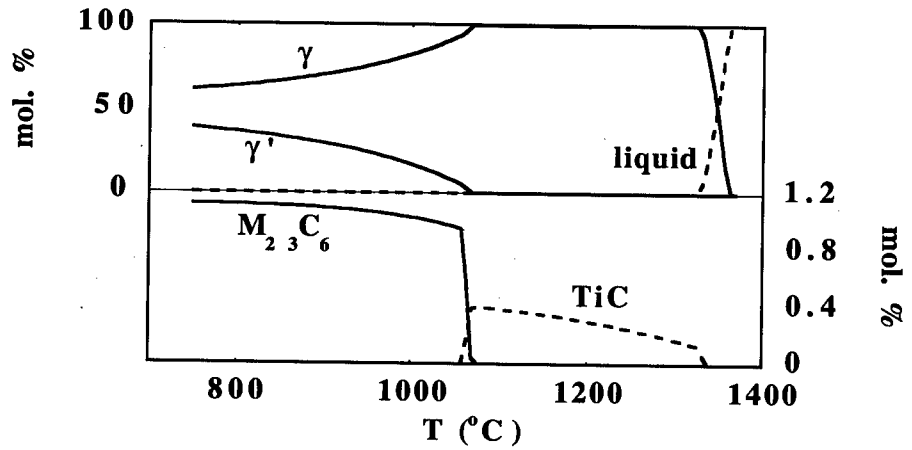

Figure 5: Calculated relative amounts of the phases expected in the selected alloy in the range 750 - 1400 °C.

CONCLUSIONS

A Gaussian processes computer modelling technique has been used to predict the yield strength and the creep rupture stress of novel nickel-base superalloys for high-temperature power-plant applications. A number of candidate alloys have been selected on the basis of their expected mechanical properties, and of their equilibrium phase diagrams at high temperatures. Promising results have been obtained.

However, further modelling is necessary, and the composition of the alloys should be refined, taking into account both metallurgical concepts and industrial requirements. For example, the alloys should not contain too much Al and Ti, since they are likely to increase the flow stress through γ' precipitation, and consequently to reduce the high temperature formability. Small amounts of boron and silicon should be added to ensure a good grain boundary quality and weldability, respectively. Finally, it will be necessary to predict the influence of other elements on both the mechanical properties and the phase equilibria, such as impurities (P, S...), or elements (Fe) whose presence can be due to the use of industrial scrap instead of pure raw materials.

ACKNOWLEDGMENTS

We are grateful to the Engineering and Physical Sciences Research Council for funding this work, and to Alstom Energy Ltd., British Steel plc., INCO Alloys Ltd., Mitsui Babcock Energy Ltd., Rolls-Royce Allen Steam Turines and the University of Wales, Swansea for partnership. The authors thank Dr Roger Reed for access to the Rolls-Royce UTC thermodynamic database on nickel-base superalloys. It is a pleasure to acknowledge all the help and support provided by Professor Colin Humphreys in the Technology Foresight Programme.

REFERENCES

[1] M.N. Gibbs, "Bayesian Gaussian processes for regression and classification", PhD Thesis, University of Cambridge, UK (1998).

[2] C.K.I. Williams and C.E. Rasmussen, in "Advances in Neural Information Processing Systems 8", MIT Press (1996).

[3] C.A.L. Bailer-Jones, H.K.D.H. Bhadeshia and D.J.C. Mackay, "Gaussian processes modelling of austenite formation in steel", to appear in Mat. Sci. Technol..

[4] F. Tancret, H.K.D.H. Bhadeshia and D.J.C. MacKay, "Comparison of artificial neural networks with Gaussian processes to model the yield strength of nickel-base superalloys", to appear in ISIJ Int..

[5] "Thermocalc", Royal Institute of Technology, Stockholm, Sweden (1999).

[6] "Tpros", Department of Physics, University of Cambridge, UK. Available on the Internet: http://wol.ra.phy.cam.ac.uk/mng10/GP/GP.html

[7] L.R. Cornwell, J.D. Embury and G.R. Purdy, Proc. 3rd Bolton Landing Conf. on Ordered Alloys, Baton Rouge, Claitors Publishing Co., (1970) p. 387.

[8] R.F. Miller and G.S. Ansell, Met. Trans., **8A** (1977) p. 1979.

[9] D. Raynor and J.M. Silcock, Metal Sci. J., **4** (1970) p. 121.

[10] A.P. Miodownik and N. Saunders, "Calculation of the APB energies in Ni-based superalloys", Thermotech Ltd., UK, Report to Rolls-Royce plc. (P24133), (1993).

[11] G.N. Maniar and J.E. Bridge, Met. Trans., **2** (1971) p. 95.
[12] Y. Mishima, S. Ochiai, N. Hamao, M. Yodogawa and T. Suzuki, Trans. Jap. Inst. of Metals, **27(9)** (1986) p. 656.
[13] J.P. Collier, P.W. Keefe and J.K. Tien, Met. Trans., **17A** (1986) p. 651.
[14] A.K. Jena and M.C. Chaturvedi, J. Mat. Sci., **19** (1984) p. 3121.
[15] K.M. Delargy, S.W.K. Shaw and G.D.W. Smith, Mat. Sci. Technol., 2 (1986) p. 1031.
[16] P. Beardmore, R.G. Davies and T.L. Johnston, Trans. Met. Soc. AIME, **245** (1969) p.1537.

Corresponding author: H.K.D.H. Bhadeshia, hkdb@cam.ac.uk

Key Engineering Materials Vols. 171-174 (2000) pp. 537-544
© 2000 Trans Tech Publications, Switzerland

Recovery of Creep Properties of Alloy 625 After Long Term Service

M.D. Mathew[1], K. Bhanu Sankara Rao[1], S.L. Mannan[1], K. Paknikar[2] and R. Singh[3]

[1] Indira Gandhi Centre for Atomic Research, Kalpakkam-603 102, India

[2] Heavy Water Board, Bombay-400 094, India

[3] National Metallurgical Laboratory, Jamshedpur-831 007, India

Keywords: Alloy 625, Creep, Life Extension, Ageing, Precipitation, Delta-Phase

ABSTRACT

Creep rupture properties of alloy 625, that has been in service for 60,000 h at 993 K, have been evaluated between 923 and 1173 K, after subjecting the service exposed material to resolution annealing treatment at 1433 K for one hour. The isostress and Larson-Miller parameter methods were employed to estimate the residual life of the service exposed material. Creep rupture strength and rupture ductility recovered substantially following re-solution annealing. The variations in rupture life and rupture ductility with creep test variables have been rationalised on the basis of the microstructural changes that occurred in the material.

INTRODUCTION

Nickel-base superalloys find widespread applications in aerospace and chemical industries. The choice for use of superalloys in chemical industries is primarily based on a good combination of its monotonic yield and tensile strength properties, good creep properties, excellent fabricability, weldability, and resistance to high temperature oxidation for prolonged exposures. A solid solution strengthened nickel base superalloy, alloy 625 containing 58 wt% (min.) nickel, 20-23 wt% chromium, 8-10 wt.% molybdenum, 5 wt.% iron, 3.15-4.15 wt.% niobium and 0.1 wt.% (max.) carbon[1] is being used as tubes in heavy water plants where ammonia is cracked into nitrogen and hydrogen. During normal operation, the cracker tubes are exposed to a temperature of

about 993 K and gas pressure of 14 MPa. At these conditions, the cracker tubes undergo creep deformation. Although the original design life of the tubes was 100,000 hours, some tubes failed after about 60,000 hours of operation necessitating premature replacement. Since replacement of the tubes is very expensive, studies have been carried out to extend the life of the service exposed tubes through rejuvenation heat treatments. It was established that a re-solution annealing treatment at 1433 K for one hour was beneficial to restore the tensile properties. The yield strength of the material decreased from 927 MPa after service exposure to 470 MPa on re-solution annealing as compared to 352 MPa for the virgin material. Similarly, the tensile elongation increased from 6% after exposure to 55% after re-solution treatment compared to 53% obtained for the virgin material. The present investigation is focussed on assessing the creep properties of the re-solution annealed tubes in the temperature range 923 to 1173 K. The microstructural changes that occurred in the alloy during stress-free thermal ageing of resolution annealed samples, and creep tested samples are discussed in detail.

EXPERIMENTAL PROCEDURE

One of the cracker tubes that failed after 60,000 hours of operation was used in the present investigation. The tube had a length of 13.5 m with an outside diameter of 88.9 mm and wall thickness of 7.95 mm. Figure 1 depicts the schematic view of the cracker tube assembly. Rectangular specimens with gauge dimensions of 25 mm length, 7 mm width and 4 mm thickness were machined from the solution annealed tubes. Two series of creep rupture tests, named as series-I and series-II, were carried out for determining the residual creep properties. The series-I tests were isostress tests conducted at six different temperatures between 1023 and 1148 K at intervals of 25 K. In all these tests, a constant stress level equal to 105 MPa was chosen, and the test temperatures were higher than the operating temperature of 993 K. The series-II tests were

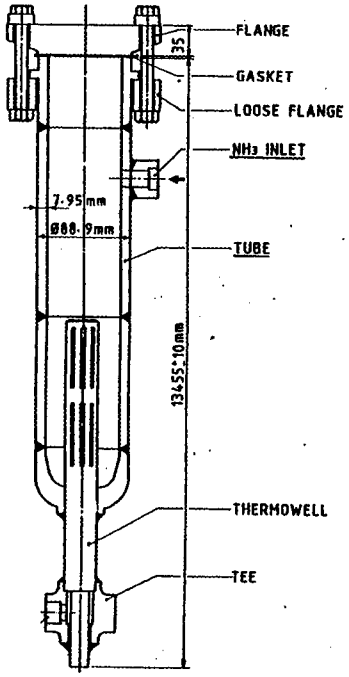

Fig.1. Schematic view of the cracker tube assembly.

conducted in a broad range of temperatures (923 to 1173 K) and stresses (100 to 600 MPa). The longest rupture time in the present investigation was about 32000 hours. In order to characterise the microstructural changes in a systematic way, samples were aged separately for 500 hours at different temperatures in the range of 923 to 1173K.

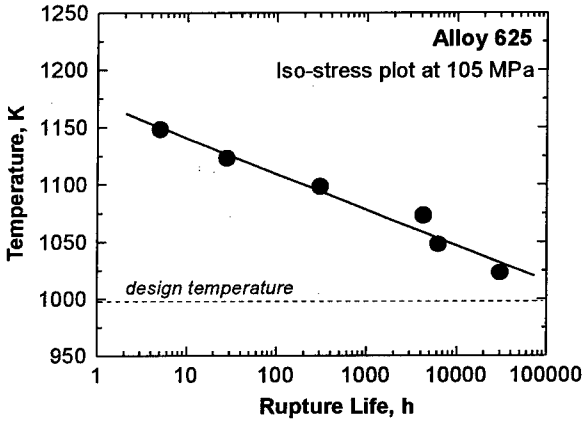

Fig. 2. An isostress plot of rupture life versus temperature of the re-solution annealed material at 105 MPa.

RESULTS AND DISCUSSION

Rupture Life

Among the various methods employed for estimating residual creep life of service exposed components, isostress method is considered to provide realistic estimates of the remnant creep life[2]. The method involves conducting a batch of creep tests at temperatures greater than the service temperature and stress close to the service stress, and then extrapolating the rupture life-temperature plot to the service temperature. On the other hand, a parametric approach is often employed to predict long-term rupture life of virgin materials using short-term laboratory data.

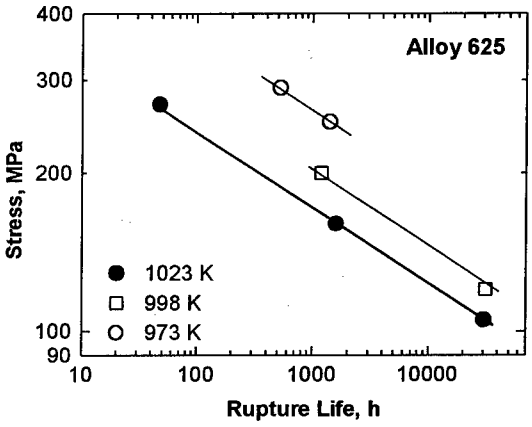

Fig. 3. Variation of rupture life with stress.

The design temperature and stress of the cracker tubes were 993 K and 70 MPa respectively. A factor of safety of 1.5 was assumed in the design taking the design stress to 105 MPa. An isostress plot of rupture life versus temperature (semi-log plot) of the re-solution annealed material at 105 MPa using series-I test results is shown in Figure 2. The

rupture life increased linearly with decrease in test temperature. Extrapolation of the statistically fitted straight line to the design operating temperature of 993 K gave a residual creep rupture life of about 250, 000 hours.

Isothermal plots of stress versus rupture life (log-log plot) at selected test temperatures using series-II test data are shown in Figure 3. Although the test program covered several temperatures in the range of 923 to 1173 K, data is not available at present at sufficient stress levels to plot the isothermals at all the test temperatures. Thus Figure 3 shows isothermal plots at 973, 998 and 1123 K only. These isothermal plots are linear and are parallel to one another with a slope of -0.16. Assuming that the Monkman-Grant relationship is valid for this material, this slope corresponds to a creep stress exponent of n=6 which suggests that the rate controlling deformation mechanism is dislocation creep.

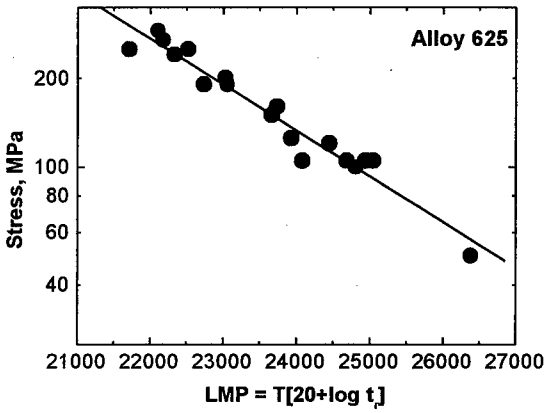

Fig. 4. Larson-Miller parameter plot.

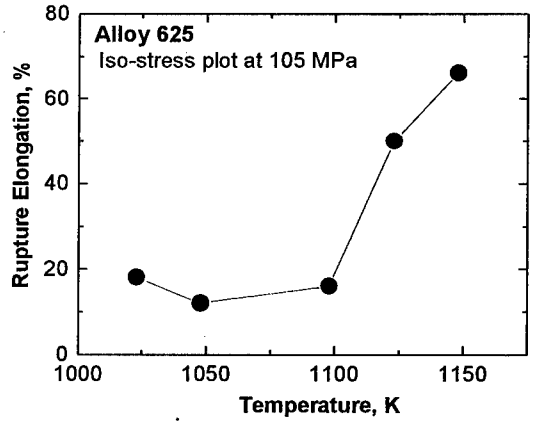

Fig.5. Variation of isostress ductility with temperature.

A Larson-Miller Parameter (LMP) analysis has been made using the data obtained from series-I and series-II tests. Figure 4 shows the variation of LMP with stress (semi-log plot). A value of 20 has been used for the constant C in the LMP equation[3] LMP = $T[C+\log t_r]$ where t_r is the rupture life and T is the temperature in K. A good statistical fit in the form $\sigma = 5.861 - 0.0001557$ LMP has been obtained, and the correlation coefficient R=0.97. Using Fig.4, a rupture life of 69,000 hours has been predicted at the design temperature of 993 K and stress of 105 MPa. This value is however lower than the rupture life predicted by the iso-stress test method by a factor of almost 3.5.

Rupture ductility

Figure 5 shows the variation of rupture elongation with temperature at a constant stress of 105 MPa. The material showed very good ductility (20-70%) at temperatures higher than 1100 K; ductility increased with increasing test temperature above 1100 K. At temperatures below 1100 K, rupture ductility varied in a narrow range of 10-20% and appeared to increase at temperatures below 1023 K. Analysis of the rupture ductility data at various temperature and stress levels from series-II tests showed that below 1050 K, the ductility was generally around 20% or less whereas at temperatures above 1050 K, rupture ductility was rather high.

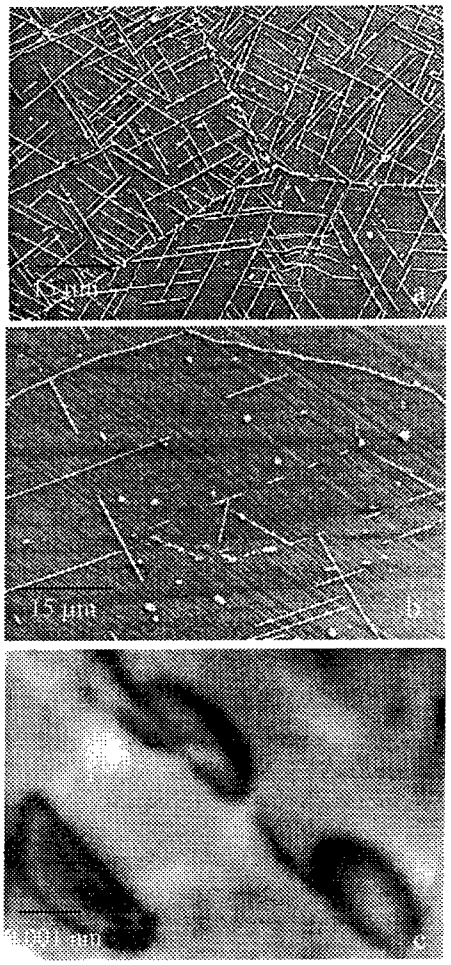

Fig. 6. δ-phase precipitates after
(a) creep tests at 1098 K for 300 h,
(b) ageing at 1173 K for 500 h and
(c) γ" precipitates after ageing at 973 K for 500 h

Precipitation Behaviour

Alloy 625 is microstructurally unstable on prolonged exposure at elevated temperatures. Carbides of type MC, M_6C, $M_{23}C_6$, and intermetallic phases of the type γ" and δ, precipitate in this alloy depending upon the temperature and duration of ageing[4,5,6,7,8,9]. γ" is a metastable phase with an ordered body centred tetragonal DO_{22} crystal structure of $Ni_3(Nb,Ti,Al)$ composition and is observed in Alloy 625 and Alloy 718 after elevated temperature ageing[4-9,10,11]. The equilibrium intermetallic precipitate is the δ-phase. This

niobium rich phase is incoherent, orthorhombic in crystal structure and precipitates typically with a needle-like morphology on ageing at high temperatures.

Microstructure of the creep tested, and aged samples were studied mainly using scanning electron microscope (SEM). The samples were given electrolytic etching using chromic acid to reveal the intermetallic phases. Below 1023 K, there was no evidence of any matrix precipitation and only grain boundary precipitates were observed. Above 1023 K, profuse precipitation of δ-phase, as identified by its acicular morphology, has been observed in the intragranular regions. Figure 6a shows δ-phase needles within the grains and carbides along the boundaries after creep testing at 1098 K for 300 hours. At still higher temperatures, there was an increase in the size and decrease in the density of the acicular precipitates. Figures 6b shows the δ-phase morphology after ageing at 1173 K. Energy dispersive analysis of x-rays was carried out on the needle shaped precipitates which confirmed that these are indeed rich in niobium as compared to the matrix. Although precipitates were not observed in SEM in material exposed upto 1023 K, it is well established that fine precipitates of γ" form in this material at temperatures above 873K [5,6]. Transmission Electron Microscopy (TEM) carried out on material aged at 973 K showed γ" precipitates with typical disc shaped morphology as shown in Fig. 6c. It is assumed that γ" precipitates of increasing size and density would be present at higher temperatures although extensive TEM studies were not performed at other ageing conditions.

Non-destructive studies conducted using stress-strain microprobe to investigate the tensile properties and hardness of this material aged at various temperatures showed a non-monotonic behaviour with a peak in yield strength, tensile strength, and hardness at 973 K[12]. This behaviour is consistent with the published literature. The peak strength and hardness are associated with the precipitation of γ" phase[7,8,10]. It is therefore suggested that the strengthening effect of γ" phase is responsible for the lower creep ductility observed below 1023 K. Precipitation and growth of δ phase results in loss of order strengthening derived from γ", and this promotes recovery of creep ductility at temperatures above 1100 K as was observed in this study. As regards the rupture life of the material is concerned, it appears that coarsening and dissolution of δ-phase does not have an adverse effect since rupture life decreased linearly with increase in test

temperature without any change in slope. But in the range of temperatures where γ" phase forms, this precipitate could have a detrimental effect on long term rupture strength and this needs to be confirmed from further tests.

CONCLUSIONS

Resolution annealing treatment was found to be beneficial to restore the creep rupture strength and ductility of service exposed Alloy 625 tubes. Isostress method predicted a residual rupture life of about 250,000 hours whereas Larson-Miller parametric method predicted a value lower by a factor of 3.5. Rupture ductility was very low at temperatures below 1023 K. Extensive precipitation of δ-phase was observed at temperatures greater than 1023 K.

ACKNOWLEDGEMENT

The authors wish to acknowledge Mr. Tiwari, NML, for his assistance in carrying out the creep tests.

REFERENCES

1. Standard specification for nickel alloy forging, ASTM E564-95A, *Annual Book of ASTM Standards*, Vol. 20.4, Section 2, 1996, American Society for Testing and Materials, USA, Vol.20.4, 1996.
2. R. Viswanathan in *Damage Mechanisms and Life Assessment of High Temperature Components*, ASM International, USA, 1990, p.59.
3. L. Ferrer, B.Pieraggi and J.F.Uginet in *Superalloys 718, 625 and Various Derivatives*, Edward E Loria (ed.), The Minerals, Metals and Materials Society, USA, 1991, p.217.
4. J.W. Brooks and P.J. Bridges in *Superalloys 1988*, S.Reichman, D.N. Dubil, G. Maurer, S. Antolovich and C. Lund (eds.), The Metallurgical Society, 1988, p.33.
5. L. Ferrer, B.Pieraggi and J.F.Uginet in *Superalloys 718, 625 and Various Derivatives*, Edward E Loria (ed.), The Minerals, Metals and Materials Society, USA, 1991, p.217.
6. M.Kohler, *ibid*,p.363.
7. R.Cozar, M.Rouby, B.Mayonobe and C.Morizot, *ibid*, p.423.
8. Chantal Vernot-Loirer and Francosis Cortial, *ibid*, p.409.
9. John F Radavich and Andrea Fort, *ibid*, p.635.
10. C.R.Conder and G.D.Smith in *Superalloys 718, 625, 706 and Various Derivatives*, Edward E Loria (ed.), The Minerals, Metals and Society, USA, 1997, p.447.
11. M.Sundararaman, P.Mukhopadhyay and S.Banerjee, *ibid*, p. 367.
12. M.D. Mathew, K.L. Murty, K.B.S. Rao and S.L. Mannan, *Mater. Sci. Engg.* A264 (1999)159.

Author for correspondence: K. Bhanu Sankara Rao, email – bhanu@igcar.ernet.in

Key Engineering Materials Vols. 171-174 (2000) pp. 545-552
© 2000 Trans Tech Publications, Switzerland

Extension of an Anisotropic Model of Creep in Single Crystal Superalloys to Variable Loading and Multiaxial Loading

H. Basoalto, M. Ardakani, R.N. Ghosh, B.A. Shollock and M. McLean

Department of Materials, Imperial College of Science, Technology and Medicine, Prince Consort Road, London SW7 2BP, UK

Keywords: Continuum Damage Mechanics, Single Crystal Superalloys, Anisotropic Deformation, Finite Element Calculations

Abstract

An understanding of the mechanisms controlling the anisotropic deformation of single crystal superalloys is a prerequisite for establishing reliable constitutive laws for engineering design. It is clear that the anisotropy in creep strength cannot be explained in terms of Schmid law concepts and the operation of a single slip system. A model, that considers the simultaneous operation of two families of slip systems, $(11\bar{1})\langle 101\rangle$ and $(100)\langle 011\rangle$, has been shown to describe well: (i) an extensive database of uniaxial creep curves in the temperature range 750 to 950°C, (ii) crystal rotations during creep deformation, (iii) specimen shape changes resulting from creep deformation. This paper will give an extension of the model to account for time dependent deformation in a range of more complex loading conditions.

1. Introduction

The increasing demand for performance and efficiency of industrial gas turbines has resulted in the introduction of single crystal superalloys as blade materials. The design of an industrial gas turbine must take into account the cost of the components during their service life, and control of costs is very much dependent of the ability to predict reliably the service life of a component. Continuum damage mechanics (CDM) has proved to be a useful means of describing the high temperature deformation of engineering alloys. It has its origins in the phenomenological single state variable model of Kachanov [1], and has been modified by various workers [2-5].

The model presented in this paper has its origins from the *CRISPEN* analysis developed by Ion. *et. al* [4]. Two state variables are used to describe the plastic creep behaviour. The first of these variables, H, attempts to describe the redistribution of stress between the matrix γ and the γ' particles of a superalloy. The second is a damage variable, ω, associated with the strain-softening arising from an increase in the density of mobile dislocations, which are confined to the γ-phase of single crystal superalloy. The constitutive equations can be expressed as

$$\begin{aligned} \dot{\varepsilon} &= \dot{\varepsilon}_0(1-S)(1+\omega) \\ \dot{S} &= \dot{\varepsilon}_0 H(1-S/S_{ss}) \\ \dot{\omega} &= C\dot{\varepsilon} \end{aligned} \qquad (1)$$

where $\dot{\varepsilon}_0, H, S_{ss}$, and C are model parameters and their values determine the shape of the

strain/time trajectory. The stress/temperature dependence of the creep strain rate has been incorporated into the model parameters (Pan. *et. al* [6]).

This paper will focus on the predictions of a generalised CDM model for cases of complex variable loading and multiaxial loading. In particular, the model will be used to determine creep curves, stress-strain response at some constant applied strain rate for the single crystal superalloy CMSX4. Also, the effect of changing test conditions on the strain-time trajectory will be addressed, and compared model predictions with strain and time hardening theories.

2. Anisotropic Slip-Formulation for Complex Loading Conditions

Consider a specimen of a single crystal superalloy stressed uniaxially in a direction $\boldsymbol{T} = <hkl>$ (see Fig. 1). The applied stress, σ, will result in a virtual force $f = \tau b$ that will drive a dislocation's motion, where τ is the shear stress acting on the slip plane and b the magnitude of the Burger's vector. Let the activated slip systems be denoted by the unit vectors $\left(\boldsymbol{m}^{(k)}, \boldsymbol{n}^{(k)}\right)$, with $\boldsymbol{m}^{(k)}$ being the slip direction and $\boldsymbol{n}^{(k)}$ is the slip plane normal. Then, the shear stress acting on the k-th slip system is given by

$$\tau^{(k)} = n_i^{(k)} \sigma_{ij} m_j^{(k)} \tag{2}$$

where σ_{ij} is the stress tensor. For single crystal superalloys it is assumed that two families of slip systems are activated: the octahedral system $\{111\}<1\bar{1}0>$ and cube system $\{001\}<110>$.

The constitutive equations (1) have been extended to anisotropic deformation by Ghosh *et. al* [5] and Pan *et. al* [6] giving rise to the following relations for each slip system:

$$\begin{aligned} \dot{\gamma}^{(k)} &= \dot{\gamma}_0^{(k)} (1 - S^{(k)})(1 + \omega^{(k)}) \\ \dot{S}^{(k)} &= \dot{\gamma}_0^{(k)} H^{(k)} (1 - S^{(k)} / S_{ss}^{(k)}) \\ \dot{\omega}^{(k)} &= \beta^{(k)} \dot{\gamma}^{(k)} \end{aligned} \tag{3}$$

$(\forall k \in G)$ where $G = \{111\}<1\bar{1}0>$ or $G = \{001\}<110>$ and $\dot{\gamma}_0^{(k)}, H^{(k)}, S_{ss}^{(k)}$, and $\beta^{(k)}$ are model parameters for the anisotropic formulation, which are directly related to the isotropic formulation model parameters through the Schmid factor.

The model parameters for equation (3) were obtained using an optimisation procedure outlined in Basoalto *et. al* [6]. Determination of the creep strain from the above equation set is carried out using the small strain approximation, i.e., that any large deformation can be viewed as been the result of consecutive smaller deformations. By discretisation of the time into a number of intervals, Δt, the incremental shear strain, $\Delta\gamma^{(k)}$, on each activated slip system can be calculated. The deformation is described in terms of a Lagragian formulation, as we are interested in predicting the uniaxial engineering stress/strain response. It can be shown that the displacement gradient tensor, ΔJ_{ij}, is given by

$$\Delta J_{ij} = \sum_{s \in G} \Delta\gamma^{(k)} n_i^{(k)} m_j^{(k)} \tag{4}$$

Using the small strain approximation, the strain tensor becomes the symmetric part of ΔJ_{ij}. This leads to:

$$\Delta\varepsilon = \frac{1}{2}\left[\Delta \boldsymbol{J} + \Delta \boldsymbol{J}^T\right] \tag{5}$$

For the case of a tensile test the engineering strain is obtained from $\Delta\varepsilon$ by projecting $d\boldsymbol{T} = \Delta\varepsilon.\boldsymbol{T}$ onto $\boldsymbol{T}$. Finally, the uniaxial creep strain at each time step is given by

$$\varepsilon_c(t_i) = (d\boldsymbol{T}).\boldsymbol{T} \tag{6}$$

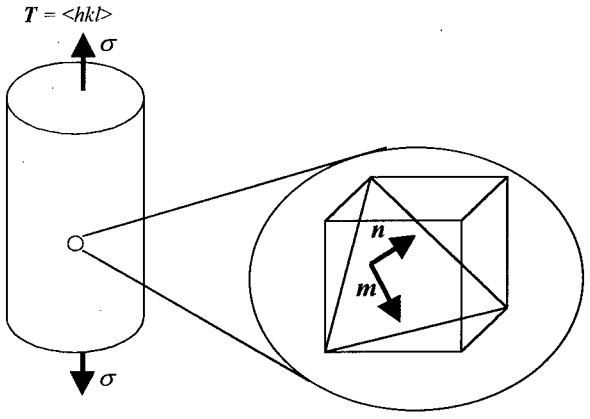

Fig. 1

So far the slip formulation has been developed for the case of a uniaxially applied constant stress. The extension of the model to complex loading conditions requires that the relationship between the applied stress and creep strain be specified. By decomposition of strain rates into an elastic and plastic (creep) response, it is possible to write the following expressions for the evolution of the applied stress, σ,

$$\dot{\sigma} = E_{.\,hkl}.(\dot{\varepsilon}_T - \dot{\varepsilon}_c) \tag{7}$$

$$\frac{1}{E_{.\,hkl}} = S_{11} + [S_{44} - 2(S_{11} - S_{12})](h^2k^2 + k^2l^2 + l^2h^2)$$

where $E_{.\,khl}$ is Young's modulus in a specified crystal direction $<hkl>$ (see Nye [7]), S_{ij} the compliance tensor, $\dot{\varepsilon}_T$ is the total strain rate, and $\dot{\varepsilon}_c$ is given by equation (6). The stress increment is calculated from the above relations for each time step Δt, and the resulting stress is projected on each active slip system to determine the shear strain.

If the appropriate boundary conditions are specified, the coupling of the constitutive equations (2) with equation (7) allows the simulation of any complex uniaxial mechanical deformation. Some common uniaxial mechanical tests are described by the following

boundary conditions:

- Constant stress creep test $\dot{\sigma} = 0$;
- Stress Relaxation $\dot{\varepsilon}_T = 0$;
- Strain controlled tensile/compressive test $\dot{\varepsilon}_T$ = constant;
- Strain controlled fatigue test $\dot{\varepsilon}_T = f(t)$.

The next section will present model predictions for some of the cases outlined above.

3. Results and Discussion of Model Predictions

Creep tests

Model predictions for constant stress creep tests are shown in Fig. 2. The model parameters were calibrated for the single crystal CMSX4 with orientation <001> and <111>. Using the numerical procedure outlined in [8], a global parameter set was determined. The term global means that the parameters obtained can describe the strain-time response for a range of stress and temperature conditions. Model predictions and experiments are in good agreement, falling within the scatter of the creep data.

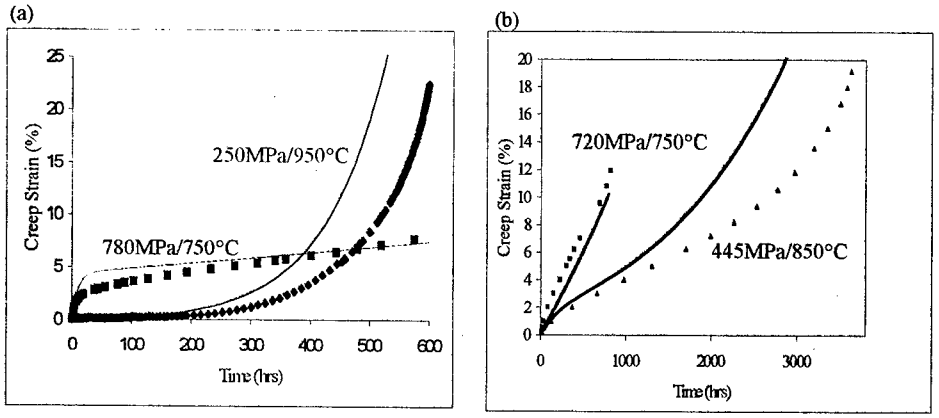

Fig. 2 Strain-time trajectories. Comparison of model predictions with experimental data. (a) CMSX4 <001>. and. (b) CMSX4 <111>.

Tensile test

Here the total strain rate, $\dot{\varepsilon}_T$, is constant throughout the test. The stress-strain response for <001> and <111> orientated at 850°C crystal are shown in Figures 3 and 4 for various strain rates. The general shapes of the $\sigma - \varepsilon_T$ curves obtained from the slip-model are in good agreement with the experimentally measured stress-strain curves. The model is able to predict reasonably the magnitude of the maximum stress and the fall in stress for as the total strain increases. The fall in the stress is a result of the accumulation damage for increasing creep strain.

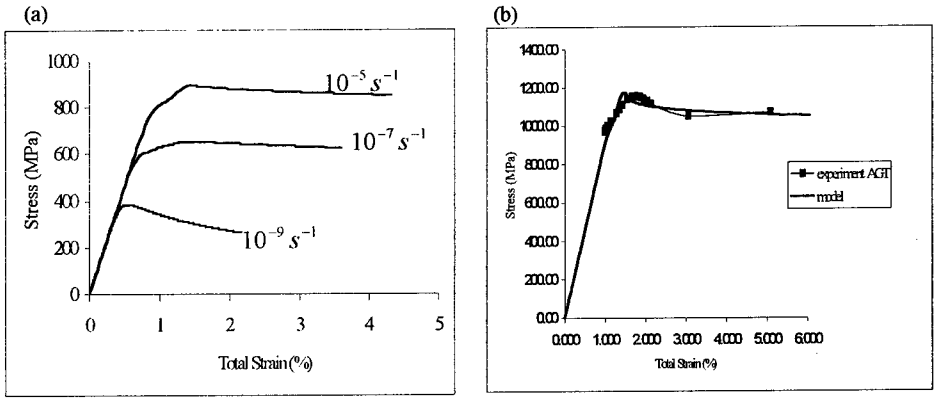

Fig. 3 Stress-strain curve predictions using the CDM model for the single crystal CMSX4 <001> at 850°C. (a) Effect of strain rate, and (b) comparison of model prediction with experimental data for $\dot{\varepsilon}_T = 0.001s^{-1}$.

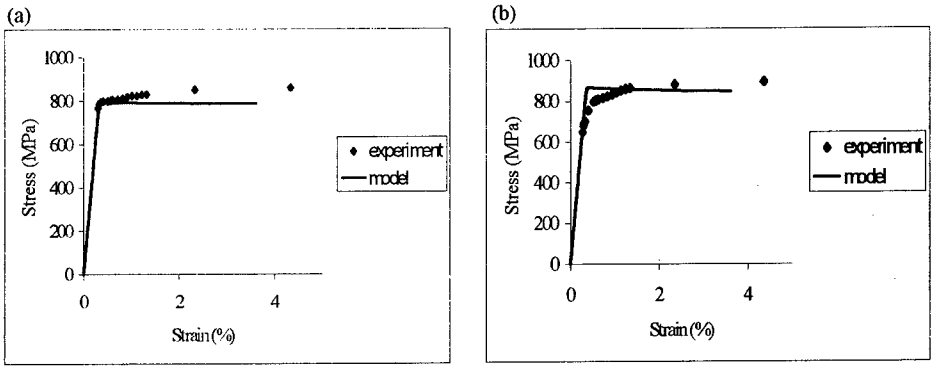

Fig. 4 Stress-strain curve predictions using the CDM model for the single crystal CMSX4 <111> at 850°C. (a) $\dot{\varepsilon}_T = 0.001s^{-1}$, and (b) $\dot{\varepsilon}_T = 0.01s^{-1}$.

Stress-Temperature Changes

An important problem in high temperature deformation is the effect of variable stress/temperature conditions on the resultant deformation. Due to the fact that most of the experimental data available are for the constant stress condition, variable stress/temperature theories have developed as an extension of the constitutive equations for constant stress. Two important constructions include strain and time hardening. Figure 5(a) shows two creep curves for 700MPa/750°C and 400MPa/850MPa given by the model, which have similar lifetimes but quite different properties of primary and tertiary creep. The prediction of the strain-time trajectory after a change in the stress/temperature conditions from 700MPa/750°C to 400MPa/850Mpa is shown in Fig. 5(b). The change was made at a time $0.3t_f$, where t_f is the time to reach a creep strain of 20% for the initial test condition (with no change in the test conditions). All three

methods (CDM, strain and time hardening) give different predictions for the resultant creep curve.

The CDM model predicts a longer lifetime than strain or time hardening. It was found that the effect of changing the test conditions was to force the hardening variable, S, to decrease. This is to be expected, since at higher temperatures primary creep in single crystal superalloys is not present. Repeating the calculation with the high temperature condition applied first gives the shortest life for the CDM prediction.

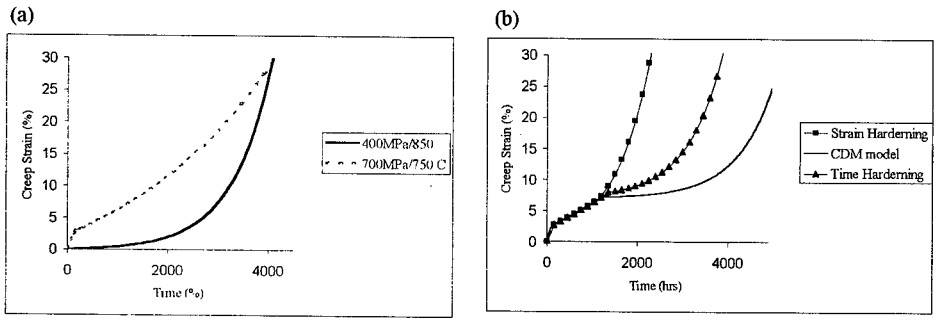

Fig. 5 Change in test conditions during creep for CMSX4 <001>. (a) Simulated creep curves for 700MPa/750°C and 400MPa/850°C. (b) Predictions of resultant creep response using CDM, strain hardening, and time hardening theories.

Finite Element Calculations

Interfacing the slip-based formulation to the commercial finite element software ABAQUS has been achieved through a user-defined subroutine for the calculation of incremental creep strain at each time step. Creep in a Bridgman notch specimen has been modeled using the C3D8 element except along the center where a C3D6 element has been used. The distribution of equivalent strain and Mises stresses after 0.5% creep strain (for Norton creep) is shown in Fig. 6. It is clear from Fig. 6 that the stress redistribution and strain accumulation are localised. The local strain near the notch root can be as large as 5% even though the overall strain is 0.5%. On the contour plots both stress and strain distributions show four-fold symmetry about the tensile axis.

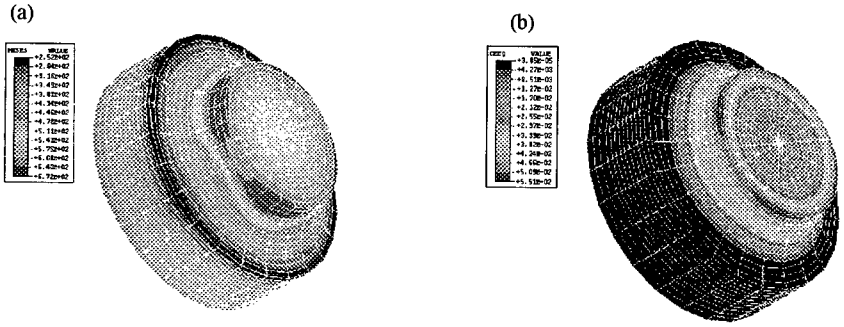

Fig. 6 Bridgman notch specimen. Finite element calculations showing the equivalent strain and stress redistribution.

Conclusion

- The CDM slip formulation expressed by equation (2) has been extended to complex variable loading formulation by the addition of equation (7).
- The model parameters were calibrated against a limited creep database for the single crystal superalloy CMSX4 with <001> and <111> orientations, from which a global parameter set was obtained. The strain-time trajectories predicted by the slip model are in good agreement with the measured creep curves (Fig. 2).
- In the case of high temperature deformation the total strain can be decomposed into elastic and plastic creep strains. For the case of a constant applied strain rate test it was found that the maximum stress was higher for a <001> than a <111> orientated crystal for a given applied strain rate (Figs. 3 and 4). The predictions again were shown to be in general agreement with the experimental data.
- Simulation of creep strain by CDM for changing stress and/or temperature gives different predictions as those for strain or time hardening.
- The slip-formulation has been incorporated into a finite element procedure.

Acknowledgements

The work was made possible by support from the Engineering and Physical Science Research Council (Grant Numbers GR/J02667, GR/K19358; Visiting Fellowship GR/L67042), the Defence Evaluation and Research Agency and BRITE EURAM III Project BE 96-3911.

References

1. L.M.Kachanov, *Izv Akad. Nauk S.S.R.* **8**, 26 (1958)

2. Yu. N.Rabotnov, *Proc. XII IUTAM Congress*, Stanford (edited by H. Hetenyi and W. G.Vincenti), p. 342, Stringer, Berlin (1969)

3. F.A.Leckie and D.R.Hayhurst, *Acta metall.* **25**, 1059 (1977)

4. J.C. Ion et al., "The Modelling of Creep for Engineering Design - I," (Report DMA A115, The National Physical Laboratory, Teddington 1986)

5. R.N. Ghosh, R.V.Curtis and M.McLean, *Acta Metall. Mater.*, 38 (1990), pp.1997

6. L-M.Pan, B.A.Shollock and M.McLean, *Proc. R. Soc. Lond.* A (1997) **453**, 1689-1715.

7. J.F.Nye, In *Physical Properties of crystals*. Oxford University Press (1957).

8. H.C.Basoalto, R.N.Ghosh, B.F.Dyson, and M.McLean, *Creep Modelling of Superalloys: Numerical Optimisation of Parameters*, Proceedings of Modelling of Microstructural Evolution in Creep Resistant Materials, 1998 (in press)

Key Engineering Materials Vols. 171-174 (2000) pp. 553-560
© 2000 Trans Tech Publications, Switzerland

Creep in Single Crystals of γ Single Phase Ni-20Cr Alloy and Evolution of Dynamic Recrystallization

T. Matsuo[1], S. Takahashi[2], Y. Ishiwari[3] and Y. Terada[1]

[1] Department of Metallurgy and Ceramics Science, Tokyo Institute of Technology, Meguro-ku, Tokyo 152-8552, Japan

[2] Graduate student, currently at IHI Co., Ltd.

[3] Graduate student, currently at Mitsubishi Material Co., Ltd.

Keywords: Creep, Single Crystal, Nickel Based Alloy, Dynamic Recrystallization, Microstructure

Abstract

The creep rate - time and the creep rate - strain curves of the single crystals of γ single phase Ni-20mass%Cr alloy have been investigated at 1173 K under the wide stress range of 19.6 to 98 MPa, and compared with those of polycrystals. The orientation corresponding to the stress axis of the single crystals were chosen within the standard stereographic triangle. The creep curve in the Ni-20mass%Cr single crystal consists of a transient stage and an accelerating stage without a steady state stage. The transient stage has two steps. In the first step, the creep rate slightly decreases, and in the second step, the decrease in creep rate becomes prominent with increasing the testing time. With decreasing the stress, the extension of transient stage becomes prominent, and by this extension, the decreasing ratio of the creep rate in transient stage is enlarged. At the lowest stress of 19.6 MPa, the most prominent extension of transient stage and the more than two order decrease in creep rate in transient stage are detected. The creep interrupting tests have been conducted at the stress of 29.4 MPa in the strain range of 0.1 to 0.6 to examine the appearance of dynamically recrystallized grains. At the strain of 0.1 corresponding to the end of the first step in transient stage, a straight subboundary parallel to slip plane appears in a wide distance of a few hundreds micrometers. With increasing the strain, the straight subboundary turns to waved one. At the strain showing the minimum creep rate, a lot of evolved subgrains appear. At the strain corresponding to the early stage of accelerating creep, dynamically recrystallized grains appear. It is confirmed that the onset of accelerating creep well corresponds to the appearance of dynamically recrystallized grains. In the single crystal creep ruptured, the whole gage portion turns to polycrystal with equiaxed grains having a diameter of 150 μm.

1. Introduction

There are many reports on the creep deformation in single crystal Ni-based superalloys [1-5]. The features of creep deformation in a γ single phase single crystal comparing to those of a polycrystal have not been understood, because of the restricted number of reports [6, 7]. Based on the reports of Ni-based single crystal superalloy, the features of creep deformation in the single crystal are characterized by the extensions of a steady state stage and an accelerating stage [8]. This understanding will be derived from the conception that the onset of accelerating creep is caused by the formation of crack at the grain boundary and the acceleration of creep rate is caused by the propagation of crack. Therefore, in the creep of single crystal without grain boundary, onset of accelerating creep and acceleration of creep rate must be fully suppressed. Using a γ single phase polycrystal alloy which has excellent ductility, it was elucidated that the onset of accelerating creep is connected not with the formation of crack, but with the appearance of dynamically recrystallized grains through the evolution of subboundary [9]. However, the increase in creep rate cannot be interpreted by the appearance of grain boundary, according to the

following equation [10];

$$\dot{\varepsilon} = A(b/d)^p(\sigma/E)^n \exp(-Q_c/RT), \quad (1)$$

where A is the material constant, b is the burgers vector, d is the average grain diameter, σ is the applied stress, E is the elasticity, Q_c is the activation energy for creep, R is the gas constant, T is the absolute temperature and p is the grain diameter exponent of creep rate. In case of dislocation creep, the value of p is zero [11], thereby the increase in grain boundary area through dynamic recrystallization does not affect the creep rate. Contrast to this, there are many reports detecting the dependence of grain diameter on creep rate [12]. The grain diameter dependence of creep rate is recently interpreted by a *Core-Mantle model* proposed in the previous paper [13]. This model is based on the conception that the predominant creep deformation occurs in the region near grain boundary. This region is named a *mantle region*. The increase in grain boundary area means the increase in the mantle region. So the appearance of dynamically recrystallized grains is resulted in the increase in creep rate. It is noteworthy that the γ single phase single crystal can be regarded as the most ductile material. By using such a ductile material, the formation of crack is fully suppressed. And it was reported in the γ single phase polycrystal that good agreement of onset of accelerating creep with the appearance of dynamically recrystallized grains is confirmed under the stress less than a certain value. So in the creep of γ single phase single crystal, firstly creep rate - time curves or creep rate - strain curves must be investigated as a function of stress.

2. Experimental

A Ni-20mass%Cr alloy, designated as Ni-20Cr in this paper, was prepared for this study. The chemical composition of the alloy is shown in **Table 1**. The alloy was melted in a high frequency induction furnace in a vacuum and was cast into a 4 kg ingot in an argon atmosphere. The ingot was hot-forged into a rod with a diameter of 13 mm. Single crystals were grown by a modified Bridgman furnace in a flow of purified argon and then solution-treated at 1523 K for 36 ks in air. The crystal orientation was determined by Laue back-reflection X-ray technique. The orientations of the stress axis in the single crystals are located within the standard stereographic triangle. In order to minimize the effect of misorientation, only crystals located near the center of the standard stereographic triangle were employed for this study. Note that all the crystals have Schmid factor above 0.46. Fullsized creep specimens with a gage portion of 30 mm in length and 6 mm in diameter were prepared.

Table 1. Chemical composition (mass%) of crystals prepared in this investigation.

Alloy	C	Si	Mn	Cr	Ni
Ni-20Cr	0.001	0.49	0.30	19.3	Bal.

The constant stress tensile creep tests were carried out at 1173 K in the wide stress range of 19.6 to 98 MPa. The constancy of stress was obtained by adjusting the auxiliary weights. The fluctuation of stress during creep was restricted within one per cent against initial stress. Creep tests at 29.4 MPa were interrupted at the strains of 0.1, 0.5, 0.73 and 0.76. Creep strain was automatically recorded through linear variable-differential transducers attached to the extensometer settled to both annular ridges of the gage portion of the specimen. Microstructures subject to creep at 29.4 MPa were examined by an optical microscope on sections parallel to the stress axis. The creep at 29.4 MPa - 1173 K showed an anisotropic deformation, therefore, the widest section parallel to the stress axis was adopted for the observation by the optical microscope. After metallographic polishing, samples were etched in a solution of orthophosphoric acid saturated with chromium trioxide with a current density of 10 mA/cm^2 for 10 minutes.

3. Results

3.1. Creep characteristics of Ni-20Cr single crystal

Creep rate - time curves of Ni-20Cr single crystals at 1173 K in the stress range of 19.6 to 98 MPa are shown in **Fig. 1**, together with those of polycrystals. The creep curves of Ni-20Cr polycrystals with the grain diameter of 200 μm were referred from the previous paper [14]. In each stress, the curve of the single crystal consists of the transient stage and the accelerating stage, and there is no steady state stage. The transient stage is divided into two steps. In the first step, creep rate slightly decreases. In the second step, the decrease in creep rate becomes prominent with increasing the testing time. At the time when the transient stage turns to the accelerating stage, creep rate shows the minimum value. The decreasing ratio of the creep rate during the transient stage becomes large with decreasing the stress, typically less than 49.0 MPa. In the transient creep stage of creep at 19.6 MPa, the decreasing ratio of creep rate becomes more than two orders of magnitude. The creep test at 29.4 MPa was interrupted at the time corresponding to the beginning of accelerating creep stage. And the creep test at 19.6 MPa was interrupted during the transient stage. Comparing the creep rate - time curves of the single crystals with that of the polycrystals, the marked difference is recognized at the stress less than 49 MPa. With decreasing the stress, the following two creep features in single crystal become prominent by comparing with those in polycrystal.

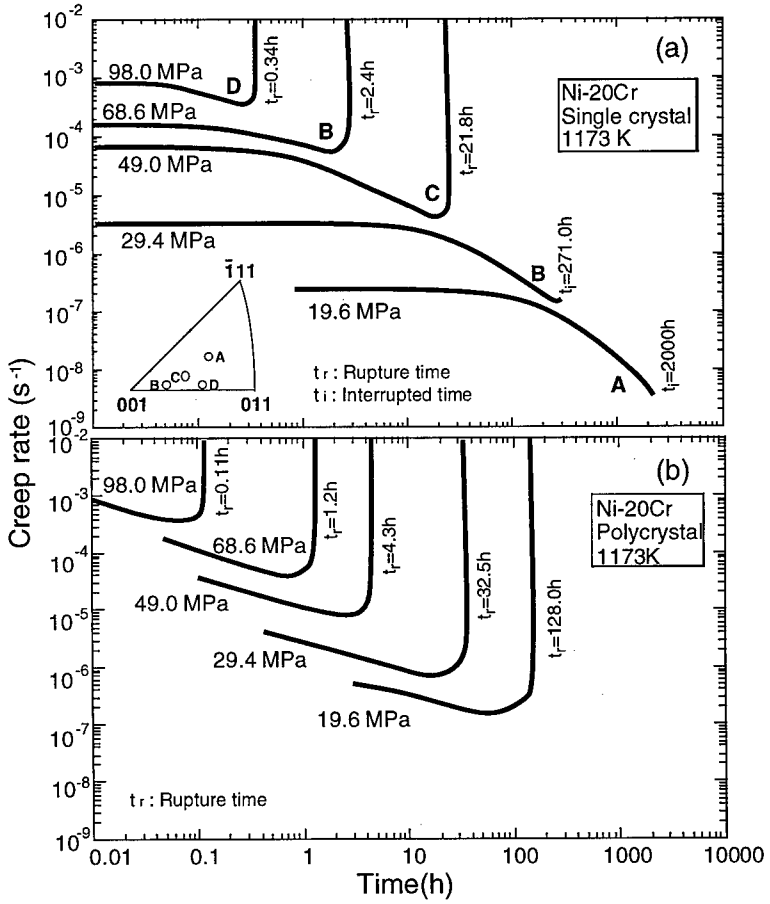

Fig. 1. Creep rate - time curves of Ni-20Cr single crystals at 1173 K in the stress range of 19.6 to 98 MPa (a), together with the curves of polycrystals (b).

1) Extension of transient stage
2) Decrease in the minimum creep rate

Creep rate - strain curves of Ni-20Cr single crystals are shown in **Fig. 2**, together with those of polycrystals [14]. The difference in the creep rate - strain curves of the single crystals comparing with those of the polycrystals is characterized by the five times larger creep strain in the single crystal. At 68.6 MPa, three times enlargement of transient creep strain was attained in the single crystal compared with that of the polycrystal. Contrast to this, the eight times enlargement of transient creep strain was obtained in the single crystal compared with that of the polycrystal. It is elucidated that the enlargement of transient creep in the single crystal compared with the polycrystal becomes larger at lower stresses.

The minimum creep rates at 1173 K in the single crystal were plotted as a function of applied stress as shown in **Fig. 3**, together with that in the polycrystal [14]. At the stress higher than 40 MPa, there is no difference in the minimum creep rate between the single crystal and the polycrystal. At the stress less than 40 MPa, the minimum creep rate in the single crystal is smaller than that in the polycrystal, and this difference in the minimum creep rate becomes prominent with decreasing the stress. This prominent decrease in the minimum creep rate in the single crystal crept at lower stress is derived by the drastic extension of transient stage.

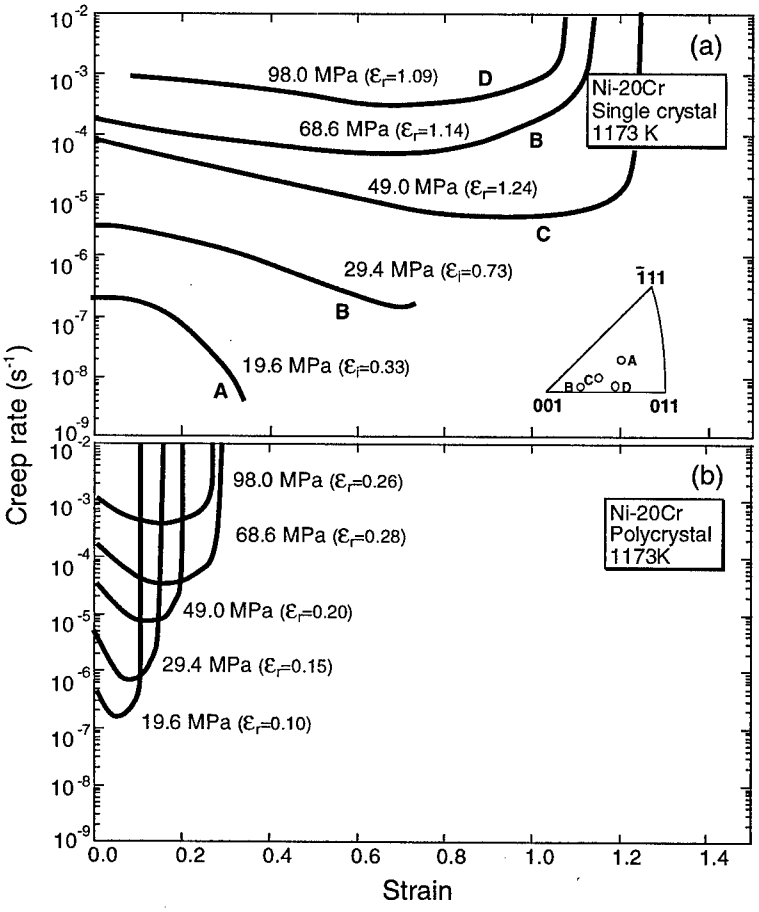

Fig. 2. Creep rate - strain curves of Ni-20Cr single crystals at 1173 K in the stress range of 19.6 to 98 MPa (a), together with the curves of polycrystals (b).

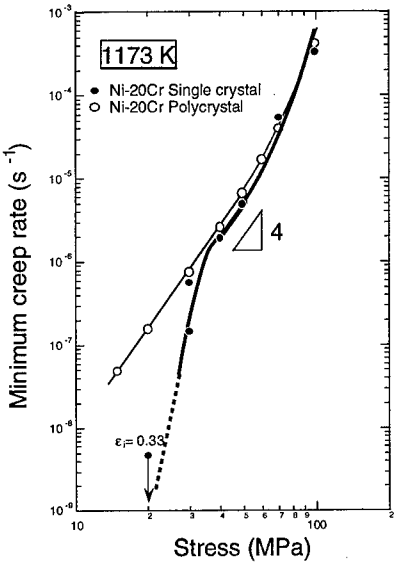

Fig. 3. Stress - minimum creep rate curve of Ni-20Cr single crystal at 1173 K, together with the curve of Ni-20Cr polycrystal.

3.2. Dynamic recrystallization in single crystal subject to creep at lower stress

The features of creep in the single crystal were emphasized at lower stresses. Then the microstructural observation for the specimen subject to creep at the lower stress must be done, and the attention must be focussed on the examination to elucidate the evolution of dynamic recrystallization. Optical micrographs of the single crystals creep interrupted at 1173 K - 29.4 MPa at the strains of 0.1 to 0.76 are shown in **Fig. 4**. Microstructural observations were done against the section parallel to stress axis and having the widest width as shown in **Fig. 4**. The direction marked by an arrow in photograph indicates the stress axis. Straight subboundaries are firstly detected in the single crystal creep interrupted at the strain of 0.1 as shown in **Fig. 4 (a)**. The straight subboundaries are located with a wide distance of a few hundreds micrometers. At the strain of 0.5, the straight subboundary turns to waved one (**Fig. 4 (b)**). At the strain of 0.73 corresponding to the strain showing the minimum creep rate, a lot of evolved subgrains appear as shown in **Fig. 4 (c)**. At the strain of 0.76 corresponding the strain at the early stage of accelerating creep, dynamically recrystallized grains appear (**Fig. 4 (d)**). In the crystal creep ruptured, the whole gage portion turns to polycrystal with equiaxed grains with a diameter of 150 μm as shown in **Fig. 4 (e)**.

4. Discussion

From the analysis of creep rate - time curves at 1173 K in the wide stress range of 19.6 to 98 MPa in γ single phase single crystals, the following features are elucidated.

1) The creep rate - time curve of single phase single crystal consists of transient stage and the accelerating stage, and steady state stage which has been considered to occupy most of the creep stage disappears.

2) The longer rupture life in single crystal than in polycrystal is resulted not in the extension of the steady state stage and the accelerating stage [8], but in the extension of the transient stage.

3) Contrast to the creep rate equation proposed under the dislocation creep condition, creep rate in γ single phase single crystal is smaller than that in polycrystal. This is resulted in the extension of transient stage.

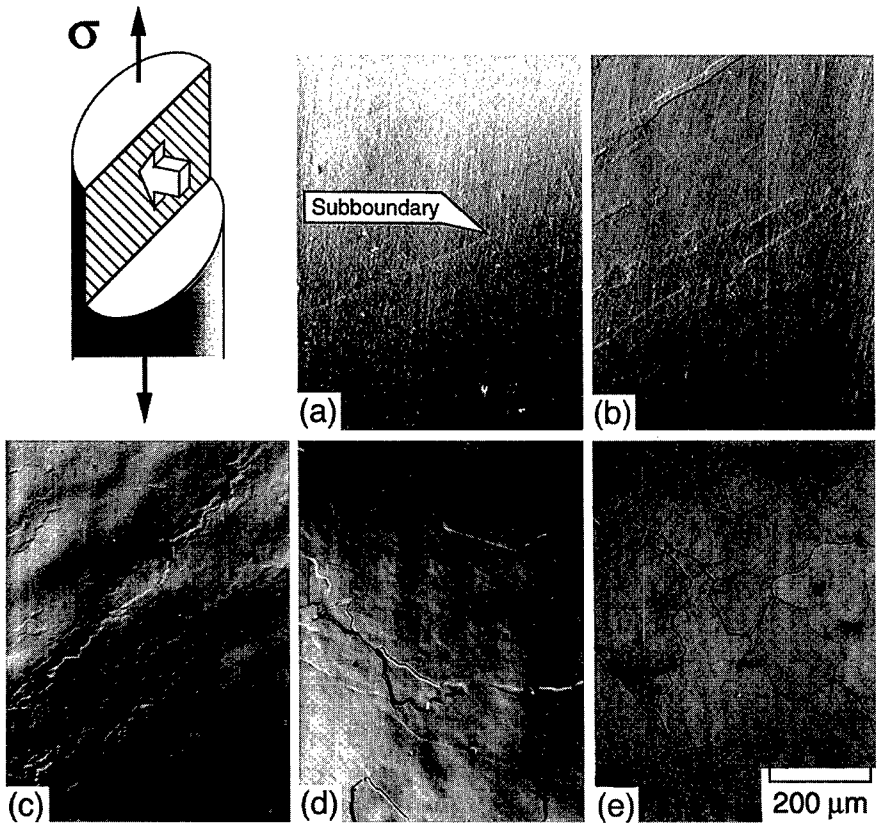

Fig. 4. Optical micrographs of the Ni-20Cr single crystals subjected creep strain of 0.1 (a), 0.5 (b), 0.73 (c), 0.76 (d) and 0.83 (e) at 1173 K - 29.4 MPa.

These features characterized in the single crystal are obtained in the single crystals whose stress axis is located within the standard stereographic triangle. Fortunately, the creep rate - time curves in the Ni-20Cr single crystals whose orientations are located at the poles of the standard stereographic triangle has been conducted at the lower stress of 29.4 MPa, and their features are substantially as same as the features obtained in this study. From the microstructural observation of the Ni-20Cr single crystal interrupting the creep test in the strain range of 0.1 to 0.76, the correlation between the creep deformation mode and the dynamic recrystallization through the evolution of subgrain is discussed and following suppositions are obtained. Schematic illustration of microstructural feature in Fig. 4 is shown in **Fig. 5**. The suppositions will be explained using Fig. 5.

1) It was elucidated that the orientation between the stress axis and the straight subboudary, as shown in **Fig. 5 (a),** becomes small with increasing the creep strain as well as a single slip plane. Therefore, in the first step of transient stage a single slip parallel to a straight subboundary is activated.

2) In the second step of transient stage where the evolution of subgrains occurs, the second and the third slip systems will be activated as shown in **Fig. 5 (b)** and **(c)**. So large decrease in creep rate occurs through the intersection of dislocations.

3) In the crystal interrupting the creep test just after onset of accelerating creep, the dynamically recrystallized grains were confirmed as shown in **Fig. 5 (d)**. So the origin of the onset of accelerating creep must be the appearance of dynamically recrystallized grains.

4) In the accelerating stage, dynamic recrystallization evolved in the whole gage portion. Increase in grain boundary area through the evolution of dynamic recrystallization enlarges the creep rate during accelerating creep. Finally, γ single phase Ni-20Cr single crystal turns to polycrystal, as shown in **Fig. 5 (e)**, subject to creep deformation under the stress less than the critical stress.

The third and the fourth microstructural features indicate the appearance and the evolution of dynamically recrystallized grains increase the creep rate.

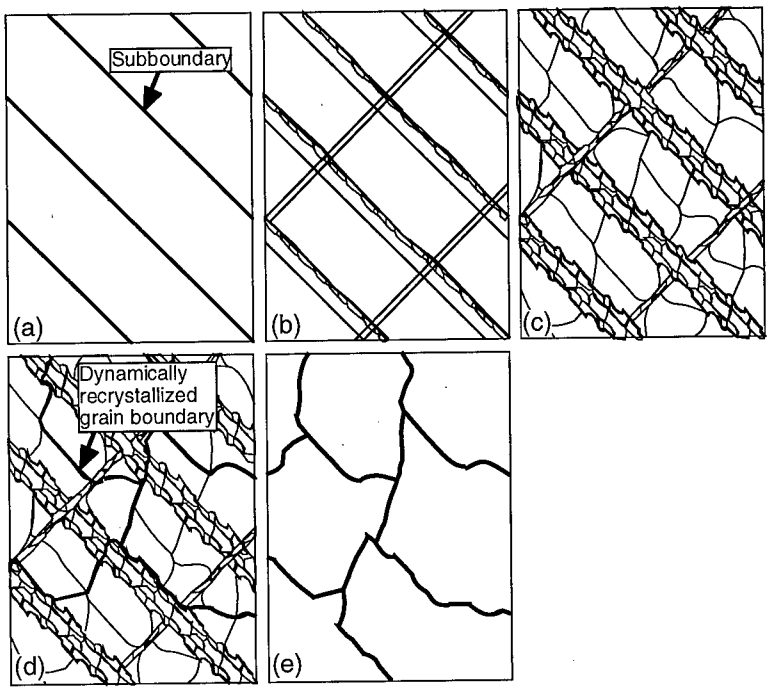

Fig. 5. Schematic illustration of microstructural features in the single crystal interrupting the creep tests at the strains of 0.1 (a), 0.5 (b), 0.73 (c) and 0.76 (d), and creep ruptured (e).

5. Conclusion

The creep tests of γ single phase Ni-20mass%Cr single crystals with the orientation within the standard stereographic triangle have been conducted at 1173 K in the wide stress range of 19.6 to 98 MPa. The creep rate - time curves and the creep rate - strain curves of single crystals have been analyzed by comparing the curves of polycrystals, and the creep deformation features of Ni-20Cr single crystal are characterized by comparing with the features in polycrystal. To elucidate the microstructural features of single crystal subject to creep at lower stress level, the correlation between the features of creep and the evolution of subgrain during creep in the single crystals has been investigated by examining the optical microstructure of the specimen interrupting the creep tests at the strains of 0.1 to 0.76 in the creep test at 29.4 MPa. The dynamic recrystallization occurs through the evolution of subboundary just at the time showing the minimum creep rate, and the single crystal turns to the polycrystal through the accelerating stage. It is found that the generation of dynamically recrystallized grains corresponds well with the onset of accelerating creep.

References

[1] B. A. Shollock, J. Y. Buffere, R. V. Curtis, M. B. Henderson and M. McLean, Scr. Mater., **36** (1997), p. 1471-1478.
[2] R. N. Ghosh, R. V. Curtis and M. McLean, Acta Metall. Mater., **38** (1990), p. 1977.
[3] V. Sass, U. Glatzel and M. Feller-Kniepmeier, Acta Mater., **44** (1996), p. 1967-1977.
[4] M. V. Nathal and L. J. Ebert, Metall. Trans., **A16** (1985), p. 427.
[5] Y. Kondo, N. Kitazaki, J. Namekata, N. Ohi and H. Hattori, *Proc. of the 8th Intern. Conf. Superalloys*, (1996), p. 279.
[6] M. Hasegawa, H. Soto and S. Karashima, Trans. JIM, **33** (1966), p. 1239.
[7] D. Sieborger and U. Gratzel, Acta Mater. **47** (1999), p. 397.
[8] J. S. Erichson, C. P. Sullivan and F. L. Versnyder, High Temperature Materials in Gas Turbines (Eds. P. R. Sahm and M. O. Speidel), Elsevier, Amsterdam, (1974), p. 315.
[9] Y. Terada, T. Matsuo and M. Kikuchi, *Stainless Steels '91*, The Iron and Steel Institute of Japan, Tokyo, (1991), p. 618-626.
[10] A. K. Mukherjee, J. E. Bird and J. E. Dorn, Trans. ASM, **62** (1969), p. 155.
[11] J. E. Bird, A. K. Mukherjee and J. E. Dorn, Quantitative Relationships between Properties and Microstructure (Eds. D. G. Brandon and A. Rosen), Israel Universities Press, (1969), p. 255.
[12] Y. Kondo, T. Matsuo, T. Shinoda and R. Tanaka, J. Iron and Steel Inst. Jpn., **65** (1979), p. 896.
[13] Y. Terada, T. Matsuo and M. Kikuchi, *Proc. of the 7th JIM Intern. Symp. on Aspects of High Temperature Deformation and Fracture in Crystalline Materials*, The Japan Institute of Metals, Sendai, (1993), p. 27-34.
[14] K. Nakajima, Dr. Thesis, Tokyo Institute of Technology, Tokyo, (1992).

* To whom all correspondence should be addressed e-mail: tmatsuo@mtl.titech.ac.jp, FAX: +81-3-5734-2874.

Key Engineering Materials Vols. 171-174 (2000) pp. 561-568
© 2000 Trans Tech Publications, Switzerland

Influencing Factors of Stress Rupture at 750 °C Temperature for Cast Nickel Base Superalloy K403

Y. Zheng and Y. Han

Beijing Institute of Aeronautical Material, P.O. Box 81, 100095, Beijing, P.R. China

Keywords: Cast Superalloy, Intermediate Temperature Stress-Rupture, Heat Treatment, Microstructure, Deformation Mechanism

Abstract The standard heat treatment of cast nickel-base superalloy K403 is the solid solution treatment of 1210 ℃/4h, air-cooling. It is very difficult to meet the requirements of the intermediate temperature stress-rupture life regulated by Aviation Standard HB5155. In order to resolve the above problem, some factors influencing intermediate stress-rupture life have been explored. The results showed that the intermediate temperature stress-rupture properties impaired by treatment of 1210 ℃/4h were due to precipitation of too small γ' phase ($< 0.2\ \mu$ m) in grains and absence of the secondary carbides at grain boundaries. The dendritic pattern appears at the fracture surface and there is no slip trace at the gauge length part of specimens treated by 1210 ℃/4h, but the crystallographic plane at fracture surface and the extensive slip can be observed for the specimens treated by 1180 ℃/4h. TEM results have shown that during intermediate temperature deformation the dislocation of 1/2<110> moves to the interface of γ/γ' and cuts γ' phase to form the high energy antiphase boundaries. The finer γ' can be cut and passed easily by dislocation and has a poor resistance to intermediate temperature creep. The finer dendrites and the microstructure containing intergranular M6C carbide with envelope of γ' and residual coarse γ' within grains were beneficial. Therefore high cooling rate during solidification and partial solid solution treatment of 1180 ℃/4h are suitable for a turbine blade alloy K403

1 Introduction

In the middle of 1960 · s, it was noted that the premature rupture of cast superalloy with enough high temperature strength occurred. Afterward metallurgists recognized that cast nickel base superalloy had ductility valley in the temperature range of 650 ~ 815 ℃, moreover variation of the stress-rupture life often reached one order of magnitude and led to early rupture during the secondary stage of creep[1]. The 760 ℃ stress-rupture strength and ductility of cast superalloy were listed in specification of superalloys in 1970 · s in the United States, because at that time the working part of blades for the civil long-life engines and the root of blades for the military engines were located in this temperature range. In China, alloy K403 is a cast nickel base superalloy developed by Beijing Institute of Aeronautical Materials (BIAM) in the early 1960 · s. It was widely used in blades and guide vanes of turbojet, turboprop, turboshaft and turbofan series. The requirements to mechanical properties at the above mentioned applied conditions can be met due to the sufficient high temperature strength of alloy K403. In the late 1980 · s, requirement for the intermediate mechanical properties of alloy K403 was proposed. The received standard of intermediate temperature stress-rupture property for ingots of alloy K403 first regulated by Aviation Standard HB5155[2] was as follows: the stress-rupture life at 750 ℃ and 645MPa be longer than

50h for as-cast or heat treated alloy by 1210 ℃/4h air-cooling. Unfortunately it was very difficult to carry out HB5155. only a few heats reached up to standard, therefore the urgent task was to explore the factors influencing 750 ℃ stress-rupture property of alloy K403.

2 Experimental Procedure

The actual composition of selected alloy K403 was controlled as Ni-5.2Co-10.8Cr-5.3W-4.0Mo-5.7Al-2.7Ti-0.01B-0.04Zr-0.14C. Master alloy used for casting blades and bars contained 50% virgin and 50% revert materials. There were three conditions of specimens: as-cast, solid solution treatment of 1210 ℃/4h and 1180 ℃/4h. The aging treatment of 900 ℃/4 ~ 16h of another set of specimens was carried out after the above mentioned solid solution treatment. Total 39 stress-rupture specimens were tested at 750 ℃, 645MPa. Microstructure and fracture surface of some representative specimens were fully analyzed and related to intermediate temperature properties.

The morphology of dendrites, the size and distribution of γ' phase and carbide, and the slipping bands near fracture surface were inspected by optical microscope (OM) and scanning electron microscope (SEM) and the dislocation structures in specimens were observed by transmission electron microscope (TEM) for the stress-rupture specimens of alloy K403 at 750 ℃, 645MPa.

3 Results

3.1 Stress-rupture life of alloy K403 at 750 ℃

The stress-rupture life at 750 ℃, 645MPa for alloy K403 with different conditions was summarized in Table 1. Compared with as-cast alloy, solid solution treatment of 1210 ℃/4h decreases the intermediate temperature stress-rupture life obviously, but solid solution treatment of 1180 ℃/4h increases life. As-cast or 1180 ~ 1210 ℃/4h solid solution treated specimens adding aging treatment of 900 ℃ have higher intermediate properties than original conditions before aging.

Table 1 Stress-rupture life at 750 ℃, 645MPa for alloy K403

condition of alloy	average stress-rupture life, h	number of specimens	range of variation, h
as-cast	69.0	9	26.8 ~ 213
1210 ℃/4h	15.7	14	1.5 ~ 91.9
1180 ℃/4h	187.9	3	65.7 ~ 284.3
as-cast+900 ℃/16h	91.5	5	60.1 ~ 226.7
1210 ℃/4h+900 ℃/4h	56.3	3	15.6 ~ 124.4
1180 ℃/4h+900 ℃/16h	223.0	5	92.8 ~ 427.1

It can be seen from Table 1 that variation of 750 ℃ stress-rupture life can reach an order of magnitude. Average life of alloy K403 with different conditions meets demand of HB5155 except 1210 ℃/4h, but the minimum life of specimens only treated by 1180 ℃/4h , as-cast+900 ℃/16h and 1180 ℃/4h+900 ℃/16h exceeds HB5155 specification. As discussed later, life variation of specimens is relative to variation of cooling rate during solidification.

3.2 Microstructure of alloy K403

Dendrite is the basic microstructure. The dendritic interspace of each specimens is different due to various cooling rate passed through the temperature range of liquidus and solidus. In the inspected 20 specimens, the dendritic interspace is in the range of 60 ~ 180 μ m. Fig. 1 shows dendritic morphology of representative bars. The finer dendritic structures usually have longer life.

Microstructure of as-cast alloy K403 is shown in Fig.2. There are primary MC carbide and < 1 vol% eutectic of $\gamma + \gamma'$ in interdendrites or at grain boundaries. The coarse secondary γ' phase precipitates within grains everywhere. The average size of this coarse γ' is in the range of 0.5 ~ 0.8 μ m with different cooling rate of specimens. A few of the fine γ' with the size of 50 ~ 100 nm distribute between the coarse γ' (pointed out by the arrow in Fig.2(b)). It is very difficult to find the secondary M6C or M23C6 carbide at grain boundaries, but one can observe the coarse γ' of 3 ~ 5 μ m which is aligned along grain boundaries.

All γ' of alloy K403 is resolved after solid solution treatment of 1210 ℃/4h, but fine γ' with 0.15 ~ 0.18 μ m size precipitates during cooling. The coarse γ' mainly distributes at grain boundaries (Fig.3(a)). The MC carbide or small amount of granular M6C carbide exists at some segments of grain boundaries occasionally (Fig. 3(b)). The treatment of 1180 ℃/4h is not full solid solution treatment, because 5 ~ 10 vol% coarse γ' is not resolved by this treatment which maintains some γ' size as-cast alloy. The resolved γ' precipitates finer γ' with the size of < 0.2 μ m during cooling. The grained M6C carbide enveloped by a thick layer of γ' is formed at grain boundary (Fig.4).

At a first glance, there is no difference in microstructure for as-cast alloy and as-cast + 900 ℃/16h treated alloy, but more details can be revealed by mono phase etching technique. Besides existence of MC carbide in as-cast alloy, the fine M23C6 and M6C carbides precipitate at grain boundary and the granular M23C6 carbide is also formed within grain after aging treatment of 900 ℃/16h (Fig.5). The specimens treatment by 1180 ~ 1210 ℃/4h + 900 ℃/4 ~ 16h maintain the microstructural characteristic of solid solution treated specimens, but the following aging treatment of 900 ℃/4 ~ 16h makes the fine γ' formed by solid solution treatment grow rather; moreover the complementary precipitation of secondary M23C6 and M6C carbides takes place at grain boundaries and within grains

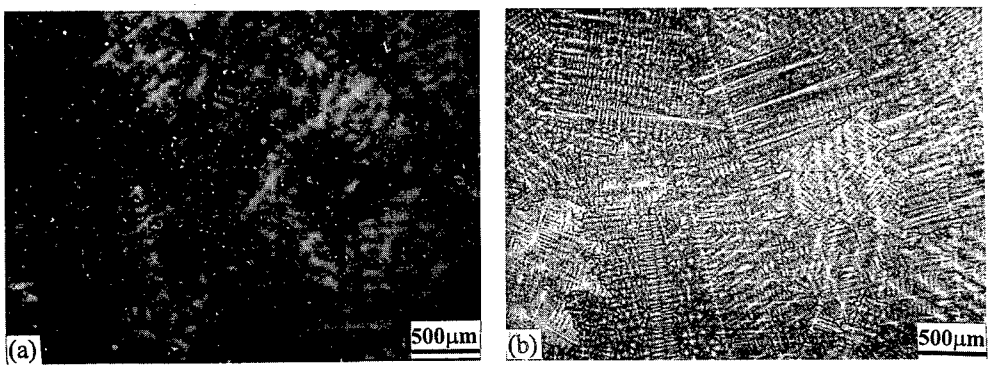

Fig. 1 Dendritic morphology of as-cast alloy K403: (a) dendritic interspace =170 μ m, life=26.8 (b) dendritic interspace = 63 μ m, life = 213h.

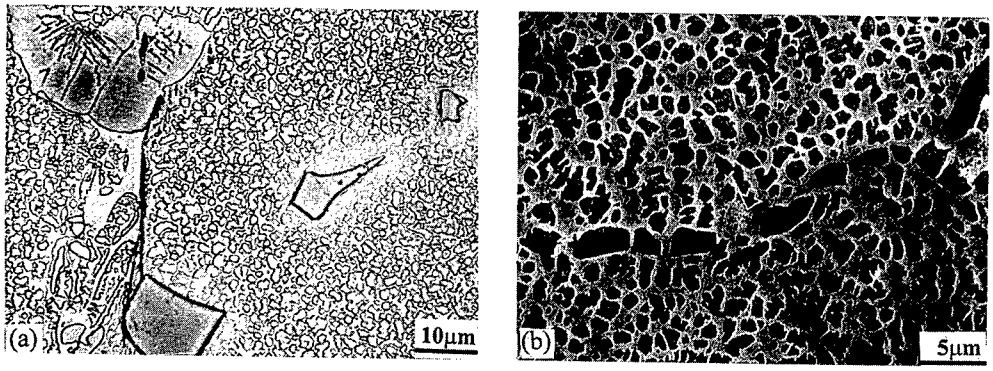

Fig.2 Microstructure of as-cast alloy K403: (a) MC carbide and eutectic (γ + γ ') in interdendrite; (b) block γ ' distributed along grain boundary.

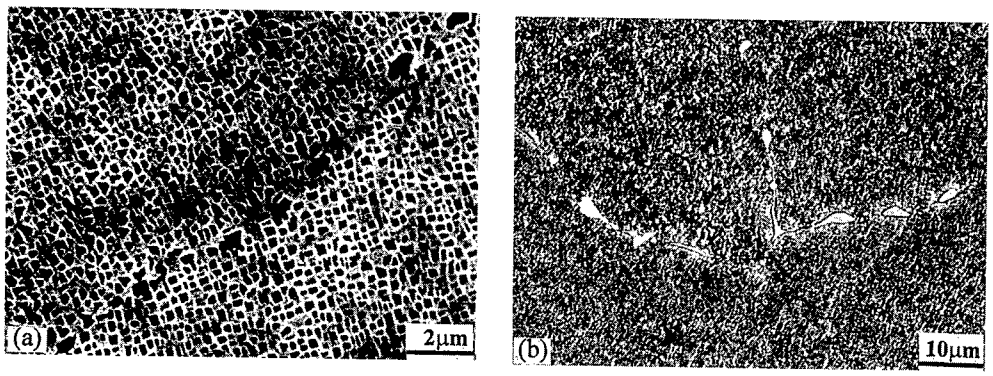

Fig. 3 Microstructure of alloy K403 after solid solution treatment of 1210 ℃/4h (a) coarse γ ' at grain boundary ; (b) MC carbide at grain boundary.

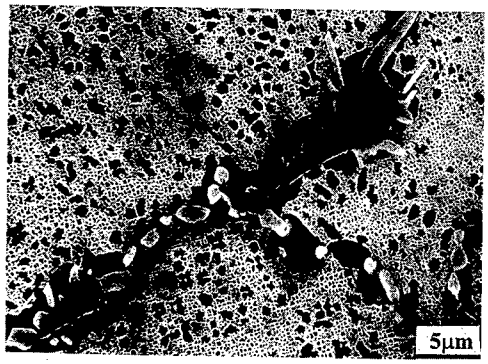

Fig.4 Microstructure of alloy K403. after treatment of 1180 ℃/4h.

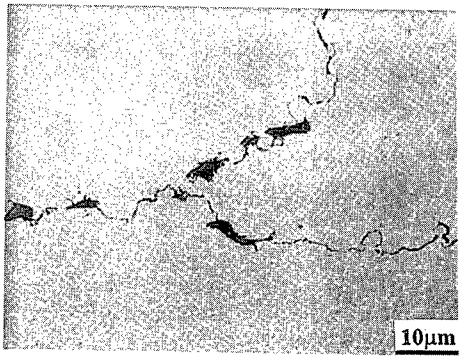

Fig.5 Microstructure of alloy K403 after as-cast +900 ℃/16h treatment.

3. 3 Fracture surface

There are two kinds of fracture surface for 750 ℃ stress-ruptured specimens: dendritic or facet fracture surface (Fig.6). For large numbers of short life specimens, fracture surface appears to be dendritic pattern and there is no slip traces at the gauge length part of specimens, especially specimens heat treated by 1210 ℃/4h (Fig.6 (a)). The specimens appeared as the crystallographic facet on fracture surface normally have long stress-rupture life and high ductility. Facet fracture surface is often fracture character of specimens treated by 1180 ℃/4h + aging (6 (b)). The size of facets is usually equal to grain size, sometimes crossing several grains.

The nature of cleavage-like fracture surface is serious slipping and decohension along slip bands. The extensive slip can be observed at gauge length of specimen (Fig.7), therefore the fracture character belongs to be ductile.

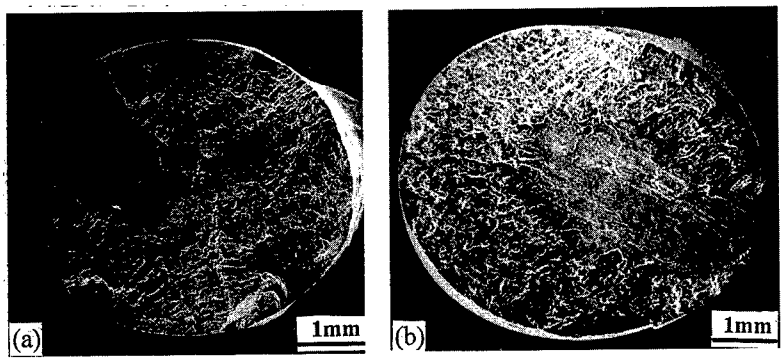

Fig.6 Typical fracture surface of alloy K403 fractured at 750 ℃, 645MPa: (a) dendritic fracture surface of specimen heat-treated by 1210 ℃/4h, having 13.2h life; (b) facet fracture surface of specimen heat-treated by 1180 ℃/4h+900 ℃/16h, having 211.5h life.

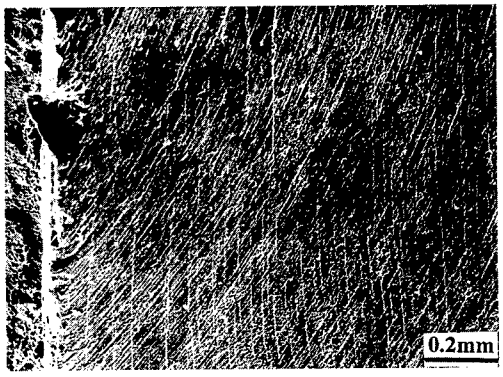

Fig.7 Extensive slip bands at gauge length of specimen with 211.5h stress-rupture life.

3. 4 Dislocation structure of ruptured specimens

Dislocation structure for the ruptured specimens of as-cast alloy at 750 ℃, 645MPa and 58.7h was

observed. The results in Fig.8 show that in this $\gamma+\gamma'$ base alloy deformation initiates at γ phase first, the dislocations density in γ phase rapidly increases and the dense dislocation networks form with increase of deformation or time. A large amount of dislocations tangles at γ/γ' interface which hardly passes γ' by shear due to the retarding effect of the ordered structure of γ' phase on deformation. As the deformation amount during creep increases further, the dislocations from matrix γ phase cut into γ' phase, therefore the dislocation contrast in coarse γ' phase of as-cast alloy remains (pointed out by the arrow in Fig.8).

The rare dislocations exist in γ' for the intermediate temperature stress-ruptured specimens treated by 1210 ℃/4h (Fig.9). The coarse and fine γ' phases exist in specimens treated by 1180 ℃ /4h+900 ℃/16h, the dislocation configuration in these γ' phase after the intermediate temperature stress-rupture is the same configuration as in the coarse γ' of as-cast alloy and the fine γ' formed by treatment of 1210 ℃/4h respectively. In order to identify the dislocation character in the coarse γ', a set of micrographs with different operating vector g was taken and specimen was located in [0 1 1] direction. There is no stacking fault fringes to appear at various g, therefore all these dislocations belong to total dislocations. As observed the dislocation configuration at g =[1 $\bar{1}$ 1] and g =[$\bar{1}$ 1 $\bar{1}$], the position and distance of dislocation pair do not change in the opposite direction of g. This results indicated that these dislocations are superlattice dislocations instead of dislocation dipoles. At g = [$\bar{1}$ $\bar{1}$ 1] and g = [0 2 $\bar{2}$] the dislocations are visible, consequently Burgers vector $\boldsymbol{b}$ within the coarse γ' is considered as [0 1 $\bar{1}$].

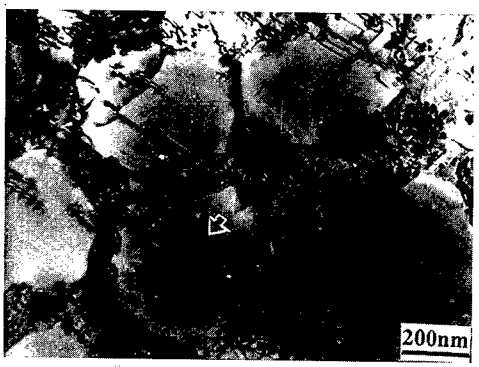

Fig.8 Dislocations in the stress-ruptured specimen at 750 ℃, 645MPa and 58.7h for as-cast alloy K403.

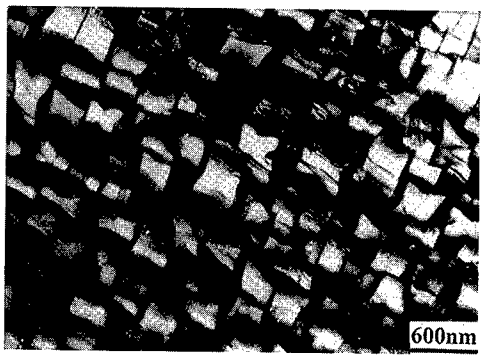

Fig.9 Dislocations in the stress-ruptured specimen at 750 ℃, 645 MPa and 4.4h for alloy K403, treated by 1210 ℃/4h.

4 Discussion

4.1 Effect of γ' size on intermediate temperature stress-rupture properties

The γ' phase is the most important phase influencing the intermediate temperature stress-rupture properties. The existing results prove that 6 ~ 14 vol% $\gamma+\gamma'$ eutectic aligned along grain boundaries or interdendrites increases the intermediate temperature stress-rupture life significantly [3]. It is confirmed from this paper that a given amount of coarse γ' with 1 μm size is necessary for maintaining the intermediate temperature stress-rupture strength of cast superalloy. The alloy

with γ' bands and coarse granular γ' not only possess long life of intermediate temperature stress-rupture, but also higher ductility of stress-rupture. Otherwise, only fine γ' with 0.15 μ m size is harmful fof intermediate temperature stress-rupture properties.

The reason concerning the effect of the amount and size of γ' phase on intermediate temperature stress-rupture properties was considered as to be related to the intrinsic characteristic of these ordered phase. Slip of matrix $\gamma+\gamma'$ in nickel base superalloy is the plane bands possessing wide interspace and this ununiform deformation causes the local stress concentration in the serious deformation region. Slip of mono-phase γ' is fine and uniform which makes slip dispersive and retrains cracking caused by slip concentration [4]. Therefore, the block γ' at grain boundaries and intrdendrites can more efficiently resist the serious deformation caused by stress concentration and is not easy to crack. The TEM results have shown that during intermediate temperature creep deformation the lattice dislocation of 1/2 <110> moves to the interface of γ/γ' and cuts γ' phase to form the high energy antiphase boundaries. The fine γ' can be cut and passed by dislocation and has a poor resistance to intermediate temperature creep [5].

4. 2 Effect of carbide on intermediate temperature properties

Generally speaking, the fine and dispersive primary MC carbides are beneficial to intermediate temperature properties, however primary MC carbide is not always distributed at grain boundaries. One of the reasons of lower intermediate temperature properties for as-cast alloy is absence of sufficient carbide at grain boundaries, therefore no matter which heat-treatment is used, besides reducing microsegregation as much as possible, the granular M6C of M23C6 carbides should precipitate at grain boundaries. 1210 ℃ exceeds the stable temperature of two kinds of carbide and it is impossible to form sufficient amount of secondary carbide at grain boundaries. In addition, intermediate temperature properties are seriously impaired due to full solid solution of all γ' phase, hence it is considered that as a turbine blade alloy the heat treatment of 1210 ℃/4h is not suitable for recommendation.

The heat treatment of 1180 ℃ makes M6C carbide precipitate at grain boundaries and maintains some part of coarse γ'. Both M6C and M23C6 precipitate and amount of the latter is higher than in the former by means of aging tretment of 900 ℃. This means that aging treatment is beneficial to as-cast or solid solution treated alloy. In summary, The satisfied intermediate temperature stress rupture properties can be obtained by heat treatment of as- cast + 900 ℃/16h or 1180 ℃/4h for turbine blade alloy K403.

5 Conclusions

1. Alloy K403 with the all fine γ' of less than 0.2 μ m size has low intermediate temperature stress-rupture properties and the mixed microstructure with about 1 and 0.2 μ m γ' is beneficial to this properties.

2. The granular M6C and M23C6 carbides enveloped by γ' phase at grain boundaries increase intermediate temperature stress-rupture properties.

3. Full solid solution treatment of 1210 ℃/4h seriously impairs intermediate temperature stress-

rupture of alloy K403 and it is not suitable for turbine blade alloy. Partial solid solution treatment of 1180 ℃/4h and treatment of as-cast +900 ℃/4h can meet intermediate temperature stress-rupture properties requirements for turbine blades of alloy K403.

References

[1] D. H. Maxwell, J. F. Bladwin, J. F. Radavidch, Metallurgica and Forming (1975) (10), p.332.
[2] Aviation Industry Standard HB5155-88,1988-04-09 issue.
[3] Yunrong Zheng, Yuling Cai, Chinese Aeronautical Science and Technology Documentation HJB830117,1983.
[4] J. E. Doherty, A. F. Giamei, B. H. Kear, Canadian Metallurgical Quarterly 13 (1) (1974), p.229.
[5] J. K. Tien, R. P. Gamble, Metall. Trans. 3 (1972), p.2157.

Correspondence: Yunrong Zheng, Fax: (8610)62456935.

Key Engineering Materials Vols. 171-174 (2000) pp. 569-576
© 2000 Trans Tech Publications, Switzerland

Study on Creep Properties and Microstructural Relation in Directionally Solidified Nickel Base Superalloy

A. Nomoto, M. Yaguchi and T. Ogata

Central Research Institute of Electric Power Industry,
2-11-1, Iwado Kita, Komae-shi, Tokyo 201-8511, Japan

Keywords: Gas Turbine Blade, Gamma Prime, Rafting

Abstract

Creep tests at temperatures ranging from 870 to 975°C and stresses ranging from 70 to 350MPa are conducted on directionally solidified(DS) nickel base superalloy used for land base gas turbine blades in order to investigate basic mechanical properties at high temperature. Creep rupture strength of the material was about 20°C higher in temperature than that of conventionally cast (CC) superalloy Inconel738LC. Ductility was a few times larger than that of Inconel738LC showing rupture elongation between 15 and 25% depending on the creep test condition. Microstructure observation performed on ruptured specimen showed so called rafted γ' precipitates specimens and aspect ratios of the precipitates varied depending on the Larson-Miller parameter. Rafting of the DS superalloy leads enlargement of particle spacing and seems to cause the acceleration of the creep rate.

Introduction

Large-scale gas turbines, as top cycle of combined cycle plants, have been extensively used in electric power plants because of high thermal efficiencies. The durability of the gas turbines limited by components operating at high temperature. First stage turbine blades are most critical parts because these are exposed under not only high temperature but also high stress. And since the replacement costs of turbine blades are getting increasing in utilities, development of the life prediction method based on the evaluations of high temperature strength of blades is required.

Nickel base superalloys have been used as material of gas turbine blades. In recent years, directionally solidified (DS) superalloys have been used for turbine blades instead of conventionally cast (CC) polycrystals (Inconel738LC for example). DS superalloys would have better high temperature strength than that of CC superalloys because these have no grain boundary vertical to the stress axis which is the main damage site in CC superalloys. There are some models evaluating the damage or predicting life for the CC materials[1-3], but that for DS materials are not available because the high temperature properties and damage mechanisms of DS materials are not clear. Therefore it is strongly needed to clarify the high temperature mechanical properties and the damage mechanisms of such kind of materials. The aim of this report is to investigate the basic creep properties of the DS superalloy and microstructural characteristics in the ruptured specimens.

Experimental Procedure

The test material was the DS nickel base superalloy. Chemical composition of the material is shown in Table 1. This is almost same as that of material used for DS gas turbine blades. Creep specimens with the dimensions ϕ6 x 30mm in gage length as shown in Fig.1 were cut from ingots by mechanical machining.

Fig.2 shows the microstructure of the material observed by optical microscopy before creep test. The crystal growth direction is the upper direction of the figure. {001} plane oriented to this direction. Few grain boundaries vertical to crystal growth direction were observed but many interfaces of dendrites were observed. Many porosities are also observed. These porosities are at the interdendritic regime as indicated in Fig.3. There are also observed γ' depleted regime and precipitates such as $M_{23}C_6$. SEM observation reveals the bimodal microstructure consisting of both coarse γ' cubes and fine γ' spheres in the specimens before test(Fig.4). Mean particle size of coarse γ' is about 0.5μm.

Creep tests were conducted at the temperatures ranging from 870 to 975°C and the stresses from 70 to 250MPa. Stress axis is parallel to the crystal growth direction. Fracture surfaces are examined by scanning electron microscope (SEM). Longitudinal cross section was cut from ruptured specimens. Surface was mechanically polished then etched by aqua regia. Microstructure observations were performed using optical microscopy and the SEM. Specimens for Transmission electron microscope (TEM) are obtained from gauge sections of ruptured specimens in longitudinal direction with respect to stress axis. TEM specimens are thinned using the twin-jet technique.

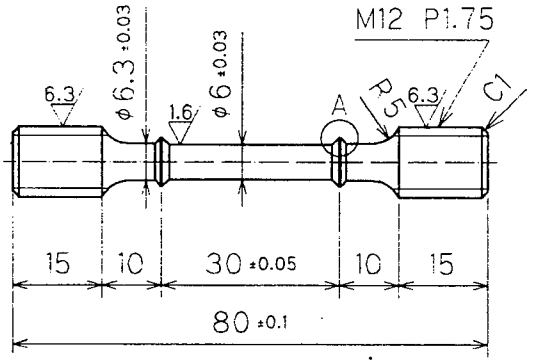

Fig.1 Specimen geometry

Table 1 Chemical composition of the material

C	Si	Mn	P	S	Ni	Cr	Mo	Co
0.1	< 0.1	< 0.05	0.004	< 0.002	60.09	13.93	1.56	9.56

W	Al	Ti	Fe	Ta	Cu	Ag	Bi
3.86	3.03	4.9	0.05	2.77	< 0.02	< 0.1 ppm	< 0.1 ppm

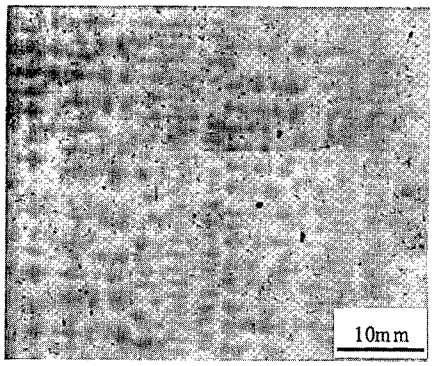

Fig.2 Optical micrograph of specimen before test

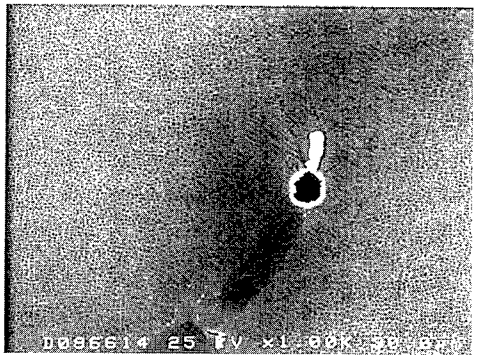

Fig.3 Interdendritic region of the DS material

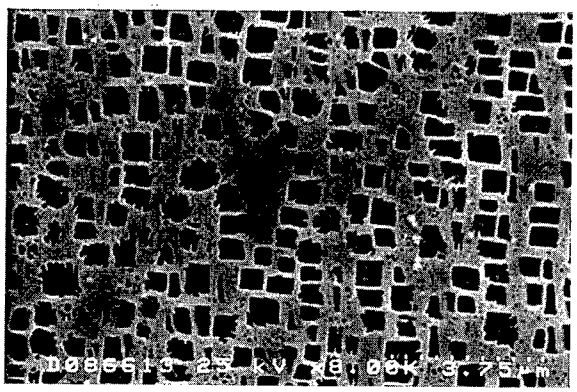

Fig.4 γ' particles of the DS material before creep test

Results and Discussion

Fig.5 shows a creep curve of the DS superalloy crept at 900°C and 250MPa. The curve of Inconel738LC CC superalloy extensively used for turbine blades crept at same temperature and stress is also shown in this figure. It is clearly demonstrated that the time and elongation to rupture of the DS superalloy are better than that of Inconel738LC. In this case, the rupture time of the DS superalloy is about 250 hours and the elongation to rupture is about 16.7%. Both the time and elongation to rupture of the DS superalloy are a few times larger than those of the CC Inconel738LC in the conditions. Fig.6 demonstrates that Larson-Miller plot of the DS superalloy and the CC Inconel738LC. The creep rupture strength of the DS alloy is about 20°C higher in temperature than that of the Inconel738LC in the conditions.

Fig.7 shows the fracture surface of the DS superalloy crept at 900°C and 200MPa. The fracture path along the dendrite interface was observed in contrast to CC superalloy such as Inconel738LC fractured at grain boundary. Fig.8 shows the results of microstructure observations of ruptured specimens by optical microscope. Large cracks were observed at the surface of specimen and relatively small cracks in the dendrite interfaces vertical to the stress axis and no cracks in dendrites.

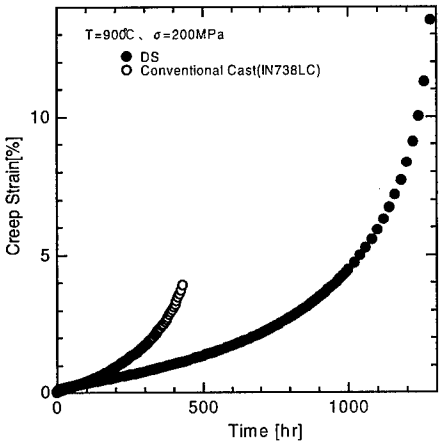

Fig.5 Creep curves of the DS and CC(Inconel738LC) superalloys

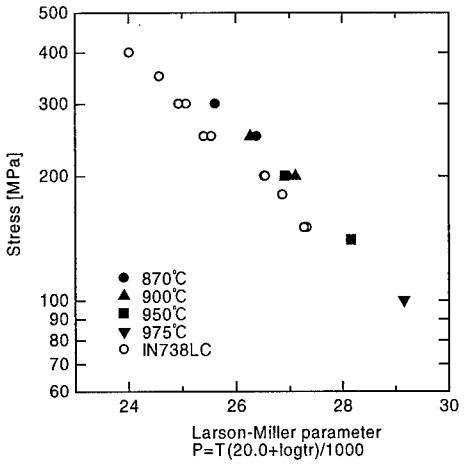

Fig.6 Larson-Miller plot of the DS and CC(Inconel738LC) superalloys

Fig.9 shows the microstructures observed by SEM at longitudinal cross sections of ruptured specimens. Fine spherical γ' particles observed before the creep test were not observed after the tests in all the conditions. On the other hand, the directional coarsening of γ' particles vertical to the stress axis, so called rafting, was observed same as other directionally and single crystal nickel base superalloy[4,5]. Other precipitates except the γ' phase were not observed. The rafting is remarkable in the specimen crept at higher temperature and lower stress. Fig.10 shows the relationship between the extent of rafting as aspect ratio of rafted γ' particle and Larson-Miller parameter. It is seen that the extent of rafting of the DS superalloy increases with increasing test temperature and/or rupture time. Maximum aspect ratio of the DS superalloy is about 3 in the conditions tested. Other DS superalloys such as CM247LC shows large aspect ratio more than 10 under similar creep conditions[4]. This indicates that the microstructure of the DS superalloy used in this study is more stable under the creep conditions.

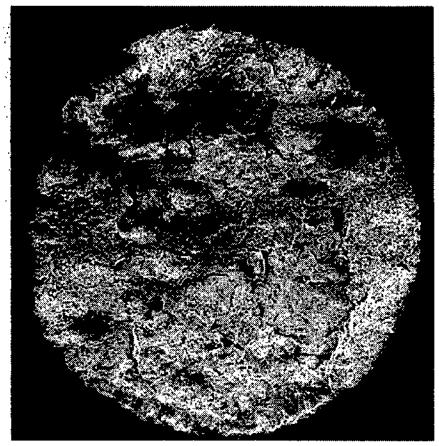

Fig.7 Fracture surface of the ruptured DS superalloy crept at 900°C and 200 MPa

Nickel base superalloy strengthened by γ' particles competing the dislocation motion in general. Therefore the geometrical changes of microstructure such as the rafting would have some effects on the change of creep strength property. Fig.11 shows change in creep rate with strain of the specimens which showed the same minimum creep rate but different aspect ratio of the γ' particles after creep to investigate the effect of rafting on the creep properties. It is demonstrated that the creep rate of the specimen with higher aspect ratio is higher than those with lowers at the later stage of creep deformation. The rafting of the γ' particles in the DS material seems to tend to accelerate the creep rate in the conditions.

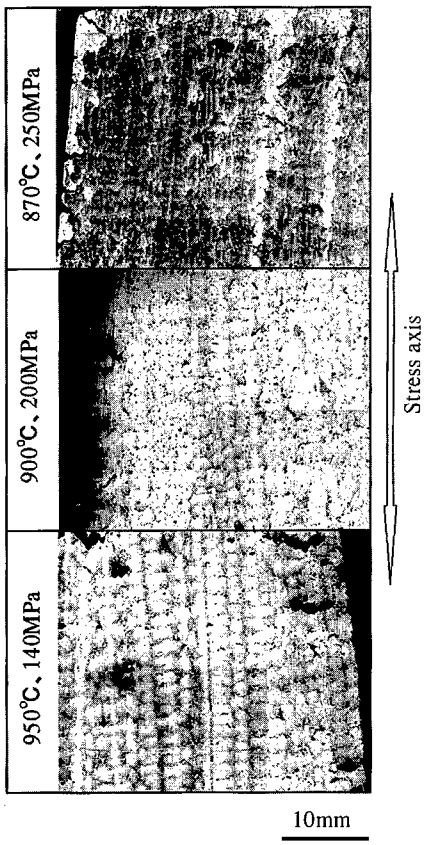

Fig.8 Optical micrograph of the ruptured DS superalloy

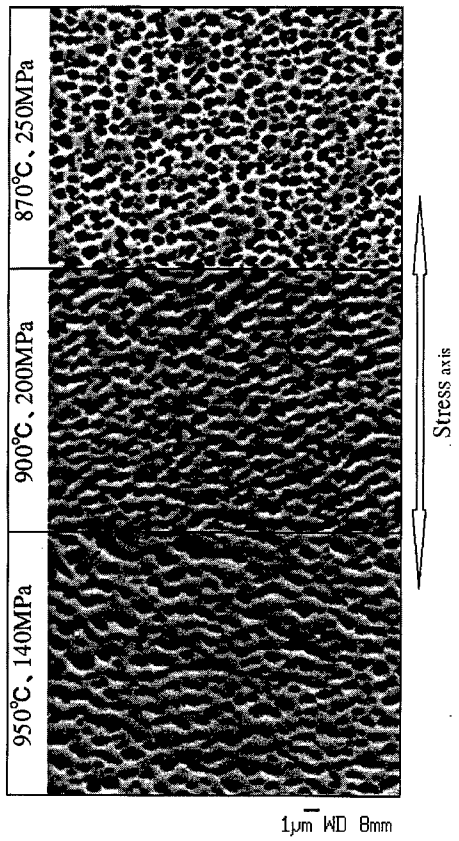

Fig.9 γ' particles of the ruptured DS superalloys

It is reported that the competing flow mechanism for γ' particle strengthened nickel base superalloy under creep deformation is dislocation climbing around the γ' particles[6] at lower creep stress and particle cutting at higher stress[7]. TEM observation of ruptured specimen of the DS superalloy crept at 870°C and 250MPa (the highest stress condition in Fig.11) shows that few dislocations cut the γ' particles (Fig.12). So it is indicated that appropriate dislocation competing mechanisms of this alloy in the conditions is the dislocation climbing around the γ' particles. In such case, the change in particle spacing and area of γ/γ' interface would be considered as the main factors accelerating creep rate. Fig.13 shows the relationship between Larson-

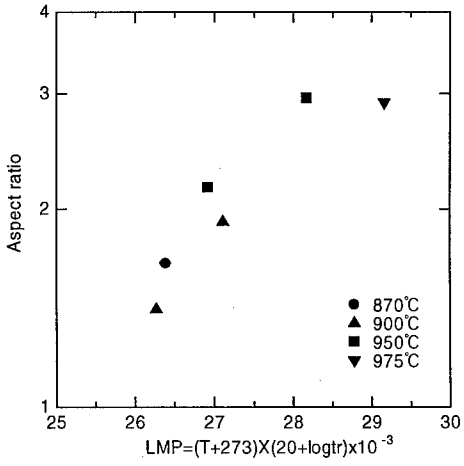

Fig.10 Relationship between aspect ratio of the γ' particles and Larson-Miller parameter

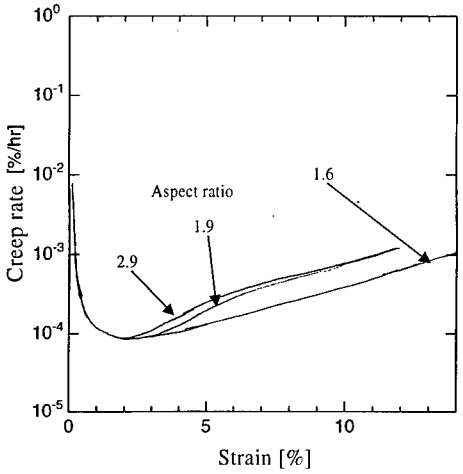

Fig.11 Effect of the aspect ratio of the γ' particles on the creep rate

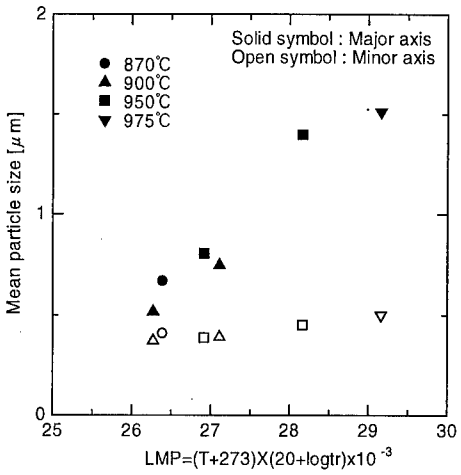

Fig.13 Relationship between major and minor axis of the γ' particles and Larson-Miller parameter

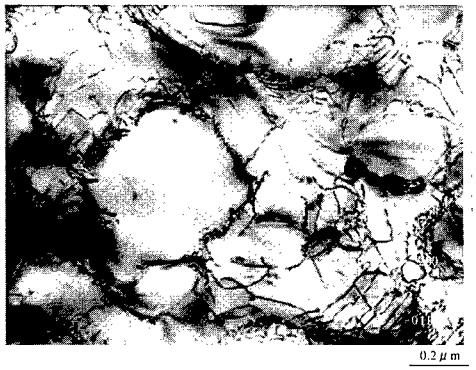

Fig.12 Dislocation structure of the ruptured specimen crept at 870°C and 250 MPa

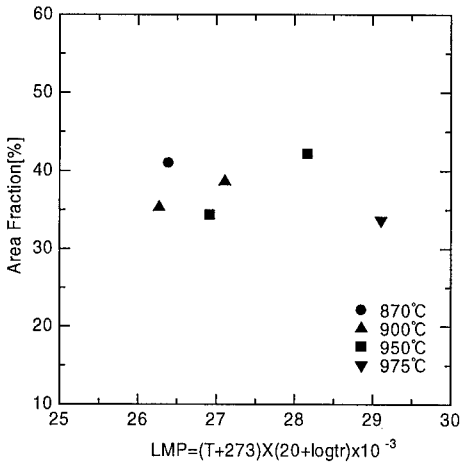

Fig.14 Relationship between the area fraction of the γ' particles and Larson-Miller parameter

Miller parameter and the size of major and minor axis of the rafted γ' particles. It is shown that the size of major axis strongly depends on test condition and increases with increasing the Larson-Miller parameter. On the other hand, the minor axis is almost constant in the all conditions tested. This means that the aspect ratio of the γ' particle correspond to the size of major axis. Fig.14 shows the volume fraction of the γ' particles obtained from SEM observations and Larson-Miller parameter. The volume fraction of the γ' particles is almost constant independent of the creep conditions. These results reveal that the increase of aspect ratio in the DS superalloy lead to the increase of the particle spacing without the change of area of γ/γ' interfaces in the conditions tested. Therefore it suggests that the acceleration of the creep rate of the DS superalloy with higher aspect ratio of γ' particle strongly depends on the enlargement of γ' particle spacing due to rafting.

Conclusions

Creep tests and microstructure observation were performed to the directionally solidified (DS) nickel base superalloy for land base gas turbine blades. The results are summarized as follows:

(1) The rupture time and elongation of the DS superalloy are about 3 times larger than those of conventionally cast (CC) Inconel738LC. Creep rupture strength of DS alloy is about 20°C higher in temperature than that of Inconel738LC.
(2) Creep crack seems to initiated at the surface of the specimen then propagated along the dendrite interface in contrast to CC superalloy fractured at grain boundary such as Inconel738LC.
(3) Raftings of γ' precipitates occurred in the ruptured specimens. Extent of the rafting of the γ' precipitates varied depending on the Larson-Miller parameter. Rafting of γ' precipitates accelerates the creep rate of the DS superalloy. It seems to be due to the increase of the particle spacing with increasing aspect ratio of γ' precipitates.

References

[1] M.Yamamoto and T.Ogata, Acta Met. Sinica, Vol.11, No.6(1998), p.470
[2] H.L.Bernstein, T.S.Grant, R.C.McClung and J.M.Allen, Auth. reprint Std. Tech. Pub. 1186 (1993), p212
[3] J.Meersmann, H.Frenz, J. Ziebs, J.Klingelhoffer and H.Kuen, 5th Int. Conf. on Biaxial/Multiaxial Fatigue and Frac. Cracow'97, Poland(1997), p.303
[4] H.Yamamoto and Y.Yoshioka, Rep. of the 123rd Commt. of Heat-Resisting Met. and Alloys, Vol.39 No.1(1998), p.17
[5] A.Royer, P.Bastie and M.Veron, Act. Mater., Vol.46, No.15(1998), p.5357
[6] P.J.Henderson and M.McLean, Act. Met., Vol.31, No.8(1983), p.1203
[7] C.Yuan, J.T.Guo, H.C.Yang and S.H.Wang, Scripta. Mater., Vol.39, No.7(1998), p.991

Key Engineering Materials Vols. 171-174 (2000) pp. 577-584
© 2000 Trans Tech Publications, Switzerland

Creep and Evolution of Dynamic Recrystallization in γ Single Phase Single Crystals Located at Poles in Standard Stereo-Triangle

H. Miyazawa[2], R. Takaku[3], D. Kawaguchi[1], Y. Terada[1] and T. Matsuo[1]

[1] Department of Metallurgy and Ceramics Science, Tokyo Institute of Technology, Meguro-ku, Tokyo 152-8552, Japan

[2] Graduate student, currently at IHI Co., Ltd.

[3] Undergraduate student, currently at The University of Tokyo

Keywords: Creep, Orientation, Single Crystal, Nickel-Based Alloy, Dynamic Recrystallization

Abstract

The effect of crystallographic orientation on creep properties was investigated on Ni-20mass%Cr single crystal with γ single phase. The single crystal with [001] orientation has the extended transient creep stage, and this creep feature leads to the longest creep life and the largest creep strain. The single crystal with [$\bar{1}$11] orientation has the smallest creep rate just after loading, but has shorter transient creep stage than that with [001] orientation. The single crystal with [011] orientation has shorter transient creep stage than that in the crystal with [001] orientation, so rupture life and total creep strain become shorter and smaller respectively than those in the crystal with [001] orientation. Then the creep life and the creep strain in the single crystal with [$\bar{1}$11] orientation become shorter and smaller respectively than those in the single crystal with [001] orientation. Only the single crystal with [011] orientation exhibits the anisotropic creep deformation. The dynamic recrystallization occurs homogeneously in the whole gage portion in the single crystals with [001] and [011] orientation. In contrast, in the single crystal with [$\bar{1}$11] orientation, the dynamically recrystallized grains with the smallest size appear locally. The important microstructural feature in the single crystal with [001] orientation is the appearance of many twins.

1. Introduction

The change in the creep deformation in γ single phase single crystal with decrease in the stress has been investigated using Ni-20mass%Cr alloy having the orientations within the standard stereographic triangle [1, 2]. The evolution of subboundary in the γ single phase single crystal was examined using a few creep interrupted specimens at 29.4 MPa [1-3]. From these studies, the onset of accelerating creep is interpreted by the appearance of dynamically recrystallized grain boundaries through the evolution of subgrains. Then, the appearance of dynamic recrystallization was also investigated as a function of stress in the range of 19.6 to 98 MPa [4]. The transient creep stage becomes shorter with increase in the stress; this is because the dynamic recrystallization takes place earlier as the stress increases. Using the single crystal oriented within the standard stereographic triangle, we found that the creep deformation in early stage is caused by a predominant slip system [1]. The number of slip systems to operate in the single crystals located at the poles of the stereographic triangle is more than that of the single crystal oriented within the standard stereographic triangle [5]. Furthermore the operative slip system among the single crystals located at the poles of the stereographic triangle may be different each other. But there is no creep data on the single crystal located at the poles of the stereographic triangle. In this study, therefore, the creep of the single crystals with [001], [011] and [$\bar{1}$11] orientations has been investigated at 1173 K under the stress of 29.4 MPa. The stress of 29.4 MPa was confirmed to be

relatively low at 1173 K for the single crystal oriented within the standard stereographic triangle [4]. The microstructures of the single crystals with [001], [011] and [$\bar{1}$11] orientations after creep deformation have been also characterized using creep rupture specimens.

2. Experimental

A Ni-20mass%Cr alloy, designated as Ni-20Cr in this paper, was melted in a high frequency induction furnace in a vacuum and cast into a 4 kg ingot in an argon atmosphere. The ingot was hot-forged into rod with a diameter of 13 mm. The chemical composition of the alloy is shown in **Table 1**. The single crystals with [001], [011] and [$\bar{1}$11] orientation, designated as [001] single crystal, [011] single crystal and [$\bar{1}$11] single crystal respectively, were successfully grown by a modified Bridgman type furnace in a flow of purified argon and then homogenized at 1523 K for 36 ks. The crystal orientations were determined by the Laue back-reflection X-ray technique. Only the crystals within three degrees of the desired orientations were employed for creep testing. Test specimens with a gage portion of 30 mm in length and 6 mm in diameter were prepared by precision grinding.

Tensile creep tests were performed at 1173 K under the constant stress of 29.4 MPa. Stress was kept constant within one per cent of the initial value during creep test by adjusting the auxiliary weights. Creep strain was measured with linear variable differential transducers through extensometers attached to annular ridges at both ends of the specimen gage portion. Microstructure subject to creep deformation was examined by an optical microscope on sections both parallel and normal to the stress axis. After metallographic polishing, samples were etched in a solution of orthophosphoric acid saturated with chromium trioxide with a current density of 10 mA/cm^2 for 10 minutes.

Table 1. Chemical composition (mass%) of crystals prepared in this investigation.

Alloy	C	Si	Mn	Cr	Ni
Ni-20Cr	0.001	0.49	0.30	19.3	Bal.

3. Results

3.1. Creep characteristics

Creep rate - time curves of the [001], [011] and [$\bar{1}$11] single crystals are shown in **Fig. 1**. Note that the creep rate is converted to the true strain rate [6]. Every creep curves are composed of the transient stage and the accelerating one, but does not have a steady-state creep stage. The creep rate remains unchanged with time at the beginning of the transient creep stage, and then gradually decreases for each orientation. The [$\bar{1}$11] single crystal exhibits the smallest creep rate just after loading. The minimum creep rate of the [$\bar{1}$11] single crystal is the same as that of the [001] single crystal. This is resulted from the shorter transient stage of the [$\bar{1}$11] single crystal than the transient stage of the [001] single crystal. The creep rate just after loading in the [011] single crystal is a little larger than that in the [001] single crystal, but the minimum creep rate in the [011] single crystal is ten times larger than that in the [001] single crystal. This increase in the difference in creep rate between two single crystals is resulted from the shorter transient stage of the [011] single crystal, in comparison with the [001] single crystal. Note that the [001] single crystal has the most extended transient stage among these three crystals.

Creep rate - strain curves of the [001], [011] and [$\bar{1}$11] single crystals are shown in **Fig. 2**. The strain at the minimum creep rate of the [$\bar{1}$11] single crystal is the smallest value of 0.23, and that of the [001] single crystal is the largest value of 1.45. The large difference in the creep strain at the minimum creep rate between the [$\bar{1}$11] and the [001] single crystals is directly resulted from the strain of transient creep. From the strain during transient creep stage, it is obvious that the [$\bar{1}$11] single crystal has large strain hardening and the [001] single crystal has small strain hardening.

It is noteworthy that the creep of the [001] single crystal was just in the beginning of accelerating creep stage when interrupted even though it already show the largest creep strain of 1.5.

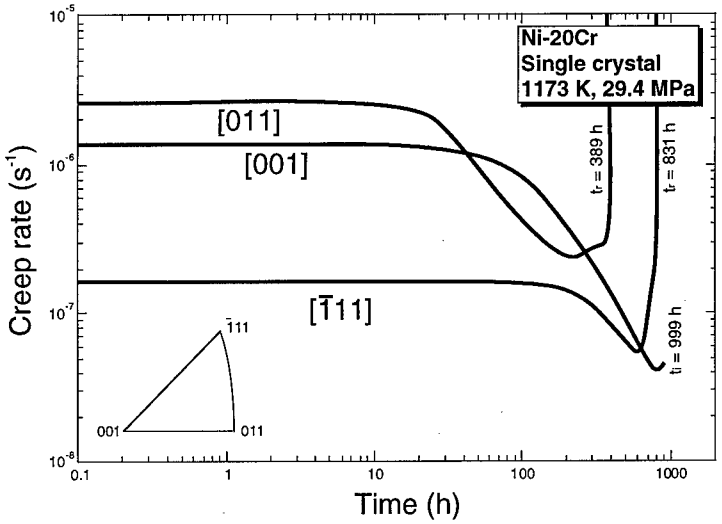

Fig. 1. Creep rate - time curves of [001], [011] and [$\bar{1}$11] single crystals of Ni-20Cr tested at 1173 K under the constant stress of 29.4 MPa.

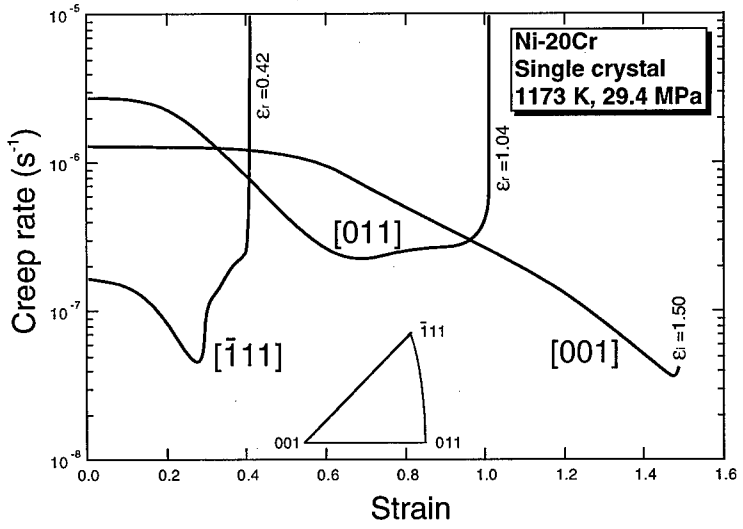

Fig. 2. Creep rate - strain curves of [001], [011] and [$\bar{1}$11] single crystals of Ni-20Cr tested at 1173 K under the constant stress of 29.4 MPa.

3.2. Difference in microstructure among three single crystals

Optical micrograph of the [001] single crystal creep interrupted at the strain of 1.5, which corresponds to the early stage of accelerating creep at 1173 K - 29.4 MPa, is shown in **Fig. 3**. Dynamically recrystallized grains in the size of 500 μm appear homogeneously in the whole gage portion, while subboundaries scarcely appear in the dynamically recrystallized grain. The striking feature in the [001] single crystal is the appearance of many twins as shown in **Fig. 4**. The twin boundaries exhibit two specific directions; one parallel to the stress axis and the other inclined 45° to the stress axis.

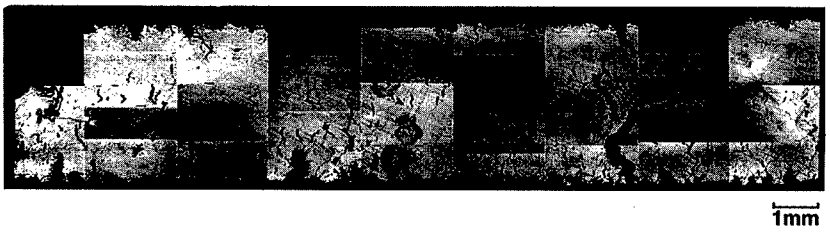

Fig. 3. Optical micrograph of the [001] single crystal of Ni-20Cr creep interrupted at the strain of 1.5 at 1173 K - 29.4 MPa. The observation was conducted on the section parallel to the stress axis.

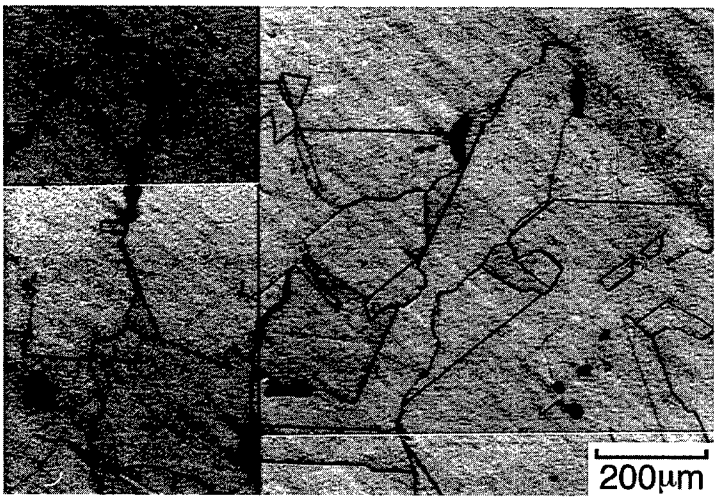

Fig. 4. Optical micrograph of the [001] single crystal of Ni-20Cr creep interrupted at the strain of 1.5 at 1173 K - 29.4 MPa.

Optical micrograph of the [011] single crystal creep ruptured at 1173 K - 29.4 MPa is shown in **Fig. 5**. Dynamically recrystallized grains are observed in the whole gage portion. Their shape is equiaxed and the grain diameter is approximately 150 μm, which is a little smaller than that in the [001] crystal. There are many cracks in the whole gage portion, and most of the cracks are formed along the direction normal to the stress axis. In most of the dynamically recrystallized grains, subboundaries can be clearly seen as shown in **Fig. 6**.

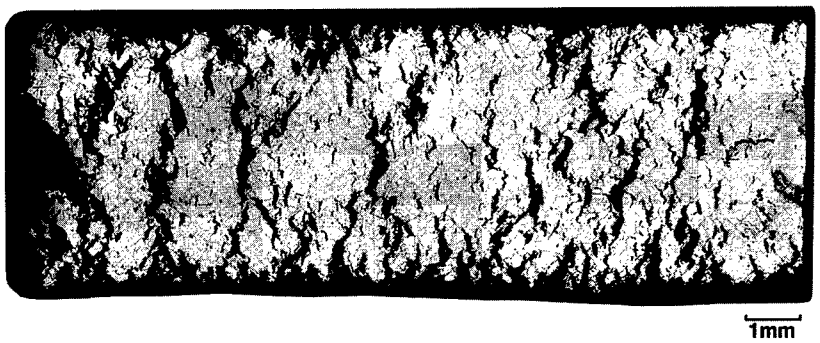

Fig. 5. Optical micrograph of the [011] single crystal of Ni-20Cr creep ruptured at 1173 K - 29.4 MPa. The observation was conducted on the section parallel to the stress axis.

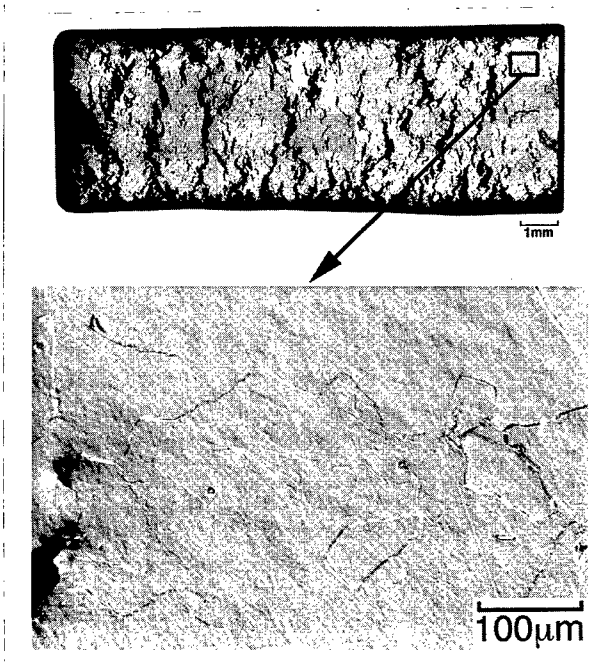

Fig. 6. Optical micrograph of the [011] single crystal of Ni-20Cr creep ruptured at 1173 K - 29.4 MPa. The observation was conducted in the interference mode in optical microscopy.

Optical micrograph of the [$\bar{1}11$] single crystal creep ruptured at 1173 K - 29.4 MPa is shown in **Fig. 7**. Dynamically recrystallized grains are observed as well, however, they are in a wide distribution range in the size. Smaller grains are detected near the cracks, which are inclined 45° to the stress axis. Subboundaries are also formed as shown in **Fig. 8**. The subboundaries within the dynamically recrystallized grain for the [$\bar{1}11$] single crystal are observed less frequently than that for the [011] single crystal.

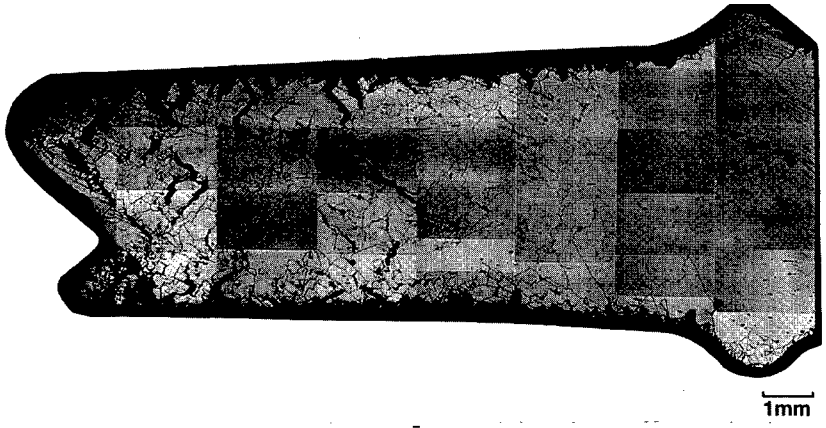

Fig. 7. Optical micrograph of the [$\bar{1}11$] single crystal of Ni-20Cr creep ruptured at 1173 K - 29.4 MPa. The observation was conducted on the section parallel to the stress axis.

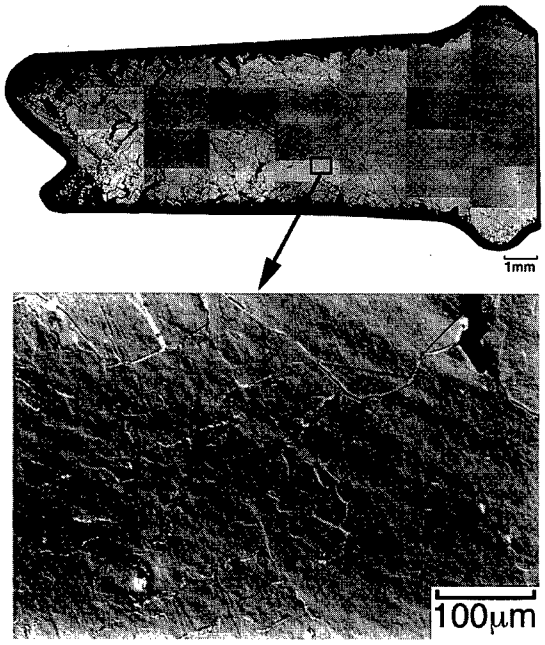

Fig. 8. Optical micrograph of the [$\bar{1}11$] single crystal of Ni-20Cr creep ruptured at 1173 K - 29.4 MPa. The observation was conducted in the interference mode in optical microscopy.

Optical micrographs of the cross sectional area of these three single crystals are shown in **Fig. 9**. These sections are cut from the outer portion of the annular ridge. The [011] single crystal shows the elliptical shape, whereas the [001] and the [$\bar{1}$11] single crystals remain circular. Consequently, anisotropic creep deformation is confirmed only for the [011] single crystal. In the section of the [001] single crystal, there is no dynamically recrystallized grain boundary. In contrast, the dynamically recrystallized grain boundaries are detected in both the [011] and the [$\bar{1}$11] single crystals. In the [011] single crystal, dynamically recrystallized grains are formed homogeneously and the grain shape looks elongated along the major axis. In the [$\bar{1}$11] single crystal, dynamically recrystallized grains are restricted in the outer region of the specimen.

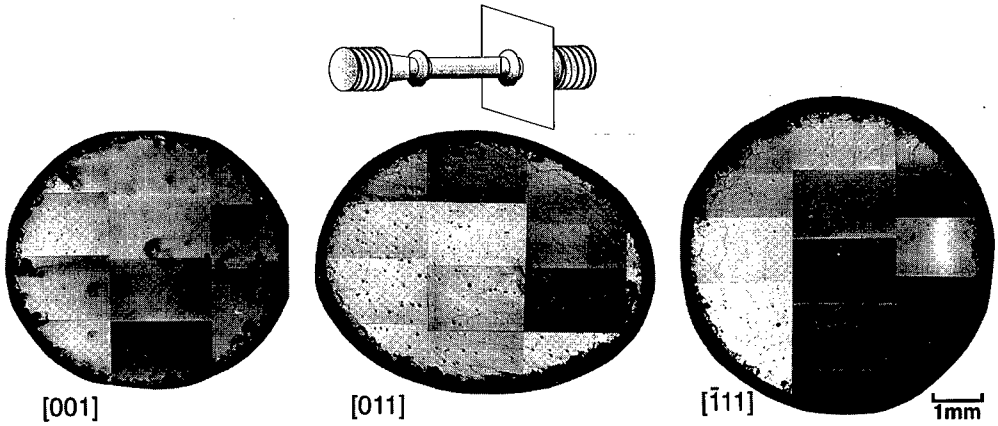

Fig. 9. Optical micrographs of the [001], [011] and [$\bar{1}$11] single crystals of Ni-20Cr creep ruptured at 1173 K - 29.4 MPa. The observation was conducted at the end of the gage portion on the section normal to the stress axis.

4. Discussion

There are marked differences in creep deformation among the [001], [011] and [$\bar{1}$11] single crystals. The minimum creep rate and the creep life are mainly dependent on the Schmid factor (S.F.) and the length of transient creep stage. The ratio of Schmid factor in the [$\bar{1}$11] single crystal (S.F. = 0.27) to that in the [001] crystal (S.F. = 0.41) is 0.66. In fact the [$\bar{1}$11] single crystal shows the smallest creep rate just after loading, but shows the minimum creep rate as same as that of the [001] single crystal. This is mainly caused by the lengthening a transient stage in the [001] single crystal. The larger transient stage leads to the decrease in creep rate. Comparing the creep rate of the [011] single crystal with that of the [001] crystal, there is no difference in creep rate between these two single crystals in the early stage of transient creep, but the transient creep stage in the [011] crystal finishes earlier than that in the [001] single crystal. As a result, the minimum creep rate in the [011] single crystal becomes larger than that in the [001] crystal. It is noteworthy that the difference in the minimum creep rate among these single crystals can be interpreted roughly by the length of transient stage. The finish of transient stage, that is onset of accelerating creep, must be discussed with appearance of dynamic recrystallization according to the microstructural observation. Each single crystal has three different microstructural features concerning the dynamically recrystallized grain as follows; 1) distribution of dynamically recrystallized grains, 2) the size of dynamically recrystallized grains, and 3) frequency of the appearance of subgrains within dynamically recrystallized grains. According to the first and the second microstructural features, the localization of the formation of dynamically recrystallized grains with small size in the [$\bar{1}$11] single crystal indicates relatively earlier occurrence of dynamic recrystallization. From the third feature, the high frequency of the appearance of subgrains within dynamically recrystallized grains indicates the continuity of evolution of subgrain.

There are two other important microstructural features dependent on the crystal orientation as follows; 1) appearance of many twins, and 2) direction of cracks. Formation of many twins for the [001] single crystal is presumably associated with the release of internal strain, results in suppression of dynamic recrystallization. The cracks occur along the dynamically recrystallized grain boundaries for all crystals, so that the crack direction is directly related to the morphology of the dynamically recrystallized grains. Thus the homogeneous formation of small and equiaxed grains observed in the [011] single crystal causes the crack direction normal to the stress axis as polycrystalline materials.

Using these five microstructural features, the correlation between shortening or lengthening of the transient stage and the dynamic recrystallization can be interpreted. In this paper, we just focused on the phenomenological aspect of creep in Ni-20Cr single crystal with the three different orientations. The detailed mechanisms of the microstructural formation have been in progress.

5. Conclusion

The effect of crystal orientation on creep rate - time curve and on microstructure of Ni-20mass%Cr single crystal with γ single phase has been investigated. The [001], [011] and [$\bar{1}$11] single crystals were creep tested at 1173 K - 29.4 MPa, and the microstructure of creep ruptured specimen was investigated on sections both parallel and normal to the stress axis. The following conclusions can be drawn from this work:

1) The [001] single crystal shows the markedly extended transient creep stage. This marked extension of transient creep stage leads to the smallest minimum creep rate and the largest strain. The [011] single crystal shows the shorter transient creep stage than that in the [001] single crystal. Anisotropic deformation is recognized in the creep of the [011] single crystal. The [$\bar{1}$11] single crystal shows the smallest creep rate just after loading and the smallest creep strain.

2) Dynamic recrystallization occurs homogeneously in the whole gage portion in the [001] and the [011] single crystals. In the [$\bar{1}$11] single crystal, the dynamically recrystallized grains appear locally at the center of the gage portion. Many twins are strikingly observed in the [001] single crystal.

3) The introduction of twin during creep may release the strain accumulated at the center of the gage portion and suppress the dynamic recrystallization. This would be the reason why the acceleration creep is suppressed in the [001] single crystal.

Acknowledgments

The authors would like to thank Associate professor M. Takeyama, Dept. of Metallurgy and Ceramics Science, Tokyo Institute of Technology, for technical discussion and manuscript preparation.

References

[1] Y. Ishiwari, M. S. Thesis, Tokyo Institute of Technology, Tokyo, (1997).
[2] T. Matsuo, T. Kashiwa, M. Nijo and Y. Terada, *Proc. of St Catherine's College Kobe Institute*, (1998), p. 147.
[3] T. Matsuo, S. Takahashi, Y. Ishiwari and Y. Terada, *Proc. of the 8th Intern. Conf. on Creep and Fracture of Engineering Materials and Structure,* Trans Tech Publications, Uetikon-Zurich, (1999), in press.
[4] Y. Terada, Y. Ishiwari and T. Matsuo, *Proc. of the 8th Intern. Conf. on Creep and Fracture of Engineering Materials and Structure,* Trans Tech Publications, Uetikon-Zurich, (1999), in press.
[5] T. Kashiwa, M. S. Thesis, Tokyo Institute of Technology, Tokyo, (1996).
[6] R. W. Hertzberg, Deformation and Fracture Mechanisms of Engineering Materials, 4th edn., Wiley, New York, (1996).

* To whom all correspondence should be addressed, e-mail: daiji@mtl.titech.ac.jp, FAX: +81-3-5734-2874.

Key Engineering Materials Vols. 171-174 (2000) pp. 585-592
© 2000 Trans Tech Publications, Switzerland

Stress Dependence of Evolution of Dynamic Recrystallization in γ Single Phase Single Crystal

Y. Terada[1], Y. Ishiwari[2] and T. Matsuo[1]

[1] Department of Metallurgy and Ceramics Science, Tokyo Institute of Technology, Meguro-ku, Tokyo 152-8552, Japan

[2] graduate student, currently at Mitsubishi Materials Corporation

Keywords: Creep, Single Crystal, Nickel Based Alloy, Dynamic Recrystallization, Microstructure

Abstract

The microstructure of the Ni-20mass%Cr single crystals creep-ruptured at 1173 K in the stress range of 19.6 - 98.0 MPa has been examined. The orientations corresponding to the stress axis of the single crystals are located within the standard stereographic triangle. The appearance of dynamically recrystallized grains in the creep-ruptured specimen drastically changes at a critical stress. In the specimen crept at lower stresses, the dynamic recrystallization occurs homogeneously in the gage portion. With increasing the stress, the microstructure turns to be heterogeneous, that is, the occurrence of dynamic recrystallization becomes more limited to the center of the specimen. The local appearance of dynamically recrystallized grains at higher stresses is discussed by correlating with the large torsion which is derived by a single slip. At lower stresses, torsion to occur seems to be small, thereby suppressing the dynamic recrystallization in early stage. This leads to the homogeneous formation of dynamically recrystallized grains.

1. Introduction

In the previous study, the characteristic of creep of γ single phase Ni-20mass%Cr single crystals with orientations inside the standard stereographic triangle was elucidated by careful analysis of the creep rate - time curves at 1173 K in the stress range of 19.6 - 98.0 MPa [1], by comparing with the polycrystalline alloy. The single crystals exhibit an unique transient creep and it consists of two steps: the step I where the creep rate almost remains unchanged, and the step II where the rate decreases gradually. With decreasing the stress, specifically below 49.0 MPa, the transient creep stage becomes unexpectedly longer, and consequently the decrease in creep rate becomes large.

The microstructural examination during creep of the single crystals at 29.4 MPa by means of interrupting the creep tests at various strains of 0.1 to 0.8 revealed that the dynamically recrystallized grains evolved from subgrains were formed at the time showing the minimum creep rate and the single crystal turns to the polycrystal during the accelerating stage [1,2]. From these evidence, we attributed the origin of accelerating creep to the occurrence of dynamic recrystallization. However, the microstructural observation has been done only at the creep condition, so that further detailed microstructural examination is needed to understand the mechanism of polycrystallization of the single crystal.

In this study, we have examined the microstructures of the creep-ruptured single crystals at a wide stress range of 19.6 to 98.0 MPa, particularly paying attention to the evolution of subgrain and appearance of dynamically recrystallized grains, and clarified the stress dependence of the microstructural evolution in the single crystals.

2. Experimental

A Ni-20mass%Cr alloy, designated as Ni-20Cr in this paper, was prepared for this study. The chemical composition of the alloy is shown in **Table 1**. The alloy was melted in a high frequency induction furnace in a vacuum and cast into a 4 kg ingot in an argon atmosphere. The ingot was hot-forged into rod with a diameter of 13 mm. Single crystals were grown by a modified

Bridgman furnace in a flow of purified argon and then solution-treated at 1523 K for 36 ks in air. The crystal orientation corresponding to the initial stress axis was determined by Laue back-reflection X-ray technique. In order to minimize the orientation effect, five crystals labeled A to E having nearly the same orientation within the standard stereographic triangle were used for this study as shown in **Fig. 1**. Then, full size creep specimens with the gage portion 30 mm in length and 6 mm in diameter were machined from the crystals. Note that all the crystals have the Schmid factor above 0.46.

Tensile creep tests were carried out at 1173 K under the constant stresses in the range of 19.6 - 98.0 MPa using the single-lever type creep machines. During the creep tests, stress was kept constant by adjusting the auxiliary weights in an accuracy within one per cent against initial stress. Creep strain was automatically recorded using linear variable-differential transducers via extensometer fitting onto annular ridges machined at both ends of the specimen gage portion. Microstructures subjected to creep deformation were observed by the optical microscope on sections both parallel and perpendicular to the stress axis. After metallographic polishing, samples were etched in a solution of orthophosphoric acid saturated with chromium trioxide with a current density of 10 mA/cm^2 for 10 minutes.

Table 1. Composition (mass%) of crystals prepared in this investigation.

Alloy	C	Si	Mn	Cr	Ni
Ni-20Cr	0.001	0.49	0.30	19.3	Bal.

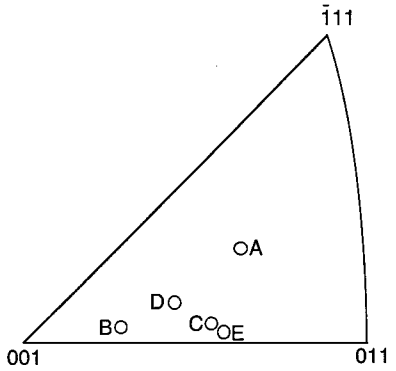

Fig. 1. Initial orientations of Ni-20Cr single crystals tested in this investigation.

3. Results

3.1. Creep characteristics

Creep rate - time curves of Ni-20Cr single crystals labeled A, B, C, D and E are shown in **Fig. 2**, where the creep rate is a true strain rate [3]. In each stress, the curve basically shows a similar shape; the creep rate initially remains constant, and then decreases to a minimum creep rate, followed by accelerating abruptly. The decrease in creep rate during the transient stage becomes large with decreasing the stress, and this effect is obvious when the stress is below 49.0 MPa. At 19.6 MPa the creep rate becomes smaller by two orders of magnitude than that of the plateau region even though the rate has not reached the minimum when the test was interrupted after 2000 h. Note that the rupture strains are around 1.0, irrespective of stress.

The stress - minimum creep rate curve of Ni-20Cr single crystal is shown in **Fig. 3**, together with the curve of Ni-20Cr polycrystalline specimen with the average grain diameter of 200 μm in the previous papers [4,5]. The minimum creep rate of the single crystal is nearly identical to that

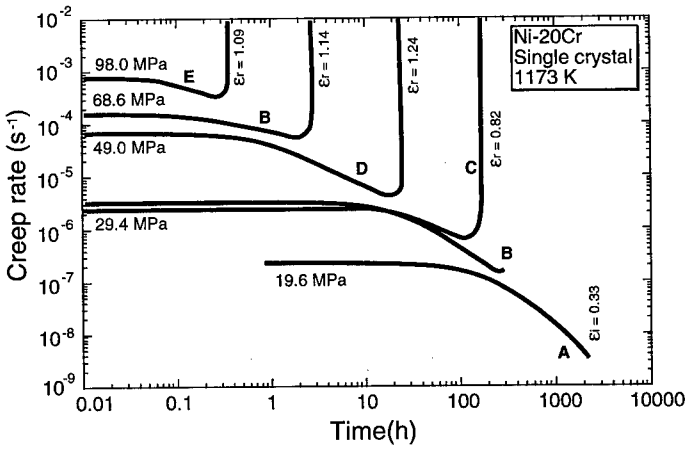

Fig. 2. Creep rate - time curves for Ni-20Cr single crystal tested at 1173 K under the constant stresses within the range of 19.6 - 98.0 MPa. The creep rate is a true strain rate [3].

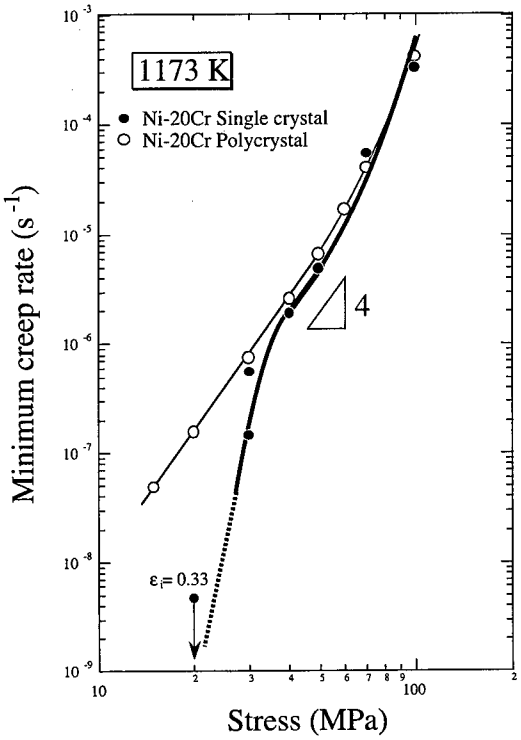

Fig. 3. Variation of minimum creep rate with applied stress for Ni-20Cr single crystal, together with the results for Ni-20Cr polycrystal obtained in the previous papers [4,5]. Tensile creep test is conducted at 1173 K under the constant stresses within the range of 19.6 - 98.0 MPa.

of the polycrystal at the stresses above 40 MPa, however below 40 MPa it becomes smaller and the difference in creep rate is enlarged with decreasing the stress. This prominent difference in the minimum creep rate with decreasing the stress is mainly caused by the extension of transient creep stage as is indicated in Fig. 2.

From these results we define the stress to lead a smaller minimum creep rate due to the extension of the transient creep stage as critical stress, and it is 40 MPa. In the following section, thus, the microstructures of the creep-ruptured specimens were examined in order to understand the mechanism causing such a stress dependent creep behavior.

3.2. Stress dependence of microstructure

Optical micrograph of the Ni-20Cr single crystals creep-ruptured at 1173 K - 29.4 MPa are shown in **Fig. 4(a)**, where the stress of 29.4 MPa is lower than the critical stress. Dynamically recrystallized grains are observed homogeneously in the whole gage portion. All of the grains are equiaxed in shape, and the average grain diameter is approximately 150 μm. Cracking takes place at the dynamically recrystallized grain boundaries perpendicular to the stress axis. Note that dynamically recrystallized grains are also detected outside the gage portion, but they are located at the center of the specimen. In the crystal crept at 49.0 MPa (**Fig. 4(b)**), dynamically recrystallized grains are formed homogeneously as well. The average diameter of dynamically recrystallized grains is about 100 μm, and it is smaller than that observed at 29.4 MPa.

In contrast, the dynamically recrystallized grains are observed in the crystal crept at 68.6 MPa, but they are formed only near the center of the creep specimen. The average diameter of the grains is about 50 μm, which is much smaller than that in the crystal crept at lower stresses. At high stress of 98.0 MPa, the region to form the dynamically recrystallized grains is more limited to the center of the specimen, as shown in **Fig. 4(d)**. The grain diameter is about 25 μm. In the crystal, subboundaries are also formed along a certain direction in the whole gage portion, although they are curved at the center of the specimen. Note that the region where many dynamically recrystallized grains are observed at the center of the specimen turns to a single line of grain boundary at the annular ridges of the specimen, and the boundary reaches to the end of the specimen. Thus, there is a marked difference in the mode of dynamic recrystallization between the crystal crept at 67.6 MPa and that at 49.0 MPa, therefore, a critical stress would exist between 49.0 MPa and 67.6 MPa.

To elucidate the morphology of the grain boundary at the center of the specimen, the microstructures of the cross section area in the ruptured specimen have been examined at the end of the gage portion. The results are shown in **Fig. 5**. The specimen is divided into three portions by dynamically recrystallized grains at the stresses lower than the critical stress (Fig. 5(a),(b)). With increasing the stress, the dynamically recrystallized grains turn to grain boundaries as shown in the crystal crept at 98.0 MPa (Fig. 5(c)).

4. Discussion

From the above result of microstructure, it appears that the dynamic recrystallization occurs during creep for the Ni-20Cr single crystal. The microstructure of the single crystal subjected to creep deformation changes drastically depending on the applied stress, as mentioned in the above section. The resulted microstructural change with stress level in the single crystals is schematically illustrated in **Fig. 6**. At lower stresses, the dynamic recrystallization occurs homogeneously in the gage portion. With increasing the stress, the grain diameter of the dynamically recrystallized grains becomes smaller under the homogeneous microstructure in the gage portion. However, the microstructure drastically turns to be heterogeneous when the stress becomes higher. The stress level which brings about the drastic change in microstructure roughly agrees with the critical stress defined from the stress - minimum creep rate curve. In the creep rate - time curves in Fig. 1, the decrease in creep rate in the transient stage becomes enlarged at the lower stresses below 49.0 MPa. This stress level corresponds to the stress below which the transient creep stage becomes extended.

The cause to change the microstructure due to dynamic recrystallization from homogeneous to heterogeneous is probably associated with the torsion of the specimen. As shown in **Fig. 7**, the creep deformation during the transient creep is caused by a single operative slip system. Since the single crystals exhibit fairly a large strain, the deformation mode makes the specimen shape off

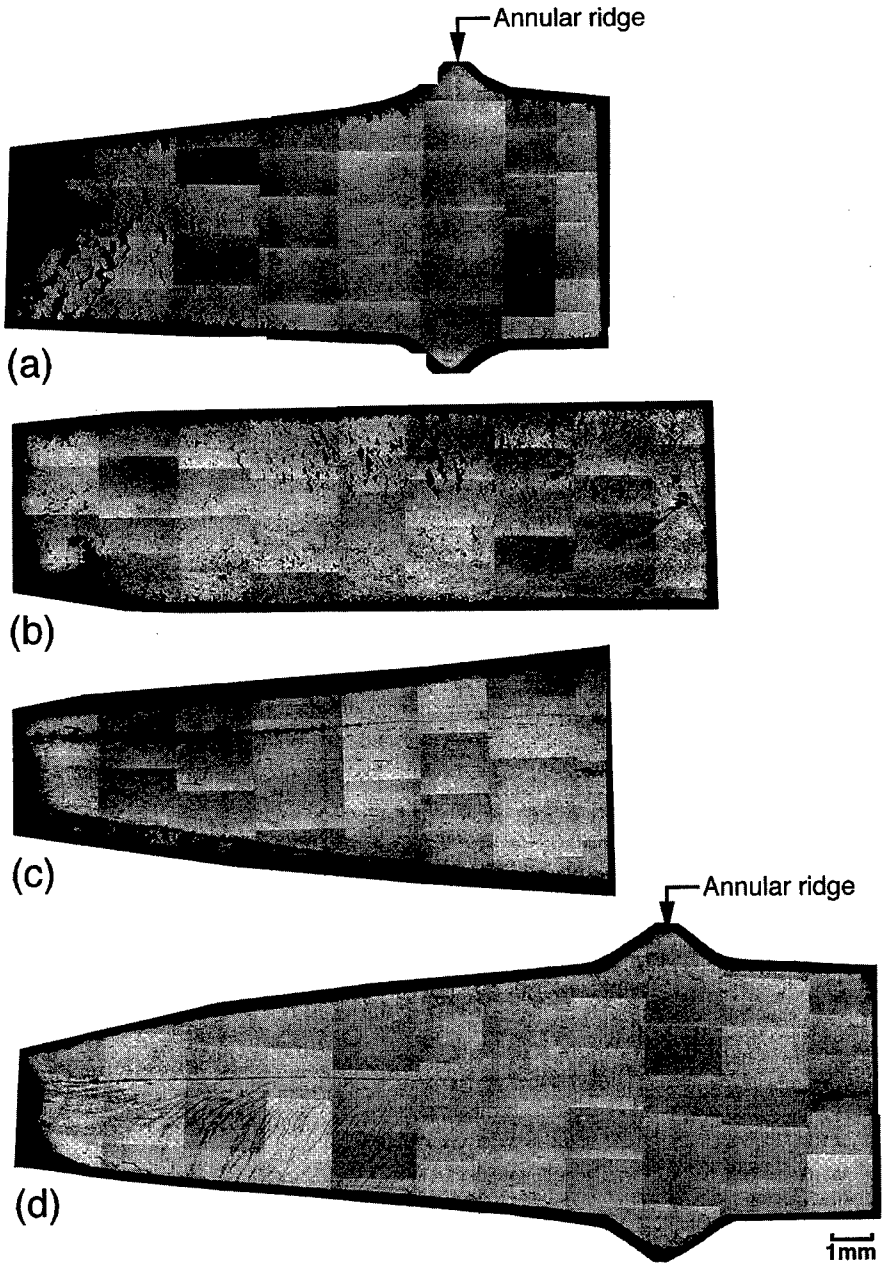

Fig. 4. Optical micrograph of Ni-20Cr single crystal creep-ruptured at 1173 K under the constant stress of 29.4 MPa (a), 49.0 MPa (b), 67.6 MPa (c) and 98.0 MPa (d). The observation is conducted on the section parallel to the stress axis.

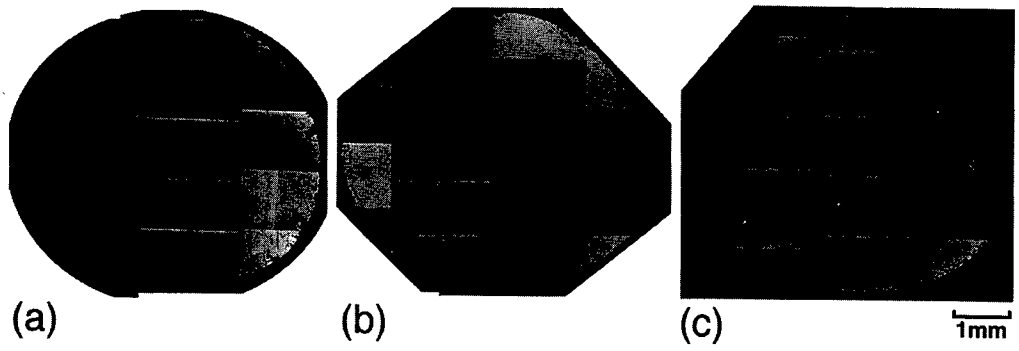

Fig. 5. Optical micrograph of Ni-20Cr single crystal creep-ruptured at 1173 K under the constant stress of 29.4 MPa (a), 49.0 MPa (b) and 98.0 MPa (c). The observation is conducted on the section perpendicular to the stress axis at the end of the gage portion.

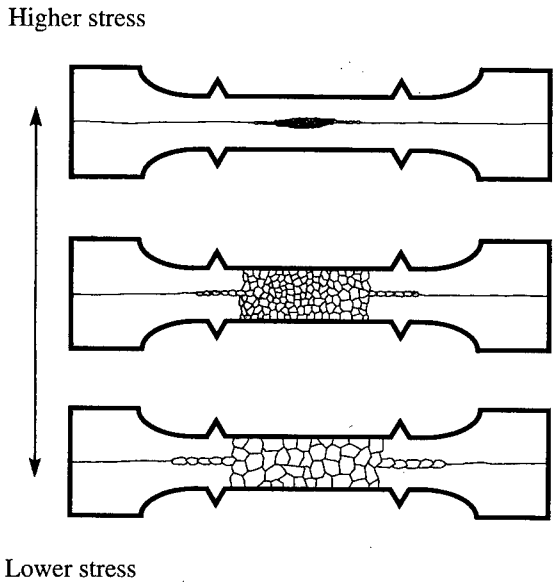

Fig. 6. Schematic illustration of microstructure for single crystal with the orientation inside the standard stereographic triangle creep-ruptured in a wide stress revel.

aligned with increasing creep strain if the specimen both ends are not constrained (Fig. 7(a), (b)) [6]. In practice, however, they are gripped in line, so that the slip plane must rotate toward the stress axis with increasing the strain, resulting in torsion of the specimen to accommodate its macroscopic shape (Fig. 7(c)). Based on this supposition, more strain is generated by torsion at the center of the specimen, rather than the outer portion. This would be responsible for the fact that the dynamic recrystallization heterogeneously occurs near the center of the specimen at higher stresses. At lower stresses, however, because of the small strain, the torsion to occur seems to be small, thereby suppressing the dynamic recrystallization in early stage. This leads to the extension of transient creep and homogeneous formation of dynamically recrystallized grains.

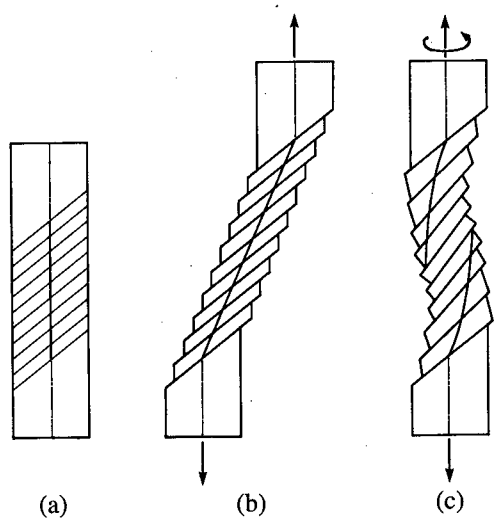

Fig. 7. Schematic illustration of cross-sectional shape change due to shear on a single slip system.

5. Conclusion

The microstructure of the Ni-20mass%Cr single crystals creep-ruptured at 1173 K in the stress range of 19.6 - 98.0 MPa has been examined. The orientations corresponding to the stress axis of the single crystals are located within the standard stereographic triangle. The results are summarized as follows;

1) The creep rate - time curve in each stress basically shows a similar shape; the creep rate initially remains constant, and then decreases to a minimum creep rate, followed by accelerating abruptly. The decrease in creep rate during the transient stage becomes large with decreasing the stress less than 49.0 MPa.

2) Dynamic recrystallization occurs homogeneously in the gage portion at the stress lower than 49.0 MPa. When the stress becomes higher, the microstructure turns to be heterogeneous, that is, the occurrence of dynamic recrystallization becomes limited to the center of the specimen.

3) The heterogeneity in dynamic recrystallization at higher stress would be associated with the torsion of the specimen caused by a single operative slip system. At lower stresses, torsion to occur seems to be small, thereby suppressing the dynamic recrystallization in early stage. This leads to the extension of transient creep and homogeneous formation of dynamically recrystallized grains.

References

[1]. T.Matsuo, S.Takahashi, Y.Ishiwari and Y.Terada, *Proc. of the 8th Intern. Conf. on Creep and Fracture of Engineering Materials and Structure*, Trans Tech Publications, Uetikon-Zurich, (1999), in press.

[2]. T.Matsuo, T.Kashiwa, M.Nijo and Y.Terada, *Proc. of St Catherine's College Kobe Institute*, (1998), p.147.

[3]. R.W.Hertzberg, *Deformation and Fracture Mechanisms of Engineering Materials, 4th edn.*, Wiley, New York, (1996).

[4]. T.Matsuo, K.Nakajima, Y.Terada and M.Kikuchi, Mater. Sci. Eng., **A146**(1991), 261.

[5]. K.Nakajima, Dr Thesis, Tokyo Institute of Technology, Tokyo, (1992).

[6]. L.-M.Pan, I.Scheibli, M.B.Henderson, B.A.Shollock and M.McLean, Acta Metall. Mater., **43**(1995), 1375.

* To whom all correspondence should be addressed, e-mail: terada@mtl.titech.ac.jp, fax: 81 3 5734 3585.

Key Engineering Materials Vols. 171-174 (2000) pp. 593-600
© 2000 Trans Tech Publications, Switzerland

Creep of Reinforced and Unreinforced AZ91 Magnesium Alloy

V. Sklenička[1], M. Pahutová[1], K. Kuchařová[1], M. Svoboda[1] and T.G. Langdon[2]

[1] Institute of Physics of Materials Academy of Sciences of the Czech Republic, Žižkova 22, CZ-616 62 Brno, Czech Republic

[2] Departments of Materials Science and Mechanical Engineering, University of Southern California, Los Angeles, CA 90089-1453, USA

Keywords: Magnesium Alloy, Alumina Short Fibres, Reinforcement, Metal Matrix Composite, Fracture, Creep Life

Abstract

Constant stress tensile creep tests were conducted at temperatures 423 and 473 K on an AZ 91 (Mg - 9wt%Al - 1wt%Zn) alloy reinforced with 20 volume % Al_2O_3 short fibres and on an unreinforced AZ 91 matrix alloy. In essence, the creep resistance of the reinforced material is shown to be considerably improved compared to the matrix alloy. The minimum creep rate for reinforced specimens is two to three orders of magnitude less than that of unreinforced specimens under the same loading. The creep life of the composite is an order of magnitude longer than the unreinforced alloy. By contrast, the presence of the reinforcement leads to a substantial decrease in the creep plasticity.

Introduction

Magnesium alloys are now being increasingly required for high-temperature structural applications where weight saving is necessary. However, the creep resistance of Mg alloys is found to be rather limited at temperatures above 423 K (150°C). A considerable improvement in the creep properties of Mg-based alloys can be potentially achieved by non-metallic short fibre reinforcement (metal matrix composites - MMCs). Although a number of studies have been reported on the creep behaviour of pure magnesium [1-4] and Mg solid solution alloys [5, 6], the creep properties of more complex Mg alloys [7-12] and short fibre reinforced Mg-based composites [9,13-16] have received only limited attention. The present study was therefore initiated to provide a comparative evaluation of the creep properties of a fibre-reinforced AZ 91 matrix composite and its matrix alloy. Attention in this paper is focused primarily on the effects of short fibre reinforcement on creep rate, lifetime and strain to fracture. It is only appropriate here to describe differences that can be inferred from a comparison between the creep characteristics of the two materials and that are relevant to the present investigation.

Experimental materials and procedures

Short fibre reinforced and unreinforced blocks of an AZ 91 alloy (Mg - 9wt%Al - 1wt%Zn - 0.3 wt% Mn) were fabricated by squeeze casting at the Department of Materials Engineering and Technology, Technical University of Clausthal, Germany. The fibre preform consists of planar randomly distributed δ - alumina short fibres (Saffil fibres from ICI, 97% Al_2O_3, 3% SiO_2, ~ 3μm in diameter with varying lengths up to an estimated maximum of ~ 150 μm). The final fibre fraction fter squeeze casting in the composite was about 20 volume %. For convenience, the

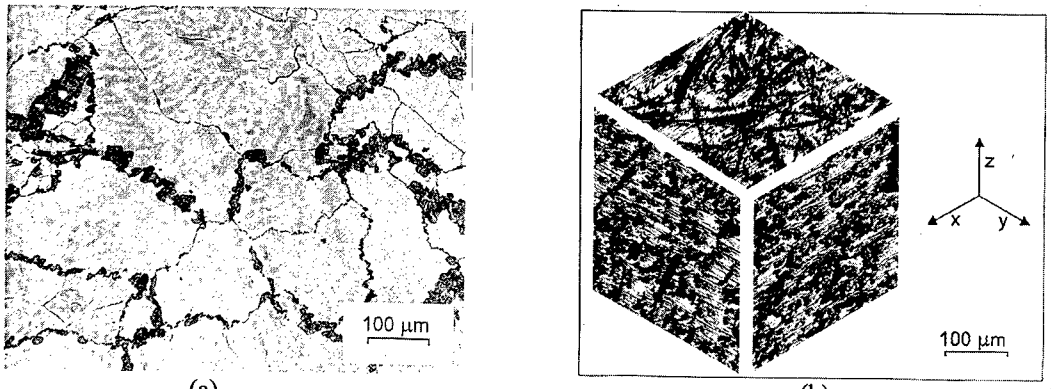

(a) (b)

Figure 1a, b. Optical micrographs showing microstructure of: (a) an unreinforced AZ 91 alloy, and (b) the AZ 91-20vol.%Al_2O_3 (f) composite.

composite is henceforth designated AZ 91 - 20 vol% Al_2O_3 (f) where f denotes fibre. Both materials were subjected to a standard T6 heat treatment (anneal for 24h at 688 K, air cool and then age for 24 h at 443 K). Examples of typical microstructures of squeeze cast monolithic AZ 91 alloy and the AZ 91 - 20 vol% Al_2O_3 (f) composite are shown in Fig. 1a, b.

Flat tensile creep specimen having gauge lengths of 25 mm and cross-sections 3 x 3.2 mm were machined from the blocks in a such way that the longitudinal specimen axes were parallel to the x - y plane (Fig. 1b). The constant stress tensile creep tests were carried out at temperatures 423 K and 473 K, respectively, and with the testing temperature continuously monitored and maintained constant to within ± 0.5 K of the desired value. The applied stress ranged from 60 to 150 MPa. The creep tests were performed in purified argon in tensile creep testing machines, making it possible to keep the nominal stress constant to within 0.1% up to a true strain of about 0.35. The creep elongations were measured using a linear variable differential transducer and they were recorded digitally continuously and computer processed using the software CRTES [17]. Almost all the specimens were run to final fracture.

Following creep testing, samples were prepared for examination by transmission electron microscopy (TEM). Observations were performed using a Philips CM 12 STEM transmission electron microscope with an operating voltage of 120 kV. Fractographic details were investigated by means of light microscopy and scanning electron microscopy (Philips SEM 505 microscope).

Experimental results

Selected creep curves for these two materials are shown in Fig. 2 in the form of strain, ε, versus time, t, for an absolute testing temperature, T, of 423 K and under comparable levels of the applied stress, σ. As demonstrated by the figure, significant differences were found in the creep behaviour of the composite when compared to its matrix alloy. First, the presence of the reinforcement leads to a substantial decrease in the creep plasticity, which is proved by the values of the total strains to fracture for the composite. Second, the composite exhibits markedly longer creep life than the alloy at the entire stress range used. Third, the shapes of creep curves for the composite and the alloy differ considerably. It should be mentioned that the creep curves shown in Fig. 2 do not clearly indicate the individual stages of creep. However, these standard ε vs. t curves can be easily replotted in the form of the instantaneous strain rate, $\dot{\varepsilon}$, versus time, t, as shown in Fig. 3. Fig. 3a presents the log $\dot{\varepsilon}$ - t curves for a temperature of 423 K and a stress of 100 MPa for both materials. It is apparent that neither curve exhibits a well-defined steady stage. In fact, this stage is reduced to

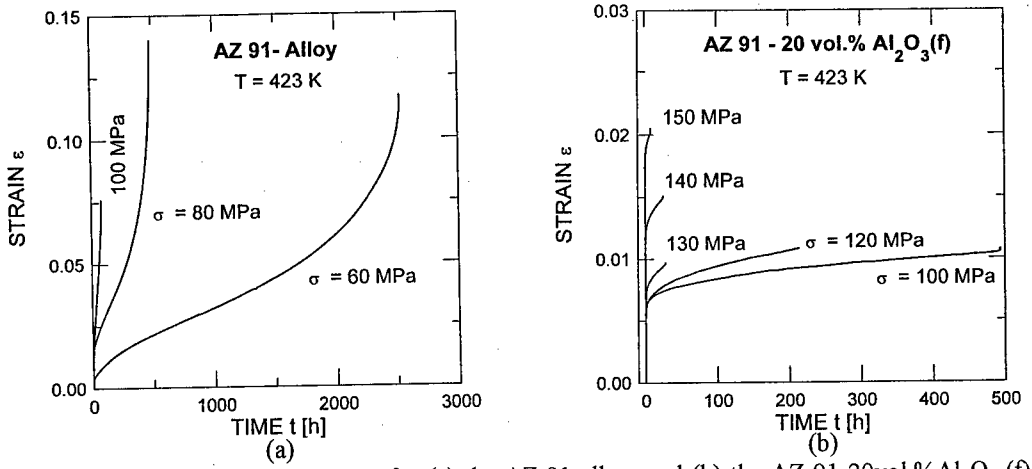

Figure 2a, b. Creep curves at 423 K for (a) the AZ 91 alloy, and (b) the AZ 91-20vol.%Al_2O_3 (f) composite.

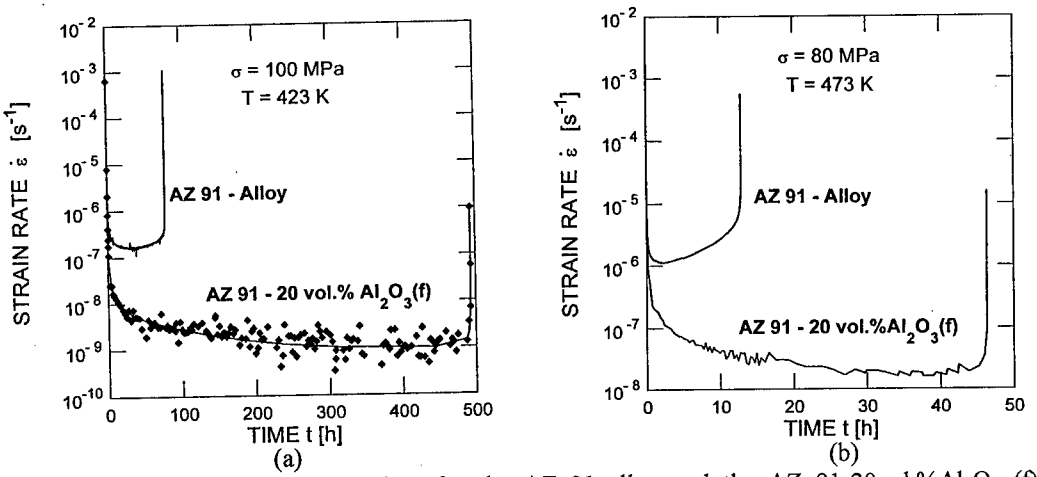

Figure 3a, b. Strain rate versus time for the AZ 91 alloy and the AZ 91-20vol.%Al_2O_3 (f) composite (a) at 423 K and 100 MPa, and (b) at 473 K and 80 MPa.

an inflection point of the $\dot{\varepsilon}$ versus t curve. Despite this similarity, the occurrence of a primary stage followed by a tertiary stage of creep in the matrix alloy is in a striking contrast with the nature of the creep curve in the composite. The latter curve shows the primary stage is fairly extensive and represents practically the whole creep test. A minimum in the creep rate is reached just before final fracture and the presence of a tertiary stage is not well-defined. This difference in the shapes of the $\dot{\varepsilon}$ - t creep curves in the matrix alloy and in the composite is confirmed and perhaps more clearly illustrated in Fig. 3b for the tests conducted at the same temperature of 473 K and stress of 80 MPa. Inspection suggests that creep in the composite is again dominated by fairly extensive primary stage. On the other hand, an extremely short primary creep in the matrix alloy is followed by a lengthy tertiary stage.

The creep data of the AZ 91 alloy and the AZ 91 - 20 vol.% Al_2O_3 (f) composite at 423 and 473 K are shown in Fig. 4a, where the minimum creep rate, $\dot{\varepsilon}_m$, is plotted against the applied stress, σ, on a logarithmic scale. Inspection of the creep data in Fig. 4a leads to two observations. First, the composite exhibits better creep resistance than the alloy over the entire stress range used; the

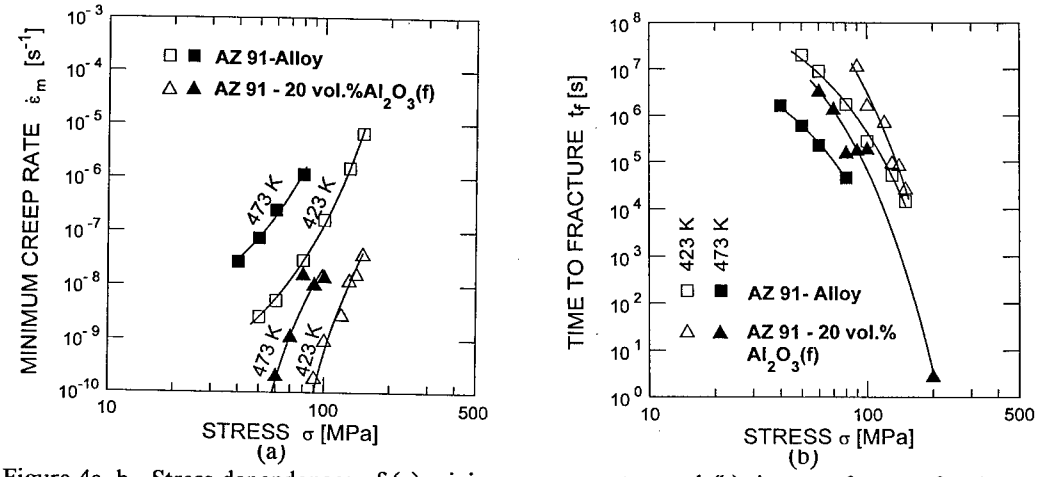

Figure 4a, b. Stress dependences of (a) minimum creep rates, and (b) times to fracture for the AZ 91 alloy and the AZ 91-20vol.%Al_2O_3 (f) composite at 423 and 473 K.

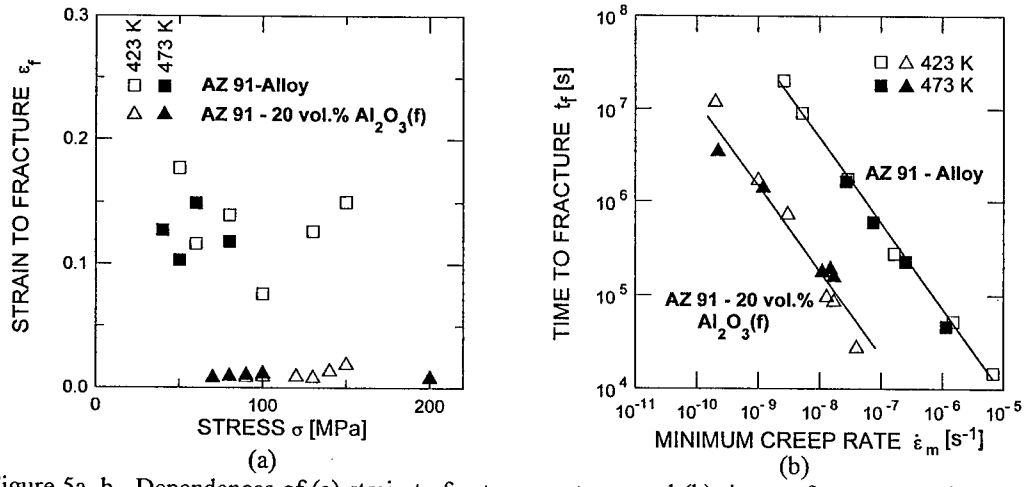

Figure 5a, b. Dependences of (a) strain to fracture on stress, and (b) time to fracture on minimum creep rate for the AZ 91 alloy and the AZ 91-20vol.%Al_2O_3 (f) composite at 423 and 473 K.

minimum creep rate for the composite is about two to three orders of magnitude less than that of the unreinforced alloy. Second, as depicted in Fig. 4a, the stress dependences of the minimum creep rates for both materials are different in trend, which is clearly demonstrated by the characteristic curvatures on the inherent curves at low stress. While the slopes and therefore the apparent stress exponents, $n_a = (\partial \ln \dot{\varepsilon} / \partial \ln \sigma)_T$, for the alloy slightly decrease with decreasing applied stress, the curvatures for the composite increase with decreasing applied stress. Such an increase of the apparent stress exponent at low stresses is usually considered to be indicative of the presence of a threshold stress representing a lower limiting stress below which creep cannot occur [18, 19]. For both materials, the double logarithmic plots of the time to fracture, t_f, as a function of applied stress are shown in Fig. 4b. It is clear from these plots that the creep life of the composite is an order of magnitude longer than the unreinforced alloy at these two temperatures. This difference consistently decreases with increasing applied stress, with a tendency at the higher stress towards no effect of the reinforcement on the lifetime. In fact, inspection of Fig. 4b reveals that at stresses higher than 200 MPa the creep life of the composite seems to be essentially equal to that of the

unreinforced matrix alloy. A variation of the strain to fracture, ε_f, with stress and temperature is shown in Fig. 5a. This figure indicates no clear effect of stress and/or temperature on the strain to fracture. The values of the strain to fracture in the composite are only 1-2%. By contrast, the strains to fracture in the matrix alloy are typically 10-15%. Experimentally determined times to fracture and strains to fracture correlate well with minimum creep rates through the Monkman-Grant relationship, $\dot{\varepsilon}_m t_f$ = constant (Fig. 5b); t_f is approximately inversely proportional to $\dot{\varepsilon}_m$. Note, however, that ε_f itself can be strongly influenced by the mechanisms of the fracture process which could explain a shift of the composite dependence towards shorter times to fracture at the same minimum creep rates.

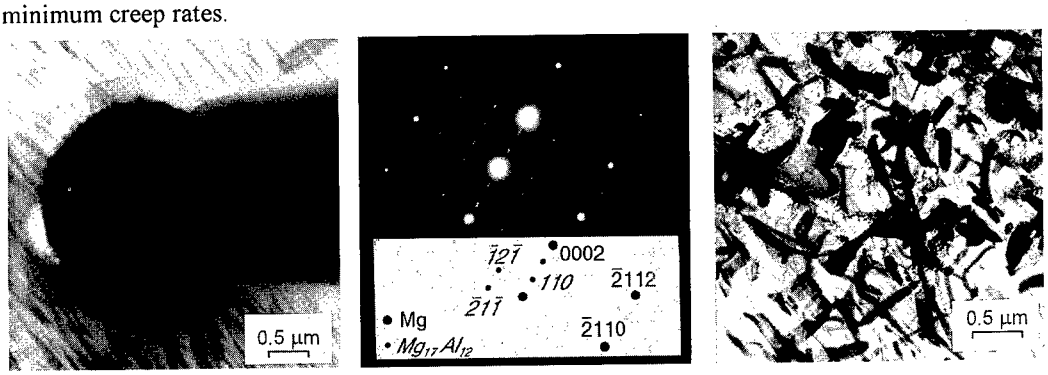

(a) (b) (c)

Figure 6a, b, c. TEM micrographs and SAED of the AZ 91-20vol.%Al_2O_3 (f) composite showing (a) alumina fibre and β-phase after T6 heat treatment, (b) SAED of coherent β-phase from region in (a), and (c) detail of coarsened coherent β-phase after creep at 423 K and 100 MPa.

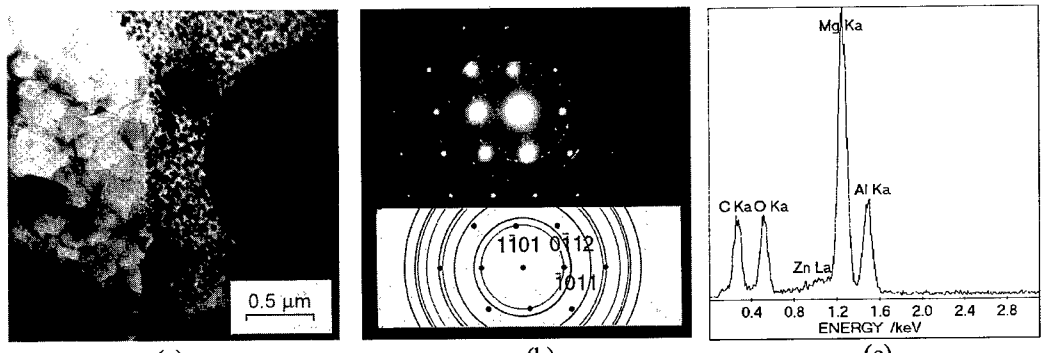

(a) (b) (c)

Figure 7a, b, c. Microstructure of the AZ 91-20vol.%Al_2O_3 (f) composite after creep at 423 K and 90 MPa: (a) TEM micrograph, (b) and (c) SAED and EDXS from MgO particles, respectively.

The microstructure of the as-cast AZ 91 alloy consists of the β - phase ($Mg_{17}Al_{12}$ [7, 20-23] and/or Mg_{17} (Al, Zn)$_{12}$ [23]) intermetallic compounds in a matrix of α magnesium solid solution. The T6 heat treatment caused partial homogenization of the microstructure of the alloy and at the same time prevented to some extent the precipitation of the massive and lamellar β - phase ($Mg_{17}Al_{12}$) particles. The microstructure of the AZ 91 - 20 vol.% Al_2O_3 (f) composite is much complex than that of the unreinforced matrix alloy [24-26]. The applied T6 heat treatment was adjusted to minimize matrix-fibre reactions in the composite. In comparison to the as-cast state the size and number of massive and lamellar $Mg_{17}Al_{12}$ precipitates is significantly reduced. However, at several sites the fibres are still interconnected by the massive β - phase "bridges" (Fig. 6a). Careful investigation by TEM revealed that the most frequent morphology of the β - phase precipitates in

the composite is coherent $Mg_{17}Al_{12}$ platelets (Figs. 6 b,c). The enhanced precipitation of the β - phase on the fibres is promoted by heterogeneous nucleation of the Al enrichment of the matrix near to the alumina fibres. Fig. 7a shows clearly a thicker zone in contact with the fibres indicating a fine internal crystalline phase. From the ring diffraction pattern and the EDS analysis this phase was identified as magnesia (MgO) particles - Figs. 7b,c. The significant microstructural changes in the composite observed after creep were fine continuous precipitation of the $Mg_{17}Al_{12}$ particles and coarsening of coherent β - phase precipitates. The longitudinal metallographic sections cut from the gauge length of creep specimens were examined using SEM to evaluate creep damage [16]. Metallographic investigation did not reveal either substantial creep fibre cracking and breakage or any debonding at the interface between the matrix and the fibres due to creep.

Discussion

It is relevant to discuss first the reason for different shapes of creep curves for the composite and the monolithic matrix alloy (Figs. 3a,b). The dominant primary stage apparent in the creep curves of the composite (Figs. 3a,b) can be a result by non-linear visco-elastic deformation of the highly-stressed central regions of the fibres; this leads to a steady-state due to matrix flow about the fibres when they are fully stretched elastically. Further, the occurrence of a lengthy primary stage of creep in the AZ 91 - 20 vol.% Al_2O_3 (f) is probably associated with the additional β - phase precipitation and with gradual change in the precipitate morphology during the creep exposure. Lastly, the observed long primary stages are not indicative of the initiation of any debonding at the interfaces between the matrix and the reinforcement and/or creep fibre breakage in accordance with the metallographic and fractographic observations. On the other hand, the tertiary creep behaviour should result from fibre fracture leading to a reduction in the fibre aspect ratio or the development of ductile tearing with off-loading of stress to the sound composite material, both factors leading to an acceleration in the creep rate. Thus, the observed extremly lengthy primary stage apparent in the creep curves of the composite in the present work does not support the prediction of the simplified mechanistic model of creep in short fibre reinforced metal matrix composite [27] derived from the creep experiments and microstructural observations on short fibre reinforced alluminium alloys (e.g. an AlSi7Cu3Mg - 15 vol.% Al_2O_3(f)) and based on three elementary microstructural processes including a multiple fibre breakage starting early in creep life. A possible explanation for this different creep behaviour in aluminium and magnesium short fibre reinforced metal matrix composites may lie in the different strength of the fibre-matrix interface (bonding) and load transfer during the creep of both composite materials.

A question naturally arises about the rate controlling mechanism(s) in creep of a fibre reinforced AZ 91 matrix composite. It should be stressed again that studies of creep behaviour and the relevant creep data of this composite are almost not available in the literature. Mordike et al. [13] conducted very limited tensile creep tests on a squeeze-cast AZ 91 + 20 vol.% Al_2O_3 (f) at temperatures 423, 473 and 523 K. For creep experiments at 423 and 523 K they obtained a value of the apparent stress exponent close to ~ 1. However, at a temperature of 473 K they reported a transition with increasing stress from $n_a \cong 1$ to $n_a \cong 3.1$ at stresses above 40 MPa. Very recently, Li et al. [15, 28] performed a comprehensive evaluation of the creep of a squeeze-cast AZ 91 - 20 vol.% Al_2O_3 (f) composite (the identical material as used in this work) using a double shear configuration. When the creep data were interpreted by incorporation of a threshold stress into the analysis, it was shown that the results are consistent with the behaviour anticipated for a magnesium solid solution alloy [5], including a true stress exponent close to 3.

The curvature on the creep curves for the composite in a double logarithmic plot of $\dot{\varepsilon}$ against σ (Fig. 4a) is indicative of the presence of a threshold stress, σ_0. When a threshold stress is present, creep occurs under an effective stress given by $(\sigma - \sigma_0)$. The values of the threshold stresses may be

estimated by using a linear extrapolation procedure in which $\dot{\varepsilon}^{1/n}$ is plotted against σ on linear axes for prior selected values of the true stress exponent n and, in the absence of any significant curvature, the plots are extrapolated linearly to intersect the stress axis at zero strain rate [19, 29]. This procedure was followed in the present investigation using prior selected values of n of 3, 5 and 8, where these three values of n represent creep by a viscous glide process [30, 31], creep controlled by dislocation climb [32] and a constant structure model of creep [33, 34], respectively. Detailed inspection of the individual plots showed that a true stress exponent of 3 yielded the best linear fit. The values of σ_0 were estimated as ~ 80 and ~ 47 MPa at the two testing temperatures of 423 and 473 K, respectively, which indicates a temperature dependence of the threshold stress. The finding $n = 3$ over a wide range of effective stress provides strong support for the adoption the suggestion of Li et al. [15, 28] that the AZ 91 composite material exhibits creep behaviour which is consistent with the behaviour anticipated for a magnesium solid solution alloys. Thus, the creep behaviour of the composite is controlled by deformation in the matrix material.

However, as depicted in Fig. 4a, the composite exhibits better creep resistance than the matrix alloy; the presence of short - fibre reinforcement leads to reduced creep rate in the composite by two to three orders of magnitude. Such difference can arise when significant load transfer partitions the external load between the matrix and the reinforcement [35-37]. In the presence of load transfer, the creep data may be successfully reconciled by putting the ratio of the creep rates of the composite, $\dot{\varepsilon}_c$, and the rates of the matrix alloy, $\dot{\varepsilon}_m$, at the same creep loading conditions equal to a factor given by $(1 - \alpha)^n$, where α is a load transfer coefficient having values lying within the range from 0 (no load transfer) to 1 (full-load transfer) [37]. The values of α inferred from the data in Fig. 4a using $n = 3$ are within the range of 0.79 to 0.90. It is interesting to correlate these experimentally determined values α with an analytical treatment. Kelly and Street [35] proposed a shear-lag approach that predicts the tensile creep behaviour of discontinuous fibre-reinforced composites. Subsequently, Nardone and Prewo [38] suggested a modified shear-lag model by considering the load transfer effect at the end of short fibres and various reinforcement geometries and arrangements (volume fraction, aspect ratio). The values of α predicted from the modified shear-lag model with 20 vol. pct of short-fibre reinforcement are $\alpha \cong 0.75$ and $\alpha \cong 0.84$ an experimentally observed fibre aspect ratios S (diameter/length) ~ 30 and ~ 50, respectively. Thus, the predicted values are in reasonable agreement with the experimental values of α inferred from the present analysis.

Conclusions

A comparison between the creep characteristics of an AZ 91 alloy reinforced with 20 vol.% Al_2O_3 short fibres and an unreiforced AZ 91 matrix alloy under comparable experimental conditions shows that creep strengthening in the composite arises mainly from the following two mechanisms: (a) the existence of a temperature - dependent threshold stress, and (b) load transfer. High values of load transfer estimated for the composite indicate good fibre/matrix interface bonding together with no substantial breakage of fibres during creep exposure lead to the conclusion that the use of alumina short fibres is very effective in improving the creep properties of the squeeze-cast Mg alloy matrix composites.

Acknowledgements

Financial support for this study was provided by the Ministry of Education of the Czech Republic under the US - Czech Programme KONTAKT ME 129, by the National Science Foundation of the United States under Grant No. INT-9602022 and by the Grant Agency of the Academy of Sciences of the Czech Republic under Grant A 2041902. We thank Professor Pavel Lukáč (Department of Metal Physics, Charles University, Prague, Czech Republic) for several helpful discussions.

References

[1] K. Milička, J. Čadek and P. Ryš, Acta Metall. 18 (1970), p. 1071.
[2] I. G. Crossland and R.B. Jones, Metal Sci. J. 6 (1972), p.162.
[3] S.S.Vagarali and T.G.Langdon: Acta Metall. 29 (1981), p. 1969.
[4] L. Shi and D.O. Northwood, Acta Metall. Mater. 42 (1994), p. 871.
[5] S. S. Vagarali and T. G. Langdon, Acta Metall. 30 (1982), p. 1157.
[6] H. Sato , Y. Masada and H. Oikawa, in: Proc. 7th JIM Symposium on Aspects of High Temper. Deformation and Fracture in Crystalline Materials, Y. Hosoi et al (eds.), Sendai, (1993), p. 107.
[7] M. Regev, E. Aghion and A. Rosen, Mater. Sci. Eng. A 234 - 236, (1997), p. 1997.
[8] W.Blum, P.Weidinger, B.Watzinger, R.Sedláček, R.Rösch and H.-G. Haldenwanger, Z.Metallkd. 88 (1997), p. 636.
[9] B.L. Mordike and P. Lukáš, in Proc. 3rd. Int. Magnesium Conference, ed. G.W.Lorimer, The Inst. of Materials, London, 1997, p. 419.
[10] W. Blum, B. Watzinger and P. Weidinger, in Magnesium Alloys and their Applications, eds. B.L.Mordike and K.U.Kainer, Werkstoff-Informationsgesellschaft mbH, Frankfurt 1998, p. 49.
[11] J.Kiehn, M.Eilers and K.U.Kainer, ibid., p. 235.
[12] M.S.Dargusch and G.L.Dunlop, ibid., p. 277.
[13] B.L.Mordike, K.U.Kainer and B. Sommer, ibid, p. 637.
[14] B.L.Mordike, K.U.Kainer, F.Moll and B. Sommer, in Magnesium 97, eds. E. Aghion and D. Eliezer, Magnesium Res. Institute Ltd., Beer-Sheva, Israel, 1998, p. 178.
[15] Y. Li, V. Sklenička and T. G. Langdon: in Creep Behaviour of Advanced Materials for the 21st Century, eds. Rajiv S. Mishra et al., TMS, Warrendale, 1999, p. 171.
[16] M. Pahutová, J.Březina, K.Kuchařová, V.Sklenička and T. G. Langdon, Mater. Letters, in press.
[17] K.Milička, F.Dobeš, J.Slaměníková and A. Orlová, Acta Metall.Mater. 43 (1995), p.26.
[18] J.C.Gibeling and W.D.Nix, Mater.Sci.Eng. 45 (1980), p.123.
[19] Y.Li and T.G.Langdon, Scripta Mater. 36 (1997), p. 1457.
[20] A.F.Crawley and B.Lagowski, Metall. Trans. 5 (1974), p. 949.
[21] J.K.Solberg, J.Tørklep, Ø. Bauger and H.Gjestland, Mater. Sci. Eng. A 134 (1991), p. 1201.
[22] E. Schaberger, D. Kahn and M. Lang, Prakt. Metallogr. 35 (1998), p. 306.
[23] E. Aghion and B. Bronfin, Proc. 3rd Intl. Magnesium Conference, ed. G. W. Lorimer, The Institute of Metals, London 1997, p. 313.
[24] K. U. Kainer, Mater. Sci. Eng. A 135 (1991), p. 243.
[25] K. Purazang, P. Abachi and K.U. Kainer, Composites 25 (1994), p. 296.
[26] J. Kiehn, K.U.Kainer, P.Vostrý and I. Stulíková, Phys. Stat. Sol. (a) 161 (1997), p. 85.
[27] A. Dlouhý, G. Eggeler and N. Merk, Acta Metall. Mater. 43 (1995), p. 535.
[28] Y. Li and T.G.Langdon, Metall. Mater. Trans. A (in press).
[29] R. Lagneborg and B. Bergman, Metal. Sci. 10 (1976), p. 20.
[30] J. Weertman, J. Appl. Phys. 28 (1957), p. 1185.
[31] F.A. Mohamed and T.G.Langdon, Acta Metall. 22 (1974), p. 779.
[32] J. Weertman, J. Appl. Phys. 28 (1957), p. 362.
[33] O.D.Sherby, R.H.Klundt and A.K.Miller, Metall.Trans. 8A (1977), p. 843.
[34] G. Gonzalez - Doncel and O. D. Sherby, Acta Metall. 41 (1993), p. 2797.
[35] A. Kelly and K.N.Street, Proc. R. Soc. London 328A (1972), p. 267.
[36] K. T. Park and F.A: Mohamed, Metall. Mater. Trans. 26A (1995), p. 3119.
[37] Y. Li and T.G.Langdon, Metall. Mater. Trans. 29A (1998), p. 2523.
[38] V.C. Nardone and K.M.Prewo, Scripta Metall. 20 (1986), p. 43.

e-mail address of the first author: sklen@ipm.cz

Key Engineering Materials Vols. 171-174 (2000) pp. 601-608
© 2000 Trans Tech Publications, Switzerland

Creep Strength of Binary Magnesium Alloys up to 0.6*Tm*

H. Sato[2], M. Suzuki[1], K. Maruyama[1] and H. Oikawa[3]

[1] Department of Materials Science, Graduate School of Engineering, Tohoku University, Aramaki-aoba, Aoba-ku, Sendai-shi, 980-8579, Japan

[2] Now with Department of Intelligent Machines and System Engineering, Faculty of Science and Technology, Hirosaki University, Bunkyo-cho 3, Hirosaki-shi, 036-8561, Japan

[3] Now with College of Industrial Technology, Amagasaki, Japan

Keywords: Aluminum, Manganese, Yttrium, Minimum Creep Rate, Normalized Creep Rate, Relative Strength

Abstract

High temperature creep characters up to $0.6T_m$ of some binary magnesium alloys are briefly summarized and discussed. Creep characteristics of magnesium-aluminum solid solutions are basically similar to that of cubic solid solutions like aluminum-magnesium, but non-dimensional normalized creep rates of magnesium alloys are relatively lower than that of aluminum alloys. The difference of creep strength in both alloys is attributed to the difference in internal stresses. Creep rates of precipitation strengthened magnesium-manganese alloys are similar to that of magnesium-aluminum solid solutions. In contrast, magnesium-yttrium alloys have higher creep resistance compared to other binary alloys even in solid solutions. Normalized creep rates (Z-value) of several alloys are presented and peculiar effects of yttrium are emphasized.

Introduction

Heart resistance is one of the important expected features of magnesium alloys as light structural materials, but information of basic deformation characteristics of the alloys at high temperatures are still insufficient. In this paper, high temperature creep characteristics of some magnesium alloys of binary systems are briefly summarized and discussed.

It is well recognized that the steady state or minimum creep rate of pure metals and solid solutions can be reasonably described by following Dorn-type equation (1) in power-law stress range.

$$\dot{\varepsilon} = A' \frac{Gb}{kT} N^{-m} \left(\frac{\sigma}{G}\right)^n \exp\left(-\frac{Q_c}{RT}\right) \qquad \text{(Eq.1)}$$

Here, A', G, b, k and R are the numerical constants, the shear modulus, the magnitude of Burgers-vector, the Boltzmann's constant and the gas constant, respectively. The values T, N and σ are the absolute temperature, the solute concentration and the applied stress which determine the creep conditions. The value m, n and Q_c characterize the creep behavior and are the concentration exponent, the stress exponent and the apparent activation energy of creep, respectively. These values are determined experimentally. In cubic solid solutions, creep characteristics depend on deformation conditions in complex manners and the bounding conditions, where creep characteristics change, depend on temperature and solute concentration[1-2]. Similar changes in creep behavior are observed in magnesium solid solutions[3-4]. The apparent activation energy of creep, Q_c, is essentially reported to be the similar value to that for diffusion in cubic solid solutions. In hcp alloys, however, it has been reported that the apparent activation energy, Q_c, depends on temperature, and the value becomes larger than that for diffusion at the temperature above $0.7T_m$(T_m: the melting temperature), while it is similar to that for diffusion below 0.7 T_m[5]. This report focuses on high temperature creep behavior of some binary magnesium alloys at the temperature up to $0.6T_m$, where apparent activation energy of creep is expected to be almost the

same with that for diffusion. Most creep data, including two engineering alloys for comparison, are quoted from references as summarized in Table 1, and creep rates of the alloys are broadly compared. Precise discussions of transition of creep characteristics are not an aim of this paper. Experimental procedure for other data presented in this paper is the same with that presented previously [4,6].

Table 1. Alloy designations and references

Designation	Alloy	Reference
0.6Al	Mg-0.59mol%Al	[4]
0.8Al	Mg-0.8mol%Al	[3]
1Al	Mg-1.04mol%Al	[4]
3Al	Mg-2.97mol% Al	[4]
5Al	Mg-4.93mol% Al	[7]
0.5Mn	Mg-0.5mol%Mn	[8]
0.2Y	Mg-0.195mol% Y	[9]
1.1Y	Mg-1.11mol%Y	[9]
1.6Y	Mg-1.62mol%Y	[9]
2.4Y	Mg-2.4mol%Y	[9]
AZ91	AZ91	[10,11]
AS21	AS21	[10,11]

Creep curves

Figure 1 shows typical creep curves of magnesium-aluminum solid solutions and magnesium-yttrium solid solutions at 550K($\approx 0.5T_m$). Shape of the creep curves shown on the figure are similar with each other, but the stress level that corresponds to the same strain rate are about four times higher in magnesium-yttrium alloys than that of magnesium-aluminum alloys. Figure 2 shows creep curves obtained at 600K in magnesium-aluminum solid solutions both under compression and tensile creep tests. The shape of creep curves changes with increasing stress in

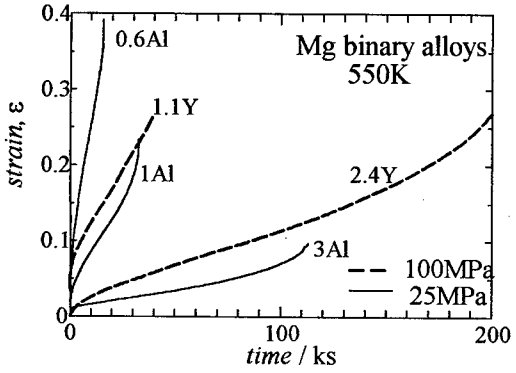

Fig.1 Examples of creep curves obtained in Mg-Al and Mg-Y solid solutions at 550K.

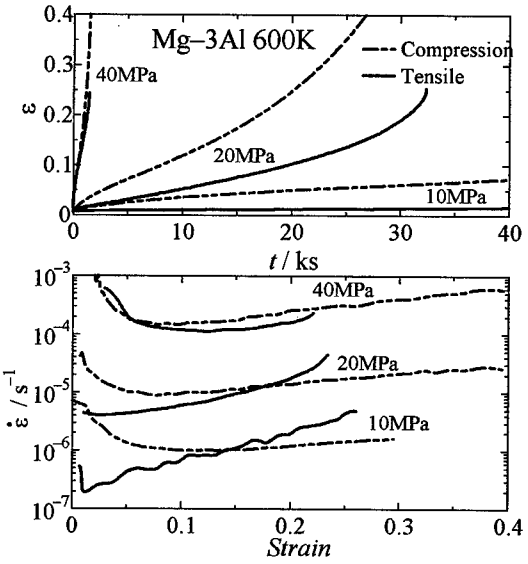

Fig.2 Comparison of the creep curves in Mg-Al solid solutions in compression and tensile creep tests.

tensile conditions, while they are not drastically changes in compression conditions. Especially at lower stress level, for example at 10MPa, the minimum creep rate appears at the beginning of creep in tensile conditions, while it appears with larger strain in compression. Minimum creep rates in compression and tensile are different, but the difference in rates are less than an order of unity at the same applied stress. The difference in the shape of creep curves between tensile and compression tests become ignorable in higher stress. The results shown in following sections are obtained by compression creep tests in magnesium-yttrium alloys and magnesium-manganese alloy, while tensile creep has performed in magnesium-aluminum solid solutions. In the following sections, stressing directions are not considered for the differences in creep rates are less pronounced.

Stress dependence of creep rate

Figure 3 shows stress dependence of the creep rate of several binary alloys as a function of the applied stress at 550K. The stress exponent, n, increases with increasing the applied stress. Three stress regions exist where n close to four, five to seven and larger than ten. The change of the stress exponent in magnesium-aluminum solid solutions is similar to that observed in cubic solid solutions. It corresponds to the change of creep characteristics and deformation mechanisms from Alloy-type to Metal-type [1-4]. The n-value takes five to seven in higher stress range in magnesium-aluminum and lower stress range in magnesium-yttrium alloys. Recovery-controlled creep is suggested from the value, n, in the stress range. The higher stress exponent, n, observed above 100MPa in magnesium-yttrium alloys corresponds to the power-law break down [12] for the normalized strain rate by self-diffusion coefficient of magnesium become larger than $10^{13}m^{-2}$.

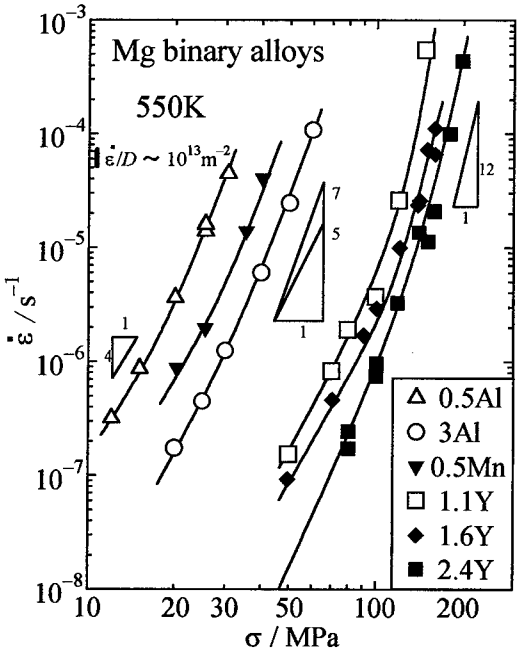

Fig.3 Creep rates in some magnesium alloys as a function of the applied stress. Open and solid marks show creep rate observed in solid solutions and alloys with precipitates, respectively.

Concentration dependence of creep rates in single phase alloys

Figure 4 shows concentration dependence of magnesium-aluminum and magnesium-yttrium alloys at 550K and 600K. Creep rates of alloys, which contain precipitates are indicated in solid marks for comparison. In magnesium-aluminum solid solutions, the concentration exponent, m, at 10MPa is unity and become smaller with increasing solute concentration at 600K. In this concentration and stress range, creep characteristics are attributed to the Alloy-type [2]. Dragging of a dislocation, which has solute atmosphere around it, is suggested as a rate controlling mechanism. With increasing the applied stress, the concentration exponents become higher and are two to three. The values are similar to that of Metal-type behavior, and recovery controlled mechanisms are suggested. The creep behaviors observed up to $0.6T_m$ are summarized as Table 2, based on the stress and concentration dependence.

Table 2. Creep parameters of Mg-Al and Mg-Y solid solution alloys up to $0.6T_m$

Type of Behavior	Alloy-type	Metal-type	Power-law Break Down
Stress exponent, n	4	6~7	10 <
Concentration exponent, m	< 1	2~3	

As described above, in the deformation condition where the Alloy-type behavior appears, the effect of solute concentration on creep rates becomes small with increasing solute concentration. This phenomenon is understood with change of dislocation mobility and its concentration dependence. When dislocations move viscously, strain-rates can be represented by the Orowan's equation, $\dot{\varepsilon} = \phi\rho_m b\bar{\upsilon}$. Here, ϕ, ρ_m and $\bar{\upsilon}$ are the geometrical factor, the mobile dislocation density, the mean dislocation velocity which is proportional to the mean effective stress, $\bar{\tau}^*$, respectively. Here, $\bar{\tau}^*$ is connected with the mean internal stress, $\bar{\sigma}_i$, as $\bar{\tau}^* = \phi(\sigma - \bar{\sigma}_i)$, and the mean internal stress $\bar{\sigma}_i$ has a square-root proportionality with a dislocation density ρ, *i.e.*, $\bar{\sigma}_i = \alpha\phi^{-1}Gb\sqrt{\rho}$. Assuming that the dislocation density ρ is the same with the mobile dislocation density ρ_m, strain rates are described by the following equation (2).

$$\dot{\varepsilon} = \frac{\phi^4}{\alpha^2 b} GB\left(\frac{\sigma}{G}\right)^3 (1-r)r^2 \qquad \text{(Eq.2)}$$

Here, B is the mobility of dislocations, α is a numerical constant and r is the ratio of the mean internal stress to the applied stress, $\bar{\sigma}_i/\sigma$. This equation suggests that the normalized strain rate mainly depend on the mobility, B, and the ratio r under the same normalized stress. Based on the TEM observations in cubic aluminum-magnesium solid solutions, the dislocation density depends only on the applied stress and that no systematic dependents on temperature nor solute concentration are observed [13]. As a consequence, the dependence of creep rates on the concentration is equal to that of the dependence of the mobility. Numerical calculations of the dislocation mobility in aluminum-magnesium solid solutions, suggests that the effect of solute concentration on the mobility become smaller with increasing solute concentration [14]. The small concentration exponent observed in magnesium-aluminum solid solutions is attributed to the decrease in the effect of concentration on the mobility of a dislocation, which has solute atmosphere[7].

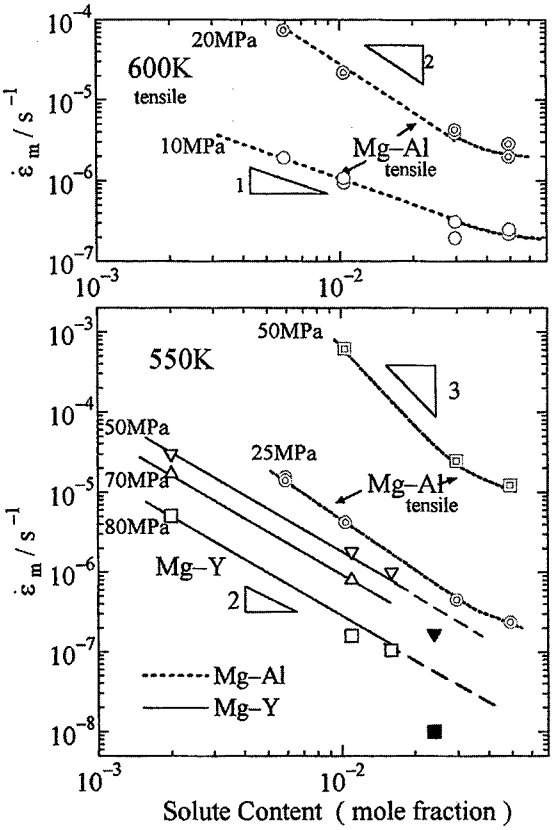

Fig. 4. Concentration dependence of strain rate in Mg-Al and Mg-Y alloys. Open marks show creep rate in solid solutions and solid marks show that in two phase alloys.

Comparison of normalized creep rates with aluminum-based solid solutions

As shown by equation (1), the strain rates can be described experimentally by the power-law. When the apparent activation energies of creep are similar with that for diffusion, the equation (1) is formed as equation (3).

$$\frac{\dot{\varepsilon}kT}{DGb} = AN^{-m}\left(\frac{\sigma}{G}\right)^{n} \qquad \text{(Eq.3)}$$

Here, D is the diffusion coefficient including the exponential term. The value, D, is the inter-diffusion coefficient, $\tilde{D}$, when solute dragging controls creep rate, or the self-diffusion coefficient, D_{self}, when recovery process controls deformation. The left-hand non-dimensional term, $\dot{\varepsilon}kT/DGb$, is defined as the non-dimensional normalized creep rate in this paper. This equation has the similar form with that proposed by Mukherjee [15], but the term of solute concentration is included instead of the term of grain size. As far as the physical coefficients are known, one can reasonably compare non-dimensional normalized strain rates between different alloy systems. In magnesium-aluminum binary system, physical coefficients have been determined and the deformation mechanisms are reasonably distinguished.

Figure 5 shows the non-dimensional normalized creep rates as a function of the normalized applied stress in both terminal solid solutions of magnesium-aluminum system obtained in tensile creep tests at 600K. Inter-diffusion coefficients, $\tilde{D}$, are used here, for the inter- and the self-diffusion coefficient in both solid solutions are close to each other. Strain rates of magnesium-aluminum solid solutions are about two orders lower than that of aluminum-magnesium solid solutions at the lower stress region where the Alloy-type appears [1]. As described in previous section, the creep rates of magnesium-aluminum solid solutions in tensile condition are lower than that in compression, but still the difference in creep rate between two phases are significant. The transition from Alloy-type to Metal-type proceeds at the normalized strain rate around 10^{-10}, independent of the phases.

When glide controlled mechanisms are considered, non-dimensional normalized strain rates are formed as equation (4).

$$\frac{\dot{\varepsilon}kT}{DGb} = \frac{\phi^4 kT}{\alpha^2 b^2}\frac{B}{D}\left(\frac{\sigma}{G}\right)^3 (1-r)r^2 \qquad \text{(Eq.4)}$$

This equation suggests the non-dimensional normalized strain rate depends on the mobility, B, and $r = \bar{\sigma}_i/\sigma$ at the same applied stress. Table 3 shows measured average internal stress obtained by strain-dip stress-transient technique in both phases at the deformation condition where Alloy-type behavior appears. The mean internal stress in magnesium-aluminum alloy is relatively higher than that in aluminum-magnesium alloy.

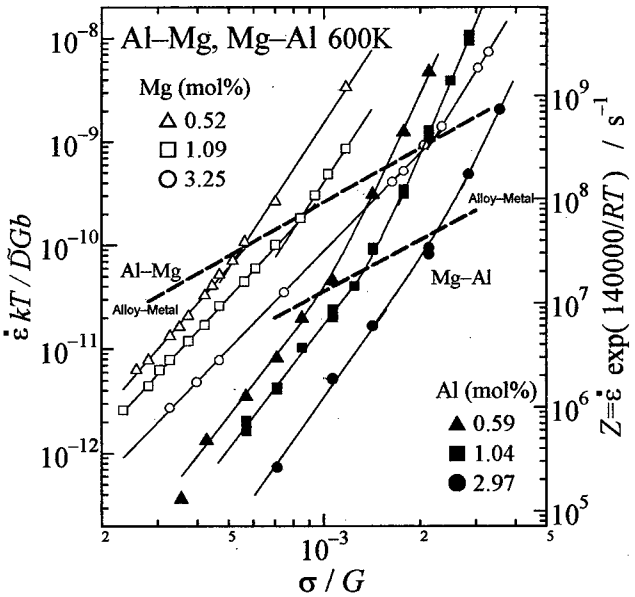

Fig. 5. Normalized strain rate as a function of the normalized applied stress in both terminal phases in Mg-Al system.

Large differences of creep rate between magnesium-aluminum and aluminum-magnesium solid solutions are attributed to the difference in the mean internal stress. Although systematic information of the mean internal stress and dislocation densities are still lacking, it seems reasonable that the average internal stress is higher in hcp magnesium-aluminum solid solutions than cubic aluminum-magnesium solid solutions, because hcp system has limited number of primary slip systems and large hardening rate is expected at this temperature range.

Table 3. Ratio of the mean internal stress to the applied stress at the non-dimensional normalized strain rate of 10^{-10} (* Interpolated value based on reference [6].)

Alloy	Mg-3Al	Al-1.09mol%Mg
σ/G	$2.1\text{x}10^{-3}$	$7.0\text{x}10^{-4}$
$r=\overline{\sigma}_i/\sigma$	0.98	0.8 *

Relative creep rates

Non-dimensional normalized creep rates are applicable when physical coefficients are well determined at the corresponding conditions. Not always, unfortunately, these physical coefficients are available. So-called Z-parameter normalized by activation energy of creep or activation energy for diffusion is another normalized creep rates, which is able to apply to many alloys including engineering alloys. Figure 6 shows dependence of Z-parameter as normalized creep rates as a function of the normalized applied stress. Broad gray curve roughly shows normalized creep rates of pure magnesium. The curve has drawn based on the figure of reference [10,11]. The activation energy used was $140\text{kJ}\cdot\text{mol}^{-1}$, which is the same with the activation energy for inter-diffusion of aluminum in magnesium used by Vagarali [3], thus the Z is defined as $Z=\dot{\varepsilon}\cdot\exp(140000/RT)$. Except AS21 and magnesium-yttrium alloys, data points tend to gather with each other and form a broad band. The band contains data both of solid solutions and alloys with precipitates. In magnesium-yttrium alloys, however, normalized creep rates are far less than that of other alloys both in solid solutions and alloy with precipitates. This fact suggests that the apparent activation energy of creep in magnesium-yttrium alloys is higher than that of other alloys. Although physical coefficients in magnesium-yttrium system are insufficient for detailed normalization and comparison, peculiar improvements of creep strength by yttrium deserve to emphasize.

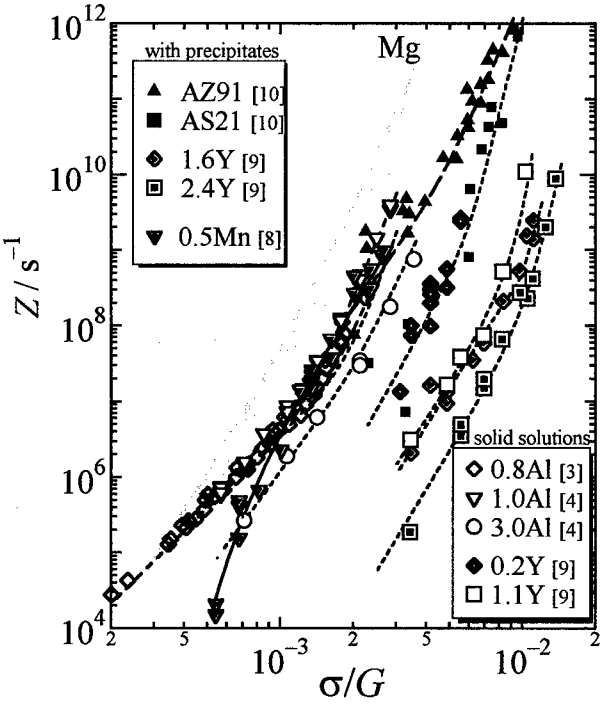

Fig. 6. Normalized creep rate as a function of the applied stress.

Summary

(1) Creep characteristics of binary magnesium alloys at the temperature up to $0.6T_m$ are briefly summarized.
(2) Magnesium-aluminum solid solutions show similar behavior of that of cubic solid solutions and both Alloy-type and Metal-type behavior appears at the temperature.
(3) Non-dimensional normalized creep rates of magnesium-aluminum solid solutions are lower than that of aluminum-magnesium solid solutions. The difference in creep rates is attributed to the difference in the mean internal stress.
(4) Yttrium improves creep strength both in solid solutions and two phase alloys. Strengthening effect of yttrium is remarkable compared with other alloying elements. Further information of high temperature properties in magnesium-yttrium system is expected including physical parameters, such as diffusion coefficients for detailed considerations of creep behavior.

Acknowledgment

This research was partly supported by Grant-in-Aid for Scientific Research (A) (Grant #07555474) and Grant-in-Aid for Scientific Research (C) (Grant #10650685) from The Ministry of Education, Science, Sports and Culture, Japan.

References

[1] H. Sato, K. Maruyama and Hiroshi Oikawa: "Aluminum Alloys, Their Physical and Mechanical Properties", ed. by T. Sato et. al., The Japan Institute of Light Metals, Japan (1998), 1355.
[2] H. Oikawa: "Hot deformation of Aluminum Alloys", ed. By T.G. Langdon, et al., TMS, Warrendale, (1991), 153.
[3] S.S. Vagarali and T.G. Langdon: Acta metall., 30(1982), 1157.
[4] H. Sato and H. Oikawa: "Strength of Metals and Alloys", ed. by D.G. Brandon et al., Freund Publishing House, Ltd., England, (1991), 463.
[5] H. Siethhoff and K. Ahlborn: Z. Metallkd., 76(1985), 627.
[6] H. Sato and H. Oikawa: Scripta Met., 22(1988), 87.
[7] H.Sato, K. Masada and H. Oikawa: "Aspects of high temperature deformation and fracture in crystalline materials", JIM, (1993), 107.
[8] M. Suzuki, H. Sato and H. Oikawa: "Strength of Materials", ICSMA10, JIM, (1994), 555.
[9] M. Suzuki, H. Sato, K. Maruyama and H. Oikawa: Mater. Sci. Eng. A, 252(1998), 248.
[10] W. Blum, B. Watzinger and P. Weidinger: Magnesium Alloys and Their Applications, Ed. By B.L. Mordike and K. U. Kainer, Werkstoff-Informationsgessellschaft mbH, Germany, (1998), 49.
[11]B.Watzinger, P. Weidinger, F. Breutinger, W. Blum, R. Rösch, H. Lipowsky and H.-G. Haldenwanger: Magnesium Alloys and Their Applications, Ed. By B.L. Mordike and K. U. Kainer, Werkstoff-Informationsgessellschaft mbH, Germany, (1998), 259.
[12] O.D. Sherby and P.M. Burke: "Mechanical Behavior of Crystalline Solids at Elevated Temperature", Prog. Mater. Sci., 13(1968), 325.
[13] H. Hayakawa, H. Nakashima and H. Yoshinaga, Nippon Kinzoku Gakkai-shi, 53(1989), 1113.
[14] H. Nakashima and H. Yoshinaga, Nippon Kinzoku Gakkai-shi, 56(1992), 254.
[15] A.K. Mukherjee, J.E. Bird and J.E. Dorn, Trans. ASM, 62(1969), 155.

Corresponding Author
Hiroyuki SATO, Department of Intelligent Machines and System Engineering,
Faculty of Science and Technology, Hirosaki University
Bunkyo-cho 3, Hirosaki-shi, 036-8561, JAPAN
Tel.& Fax. +81-172-39-3673 E-mail: g4sato@mech.hirosaki-u.ac.jp

Key Engineering Materials Vols. 171-174 (2000) pp. 609-616
© 2000 Trans Tech Publications, Switzerland

Microstructural Evolution during Creep of the Mg-Al-Alloy AZ91hp

P. Zhang[1], B. Watzinger[1], Q.P. Kong[2] and W. Blum[1]

[1] Institut für Werkstoffwissenschaften, Lehrstuhl 1,
Martensstraße 5, DE-91058, Erlangen, Germany

[2] Institute of Solid State Physics, Academia Sinica, Hefei 230031, P.R. China

Keywords: Microstructure, Compression Creep, Mg-Al-Alloy AZ91hp, Dislocation Spacing, Precipitates, Precipitation Hardening

Abstract

The light-weight pressure die-cast Mg-Al-base alloy AZ91hp used in automotive application in the as cast state was investigated with regard to evolution of the microstructure during annealing at 150°C and creep at 135°C and 210 MPa. Due to the fast cooling during die casting the microstructure is unstable. Annealing for 1 h at 150°C leads to beginning of precipitation of coherent β-particles. Creep for 34 min at 135°C causes precipitation of β on a large scale, but with strong local variation and formation of a subgranular dislocation structure with a spacing of free dislocations of about $4\,b\,G/\sigma$ and a subgrain size of about $15\,b\,G/\sigma$, similar to the characteristic dislocation spacings in the steady state of deformation of cubic metals. These microstructural changes must be taken into account in the constitutive description of deformation of AZ91 at intermediate temperatures.

1. Introduction

The creep behavior of die-cast magnesium alloys is relevant with regard to their application in automobiles. For a full constitutive description of creep one needs information not only on the kinetics of creep, but also on the evolution of the microstructure. So far the knowledge on the microstructure of Mg-alloys is limited. The present work examines the changes in phase structure and dislocation structure of AZ91 accompanying creep.

2. Experimental

The high-purity magnesium alloy AZ91hp (composition in wt.%: Al 8.9, Zn 0.79, Mn 0.21, Si 0.01, Fe 0.003, Cu 0.001, Ni 0.001, Be 0.0007) was produced by pressure die casting. The thickness of the castings varies in steps from 2.5 mm to 25 mm. The specimens for compression tests were taken from the section with 5 mm thickness. Compression was done at 135°C and constant stress σ (load per average cross section). Fig. 1 shows the strain rate $\dot{\epsilon}$ - strain ϵ - curve of the specimen investigated in this work. The minimum rate of deformation was reached at $\epsilon \approx 0.14$.

For light optical (LOM) and scanning electron microscopy (SEM, with JEOL JSM6400), sections of the specimens parallel to the normal of the cast plate and the direction of compression, respectively, were prepared by mechanical polishing (final step: 0.3 μm sized Al_2O_3-powder) followed by etching in a solution of nitric acid (volume fraction 1:25) in ethanol. The foils for transmission electron microscopy (TEM, with Philips EM 400) were prepared by a combination of mechanical and ion thinning techniques: Discs of 3 mm diameter and 50 μm thickness were prepared by cutting slices of 1 mm thickness from the bulk specimens with a low speed diamond saw, grinding and punching; final thinning was performed on an ion beam etching machine, operating at 4 kV with an incident angle of 5°. The density ρ_f of free dislocations

inside (sub)grains was determined by counting the points where dislocations intersect the foil surfaces. The size of subgrains (crystallites partially bounded by low angle boundaries) was quantified by the line intersection technique.

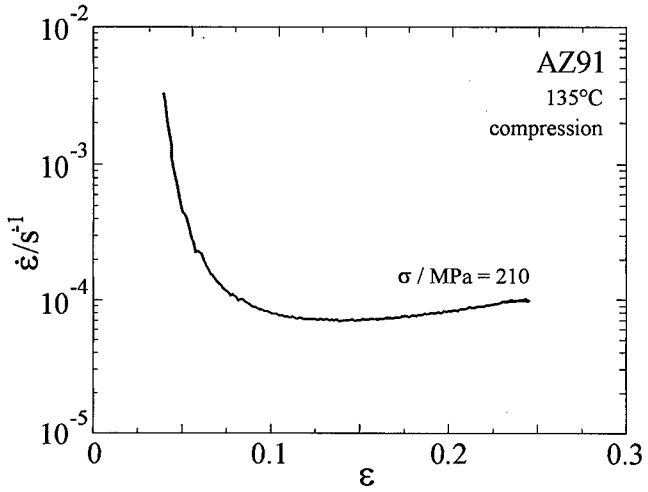

Figure 1: Strain rate $\dot{\epsilon}$ as function of strain for compression at 135°C and 210 MPa interrupted at $\epsilon = 0.24$ after 34 min of deformation and about 1 h of soaking at test temperature prior to deformation.

3. Microstructural Results

From the literature, e.g.[1, 2] it is known that as cast AZ91 is made up from primary grains of α-phase surrounded by a eutectic layer consisting of large particles of β-phase ($Mg_{17}Al_{12}$ embedded in supersaturated α-Mg-Al phase). These structure elements can be seen in Fig. 2. The grain size d is about 10 to 18 μm. The TEM-micrograph of Fig. 2c shows a grain (or subgrain) of α with some large eutectic β-precipitates preferentially located at the boundaries and a density of free dislocations $\rho_f = 12 \times 10^{12}/m^2$. Quantitative evaluation of SEM micrographs like Fig. 2b yielded a volume fraction of β-phase $f_\beta = 0.14 \pm 0.02$. From the binary phase diagram Mg-Al one expects $f_\beta = 0.17$. These figures are consistent with the expectation that α is supersaturated with Al.

Annealing will move the system towards equilibrium. However, after annealing by 1 h at 150°C no micostructural change relative to the as cast state was found; in particular the contrast between eutectic and primary α still existed indicating that little precipitation of β had occurred. This is consistent with the observation of [3] that nucleation of β-precipitates needs a time interval in the order of 45 min at 200°C. However, TEM observation shows that formation of small coherent β-particles is beginning in the eutectic as well as in the primary α-phase (Fig. 3).

In contrast to annealing at 150°C, 1h of creep at 135°C and 210 MPa to a compressive strain of 0.24 (after about 1 h of soaking at test temperature) has a pronounced effect on the microstructure. Fig. 4a (SEM) shows that the grains have been compressed, the boundary between primary and eutectic α has disappeared, and β has precipitated along lines which probably mark large angle grain boundaries. TEM shows additional details. In the primary α region numerous β-precipitates with relatively rounded shapes can be seen. In regions which probably correspond to the eutectic α-phase β-particles appear locally with a large volume

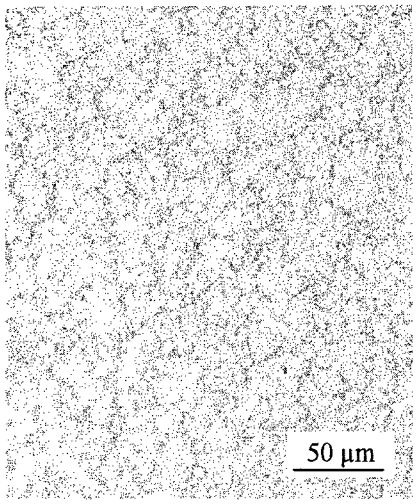

a

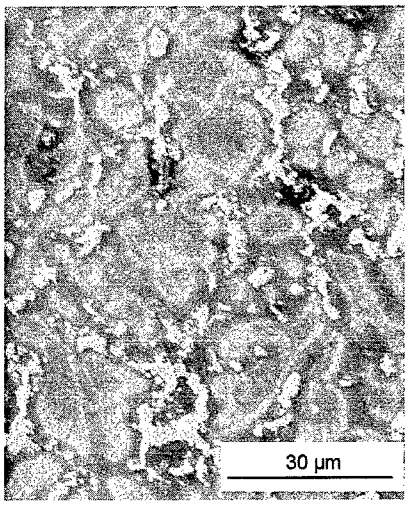

b

c

Figure 2: As cast AZ91:
a) Large β-particles (dark) surrounding α-phase (LOM of weakly etched section),
b) Large β-particles (white) in eutectic α-phase (dark); bounding the primary α-grains (grey) (SEM with secondary electrons),
c) α-(sub)grain with dislocations and large eutectic β-particles (TEM). The boundary between primary and eutectic α is invisible.

fraction apparently exceeding the value of 0.17 expected for an Al-content of 9 wt.%. The density of free dislocations is $\rho_f = 100 \times 10^{12}/m^2$ has strongly increased relative to the initial state. Free dislocations lie predominatly on basal planes, but there are also some segments of dislocation lying on non-basal planes confirming the finding of Regev et al. [6]. In addition, subgrains have formed. The term subgrain is used because some of the boundaries can be identified as dislocation networks. However, there are indications that there are also twin boundaries incorporated in the structure implying that twinning is an active mode of deformation at the present conditions. The subgrain structure is qualitatively confirmed by LOM (Fig. 5) showing a granular structure with crystallite sizes in the order of several μm, i.e. distinctly smaller than the size of the primary α-grains. The subgrains are not equiaxed; determination of the subgrain size w in the directions of 0°, 45° and 90° to the direction of subgrain elongation yielded $w_{00} = 483$ nm, $w_{45} = 367$ nm, and $w_{90} = 293$ nm. The statistical error of these values is about 15%.

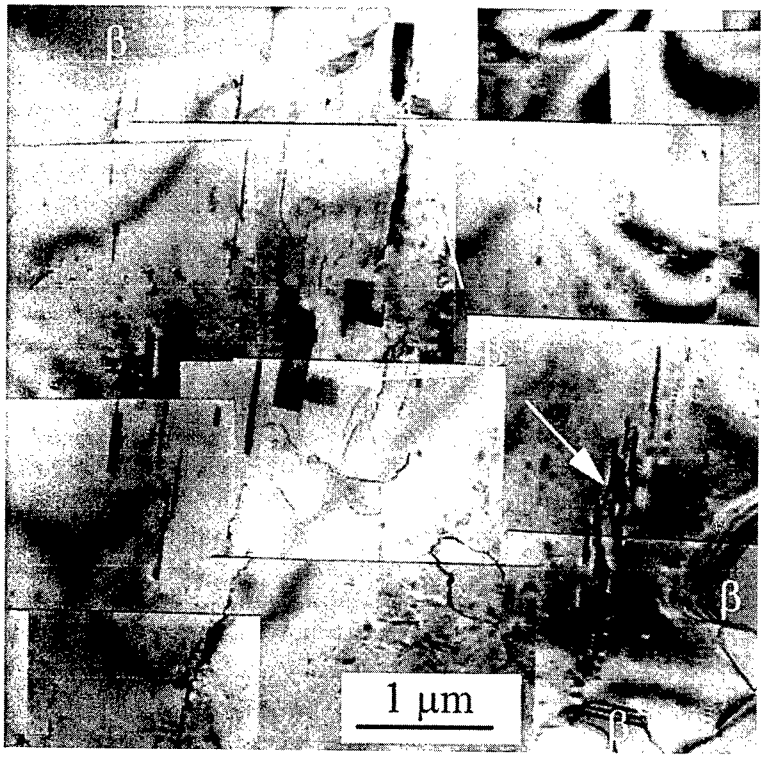

Figure 3: Coherent precipitates of β (partially marked by arrows) after 1 h of annealing at 150°C (TEM); at the upper left and the lower right large eutectic β-particles are visible.

a

c

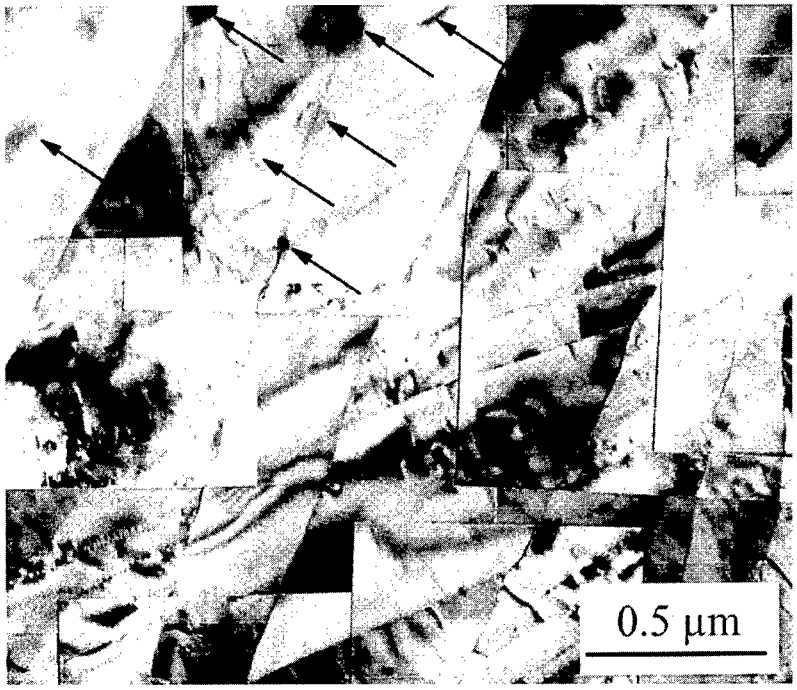

b

Figure 4: Microstructure after creep by $\epsilon = 0.24$ at 135°C and 210 MPa:
a) β-phase appears not only in the eutectic form bounding primary α but also aligned along boundaries. Note disappearance of contrast between primary and eutectic α (SEM with secondary electrons).
b) Subgranular dislocation structure and β-particles (partially marked by arrows) in primary α-phase (TEM).
c) Region (presumably in eutectic α-phase) with high volume fraction of β-precipitates (TEM).

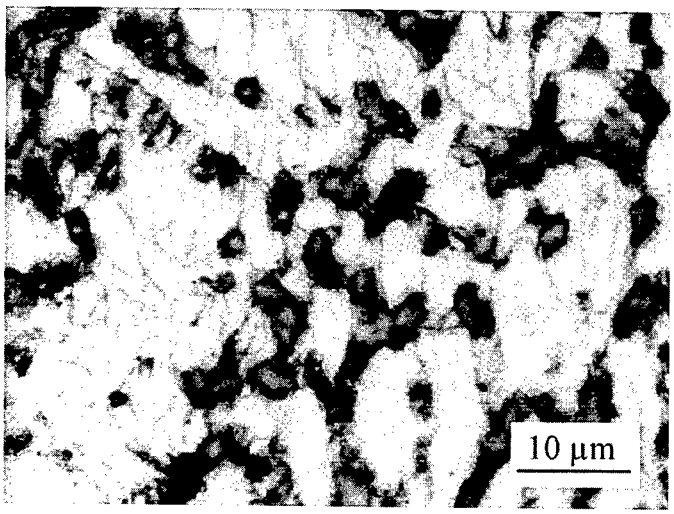

Figure 5: Microstructure of strongly etched section of the crept specimen of Fig. 4 (LOM).

4. Discussion

The present results clearly show that the phase structural changes in the unstable as cast state of the alloy AZ91 are strongly accelerated by concurrent creep at 135°C. It appears that the dislocation activity caused by the rapid deformation in the beginning of creep triggers nucleation of β-phase allowing for fast decrease of the supersaturation with Al in the primary as well as in the more strongly supersaturated eutectic α-phase. This precipitation will increase the creep resistance. The assumption of precipitation hardening is consistent with the conclusion of Dargusch et al. [2] and Blum et al. [5] and implies that β is a hard phase at least at the test temperature of this work, 135°C. The observed precipitation also backs the interpretation of Blum et al. [5] for the influence of high temperature annealing on the maximum creep resistance (which is even higher than for as cast material because the large primary β-particles are dissolved during annealing at 413°C and precipitation hardening is consequently enhanced).

In addition to precipitation hardening the effect of the relatively high initial density of dislocations, the small grain size and the eutectic which probably constitutes a relatively hard region due to large supersaturation with Al and hardening by eutectic β influence the creep response and cause a relatively short primary stage of creep as compared to the annealed, large grained AZ91 (compare Fig. 1 and [5]).

The observed increase in creep rate $\dot{\epsilon}$ for $\epsilon > 0.15$ (Fig. 1) is probably of microstructural origin as the macroscopic deformation was apparently uniaxial, and showed no indications of mechanical instability. At present it cannot be decided whether loss of solid solution hardening by precipitation of Al or loss of precipitation hardening due to coarsening of the precipitates or chang in texture is the major reason of the observed softening.

The observation of subgrain formation confirms the results reported previously for crept [5] and and for hot worked AZ91 [7] and is in line with the general findings of subgrain structures in the steady state of deformation for materials of different crystallographic structures.

It is known [8] that the characteristic dislocation spacings are mainly (though not completely) determined by applied stress. This holds also in the present case. Fig. 6 shows the subgrain

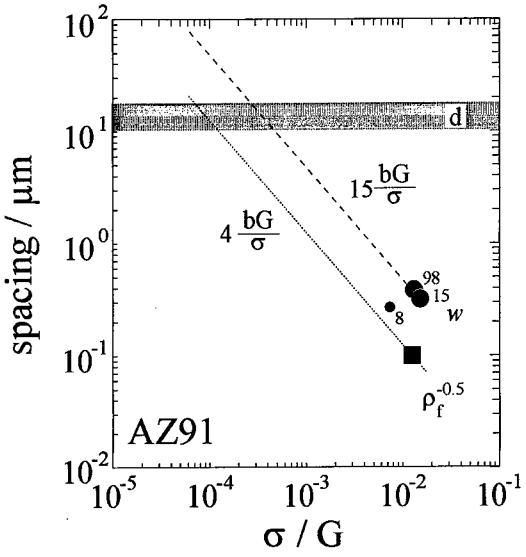

Figure 6: Subgrain size w and spacing $\rho_f^{-0.5}$ plotted against stress σ normalized by the shear modulus G=16.6×(1−5.3×10^{-4}(T/K − 300)) GPa [4]. The number of investigated subgrains is given beside the w-symbols. The small full circle represents the w-value reported in [5]. The lines with slope -1 are shown for the sake of comparison only. The shaded band marks the initial grain size d.

size and the spacing of free dislocations plotted against shear modulus normalized stress. It is seen that the average subgrain size w lies in the order of $15\,bG/\sigma$ and the average spacing of free dislocations is about $4\,bG/\sigma$. These figures correspond to the results obtained for materials with other crystal structures, in particular fcc materials [8].

5. Summary

1. Die cast AZ91hp consisting of primary α-phase surrounded by eutectic mixture of supersaturated α- and β-phase is in an unstable state. Annealing by 1 h at 150°C causes only minor changes; however, the beginning of precipitation of small coherent β-particles can be seen by TEM.

2. Creep at 135°C and 210 MPa causes severe microstructural changes: β precipitates in each component of the microstructure, but with marked local variation in volume fraction inside the α-phase and with preference of precipitation at grain boundaries. These observations support the interpretation of the creep behavior of AZ91 in terms of precipitation hardening. The dislocation structure develops towards a steady state subgrain structure. The average subgrain size and spacing of free dislocations lie in the order of magnitude expected from approximate inverse relation to shear modulus normalized stress as commonly found for materials with cubic crystal structure.

Acknowledgements

Thanks are due to Audi AG for cooperation and the Bayerische Forschungsstiftung for supporting this cooperation and granting a scholarship for P. Zhang.

References

[1] G.L. Dunlop, W.P. Sequeira and M.S. Dargush. Microstructure and Properties of Magnesium Alloy High Pressure Die Castings. In E. Aghion and D. Eliezer, editors, *Proc. of the First Israeli International Conference on Magnesium Science & Technology*, pages 108–115, Israel, 1997. Magnesium Research Institute (MRI) LTD.

[2] M. Dargusch, M. Hisa, C.H. Cáceres and G.L. Dunlop. Elevated Temperature Deformation of Die Cast Mg Alloy AZ91D. In G.W. Lorimer, editor, *Proceedings of the Third International Magnesium Conference*, pages 153–165, London, 1997. The Institute of Materials.

[3] S. Celotto, T.J. Bastow, P. Humble and C.J. Betteles. A Study of the Kinetics of Precipitation in Binary Mg–Al Alloys and AZ91E using Nuclear Magnetic Resonance. In G.W. Lorimer, editor, *Third International Magnesium Conference*, pages 391–402, London, 1997. Institute of Materials.

[4] H.J. Frost and M.F. Ashby. *Deformation-Mechanism Maps*. Pergamon Press, Oxford, 1982.

[5] W. Blum, B. Watzinger and P. Weidinger. Creep Resistance of Mg-base Alloys. In B.L. Mordike and K.U. Kainer, editors, *Proc. of the International Conference on Magnesium Alloys and Their Applications, Wolfsburg*, pages 49–60, Frankfurt, 1998. Werkstoff-Informationsgesellschaft mbH.

[6] M. Regev, E. Aghion, S. Berger, M. Bamberger and A. Rosen. Dislocation Analysis of Crept AZ91D Ingot Castings. *Mat. Sci. Engng.*, A257:349–353, 1998.

[7] M.M. Myshlyaev, A. Mwembela and H.J. McQueen. Microstructural Development in Hot Worked Mg-Al-Zn Alloy. *Submitted to Can. Metal. Quart.*, 1997.

[8] W. Blum. Plastic Deformation and Creep of Crystalline Materials. In H. Mughrabi, editor, *Plastic Deformation and Fracture of Materials*, volume 6 of Materials Science and Technology, pages 359–405. VCH Verlagsgesellschaft, Weinheim, R.W. Chan and P. Haasen and E.J. Kramer, 1993.

Corresponding author: P. Zhang
e-mail: pzhang@ww.uni-erlangen.de

Key Engineering Materials Vols. 171-174 (2000) pp. 617-624
© 2000 Trans Tech Publications, Switzerland

Effect of Liquid Phase on Creep and Fracture Behavior of Al-5%Mg

H. Iwasaki[1], T. Mori[1], M. Mabuchi[2] and K. Higashi[3]

[1] Department of Materials Science and Engineering, Himeji Institute of Technology, Shosha, Himeji, Hyogo, Japan

[2] National Industrial Research Institute of Nagoya, Hirate-cho, Kita-ku, Nagoya, Japan

[3] Department of Metallurgy and Materials Science, Osaka Prefecture University, Gakuen-cho, Sakai, Osaka, Japan

Keywords: Shear Test, High Temperature Deformation, Liquid Phase, Aluminum Alloy, Stress Exponent

Abstract

Shear tests have been carried out over a wide temperature range of 753 ~ 893K, including temperatures below and above the solidus temperature, for an Al-5wt.%Mg alloy. The deformation behavior in a semi-solid state is divided into two regions; one is in a semi-solid state containing the discontinuous liquid and another is in a semi-solid state containing the continuous liquid. An analysis of the deformation mechanisms suggested that the deformation of the latter is associated with the lubricated flow. On the other hand, the deformation of the former is likely a transition from the viscous glide creep in a solid state to the lubricated flow in a semi-solid state containing the continuous liquid.

1. Introduction

The deformation behavior in a semi-solid state is phenomenologically divided as follows; plastic deformation of solid phases, sliding between solid phases, flow of liquid incorporating solid phases and liquid flow [1]. For compressive deformation, because the liquid is squeezed out of boundaries experiencing compressive stresses in a very short time [2], it is difficult to investigate the deformation related to the liquid flow. In the present investigation, shear tests are carried out over a wide temperature range of 753 ~ 893K, including temperatures below and above the solid temperature, for Al-5wt.% Mg alloy to investigate the deformation behavior in semi-solid states at early states of melting. Pharr et al.[3] showed that the liquid significantly affects the creep behavior when a significant portion of grain boundary area, in excess of 70 %, is wet. This study revealed that the volume fraction of the liquid phase is an important factor in the deformation characteristics in a semi-solid state. The same trend has been reported in a semi-solid state at solidification [4]. However, the deformation in a semi-solid state is very complicated and can not be described only by the volume fraction of the liquid phase. In the present investigation, the deformation characteristics in a semi-solid state at the early states of melting are investigated from the viewpoint of the distribution of the liquid phase.

2. Experimental Procedure

A material used in the present investigation was a commercial Al-5Mg (5056) alloy. The chemical composition of the alloy is 5.05 Mg, 0.10 Cu, 0.10 Zn, 0.40 Fe, 0.30 Si, 0.15Cr and 0.15Mn in weight pct. The grain are almost equiaxed and the grain size is 20.83 μm. Double shear

specimens were machined from as-received material. All tests were conducted double-shear conditions, using specimens having twin gauge lengths 2.5 mm long and 3 mm in diameter as shown in Fig. 1, in a strain rate range of mainly $10^{-3} \sim 2\ s^{-1}$ and in a wide temperature range of 753 ~ 893 K. The test temperature range includes temperatures below and above the solidus temperature. Much attention was paid to control of the test temperatures. The electric furnace with three zones was used for strict control of the test temperatures. As a result, the test temperatures were rigidly maintained within ±0.1 K. For the testing machine used, the reliable stress values are more than 0.02 MPa because of the detection limit of the load cell. Therefore, tests were not conducted at low strain rates below 10^{-1} or 5×10^{-1} /s at more than 890 K.

The annealed and the deformed specimens were rapidly quenched to investigate the microstructure. The quenched specimens were mechanically polished and then etched. Differential scanning calorimeter (DSC) experiments were carried out for the as-received material to investigate the solidus temperature. The solidus temperature of the alloy was 853 K.

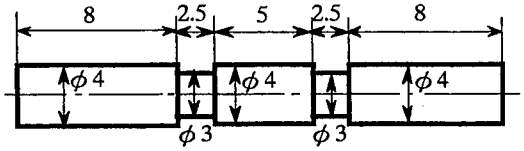

Fig. 1 Illustration of the test specimen.

3. Results

3.1 Microstructure

Microstructures of the specimens annealed at the given temperatures above the solidus temperature (= 853 K) are shown in Figs 2 & 3, where the annealing time is 1.8ks. It can been seen that partial melting preferentially occurs at the triple points of grain boundaries, as shown in the specimen annealed at 863 K, and then partial melting develops along grain boundaries with increasing temperature. Inspection of the microstructures reveals that all areas of grain boundaries are not wet at temperatures ≤888 K, but all areas of grain boundaries are wet at temperatures ≥890 K. Therefore, the temperature range in the present investigation can be divided into three states; a region of solid state between 753 and 833 K, a region of semi-solid state containing a discontinuous intergranular liquid between 863 and 888 K, and a region of semi-solid state containing the continuous intergranular liquid between 890 and 893 K. Partial melting occurs in the interior of the solid phase as well as at grain boundaries, however, each liquid phase in the interior of the solid phase is isolate at all the testing temperatures. Pores are found in the interior of the solid phase. The pores are probably formed during solidification of liquid inclusions by rapid quenching.

The average diameter of the solid phase and the average thickness of the liquid phase at 890 ~ 893 K are quantitatively measured using a LUZEX F Stereo Analyzing System. The results are listed in Table 1. It is noted that the thickness of the liquid phase significantly depends on the temperature. Microstructures of the specimens deformed at 890 K to $\gamma = 0.18$ and 0.44 are shown in Fig. 4, where the shear rate is $1\ s^{-1}$. The phase at 890 K is the semi-solid state containing the continuous liquid. However, no aggregation of the liquid phase was found and there were no boundaries where the liquid was squeezed out of up to $\gamma = 0.1$. In addition, inspection of Fig. 4 reveals that cavities and cracks are not formed at liquid boundaries. Another important observation is that the size and shape

of the solid phase in the deformed specimens are the same as those in the annealed specimen. This suggests that deformation does not occur in the interior of the solid phase and the deformation mechanism is associated with the flow of liquid incorporating solid phases.

Table 1 The thickness of the liquid phase and the size of the solid phase at 890-893 K.

Temperature (K)	Thickness of the liquid phase (μm)	Size of the solid phase (μm)
890	9.3	125.2
891	14.6	133.4
893	23.6	136.3

3.2 Deformation Behavior

The shear stress - shear strain curves at 773, 888 and 891 K are shown Fig. 5, where the shear rate is 1 s^{-1}. It can be seen that the flow stress is almost constant to large strain of about 1.5 and the shear strain to failure is large at 773 K where the phase is a solid state, however, the flow stress rapidly decreases after a maximum stress is attained and the shear strain to failure is very small at 888 and 891 K where the phase is the semi-solid state. The same trend of the yield behavior in a semi-solid state has been reported in thixotropic metals [5].

The variation in shear stress as a function of shear strain rate at 753 ~ 893 K is shown in Fig. 6. The shear stresses were determined at a small strain of $\gamma = 0.05$ because there was no aggregation of the liquid phase at $\gamma = 0.05$. It follows from Fig. 6 that the stress exponent, n ($=\partial \ln\tau/\partial \ln\dot{\gamma}$, where τ is the shear stress and $\dot{\gamma}$ is the shear strain rate), is about 3 at 753 ~ 833 K where the phase is a solid state. Many solid-solution alloys such as Al-Mg alloys show creep behavior with n = 3 because of viscous dislocation glide [6-9]. The fact that the stress exponent was 3 at 753 ~ 833 K indicates that the deformation mechanism is viscous dislocation glide creep. On the other hand, the stress exponent decreases with increasing temperature in a temperature range of 863 ~ 888ΛK, where the phase is the semi-solid state containing the discontinuous liquid, in particular, the low stress exponent of about 2 is attained at 888 K. Many superplastic metals show the low stress exponent of 2 [10]. The dominant deformation process of superplastic flow is grain boundary sliding [11-14]. Therefore, the deformation at 863 ~ 888 K may be associated with grain boundary sliding enhanced by the liquid phase. At 890 ~ 893 K, the very low value of n = 1 is attained at high strain rates of more than 1 s^{-1}.

On the other hand, the stress exponent appears to be high at low strain rates of less than 1 s^{-1} at 890 ~ 893 K, however, we could not investigate the stress-rate relation at low strain rates of less than 1 s^{-1} at 890 ~ 893 K because the flow stresses were close to the detection limit of the load cell used in the present investigations.

3.3 Fracture Behavior

The specimens deformed to failure by the shear tests are shown in Fig.7. Clearly, the shear strain to failure at 863 ~ 893 K, where the phase is the semi-solid state, is much smaller than that at 753 ~ 833 K, where the phase is a solid state. The variation in shear strain to failure as a function of

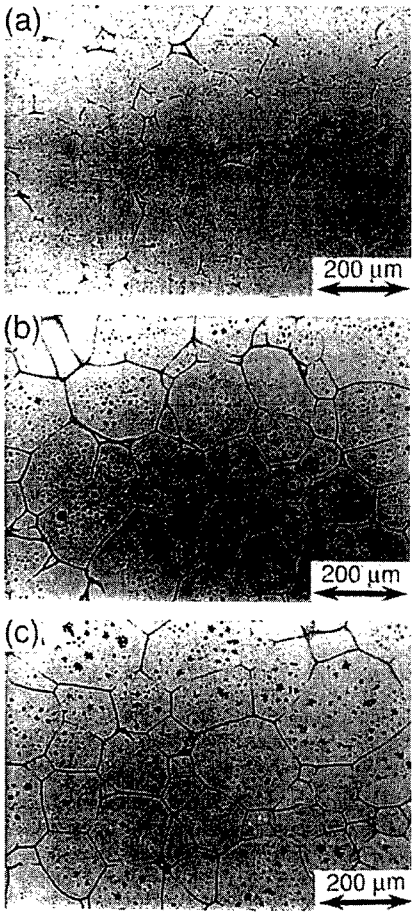

Fig. 2 Microstructures of the specimens annealed at (a) 863 K, (b) 883 K and (c) 888 K, where the annealing time is 1.8 ks.

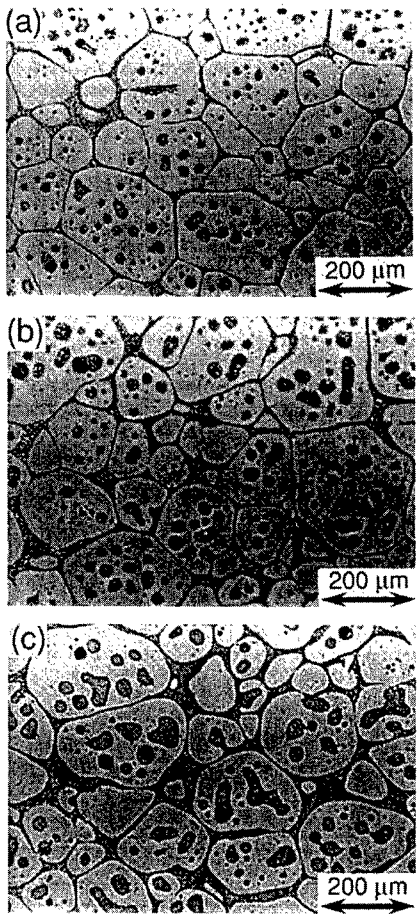

Fig. 3 Microstructures of the specimens annealed at (a) 890 K, (b) 891 K and (c) 893 K, where the annealing time is 1.8 ks.

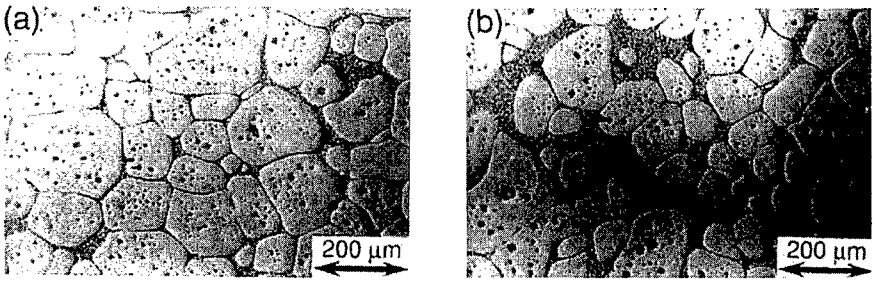

Fig. 4 Microstructures of the specimens deformed at 890 K: (a) $\gamma = 0.1$ and (b) $\gamma = 0.4$.

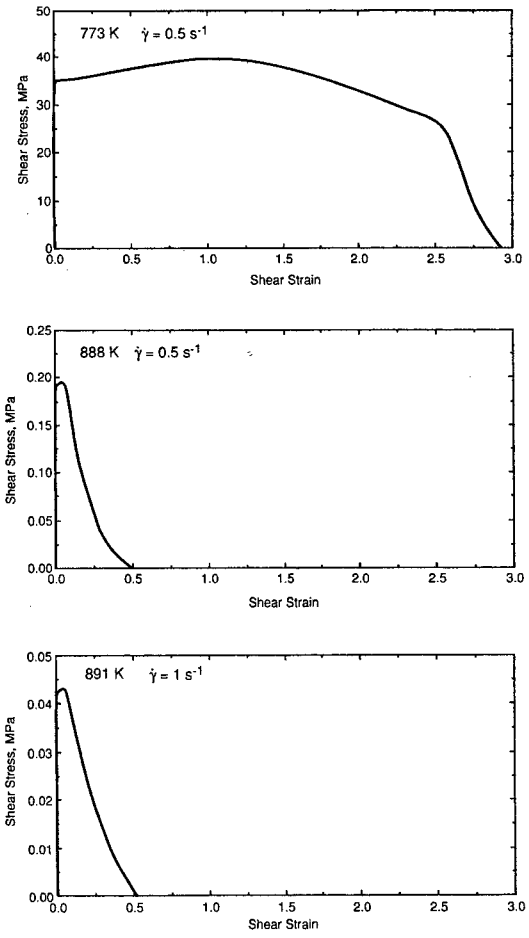

Fig. 5 The shear stress-shear strain curves at 773, 888 and 891 K.

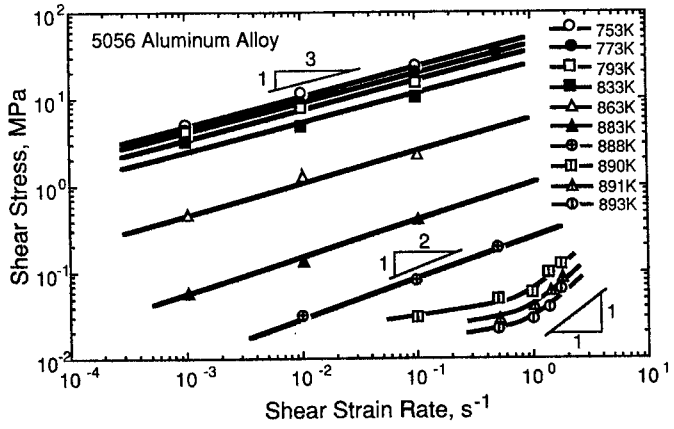

Fig. 6 The variation in shear stress as a function of shear strain rate at 753-893 K.

temperature is shown in Fig. 8, where the shear strain rate is 10^{-1} s^{-1} at 753 ~ 888 K and 1 s^{-1} at 890 ~ 893 K. It can be seen that the shear strain to failure significantly decreases at the solidus temperature. Roth et al. [15] noted that the embrittlement observed by high temperature impact testing is associated with the presence of the liquid phases in Al alloys containing low-melting-point inclusions of Bi, Cd or Pb . The low ductility in the semi-solid state is probably attributed to intergranular decohesion at liquid grain boundaries. Recently, it was reported that superplastic elongation is enhanced by the presence of a liquid phase [16-18]. In this case, the thickness of a liquid phase is very thin (≤ 30 nm) [19]. In the present investigation, however, the thickness of the liquid phase is much larger than that for the superplastic materials. The critical stress, below which decohesion is not caused at liquid boundaries, decreases with increasing thickness of the liquid phase [19]. Therefore, the thick liquid phase is likely responsible for the low ductility in the semi-solid state in the presentinvestigation.

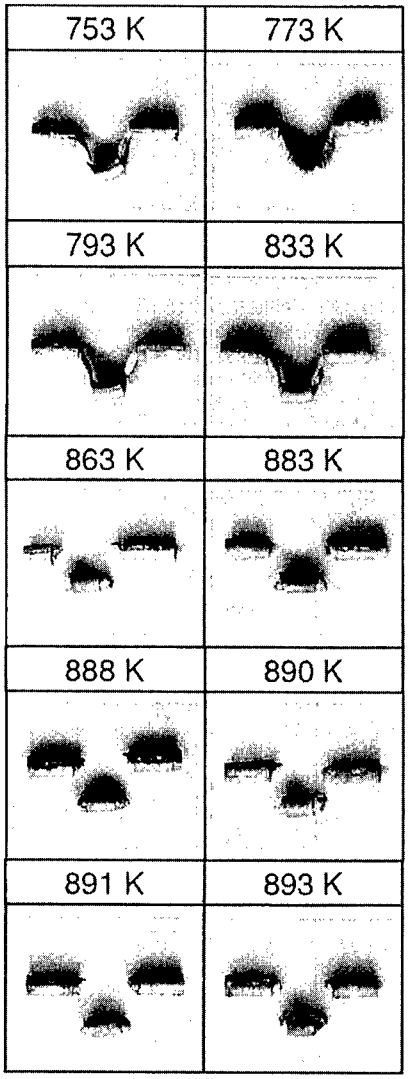

Fig. 7 Examples of the specimens deformed to failure.

4. Surmary

(1) Shear tests and microstructural observation were carried out over a wide temperature range of 753 ~ 893K, including temperatures below and above the solid temperature, for Al-5%Mg alloy.

(2) Microstructural observation showed that the phase at 753 ~ 833 K is a solid state, the phase at 863 ~ 888 K is a semi-solid state containing the discontinuous intergranular liquid, and the phase at 890 ~ 893 K is a semi-solid state containing the continuous intergranular liquid.

(3) When the phase is a solid state, the stress exponent is 3 and the deformation mechanims is considered to be the viscous glide creep.

(4) The deformation behavior in the semi-solid state depended on the distribution of the liquid phase. When the liquid phase is continuous, the stress exponent is unity and the dominant deformation

process is likely to be the lubricated flow.

(5) On the other hand, when the liquid phase is discontinuous, the stress exponent depended on the temperature. This region is likely a transition from the viscous glide creep to the lubricated flow.

Acknowledgments

H.I. and K.H. gratefully acknowledge the financial support of the Ministry of Education Science and Culture of Japan.

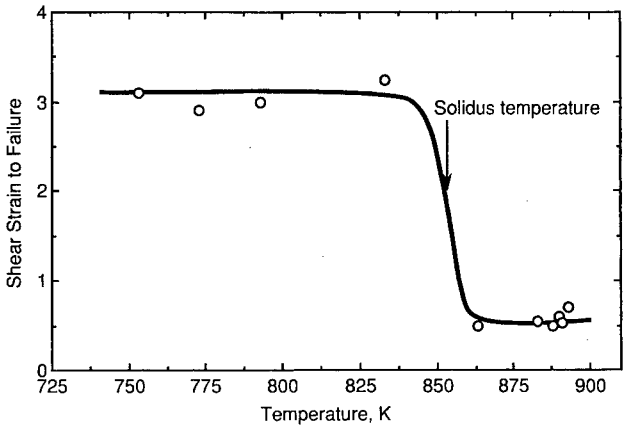

Fig. 8 The variation in shear strain to failure as a function of temperature.

References

1. C.P.Chen and C.-Y.A.Tsao, Acta mater., 45, (1997) 1955.
2. B.L.Vaandrager and G.M.Pharr, Acta metall., 37, (1989) 1057.
3. G.M.Pharr, P.S.Godavarti and B.L.Vaandrager, J. Mater. Sci., 24, (1989) 784.
4. M.C.Flemings, Metall. Trans., 22A, (1991) 957.
5. S.Sannes, H.Gjestland, L.Arnberg and J.K.Solberg, Proc. 3th International Conf. on Processing of Semi-Solid Alloys and Composites, M.Kiuchi ed., Inst. Industrial Science, University of Tokyo, Tokyo, (1994), p. 271.
6. O.D.Sherby and P.M.Burke, Prog. Mater. Sci., 13, (1968) 325.
7. W.R.Canon and O.D.Sherby, Metall. Trans., 1, (1970) 1030.
8. F.A.Mohamed and T.G.Langdon, Acta metall., 22, (1974) 779.
9. P.Yavari, F.A.Mohamed and T.G.Langdon, Acta metall., 29, (1981) 1495.
10. O.D.Sherby and J.Wadsworth, Prog. Mater. Sci., 33, (1989) 169.
11. K.Matsuki, H.Morita, M.Yamada and Y.Murakami, Met. Sci., 11, (1977) 156.
12. R.C.Gifkins, J. Mater. Sci., 13, (1978) 1926.
13. R.Z.Valiev and O.A.Kaibyshev, Acta metall., 31, (1983) 2121.
14. T.G.Langdon, Mater. Sci. Eng., A174, (1994) 225.
15. M.C.Roth, G.C.Weatherly and W.A.Miller, Acta metall., 28, (1980) 841.
16. J.Koike, M.Mabuchi and K.Higashi, Acta metall. mater., 43, (1995) 199.
17. K.Higashi, T.G.Nieh, J.Wadsworth and M.Mabuchi, Scripta metall. mater., 32, (1995) 1079.
18. K.Higashi, T.G.Nieh and J.Wadsworth, Acta metall. mater., 43, (1995) 3275.
19. M.Mabuchi and K.Higashi, J. Mater. Res., 12, (1997) 2332.

Key Engineering Materials Vols. 171-174 (2000) pp. 625-632
© 2000 Trans Tech Publications, Switzerland

High Temperature Strengths of Ir-Based Refractory Superalloys

Y.Yamabe-Mitarai[1], X. Yu[1], Y. Gu[1], Y. Ro[1], S. Nakazawa[1], T. Maruko[2] and H. Harada[1]

[1] National Research Institute for Metals, 1-2-1 Sengen, Tsukuba, Ibaraki, 305-0047, Japan

[2] Furuya Metals Co. Ltd., 1915 Morizoeshima, Shimodate, Ibaraki, 308-0861, Japan

Keywords: Precipitation Hardening, Compression Strength, High Temperature Materials, Fcc and $L1_2$ Two Phase Coherent Structure

ABSTRACT

The microstructurs and compression strengths of Ir-based binary alloys (Ir-X, where X is V, Ti, Ta, Nb, Hf, or Zr) at temperatures between room temperature and 1800 °C were investigated. Several Ir-based alloys displayed superior strength throughout the temperature range. An fcc and $L1_2$ two-phase structure was observed in the Ir-based alloys by a transmission electron microscope and is believed to be an important element of the strength performance. Precipitate shape was observed to depend upon the lattice parameter misfit between an fcc matrix and $L1_2$ precipitates. Cuboidal $L1_2$ precipitates were formed in the Ir-Nb and Ir-Ta alloys with lattice misfit about 0.3%. Plate-like precipitates were formed in the Ir-Hf and Ir-Zr alloys with lattice misfit about 2%, and these precipitates formed a three-dimensional maze structure. Precipitation hardening was investigated in the Ir-Nb and Ir-Zr alloys, but was larger in the Ir-Zr alloy. We observed different deformation mechanisms, shearing mechanism and bypass mechanism in the Ir-Zr and Ir-Nb alloys, respectively.

INTRODUCTION

We have investigated Ir-based alloys as attractive ultra-high temperature materials [1-5]. Ir was selected as the base material because of high melting temperature of Ir (2447 °C). In Ir-V, Ir-Ti, Ir-Nb, Ir-Ta, Ir-Hf, and Ir-Zr binary systems, the fcc structure equilibrates with the $L1_2$ structure [6]. Thus the fcc and $L1_2$ two-phase coherent structure is expected in these alloys. In well known Ni-based superalloys, the fcc and $L1_2$ two-phase coherent structure plays important role to strengthen the alloy around from 800 to 1100°C. For example, both the single-phase alloy with the $L1_2$ structure, and the single-phase alloy with the fcc structure are less resistant to creep deformation than the fcc and $L1_2$ two-phase alloys [7]. These two-phase alloys are more resistant to creep deformation since precipitates form in the matrix with coherent interfaces, and these coherent interfaces prevent movement of dislocations and coarsening of the precipitates [8]. If the fcc and $L1_2$ two-phase coherent structure is formed in the Ir-based alloys, we can expect that Ir-based alloys also show high strength at high temperature which can not be used for Ni-based superalloys. We defined the alloy with the fcc and $L1_2$ two-phase coherent structure and yet with considerably high melting temperatures as "refractory superalloys".

As a high temperature materials, platinum group metals and their alloys have been investigated. Liu et al. observed that the addition of small amounts of W or Th to Ir with an fcc structure improves the ductility of Ir. An Ir-0.3%W alloy is used in the primary containment of space power systems or general purpose heat sources [9, 10]. RuAl and RuSc with a B2 structure [11-14] and IrNb and RuTa with an $L1_0$ structure [14], and Ir_3Nb and Ir_3Zr [15] with an $L1_2$ structure have also been investigated. However there is little research about the platinum group metals based fcc and $L1_2$ two-phase alloys.

In this paper, we investigated strength behavior of the Ir-based binary alloys up to 1800°C. Deformation mechanisms in the Ir-Nb and Ir-Zr alloys as representative are discussed by observation of microstructure and dislocation structure using transmission electron microscope (TEM).

EXPERIMENTAL PROCEDURES

We chose V, Ti, Nb, Ta, Hf, and Zr as the alloying elements of the Ir binary alloys. All Ir binary alloys with second element contents up to 25 at% were prepared as 70g button ingots by arc melting

in an argon atmosphere. This composition range include the fcc single-phase region, the fcc and $L1_2$ two-phase region, and $L1_2$ single-phase region. The table 1 summarized the phase composition of tested alloys, the phase, and heat treatment. We cut 3mm-diameter cylindrical samples from the binary alloy ingots and heat treated them. Heating at 1200°C was carried out with the samples encapsulated in quartz tubes filled with argon gas, followed with water quenching. Heating above 1200°C was carried out in the vacuum furnace. First, we observed the microstructure of these heat treated alloys using a TEM. Next, the compression test was carried out for heat treated samples in air for tests at both room temperature and 1200°C, and in argon for tests at 1800°C. For the tests at 1200°C and 1800°C, the samples remained at the test temperature for 15 minutes before loading. The initial compressive strain rate for every compression test was 3.0×10^{-4}/s. The compression test was stopped when the plastic strain reached about 3%. After the compression test, thin discs were cut from deformed samples, the dislocation structure was observed using TEM. To observe microstructure in the heat treated samples and dislocation structure in the deformed samples, thin discs were cut from samples and were ion-milled. Images were taken in the beam direction of [001], [101], and [112]. Dark-field images were taken with superlattice reflections (**g** =110) from the $L1_2$ phase in the beam direction of [001].

Table 1 Alloy composition (at%), related phase, and heat treatment of tested alloys.

Alloy composition	Phase	Heat treatment for compression test
Ir-9Ti	fcc	1200°C 1 hour
Ir-15, 17Ti	fcc +$L1_2$	1200°C 168 hours
Ir-25Ti	$L1_2$	2000°C 17 hours
Ir-10Nb	fcc	2000°C 72 hours
Ir-15, 17Nb	fcc +$L1_2$	1200°C 72 hours
Ir-25Nb	$L1_2$	2000°C 72 hours
Ir-2Hf	fcc	1800°C 1 hour
Ir-13, 15Hf	fcc +$L1_2$	1400°C 168 hours
Ir-24Hf	$L1_2$	2000°C 72 hours
Ir-2Zr	fcc	1800°C 1 hour
Ir-12, 15Zr	fcc +$L1_2$	1200°C 10 hours
Ir-25Zr	$L1_2$	2000°C 72 hours
Ir-18Ta	fcc +$L1_2$	1200°C 72 hours
Ir-18V	fcc +$L1_2$	1200°C 168 hours

RESULTS

The fcc and $L1_2$ two-phase coherent structure was formed in Ir-based alloys after heat treatment at 1200 or 1400°C for 168 hours in Fig. 1. The phases with bright contrast are Ir_3V, Ir_3Ti, Ir_3Nb, and Ir_3Zr with the $L1_2$ structure (Figs. 1(a), (b), (c), and (f), respectively). Precipitates shape depends on lattice misfit between the fcc matrix and the $L1_2$ precipitates, $\Delta a = \frac{a_{prcipitate} - a_{matrix}}{a_{matrix}}$. In Fig.1, L.M. shows the lattice misfit of these alloys [3]. When lattice misfit is small (less than 0.2%), irregularly shaped precipitates were formed in the Ir-V and Ir-Ti alloys (Figs. 1(a) and (b)). Cuboidal precipitates with coherent interfaces between 100nm and 200nm in size were observed in the Ir-Nb and Ir-Ta alloys with moderate lattice misfit (Figs. 1(c) and (d)). Plate-like precipitates with coherent interfaces were formed and a three-dimensional maze structure appeared in the Ir-Hf and Ir-Zr alloys with large lattice misfit near 2% (Fig. 1(e) and (f)). In the Ir-Hf and Ir-Zr alloys, semi-coherent precipitates were also observed in addition to the coherent precipitates (Fig. 1(g) and (h)). Semi-coherent precipitates are larger than coherent precipitates, and misfit dislocations were observed at interfaces between matrix and semi-coherent precipitates.

The temperature dependence of the 0.2% flow stress of the Ir-based binary alloys with 50% precipitates is shown in Fig. 2. Four well-known materials are also plotted for comparison. First is the 0.2% flow stresses of a Ni-Al-Cr alloy with 40% $L1_2$ phase [16]. The second is the 0.2% flow stresses of a commercially available Ni-based superalloy, MarM247 (Ni-10Co-10W-8.5Cr-5.5Al-0.7Mo-3Ta-1.4Hf wt%) [17]. The third is the tensile yield stresses of a third generation single crystal Ni-based superalloy, CMSX-10 (Ni-2Cr-3Co-0.4Mo-5W-8Ta-6Re-0.1Nb-5.7Al-0.2Ti-0.03Hf wt%) [18]. The fourth is the tensile yield stresses of a W-based HfC dispersion hardening alloy (W-0.35wt%Hf-0.025wt%C) [17]. The strengths of the Ir-Nb, Ir-Ta, Ir-Hf, and Ir-Zr alloys were equivalent to or far higher than the strengths of MarM247 and CMSX-10 at temperatures below 1000°C. The strengths of these alloys were above 400 MPa even at 1200°C and much higher than that of MarM247 (50 MPa). At 1800°C, the strengths of these alloys were about 200 MPa, equivalent to the strength of the W-HfC alloy (197 MPa), which is the strongest known metallic material available at these temperature. The strengths of the Ir-Ti and Ir-V alloys were low at all testing temperatures.

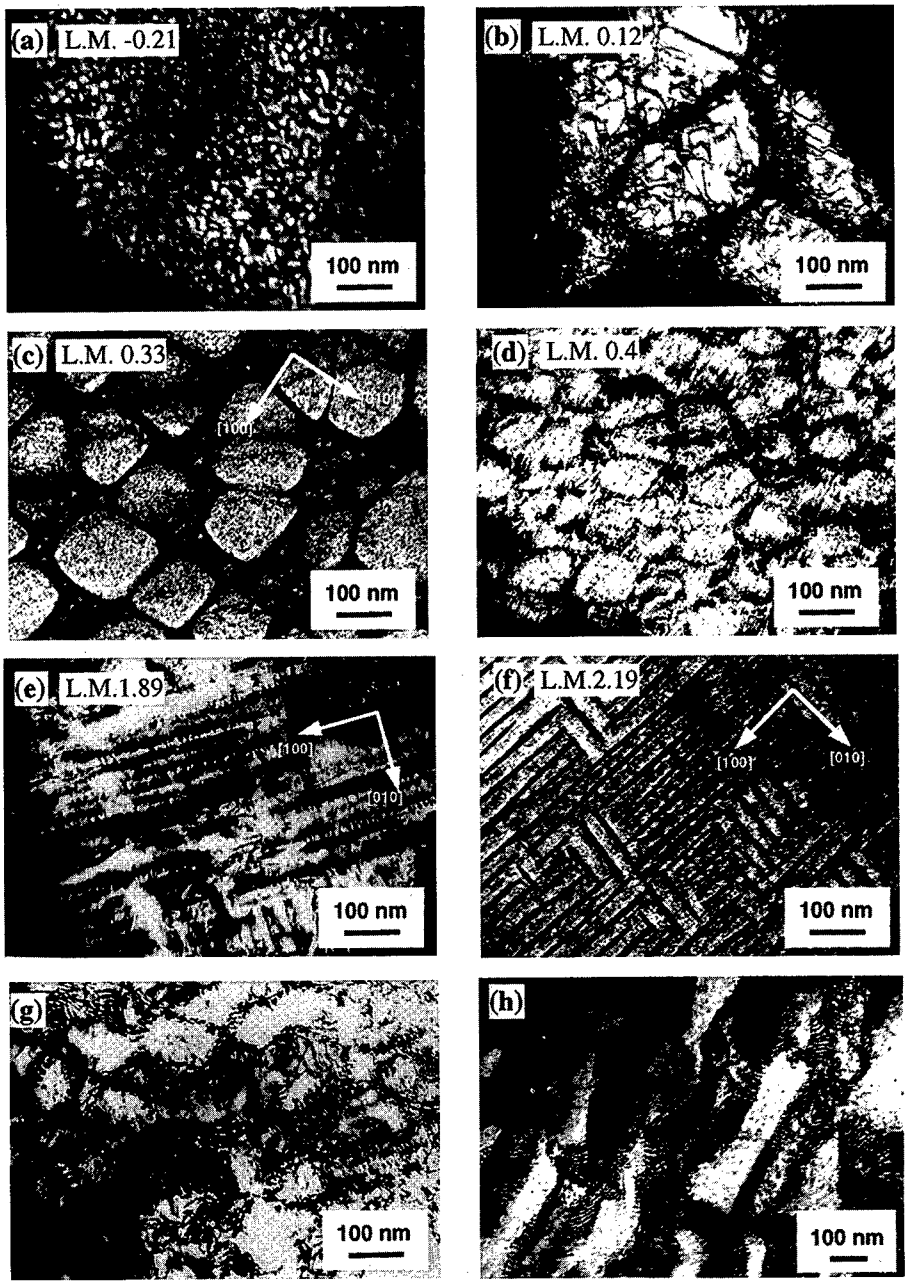

Fig. 1 Microstructure of the Ir-15at% (a)V, (b)Ti, (c)Nb, (d)Ta, (e),(g)Hf, and (f),(h)Zr alloys. (d), (e),(g), and (h) are bright-field images.(a), (b), (c), (f) are dark-field images. They were taken in the beam direction of [001]. Only (h) was taken in beam direction of [101]. All dark-filed images were taken with a superlattice reflection (g=110) from the $L1_2$ structure. The alloys except for the Ir-Hf alloy were heated at 1200°C for 168 hours. Only the Ir-Hf alloy was heated at 1400°C for 168 hours.

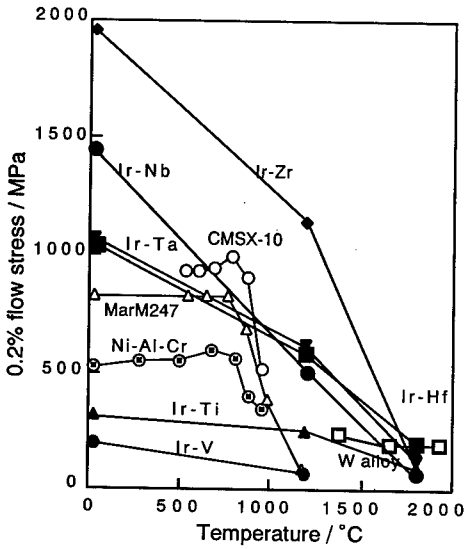

Fig. 2 Temperature dependence of 0.2% flow stress determined by compression tests in Ir-based binary alloys with 50% precipitates in volume fraction, and strength of the Ni- and W-based alloys.

To clearly understand the effects of precipitate shape upon strength, concentration dependence of the strength was investigated for these alloys. Here, only the strength of the Ir-Zr alloys is shown in Fig. 3a to understand clear. The strengths of the two-phase alloys at room temperature and 1200°C were higher than those of the samples with the fcc or $L1_2$ single-phases. This is attributed to the precipitation hardening. We estimated the precipitation hardening of these alloys. First, the contribution of solid-solution hardening to alloy strength can be estimated by the law of mixture for composite materials, as a linear combination of the strengths of the fcc matrix and the $L1_2$ precipitates (dotted lines in Fig. 3a). The difference between the experimentally determined strength and the strength due to solid solution hardening is caused by precipitation hardening (arrow in Fig. 3a). The precipitation hardening at 1200°C is plotted as a function of precipitate volume fraction determined by phase diagrams [6] (Fig. 3b). The precipitation hardening was more effective in the Ir-Zr alloys with plate-like precipitates than in the Ir-Nb alloys with cuboidal precipitates. The precipitation hardening of the Ir-Hf alloy was lower than those of the Ir-Nb alloy although plate-like precipitates were formed. In the Ir-Ti alloys, clear precipitation hardening was not observed.

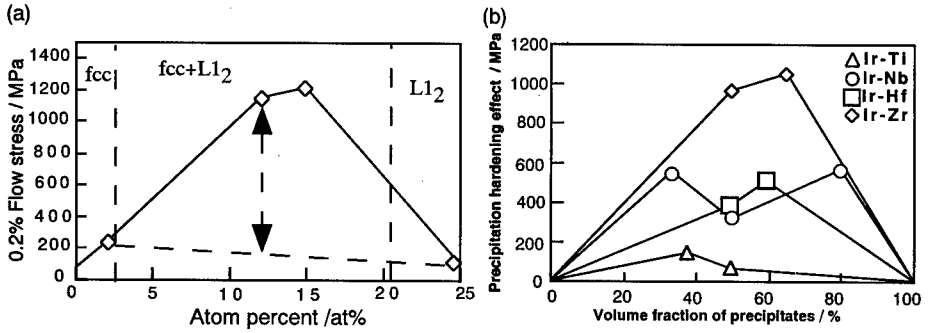

Fig. 3 (a) Concentration dependence of 0.2% flow stress in compression at 1200 °C after heat treatment at 1200°C. (b) Precipitation hardening effect as function of volume fraction of precipitates at 1200 °C.

Dislocation structure of the Ir-Nb and Ir-Zr alloys compressed about 3% at 1200°C are shown in Fig. 4. Cuboidal precipitate shape remained and some dislocations were observed at the interface between precipitates and the matrix in the Ir-Nb alloys (Fig. 4a). However, no difference between heat-treated samples and deformed samples was observed. In the Ir-Zr alloys, the dislocation network was observed at the interface and shearing by bowed dislocations in precipitates was also observed (Fig. 4b). In addition, some dislocations bowed into the precipitates from the interface (A in Fig. 4b).

To understand deformation mode of the Ir-Nb alloy, compression test was carried out for samples heat treated at different temperature. When heat treatment at 1200°C for 168 hours was carried out, 200 nm cuboidal precipitates were formed (Fig. 1c). However, after heat treatment at 1500°C for 168 hours, not only 200 nm cuboidal precipitates in the fcc matrix, but also needle or plate-like fcc phases were formed in the cuboidal $L1_2$ precipitates(Fig 5a). Habit planes between cuboidal $L1_2$ precipitates and the fcc matrix were {100} planes. Habit planes between either needle or

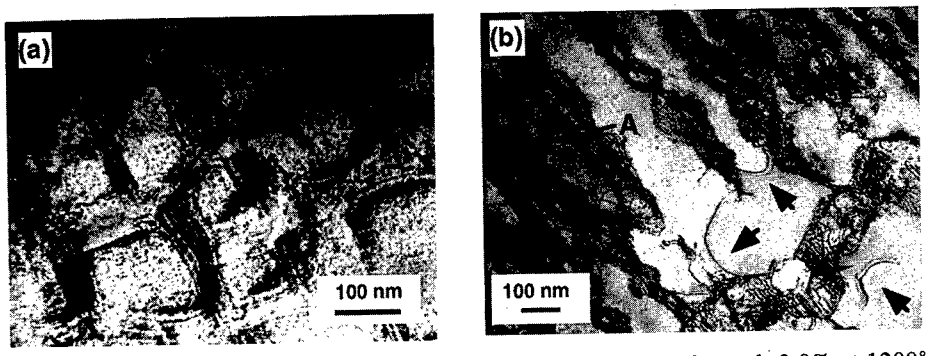

Fig. 4 Bright-field images of the (a) Ir-15at% Nb alloys plasticaly deformed 3.0% at 1200°C and (b) Ir-15at%Zr alloy plastically deformed 3.2% at 1200 °C. The images were taken in the beam directions of (a) [112], (g=$\bar{2}$20) and (b) [101], (g=020).

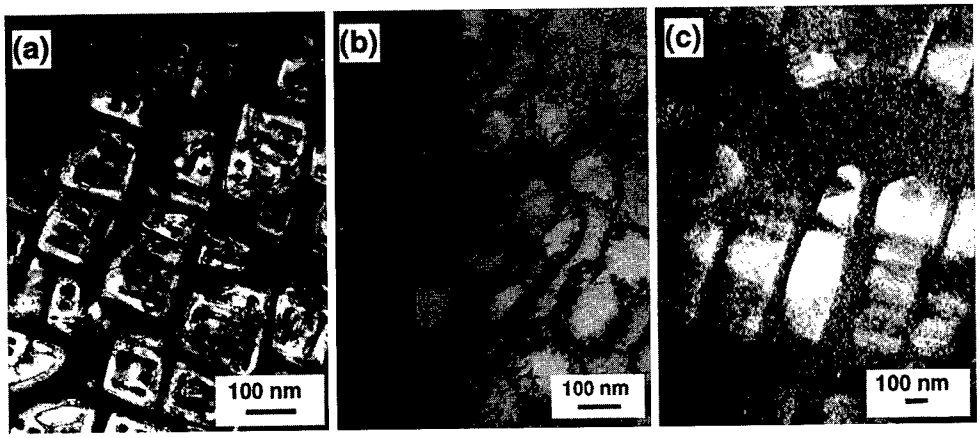

Fig. 5 Dark-field images of Ir-15at% Nb alloys heat treated at (a) 1500 and (c)1800°C for 168 hours. All dark- field images were taken with a superlattice reflection (g=110) from the $L1_2$ structure in the beam direction of [001]. (b) Bright-field image of Ir-15at% Nb alloys heat treated at 1800°C for 72 hours in the beam direction of [001].

plate-like fcc phases and $L1_2$ precipitates were also {100} planes. After heat treatment at 1800°C for 72 hours, spherical precipitates with misfit dislocation were distributed uniformly in the matrix(Fig. 5b). However after heat treatment at 1800°C for 168 hours, precipitates shape was cuboidal or rectangular(Fig. 5c). These $L1_2$ precipitates grew to about 400 nm in size. The precipitates were continuous and were found in arrays along the <100> direction. Therefore, some of the fcc channels grew to about 300 nm, compared with 10 to 100 nm for the fcc channels in alloys heat treated at 1200 and 1500°C.

Figure 6 shows the temperature dependence of the compressive strength of the alloys. The strength of the samples heat treated at 1200°C was about 1200 and 800MPa at room temperature and 1200°C, respectively. Above 1200°C, the strength decreased to about 130MPa at 1800°C. Other samples heat treated at 1500 and 1800°C showed similar behavior. The strength of the samples heat treated at 1800°C for 168 hours was lower than those of the samples heated at 1200 and 1500°C. On the other hand, for the samples heat treated at 1800°C for 72 hours, the strength at room temperature and 1200°C was equivalent to that of the samples heat treated at 1200°C. Compared with the strength of the samples heat treated at 1200 and 1500°C, at room temperature the strength of the samples heat

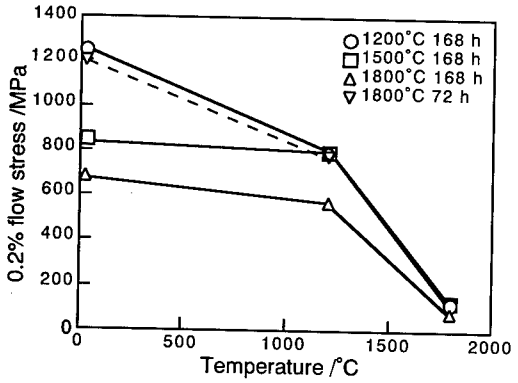

Fig. 6 Temperature dependence of compressive strength in Ir-15at% Nb alloys heat treated at 1200, 1500, and 1800°C for 72 hours and 168 hours.

treated at 1500°C was lower than that of the samples heat treated at 1200°C. At 1800°C, there was no significant effect of the heat-treatment temperature on the compressive strength of the samples.

DISCUSSION

Here we discuss precipitation-hardening mechanisms. Under compression testing conditions with high strain rate, the climb of the matrix dislocations can not occur because thermal activation is needed to climb, and thus the sample must deform by bypass mechanism with an Orowan loop or shearing mechanism. Bypass of dislocations with an Orowan loop around plate-like precipitates may be difficult in the Ir-Zr alloy. In this case, shearing of precipitates becomes predominant in compressive condition. We observed shearing of dislocation into precipitates in the Ir-Zr alloys. Thus we concluded that the Ir-Zr alloys deforms by shearing of dislocations. In the Ir-Nb alloys, we did not clearly observe evidence of bypass or shearing mechanisms. In Fig. 6, the strengths of the Ir-Nb alloys heat treated at 1200 and 1500°C were almost equivalent, except for the strength at room temperature. If the alloy deforms by shearing, the strength of the samples heat treated at 1500°C will be higher than those heat treated at 1200°C, because dislocations will meet not only coherent interfaces between $L1_2$ precipitates and the fcc matrix, but also coherent interfaces from the fcc phase in the $L1_2$ precipitates. The equivalent strength of both samples heat treated at 1200 and 1500°C shows that Ir-Nb alloys deform by the bypass mechanism. From above discussion, we conclude that the Ir-Zr alloy deforms by shearing mechanism and the Ir-Nb alloy deforms by bypass mechanism. The precipitation hardening effect was larger in the Ir-Zr alloy than in the Ir-Nb alloy. One of the reasons is that dislocations in the matrix will be trapped at the coherent interface with large coherency strain and at semi-coherent interface by many misfit dislocations in the Ir-Zr alloy than in the Ir-Nb alloy. This causes high precipitation hardening in the Ir-Zr alloy.

Next we discuss microstructure and strength of the Ir-Nb alloy in detail. The precipitate shape is determined by minimizing the sum of the elastic strain energy of the lattice misfit between the matrix and precipitate, and of the interfacial energy [for example 19]. The fcc plate in the $L1_2$ precipitates observed in the samples heat treated at 1500°C, and arrays of precipitates observed in the samples heat treated at 1800°C are attributed to elastic effect although we do not have data for the elastic constants of Ir_3Nb. Spherical precipitates and cuboidal precipitates were observed by the heat treatment at 1800°C for 72 hours and 168 hours, respectively. We conclude that both of spherical and cuboidal precipitates are stable at this temperature similar to Ir-Zr alloy in which we observed both of coherent plate precipitates and semi-coherent structure.

At room temperature, the strength of the sample heated at 1200°C was higher than that of the sample heated at 1500°C in the Ir-Nb alloy. This is because in the sample heated at 1200°C, fine precipitates formed during cooling strengthen the alloy. At 1200°C, these cooling precipitates are dissolved in the matrix, thus there is no large difference between strengths of samples heated at 1200 and 1500°C. The strengths of samples heat treated at 1800°C for 168 hours were lower than those at lower heat-treatment temperatures because of large, wide fcc channels. Dislocations do not need to bypass precipitates and can move even if confined to the fcc matrix. On the other hand, the strength of the samples heat treated at 1800°C for 72 hours were equivalent to the strengths of the sample heat treated at 1200°C, because of uniformly distributed 200 nm spherical precipitates.

Finally, we discuss possibility of the Ir-based alloys as high temperature materials. Among the Ir-based binary alloys, the Ir-Zr and Ir-Nb alloys are promising as high temperature materials because of their high precipitation hardening effect. The strengths of the Ir-Ta alloy were similar to that of the Ir-Nb alloy. Although the precipitation hardening effect of the Ir-Ta alloy was not investigated, the Ir-Ta alloy is also promising material.

CONCLUSIONS

Compression strength up to 1800°C and precipitation hardening were investigated in Ir-based refractory superalloys with the fcc and $L1_2$ two phase structure. The compression strengths of several Ir-based alloys were superior throughout the temperature range. The precipitate shape of the Ir-based alloys (Ir-Zr and Ir-Hf) with large lattice misfits is a coherent or semi-coherent plate. Coherent plate-like precipitates made a three dimensional maze structure. The precipitate-shape of the Ir-based alloys (Ir-Nb and Ir-Ta) with moderate lattice misfit is cubical. Precipitation hardening of the Ir-Zr alloys with plate-like precipitates is higher than that of the Ir-Nb alloys with cuboidal precipitates at 1200°C. We conclude that the Ir-Zr and Ir-Nb alloys deform by the shearing of dislocation and bypass mechanism, respectively. Although deformation mode of the Ir-Zr and Ir-Nb alloys is different, the strength of them was about 800 MPa at 1200°C. We conclude that Ir-Zr, Ir-Nb and Ir-Ta are promising high temperature materials.

ACKNOWLEDGEMENTS

We are grateful to Mr. S. Nishikawa of Furuya Metal Co., Ltd. for preparing the Ir-based alloy ingots.

REFERENCES

[1] Y. Yamabe, Y. Koizumi, H. Murakami, Y. Ro, T. Maruko, and H. Harada, Scripta Mat., **35(2)**, (1996), p. 211.
[2] Y. Yamabe-Mitarai, Y. Koizumi, H. Murakami, Y. Ro, T. Maruko, and H. Harada, Mat. Res. Soc. Symp. Proc, **460**, (1996), p.701.
[3] Y. Yamabe-Mitarai, Y. Ro, T. Maruko, T. Yokokawa, and H. Harada, in the Second International Symp. of Structural Intermetallics/1997, M. V., Nathal, R. Darolia, C. T. Liu, P. L. Martin, D. B. Miracle, R. Wagner, and M. Yamaguchi, Editors, Structural Intermetallics 1997, TMS, Warrendale, PA (1997), p. 805.
[4] Y. Yamabe-Mitarai, Y. Ro, T. Maruko, and H. Harada, Met. Trans A, **29A**, (1998), 537.
[5] Yuefeng Gu, Y. Yamabe-Mitarai, Y. Ro, T. Yokokawa, and H. Harada, Scripta Mat., 39, 6 (1998) p.723
[6] T. B. Massalski et al., *ed.*, Binary Alloy Phase Diagrams, ASM International, Materials Park, OH, (1992), p. 2082, 2330, 2355, 2361, 2366.
[7] Y. Ro, Y. Koizumi, and H. Harada, Mat. Sci. Eng., **A223**, (1997), p. 59.
[8] D. D. Pearson, F. D. Lemkey, and B. H. Kear, in Superalloys/1980, J. K. Tien, S. T. Wlodek. H. Morrow III, M. Gell, and G. E. Maurer, Editors, Superalloys 1980, ASM, Seven Springs, (1980), p. 513.
[9] C. T. Liu, H. Inoue, and A. C. Schaffhauser, Metall. Trans., **12A**, (1981), p.993.
[10] D. E. Harasyn, R. L. Heestand, and C. T. Liu, Mat. Sci. Eng., **A187**, (1994), p. 155.
[11] I. M. Wolff, Met. Trans. A, **27A**, (1996), p. 3688.
[12] I. M. Wolff and G. Sauthoff, Acta Metall. Mater., **45(7)**, (1997), p. 2949.
[13] I. M. Wolff, G. Sauthoff, L. A. Cornish, H. DeV. Steyn, and R. Coetzee, in the Second International Symp. of Structural Intermetallics/1997, M. V., Nathal, R. Darolia, C. T. Liu, P. L. Martin, D. B. Miracle, R. Wagner, and M. Yamaguchi, Editors, Structural Intermetallics 1997, TMS, Warrendale, PA (1997), p. p. 815.
[14] R. L. Fleischer, Platinum Metals Rev., **36(3)**, (1992), p.138.
[15] A. M. Gyurko and J. M. Sanchez, Mat. Sci. Eng., **A170**, (1993), p. 169.
[16] P. Beardmore, R. G. Davies, and T. L. Johnston, TMS-AIME, **245**, (1969), p. 1537.
[17] W. F. Brown, Jr., H. Mindin, and C. Y. Ho, Aerospace Structural Metals Handbook, vol. 5, CINDAS/Purdue University, U. S.(1992), p. 4218, 5502.
[18] G. L. Elickson, in Superalloys/1996, R. D. Kissinger, D. J. Deye, D. L. Anton, A. D. Cetel, M. V. Nathal, T, M, Pollock, and D. A. Woodford, Editors, Superalloys 1996, TSM, Seven Springs, (1996), p. 35.
[19] T. Miyazaki, K. Nakamura, and H. Mori, J. Mat. Sci., 14, (1979), p.1827.

Key Engineering Materials Vols. 171-174 (2000) pp. 633-638
© 2000 Trans Tech Publications, Switzerland

Creep Behavior of Aluminum Alloy Foils for Microelectronic Circuits

Q. Zhou[1] and G. Itoh[1,2]

[1] Department of Mechanical Engineering, Nagaoka University of Technology, Nagaoka, Niigata Pref., 940-2188 Japan

[2] Graduate student

Keywords: Al-1%Si-0.5%Cu Alloy, Thin Foil, Thickness, Grain Size, Subgrain, Texture, Microelectronic Circuit

Abstract

Creep behavior of Al-1mass%Si-0.5mass%Cu alloy foils with different thicknesses (10-500μm) produced by rolling and subsequent annealing has been investigated. The results showed that the stress exponent varied from 7.9 to 10.4, depending on the specimen thickness. Taking the presence of silicon phase particles into account, threshold stress σ_{th} was introduced to interpret the high stress exponent. The modified stress exponent was about 5 with the effective stress, σ-σ_{th}, where σ is the applied stress. Subgrains were observed by TEM in the specimens during the steady state creep. Thus, it was reasonably deduced that the creep proceeded following the mechanism in which the deformation was controlled by dislocation climb. The creep rate of the specimens with the same texture decreased with increasing specimen thickness. Another possible factor affecting the creep rate was the texture formed in rolling and subsequent annealing. The textures of specimens with different thicknesses were assessed by orientation distribution function.

Introduction

In recent years, the dimension of interconnect lines in microelectronic circuits has been decreased with the sharp increase in the scale of integration of the circuits. A typical aluminum interconnect line is about 0.2μm in thickness with the scale of 6.4×10^6 bit DRAM. With the decrease in dimension, some serious problems have been observed in aluminum interconnect lines [1, 2]. Stress migration is one of the problems and a phenomenon of failure which takes place in the line when the circuit is kept at about 200°C with no electric current. This failure is caused by the thermal stress originated from that the line is surrounded by passivation and insulation films both having expansion coefficients smaller than that of aluminum line [3], and that the final process (passivation coating) is performed at a high temperature of about 450°C.

The failure has frequently been attributed to diffusion creep [4]. However, no evidence of this mechanism has been obtained so far. Moreover, in bulk metals and alloys, diffusion creep is a deformation mechanism which is dominant at higher temperature ($>0.6T_m$) [5, 6]. To understand the mechanism of stress migration, it is necessary to study the deformation behavior of thin foils at elevated temperature. This paper describes a summary by the authors [7-11] on the creep behavior of thin foils of a low-alloyed aluminum, which is currently used for the connect lines, as a main function of specimen thickness and grain size.

Experimental procedure

The specimens used in this study were Al-0.95mass%Si-0.43mass%Cu alloy thin foils with thicknesses ranging from 10 to 500μm prepared by melting, casting, rolling and annealing. The detail on the preparation of the specimens of 50 to 500μm thicknesses has been described elsewhere [7-10]. The final rolling from the thickness of 500μm to 10 and 30μm was carried out by Rikazai Co. Ltd. with a different rolling mill. Tensile test pieces with gauge length of 10mm and gauge width of 6mm were cut from the foils, and subsequently annealed at 450°C for 1 h. The annealing corresponds to the heat treatment of passivation coating carried out in the final manufacturing process of the actual microelectronic circuits. The creep tests were performed in the constant load mode at initial applied stress, σ, of 20-50MPa at 200°C in air atmosphere. The

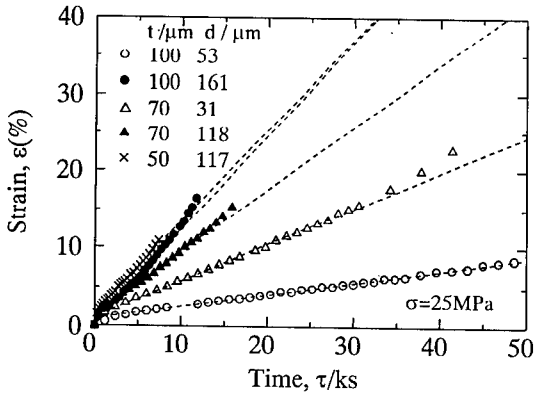

Fig. 1 Creep curves of the specimens with different thicknesses, t, and grain sizes, d, at a fixed applied stress, σ, of 25MPa.

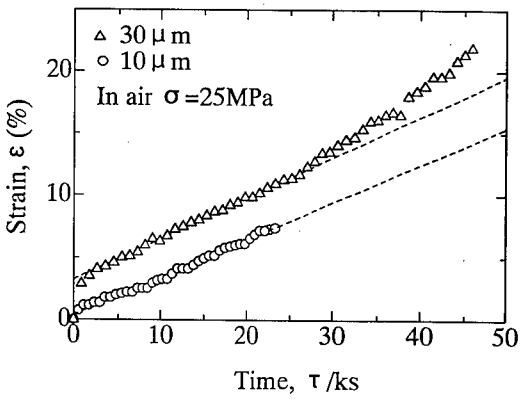

Fig. 2 Creep curves of thinner specimens.

specimens with 10 and 30μm thickness were also tested in a silicone oil bath in order to prevent oxidation during the test. The change in the gauge length was measured photographically using a camera, as mentioned in detail in the previous papers [7-10]. The L-ST section of the specimens prior to the test was subjected to metallographic observation for grain size measurement, and the grain size in L direction, d, was measured by the mean intercept method. A 3mm-diameter disk as TEM specimen was cut from the test piece which was in the course of the steady state creep at an applied stress of 25MPa with a testing time of 6ks. Then, the dislocation structure was observed with a JEOL-2010 TEM. The texture of each foil was examined with a Rigaku X-ray diffractometer, Geigerflex using Cu K_α radiation operated at 50kV/150mA. Orientation distribution function (ODF) was obtained to characterize the texture.

Experimental Results and Discussion:

1. Effects of specimen thickness and grain size:

Creep curves of the specimens with different thicknesses and grain sizes tested in air are shown in Fig. 1. The three regimes of creep states are clearly seen in Fig. 1. Regression lines were drawn in the steady state of the curves as boken lines in the figure. Creep curves of thinner specimens are shown in Fig. 2. The same result is obtained with respect to the three regimes of creep curve as that in Fig. 1. The same result was also obtained when tested in silicone oil, although not actually shown here.

Steady state creep rate obtained from the slope of such regression lines as mentioned above is abbreviated simply to 'creep rate' and is plotted as a function of specimen thickness, t, at a fixed stress in Fig. 3. Creep rate is increased with decreasing specimen thickness when the thickness is over 50μm, while it is decreased with decreasing specimen thickness for the specimen thickness below 50μm. Although

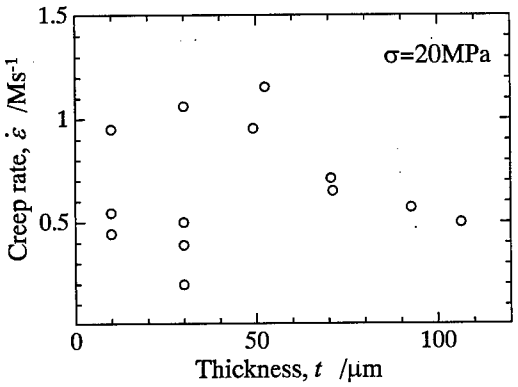

Fig. 3 Plot of creep rate vs. specimen thickness ranging from 10 to 100μm

not shown here, it was demonstrated that the dependence of the creep rate on t/d was more manifested than that on t in the range from 50 to 500μm [7]. The creep rate data obtained in the present study have then plotted in Fig. 4 as a function of t/d in double logarithmic coordinate. The creep rate is increased with decreasing t/d, being consistent with the other result obtained [7, 10].

2. Deformation mechanism:

Correlation between the creep rate and the applied stress is exhibited in Fig. 5 in double logarithmic coordinate. The stress exponents of high values over 8 have been obtained from all of the plots although slightly dependent on the specimen thickness. Since dispersion of Si phase particles was observed in the specimens by the TEM examination [7, 10], threshold stress (σ_{th}) should be introduced into the relationship of the creep rate with the stress [5]. From the fact that slip steps were observed on the specimen surface after the creep test [7], dislocation creep, not diffusion creep, was presumed to be the mechanism which operates in the tested conditions. There are two types of dislocation creep mechanisms, in which the deformation process is controlled by: (i) viscous glide of dislocation where stress exponent of 3 and uniform distribution of dislocation should be observed, and (ii) dislocation climb where stress exponent of 5 and subgrain formation is expected. To determine the threshold stress and to elucidate which of the two types mentioned above is operating, the $1/n'$-th power of strain rate, $\dot{\varepsilon}$, was plotted as a function of σ both in linear coordinate [11], assuming the n' value of 3 and 5. The results obtained for n'=3 and 5 are shown in Fig. 6 and 7, respectively. In these figures, regression coefficient (r^2) for three specimen thicknesses, are also indicated. By comparing the regression coefficient values of the lines in the two figures, it is found that they are greater for n'=5 than for n'=3 in all three specimens. Thus, it seems reasonable to choose 5 as the n' value, supporting the climb-controlled creep mechanism. Moreover, TEM microstructure obtained from the specimen in the course of steady state creep, shown in Fig. 8, demonstrates a subgrain structure. This is also

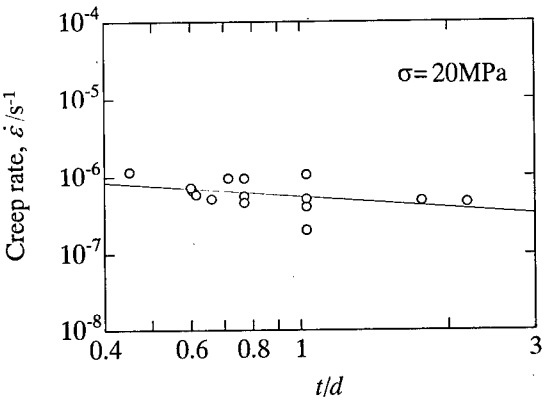

Fig. 4 Double logarithmic plot of creep rate vs. t/d.

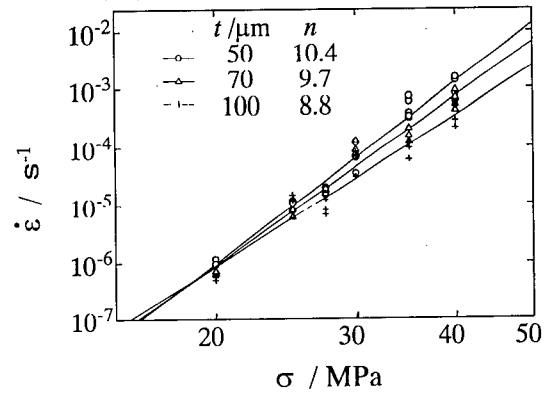

Fig. 5 Double logarithmic plots of creep rate vs. applied stress. All the data are in the range of t/d<1

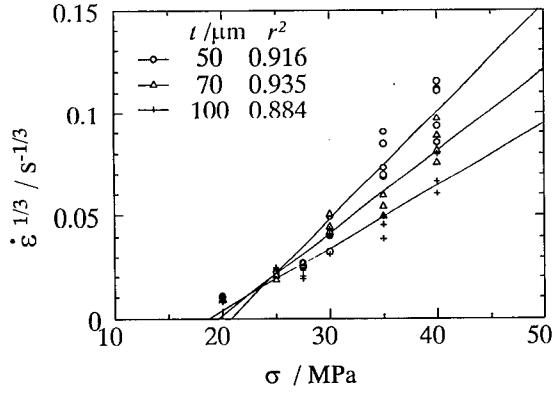

Fig. 6 Plot of $\dot{\varepsilon}^{1/3}$ vs. σ assuming the true stress exponent of 3.

considered to be an evidence of the dislocation creep controlled by climb [5, 6].

3. Effect of texture:

Besides the specimen thickness and grain size, texture has been examined as another factor on which may influence the creep behavior. The textures of the specimen of the thicknesses 30 and 70μm are shown in Fig. 9 in which sections of ODF is illustrated. From Fig. 8 (a), the specimen of 30μm thickness shows sharp S {123}<634> and Goss {011}<100> components, while from Fig. 8 (b), the specimen of thickness 70μm shows a mild Cube {001}<100> component. The ODF's of the other specimens with thickness from 10 to 100μm were also obtained, although not shown here. The texture for the thickness of 10μm was almost identical with that for 30μm with higher density of S components. In the specimen thickness range from 50 to 100μm, textures are almost constant, i.e., the same as that of specimen of 70μm thickness, in which the Cube component is slightly prominent. In section 1, the creep rate has been found to decrease with decreasing specimen thickness when the specimen thickness is below 50μm, contrary to the tendency for the specimen thickness over 50μm. This might be attributed to the above-mentioned difference in texture. The relationship between creep rate and texture will be investigated further in detail in the near future.

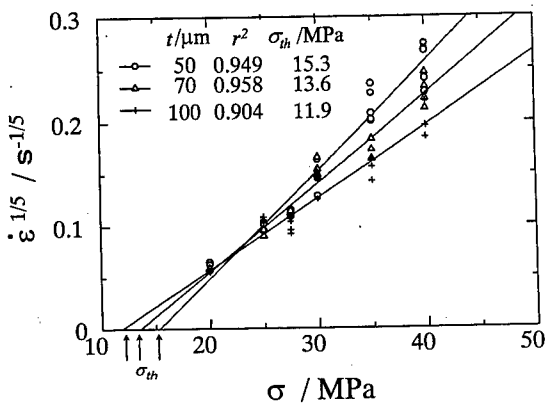

Fig.7 Plot of $\dot{\varepsilon}^{1/5}$ vs. σ assuming the true stress exponent of 5. Threshold stress values, calculated by extrapolating the line as indicated by arrows, are shown in the figure.

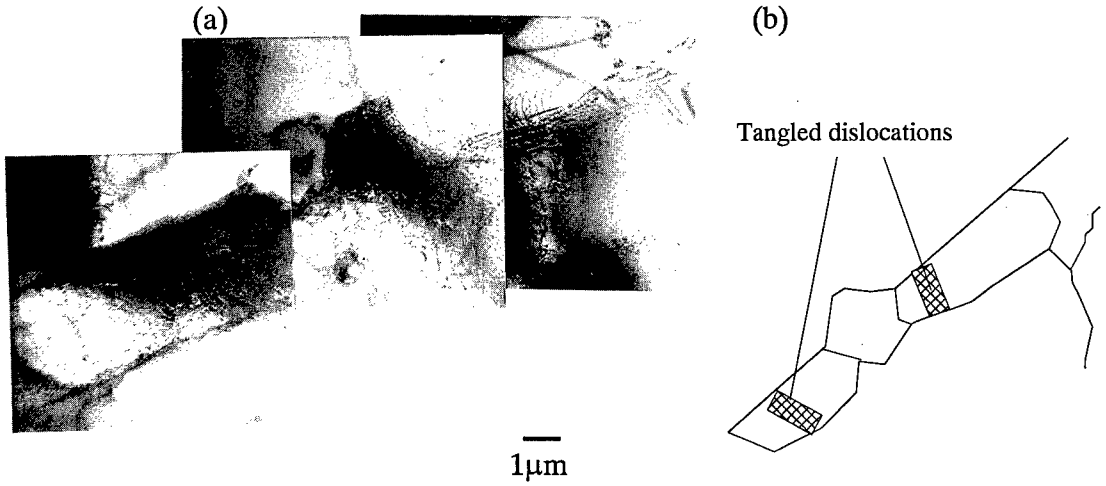

Fig. 8 A TEM photograph taken from the specimen of t=50μm crept at 25MPa for 6ks (a), and corresponding schematic drawing showing substructure (b).

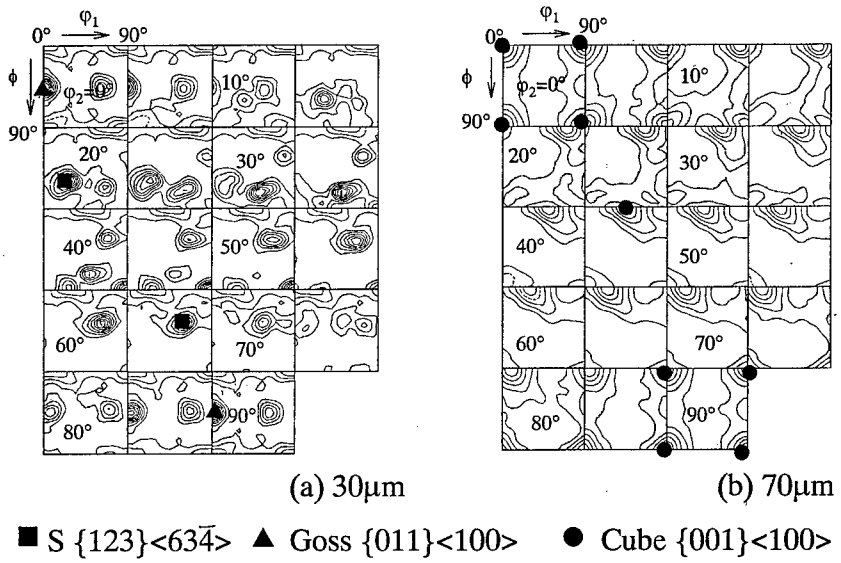

Fig. 9 Sections of orientation distribution function (ODF) of the specimen prior to the creep with thickness 30μm (a) and 70μm (b). Primary components are indicated below the graphs.

Conclusion:

Creep behavior of Al-1%Si-0.5%Cu alloy thin foils with thicknesses ranging from 10 to 500μm has been investigated. Creep rate increases with decreasing specimen thickness when the thickness is over 50μm, while on the contrary, the creep rate decreases with decreasing thickness in the thickness range below 50μm. The dependence of creep rate on applied stress follows power law with stress exponents ranging from 7.9 to 10.4. By applying threshold stress method, the true stress exponent is modified to 5 which indicates the dislocation creep mechanism controlled by climb. The TEM observation on the specimen during steady state creep showing subgrain structure further supports this conclusion. Texture examination by ODF shows that S and Cube textures develop in the specimens with the thickness ranges of 10 to 30μm and 50 to 100μm, respectively.

Acknowledgments

The authors wish to acknowledge the financial support from the Light Metal Educational Foundation, from Iketani Science and Technology Foundation, and Grant-in-Aid for Scientific Research (C) from Ministry of Education, Science Sports and Culture of Japan. They would also like to thank the staff in SKY Aluminum Co. Ltd., where texture examination was kindly carried out, and to thank Mr. T. Yamashita, a graduate student, for his experimental assistance in creep test.

Reference

[1] K. Hinode, Bul. Japan Inst. Metals, 28(1989), 40.
[2] T. Nishida, Materia Japan, 33(1994), 755.
[3] K. Hinode, I. Asano, T. Ishiba and Y. Homma, J. Vac. Sci. Technol., B8(1990), 495.
[4] K. Hinode, N. Owada, T. Nishida and K. Mukai, J. Vac. Sci. Technol., B5(1987), 518.
[5] K. Maruyama: *Materials Science of High-Temperature Strength*, Uchida Rokakuho Publishing Co. LTD., (1997), p.93.
[6] A. S. Argon: *Physical Metallurgy*, ed. by R. W. Cahn and P. Haasen, North Holland, (1996), p. 1958.
[7] G. Itoh and T. Nitta, *Proceedings of the International Symposium on Design, Processing and Advanced Engineering Materials,* ed. by JSPS AEM 156 Committee, (1998), p. 355.

[8] T. Yamashita, G. Itoh and T. Nitta, *Proceedings of the 6th International Conference on Aluminum Alloys, ICAA-6*, edited by T. Sato et. al., The Japan Institute of Light Metals, (1998), p. 1379.
[9] T. Yamashita, G. Itoh and T. Nitta, *The third Pacific Rim International Conference on Advanced Materials and Processing (PRICM3)*, edited by M. A. Imam et. al., The Minerals, Metals & Materials Society, (1998), p 2713.
[10] T. Nitta and G. Itoh, J. Japan Inst. Metals, 63(1999), 196.
[11] Q. Zhou, G. Itoh and T. Yamashita, Mater. Trans., JIM, 40(1999), 443.
[12] R. S. Mishra, A. B. Pandey and A. K. Mukherjee: Mater. Sci. Eng., A201(1995), 205.

Key Engineering Materials Vols. 171-174 (2000) pp. 639-646
© 2000 Trans Tech Publications, Switzerland

Creep and Evolution of Dynamic Recrystallization in Single Crystals of Ti-48at%Al with Different Orientation between Stress Axis and γ Lamellar Plate

N. Shiratori[1,2,3], S. Hirata[1,2], T. Asai[1,2], M. Takeyama[1] and T. Matsuo[1]

[1] Department of Metallurgy and Ceramics Science, Tokyo Institute of Technology, Meguro-ku, Tokyo 152-8552, Japan

[2] Graduate student

[3] Currently JGC

Keywords: Creep, Titanium Aluminide, Single Crystal, Lamellar, Dynamic Recrystallization

Abstract

Creep deformation of Ti-48at%Al PST crystals with various lamellar orientation angles ϕ with respect to the stress axis has been investigated at 1148 K under the stress of 68.6 MPa. The specimen with a lamellar orientation nearly parallel to the stress axis (ϕ=3°) shows the smallest creep rate and the extended transient creep stage, whereas the specimen with ϕ=63° exhibits the largest creep rate and the shortest rupture life. The former exhibits no macroscopic change in the lamellar morphology even after creep tested for 5200 h. However, the specimen with the ϕ=63° ruptured only after 920 h shows many bent lamellar plates and dynamically recrystallized grains near the middle of the specimen. The dynamic recrystallization is caused by the following sequence: (1) breakup of lamellar plates, (2) formation of subboundaries running parallel to the stress axis, (3) further collapse and distortion of the lamellar plates, (4) occurrence of dynamically recrystallized grains along the subboundaries. The orientation dependence of the occurrence of dynamic recrystallization is associated with the rotation of the lamellar plates, and can be interpreted in term of the difference in mode of slip deformation.

1. Introduction

Creep properties of Ti-rich gamma TiAl based alloys with fully lamellar structure have been extensively studied recently, because of a simple principal reason that these alloys show better room-temperature ductility than gamma single phase alloys [1-4]. However, most of the studies have been focused on alloy development to realize high-temperature applications, so that one important concept has been left behind, that is, no conclusive mechanism has been proposed on the role of the lamellar morphology on creep deformation [5, 6].

Matsuo et al. [7-10] recently reported that the lamellar plates play an important role in preventing the dynamically recrystallized grains occurred along the grain boundaries from developing toward the grain interior during creep, by comparing the creep properties of fully lamellar Ti-48at%Al with those of single phase Ti-50at%Al alloys. They also reported that the suppression of the dynamic recrystallization drastically delays the onset of accelerating creep, thereby resulting in the longer rupture life.

In case of a single crystal with fully lamellar structure (PST) [12], the creep properties may be superior to those of the polycrystalline lamellar alloys, because no grain boundaries at which the dynamic recrystallization preferentially occurs exist. Based on this concept, we have examined the creep properties of the PST crystals having various orientation angles ϕ between the lamellar plate and the tensile stress axis in the range of 3~63°, and found that the creep properties are very sensitive to the ϕ. These results suggest that the difference in creep properties of these PST

specimens could possibly be associated with the different formation mode of dynamic recrystallization.

In this study, we will present the orientation dependence of creep properties of the PST specimens in detail, and have examined the microstructure changes during creep deformation. Since we found that dynamic recrystallization occurs in the specimens with large ϕ values, the formation process has been discussed.

2. Experimental

The alloy made in this study has a chemical composition of Ti-47.5at%Al containing 300 ppm oxygen and 70 ppm nitrogen by weight. This alloy was prepared by induction skull melting, followed by centrifugally casting into bars with 12 mm in diameter and 180 mm in length, and then HIPed at 1473 K/176.4 MPa for 3 h. The bars were single-crystallized by an optical floating zone method at a growth rate of 30 mm/h in a flowing purified argon. Seven PST crystals were grown. The orientation angle ϕ between the stress axis (growth direction) and lamellar plate was measured optically for each crystal cut normal to the lamellar plate along the growth direction, and it was in the range of 3° to 77°. Tensile creep specimens with a gauge portion of 30 mm in length and 6 mm in diameter were machined from the grown crystals.

Tensile creep tests were conducted at 1148 K under the constant stress of 68.6 MPa in air using the single-lever type creep machines. The constancy of stress during creep was kept in an accuracy within one per cent against initial stress by adjusting the auxiliary weights. Creep strain was automatically recorded by linear variable-differential transducers through extensometers attached to annular ridges at both ends of the specimen gauge portion. The creep tests were interrupted for some of the specimens by rapid air cooling under load using a compressed air, followed by water quenching. Macro- and microstructure observations were made using optical and scanning electron microscopes.

3. Results

3. 1 Initial microstructure

Backscattered electron images of as grown crystals with ϕ=3° and 63° are shown in Fig. 1, where the transverse direction is the growth direction, identical to the stress axis. Both exhibit a fully lamellar structure consisting of α_2-Ti_3Al (white contrast) and γ phases, with no grain boundaries.

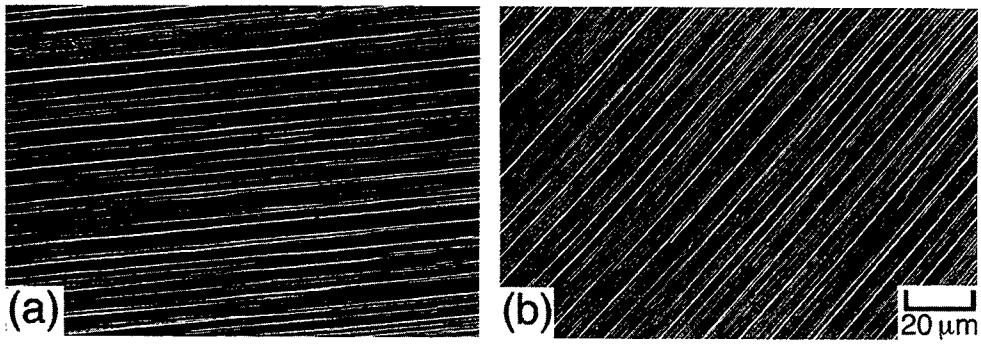

Fig. 1. Backscattered electron images of Ti-48at%Al PST specimens before creep test: (a) ϕ=3°, (b) ϕ=63° (Growth direction: horizontal)

Among all grown crystals, the volume fraction of α_2 phase (~15%), average thickness of the α_2 plates (<0.5 μm) and the interphase spacing of the α_2 plates (~2.3 μm) are nearly the same, regardless of the angle ϕ.

3. 2 ϕ dependence of creep rate

Fig. 2 shows creep rate-time curves of PST specimens with various ϕ ($3° \leqq \phi \leqq 77°$), together with that of the polycrystalline lamellar specimen (FL) for comparison [8]. The specimen with ϕ=3° and 23° were intentionally interrupted after testing for 5200 h at minimum creep stage and for 3390 h at the accelerating creep stage, respectively. The specimen with ϕ=63° exhibits the largest creep rate during overall creep and the shortest rupture life. The creep rate decreases even though the ϕ becomes either smaller or larger than 63°. In comparison of the curves of the specimens with ϕ=3° and 63°, the difference in creep rate just after loading is relatively small, but becomes larger with time, and finally reaches more than three orders of magnitude at minimum creep rate. It should be noted that the creep rate starts accelerating only after 100 h for the specimen with ϕ=63°, whereas it decreases continuously even after testing for more than 5000 h for the specimen with ϕ=3°.

The creep rate plotted as a function of creep strain of these PST crystals is shown in Fig. 3. The specimen with ϕ=63° shows the largest creep rupture strain of 0.65. The creep strain to reach the minimum creep rate shows maximum when the ϕ is 63°, and it becomes smaller with ϕ being either smaller or larger, similar to the ϕ dependence of the creep rate, as shown in Fig. 2. It is obvious that the specimen with ϕ=3° shows only 0.007 strain.

3. 3 Microstructures after the creep test

Fig. 4 shows the macroscopic view of the longitudinal section of the specimen with ϕ=3° after creep testing for 5200 h, together with the corresponding BEI showing the lamellar morphology. Since the specimen was deformed only by 0.007 strain, macroscopically and microscopically no obvious change in microstructure was observed. The same observation was done on the specimen with ϕ=63°, ruptured at 920 h, as shown in Fig. 5. The specimen was heavily deformed, and surprisingly an unusual microstructure was formed in the middle of the specimen encircled by the line in Fig. 5 (a). The high magnification view of the area clearly shows that the lamellae are heavily bent and the dynamically recrystallized γ as well as spheroidal α_2 particles were formed there (Fig. 5 (b)). The rest of the region, however, exhibits a sound lamellar structure, although the ϕ becomes smaller as the area approaches to the fractured surface.

3.4 Microstructure change during creep

The fractured microstructure of the specimen with ϕ=63° is such that, in order to examine the process to collapse the lamellar morphology, other PST specimens with similar ϕ values of 67° and 65° were creep interrupted at the minimum and accelerating creep stages.

In the specimen interrupted at the minimum creep stage with 0.06 strain, no obvious change in microstructure was detected. However, in the specimen interrupted at the accelerating creep stage with 0.17 strain, a few subboundaries running parallel to the stress axis were observed, and they were traced macroscopically as shown in Fig. 6 (a). The higher magnification view shown in Fig. 6 (b) reveals that at the boundaries the lamellar plates are broken and misoriented by a few degrees. In the specimen interrupted with 0.27 strain, heavily curved lamellar regions were macroscopically observed in the middle of the specimen as marked in Fig. 7 (a), and many gamma grains are clearly formed there (Fig. 7 (b)).

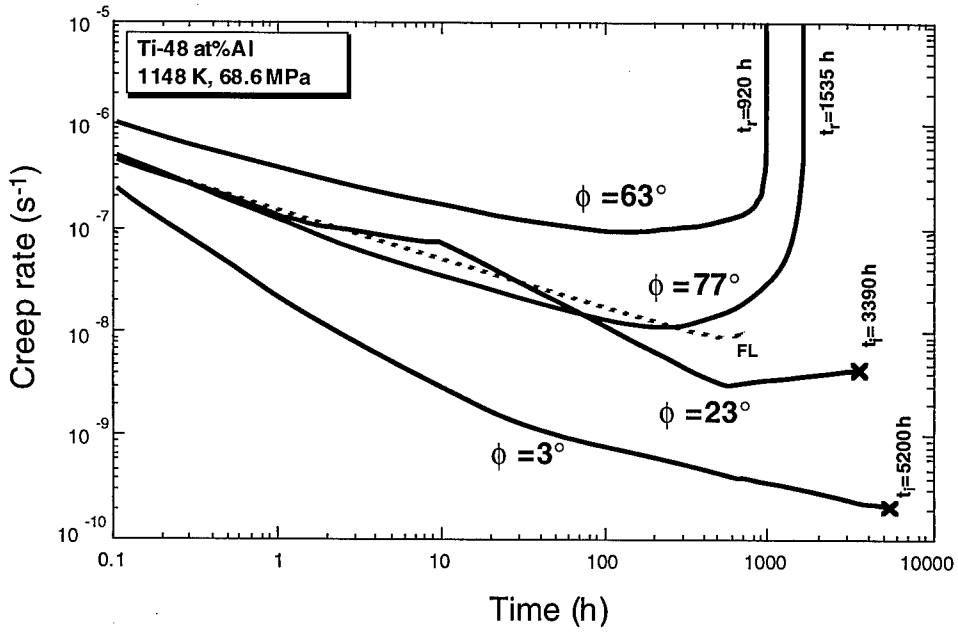

Fig. 2. Creep rate-time curves of Ti-48at%Al PST specimens with various ϕ at 1148 K/68.6 MPa, together with that of the polycrystalline FL specimen.

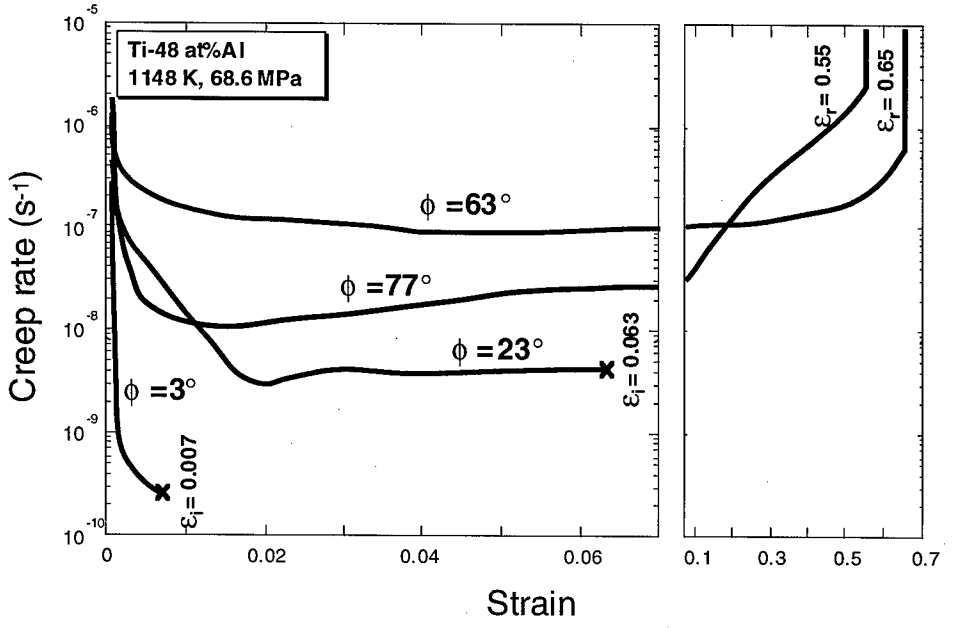

Fig. 3. Creep rate-strain curves of Ti-48at%Al PST specimen with various ϕ at 1148 K/68.6 MPa.

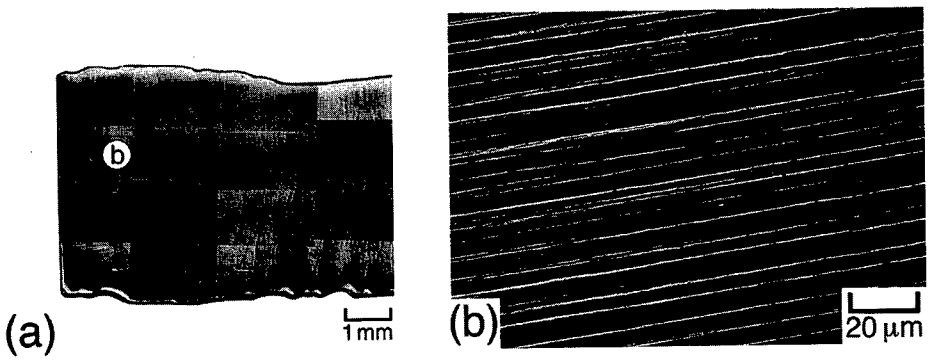

Fig. 4. Optical and backscattered electron images of Ti-48at%Al PST specimen with ϕ=3° creep interrupted after testing for 5200h at 1148 K/68.6 MPa. (a) macroscopic view of the longitudinal section, (b) the high magnification of the portion marked in (a).

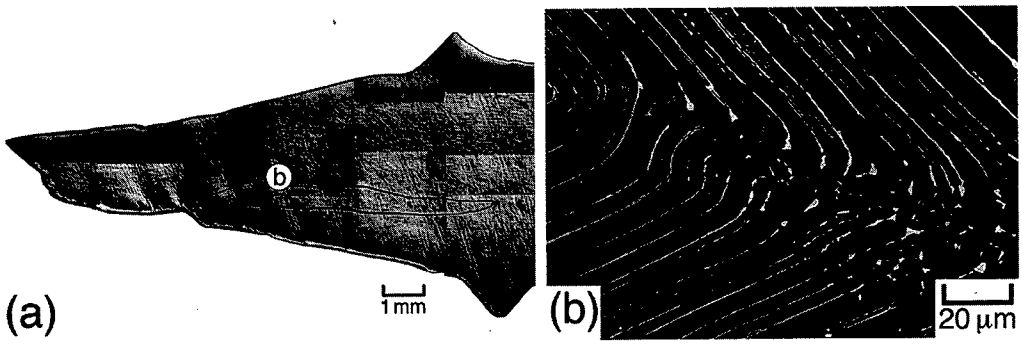

Fig. 5. Optical and backscattered electron images of Ti-48at%Al PST specimen with ϕ=63° creep ruptured at 1148 K/68.6 MPa. (a) macroscopic view of the longitudinal section, (b) the high magnification of the portion marked in (a).

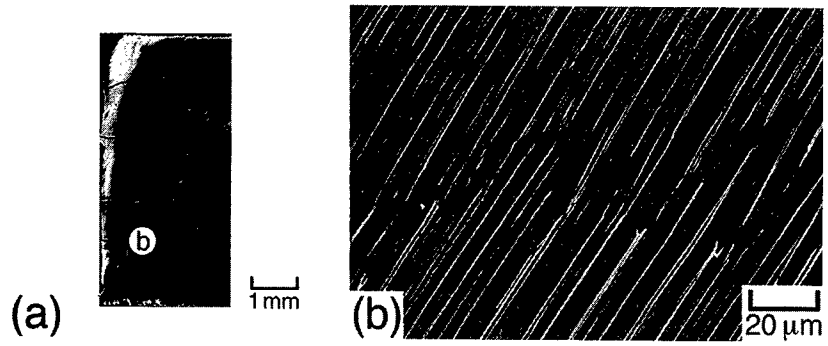

Fig. 6. Optical and backscattered electron images of Ti-48at%Al PST specimen with ϕ=63° creep interrupted at a strain of 0.17 at 1148 K/68.6 MPa. (a) macroscopic view of the longitudinal section, (b) the high magnification of the portion marked in (a).

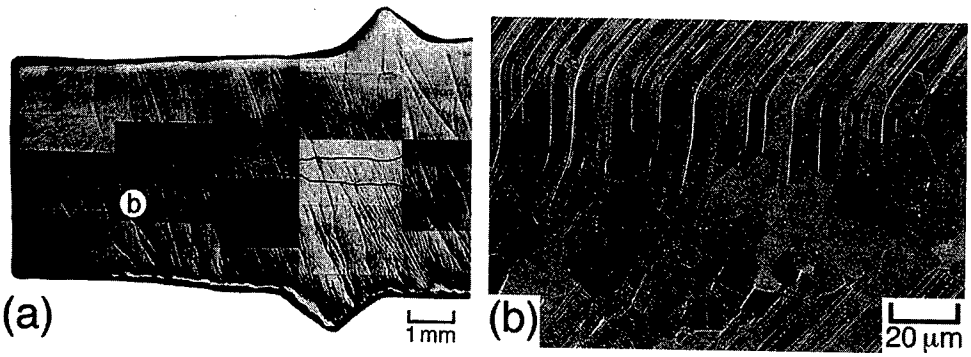

Fig. 7. Optical and backscattered electron images of Ti-48at%Al PST specimen with ϕ=63° creep interrupted at a strain of 0.27 at 1148 K/68.6 MPa. (a) macroscopic view of the longitudinal section, (b) the high magnification of the portion marked in (a).

4. Discussion

The present study clearly demonstrates that the creep properties of Ti-48at%Al single crystals depend strongly on the lamellar orientation and that the single crystallization does not necessarily make the creep properties better than those of the polycrystalline alloy (Fig. 2). The microstructure observation clearly reveals that the dynamically recrystallized grains are observed only for the specimen accelerated earlier but no such microstructure is observed for the specimen having a lamellar orientation nearly parallel to the stress axis and, instead, an extensive period of transient creep appears (Figs. 4 and 5). These results clearly supports our concept that dynamic recrystallization is a major cause to accelerate the creep rate even for the single crystal materials.

The ϕ dependence of the occurrence of dynamic recrystallization is associated with the deformation mode of the crystals. As shown in Fig. 6 and 7, the microstructure observation during creep deformation for the specimens with the large ϕ values phenomenologically suggests the formation process of the dynamically recrystallized grains in a following sequence: (1) breakup of the lamellar plates, (2) formation of subboundaries running through the gauge portion, (3) further collapse of the lamellar plate along the subboundaries, (4) occurrence of dynamic recrystallization at the subboundaries, resulting in the γ grains. Unlike the specimen with ϕ=3°, which shows only 0.007 strain at the minimum creep stage, the specimen with ϕ=63° already exhibits an order of magnitude larger strain of 0.06 at the same stage (Fig. 3). It is thus no doubt that during the transient creep the deformation of PST crystal with ϕ=63° occurs mainly by the primary slip systems parallel to the lamellae [8]. However, as the creep strain increases, the primary slip planes rotate toward the stress axis since the both ends of the specimen are gripped in line, as mentioned in Fig. 5. The rotation would activate other slip systems to cross the lamellae and cause the stress concentration at the lamellar interfaces. Such a deformation process is responsible for the collapse of the lamellar plates and results in the subboundary formation to accommodate the macroscopic strain. As the creep deformation proceeds further, high stress concentration occurs along the subboundaries, and eventually causes the dynamic recrystallization.

In the specimen with lamellar plates nearly parallel to the stress axis, the primary slip systems could not easily be activated since the Schmid factors are nearly zero, so that the rotation of the lamellar plates never occurs. Alternatively the creep deformation has to be caused by the slip to cross the lamellae. However, such a slip is constrained with the lamellar width, thereby resulting in a very small creep strain (Fig. 3). This is responsible for the extensive period of the transient creep stage for the specimen with ϕ=3° and absence of dynamic recrystallization.

Acknowledgements

This research is supported by the research grant on "Research for the Future Program" from Japan Society for the Promotion of Science (96R12301). We acknowledge Central Research Laboratories, Mitsubishi Materials Corporation for providing the alloy ingots.

References

[1] S. Mitao, S. Tsuyama and K. Minakawa, Mater. Sci. Eng., **A143**(1991), 51.
[2] T. A. Parthasarathy, M. G. Mendiratta and D. M. Dimiduk, Scr. Mater., **37**(1997), 315.
[3] M. Es-Souni, A. Bartels and R. Wagner, Acta metall. mater., **43**(1995), 153.
[4] Y.W.Kim, J. Metals, 46 (1994), 30.
[5] K. Maruyama, R. Yamamoto, H. Nakakuki and N. Fujitsuna, Mater. Sci. Eng., **A239**(1997), 419.
[6] B. D. Worth, J. W. Jones and J. E. Allison, Metall. Mater. Trans., **A26**(1995), 2947.
[7] T. A. Parthasarathy, M. G. Mendiratta and D. M. Dimiduk, Scr. Mater., **37**(1997), 315.

[8] T. Matsuo, T. Nozaki, T. Asai, S. Y. Chang and M. Takeyama, Intermetallics, **6**(1998), 695
[9] T. Nozaki, R. Izawa, S. Y. Chang, M. Takeyama and T. Matsuo, in Pro. The Third Pacific Rim Int. Conf. on Adv. Materials and Processing. PRICM 3, TMS, Warrendale, PA, (1998), p. 2461.
[10] T. Nozaki, K. Araki, M. Takeyama and T. Matsuo, in Pro. Int. Conf. on Thermomechanical Processing of Steels and Other Materials. THERMEC'97, TMS, Warrendale, PA, (1997), p. 1415.
[11] K. Araki, M. Takeyama, T. Matsuo and M. Kikuchi, The Abstracts of the 117th Fall Meetings of Japan Inst. Metals and Inter. Symp. on Adv. Materials and Tech. for the 21st Century, (1995), p. 292.
[12] T. Fujiwara, A. Nakamura, M. Hosomi, S. R. Nishitani, Y. Shirai and M. Yamaguchi, Phil. Mag., **61**(1990), 591.

* To whom all correspondence should be addressed, e-mail: tetsuya@mtl.titech.ac.jp, fax:+81-3-5734-3585.

Key Engineering Materials Vols. 171-174 (2000) pp. 647-654
© 2000 Trans Tech Publications, Switzerland

Anomalous Creep Curve of Cu-30 Mass%Zn Alloy

A. Muto, S. Goto and M. Tagami

Department of Materials Science and Engineering, Faculty of Engineering and Resource Science, Akita University, Tegata Gakuencho, Akita, 010-8502, Japan

Keywords: High Temperature Deformation, Brass, Fine Grain, Work-Hardening, Grain Boundary Sliding, Void Formation

Abstract

In order to clarify the feature of high temperature deformation in fine-grained α Brass, a Cu-30 mass%Zn specimen with a grain size of 0.012mm diameter was prepared by annealing for 3.6ks at 723K. A constant stress creep test was conducted for the specimen under various stresses at 623 and 673 K in a salt bath. Their creep curves were compared with each other. The test under a stress of 47.4MPa at 623K reveals a normal type of creep curve consisting of transient creep (the 1st creep), steady-state creep (the 2nd creep) and accelerating creep (the 3rd creep). While the test under the stresses less than 29.4MPa at 673K reveals an anomalous type of creep curve in which the strain rate at the 3rd creep increases with increasing strain in the beginning, attains peak value and decreases again. It is certain that the form of the creep curve depends on stress and temperature, and in particular during the 3rd creep the curves at 673K show a sudden decrease in strain rate, which we call the 4th creep.Under the anomalous creep conditions the amounts of strain to the 2nd creep, the peak strain rate and the creep fracture do not depend on the stress and correspond to 0.35, 0.57, and 0.67 in true strain, respectively.The reason for the anomalous type of creep curve is discussed mainly from view points of grain growth during creep deformation, work hardening and grain boundary sliding.

Introduction

Although 70-30 brass which is a single-phase alloy has high ductility at room temperature, an embrittlement is known at an intermediate temperature range[1-5]. However tensile test revealed that 70-30 brass specimens having coarse grain sizes showed the intermediate temperature embrittlement and as grain size gets smaller, fractured elongation increased above 200% at the intermediate temperature range in a salt bath [6,7]. High temperature creep test revealed that 70-30 brass specimens having fine grain sizes showed anomalous creep curve at the intermediate temperature range around 673K in a salt bath, that was in the beginning of this process the creep rate of the specimen shows 1st creep , 2nd creep and 3rd creep, and at the end of the process the increasing creep rate markedly transforms to decreasing creep rate, that is to say, 4th creep state appears [8,9]. Some irregular creep curves are well-known phenomenon for metals and alloys [10-13], but the 4th type of creep curves have not been so far reported.

The purpose of this paper is to consider the peculiarity of the creep curve and creep-deformation behavior of a Cu-30mass%Zn alloy with a grain size of 0.012mm diameter considering the effects of temperature and stress.

Materials and Experimental Procedure

The materials used in this experiment are a 70-30 brass sheet having a thickness of 1.6mm

on the market. The specimen was analyzed as follows : Cu 70.67, Fe 0.001, Pb 0.001, Ag≤0.001, Sn≤0.001, S 0.001 and O 0.001 mass% and Zn remainder. The specimen cold rolled has a gauge section having length 25.0mm and width 5.0mm, in which longitudinal direction of the specimen is parallel to the rolling direction. The test pieces are annealed in an argon atmosphere at 723K for 3.6ks, and the resultant average grain size is 0.012mm. The grain sizes are not uniformity but duplex grain structure.

Constant stress creep tests were carried out in the same manner as method reported elsewhere[8,13]. That is to say, the creep testing machine is of a modified lever type, in which load is controlled to get a constant stress condition by means of decreasing the load. The test was conducted under stresses of 38.2, 47.4, 59.2, 71.3 and 83.9MPa at 623K, and also under stresses of 9.8, 16.4, 19.6, 24.7, 29.4 and 39.2MPa at 673K in salt consisting of 50% $NaNO_3$ and 50% KNO_3. Their creep curves and microstructures were compared with each other.

Experimental Results

Figure 1 shows the creep curves of the specimens tested under stresses of 38.2, 47.4, 59.2, 71.3 and 83.9MPa at 623K. The time interval between doting points is 7.2ks (= 2h). The figure indicates that the fracture strains are relatively large and little difference for stresses. In any event, the creep curves have processes of 1st, 2nd and 3rd creep and show fracture. **Figure 2** shows the creep curves of the specimens tested under stresses of 9.8, 16.4, 19.6, 24.7, 29.4 and 39.2MPa at 673K. Although the creep curve under 39.2MPa shows normal shape, the curves under the stresses less than 19.6MPa reveal unusual shape. That is to say, these creep curves show 1st, 2nd, 3rd creep curves and a peculiar state, namely, a different deformation process which indicates a marked change in state under the stresses less than 19.6MPa. Because of clarifying the tendency of the curves, **Fig.3** and **4** show the creep rate calculated on the basis of Fig.1 and Fig.2 under each applied stress. In spite of presenting larger side in time-axis compared with that of Fig.2, the specimen does

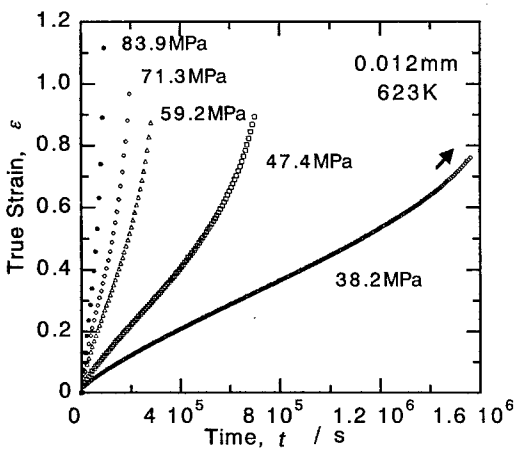

Fig.1 Creep curves of the Cu-30mass%Zn specimens tested under various stresses at 623K.

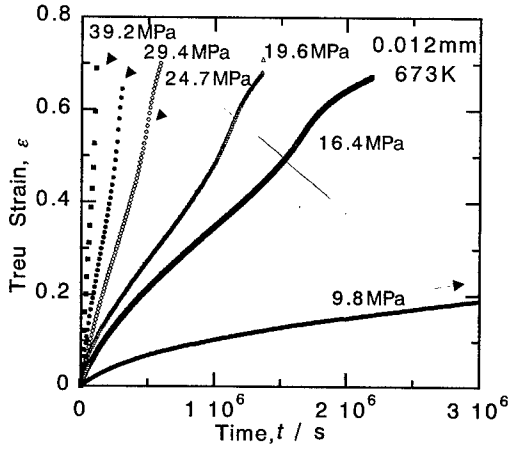

Fig.2 Creep curves of the Cu-30mass%Zn specimens tested under various stresses at 673K.

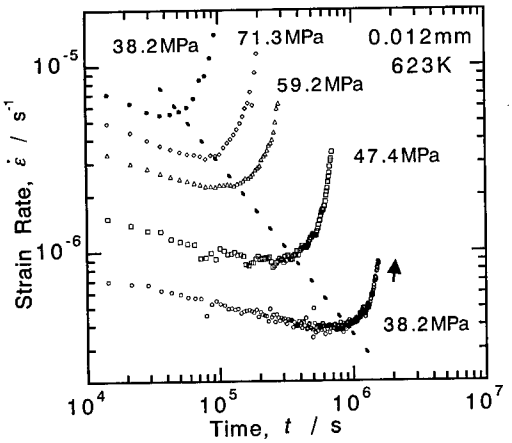

Fig.3 The relation between the strain rate and the time of the specimens tested under various stresses at 623K.

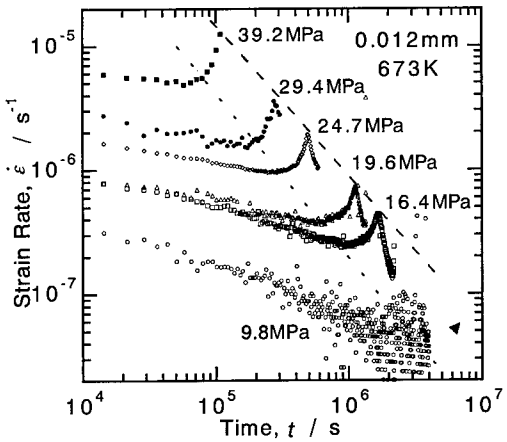

Fig.4 The relation between the strain rate and the time of the specimens tested under various stresses at 673K.

not rupture under 9.8MPa at 673K as shown in Fig.4. Figure 3 shows the familiar 1st, 2nd and 3rd creep states, while Fig.4 reveal all the details of the event explained. As the diagram on Fig.4 indicates, as the location of showing the steady state deformation rate shifts to larger range in time-axis, increasing with applied stress for the specimen. In addition, the creep curve of the specimen shows clearly the state of 4th creep, namely, a deformation process which indicates a marked decrease of strain rate at the end of 3rd creep. The ratio of the time showing 4th creep state to the time of total creep states is large, and the state of 4th creep increases with decreasing stress in the ratio. **Figures 5** and **6** show the strain rate-true strain curves on the basis of Figs.1 and 2 under each

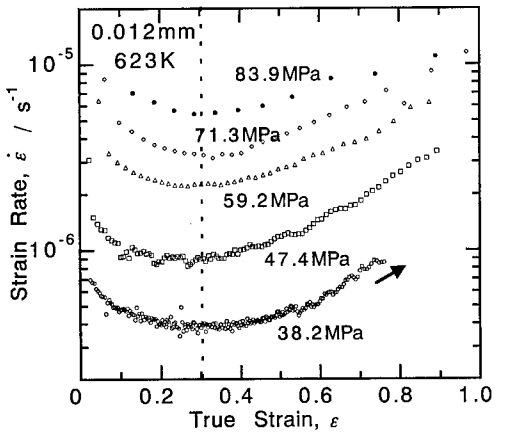

Fig.5 The relation between the strain rate and the true strain of the specimens tested under various stresses at 623K.

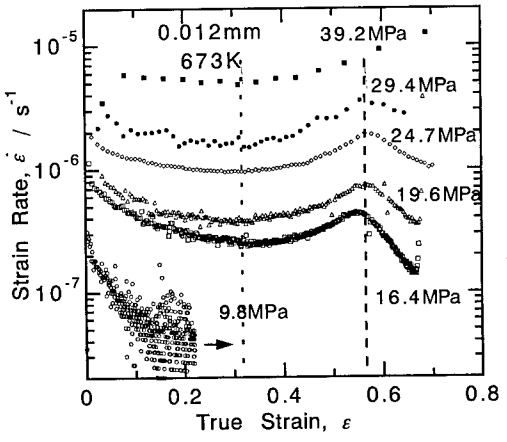

Fig.6 The relation between the strain rate and the true strain of the specimens tested under various stresses at 673K.

applied stress. These diagrams in Fig.5 tell us that at the beginning of this process the creep rate of the specimen shows the 1st creep decreasing with strain, the next 2nd creep showing steady state creep which includes the minimum strain rate and presents the 3rd creep. And Fig.6 shows peculiarly the increasing creep rate at the 3rd creep state markedly transforms to decreasing creep rate at the end of process, that is to say, the 4th creep state appears. As a results the creep rate curve had a peak. The value of steady state strain and that of the strain showing peaks were about 0.32 and about 0.56, respectively independently of applied stress at 673K.

Optical microstructures of the specimens were observed at several states of creep. **Figure 7** shows the grain structure at the gauge part and gripped part of the specimens in which the photograph alphabet notation corresponds to that of the figure set in Fig.7. Photograph (a) shows the initial grain structure of the specimen. Photographs (b) to (f) show microstructure at various location on the figure of strain rate vs. strain curve of the gauge section of the specimens tested under the stress of 19.6MPa at 673K . Photograph (e-0) shows the structure of the gripped section of the specimens at the location (e) at the same creep tested condition. Generally, the grain size increases with increasing the strain. In this connection grain sizes of the gauge and the gripped section are similar at location (e) of the 4th creep state. At the 2nd creep state (c), voids were observed at grain boundary. After that the voids (aggregation of vacancies) grew keeping round shape with increasing strain. As shown at (e) the grains and voids are similar in size.

Discussion

Cu-30 mass%Zn specimen with a grain diameter of 0.012mm shows normal creep curve known to all at 623K. On the other hand, the same specimen shows anomalous creep curve at 673K under stresses less than 39.2MPa. The latter creep curves shows the 1st, the 2nd, the 3rd creep and a peculiar the 4th state, namely, a different deformation process which indicates a marked change in state. On the relation between strain rate and time or strain, the creep rate curve at 673K had a peak. For the specimen tested under the stress of 19.6MPa at 673K and shows the 4th creep, the relation between the mean grain size and the true strain is revealed as shown in **Fig.8**, in which the open marks show the gripped section and the solid marks show the gauge section of the specimen. In this case the both grain size monotonously increases with increasing strain in the same size. But the grain size of the specimen tested at 623K holed in size during creep. It seems to be due to the low diffusion rate (low grain growth rate) at the lower temperature and the short time on creep. On the one hand let us look closely at the void. **Figure 9** shows the changes in the mean void number density and the total void area ratio as a function of true strain, which was calculated by the optical microstructures observed at the several states of the creep. In this case the mean void number density and the total void area ratio monotonously increase also with increasing strain. In those circumstance source of the 4th creep sudden occurring at the end of 3rd creep is hard to understand.

Figure 10 shows effect of the true strain on the integral width and the half value width of Xray diffraction profile for (220) lattice plane of the specimen tested under a stress of 19.6MPa at 673K. There is a marked increase in the amount of the widths, after the maximum strain rate position. It suggests that dislocation density increases markedly during the creep process. Consequently, the specimen at the 4th creep state is considered to have higher strength than at the 3rd creep state. Around these states, however, it is also concerned that the specimen becomes softening because of notable void formation. That is to say, the increase in strength of the specimen containing voids overcomes specimen's softening which was brought by void formation and grain growth. Effect of these behavior seems to induce the 4th creep.

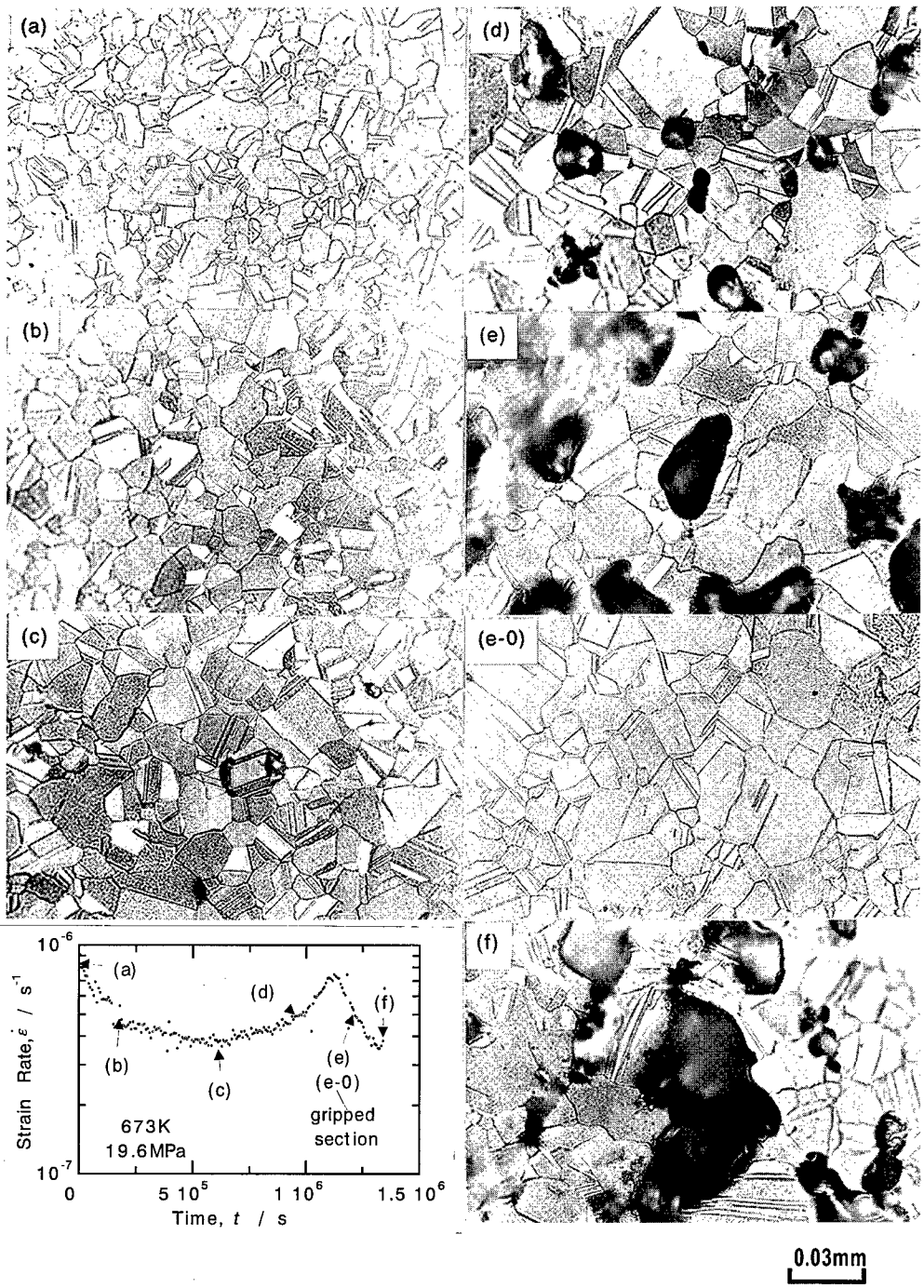

Fig.7 Microstructures of the gauge part and the gripped section of the specimen tested under a stress of 19.6MPa at 673K. Photo.(a) to (f) correspond to the alphabets on the figure showing the relation between strain rate and time.

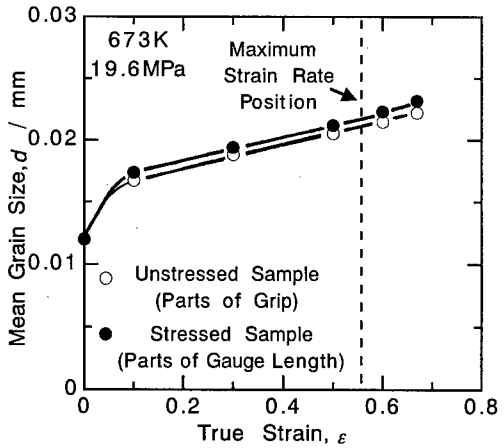

Fig.8 The relation between the mean grain size and the true strain of unstressed part (grip) and stressed part (gauge) in the specimen tested under a stress of 19.6MPa at 673K.

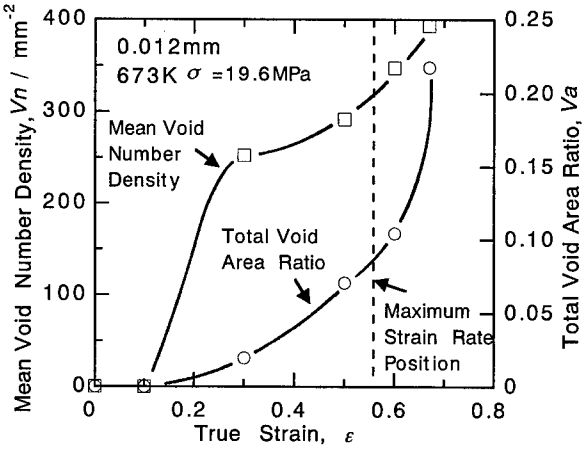

Fig.9 The relation between the mean void number density, the total void area ratio and the true strain of the specimen tested under a stress of 19.6MPa at 673K.

Consequently it follows from what has been said that the shape of the anomalous strain rate curve depends on the details which crystal grain growing statically at the 3rd creep is work-hardened and is more difficult to grain boundary sliding because of grain growth concurrently. Therefore the marked decrease in creep rate would induce the whole specimen to be work-hardened. Viewed in this light, which creep curves at 623K for Fig.1 does not show peculiarity, creep curves at 673K for Fig.2 show that, because of the ease of grain growth in the case, namely, high temperature deformation.

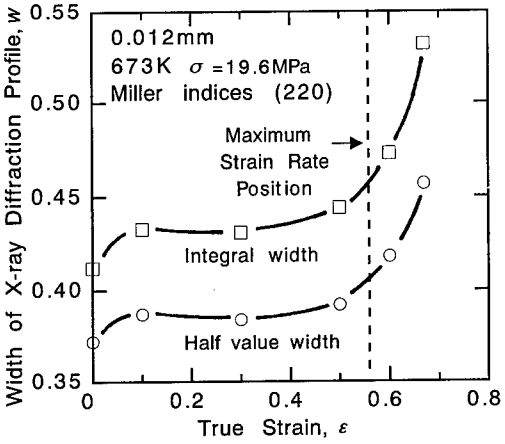

Fig. 10 The relation between the width of the Xray diffraction profile and the true strain of the specimen tested under a stress of 19.6MPa at 673K.

Conclusions

By using a constant stress creep machine, 70-30 brass specimens, with a grain diameter of 0.012mm, were creep-tested under different stresses at 623K and 673K. From the facts described in the above chapters, we may conclude that:

1. Creep curves for 70-30 brass specimens depend on temperature. The creep curve diagrams show the 1st, the 2nd and the 3rd creep at 623K. But at 673K, the curves show the 4th creep which indicates a marked decrease of the strain rate during the 3rd creep. As a result the creep rate curve at 673K exhibits a peak.
2. The steady state creep has a tendency to appear at lower strains with increasing temperature. The strain, which causes the 4th creep on the creep curve, has the same tendency.
3. The state of the 4th creep can be explained as the results of the grain growth and the increasing sudden work-hardening.

References

[1] O. Izumi and Y. Harada , Trans. JIM.**11** (1970), p. 284.
[2] C. C. Koch and A. R. Troiano, Trans. ASM. **57** (1964) , p. 519.
[3] Von K l, Hanser and Osnabruck, Z. Metallk. **18** (1926) , p. 247.
[4] J. N. Greenwood, D. R. Miller and W. Suitew, Acta Met. **2** (1954) , p. 250.
[5] M. Ohmori, K. Wakasa and Y. Yoshinaga, Trans. Jpn. Inst. Metals, **37**(1973) , p. 1188.
[6] A. Muto, S. Goto, M. Tagami and S. Aso, Trans. Jpn. Inst. Metals, **58**(1994) , p. 146.
[7] A. Muto, S. Goto, M. Tagami and S. Aso, Trans. Jpn. Inst. Metals, **59** (1995), p. 23.
[8] A. Muto, S. Goto, M. Tagami and S. Aso, Trans. Jpn. Inst. Metals, **62** (1998), p. 343.
[9] A. Muto, S. Goto, M. Tagami and S. Aso, J. Mat. Sci. Soc. Jpn. **35** (1998), p. 251.
[10] H. Conrad, W. D. Robertson , Trans. AIME. **212** (1958) , p.536.
[11] E. M. Howard, W. C. Barmore, J. D. Mote and J. E. Dorn , Trans. AIME. **227** (1963), p. 1061.
[12] R. W. Fountain and M. Korchynsky , Trans. ASM. **51** (1959), p.108.
[13] G. J. Richardson, C. M. Sellars and W. J. McG. Tegart , Acta Metall. **14** (1966), p.1225.

Key Engineering Materials Vols. 171-174 (2000) pp. 655-662
© 2000 Trans Tech Publications, Switzerland

Deformation Mechanisms in Tin and Tin-Based Electronic Solder Alloys

M.D. Mathew[1], S. Movva[2] and K.L. Murty[2]

[1] Indira Gandhi Center for Atomic Research, Kalpakkam 603 102, India

[2] North Carolina State University, Raleigh NC 27695-7909, USA

Keywords: Tin, Sn-3.5Ag, Sn-5Sb, Creep, Solder, Activation Energy

ABSTRACT

Creep deformation mechanisms in tin, and Sn-3.5Ag and Sn-5Sb electronic solder alloys, have been studied at various temperatures between ambient and 473 K. Power-law relationships between strain rate and stress were generally observed. Stress exponent n = 7.6 ± 0.2, 5.0 ± 0.2 and 5.0 ± 0.3, and activation energy for creep $Q_c = 60.3 \pm 3.8$, 60.7 ± 6.6 and 44.7 ± 3.7 kJ/mole were obtained in the case of tin, Sn-3.5Ag and Sn-5Sb respectively. It is suggested that the rate controlling deformation mechanism is dislocation climb controlled by lattice diffusion in pure tin and Sn-3.5Ag alloy, and viscous glide controlled by pipe diffusion in Sn-5Sb alloy. Sn-5Sb alloy is found to be more creep resistant than Sn-3.5Ag alloy.

INTRODUCTION

Sn-3.5Ag eutectic and Sn-5Sb solid solution alloys are two potential candidate materials for replacing lead-bearing solder materials for interconnection and packaging of commercial microelectronics assemblies[1]. During normal service conditions, the low melting solder alloys are subjected to creep and fatigue deformation. Even at ambient temperature of operation, the homologous temperature for these alloys is high, around 0.6, while the interconnect temperatures can reach as high as 350 K due to local heating, thereby causing creep deformation in the solder material. Automotive under-hood, mainframe and supercomputer applications impose much higher operating temperatures. Fatigue deformation occurs due to induced stresses from differential thermal expansion between the substrate and the solder joints. Therefore, creep and thermal fatigue are two major mechanical properties that control the reliability of solder joints. In this paper, we discuss our recent results on the creep deformation behaviour of tin, Sn-3.5Ag, and Sn-5Sb alloys. Pure tin metal has been included in this study to facilitate understanding the role of alloying elements on the deformation behaviour of the two alloys.

MATERIALS AND EXPERIMENTAL METHODS

Tin samples were annealed at 453 K for 30 minutes before creep testing (melting temperature of pure tin[2] is 505 K). Following annealing, the grain size increased from 25 μm to 150 μm. Sn-3.5Ag and Sn-5Sb alloys were tested in the as-received condition. The average grain size of Sn-3.5Ag and Sn-5Sb alloys were about 20 and 25 μm respectively. Creep specimens with a gauge length of 25 mm, gauge width of 4 mm and gauge thickness of 1 mm were used for the tests. Constant load creep tests were performed in air at 296, 327, 373, 423, 448 and 473 K, and at stresses varying from 1 to 30 MPa. A single specimen was used at each test temperature. In the steady state creep region, the stress was increased in steps of about 2 MPa; once steady-state region was attained at the new stress level, the stress was further increased till the sample fractured.

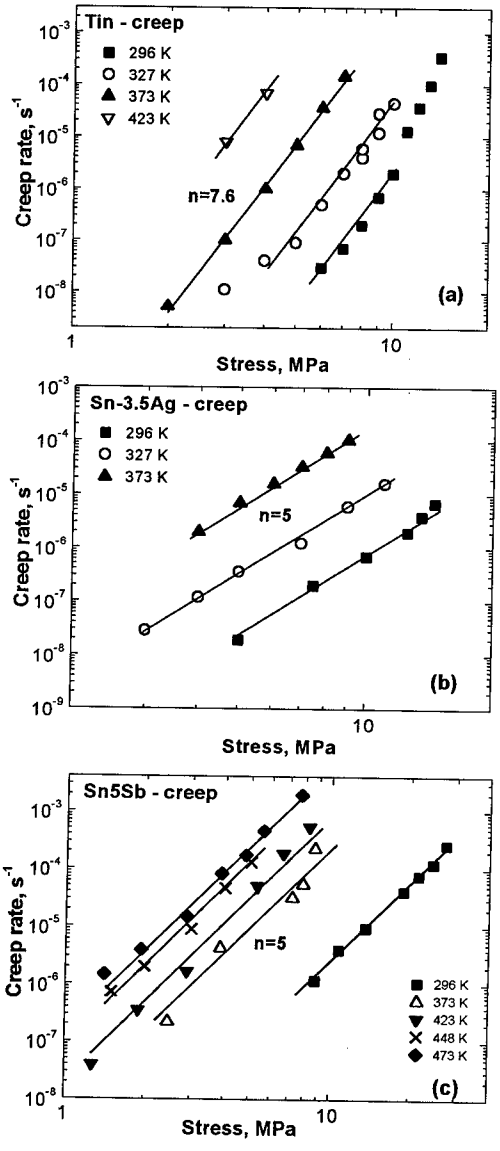

Fig.1. Stress-dependence of creep rate.

RESULTS

Figures 1a-1c show the variation of steady-state creep-rate ($\dot{\varepsilon}$) with applied stress (σ) at various temperatures for tin, Sn-3.5Ag and Sn-5Sb respectively. A power law relationship of the form $\dot{\varepsilon}=A\sigma^n$ was found to be followed over the entire stress range, and at all the temperatures, for the three materials. Tin showed a deviation from power law relationship in the high stress region at room temperature. Sn-Ag and Sn-5Sb alloys yielded values of $n = 5.0 \pm 0.2$ and 5.0 ± 0.3 respectively over the entire temperature range, and pure tin exhibited a higher value of $n = 7.6 \pm 0.2$.

The activation energy for creep deformation (Q_c) was determined from an Arrhenius plot of ln ($\dot{\varepsilon}$) versus reciprocal of absolute temperature at a constant σ/E value where E is the elastic modulus at the test temperature. These plots are shown in Fig. 2 for the three materials corresponding to $\sigma = 2.0 \times 10^{-4} E$. The estimated values of Q_c are 60.3 ± 3.8 kJ/mole for tin, 60.7 ± 6.6 kJ/mole for Sn-3.5Ag and 44.7 ± 3.7 kJ/mole for Sn-5Sb. Thus both tin and Sn-3.5Ag alloy gave almost the same activation energy whereas the value obtained for Sn-5Sb alloy was lower than that for pure tin.

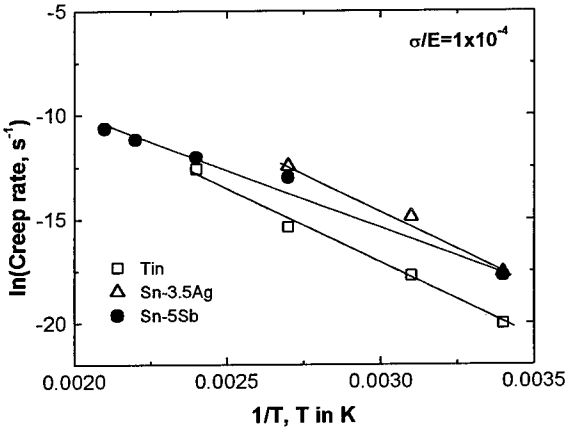

Fig.2. Arrhenius plot to determine Q_c.

DISCUSSION

Tin

The estimated values of creep activation energy have been used to present the isothermal plots (Figs. 1a to 1c) in the form of a temperature compensated strain rate (εkT/DEb) versus normalized stress (σ/E) master plot. Here, k is the Boltzmann constant, D is the diffusivity and b is the Burgers vector. In calculating D, the frequency factor D_o was taken to be equal to 0.78 cm^2/s for the three materials[3]. These plots (Fig. 3) show that for a given material, the data points obtained at different temperatures fall on a single straight line.

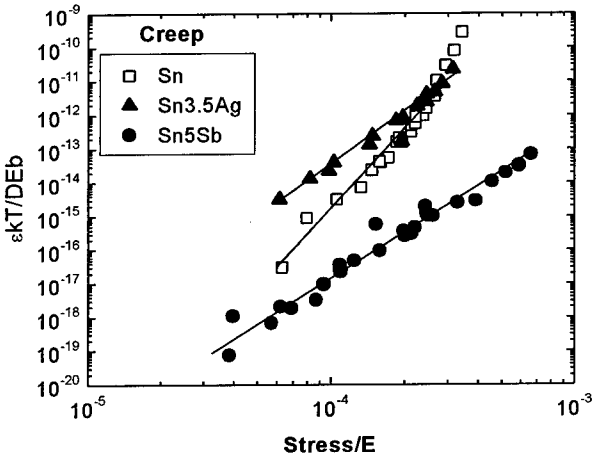

Fig.3. Normalised strain rate versus normalised stress

Creep deformation mechanisms are identified by the value of the stress exponent n and the activation energy Q_c[4,5,6]. Dislocation creep occurs as a result of glide and climb of edge dislocations. These are sequential processes so that the slower process becomes the rate controlling step. Dislocation creep in pure metals is characterized by a value of n = 5, and climb of edge dislocations is the rate controlling mechanism since velocity of climb is slower than velocity of glide. The

activation energy for creep corresponds to the activation energy for self-diffusion or pipe diffusion, depending upon the predominant path of diffusion, which in turn depends on the deformation temperature.

From a review of the published literature on tin, it becomes apparent that there is no clear agreement on the self-diffusion data reported for this material, and also on the expected equivalence between the activation energy for creep deformation and activation energy for self-diffusion. Earlier work on the creep of polycrystalline tin by Breen and Weertman[7], in the temperature range of ambient to near melting point, yielded values of n = 12 and 4.5, at low and high temperatures respectively. Two activation energy values for creep were reported; Q_c = 108 kJ/mole at high temperatures (423 to 497 K) and Q_c = 46 kJ/mole at low temperatures (293 to 423 K). The activation energy values for creep did not agree with the value for self-diffusion in single crystal tin, namely, 25 and 44 kJ/mole in the low and high temperature regions respectively. This disagreement was attributed to the high anisotropy in diffusion exhibited by single crystal tin. In β-tin single crystals, Meakin and Klokholm[8] measured activation energy for self-diffusion of 107 and 97.4 kJ/mole along directions parallel and perpendicular to the c-axis. Mohammed et al.[9] confirmed that at low stresses and high temperatures, tin gave stress exponents of 6 - 8 and activation energy for creep of 96 kJ/mole. A stress exponent of 1 was observed at 495 K at strain rates below 10^{-8} s^{-1}, which was attributed to Harper-Dorn creep mechanism.

Sherby and Weertman[10] rationalised the inconsistencies observed in the activation energy values for diffusion and creep for pure tin, from the well-established equivalence between the values of Q_c and Q_{ld}, where Q_{ld} is the activation energy for lattice diffusion. It is generally observed that as the homologous temperature is decreased from a high value, there is a transition from lattice diffusion controlled creep to pipe diffusion controlled creep such that $Q_c = Q_{pd}$ where Q_{pd} is the activation energy for pipe or core diffusion. The transition temperature γ is usually about 0.5-0.6 for most metals. The activation energy for self-diffusion through the crystal lattice is a function of melting temperature T_m, crystal structure and valence K, while the activation energy for diffusion through dislocation core is a function of the melting temperature only. These activation energies can be expressed as $Q_{ld} = RKT_m$ and $Q_{pd} = 11RT_m$. From these equations, it can be shown that $\gamma = (11-K)/\log(200(\sigma/E)^2)$. The transition temperature thus depends on the values of (σ/E) and K. A value of K=24 is reported for tin which is much higher than the value for other metals. Hence it follows that $\gamma = 0.90$ when $\sigma/E = 5\times10^{-5}$ and $\gamma = 0.99$ when $\sigma/E = 1\times10^{-5}$. Thus creep deformation in tin would be governed by dislocation core diffusion upto temperatures close to T_m. The activation energy for pipe diffusion can be estimated from the previous equation as Q_{pd} = 46 kJ/mole. The ratio Q_{pd}/Q_{ld}

although is a constant is known to vary with the material. For example, values of 0.3 to 0.4 for silver, 0.6 for gold and aluminum, and 0.4 to 0.7 for tin have been suggested[10]. So, in the case of tin, Q_{pd} can be estimated to vary from 66 kJ/mole corresponding to $Q_{pd}/Q_{ld} = 0.7$ to 115 kJ/mole corresponding to $Q_{pd}/Q_{ld} = 0.4$. We feel that it is unrealistic to consider that deformation is controlled by pipe diffusion at temperatures even near the melting point. In the analysis of our experimental results from ambient to 0.83 T_m, we therefore assume a value of $Q_{pd}/Q_{ld} = 0.7$ and so the corresponding estimated value of Q_{ld} = 66 kJ/mole. The experimentally determined value of about 60 kJ/mole for Q_c is thus found to be in reasonably good agreement with this analysis. So we suggest that dislocation creep controlled by lattice diffusion is the rate controlling mechanism for the range of conditions investigated. The value of n = 7.6 falls in the range reported in the literature (3.6 to 12), although, as a pure metal, one would expect a value of n = 5.

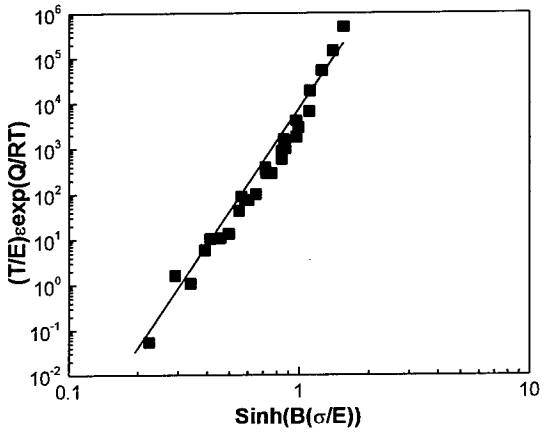

Fig. 4. Double log plot of strain rate versus sinh(Bσ/E).

The high stress data at 298 K deviate from the power law relationship apparently due to power-law breakdown. In this region, exponential stress dependence is usually noted. The experimental data points are fit to a single sinh function which can combine the low and high stress data, i.e., $\dot{\varepsilon} = A \frac{E}{T} e^{-Q/RT} \sinh (B\frac{\sigma}{E})^{7.6}$ where A = 4,514 and B = 3,610. Figure 4 is a double-log plot of temperature compensated strain-rate versus sinh(Bσ/E), and it can be seen that the data at various temperatures follow a single line with a slope of 7.6.

Sn-3.5Ag Alloy

In Sn-3.5Ag eutectic system, most of the silver resides in Ag_3Sn intermetallic particles that are distributed in the matrix in the form of fine rod shaped precipitates. Thus, although one may expect that these particles would act as dispersion strengtheners thereby resulting in n value much higher than 5, which is generally the case with precipitation strengthened materials, the present study yielded a value of n = 5. The activation energy obtained (Q_c = 60.7 kJ/mole) is almost exactly the same as that obtained for pure tin. It should be pointed out that the published literature on the deformation behavior of this alloy system is very limited. In the case of lead-tin

eutectic, Grivas et al.[11] obtained a stress exponent of n = 2 in the low stress region which was attributed to grain boundary sliding. A much higher value of n = 7 was observed at higher stresses apparently due to the dominance of dislocation climb. From creep tests in the temperature range of 300 to 405 K, Darveaux[12] observed a stress dependence of 5.5 and activation energy of 38 kJ/mole. The stress exponent and activation energy obtained in this study compare favourably with the results from the analysis on pure tin thereby suggesting that creep takes place by lattice diffusion-controlled dislocation creep in Sn-3.5 Ag also, in the temperature range of investigation. A separate iso-stress creep test at 5 Mpa, at several temperatures between ambient and 447 K, yielded a value of Q_c = 65 kJ/mole.

Sn-5Sb Alloy

Sn-5Sb is a solid solution alloy, and solid solution alloys are broadly categorised as class-M alloys if the value of n is equal to 5, and class-A alloys if the value of n is equal[13] to 3. In class-M alloys, the rate controlling mechanism is the climb of edge dislocations just as in the case of pure metals. In class-A alloys, the rate controlling mechanism is solute-diffusion controlled dislocation glide since solute atmospheres lock the dislocations such that the rate of glide becomes slower than the rate of climb. Such a mechanism, which is also known as microcreep, predicts activation energy for creep which is equal to the activation energy for diffusion of solute elements. In either case, recovery takes place by the climb of edge dislocations. In class-A alloys where creep is controlled by viscous glide of dislocations, one would expect the dislocations to break away from the solute atmospheres as high stresses are approached. Hence, at higher stresses, climb would be the rate controlling mechanism, as in pure metals, with a value of n = 5 and $Q_c = Q_{ld}$. As Murty[14] has shown in the case of an Al-Mg alloy, the critical stress for the transition from viscous glide to climb in the range of $2x10^{-4}$ E to $1x10^{-3}$ E. Such transitions were reported in many class-A alloys[5]. The transition stress in the present investigation does fall in this regime, and thus the present creep results on Sn-5Sb alloy could correspond to the climb of the edge dislocations. However, the activation energy of 44.7 kJ/mole determined from the creep experiments is around 0.7 times the activation energy determined in pure tin. This value is comparable to the estimated activation energy for low temperature dislocation climb, assisted by vacancy diffusion through dislocation core (46 kJ/mole). However, in that case, the stress exponent will be higher by a value of 2, i.e., equal[13,15] to 7 whereas we obtained a value of n = 5. It is possible that viscous glide is the rate controlling mechanism in Sn-5Sb alloy under the present test conditions. Solute diffusion through dislocation core would then dominate so that the strain-rate would be proportional to the dislocation density, ρ, i.e., $\dot{\varepsilon} = A_1 \rho e^{-Q_{pipe}} \sigma^3$. Since $\rho \propto \sigma^2$, $\dot{\varepsilon} = A' e^{-Q_{pipe}} \sigma^5$. The stress exponent of 5 and

the activation energy of 44.7 kJ/mole obtained in our experiments are in good agreement with the low-temperature viscous glide mechanism.

CONCLUSIONS

Creep deformation mechanisms in pure tin, Sn-3.5Ag and Sn-5Sb alloys were studied in the temperature range of ambient to 473K. Stress exponent of n = 7.6 ± 0.2, 5.0 ± 0.2 and 5.0 ± 0.3 and activation energy for creep Q_c equal to 60.3 ± 3.8, 60.7 ± 6.6 and 44.7 ± 3.7 were obtained for tin, Sn-3.5Ag and Sn-5Sb alloys respectively. From phenomenological analyses, activation energies for self-diffusion through the lattice and dislocation core for tin were estimated as 65 and 46 kJ/mole. Based on the experimentally determined stress exponent and activation energy values, it is suggested that the creep deformation mechanisms are dislocation climb creep controlled by lattice diffusion in pure tin and Sn-3.5Ag alloy, and viscous glide controlled by pipe diffusion in Sn-5Sb alloy.

ACKNOWLEDGEMENTS

One of the authors (MDM) wishes to acknowledge the financial support received from the U.S. National Science Foundation and INEEL University Research Consortium. Thanks are also due to Taracorp Imaco Inc., Alpha Metals Inc., and Indium Corp. for supplying the materials.

REFERENCES

1. P. T. Vianco and D. R. Frear, J. of Metals, 45 (1993) 14.
2. L. E. Felton, C. H. Taeder and D. B. Knorr, J. of Metals, 45 (1993) 28.
3. J. Askill, Tracer Diffusion Data for Metals, Alloys and Simple Oxides, IFI Plenum, New York (1970) 39.
4. J. E. Bird, A. K. Mukherjee and J. E. Dorn in Quantitative Relation Between Properties and Microstructure, Israel University Press, Jerusalem (1969) 255.
5. K. L. Murty, in Creep and Fracture of Engineering Materials and Structures, (eds.) J.C. Earthman and F. A. Mohamed, The Minerals, Metals and Materials Society, Warrendale, PA. (1997) 739.
6. K. L. Murty and O. Kanert, J. of Applied Physics, 67 (1990) 2866.
7. J. E. Breen and J. Weertman, J. of Metals, 72 (1955) 1230.
8. J. D. Meakin and E. Klokholm, Tran. Met. Soc., AIME, 218 (1960) 463.
9. F. A. Mohamed, K. L. Murty and J. W. Morris, Met. Trans., 4 (1973) 935.
10. O.D. Sherby and J. Weertman, Acta Metall., 27(1979) 387.

11. D. Grivas, K. L. Murty and J. W. Morris, Acta Met., 27 (1979) 731.
12. R. Darveaux,.Hybrids and Manufacturing Tech., 15 (1992) 1013.
13. O. D. Sherby and P. M. Burke, Prog. Mater. Sci., 1. (1967) 325.
14. K. L. Murty, Scr. Metall., 7 (1973) 899.
15. K.L.Murty, M.D.Mathew, Y.Wang and Fahmy M Haggag , Modeling the Mechanical Response of Structural Materials, (ed.) Eric M Taleff and Rao K Mahidhara, The Minerals, Metals and Materials Society, Warrendale, PA (1997) 145.

Author for correspondence: M.D. Mathew; email – mathew@igcar.ernet.in

Key Engineering Materials Vols. 171-174 (2000) pp. 663-668
© 2000 Trans Tech Publications, Switzerland

Effect of Microalloying on the Creep Strength and Microstructure of Eutectic Sn-Pb Solders

N. Wade[1], T. Akuzawa[2], J. Kunii[3] and K. Miyahara[3]

[1] Technical R&D Lab., Topy Industries Ltd., Toyohashi 441-8510, Japan

[2] Nippon Filler Metals, Chiba-pref., 270-0203 Japan

[3] Dept. of Molecular Design and Eng., Nagoya Univ., Nagoya 464-8603, Japan

Keywords: Microalloying, Solder, Creep Strength, Rupture Strength, Particle Dispersion Strengthening, Sn-Pb Eutectic Alloy, Microstructure

Abstract Electronic devices are recently much more frequently loaded into more severe environments of higher temperature and/or fluctuating stress and temperature. Accordingly, the improvement of creep strength properties and mechanical and thermal fatigue ones of the electronic joining material of solder is strongly demanded. The objective of the present study is to improve the creep strength of Sn-Pb eutectic solder by the addition of small amount of effective elementsof Sb, Ag, Cu and Ga, which are selected by preliminary experiments and statistical analysis. Creep tests indicated that the microalloying improved significantly the creep strength comparing with that of the regular Sn-Pb eutectic solder.

Introduction

Recently, electronic devices are much more frequently loaded into the more severe environments, such as the condition of higher temperature and/or fluctuating stress and temperature, which induces the higher temperature creep fracture and/or the enhanced mechanical and thermal fatigue in the electronic joining materials of solder[1,2]. Accordingly, the improvement of creep strength and mechanical and thermal fatigue strength is strongly demanded in a technical field of electronic materials joining.

The present authors have investigated the effect of the small amount of addition of Sb, Ag, Cu and Ga on the creep strength of the regular Sn-Pb eutectic solder . These elements have shown significant improvement of the creep and rupture strength, although there is no difference between the activation energies for the minimum creep-rate deformation of the microalloyed solder and the regular Sn-Pb eutectic alloy. TEM (transmission electron microscope) observation indicates that there are no precipitate particles in the Pb side phase, but tiny particles are formed and distribute densely in the Sn side phase which is a major part of the matrix of the Sn-Pb eutectic alloy. Accordingly, it is considered that this dense distribution of the small particles improves the creep and rupture strength of the microalloyed material.

Experimental procedures

Table 1 shows the chemical compositions of the materials used. The alloy A is a regular Sn-Pb eutectic solder alloy. The alloy B contains 0.5%Sb, 0.5%Ag, 0.1%Cu and 0.003%Ga. The previous research[3] indicated that this combined addition of Sb, Ag, Cu and Ga to the regular eutectic solder alloy was very beneficial for the improvement of thermal fatigue strength. These alloys were cast into metallic dies and the creep test specimens were machined from the ingots. Creep test was performed at the temperature range of 313 to 378K and the stress level of 5 to 15MPa. Optical microscope (OM) and TEM observation were made on the specimens of the alloy B

Table 1 The chemical compositions of the materials used (mass %)

Materials	Sn	Pb	Sb	Ag	Cu	Ga
Solder alloy A	Bal.	37.0	---	---	---	---
Solder alloy B	Bal	37.0	0.5	0.5	0.1	0.003

which were aged at 423K for 3.6Ms after the casting into the metallic dies.. Vickers hardness measurement was also done at room temperature to clarify whether there is a age-hardening phenomenon due to the addition of the microalloying elements in the alloy B.

Experimental results and discussion

Figure 1 shows the results of Vickers hardness measurement during the aging treatment at 353K for 1800ks of the alloys A and B which were cast into the metallic dies. This indicates that although there is no age-hardening effect even in the alloy B, the strength of the alloy B is larger than that of the alloy A. Figure 2 shows typical creep curves of the alloys A and B at 333K and 5 to 10MPa. It can be understood that the alloy B has larger creep strength than the alloy A. In Fig.3, a creep rate curve is shown with a usual creep curve of the alloy B. The minimum creep rate ($\dot{\varepsilon}_{min}$) can be obtained from the minimum point of this curve. The $\dot{\varepsilon}_{min}$ of the alloy B is smaller than that of the alloy A at the same creep condition (stress and temperature). The stress dependences of $\dot{\varepsilon}_{min}$ of the alloys A and B are shown in Figs.4 and 5, respectively. Stress exponent, which is designated to be an exponent, n, to satisfy the following equation,

$$\dot{\varepsilon}_{min} \propto \sigma^n \quad \text{---------- (1)}$$

, where σ is a creep stress, is also shown in Figs. 4-(a) and (b). It is generally recognized that the n value increases with the increasing of creep strength and decreases at higher creep test tempearature. The n valuses shown in Figs.4 and 5 also indicate this tendency. When we express the $\dot{\varepsilon}_{min}$ by the Eq. (2),

$$\dot{\varepsilon}_{min} = C\,\sigma^n e^{-Q/RT} \quad \text{-------- (2)}$$

, where C is constant, Q:the activation energy for the minimum rate creep, R:gas constant and T is the absolute creep test temperature, Q of the alloys A and B are obtained in Figs.5 (a) and (b). These values of 81 to 103kJ/mol are roughly near to the activation energy (108kJ/mol) for the self diffusion of the each element of Sn and Pb[4]. Accordingly, it can be an understanding that the creep strengthening of the alloy B is due to the decrease of the frequency factor, C in Eq.(2).

Figure 6 shows the creep-rupture curves, which

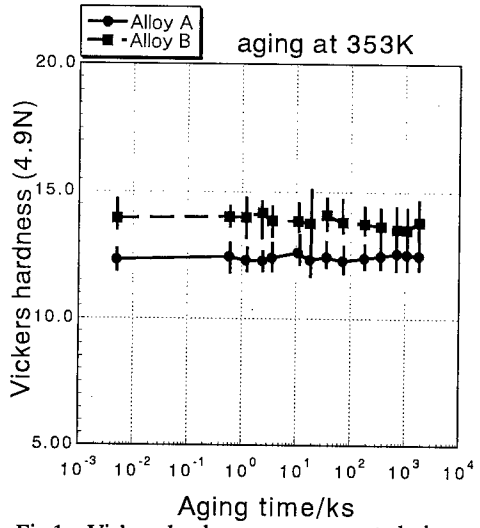

Fig.1 Vickers hardness measurement during the aging treatment at 353K for 1800ks after the casting into the metallic dies.

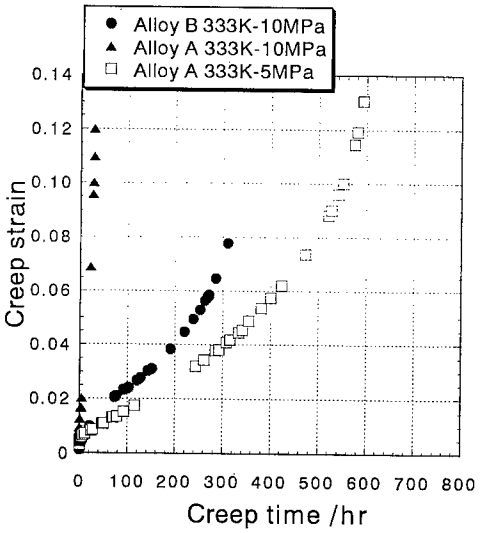

Fig.2 Typical creep curves of the alloys A and B at 333K and 5 to 10MPa.

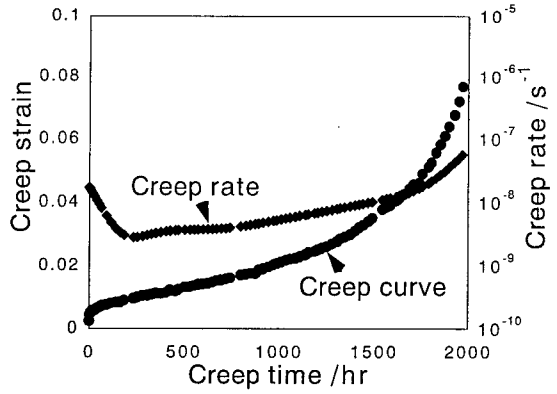

Fig.3 A creep rate curve and a regular creep curve of the alloy B at 10MPa and 313K.

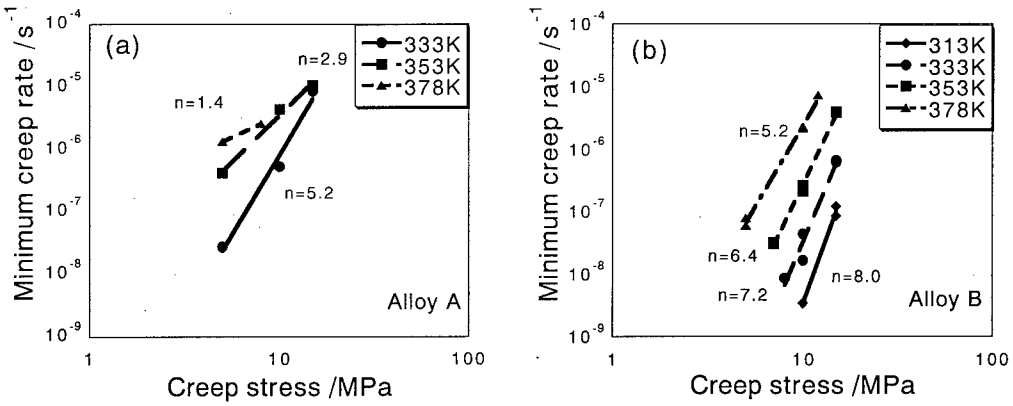

Fig.4 Stress dependence of the minimum creep rate ($\dot{\varepsilon}_{min}$) of the alloys A and B
(a) alloy A, (b) alloy B

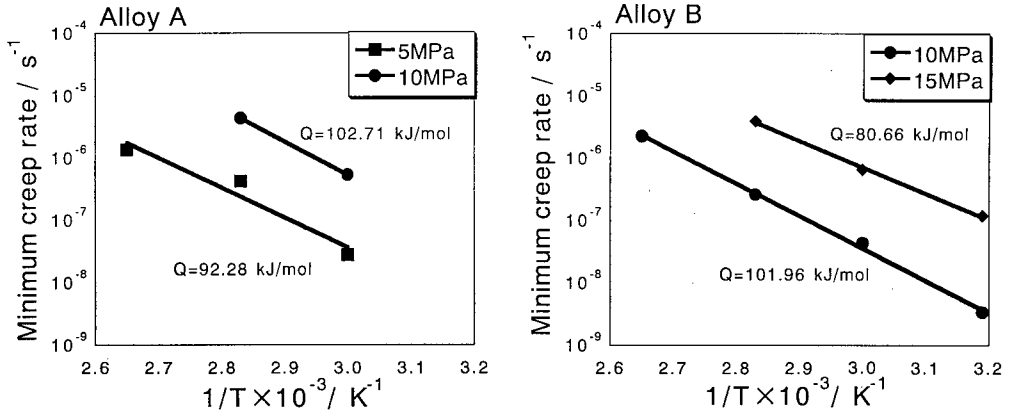

Fig.5 Activation energy for the minimum rate reeep of the alloys A and B
(a) alloy A, (b) alloy B

indicates the relationship between creep-rupture stress and rupture time of the alloys A and B. At the same test condition (stress and temperature), rupture time of the alloy B is larger by one order than that of the alloy A. Accordingly, it can be seen that the addition of Sb, Ag, Cu and Ga is very beneficial for the improvement of the creep and rupture strength of the regular eutectic solder alloy A.

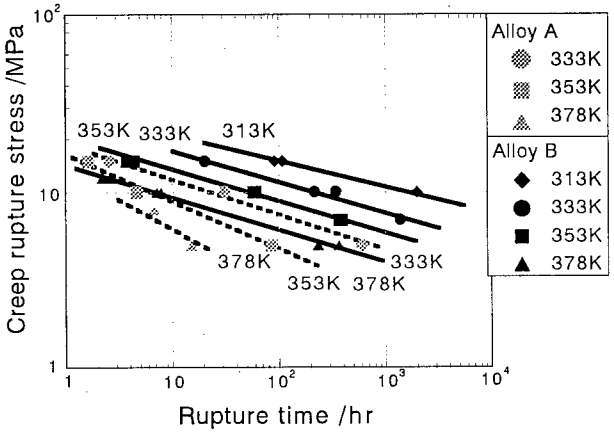

Fig.6 Creep-rupture curves (relationship between creep-rupture stress and rupture time) of the alloys A and B

Figure 7 shows the optical micrographs of the alloys A and B which are aging-treated at 313K for 36ks. No significant difference can be observed between the Photos. (a) and (b). Figure 8-(a) shows the TEM observation of the Pb phase in the alloy B after the aging treatment at 423K for 3.6Ms. There is no precipitates in the Pb phase. On the other hand, Fig. 8-(b) indicates that a fairly large number of tiny particles disperses in the Sn phase matrix. The constituent elements of the tiny particles are not yet analyzed by the method of EDX et al., but these can be considered to be intermetallic compounds formed by the combination of the elements of Sn, Ag and/or Cu. The

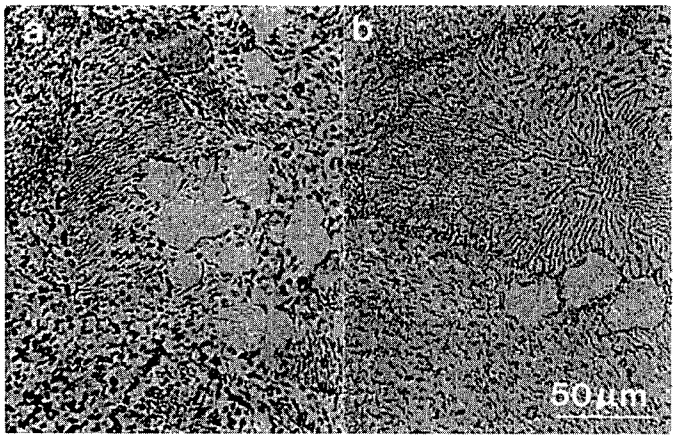

Fig. 7 Optical micrographs of the alloys A and B aging treated at 313K for 36ks. (a) alloy A, (b) alloy B

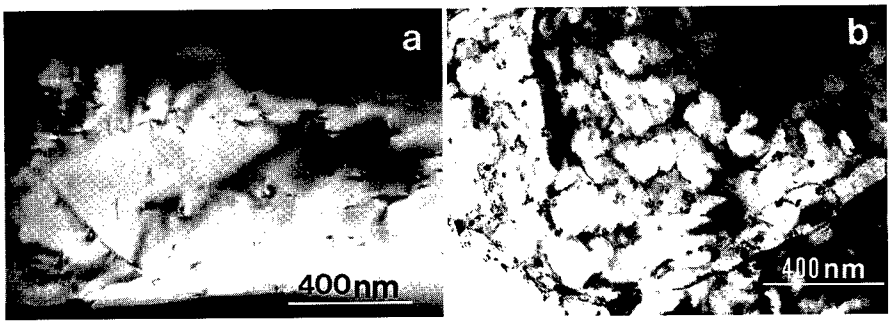

Fig. 8 TEM observation of the alloy B aging-treated at 423K for 3.6Ms.
(a) Pb phase, (b) Sn phase

dispersion of these particles strengthen the Sn phase which is a major part of matrix in the Pb-Sn eutectic alloy. Seeing that the activation energiy, Q for the minimum rate creep of tha alloys A and B is roughly same, but the frequency factor, C of the alloy B in the Eq.(2) is smaller than that of the alloy A, it is considered that the tiny particles dispersion decreases the sweeping area of dislocation after a thermal activation event, such as a climb motion or cross slip of dislocation blocked by some kinds of barriers. Accordingly, these partciles are considered to have a particle dispersion strengthening to contribute to the significant improvement of the creep and rupture strengthes of the alloy B.

Conclusion

The combined addition of 0.5%Sb, 0.5%Ag, 0.1%Cu and 0.003%Ga on the regular Sn-Pb eutectic solder alloy has significantly improved the creep and rupture strengthes. TEM observation indicates that there is no precipitates in the Pb phase but a large number density of tiny particles are formed and dispersed in the Sn phase. These particles are considered to contribute to the significant improvement of the creep and rupture strengthes of the alloy B.

References

1. E.E.de Kluizenaar, Soldering and Surface Mount Technology, No.5, June, 56 (1990).
2. M. Ohtsuka, Material Life, 8, 72 (1906).
3. N.Wade, S.Yamada, T.Akuzawa, Y.Hosaka and K.Miyahara, Proc. of the 5th Symp. on Microjoining and Assembly Technology in Electronics "Mate '99" (Feb., 4-5, 1999, Yokohama, Japan), p.63.
4. Metal data book, (edited by Japanese Inst. of Metals, 1984, Maruzen Pub. Co. Ltd.), p.27.

Key Engineering Materials Vols. 171-174 (2000) pp. 669-676
© 2000 Trans Tech Publications, Switzerland

Microstructures and Fracture Behaviours of Ir-Nb Two-Phase Refractory Superalloys Containing Various Amounts of Nb, Ni, Mo, C and B

Y.F. Gu, Y. Yamabe-Mitarai, Y. Ro and H. Harada

National Research Institute for Metals, 1-2-1 Sengen, Tsukuba, Ibaraki 305-0047, Japan

Keywords: Ir-Nb *f*cc-$L1_2$ Two-Phase Alloys, Third Elements (Ni, Mo, C, B), Microstructure, Fracture Behaviour

Astract The effects of various Nb, Ni, Mo, B, and C content on the microstructures and deformation behaviours of Ir-Nb *f*cc-$L1_2$ two-phase refractory superalloys were investigated at both room and high temperatures. The results showed that the intergranular fracture occurring in Ir single-phase alloys could be governed by controlling the microstructures around GBs and alloying Ni, B and C in Ir-15at%Nb two-phase alloys. The results also showed that Ir-15at%Nb two-phase refractory superalloys alloyed with about 10at% Ni were superior to the binary Ir-15at%Nb two-phase alloy as an ultra-high temperature structural material in terms of strength, fracture behavior, and density.

1 Introduction

Ni-based superalloys are among the most well known and successful materials in the history of aeronautics and gas turbine industries[1]. However, new high temperature structural materials with operating temperatures exceed those of conventional Ni-based superalloys are required in various fields[2,3]. Recently, we develope a new class of two-phase superalloys, namely, refractory superalloy, based on platinum group metals (PGMs)[4-7]. These refractory superalloys have a coherent *f*cc-$L1_2$ structure, similar to γ/γ' microstructure in nickel-base superalloys, and have good potentiality as structural materials used at ultra-high temperatures up to 2000 °C. Preliminary results showed that, of these refractory superalloys, Ir-based *f*cc-$L1_2$ two-phase alloys, such as Ir-15at%Nb, Ir-15at%Hf and Ir-15at%Zr alloys, are superior in high temperature strength and oxidation resistance[7].

Despite the importance of the relationship between the microstructures and the deformation behaviours of these refractory superalloys for practical applications, the fracture behaviour has also needed to be understood. The aims of the present study are: (i) to examine the effects of various niobium (Nb) contents on the microstructures and fracture behaviours of Ir-Nb two-phase refractory superalloys, (ii) to identify the effects of third element (Ni, Mo, C, and B) addition on the microstructures and fracture behaviours of Ir-15at%Nb alloy, and (iii) to determine the relationship between the microstructure and fracture behaviour of the alloy. Our results show that the intergranular fracture occurred in Ir single-phase alloys could be governed by controlling the microstructures around grain-boundary (GB) and alloying some third elements.

2 Experimental Procedures

Samples were arc melted into disk-shaped ingots using as high-purity components as reasonably available (>99.9at%). Table 1 lists the alloy compositions, heat treatment conditions, phase constituent and the volume fractions of the phase with $L1_2$ structure, which calculated from the binary phase diagram[8]. All samples were electro-machined and polished to Ø3 × 6 mm. Compression tests were done in air in the range from 293K to 1473K at an initial strain rate of 3.0×10^{-4} s^{-1} and strains were determined from the load-displacement curves recorded from a strip chart.

We examined the microstructures of the annealed specimens by using a scanning electron microscope (SEM) and a transmission electron microscope (TEM). The polished specimens were

electrolytically etched in a 5% HCl ethyl alcohol solution. Using an energy-disperse X-ray spectroscope (EDS) and a back-scattered electron (BSE) imaging unit attached to the SEM, we determined the phases and microstructures around the GB. For fracture surface investigation, fractures surfaces developed during compression test were examined used the SEM.

Table 1. Experimental Alloys

Alloy Number	Nominal Composition (at. pct)	Volume Fraction % ($L1_2$)	Heat Treatment (°C-h)	Structure
1	$Ir_{75}Nb_{15}$	31	1800-72	primary Ir + eutectic (Ir_3Nb + Ir)
2	$Ir_{83}Nb_{17}$	49	1800-72	eutectic(Ir_3Nb + Ir)
3	$Ir_{80}Nb_{20}$	68	1800-72	primary Ir_3Nb + eutectic (Ir_3Nb + Ir)
4	$Ir_{75}Nb_{15}Ni_{10}$	33	1300-168	fcc + $L1_2$
5	$Ir_{65}Nb_{15}Ni_{20}$		1300-168	fcc + $L1_2$
6	$Ir_{55}Nb_{15}Ni_{30}$		1300-168	fcc + $L1_2$ + $(Ir,Ni)_{11}Nb_9$
7	$Ir_{80}Nb_{15}Mo_5$		1300-168	fcc + $L1_2$
8	$Ir_{75}Nb_{15}$+ 500 ppm wt%B		1300-100	fcc + $L1_2$
9	$Ir_{75}Nb_{15}$+ 500 ppm wt%C		1300-100	fcc + $L1_2$

3 Results

3.1 Microstructure

The microstructures of tested alloys are shown in Fig. 1. The following can be seen.

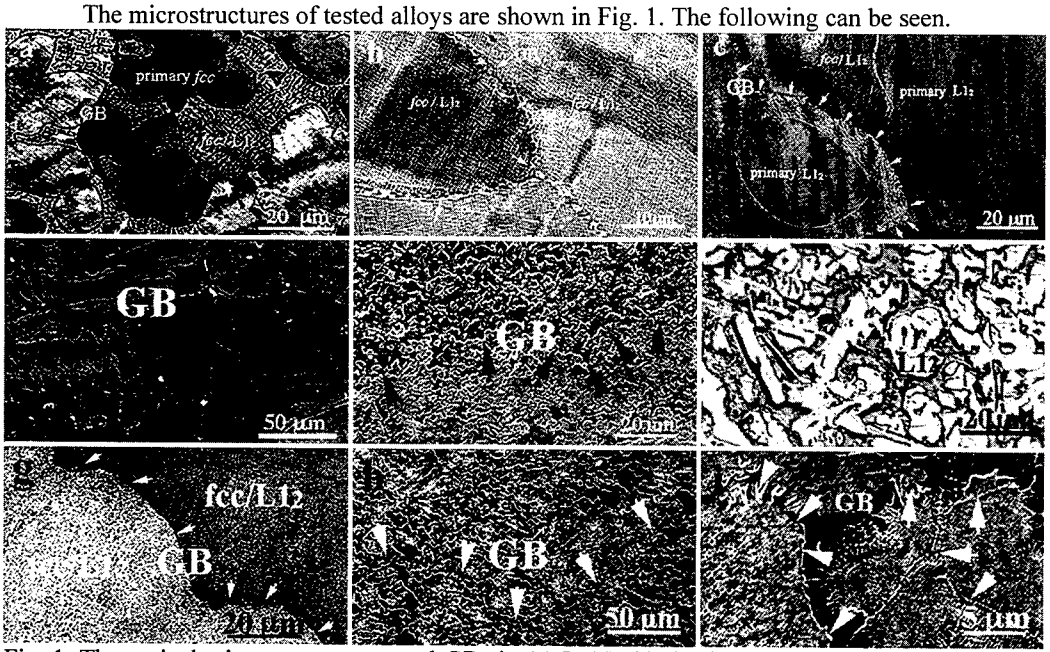

Fig. 1. The typical microstructure around GBs in (a) Ir-15at%Nb, (b) Ir-17at%Nb, (c) Ir-20at%Nb, (d) Ir-15at%Nb-10at%Ni, (e) Ir-15at%Nb-20at%Ni, (f) Ir-15at%Nb-30at%Ni, (g) Ir-15at%Nb-5at%Mo, (h) Ir-15at%Nb-500 ppm wt%B, and (i) Ir-15at%Nb-500 ppm wt%C

Ir-Nb. BSE imagines and EDS analysis show that the microstructures for the Ir-Nb two-phase refractory superalloys could be categorized into three types (I, II, and III). The microstructures of

the alloys containing less than 17at%Nb showed a dendritic structure, and thus was type I. Type I structure was characterized by the dendritic cones that were formed by $f$cc phase (according to the Ir-Nb binary phase diagram) and by the $f$cc / $L1_2$ two-phase mixture structure between the dendritic cones. We noted that most part of the GBs for the type I alloys was made up by the connection of single $f$cc phase or the single $f$cc phase with $f$cc/$L1_2$ two-phase (Fig.1a). The microstructure of the alloy containing 17at% Nb showed a eutectic structure, and thus was type II. Type II was characterized by the $f$cc / $L1_2$ two-phase mixture structure within grains and along GBs. The GBs in the alloy were formed by the connection of the $f$cc / $L1_2$ two-phase mixture structure (Fig.1b). The microstructures of the alloy containing more than 17at% Nb showed another dendritic structure, and thus was type III. Type III structure was characterized by dendrite cones formed by $L1_2$ phase (according to the phase diagram) and the $f$cc / $L1_2$ two-phase mixture structure between the dendrite cones. The most part of the GBs in these type III alloys was also formed by the connection of the $f$cc / $L1_2$ two-phase structure (Fig.1c).

Ir-Nb-Ni. The average phase sizes of the Ni containing Ir-15at%Nb alloys became coarser with the Ni content increasing (Figs.1d-1f). The GBs in the alloy containing 10at%Ni were formed by the connection of the $f$cc / $L1_2$ two-phase structure (Fig.1d), such as the GB's structure in Ir-Nb two-phase alloys with type II or III structures. The connections of different sizes and morphologies of the fcc (dark part in Fig.1e) and $L1_2$ phase (irregular white part in Fig.1e) formed the GBs of Ir-15at%Nb-20at%Ni. The results of the EDS showed that there was a third phase existing when the Ni content was 30at%(Fig.1f).

Ir-15at%Nb-5at%Mo. The microstructure of the Ir-15at%-5at%Mo alloy was characterized by the $f$cc / $L1_2$ two-phase mixture structure within grains. But along the GBs in the alloy, there were thin layers of fcc phase (Fig.1g). Therefore, the GB structure of this alloy was same as the type I alloy.

Ir-15at%Nb-500 ppm wt% B or C. Doping 500 ppm wt% B or C to Ir-15at%Nb changed the microstructure greatly (Fig.1a, 1h and 1i). Most part of the GBs in these two doped alloys were formed by the connection of the $f$cc / $L1'_2$ two-phase structure, and thus were same as type II or III alloys.

3.2 Mechanical properties

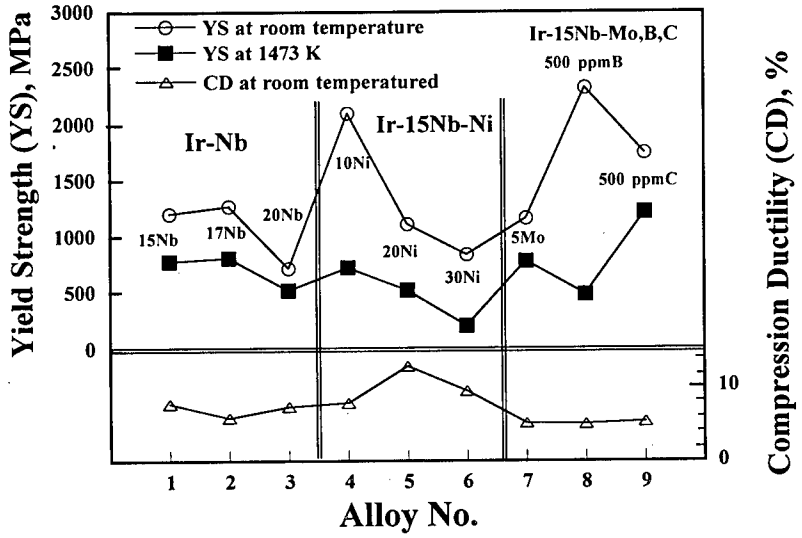

Fig.2. Compression properties of the tested alloys

The results of the room- and high-temperatures compression tests are shown in Fig.2. The significant trends are as follows:

- For the Ir-Nb two-phase alloys, the yield strengths increases with increasing Nb content up to 17at%, where the volume fraction of the $L1_2$ phase was about 50%, both at room temperature and 1473 K. When the Nb content exceeded 17at%, the yield strengths decreased with increasing the Nb content. However, the Ir-17at%Nb alloy had the lowest compression ductility, 6.2%.
- In the case of Ir-15at%Nb-Xat%Ni (X=10, 20, and 30) alloys, the yield strength of the Ir-15at%Nb-10at%Ni alloy was 2150 MPa at room temperature, which was much greater than that of the binary Ir-15at%Nb alloy, and the yield strength was 728 MPa at 1473 K, similar to that of the binary alloy. The yield strengths of the other Ni containing Ir-15at%Nb alloys were lower than that of the binary Ir-15at%Nb, both at room and high temperatures. The results also showed the Ni addition was beneficial to the compression ductility of the Ni containing alloys at room temperature even when the Ni content researched 30at%. The maximum value was obtained in the Ir-15at%Nb-20at%Ni alloy, and was 13%.
- For the Ir-15at%Nb-5at%Mo alloy, the addition of 5at%Mo had little effect on the strength and ductility of the Ir-15at%Nb alloy. 500 ppm wt%B addition to Ir-15a%Nb improves the room temperature strength of the doped alloy from 1258 MPa to 2324 MPa. But it lowered the strength from 1032 MPa to 486 MPa at 1473K. 500 ppm wt%C doping raised the yield strength of Ir-15at% alloy at both room temperature and 1473 K. The ductilitity of the binary Ir-15at%Nb alloys doped with B or C was almost same with the binary alloy at room temperature.

3.3 Fractography

The fracture surfaces of the tested alloys after compression tests at room temperature are shown in Fig.3. These show the following behaviours:

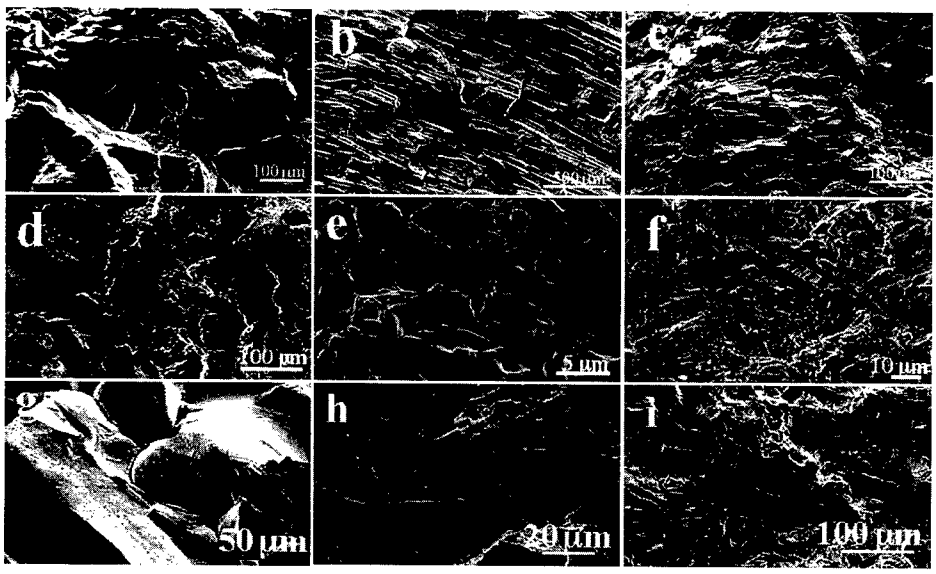

Fig. 3. The fracture surfaces of the tested alloys after compression at room temperature
(a) Ir-15at%Nb, (b) Ir-17at%Nb, (c) Ir-20at%Nb, (d) Ir-15at%Nb-10at%Ni, (e) Ir-15at%Nb-20at%Ni, (f) Ir-15at%Nb-30at%Ni, (g) Ir-15at%Nb-5at%Mo, (h) Ir-15at%Nb-500 ppm wt%B, and (i) Ir-15at%Nb-500 ppm wt%C

- In the Ir-Nb two-phase alloys, intergranular fracture occurred for the alloys with the type I structure (Fig.3a) and transgranular fracture occurred for the alloys with the type II and III structures (Fig.3b and 3c). Cleavage fracture was the predominant fracture mode on the surfaces of the transgranular areas, which were indicated by the river patterns and many cleavage steps microstructure.
- The fracture surfaces of the Ir-15at%Nb-10at%Ni alloy exhibited transgranular fracture in compression (Fig.3d), whereas the other Ni containing Ir-15at%Nb alloys exhibited a mixture of the intergranular and transgranular fracture (Fig.3e and 3f). A close observation showed that the cleavage fracture was still a predominant fracture on the surfaces of the transgranular areas. The result of Auger spectroscopy analysis showed that no significant segregation of Ni at the GBs in Ni-alloyed Ir-15at%Nb alloys.
- The intergranular fracture occurred for the Ir-15at%-5at%Mo alloy, which GB had the type I structure. 500 ppm wt%B or C doping changed fracture mode from the intergranular fracture in Ir-15at%Nb to the transgranular fracture in the doped Ir-15at%Nb alloys. However, the cleavage fracture was still a predominant fracture on the surfaces of the transgranular areas. The result of EDS analysis showed that there was more B or C concentration at the GBs for the doped alloys than the bulk concentration.

The interactions for the deformation bands with GBs and cracks propagate in some of the tested alloys are shown in Fig. 4. The left-side photos in Fig.4 show the microstructures during the deformation while the right-side photos show the microstructures after deformation.

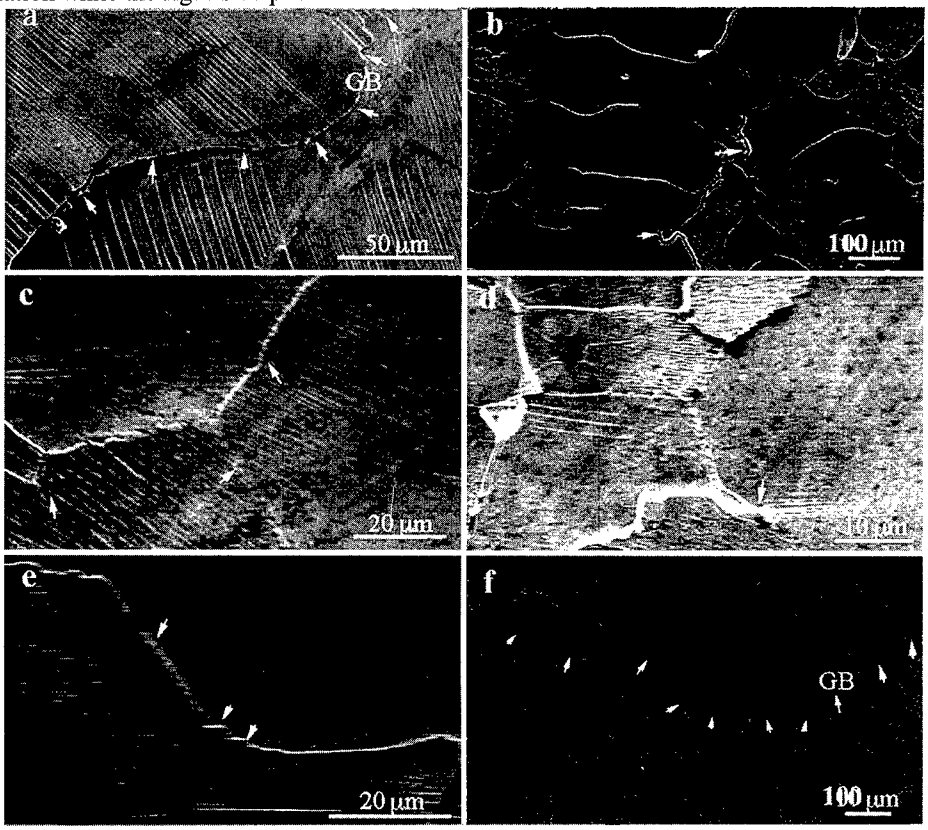

Fig. 4. The deformation microstructure of Ir-Nb two-phase alloys
(a), (b) Ir-15at%Nb, arrows in (a) and (b) indicate the GB
(c), (d) Ir-17at%Nb, arrows in (c) indicate slip bands across the GBs, arrow in (d) indicate crack across the GBs
(e), (f) Ir-20at%Nb, arrows in (e) indicate slip bands across the GBs, arrow in (f) the GBs

For the Ir-15at% Nb alloy, the slip bands (white lines in Fig.4a) had difficulty in crossing the GB during the deformation and therefore terminated at the GB (Fig.4a). Because the matrix slip bands terminated at the GB, large stress concentrated at the GB and caused cracks to initiate and to propagate along the GB (Fig.4b). For the Ir-17at%Nb (Fig.4c) and Ir-20at%Nb (Fig.4e), the slip bands crossed the GBs during the deformation. This crossing prevented a build-up of stress at the GBs, thus allowed the cracks to transfer from one grain to another (Fig.4d for Ir-17at%Nb and Fig.4f for Ir-20at% Nb).

4 Discussion

The strength of two-phase alloy systems is essentially due to the interaction between dislocations and particles of the second phase. In the last three decades, remarkable advances have been made in understanding the dislocation-particle interaction mechanism[2]. The volume fraction and the size of $L1_2$ precipitates and $f$cc / $L1_2$ lattice misfit are the main factors affecting the strength of Ni-based two-phase superalloys[9]. The strength of Ni-based superalloys peaks at a particular volume fraction of the precipitates, normally between 60% and 70%[10]. Because the structure of the alloys that we study here is similar to that of Ni-based superalloys, these parameters may be still the main factors in our alloys. In our study, for Ir-Nb binary two-phase alloys, the fcc/$L1_2$ lattice misfits do not change because the compositions of fcc and $L1_2$ phases were same for all of the tested Ir-Nb binary alloys. Therefore, the volume fraction and the size of $L1_2$ precipitates would be the governing factors for the strengths of these alloys. According to our results, the maximum strength occurred when the alloy contained about 50% volume fraction of the $L1_2$ precipitate. The effect of $L1_2$ precipitate size on the strength was a yet more complicated problem and remains to be resolved. For the Ni alloyed Ir-15at%Nb two phase alloys, our results show that the addition of Ni was effective in raising the room temperature strength of the alloy when Ni content was about 10 at%. Possible factors contributing to this strength improvement were (a) solid solution hardening, (b) precipitate hardening, and (c) grain boundary effect. More work needs to be done to understand the detail mechanisms of the Ni alloyed alloys. The effects of doping B or C on the strength of Ir-15at%Nb alloys are not fully understood now, more data and investigation are needed to clear their mechanisms.

The fracture modes observed in some Ir-Nb and Ir-15at%Nb alloyed with 10at%Ni, or 5at%Mo, or 500 ppm wt% B ro C alloys are quite different from the morphologies of GBs fracture generally observed in polycrystalline Ir and Ir alloys[11]. Because it was reported that intergranular brittleness in polycrystalline Ir and Ir alloys are intrinsic and are not due to impurities at the GBs[12], the GBs in these alloys may always be weak points. Liu *et al.*[13] found that GB fracture of the Ir-0.3 pct W could be suppressed by doping 200 ppm Th and they contributed this suppression to the GB segregation of Th. Wolff and Sauthoff[14] showed that a small amount of B could improve the ductility and strength in the $Ir_{84}Nb_{14}$ alloy. They also associated this improving with the segregation of B to the GBs. Therefore, the fracture mode changes for Ir-15at%Nb doped with B or C in this research may be contributed to the segregation of B or C to the GBs. However, for the Ni alloyed $Ir_{85}Nb_{15}$ alloys, we could not find the segregation of Ni to the GBs. This implies that the mechanism for Ni suppression the GB fracture in the Ni alloyed $Ir_{85}Nb_{15}$ alloys is different to that of B, C and Th. According to this research, the microstructure of the GBs in the two-phase refractory superalloys may govern the intergranular fracture, such as in other two-phase alloys[15,16]. When the microstructures around GBs have similar fcc/$L1_2$ mixture structure (type II and III), the GB cohension would be improved, and thus incompatibilities in stress and strain at the GB would be avoided. Therefore, the fracture modes of the alloys can be changed. More research should be conducted to understand this mechanism.

5 Conclusions

1. For the Ir-Nb two-phase alloys, the yield strengths of the alloys reached the maximum value when Nb content was 17at%, where the volume fraction of the $L1_2$ precipitate was about 50 at%.

The fracture modes of the alloys ranged from predominant intergranular in the alloys whose Nb content was less than 17 at%, to transgranular in the alloys whose Nb content was at least 17 at%.

2. For the Ni alloyed Ir-15at%Nb alloys, the Ni addition was beneficial to the compression ductility even when the Ni content researched 30 at%. The yield strength of Ir-15at%Nb-10at%Ni was much greater than that of the binary alloy at room temperature and remained at a level similar to that of the binary alloy at 1473K. Ni addition changed the fracture mode from predominant intergranular in Ir-15at%Nb to transgranular in Ir-15at%Nb-10at%Ni and a mixture of intergranular and transgranular fracture in the other Ni alloyed Ir-15at%Nb alloys.

3. The addition of 5at%Mo had little effects on the strength, ductility and fracture behaviour of the Ir-15at%Nb alloy.

4. The strengths of Ir-15at%Nb doped with 500 ppm wt%B or C were greater than that of the undoped alloy at both room temperature and 1473K. The fracture mode changed from intergranular fracture in undoped alloy to transgranular fracture in doped alloy. The compression ductilities were almost same for the undoped and doped alloys.

5. Ir-15at%Nb two-phase refractory superalloys alloyed with about 10at% Ni were superior to the binary Ir-15at%Nb two-phase alloy as an ultra-high temperature structural material in terms of strength, fracture behavior, and density

Acknowledgements

We thank Mr. S. Nishikawa and Mr. T. Maruko of Furuya Metal Co. Ltd. for preparing the alloys ingots. This research was done under the Japanese Science and Technology Agency (STA) Fellowship program. Y. F. Gu expresses his gratitude for the award of an STA post-doctoral fellowship, tenable at the National Research Institute for Metals, Tsukuba, Japan.

References

1. R. R. Jensen, and J. K. Tien: Metall. Trans. A, vol. 16A(1985), p1049.
2. M. Feller-kniepmeier, and T. Link: Mater. Sci. Engng. A, vol. 113(1989), p191
3. J. M. Shoji: Air Force Rocket Propulsion Laboratory Report, TR-84-057, 1985.
4. Y. Yamabe, Y. Koizumi, H. Murakami, Y. Ro, T. Maruko, and H. Harada: Scripta Mat., vol. 35(1996), p211.
5. Y. Yamabe-Mitarai, Y. Koizumi, H. Murakami, Y. Ro, T. Maruko, and H. Harada: Scripta Mat., vol. 36(1997), p 393.
6. Y. Yamabe-Mitarai, Y. Ro, T. Maruko, T. Yokokawa, and H. Harada: Structural Intermetallics, 1997, p805.
7. Y. Yamabe-Mitarai, Y. Ro, T. Maruko, and H. Harada: Met. Trans., vol. 29(1998), p 537.
8. Thaddeus B. Massalski: Binary Alloy Phase Diagrams, 2nd ed., ASM Metals Park, OH, 1992, vol. 3.
9. A. Royer, P. Bastie, and D. Bellet: Phil. Mag. A, vol. 72(3)(1995), p669.
10. A. Muller, Th. Gnaupel-Herold, and W. Reimers: Phys. Status Solidi (a), vol.159(1997), p375.
11. A. S. Darling: Intern. Met. Rev.,vol.18(1973), p91.
12. S. P. Chen: Phil. Mag. A, vol. 66(1992), p1.
13. C. T. Liu, H. Inouye, and A. C. Schaffhauser: Metall. Trans. A, vol. 12A(1981), p993.
14. M. Wolff, and G. Sauthoff: Metall. Trans. A, Vol. 27A(1996), p2642.
15. W. J. Mills, Metall. Trans. A, 1980, Vol. 11A(1980), p1089.
16. E. Hornbogen and H. Kreye, J. of Materials science, 17(1982) p979.

Key Engineering Materials Vols. 171-174 (2000) pp. 677-684
© 2000 Trans Tech Publications, Switzerland

Investigation on Microstructure and Fracture of Quaternary Ir-Based Alloys

X.H. Yu, Y. Yamabe-Mitarai, Y. Ro and H. Harada

High Temperature Materials Research Group, National Research Institute for Metals,
1-2-1 Sengen, Tsukuba, Ibaraki 305-0047, Japan

Keywords: Microstructure, Fracture, Quaternary, Ir-Nb-Ni-Al, Ir-Ta-Ni-Al, Ductility

ABSTRACT The microstructure and the fracture of the new developed Ir-Nb-Ni-Al and Ir-Ta-Ni-Al were investigated. At 1300°C, three-phase equilibrium-fcc, $L1_2$-Ni_3Al and Ir_3Nb were observed in alloys Ir-5Nb-62.4Ni-12.6Al, Ir-15Nb-20.8Ni-4.2Al and three-phase equilibrium-fcc, $L1_2$-Ni_3Al and Ir_3Ta existed in alloys Ir-3.75Ta-62.4Ni-12.6Al and Ir-11.25Ta-20.8Ni-4.2Al; four-equilibrium–fcc, B2-IrAl, $L1_2$-Ni_3Al and Ir_3Nb or Ir_3Ta were observed in alloy Ir-10Nb-41.6Ni-8.4Al or Ir-7.5Ta-41.6Ni-8.4Al. At 1400°C, the three-phase equilibrium existed in all of the alloys. The compressive strengths at 1200°C were from 79 to 616 MPa. The compressive strain of the quaternary was greatly improved compared with Ir-based alloys (below 10%). The lowest one was 18. The precipitation hardening of quaternary alloys can be caused by the precipitate-shearing mechanism. The compressive strength of quaternary alloys can be attributed to the precipitation and solid solution hardening as well as to the interface strengthening.

INTRODUCTION

More and more refractory elements, Re, Mo, W, Ta etc is added into Ni-based superalloys to increase the temperature capability. However, the melting temperature of Ni (1455°C) limits the temperature capability. The platinum group metals may be the promising candidates as a matrix for ultra-high temperature use, especially Ir (melting temperature is 2240°C) is a stronger candidate. Yamabe-Mitarai et al. [1,2] found the Ir-based refractory superalloys are of fcc/$L1_2$ coherent structure similar to Ni-based superalloys and have higher strength at high temperature. But the intergranular fracture in polycrystalline existed in the Ir-based superalloys and the ductility of the Ir-based superalloys was lower [3,4], which limit the application of the Ir-based superalloys. The another problem is the cost of Ir, which is very expensive due to the supply in the all of the world is about 3000 kg/year.

To enhance the temperature capabilities of Ni-based superalloys and improve the ductility of Ir-based superalloys, a novel approach to improve the disadvantage both of Ir- and Ni-based superalloys were found. It is to combine Ir-based with Ni-based binary alloys in different proportions to prepared quaternary superalloys. A sketch of a portion of the quaternary phase diagram is shown in Fig.1. The details were described in Ref.(5,6).

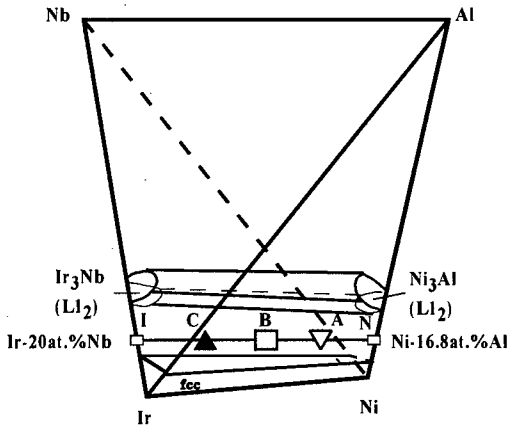

Fig.1 A sketch of a portion of the quaternary Ir-Nb-Ni-Al phase diagram at 1400°C

Two kinds of novel quaternary Ir-Nb-Ni-Al and Ir-Ta-Ni-Al alloys were investigated. The object is to take the advantage of Ir-based alloys (high strength at high temperature) and Ni-based alloys (good ductility and relatively lower density and cost).

The fracture mode both of pure Ir and Ir-based binary superalloys belongs to the intergranular fracture. Although the fracture mode of ternary Ir-15Nb-xNi can be changed from intergranular mode into transgranular by adding Ni to Ir-15at.%Nb [3], the ductility was not improved enough. Ni-based single-crystal superalloys are of the γ/γ' coherent structure, the fracture is of the characteristic of square-like facets oriented on <001> planes [7,8]. However, the fracture mode and ductility of quaternary Ir-based superalloys have never been investigated.

In this paper, the microstructure and the fracture mode of quaternary Ir-Nb-Ni-Al and Ir-Ta-Ni-Al refractory superalloys is investigated and the strengthening mechanism is discussed.

EXPERIMENT PROCEDURE

Quaternary Ir-based refractory superalloys were prepared by two kinds of binary alloys, which consist of fcc and $L1_2$ two phase, in different proportions. They are Ir-20at.%Nb or Ir-15at.%Ta and Ni-16.8at.%Al. The proportions of Ir-based and Ni-based binary alloys were: Ir-based : Ni-based = 25:75, 50:50 and 75:25. In abbreviation, e.g. in the case of quaternary alloys with the proportion of Ir-based : Ni-based = 25 : 75, it is called "with 75% Ir-based alloy" for short. The nominal composition is listed in Table 1. The ingots of quaternary alloys were prepared by arc melting in an argon atmosphere. Cylindrical sample with 3mm diameter and 6mm long were cut from the each ingot for compression test. These samples were heated at 1300 and 1400°C for 168h in vacuum furnace. The compression tests were carried out at 1200°C. Samples were kept at 1200 °C for 10 minutes before loading. The initial compressive strain rate was 4×10^{-3}/s.

The microstructure and the fractured surface of samples were observed by scanning electron microscopy (SEM) and transmission electron microscopy (TEM). The phase analysis was investigated by X-ray diffractometry (XRD) and the compositions were measured by energy dispersive X-ray spectroscopy (EDX) attached to SEM. These samples were etched with 5% HCl ethanol solution at AC 10V for 10 min before observed by SEM. The specimens with 3mm in diameter were ion milled for TEM observation.

Table 1 The nominal composition of Ir-based refractory superalloys (at.%)

Quaternary	Sample	Proportion of Ir-based: Ni-based	Nominal composition (at.%)
Ir-Nb-Ni-Al	Alloy A	25:75	Ir-5Nb-62.4Ni-12.6Al
	Alloy B	50:50	Ir-10Nb-41.6Ni-8.4Al
	Alloy C	75:25	Ir-15Nb-20.8Ni-4.2Al
Ir-Ta-Ni-Al	Alloy A	25:75	Ir-3.75Ta-62.4Ni-12.6Al
	Alloy B	50:50	Ir-7.50Ta-41.6Ni-8.4Al
	Alloy C	75:25	Ir-11.25Ta-20.8Ni-4.2Al

RESULTS

1. MICROSTRUCTURES AND PHASE ANALYSIS

All of the as cast microstructures of these two kinds of quaternary alloys, Ir-Nb-Ni-Al and Ir-Ta-Ni-Al, were of dendrite structure. In alloy A, the dendrite structure was fcc matrix, but the dendrites were $L1_2$-Ir_3Nb or Ir_3Ta in alloy B and C.

Figs.2a~c shows the microstructures of quaternary Ir-Nb-Ni-Al after heat-treated at 1300 °C for 168hrs. The results of X -ray and composition analysis indicated that fcc and two kinds of $L1_2$-Ir_3Nb and Ni_3Al existed in the three alloys. B2 phase was observed in alloy B in addition to the three phases. More, a lot of lamella structure were formed by fcc with Ni_3Al or Ir_3Nb in alloy A (Fig.1a). The lamella space was about 1.6~2.5μm. Compared with the as cast microstructure, a lot of particles precipitated and the fcc/$L1_2$ coherent structure formed in the fcc matrix (Fig.3).

The microstructure of quaternary Ir-Ta-Ni-Al (see Figs.2d,e,f) was similar to that of quaternary Ir-Nb-Ni-Al except of the alloy A. There was no lamella structure in the alloy A (Fig.2d). The X-ray phase analysis of Ir-Ta-Ni-Al heated at 1300°C for 168hrs is shown in Fig.4. The results of X-ray indicated that there were fcc and $L1_2$-Ir_3Ta and Ni_3Al in the alloy A and C; B2-IrAl phase also existed in alloy B in addition to the fcc and Ir_3Ta and Ni_3Al. This means there were the similar constituents in both of quaternary Ir-based refractory superalloys, i.e. three-phase equilibrium (fcc, Ir_3Nb and Ni_3Al or fcc, Ir_3Ta and Ni_3Al) in alloy A and C; four-phase equilibrium (fcc, B2, Ir_3Nb and Ni_3Al or fcc, B2, Ir_3Ta and Ni_3Al) in alloy B at 1300°C.

After heated at 1400°C for 168hrs, the biggest change, compared with that formed at 1300°C for 168hrs, is the disappearance of B2 phase from alloy B in both of quaternary superalloys. The amount of fine $L1_2$ particles in the matrix in all alloys at 1400°C exceeded that heat treated at 1300°C. In alloy A and C, the phase structure did not change between 1300°C and 1400°C.

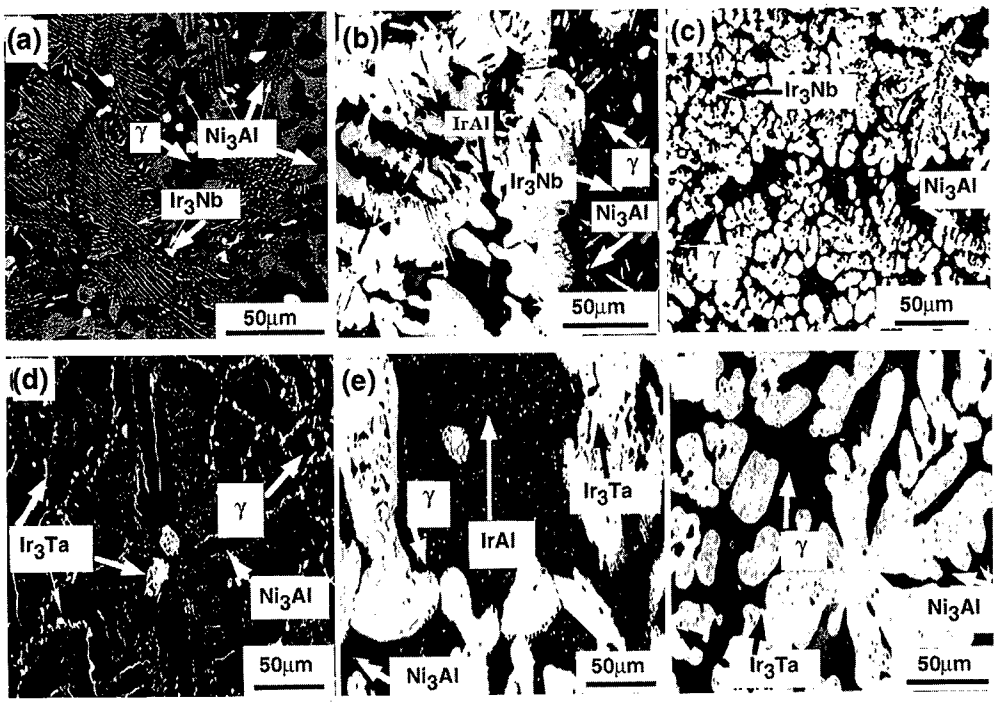

Fig.2 The microstructure of (a) Ir-5Nb-62.4Ni-12.6Al (alloy A), (b) (Ir-10Nb-41.6Ni-8.4Al (alloy B), (c) Ir-15Nb-20.8Ni-4.2Al (alloy C), (d) Ir-3.75Ta-62.4Ni-12.6Al (alloy A), (e) Ir-7.5Ta-41.6Ni-8.4Al (alloy B) and (f) Ir-11.25Ta-20.8Ni-4.2Al (alloy C) heated at 1300°C for 168hrs

The compressive tests were carried out 1200°C. These samples were heated at 1400°C for 168hrs before the compressive tests. The Figure 5 shows close-up view from the base of cylindrical sample of quaternary Ir-Ta-Ni-Al after being compressed at 1200°C. The Fig.5a shows unloaded sample of alloy A after the compressive strain was about 15%. No macro-crack could be observed on the surface of tested sample. We tried to fracture the specimen, but the specimen of alloy B did not fracture even the strain reached up to 90% (see Fig.5b) and the specimen changed from cylindrical to disc shape. Among all of the compressive tests for both of quaternary Ir-Nb-Ni-Al and Ir-Ta-Ni-Al alloys, only the specimen of alloy C in quaternary Ir-Ta-Ni-Al could be fractured during the compressive test (Fig.5c) when the compressive strain was 18.6%. This means the ductility of quaternary Ir-based superalloys has been improved greatly compared with that of Ir-based binary alloys and ternary alloys (lower than 10%).

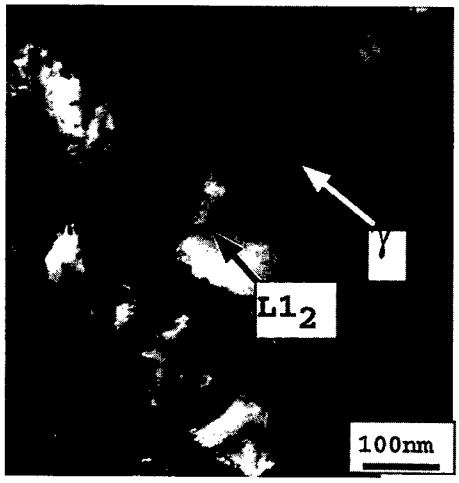

Fig.3The fcc/$L1_2$ coherent structure taken from the fcc matrix

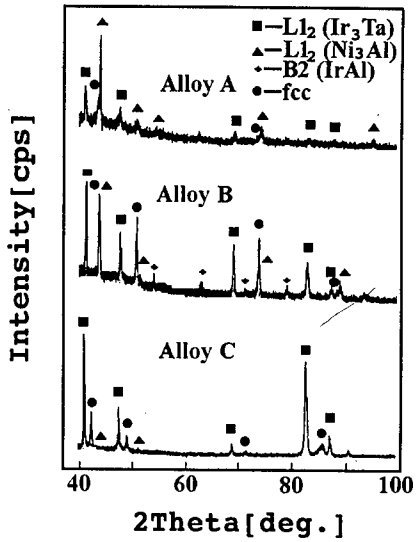

Fig.4 X-ray intensity of quaternary Ir-Ta-Ni-Al superalloys heated at 1300°C for 168hrs

The 0.2% flow stress of quaternary Ir-based superalloys is plotted in Fig.6a. For reference, the 0.2% flow stress of the binary Ir-20at.%Nb and Ir-15at.%Ta alloys [1] as well as commercial Ni-based superalloys, MarM247 [9], at 1200°C were also plotted. The 0.2% flow stress of quaternary alloys at 1200°C were from 79 to 616 MPa, which was higher than that of Ni-based superalloys (MarM247, 50MPa) but lower than that of Ir-based alloy (Ir-15at.%Ta, 750MPa). The effect of heat treatment on the 0.2% flow stress at 1200°C of quaternary Ir-Nb-Ni-Al were also investigated and is shown in Fig.6b. These samples were heated at 1300°C for 168hrs, and one sample of alloy C was heated at 1500°C for 72hrs. For comparison, the 0.2% flow stress at 1200°C of quaternary In-Nb-Ni-Al heated at 1400°C is also plotted in Fig.6b. Compared with the 0.2% flow stress at 1200°C of the samples heat treated at 1300 and 1400°C for 168hrs, the strength of alloy A was considerably increased about 2.5 times but that of the alloy B was decreased. There is no significant effect of heat treatment at 1300 or 1400°C for 168hrs on the compressive strength of alloy C. However, when the alloy C was heat-treated at 1500°C for 72hrs, the 0.2% flow stress, 467MPa, was increased greatly and was very closed to that of Ir-20at.%Nb binary alloy.

As mentioned above, most of these samples could not be fractured during the compress test. These samples were bent to fracture to observe the fracture surface. The fractures of the two kinds of quaternary Ir-Nb-Ni-Al and Ir-Ta-Ni-Al heated at 1300°C for 168hrs were investigated. No significant macro-fracture surface differences existed for the four alloys with 25% Ir-based alloy (alloy A) and 50% Ir-based alloys (alloy B). The scanning electron fractograghs (Fig. 7a,b,d,e) indicate ductile dimple fracture morphology in bonded precipitates of all size, tear ridges, and no cleavage for all the alloy A and B alloys in the two kinds of quaternary alloys. The four alloys also contain amounts of precipitates fracturing via ductile dimples. These micro-fracture morphologies

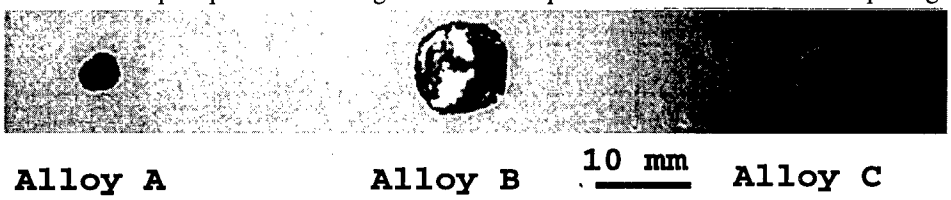

Fig.5 The macro-photos of quaternary Ir-Ta-Ni-Al after compressed at 1200°C. (a) Ir-3.75Ta-62.4Ni-12.6Al (alloy A), (b) Ir-7.5Ta-41.6Ni-8.4Al (alloy B), and (c) Ir-11.25Ta-20.8Ni-4.2Al (alloy C)

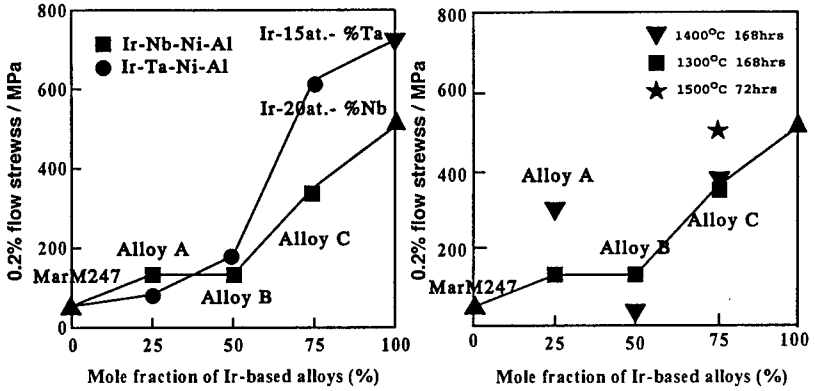

Fig.6 (a) The 0.2% flow stress of quaternary Ir-based superalloys at 1200°C, (b) The effect of heat treatment on 0.2% flow stress at 1200°C of quaternary Ir-Nb-Ni-Al

can be classified as ductile. The Fig.7c,f shows the scanning electron fractographs of alloy C of the two kinds of quaternary alloys. Here, the predominantly ductile dimpling with a lot of precipitates fracturing can be observed. Compared with the precipitates fracturing in alloy A and B, the size of the precipitates fracturing in alloy C was larger. Therefore, The above micro-fracture morphology can be classified here as globally ductile and locally brittle. The fracture mode is different from that of Ni-based superalloys and Ir-based superalloys.

The morphology of precipitates and the dislocations were observed by TEM after the quaternary Ir-Nb-Ni-Al superalloys were deformed about 15% at 1200°C (the compression strain were calculated by the change in specimen height before and after the compression test), the $L1_2$ precipitates were still dendrite or cubic. Only a few dislocations were observed in fcc matrix. An interfacial dislocation was observed at the interface between the matrix and the dendrite structure(Fig.8a). Shearing by bowed dislocation was also observed in the larger dendrite $L1_2$ structure (Fig.8b). In a few places, stacking fault left by the shearing of cubic precipitates on a plane was observed (see Fig.8c).

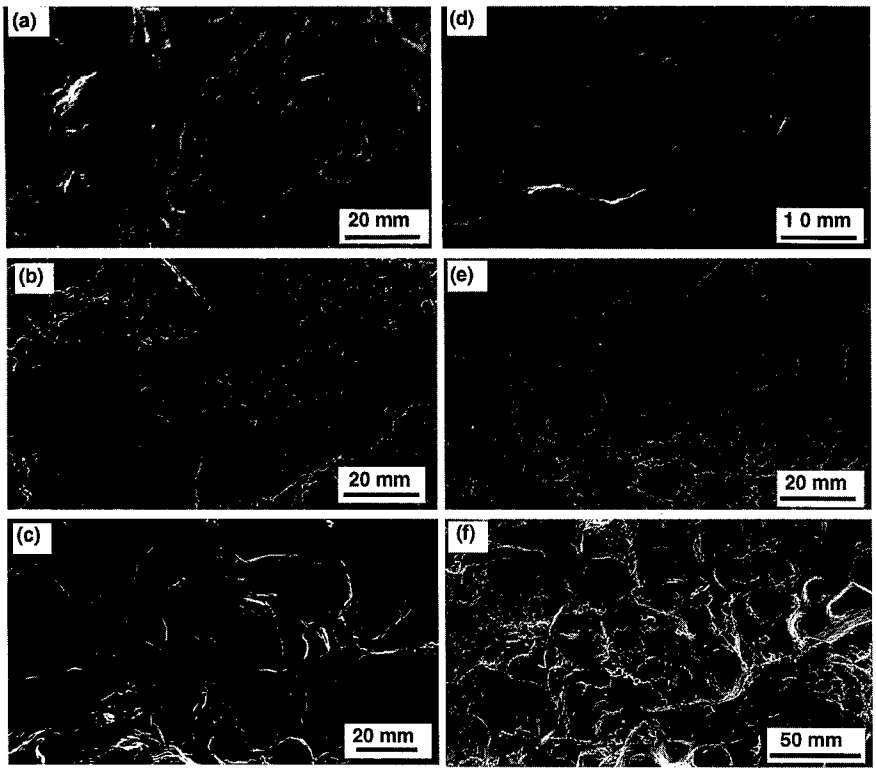

Fig.7 The scanning electron fractographs of two kinds of quaternary Ir-based alloys. (a) Ir-5Nb-62.4Ni-12.6Al (alloy A), (b) (Ir-10Nb-41.6Ni-8.4Al (alloy B), (c) Ir-15Nb-20.8Ni-4.2Al (alloy C), (d) Ir-3.75Ta-62.4Ni-12.6Al (alloy A), (e) Ir-7.5Ta-41.6Ni-8.4Al (alloy B), and (f) Ir-11.25Ta-20.8Ni-4.2Al (alloy C)

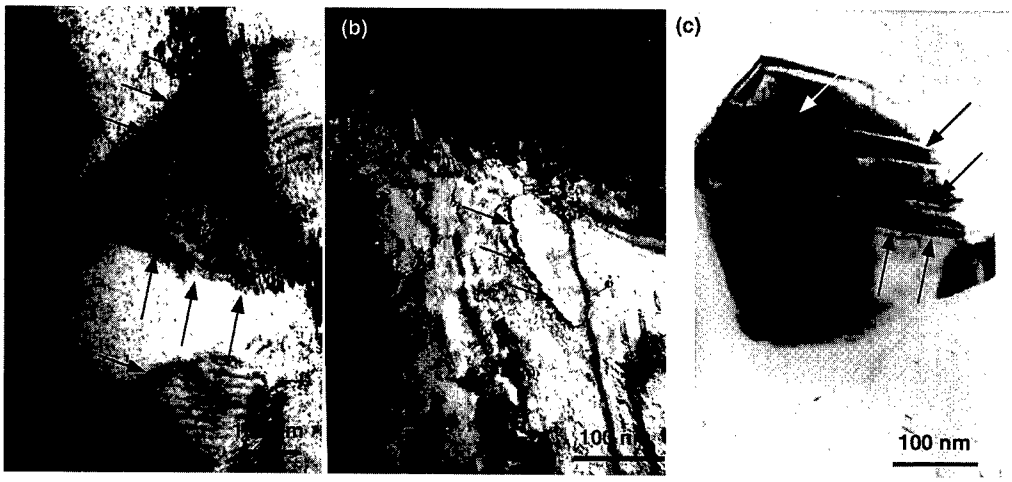

Fig.8 Dislocations of quaternary Ir-Nb-Ni-Al superalloys compressed at 1200°C. (a) interfacial dislocation at the interface between the matrix and the dendrite precipitate, (b) bowed dislocation in larger dendrite structure, (c) stacking fault left by the shearing of precipitates on a plane

Discussion

Here we will discuss the strengthening behavior of the quaternary alloy. The strength of quaternary alloys can be estimated by the law of mixture strength of composite materials, as a linear combination of the strength of the two types of component binary alloys. From Fig. 6a, we see that the strengths of quaternary alloys are located between the strengths of Ni- and Ir-based binary alloys and the strength of quaternary alloys increased with increasing concentration of Ir-based alloys. The compressive strength of quaternary Ir-Nb-Ni-Al refractory superalloys is higher than that of Ni-based superalloys but lower than that of Ir-based superalloys. Compared with quaternary Ir-Ta-Ni-Al alloys, the compressive strength of alloy A, which included 25% Ir-based alloy, was about 60% higher, but that of alloy C, which included 75% Ir-based alloy, was about 43% lower. For Ir-Ta-Ni-Al alloys, there were many larger precipitate particles at the grain boundaries in alloy A and these particles weakened the strength of the grain boundary. For alloy C of quaternary Ir-Ta-Ni-Al alloys, the fcc matrix include more Ir (5). Therefore, it is reasonable that the strength of alloy C in the Ir-Ta-Ni-Al quaternary alloy was higher than that of alloy C in the Ir-Nb-Ni-Al quaternary alloy.

Similar to the characteristics of Ni-based superalloys that contribute to their compressive strength, the compressive strength of quaternary alloys can be attributed to the precipitation and solid solution hardening as well as to the interface strengthening. The solid solution hardening caused by the increasing of Ir content was observed in many kinds of Ir-based alloys [10]. Therefore, the increment of 0.2% flow stress of alloy C in Ir-Ta-Ni-Al compared to that in Ir-Nb-Ni-Al could be contributed to the increment of Ir content in matrix.

There were coherent and incoherent $L1_2$ precipitates in the quaternary alloys. For incoherent precipitates (dendrite structure), the interfacial dislocations were left by shearing of precipitates or just stopped at interfacial when the movement dislocation slipped in the matrix and met larger dendrite structure (Fig.8a). The bowing dislocation showed the shearing of dislocation in the dendrite structure (Fig.8b). The similar dislocations were also observed in Ir-based superalloys [11,12]. For coherent precipitates, stacking fault were left after the dislocation passed the precipitates (Fig.8c). Therefore, the precipitation hardening can be caused by the precipitate-shearing mechanism (Fig.8). The existence of bowing dislocation and stacking fault indicated that the dislocation was shearing or had sheared the precipitates. The shearing trace of dislocation can also be observed from the fractographs (Fig.7). The shearing of dislocation resulted in the precipitate fracture.

The effect of heat treatment on the strength is considered as follow. The increment in strength of alloy A heat-treated at 1300°C compared to that heat treated at 1400°C is associated with geometrical hardening term. Since there were a lot of fcc/ $L1_2$ lamella structure at 1300°C but only a few lamella structure existed at 1400°C. The interface of lamella structure as a barrier prevented from the movement of dislocation. In this case, the strength at 1300°C will be higher. The decrease of strength of alloy B heat-treated at 1300°C for 168hrs may be associated with the existence of IrAl. It needs more detailed work in the future. The microstructure was similar to each other at 1300, 1400 and 1500°C, three-phase equilibrium existed in the three temperature. The volume of fine cubic precipitates in fcc matrix did not change significantly at both 1300 and 1400°C for 168hrs, but had a significantly increment after it was heated at 1500°C for 72hrs. Therefore the increment in strength of alloy C heat-treated at 1500°C for 72hrs can be attributed to the precipitation hardening. Fine precipitates can act as a barrier to dislocation movement because of the small inter-particles spacing and the high interfacial energy.

CONCLUSIONS

The microstructure and the fracture of the new developed Ir-Nb-Ni-Al and Ir-Ta-Ni-Al were investigated. At 1300°C, three-phase equilibrium-fcc, $L1_2$-Ni_3Al and Ir_3Nb were observed in alloys Ir-5Nb-62.4Ni-12.6Al, Ir-15Nb-20.8Ni-4.2Al and three-phase equilibrium-fcc, $L1_2$-Ni_3Al and Ir_3Ta existed in alloys Ir-3.75Ta-62.4Ni-12.6Al and Ir-11.25Ta-20.8Ni-4.2Al; four-equilibrium–fcc, B2-IrAl, $L1_2$-Ni_3Al and Ir_3Nb or Ir_3Ta were observed in alloy Ir-10Nb-41.6Ni-8.4Al or Ir-7.5Ta-41.6Ni-8.4Al. At 1400°C, the three-phase equilibrium existed in all of the alloys. The compressive strengths at 1200°C were from 79 to 616 MPa. The compressive strain of the quaternary was greatly improved compared with Ir-based alloys (below 10%). The lowest one was 18%. The pure transgranular fracture mode could be found in four alloys with 25% and 50% Ir-based alloys (alloy A and B) in the two quaternary alloys. The alloys with 75% Ir-based alloy were of the mix mode fracture with a few proportions of intergranular fractures. The precipitation hardening of quaternary alloys can be caused by the precipitate-shearing mechanism. The compressive strength of quaternary alloys can be attributed to the precipitation and solid solution hardening as well as to the interface strengthening. The effect of heat treatment on the strength is contributed to geometrical hardening term for alloy Ir-5Nb-62.4Ni-12.6Al and the precipitation hardening for alloy Ir-15Nb-20.8Ni-4.2Al.

REFERENCE

[1] Y. Yamabe-Mitarai, Y.Ro, T.Maruko and H.Harada, Metall. Mat. Trans.A, Vol.29A (1998), p. 537

[2] Y. Yamabe-Mitarai, Y.Ro, T.Maruko, T.Yokokawa and H.Harada, Structural Intermetallics 1997, Eds. M.V. Nathal, R.Darolia, C.T.Liu, P.L.Martin, D.B.Miracle, R. Wagner and M.Ramaguchi, The Minerals, Metals &Materials Society, (1997), p.805

[3] Yuefeng Gu, Y. Yamabe-Mitarai, Y.Ro, T.Yokokawa, and H.Harada, Scripta Materialia, Vol.39, No.6 (1998), p.723

[4] Yuefeng Gu, Y. Yamabe-Mitarai, Y.Ro, T.Yokokawa, and H.Harada, Scripta Materialia, accepted (1999)

[5] Xihong Yu, Yoko Yamabe-Mitarai, Yoshikazu Ro, Yuefeng Gu and Hiroshi Harada, Script Materialia, accepted in (1999)

[6] Xihong. Yu, Yoko.Yamabe-Mitarai, Yuefeng.Gu, and Hiroshi.Harada, Abstract of the Japan Institute of Metals, No.123(1998), p. 331

[7] M.marchionni, D.Goldschmidt, M.Maldini, Superalloys 1992. Edited by S.D. Antolovich, R.W.Stusrud, R.A.MacKay, D.L.Anton, T.Khan, R.D.Kissinger, D.L.Klarstrom, The Minerals, Metals & Materials Society (1992), p. 775

[8] S.H.Ai, V.Lupinc, M.Maldini, Script Materialia, Vol.26 (1992), p. 579

[9] Y. Yamabe, Y.Koizumi, H.Murakami, Y.Ro, T.Maruko and H.Harada, Script Materialia, Vol.35, No.2, 211 (1996)

[10] Y. Yamabe-Mitarai, Y.Ro, T.Maruko, and H.Harada, Intermetallics 7, 49 (1999)

[11] Y. Yamabe-Mitarai, Y.Ro, T.Maruko, and H.Harada, , Script Materialia, Vol40, No.1 (1999), p.109

[12] Y. Yamabe-Mitarai, Y.Ro, T.Maruko, T.Yokokawa, Yuefeng Gu, and H.Harada, Materials for Advanced Power Engineering 1998, Edited by J.Lecomte-Beckers, F.Schubert and P.J.Ennis, Forschungszentrum julich, GmbH, Germany (1998), p.1147

For correspondence: Dr. X.H.Yu, High Temperature Materials Research Group
National Institute Research for Metals, 1-2-1 Sengen, Tsukuba, Ibaraki 305-0047, Japan
Tel: 0081-0298-59-2527, Fax: 0081-0298-59-2501
Email: xhyu@nrim.gp.jp

Key Engineering Materials Vols. 171-174 (2000) pp. 685-692
© 2000 Trans Tech Publications, Switzerland

Role of Interfacial Dislocations on Creep of a Fully Lamellar TiAl

T.G. Nieh and L.M. Hsiung

Lawrence Livermore National Laboratory, L-350, P.O. Box 808, Livermore, CA 94551, USA

Keywords: Intermetallic Alloy, Creep, Interface, Interface Sliding, Deformation Twinning, Laminate, Dislocation Pileup

Abstract

Deformation mechanisms of a fully lamellar TiAl (γ lamellae: 100 ~ 300 nm thick, α_2 lamellae: 10 ~ 50 nm thick) crept at 760°C have been investigated. It was found that, as a result of a fine structure, the motion and multiplication of dislocations within both γ and α_2 lamellae are limited at low creep stresses (< 400 MPa). Thus, the glide and climb of lattice dislocations have insignificant contribution to creep deformation. In contrast, the motion of interfacial dislocations on γ/α_2 and γ/γ interfaces (i.e. interface sliding) dominates the deformation at low stresses. The major obstacles impeding the motion of interfacial dislocations was found to be lattice dislocations impinging on lamellar interfaces. The number of impinging lattice dislocations increases as the applied stress increases and, subsequently, causes the pileup of interfacial dislocations on the interfaces. The pileup further leads to the formation of deformation twins. Deformation twinning activated by the pileup of interfacial dislocations is suggested to be the dominant deformation mechanism at high stresses (> 400 MPa).

Introduction

Two-phase [TiAl (γ)-Ti_3Al (α_2)] TiAl alloys have recently attracted more attention than single-phase γ-TiAl alloys because of their superior combination of room-temperature mechanical properties. Great efforts have been made to improve the creep resistance of two-phase TiAl alloys through alloy design and microstructural optimization. By controlling thermomechanical treatments, three different types of microstructures [equiaxed, duplex, and fully lamellar (*FL*)] have been developed [1]. It is well known that the creep resistance of two-phase alloys with a *FL* microstructure is better than that of the alloys with equiaxed and/or duplex microstructures [1-4]. Also, the creep resistance of powder metallurgy *FL*-TiAl alloys is superior to that of ingot metallurgy *FL*-TiAl alloys as a result of a refined lamellar microstructure [2]. Although a significant progress has been made in improving the creep resistance of TiAl alloys, little is known about the underlying creep mechanisms. Several studies on the creep behavior of *FL*-TiAl alloys have been made [3,5], only a few of the creep models have considered the contribution of interface sliding. The motion of interfacial dislocations was recently demonstrated to play an important role during the creep of *FL*-TiAl [6-8].

In a manner similar to other TiAl alloys, creep of fully lamellar *FL*-TiAl alloys revealed two distinct regimes, i.e. low stress (*LS*) and high stress (*HS*), as shown in Fig. 1 [8]. A nearly linear creep behavior was observed in the *LS* regime (< 400 MPa), i.e. $\dot{\varepsilon} = K \cdot \sigma^n$ and n = 1.2 ~1.6, and a power-law creep behavior with n = 6.7 ~ 10.1 in the *HS* regime (> 400 MPa.). An apparent activation energy Q of 160.4 kJ/mole was also obtained [8]. This value is much lower than the

activation enthalpy (Q_v = 295 kJ/mole [9,10], 330 kJ/mole [11]) for lattice diffusion of Ti in γ-TiAl. However, it is close to the activation enthalpy for diffusion of O in γ-TiAl (177 kJ/mole) [12], O in Ti (168 kJ/mole) [13], O in Ti-6Al-4Zr-2Mo-2Sn (167.2 kJ/mole) [14], and C in Ti (127.6 kJ/mole) [15]. Also, the value is also close to the activation enthalpy for dislocation core diffusion ($Q_c/Q_v \approx 0.6$, i.e. 177 ~ 198 kJ/mole). This result indicates that the dislocation climb assisted by lattice diffusion within γ laths is probably not responsible for the creep deformation of refined *FL*-TiAl at low applied stresses. The purpose of the present investigation is to correlate creep behavior with deformation (interfacial) substructure to elucidate further the creep mechanisms of refined *FL*-TiAl.

Experimental

A *FL*-TiAl alloy with a nominal composition: Ti-47Al-2Cr-2Nb (in at. %) was used for this study. The alloy was fabricated by a hot-extrusion of gas-atomized titanium aluminide powder at 1400°C. The interstitial impurities [in parts per million (ppm) by weight] of the alloy are O: 780; N: 40; C: 260. Test specimens with a gauge dimension of 24.4 x 5.08 x 1.52 mm were prepared from the annealed alloy by electrical discharge machining. Creep tests were conducted in a dead-load creep machine with a lever arm ratio of 16:1. Tests were performed in air in a split furnace with three zones at 760°C. Detail information regarding the creep experiment and experimental data was reported elsewhere [2,8]. For current study, the deformation substructures of two tested specimens [one crept at a stress of 138 MPa (creep strain: ~0.25%) in the *LS* regime, and the other crept at a stress of 518 MPa (creep strain: ~3.6%) in the *HS* regime] were investigated. TEM foils were prepared by twin-jet electropolishing in a solution of 60 vol. % methanol, 35 vol. % butyl alcohol and 5 vol. % perchloric acid at ~15 V and –30°C. The microstructures of the crept alloys were examined using a JEOL-200CX transmission electron microscope equipped with a double-tilt goniometer stage. Images of dislocations were recorded using a weak–beam dark field (WBDF) imaging technique under *g (3g)* diffraction conditions.

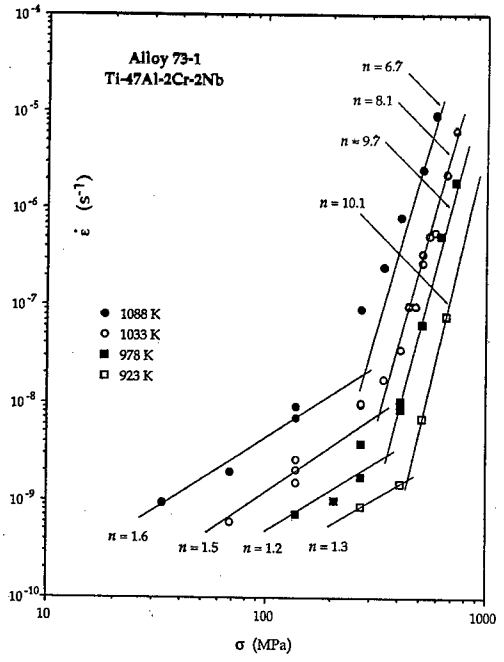

Fig. 1 Plots of steady state creep rates versus applied stress at testing temperatures between 650 and 815°C [8].

Results and discussion

Microstructure of As-Fabricated Alloy

A typical edge-on lamellar microstructure of the as-fabricated alloy is shown in Fig. 2 (left). The thicknesses of lamellae were measured to be in the range of 100 ~ 300 nm and 10 ~ 50 nm for γ and α_2, respectively. A WBDF image showing the dislocation substructure of the alloy is shown in Fig. 2 (right). Both lattice dislocations (*LD* hereafter), formed within γ lamellae, and interfacial dislocations (*ID* hereafter), formed on lamellar interfaces, can be readily seen. Evidently, the population of *ID* is much greater than that of *LD*. Here, *LD* includes both threading dislocation (i.e. dislocation terminates on the lamellar interfaces) and free dislocation (i.e. dislocation which is physically distant from the lamellar interfaces). It is noted that the density of threading dislocation is greater than that of free dislocation.

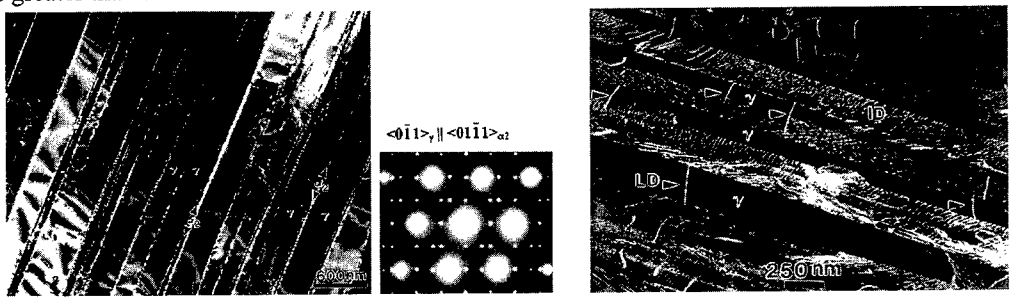

Fig. 2 Dark-field images showing typical dislocation substructures observed from an as-fabricated alloy sample; (left) edge-on view, and (right) tilt view.

Creep Deformation in the Low Stress (*LS*) regime

Deformation in a lamellar alloy is, in principle, caused by the multiplication and motion of *ID* and *LD*. Since α_2 is stronger than γ, and also the volume fraction of α_2 lamella is small ($\leq$ 10%), deformation by the motion of *LD* is expected to occur mainly in the γ lamellae. Furthermore, due to the short moving distance of free dislocations the motion (bowing) of threading dislocations contributes primarily to deformation within the γ lamellae. In general, an applied shear stress must exceed the critical resolved shear stress in order to bow the threading dislocations. The critical resolved shear stress ($\tau_b \approx \mu b/d$) is dependent upon the thickness (d) of γ lamellae. Taking μ = 59 GPa (at 760°C), b = 0.28 nm, and d = 100 ~ 300 nm, the critical resolved shear stress is calculated to be τ_b = 55 ~ 165 MPa. Thus, the applied stress ($\sigma \approx 2\tau_b$) required to bow the threading dislocations is estimated to be greater than 110 ~ 330 MPa. Taking into account the fact that the motion and multiplication of *LD* in both γ and α_2 lamellae are limited in the *LS* regime, as a result of the refined lamellae, the motion of pre-existing *ID* is expected to become important to deformation. It is worth noting that the cooperative motion of *ID* in *FL*-TiAl deformed at room temperature has been observed previously in an *in situ* straining experiment [7]. We now present an indirect evidence of the motion of *ID* in FL-TiAl creep deformed at 760°C.

The interfacial substructure of a soft lamellar grain (oriented nearly ~45° with respect to the stress axis) in a sample crept at 138 MPa is shown in Fig. 3 (left). The appearance of fringe contrasts trailing along *ID* can be readily observed. The fringe contrasts can be best viewed when $2\pi \boldsymbol{g} \bullet \boldsymbol{R}$ = 2/3 or 4/3, where $\boldsymbol{g}$ is the reflection vector and $\boldsymbol{R}$ (= 1/3[111]) is the displacement vector of stacking fault in γ lamella; this suggests the formation of stacking faults on the wake of *ID*. The triangular features are presumably formed by the motion of three sets of *ID* arrays with Burgers vectors: $1/6[\bar{1}\,\bar{1}\,2]$, $1/6[1\bar{2}\,1]$ and $1/6[\bar{2}\,11]$. The formation mechanism is schematically illustrated in Fig. 3 (right), where the equilibrium γ/α_2 interface resulted from both *ID* motion (pure shear) and chemical diffusion is lagging behind the non-equilibrium interface created solely by the motion of *ID*. Here, a stacking fault is formed as the first Shockley partial, $1/6[\bar{1}\,\bar{1}\,2]$, glides along the

interface, but is terminated by the glide of the second Shockley partial, 1/6[1$\bar{2}$ 1]. Then, another stacking fault is formed as the third Shockley partial, *1/6*[$\bar{2}$ 11], glides along.

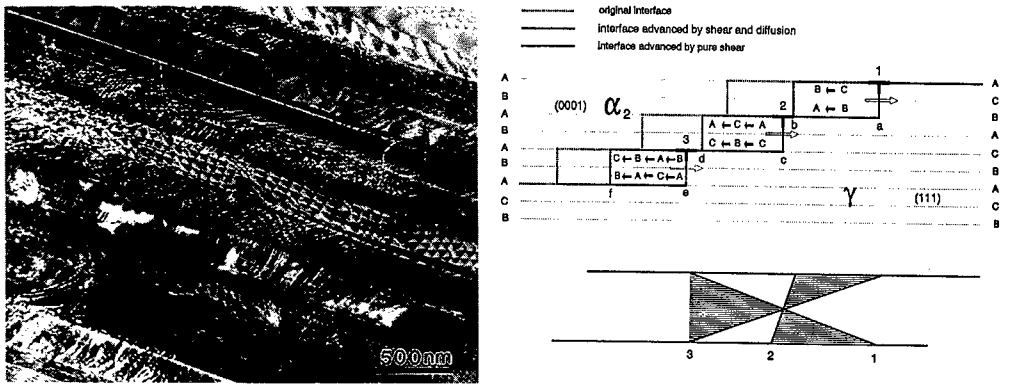

Fig. 3 (left) A WBDF image showing the appearance of fringe contrast trailing along *ID* on γ/α_2 and γ/γ interfaces, (right) a schematic illustration of the migration of γ/α_2 interface resulted from the cooperative motion of *ID* and chemical diffusion. Notice that the equilibrium interface is lagging behind the non-equilibrium interface generated by a pure shear. The triangular fault ribbons resulted from the motion of three different Shockley partials are also illustrated. The letters A, B and C stand for the stacking sequence.

It is noted that the highly populated *ID* and stacking faults on lamellar interfaces are expected to be the preferential sites for solute or impurity segregation. In fact, experimental evidence of solute segregation to γ/α_2 and γ/γ interfaces has recently been reported [16]. These solute segregants can act as short-range barriers for the motion of *ID*, in a manner similar to that of *Cottrell* atmosphere and *Suzuki* effect [17]; this results in the viscous glide of *ID*. The steady state creep rate may be described using the Orowan equation given below:

$$\dot{\varepsilon} = \Phi \rho_m b \bar{v} \qquad (1)$$

where Φ is a geometrical factor (for isotropic polycrystals: inverse of Taylor factor, for single crystal: Schmid factor), ρ_m is the density of mobile dislocations, b is the Burgers vector, and $\bar{v}$ is the average dislocation velocity. Since the multiplication of lattice dislocations within refined γ and α_2 lamellae is very limited when the material is deformed at low stress, the glide of pre-existing *ID* arrays becomes the predominant deformation mechanism. That is, the mobile dislocation density (ρ_m) is approximately equals to the density of *ID*. Under small creep-strain, low creep stress and strain-rate, it is plausible to assume that *ID* arrays are moving with a constant spacing so that the density of mobile dislocations is insensitive to the applied stress, i.e. $\rho_m \neq F(\sigma)$. Accordingly, the steady state creep rate ($\dot{\varepsilon}$) is mainly controlled by the average velocity ($\bar{v}$) of *ID* arrays [i.e. $\dot{\varepsilon} = F(\bar{v})$], which are considered to be drifting with the pinning solute (impurity) atoms at low applied stresses.

Let there be m solute atoms per unit length of dislocation line which effectively pin a dislocation line. When a unit length of *LD* drifts one atomic distance under an external stress σ, the estimated drift velocity of the dislocation line is of the order [17,18]:

$$\bar{v} = (\sigma b^3 \nu / mkT) \exp(S/k) \exp(-Q/kT) \qquad (2)$$

where ν (~10^{12}/sec) is the average vibration frequency of the dislocation line, S is the entropy of activation for the motion, and Q is the activation energy associated with the jump of a pinning

$$\dot{\varepsilon} = M\,(\dot{N}\bullet\Delta t)\,L\,b\,\bar{v} \qquad (5)$$

where, M is the number of twin sources per unit volume, $(\dot{N}\bullet\Delta t)$ is the number of twinning dislocations emitted from a twin source, L is the length of twinning dislocation, b is the length of Burgers vector, and $\bar{v}$ is the average velocity of twinning dislocation. Quantitatively, $M, \dot{N}$, and $\bar{v}$ in the equation are dependent upon the applied stress and initial microstructure. A rigorous quantitative creep model based upon the twinning process is currently underway.

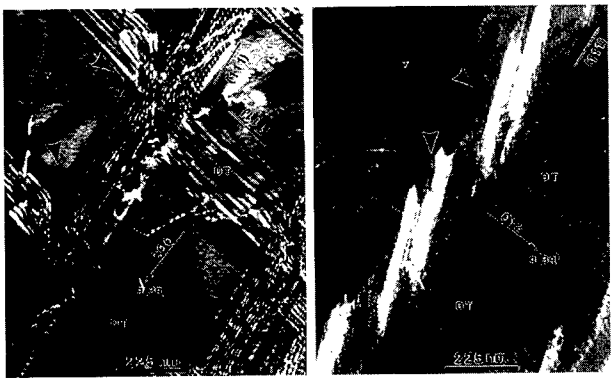

Fig. 6 Paired WBDF images showing the existence of *1/6*[011] stair-rod dislocations at the intersections (indicated by arrows) between the $(\bar{1}\,11)$ type *DT* and a α_2 lamella. (Left) Invisible at $\boldsymbol{g} = 200$ $(\boldsymbol{g}\bullet\boldsymbol{b} = 0)$, (right) visible at $\boldsymbol{g} = 021$, **Z** (zone axis) $\approx [0\,\bar{1}\,2]$.

Summary

Creep mechanisms of *FL*-TiAl with a refined lamellar microstructure (γ lamellae: 100 ~ 300 nm thick, α_2 lamellae: 10 ~ 50 nm thick) have been investigated. In the low stress regime (< 400 MPa). the motion and multiplication of lattice dislocations are limited because the refined lamellar spacing, a cooperative motion of interfacial dislocations (i.e. interface sliding) is proposed to be the dominant deformation mechanism. During the sliding of lamellar interfaces, the motion of interfacial dislocations is interrupted by the impinged lattice dislocations on the interfaces and results in the pileup of interfacial dislocations. This is a prevalent process especially at high stresses. To relieve stress concentration at the head of dislocation pileup, $(\bar{1}\,11)$-type deformation twins are observed to emit from the interfaces through the dissociation reaction of interfacial dislocations: $1/6[\bar{1}\,2\,\bar{1}]_{(111)} \rightarrow 1/6[011]_{(100)} + 1/6[\bar{1}\,1\,\bar{2}]_{(\bar{1}11)}$. It is thus suggested that deformation twinning activated by the pileup of interfacial dislocations is the dominant deformation mechanism in the high stress regime (> 400 MPa).

Acknowledgment

This work was performed under the auspices of the U.S. Department of Energy by Lawrence Livermore National Laboratory under contract No. W–7405–Eng–48.

References

1. Y –W. Kim, *Acta Metall. Mater.* **40**, 1121 (1992).
2. J. N. Wang, A. J. Schwartz, T. G. Nieh, C. T. Liu, V. K. Sikka and D. R. Clemens, in *Gamma Titanium Aluminides*, ed. Y-W. Kim et al., TMS (1995), p. 949.
3. J. Beddoes, W. Wallace and L. Zhao, *Intr. Mater. Rev.*, **40**, 97 (1995).
4. C. T. Liu, P. J. Maziasz and J. L. Wright, *Mat. Res. Soc. Symp. Proc.*, **460**, 83 (1997).
5. T. A. Parthasarathy, M.G. Mendiratta and D.M. Dimiduk, *Scripta Mater.*, **37**, 315 (1997).
6. L. M. Hsiung and T. G. Nieh, *Mater. Sci. Engrg.*, **A239-240**, 438 (1997).
7. L. M. Hsiung, A. J. Schwartz and T. G. Nieh, *Scripta Mater.* **36**, 1017 (1997).
8. J. N. Wang and T. G. Nieh, *Acta Mater.*, **46**, 1887 (1998).
9. H. Mehrer, W. Sprengel and M. Denkinger, in *Diffusion in Ordered alloys*, Eds. B. Fulta et al., TMS (1993), p. 51.
10. W. Sprengel, N. Oikawa, H. Nakajima, *Intermetallics*, **4**, 185 (1996).
11. H. Oikawa, in *High Temperature Aluminides and Intermetallics*, Eds. S. H. Whang et al., TMS (1989), p. 353.
12. Y. A. Chang, R. Kieschke, J. DeKock and M. X. Zhang, in *Control of Interfaces in Metal and Ceramics Composites*, edited by R. Y. Lin and S. G. Fishman, TMS (1993), p. 3.
13. C. R. Brooks, in *Metals Handbook* (Desk Edition, 1985), edited by H. E. Boyer and T. L. Gall, ASM (Metals Park, OH), 28•66(T).
14. R. N. Shenoy, J. Unnam and R. K. Clark, in *Oxidation of Metals*, **26**, 105 (1986).
15. A. I., Nakonechnikov and L. V. Parlinov, *Diffusion Data*, **6**, 573 (1972).
16. C. T. Liu, P. J. Maziasz, and D. J. Larson, in *Interstitial and Substitutional Solute Effects in Intermetallics*, Eds. Baker et al., TMS (1998), p. 179.
17. J. Weertman and J. R. Weertman, *Elementary Dislocation Theory*, Macmillan, NewYork (1964).
18. J. P. Hirth and J. Lothe, *Theory of Dislocations*, McGraw-Hill, New York (1968).
19. J. D. Eshelby, F. C. Frank and F. R. N. Nabarro, *Phil. Mag.* **42**, 351 (1951).
20. T. Mori and H. Fujita, *Acta Metall.*, **28**, 771 (1980).
21. M. H. Yoo, *Scripta Mater.*, **39**, 569 (1998).

Key Engineering Materials Vols. 171-174 (2000) pp. 693-700
© 2000 Trans Tech Publications, Switzerland

Microstructural Evolution Associated with Creep Rate Minima in Pure- and Near-γ TiAl Intermetallics

A. Dlouhý, K. Kuchařová and T. Horkel

Institute of Physics of Materials, Academy of Sciences of the Czech Republic,
Žižkova 22, CZ-616 62 Brno, Czech Republic

Keywords: Intermetallics, TiAl, Creep, TEM, Twinning, Microstructural Evolution

Abstract Interrupted tensile and compression creep tests were performed at 1100K and 100MPa to study strain dependent microstructural changes in pure-γ Ti-52Al. A mean twin spacing (MTS) and dislocation densities were investigated in the range of strain where sharp creep rate minima occur. It has been found that the overall dislocation density approaches a stationary value at strains close to 1%. On the other hand, strains as large as 7% are not sufficient to establish a dynamic equilibrium for deformation twinning.
Based on these results it is suggested that, in the pure- and near-γ equiaxed grain microstructures, the increase of creep rate after minimum and its new gradual saturation reflects a sluggish nucleation of deformation twins. A simple model has been proposed which addresses competitive effects of strain hardening and strain softening associated with the twinning process.

Introduction Takahashi and co-workers [1] first reported on sharp creep rate minima (SCRMa) during creep in pure-γ TiAl. A similar type of creep rate minimum was recently found for near-γ Ti48Al2Cr2Nb-1B with an equiaxed grain microstructure [2,3]. The sharp minimum of creep rate is associated with an improved resistance of the equiaxed grain microstructures to primary creep. However, this advantage has to be balanced against a substantially lower ductility as compared to the fully lamellar alloy modification [3]. Therefore a thorough understanding of underlying microstructural processes is required to profit from both, the good creep resistance and improved ductility of near-γ TiAl in engineering applications.
Slip processes in γ-TiAl intermetallics, which also contribute to creep strain, exhibit some specific features caused by the $L1_0$ crystal lattice structure. Slip displacements with *zero* component into the tetragonal c-axis (dislocations with Burgers vector 1/2<110> referred to as <a>-dislocations throughout this study) can be easily activated [4] because they are not associated with the creation of anti-phase boundaries (APBs). Two types of displacement with *non-zero* component into the c-axis are usually observed [4]: (i) the <101>-type superdislocations (<c>-dislocations in this study) and (ii) deformation twins (DT) which nucleate and spread due to the slip of 1/6<112>-type partial dislocations.
Contributions of both, the <a>-dislocations and DT to creep strain were observed by Ishikawa and Oikawa [5]. Recently, there also were studies which concentrated on various aspects of twinning during creep of near-γ TiAl alloys [6-8]. However, no microstructurally based explanation has been proposed so far which would clarify the relation between SCRMa and elementary deformation processes. Therefore, the present study is aimed at (i) performing a quantitative assessment of microstructural changes with increasing creep strain and (ii) discussing possible microstructural sources of the SCRMa.

Experimental All details on the preparation of the experimental alloy Ti-52at%Al and on creep testing were already given elsewhere [2,3]. Metallographic cross-sections were studied by a conventional light microscopy and SEM in order to describe the influence of creep on grain size and mean twin spacing λ (MTS). The metallographic surfaces were electro-polished (electrolyte 25ml $HClO_4$ and 7.5ml HNO_3 in 500ml ethanol) and electro-etched using the 5% solution of HBF in water. A computer assisted image analysis was adopted [9] to collect representative data on grain structure.
A special care was also given to the preparation of transmission electron microscopy (TEM) foils to avoid any damage due to the foil thinning. Slices cut out of the creep specimen gauge length and the specimen head were ground on emery papers to thickness of 0.3mm. From this point on only chemical methods

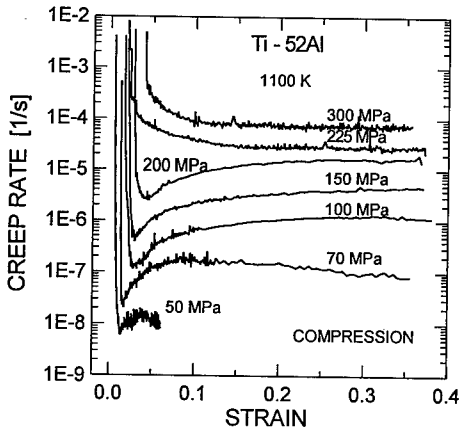

Fig.1: Compression creep curves of Ti-52Al obtained at 1100K and in the applied stress range 50-300MPa. The curves change their shape from standard form (above 200MPa) to sharp minimum form (below 200MPa). At low stresses the minimum becomes less apparent, see the curve obtained at 50MPa.

were applied during subsequent thinning. The double jet TENUPOL equipment was used for final perforation of the foil. The electrolyte $HClO_4$ (5%) and methanol (95%) was kept at -50°C. The method proposed by Ham [10] was used to estimate dislocation densities. A foil thickness was obtained either with the convergent beam [11] or with the stereo-pair [12] technique.

Creep tests Compression creep curves of pure-γ Ti-52Al are plotted in Fig.1 and results of interrupted creep tests performed at 1100K and 100MPa are shown in Fig.2. At the temperature 1100K and for applied stresses below 200MPa the creep curves exhibit a sharp minimum. The minimum is independent of loading mode as it has been reported earlier [2,3]. Curves in Fig.2a represent three test in compression interrupted at strains 2%, 8% and 38%. A similar set of tension tests is presented in Fig.2b, where terminal strains are 0.9%, 2.7% and 6.8%. In passing we note that the points in which the tests were interrupted are indicated by full symbols.

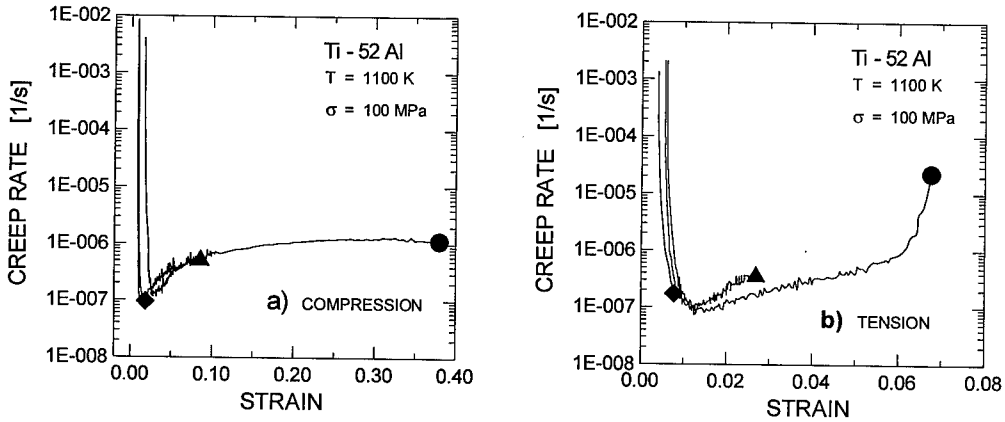

Fig.2: Interrupted creep (full symbols indicate test terminations) of Ti-52Al at 1100K and 100MPa: **a)** compression – terminal strains 2, 8 and 38%, **b)** tension – terminal strains 0.9, 2.7 and 6.8%.

Metallography Four micrographs in Fig.3 show cross-sections of Ti-52Al in the undeformed state (Fig.3a) and after tensile creep (Figs.3b-d) to three different levels of strain (creep curves presented in Fig.2b). In contrast to the undeformed state, thin deformation twins can be observed in Fig.3b. The number and the width of deformation twins increase in the range of strain where creep rate accelerates after the minimum as it is documented in Fig.3c (strain 2.7%) and in Fig.3d (strain 6.8%). There is not to much evidence for necklace recrystallization in micrographs of Fig.3 even though it was often reported in literature [5]. Grain boundaries become increasingly wavy with increasing creep strain which can be

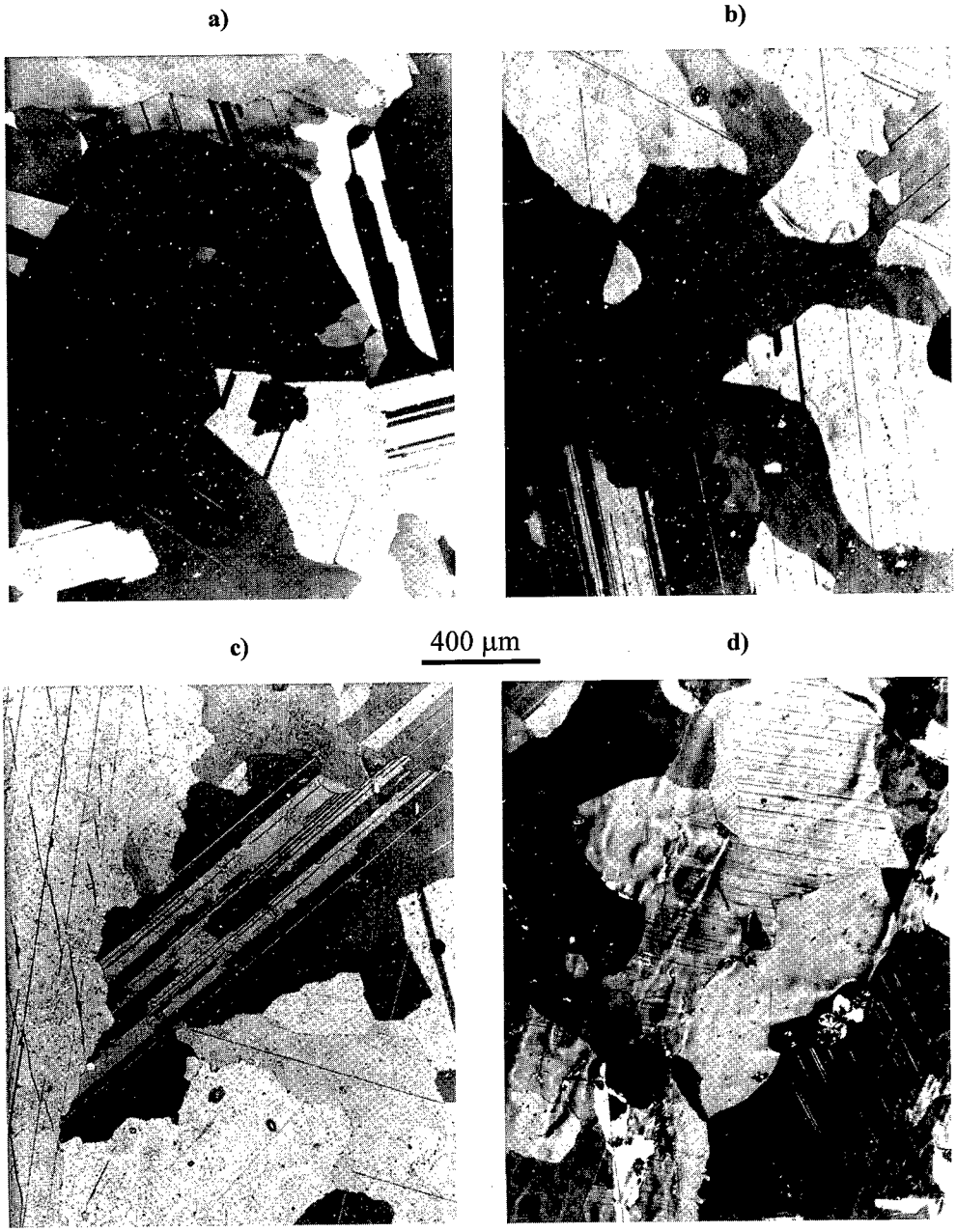

Fig.3: Metallographic cross-sections prepared from Ti-52Al specimens after interrupted tensile creep tests. Corresponding strains increase in the succession: **a)** 0% - specimen head, **b)** 0.9%, **c)** 2.7% and **d)** 6.8%. There are almost no deformation twins observed in the undeformed specimen head in a) and the number of twins in individual grains increases with increasing tensile strain in b), c) and d).

associated with forces acting on the grain boundaries from a gradually evolving subgrain structure. Metallographic cross-sections were also prepared from specimens after interrupted compression creep. These cross-sections were processed by image analysis to evaluate grain size and its changes with compression strain. Results are shown in Fig.4 where cumulative relative distributions of the maximum grain diameter D_{max} are plotted. The results suggest that grains of the Ti-52Al alloy grow during creep. The mean twin spacing λ was measured after interrupted tensile creep (Figs.2b and 5). The dependence plotted in Fig.5 indicates that the MTS steadily decreases through the whole investigated range of strain and after 7% of strain the deformation twinning still does not come to dynamic equilibrium.

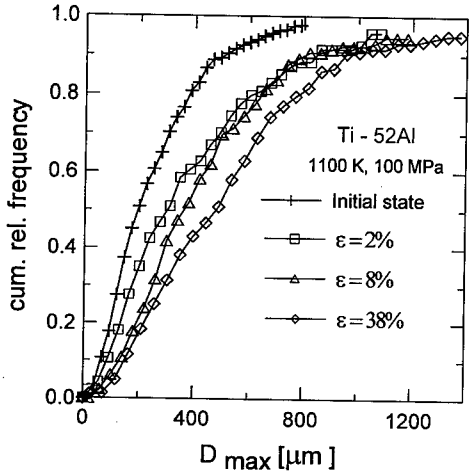

Fig.4: Grain growth with increasing compression creep strain in Ti-52Al at 1100K and 100MPa.

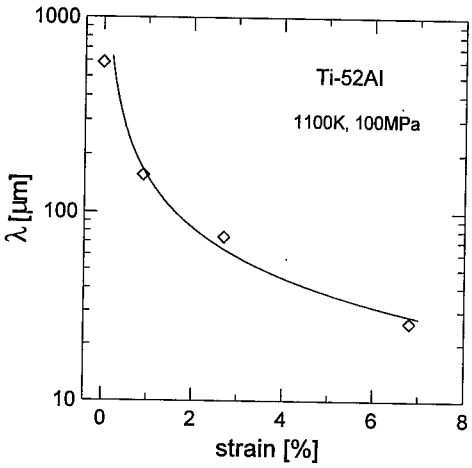

Fig.5: Evolution of mean twin spacing with creep strain in Ti-52Al at 1100K and 100MPa.

Transmission electron microscopy TEM micrographs taken with **g**={111} and presented in Fig.6 demonstrate changes of dislocation structure with strain in interrupted tensile creep tests of Fig.2b. A low dislocation density in undeformed specimen head is shown in Fig.6a. Dislocations which originated from the deformation process move either individually or start to form new subgrain walls after approximately 1% of strain (Fig.6b). With still increasing strain, dislocation networks in subgrain boundaries become more regular (Fig.6c) and after 7% deformation a considerable part of dislocation density is organized in subgrain structure (Fig.6d). Majority of dislocations observed in micrographs of Fig.6 are ordinary <a>-dislocations. Deformation twins are rarely seen in TEM micrographs since the smallest measured MTS value (26μm) is still much larger as compared to dimensions of TEM micrographs in Fig.6.
A summary of dislocation density measurements is presented in Fig.7. Two important points should be highlighted: (i) there is a detectable density of <c>-dislocations which represents approximately 1/4 of the overall dislocation density (<a>&<c>-dislocations) and (ii) both densities, <c>-dislocations and also <a>&<c>-dislocations, exhibit the most intensive growth during initial 1% of creep strain. Only a limited increased of both densities could be observed in later stages of creep.

Correlation between microstructure and creep rate It was shown by Mecking et al. [13] that all the three types of shear (<a>-dislocations, <c>-dislocations and DT) are needed to fulfil the von Mises criterion of strain continuity. If one of the displacements were missing, severe accumulation of internal stress would be expected unless (i) a missing displacement is activated later in creep or (ii) a process controlled by fast diffusion would be able to supply required displacements and relax the stress field.
Results presented in Figs.5 and 7 suggest that <a>- and <c>-dislocation densities approach a dynamic equilibrium with a transition primary strain of the order of 1%. In contrast, 7% strain is not sufficient to reach a similar equilibrium for the twinning process. Consequently, it can be stated, in agreement with the conclusion of Farenc et al. [14], that the nucleation of DT at the beginning of creep requires a markedly

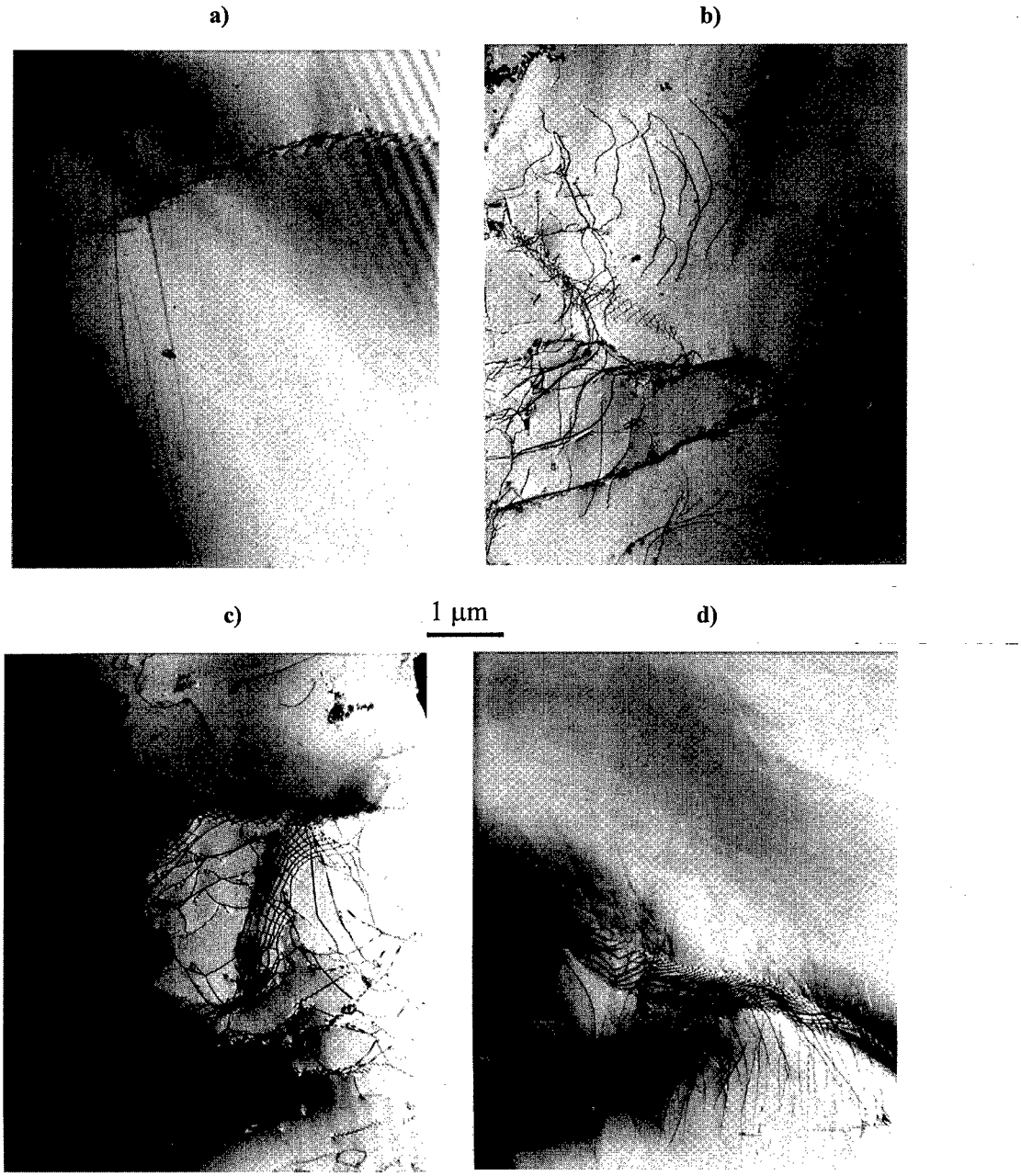

Fig.6: TEM micrographs taken with **g**={111} demonstrate changes of dislocation structure with increasing strain in tensile creep tests interrupted at strains: **a)** 0% - undeformed specimen head, **b)** 0.9%, **c)** 2.7% and **d)** 6.8%. Dislocation structures shown in this figure contain almost exclusively <a>-dislocations. The formation of new subgrain walls starts early in the creep life as it is documented in the micrograph b).

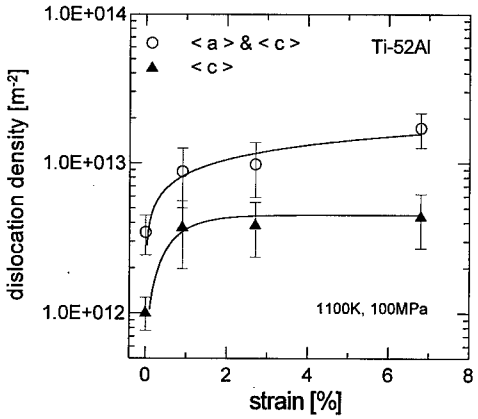

Fig.7: Summary of <c>- and <a>&<c>-dislocation density measurements after varying amount of tensile creep strain accumulated at 1100K and 100MPa in Ti-52Al alloy. Both dislocation densities reach almost stationary value after 1% primary strain transition. The density of <c>-dislocations represents approximately 1/4 of the overall dislocation density of <a>&<c>-dislocations.

higher resolved shear stress as compared to the nucleation of <a>-dislocation slip. A consequence of DT being a "hard" mode of deformation is that considerable internal elastic strains build up at the early stages of creep which substitute the missing DT displacements. These mismatch strains (elastic) are associated with internal stresses that, on one hand, hinder the <a>-dislocation slip but, on the other hand, they support the nucleation and spreading of DT. Once the stress state required for the twin nucleation is locally created, the twinning starts and relaxes the mismatch stresses. The evolution of deformation twinning thus contributes to the acceleration of creep rate after the creep rate minimum. In summary, the sharp minimum of creep rate results from a superposition between a "normal" metal-type primary transition for deformation carried by <a>-dislocations and "inverse" alloy-type primary transition for deformation due to twinning. Contrary to the commonly accepted view that DT acts as a strain hardening process during creep of pure- and near-γ TiAl intermetallics, e.g. [6], our results show, that DT can also act as a strain softening process since with the increasing intensity of twinning the overall creep rate increases after the sharp minimum.

Strain hardening and strain softening due to deformation twinning In order to demonstrate the mentioned competitive effects of strain hardening and strain softening associated with DT, we develop here a simplified description which can account for the dependence of creep rate on the mean twin spacing λ. The description is based on the Orowan equation

$$\dot{\varepsilon} = M \cdot b \cdot \rho \cdot \mathrm{v} \tag{1}$$

where M is appropriate orientation factor, b is the Burgers vector, ρ is mobile dislocation density and v is a mean velocity of dislocations. Since at least two distinct dislocation families, namely <a>-dislocations and partial 1/6<112>-twinning dislocations (<T>-dislocations) have to be considered, the Eq.1 should be applied to both systems individually. However, in our treatment we adopt two basic simplifications: (i) M and b are approximately the same for both families and (ii) the velocity of dislocations in both families and its functional dependence on driving forces are also approximately the same. Then the Eq.1, with $\rho_{<T>}$ for a density of twinning dislocations and $\rho^{m}_{<a>}$ for mobile density of <a>-dislocations, becomes

$$\dot{\varepsilon} = M \cdot b \cdot (\rho^{m}_{<a>} + \rho_{<T>}) \cdot \mathrm{v}\,. \tag{2}$$

The dependence of dislocation velocity on driving force is approximated by a power law

$$\mathrm{v} = B \cdot \left(\frac{\sigma - \sigma_D - \sigma_M - \sigma_O}{\mu} \right)^{n} \tag{3}$$

where B is a rate parameter, n - driving force exponent, μ - shear modulus, σ - applied stress, $\sigma_D = \mu \cdot b \cdot \sqrt{\rho_{<a>} + \rho_{<T>}}$ - mean internal stress due to the overall dislocation density, σ_M - mean internal stress resulting from the strain mismatch and $\sigma_O = \mu \cdot b \cdot (\lambda)^{-1}$ represents the Orowan back-stress

associated with the presence of twin boundaries (λ is the mean twin spacing). The density of twinning dislocations can be further expressed as

$$\rho_{<T>} = \rho^{1}_{<T>} \cdot \frac{D}{\lambda} \tag{4}$$

with $\rho^{1}_{<T>}$ being the dislocation density which propagates in one twinning event and with D being the mean grain size. Thus the overall mobile dislocation density can be written in the form

$$\rho^{m}_{<a>} + \rho_{<T>} = \rho^{m}_{<a>} \cdot \left(1 + \frac{\rho^{1}_{<T>}}{\rho^{m}_{<a>}} \cdot \frac{D}{\lambda}\right). \tag{5}$$

There is only limited knowledge on the mobile density of <a>-dislocations, however we estimate that the ratio $r = \rho^{1}_{<T>} \cdot (\rho^{m}_{<a>})^{-1}$ in Eq.5 can be fairly well approximated by a factor of the order of unity for twin widths in the range of 100nm. Thus with σ_M=0 the Eq.2 becomes

$$\dot{\varepsilon} = M \cdot b \cdot \rho^{m}_{<a>} \cdot B \cdot (1 + r \cdot \frac{D}{\lambda}) \cdot \left(\frac{\sigma}{\mu} - b \cdot \sqrt{\rho_{<a>} + \rho_{<T>}} - \frac{b}{\lambda}\right)^{n} \tag{6}$$

or in a simplified form

$$\dot{\varepsilon} = A \cdot S(\lambda) \cdot h(\lambda) \tag{7}$$

where $A = M \cdot b \cdot \rho^{m}_{<a>} \cdot B$, the strain softening term

$$S(\lambda) = \left(1 + r \cdot \frac{D}{\lambda}\right) \tag{8}$$

and the strain hardening term

$$H(\lambda) = A \cdot h(\lambda) = A \cdot \left(\frac{\sigma}{\mu} - b \cdot \sqrt{\rho_{<a>} + \rho_{<T>}} - \frac{b}{\lambda}\right)^{n}. \tag{9}$$

Creep rate given by Eq.6 is plotted in Fig.8 together with strain softening S(λ) and strain hardening H(λ) terms. Following set of input parameters was used when calculating the dependencies of Fig.8: σ=100MPa, b=2.8×10^{-10}m, μ=60GPa, D=200μm, r=0.8, $\rho_{<a>} + \rho_{<T>}$ = 3×10^{13}m^{-2}, n=1 and A=2×10^{-4}s^{-1}. Values of the input parameters were taken either from literature or their selection was guided by the experimental results obtained in the present study.

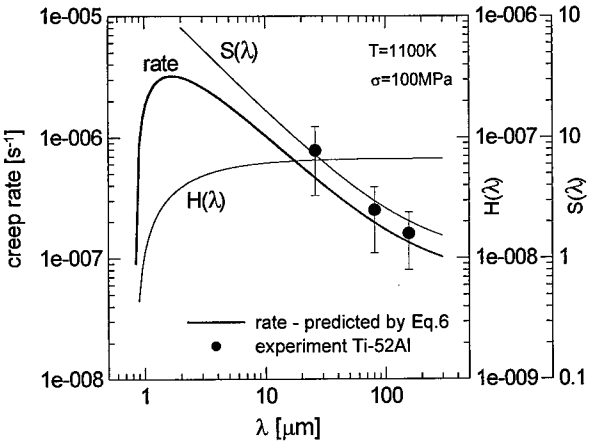

Fig.8: Correlation between creep rate of pure-γ Ti-52Al and mean twin spacing λ as predicted by Eq.6 and as measured in interrupted creep tests. The predicted curve results from superposition of softening S(λ) and hardening H(λ) terms. Hardening controls creep rate in submicron range of λ.

As it is evident from Fig.8, creep rate increases with decreasing λ (twinning causes strain softening) up to the moment when distance between neighbouring twins approaches 1μm range. From this point on creep rate starts to decrease and on further decrease of λ quite sharp drop of creep rate is expected. Therefore,

for submicron values of λ the hardening effect associated with the twinning process dominates the creep rate. Three experimental points shown in Fig.8 demonstrate the correlation between instantaneous creep rate and the mean twin spacing observed in the interrupted creep tests. In order to facilitate the comparison of experimental results and calculated curves we note that strain in interrupted tests increases with decreasing value of λ. It can be seen that the agreement of experimentally based correlation and model predictions given by Eq.6 is quite satisfactory.

Conclusions The evolution of microstructure with creep strain in pure-γ Ti-52Al at 1100K and 100MPa has been investigated in the range of strain where sharp creep rate minima are observed. Results of the quantitative metallographic and TEM study can be summarized as follows:

1) Grain structure of the alloy is unstable during creep and the initial grain size of 200μm changes to 500μm after 38% of compression creep. However, the sharp creep rate minima were shown to be independent of these grain size changes [2,3].

2) Deformation twinning contributes to the creep strain such that the mean twin spacing λ continuously decreases during initial 7% of strain after which the value λ=26μm has been found.

3) Dislocations with non-zero component of Burgers vector into the tetragonal c-axis of $L1_0$ lattice (<c>-dislocations) and their densities were evaluated from **g**=(002) TEM bright field micrographs. The density of these dislocations is at least four times lower than the integral dislocation density.

4) Both the <c>-dislocation density and the integral dislocation density grow in the early stages of creep and approach a stationary level after only 1% of creep strain.

5) The sharp creep rate minima result from the superposition of normal (metal-type) primary transition associated with the multiplication and motion of <a>-dislocations and inverted (alloy-type) primary transition due to the activation of deformation twinning.

6) The role of deformation twinning (DT) in creep of equiaxed pure- and near-γ [2,3] TiAl alloys is two-fold since DT contributes to both, strain hardening and strain softening. Which effect prevails in the macroscopic creep response depends primarily on the mean twin spacing λ. In the submicron range of λ, the hardening contribution dominates while for higher values of λ the strain softening effect controls the creep behaviour.

Acknowledgement The authors would like to thank Mr. M. Daniel for preparation of TEM foils, Mrs. L. Poláčková and Mr. J. Březina for technical assistance during metallographic investigation and Mrs. L. Adamcová for preparation of final TEM micrographs. The financial support was received from GA CR under the contract no. 106/95/1522 and from Ministry of Education CR under the contract no. OC 522.100.

References

[1] T. Takahashi, H. Nagai and H. Oikawa, Mat. Sci. Eng. A 114 (1989), p.13.
[2] A. Dlouhý, K. Kuchařová and T. Horkel, in: Materials for Advanced Power Engineering 1998, Part III, Proceedings of the Sixth Liège Conference, edited by J.Lecomte-Beckers et al., Forschungszentrum Jülich 1998, p.1219.
[3] A. Dlouhý, K. Kuchařová and T. Horkel, in: Creep Behaviour of Advanced Materials for the 21st Century, Proceedings of the 1999 TMS Annual Meeting, ,edited by R. S. Mishra et al., TMS, Warrendale 1999, p.207.
[4] D. Shechtman, M.J. Blackburn and H.A. Lipsit, Met. Trans. 5 (1974), p.1373.
[5] Y. Ishikawa and H. Oikawa, Mater. Trans. JIM 35 (1994), p.336.
[6] M.A. Morris and M. Leboeuf, Intermetallics 5 (1997), p.339.
[7] B. Skrotzki, M. Ünal and G. Eggeler, Scripta Mater. 39 (1998), p.1023.
[8] J.G. Wang, L.M. Hsiung and T.G. Nieh, Scripta Mater. 39 (1998), p.957.
[9] J. Němec A. Dlouhý, K. Kuchařová and M. Cans, Pract. Metallography 33 (1996), p.198.
[10] R.K. Ham, Phil. Mag. 6 (1961), p.1183.
[11] P.M. Kelly, A. Jostons, R.G. Blake and J.G. Napier, Phys. Stat. Sol. A 31 (1975), p.771.
[12] A. Dlouhý and J. Pešička, Czech. J. Phys. 40 (1990), p.539.
[13] H. Mecking, Ch. Hartig and U.F. Kocks, Acta Mater. 44 (1996), p.1309.
[14] S. Farenc, A. Coujou and A. Couret, Phil. Mag. A 67 (1993), p.127.

e-mail address: dlouhy@ipm.cz

Key Engineering Materials Vols. 171-174 (2000) pp. 701-708
© 2000 Trans Tech Publications, Switzerland

A New Microstructural View of Creep in Near-γ TiAl-Alloys

B. Skrotzki

Ruhr-University Bochum, Dept. of Mechanical Engineering, Institute for Materials,
DE-44780 Bochum, Germany

Keywords: Creep Mechanism, Duplex Microstructure, Microstructural Evolution, Dislocations, Mechanical Twinning, Dynamic Recrystallization, Interface Spacing, Back Stress

Abstract The microstructural evolution during creep of a near-γ TiAl-alloy with duplex microstructure was studied. Three elementary processes have been identified in the γ-phase, which contribute to the overall creep deformation mechanism: (i) Ordinary dislocation plasticity and (ii) mechanical twinning contribute to creep deformation from the beginning on. Both deformation modes build up back stresses due to elastic incompatibilities that arise due to the crystallography of the ordered $L1_0$ lattice of the γ-phase. (iii) When the strain rate minimum is reached, dynamic recrystallization starts to contribute to creep in two ways: (a) the density of ordinary dislocations is decreased and, consequently, back stresses are relaxed; (b) grains may be formed in those orientations, which allow plastic deformation in directions, which are required for homogeneous macroscopic deformation. These three elementary processes are coupled and jointly control the creep behavior.

Introduction

Intermetallic near-γ Titanium Aluminides are regarded as promising candidate materials for high temperature applications. They show attractive properties such as low density combined with high strength and high Young's modulus which are retained at high temperature, and good corrosion resistance. The temperature and stress regime of envisaged applications of near-γ TiAl-alloys (such as turbine blades) is well within a range where creep processes take place. Therefore, the mechanical behavior has to be well characterized and a number of creep studies have been carried out in the last years (e.g. see [1 - 7]). Most creep studies focused on nearly or fully lamellar microstructures, which show the best creep resistance and fracture toughness but their ductility is low. Duplex alloys which the present work concentrates on exhibit lower creep strength but provide a good compromise between room temperature ductility and high temperature mechanical properties.

Beside the microstructure, which strongly controls the deformation behavior of near-γ TiAl-alloys, the crystal structure of the two intermetallic phases has to be considered to understand the deformation mechanism. The ordered $L1_0$ structure of γ-TiAl exhibits a tetragonal distorted fcc unit cell (c/a = 1.02) where lattice planes with Al and Ti atoms alternate in the c-direction (Fig. 1). Slip occurs by ordinary dislocations with $\mathbf{b}_o = 1/2 <110]$ and by superdislocations with $\mathbf{b}_{s1} = <101]$ and $\mathbf{b}_{s2} = 1/2 <112]$ [8, 9]. Deformation twins form on {111} planes but only those <112> twinning directions are observed, which preserve the order of the $L1_0$ lattice [10]. α_2-Ti_3Al possesses a hexagonal ordered $D0_{19}$ structure. Slip occurs in this crystal structure by dislocations with $\mathbf{b} = 2/3 <11\bar{2}0>$ on the basal, prismatic and pyramidal planes [9].

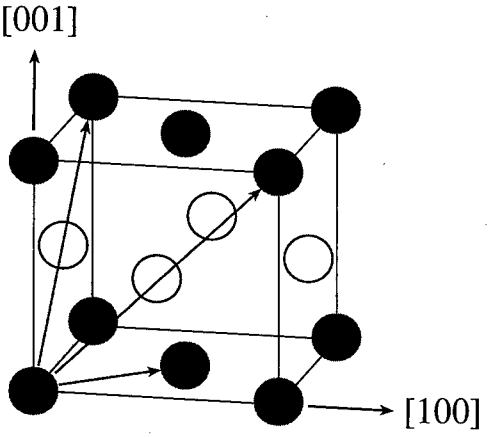

Fig. 1: Tetragonal distorted fcc unit cell of the ordered $L1_0$ superlattice of γ-TiAl.

So far, no clear overall microstructural description of creep in near-γ TiAl-alloys has yet evolved which rationalizes how elementary microstructural processes combine to yield the experimental stress and temperature dependence of the creep rate. Therefore, the main objective of the present work was to study the microstructural evolution of a near-γ TiAl-alloy with duplex microstructure during creep to identify the key elements of the overall creep deformation mechanism.

Material and Experimental Procedure

An alloy of type Ti-47Al-2Mn-2Nb + 0.8 vol. % TiB_2 XD^{TM} produced by Howmet Corporation (Whitehall, Mich., USA) was investigated. Its actual chemical composition is given in Table 1. The content of interstitial elements was determined to be 507 ppm O, 70 ppm C, 73 ppm N and 5 ppm H (in wtppm). Cast rods of 15 mm diameter and 200 mm length were HIPed (1260 °C/172 MPa) followed by a heat treatment in vacuum at 1010 °C for 50 h. The mean grain size was measured to be 15 μm for the γ-grains and 30 μm for the lamellar grains with a volume fraction of lamellar grains of 15 to 20 %.

Table 1: Chemical composition of the investigated alloy.

	Ti	Al	Nb	Mn	Fe	Cu	Si	B
wt. %	Bal.	32.44	4.89	2.85	0.05	0.05	0.04	0.32
at. %	Bal.	46.62	2.04	2.01	0.03	0.03	0.06	1.15

Creep tests were carried out in air under constant tensile load at temperatures of 650, 700 and 750 °C and initial stresses varying between 150 and 350 MPa. The majority of tests were interrupted after reaching 1 or 2 % plastic creep strain and only a few tests were deformed to fracture. Further details of creep testing as well as mechanical data are reported in [11].

A JEOL JSM 840 scanning electron microscope (SEM) operating in backscatter mode was employed to characterize the as received and deformed material. Standard metallographic techniques were applied to prepare thin foils for transmission electron microscopy from slices cut from the creep specimens perpendicular to the stress axis. The samples were electrolytically

polished using the twin jet method in a solution of 600 ml methanol, 360 ml butylcellosolve and 60 ml perchloric acid at –30 °C. The thin foils were investigated using a Philips CM20 transmission electron microscope at an accelerating voltage of 200 kV. Lamellar grains and γ-grains were investigated separately. All grains were tilted to have the lamellar interfaces and twin interfaces edge on, i.e. the interfaces were parallel to the electron beam. The mean interface spacing was then measured by counting the number of intersections of a test line (being perpendicular to the interface) with the lamellae or twin interfaces.

Results and Discussion

Electron microscopy combined with quantitative image analysis was applied to study the microstructural evolution during creep and to identify the elementary processes that combine to the overall creep mechanism. Some of the reported results were published previously [12, 13]. The main microstructural features of the creep deformation process are (i) ordinary dislocation plasticity, (ii) mechanical twinning and (iii) dynamic recrystallization.

During primary and secondary creep, the density of superdislocations remains constant while ordinary dislocation density increases in the γ-phase with increasing strain [14]. In agreement with other studies (e.g. [1, 5]), it was found that the majority of dislocations observed are ordinary dislocations. An example is given in Fig. 2, which shows two TEM bright field images of a γ-grain after creep under two different diffraction conditions. Fig. 2a was taken with $\mathbf{g} = 002$ and only a few dislocations are present. Fig. 2b was taken with $\mathbf{g} = 020$ and a considerable number of dislocations is visible. However, the majority of dislocations is invisible with $\mathbf{g} = 002$ and are therefore ordinary dislocations with $\mathbf{b}_o = 1/2 <110]$. It is important to note that ordinary dislocations do not provide any deformation in c-direction (cf. Fig. 1).

(a) (b)

Fig. 2: TEM bright field images of a γ-grain after creep (750 °C/204 MPa/2 %) (a) $\mathbf{g} = 002$ and (b) $\mathbf{g} = 020$. The majority of dislocations are ordinary dislocations with $\mathbf{b}_o = 1/2 <110]$.

Early studies on γ-TiAl already reported that mechanical twins (or deformation twins) are formed during plastic deformation [15, 16]. Mechanical twinning was identified to be an important

deformation mechanism during creep as well. However, traditional creep theories do not take into account any contribution by mechanical twinning to the creep deformation process. Mechanical twinning contributes from the beginning on in the γ-phase, both in the equiaxed grains as well as in the γ-lamellae [13]. Quantitative image analysis on SEM micrographs revealed that mechanical twinning occurs in the γ-phase already after loading and at stresses as low as 150 MPa. Fig. 3 shows that the fraction of twinned γ-grains increases with increasing stress and strain. After fracture, more than 50 % of the γ-grains were found to have twins but only part of the grains are favorably oriented for twinning since the texture in the studied material is random and, therefore, grain orientations are statistically distributed.

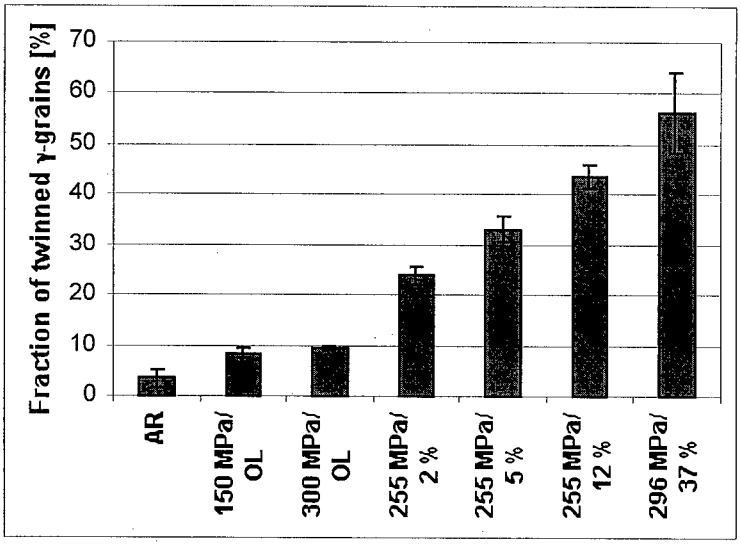

Fig. 3: Volume fraction of twinned γ-grains in the as received state (AR), after loading (OL) and after creep deformation at 750 °C.

Fig. 4 shows the results of a quantitative analysis of both grain types. The interface spacing of the lamellar grains decreases significantly already after small creep strains (0.3 %) but remains almost constant during further deformation [13]. In contrast to the lamellar spacing, the twin spacing of the γ-grains continuously decreases with increasing stress and strain. The early formation of mechanical twins shows that this deformation mode contributes to creep from the beginning on. Obviously, mechanical twinning is an easy deformation mode in γ-TiAl favored by the low intrinsic stacking fault energy [17, 18].

Further quantitative image analysis on SEM micrographs proved that the grain size of the γ-grains changed during creep [12]. The grain size is not affected by small strains (2 %) as compared to the as received condition (AR). Creep strains of 5 % or higher result in a shift towards smaller grain sizes, which implies that dynamic recrystallization occurred during creep. TEM results indicate that the first small dislocation free grains are present already after 2 % strain. More and more such grains form as strain increases and these dynamically recrystallized grains undergo plastic deformation during subsequent deformation. Dynamic recrystallization starts at high angle grain boundaries, which impede dislocation motion and deformation twinning. High stress concentrations result in these regions which represent locations where the new grains form. Dynamic

recrystallization (rather than recovery processes with subgrain formation) is favored in γ-TiAl due to its low stacking fault energy [19].

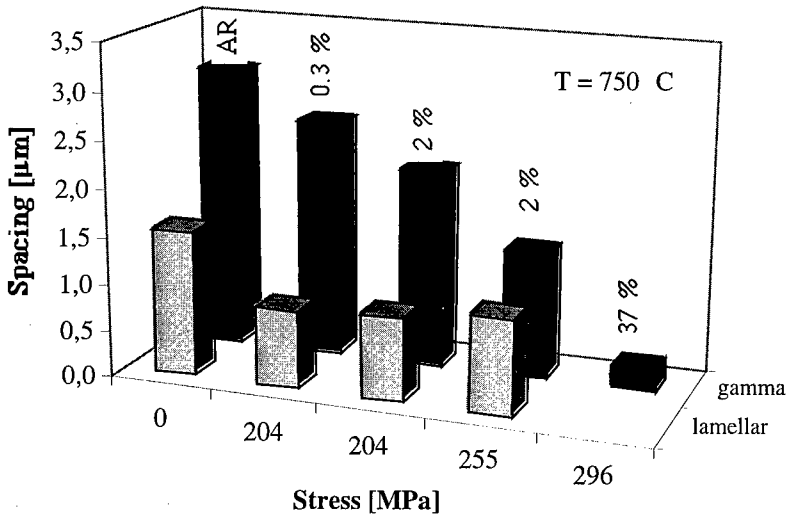

Fig. 4: Mean interface spacing of lamellar grains and mean twin spacing of γ-grains before (AR) and after creep deformation at 750 °C.

The microstructural results suggest that ordinary dislocation activity and mechanical twinning jointly control primary creep. From the fact that mechanical twinning is already observed from the beginning on, it is concluded that this deformation mechanism is equally important in early plastic creep deformation as ordinary dislocation mobility. Both processes are driven by the intensity of the resolved shear stress in individual γ-grains and -lamellae.

It is important to note that ordinary dislocations with $\mathbf{b}_o = 1/2 <110]$ do not provide any deformation in [001] direction (see Fig. 1). When only ordinary dislocations contribute to deformation, elastic incompatibilities arise due to the absence of plastic deformation in c-direction, which result in back stresses. Superdislocations, which would provide strain in [001] direction, were only rarely observed. However, Fig. 5 reveals that mechanical twinning does contribute to deformation in c-direction and it can be easily shown that it results in a shortening of the γ-crystal in [001]-direction [20]. Therefore, mechanical twinning can reduce the back stresses caused by ordinary dislocations. On the other hand, deformation twins also build up local elastic constraints at grain boundaries and twin intersections, which in turn provide driving forces for ordinary dislocations.

If only one of these two processes is active in a grain (due to its orientation with respect to the external creep stress), back stresses quickly increase and are reduced as the second process starts to contribute. However, it has been shown by Mecking et al. [10] that the von Mises criterion, which requires five independent slip systems for the accommodation of strain, is not satisfied by the contribution of ordinary dislocations and mechanical twinning. Based on microstructural results it is suggested that dynamic recrystallization is the third process which contributes to creep deformation: it decreases the overall dislocation density when the new grains are formed and, consequently, the back stresses due to ordinary dislocations are reduced. Besides, new grains might be formed in orientations, which are favorably oriented for plastic deformation in directions that are required to allow for homogeneous macroscopic deformation. Currently, texture measurements are being carried out to identify the recrystallization texture established during dynamic recrystallization. It is

expected that the results will provide information with respect to the orientation of the newly formed γ-grains.

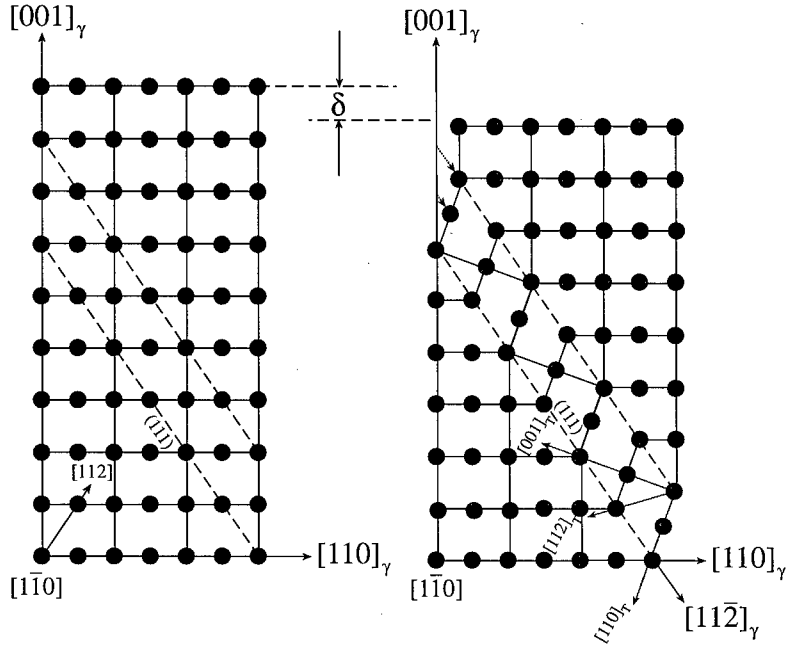

Fig. 5: (a) Parent γ-crystal cut through the (1$\bar{1}$0) plane. Dashed lines mark the (111)-twinning plane. (b) γ-crystal with (111)[11$\bar{2}$] deformation twin. The original γ-crystal is shortened by the amount of δ in c-direction [001] and lengthened in [110] direction.

The mechanical data published elsewhere [11] showed that the strain rate rapidly decreases during primary creep until a creep rate minimum is reached between 1 to 2 % strain. In contrast to model materials, near-γ TiAl does not exhibit a wide secondary creep regime with constant creep rate. The creep rate rather slowly increases again when the minimum is exceeded. Necking is not observed in this stage of deformation. Later on, the creep rate quickly increases and necking takes place at about 10 % strain. The results provided by microstructural analysis of the duplex near-γ TiAl-alloy suggest that the decrease of the strain rate in the primary regime is accompanied by an increase of ordinary dislocation density and the formation of deformation twins. High stress concentrations arise at high angle grain boundaries, which represent obstacles to dislocations and to deformation twins. Both deformation modes are associated with macroscopic and microscopic back stresses and influence the strain rate. When the creep rate minimum is reached dynamic recrystallization starts at these locations of high stress concentrations and begins to contribute to creep as a third mechanism. As a consequence, the minimum creep rate increases again. During the early stages of the tertiary creep regime, the volume fraction of recrystallized grains grows and causes the creep rate to further increase. Later on during creep life, the creep rate accelerates due to necking and formation of voids.

Summary and Conclusion

Microstructural results were presented and discussed with respect to the creep deformation mechanism in a duplex near-γ TiAl-alloy. The following conclusions were drawn:

- Ordinary dislocation plasticity and mechanical twinning contribute to creep from the beginning on. Both deformation modes build up back stresses due to incompatibility strains.
- Superdislocations are only infrequently observed and, therefore, do not reduce strain incompatibilities.
- Dynamic recrystallization contributes to plastic deformation: (i) by decreasing the dislocation density and, therefore, back stresses due to incompatibility strains and (ii) possibly by providing grains in those orientation which allow plastic deformation in directions that are needed for homogeneous macroscopic deformation.
- These three elementary processes (i) movement of ordinary dislocations, (ii) mechanical twinning, and (iii) dynamic recrystallization are coupled and govern the overall creep rate.

Acknowledgement

This work was supported by MTU (Motoren- und Turbinen-Union München GmbH) who also supplied the TiAl material. The author also appreciates funding in the framework of the European research project COST 513. Thanks are due to T. Rudolf who contributed microstructural results and to G. Eggeler for fruitful discussion.

References

[1] F. Appel, R. Wagner, Mater. Sci. Eng. R22 (1998) 187 – 268
[2] J. Beddoes, W. Wallace, L. Zhao, Int. Mater. Rev. 40 (1995) 197 – 217
[3] L. M. Hsiung, T. G. Nieh, Mater. Sci. Eng. A239-240 (1997) 438 – 444
[4] M. Lu, K. J. Hemker, Acta mater. 45 (1997) 3573 – 3585
[5] M. A. Morris, M. Leboeuf, J. Mater. Res. 13 (1998) 1 - 15
[6] M. A. Morris, T. I. Lipe, Intermetallics 5 (1997) 329 – 337
[7] D. Y. Seo, T. R. Bieler, S. U. An, D. E. Larsen, Met. Mater. Trans. 29A (1998) 89 – 98
[8] B. Viguier, et al., Phil. Mag. A 71 (1995) 1295 - 1312
[9] M. Yamaguchi, Y. Umakoshi, Prog. Mat. Sci. 14 (1990) 1 - 148
[10] H. Mecking, C. Hartig, U. F. Kocks, Acta mater. 44 (1996) 1309 – 1321
[11] B. Skrotzki, T. Rudolf, G. Eggeler, Z. Metallkde (1999) (in print)
[12] B. Skrotzki, T. Rudolf, A. Dlouhy, G. Eggeler, Scripta mater. 39 (1998) 1545 - 1551
[13] B. Skrotzki, M. Ünal, G. Eggeler, Scripta mater. 39 (1998)1023 – 1029
[14] T. Rudolf, B. Skrotzki, G. Eggeler, unpublished results
[15] D. Shechtman, M. J. Blackburn, H. A. Lipsitt, H. A., Metall. Trans. 5 (1974) 1373 - 1381
[16] H. A. Lipsitt, D. Shechtman, R. E. Schafrik, Metall. Trans. 6A (1975) 1991 - 1996
[17] C. L. Fu, M. H. Yoo, Scripta mater. 37 (1997) 1453 - 1459
[18] G. Hug, A. Loiseau, P. Veyssière, Phil. Mag. A 57 (1998) 499 – 523
[19] F. J. Humphreys, M. Hatherly, Recrystallization and Related Annealing Phenomena, Elsevier Science Ltd., Oxford, UK (1995)
[29] B. Skrotzki, unpublished results

Correspondence to:
E-mail: birgit.skrotzki@ruhr-uni-bochum.de; Fax: ++49-234-7094-235

Key Engineering Materials Vols. 171-174 (2000) pp. 709-716
© 2000 Trans Tech Publications, Switzerland

Creep Deformation of Polysynthetically Twinned (PST) Ti-48mol%Al

G. Wegmann[1], T. Suda[2] and K. Maruyama[2]

[1] GKSS Research Centre, Institute for Materials Research,
Max-Planck-Straße, DE-21452 Geesthacht, Germany

[2] Department of Materials Science, Graduate School of Engineering, Tohoku University,
Aobayama 02, Sendai 980-8579, Japan

Keywords: Titanium Aluminides, High Temperature, Fully Lamellar Structure, PST Crystal, Creep Rate, Creep Resistance, Orientation, Schmid Factor, Twinning

Abstract To investigate the influence of the orientation of the lamellar plates, present in two-phase ($\alpha_2+\gamma$) Ti-Al alloys, on the creep resistance, four orientation variants of a PST crystal of the nominal composition Ti-48mol%Al were deformed in compression for different applied stresses at 1150 K. When the angle of the lamellar interfaces with respect to the compression axis is denoted as ϕ, the investigated variants were A (ϕ=0°), B1 (ϕ=35°), B2 (ϕ=55°), and N (ϕ=90°). The soft orientation variant B1 featured normal creep behavior, however, in the case of the soft orientation variant B2 no tertiary creep was encountered within strains up to 0.15. This basically different behavior under creep condition was attributed to the rotation of the PST crystal with strain. The orientation variant B1 rotates towards the softer 45° orientation, whereas the orientation variant B2 rotates towards the hard orientation N. The rotational hardening in the case of orientation B2 explains the absence of tertiary creep. The hard PST orientations revealed an entirely different behavior with distinct creep rate minima at plastic strains around 0.02-0.03. The lowest minimum creep rates and longest creep lives at all investigated stresses were given by orientation variant N. This is to be understood on the basis of the resolved shear stress criterion. The Schmid factors for the orientation variant N are in all six domains lower than in the other hard orientation variant A. The soft orientations revealed a transition stress near 200 MPa. For the low stress regime a high stress exponent of about 9 was evaluated but for the high stress regime the stress exponent equals unity. The hard PST orientations exhibit for all considered stresses a constant stress exponent of 7.3. The low stress exponent for the soft orientations at high stresses was ascribed to microstructural instability in the consequence of mechanical twinning parallel to the lamellar interfaces, which becomes significant for stresses higher than 200 MPa.

1 Introduction

Titanium aluminides have received great attention as a new light-weight material for structural applications because of their attractive properties such as low density, relatively high melting temperature, strength, and modulus retention with temperature [1]. Since two-phase TiAl/Ti_3Al alloys exhibit better ductility and toughness than single-phase TiAl alloys the main interest concentrates on two-phase materials. The prospective usage of these materials is in aircraft gas turbines, e.g. turbine blades. One of the primary requirements for this application is a high creep resistance at elevated temperatures. By controlling thermomechanical processing and subsequent heat treatment, four types of microstructures can be produced: fully lamellar, near lamellar, duplex and near gamma. Lamellar microstructures with colonies composed of the stacking of parallel aligned α_2 and twin related γ lamellae are considered as the most favorable for forthcoming applications owing to their higher strength and creep resistance [2-8]. The γ phase forms with the particular crystallographic orientation

relationship during cooling from the α single phase field: $\{111\}_\gamma // (0001)_{\alpha 2}$ and $\langle 1\bar{1}0\rangle_\gamma // \langle 11\bar{2}0\rangle_{\alpha 2}$ known as the Blackburn relationship [9]. The lamellar interface is given by $(111)_\gamma$. Due to the slight tetragonality of the $L1_0$-structure of TiAl the $\langle 1\bar{1}0\rangle$ directions are not equivalent and three domains exist rotated about the [111] axis by multiples of 120° within the matrix and the twinned lamellae. The basic understanding of the deformation characteristics of the lamellar microstructure has been substantially pushed forward by the research work of Yamaguchi and his co-workers using a fundamental unit of the lamellar structure without grain boundaries, namely polysynthetically twinned (PST) crystals [10-18]. Many important aspects of the deformation characteristics of the lamellar α_2/γ structure have been successfully worked out at a large range of temperatures up to 1273 K, but the mechanical behavior of a PST crystal under creep condition has not been addressed so far.

2 Experimental procedures

The material used in this study was an as-grown polysynthetically twinned (PST) Ti-Al crystal, which was fabricated with a growth rate of 1.4×10^{-3} mms^{-1} by Kyoto University, Japan. The nominal composition is binary Ti-48mol%Al. Details of the crystal growing process are described elsewhere [10]. This PST crystal was oriented using a Laue camera equipped with a two-axis goniometer. Parallelepipeds of the average size of $2 \times 2 \times 3$ mm^3 were cut with a diamond saw.

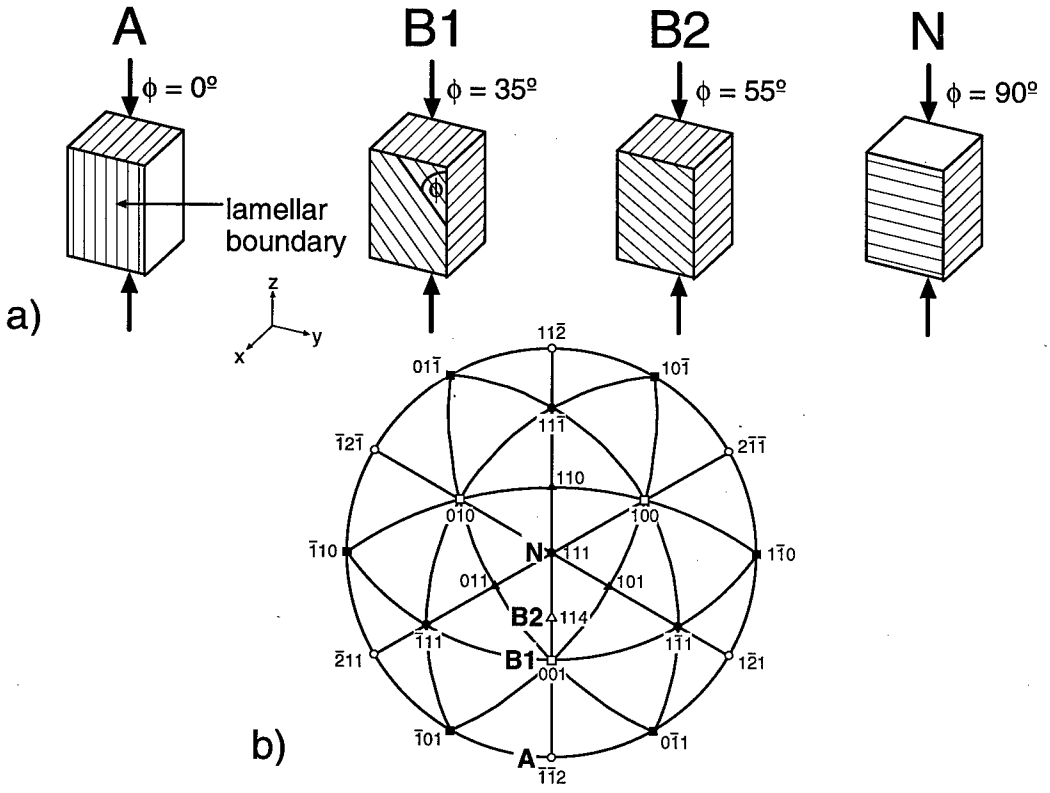

Fig. 1 Illustration of four orientation variants of the PST specimens. a) specimen sketches, b) position of the compression axes in the (111) stereographic standard projection of the γ phase.

Before application of the creep load the specimens were held at the creep testing temperature for in average 7.2×10^3s in order to have a stable elongation signal. The creep tests were terminated after different strains, e.g. in the primary creep regime, in the creep rate minimum, or in the tertiary creep regime. The specimens were cooled down to room temperature at an initial cooling rate of 0.25 Ks^{-1} under full load in order to retain the deformation microstructure.

Four orientation variants were studied with different angles ϕ as illustrated in Fig. 1, i.e. 0° (orientation A), 35° (orientation B1) 55° (orientation B2), and 90° (orientation N). The angle ϕ denotes the angle of the lamellar plates with respect to the compression axis about the x-axis parallel to $\langle 11\bar{2}0\rangle$. According to the work of Inui et al. [16] and Kishida et al. [18] the compression axes are indicated with respect to the six domains of the γ phase as shown in Table 1. The testing temperature of 1150 K was always kept constant within ±1 K. The creep tests were carried out in an argon atmosphere to protect the specimens against oxidation.

Table 1: Miller Indices of the compression axes in each domain of the γ phase

Orientation	Miller Indices					
	I Matrix	I Twin	II Matrix	II Twin	III Matrix	III Twin
A	$\bar{1}\bar{1}2$	$11\bar{2}$	$\bar{1}2\bar{1}$	$1\bar{2}1$	$2\bar{1}\bar{1}$	$\bar{2}11$
B1	001	$22\bar{1}$	010	$2\bar{1}2$	100	$\bar{1}22$
B2	114	110	141	101	411	011
N	111	111	111	111	111	111

3 Results

The creep curves of the two soft PST orientations B1 and B2 for various applied stresses are displayed in Fig. 2a and Fig. 3a, respectively. It can be seen that for the soft orientation B1 with the angle ϕ of 35° normal creep behavior was found with the three characteristic regimes: primary creep, a more or less extended stationary regime followed by tertiary creep with an increasing slope of the creep curve (Fig. 2a).

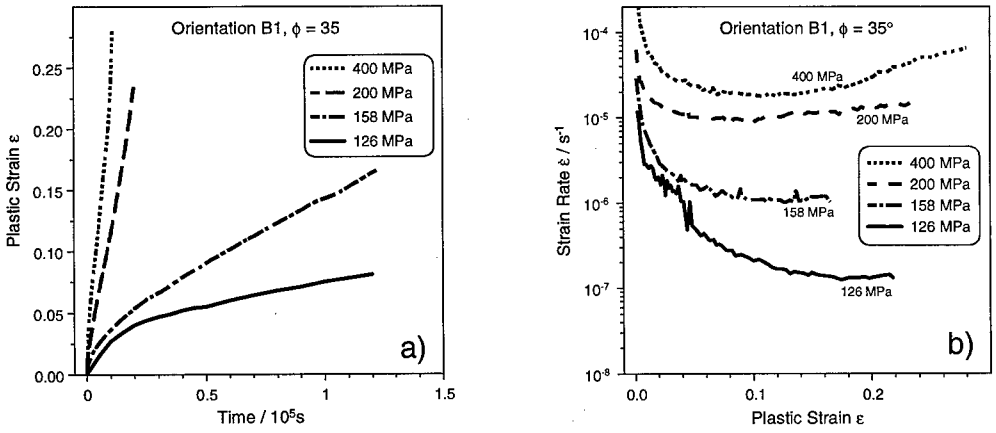

Fig. 2 Effect of the applied stress on the creep behavior of the soft PST orientation B1. a) plastic strain vs. time, b) creep rate vs. plastic strain.

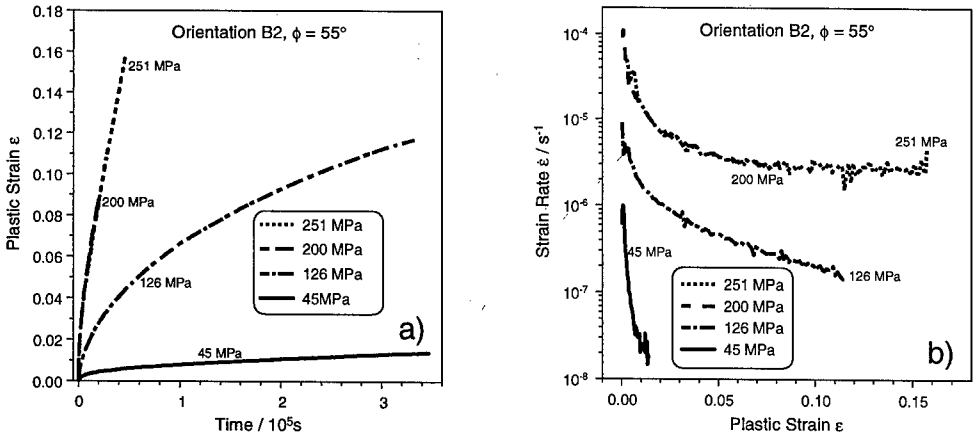

Fig. 3 Effect of the applied stress on the creep behavior of the soft PST orientation B2. a) plastic strain vs. time, b) creep rate vs. plastic strain.

The creep curves for the orientation B2 with the angle ϕ of 55° showed also a primary creep regime, which is connected to a indefinite regime of infinite decreasing slope of the creep curve (Fig. 3a). In contrast to the observation of a distinct tertiary regime for all specimens of the orientation B1 no tertiary regime was observed for none of the 4 creep specimens of the orientation B2 at least up to the termination strains used for these creep tests.

When comparing the function of the strain rate plotted versus the plastic strain of the two soft orientation variants the basic difference is more clearly visible (Fig. 2b and Fig. 3b). Whereas all creep specimens of the orientation B1 for all investigated stresses show at least a slight increase of the strain rate after passing through a stationary regime (Fig. 2b), no such tertiary creep acceleration is to be observed for none of the investigated specimens of the orientation B2 irrespective of the plastic strain at the termination point of the particular creep experiment (Fig. 3b). For the stresses of 126, 200 and 251 MPa (orientation B2) the strain rate becomes nearly a linear function of the plastic strain with a negative or almost zero slope. The creep experiment at a stress of 45 MPa was definitely terminated to early in the primary creep regime so that no statement about the development of the strain rate at higher strains can be provided.

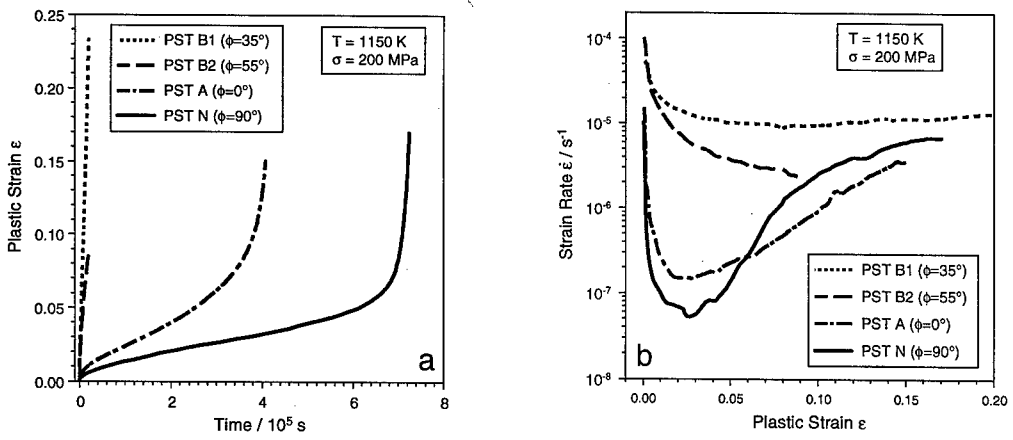

Fig. 4 Effect of the lamellar orientation on the creep behavior for the applied stress of 200 MPa. a) plastic strain vs. time, b) creep rate vs. plastic strain.

An entirely different creep behavior of the hard PST orientations A and N was observed. Fig. 4 shows the effect of the lamellar orientation on the creep behavior in terms of the creep curves (Fig. 4a) and the strain rate versus the plastic strain (Fig. 4b) for the applied stress of 200 MPa. In contrast to the creep behavior of the soft orientations described in the forehand both hard PST orientations exhibit distinct creep rate minima at relatively low plastic strains around 0.02-0.03. After passing through the minima sharp creep rate accelerations follow, which is even more pronounced for the orientation N than for the orientation A. The lowest minimum creep rates were measured for the orientation N (Fig. 5). The orientation A shows minimum creep rates that are about twice of that of the orientation N.

When plotting the minimum or stationary strain rate versus the applied stress, shown in Fig. 5, two regimes are to be distinguished for the soft orientations. For low stresses up to 200 MPa a high stress exponent of 9.1 was evaluated. In the case of the orientation B2 no real minimum creep rates were measured. However, the strain rates at the termination point were probably close to the final minimum creep rate in the case of the high stresses 200 and 251 MPa (cf. Fig. 3b), but the strain rate at the termination point was probably less close to the final minimum creep rate in the case of the low stress of 126 MPa. This fact is reflected by the arrow downwards for the data point at 126 MPa for orientation B2 in Fig. 5. In the consequence of a lack of successful experiments in the case of orientation B2 only a lower limit for the stress exponent for low stresses up to 200 MPa of 6.2 can be stated at the present time of knowledge. Nevertheless, the presented data supports the view that both soft orientations show a similar transition stress of about 200 MPa. At high stresses above 200 MPa stress exponents near unity were evaluated. The hard PST orientations A and N exhibit both a stress exponent of 7.3 for the investigated stresses above 200 MPa.

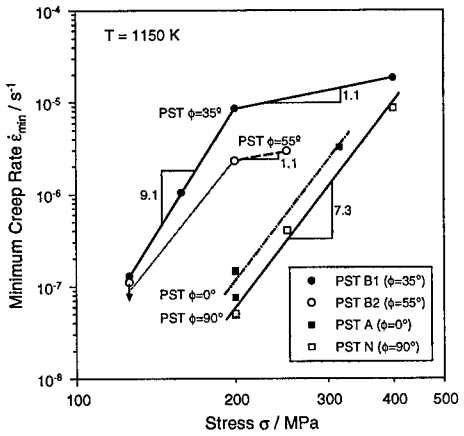

Fig. 5 Effect of the applied stress on the minimum creep rate at 1150 K for the different considered lamellar orientations.

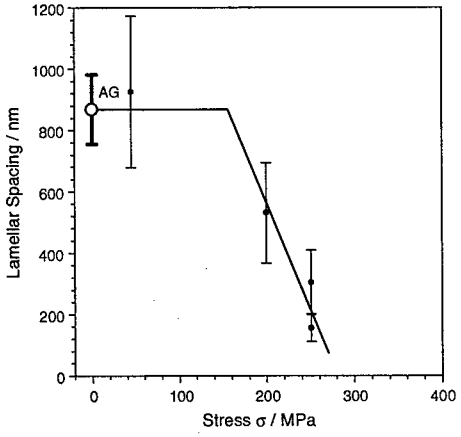

Fig. 6 Dependence of the lamellar spacing on the applied stress for soft PST orientations. The error bars mark the 95% confidence interval. AG: As grown condition. Data taken from [22].

4 Discussion

The effect of the lamellar orientation on the creep resistance is discussed on the basis of the resolved shear stress, which is given by the product of the Schmid factor and the applied stress. Since the γ phase is considerably weaker than the α_2 phase at high temperatures the creep resistance is expected to be controlled by the deformation of the γ constituent. Slip systems with a lattice translation vector

contained in the (111) lamellar plane are regarded to as soft modes and slip systems with a lattice translation vector contained in a glide plane inclined to the lamellar interfaces are regarded to as hard modes in accordance to the work of Inui et al. [16] and Kishida et al. [18]. The creep experiments with the applied stress of 200 MPa (cf. Fig. 4) show that the hard PST orientations exhibit substantially longer creep lives than the soft PST orientations. The pronounced orientation effect is easily understandable due to the high Schmid factors for soft slip modes in four of the six γ domains and for the soft parallel twinning mode in all γ domains in the case of the soft PST orientations [19]. In contrast to the soft PST orientations the hard PST orientations do not have any resolved shear stress on any of the soft deformation modes. In a previous study we demonstrated by TEM observations that the deformation structures of soft PST orientations are dominated by soft deformation modes and that the deformation structures of the hard PST orientations are dominated by hard slip systems inclined to the lamellar interfaces and by cross twinning [19].

Table 2: Maximum Schmid factors for the two soft orientations in all existing domains. Ordinary dislocation slip, superdislocation slip, and twinning systems are analyzed.

Orientation	I Matrix	I Twin	II Matrix	II Twin	III Matrix	III Twin
B1, 35°	0.471	0.471	0.408	0.408	0.408	0.408
B2, 55°	0.471	0.471	0.454	0.408	0.454	0.408

In contrast to the expectations derived from the Schmid factors the soft orientation B2 appears harder than the orientation B1 for the investigated creep conditions. When considering the maximum Schmid factor as the governing criterion for the strength of a particular orientation variant (Table 2), the orientation B2 should be slightly softer than the orientation B1 since the matrix domains II and III offer higher Schmid factors with 0.454 than the matrix domains of the orientation B1 with 0.408. The matrix domain I and the twin domains of both orientation variants have identical maximum Schmid factors. In the very early state of creep at low stains (< 0.005) the maximum Schmid factor criterion holds and the orientations B1 and B2 show a similar creep behavior (cf. Fig. 4b). But with increasing strain the orientation B2 exhibits an increasingly higher creep resistance compared with the orientation B1. This unexpected behavior is associated with the crystal rotation. During creep deformation the orientation B1 is rotating about the $[1\bar{1}0]$ axis in the direction of a 45° orientation, and the orientation B2 is rotating towards the hard orientation N. The Schmid factors for the dominating soft deformation modes are increasing in the case of orientation B1, whereas they are decreasing in the case of orientation B2 (rotational hardening). In the consequence of this, the specimen of the orientation B1 becomes weaker in the course of creep deformation, but the specimen of the orientation B2 becomes harder. The decreasing Schmid factors in the orientation B2 result in a higher creep resistance. In addition to that, the continuous hardening of the orientation B2 in the course of deformation is responsible for the difficulty to establish a stationary or a minimum creep rate (cf. paragraph 3).

The stress exponents for the soft PST orientations below 200 MPa and for the hard PST orientations are significantly higher than 4-5, which in general indicates a climb controlled creep mechanism. A possible explanation for the high stress exponents of 9.1 and 7.3 is the existence of a threshold stress due to the abundance of the lamellar interfaces in accordance to the concept of Gibeling and Nix [20]. The remarkably low stress exponent of 1.1 for the soft orientations at applied stresses above 200 MPa can be attributed to the microstructural instability of the PST specimens during creep at 1150 K. A stress exponent in the range of unity is usually associated with diffusion controlled creep mechanisms [21], which are certainly not the rate controlling mechanisms for the soft PST orientations at the considered conditions. In a previous study [22] we were able to demonstrate that the

lamellar microstructure is considerably modified during creep deformation owing to the mechanism of parallel twinning. Severe parallel twinning took place during creep with applied stresses above 200 MPa in the soft orientations. By the parallel twinning activity the lamellar spacing was particularly reduced from 868nm in the undeformed condition to 304nm after creep deformation in the case of the specimen of orientation B2 tested with 251 MPa. As shown in Fig. 6 the reduction of the lamellar spacing that is brought about by parallel twinning is greatly increased with increasing applied stress for high stresses, at least above 200 MPa. Not only by the research work of the co-author's laboratory [23] but also by other groups [24-26] it is well accepted that the creep resistance is enhanced by a reduction of the lamellar spacing. The mechanical twinning parallel to the lamellar interfaces strengthens the lamellar structure of a soft orientation in the course of creep. The strengthening effect becomes more pronounced with increasing applied stress, which results in the evaluated stress exponent of about 1.1.

The observation of a transition stress for the stress exponent of the soft PST orientations may suggest a critical stress for the occurrence of parallel twinning. Even though the number of data points in Fig. 6 is too low to establish an exact amount of the proposed critical stress, the existence of such a critical stress is supported by the lamellar spacing data. Such a critical stress for parallel twinning would rationalize the observed transition from a high stress exponent at low stresses to a low stress exponent at high stresses in the case of the soft orientations. The activity of parallel twinning in the hard PST orientations was much less than in the soft orientations, what can be understood by the absence of a resolved shear stress for this deformation mode in the hard PST orientations. Therefore, only a moderate microstructural modification in terms of a lamellar refinement was encountered in the hard PST orientations, which obviously did not reduce the stress exponent as severe as in the case of the soft PST orientations.

5 Conclusions

1. PST orientations with their lamellae parallel (A) or perpendicular (N) to the compression axis show higher creep lives and lower minimum creep rates than soft oriented PST specimens. The hard PST orientations deform mainly by hard deformation modes oblique to the lamellar interfaces, whereas the soft orientation deform by slip and twinning parallel to the lamellar interfaces in accordance to the resolved shear stress criterion for the operative deformation modes.
2. The higher creep resistance of the soft orientation B2 compared with the orientation B1 was interpreted as the result of the crystal rotation that takes place during creep deformation. The specimens of the orientation B1 rotate towards a softer 45° orientation and the orientation B2 rotates towards the hard orientation N.
3. A remarkably low stress exponent value for the soft PST orientations was evaluated for high applied stresses above 200 MPa. This was interpreted as the result of microstructural instability during creep at 1150 K due to mechanical twinning parallel to the lamellar interfaces, which leads to a lamellar refinement and self-strengthening of the lamellar structure in the course of creep deformation. A critical stress (≈200 MPa) for the operation of parallel twinning is proposed, which would explain the transition from a high stress exponent of 9.1 at low stresses (< 200 MPa) to a low stress exponent near unity at high stresses.

Acknowledgments

This work was supported by JSPS (No. JSPS-RFTF96R12301) and by the Ministry of Education, Science, Sports and Culture, Japan (No.08455313). The PST crystals used for this research were kindly provided by Prof. Yamaguchi, Kyoto University, Japan.

References

[1] Y.-W. Kim, JOM, 46 (1994), p. 30.

[2] C.T. Liu, J.H. Schneibel, J.L. Wright and D.S. Easton, Intermetallics, 4 (1996), p. 429.

[3] P.J. Maziasz and C.T. Liu, Metall. Mater. Trans. A, 29 (1998), p. 105.

[4] C.T. Liu and P.J. Maziasz, Intermetallics, 6 (1998), p. 653.

[5] B.D. Worth, J.W. Jones and J.E. Allison, in Gamma Titanium Aluminides, ed. Y.-W. Kim, R. Wagner and M. Yamaguchi, TMS, Warrendale, PA, USA (1995), p. 931.

[6] B. D. Worth, J.W. Jones and J.E. Allison, Metall. Mater. Trans A, 26 (1995), p. 2947.

[7] M. Es-Souni, A. Bartels and R. Wagner, Acta metall. mater., 43 (1995), p. 153.

[8] M.A. Morris and T. Lipe, Intermetallics, 5 (1997), p. 329.

[9] M.J. Blackburn, The Science and Technology and Application of Titanium, eds. R.T. Jaffe and N. Promisel, Pergamon, Oxford (1970), p. 633.

[10] T. Fujiwara, A. Nakamura, M. Hosomi, S.R. Nishitani, Y. Shirai and M. Yamaguchi, Phil. Mag. A, 61 (1990), p. 591.

[11] H. Inui, M.H. Oh, A. Nakamura and M. Yamaguchi, Phil. Mag. A, 66 (1992), p. 539.

[12] H. Inui, M.H. Oh, A. Nakamura and M. Yamaguchi, Phil. Mag. A, 66 (1992), p. 557.

[13] H. Inui, M.H. Oh, A. Nakamura and M. Yamaguchi, Acta Metall. Mater., 40 (1992), p. 3095.

[14] M. Yamaguchi and H. Inui, in: Structural Intermetallics 1993, eds. R. Darolia, J.J. Lewandowski, C.T. Liu, P.L. Martin, D.B. Miracle and M.V. Nathal, TMS, Warrendale, PA, USA (1993), p. 127.

[15] K.-F. Yao, H. Inui, K. Kishida and M. Yamaguchi, Acta metall. mater., 43 (1995), p. 1075.

[16] H. Inui, K. Kishida, M. Misaki, M. Kobayashi, Y. Shirai and M. Yamaguchi, Phil. Mag. A, 72 (1995), p. 1609.

[17] H. Umeda, K. Kishida, H. Inui and M. Yamaguchi, Mater. Sci. Eng. A, 239-240 (1997), p. 336.

[18] K. Kishida, H. Inui and M. Yamaguchi, Phil. Mag. A, 78 (1998), p. 1.

[19] G. Wegmann, T. Suda and K. Maruyama, Intermetallics, submitted for publication.

[20] J.C. Gibeling and W.D. Nix., Mater. Sci. Eng. A, 45 (1980), p. 123.

[21] J. Cadek, Creep in Metallic Materials, Elsevier, Amsterdam, Oxford, New York, Tokyo (1988), p. 205.

[22] G. Wegmann and K. Maruyama, Phil. Mag. A, accepted for publication.

[23] K. Maruyama, R. Yamamoto, H. Nakakuki and N. Fujitsuna, Mater. Sci. Eng. A 239-240 (1997), p. 419.

[24] T.A. Parthasarathy, M. Keller and M.G. Mendiratta, Scr. Mater., 38 (1998), p. 1025.

[25] J. Beddoes, L. Zhao, P. Au, D. Dudzinski, and J. Triantafillou, in: Structural Intermetallics 1997, eds. M.V Nathal, R. Darolia, C.T. Liu, P.L. Martin, D.B. Miracle, R. Wagner and M. Yamaguchi, TMS, Warrendale, PA, USA (1997), p. 109.

[26] W.R. Chen, J. Triantafillou, J. Beddoes and L. Zhao, Intermetallics, 7 (1999), p. 171.

Corresponding author: Dr. Gerhard Wegmann, GKSS Research Centre, Institute for Materials Research, Max-Planck-Straße, 21452 Geesthacht, GERMANY, phone: 0049-4152-87-2597, fax: 0049-4152-87-2595, e-mail: gerhard.wegmann@gkss.de

Key Engineering Materials Vols. 171-174 (2000) pp. 717-724
© 2000 Trans Tech Publications, Switzerland

Effect of Lamellar Spacing on Creep Strength of Ti-42mol%Al Alloy with Fully Lamellar Structure

R. Yamamoto[2], K. Mizoguchi[1] and K. Maruyama[1]

[1] Department of Materials Science, Graduate School of Engineering, Tohoku University Aoba-yama 02, Sendai 980-8579, Japan

[2] Graduate Student, now with Mitsubishi Heavy Industries, Ltd., 2-1-1 Shinhama Arai-cho, Takasago, Hyogo Prefecture 676-8686, Japan

Keywords: Titanium Aluminide, High Temperatured Creep, Lamellar Structure, Acceleration Creep

Abstract

High temperature creep of a binary Ti-42mol%Al alloy with a fully lamellar structure was studied in order to clarify the effects of lamellar spacing on creep strength. Specimens having three different values of lamellar spacing (0.1, 0.25, and 1.5 μm) were prepared by changing the cooling process after the solution treatment. All the specimens had the same grain size of 180 μm. Creep tests were carried out at 1100 K and 1200 K under stresses from 60 MPa to 500 MPa.

At high stresses, the decrease of creep rate (strain hardening) in the primary creep stage was more significant in the finer lamellar structure, and creep rate acceleration in the tertiary creep stage was independent of lamellar spacing. Therefore, the creep rate of the lamellar structure decreases with decreasing lamellar spacing, suggesting that a finer lamellar structure is better for improving creep strength. At low stress, on the other hand, the dependence of creep strength on lamellar spacing diminished, since the creep rate acceleration in the tertiary creep stage was substantial in the finer lamellar structure.

Lamellar spacing affects creep strength differently at different stress levels. The strain softening, which is due to microstructural degradation (spheroidization and discontinuous coarsening) of the lamellar structure, is the major cause of the disappearance of the lamellar spacing dependence of creep strength at low stresses.

1. Introduction

TiAl based intermetallic alloys have low specific gravity and good elevated temperature strength. Because of these beneficial properties, they are a candidate for high temperature structural applications [1]. Even for high temperature applications, however, structural materials must also have sufficient ductility at room temperature. To fulfill this requirement, dual phase "TiAl alloys" composed of γTiAl and α_2Ti_3Al phases have attracted the attention of many researchers [2,3]. TiAl alloys take various microstructures depending on their heat treatment. Among these microstructures, a fine grained fully lamellar structure provides a good combination of room temperature ductility and high temperature creep strength [3].

It is known that lamellar spacing has significant effects on high temperature strength. For example, the creep strength of directionally solidified eutectic alloys increases with decreasing lamellar spacing when their lamellar interfaces are aligned parallel to the stress axis [4,5]. The high strength has been explained by enhanced strain hardening of the fine lamellar structure [6-8].

Several inconsistent results have been reported on the creep of fully lamellar TiAl alloys. Lamellar structures usually give a lower creep rate than the constituent single phase materials [8-12]. This result supports the strengthening by the lamellar structure. In a report by Beddos et al. [13], a fine lamellar structure (lamellar spacing, λ = 0.12 μm) of Ti-48mol%Al showed a higher creep strength than a coarse one (λ = 0.45 μm). On the other hand, Jones et al. [14,15] reported that a specimen with intermediate lamellar spacing (λ = 0.12 μm) had the highest creep strength among Ti-48Al-2Nb-2Mn specimens. It is thus necessary to know the cause of the different effects of lamellar spacing on the creep strength of TiAl alloys with fully lamellar structure.

Two kinds of structural change are found in tertiary creep. The first is void or crack formation along grain boundaries and γ/α_2 interfaces [16]. The second is the spheroidization of lamellar plates (small dynamically recrystallized grains) along grain boundaries, which is important because creep rate is known to increase with increasing numbers of spheroidized grains [6]. Though it is clear that both void (crack) formation and spheroidization influence tertiary creep deformation behavior, it is not well known how this influence changes with creep conditions.

In the present paper, effects of lamellar spacing on creep rate are studied with a fully lamellar TiAl alloy over wide ranges of stress and temperature. It is also discussed how and why the effects of lamellar spacing change with stress level based on structural changes during creep.

2. Experimental Procedure

The material studied was a binary Ti-42mol%Al alloy having almost equal volume of γ and α_2 phases. The alloy was arc-melted in a vacuum, and then hot extruded at 1473 K. The reduction of area was 80%. Compression creep specimens, 2 mm×2 mm in cross section and 3 mm in height, were cut from the extruded rod. Their stress axis was parallel to the direction of extrusion. They were annealed in a vacuum at 1500 K for 600 s. This annealing (solution treatment) in the α single phase regime determines the prior α grain size and the subsequent grain size of the fully lamellar structure. All specimens thus had the same grain size of about 180 μm. Lamellar spacing was controlled by a cooling procedure after the annealing. The procedures are listed in Table 1 together with the average lamellar spacing of each specimen. Hereafter, the specimens having the three different lamellar spacings will be referred to as Sp.A, Sp.B and Sp.C. Sp.A was furnace cooled at an initial cooling rate of 0.6 K/s. During the cooling, Sp.B was held for 43.2 ks at 1375 K, a little below the eutectoid temperature. Sp.C was initially furnace cooled to 1450 K and then slowly cooled at 1.7×10^{-3} K/s to make the coarse lamellar spacing. In this paper, the lamellar spacing is taken as the average thickness of each phase lamella, and is the same in both γ and α_2 phases. The grain boundary morphology changes with cooling rate: Sp.A has a smooth grain boundary, Sp.B a wavy grain boundary, and Sp.C a zig-zag grain boundary with a blocky-γ-phase.

Table 1 Heat treatment used for making the different lamellar spacings.

Specimen	Solution treatment	Cooling procedure	Lamellar spacing	Grain size
Sp.A	1500 K, 600 s	Furnace cool	0.1 μm	180 μm
Sp.B	1500 K, 600 s	1375 K, 43.2 ks hold	0.25 μm	180 μm
Sp.C	1500 K, 600 s	0.0017 K/s from 1450 K	1.5 μm	180 μm

Creep tests were carried out in an argon gas atmosphere. Creep stress was kept constant within ±1% deviation. Some creep tests were interrupted to study microstructural changes during creep.

3. Results and Discussion

3.1 Effects of Lamellar Spacing on Creep Rate

Minimum creep rates of the three different lamellar structures are compared in Fig. 1. The stress exponent n decreased with decreasing lamellar spacing: n = 4.5, 4.1, and 3.7 in Sp.A, B and C, respectively. At the high stresses, the fine lamellar spacing gave a lower creep rate, suggesting that the refinement of lamellar spacing was effective in improving creep

strength. At the low stresses, on the other hand, the difference in minimum creep rate diminished.

The activation energies Q for creep rate did not evidently vary among the three lamellar structures: Q = 400, 380, and 420 kJ/mol in SpA, Sp.B and Sp.C, respectively. This finding indicates that the effects of lamellar spacing varied with stress level, but did not change with temperature.

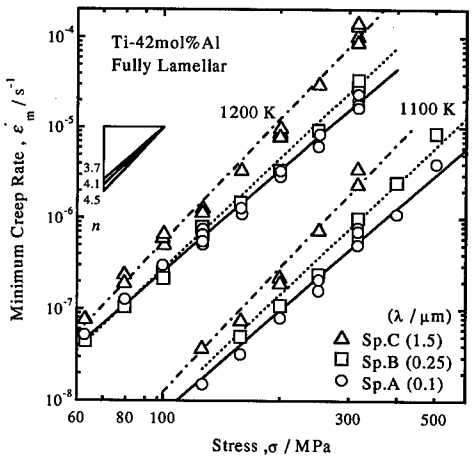

Fig. 1. Comparison of minimum creep rate among Sp.A, B and C (λ:lamellar spacing).

3.2 Cause of the Lamellar Spacing Dependence of Creep Rate

Minimum creep rate is attained by a balance between strain hardening and softening [17]. In primary creep, a decrease of creep rate occurs due to strain hardening, and becomes more significant with the decreasing lamellar spacing, as is the case in directionally solidified eutectic alloys [4,5]. On the other hand, microstructural degradation also takes place during creep, causing a creep rate acceleration in the tertiary creep stage. The extensive degradation makes the creep rate acceleration more remarkable.

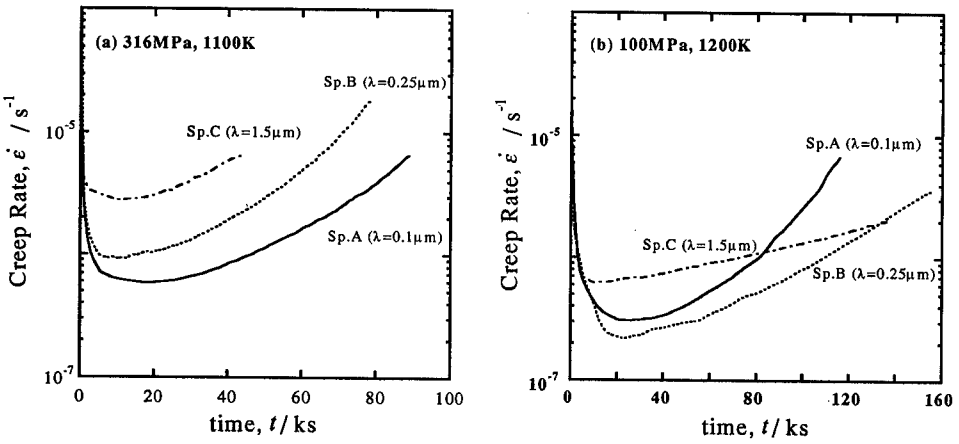

Fig. 2. Representative creep curves of the three different lamellar microstructures. (a) at high stress, and (b) at low stress.

Figure 2 shows representative creep curves of the three lamellar microstructures.

Variation of creep rate during each creep test is drawn as a function of test duration. At the high stress (see Fig. 2(a)), the creep rate acceleration in the tertiary creep stage is similar among the three different lamellar structures. The creep rate deceleration in the primary creep stage becomes more significant as the lamellar spacing decreases. The lower creep rate of the finer lamellar structure can be explained by this structure enhanced strain hardening [6-8].

At the low stress (see Fig. 2(b)), however, the creep acceleration is more significant with decreasing lamellar spacing. This adverse effect of fine lamellae on creep acceleration cancels the beneficial effect on strain hardening. As will be shown in Section 3.3, the rapid acceleration is ascribed to microstructural degradation at the grain boundaries. This degradation is a cause of the lamellar spacing insensitive creep rate and the further increase in creep rate of the fine lamellar microstructure at low stresses.

3.3 Degradation of the Lamellar Structure

Backscattered electron SEM (BS-SEM) micrographs of Sp.A, which was crept at 1200K under 100 MPa to ε=0.051, are shown in Fig. 3, where the dark areas are γ phase and the bright areas are α_2 phase. Before creep, there were no small grains along the grain boundaries. The formation of small grains along grain boundaries is shown Fig. 3(a), and indicates the spheroidization of lamellar plates during high temperature deformation. This spheroidization, which corresponds to a nucleation type of dynamic recrystallization (DRX), has been reported by other researchers [6,18] and has been demonstrated to increase the creep rate of lamellar TiAl alloys [6]. Grains having coarse lamellae can be seen at the grain boundaries in Fig. 3(b). This changing lamellar structure is called discontinuous coarsening (DC), and is often observed after annealing TiAl alloys at high temperature [19]. The discontinuous coarsening is accompanied by migration of grain boundaries and corresponds to a bulging type DRX. The migrating grain boundaries sweep away the dislocations that caused the strain hardening in the primary creep, resulting in the softening of the lamellar microstructure during the tertiary creep.

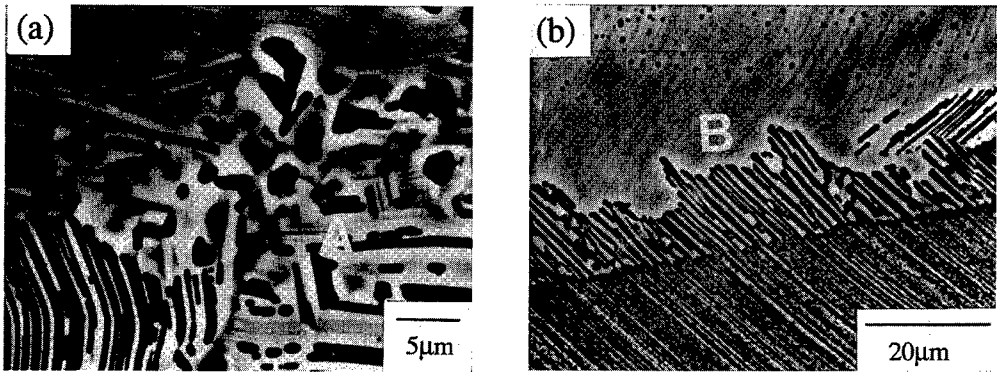

Fig. 3. BS-SEM micrograps of Sp.A crept to 5.1% strain at 1200K under 100MPa.

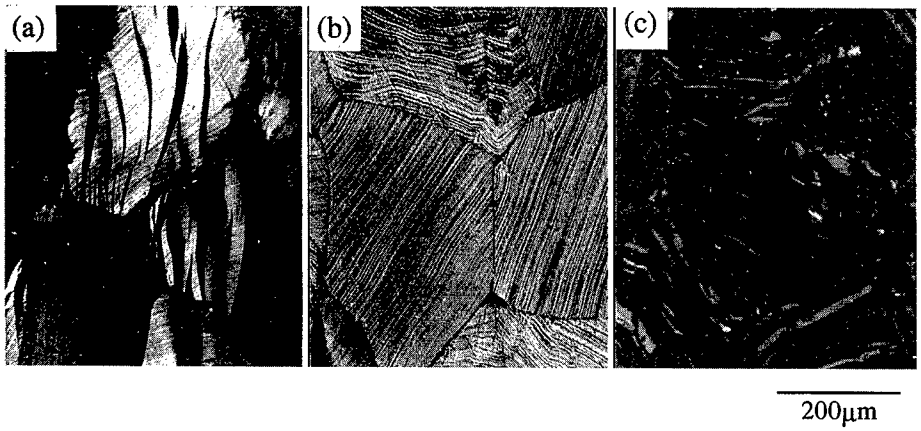

Fig. 4. Optical micrographs of crept specimens; (a) and (b) Sp.A, (c) Sp.C. The specimens were crept to 15% strain at 1200K under (a) and (c) 100MPa, and (b) 316MPa.

Optical micrographs of Sp.A and C after creep tests are shown in Fig. 4. Before creep, there were no small grains along the grain boundaries of Sp.A, but Sp.C had some gamma grains formed during heat treatment. After creep, dynamic recrystallized (DRX) grains (nucleation + bulging types of DRX) were evident in the fine lamellar specimen (Sp.A) at the low stress (Fig. 4(a)). As seen in Fig. 4(b), the microstructural degradation was not so evident at the high stress, even in the fine lamellar specimen. At high stress the spheroidization occurs more frequently, while discontinuous coarsening is dominant at low stress. The microstructural degradation was not seen in the coarse lamellar specimen, Sp.C, even at the low stress (Fig. 4(c)).

The area fraction of DRX region (nucleation + bulging types of DRX) is given in Fig. 5 as a function of creep stress. The fraction is small in all the specimens at high stresses, but increases with decreasing lamellar spacing at low stresses. The prominent DRX of the fine lamellar structure at low stresses was responsible for the rapid creep acceleration and the consequent increase in minimum creep rate of Sp.A at low stress (see Fig. 2(b)). This instability at the grain boundaries was responsible for the increased creep rate of the fine lamellar structure at low stresses. Therefore, in order to utilize the strengthening by a fine lamellar structure, the grain boundaries must be stabilized by some means.

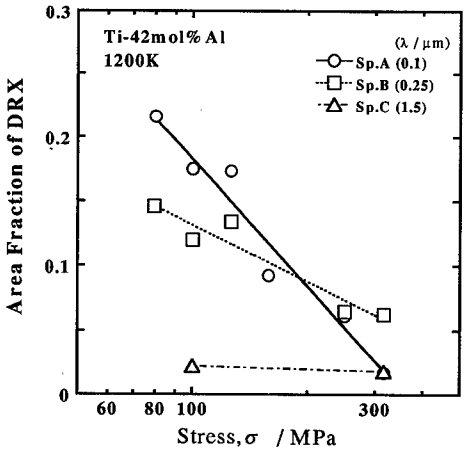

Fig 5. Area fraction of dynamically recrystallized grains after 15% creep deformation at 1200K.

4. Summary

Creep of fully lamellar Ti-42mol%Al with three different lamellar spacings was investigated, and the following results were obtained:

(1) The decrease in strain rate (strain hardening) during the primary creep stage was more significant in the finer lamellar structure. The minimum creep rate of fully lamellar TiAl alloys, therefore, decreases with decreasing lamellar spacing at high stresses.

(2) Microstructural degradation (discontinuous coarsening of the lamellar microstructure and spheroidization of the lamellar plates) took place along grain boundaries, especially in the fine lamellar structure at low stresses. This microstructural degradation caused the increase in creep rate of the fine lamellar spacing at low stresses.

Acknowledgments

This research was supported by grants from JSPS (No. JSPS-RFTF96R12301) and the Ministry of Education, Science, Sports and Culture of Japan (No. 08455313), and by the Iron and Steel Institute of Japan. The material used was kindly provided by Kobe Steel, Ltd., Kobe, Japan.

References

[1] D. Eylon, M. M. Keller and P. E. Jones, Intermetallics, **6**(1998), 703.
[2] Y.W. Kim and D.M. Dimiduk, JOM, **43(8)**(1991), 40.
[3] Y.W. Kim, JOM, **46(7)**(1994), 30.
[4] R.D. Schmidt-Whitley, Z. Metallk., **64**(1973), 552.
[5] B. Bullock, M. Mclean and D.E. Miles, Acta Metall., **25**(1977), 333.
[6] J.A. Wert and M.F. Bartholomeusz, Metall. Mater. Trans., **27A**(1996), 127.
[7] P.P. Rao and K. Tangri, Mater. Sci. Eng., **132A**(1991), 49.
[8] M.F. Bartholomeusz and J.A. Wert, Metall. Mater. Trans., **25A**(1994), 2161.
[9] B.D. Worth, J.W. Jones and J.E. Allison, Metall. Mater. Trans., **26A**(1995), 2947.
[10] B.D. Worth, J.W. Jones and J.E. Allison, Metall. Mater. Trans., **26A**(1995), 2961.
[11] S.C. Huang, Metall. Trans., **23A**(1992), 375.
[12] H. Oikawa and K. Maruyama, Gamma Titanium Aluminides, ed. Y.W. Kim et al. (Warrendale, PA: TMS, 1995), 919.
[13] J. Beddoes, J. Triantafillou and L. Zhao: MRS Symp. Proc., **460**(1997), 293.

[14] P. D. Crofts, P. Bowen and I. P. Jones, Scripta Mater., **35**(1996), 1391.
[15] F. Herrouin, P. Bowen and I. P. Jones, MRS Symp. Proc., **460**(1997), 287.
[16] J. Triantafillou, J. Beddoes, L. Zhao and W. Wallace, Scr. Metall. Mater., **30**(1994), 1387.
[17] K. Maruyama and H. Oikawa, Trans. Japan Inst. Metals, **28**(1987), 291.
[18] M. Es-Souni, A. Bartels and R. Wagner, Acta Metall. Mater., **43**(1995), 153.
[19] S. Mitao and L. A. Bendersky, Acta Metall. Mater., **45**(1997)4475

Key Engineering Materials Vols. 171-174 (2000) pp. 725-732
© 2000 Trans Tech Publications, Switzerland

Alternative Approaches to Creep Data Analyses for Ceramic-Fibre-Reinforced Ceramic-Matrix Composites

B. Wilshire[1] and F. Carreño[2]

[1] Department of Materials Engineering, University of Wales, Swansea, SA2 8PP, UK

[2] Now at Centro Nacional de Investigaciones Metalúrgicas, CSIC, ES-28040 Madrid, Spain

Keywords: Ceramic-Matrix Composites, Creep, Fracture, SiC_f/Al_2O_3, SiC_f/SiC

Abstract

A variety of approaches, ranging from microstructural studies to analyses of creep curve shapes, have been used to identify the processes controlling the high temperature creep and creep rupture properties of SiC_f/SiC and SiC_f/Al_2O_3 composites produced with similar fibre types, volume fractions and architectures.

Introduction

At high temperatures, most materials display normal creep curves, ie after the initial strain on loading, the creep rate decays with time during the primary stage until a minimum or secondary rate is attained, after which the rate accelerates during the tertiary stage which leads to fracture. However, many ceramics and other creep-brittle materials exhibit creep curves with little or no tertiary period, so the creep rate decreases to a minimum value which is reached essentially at the point of failure. Yet, irrespective of the shapes of the recorded creep curves, it has become common practice to discuss creep and creep fracture properties in terms of just a few standard parameters, conventionally, the minimum creep rate, the time to fracture and the creep ductility. Since the fracture times often depend inversely on the minimum creep rate[1], creep behaviour patterns are then generally described through the stress (σ) and temperature (T) dependences of the minimum rate ($\dot{\varepsilon}_m$) and rupture life (t_f), using equations of the form

$$\dot{\varepsilon}_m = M/t_f = A\sigma^n \exp -Q_c/RT \qquad (1)$$

where A and M are considered as constants, n is the stress exponent and Q_c is the activation energy for creep (in units of $Jmol^{-1}$ when the gas constant, $R = 8.314\,JK^{-1}mol^{-1}$). The fact that n and Q_c are themselves functions of stress and temperature has then usually been explained by assuming that different mechanisms become dominant in different stress/temperature regimes. Conversely, the dominant creep mechanism has traditionally been identified by comparing measured n and Q_c values with the values predicted theoretically for different creep processes.

The limitations of these conventional approaches are illustrated by reference to tensile creep data obtained for two ceramic-fibre-reinforced ceramic-matrix composites (CFCCs), namely,
(a) a SiC-fibre-reinforced SiC matrix (SiC_f/SiC) composite[2] and
(b) a SiC-fibre-reinforced Al_2O_3-matrix (SiC_f/Al_2O_3) material[3, 4].
Although both CFCCs were reinforced with 0.38 volume fractions of ~20μm diameter Nicalon NL202 fibres (Nippon Carbon, Japan) aligned parallel and normal to the tensile stress direction, significant differences in creep and creep fracture properties were noted. Even so, by supporting microstructural studies with qualitative and quantitative analyses of creep curve shapes, all features of the creep behaviour patterns observed for these high-performance CFCCs can be interpreted in terms of the processes governing creep strain accumulation and creep ductility.

Experimental Procedures

With both CFCCs, bundles of fibres were woven into 2D layers or plys which were aligned, stacked and densified to produce multi-layer samples having 0/90° fibre architectures. Yet, while the SiC_f/SiC composite had a plain weave, an eight-harness satin weave reinforced the SiC_f/Al_2O_3 material. In addition, these products had different fibre coating types and porosity distributions[2-4].

(a) Carbon layers (<0.5μm) provided the fibre/matrix interfaces of the SiC_f/SiC samples, whereas thin boron nitride interfaces surrounded by dense SiC coatings (~5μm thick) introduced double BN/SiC layers between the fibres and matrix of the SiC_f/Al_2O_3 specimens (Fig. 1).

(b) While pores (~1 to ~20μm) were readily apparent within the fibre bundles of each composite, only in the SiC_f/SiC samples were macropores (up to several 100μm in length) widely observed in the matrix regions between the interwoven fibre bundles.

Tensile creep data for these 0/90° CFCCs were obtained using high-precision machines[2, 5], with the tensile stress applied parallel to one fibre direction. Tests were completed in air over a range of stresses at 1573K for the SiC_f/SiC specimens[2] and at 1473K, 1573K and 1673K for the SiC_f/Al_2O_3 testpieces[3, 4]. Under all conditions, continuously decaying creep curves were recorded, essentially, with no tertiary stages displayed, (Fig. 2).

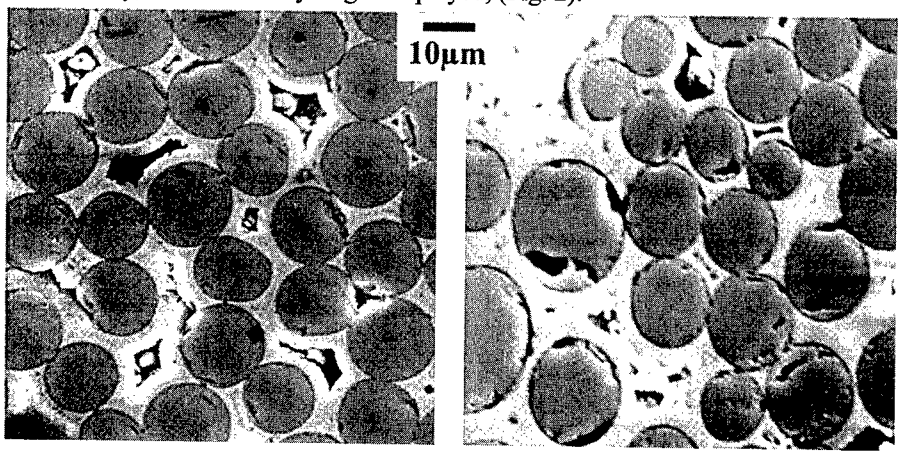

Figure 1. Scanning electron micrographs showing (a) the carbon-coated fibres in the SiC_f/SiC composite[2] and (b) the fibres, with double BN/SiC coatings, in the SiC_f/Al_2O_3 material[3, 4].

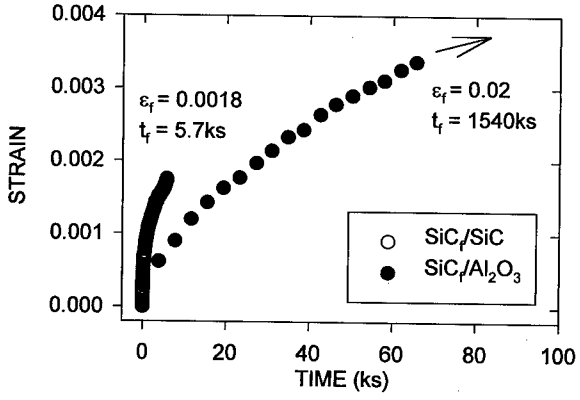

Figure 2. Creep curves obtained for the SiC_f/SiC and SiC_f/Al_2O_3 composites in air at 1573K under a stress of 75 MPa, showing early curve termination for the low-ductility SiC_f/SiC material[4].

Power Law Representation of Creep Data

Figs. 3 and 4 show the stress/creep rate results for each composite, together with data available at 1573K under argon for Nicalon fibres[6], plotted according to eqn. 1.

(a) Fig. 3 reveals that, at the same stress, the creep rates recorded for the SiC_f/SiC samples at 1573K are about ten times faster than those reported for the SiC_f/Al_2O_3 material.

(b) At 1573K, similar high n values are found for both composites (Fig. 3) but, particularly at 1673K, n decreases with decreasing stress from the very high values (~50) displayed in short-term tests carried out for the SiC_f/Al_2O_3 samples (Fig. 4).

From Fig. 3, it is evident that stresses about five times higher must be applied to the Nicalon fibres in order to achieve creep rates comparable with those exhibited by the Nicalon-fibre-reinforced composites (Fig. 3). The creep properties of both 0/90° CFCCs must therefore be governed by the longitudinal fibres, which occupy approximately one fifth of the specimen cross-sections[2, 3]. Moreover, the creep strength of Nicalon fibres deteriorates with time at temperatures above ~1500K[6-8]. Hence, the decrease in n with increasing test duration (Fig. 4) is a consequence of microstructural instability of the Nicalon fibres at high temperature rather than any change in basic creep mechanism[3].

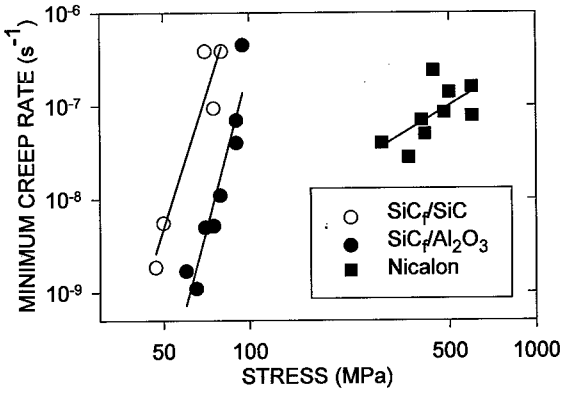

Figure 3. The stress dependences of the minimum creep rates for the SiC_f/SiC composite[2], for the SiC_f/Al_2O_3 material[3, 4] and for Nicalon NL202 fibres[6] at 1573K.

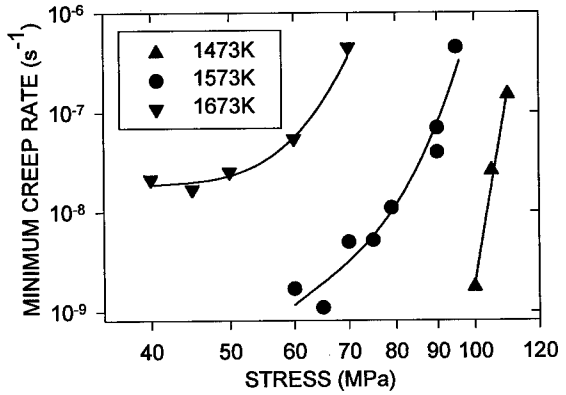

Figure 4. The stress dependences of the minimum creep rates recorded in air at 1473, 1573 and 1673K for the SiC_f/Al_2O_3 composite[3].

Creep Fracture Properties

At 1573K, the creep rates for the SiC_f/SiC composite are about an order of magnitude faster than those for the SiC_f/Al_2O_3 material (Fig. 3) but, even for the same creep rate, the rupture lives of the SiC_f/SiC product are a further order of magnitude lower than those for the SiC_f/Al_2O_3 (Fig. 5). Yet, since the creep strengths are determined by the fibres, similar property values would be expected for these 0/90° CFCCs, both of which were produced with comparable fibre types, volume fractions and architectures. In fact, as evident from Fig. 2, the initial creep rates differ only by a factor of four under the same test conditions. However, when decaying creep curves are displayed under uniaxial tension (Fig. 2), the creep rate ($\dot{\varepsilon}$) decreases with time (t) such that $\dot{\varepsilon} \rightarrow \dot{\varepsilon}_m$ and $t \rightarrow t_f$ as the creep strain (ε) approaches the limiting creep ductility (ε_f). Consequently, the minimum creep rate and rupture life are affected by the magnitude of the creep strain to failure[4].

(a) With the SiC_f/SiC samples, the strains to failure are low at all stresses (Fig. 6), so the creep curves terminate early (Fig. 2) giving high $\dot{\varepsilon}_m$ and low t_f values (Figs. 3 and 5).

(b) With the SiC_f/Al_2O_3 specimens, ε_f increases with decreasing stress (Fig. 6). Hence, particularly in long-term tests, the creep rate decays until fracture occurs at relatively high strains (Fig. 2), resulting in lower minimum creep rates and much longer times to fracture (Figs. 3 and 5).

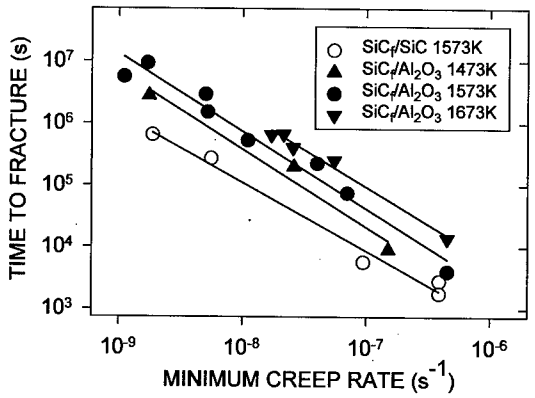

Figure 5. The relationships between the minimum creep rate and the time to fracture for the SiC_f/SiC composite at 1573K and for the SiC_f/Al_2O_3 material at 1473 to 1673K[2, 3].

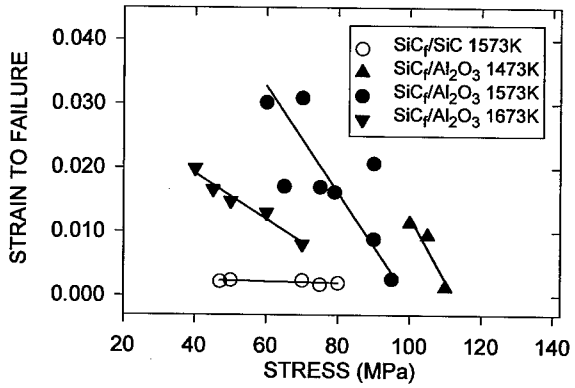

Figure 6. The stress dependences of the creep strains to failure for the SiC_f/SiC composite at 1573K and for the SiC_f/Al_2O_3 material at 1473 to 1673K[2, 3].

Analysis of Creep Curve Shapes

The results in Fig. 5 indicate that, while the rupture life varies inversely with the minimum creep rate for the SiC_f/SiC samples (ie M in eqn. 1 is a constant), the value of M increases with decreasing stress for the SiC_f/Al_2O_3 specimens at all temperatures. Even so, for both CFCCs,

$$\dot{\varepsilon}_m . t_f = M = X\varepsilon_f \quad (2)$$

with $X \cong 0.5$ for the SiC_f/SiC composite at 1573K and for the SiC_f/Al_2O_3 material at 1473 and 1573K but with $X \cong 0.75$ for the alumina-matrix material at 1673K (Fig. 7). This dependence of $\dot{\varepsilon}_m.t_f$ on ε_f has been explained quantitatively[4] by describing decaying curves (Fig. 2) as[9,10]

$$\varepsilon = \theta_1[1-\exp(-\theta_2 t)] + \theta_3\theta_4 t \quad (3)$$

where θ_1 scales the primary strain, θ_2 quantifies the curvature of the primary stage and $\theta_3\theta_4 = \dot{\varepsilon}_m$. However, more simply, the various creep curves recorded for each 0/90° CFCCs can be superimposed (Fig. 8) using the expression

$$\varepsilon = at^x \quad (4)$$

accounting for eqn. 2 when x = X. With the SiC_f/Al_2O_3 composite, the ratio $\dot{\varepsilon}_m.t_f/\varepsilon_f$ (= X in eqn. 2) then increases from 0.5 to 0.75 (Fig. 7) as the curvature of the primary stage diminishes with increasing test temperature (equivalent to $x \rightarrow 1$ in eqn. 4).

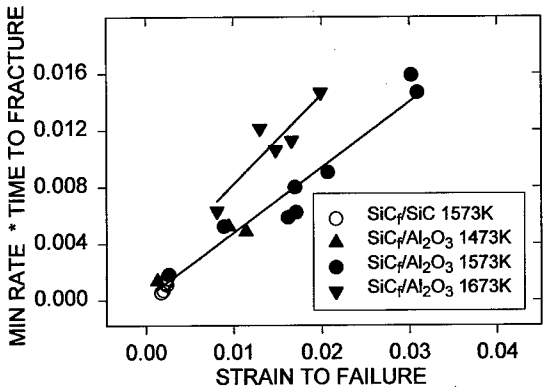

Figure 7. The dependences of the product $\dot{\varepsilon}_m.t_f$ on creep ductility for the SiC_f/SiC composite at 1573K and for the SiC_f/Al_2O_3 material at 1473, 1573 and 1673K.

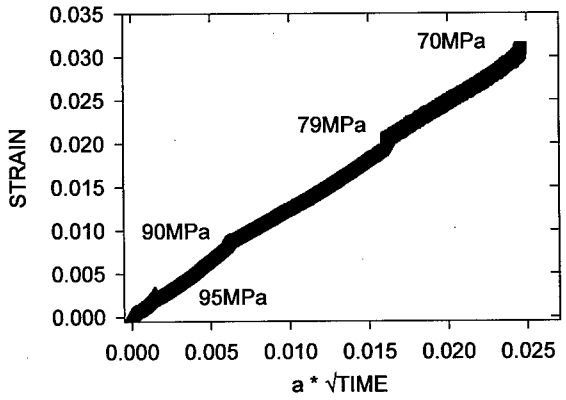

Figure 8. Superimposition of the creep curves recorded at 1573K under different applied stresses for the SiC_f/Al_2O_3 composite, showing progressively later curve termination with decreasing stress.

Creep Damage Processes

For both 0/90° CFCCs, differences in the stress dependences of the creep rate (Fig. 3), the rupture life (Fig. 5) and the product $\dot{\varepsilon}_m.t_f$ (Fig. 7) can be explained qualitatively and quantitatively in terms of ductility variations (Figs. 2 and 8). Yet, while the ductility patterns differ substantially (Fig. 6), the process governing creep and creep fracture are broadly comparable for both composites. Thus, the longitudinal fibres control the rate of creep strain accumulation (Fig. 3), with creep of the fibres accompanied by cracking of the weak porous matrices. The cracks grow relatively easily through the transverse fibre bundles and through the fibre-free matrix regions between the interwoven fibre bundles (Fig. 9) but, on growing into the longitudinal bundles, the cracks become bridged by fibres. Hence, the deformation rates and the crack growth rates are determined by the longitudinal fibres, accounting for the observed dependence of the rupture life on creep rate (Fig. 5). However, during tests in air, oxygen penetration accelerates failure of the crack-bridging fibres[11-13], so that cracks grow with fibre fracture occurring essentially in the crack plane[4]. The cracks then grow until the remaining numbers of unfractured longitudinal fibre bundles cannot sustain the creep load. For both CFCCs, the resulting fracture surfaces therefore show crack-growth zones with in-plane fibre failure and regions where final failure has occurred by fibre pull-out (Fig. 10).

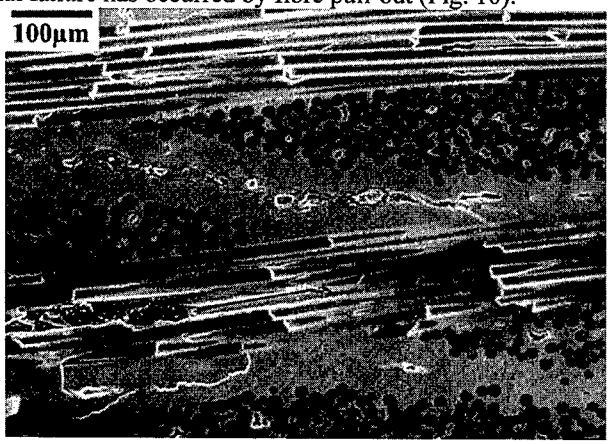

Figure 9. Cracks developing in the matrix regions between the interwoven fibre bundles during creep of the SiC_f/SiC composite.

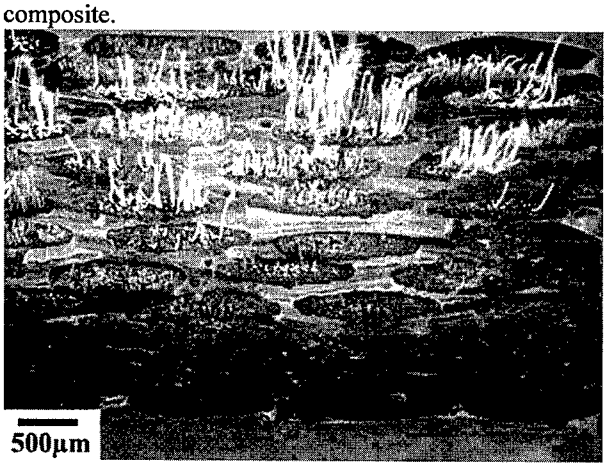

Figure 10. Typical appearance of the fracture surfaces of the SiC_f/SiC composite. Fractographs showing crack growth zones and fibre pull-out regions were also found with the SiC_f/Al_2O_3 samples.

Creep Crack Growth Rates

Although the processes controlling creep and creep fracture are broadly similar for both 0/90° CFCCs, the crack growth rates (and, therefore, the creep ductilities) are microstructure dependent. With the SiC_f/SiC testpieces, cracks nucleate preferentially at macropores present in the matrix regions between the interwoven fibre bundles (Fig. 11). Surface-nucleated cracks then grow and link up, resulting in low-ductility failure at all stress levels (Fig. 6) as a dominant crack grows rapidly through the longitudinal fibre bundles by direct oxygen penetration along the growing crack. In contrast, in the as-processed state, the SiC_f/Al_2O_3 samples contain residual stress-induced microcracks[14]. During creep, cracks therefore form extensively throughout the alumina-matrix composite (Fig. 12). However, in this case, the crack growth rates are reduced by
(a) the protection conferred by the double BN/SiC coatings on the Nicalon fibres (Fig. 1b) and/or
(b) low rates of indirect oxygen ingress through the micro-cracked alumina matrix[4].
Low crack growth rates then defer fracture to longer times and higher strains (Fig. 2). Consequently, the creep strain to failure increases (Fig. 6) as the critical crack area/specimen cross-section ratio required to cause sudden failure by fibre pull-out (Fig. 10) increases with decreasing applied stress[4].

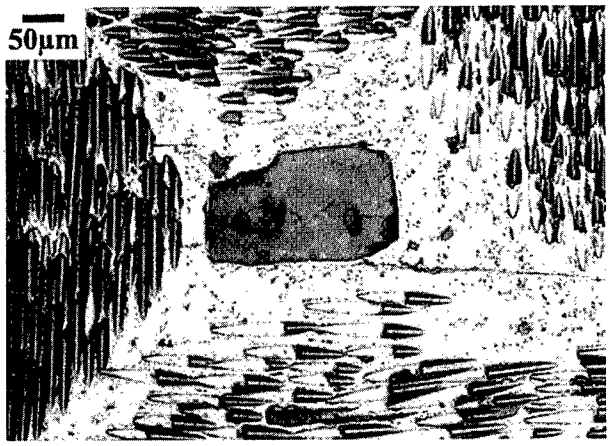

Figure 11. Scanning electron micrograph showing the development of cracks from a macropore in matrix regions between the interwoven fibre bundles in the SiC_f/SiC composite.

Figure 12. Scanning electron micrograph showing the extensive development of cracks during creep of the SiC_f/Al_2O_3 testpieces.

Conclusions

The complex creep behaviour patterns observed for 0/90° CFCCs have been rationalized by supporting conventional data comparison methods not only with microstructural studies but also with qualitative and quantitative analyses of creep curve shapes[4]. Using this combination of approaches, the tensile creep properties of SiC_f/SiC and SiC_f/Al_2O_3 composites are shown to be determined by the fibres, with microstructural instability of the Nicalon fibres rather than mechanism changes accounting for the recorded variations in n value with changing stress and temperature conditions[3]. Creep of the fibres is accompanied by matrix crack formation. These cracks can develop relatively easily through the transverse fibre bundles and through the matrix regions between the interwoven fibre bundles whereas, on growing into the longitudinal bundles, crack growth rates become limited by crack-bridging fibres. Even so, oxygen penetration accelerates failure of the crack-bridging fibres, with fracture then taking place when the crack area/cross-section ratio reaches the critical value needed to cause sudden failure by fibre pull-out. Although the 0/90° composites were produced with similar fibre types, volume fractions and architectures, the superior creep and creep fracture properties of the SiC_f/Al_2O_3 composite can be rationalized in terms of variations in crack growth rates and creep ductilities which, in turn, depend on the susceptibility of the crack-bridging fibres to oxidation-assisted failure[4].

Acknowledgements

The provision of a post-doctoral research fellowship for Dr Carreño under the EC Human Capital and Mobility Programme (Contract No. ERBCHBGCT9330303) and the support received through the British Council UK/Spain research collaboration initiative are gratefully acknowledged. The authors also wish to thank Rolls-Royce for financial support and materials supplies.

References

[1] F.C. Monkman and N.J. Grant, Proc. ASTM. 56 (1956), p.593.
[2] B. Wilshire, F. Carreño and M.J.L. Percival, Scripta Mater. 39 (1998), p.729.
[3] B. Wilshire and F. Carreño, Mater. Sci. Eng. (1999), to be published.
[4] B. Wilshire and F. Carreño, J. Eur. Ceram. Soc., to be published.
[5] B. Wilshire and H. Jiang, Brit. Ceram. Trans. 93 (1994), p.213.
[6] G. Simon and A.R. Bunsell, J. Mater. Sci. 19 (1984), p.3670.
[7] T. Mah, N. Hecht, D. McCullum, J. Hoenigman, H. Kim, A. Katz and H.A. Lipsitt, J. Mater. Sci. 19 (1984), p.1191.
[8] K. Luthra, J. Amer. Ceram. Soc. 69 (1986), p.231.
[9] R.W. Evans and B. Wilshire, 'Creep of Metals and Alloys', The Institute of Metals, London, 1985.
[10] R.W. Evans, P.J. Scharning and B. Wilshire, 'Creep Behaviour of Crystalline Solids' (Ed. B. Wilshire and R.W. Evans), Pineridge Press, Swansea, 1985, 201.
[11] C.H. Henager and R.H. Jones, Mater. Sci. Eng. A166 (1993), p.211.
[12] A.G. Evans and C. Weber, Mater. Sci. Eng. A208 (1996), p.1.
[13] H.C. Cao, E. Bischoff, O Shaizero, M. Rühle, A.G. Evans, D.B. Marshall and J.J. Brennan, J. Amer. Ceram. Soc. 73 (1990), p.1691.
[14] F.E. Heredia, A.G. Evans and C.A. Anderson, J. Amer. Ceram. Soc. 78 (1995), p.2790.

Key Engineering Materials Vols. 171-174 (2000) pp. 733-740
© 2000 Trans Tech Publications, Switzerland

Elasticity, Stress Relaxation and Creep in SiC Particle Reinforced Oxynitride Glass

T. Rouxel, J.-C. Sanglebœuf, P. Verdier and Y. Laurent

Laboratoire 'Verres et Céramiques', UMR-CNRS 6512, Université de Rennes 1, campus de Beaulieu, FR-35042 Rennes cedex, France

Keywords: Brittle Particulate Composites, Stress Relaxation, Creep, Viscosity, Rheology

Abstract - SiC particle reinforced oxynitride glass composites with remarkable mechanical properties and suitability to viscoplastic forming techniques were successfully synthesized. In order to better understand the complex nature of flow in these composites, the stress relaxation and creep behaviors were characterized for particle size and volume fraction from 3 to 150 μm and 0 to 40 % respectively. A good modelling of the relaxation curves was reached using the Kohlrausch-Williams-Watt analytical expression. The viscosity coefficient, as calculated from relaxation data by means of the Boltzmann superposition principle, is very close to the creep viscosity, as determined from the stationary creep regime. The presence of rigid particles results in significant decreases in the relaxation kinetics and creep rates. The smaller the particle size or the higher the particle volume fraction is and the lower the flow kinetics becomes. Furthermore, the apparent viscosity of the composites exhibits a strain-hardening behavior, and a critical strain at which flow is apparently blocked, depending on both particle size and volume fraction, has been successfully introduced to interpret the data.

I. MATERIALS

The oxynitride glass, with stoichiometric composition $Y_{0.124}$-$Mg_{0.160}$-$Si_{0.414}$-$Al_{0.302}$-$O_{1.4}$-$N_{0.151}$, hereafter referred as YBC6, has been prepared by heating up to 1700°C under nitrogen atmosphere a mixture of Y_2O_3, MgO, SiO_2, AlN and Al_2O_3 powders, and subsequent quenching. The silicon carbide has been synthesized by reaction between silicon and carbon at elevated temperature under nitrogen atmosphere. The SiC particle size ranges from 1 to 10 microns. Composites are fabricated from glass and SiC powders, by mixing various amounts of each constituent and hot-pressing under nitrogen atmosphere [1,2]. Dense and homogeneous materials were prepared (Fig.1).

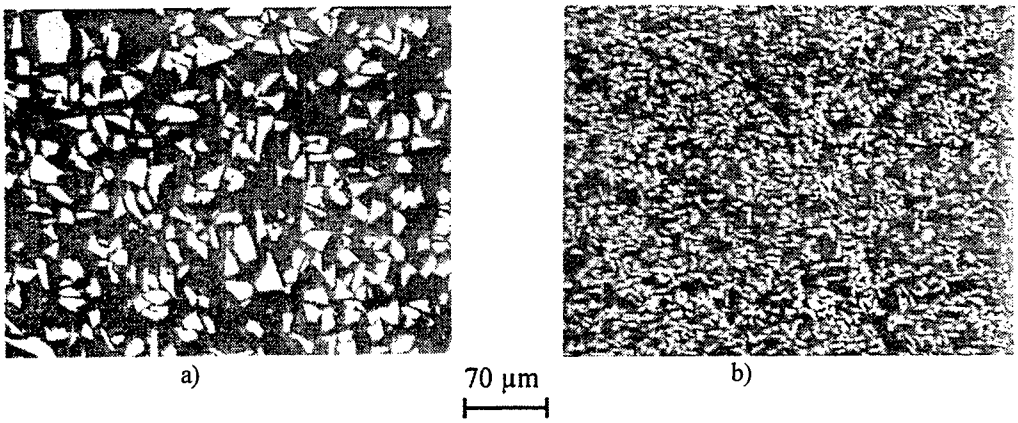

Fig.1 - Scanning electron microscope picture of a polished section of (a) a composite with 28 vol.% particles, 16 microns in diameter, and (b) a composite with 28 vol.% particles, 6 microns in diameter.

The mode 1 fracture toughness, K_{1c}, was estimated by means of Vickers indents. K_{1c} was calculated using the equation derived by Marshall et al. [3]:

$$K_{1c} = 0.036\, E^{0.4}\, F^{0.6}\, (d/2)^{0.8}\, c^{-1.5} \qquad (1)$$

where F (N) is the load applied on the indent, d (m) is the length of the inverse pyramid diagonal, and c (m) is half the crack length. A load of 98.1 N was chosen to favour the median (half-penny shaped) crack system, and to ensure a much larger size for the indent than the microstructural scale. It is noteworthy that such a high load did not induce chipping, whereas chipping occurs at much lower load in oxide glasses. The elastic moduli were measured by means of an ultrasonic technique, with 10 MHz piezoelectric transducers, in direct contact with the specimen. The fracture toughness, K_{1c}, and the effective fracture surface energy, γ_{eff}, of oxynitride glass(m) / SiC(p) brittle particulate composites were also measured by means of stable fracture tests, using chevron-notch three-point bend specimens [4] (Table 1).

Table 1. Physical and mechanical properties of the materials.

	$\alpha(10^{-6}\,°C^{-1})$ 100-500°C	σ_r(MPa) 3-pts	K_{1c}(MPa.m$^{0.5}$) 10 kg, 10 ind.	K_{1c}(MPa.m$^{0.5}$) Chevron Notch.	E(GPa)	ν
SiC*	4.0 ± 0,1	450 ± 20 (30 spe.)	3.5 ± 0.2	/	420 ± 1	0.16
Window glass	10.3 ± 0.1	119 ± 19 (3 spe.)	0.6 ± 0.2	0.63 ± 0.10	74 ± 1	0.23
YBC6	7.3 ± 0,1	116 ± 30 (3 spe.)	1.2 ± 0.2	1.18 ± 0.10	134 ± 1	0.28
YBC6+28% SiC	/	251 ± 42 (3 spe.)	2.6 ± 0.2	2.15 ± 0.10	194 ± 1	0.24
YBC6+40% SiC	/	317 ± 23 (3 spe.)	2.8 ± 0.2	2.49 ± 0.10	216 ± 1	0.23

**: data from "Céramiques & Composites", CCSiC-100.*

In comparison to oxide glasses, the oxynitride glass matrix is noticeably tougher: K_{1cm} = 1.2 MPa.√m and γ_{eff} = 5 J/m^2. The addition of SiC particles, 6 μm in diameter, results in a significant toughening: K_{1c} = 2.5 MPa.√m and γ_{eff} = 9.1 J/m^2 for the composite with 40 vol% SiC [3,4]. In such systems, with strong particle-matrix interfacial bonding, and where (E_p, K_{1cp}, σ_{rp}) > (E_m, K_{1cm}, σ_{rm}), the main toughening contribution is due to a discrete pinning of the crack by particles near the crack tip in conjunction to bowing of the crack front between particles, and to a small scale bridging mechanism [4].

II. THE VISCOPLASTIC FORMING RANGE: AN ULTRASONIC STUDY

Young's modulus was used as a probe to follow the materials evolution during heating from the room temperature up to 1100°C. A schematic drawing of the experimental device is shown in Fig.2. Ultrasonic longitudinal short pulses are generated by a 300 kHz magnetostrictive transducer in a thin tungsten wave guide coupled to the sample. Data analysis is based on the "long bar mode" approximation. Young's modulus, E, is calculated from the longitudinal wave velocity, V_l, and from the sample specific mass, ρ, using:

$$E = \rho\, V_l^2 \qquad (2)$$

Results obtained on the matrix and on composites with 30.9 and 50.2 vol.% SiC particles are plotted together in Fig.3.

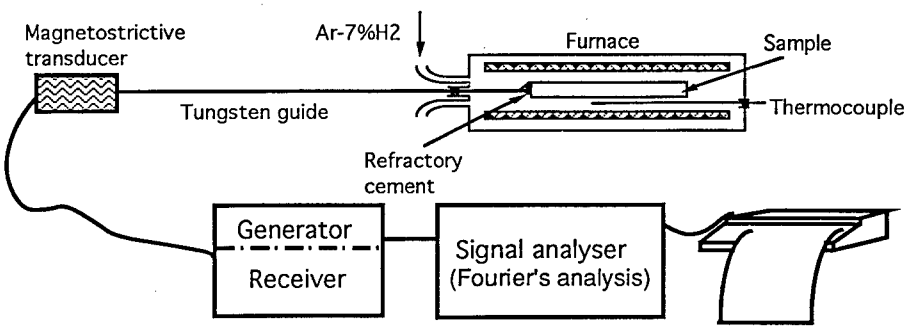

Fig.2 - Schematic drawing of the high temperature ultrasonic testing equipment

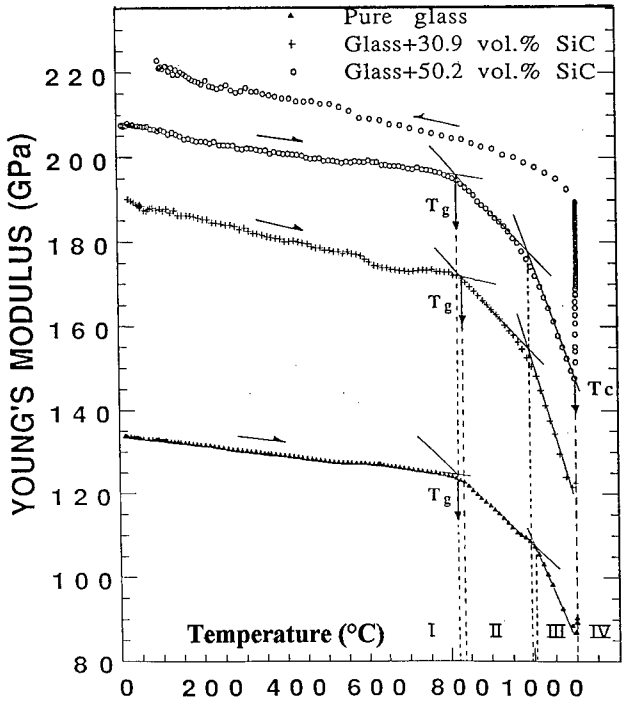

Fig.3 - Temperature dependence of Young's modulus

E decreases slowly and almost linearly up to 800°C, with a slope $(dE/dT)_g \approx -11$ MPa °C^{-1}. This slope characterizes the glassy state. Then E decreases more rapidly due to the rapid softening of the glass in the supercooled liquid state, with again for all grades: $(dE/dT)_{liq} \approx -105$ MPa °C^{-1}. According to the conventional way of determination of the glass transition range, Tg is obtained by intersecting the lines corresponding to the glassy (region I) and to the supercooled liquid (region II) behaviors. This way of determination results in Tg between 820 and 840°C, slightly below the dilatometric result: $Tg_{dil} \approx 863$°C. A detailed inspection of the curves reveals that the supercooled

liquid range can be divided into two stages, corresponding to different softening rates. The second stage (region III) extends from 1000 to 1100°C and is associated to a fast decrease of E with rising temperatures: $dE/dT_{III} = 270$ MPa °C^{-1}. This peculiar behavior has not been observed in standard oxide glasses (Ca,Al silicates). It is suggested that the softening is hierarchically constrained, with the weakest interatomic bonds controlling the first softening regime while the strongest ones relays on in region III. With regards to the selected heating rate of 5°C min.$^{-1}$, crystallization starts at 1100°C with the precipitation of yttrium and magnesium silicates, inducing a net improvement of the materials stiffness. X-ray diffraction spectra were recorded in-situ at 1100°C during the glass to glass-ceramic transformation. The main crystallized phases are $MgAl_2O_4$ (magnesium spinel), $MgSiO_3$ (clinoenstatite), z- and δ-$Y_2Si_2O_7$ idiomorphic phases.

For a glass to be plastically deformed at a speed suitable for shaping techniques, the temperature must be higher than Tg but lower than the first crystallization temperature. In the present case, the viscoplastic forming range is in-between 850 and 1050°C.

III. RELAXATION AND CREEP

III.1 Experimental method

Relaxation and creep experiments were carried out both in compression, on 3x3x7 (height) mm^3 rectangular specimens, and in 3-point bending (SiC device) on 3(height)x4(width)x25 mm^3 rectangular bars, with a span length of 20 mm. However, because results obtained in compression show exactly same trends as in bending [5], only these latter results are discussed in this paper.

Relaxation experiments were performed with an electro-mechanical testing machine (INSTRON 8562) using silicon carbide pistons and bending device. After a rapid loading of the specimen at a rate of 1000 N.min^{-1} to a stress σ_0 at time origin of 50 MPa, the distance between the upper and lower pistons was kept constant by enslaving the actuator position on the value of a differential displacement measuring device (LVDT), using alumina rods in contact with the bending device in the hot zone, which gives the actual specimen displacement. It must be emphasized that the specimen deformation is much smaller than the actuator displacement, especially at relatively low temperature ($T \approx T_g$), when the specimen deforms little while the thermal equilibrium of the whole equipment takes much time to be reached. A rapid loading is required to insure a quasi-elastic regime during this stage, so that the relaxation curve won't be affected by this stage through a memory effect. Relaxation experiments were fully computerized and an average of 2000 points were recorded for a single experiment. Such a large number of (stress, time) points is required to model the behavior by means of analytical expression, especially during the early relaxation stage, when the relaxation kinetics is very fast.

The creep behavior was studied with a dead-load machine, at a stress of 40 to 50 MPa, with a differential displacement measuring device using an LVDT.

The apparent viscosity of the specimen, η_a, was determined from the strain-rate corresponding to the quasi stationary creep stage, using the relationship stemming from the well-known analogy between Hookean elasticity and Newtonian flow:

$$\eta_a = \frac{\sigma}{2(1+\nu)\dot{\varepsilon}} \quad (3)$$

where σ, $\dot{\varepsilon}$ and ν are the flow stress, the strain-rate and Poisson's ratio respectively.

III.2 Results and discussion

Typical relaxation curves obtained on the matrix between 840 and 900°C, and on composites with 28 and 40 vol.% SiC at 860°C, are plotted in Figs.4a and b respectively. A good fitting of the relaxation curves is obtained by the so-called Kohlrausch-Williams-Watt (KWW) [6] analytical expression for the relaxation function:

$$\phi(t) = \exp[-(t/\tau)^b] \quad (4) \quad (\phi(t) \text{ is defined as: } \phi(t) = \sigma(\tau)/\sigma_0)$$

where b is named correlation factor and ranges between 0 and 1, and τ is the relaxation time constant.

a)

b)

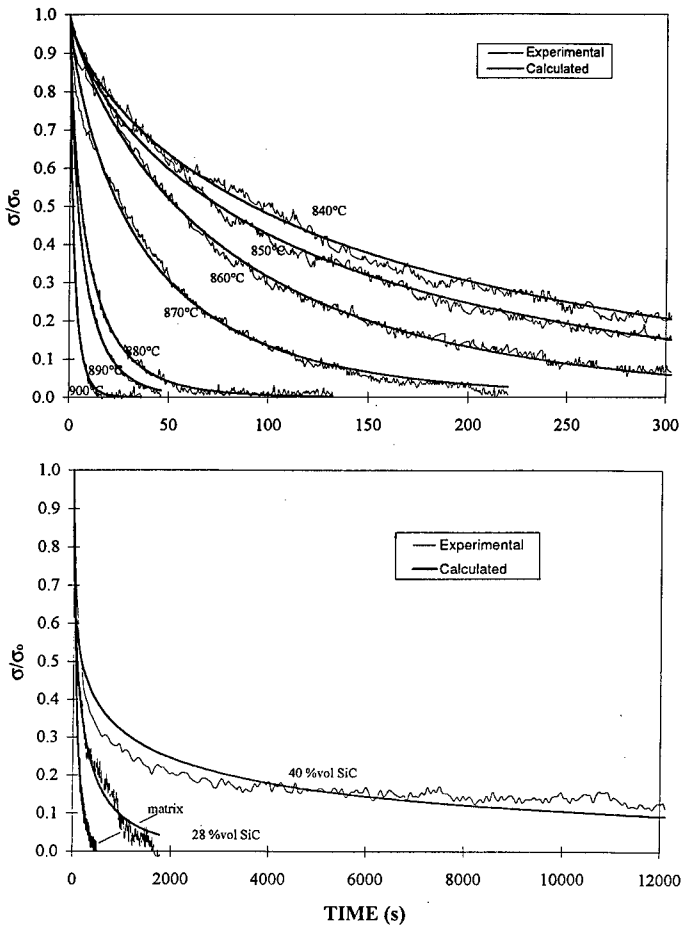

Fig.4 - Stress relaxation for an initial stress of 50 MPa: a) glass matrix; b) composites with 28 and 40 vol.% SiC particles 6 microns in diameter, at 860°C.

Values for b and τ as a function of the temperature are summarized in table 2. The exponent b increases from 0.33 at 780°C to an average value of 0.75 above Tg. Following previous works [7,8], this parameter can be tentatively regarded as a structural factor reflecting the correlation between the different possible molecular movement in the glass atomic network. At T<Tg the correlation is very high, or in other terms the very strong intermolecular coupling allows for elastic deformation only, and b approaches zero. On the contrary, at T>Tg the correlation becomes weaker and weaker as the matter state get closer to the liquid state, and b becomes high, between 0.7 and 0.8 in the present case, 1 for the simple Debye relaxation (Maxwell description). The decrease of τ with rising temperatures, from 40 min at 780°C to 2.54 sec at 915°C, seems to be faster in the supercooled liquid range (i.e. for T>Tg) than in the glassy state region.
The higher the particles content is and the smaller the relaxation rate becomes. For instance, at 860°C, a given value of the stress relaxation, say ϕ=0.368 to get t=τ in eq.4, corresponds to annealing times of 78 sec for the matrix, and 186 and 347 sec for the 28 and 40 vol% SiC composites respectively. It

is noteworthy that the KWW analytical form for ϕ is no longer suitable to describe the behavior of composites with more than 28 vol% SiC.

Table 2. Parameters derived from - or used to model - the relaxation data.

T (°C)	μ (GPa) matrix	b matrix	τ (sec.) matrix	η creep (Pa.sec)	η relax (Pa.sec)	μ (GPa) 28%SiC	b 28%SiC	τ (sec.) 28%SiC	η relax (Pa.sec) 28%SiC
780	49.85	0.33	2374	/	$7.3.10^{14}$	73.05	/	/	/
810	49.58	0.46	934	/	$1.1.10^{14}$	72.78	/	/	/
820	49.41	0.54	520	8.10^{13}	$4.5.10^{13}$	72.61	0.50	2214	$3.0.10^{14}$
830	49.24	0.58	414	/	$3.2.10^{13}$	72.44	0.60	1285	$1.4.10^{14}$
840	49.02	0.69	155	$1.6.10^{13}$	$9.7.10^{12}$	72.22	0.65	512	$5.1.10^{13}$
850	48.65	0.72	124	/	$7.4.10^{12}$	71.85	/	/	/
860	48.26	0.81	83.4	$2.9.10^{12}$	$4.5.10^{12}$	71.46	0.53	185	$2.4.10^{13}$
870	47.90	0.76	39.8	/	$2.2.10^{12}$	71.10	/	/	/
880	47.50	0.71	9.68	/	$5.7.10^{11}$	70.70	0.58	94	$1.0.10^{13}$
890	47.20	0.74	6.89	$5.4.10^{11}$	$3.9.10^{11}$	70.40	0.54	53	$6.5.10^{12}$
900	46.86	0.80	2.54	/	$1.4.10^{11}$	70.06	/	/	/

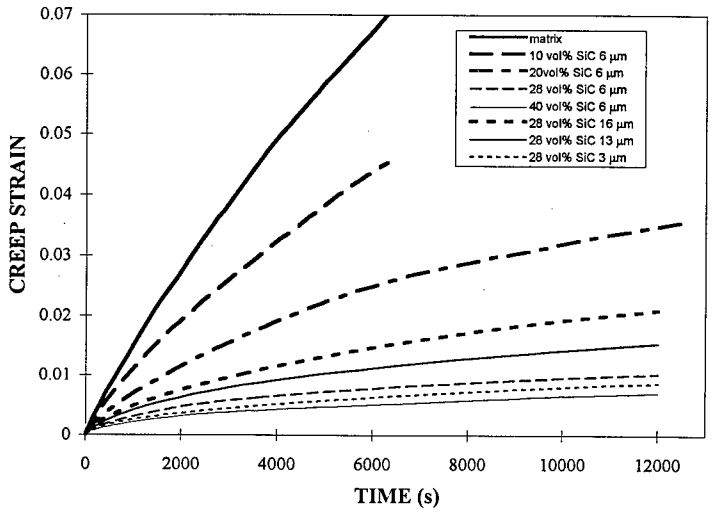

Fig.5 - Three-point bending creep at 860°C under 53.3 MPa

As shown in Fig.5, the creep resistance increases with decreasing particle size or with rising second phase volume fraction. The creep strain-rate keeps decreasing according to a linear hardening behavior expressed as follow:

$$\dot{\varepsilon} = \dot{\varepsilon}_0(1-\varepsilon/\varepsilon_\infty) \quad (5)$$

where $\dot{\varepsilon}_0$ is an extrapolated strain rate value corresponding to the stationary flow regime that would be observed in the absence of any transient stage, immediately after loading (i.e. at $\varepsilon=0$). ε_∞ represents an upper limit for the creep strain, which has the meaning of a rigidity threshold occurring under constant stress (creep testing) with respect to the linear hardening considered here. In fact, as ε approaches this value a slower diffusional flow regime may occur, with a creep rate of less than 10^{-6}sec^{-1}. According to this phenomenological relationship, the apparent actual viscosity is given by:

$$\eta_a = \frac{\eta_o}{1 - \frac{\varepsilon}{\varepsilon_\infty}} \quad (6)$$

where η_o is the viscosity coefficient extrapolated to zero strain,

$$\eta_o = \frac{\sigma}{2(1+\nu)\dot{\varepsilon}_o} \quad (7)$$

and is close to the value obtained from relaxation data as long as $f_p<0.4$ and $\phi_p \geq 6$ μm (see table 2).
It follows from the Boltzmann superposition principle that the creep viscosity (η) relates to the relaxation kinetics, and in the present case where $\phi(t)$ is expressed by the KWW relationship, the following expression can be derived for the viscosity:

$$\eta = \frac{\mu}{b}\tau\,\Gamma\left(\frac{1}{b}\right) \quad (8)$$

where where μ is the shear modulus and Γ is the gamma function.
The viscosity of the matrix follows an Arrhenius law with an apparent activation energy of 785 kJ mol^{-1}, over the whole temperature range. For a composite with 28 vol.% particles, 6 microns in diameter, the calculated viscosity exhibits the same activation energy as for the matrix, but the viscosity is 60 to 80 times higher than that of the matrix at a given temperature, and for a given viscosity a temperature shift of about 30°C is observed. However, a viscosity coefficient can hardly be given a physical meaning in the case of composites with more than 28 vol% SiC because the flow behavior becomes then clearly strain-dependent.

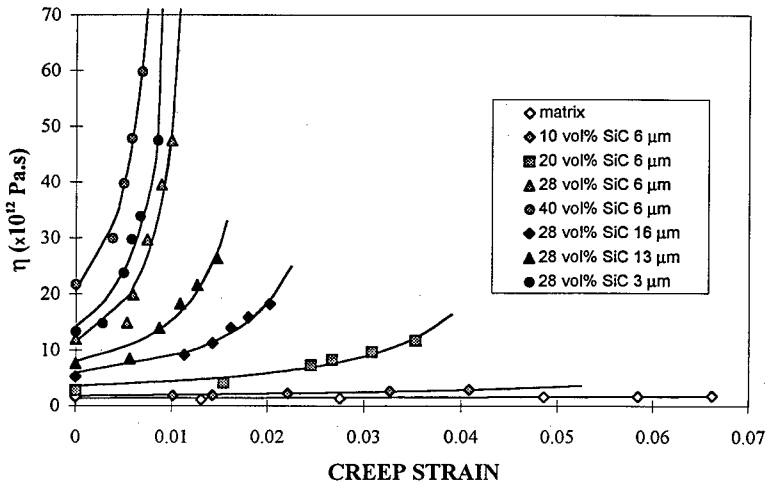

Fig.6 - Apparent creep viscosity as a function of the creep strain. The experimental data are fitted by means of eq.6.

Beside the elasticity-based models, experimental studies of the rheology of suspensions gave birth to several semi-empirical models, among which the widely used Krieger and Dougherty's model [11]. The normalized viscosities, η/η_o, of the studied composites, are well described by the Krieger and Dougherty's equation,

$$\eta_o/\eta_m = \left(1 - \frac{f_p}{f_{pc}}\right)^{-k_h f_{pc}} \quad (9)$$

where f_p is the particle volume fraction, f_{pc} is the critical second phase volume fraction at which the flow is blocked, and k_h is defined as a shape factor, which is close to 2.5 for spherical particles and can increase up to 5 for acicular particles, as particle rotation produces a large hydrodynamic volume. f_{pc} is close to the maximum particle packing fraction, which can been estimated from the apparent specific volume (ASV) of powders with different particle sizes using:

$$f_{pc} = \frac{1}{ASV\ \rho_{SiC}} \quad (10)$$

where ρ_{SiC} is the SiC specific mass ($\rho_{SiC} = 3.22\ g.cm^{-3}$).
A value of 3.7 was determined for k_h by fitting of the experimental viscosity data.
In the present study, a good description of the strain- and second phase characteristics- dependence was reached using eq.6 for the apparent viscosity (Fig.6). In this equation, the upper limit for the creep strain, ε_∞, characterizes the strain-hardening behavior. This parameter is found to depend on the particle size and volume fraction according to:

$$\varepsilon_\infty = \left(\frac{f_{pc}}{f_p} - 1\right)^{\alpha} \quad (11)$$

where f_{pc} is the only and purely size dependent factor. The exponent α is close to unity, and f_{pc} increases from 0.33 to 0.49 as f_p increases from 0.1 to 0.4 with a rapid increase for f_p smaller than 0.2 (see ref.[5] for detail).

REFERENCES:

[1] B. Baron, "Elaboration, caractérisation et mise en forme par déformation viscoplastique de composites particulaires verre oxyazoté-SiC", *Ph.D dissertation*, University of Rennes 1 (France), Oct. 1996.

[2] B. Baron, T. Chartier, T. Rouxel, P. Verdier and Y. Laurent, "SiC particle reinforced oxynitride glass: processing and mechanical properties", *J. Europ. ceram. Soc.* **17**, 773-780 (1997).

[3] D.B. Marshall and A.G. Evans, "Reply to 'Comment on elastic/plastic indentation damage in ceramics: the median/radial crack system', *Journal of the American Ceramic Society* **64**, C-182-183 (1981).

[4] T. Rouxel and Y. Laurent, "Fracture characteristics of SiC particle reinforced oxynitride glass using chevron-notch three-point bend specimens", *Int. J. Fract.* **91**, 83-101 (1999).

[5] T. Rouxel, B. Baron, P. Verdier and T. Sakuma, "SiC particle reinforced oxynitride glass: stress relaxation, creep and strain-rate imposed experiments", *Acta materialia,* 46 6115-6130 (1998).

[6] R. Kohlrausch, Ann. Phys. (Leipzig) **12**, 393 (1987). See also: "Fundamentals of inorganic glasses", Ed. A.K. Varshneya, Pub. Academic Press Inc. (Boston, San-Diego, New-York, London, 1994).

[7] K.L. Ngai, A.K. Rajagopal and S. Teitler, "Slowing down of relaxation in a complex system by constraint dynamics", *J. Chem. Phys.* **88**, 5086-94 (1988).

[8] J. Perez, J.Y. Cavaillé, S. Etienne and C. Jourdan, "Physical interpretation of the rheological behavior of amorphous polymers through the glass transition", *Revue Phys. Appl.* **23**, 125-135 (1988).

[9] R.M. Christensen, "A Critical Evaluation for a Class of Micromechanics Models", *J. Mech. Phys. Solids* **38**, 379-404 (1990).

[10] E. Hervé and A. Zaoui, "n-layered inclusion-based micromechanical modelling", *Int. J. Engng Sci.* **31**, 1-10 (1993).

[11] I.M. Krieger and T.J. Dougherty, "A mechanism for non-Newtonian flow in suspensions of rigid spheres", *Trans. Soc. Rheol.* **III**, 137-152 (1959).

[12] R.E. Dutton and M.N. Rahaman, "Creep viscosity of glass-matrix composites near the percolation threshold", *J. Mat. Sci. Lett.* **12**, 1453-1456 (1993).

[13] A. Tewari, V.S.R. Murthy and G.S. Murty, "Rheological behaviour of SiC (particulate)-borosilicate composites at elevated temperatures", *J. Mat. Sci. Lett.* **15**, 227-229 (1996).

Key Engineering Materials Vols. 171-174 (2000) pp. 741-746
© 2000 Trans Tech Publications, Switzerland

Improvement of High Temperature Strength and Creep of α-Sialon by Grain Boundary Crystallization

T. Nishimura[1], M. Mitomo[1], A. Ishida[2] and H. Gu[3]

[1] National Institute for Research in Inorganic Materials,
1-1 Namiki, Tsukuba, Ibaraki 305-0044 Japan

[2] Isuzu Ceramics Research Institute Co., Ltd.,
8 Tsutsidana, Fujisawa-shi, Kanagawa, 252-851 Japan

[3] Japan Science and Technology Corporation,
2-4-1 Mutsuno, Atsuta-ku, Nagoya-shi 456-8587 Japan

Keywords: Y-α-Sialon, Yttrium Aluminum Garnet, Amorphous Phase

Abstract

Effect of grain boundary crystallization on high temperature strength and creep of Y-α-sialon was investigated. Powder mixture of Si_3N_4, AlN and Y_2O_3 was sintered by hot pressing at 1750 °C for 1h with sintering additives of yttrium aluminum garnet (YAG) composition. The as-sintered material was mainly consisted of α-sialon, Y-Si-Al-O-N crystalline phases and amorphous phase. Annealing at 1550 °C for 4 hs was conducted for crystallization of grain boundary. The annealed one was consisted of α-sialon, YAG and amorphous phase. Strength of as-sintered material decreased with the increase of temperatures up to 1300 °C, recovered between 1400 and 1500 °C and then decreased at 1600 °C. The strength recovery might be due to crystallization of grain boundary. The strength of annealed one was almost constant until at 1300 °C and, at higher temperature, decreased with the increase of temperature. Deformation behavior of as-sintered material under compressive stress of 198 MPa at 1200 °C was almost same as that of annealed one at 1300 °C under the same stress condition.

1 Introduction

Sialon is a solid solution of silicon nitride and a candidate for structural use at high temperature[1,2]. It is conventionally fabricated by liquid phase sintering method. Sintering additives, usually metal oxide and/or nitrides, are added to raw powder in order to assist the densification and grain growth. They form liquid phase during heating, reacting with silicon dioxide on the surface of raw silicon nitride powder. The existence of liquid phase is helpful for grain movement and mass transportation. The liquid solidifies at grain boundary of sialon grains and/or diffuses into the grains. The solidified phase, called grain boundary phase, is usually amorphous and softens at high temperatures, which means that high temperature properties of the material are dominated by the grain boundary phase. An α-sialon has α-Si_3N_4 structure in the system Me-Si-Al-O-N (Me: metal) [3]. General formula in Si_3N_4-Y_2O_3-AlN system is written below.

$$(4-1.5x)Si_3N_4+0.5x(Y_2O_3+9AlN) \rightarrow Y_x(Si_{12-4.5x}Al_{4.5x})(O_{1.5x}N_{16-1.5x}) \quad (0<x\leq 2)$$

The α-sialon can incorporate many cations of the additives in their interstitial holes. Therefore, a material with small amount of residual glass may possibly obtained, which is advantageous to heat resistance. Crystallization of the grain boundary phase has been investigated with respect to the improvement of high temperature properties. Sialon ceramics with yttrium aluminum garnet ($Y_3Al_5O_{12}$: YAG) grain boundary phase have been investigated [4-6]. Lewis et al. [4]

investigated effect of crystallization of garnet phase in normal pressure sintered β-sialon with Y or Nd additives on mechanical properties. Strength at higher temperature than 1000 °C was improved by the crystallization. Creep resistance of α/β-sialon with YAG grain boundary phase is higher than that of β-sialon with YAG by complete removal of residual amorphous phase [5]. Bandyopadhyay suggested that high temperature strength of gas pressure sintered Y-α-sialon was improved by crystallization of YAG [6]. Therefore, improvement of high temperature properties of α-sialon with YAG is expected by reduction of amorphous phase and crystallization of grain boundary. Until now, effect of YAG crystallization on high temperature properties of α-sialon has never been reported. For the purpose, phase relationships and microstructural change were preliminary investigated. Y-α-sialon was stable with YAG liquid composition at 1750 °C which could be devitrified to YAG by post sintering annealing at 1500 °C for 4 h [7]. Phase and microstructural change due to post sintering annealing of R-α-sialon with rare earth aluminum garnet (RAG) was examined (R: Nd, Dy, Y and Yb). For R is Y, only α-sialon was detected after sintering and α-sialon and YAG after annealing at 1450 °C for 72 h. Grain boundary film thickness between sialon grains decreased by the annealing [8]. In the present paper, effect of crystallization of YAG on high temperature properties of Y-α-sialon is investigated.

2 Experimental procedure

Si_3N_4(Ube Industries Co., Tokyo, Japan, SN-E10), Y_2O_3 (Shin-Etsu Chemical Co., Tokyo, Japan, 99.9% pure) and AlN (Tokuyama, Tokyo, Japan, Type F) powders were mixed in a Si_3N_4 pot with hexane and Si_3N_4 balls for 2 hs using planetary mill. The composition of the powders was chosen as x=0.45 in the general formula of α-sialon. Al_2O_3 (Sumitomo Chemical Co. ltd., Osaka, Japan, AKP20) and Y_2O_3 with YAG composition were added to the mixed powder as sintering aids. The amount of the additives was totally 10 mass%[6,7]. The mixed powder was hot-pressed in a carbon die coated with boron nitride powder at 1750 °C for 1h under compressive stress of 20 MPa in static nitrogen of 0.1 MPa. Rectangular plates with dimension of about 3.5 x 21 x 25 mm^3 were obtained (designated as-sintered material in this paper). Post sintering annealing was conducted at 1550 °C for 4 hs in nitrogen atmosphere (designated annealed material). Bending specimens with dimension of 2.5 x 3 x 25 mm^3 were prepared from the plates by cutting, grinding and polishing. Bending strength was measured at elevated temperatures up to 1600 °C. Four-point jig with inner and outer span of 10 mm and 20 mm was used. Atmosphere at room and high temperatures was air and nitrogen, respectively. Constant crosshead speed of 0.5 mm/min was used for room and high temperature. High temperature strength was also measured at slower crosshead speed of 0.005 mm/min, in order to investigate effect of slow crack growth. Creep behavior was measured in nitrogen atmosphere at 1200-1500 °C under compressive stress of 198 MPa. Microstructures were investigated by scanning transmission electron microscope(STEM). High resolution electron microscope (HREM) was used for observing grain boundary film.

3 Results and discussion

3.1 Microstructural change by annealing

Bulk density of as-sintered and annealed material was 3.31 Mg/m^3 and 3.36 Mg/m^3, respectively. Crystalline phases were identified by X-ray diffraction analysis. The primary crystalline phase of as-sintered material was α-sialon. Weak peaks of melilite ($Y_2Si_3N_4O_3$) and 12H sialon ($SiAl_5O_2N_5$) were observed, but YAG phase was not detected. From the annealed material, α-sialon, YAG and small amount of β-sialon were detected. Only α-sialon was detected from as-sintered material and α-sialon and YAG from the material annealed at 1500 °C in the previous work [7,8]. The difference might result from larger sample dimension and higher annealing temperature.

Figure 1 shows typical STEM dark field image of both materials. Dark part corresponds to sialon and other crystalline phases and white part amorphous grain boundary phase. The amorphous phase in as-sintered material exists continuously both between silicon nitride grains and at grain boundary pockets (Fig. 1 (a)). That in annealed material exists isolatedly mainly at grain boundary pockets (Fig. 1 (b)). These microstructural features are consistent to that of small samples from same powder[6,7].

In the Fig. 1 (b), grain boundary film between sialon grains cannot be observed. So, grain boundary between sialon grains of annealed material was observed by HREM. Typical image is shown in Fig. 2. Amorphous grain boundary film with thickness of about 1 nm is observed. Grain boundary film thickness reduces by annealing, but the film still exists. Lewis et al. [5] reported that thickness of amorphous film between sialon grains decreased and crystallized YAG distributed isolatedly in β'/α'-sialon. Curved interface between YAG and sialons resulted from equilibration of triple phase junctions. The authors claimed that the interface was evidence for complete removal of non-stoichiometric glass-stabilizing elements by solid solution within α'. In the present annealed material, amorphous phase still exists. It could be removed by precise control of initial chemical composition.

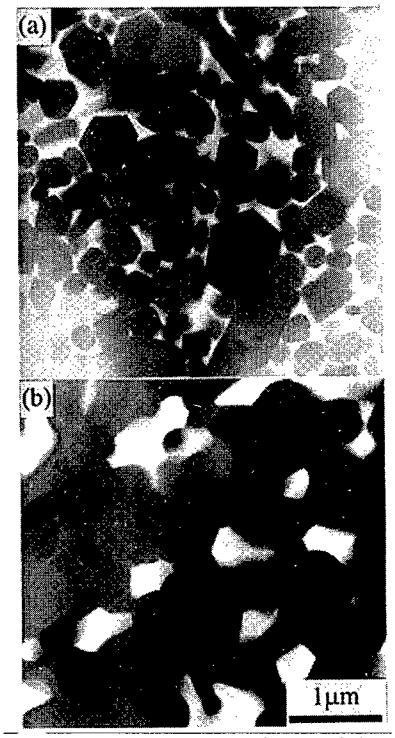

Fig. 1 Microstructure of Y-α-sialon before (a) and after (b) annealing.

3.2 High temperature strength

Bending strength was measured at cross head speed of 0.5 mm/min at elevated temperature. The results were plotted in Fig. 3 together with the data in reference 5 and 6. Strength of as-sintered material at 800 and 1000 °C is slightly lower than that at room temperature. The strength decreases with the increase of temperature up to 1400 °C, recovers at 1500 °C once, and decreases again at 1600 °C. Load-displacement curves of as-sintered material are almost linear up to maximum load at 1000, 1200 and 1500 °C and shape of the curve is rather convex at 1300, 1400 and 1600 °C. Fractured surfaces after bending test were rough at 800-1200 °C and flat at 1300 °C and higher. The strength of annealed material is almost constant up to 1300 °C and, at higher temperature, decreases with increase of temperature. The load-displacement curves are linear at 1000-1400 °C and convex at 1500 and 1600 °C. Fractured surfaces were rough up to 1400 °C and flat at 1500 and 1600 °C. Strength degradation, fracture behavior and observation of fractured surfaces suggest that, in the fracture of as-sintered material, slow crack growth starts from 1000 °C and becomes dominant at 1200 °C and higher. Softening point of Y-Si-Al-O-N glass

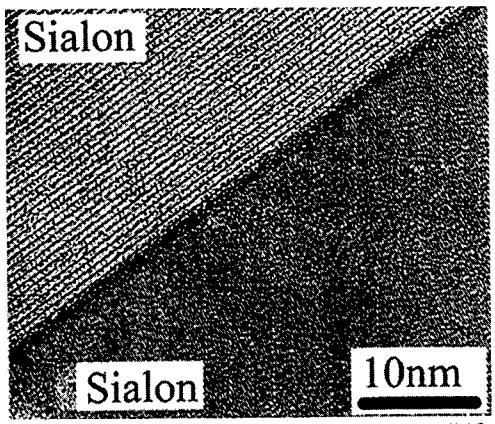

Fig. 2 Grain boundary film in annealed Y-α-sialon.

was reported to be within a range 865-975 °C [9]. The strength degradation at 800-1400 °C could be explained by the softening. Recovery of strength at 1500 °C resulted from crystallization of grain boundary, which was confirmed by XRD analysis of the sample after test. For the annealed material, slow crack growth starts from 1400 °C and is dominant at 1500 °C and higher. Softening of residual amorphous might occur between 1300 and 1400 °C. The residual amorphous phase has different chemical composition from amorphous phase before annealing.

At 1500 and 1600 °C, strength of as-sintered and annealed materials is almost same. This suggests that residual amorphous phase after crystallization softens at that temperature and crystallization of grain boundary is effective up to 1400 °C. Strength of β'-sialon with amorphous grain boundary phase decreased at about 800 °C and that with crystalline grain boundary phase was constant up to 1000 °C. For the material, high temperature strength was improved by the crystallization, but the strength of the material with crystalline grain boundary phase decreased at 1200 °C, which is 200 °C lower than the present result. Strength at 1200 °C of α-sialon was recovered from 328 to 430 MPa by crystallization of grain boundary to YAG. The improved strength was almost same as room temperature strength of the initial material. At 1350 °C, the strength was improved by the crystallization, but the value was 361 MPa, which is lower than that at 1200 °C, 430 MPa. Crystallization of YAG contributed to the strength, but the strength of annealed material with elevated temperature is not investigated. The present result suggests that the crystallization is effective on the strength within a certain temperature range. Higher limit for effect of crystallization has never been reported.

Fatigue is one of important evaluation for application of ceramics. Precise evaluation did not conducted in the work, but bending strength was measured at slower crosshead speed, 0.005 mm/min at 1200-1500 °C in order to estimate the effect of slow crack growth on dynamic fatigue. The strength was plotted with the data measured at crosshead speed of 0.5 mm/min (Fig. 4). The

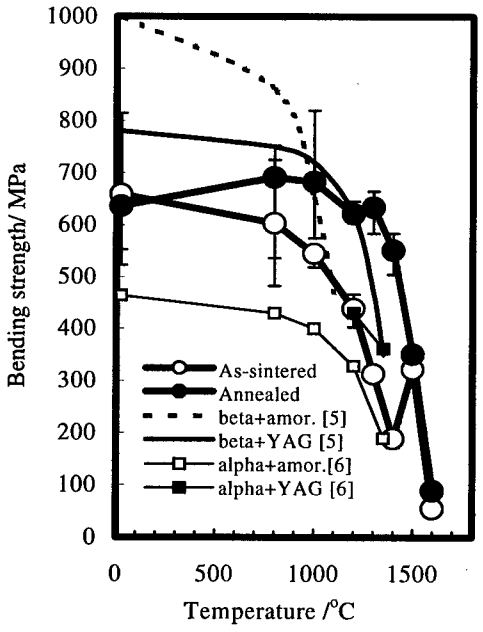

Fig. 3 Effect of grain boundary crystallization on high temperature strength of Y-α-sialon.

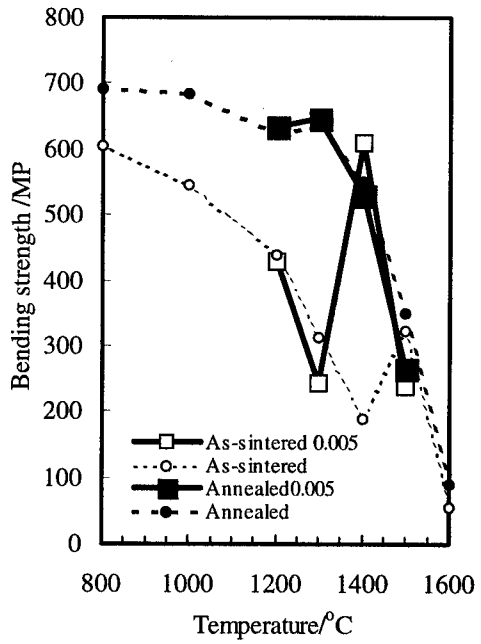

Fig. 4 Effect of crosshead speed on high temperature strength of Y-α-sialon

strength of as-sintered material decreases with the increase of temperature recovers at 1400 °C and decreases again at 1500 °C. Temperature of the strength recovery is lowered. The strength at 0.005 mm/min is almost the same as that at 0.5 mm/min at 1200 °C but lower at 1300 and 1500 °C. Load-displacement curves of as-sintered material are almost linear at 1200 and 1400 °C and convex at 1300 and 1500 °C. Fractured surface was rough at 1200 and 1400 °C and flat 1300 and 1500 °C. Crystallization of YAG was confirmed by XRD analysis of sample after test at 1400 °C. It might be a reason for the strength at 1400 °C. The strength of annealed material at 0.005 mm/min is almost same as that at 0.5 mm/min at 1200, 1300 and 1400 °C and is lower than that at 0.5 mm/min at 1500 °C. The load-displacement curves of annealed material is linear at 1200, 1300 and 1400 °C and convex at 1500 °C. Fractured surface was rough at 1200-1400 °C and flat at 1500 °C. The results suggest that slow crack growth is already dominant at 1200 °C in the as-sintered material. In the annealed material, slow crack growth starts 1400 °C and is dominant 1500 °C, i.e. dynamic fatigue is apparent at 1300 °C for the fracture of as-sintered material and at 1500 °C for that of annealed material.

Strength of as-sintered material recovered at 1500 °C, 0.5 mm/min, and 1400 °C, 0.005 mm/min. YAG crystallization was confirmed by XRD analysis. At 1400-1500 °C, deformation and crystallization of YAG are competing. The time for fracture was within five minutes at 0.5 mm/min and longer than one hour at 0.005 mm/min. When the cross head speed is low, the time for crystallization is long enough, though crystallization rate is low even at low temperature.

Fracture behavior of as-sintered material might be explained below:

$T<1000$ °C: Brittle fracture dominated by a defect.

$1000\leq T\leq 1300$ °C: Fracture by softening of amorphous phase.

$1300<T<1500$ °C: Softening of amorphous phase and crystallization occur simultaneously.

1500 °C$\leq T$: Fracture by softening of residual amorphous phase after crystallization.

Fracture behavior of annealed material is more simple,

$T\leq 1300$ °C: Brittle fracture dominated by a defect

1300 °C$\leq T$: Softening of residual amorphous phase.

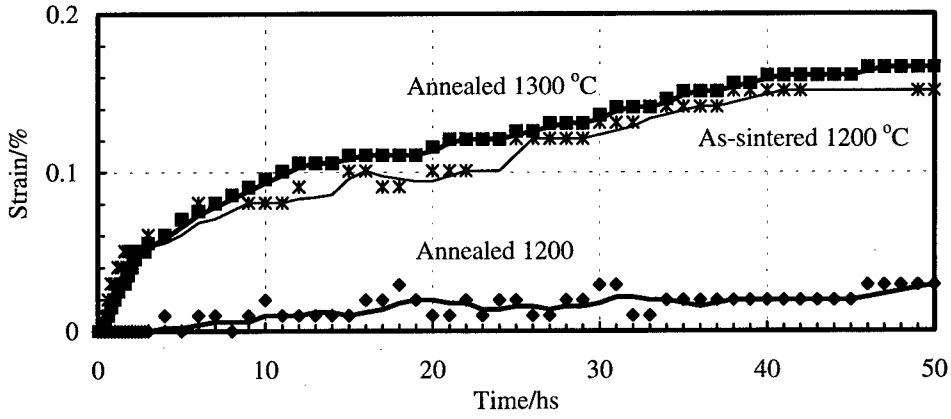

Fig. 5 Effect of grain boundary crystallization on creep of Y-α-sialon.

3.3 Creep

Creep behavior of both samples was measured at 1200 and 1300 °C in nitrogen under compressive stress of 198 MPa. Strain curves are shown in Fig. 4. Data plot of annealed material at 1200 °C is scattered. Absolute deformation was so small and in same level of precision of measurement, which might be a reason of the scattering. The strain is believed to increase monotonously. At 1200 °C, the final strain of as-sintered material is 0.15 %, which is five times of that of annealed material. The strain curves of as-sintered material at 1200 °C is almost the same as that of annealed material at 1300 °C. Creep measurement of annealed material was conducted up to 1500 °C. Relationship between creep rate and inverse of temperature is plotted in Fig. 5. Steady-state creep rate of annealed material is about one tenth of that of as-sintered material. Creep resistance of Y-α-sialon is improved by the crystallization of YAG. Apparent activation energy of annealed material is calculated from the slope of plots. It is 294 kJ/mol. In order to discuss on effect of crystallization on creep resistance, more experiments are necessary. It will be reported elswhere future.

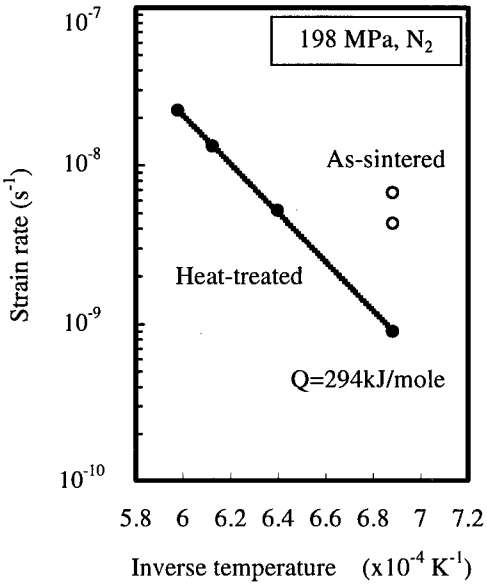

Fig. 6 Creep behavior of Y-α-sialon ceramics.

References

[1] Y. Oyama, O. Kamigaito, Japan. J. Appl. Phys., 10 (1971) p. 1637.
[2] K. H. Jack, W. I. Wilson, Nature Phys. Sci., 238 (1972) p. 28.
[3] M. Mitomo, J. Ceram. Soc. Japan (Yogyo-Kyokai-Shi) 85 (1977) p. 408.
[4] M. H. Lewis, G. Leng-Ward, C. Jasper, Ceramic Transactions: Ceramic powder science II, ed. G. L. Messing, (1988) p.1019.
[5] M. H. Lewis, Materials research society symposium proceedings vol. 287, Silicon nitride ceramics scientific and technological advances, ed. I-W. Chen, P. F. Becher, M. Mitomo, G. Petzow, T.-S. Yen, (1993) p.159.
[6] S. Bandyopadhyay, M. J. Hoffmann, G. Petzow, J. Am. Ceram. Soc., 79 (1996) p.1537.
[7] J.-W. Min, M. Mitomo, Ceramics International, 21 (1995) p. 427.
[8] M. Mitomo, A. Ishida, J. Euro. Ceram. Soc., 19 (1999) p. 7.
[9] C. O'Meara, G. D. Dunlop, R. Pompe, J. Euro. Ceram. Soc. 8 (1991) p. 161.

Corresponding address
Dr. Toshiyuki Nishimura
National Institute for Research in Inorganic Materials, 1-1 Namiki, Tsukuba, Ibaraki 305-0044, Japan, Tel: 0298-51-3354 ext. 570, Fax: 0298-51-3613, e-mail: nishimur@nirim.go.jp

Key Engineering Materials Vols. 171-174 (2000) pp. 747-754
© 2000 Trans Tech Publications, Switzerland

Creep Processes in the Advanced Silicon Nitride Ceramics

F. Lofaj[1,3], A. Okada[2], Y. Ikeda[2] and H. Kawamoto[2]

[1] Institute of Materials Research of the Slovak Academy of Sciences, 043 53 Košice, Slovakia

[2] Japan Fine Ceramics Center, Atsuta-ku, Nagoya 456-8587, Japan

[3] Current address: National Institute of Standards and Technology, Gaithersburg, MD 20899, USA

Keywords: Silicon Nitride, Tensile Creep, Cavitation, Grain Boundary Sliding, Viscous Flow

Abstract Tensile creep behavior and creep damage in SN 281, SN 88M and ST 1 silicon nitride ceramics have been investigated at 1200°C - 1400°C in order to reveal basic creep mechanisms. HIP-ed SN 281 exhibits the highest creep resistance and the lowest failure strains less than 0.7% at 1400°C-1450°C. The minimum strain rates in the gas-pressure sintered (GPS) SN 88 M are two orders of magnitude higher and the failure strains are ≤ 3.5%. The nano-sized GPS grade, ST 1, exhibits a transition from creep resistant to quasi-ductile behavior at temperatures above 1300°C. Creep above 1300°C was strongly affected by oxidation, and the failure stains were around 20%. Despite the very wide range of failure strains and minimum strain rates, the common features of creep behavior in all materials are cavitation and secondary phase evolution. Multigrain junction cavities are present in each material and their apparent density is proportional to the strain. Cavitation according to the recent model of Luecke and Wiederhorn was concluded to be the common creep mechanism. This model is based on a repeated sequence of grain boundary sliding, viscous flow and cavitation due to the redistribution of secondary phases between the multigrain junctions. The gradual changes in secondary phases related to oxidation and/or phase transformation are also involved in the long-term creep processes. These effects change the properties of the secondary phases and indirectly affect cavitation and creep behavior. A simple model including the effect of secondary phase evolution on cavitation is proposed. Different creep behavior of silicon nitride ceramics can be explained by differences in the properties of the secondary phases.

I. Introduction

Silicon nitride ceramics are two-phase materials which consist of elongated β-Si_3N_4 grains embedded in the secondary phases originating from the sintering additives. Tailoring the microstructure via control of a grain size distribution and properties of the secondary phases results in the materials with high strength, high fracture toughness or high creep resistance depending on the requirements for their applications [1-3].

Since creep is one of the principal design limitations for the components in gas turbines, and silicon nitride is the most promising high temperature material, a number of silicon nitride ceramics with high creep resistance have been developed over the last decade [1-13]. The microstructure of these materials usually has a bimodal grain size distribution with the matrix grain size in the range of 0.5-1 μm and considerably larger elongated grains used for reinforcement [12-14]. HIP-ed grades are often more creep resistant than GPS ones because of lower content of the secondary phases. The stress exponents, n, are usually in the range from 4 to 10 in both GPS and HIP-ed grades [4-13]. Creep models based on diffusional mechanisms cannot explain such a strong stress dependence. Since cavitation is always present in the deformed materials, the enhancement of cavitation in tension and its suppression in compression are considered to be responsible for the high values of stress exponents and creep asymmetry [4, 6-8]. Several recent works suggest that cavitation plays a dominant role in creep deformation [12-18]. Luecke and Wiederhorn developed a creep model based on cavitation at multigrain junctions [16]. They assumed that any sliding in a fully dense, granular material causes its

dilatation. This results in a build-up of the local hydrostatic tensile stresses in the viscous phase in multigrain junctions. Cavities are nucleated in the pockets with maximum stresses. The stress gradients between the cavitated junctions and the adjacent junctions without cavities drive the redistribution of the secondary phase toward the cavity free junctions by viscous flow or solution-precipitation, leading to their expansion [16, 18]. The stress dependence of the minimum strain rate is described as [16]

$$\dot{\varepsilon}_s = A_c \sigma \exp(-Q_c/RT) \exp(\beta_c \sigma) , \quad (1)$$

where A_c and Q_c are a dimensional constant and an apparent activation energy, respectively, and β_c is the ratio of the critical stress necessary for cavity nucleation to the square width of a stress distribution at multigrain junctions. The model predicts an increase in stress dependence at high stress and a decrease of creep asymmetry at low stresses. This prediction agrees very well with the experimental data obtained on SN 88 [16, 18]. However, it is not clear if this model is valid in the other silicon nitride materials with high and low creep resistance, respectively.

The current study summarizes tensile creep investigations in three different silicon nitride ceramics performed within Japanese national project "Research and Development of the Ceramic Gas Turbines (300 kW class)". The aim of the work is to investigate the role of cavitation in silicon nitride ceramics with very different creep behavior, from highly creep resistant up to quasi-ductile, in order to verify the dominant creep mechanism in silicon nitride ceramics.

II. Experimental Procedure

Three types of silicon nitride ceramics have been investigated. The first material studied is designated as SN 281. It is relatively new grade produced by hot isostatic pressing (Kyocera Corp., Kyoto, Japan). It consists of matrix grains with a mean diameter of ~1 μm and an aspect ratio from 2 to 4, and a small number of large grains with the length from 6 to 30 μm and diameter of 3-6 μm [12]. The second material is a gas-pressure-sintered, self-reinforced nano-composite silicon nitride designated as SN 88M (NGK Insulator Co., Ltd., Nagoya, Japan). The grade is a modified version of the commercial grade, SN 88. The microstructure of this material consists of large silicon nitride grains (up to 50-80 μm long, diameter 5-10 μm) embedded in a fine matrix of β-Si_3N_4. The mean size of the matrix grains is approximately 0.5 - 0.8 μm with an aspect ratio of 3 to 5. Secondary phases contain Yb and Y cations [12-14, 17]. The third material, ST 1, is high strength, self-reinforced, nano-sized silicon nitride produced by gas-pressure sintering by NGK Spark Plug, Co., (Nagoya, Japan). The mean grain size of the matrix grains is approximately 0.2 μm, and their aspect ratio is less than 3. The diameters of the reinforcing grains are 0.5-1.5 μm and the aspect ratios are from 5 to 10. Secondary crystalline phases contain Yb and Al cations [10, 19].

Most of the tensile tests were performed on flat dog-bone shape specimens with rectangular cross section (4 x 2.5 mm^2). The specimens were tested in nine creep machines with the four pin SiC hot jigs, and dead weight loading at temperatures ranging from 1200°C to 1450°C in air. The bending strains were minimized to less than 5% under a load corresponding to the applied stress. The details of specimen geometry and testing are described elsewhere [12-14].

Creep damage introduced during the deformation was investigated by transmission electron microscopy (TEM) (models JEM 100 CX II, JEM 2010 and JEM-4000 FX, JEOL, Japan, respectively) on thin foils prepared from the bulk of 8 creep tested specimens of material SN 88M, 5 specimens of material SN 281 and 10 specimens from ST 1. X-ray diffraction was used to investigate the phase changes in each material after testing.

III. Results

1. Creep Behavior and Stress Exponents

The materials studied exhibit significant differences in creep behavior depending on the temperature and stress. SN 281 has the highest creep resistance: its deformation starts at the temperatures above 1350°C and stresses above 150 MPa whereas the onset of the deformation in SN 88M is below 1250°C (Fig. 1 (A)-(B)). ST 1 is the least creep resistant material, however, its behavior strongly depends on temperature. At the temperatures below 1300°C it is comparable to SN 88M, at higher temperatures it

transforms into "quasi-ductile" material with maximum failure strains around 20% accumulated during prolonged accelerated stage (Fig. 1 (C)) [10, 19]. The maximum failure strains obtained in SN 88M are around 3.5% [13] whereas in SN 281 are less than 0.6% [12]. The accelerated stage was not observed in SN 281 at 1400°C - 1450°C.

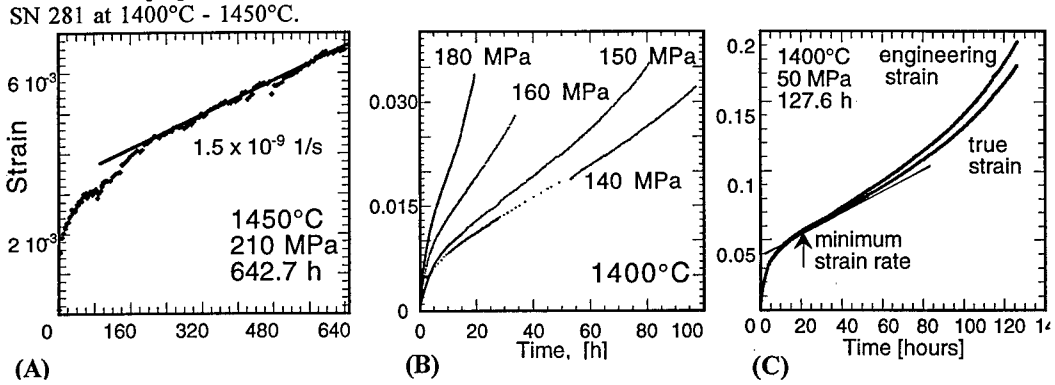

Fig. 1. The comparison of tensile creep curves in SN 281 - (A), SN 88M - (B) and ST 1 - (C).

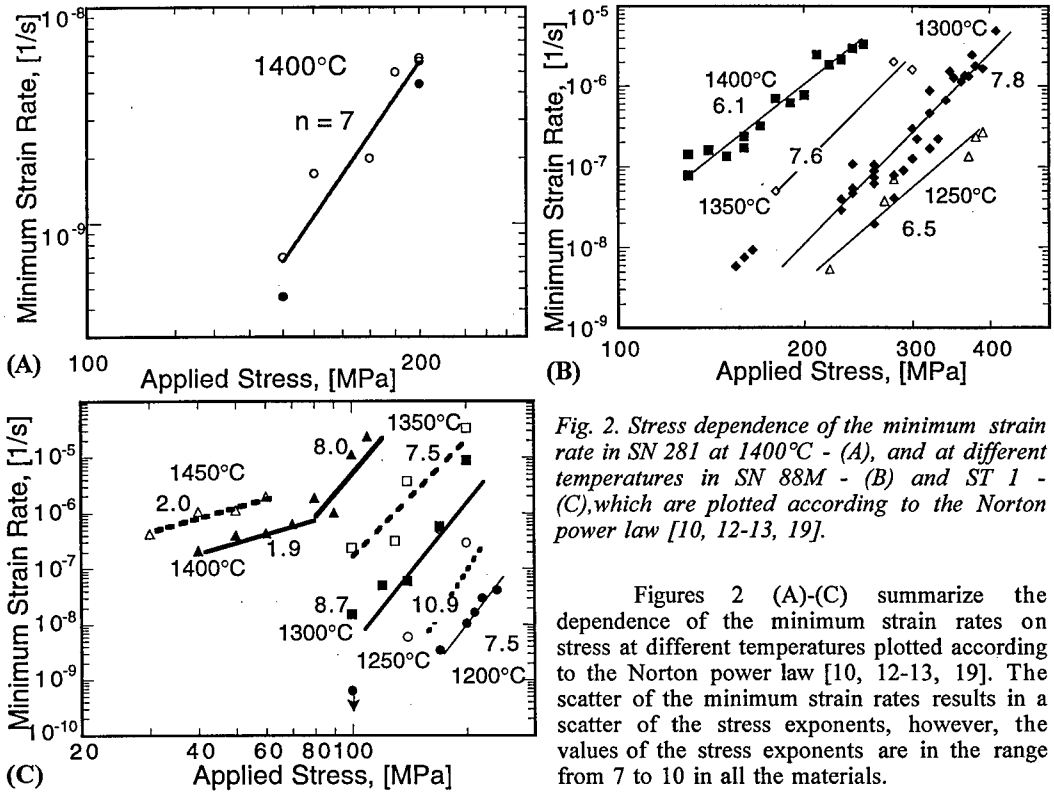

Fig. 2. Stress dependence of the minimum strain rate in SN 281 at 1400°C - (A), and at different temperatures in SN 88M - (B) and ST 1 - (C),which are plotted according to the Norton power law [10, 12-13, 19].

Figures 2 (A)-(C) summarize the dependence of the minimum strain rates on stress at different temperatures plotted according to the Norton power law [10, 12-13, 19]. The scatter of the minimum strain rates results in a scatter of the stress exponents, however, the values of the stress exponents are in the range from 7 to 10 in all the materials.

2. Cavitation

Creep damage was investigated in detail for SN 88M and the creep defects were classified in two groups depending on the phase in which they formed (see Table 1) [12, 14, 20]. The first group, called inter-granular creep defects, consists of defects in the boundary phase. The second group, intra-granular defects, are formed in the silicon nitride grains. The most common in all the materials studied were the **multigrain junction cavities**. Fig. 3 (A)-(C) illustrate such cavities in SN 281, SN 88M and ST 1, res-

*Table 1. Classification of creep damage in different silicon nitride ceramics (GBS - grain boundary sliding, *-crack formation depends on the creep conditions).*

CREEP DAMAGE IN	HIGH STRESSES)	LOW STRESSES	SN 281	SN 88M	ST 1	POSSIBLE MECHANISMS
AMORPHOUS BOUNDARY PHASE	Multigrain Junction Cavities		✓ **few**	✓	✓ **many**	**GBS + Viscous Flow**
	Two Grain Junction Cavities		not found	✓ **few**	not found	**GBS + Viscous Flow**
	Microcracks		*not found	*✓	*✓	**GBS + Viscous Flow** +(solution-precipitation)
	Cracks			*✓	*✓	
	Main Crack		*✓	*✓	*✓	
SILICON NITRIDE GRAINS	Broken Large Grains		not found	✓ **few**	not found	GBS+Viscous Flow **Fast Fracture** + (Viscous Flow)
	NO	Symmetrical and Asymmetrical Cavities	not found	✓ **few**	not found	(GBS + Viscous Flow) + **Solution-Precipitation**
	NO	Crack-like Cavities	not found	✓ **very few**	not found	(GBS + Viscous Flow) + **Stress-Solution-Precipitation**

pectively. Their shapes are similar and varied depending on the geometry of the grains. The size of the individual multigrain junction cavities is comparable with the size of matrix grains. The main difference between the materials after creep at similar conditions is the apparent density of the cavities estimated from TEM micrographs. The local density of cavities in SN 281 with the failure creep strain of ~ 0.6% is lower, than in SN 88M with six times higher strains. A very high concentration of cavities is present in ST 1 for strains of ~20%. **Two-grain junction cavities** inside the glassy phase were observed only in SN 88M and very rarely in comparison with the multigrain junction cavities [12]. They were not found in SN 281 and ST 1 materials. **Creep cracks** formation was inversely proportional to the failure strains. A high concentration of large cracks was observed in ST 1, whereas the number of cracks in SN 281 was negligible The morphology of the creep cracks in SN 88M suggests that they formed most probably by interconnection of numerous multigrain junction cavities. **Broken large grains** were observed in SN88M after both short-term and long-term tests under high and low loads, respectively.

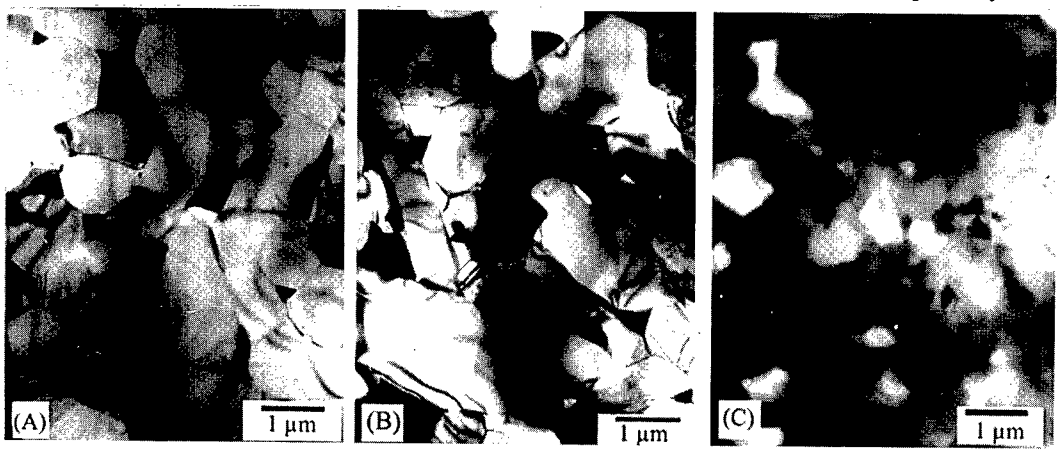

Fig. 3. Multigrain junction cavities formed in SN 281 after creep at 1400°C under a stress of 150 MPa after 2804 hours - (A), in SN 88M at 1350°C, 180 MPa after 497 hours - (B) and in ST 1 at 1450°C under a stress of 60 MPa and 25 hours - (C).

Small symmetrical and asymmetrical cavities: The cavities symmetrically penetrating into the Si_3N_4 grains were found at two grain junction boundaries with very thin boundary phase [12-14]. The geometry of these cavities is very similar to the lenticular cavities reported in other silicon nitride ceramics [5, 7-8]. **Crack-like intragranular cavities** were found in SN 88M simultaneously with the small **asymmetrical cavities** in some of the large grains after long-term tests [12-14, 20]. Intergranular creep defects were not present in ST 1. Although they were not found in SN 281, their presence and the presence of two-grain junction cavities or other defects cannot be excluded.

3. Evolution of Phase Composition

The X-ray diffraction analysis revealed significant phase changes in the secondary phases after heat treatment and creep in the interior of the materials (Fig. 4). In SN 88M, the $Yb_4Si_2N_2O_7$ phase in the as-received material evolved into $Yb_2Si_2O_7$ after creep (Fig. 4 (A)) [21-22]. The secondary phases in SN 281 were not identified, however, the changes are also visible (Fig. 4 (B)). The most pronounced phase

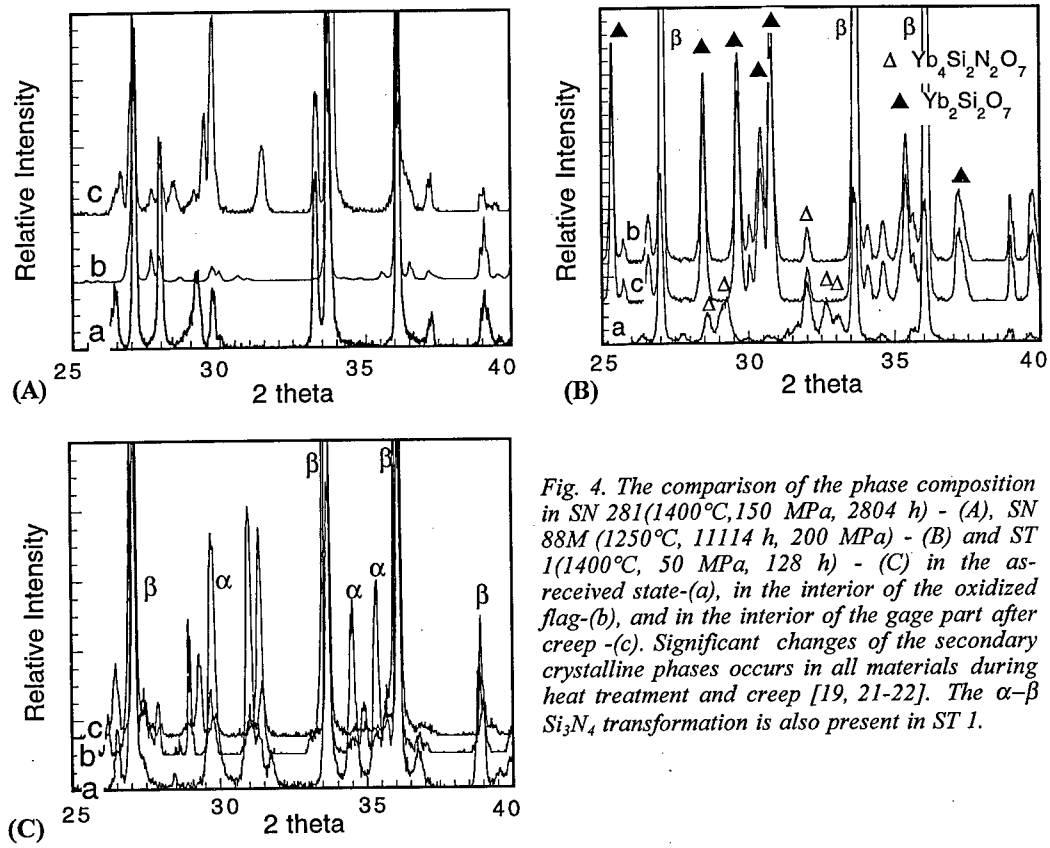

Fig. 4. The comparison of the phase composition in SN 281(1400°C,150 MPa, 2804 h) - (A), SN 88M (1250°C, 11114 h, 200 MPa) - (B) and ST 1(1400°C, 50 MPa, 128 h) - (C) in the as-received state-(a), in the interior of the oxidized flag-(b), and in the interior of the gage part after creep -(c). Significant changes of the secondary crystalline phases occurs in all materials during heat treatment and creep [19, 21-22]. The α–β Si_3N_4 transformation is also present in ST 1.

changes were observed in ST 1 ceramics at temperatures above 1300°C, and they were related to oxidation which drives redistribution of Yb cations toward the surface [10, 19]. A thick white layer, consisting of large elongated grains of $Yb_2Si_2O_7$ embedded in the amorphous phase, likely silica, was formed at the surface. The first subsurface layer was almost pure β-Si_3N_4. The precipitates in the following layer containing Yb and Al were identified as $Yb_4Al_2O_9$ [19]. The crystalline secondary phases in the core zone of the specimen, besides β-Si_3N_4, were unidentified, however, their composition is completely different from the initial composition (Fig. 4 (C)). The thickness of the oxidation related layers was larger and new phases formed under the effect of stress, as compared to that oxidized at the same conditions (see Fig. 4 (C)) [10, 19]. The disappearance of the residual α-Si_3N_4 phase in the creep-tested specimen confirms the presence of solution-precipitation.

IV. Discussion

The difference in minimum creep rate between ST 1 at 1450°C under 60 MPa and SN 281 at the same temperature, however, much higher stress of 210 MPa, is approximately 3 orders of magnitude. Creep resistance of SN 88M is in between those two materials. However, cavitation and secondary phase changes are the common features in all three materials. In SN 88M silicon nitride, the contribution of cavities to the total tensile strain was found to exceed 90% [17]. From the viewpoint of cavitation, the only principal difference between the materials with the highest and the lowest creep resistance is the density of the cavities. Very low densities were observed in SN 281 at low strains whereas high densities were seen in ST 1 with high strains (Fig. 3). The multigrain junction cavities are present in all the materials studied (Table 1) while other types have been observed only in SN 88M. Thus, the multigrain junction cavities are the most important type of cavities for volume generation and for creep behavior. Creep deformation via cavitation at multigrain junctions is involved in the creep model of Luecke and Wiederhorn. The strain rate dependence on stress is described in this case by the Eq. 1 [16]. If this is a general model for creep in two-phase materials such as silicon nitride, strain rate data have to fit Eq. 1. Fig. 5 (A) - (C) show the fits of the data taken from Fig. 2 (A)-(C), plotted according to this equation. It can be seen that the data agree very well with the expected dependence. In the case of ST 1, even the transition from high to low stress exponents at low stresses is eliminated [19]. The agreement between the data in different silicon nitride ceramics and cavitation creep model suggests that cavitation at multigrain junction is the main and common creep mechanism in materials with behavior varying from negligible creep up to quasi-ductile deformation.

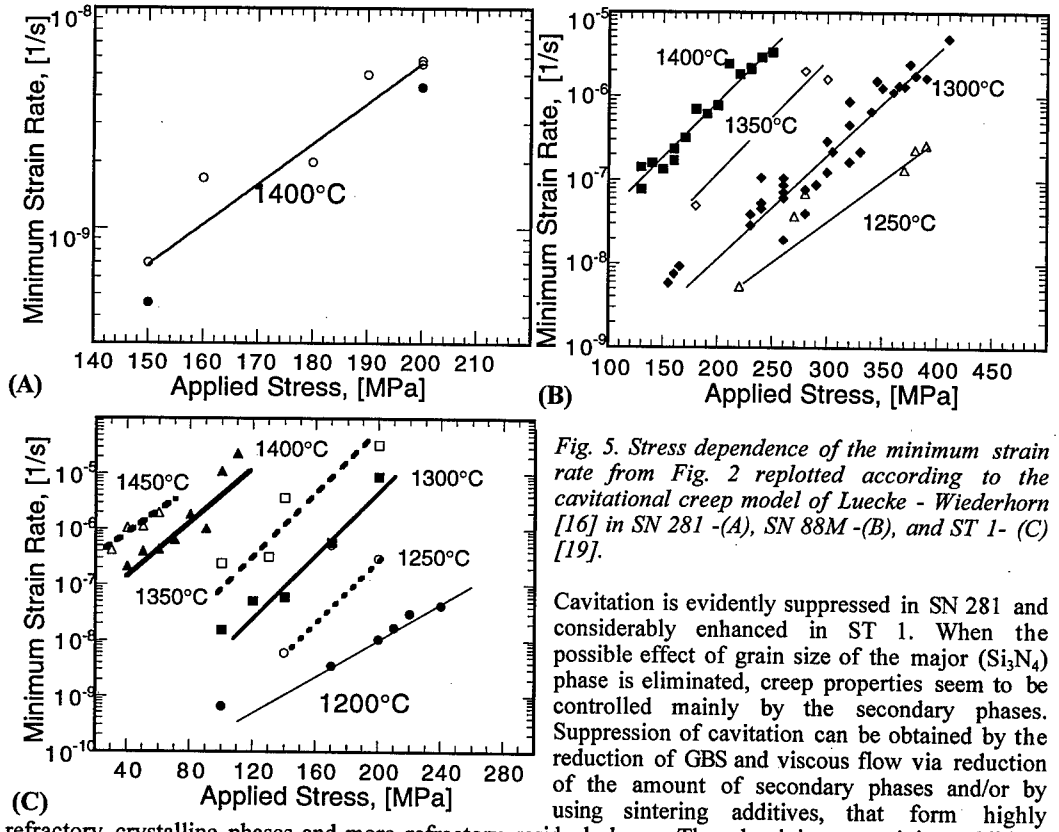

Fig. 5. Stress dependence of the minimum strain rate from Fig. 2 replotted according to the cavitational creep model of Luecke - Wiederhorn [16] in SN 281 -(A), SN 88M -(B), and ST 1- (C) [19].

Cavitation is evidently suppressed in SN 281 and considerably enhanced in ST 1. When the possible effect of grain size of the major (Si_3N_4) phase is eliminated, creep properties seem to be controlled mainly by the secondary phases. Suppression of cavitation can be obtained by the reduction of GBS and viscous flow via reduction of the amount of secondary phases and/or by using sintering additives, that form highly refractory crystalline phases and more refractory residual glasses. The aluminium-containing additives present in ST 1 besides Yb cations, significantly reduce the softening temperature of the glassy phase at the grain boundaries. Ytterbium- and yttrium-containing additives without Al in SN 88M result in more refractory secondary phase and less cavitation. Reduction of the amount of additives via HIP-ing and

high refractory rare-earth oxides in SN 281 result in an increase of creep resistance by almost 100°C in comparison with SN 88M. Additional effects may result from the evolution of the secondary phases (Fig. 4). These changes are connected either with oxidation and stress enhanced redistribution of additives between the surface and bulk, as it is in ST 1 at temperatures over 1300°C [10, 19], or from oxidation at the surface and Yb-oxynitride ⇨ Yb-disilicate phase transformation in the bulk, as observed in SN 88M [21-22]. The phase evolution in SN 88M can be described by a reaction [21-22]

$$2\,Yb_4Si_2N_2O_7 + 7\,SiO_2 \rightarrow 4\,Yb_2Si_2O_7 + Si_3N_4\,. \quad (2)$$

which is similar to the YAM → apatite transformation in yttria-aluminium nitride doped silicon nitride [23]. In both cases, silica at the grain boundaries is consumed. This reduces the possibilities for GBS, viscous flow, solution precipitation contributing to cavitation. Possibly, this is one of the reasons the creep lifetime of GPS SN 88M at 1400°C is even better than that of HIP-ed grade NT 154 [12].
GBS and viscous redistribution of the glassy phase are the principal mechanisms to generate high local tensile stresses required for cavity nucleation and development [4 - 20]. Solution-precipitation may also contribute to the formation of some of creep defects (see Table 1). As a result, GBS, viscous flow and solution-precipitation are the basic mechanisms necessarily involved in creep damage development. Figure 6 is a simplified flow chart of these mechanisms resulting in the formation of different types of cavities. Each of them contributes into the volume conservative deformation which can account for up to 10 % of the total tensile strain [17]. However, more than 90 % of the total tensile strain results from non-conservative processes, predominantly from the volume of cavities at multigrain junctions. The linear dependence of cavitation strain contribution on strain is possible due to repetition of the sequence "GBS ⇨ cavitation at multigrain junctions ⇨ viscous flow". Crucial to this process is a release of the contacts between the grains via the redistribution of the secondary phase among the cavity free pockets.

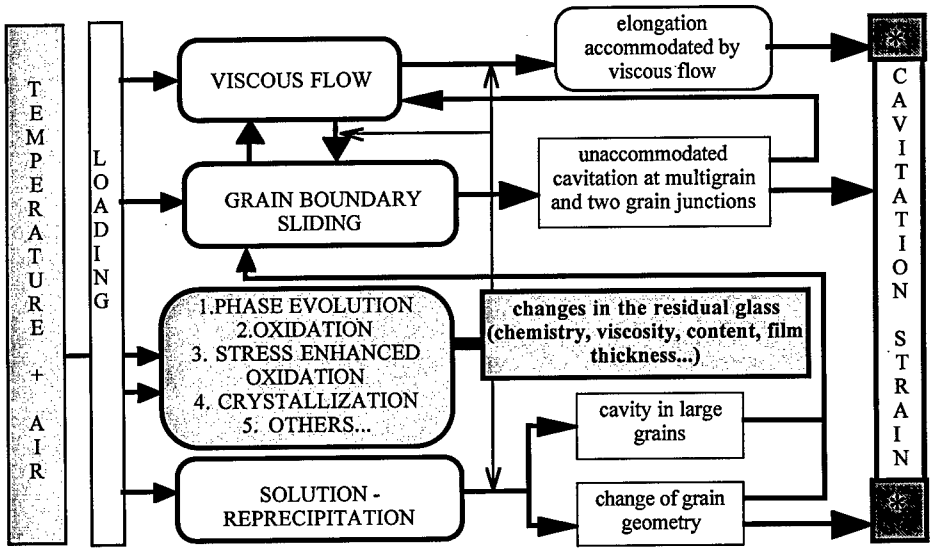

Fig. 6. A scheme of the relationships between different creep mechanisms for cavitation including the effects of oxidation, phase transformation and others. The changes in the secondary phases influence cavitation via modification of the properties of the residual glass (- volume conservative strain).*

Phase transformation, crystallization, and additive/impurity redistribution associated with oxidation modify the amount and viscosity of the residual glassy phase. These changes affect the mechanisms involved in cavitation and consequently, creep behavior (Fig. 6). The model implies that the key issue in increasing the high temperature properties of silicon nitride ceramics is residual glass engineering (RGE). The use of high refractory rare-earth oxide additives, reduction of impurity content, HIP and

the intentional introduction of the metastable boundary phases, such as oxynitrides or apatites, are the possible RGE methods resulting in the reduction of cavitation and ceramics with higher creep resistance.

V. Conclusions

Tensile creep behavior ranging from highly creep resistant (SN 281) to "quasi-ductile" (ST 1) exhibits common features, which include cavitation at multigrain junctions and secondary phase evolution. Cavitation according to the recent model of Luecke and Wiederhorn was concluded to be the main creep mechanism despite differences in microstructure and creep behavior in the materials. This model is based on a repeated sequence of grain boundary sliding, viscous flow and cavitation, which are possible due to the redistribution of secondary phases between the multigrain junctions. The gradual changes in secondary phases related to crystallization, oxidation and phase transformation are also involved in the long-term creep processes. These effects change the properties of the secondary phases and indirectly affect cavitation and creep behavior. The differences in creep resistance between different ceramics can be explained by differences resulting from different properties of the secondary phases.

Acknowledgments This work was supported by the NEDO Project "Research and Development on Ceramic Gas Turbine (300 kW Class)" (Japan), VEGA Grant No. 2/5162/98 (Slovakia) and British Council Academic Link Program (UK). The supports for F. Lofaj from STA and Iketani Science and Technology Foundation (Japan), and NIST and J.W. Fulbright Commission (USA) are gratefully acknowledged. The help and the discussions with S.M. Wiederhorn and W.E. Luecke are highly appreciated.

References

[1] Y. Ukyo, S. Wada, *J.Ceram.Soc.Japan,* **97** [8] (1989), p. 872.
[2] C.W. Li, J. Yamanis, *Ceram.Eng.Sci.Proc.,* **10** [7-8] (1989), p. 632.
[3] Y. Tajima, *Silicon Nitride Ceramics. Scientific and Technological Advances*. Mat. Res. Soc. Symp. Proc., **287,** MRS, Pittsburgh, PA (1993), p. 3453.
[4] M.K. Ferber, M.G Jenkins, *J.Am.Ceram.Soc.,* **75** [9] (1992), p. 2453.
[5] S.M. Wiederhorn, B.J. Hockey, D.C. Cranmer, R.L. Yeckley, *J.Mater.Sci.,* **28** (1993), p. 4445.
[6]T. Ohji, Y. Yamauchi, *J.Am.Ceram.Soc.,* **76** [12] (1993), p.3105.
[7] M.K. Ferber, M.J. Jenkins, T.A. Nolan, R.L. Yeckley, *J.Am.Ceram.Soc.,* **77** [3] (1994), p.657.
[8] M.N. Menon, H.T. Fang, D.C. Wu, M.J. Jenkins, M.K. Ferber, K.L. More, C.R. Hubbard, T.A. Nolan, *J.Am.Ceram.Soc.,* **77** [5] (1994), p. 1217.
[9] Ch.J. Gasdaska, *J.Am.Ceram.Soc.*, **77** [9] (1994), p. 2408.
[10] F. Lofaj, H. Usami, Y. Ikeda, Y. Mizuta, H. Kawamoto, *Proc. of the 1995 Yokohama International Gas Turbine Congress,* Gas Turbine Soc. of Japan, Japan, (1995), vol. 3, p. 37.
[11] A.A. Wereszczak, M.K. Ferber, T.P. Kirkland, K.L. More, M.R. Foley, R.L. Yeckley, *J.Am.Ceram.Soc.,* **78** [8] (1995), p.2129.
[12] F. Lofaj, J.-W. Cao, A. Okada, H. Kawamoto, *Proc. 6th Int. Symp. on Ceramic Materials and Components for Engines*, Technoplaza Co., Ltd., Tokyo, Japan, (1998), p. 713.
[13] F. Lofaj, H. Usami, A. Okada, H. Kawamoto, *Engineering Ceramics '96: Higher Reliability through Processing*. Kluwer Academic Publ., The Netherlands, (1997), p.337.
[14] F. Lofaj, A. Okada, H. Usami, H. Kawamoto, *J.Am.Ceram.Soc.*, **82** [4] (1999), p. 1009.
[15] W.E. Luecke, S.M. Wiederhorn, B.J. Hockey, R.F. Krause, Jr., G.G. Long, *J.Am.Ceram. Soc.,* **78** [8] (1995), p. 2085.
[16] W.E. Luecke, S.M. Wiederhorn, *J.Am.Ceram. Soc.,* (1999), in print.
[17] F. Lofaj, A. Okada, H. Kawamoto, *J.Am.Ceram.Soc.*, **80** [6] (1997), p. 1619.
[18] R.F. Krause, Jr., W.E. Luecke, J.D. French, B.J. Hockey, S.M. Wiederhorn, *J.Am.Ceram. Soc.,* **82** [5] (1999), 1233.
[19] F. Lofaj, A. Okada, Y. Ikeda, Y. Mizuta, H. Usami, H. Kawamoto, *Proc. Engineering Ceramics '99*, Trans Tech Pub., Switzerland (1999), in print.
[20] F. Lofaj, A. Okada, H. Usami, H. Kawamoto, *Ceram. Trans.,* **71,** (1996), p. 585.
[21] F. Lofaj, H. Gu, A. Okada, H. Kawamoto, *Mat.Sci.Forum Vols.* **294-296,** (1999), p. 621.
[22] F. Lofaj, H. Gu, A. Okada, H. Kawamoto, submitted to *J.Am.Ceram.Soc.*, (1999).
[23] R. Stemmer, G. Roebben, O. van der Biest, *Acta Mater.,* **46** [15] (1998), p. 5599.

Key Engineering Materials Vols. 171-174 (2000) pp. 755-762
© 2000 Trans Tech Publications, Switzerland

Creep Deformation and Fracture of SiC/SiC Composites

S. Zhu[1], M. Mizuno[2], Y. Kagawa[3] and Y. Ochi[1]

[1] The University of Electro-Communications, Chofu, Tokyo, Japan

[2] Japan Fine Ceramics Center, Atsuta-ku, Nagoya, Japan

[3] Institute of Industrial Sciences, University of Tokyo, Tokyo, Japan

Keywords: Creep, SiC/SiC Composite, Stress Exponent, Activation Energy, Deformation, Fracture

Abstract

The tensile creep tests of SiC fiber reinforced SiC composites at 1000-1300 C were conducted. The apparent stress exponent and activation energy for creep increase with a decrease in stress. The threshold stress approach was used to interpret the experimental data. Creep of SiC matrix is attributed to the rate-controlling process for the creep of the SiC/SiC composites. Creep fracture mechanism and life prediction method were also discussed.

Introduction

Creep behavior of continuous fiber reinforced ceramic matrix composites was recently investigated [1-17]. The incorporation of SiC fiber into Si_3N_4 results in substantial improvements in creep resistance [7]. Multiple fiber fracture rather than multiple matrix cracking was observed and creep mechanism was a repetitive matrix stress relaxation-fiber rupture-load transfer and distribution scheme [7]. Moreover, a threshold stress was found for tensile creep of unidirectional SiC_f/HPSN (Hot Pressed Silicon Nitride) composite, which was much higher than proportional limit [4,5].

The different mechanisms were found in creep of SiC_f/glass-ceramics at 1200 °C at different tensile stress levels [8]. At low stresses, cavities formed in the matrix with no significant fiber or matrix damage [8]. At moderate stresses, periodic fiber rupture occurred and at high stresses matrix fracture and rupture of the highly stressed bridging fibers limited creep life [8]. Since grain growth in Nicalon fibers enhanced creep resistance, creep deformation was found transient in nature at 1200 °C [9].

For SiC_f/SiC, flexural creep experiments in vacuum were reported at the temperatures of 1000 to 1400 °C [14-17]. A threshold stress for creep was found, which corresponded to the stress for matrix cracking. Considering that the state of stress in a flexural specimen is a strong function of time and temperature during creep, tensile creep tests are necessary to be carried out in order to understand creep behavior and mechanism of SiC/SiC and to establish a method for creep life prediction in SiC/SiC composites [18-20]. Carbon layer in SiC/SiC leads to low oxidation resistance at high temperatures [21-26]. Therefore, the tensile creep tests of the SiC/SiC composite were conducted in argon in this paper.

Experimental Procedure

The composites used in the investigation were processed by chemical vapor infiltration (CVI) of SiC into plain-woven 0°/90° Nicalon-fiber preforms (made by Du Pont Lanxide Composites Inc., U.S.A.). Before the infiltration the preforms were coated with carbon by CVD to decrease interface bonding between fibers and the matrix lead to increases in strength and toughness. The composites, processed as 200 mm X 200 mm panels with a thickness of 3.4 mm and 11 plies, contained 40 vol%

Nicalon fibers and 9.7 % porosity. The diameter of fibers was about 12 μm and each bundle consisted of 500 fibers. The density of the composite was 2.58 g/cm^3.
The tensile specimens were machined from the panels using diamond cutting tools. The dimensions of the plate-shaped specimens for tensile creep tests were 30 x 8 x 2.2 mm [19,27]. The surfaces of the specimens were machined by 800 grit grinding wheel before testing.
The monotonic tensile and constant load tensile creep tests were performed in argon and air at the temperatures of 1000 to 1300 °C with MTS 810 testing system. The alignment between the upper and lower grips of the load unit was adjusted using a steel specimen to allow the bending strain below 5 %. The displacement rate for monotonic tensile tests was 0.5 mm/min. The specimens were allowed to soak over 30 min. at the testing temperatures before starting tensile creep tests. Young's modulus during creep tests was measured by periodically unloading and reloading. The unloading and reloading rate was 2 MPa s^{-1}. The amount of unloading was 10 MPa. The crept specimens were observed by both optical microscopy and scanning electron microscopy (SEM).
For high temperature tests, MTS 659 controlled atmosphere furnace was used. The chamber was first allowed to pump down to less than 13.3 Pa (100 millitorr) and then backfill the chamber with high purity argon gas. The steps were repeated three times to ensure a thorough purge. The argon gas was flowed through the chamber enough to equal five times the chamber volume. The volume percentage of oxygen in the high purity argon gas was less than 1 ppm.

Results

Creep Deformation
A constant tensile load produces an instantaneous strain response followed by a time dependent strain [19]. The instantaneous strain consists of recoverable (elastic) strain at low stresses and nonrecoverable strain at high stresses. The time dependent (creep) strain is transient, and continuously decreasing strain rate (primary stage) appears at first. Then it goes to a steady state (constant strain rate, secondary) stage, at last accelerating (tertiary stage) to rupture. The existence of one or two or three stages depends on stress and temperature conditions. At high stresses, there is no tertiary stage or even no secondary stage. The accelerating creep stage appears after the steady state creep at low stresses. Abbé et al [14,15] also found steady state creep in flexure tests of SiC/SiC in vacuum at temperatures of 1100 to 1400 °C.
The minimum creep strain rate as a function of stress is shown in Fig. 1. The minimum creep strain rate ($\dot{\varepsilon}_m$) can be described by power law

$$\dot{\varepsilon}_m = A \cdot \sigma^n \cdot \exp(-Q/RT) \qquad (1)$$

where A is a constant, n is the apparent stress exponent for creep, Q is the apparent activation energy for creep, R is gas constant and T is the absolute temperature. The apparent stress exponent for creep increases with decreasing stress. The minimum apparent stress exponent is 5 and the maximum is 25. Moreover, an apparent threshold stress exists at a given temperature, below which creep strain rate falls below the detectable level. The apparent threshold stress is 75 MPa at 1000 and 1100 °C, 60 MPa at 1200 °C, and 30 MPa at 1300 °C. The apparent activation energies for creep calculated from equation (1). The apparent activation energy for creep decreases with increasing stress and tends to be a constant value at high stresses.

Creep Rupture

Young's modulus during creep was periodically measured to examine the cracking evolution. It was found that the variation of the Young's modulus was related to the evolution of matrix cracks (Fig. 2). The modulus decreases with time at stresses (120 and 180 MPa) higher than the matrix cracking

stress and remains constant at lower stresses (45 and 60 MPa).

The creep rupture time versus stress can be fitted by the empirical relation

$$t_r = B \cdot \sigma^{-N} \qquad (2)$$

where t_r is time to rupture, B is a constant and N is the stress exponent for stress rupture. According to equation (2), N is 5.8 at 1000 °C, 4.1 at 1100 °C, 8.1 at 1200 °C and 4.2 at 1300 °C. Most of them are similar to the stress exponents for creep at high stresses. The value at 1200 °C is unusually higher than others, since the data at 75 MPa are offset from others.
The steady state creep strain rates versus time to rupture is shown in Fig. 4. The data fall into a straight line, i.e., fit Monkman-Grant relation [38]

$$t_r \cdot \dot{\varepsilon}_m^q = C_{M-G} \qquad (3)$$

where q is the strain rate exponent and C_{M-G} is a constant. Fig. 3 shows that q is 0.72. Monkman-Grant relation provides a method for creep life prediction of SiC/SiC composite. If

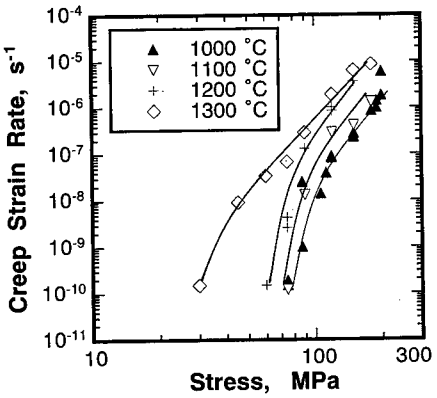

Fig. 1 Tensile minimum creep strain rate versus stress in argon at 1000, 1100, 1200 and 1300 °C.

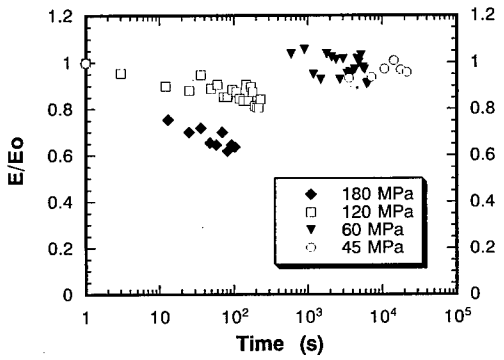

Fig. 2 Variation of Young's modulus measured by partial unloadings with time during creep at 1300 °C, E_o is the modulus in the linear portion during loading.

the steady state creep rate is known, the creep life can be easily calculated by the equation (3). However, creep rate is often difficult to be measured for a component in structures. In this case, some parameters may be useful for creep life prediction.

Larson-Miller parameter (P) [39] is one of the useful parameters used for predicting creep life in metallic materials. The basic assumptions of it are that q = 1 and Q is a function of stress. The present results are approximately satisfied with these assumptions. It can be used for correlating stress-temperature-life relationship in SiC/SiC composite in the following expression:

$$P = T \cdot (C + \log t_r) \qquad (4)$$

It was found that data at different temperatures fall on the same line with the best fit when the constant C is between 5 and 10, when the curves of log t_r vs $1/T$ were drawn. Fig. 4 shows the relation of stress with Larson-Miller parameter with C of 7. The constant (C) of Larson-Miller parameter is 20 for metals and alloys. For monolithic silicon nitride, it is among 30 and 40,

depending on grades of silicon nitride [40,41]. For oxides, it ranges from 10 to 22 [42]. The values of the constant for SiC/SiC composite are 5-10, determined by the data at four temperatures.

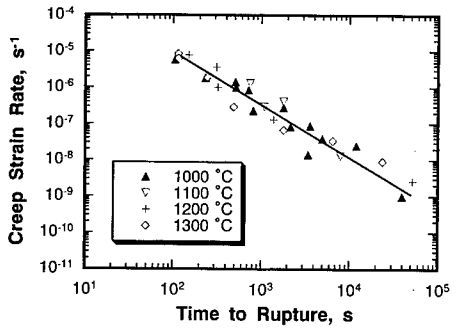

Fig. 3 Tensile minimum creep strain rate versus time to rupture at different stresses in argon at 1000, 1100, 1200 and 1300 °C.

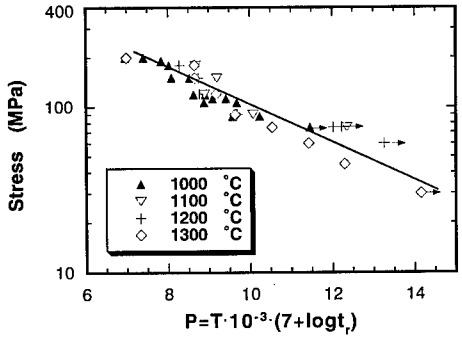

Fig. 4 Tensile stress versus Larson-Miller parameter at different stresses in argon at 1000, 1100, 1200 and 1300 °C.

Creep rupture surfaces exhibit that the fracture mode prefers to main 0° bundles' fracture. This is different from the fracture mode of monotonic tension at elevated temperatures, in which both 0° and 90° bundles fracture [27]. At low stresses, fracture surfaces consist of two regions: one is rough, with evident fiber pullout; another is plain, flush with the matrix. The lateral section of creep ruptured specimens shows that the matrix cracking occurs in the rough region, similar to that at high stress (Fig. 5 (a) and (b)). In the plain region, fibers fracture flush with the matrix and there are few cracks in the matrix (Fig. 5 (c)). At high stresses, cracks initiated at large pores between fiber bundles are bridged by intact 0° fibers. Crack propagation in 90° bundles is along fibers-matrix interfaces or connected by pores in the bundles. Crack propagation in 0° bundles at high stresses is similar to that in unidirectional fiber reinforced CMCs. A difference is that there is bundle's bending in plane woven CMCs, which produces stress concentration at the crossover points of fiber weaving structures. This may be why fiber pullout length in plane woven materials is smaller than that in unidirectional materials. The crack cuts through the 0° fibers. This means that creep fracture first took place in the plain region and finally in the rough region.

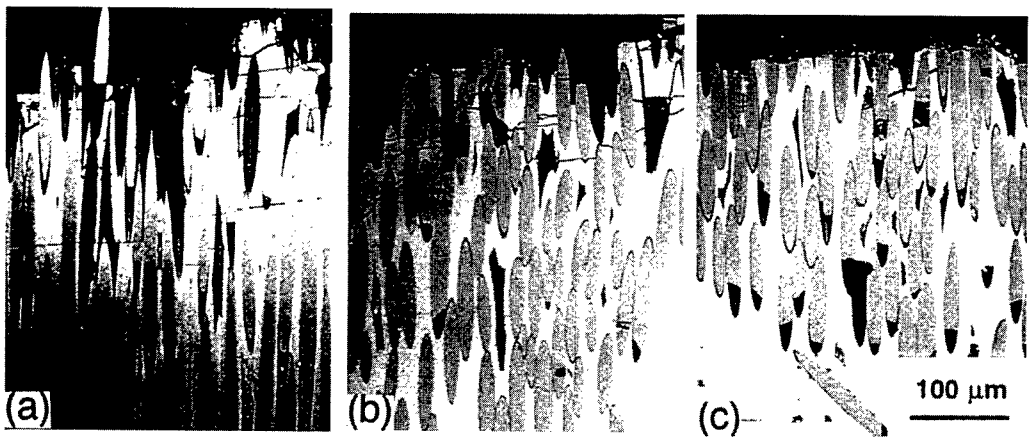

Fig. 5 Crack propagation paths on cross sections of crept specimens in argon. (a) 1300 °C, 180 MPa; (b) and (c) 1300 °C, 45 MPa.

Discussion

Since little is known about creep behavior of CVI SiC matrix at the temperatures of 1000-1300 °C, it is difficult to say if creep rate of the matrix is higher than that of the fiber in SiC/SiC although it was classified to the creep mismatch ratio < 1 [6]. The minimum steady-state creep rate of CVD SiC is 9.3 x 10^{-10} s^{-1} in argon at 1400 °C and 220 MPa [28], which is lower than the that (10^{-7}-10^{-8} s-1) of Nicalon fiber in argon at 1300 °C and 200 MPa extrapolating from the data at high stresses [29,30]. If CVI SiC in the composite is considered to be similar to CVD SiC, SiC/SiC composite should be classified to creep mismatch ratio > 1. Therefore, a time dependent redistribution in stress will be from the less creep resistant fibers to the more creep resistant matrix after loading. In this case, the stress transfer to the matrix will cause matrix cracking. However, this is base on no matrix cracking during the initial loading and a good stress transfer through interfaces.

Since the thermal expansion coefficient of SiC matrix is larger than that of Nicalon fibers, the residual stress on the fibers is compressive when the temperature is lower than the processing temperature, and relaxes with increasing temperature. Because the CVI processing temperature is about 1000 °C, the residual stress on the fibers is close to zero at 1000 °C and above 1000 °C. The stress state at the interface and the weak interface caused by carbon coating are inferior to stress transfer of the interface. Therefore, the extent of the stress redistribution according to CMR is very difficult to be estimated.

At high stresses, there is only transient creep stage. This is similar to creep behavior of Nicalon fibers [29,30]. Fibers creep is likely to be attributed to the rate controlling creep mechanism for the composite in tension. However, creep strain of SiC/SiC composite is one order of magnitude lower than that of Nicalon fibers at a given rupture time [29-31]. This means that creep of fibers is constrained by either the matrix or the weaving architecture. Moreover, the stress exponent and activation energy for creep of the composite are inconsistent with those of Nicalon fibers, as described later.

At low stresses, there are three stages of creep: transient, steady-state and tertiary stages. The steady-state stage is sometimes short and only exhibits a minimum creep rate. The tertiary stage is evident and covers a large portion of the creep strain. The progressive debonding of interfaces and the statistical rupture of fibers were attributed to the mechanism of tertiary creep in an Al_2O_3(f)/CVI-SiC composite with a 2D woven fiber architecture [13]. Since the stress is lower than the matrix cracking stress, few matrix cracks exist in the crept specimens (Fig. 5(c)). The stiffness remains constant with time (Fig. 2) and the flat fracture surfaces appear (Fig. 6(b)). Evans and Zok [32] stated that the rupture ductility of the ceramic fibers is typically quite low, and consequently, matrix cracking by stress transfer often leads to creep rupture with brittle characteristics.

The present tensile creep strain rates at a given stress and temperature were in the same order of magnitude as the flexural creep rates by Vicens et al [33]. The apparent activation energy for tensile creep was also similar to that for flexural creep [33]. However, the stress exponent for tensile creep was found to be larger than that for flexural creep. The phenomena were often seen in creep tests in monolithic ceramics [34]. In monolithic ceramics, the higher stress exponent in tensile creep than in flexural creep is generally attributed to cavitation or microcracking in tension but not in compression.

To examine the effects of fibers, we compare the present results with the tensile creep behavior of an Al_2O_3(f)/CVI-SiC composite (Al_2O_3/SiC) with a 2D woven fiber architecture [12,35]. The steady-state creep rate in Al_2O_3/SiC exhibited two distinct regimes depending on creep stress at the temperatures of 950 to 1100 °C. The stress exponent for creep was 9.5 at low stresses and 4.5 at high stresses. This result is similar to the present result in the similar temperature and stress conditions. However, creep strain of Al_2O_3/SiC is one order of magnitude higher than that of SiC/SiC. Although Al_2O_3 fibers are less creep resistant than Nicalon fibers, their creep onset temperatures and creep ductility are similar [36]. Since the difference in thermal expansion coefficient between the fibers and matrix in Al_2O_3/SiC is larger than that in SiC/SiC, the matrix

cracking in Al_2O_3/SiC is much more extensive than that in SiC/SiC. Thus, the constraint of the matrix on creep of fibers in Al_2O_3/SiC is less. The stress exponent for creep of Al_2O_3/SiC is similar to that of Al_2O_3 fibers. Therefore, it was suggested that creep rate of Al_2O_3/SiC was controlled by creep of the bridging fibers at high stresses. Evidently, creep behavior of SiC/SiC is different from that of Al_2O_3/SiC.

2D SiCf/CAS composite has the same fibers and different matrix as SiC/SiC. Creep strain of SiC/CAS [8] is also one order of magnitude higher than that of SiC/SiC. Here it should be noted that the matrix contributes little resistance to creep strain of the composite in SiCf/CAS at 1200 °C. Moreover, the stress exponent for creep of SiCf/CAS is consistent with that of Nicalon fibers, indicating that the composite creep rate appears to be primarily controlled by creep of Nicalon fibers.

From creep of Al_2O_3/SiC and SiC/CAS, we can conclude that creep of fiber controls the creep of the composite only when the matrix contributes little to creep deformation of the composite. SiC/SiC does not satisfy the prerequisite, since the matrix cracking is not very extensive and creep resistance of the matrix is higher than that of Nicalon fibers. The apparent stress exponents for creep of SiC/SiC are much higher than those of SiC fibers (1-2 [29]). The apparent activation energies for creep of the composite at high stresses are lower than those of the fibers (370-490 kJ/mol [29]).

In fact, a crack propagation in the matrix depends on both creep of the bridged fibers in wake of crack and creep of the matrix in front of crack tip. Since the both processes are intercorrelated, the lowest one is the rate-controlling process. Compression creep of CVD SiC showed that the stress exponent for creep is 2.3 and the activation energy is 175 kJ/mol [28]. The latter is very close to that of the composite at high stresses (Fig. 6). The stress exponent for compressive creep of CVD SiC is similar to that for flexural creep of the composite [14]. Therefore, creep of the composite might be controlled by creep of the matrix.

The apparent stress exponent and activation energy for creep of SiC/SiC increase with decreasing stress (Fig. 2). This is similar to creep behavior of SiC whiskers reinforced aluminum composites [37]. It was explained by introducing a resisting stress (threshold stress) which may be related with the interaction of whiskers with dislocations in the matrix. Following this approach, we phenomenologically treat the present creep data of SiC/SiC.

If we ploted $\dot{\varepsilon}_m^{1/n}$ with σ, n was 5 for a best fit of a linear relation (Fig. 6). Defining the threshold stress as the applied stress to which zero creep rate corresponded at a given temperature, the values of the threshold stress (σ_{th}) could be calculated at different temperatures. Then, the creep rates normalized to $\exp(-Q_L/RT)$ (Q_L is the activation energy (175 kJ/mol) for creep of CVD SiC [28]) were plotted against the effective stress ($\sigma - \sigma_{th}$), as shown in Fig. 7. It can be seen that all the data points can be well fitted by a single straight line with a slope of 5. However, if the activation energy for creep of Nicalon fibers was used to normalize creep rates, all the data could not fall on the same line. This means that creep of the composite is controlled by creep of the matrix.

Introducing the threshold stress, the equation (1) becomes

$$\dot{\varepsilon}_m = A \cdot (\sigma - \sigma_{th})^{n'} \cdot \exp(-Q'/RT) \qquad (5)$$

where $n' = 5$ and Q' is the activation energy of the matrix (175 kJ/mol). Combining this equation with Eqs. (1) and assuming that the modulus of the matrix does not vary with temperature, the apparent stress exponent and apparent activation energy for creep

$$n = \frac{5 \cdot \sigma}{\sigma - \sigma_{th}} \qquad (6)$$

and

$$Q = Q' - \frac{n' RT^2}{\sigma - \sigma_{th}} \frac{d\sigma_{th}}{dT} \qquad (7)$$

is obtained. It can be seen that both the apparent stress exponent and activation energy decrease with increasing temperature from Eqs. (6) and (7).

Conclusions

Tensile creep behavior of SiC-fiber reinforced SiC composite has been investigated in argon at the temperatures of 1000-1300 °C. The apparent stress exponents for creep of the composite and the apparent activation energies for creep increase with the decrease of stress. The threshold stress approach can be used to treat the data. Creep of the matrix controls creep of the composites. The relationship between creep rate and time to rupture can be described by Monkman-Grant equation. Moreover, Larson-Miller parameter can also be used for creep life prediction of the composite when a proper constant is selected.

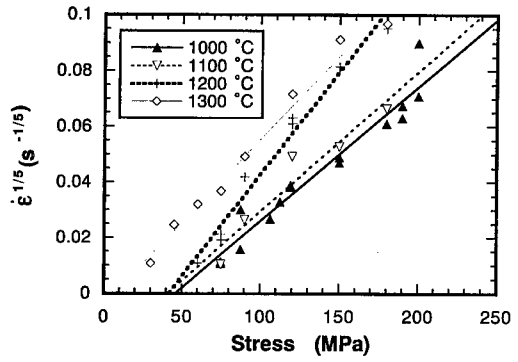

Fig. 6 Relationship between $\dot{\varepsilon}_m^{1/n}$ and σ (n is 5).

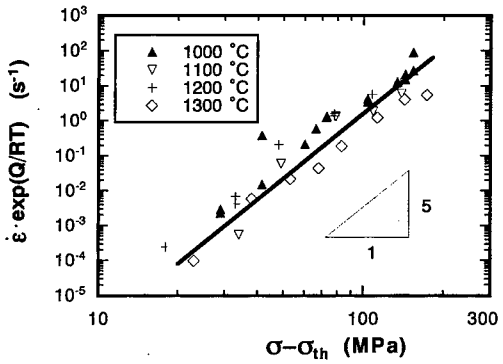

Fig. 7 Creep strain rates normalized to $\exp(-Q_L/RT)$ versus the effective stress $(\sigma - \sigma_{th})$, Q_L is 175 kJ/mol, the activation energy for creep of CVD SiC [28].

References

1. J. W. Holmes, J. Am. Ceram. Soc., 74 (1991), p. 1639.
2. J. W. Holmes, J. Mater. Sci., 26 (1991), p. 1808.
3. Y. H. Park and J. W. Holmes, J. Mater. Sci., 27(1992), p. 6341.
4. J. W. Holmes, Y. Park and J. W. Jones, J. Am. Ceram. Soc., 76 (1993), p. 1281.
5. J. W. Holmes and J. L. Chermant, High Temperature Ceramic Matrix Composites, ed. R. Naslain, J. Lamon, D. Doumeingts (Woodhead Publishing Limited, 1994), p. 633.
6. J.L.Chermant and J.W. Holmes, High Temperature Ceramic Matrix Composites I: Design, Durability and Performance, ed. A.G. Evans and R. Naslain (The American Ceramic Society, 1995), p. 95.
7. R. B. Thayer and J.-M. Yang, Mater. Sci. Eng., A160 (1993), p. 169.
8. X. Wu and J. W. Holmes, J. Am. Ceram. Soc., 76 (1993), p. 2695.
9. C. H. Weber, J. P. A. Lofvander and A. G. Evans, J. Am. Ceram. Soc., 77 (1994), p. 1745.
10. D. W. Meyer, R. F. Cooper and M. E. Plesha, Acta Metall. Mater., 41 (1993), p. 3157.

11. M. Khobaib and L. Zawada, Ceram. Eng. Sci. Proc., 12 (1991), p. 1537.
12. F. Lamouroux, M. Steen & J. L. Valles, J. Euro. Ceram. Soc., 14 (1994), p. 529.
13. F. Lamouroux, J. L. Valles & M. Steen, J. Euro. Ceram. Soc., 14 (1994), p. 539.
14. F. Abbe, J. Vicens and J. L. Chermant, J. Mater. Sci. Lett., 8 (1989), p. 1026.
15. F. Abbe and J. L. Chermant, Creep and Fracture of Engineering Materials and Structures, ed. W. Wilshire and R. W. Evans (London, UK: The Institute of Metals, 1990), p. 439.
16. J. L. Chermant, F. Abbe and D. Kervadec, Creep and Fracture of Engineering Materials and Structures, ed. W. Wilshire and R. W. Evans (London, UK: The Institute of Metals, 1993), p. 37.
17. D. Kervadec and J. L. Chermant, Fracture Mechanics of Ceramics, Vol. 10, ed. R. Bradt, et al (New York, NY: Plenum Press, 1992), p. 459.
18. S. Zhu, M. Mizuno, Y. Kagawa, J. Cao, Y. Nagano and H. Kaya, Mater. Sci. Eng., A225 (1997), p. 69.
19. S. Zhu, M. Mizuno, Y. Nagano, Y. Kagawa and H. Kaya, Comp. Sci. and Tech., 57 (1997), p. 1629.
20. S. Zhu, M.Mizuno, Y.Nagano, J. Cao, Y.Kagawa and H. Kaya, J. Am. Ceram. Soc., 81 (1998), p. 2269.
21. N. Frety, R. Molins, M. Boussuge, J. Mater. Sci., 27 (1992), p. 5084.
22. L. Filipuzzi, G. Camus, R. Naslain, J. Thébault, J. Am. Ceram. Soc., 77 (1994), p. 459.
23. M. Huger, D. Fargeot, C. Gault, J. Am. Ceram. Soc., 77[10] (1994), p. 2554.
24. M. L. Bouchetou, T. Cutard, M. Huger, D. Fargeot,C. Gault, High-temperature Ceramic-matrix Composites I: Design, Durability, and Performance, Ed. A.G. Evans, and R. Naslain, (American Ceramic Society, 1995), p. 181.
25. M. Elahi, K. Liao, K. Reifsnider, T. Dunyak, Ceram. Eng. & Sci. Proc., 16 (1995), p. 75.
26. D. S. Fox, Ceram. Eng. & Sci. Proc., 16 (1995), p. 877.
27. M. Mizuno, S. Zhu, Y. Nagano, Y. Sakaida, Y. Kagawa, M. Watanabe, J. Am. Ceram. Soc., 79 (1996), p. 3065.
28. C. H. Carter, Jr., R.F. Davis, J. Am. Ceram. Soc., 67(1984), p. 732.
29. G. Simon, A. R. Bunsell, J. Mater. Sci., 19 (1984), p. 3658.
30. N. Jia, R. Bodet, and R. E. Tressler, J. Am. Ceram. Soc., 76 (1993), p. 3051.
31. R. Bodet, X. Bourrat, J. Lamon, R. Naslain, J. Mater. Sci., 30 (1995), p. 661.
32. A. G. Evans and F. W. Zok, J. Mater. Sci., 29 (1994), p. 3857.
33. J. Vicens, M.-H. Rouillon, P. Fourvel, F. Abbe, M. Gomina and J.-L. Chermant, Microsc. Microanal. Microstruct., 2 (1991), p. 75.
34. M.K. Ferber and M.G. Jenkins, J. Am. Ceram. Soc., 75 (1992), p. 2453.
35. J. N. Adami, These de Docteur és Science Techniques, (L'École Polytechnique Fédérale de Zürich, 1992).
36. J.A. DiCarlo, Comp. Sci. Tech., 51 (1994), p. 213.
37. J. Èadek, H. Oikawa, V. Sustek, Mater. Sci. Eng., A190 (1995), p. 9.
38. F.C. Monkman and N.J. Grant, Proc. Am. Soc. Test. Mater., 56 (1956), p. 593.
39. F. R. Larson and J. Miller, Trans. ASME, 74 (1952), p. 765.
40. M. Masuda, T. Makino, Y. Nakasuji and M. Matsui, Fracture Mechanics of Ceramics, ed. R.C. Bradt, et al, Vol. 9 (New York, NY: Plenum Publ. Corp., 1992), p. 481.
41. S. M. Wiederhorn, J. D. French, W. E. Luecke, Ceramic Materials and Components for Engines, ed. D.S. Yan, X.R. Fu, S.X. Shi (Singapore, World Scientific, 1994), p. 145.
42. S. Deng and R. Warren, J. Europ. Ceram. Soc., 15 (1995), p. 513.
43. M.R. Begley, B.N. Cox and R.M. McMeeking, Acta Metall.Mater., 43 (1995), p. 3927.
44. M.R. Begley, A.G. Evans and R.M. McMeeking, J. Mech. Phys. Solids, 43 (1995), p. 727.
45. A.G. Evans and C. Weber, Mater. Sci. Eng., A208 (1996), p. 1.
46. C.R. Jones, C.H. Henager, Jr. and R.H. Jones, Scr. Metall. Mater., 33 (1995), p. 2067.

Key Engineering Materials Vols. 171-174 (2000) pp. 763-770
© 2000 Trans Tech Publications, Switzerland

Cavitation Failure in a Superplastic Alumina with Zirconia-Particle Dispersion

K. Hiraga, Y. Sakka, T.S. Suzuki and K. Nakano

National Research Institute for Metals, 1-2-1, Sengen, Tsukuba-shi, Ibaraki 305-0047, Japan

Keywords: Cavity Formation and Growth, Cavity Interlinkage, Microcracking, Crack Propagation, Tensile Ductility

Abstract High temperature tensile failure in a fine-grained alumina with zirconia particle dispersion is found to relate closely to the separation distance among micrometer-sized cavities growing from preexistent defects and from newly formed ones during deformation. As the separation distance is decreased to a certain level with an increase in both density and size of such cavities, extensive cavity interlinkage starts to cause microcracking, and the microcracking leads to the occurrence of macroscopic cracks propagating in a direction perpendicular to the tensile axis toward the final failure. The dependence of the onset strain of microcracking on temperature and grain size is also found to relate closely to the dependence of cavity formation and growth rates on these factors.

1. Introduction

Earlier studies [1-4] have often pointed out that failure in fine-grained ceramics undergoing superplastic or superplastic-like tensile deformation is controlled by microcracks propagating in a direction perpendicular to the tensile axis. In spite of the general accordance of such qualitative observation for the final process of tensile failure, however, mechanisms relating to the microcracking have still been unclear owing to rather limited information on the evolution of damage accumulation in superplastic ceramics. For example, even the nature of microcracking noted in the earlier studies is essentially different to each other. Kim et al. [1] proposed that microcracks occur from preexistent defects and propagate from the beginning of tensile deformation to failure in a brittle manner. In contrast, Schissler et al. [2] and Chokshi et al. [3, 4] associated the microcracking with extensive cavity interlinkage. In this process, plastic deformation is latently assumed for internal necking in the matrix lying between the adjacent cavities. To obtain a definite basis for discussing the mechanisms of tensile failure in superplastic ceramics, quantitative information is therefore necessary on the occurrence and growth of microcracks. From this point of view, the present study examine the damage evolution in a superplastic alumina containing 10 vol% zirconia particles [5, 6]. An emphasis was placed on the relationship between cavity damage accumulation and microcracking.

2. Experimental Procedure

Colloidal processing [6] was applied to high purity α-Al_2O_3 (>99.99%, TM-DAR, Taimei Chemical) and 3 mol% yttria-stabilized tetragonal zirconia (>99.97%, TZ-3Y, Tosoh) powders with nominal particle diameters of 0.2 μm and 0.03 μm, respectively. An aqueous suspension prepared electrosterically from these powders and an ammonium polycarboxylate was consolidated by slip casting followed by cold-isostatical pressing at 400 MPa. Sintering at 1673 K for 2 h in air resulted in a relative density of 99.6 % and an equiaxed grain structure with uniform dispersion of

zirconia particles with an average size of 0.1 μm. The average alumina grain size, d_0, was 0.45 μm, where the size was determined by scanning electron microscopy (SEM) and defined as 1.56 times the average intercept length of grains corrected for second phase dispersion [7]. Some of the sintered compacts were aged at 1773 K for 9 h and 1873 K for 22 h to obtain coarser grain sizes of 0.95 and 2.0 μm, respectively.

From the compacts with and without aging, dog-bone-shaped flat tensile specimens were machined with gauge dimensions of '10-'3-"3.5 mm. By using an Instron-type machine, the specimens were deformed to prescribed tensile strains at 1673-1773 K, at an initial strain rate of $\dot{\varepsilon}_0=1.7\times10^{-4}$ s^{-2}. After loading, a surface layer of about 500 μm was removed from each deformed specimen for polishing to a 1 μm diamond finish.

Quantitative microstructural examination for the numerical density, size and shape of cavities [8, 9] was carried out near the center of the as-polished gauge portion using an optical microscope equipped with an image analyzer. The resolution of the examination was set to 1.0 μm and cavity numbers counted were $(1\sim2)\times10^4$ for each specimen.

3. Results and Discussion

3. 1. Tensile Flow Behavior

As shown in Fig. 1, the as-sintered material shows substantial superplasticity, where tensile elongation to failure reaches 300 and 550 % at 1723 and 177 K, respectively. The dependence of tensile behavior on temperature and grain size is consistent with the general trend reported in some fine-grained oxides such as tetragonal zirconia [10] and magnesia doped alumina [11]: a decrease in temperature or an increase in grain size heightens the level of flow stress and results in decreased tensile ductility. A noticeable decrease in flow stress with increasing strain appearing at 1773 K for d_0=2.0 μm and at 1673 K for d_0=0.45 μm is due to active cavity damage accumulation as will be shown in the following sections.

3.2 Aspects of Damaged Microstructure

Damaged microstructures were observed as a function of true strain normalized with failure strain, $\in/\in_f$. Regardless of the variation in tensile behavior due to the difference in temperature and grain size as shown in Fig. 1, there was close resemblance in the aspects of damaged microstructures against the $\in/\in_f$-value. At strains up to $\in/\in_f\sim0.8$, more than 95% of cavities were rounded with aspect ratios (=major axis length/minor axis length) smaller than 2.0 and dispersed uniformly with a very little indication of coalescence. At larger strains, although cavity coalescence had already started, it was localized in a region around individual cavities and their sizes stayed smaller than 10 μm (Fig. 2(a)). As the $\in/\in_f$-value exceeded about 0.8, extensive interlinkage occurred among the cavities. The extensive interlinkage was enhanced with an increase in the $\in/\in_f$ value, resulting in microcracks growing in a direction perpendicular to the stress axis with sizes

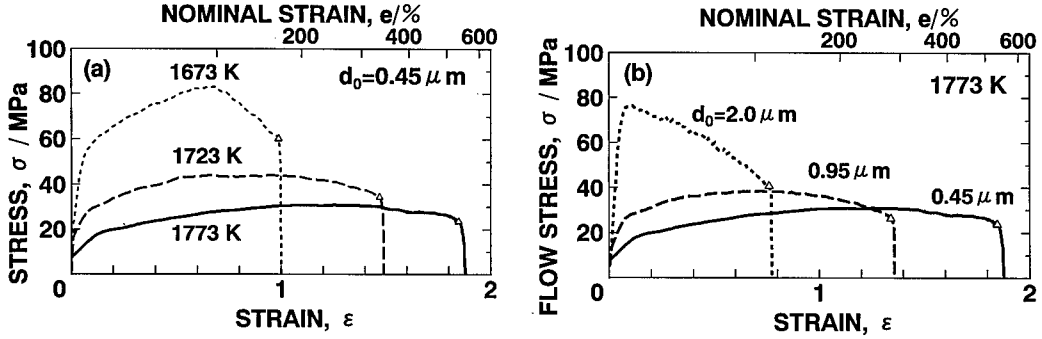

Fig. 1 The dependence of tensile flow on (a) temperature and (b) grain size.

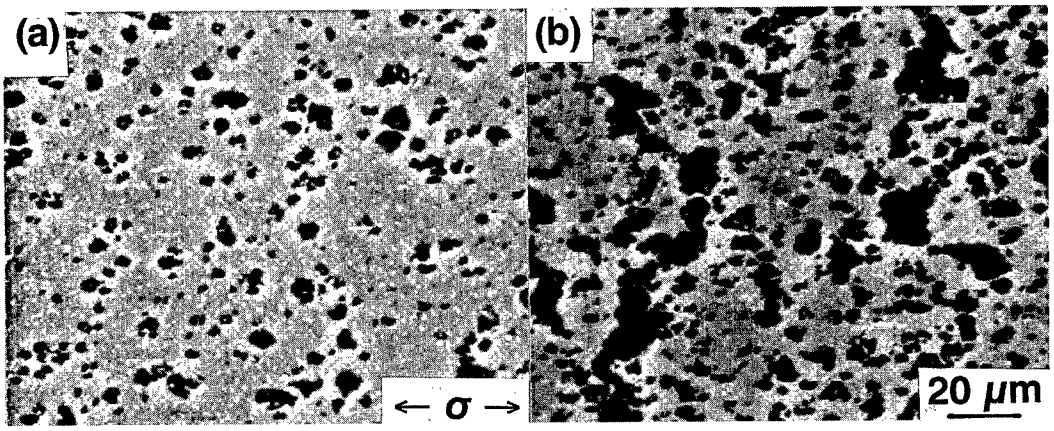

Fig. 2 Cavitated microstructures (1773 K, d_0=0.45 μm). (a) $\in/\in_f$=0.85. (b) $\in/\in_f$=0.93.

larger than 20 μm (Fig. 2(b)). From this observation, cavities with major axis lengths larger than 20 μm and with aspect ratios smaller than 2.0 are noted as microcracks in the following examination. As shown in Fig. 3, the final failure in each specimen took place by the propagation of one or more macroscopic cracks. The sign of such macroscopic cracking was not observed until the $\in/\in_f$-value exceeded 0.9~0.95. The present observation typically shown in Fig. 3(a) indicates that the macroscopic cracks occurred from the interlinkage of the microcracks.

Extensive observation of failed and interrupted specimens drew the following information on the nature of the macroscopic cracks. Large crack opening (Figs. 3(a) and (b)), heavy damage zone beside the cracks (Fig. 3(b)) and winding crack paths (Fig. 3(a)) are characteristics of the macroscopic cracks propagating in the present material. These are the strong indications that the cracks did not propagate in such a fully brittle manner as proposed by Kim et al. [1], but that plastic deformation did pertain during propagation.

To obtain a support to this observation, examination was made on the critical stress intensity factor, K_c for the final failure. In specimens pulled to failure, observation along the crack axis enabled us to distinguish the portion of gradual crack propagation from that of rapid propagation toward the final failure and hence to evaluate the crack length just before the rapid propagation had

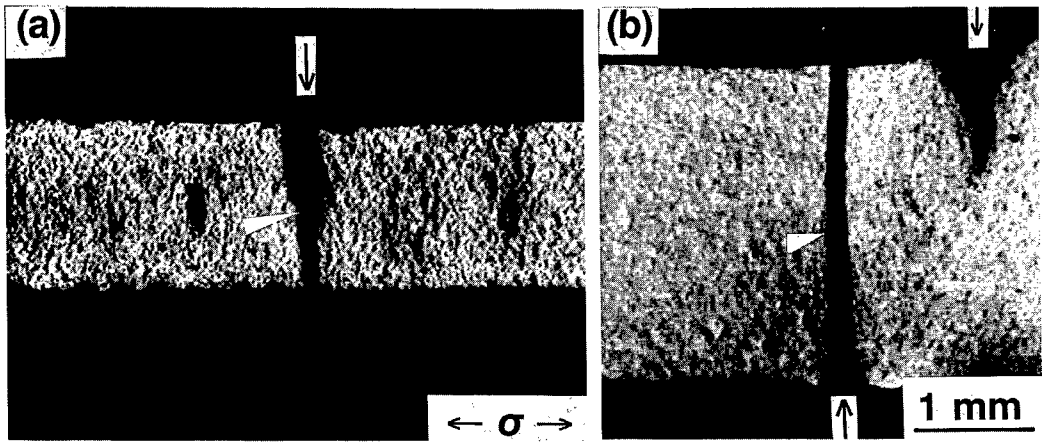

Fig. 3 Macroscopic view of crack propagation. (a) 1773 K, d_0=0.45 μm. (b) 1773 K, d_0=2.0 μm. Arrows indicate the direction of crack propagation and white arrows indicate the detected onset points of rapid propagation, respectively.

Table 1 Evaluation of K_c-values.

T/K	d_0/μm	A_d^*	K_c/MPam$^{1/2}$
1773	0.45	0.39	5.7
1723	0.45	0.34	5.5
1673	0.45	0.26	12.1
1773	0.95	0.27	3.0
1773	2.0	0.24	5.7

* damaged area fraction just befor failure.

started. The onset stress of the rapid crack propagation can be evaluated by regarding the point from which steep reduction in flow stress appears just before failure (see open triangles in Fig. 1) as the initiation of the rapid propagation. Table 1 lists the K_c-value evaluated from the crack length and the onset stress which was obtained directly from the load-displacement curve and the dimensions beside the crack in each failed specimen. Although little information is available on the high temperature fracture toughness of zirconia dispersed alumina, values for fine-grained alumina at room temperature can be regarded as an upper bound for fully brittle fracture in the present specimens. This is because, at the temperatures used in this study, toughening by phase transformation in zirconia particles does not work and a decrease in Young's modulus is expected to decrease fracture toughness. We should also note that porosity in deformed specimens causes a reduction in fracture toughness as $K_{IC} \simeq K_{IC0}\exp(-4.2P_f)$ in alumina [12], where K_{IC0} is the fracture toughness without porosity and P_f is the fraction of porosity. Applying the best K_{IC0}-values of 3.5~5.5 MPam$^{1/2}$ for virgin alumina with d_0~1 μm [12] and the damaged area fraction, A_d, listed in Table 1 to this equation yields K_{IC}=0.7~2.2 MPam$^{1/2}$ as the upper bound of the present consideration. The K_c-values evaluated in Table 1 are markedly higher than this upper bound. Fully brittle fracture can thus be ruled out in the present specimens. Intervention of plasticity during crack propagation is therefore the most reasonable explanation for such large K_c-values and the features of cracks observed in Fig. 3.

3.3. Microcracking in Relation with Cavitation Damage

To obtain quantitative information on microcracking, the numerical density of microcracks was examined as a function of local strain defined as $\in_l=\ln(S_0/S)^*$, where S_0 is the cross-sectional area of the gauge portion before deformation and S is the cross-sectional area of the gauge portion at

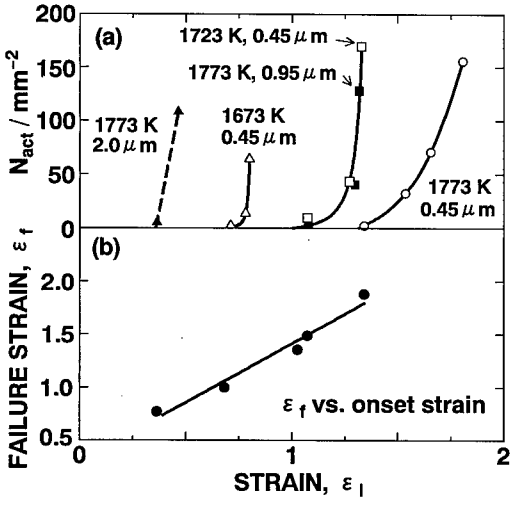

Fig. 4 Occurrence of microcracking ((a)) and failure strain as a function of the onset strain of microcracking ((B)).

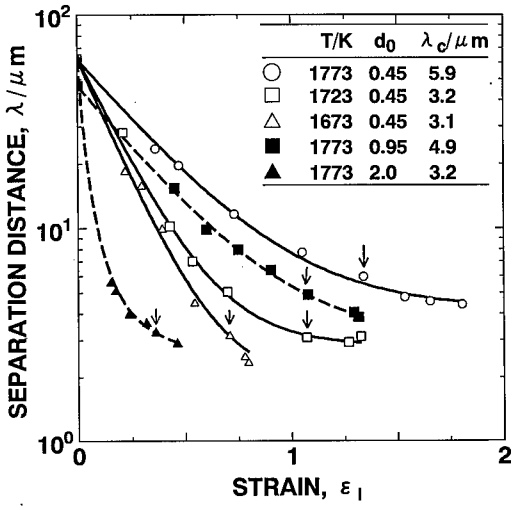

Fig. 5 Cavity separation distance as a function of local true strain. Arrows indicate the onset of microcracking

* By use of ε_l, we can avoid interference from deformation at the specimen shoulders and from broad necking which occur at strains near failure.

which the measurement was performed. In this examination, the crack density is corrected against areal expansion due to cavitation damage as $N_{acr}=N_{at}/(1-A_d)$, where N_{at} is the total number of microcrack per unit area and A_d is the damaged area fraction at each strain. The results shown in Fig. 4(a) reveal a threshold-like feature in microcracking: as tensile strain reaches to a certain level, microcracks start to occur and the microcrack density increases steeply with an increase in strain. As demonstrated in Fig. 4(b), tensile true strain to failure is proportional to the onset strain of microcracking. Microcracking is thus a strong indication of the initiation of failure process in the present material.

Since the brittle propagation is not the case for the macroscopic cracks, intervention of plasticity is a reasonable assumption for microcracking, that is, internal necking in the matrix between cavities is assumed to control microcracking. According to the models for internal necking [13, 14], the onset strain of internal necking is a strong function of the separation distance among the existent cavities. To examine this point, the cavity separation distance, λ, was evaluated as

$$\lambda=l_{av}-D_{av}$$

$$=(4/\pi\Sigma N_{ai})^{1/2}-\Sigma N_{ai}D_i/\Sigma N_{ai}, \quad (1)$$

where l_{av} and D_{av} are the average center to center spacing and the average area-equivalent circle diameter of cavities larger than 1.0 μm, respectively, N_{ai} is the cavity density and D_i is the cavity diameter of size class i. As shown in Fig. 5, the separation distance decreases with an increase in strain owing to an increase in both density and size of cavities. Comparison with Fig. 4(a) reveals that microcracking starts when the separation distance decrease to a critical value, λ_c, of about 4±1 μm except for a slightly large value at 1773 K for d_0=0.45 μm. The onset of microcracking from λ_c=3~4 μm has also been observed in an earlier study [9] on a zirconia-dispersed alumina prepared by conventional processing and a magnesia-doped alumina deformed at 1723 K. Such a close relationship between the cavity separation distance and microcracking strongly supports the internal necking mechanism. A trend of increasing λ_c-value with increasing temperature or decreasing grain size also support this mechanism, because a decrease in flow stress due to smaller grain sizes and/or higher temperatures is expected to decrease the λ_c-value.

3. 4. Temperature and Grain Size Dependence of Microcracking

As expressed by Eq. (1), the cavity separation distance is a function of the numerical density and size of cavities. This means that the onset strain of microcracking depends on cavity formation* and/or growth rates. Figure 6 represents the total cavity density, $N_{acr}=\Sigma N_{ai}/(1-A_d)$ as a function of local strain. The nonlinear dependence of cavity formation on strain at $\in<\sim 0.8\in_f$ relates to a constraint for growth of cavity nuclei into sizes larger than the current grain size [15], and the tendency toward saturated density near failure is due to extensive cavity coalescence. The figure demonstrates that the total cavity density depends strongly on temperature and grain size: the density noticeably increases either with a decrease in temperature for a given temperature or with an increase in grain size for a given temperature. Quantitative examination by SEM [15] confirmed that the temperature and grain size dependence of cavity formation reflects the dependence of cavity nucleation rate on these factors.

To get information on cavity growth without interference from continuous cavity formation, the average cavity diameter, D_{av}, was evaluated in the tail of each cavity size distribution as

$$D_{av}=\sum_{i=j-k}^{j} N_{aci}D_i \Big/ \sum_{i=j-k}^{j} N_{aci}, \quad (2)$$

* Since the examination was confined to cavities larger than 1.0 μm, the usual term *cavity nucleation* was not used.

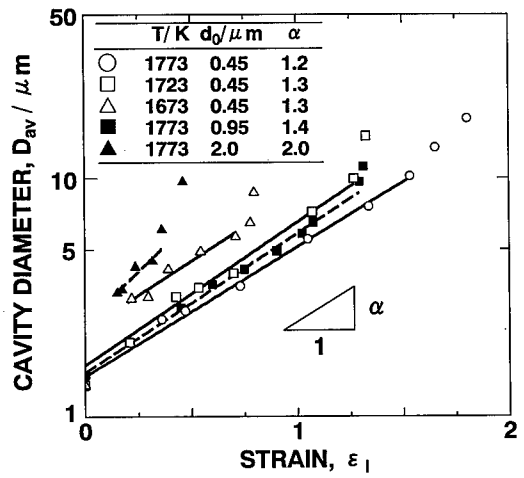

Fig. 6 Total cavity density as a function of local true strain.

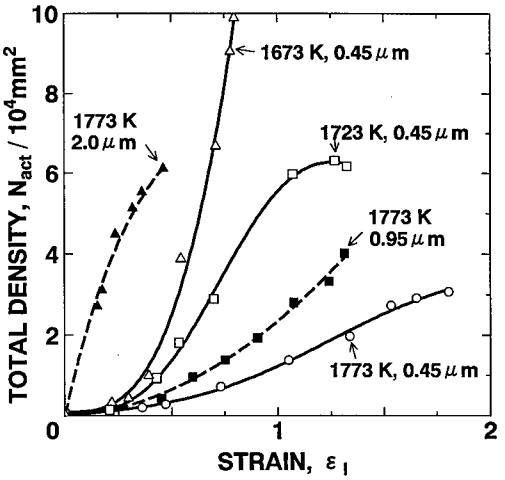

Fig.7 Average cavity diameter as a function of local true strain.

where $N_{aci}=N_{ai}/(1-A_c)$ is the corrected numerical density of cavities in size class i and j is the largest size class in each size distribution. The range of size class, k, is determined so that ΣN_{aci} remains constant for the respective size distributions at different strains. Setting ΣN_{aci}=400 mm^{-2}, which is the cavity density before deformation, Eq. (2) gave the average cavity sizes plotted in Fig. 7. For strains where extensive cavity interlinkage was inactive, a linear relationship holds between ln (D_{av}) and ε_l in each specimen. This leads to the following growth law, which also appears in a magnesia-doped alumina [9] and a tetragonal zirconia [16]:

$$D_{av}(\varepsilon)=D_{av0}\exp(\alpha\varepsilon), \qquad (3)$$

where D_{av0} is the diameter from which cavity growth obeys Eq. (3) and α is the rate constant. At 1723~1773 K for d_0=0.45~0.95, both α-value and intersection to the ordinate are almost the same, that is, the growth behavior is almost the same under these conditions. The data indicate, however, that a lowered temperature (1673 K for d_0=0.45 μm) or a larger initial grain size (d_0=0.2 μm at 1773 K) enhances cavity growth, since the cavity tends grow more rapidly to about 3 μm than the prediction of Eq. (3) and a larger α-value appears for d_0=2.0 μm. Such a trend may possibly be correlated with localized cavity coalescence in sizes finer than the resolution of optical microscopy, which was observed by SEM for these cases.

From Figs. 5 through 7 and Eq. (1), the dependence of microcracking and hence tensile ductility (Fig. 4(b)) on temperature and grain size can be explained as follows. For higher temperatures or smaller grain sizes, namely at 1723~1773 K for d_0=0.45~0.95, cavity growth is not closely associated with a difference in the onset strain of microcracking. Under these conditions, the rate of cavity formation controls the onset of microcracking. A lowered temperature (1673 K, d_0=0.45 μm) or a larger initial grain size (1773 K, d_0=2.0 μm) enhances both growth and formation of cavities and thereby decrease the onset strain of microcracking and tensile ductility.

4. Summary and Conclusions

(1) In a zirconia-dispersed alumina with initial grain sizes of 0.45~2.0 μm, tensile failure during superplastic or superplastic-like deformation at 1673~1773 K takes place through the propagation of one or more macroscopic cracks in a direction perpendicular to the stress axis. Evidence is

obtained that the cracks do not propagate in such a brittle manner as proposed in earlier work.
(2) The macroscopic cracks are formed at strains larger than 90~95% of failure strain by the interlinkage of microcracks. The microcracks start to occur as the separation distance of micrometer-sized cavities decreased to a certain level, indicating that internal necking of the matrix between the adjacent cavities controls microcracking.
(4) The dependence of tensile ductility on temperature and grain size arises from the dependence of cavity formation and growth rates on these factors: lower temperatures and larger initial grain sizes enhance cavity formation and/or growth, and thereby decrease the onset strain of microcracking and tensile ductility.

Acknowledgement

The authors thank Dr. T. Tanabe for his advice on high-temperature experiments.

References

[1] W-J. Kim, J. Wolfenstine and O. D. Sherby, Acta metall.mater. 9(1991), p. 199.
[2] D. J. Schissler, A. H. Chokshi, T. G. Nieh and J. Wadsworth, Acta. metall. mater. 39(1991), p. 3227.
[3] A. H. Chokshi, T. G. Nieh and J. Wadsworth, J. Am. Ceram. Soc. 74(1991), p. 869.
[4] A. H. Chokshi, Mater. Sci. Forum, 304-306(1998), p. 387.
[5] K. Nakano, T. S. Suzuki, K. Hiraga and Y. Sakka, Scr. Mater. 39(1998), p. 1273.
[6] Y. S. Suzuki, Y. Sakka, K. Nakano and K. Hiraga, Mater. Trans. JIM 39 (1998), p. 689.
[7] K. J. C. Wurst and J. A. Nelson, J. Am. Ceram. Soc. 55(1972), p. 109.
[8] K. Hiraga, K. Nakano, T. S. Suzuki and Y. Sakka, Scr. Mater. 39(1998), p. 1273.
[9] K. Hiraga, K. Nakano, Y. S. Suzuki and Y. Sakka, Mater. Sci. Forum 304-306(1998), p. 431.
[10] T. Kondo, Y. Takigawa and T. Sakuma, Mater. Sci. Eng. A231(1997), p. 163.
[11] Y. Yoshizawa and T. Sakuma, Acta metall. mater. 40(1992), p. 2943.
[12] R. W. Rice, J. Mater. Sci. 31(1996), p. 1969.
[13] P. F. Tomason, Acta metall. 33(1985), p. 1079.
[14] T. Pardoen, I. Doghri and F. Delannay, Acta mater. 46(1998), p. 541.
[15] K. Hiraga, K. Nakano, T. S. Suzuki and Y. Sakka, to be published.
[16] K. Hiraga and K. Nakano, Mater. Sci. Forum 243-245(1997), p. 387.

e-mail address: hiraga@nrim.go.jp

Key Engineering Materials Vols. 171-174 (2000) pp. 771-778
© 2000 Trans Tech Publications, Switzerland

Tensile Deformation of Both ZrO_2/TiC Composite and Al_2O_3/TiC Composite at High Temperature

H. Miyazaki[1], K. Kubobuchi[1], K. Yamaguchi[1], T. Iseki[1] and T. Yano[2]

[1] Department of Inorganic Materials, Faculty of Engineering, Tokyo Institute of Technology, 2-12-1 O-okayama, Meguro-ku, Tokyo 152-8552, Japan

[2] Research Laboratory for Nuclear Reactors, Tokyo Institute of Technology, 2-12-1 O-okayama, Meguro-ku, Tokyo 152-8550, Japan

Keywords: Al_2O_3/TiC Composite, ZrO_2/TiC Composite, Rheological Model, Zener's Pinning Effect

Abstract

Effect of second-phase particles upon the deformation behavior was studied using both ZrO_2/TiC composite and Al_2O_3/TiC composite whose contents of TiC varied from 0 to 26 vol%. These composites were deformed at a strain rate of $8\times10^{-4}s^{-1}$ and at 1600 °C, where grain coarsening of matrix phase was expected. The flow stress of ZrO_2/TiC composite increased with increasing fraction of TiC, whereas elongation of the composite decreased with increasing TiC content. On the contrary to the ZrO_2/TiC composite, the Al_2O_3/TiC composite with 8 vol% TiC deformed with the lowest stress among the other low and high TiC content specimens and showed maximum elongation. Grain growth due to the deformation was negligible in the specimen with 26 vol% TiC, whereas severe grain growth was observed in the Al_2O_3/TiC composite with less amount of TiC. It was supposed that the role of TiC particles in Al_2O_3/TiC composite was inhibition of the grain growth at high temperatures. The difference in the effects of TiC on the deformation behavior of both composites was discussed with both rheological model and the pinning effect of TiC on the grain growth of matrix.

I. Introduction

Superplasticity of Al_2O_3/TiC composite was reported by Katsumura et al. and Nagano et al [1,2]. The composite is a unique superplastic ceramics since it consists of relatively large grains, 1.2 μm [2]. However, there are few studies of the composite regardless of the uniqueness. In this study, effect of TiC content upon the flow stress of the composite was compared with that of superplastic-like ZrO_2/TiC composite. In general, grain size of TZP is stable during the superplastic deformation, whereas that of alumina grows during the deformation. It is expected that pining effect of TiC particles upon the matrix grains would be significant in case of Al_2O_3/TiC composite. Both composites were deformed at 1600°C and at a strain rate of 8×10^{-4} s^{-1}, then the effect of fraction of TiC particles upon the flow stress of both composites was studied. The

dependence of the flow stress upon the fraction of TiC was analyzed by combination of the rheological model [3] with the Zener's pinning effect against grain growth of matrix phase [4].

II. Theory

(1) When grain size of major phase is not affected by minor phase:

Flow stress of the composite with hard inclusion is estimated using rheological model when stress exponent, n is constant regardless of the fraction of minor phase [3,5,6].

$$\sigma^n = (1-f)^{-2-(n/2)} A \times \dot{\varepsilon} \times D^p \qquad \text{Eq. 1}$$

Where σ is the true stress, D is the grain size of major phase, p is the grain size exponent, $\dot{\varepsilon}$ is the true strain rate, f is the volume fraction of minor phase and A is a constant depending on the material. The equation indicates increment of flow stress of the composite with higher fraction of minor phase.

(2) When grain size of major phase is controlled by minor phase whose growth rate is slower than that of major phase:

Grain size of the major phase is known to follow the Zener's relation [4,7,8],

$$D = 4d/(3f) \qquad \text{Eq. 2}$$

where d is the grain size of minor phase. Then the flow stress of the composite is estimated as follows:

$$\sigma^n = (1-f)^{-2-(n/2)} A \times \dot{\varepsilon} \times \{4\, d/(3f)\}^p \qquad \text{Eq. 3}$$

When the composite with different fraction of minor phase is deformed under the same condition, i.e., deformation temperature and strain rate, dependence of the flow stress upon the fraction of minor phase is estimated as follows:

$$\sigma = (1-f)^{-(2/n)-1/2} f^{-p/n} \times d^{p/n} \{\dot{\varepsilon} \times A \times (4/3)^p\}^{1/n} \qquad \text{Eq. 4}$$

III. Experimental procedure

The starting powder of the ZrO_2 composite was fine-grained co-precipitated zirconia containing 3 mol% of yttria in solid solution (TZ-3Y, Tosoh, Tokyo, Japan) with an average particle size of 0.027μm. TiC powder (TiC-007N, Nippon Shin-kinzoku, Japan) with an average grain size of 0.63 μm was added to the matrix powder. The fraction of TiC was varied from 0 to 26 vol%. The powders were mixed using ball-mill with zirconia balls for 24h in ethanol. The mixed powder was hot-pressed with a graphite resistance furnace (Hi-Multi 5000, Fuji-dempa, Japan) in vacuum under compressive stress of 30MPa for 30 min. The sintering temperature of the monolithic ZrO_2 was 1400°C, whereas those of the composites with 8 and 26 vol% were 1450 and 1550 °C, respectively. The relative densities of the composites were > 98%. X-ray

diffraction of the specimen revealed that the main phase of ZrO_2 was tetragonal and that small amount of cubic phase existed.

Al_2O_3/TiC composite was synthesized from high-purity (>99.99%) alumina (TM-D, Taimei Chemicals, Tokyo, Japan) with an average particle size of ~0.2 μm. The same TiC powder mentioned above was added to the matrix powder. An amount of TiC was 0, 0.8, 2.4, 8 and 26 vol%. The synthesis procedure of the composite was almost the same as that of the ZrO_2/TiC composite except hot-pressing temperature. The hot-pressing temperature of the monolithic Al_2O_3 and that of the Al_2O_3/TiC composite was varied from 1250 to 1650 °C according to the fraction of TiC, which was determined to obtain the relative density of the composite of more than 95%.

The tensile specimens were diamond-machined from the as-sintered plates. The tensile specimens had the gage length of 10 mm and rectangular cross section of 2 mm×2 mm. Tensile tests at a constant cross-head speed were conducted in vacuum at 1600°C, using a universal testing machine. The initial strain rate was $8\times10^{-4}s^{-1}$. The elongation of the specimens was measured from the displacement of the cross-head. The polished surfaces of both the as-sintered and the deformed ZrO_2/TiC composites were thermally etched in vacuum at 1400 °C for 10~20 min. Al_2O_3/TiC composite was also etched at 1300 °C for 5~20 min. The surfaces of the deformed specimens contained the tensile axis. Microstructure of the as-sintered and the deformed specimens was observed by scanning electron microscopy (S800, S3500, Hitachi, Japan).

IV. Results and discussion

(1) Deformation behavior of ZrO_2/TiC composite

Fig.1 shows the deformation behavior of ZrO_2/TiC composite at 1600°C. The flow stress of the composite increased with increasing TiC content, whereas the elongation at fracture decreased at higher ratio of TiC. It is supposed that hard TiC particles [9,10] suppressed the superplastic-like flow of TZP.

Fig. 2 shows the microstructure of the composite both before and after the deformation. The grain sizes of the as-sintered ZrO_2/TiC composite of 0, 8 and 26 vol% TiC were 0.4, 0.5 and 0.6 μm, respectively. Little grain growth occurred after the deformation of each composite. After the deformation, the grain size of monolithic TZP was larger than that of the composites. This may be attributed to 3 times longer deformation time of the monolithic specimen than that of the composite. It is supposed that the grain size of the composite and monolithic at a small strain was almost the same. Then, grain growth of ZrO_2 phase was slightly affected by the presence of TiC particles. Okada et al. showed that little difference was observed in the growth rate of zirconia particles in the pure TZP and in the TZP with 6.7 vol% Al_2O_3 [8]. They attributed the small effect of alumina grain upon the growth of zirconia grain to sluggish grain growth of

zirconia particles. Therefore, it is reasonable to suppose that the little influence of TiC particles upon grain growth of zirconia in the ZrO_2/TiC composite was also caused by sluggish grain growth of zirconia particles.

The dependence of the flow stress upon the fraction of TiC is shown in Fig. 3, where the strain is 0.03. The observed stress exponent (n) of the ZrO_2/ 8 vol% TiC composite was 2.1, which was almost the same as that of reported value for 3Y-TZP. Then the flow stress of the ZrO_2/TiC composite was calculated with Eq. 1 by assuming that grain size exponent p=2 (solid line in Fig. 3). It is clear that the rheological model, i.e. Eq. 1, is valid for the ZrO_2/TiC composite. Wakai et al. reported the effect of fraction of alumina upon the superplasticity of TZP/Al_2O_3 composite [6,11]. They indicated that larger fraction of alumina increased the flow stress of the composite and that rheological model which was proposed by Chen [3] was effective to analyze the superplastic behavior of the composite. All these results reveal that the effect of TiC in ZrO_2/TiC composite is suppression of the grain boundary sliding.

It is strange that the observed elongation of the monolithic ZrO_2 was c.a. 1/3 of that of 3Y-TZP reported by Wakai et al [12]. The origin of the small elongation of our sample might be our unique synthesize procedure of the samples since 3Y-TZP is usually fabricated in air, whereas our samples were hot-pressed using graphite jig. Koike et al. reported that the deformation behavior of MgO-doped alumina was affected by the segregation of carbon impurity at the grain boundary [13]. They explained that the origin of the contamination of carbon was a graphite susceptor which was used in HIPing the samples [14]. Farther experiments to clarify the effect of carbon impurity on the superplastic behavior of the 3Y-TZP are now on going [15].

(2) Deformation behavior of Al_2O_3/TiC composite

Fig.4 shows the true strain versus true stress curves of the Al_2O_3/TiC composite tested at 1600°C. The monolithic Al_2O_3 fractured immediately after start of the test and plastic behavior was not observed. When the fraction of TiC was below 8 vol%, the flow stress of the composite decreased with increasing TiC content and the elongation increased, concurrently. In contrast, the flow stress increased above 8 vol% TiC composite and the elongation decreased, concurrently. These phenomena were against the prediction from the rheological model described in section II. (1).

Fig. 5 shows the microstructure of the composite both before and after the deformation. Before the deformation, grain size of the major phase of the composite decreased from 2.5 to 1.2 μm with increasing the fraction of TiC. The decrease in the grain size of matrix with increase of TiC content regardless of higher sintering temperature indicates that grain growth of alumina during sintering was suppressed by pinning effect of TiC particles. However, the pinning effect of TiC in Al_2O_3/ 26 vol% TiC composite was not so significant as expected. This is probably caused by the agglomeration of TiC particles in Al_2O_3/ 26 vol% TiC composite. In Al_2O_3/26 vol% TiC composite, 2~3 TiC particles coalesced into a large grain whose size was c.a. 1.5 times

larger than the size of TiC particles in other composites with lower content of TiC. Large grain growth was observed after the deformation of both the monolithic and the composite with lower fraction of TiC. Grain growth was slightly observed in the composite with higher content of TiC. It is obvious that grain growth was inhibited by the TiC particles.

Xue and Chen examined the superplastic deformation of Al_2O_3 composite with ZrO_2 in temperature range of 1200 to 1400 °C [16]. He showed that second-phase particles inhibited the grain growth of matrix during deformation and improved the superplasticity. The reduction of the flow stress of Al_2O_3/TiC may be explained by the pining effect of TiC as well. It is reasonable to suppose that the simple rheological model is not suitable to analyze the dependence of the flow stress upon the TiC content since grains size differed depending on the content of TiC.

Okada et al. examined the grain-size distribution in Al_2O_3/ZrO_2 generated by high-temperature annealing [8]. They showed the constant ratio of grain size of alumina to that of zirconia in Al_2O_3/ 6.7 vol% TZP regardless of annealing time. It is considered that growth rate of alumina grain in the composite is controlled by the zirconia grains. The relation of grain size of major phase and minor phase follows Zener's equation in their experiments. Then, the grain size of alumina grain in the Al_2O_3/TiC composite also can be approximated by using Zener's equation [15]. The rheological model used in Eq. (4) is based on the assumption that the minor phase is harder than major phase. TiC is harder than Al_2O_3 at 1600°C [17]. Therefore, Eq. (4) is appropriate to analyze the tendency of flow stress in the Al_2O_3/TiC composite with different TiC content.

The flow stress at ε =0.03 are plotted against the fraction of TiC in Fig. 6. The flow stress was calculated by substituting the observed stress exponent n =2.4 into Eq. 4 and by assuming that the grain size exponent p=2[18](line in the Fig. 6). From these results, it is clear that the suppressed grain growth due to TiC particles reduces the flow stress of the composite, whereas the large addition of TiC cancels the merit of small grain size since the resistance against grain-boundary sliding is increased by hard TiC particles.

V. Summary

In order to study the effect of TiC particles on the deformation behavior of oxide composite, both ZrO_2/TiC and Al_2O_3/TiC composites were synthesized by hot pressing. The content of TiC in the composites was varied from 0 to 26 vol%. These composites were deformed at 1600°C under tensile stress with initial strain rate of $8\times10^{-4}s^{-1}$. Effects of TiC particles upon the flow stress of both the composites were compared. In the case of ZrO_2/TiC composite, the flow stress increased with increasing the fraction of TiC, whereas the elongation of the composite decreased. On the contrary, the flow stress of the Al_2O_3/TiC composite went through minimum when the fraction of TiC was around 8 vol%. The grain growth of alumina during both the sintering and the deformation was suppressed when TiC content increased. The reduction of the flow stress

due to small amount of TiC in the Al_2O_3/TiC composite was attributed mainly to the pinning effect of TiC particles against the grain growth of alumina. The increment in the flow stress at higher fraction of TiC was accounted by the increased resistance against grain-boundary sliding that canceled the merit of small grain size. The dependence of the flow stress upon the fraction of the TiC could be explained quantitatively with the combined equation of the rheological model and Zener's pinning effect on the grain growth of matrix particles.

References

1. Y. Katsumura and M. Fukuhara, High Tech Ceramics. Edited by Vincenzini (1987) pp. 2735-2745 (Elsevier Science Publishers B.V., Amsterdam).
2. T. Nagano, H. Kato and F. Wakai, J. Am. Ceram. Soc. **74** [9] (1991), p. 2258.
3. I-W. Chen, in Superplasticity, pp. 5.1-5.20, ed. Baudelet, B. and Suery, M. Centre National de la Recherche Scientifique, Paris, Grenoble, France, 1985.
4. C. S. Smith, Trans. Metal. Soc. AIME. **175** (1948), p. 15.
5. C-K. Yoon and I-W. Chen, J. Am. Ceram. Soc. **73** [6] (1990), p. 1555.
6. F. Wakai and H. Kato, Adv. Ceram. Mater. **3** [1] (1988), p. 71.
7. T. Nishizawa, Tetsu to Hagane **70** [15] (1984), p. 1984.
8. K. Okada, Y. Yoshizawa and T. Sakuma, J. Am. Ceram. Soc. **74** [11] (1991), p. 2820.
9. Engineering property data on selected ceramics, volume III. Single oxide, in p. 5.4.5-18, Metals and ceramics information center, Battelle, Columbus laboratories, 505 King Avenue Columbus, Ohio 43201, A Department of Defense Information Analysis Center, July 1981.
10. Engineering property data on selected ceramics, volume II. Carbide, in pp. 5.2.4-11-13, Metals and ceramics information center, Battelle, Columbus laboratories, 505 King Avenue Columbus, Ohio 43201, A Department of Defense Information Analysis Center, August 1979.
11. F. Wakai, Y. Kodama, S. Sakaguchi N. Murayama, H. Kato and T. Nagano, in MRS Intl. Meeting on Advanced Materials Vol 7 (IMAM-7, Superplasticity) pp. 259-266, ed. M. Doyama, S. Somiya and R. P. H, Chang, Materials Research Society, Pittsuburgh, PA, 1989.
12. F. Wakai, S. Sakaguchi and Y. Matsuno, Adv. Ceram. Mater. **1** [3] (1986), p. 259.
13. J. Koike, K. Maruyama and H. Oikawa, Mater. Sci. Forum, 233-234 (1979), p 351.
14. J. Koike, S. Tashima, S. Wakiya, K. Maruyama and H. Oikawa, Mater. Sci. Eng. A220, (1996), p. 26.
15. H. Miyazaki, T. Iseki and T. Yano, in preparing for submission.
16. L-A. Xue and I-W. Chen, J. Am. Ceram. Soc. **79**[1] (1996), p. 233.
17. Engineering property data on selected ceramics, volume III. Single oxide, in pp. 5.4.1-27-28, Metals and ceramics information center, Battelle, Columbus laboratories, 505 King Avenue Columbus, Ohio 43201, A Department of Defense Information Analysis Center, July 1981.
18. I-W. Chen and L-A. Xue, J. Am. Ceram. Soc. **73**[9] (1990), p. 2585.

Acknowledgements

The authors would like to thank to the Grant-in-Aid for Scientific Research on the Priority Area "Innovation in Superplasticity" No.08242101 from the Ministry of Education, Science and Culture, Japan for financial support of this study. Mr. R. Ooki and Mr. M. Imai are acknowledged for excellent supports to our experiments. We are grateful to Prof. Y. Matsuo and Associate Prof. K. Yasuda for valuable discussion.

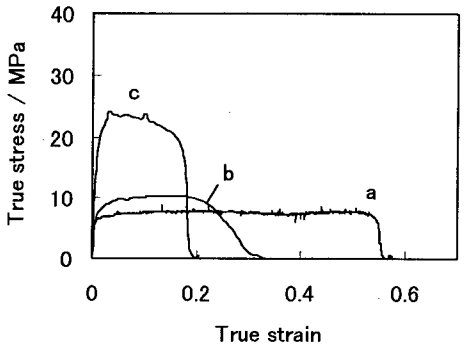

Fig. 1. Deformation behavior of ZrO_2/TiC composite at initial strain rate of $8\times10^{-4}s^{-1}$ and at 1600°C. Volume fraction of TiC are a: 0, b: 8 and c: 26 %, respectively.

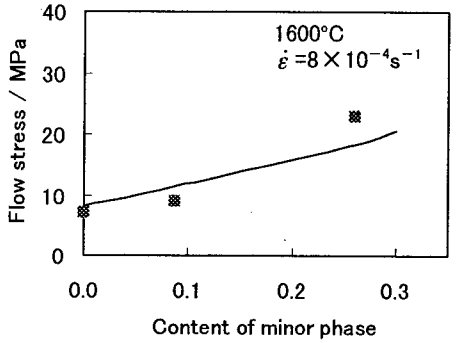

Fig. 3. Dependence of the flow stress upon the fraction of TiC at true strain, $\varepsilon=0.03$. The line shows the calculated flow stress using Eq. 1.

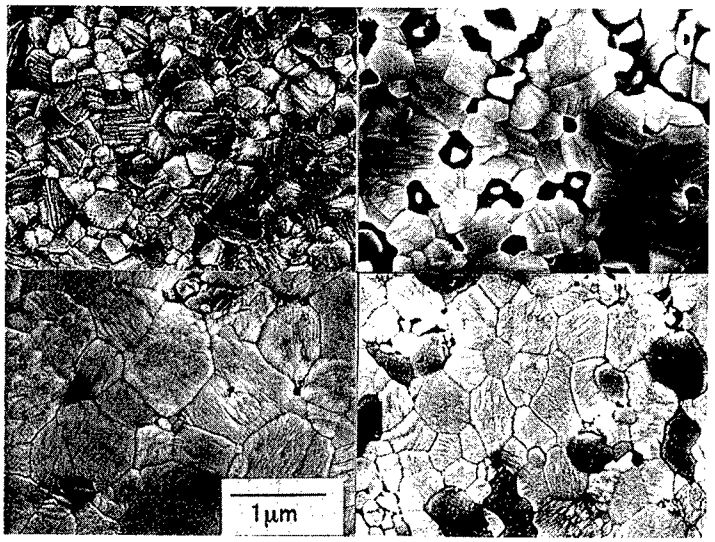

monolithic ZrO_2 ZrO_2/ 26vol% TiC composite

Fig. 2. SEM micrographs of ZrO_2/TiC composite both before (upper two) and after the deformation (lower two). The dark and bright contrasts correspond to TiC and ZrO_2 grains. Dark spots in ZrO_2/ 26vol% TiC composite before deformation are probably pores caused by thermal etching.

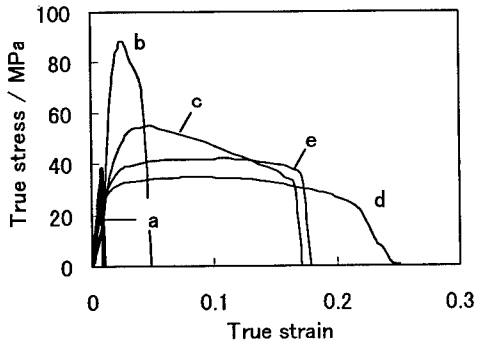

Fig. 4. Deformation behavior of Al_2O_3/TiC composite at initial strain rate of $8\times10^{-4}s^{-1}$ and at 1600°C. Volume fraction of TiC are a: 0, b: 0.8, c: 2.4, d: 8 and e: 26 %, respectively.

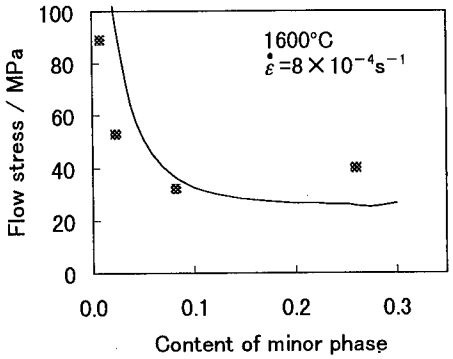

Fig. 6. Dependence of the flow stress upon the fraction of TiC at true strain, $\varepsilon=0.03$. The line indicates calculated flow stress using Eq. 4.

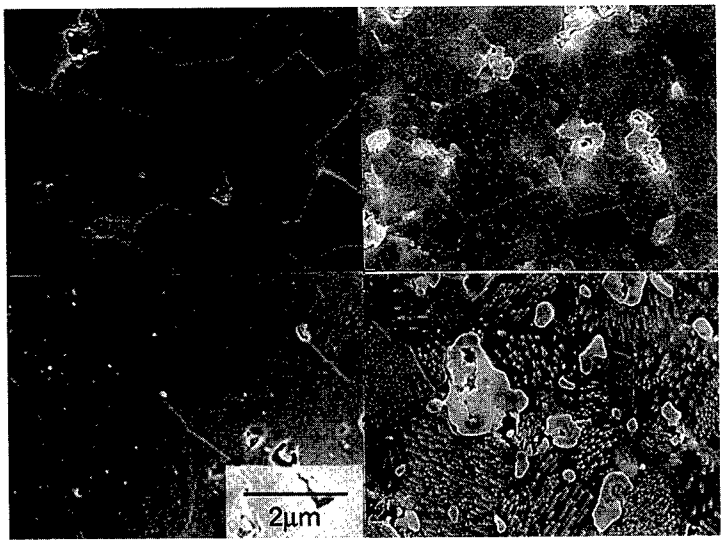

Al_2O_3/ 0.8 vol% TiC composite Al_2O_3/ 8vol% TiC composite

Fig. 5. SEM micrographs of Al_2O_3/TiC composite both before (upper two) and after the deformation (lower two). The dark and bright contrasts correspond to Al_2O_3 and TiC grains.

For correspondence with readers: H. Miyazaki, e-mail: hmiyazak@o.cc.titech.ac.jp,
Fax: +81-3-5734-3352

Key Engineering Materials Vols. 171-174 (2000) pp. 779-786
© 2000 Trans Tech Publications, Switzerland

Is there Diffusion Creep in Alumina?

R.S. Kottada and A.H. Chokshi

Department of Metallurgy, Indian Institute of Science, Bangalore 560 012, India33

Keywords: Grain Growth, Grain Shape, Stress Exponent, Alumina, Diffusion Creep

Abstract Although early studies on polycrystalline alumina attributed creep to diffusional processes, a re-analysis of the data and additional experimental results indicated that the creep behavior was non-linear, with a stress exponent of n~2, where $\dot{\varepsilon} \propto \sigma^n$ and $\dot{\varepsilon}$ and σ are the strain rate and stress, respectively. Recently, there has been renewed interest in characterizing the mechanical properties of alumina-based ceramics, in view of the possibility of obtaining superplastic-like large elongations in such materials. However, the occurrence of concurrent grain growth and extensive cavitation has precluded a complete characterization of the mechanisms of tensile flow. This paper reviews some of the earlier studies, and then describes results from recent experimental results on alumina doped with 300 ppm magnesia. The mechanical testing was accompanied by detailed microstructural investigations on grain growth, changes in grain shape and cavitation. These experimental results and appropriate analysis are used to critically examine the possibility of diffusion creep in polycrystalline alumina.

Introduction The time dependent plastic deformation of materials, termed creep, is an important design criterion for structural applications at elevated temperatures. Creep deformation can occur generally by the movement of dislocations, grain boundary sliding and diffusion creep processes [1]. High temperature deformation can be characterized in terms of the following rate equation:

$$\dot{\varepsilon} = \frac{ADGb}{kT}\left(\frac{b}{d}\right)^p\left(\frac{\sigma}{G}\right)^n \qquad (1)$$

where $\dot{\varepsilon}$ is the strain rate, A is a dimensionless constant, D is the appropriate diffusivity, G is the shear modulus, b is the magnitude of the Burgers vector, k is Boltzmann's constant, T is the absolute temperature, d is the grain size, p is the inverse grain size exponent, σ is the stress and n is termed the stress exponent. The diffusion coefficient may be expressed as $D=D_0 \exp(-Q/RT)$, where D_0 is a frequency factor, Q is the activation energy and R is the gas constant.

Theoretically, it is anticipated that at sufficiently low stresses, where dislocation mobility is limited, deformation will occur largely by diffusion creep mechanisms. Consequently, an understanding of diffusion creep mechanisms is a matter of considerable interest, from both theoretical and practical viewpoints. The theoretical foundations of diffusion creep processes were developed over fifty years ago, and there are no significant arguments regarding the theoretical basis for diffusion creep models [2-4]. An application of stress biases the production of vacancies on grain boundaries, so that the vacancy concentration is either increased or decreased over the thermal equilibrium value with the application of a tensile or compressive stress component. The gradient in vacancy concentration then leads to a flow of vacancy, and this process is termed

diffusion creep. The Nabarro-Herring creep model [2,3] involves vacancy flow through the lattice whereas the Coble model [4] involves vacancy flow along grain boundaries. While both models lead to a stress exponent of n=1, the Nabarro-Herring process involves $Q=Q_L$ and p=2 whereas the Coble model leads to $Q=Q_{GB}$ and p=3; here Q_L and Q_{GB} are the lattice and grain boundary activation energies, respectively.

Recently, there has been considerable debate in the literature regarding the experimental validity of the diffusion creep models, and various discrepancies have been noted between the theoretical expectations and the experimental observations [5-8].

In contrast to metallic materials, there have been numerous reports of stress exponent of ~1 in ceramics, and these have been attributed largely to diffusion creep mechanisms [1]. As noted elsewhere, these observations arise probably from the fine grain sizes of ceramics that are produced usually from powders, and the possibility of a change in the rate controlling diffusing ion so that the transition from diffusion to dislocation creep is increased to higher stress levels [1].

Following preliminary studies on the torsional creep behavior of alumina in the 1950's [9,10], creep experiments conducted largely in bending mode revealed a stress exponent of n~1 [11,12], and such data were attributed to either Nabarro-Herring or Coble diffusion creep. A reanalysis of the early data and more recent experimental results indicated that deformation in alumina was associated more with a stress exponent of n~2 [13-15]. These experimental results have been attributed variously to grain boundary sliding, interface reaction controlled diffusion creep and a transition from diffusion creep to dislocation creep.

The fine grain size of alumina, the measurement of a significant contribution by grain boundary sliding [16] and a stress exponent of n~2 are all factors consistent with reports of superplasticity in metallic alloys [17,18]. Consequently, there has been renewed interest in characterizing the tensile creep properties of alumina, following the observation of large strains in compression [19,20] and the large ductility reported in zirconia based ceramics [21-23]. The occurrence of significant grain growth and extensive cavitation has precluded the complete characterization of the deformation characteristics of polycrystalline alumina [24-27].

The present report describes experimental results from a recent study on alumina doped with 300 ppm magnesia. Following the pioneering work by Coble [28], it is recognized that magnesia doping assists densification of alumina, and the retention of a fine and uniform grain size. The mechanical testing is accompanied by detailed microstructural characterization in terms of changes in grain size and shape as well as cavitation.

Experimental Materials and Procedures Alumina powders doped with 300 ppm magnesia were obtained from Ceralox, U.S.A. Flat, dog-bone shaped tensile specimens were prepared by cold pressing and sintering at 1773 K for 4 hours, using a procedure described elsewhere [29]. Selected specimens were annealed at temperatures between 1773 and 1873 K for periods up to 10 hours for characterizing static grain growth.

Tensile testing was conducted on a modified Instron machine operating at a constant cross head velocity. The specimens were soaked at 1773 K for one hour, and then taken quickly to the testing temperature prior to loading. Most of the specimens were pulled to failure over a range of conditions. Tests on selected specimens were interrupted prior to failure for characterizing microstructural evolution. Densities of the gauge sections of deformed specimens were measured using Archimedes principle.

The gauge and the gripping sections of deformed specimens were polished metallographically, and etched thermally at 1723 K for one hour. Quantitative image analysis techniques were used to determine the mean grain size parallel (L_1) and perpendicular (L_2) to the tensile axis. The mean linear intercept grain size was defined as $d = (L_1 L_2^2)^{1/3}$, and the grain aspect ratio was defined as L_1/L_2. Scanning electron microscopy was utilized for characterizing cavitation.

Experimental Results

Initial Material Characterization Figure 1a is a scanning electron micrograph of the as-sintered specimen, illustrating a reasonably uniform and equiaxed grain size and a lack of porosity. The density of the as-sintered specimens were estimated to be >99%, based on a theoretical full density of 3.96 Mgm m^{-3} for pure alumina. The as-sintered grain size was 2.0±0.1 μm, and the aspect ratio (L_1/L_2) was 1.06±0.05. Since cavities nucleate frequently at very coarse grains in a fine microstructure, it was necessary to characterize the distribution of grain sizes in the material [30,31]. Figure 1b is a histogram depicting the frequency distribution of grain sizes in an as-sintered specimen; the distribution is clearly log-normal, and there was no evidence for abnormally large grains in the microstructure.

Since grain growth is a very common occurrence during high temperature deformation in fine grained materials, the static grain growth characteristics were obtained over a range of annealing times and temperatures. Grain growth is usually represented in a form: $d^N - d_0^N = K_g t$, where d_0 is the initial grain size, d is the grain size at time t, and K_g is a constant. The temperature dependence of grain growth can be expressed as $K_g = K_0 \exp(-Q_g/RT)$, where K_0 is a constant and Q_g is the activation energy for grain growth. Analysis of all the data revealed that values of N between 2 and 4 all yielded fits with regression coefficients of >0.99. Using N=3, the present analysis yielded a value of $K_g \sim 2\times10^{-21}$ $m^3 s^{-1}$, and an activation energy $Q_g \sim 630$ kJ mol^{-1}.

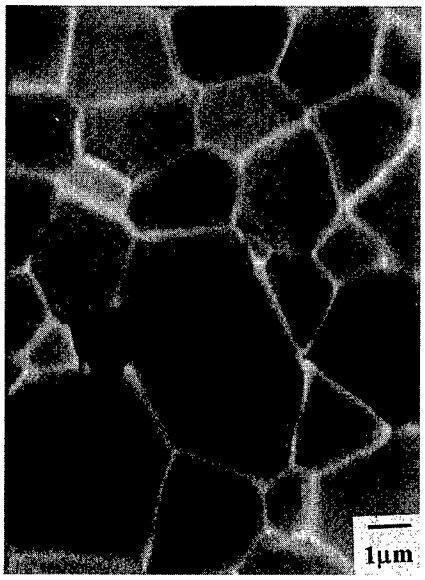

Fig. 1 Scanning electron micrograph of as-sintered specimen.

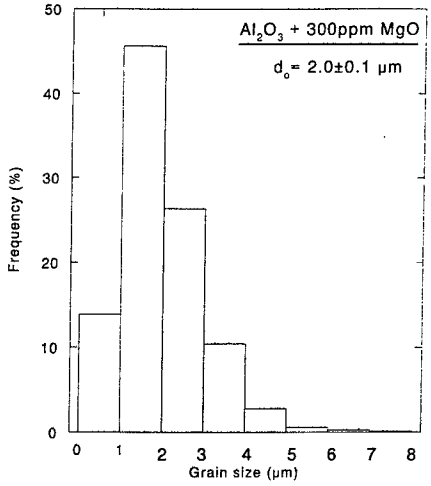

Fig. 2 Grain size distribution in an as-sintered specimen.

Microstructural Observations Concurrent cavitation was noted in deformed specimens by both density measurements as well as microstructural characterization. Figure 3a is a scanning electron micrograph illustrating the formation of voids during tensile deformation. The cavities appear to nucleate predominantly at triple points, and grow into grain boundary facet cracks perpendicular to the tensile axis, in a manner similar to a superplastic zirconia-alumina composite [32]. Density measurements indicated that the levels of cavitation varied from ~1 to 6% depending on the experimental conditions.

Concurrent grain growth was observed under all experimental conditions. However, as illustrated in Fig. 3b, measurements revealed that the grain sizes were essentially identical in the deformed gauge sections and the undeformed gripping sections, thereby indicating that grain growth was essentially a time related process. In view of this observation, additional small pieces of the as-sintered specimens were annealed for periods corresponding to the times taken to reach the maximum stresses during tensile testing, and these grain sizes are referred to as d_m in subsequent analysis. Measurements revealed also that the grains retained their equiaxed shapes after significant tensile deformation (fig. 3a), with the grain aspect ratio ranging from 0.97 to 1.04 for all specimens tested with an initial grain size of 2.0 μm.

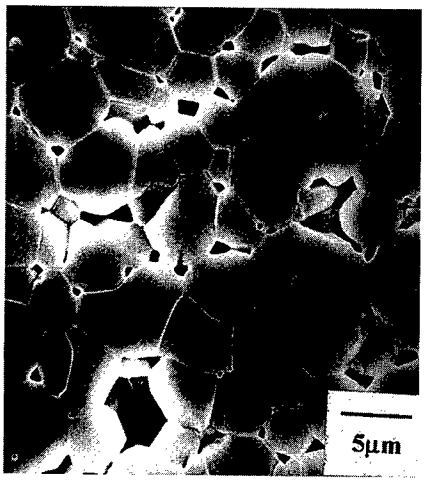

Fig. 3a Scanning electron micrograph depicting cavitation and retention of equiaxed grain size; the tensile axis is vertical.

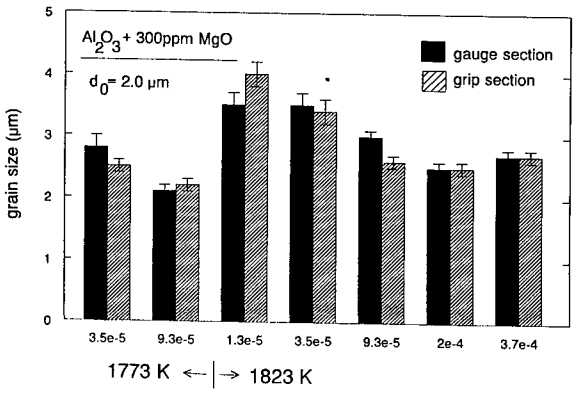

Fig. 3b Variation in final grain sizes in the gauge and gripping sections of specimens tested at 1773 and 1823 K.

Mechanical Properties Figure 4 illustrates the shapes of the tensile specimens during processing and after superplastic deformation. The top specimen is in the as-pressed green state whereas the middle specimen is in the as-sintered state, ready for tensile testing. The bottom specimen depicts the uniformity of deformation under optimum conditions, corresponding to an elongation to failure of 44%.

The variation in flow stress with elongations is shown in Fig. 5 for specimens with different initial grain sizes from 2.0 to 4.9 μm tested at 1823 K and an initial strain rate of 3.5×10^{-5} s^{-1}. In general, high strain rates, low temperatures and coarser grain sizes led to a sharp peak in the flow behavior. At lower strain rates, higher temperatures and finer grain sizes, the data seemed to favor steady-state type behavior.

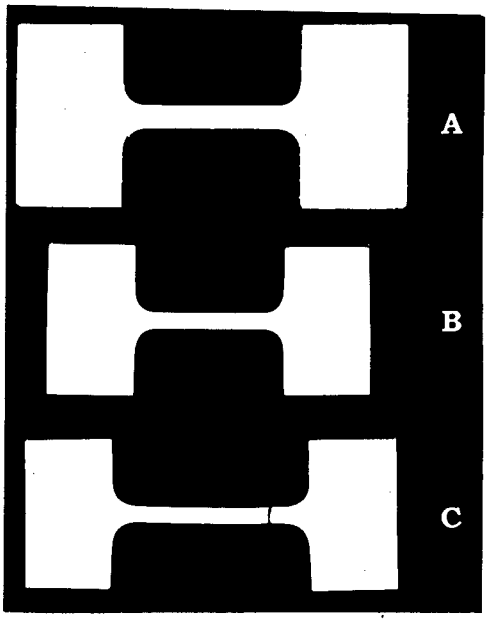

Fig. 4 Shapes of tensile specimens after cold pressing (top), sintering (middle) and optimum tensile testing (bottom).

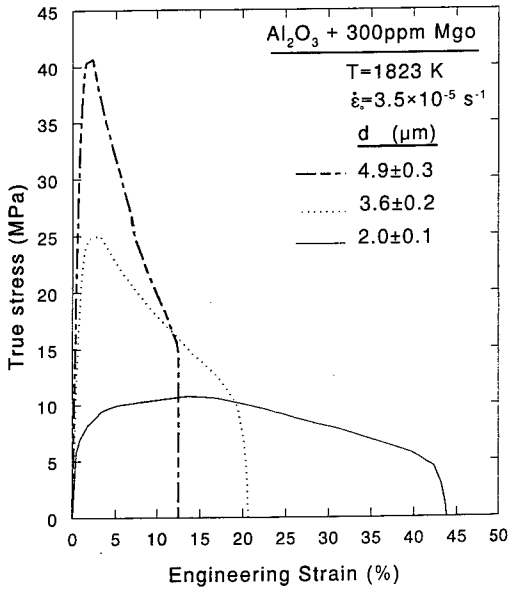

Fig. 5 Variation in flow stress with elongation for specimens with different initial grain sizes.

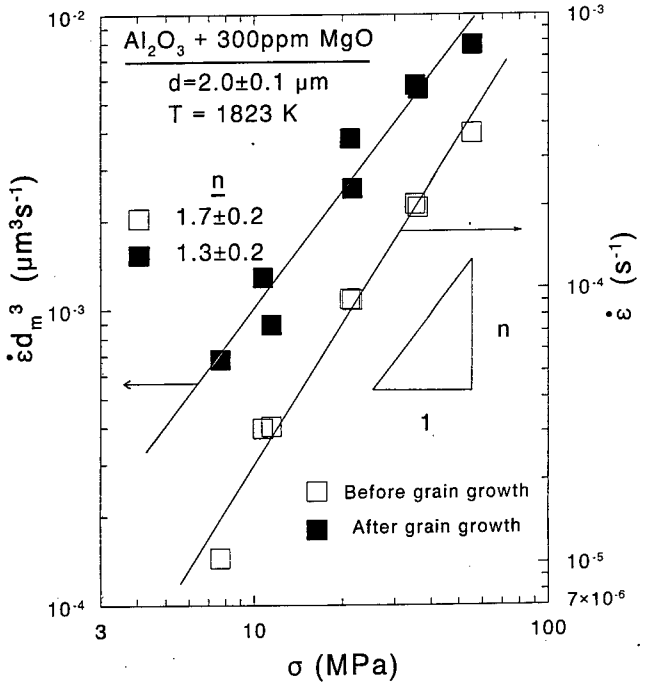

Fig. 6 Variation with stress in strain rate (right axis) and grain size compensated strain rate (left axis) for specimens with an initial grain size of 2.0 μm tested at 1823 K.

Figure 6 illustrates the variation in strain rate with stress on a logarithmic scale (right axis); the stresses correspond to the maximum values noted from appropriate stress-strain curves. The slope of the curve gives a stress exponent of n~1.7. However, it is clear from eqn. 1, that the stress exponent can be calculated in such a manner only when the temperature and grain size are kept constant. As noted in Fig. 3b, there was considerable grain growth during tensile testing, and the level of grain growth varied with testing time. Consequently, it is necessary to compensate the data for varying grain sizes.

Experiments such as those shown in Fig. 5 were utilized to characterize the inverse grain size exponent p. Logarithmic plots of flow stress versus grain sizes at maximum stress, at two different strain rates, yielded an average value of p~3 [33].

From eqn. 1, it follows that variations in grain size during testing can be compensated by plotting data in the format $\dot{\varepsilon} d^p$ vs σ on a logarithmic scale. The grain growth compensated data are also shown in Fig. 6, with a value of p=3. It is clear that when grain growth is taken into account, the true stress exponent for deformation is n=1.3±0.2, which is close to the value anticipated for diffusion creep (n=1).

Discussion Microstructural observations and quantitative measurements of grain size distributions did not reveal the development of abnormally coarse grains, so that ductility was not limited by the formation of cavities at such sites.

Many of the early studies on alumina reporting values of n in the range of ~1 to 2 were performed in 3-point or 4-point bending mode [11-16]. As recognized now, the analysis of such data is quite complex, in view of the possible differences in cavitation and deformation behavior in tension and compression [34].

Many recent studies in tension in alumina-based materials have noted the occurrence of grain growth. The stress exponents reported under such conditions have typically been in the range of ~1.7 to 2.1 [24-27]. However, as clear from eqn. 1, and demonstrated above in Fig. 6, the occurrence of grain growth can lead to errors in determination of the stress exponent. Detailed analysis of the present data, incorporating grain growth, shows clearly that the material is deforming with a true stress exponent of n~1, which is consistent with diffusion creep.

The grain size dependence of creep is given by the exponent p~3, which is consistent with Coble diffusion creep, involving vacancy flow along grain boundaries. Since alumina is stoichiometeric and has a high energy for defect formation, it acts as a highly extrinsic material; consequently, it is anticipated that the diffusion coefficients will vary significantly with the exact levels of additives and trace impurities. In view of this behavior, and the considerable variations reported in the activation energies for diffusion in alumina, it is not possible to utilize measurements of activation energies to confirm grain boundary diffusion control of creep deformation.

One of the major predictions of standard diffusion creep models is that the grains will elongate along the tensile axis. In most experimental studies attributed to diffusion creep, the strain rates for deformation are relatively slow and the total strains accrued are very limited. Consequently, it has not been possible to experimentally evaluate critically the existence of grain elongation along the tensile axis. In the present study, substantial elongations of up to 44% were obtained, so that significant grain elongation is anticipated. However, in contrast to anticipated

grain aspect ratios of up to ~1.7, the experimental measurements indicate clearly that grains essentially maintain their original equiaxed shapes.

It is argued below that grain elongation is not likely during diffusion creep. In general, diffusion creep involves mass transport over distances on the order of the grain sizes, whereas grain growth involves mass transport over much shorter distances. Therefore, conditions favoring diffusion creep are also likely to encourage grain growth. Consequently, it is anticipated that grain growth will occur concomitantly with diffusion creep. As recognized earlier by Smith [35] and Burke and Turnbull [36], grain growth topologically involves the elimination of small grains in a distribution as well as exchange of grain neighbors. This process is similar to the model developed by Ashby and Verrall [37] for superplasticity essentially involving diffusion creep with grain exchange. It is suggested that the process of grain rearrangement, occuring as a consequence of grain growth, will mask the development of an elongated grain structure during diffusion creep. Consequently, the retention of an equiaxed grain shape is not inconsistent with the occurrence of diffusion creep.

Lifshitz [38] pointed out that grain boundary sliding must accompany diffusion creep in order to maintain grain contiguity. In a parallel study on compression creep on the same batch of alumina, microstructural surface observations on polished and deformed specimens provided ample evidence for the occurrence of grain boundary sliding.

It is clear from the above discussions that the tensile deformation and microstructural characteristics of polycrystalline alumina doped with 300 ppm magnesia are consistent with Coble diffusion creep.

Summary and Conclusions

Tensile experiments at elevated temperatures indicate that deformation in magnesia doped alumina is associated with a stress exponent of ~1.7. However, microstructural examination reveals that there is considerable grain growth during the tensile deformation of polycrystalline alumina. When the mechanical data are corrected for concurrent grain growth, it is noted that the true stress exponent for deformation is ~1.3. The stress exponent of ~1 and a inverse grain size exponent of ~3 are consistent with deformation by diffusion creep. It is argued that the occurrence of concurrent grain growth, and the associated grain rearrangement, will mask the appearance of grain elongation, so that microstructural observations indicating a retention of an equiaxed grain shape as well as grain boundary sliding are also consistent with deformation by diffusion creep.

Acknowledgments

This work was supported by a Swarnajayanti Presidential Young Scientist Award to AHC. Additional support from the Aeronautical Research and Development Board as well as the Department of Science and Technology is also acknowledged gratefully.

References

1. A.H. Chokshi and T.G. Langdon, Mater. Sci. Tech. **7** (1991) 577.
2. F.R.N. Nabarro, *Report on a Conference on Strength of Solids*, p. 75. The Physical Society, London (1948).
3. C. Herring, J. App. Phys. **21** (1950) 437.
4. R.L. Coble, J. App. Phys. **34** (1963) 1670.

5. O.A. Ruano, J. Wadsworth, J. Wolfenstine and O.D. Sherby, Mater. Sci. Eng. **A165** (1993) 133.
6. G.W. Greenwood, Scripta Metall. Mater. **30** (1994) 1527.
7. G.W. Greenwood, *Creep Behavior of Advanced Materials for the 21st Century* (eds. R.S. Mishra, A.K. Mukherjee and K.L. Murty) p. 413. The Minerals, Metals and Materials Society, Warrendale, PA, U.S.A. (1999).
8. J. Wadsworth, O.A. Ruano and O.D. Sherby, *Creep Behavior of Advanced Materials for the 21st Century* (eds. R.S. Mishra, A.K. Mukherjee and K.L. Murty) p. 425. The Minerals, Metals and Materials Society, Warrendale, PA, U.S.A. (1999).
9. J.A. Stavrolakis and F.H. Norton, J. Am. Ceram. Soc. **33** (1950) 263.
10. R.L. Coble and W.D. Kingery, J. Am. Ceram. Soc. **39** (1956) 377.
11. R.C. Folweiler, J.App. Phys. **32** (1961) 773.
12. R.L. Coble and Y.H. Guerard, J. Am. Ceram. Soc. **46** (1963) 353.
13. A.H. Heuer, R.M. Cannon and N.J. Tighe, *Ultrafine-Grain Ceramics* (eds. J.J. Burke, N.L. Reed and V. Weiss) p. 339. Syracuse University Press, Syracuse, NY (1970).
14. R.M. Cannon, W.H. Rhodes and A.H. Heuer, J. Am. Ceram. Soc. **63** (1980) 46.
15. A.H. Chokshi and J.R. Porter, J. Mater. Sci. **21** (1986) 705.
16. A.H. Chokshi, J. Mater. Sci. **25** (1990) 3231.
17. A.H. Chokshi, A.K. Mukherjee and T.G. Langdon, Mater. Sci. Eng. **R10** (1993) 238.
18. T.G. Nieh, J. Wadsworth and O.D. Sherby, *Superplasticity in Metals and Ceramics*, Cambridge University Press (1997).
19. J.D. Fridez, C. Carry and A. Mocellin, *Structure and Properties of MgO and Al_2O_3 Ceramics* (ed. W.D. Kingery) p. 720. The American Ceramic Society, Columbus, Ohio, U.S.A. (1984).
20. W.R. Cannon, *Structure and Properties of MgO and Al_2O_3 Ceramics* (ed. W.D. Kingery) p. 741. The American Ceramic Society, Columbus, Ohio, U.S.A. (1984).
21. F. Wakai, S. Sakaguchi and Y. Matsuno, Adv. Ceram. Mater. **1** (1986) 259.
22. F. Wakai, Y. Kodama and T. Nagano, JJAP Series 2 (1989) 57.
23. T. Sakuma, Mater. Sci. Forum **243-245** (1997) 327.
24. A.G. Robertson, D.S. Wilkinson and C.H. Caceres, J. Am. Ceram. Soc. **74** (1991) 915.
25. A. Xu and A.A. Solomom, J. Am. Ceram. Soc. **75** (1992) 985.
26. Y. Yoshizawa and T. Sakuma, Acta Metall. Mater. **40** (1992) 2943.
27. F. Wakai, T. Nagano, T. Iga, J. Am. Ceram. Soc. **80** (1997) 2361.
28. R.L. Coble, J. App. Phys. **32** (1961) 793.
29. L.N. Satapathy, R.S. Kottada and A.H. Chokshi, to be published.
30. A.H. Chokshi and J.R. Porter, J. Am. Ceram. Soc. **70** (1987) 197.
31. A.H. Chokshi, T.G. Nieh and J. Wadsworth, J. Am. Ceram. Soc. **74** (1991) 869.
32. D.M. Owen, A.H. Chokshi and S.R. Nutt, J. Am. Ceram. Soc. **80** (1997) 2433.
33. R.S. Kottada and A.H. Chokshi, to be published.
34. R.F. Krause, J. Am. Ceram. Soc. **75** (1992) 1307.
35. C.S. Smith, *Metal Interfaces*, p. 65. The American Society for Metals, Cleveland, OH, U.S.A. (1952).
36. J.E. Burke and D. Turnbull, Prog. Metal Phys. **3** (1952) 220.
37. M.F. Ashby and R.A. Verrall, Acta Metall. **21** (1973) 149.

Key Engineering Materials Vols. 171-174 (2000) pp. 787-792
© 2000 Trans Tech Publications, Switzerland

High Temperature Mechanical Behavior of YSZ Nanocrystals

F. Gutiérrez-Mora[1], M. Jiménez-Melendo[1], A. Domínguez-Rodríguez[1] and R. Chaim[2]

[1] Departamento de Física de la Materia Condensada, Universidad de Sevilla, Aptdo. 1065, ES-41080 Sevilla, Spain

[2] Department of Materials Engineering, Technion-Israel Institute of Technology, Haifa 32000, Israel

Keywords: Zirconia, Nanocrystals, Superplasticity, Creep

Abstract. Compressive deformation experiments were carried out at temperatures T ~ 0.5 T_m over a range of stresses and strain rates on fully dense samples of nanocrystalline 4 mol% Y_2O_3-partially stabilized ZrO_2 with an average grain size of 40 nm. The measured creep rates are comparable or even lower than the corresponding coarse-grain rates. Microstructural observations show the formation of cavities at moderate strains. These results are opposite to expectations of enhanced superplasticity in nanocrystalline ceramics.

1. Introduction

In the last decade, many investigations have studied the high temperature plastic deformation of Y_2O_3-stabilized ZrO_2 (YSZ) polycrystals. A like-metal superplasticity has been observed in YSZ with submicronic grain sizes (0.2 μm - 1 μm) [1-4]. Based on these results, high strain rate and low temperature superplasticity would be then expected in materials prepared with sufficiently small grain sizes. A variety of processing techniques are now available which allow the production of ceramics, as well as metals and intermetallics, with grain sizes below 100 nm [3,5]. In this paper, the preliminary results of high temperature deformation of fully dense nanostructured YSZ are reported. These results are compared to the expected flow behavior based on superplasticity observed in submicronic YSZ.

2. Experimental procedure

Nanocrystalline 4 mol% Y_2O_3-ZrO_2 powders of 10 nm in size were obtained by chemical precipitation from mixed nitrate solutions. The calcined powders were cold pressed at 300 MPa into cylinders and then sintered at 1100°C in air for 2 hours. The resulting green bodies were hot-isostatically pressed (HIP) in argon pressure of 150 MPa at 1350°C for 4 hours. A detailed description of the processing procedure can be found elsewhere [6]. After HIP, the density of the samples, measured by Archimedes' method, was close to the theoretical density. Rectangular specimens 4 x 2 x 2 mm^3 were used for mechanical tests. Compression experiments were carried

out in air at temperatures between 1100°C and 1200°C at constant cross-head speed in an Instron universal testing machine and at constant load in a creep machine. The recorded data were plotted as σ - ε or log $\dot{\varepsilon}$ - ε curves, where σ and ε are the engineering stress and strain, respectively, and $\dot{\varepsilon}$ the strain rate. The microstructural characterization of the as-received and deformed samples was carried out using scanning (SEM) and transmission (TEM) electron microscopy (Microscopy Service, University of Sevilla, Spain). Line broadening of X-ray diffraction spectra was also used to evaluate the grain size before and after testing.

3. Results and discussion

X-ray diffraction showed that the material consisted of 40 vol% monoclinic-phase and 60 vol% tetragonal-phase grains. An average grain size d of 40 nm was estimated from the line broadening in these spectra. A slightly larger grain size of 60 nm was found from TEM observations. However, twinning effect complicated these observations, which could result in an underestimation of the number of the finer grains, thus shifting the mean grain size to higher values. The grains were equiaxed and well faceted. No porosity was detected in the as-received materials, in agreement with density measurements.

Fig. 1 shows a creep curve plotted as log $\dot{\varepsilon}$ - ε showing several determinations of the stress exponent and the activation energy by stress and temperature changes, respectively. There are very small transients, the steady-state stage being reached almost immediately upon loading. The maintenance of the strain rate level after positive and negative temperature changes evidences that

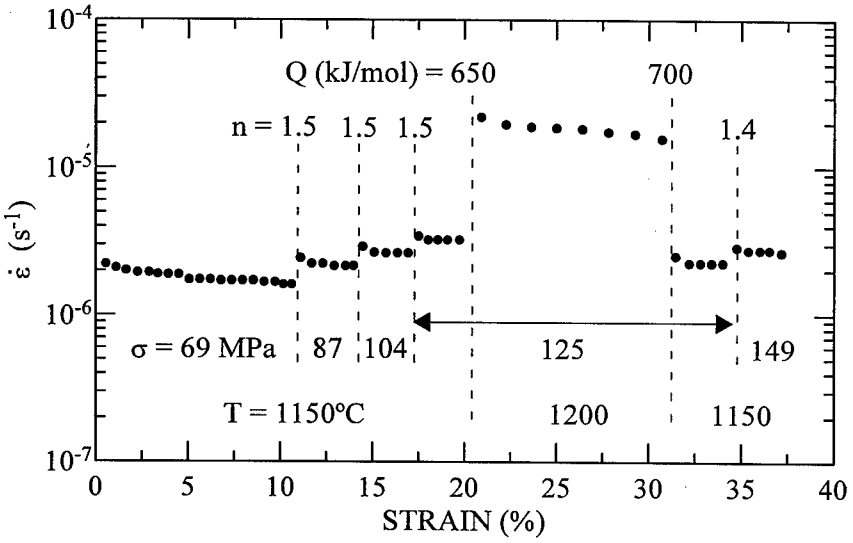

Fig. 1. Creep curve for 4 mol% Y_2O_3-stabilized ZrO_2 nanocrystals (d = 40 nm). Several determinations of the stress exponent n and the activation energy Q are shown.

the grain size was quite stable during deformation. This point was confirmed by line broadening of X-ray spectra taken from deformed samples.

The mechanical data have been analyzed using the standard high temperature power law for steady state deformation:

$$\dot{\varepsilon} = A\sigma^{n} d^{-p} \exp(-Q/RT) \quad (1)$$

where A is a constant, n the stress exponent, p the grain size exponent and Q the activation energy for flow. Average values of $n = 1.4 \pm 0.2$ and $Q = 660 \pm 40$ kJ/mol were estimated from eq. (1). Chen et al. [7] have reported $n = 2$ and $Q = 585$ kJ/mol in a 2.2 mol% Y_2O_3-stabilized ZrO_2 with a grain size ranging from 60 to 150 nm at temperatures between 1075 and 1150°C. The creep parameters, and the absolute magnitude of the strain rate as well, are far from those expected for an enhanced superplastic material, as discussed below. Secondary creep regimes were also found in Instron experiments at an initial strain rate $\dot{\varepsilon}_o = 5\text{x}10^{-6}$ s^{-1} between 1100 and 1200°C. By contrast, a brittle behavior was observed at $\dot{\varepsilon}_o = 2\text{x}10^{-5}$ s^{-1} at 1100°C; the failure occurred at only $\varepsilon = 0.03$ after a peak stress of 900 MPa was achieved.

SEM observations of deformed samples showed a high level of cavitation after moderate strains, as can be seen in Fig. 2 for a specimen tested to a total strain of 0.55 at a temperature of 1200°C. A large density of small cavities was distributed throughout the sample. Large cavities of a few micrometers in size, formed by coalescence of the small ones, could be also found in some regions, which were likely the source of eventual failure. This feature is opposite to that found in submicronic YSZ, where very large macroscopic strains are reached without significant

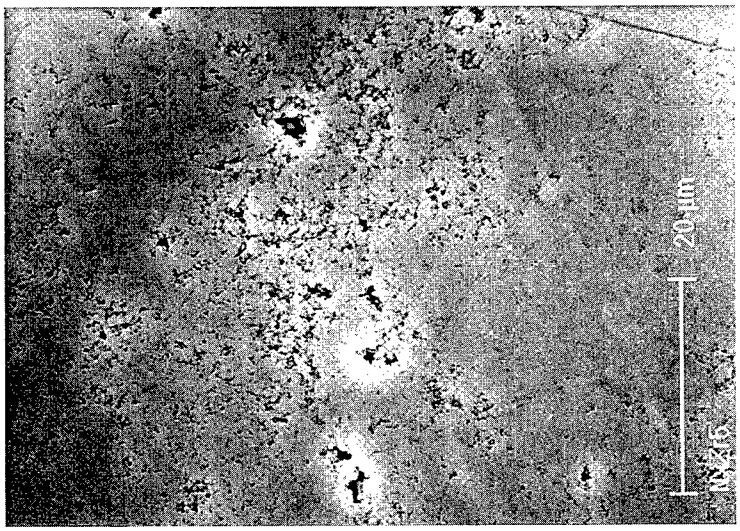

Fig. 2. SEM micrograph of nanocrystalline 4 mol% Y_2O_3-stabilized ZrO_2 tested at 1200°C up to a total strain $\varepsilon = 0.55$.

microstructural changes. It should be noted, however, that extensive intergranular cavitation has been reported in microcrystalline YSZ deformed at very low stresses [8], where the stress exponent seems to be close to unity [4].

It is interesting to compare the deformation results on Y_2O_3-stabilized ZrO_2 with different grain sizes. Fig. 2a shows the $\dot{\varepsilon}$ - σ curves at 1150°C for YSZ with grain sizes ranging from 0.1 μm to 1.2 μm [1-3,9], along with the present results. In order to have a single reference, all the grain sizes reported in these investigations have been converted to $d = 1.78\,\bar{L}$, where $\bar{L}$ is the mean linear intercept length. As can be seen, the magnitude of strain rate for nanocrystalline YSZ is similar, and even lower, than that corresponding to submicronic materials. The comparison is more dramatic if the strain rate is compensated with grain size, as shown in Fig. 3b. On this normalized basis, the strain rates for nanocrystals fall two orders of magnitude below those of the submicronic YSZ (the use of d^3 instead of d^2 compensation in Fig. 3b leads to higher differences between both grain size ranges). Recently, Jiménez-Melendo et al. [4] have noted that the superplastic data of YSZ with submicronic grain sizes at temperatures ranging from 1250 to 1450°C can be represented by a generalized equation with $n = 2$, $p = 2$ and $Q = 460$ kJ/mol, with a threshold stress σ_0 below which grain boundary sliding cannot proceed. The prediction of such an equation in the superplastic region ($\sigma_0 = 0$) is shown in Fig. 3b (dotted line). A rather good correlation with experimental data for submicron-grained YSZ can be seen. Similar results are found at 1100 and 1200°C.

The low strain rates, along with the extensive damage exhibited by the samples, indicate that grain boundary sliding is not an easy deformation mechanism in nanocrystalline YSZ, at least in the present experimental conditions. In the threshold stress formalism developed for submicronic YSZ [4], grain boundary sliding is increasingly inhibited as the applied stress approaches the threshold value and another deformation mechanism must be operative at very low stresses. Diffusional creep is the likely mechanism responsible for this stress region, as predicted for all creep theories at sufficiently low stresses. Since the stress range used in this investigation is well below the threshold stress predicted for this temperature and grain size [4], the low values of n and the presence of cavitation are consistent with this idea. However, our results are clearly too preliminary to make definite conclusions. Further work, particularly TEM observations of the as-received and deformed specimens, is required to understand the mechanisms responsible for the mechanical behavior at elevated temperatures of nanocrystalline YSZ and to critically test whether the framework developed for submicronic YSZ is applicable.

In this regard, it is interesting to note that a change in flow behavior has been also found in nanocrystalline metals with respect to coarse-grained ones. For example, a transition in stress exponent from 2.5 to 1.2 has been reported in Ni-P alloy with decreasing the grain size from 0.3 μm to 30 nm [10]; in addition, the strain rate increased only by a factor of 2, while d decreased by a factor of 10. A similar trend has been reported in nanocrystalline titanium aluminide (d = 25 – 50

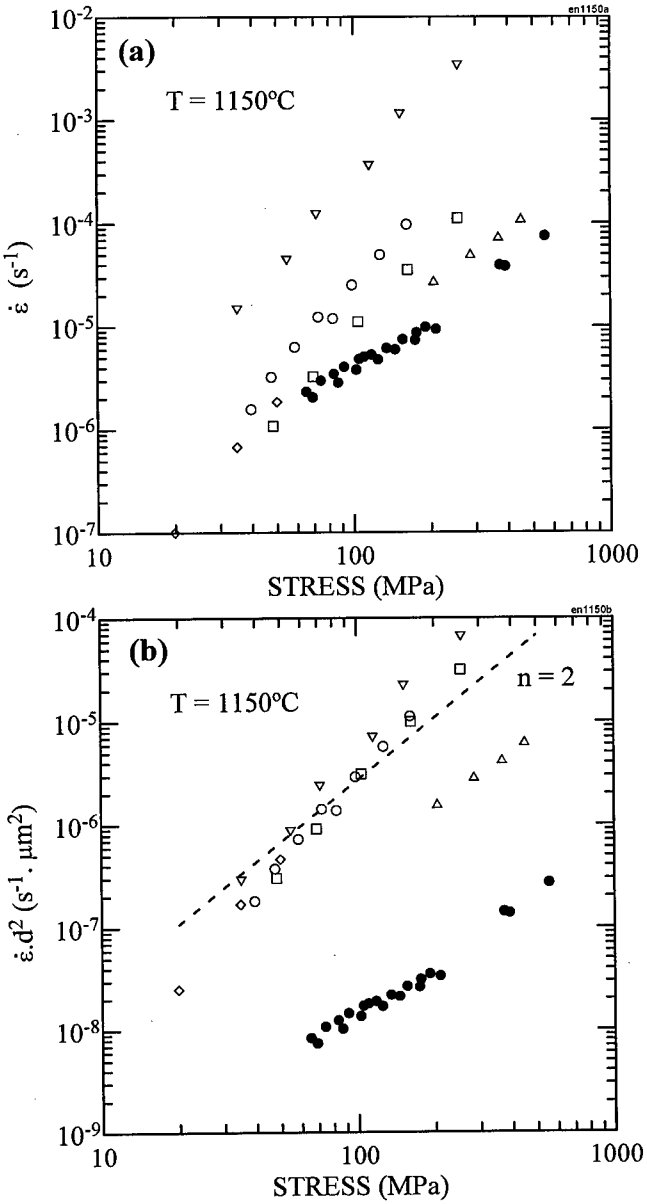

Fig. 3. (a) Variation of strain rate with stress at 1150°C for submicronic (△: 0.24 μm [1]; ○: 0.34 μm [2]; ◇: 0.5 μm [9]; □: 0.53 μm [3]; ▽: 0.14 μm [3]) and nanocrystalline (●: present work) YSZ polycrystals. (b) Grain-size compensated strain rate vs stress. Prediction of the generalized equation derived by Jiménez-Melendo et al. [4] for superplasticity (n = 2) in YSZ is also shown (dotted line).

nm) [11], nickel aluminide (d = 50 nm) [12] and Cu and Pd (d = 10 - 55 nm) [13], where the measured creep rates are also two to four orders of magnitude smaller than the creep rates extrapolated from the corresponding coarse-grained materials.

4. Conclusions

The high temperature mechanical properties of 4 mol% Y_2O_3-partially stabilized ZrO_2 polycrystals with a mean grain size of 40 nm have been studied. Compression tests were performed at constant load and at constant initial strain rate in the temperature range 1100 - 1200°C. Grain growth was minimal at the present experimental conditions. The measured creep rates are similar to those found in submicronic YSZ, which means a much higher creep resistance than that expected for very fine-grained materials. In addition, the samples exhibited extensive cavitation after moderate strains. Therefore, a grain size reduction does not results in a shifting of the grain boundary sliding mechanism to lower temperatures, as would be expected.

Acknowledgements. This research has been supported by CICYT under grants Nos. MAT97-0562-C02-01 and MAT97-1007-C02 (Ministerio de Educación y Ciencia, Madrid, Spain).

REFERENCES

[1] C-M.J. Hwang and W-W. Chen, J. Amer. Cer. Soc. 73 (1990), p. 1626.
[2] J.R. Seidensticker and M.J. Mayo, Scripta Met. Mater. 31 (1994), p. 1754.
[3] M. J. Mayo, Materials & Desing 14 (1993), p. 323.
[4] M. Jiménez-Melendo, A. Domínguez-Rodríguez and A. Bravo-León, J. Am. Ceram. Soc. 81 (1998), p. 2761.
[5] A.J. Burggraaf, A.J.A. Winnubst and H. Verweij, in Third Euro-Ceramics Vol. 3: Engineering Ceramics, pp. 561-576. Ed. by P. Durán and J.F. Fernández, Faenza-Editrice Ibérica, Castellón, Spain, 1993.
[6] R. Chaim and M. Hefetz, J. Mater. Res. 13 (1998), p. 1875.
[7] L. Chen. T. Rouxel and R. Chaim, Mater. Sci. Forum 243-243 (1997), p. 245.
[8] A. Bravo-León, M. Jiménez-Melendo and A. Domínguez-Rodríguez, Scripta mater. 35 (1996), p. 551.
[9] K.D. Debschütz, B. Caspers, G.A. Schneider and G. Petzow, J. Am. Ceram. Soc. 76 (1993), p. 2468.
[10] J. Deng, D.L. Wang, Q.P. Kong and J.P. Shui, Scripta Metall. Mater. 32 (1995), p. 349.
[11] R.S. Mishra, A.K. Mukherjee, D.K. Mukhopadhyay, C. Suryanarayana and F.H. Froes, Scripta. Mater. 34 (1996), p. 1765.
[12] R.S. Mishra, R.Z. Valiev, S.X. McFadden and A.K. Mukherjee, Mater. Sci. Eng. A252 (1998), p. 174.
[13] P.G. Sanders, M. Rittner, E. Kiedaisch, J.R. Weertman, H. Kung and Y.C. Lu, NanoStructured Mater. 9 (1997), p. 433.

E-mail address: melendo@cica.es

Key Engineering Materials Vols. 171-174 (2000) pp. 793-800
© 2000 Trans Tech Publications, Switzerland

Yttrium in Polycrystalline α-Alumina

M.A. Gülgün and M. Rühle

Max Planck Institut für Metallforschung, Seestr 92, DE-70174, Stuttgart, Germany

Keywords: Alumina, Yttrium, Grain Boundary Segregation, Microstructure, Microchemistry, Sintering, Grain Growth

Abstract:

Depending on its concentration, yttrium in polycrystalline α-alumina can exist as solute/segregant or as solute/segregant/in precipitates. At low concentrations and/or very small grain sizes, yttrium occurs as solute in the bulk and segregant at the grain boundaries. As the dopant concentration is increased and/or the ceramic is heat treated such that grain growth happens, yttrium is also accommodated in yttrium aluminate precipitates in addition to being a solute and a segregant.

Alpha alumina samples doped with varying amounts of yttrium (from 0 to 3000 wt ppm Y_2O_3) were prepared by pressureless sintering in air. Their sintering behavior, microstructure, and microchemistry were investigated.

In the solute/segregant regime (I), the excess concentration of yttrium at the grain boundaries increased in a predictable manner, proportional to the amount added and inversely related to the available interface area. The grain size was uniform and small (1-2 μm). In the solute/segregant/precipitate regime (III), however, the average excess concentration of yttrium atoms at grain boundaries was unexpectedly low. In this regime III, explosive grain growth was observed. Grains of sizes 50-100 μm existed in the microstructure, and with successive annealing, a large and uniform grain size microstructure was obtained.

This explosive grain growth may be closely related to the peculiar creep deformation behavior of yttrium-doped α-aluminum oxide ceramic.

Introduction

Additions of small amounts of various rare-earth oxides were shown to enhance the creep resistance of polycrystalline α-alumina [1-5]. Among these, yttrium appears to be the most effective cation in reducing the strain rate of the ceramic during high temperature deformation (about 2 orders of magnitude reduction in strain rate with yttrium additions) [1,4-6]. Yttrium's influence is closely related to its limited solubility (6-10 ppm [7-8]), and consequent segregation behavior in α-alumina. Numerous studies have shown that yttrium strongly segregates to the grain boundaries and/or precipitates as yttrium aluminate garnet phase [9-10] depending on the total amount of the dopant and/or the grain size of the ceramic.

Carry and his co-workers conducted experiments with fine grained, MgO-doped, polycrystalline α-aluminas which were co-doped with two different amounts of yttrium (500 and 1500 wt ppm Y2O3) [11]. In 500 wt ppm yttrium co-doped, fine grained alumina , the dopant existed as solute in the bulk and segregant at the grain boundaries (regime I). It was shown that yttrium was an effective suppressant of the creep rate as a segregant. Highly yttrium co-doped sample (1500 wt ppm) where the dopant existed as solute/segregant/precipitate (regime III) exhibited similar creep behavior. In a cleverly devised experiment where the transition between regime I and regime III due to grain growth occurred during creep rate measurements, Priester et al [3] observed a plateau region in the strain rate versus grain size plots. During this plateau, strain rate remained almost constant although the grain size doubled. An explanation for this behavior as well as a possible mechanism for yttrium's role in reducing creep rate in α-alumina are still elusive. Several mechanisms have been put forward by different groups: (i) One involving a hindered accommodation process of dislocations at the segregated boundaries [3], (ii) another one suggesting reduced diffusion rate of cations along the segregated grain boundaries which assumes large rare-earth cations plugging the "fast diffusion paths" along the boundaries [4], and (iii) or existence of a sub-monolayer coverage second phase which interferes with dislocation motion (and hence grain boundary sliding and/or dislocation accommodation processes) and diffusion of ions along the segregated grain boundaries [10, 12-13]. Although all these suggested mechanisms are plausible, no clear experimental evidence exists to clarify the issue.

Yttrium's effect in sintering and densification of α-alumina has been addressed by two separate groups [11, 14-15]. Carry et al. [11] conducted experiments with two different amounts of yttrium/MgO co-doping and reported a peculiar final stage densification behavior in α-alumina ceramic when doped with yttrium. Harmer and co-workers studied heavily doped and hence precipitated (regime III) alumina and concluded that yttrium also suppressed sintering and densification processes similar to its role in reduced creep deformation.

In order to clarify yttrium's role in sintering and densification, as well as creep deformation, a systematic study of microstructure and microchemistry of polycrystalline α-alumina doped only with varying amounts of yttrium was conducted. The somehow unexpected results are presented and discussed in this publication.

Experimental Procedure

Pure alumina powders (AKP3000 or AKP53, Sumitomo Chem., Osaka, Japan) were doped with 0, 150, 300, 500, 1000, 1500, and 3000 wt ppm Y_2O_3. Yttrium was added to the powders as stoichiometric amount of $Y(NO_3)_3 \cdot 6H_2O$ (Strem Chem., Newburyport, MA). One set of green compacts were prepared by the temperature induced forming technique (TIF) [16]. Other samples (CIP) were prepared from powders that were mixed with zirconia milling balls (later with 99.7% pure alumina milling balls) in 200 proof isopropanol. Dried powders were then uniaxially pressed in cylindrical dies under 20 MPa, and subsequently cold isostatically pressed at 800 MPa for one minute. Green compacts were pressureless sintered in air at temperatures

ranging from 1500 to 1650°C for periods of 2 to 24 hours. All samples were thermally etched at 1400°C for half an hour.

The microstructure and microchemistry of the sintered bodies were analized with optical microscopy (OM), scanning electron microscopy (SEM), transmission electron microscopy (TEM), and analytical electron microscopy (AEM). Quantification of the segregated yttrium at the grain boundaries was performed using the procedure detailed in previous publications [10].

Results and Discussion

Samples were analized before and after sintering using optical emission spectrometry (ICP-OES). Table I lists the amount of various cations in different samples. Silicon and calcium in the first set of samples were most likely introduced to the samples during TIF processing of the green compacts. Second set of samples were produced through conventional ceramic processing routes, and zirconia was the only detected impurity at the detection limits for the available OES equipment. Yttrium concentrations followed the intended dopant level in lightly doped samples, deviated from the intended amount for highly doped samples.

Table 1. Concentrations of cations other than Al in the samples (ICP-OES).

Sample	Y [wt ppm]	Si [wt ppm]	Ca [wt ppm]	Mg [wt ppm]	Zr [wt ppm]
TIF Y0	<2	300 ±50	20 ±10	40 ±10	-
TIF Y150	123 ±6	300 ±50	220 ±20	30 ±10	-
TIF Y300	242 ±12	300 ±50	30 ±10	40 ±10	-
TIF Y500	400 ±20	330 ±50	30 ±10	40 ±10	-
TIF Y1000	824 ±40	300 ±50	30 ±10	40 ±10	-
TIF Y1500	1110 ±60	320 ±50	30 ±10	30 ±10	-
TIF Y3000	1320 ±70	370 ±50	30 ±10	40 ±10	-
CIP Y0	<2	<200	<10	<10	<10
CIP Y150	136 ±6	<200	<10	<10	30 ±10
CIP Y300	334 ±17	<200	<10	<10	60 ±10
CIP Y500	472 ±25	<200	<10	<10	80 ±10
CIP Y1000	1000 ±60	<200	<10	<10	80 ±10
CIP Y3000	1730 ±150	<200	<10	<10	30 ±10

"safe detection" limit for Si about 100 ppm, for Zr, Mg and Ca 10 ppm

Figures 1 a-f show the microstructure of TIF series α-alumina doped with 0, 150, 300, 500, 1000, and 1500 wt ppm Y_2O_3 sintered at 1550°C for 2 hrs except for 0 wt ppm sample which was sintered at 1500°C for 2 hrs. Respective average grain sizes given as mean linear intercept length are 1.85 (Y0), 2.14 (Y150), 2.10 (Y300), 2.06 (Y500), 7.49 (Y1000), and 13.8 μm (Y1500). In these samples, relatively high silicon and calcium impurity contents (especially in Y150 sample) caused few grains to grow exaggeratedly. Undoped sample and samples with small amounts of yttrium addition had grain sizes in the order of 1-2 μm whereas the highly doped samples exhibited an explosive grain

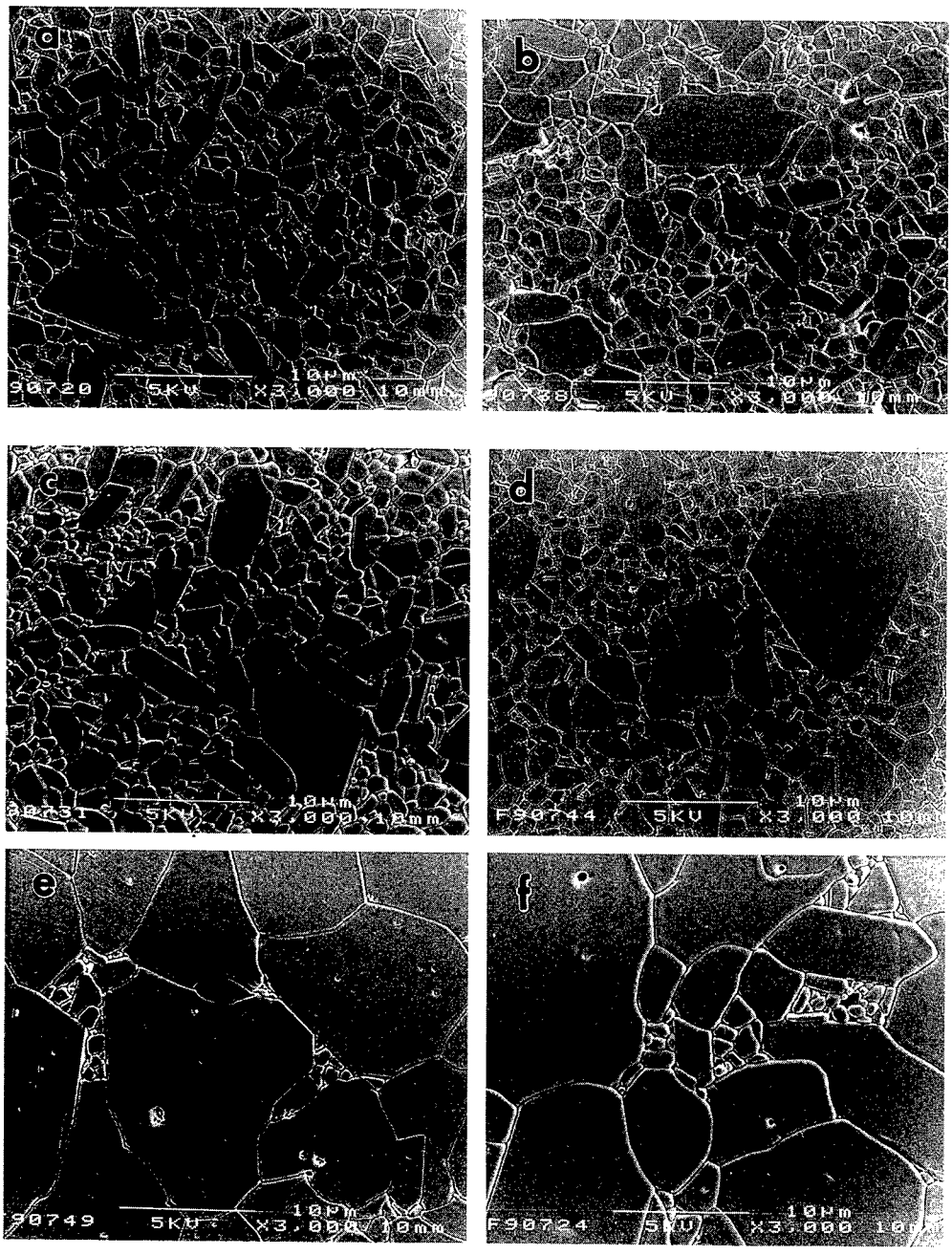

Figure 1. SEM micrographs of Y-doped α-alumina samples prepared through TIF-process and sintered at 1550°C for 2 hrs. Microstructures shown are from (a) "pure", (b) 150 wt ppm, (c) 300 wt ppm, (d) 500 wt ppm, (e) 1000 wt ppm, and (f) 1500 wt ppm Y_2O_3 doped samples. A sudden jump in grain size was observed in (e) and (f).

growth under identical sintering conditions and impurity levels. In 1000 wt ppm and 1500 wt ppm Y_2O_3 doped samples, precipitates of YAG were observed. Samples with lesser amounts of the dopant were free from precipitates. Similar observation were made with silicon and calcium free samples which were doped with 0, 150, 300, and 500 wt ppm Y_2O_3 and sintered at temperatures between 1500, 1550, and 1650 °C for various times between 2 and 24 hrs. Undoped (Y0) or lightly doped samples (Y150) had a very fine grain size distribution. Samples with 300 wt ppm and 500 wt ppm doping had a fine grain size when sintered at lower temperatures for shorter times. However, as the sintering time or temperature were increased, again explosive grain growth was observed. Figures 2 a-c show the change in the grain size with increasing sintering time at 1550°C for 500 wt ppm Y_2O_3 doped sample. Despite the sudden jump in the average grain size between figures 2 (a) and (c), the grain size distribution of both microstructures is uniform. During the transition (figure 2 (b)), few grains grow making the microstructure look like few scattered basketballs in a field of tennis balls. This bimodal uniformity is in strong contrast to the samples that contained silicon and calcium impurities and hence exhibited few exaggeratedly grown slab-like grains.

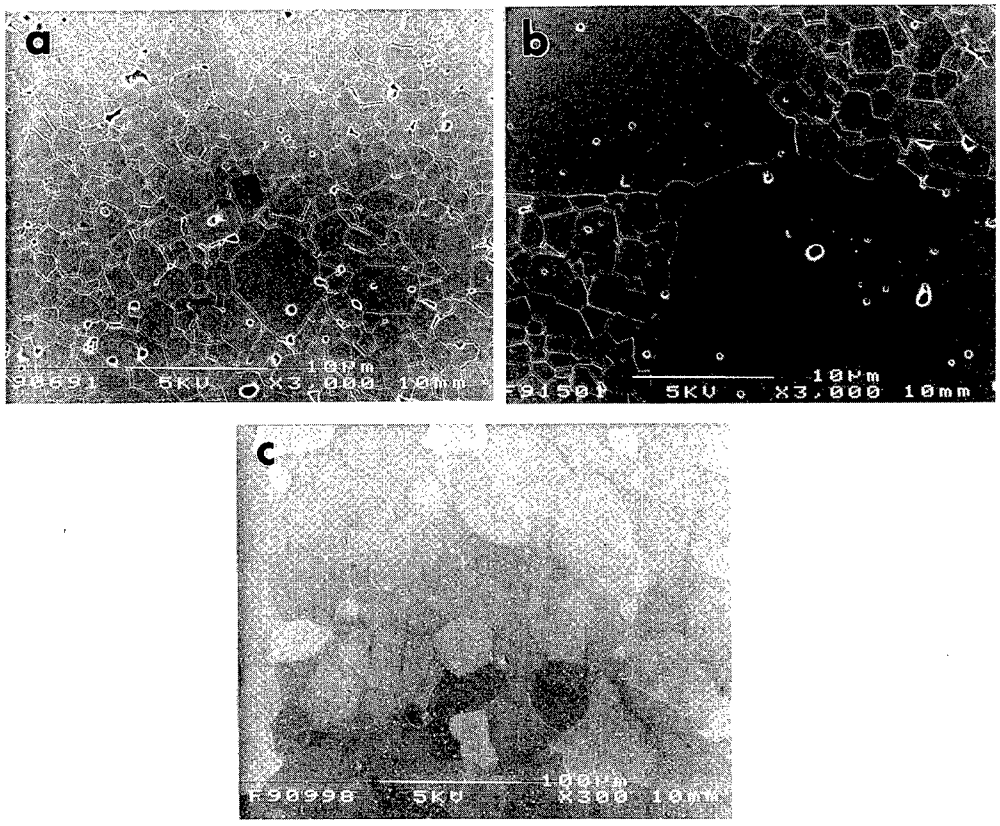

Figure 2. SEM Micrographs of CIP-Y500 samples sintered at 1550°C for (a) 2 hrs, (b) 6 hours and (c) 12 hrs. The transition from a uniform fine grained microstructure to a uniform large grained microstructure is illustrated in the micrographs.

Chemistry of the grain boundaries were quantified using a dedicated scanning transmission electron microscope (STEM) and procedures outlined in an earlier publications [10]. Figure 4 shows the measured mean linear intercept (TIF-samples) and calculated yttrium excess concentration at the boundaries assuming no precipitation would occur [17]. Experimental yttrium excess concentration at the grain boundaries in two samples, TIF-Y500 and TIF-Y3000, are also indicated on the same plot. The amount of excess yttrium atoms (ions) at the GBs of the sample doped with 500 wt ppm is almost twice as high as the one in the sample doped with 3000 wt ppm Y_2O_3. TEM analysis of the same samples indicated that the Y3000 sample contained large number of YAG precipitates whereas, no YAG particles were observed in the Y500 sample. AEM analysis of both set of samples (TIF and CIP) revealed that the concentration of excess yttrium at the boundaries increases with increasing total amount of the dopant up to a level (approximately 6 yttrium atoms/nm^2) where precipitation occurs. After the precipitation, the excess concentration settles at a level (~ 3.5 yttrium atoms/nm^2) which is lower than the highest measured yttrium excess before precipitation.

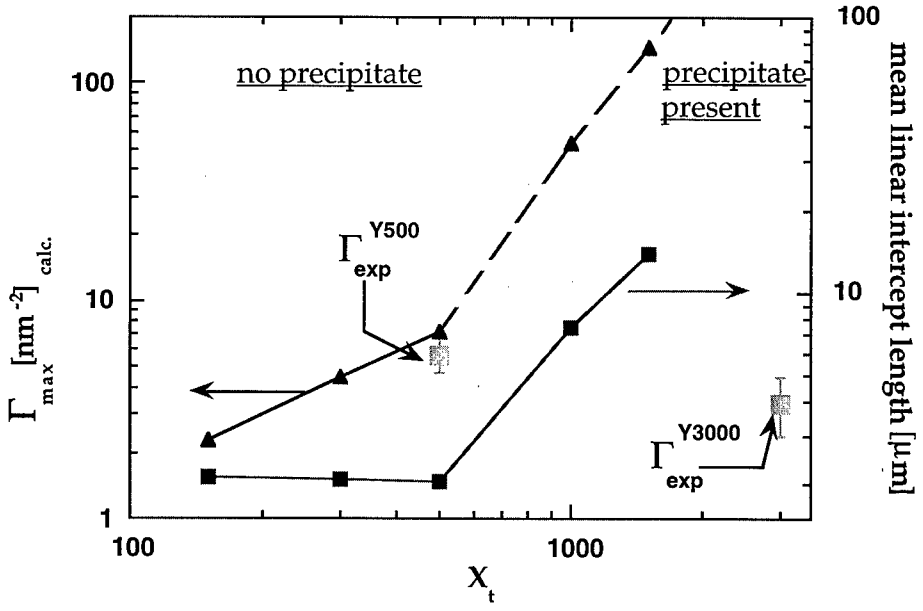

Figure 3. Yttrium excess concentration and grain size versus total amount of yttrium added to alumina. Y-excess concentration is calculated assuming no precipitates. Experimental yttrium excess for TIF Y500 and Y3000 samples are also indicated.

From the results it is obvious that the explosive grain growth observed in the precipitated samples is closely linked to the super-saturation of the boundaries and the

consequent precipitation. However, the question about when exactly the explosive grain growth occurs, i.e. whether at the super-saturation, or after precipitation, or during the transition is yet to be answered. The issue of how the structure of the segregated grain boundaries changes during this transition is addressed in another comprehensive publication on the subject [17]. An explanation of this phenomenon also holds the key to understand the peculiar, superplastic-like plateau regime in the high temperature deformation of yttrium doped, fine grained α-alumina. Currently, experiments with ultra-pure α-alumina samples containing only yttrium as the foreign cation are underway to clarify these points.

Another important observation is the uniformity of the grain sizes and grain morphology in the absence of excessive amounts of silicon and calcium impurities. In the CIP-type specimens where the only unintented impurity was zirconium, the grain size distributions in both, fine grained and large grained samples were uniform. Slab-like, large grains that were observed in silicon and calcium contaminated aluminas were not found in these samples and most of the grain were nearly equi-axed. This would indicate that yttrium does not show a preferential segregation towards a certain plane in α-alumina. Further analytical electron microscopy studies are underway to support this conclusion.

Conclusions

Yttrium can exist in alpha alumina as solute, segregant at the grain boundaries or surfaces, and/or as in YAG precipitates depending on its total concentration and the grain size of the ceramic. Experiments with polycrystalline α-alumina doped with varying amounts of yttrium indicated that the excess concentration of yttrium at the grain boundaries increases with increasing doping levels and/or increasing grain size of the ceramic up to a level (~6 yttrium atoms/nm^2) where precipitation occurs. After the precipitation, the average excess yttrium at GBs was approximately 3.5 yttrium atoms/nm^2.

The microstructure of the samples with small additions of yttrium is made up of small and uniform grains (1-2 μm). However, the grain size in the precipitated samples is more than an order of magnitude larger but yet uniform. Grains in both microstructures are nearly equi-axed. Results indicate that the saturation/precipitation behavior is closely linked to the explosive jump in the grain size.

Acknowledgements:
We are indebted to Dr. N. Bell and Prof. W. Sigmund for preparing the TIF-specimens. Acknowledgements are also due to Miss Kallfass, Dr. Bischoff and Dr. Scheu for OM, SEM quantitative image analysis, and STEM analysis of various samples. MAG would like to thank the CFEMS-8 organizing committee for the financial support in form of Young Researcher Award.

References:

[1] S. Lartigue et al., Colloque Phys., **C1-51** (1990) p. C1-985.
[2] S. Lartigue et al., Mat. Sci. Eng., **A164** (1993), p. 211.

[3] L. Priester et al., Proceedings. JIMIS-8 (1996), p. 134.
[4] J. Cho et al. J. Am. Ceram. Soc., 80 (1997), p. 1013.
[5] H. Yoshida et al. , Intern. Symp. Cer. Mat. Comp. Engines (1997), p. 695.
[6] J. D. French et al., J. Am. Ceram. Soc., **77** (1994), p. 2857.
[7] J. D. Cawley and J. W. Halloran, J. Am. Ceram. Soc., **69** (1986), p. C-195.
[8] R. C. McCune et al., J. Am. Ceram. Soc., **69** (1986), p. C-196.
[9] D. Bouchet et al., Microsc. Microanal. Microstruct., 4 (1993), p. 561.
[10] M. A. Gulgun et al., J. Am. Ceram. Soc., **82** (1999), p. ?
[11] E. Sato and C. Carry, J. Am. Ceram. Soc., **79** (1996), p. 2156.
[12] M. A. Gulgun et al., Mat. Sci. Forum, **294-296** (1999), p. 289.
[13] S. Lartigue, private communication (1999).
[14] P. Gruffel and C. Carry, J. Euro. Ceram. Soc., 11 (1993), p. 189.
[15] J. Fang et al., J. Am. Ceram. Soc., **80** (1997), p. 2005.
[16] N. Bell, and W. Sigmund, unpublished work (1998).
[17] M. A. Gulgun et al., in preparation (1999).

for correspondance: For both authors
Fax # ++49-711-2095-320
m-gulgun@hrem.mpi-stuttgart.mpg.de
ruehle@hrem.mpi-stuttgart.mpg.de

Key Engineering Materials Vols. 171-174 (2000) pp. 801-808
© 2000 Trans Tech Publications, Switzerland

Slip Systems in Erbia Single Crystals

A.A. Sharif, A. Misra, J.J. Petrovic and T.E. Mitchell

Center for Materials Science, MS K765, Los Alamos National Laboratory,
Los Alamos, NM 87544, USA

Keywords: Erbium Oxide, Rare-Earth, Shear Strength, Burgers Vector, Dissociation, Ia3

ABSTRACT

Dislocation motion during high-temperature deformation of erbia single crystals has been investigated. Compressive deformation along various crystallographic axes at 1640°C resulted in slip on {110} planes. The Burgers vector was determined to be $\bar{b} = 1/2 < 1\bar{1}1 >$. Dislocations with such a large Burgers vector, (9.1 Å), can dissociate into $1/4 < 1\bar{1}0 >$ and $1/4 < 1\bar{1}2 >$ partials. The critical resolved shear stress of the samples at 1640°C was estimated to be about 38 MPa. Cleavage at room temperature was found to be on {111} planes.

INTRODUCTION

Erbia (Er_2O_3) is a rare-earth oxide with an excellent chemical and thermal stability at high temperatures. The free energy of formation of Er_2O_3 is one of the lowest among all binary oxide ceramics [1,2]. Because of its high thermal neutron absorption cross section, Er_2O_3 is a good candidate for applications as a barrier to migration of fission products [3]. However, knowledge of the fundamental mechanical properties of Er_2O_3 is lacking. Difficulties in preparing large samples of single crystalline rare-earth sesquioxides for high-temperature deformation have prevented the experimental investigation of plasticity in these materials. Knowledge of plastic deformation in rare-earth sesquioxides is limited to analogies extended from the study of yttria (Y_2O_3) to other sesquioxides [4]. With advances in the science and technology of single crystal growth, the direct study of dislocation motion in Er_2O_3 single crystals is possible.

Er_2O_3 has the cubic rare-earth type-C bcc crystal structure with a large complex unit cell comprised of 16 Er_2O_3 sesquioxide units with a 10.55Å lattice parameter [2]. Er_2O_3 belongs to the Ia3 space group, which is different from the fluorite structure in missing one fourth of the sites in the anion sub-lattice in <111> directions. The oxygen octahedra are distorted, resulting in a distortion of the {110} planes of high density on which dislocation movement is expected.

The aim of this investigation is to extend the scope of knowledge on the fundamental mechanical properties and plasticity of Er_2O_3 rare-earth sesquioxide at high temperatures. The focus is to determine the nature of dislocations in Er_2O_3 and test the validity of the analogies made from studies on Y_2O_3. Furthermore, this investigation aims to elucidate the characteristics of dislocations in such complex crystal structure.

EXPERIMENTAL PROCEDURE

A xenon optical float zone single crystal growth unit was used to prepare single crystals of Er_2O_3. Er_2O_3 rods were cold isostatically pressed from commercially available powders (Rhone-Poulenc, Shelton, CT) with 99.9 % purity. These rods were used as seeds and feeds to prepare crystals with about 4 mm diameter and 60 mm long. The details of crystal growth conditions are given elsewhere [5]. Crystals were annealed 4 hours at 1600°C in air to achieve stoichiometry. Crystal orientations were determined using Laue x-ray back reflection method. Samples for compression testing were sectioned from these crystals using a diamond saw. High-temperature deformation experiments were conducted at 1640° in compression on samples with different orientations. An ATS (Butler, PA) furnace mounted on an Instron (Canton, MA) testing instrument was used for high temperature deformation experiments. Constant strain rate and constant stress loading modes were used to deform the samples. Transmission optical microscopy (OM), scanning electron microscopy (SEM), and transmission electron microscopy (TEM) were used to characterize the samples.

RESULTS

Since crystal growth took place in an inert atmosphere, all the as-grown crystals were substoichiometric. Substoichiometry in cubic C-type Er_2O_3 imparts a dark black color to the crystals [6]. Annealing the black as-grown crystals in air resulted in stoichiometric samples of pink color. The presence of cracks in the translucent stoichiometric samples was clearly visible by naked eye examination. Imperfections present in single crystals of as-grown Er_2O_3 posed difficulties in studying dislocation motion. Microcracks were present in all samples because of thermal shock experienced by the sample during crystal growth. Without using a single crystalline seed, all crystals grew in <111> directions. The cross section of the crystal perpendicular to the growth axis deviated from circular by faceting on two opposite sides. Laue x-ray back reflection analysis showed that these facets were always $\{\bar{2}11\}$ planes. The planes normal to the facets and parallel to the growth axis were $\{0\bar{1}1\}$ planes. The facets on the crystals twisted around the growth axis, <111>, by about 1° per 14 mm growth. The presence of low angle boundaries normal to the growth axis was confirmed from Laue patterns from the side of the crystals. Samples containing boundaries were not used for deformation experiments.

Planar cleavage was not observed at high temperatures and high stresses. Easy cleavage at room temperature was observed in these crystals during sample thinning to make TEM foils (Figure 1). At room temperature, large crystals subjected to bending stresses always fractured on parallel {111} planes. Laue x-ray pattern confirmed that fracture of samples occurred on {111} cleavage planes.

Preliminary attempts to deform single crystals of Er_2O_3 at and below 1600°C resulted in brittle fracture of the samples. These samples failed by crack propagation; OM and TEM examinations could reveal no evidence of plastic deformation. Hence, the temperature was raised to 1640°C, which was the limit of the furnace on the Instron testing machine. The yield strength of the samples at 1640°C was estimated from the 0.2% strain offset. The typical yield strength of the samples was approximately 95 MPa. Examples of stress vs. strain behavior for samples deformed along $[\bar{1}\bar{1}2]$ and $[\bar{1}10]$ crystal axes at 1640°C are shown in Figure 2. The load on the samples was removed after about 0.1% strain in order to prevent catastrophic failure and preserve the sample for further analysis. Cracks were observed in all the samples that had undergone deformation. These cracks grew under stress from microcracks developed during crystal growth and were not on

cleavage planes. Due to the presence of these cracks, an increase in the dimensions of the samples was detected after deformation, compared to the dimensions before deformation. Hence, the total strain in the samples could not be calculated accurately from the sample dimensions measured before and after deformation.

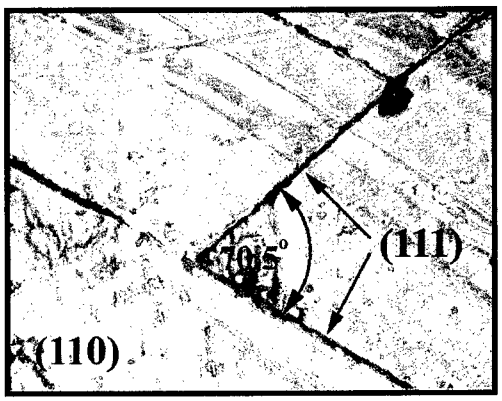

Figure 1. Light micrograph of a thin section showing {111} cracks in single crystalline Er_2O_3.

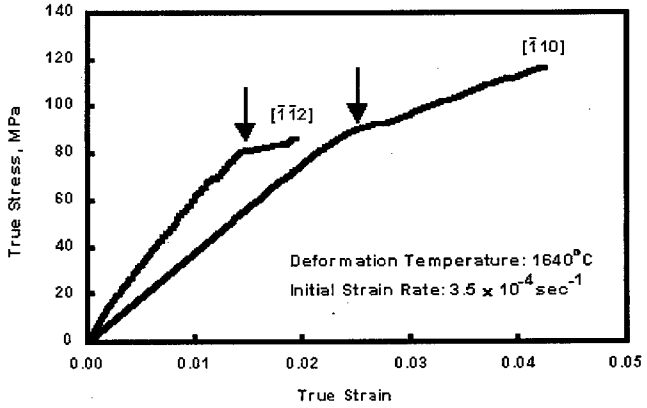

Figure 2. Estimation of the yield strength of Er_2O_3 single crystals by 0.2% strain offset method for samples deformed along [$\bar{1}\bar{1}$2], [$\bar{1}$10] directions. Arrows indicate yielding. The slopes of the "elastic" lines include effects of machine softness.

In samples with only a small density of cracks, after deformation at 1640°C slip traces were observed on the surfaces of the samples (Figure 3). Standard trace analysis was used to calculate the slip planes for samples deformed along [111], [$\bar{1}\bar{1}$2], [$\bar{1}$10] and [123] crystallographic axes. An example of observation of slip planes and slip traces is shown in Figure 3 for a sample deformed along [111]; all the slip planes that could be identified were {110} planes.

A number of dislocations were studied by TEM to determine the type of Burgers vector operating during deformation at 1640°C. For slip on {110} planes, the possible Burgers vectors are $1/2\langle 111\rangle$, <110>, and <100>. Of these possibilities, <110> appears to be unlikely due to its large magnitude of 15 Å. In the dislocation analysis, enough $\vec{g}$-vectors were used to determine $\vec{b}$

unambiguously. Dislocations were imaged with the three $\bar{g}=4\bar{4}0$ type reflections in the [111] zone and $\bar{g}=400$ type vectors for the three <110> type zone axes at 35° from the [111] zone. In most cases, clear invisibility was obtained with only one $\bar{g}$-vector. However, most possibilities for $\bar{b}$ could be eliminated just by visibility conditions. For example, the dislocation in the upper left corner of Figure 4 was visible with $\bar{g}=040$ and $\bar{g}=400$, eliminating $\bar{b}=[100]$, $\bar{b}=[010]$, $\bar{b}=[001]$, $\bar{b}=[011]$, $\bar{b}=[0\bar{1}1]$, $\bar{b}=[101]$, and $\bar{b}=[\bar{1}01]$. This dislocation was invisible with $\bar{g}=04\bar{4}$, eliminating $\bar{b}=[110]$, $\bar{b}=[1\bar{1}0]$, $\bar{b}=[1\bar{1}1]$, $\bar{b}=[11\bar{1}]$ and resulting in possible $\bar{b}$ of $1/2[\bar{1}11]$ or $1/2[111]$. Visibility with $\bar{g}=4\bar{4}0$ rules out the possibility of $\bar{b}=1/2[111]$. Hence, the Burgers vector of this dislocation was determined as $1/2[\bar{1}11]$. Any dislocation whose Burgers vector could be identified unambiguously had a $1/2<111>$ Burgers vector.

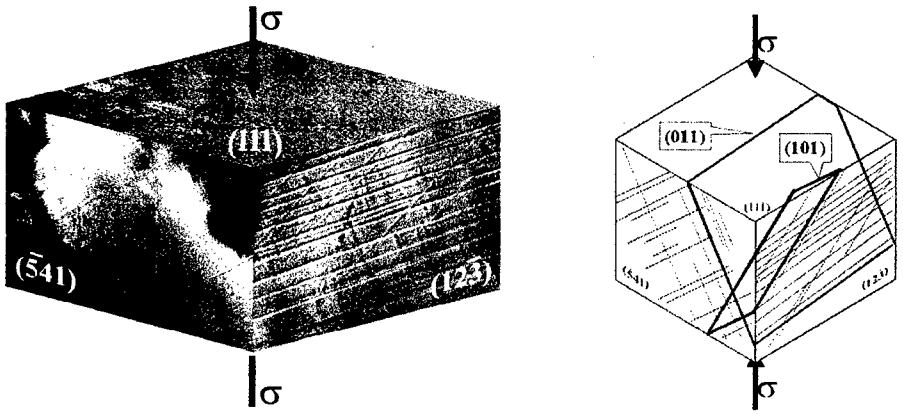

Figure 3. Observation of the (110) slip planes from $(\bar{5}41)$ and $(12\bar{3})$ side traces of a crystal deformed along [111].

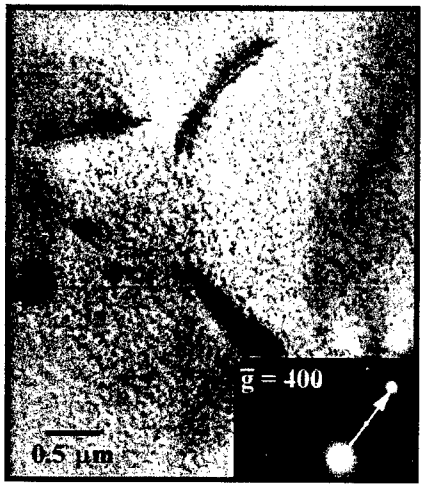

Figure 4. Dislocations in a sample deformed along [111] crystal axis at 1640°C.

DISCUSSION

Twist

Rotation of the crystal orientation about the growth axis is likely to be due to the stress imposed on the cooling liquid during crystal growth. In order to obtain uniform mixing throughout the molten zone during crystal growth, the seed and feed rods were rotated at 55 rpm in opposite directions. As the molten zone was transferred from one end of the feed rod to the other end incrementally, molten Er_2O_3 started to cool down and its viscosity started to increase until it crystallized. It was at this stage of the cool down process that the shear stress imposed by the surrounding high viscosity liquid caused the crystallizing planes to rotate on the seed incrementally. This rotation resulted in the creation of twists, which were seen as a doubled pattern in Laue x-ray back reflection.

During crystal growth, the power input is adjusted whenever a change in the ratio of the molten zone neck diameter to its height is observed. It was found experimentally that keeping this ratio to 3/4 resulted in the growth of crystal with least defects. Deviation from this condition due to the power deficit or excess resulted in a deviation from equilibrium growth conditions and defects including twists in the crystal. The presence of twists was not observed in most samples by Laue x-ray back reflection after the crystals were sectioned. Hence, despite the appearance of continuity of the rotation of the crystals to the naked eye, twisting in the crystals was localized at twist boundaries.

Cleavage

Brittle fracture in crystalline materials generally occurs along cleavage planes of high atomic density. Cleavage planes are usually planes of normal growth of the crystal [7]. In Er_2O_3 single crystals, fracture at room temperature and low stresses always occurred on {111} planes, which are the normal growth planes of the crystal. At high stresses microcracks, which are already present in the samples, have propensity to grow rapidly. This resulted in the propagation of cracks on random crystallographic planes during deformation at 1640°C and relatively high stresses.

Yield Strength

Sample failure under high-temperature and high-stress conditions occurred by propagation of microcracks that were present in the as-fabricated samples. The presence of these microcracks often resulted in the failure of the samples below the yield strength of the material. A drop in the load during constant-strain-rate-deformation experiments and a sudden crosshead movement during constant-load experiments marked the sample failure by crack propagation. The presence of microcracks generated during crystal growth in the samples prevented obtaining consistent results for yield strengths during deformation experiments.

No reliable difference in strength could be attributed to different compression axes. Calculating the value of the ratio of the Young's modulus (E) in [111] direction to that in [100] direction, $E_{[111]}/E_{[100]}$, to determine the maximum anisotropy in Er_2O_3 single crystals resulted in the value of 1.3 indicating some orientation dependence of Young's modulus for Er_2O_3 crystals. The values of E in various orientations were calculated from the elastic constants obtained by using the ultrasonic resonance technique [8]. Anisotropy in elastic behavior observed in different orientations in Er_2O_3 single crystals does not result in different values of yield strength during compressive deformation in different orientations. The Schmid factors for slip on {110} planes and <111> directions along $[\bar{1}\,\bar{1}2]$ and $[\bar{1}10]$ are identical with a value of 0.41. Although in Figure 2 yield

strength of the sample deformed along $[\bar{1}10]$ direction is slightly higher than that for the sample deformed along $[\bar{1}\,\bar{1}2]$ direction, due to the scatter in the data the effects of anisotropy on yield strength could not be isolated affirmatively for all directions examined. The values of the yield strength of these samples were affected by the presence of imperfections in the crystals. Cracks were observed in all samples after deformation. Propagation of these cracks resulted in the premature failure of some samples. The critical resolved shear stress of the samples for all directions was about 38 MPa. The difference in the slopes of the elastic regions observed for these samples in Figure 2 is a result of the machine softness and does not have a significance.

To prevent crack propagation and to promote plasticity in Er_2O_3 single crystals, deformation experiments must be conducted at temperatures higher than 1640°C. Although plastic deformation was observed in some samples at 1640°C, rapid crack propagation in most samples indicated that the brittle-to-ductile transformation temperature of the samples was above 1640°C.

Slip System

In general, the slip plane is the plane of maximum packing in metals. In ionically bonded compounds, slip can not occur easily on the close-packed planes because of electrostatic repulsion forces caused by passing like charged ions near one another [9]. There are three crystallographic slip planes commonly observed in bcc metals, namely, {110}, {211}, and {321}. Screw dislocations may move on any combination of these planes that is favored by stress. Hence slip lines in bcc metals often are not very well defined and are wavy. Slip planes in the bcc crystal structure vary with composition, crystal orientation, temperature, and strain rate [10].

A number of slip systems have been observed in cubic rare-earth type-C crystal structure by studying Y_2O_3 single crystals. At low temperatures and high stresses, {001}<110> slip system is reported to be active in Y_2O_3 [11,12]. {001} planes do not contain the shortest Burgers vector for this structure which is $\vec{b} = 1/2 < 111 >$, (9.1 Å), and results in a large Burgers vector of $\vec{b} = < 110 >$, (15 Å). The occurrence of such a large Burgers vector in Y_2O_3 is explained by dissociation of <110> into four collinear partials, which may glide on {001} planes [13]. Other Burgers vectors observed in Y_2O_3 after undergoing deformation at ~0.58 T_m are $\vec{b} = 1/2 < 111 >$ and $\vec{b} = < 100 >$ [14]. The Burgers vector identified here, $\vec{b} = 1/2 < 1\,\bar{1}1 >$ at ~0.67 T_m, has a magnitude of 9.1 Å. Due to the differences in deformation temperatures between the two studies, direct comparison is not possible. No plastic deformation in Er_2O_3 was observed at temperatures below 0.67 T_m. It is possible that different slip systems become active at different temperatures.

In general, the Burgers vector of a dislocation in bcc materials is a $\vec{b} = 1/2 < 1\,\bar{1}1 >$ type. Such a dislocation can glide on {110} planes. In metals the $1/2 < 1\,\bar{1}1 >$ Burgers vectors may dissociate into three partials of the type $1/6 < 1\,\bar{1}1 >$ [10]. However, in erbia, due to the distribution of dissimilar charges, these partials can not form at 1640°C. Another possibility for the dissociation of $< \bar{1}11 >$ Burgers vectors is $1/2\langle\bar{1}11\rangle \rightarrow 1/4\langle\bar{1}10\rangle + 1/4\langle\bar{1}12\rangle$. Such dissociation has been observed in Y_2O_3 single crystals deformed at 0.58 T_m [13].

Burger vectors of $\vec{b} = < 100 >$, although only slightly larger in length (10.55 Å) than $\vec{b} = 1/2 < 1\,\bar{1}1 >$, (9.1 Å), were not observed in Er_2O_3. The $\vec{b} = < 100 >$ Burgers vectors observed in Y_2O_3 crystals is probably developed by association of two <111> or <110> Burgers vectors as $1/2[111] + 1/2[1\,\bar{1}\,\bar{1}] \rightarrow [100]$ or $1/2[110] + 1/2[1\,\bar{1}0] \rightarrow [100]$ [13,14]. An increase in the density of

$\vec{b} = 1/2 < 111 >$ dislocations at high temperatures (1550-1800°C) in Y_2O_3 has been observed to induce dislocation junctions with a Burgers vector of $\vec{b} = < 100 >$ [15]. Deformation of Er_2O_3 at 1640°C resulted in a very low dislocation density. It is likely that the reason that $\vec{b} = < 100 >$ Burgers vectors were not observed here is that the dislocation density was never high enough for $\vec{b} = 1/2 < 111 >$ Burgers vectors to interact.

Since strong slip traces were observed on the surfaces of the plastically deformed samples, high dislocation densities were expected to be present in the samples after plastic deformation. It appears that the climb of dislocations during deformation resulted in the annihilation of dislocations.

All dislocations observed were deformation dislocations since no dislocations were observed in undeformed samples during TEM examinations. Most dislocations were observed as double lines as seen in Figure 4. It is likely that very high-energy $\vec{b} = 1/2 < \bar{1}11 >$ Burgers vectors dissociate into partials to reduce their energy. Dissociation of $\vec{b} = 1/2 < 111 >$ into partials is perhaps the source of the double images observed for these dislocations.

Examination of the slip planes, {110} planes, of an Er_2O_3 crystal reveals that there are no possibilities of dissociation for $\vec{b} = 1/2 < 111 >$ without creating high-energy stacking faults. The most likely dissociation of $\vec{b} = 1/2 < 111 >$ on {110} planes seems to be dissociation into $1/4 < 110 >$ and $1/4 < 112 >$ partials as illustrated schematically in Figure 5. Weak beam TEM examinations have not been performed yet to elucidate the source of double images observed.

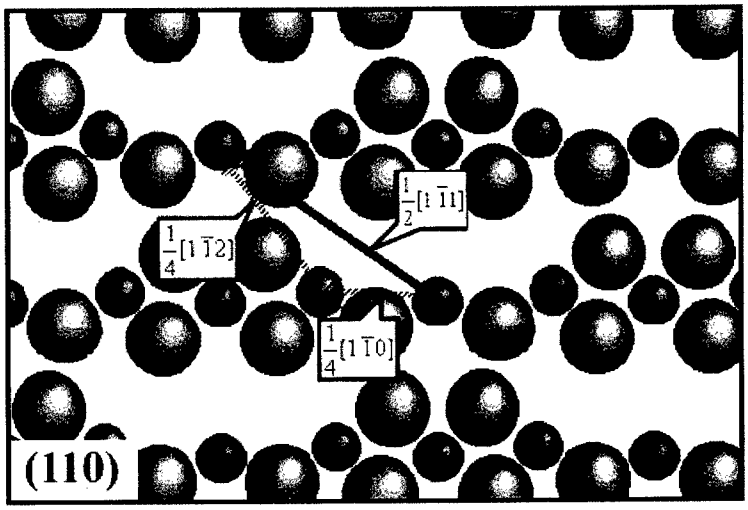

Figure 5. Dissociation of $1/2[1\,\bar{1}1]$ Burgers vector to $1/4[1\,\bar{1}0]$ and $1/4[1\,\bar{1}2]$ partials on (110) plane. The large atoms are oxygen ions and the small ones are erbium ions.

CONCLUSIONS

The brittle-to-ductile transition temperature of single crystalline Er_2O_3 is above 1640°C. No plasticity in Er_2O_3 was detected below 1640°C and limited plasticity was observed at 1640°C. For most samples, crack growth during high-temperature deformation prevented the stress on the

samples from reaching the yield stress. The value of the critical resolved shear stress for all directions at 1640°C under compression was about 38 MPa. Slip occurred on {110} planes regardless of the crystal orientation. At 1640°C, the slip system in Er_2O_3 rare-earth cubic type-C was determined to be {110}<111>. It is believed that $1/2<111>$ Burgers vectors dissociates into $1/4<110> + 1/4<112>$ partials.

ACKNOWLEDGEMENT

This research is sponsored by the US Department of Energy, Office of Basic Science, Division of Materials Science. The authors would like to acknowledge Russell Romero's contribution of growing erbia single crystals.

REFERENCES

[1] J.P. Coughlin, U.S. Bureau of Mines Bulletin, (1954), p. 542.

[2] L. Eyring, "The Binary Rare Earth Oxides," in Handbook on the Physics and Chemistry of Rare Earths, edited by Karl A. Gschneider Jr. and LeRoy Eyring (North-Holland Publishing Co., Amsterdam, (1979), Vol. 3, pp. 337-398.

[3] M.F. Berard and D.R. Wilder, J. Amer. Ceram. Soc., 52 (1969), pp. 85-88.

[4] M. Boisson and R.J. Gaboriaud, J. Mater, Sci,, 16 (1981), pp. 3452-3460.

[5] A.D. Neuman, M.J. Blacic, M. Platrero,R.S. Romero,K.J. McClellan, and J.J. Petrovic, Ceram. Eng. & Sci. Proc., 19 (1998), pp. 423-429.

[6] A.E. Miller and A.H. Daane, J. Inorg. Nucl. Chem., 27 (1960), pp. 1955-1960.

[7] W.D. Kingery, H.K. Bowen, and D.R. Uhlmann, Introduction to Ceramics, 2 ed. John Wiley & Sons, New York, (1975), p. 783.

[8] J.J. Petrovic and F. Chu, Private Communications, (1999).

[9] D.W. Lee and J.S. Haggerty, J. Amer. Ceram. Soc., 52 (1969), pp. 641-647.

[10] D. Hull and D.J. Bacon, Dislocations, 3 ed. Pergamon Press, Inc., Oxford, UK, (1984), pp. 47-111.

[11] R.J. Gaboriaud, Ph.D. Dissertation, Poitiers, France, (1978).

[12] R.J. Gaboriaud and M.F. Denanot, J. Microscop. Spectroscop. Electroniq., 3 (1978), pp. A4-A4.

[13] R.J. Gaboriaud, M.F. Denanot, M. Boisson, and J. Grilhe, Phys. Stat. Sol. (A), 46 (1978), pp. 387-396.

[14] R.J. Gaboriaud and J. Cadoz, Phys. Stat. Sol. (A), 52 (1979), pp. 95-101.

[15] R.J. Gaboriaud, Phil. Mag. (A), 44 (1981), pp. 561-587.

Please send correspondence to Adel A. Sharif at adel@lanl.gov, fax (505) 665-2992.

Key Engineering Materials Vols. 171-174 (2000) pp. 809-816
© 2000 Trans Tech Publications, Switzerland

A Critical Factor to Determine the High-Temperature Creep Resistance in Cation-Doped Polycrystalline Al_2O_3

H. Yoshida, Y. Ikuhara and T. Sakuma

Department of Materials Science, Graduate School of Engineering, the University of Tokyo,
7-3-1 Hongo, Bunkyo-ku, Tokyo 113-8656, Japan
E-Mail: yoshida@ceramic.mm.t.u-tokyo.ac.jp

Keywords: Al_2O_3, Creep Resistance, Grain Boundary Segregation, Molecular Orbital Calculations

Abstract

A small dopant effect on the high-temperature creep resistance in high-purity, polycrystalline Al_2O_3 is examined by uniaxial compression creep testing in air at temperatures between 1150 $\sim$ 1350 °C under the applied stress of 10 $\sim$ 200 MPa. High-temperature creep resistance in polycrystalline Al_2O_3 is highly improved by zirconium or lanthanoid ions in the level of about 0.05mol%. High resolution electron microscopy (HREM) and X-ray energy dispersive spectroscopy (EDS) analyse revealed that the dopant cation segregate in grain boundaries, and is likely to influence grain boundary diffusion. This paper aims to show a critical parameter to describe the high-temperature creep rate in cation-doped Al_2O_3.

1 Introduction

It has been reported that high-temperature mechanical property in polycrystalline Al_2O_3 is highly improved by ZrO_2 dispersion[1–5]. Okada *et al.* found that the flow stress of Al_2O_3–ZrO_2 with a composition range from 2 to 20 wt% ZrO_2(2.5mol%Y_2O_3) has a flow stress in excess of 100 MPa at 1400°C, which is much higher than that of undoped Al_2O_3[3,4]. According to the data of Wakai *et al.*, the creep rate of Al_2O_3–20wt%ZrO_2(3mol%Y_2O_3) is about 40 times lower than that of Al_2O_3 at 1250 and 1300°C[5]. The excellent high-temperature mechanical properties were explained in terms of the dispersion of ZrO_2 particles in Al_2O_3 grain boundaries [5,6].

More recently, we reported that the major effect of the improved creep resistance in Al_2O_3–ZrO_2 is caused by the segregation of zirconium ions in grain boundaries rather than the dispersion effect of ZrO_2 particles[7]. The improved creep resistance due to grain boundary segregation of cations has been found in various dopants[8,9]. The present paper aims to briefly summarize our experimental data on the small dopant effect on the high-temperature creep resistance and to show that the change in chemical bonding state in grain boundaries with dopant segregation is responsible for the improvement of creep resistance.

2 Results and Discussion

2.1 Improvement of Creep Resistance in Al_2O_3 with ZrO_2-doping

High-temperature creep resistance in high-purity, polycrystalline Al_2O_3 is highly improved by a small amount of Zr addition as shown in Figure 1, which shows the creep curves at 1300°C under an applied stress of 26MPa in high-purity Al_2O_3 with a purity of 99.99%, 0.1wt% ZrO_2-doped single phase Al_2O_3 and Al_2O_3-10wt% ZrO_2(2.5mol% Y_2O_3) containing

ZrO_2 dispersion[7]. The creep rate is very much suppressed by the small amount of ZrO_2 doping, and further reduced by ZrO_2 dispersion in Al_2O_3. The difference in creep rate is not caused by grain size difference or grain growth, because the grain size is nearly the same in the three materials and grain growth during creep deformation is negligible.

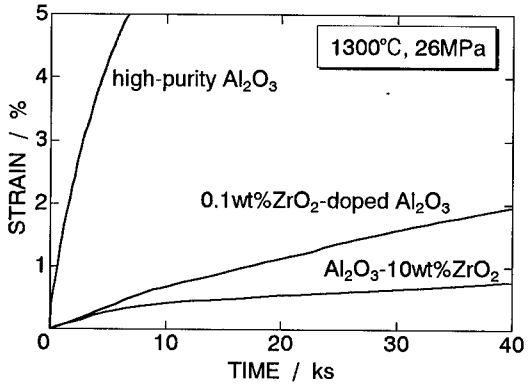

Figure 1. The creep curves in high- purity Al_2O_3, 0.1wt% ZrO_2- doped Al_2O_3 and Al_2O_3- 10wt% ZrO_2 (2.5mol%Y_2O_3) under an applied stress of 26MPa at 1300°C.

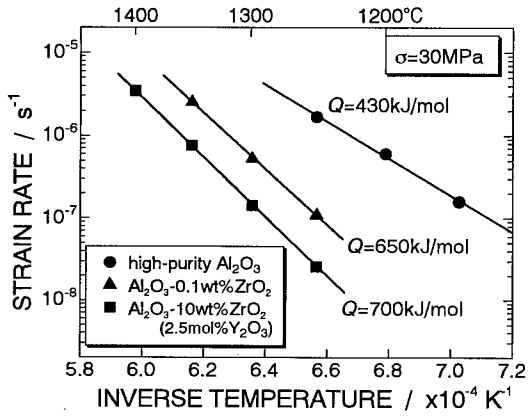

Figure 2. An Arrhenius plot of creep strain against inverse temperature in high- purity Al_2O_3, 0.1wt% ZrO_2 -doped Al_2O_3 and Al_2O_3–10wt%ZrO

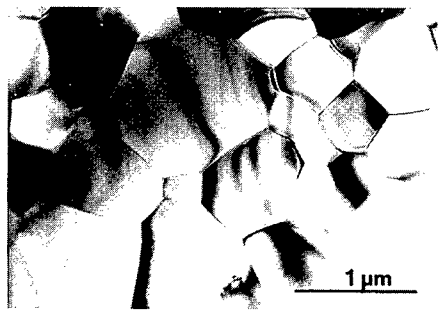

Figure 3. A bright-field transmission electron micrograph of as-sintered 0.1wt%ZrO_2- doped Al_2O_3.

The activation energy for creep deformation was obtained from an Arrhenius plot of creep strain rate at an applied stress of 30 MPa against inverse temperature as shown in Figure 2. The activation energy for creep deformation is 430 kJ/mol in high-purity Al_2O_3, 650 kJ/mol in 0.1wt%ZrO_2-doped Al_2O_3 and 700 kJ/mol in Al_2O_3-10wt%ZrO_2 at temperature range of 1150 $\sim$ 1400 °C under the applied stress of 30 MPa. The activation energy values correspond well with the creep resistance in these materials. It is noted that the doping of zirconium even in the level of 0.1 wt% yields a drastic increase of activation energy.

Figure 3 is a conventional bright field image of 0.1wt%ZrO_2-doped Al_2O_3. The grains are nearly equiaxed without second phase. The 0.1wt%ZrO_2-doped Al_2O_3 was confirmed to be a single phase material as well as high-purity Al_2O_3. Figure 4 is a HREM image of 0.1wt%ZrO_2–doped Al_2O_3 (a) together with the EDS spectra taken from the matrix (b) and from the grain boundary (c). HREM image was taken for the boundary at the edge-on view, and EDS spectra were obtained with a probe size of about 1nm at the indicated areas shown as the circles in Figure 4 (a). The presence of zirconium ions is detected in the grain boundary but not in the matrix. This must be the evidence of Zr ions' segregation in grain boundaries.

The activation energy for high-purity Al_2O_3 is in good agreement with the activation energy for Al^{3+} grain boundary diffusion which is reported to be 418 kJ/mol[10]. In contrast, the activation energy for diffusion in ZrO_2-doped Al_2O_3 has not been reported so far, but is estimated from indirect methods. For example, Wang and Raj obtained the activation energy of 700 $\pm$ 100 kJ/mol from sintering experiments in Al_2O_3–ZrO_2 with a composition range from 5 to 95 vol% ZrO_2 on the assumption that sintering is controlled by grain boundary diffusion[2, 12]. Wakai reported an activation energy of 754 kJ/mol for superplastic flow in Al_2O_3–20wt%ZrO_2(2.5mol%Y_2O_3)[5]. Since the superplastic flow takes place mainly by grain boundary sliding, the activation energy may be associated with grain boundary diffusion of constituent ions. Okada

and Sakuma obtained the activation energy of 732 kJ/mol for grain growth in Al_2O_3–6.7 vol%ZrO_2[13]. From these results, it seems reasonable that the activation energy for grain boundary diffusion in ZrO_2-doped Al_2O_3 is about 700 kJ/mol. These values are not so different from the activation energies for steady-state creep rate in 0.1wt%ZrO_2-doped Al_2O_3 and Al_2O_3–10wt%ZrO_2. The present result indicates that the grain boundary diffusivity of Al ions must be retarded by the segregation of Zr ions in grain boundaries.

2.2 High-temperature Creep Resistance in Lanthanide Ion-doped Al_2O_3

The small dopant effect on the creep resistance in polycrystalline Al_2O_3 is not a special case for zirconium ion but appears in other dopants such as lanthanoid ions even in the level of 0.05 mol%. Figure 5 shows the creep curves at 1250°C under an applied stress of 50MPa in high-purity Al_2O_3 and Al_2O_3 with 0.05mol% of Y_2O_3, Sm_2O_3, Eu_2O_3, Tm_2O_3 or Lu_2O_3[9]. These materials were fabricated by sintering in air at temperatures of 1300°C $\sim$ 1400°C in order to obtain an average grain size of about 1 μm. The creep deformation of polycrystalline Al_2O_3 is very much suppressed by the lanthanoid oxide doping. The dopant effect is dependent on the type of cation; the improvement of creep resistance is in the order, Sm < Tm < Eu < Y $\simeq$ Lu. Lu_2O_3 and Y_2O_3 are particularly effective to improve the creep resistance in Al_2O_3 in comparison with other dopants. The difference in creep rate in the materials is not caused by the change of grain growth rate, because the grain growth during creep deformation was negligible in the present materials at the temperature range examined.

The creep rate in the lanthanoid-doped materials reduces with increasing time. Time or strain at the onset of the steady-state creep rate depends on testing condition, and we tentatively define the steady-state rate where the change of strain rate with time is in the level of $\pm 1 \times 10^{-9}$ s^{-1}. The steady-state creep rate is plotted against applied stress in the four materials at 1250 °C in Figure 6.

The creep strain rate in Sm_2O_3-doped Al_2O_3 is about 50 times, and that in Y_2O_3- or Lu_2O_3-doped Al_2O_3 is about 200 times lower than that of high-purity Al_2O_3 at 1250°C for

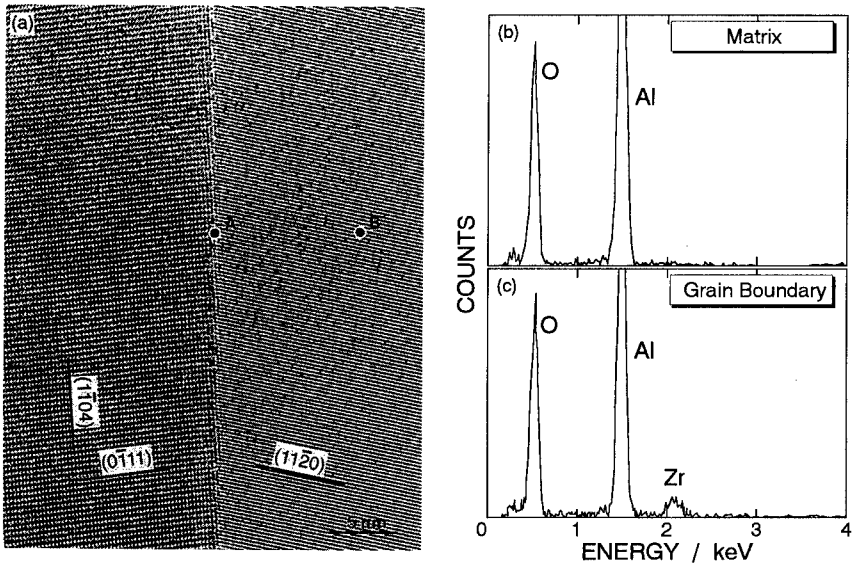

Figure 4. HREM image of as-sintered 0.1wt%ZrO_2-doped Al_2O_3 (a), and the EDS spectra taken from (b) the matrix in (a) and (c) the grain boundary. The analysed area is marked by the circles.

the same applied stress. In each material, the log-log plot of creep strain rate against applied stress is approximated to be a single straight line with a stress exponent n of about 2. This value can be explained in terms of either an interface reaction-controlled diffusional creep[14] or a grain boundary sliding[15–17]. Since no dislocation activity is observed in the crept samples, the creep deformation must be induced by a diffusional process.

The activation energy for creep deformation was obtained in a conventional way from an Arrhenius plot of creep strain rate at an applied stress of 100MPa against inverse temperature as demonstrated in Figure 7, in which a calculated creep strain rate of aluminum ion lattice diffusional creep (Nabarro–Herring creep)[18] for high-purity Al_2O_3 is also plotted. From the slope of these lines, the Q values are calculated to be 410 kJ/mol for undoped-Al_2O_3, 790 kJ/mol, 830 kJ/mol and 780 kJ/mol for Sm_2O_3-, Y_2O_3- and Lu_2O_3-doped Al_2O_3, respectively. The activation energies for lanthanoid-doped Al_2O_3 are about twice as large as that of undoped-Al_2O_3 as well as ZrO_2-doped one. The improved creep resistance due to the lanthanoid-doping is mainly caused by an increment in the activation energy.

Figure 8 is an example of HREM of a grain boundary and EDS spectra taken from grain interior and grain boundary in 0.05mol% Lu_2O_3-doped Al_2O_3. No second phase or amorphous phase is seen in the grain boundary, and the segregation of lutetium ions in the grain boundary is

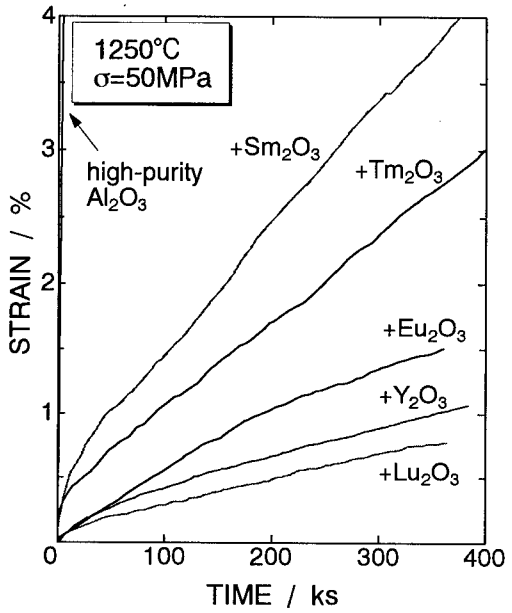

Figure 5. The creep curves in undoped Al_2O_3 and Ln_2O_3 (Ln: Y, Sm, Eu, Tm, Lu)-doped Al_2O_3 under an applied stress of 50MPa at 1250°C.

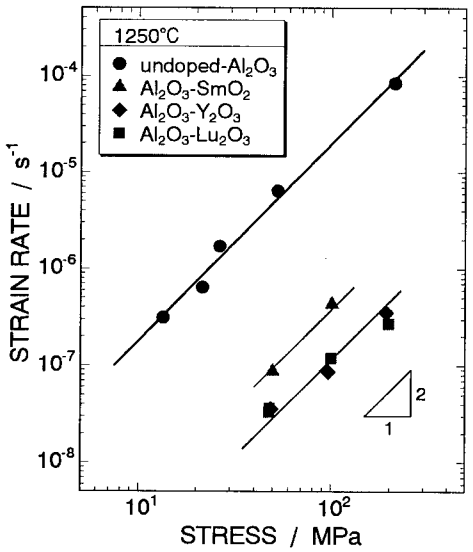

Figure 6. A log-log plot of the steady state creep rate against the applied stress in undoped Al_2O_3 and Sm_2O_3 or Y_2O_3 or Lu_2O_3-doped Al_2O_3 at 1250°C.

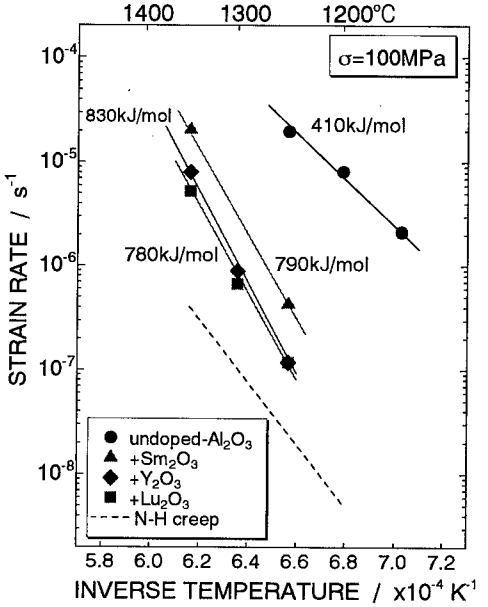

Figure 7. An Arrhenius plot of creep strain against inverse temperature in undoped Al_2O_3, Sm_2O_3-doped, Y_2O_3-doped and Lu_2O_3-doped Al_2O_3. The slope of these lines represent the activation energies.

clearly detected in the EDS spectrum as well as Zr ions. The microstructure in Al_2O_3 with other dopant cation is essentially the same with that in the Lu_2O_3-doped Al_2O_3.

Since the activation energy for high-purity Al_2O_3 is in good agreement with that for Al^{3+} grain boundary diffusion, it seems reasonable that creep rate in undoped-Al_2O_3 is controlled by grain boundary sliding accommodated by grain boundary diffusion. The activation energy of about 800 kJ/mol in Ln-doped Al_2O_3 is much larger than that in undoped-Al_2O_3. Since the dopant cations tend to segregate in Al_2O_3 grain boundaries as well as zirconium ions, and since the creep rate in Ln-doped Al_2O_3 is still larger than that of lattice diffusion creep

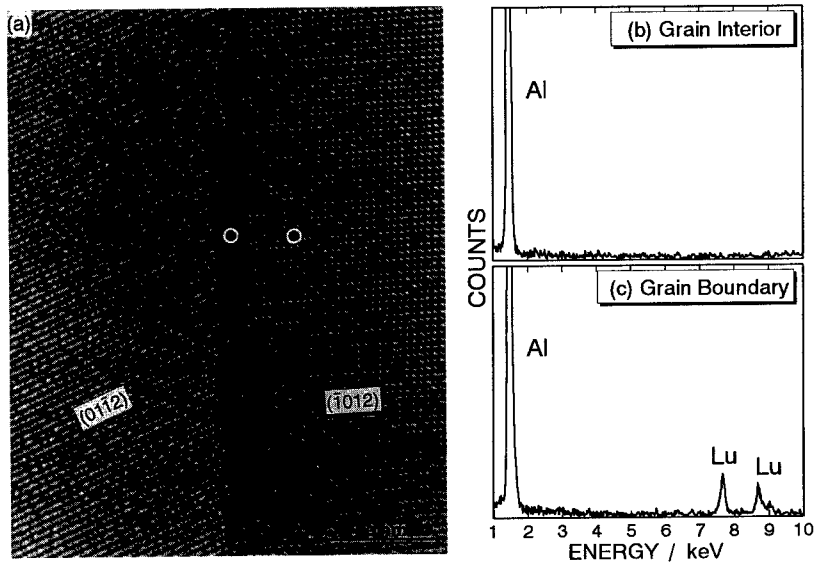

Figure 8. A high-resolution electron micrograph of a grain boundary in as-sintered 0.05mol% Lu_2O_3- doped Al_2O_3 (a), together with EDS spectra taken with a probe size of about 1 nm from (b) grain interior and (c) grain boundary.

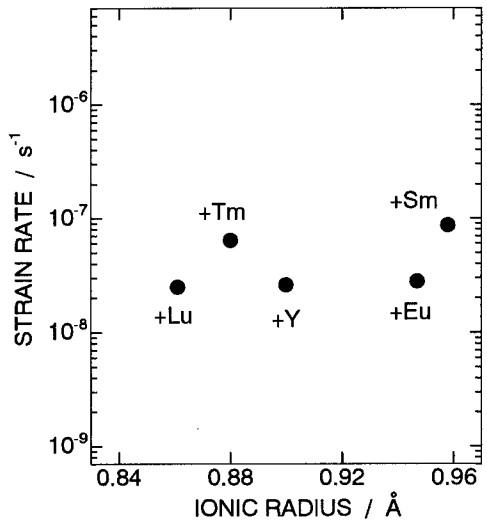

Figure 9. A Plot of creep strain rate at 1250°C under the applied stress of 50 MPa in the present materials against the dopant cation radius[22].

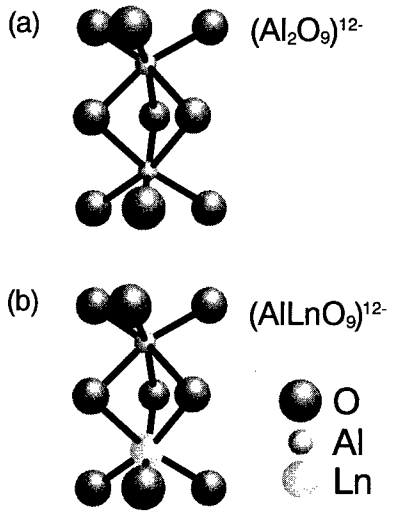

Figure 10. Atomic structure of cluster models (a) $(Al_2O_9)^{12-}$ and (b) $(AlLnO_9)^{12-}$.

expected for high-purity Al_2O_3 as shown in Fig.7, the high activation energy in Ln-doped Al_2O_3 is likely to result from the suppression of grain boundary diffusion by the segregation of Ln ion in grain boundaries. It is expected that the grain boundary diffusion of aluminum ions will be restricted by the segregation, and the creep resistance will be improved when the creep deformation is controlled by grain boundary diffusion.

The present result demonstrates that the creep resistance is dependent on the type of dopant cation. Fig.9 shows the creep strain rate in lanthanoid ion-doped Al_2O_3 under 50MPa at 1250°C against dopant ionic radius which is defined for six-fold coordination[22]. Lutetium ion, which has the smallest ionic radius in the dopant cations, is the most effective to reduce creep strain rate, but the dopant effect cannot be explained in terms of the ionic radius of cation; for example, Sm and Eu ions have similar ionic radii, but the observed creep rate is different between Sm_2O_3- and Eu_2O_3-doped Al_2O_3. To find a factor to describe the dopant effect, the change in electronic structure, the net charge and the bond overlap population of Al^{3+} and O^{2-} ions with dopant cations was evaluated.

2.3 Chemical Bonding State in Al_2O_3

In order to estimate the ionic bonding state in the presence of Ln ions in Al_2O_3, a first-principles molecular orbital calculation was conducted by the discrete-variational (DV)–Xα method developed by Adachi[23]. The model clusters of undoped- Al_2O_3 and Al_2O_3 with Ln cation used are shown in Figure 10[24]. Figure 10(a) shows a model cluster for pure Al_2O_3, $(Al_2O_9)^{12-}$, which represents a part of the corundum structure. Figure 10 (b) shows a model cluster of $(AlLnO_9)^{12-}$, in which a lanthanoid ion is substituted at , one of the aluminum ion's site. The model clusters used for the calculation are very simple ones, but it has been reported that the energy level structure and the charge density profile in Al_2O_3 can reasonably be evaluated using the $(Al_2O_9)^{12-}$ cluster [25,26]. The net charges of each ion and the bond overlap population between atoms can be obtained from the first-principles molecular orbital calculations. They correspond to the ionicity in the atoms and the covalency between the atoms, respectively[23,25–28].

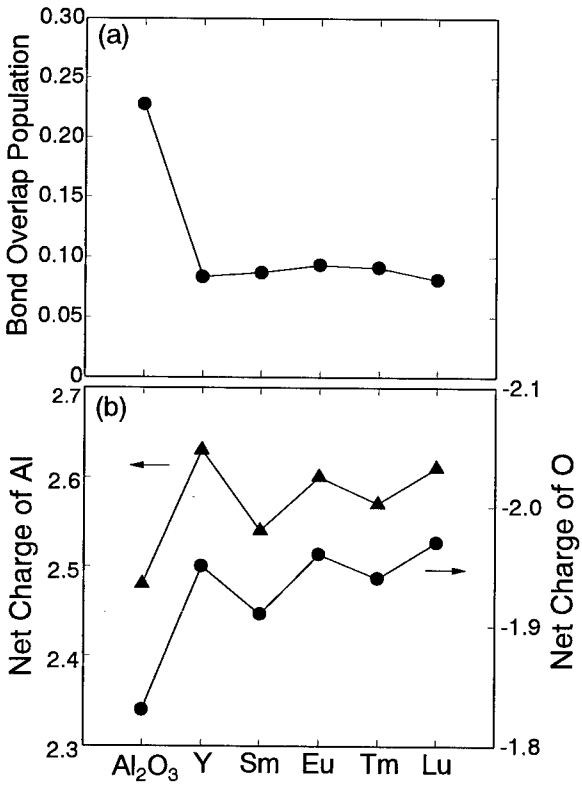

Figure 11. Bond overlap population between Al and O (a) and net charges for Al and O (b) obtained by molecular orbital calculations using the model clusters shown in Figure 9.

Figure 11 shows the bond overlap population between Al and O atoms (a) and the net charge in Al and O atoms (b) obtained from the cluster models of $(Al_2O_9)^{12-}$ and $(AlLnO_9)^{12-}$ in Figure 10. The bond overlap populations in Ln ion-doped clusters are smaller than that in undoped-Al_2O_3, but is not a factor to explain the difference in the type of dopant cation on the creep resistance in Al_2O_3. In contrast, the absolute values of Al and O net charges are larger in Y or Eu or Lu-doped cluster than that in undoped-one or the clusters with other-dopants. This result indicates that the net charge is a critical factor

for the creep resistance in Ln-doped Al_2O_3.

Figure 12 shows the creep strain rate in undoped-Al_2O_3 and Ln-doped Al_2O_3 in Fig.5 against (a) the bond overlap population and (b) the products of Al and O net charges. As shown in Fig.12, the effect of dopant cations on the creep strain rate cannot be explained from the order of bond overlap population in Ln -doped Al_2O_3, but the product of net charges is correlated well with the creep strain rate in Ln-doped Al_2O_3. The increment in the absolute value of the product corresponds to the increase of ionicity between Al and O ions. Since the bond strength in Al_2O_3 is mainly caused by ionic bonding, i.e. a Coulomb's electrical attraction force between cations and anions[29], the present result suggests that the creep resistance in Al_2O_3 is influenced by the change in the ionic bonding state between Al and O atoms in grain boundaries with the segregation of lanthanoid cations. In the present study, the change in the atomic bonding state is estimated for corundum structure, and not for grain boundaries. The configuration of dopant ions at grain boundaries in Al_2O_3 must be different from that of Fig.10, but it is very hard to define a suitable cluster for grain boundaries in Al_2O_3 and to determine the location of dopant ions in the cluster. If we find more adequate clusters for grain boundaries, more quantitative agreements will be available for grain boundary diffusivity or for high-temperature creep resistance in polycrystalline Al_2O_3.

3 Conclusion

The creep resistance of polycrystalline Al_2O_3 with a grain size of about 1 μm is highly improved by the doping of zirconium or lanthanoid ion even in the level of about 0.05mol% at temperatures between 1250 and 1350°C and an applied stress in a range of 10 $\sim$ 200MPa. The change in the creep resistance is caused by the segregation of dopant cations in alumina grain

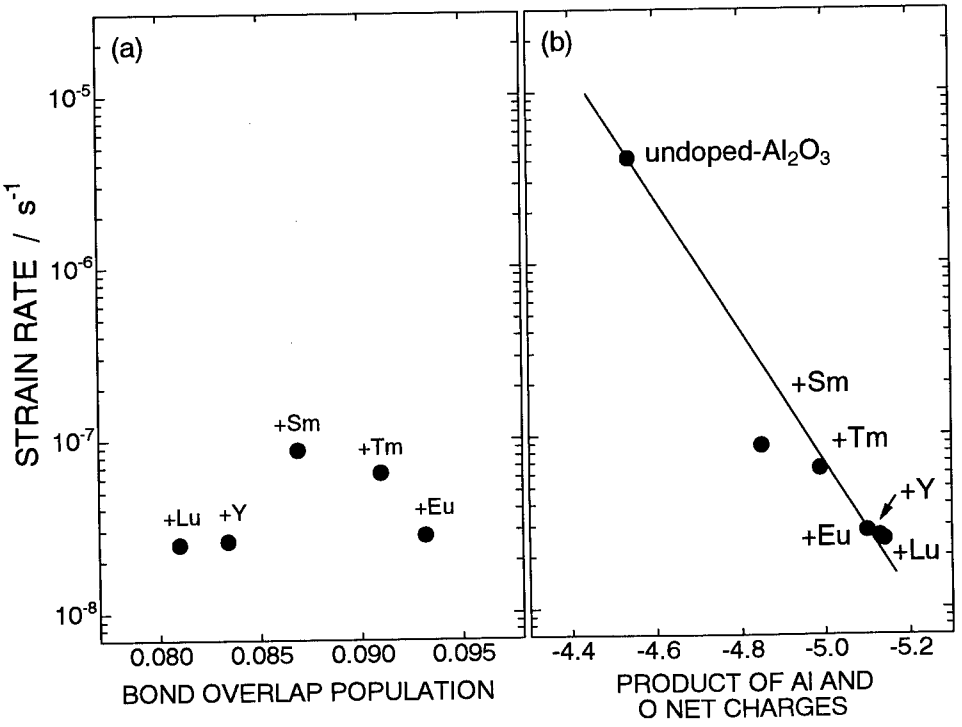

Figure 12. A Plot of creep strain rate at 1250°C under the applied stress of 50 MPa in the present materials against (a) the bond overlap population between Al and O and (b) the product of Al and O net charges.

boundaries. Among the dopant cations examined, Y and Lu ions are particularly effective to improve the creep resistance. It is suggested that high-temperature creep deformation is likely to take place mainly by grain boundary sliding accommodated by grain boundary diffusion. The grain boundary diffusivity must be retarded by the segregation of zirconium or lanthanoid ions. The results of a first-principles molecular orbital calculation based on a model cluster of $(Al_2O_9)^{12-}$ suggest that the creep strain rate is well correlated with the product of the net charge on cations and anions.

Acknowledgment

The authors wish to express their gratitude to the Ministry of Education, Science and Culture, Japan, for the financial support by a Grant-in-Aid for Developmental Scientific Research (2)–10450254 for Fundamental Scientific Research. A part of this study was supported by Kurata Science and Technology Foundation.

References

[1] J. Wang and R. Stevens, *J. Mater. Sci.*, **24** (1989) 3421–3440.
[2] J. Wang and R. Raj, *Acta metall. mater.*, **39** (1991) 2909–19.
[3] K. Okada, Y. Yoshizawa and T. Sakuma, Ed. by S. Hori, M. Tokizane and N. Furushiro, The Japan Society for Research on Superplasticity, pp.227-32 (1991).
[4] K. Okada, Y. Yoshizawa and T. Sakuma, in the Proc. of the 1st International Symposium on the Science of Engineering Ceramics, Ed. by S. Kimura, and K. Niihara, The Ceramic Society for Japan, Tokyo, pp.251-56 (1991).
[5] F. Wakai, T. Iga and T. Nagano, *J. Ceram. Soc. Jpn.*, **96** (1988) 1206–09.
[6] N. Claussen, *Science and Technology of Zirconia II,* Advances in Ceramics volume12, (edited by N. Claussen, M. Rühle and A.H. Heuer), p. 325. The American Ceramic Society, Inc., Columbus, Ohio (1983).
[7] H. Yoshida, K. Okada, Y. Ikuhara and T. Sakuma, *Phil. Mag. Lett.*, **76** (1997) 9–14.
[8] J. Cho, M.P. Harmer, H.M. Chan, J.M. Rickman and A.M. Thompson, *J. Am. Ceram. Soc.*, **80** (1997) 1013–17.
[9] H. Yoshida, Y. Ikuhara and T. Sakuma, *J. Mater. Res.*, **13** (1998) 2597–2601.
[10] R.M. Cannon, W.H. Rhodes and A.H. Heuer, *J. Am. Ceram. Soc.*, **63** (1980) 46–53.
[11] J. Wang and R Raj, *J. Am. Ceram. Soc.*, **73** (1990) 1172–75.
[12] J. Wang and R Raj, *J. Am. Ceram. Soc.*, **74** (1991) 1959–63.
[13] K. Okada and T Sakuma, *Brit. Ceram. Trans.*, **93** (1994) 71–74.
[14] B. Burton, *Mater. Sci. Eng.*, **10** (1972) 9–14.
[15] A.K. Mukherjee, *Mater. Sci. Eng.*, **8** (1971) 83–89.
[16] R.C. Gifkins, *Metall. Trans. A*, **7A** (1976) 1225–32.
[17] A. Arieli and A.K. Mukherjee, *Mater. Sci. Eng.*, **45** (1980) 61–70.
[18] C. Herring, *J. Appl. Phys.* , **21** (1950) 437-445.
[19] Y. Oishi and W.D. Kingery, *J. Chem. Phys.*, **33** (1960) 480–86.
[20] M.L. Gall, B. Lesage and J. Bernardini, *Phil. Mag. A*, **70** (1994) 761–73.
[21] D. Prot and C. Monty, *Phil. Mag. A*, **73** (1996) 899–917.
[22] R.D. Shannon, *Acta. Cryst.*, **A32** (1976) 751–767.
[23] H. Adachi, M. Tsukada and C. Satoko, I. Application to Metal Clusters, " *J. Phys. Soc. Jpn.*, **45** (1978) 875–883.
[24] H. Yoshida, Y. Ikuhara and T. Sakuma, *Phil. Mag. Lett.*, **79** (1999) 249–256.
[25] I. Tanaka, J. Kawai and H. Adachi, *Solid State Commun.*, **93** 533–36 (1995).
[26] H. Adachi, *Ceramics*, **27** (1992) 495–501.
[27] Y. Ikuhara, Y. Sugawara, I. Tanaka and P. Pirouz, *Interface Science*, **5** (1997) 5.
[28] Y. Ikuhara, T. Watanabe, T. Saito, H. Yoshida and T. Sakuma, *Mater. Sci. Forum*, 294-296 (1999) 273-276.
[29] W.D. Kingery, H.K. Bowen and D.R. Uhlman, pp. 44–46 in *Introduction to Ceramics.* New York: John Wiley and Sons (1976).

Key Engineering Materials Vols. 171-174 (2000) pp. 817-824
© 2000 Trans Tech Publications, Switzerland

Compressive Creep and Stress Relaxation Kinetics in a High Purity Silicon Nitride Ceramics in the 1400-1650 °C Range

S. Testu[1], J.L. Besson[1], T. Rouxel[2] and G.B. Granger[3]

[1] ENSCI, Science des Procédés Céramiques et Traitements de Surface, UMR-CNRS 6638, 47 Av. A. Thomas, FR-87065 Limoges cedex, France
E-Mail: s.testu@ensci.fr, Fax: 05 55 79 09 98

[2] Laboratoire "Verres et Céramiques", UMR-CNRS 6512, Université de Rennes I, Campus Beaulieu, FR-35042 Rennes Cedex, France

[3] Céramiques Techniques Desmarquest, Saint-Gobain, ZI n°1, rue de l'Industrie, FR-27025 Evreux Cedex, France

Keywords: GPS Silicon Nitride, Stress Relaxation, Creep, Microstructure

Abstract

The paper presents the study of the mechanical behaviour at high temperature under compressive stresses of a Gas Pressure Sintered silicon nitride. It is the last generation of Si_3N_4 materials with elongated grains and a very few amount of glassy phase that explains a strong creep resistance up to 1400°C. Stress relaxation and creep tests were achieved in the 1400–1650°C temperature range. The Kolhraush-Williams-Watt empirical expression is used to fit the stress relaxation curves. The primary creep could be modelled as a delayed deformation ending by a plateau dependent on temperature. Both creep and stress relaxation curves parameters suggest the existence of strong microstructural changes during testing above 1450°C.

Material

The material, supplied by Norton-Desmarquest [1] is a fully dense silicon nitride sintered at 1800°C under a nitrogen pressure of 5 MPa. The GPS method uses two commercials α-Si_3N_4 (SN-E-10, UBE) and α-YSiAlON (SY5, UBE, $Y_{0.5}Si_{9.75}Al_{2.25}O_{0.75}N_{15.25}$) powders without additive. The microstructure of the as-sintered material is essentially made of β-SiAlON elongated grains and α-YSiAlON grains in an approximate β/α ratio of 80/20. The grain size distribution is difficult to assess but the SEM observations of the plasma etched[1] material have revealed some main characteristics (Fig.1): β elongated grains (7 to 9 μm in length) are frequently observed together with some extra large grains (30 μm) resulting from abnormal grain growth during the GPS process [2,3]. The high density (3.22 g/cm^3) of this randomly oriented elongated grain structure is due to the filling of the interstitial space with smaller β and α grains (between 0.4 and 4 μm). The α grain morphology is the same than that of the glassy pockets generally observed in silicon nitride materials sintered with Y_2O_3 or Al_2O_3 aids

[1] Acknowledgements: The author would like to thank Mr Pesant and Mrs Legrand for the plasma etching at the Institut d'Electronique et de Microélectronique du Nord, A^{ve} Poincaré, BP 69, 59652 Villeneuve d'Ascq cedex, France.

[4]. No amorphous film could be observed between silicon nitride grains in TEM, and the sintered material seems to have a very insignificant amount of small glassy pockets. Such a microstructure explains the high creep resistance observed up to 1400°C for stresses in the order of 100MPa.

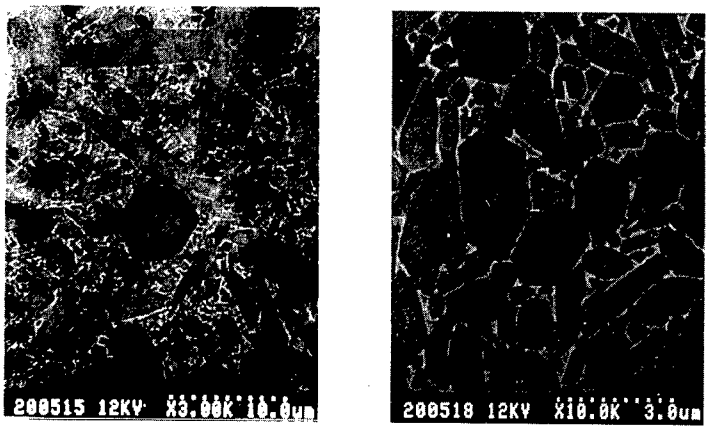

Fig. 1: SEM micrographs of the GPS silicon nitride after SF_6 plasma etching.

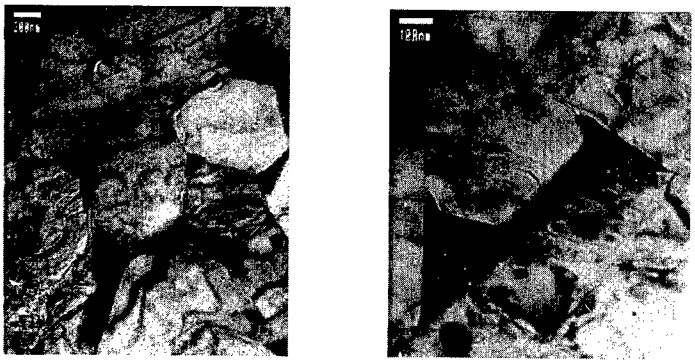

Fig. 2: TEM micrographs of the as-sintered material: general view (left) and enlarged view of the YSiAlON crystallised phase (right).

High temperature mechanical tests

The creep and stress relaxation tests were conducted on a high temperature (1800°C) mechanical (Instron 8562) testing machine detailed in a previous paper [5]. To limit Si_3N_4 oxidation and decomposition, the tests were carried out under a nitrogen atmosphere. The compressive samples (7x3x3) mm^3 were placed between two SiC pistons. The heating and cooling rates were 10°C/min. A differential measurement device, by means of a LVDT and mechanical contacts with the specimen was used to accurately measure the specimen height. During creep test, the load was electronically maintained constant by enslavement of the actuator on the load, whereas the sample deformation was maintained constant for relaxation test. The PC acquisition of data gives about 2000 points for each curve.

Stress Relaxation Results

The influence of temperature on the relaxation kinetics was studied between 1400 and 1650°C, for an initial applied stress of 100 MPa.

During the stress relaxation process, the macroscopic load decrease is associated to the conversion of elastic deformation into plastic deformation. The stress relaxation kinetics $\sigma(t)$, normalised by the initial stress σ_o, is here analysed by the Kolhraush-Williams-Watt equation:

$$\sigma / \sigma_o = \exp [- (t / \tau_1)^{b1}] \qquad \text{Eq. 1,}$$

where τ_1 is an apparent relaxation time and b_1 a parameter between 0 and 1 associated to the relaxation time distribution spectrum. The experimental and calculated (Eq.1) stress relaxation curves are represented on Fig. 3.

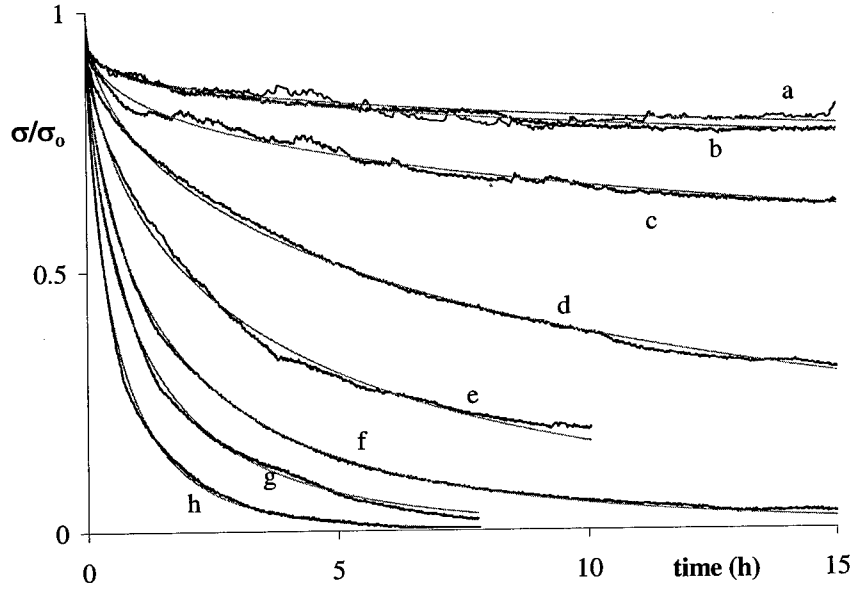

Fig. 3: Stress relaxation curves from an initial stress of 100MPa, at different temperatures: 1400°C (a), 1450°C (b), 1500°C (c), 1550°C (d), 1575°C (e), 1600°C (f), 1625°C (g), and 1650°C (h).

T (°C)	1400	1450	1500	1550	1575	1600	1625	1650
b_1	0.23	0.26	0.35	0.53	0.54	0.59	0.62	0.67
τ_1 (h)	5602	2016	127	10.6	3.85	1.63	1.07	0.59

Table 1: KWW equation parameters of the stress relaxation curves (Fig. 3).

The KWW equation parameter's, calculated to fit the experimental curves at the different temperatures, are given in Table1. First, it could be noted that the relaxation kinetics of the GPS material is very slow. For a silicon nitride with continuous intergranular glassy films, Rouxel and Wakai [6] gave relaxation times between 15 and 0.4 minutes in the same

temperature range. The decrease of the relaxation time, when the temperature increases, can be regarded as due to a thermally activated process with an average apparent activation energy of 1070 kJ/mol. This high value is similar to the value obtained by Donzel and al. [7] for a YSiAlON glass studied by mechanical spectroscopy, but really far from the 470 kJ/mol value obtain in reference [6]. In fact, the change of log τ_1 with the reciprocal absolute temperature exhibits a S-shape (Fig. 4). This could result from modifications of the microstructure coming from melting of yttrium containing crystalline phases.

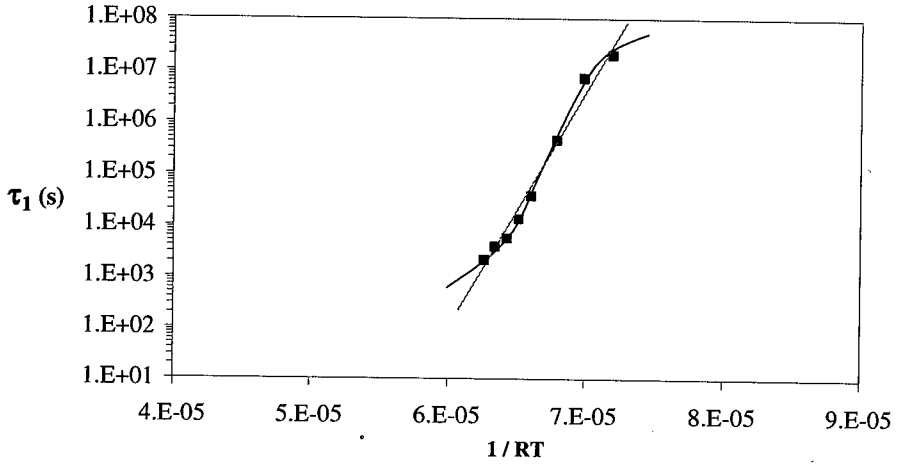

Fig. 4: Activation energy of the relaxation time τ_1 between 1400 and 1650°C.

Besides, there is an evolution of the parameter b_1 whereas it is generally constant and equal to 0.5 in glasses [8]. According to Perez et al. [9] and Ngai et al. [10], b_1 is a correlation factor and can be tentatively related to the mobility of the structural unit at the atomic or molecular scale: b_1 is null when the correlation is high (elastic solids) and tend to unity when the correlation is low (b_1=1 in liquids). The evolution observed in our study (Table 1) reflects a smooth transition between a quite rigid state toward a more fluid state.

Creep Results

The stress dependence of creep was studied at 1550°C for 50, 100 and 200 MPa initial stresses (Fig. 5), and the temperature dependence for an initial stress of 100 MPa at different temperatures between 1450 and 1600°C (Fig. 6). The deformation measured under a stress of 100MPa at 1400°C was under the experimental sensitivity.

The creep curves $\varepsilon(t)$ can be analysed as the sum of two components: $\varepsilon = \varepsilon_d + \dot{\varepsilon}_s t$.

ε_d, corresponding to the delayed elastic deformation, is given by (Eq.2) where ε^∞ is an asymptotic deformation, τ_2 is a retardation time and b_2 is the exponent of the extended exponential associated to the retardation time distribution spectrum.

$$\varepsilon_d = \varepsilon^\infty [1 - \exp(-(t/\tau_2)^{b2})] \qquad \text{Eq. 2.}$$

$\dot{\varepsilon}_s t$ corresponds to the viscous permanent deformation (Eq.3).

$$\dot{\varepsilon}_s = A\, \sigma^n \exp(-Q_2/RT) \qquad \text{Eq. 3.}$$

The strain rate $\dot{\varepsilon}_s$, reported in Table 2 and Table 3, increases with stress and temperature according to the Eq. 3. The stress exponent value is n=1.8 and the apparent activation energy, Q_2=1069 kJ/mol, is very high.
It is interesting to note that Bernard Granger [1] obtain n=1 and a smaller creep activation energy of 770 kJ/mol in the 1280-1400°C range for the same material. So, the deformation mechanisms are certainly different under and above 1450°C.

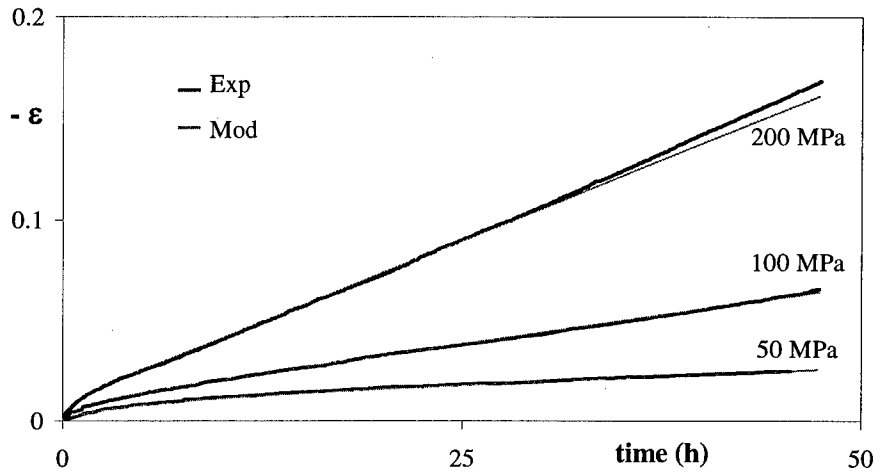

Fig. 5: Silicon nitride compressive creep curves under nitrogen at 1550°C.

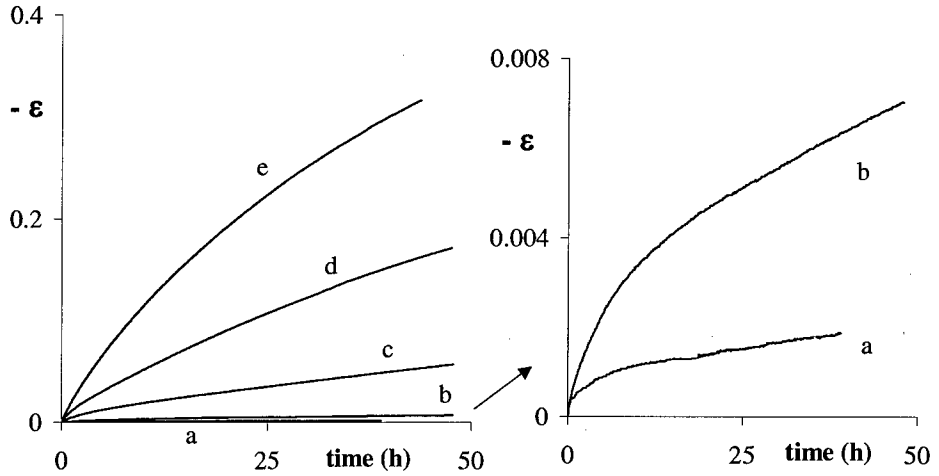

Fig. 6: Silicon nitride compressive creep curves under nitrogen at an initial stress of 100MPa and for different temperature: 1450°C (a), 1500°C (b), 1550°C (c), 1575°C (d) and 1600°C (e).

According to the results in Table 2 and Table 3, the main transient creep parameter ε^{∞} is independent of stress but increases rapidly with temperature. At constant temperature, the retardation time, τ_2, decreases when the stress increases.

σ (MPa)	$\dot{\varepsilon}_s$ (s^{-1})	ε^∞	τ_2 (h)	b_2
50	$9.31\ 10^{-8}$	0.0099	4.9 ±0.1	0.75 ±0.05
100	$3.22\ 10^{-7}$	0.0097	1.9 ±0.1	0.65 ±0.05
200	$8.93\ 10^{-7}$	0.0096	0.6 ±0.1	0.85 ±0.05

Table 2: Creep curves parameters at 1550°C (Fig. 5).

T (°C)	1450	1500	1550	1575	1600
$\dot{\varepsilon}_s$ (s^{-1})	$6.86\ 10^{-9}$	$2.39\ 10^{-8}$	$2.68\ 10^{-7}$	$9.83\ 10^{-7}$	$2.06\ 10^{-6}$
ε^∞	0.0009	0.003	0.011	0.020	0.045

Table 3: Creep curves parameters under 100MPa for the different temperatures (Fig. 6).

In silicon nitride, the primary creep could be explain by a redistribution of the glassy phase until the grains come in contact [11,12]. Then, the creep becomes stationary. Upon loading, the secondary glass phase flows from compressive zones to tensile ones [13,14]. Let us consider a material composed of rigid grains embedded in a secondary viscous phase the quantity of which depends on temperature. In this model, the ε^∞ value is reached when all the secondary phase has flowed out. Above 1550°C, there is a certain quantity of liquid secondary phase. The increase in ε^∞reflects the increase of the liquid phase with temperature (Table 3). As the applied stress increases, the grain rearrangement becomes faster, ε^∞ is reached more rapidly and the retardation time, τ_2, decreases (Table 2). The present results don't permit to clearly understand the evolution of τ_2 with temperature because there is several mechanisms in competition: the average distance between the grains increases with temperature as ε^∞ does, the secondary phase viscosity changes with temperature and composition. For instance, if the glass nitrogen content increases, the glass viscosity rapidly increases [15] whereas it decreases when the temperature rises. Only in situ composition analyses could reveal the truth on this ambiguity.

Conclusion

This GPS silicon nitride is strongly resistant up to 1400°C, because its microstructure consists in randomly oriented β-Si_3N_4 grains without glassy film at room temperature. Both relaxation and creep analyses in the 1400-1650°C range show a transition in the mechanical behaviour around 1450°C. Above this temperature, b_1 tends to the value for the liquid state, and the asymptotic value of the delayed deformation rises with temperature. According to UBE information about the starting powders, it could be argue that there is formation of liquid phase due to melting of YSiAlON crystallise phase during testing at these temperatures. This hypothesis is supported by our microstructural TEM observations after testing. Much more glassy pockets than in the as sintered material was observed in a material deformed at 1650°C. Besides, SEM observations (retro-diffused mode) of several tested samples have shown that an important redistribution of yttrium occurs above 1450°C (Fig. 7). These phenomena necessary need the presence of a liquid phase during testing.

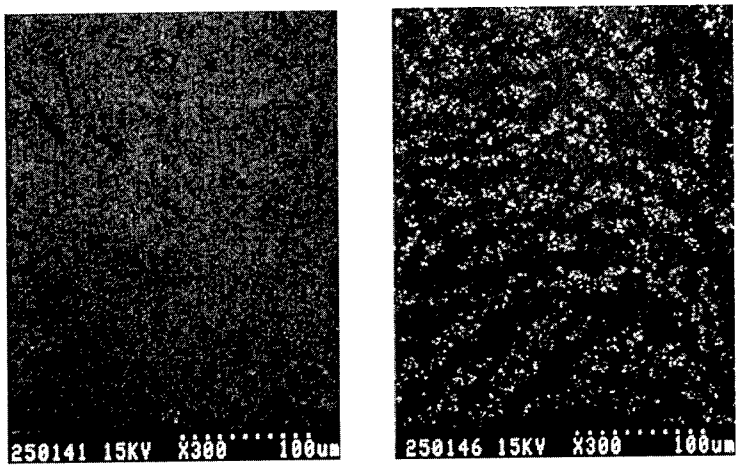

Fig. 7: White yttrium repartition observed in the silicon nitride after 1400°C (left) and 1600°C (right) stress relaxation test.

So, microscopic observations, compressive creep and relaxation tests lead to the conclusion of a microstructural transformation by liquid phase formation, that modifies the mechanism of the deformation above 1450°C.

References

1 G. Bernard Granger, J. Crampon, R. Duclos, B. Cales, J. Eur. Ceram. Soc. 17 (1997), p.1647.
2 W. Dressler, H.J. Kleebe, M.J. Hoffmann, M. Ruhle, G. Petzow, J. Eur. Ceram. Soc. 16 (1996), p.3.
3 D.S. Park, S.Y. Lee, H.D. Kim, B.J. Yoo, B.A. Kim, J. Am. Ceram. Soc. 81 (1998), p.1876.
4 C.C. Ahn, G. Thomas, J. Am. Ceram. Soc. 66 (1983), p.14.
5 D. Murat, Thèse à l'Université de Limoges / France (1995).
6 T. Rouxel, F. Wakai, Acta Metall. Mater. 41 (1993), p.3203.
7 L. Donzel, R. Schaller, Journal de Physique IV C8-663 (1996).
8 J. De Bast, P. Gilard, Comptes rendus de recherches de l'IRSIA n°32 (1965).
9 J. Perez, J.Y. Cavaille, S. Etienne, C. Jourdan, Revue Phys. Appl. 23 (1988), p.125.
10 K.L. Ngai, A.K. Rajagopal, S. Teiler, J. Chem. Phys. 88 (1988), p.5086.
11 FF Lange, BI Davis, DR Clarke, J. Mat. Sci. 15 (1980), p.601.
12 J.R. Dryden, D. Kocerovsky, D.S. Wilkinson, D.F. Watt, Acta Metall. 37 (1989), p.2007.
13 C.M. Wang, M. Mitomo, T. Nishimura, Y. Bando, J. Am. Ceram. Soc. 80 (1997), p.1213.
14 Q Jin, XG Ning, D Wilkinson, G Weaherly, J. Am. Ceram. Soc. 80 (1997), p.685.
15 T. Rouxel, M. Huger, J.L. Besson, J. Mat. Sci. 27 (1992), p.279.

Key Engineering Materials Vols. 171-174 (2000) pp. 825-832
© 2000 Trans Tech Publications, Switzerland

Dislocation Structure and Activated Slip Systems in ß-Silicon Nitride during High Temperature Deformation

K. Kawahara[1], S. Tsurekawa[1] and H. Nakashima[2]

[1] Department of Machine Intelligence and Systems Engineering, Graduate School of Engineering, Tohoku University, Sendai, Miyagi 980-8579, Japan

[2] Department of Molecular and Material Sciences, Graduate School of Engineering Sciences, Kyuschu University, Kasuga, Fukuoka 816-8580, Japan

Keywords: Silicon Nitride, High Temperature Deformation, Weak-Beam Method, Slip System

ABSTRACT

ß-Silicon nitride (Si_3N_4) with sintering additives of 5mass% Y_2O_3 and 4mass% Al_2O_3 was deformed by compression at temperatures from 1820 to 2020K and at strain rates from 9×10^{-6} to 2×10^{-4} s^{-1}. Dislocation structures were examined by transmission electron microscopy (TEM) to identify the slip systems activated during high temperature deformation.

It was found that the high temperature deformation behavior of ß-Si_3N_4 depended strongly on the deformation condition. A good ductility as well as 10% in plastic strain occurred without crack formation under the limited condition of higher temperatures and lower strain rates. Both from the Burgers vector analysis using the weak-beam method and from the trace analysis on TEM, most of dislocations operating during deformation were found to be ***c*** dislocations belonging to the $\{10\bar{1}0\}[0001]$ primary slip system. In addition to ***c*** dislocations, ***a*** dislocations on a $\{10\bar{1}0\}<1\bar{2}10>$ prism slip were often observed. However, ***a+c*** dislocations on the $\{11\bar{2}1\}<\bar{2}113>$ pyramidal slip were only activated under the limited conditions where a good ductility had been appeared by compression. It has been considered, therefore, that the occurrence of ductility would be closely related to the activation of the pyramidal slip system.

1. INTRODUCTION

Since silicon nitride has an excellent high temperature strength, a low density and a low coefficiency of thermal expansion, it has been expected as a structural material used at high temperatures. However, Si_3N_4 has been restricted to a practical use for a structural material because of the lack of reliability coming from the brittleness. ß-Si_3N_4 has a hexagonal structure, so that secondary slip systems such as the pyramidal slip should be activated on the primary one for polycrystalline ß-Si_3N_4 to plastically deform without crack formation. Therefore, it is of great importance to clarify whether the secondary slip systems can be activated during high temperature deformation. To the present authors' knowledge, however, there are only a few investigations on slip systems of Si_3N_4. Butler[1] observed the dislocation structures in ß-Si_3N_4 and found that the $\{10\bar{1}0\}[0001]$ was the primary slip system in ß-Si_3N_4. Evans and Sharp[2], and Lee and Hilmas[3] analyzed the Burgers vector by TEM on the basis of the $\boldsymbol{g}\cdot\boldsymbol{b}=0$ invisibility criteria, where ***g*** and ***b*** were general meanings, and reported that ***a*** and ***a+c*** dislocations operated on ***c*** dislocations. However, slip planes of these ***a*** and ***a+c*** dislocations have never experimentally identified so far. Recently, Milhet *et al.*[4] found that the $\{11\bar{2}0\}[0001]$ slip was activated at 1073K on the $\{10\bar{1}0\}[0001]$ primary slip. They supposed that the ***c*** dislocations on $\{11\bar{2}0\}$ were probably as a result of the cross-slip of ***c*** dislocations with the screw component on the $\{10\bar{1}0\}$ primary slip planes onto the $\{11\bar{2}0\}$ planes. However, the relation between the deformation behavior and the activated slip systems has not been completely understood yet.

In the present investigation, high temperature deformation behavior of ß-Si_3N_4 was examined by compression, then dislocation structures were analyzed by TEM using the weak-beam method to identify the activated slip systems during high temperature deformation. From these results, the

deformation behavior has been discussed from the viewpoint of the activated slip systems.

2. EXPERIMENTAL PROCEDURE

2. 1. Specimen preparation

The material used in this study was a hot-pressed ß-Si_3N_4 with sintering aids of 5mass% Y_2O_3 and 4mass% Al_2O_3. The mean grain size was about 0.6μm and the density was 3.26Mg/m^3, which was 99.7% in theoretical density. Specimens for compression tests were cut from the sintered material using a low speed diamond saw and mechanically polished to a final size of about 2mm×2mm×3mm. Then, the side planes of specimens were buff-finished to mirror planes with a diamond paste of 1μm in particle size.

2. 2. Compression test

High temperature compression tests were carried out under a nitrogen atmosphere at temperatures from 1820 to 2020K and at strain rates from 9×10^{-6} to $2\times10^{-4}s^{-1}$. The details of the experimental procedure were the same as those described in the previous paper[5]. In this study, compression rods made of sintered SiC were used. The compression faces of the rods were painted with high purity hexagonal BN for lubrication and seizure proof.

The specimens deformed to 3~10% in strain were rapidly cooled under loading by switching-off the radio frequency heating current to freeze-in the dislocation structures developed during high temperature deformation.

2. 3. TEM observation

Thin foils suitable for TEM observation were prepared by the following way. Sheets of about 0.5mm in thickness were cut from the deformed samples parallel to the compression axis using a low speed diamond saw and mechanically polished to less than 50μm in thickness. Then, they were buff-finished to mirror plane using a diamond paste of 1μm in particle size and A^+ ion milled into foils under the condition of 4.0kV, 0.4mA and 15° in beam angle. In addition, the foils were coated with carbon to prevent from charging-up during TEM observation. A JEOL JEM-2000EX/T electron microscope, which was modified to achieve ±25° double tilt, was worked with an acceleration voltage of 200kV.

2. 4. Identification of slip system

A slip system is defined as the combination of a slip plane and a slip direction. The slip direction is relevant to the Burgers vector, and the slip plane is defined as the plane containing both the Burgers vector and the dislocation line direction. Therefore, if the Burgers vector and the dislocation line direction are determined, the slip system can be identified except the case for a pure screw dislocation.

In this study, the weak-beam method was applied to determine the Burgers vector of a dislocation[6]. Under the weak-beam condition, fine-spaced thickness fringes appear in a dark-field image of wedge-shaped specimen. If the foil contains a dislocation, some of the fringes terminate at the end of the dislocation as shown in Fig. 1. According to Ishida *et al.*[6], the number of the terminating fringes, N, is closely related to the Burgers vector, $\boldsymbol{b}$, of the dislocation. They give a equation with the following form,

$$\boldsymbol{g}\cdot\boldsymbol{b}=\mathrm{sgn}(s)N, \qquad (1)$$

where, $\boldsymbol{g}$ is the reflection vector and sgn(s) the sign of the deviation vector from the ideal Bragg

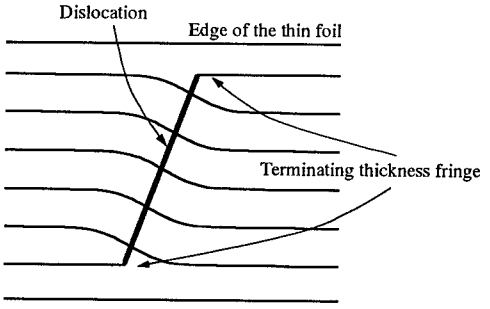

Fig. 1 Schematic illustration of a weak-beam image of a thin foil containing a dislocation. The number of terminating thickness fringes, N, is +1.

condition, s. The sign of s was defined as plus when the deviation vector, s, turned to outside of the Ewald sphere. The number of terminating fringes, N, was taken as positive sign when the fringes terminated at the right-hand side of the end of the positive dislocation line direction, where the positive dislocation line direction was the direction towards the edge of the thin foil. For example, the number of the terminating fringes is +1 for Fig. 1. Therefore, the Burgers vector can be determined from three weak-beam images of the same dislocation with independent reflection vectors.

The trace analysis was applied for the determination of a dislocation line direction. Figure 2 is a schematic explanation of the trace analysis. The true dislocation line $\overline{ab}$ is observed as the projected image $\overline{a'b'}$ on the normal plane to the incident beam direction, $\boldsymbol{B}_A$. As shown in Fig. 2, the plane containing both $\boldsymbol{B}_A$ and $\overline{a'b'}$ also contains the true dislocation line $\overline{ab}$. Micrograph taken in any other beam direction, $\boldsymbol{B}_B$, results in second projected image $\overline{a''b''}$. Then, the other plane is defined by $\overline{a''b''}$ and $\boldsymbol{B}_B$. Consequently, the intersection of these two planes gives the true direction of the dislocation $\overline{ab}$.

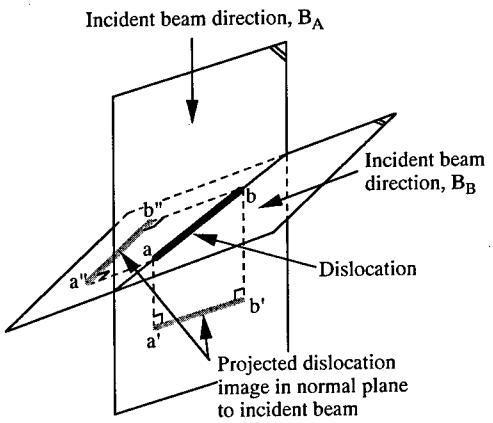

Fig. 2 Schematic explanation for the determination of the true dislocation line direction. The true dislocation line direction is determined as the intersection of the two distinct planes, which contain the incident beam direction and the projected dislocation line direction.

3. RESULTS AND DISCUSSION

3. 1. Compression test

Figure 3 shows stress-strain curves of ß-Si_3N_4 compressed at 1970K and at various strain rates indicated in this figure. High temperature deformation behavior of ß-Si_3N_4 depends strongly on the strain rate. The flow stress decreases with decreasing strain rate. The stress-strain curves show a peak followed by monotonous decrease in flow stress. The decrease in the flow stress after the peak occurs abruptly at higher strain rates than $2\times10^{-5}s^{-1}$ because of either crack initiation or propagation, while the stress reduction occurs gradually at a strain rate of $9\times10^{-6}s^{-1}$. It was found that any cracks were not observed on the surfaces of the samples deformed at $9\times10^{-6}s^{-1}$. Also, the temperature dependence of deformation behavior was similar to the strain rate dependence.

Figure 4 shows the relation between the plastic strain rate, $\dot{\varepsilon}_p$, and the peak stress compensated by the shear modulus, σ_{peak}/G. The shear modulus was estimated by an extrapolating the temperature dependence of the shear modulus measured at temperature range from R.T. to 1673K for hot-pressed ß-Si_3N_4[7]. The slope in the double loga-

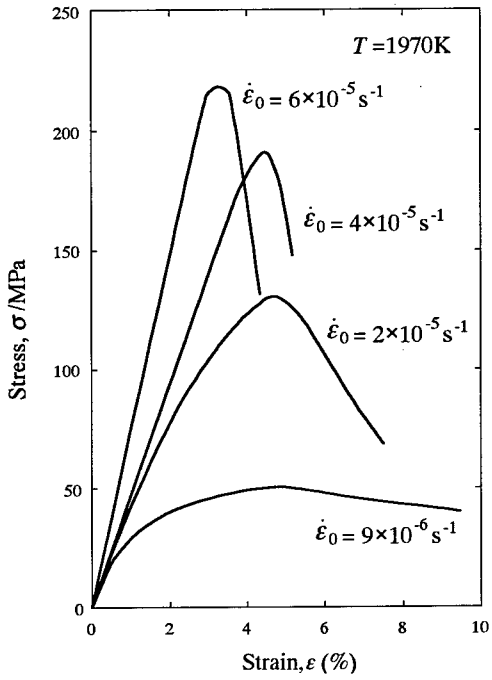

Fig. 3 Stress-strain curves for ß-Si_3N_4 compressed at 1970K and at various strain rates.

rithm plot shown in Fig. 4 gives the stress exponent, n. It is seen that there are two distinct regions with different stress exponents depending on the strain rate except at 1820K. The stress exponent, n, is about 3 in the higher strain rate region (HSR), whereas 1 in the lower strain rate region (LSR). In addition, the transition from HSR to LSR region was in good agreement with the brittle- ductile transition from the viewpoint of crack formation.

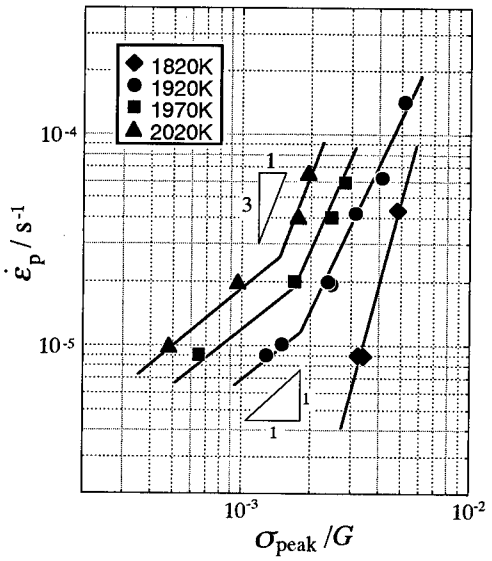

Fig. 4 Relation between the strain rate, $\dot{\varepsilon}_p$, and the peak stress compensated by shear modulus, σ_{peak}/G, at various temperatures.

3. 2. TEM observation

Figure 5[8] shows the dislocation structure of ß-Si_3N_4 deformed at 1920K at a strain rate of $9\times10^{-6}s^{-1}$. Figures 5 (a) and (b) were taken at the same area with different reflection vectors; (a) $\boldsymbol{g}=000\bar{2}$, (b) $\boldsymbol{g}=3\bar{2}\,\bar{1}0$. The dislocation distribution is homogeneous and subboundaries are scarcely observed. Moreover, most of dislocations are bowing out, indicating that these dislocations are mobile. According to the $\boldsymbol{g}\cdot\boldsymbol{b}=0$ invisibility criteria, $\boldsymbol{a}$ dislocations having the Burgers vector of $a/3\langle11\bar{2}0\rangle$ should be invisible if it is imaged with the reflection vector of $\boldsymbol{g}=000\bar{2}$ (Fig. 5 (a)), while $\boldsymbol{c}$ dislocations with the Burgers vector of $c[0001]$ is invisible with $\boldsymbol{g}=3\bar{2}\,\bar{1}0$ (Fig. 5 (b)). Furthermore, $\boldsymbol{a}+\boldsymbol{c}$ dislocations, $a/3\langle11\bar{2}0\rangle+c[0001]$, should be in contrast with both of the reflections. Therefore, we can see that most of dislocations observed in Fig. 5 are $\boldsymbol{c}$ dislocations. In addition, some $\boldsymbol{a}$ dislocations are present but the $\boldsymbol{a}+\boldsymbol{c}$ dislocation cannot be observed in this area. The ratio of the dislocation densities of $\boldsymbol{c}$ and $\boldsymbol{a}$ dislocations was roughly estimated to be 10 : 1. The dislocation structure shown

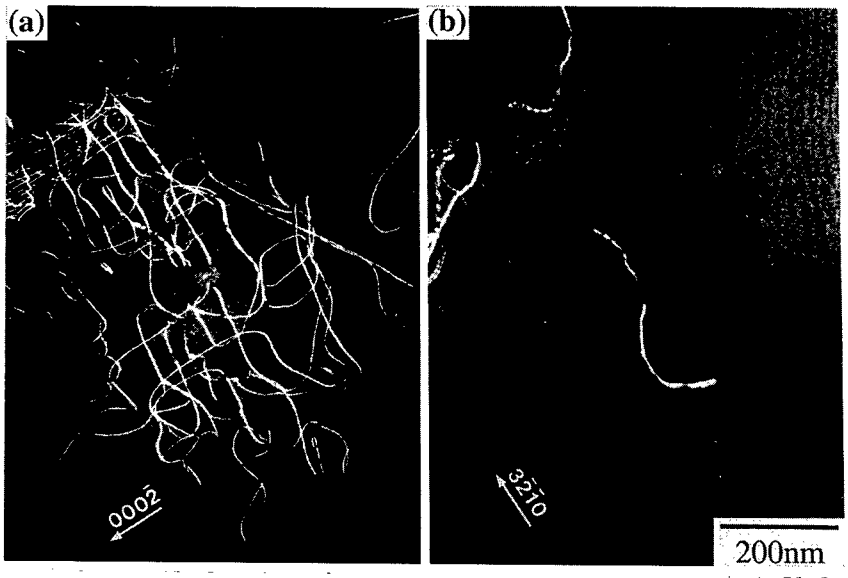

Fig. 5 Dislocation structure observed in the sample 10% deformed at 1920K and at a strain rate of $9\times10^{-6}s^{-1}$. Micrographs (a) and (b) were taken at the same area with different reflection vectors; (a) $\boldsymbol{g}=000\bar{2}$, (b) $\boldsymbol{g}=3\bar{2}\,\bar{1}0$ [8].

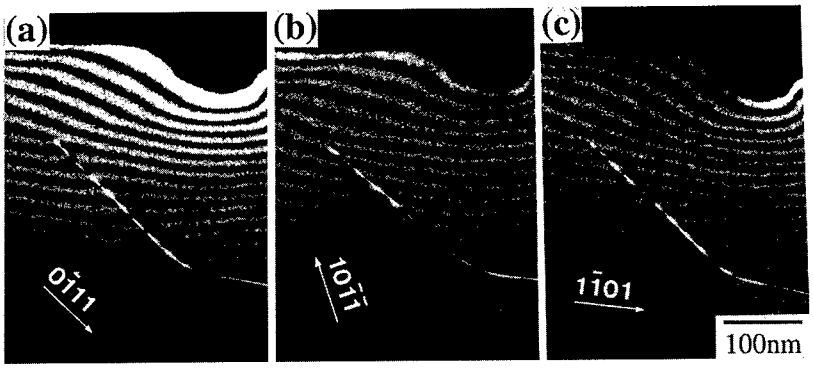

Fig. 6 Weak-beam images of a ***c*** dislocation with three independent reflection vectors[8].

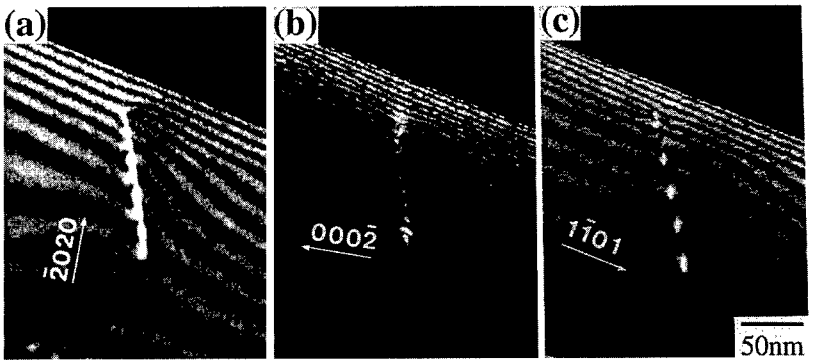

Fig. 7 Weak-beam images of an ***a*** dislocation with three independent reflection vectors[8].

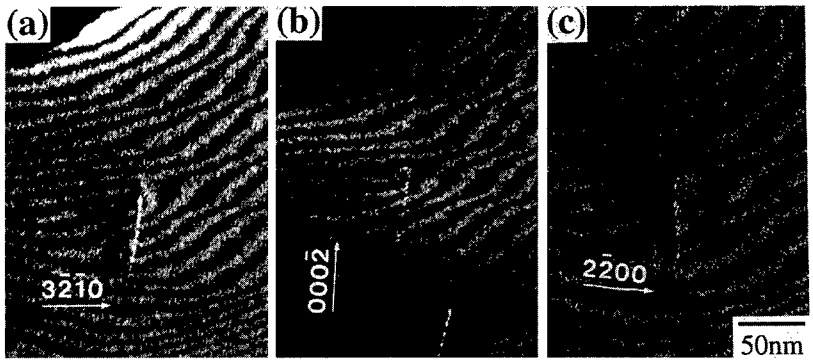

Fig. 8 Weak-beam images of an ***a+c*** dislocation with three independent reflection vectors[8].

in Fig. 5 was the typical one developed during high temperature deformation of ß-Si_3N_4. The dislocation density ratio of ***c*** and ***a*** was found to be independent of deformation conditions.

3. 3. Identification of slip system

Figures 6, 7 and 8[8] show weak-beam images of dislocations, each of which was taken with three independent reflection vectors. Dislocations shown in Figs. 6 and 8 were observed after deformation to 5% in strain at 1920K and at a strain rate of $1\times10^{-5}s^{-1}$, those in Fig. 7 being after deformation to 10% at 2020K and at a strain rate of $2\times10^{-5}s^{-1}$. One thickness fringe is terminating at the left-hand side of the end of the positive dislocation line direction in figs. 6 (a) and (c), while one fringe is

terminating at the right-hand side in fig. 6 (b). According to the definition as mentioned above, the number of terminating fringes, N, are -1, +1 and -1 for Figs. 6 (a), (b) and (c), respectively. The sign of deviation vector from the ideal Bragg condition, sgn(s), was minus for each diffraction condition of Figs. 6 (a), (b) and (c). If the Burgers vector of the dislocation in Fig. 6 is assumed to be $\boldsymbol{b}=[h\,k\,i\,l]$, the following equations are given,

$$-k+i+l=1 \qquad (2)$$
$$h-i-l=-1 \qquad (3)$$
$$h-k+l=1. \qquad (4)$$

By solving the eqs. (2)-(4) with taking account of the manner of Miller index for the hexagonal coordination, *i.e.*, $h+k+i=0$, the Burgers vector of the dislocation in Fig. 6 is confirmed to be $\boldsymbol{b}=c[0001]$. The same procedure applied for the dislocations in Fig. 7 and 8 revealed that the dislocations in Fig. 7 and 8 were $\boldsymbol{a}$ and $\boldsymbol{a}+\boldsymbol{c}$ dislocations, respectively. The reflection vectors, $\boldsymbol{g}$, the number of terminating fringes, N, the sign of the deviation vector from the ideal Bragg condition, sgn(s) and determined Burgers vectors, $\boldsymbol{b}$, for Figs. 6, 7 and 8 are summarized in table 1.

Table 1 Reflection vectors, $\boldsymbol{g}$, numbers of terminating thickness fringes, N, sign of the deviation vectors from the exact Bragg's diffraction condition, sgn(s), and analyzed Burgers vectors, $\boldsymbol{b}$, for figs. 6, 7 and 8.

		$\boldsymbol{g}$	N	sgn(s)	$\boldsymbol{b}$
Fig. 6	(a)	$0\bar{1}11$	-1	–	$c[0001]$
	(b)	$10\bar{1}\bar{1}$	+1	–	
	(c)	$1\bar{1}01$	-1	–	
Fig. 7	(a)	$\bar{2}020$	+2	–	$\frac{a}{3}[2\bar{1}\bar{1}0]$
	(b)	$000\,\bar{2}$	0	+	
	(c)	$1\bar{1}01$	-1	–	
Fig. 8	(a)	$3\bar{2}\bar{1}0$	-3	–	$\frac{a}{3}[2\bar{1}\bar{1}0]$ + $c[000\,\bar{1}]$
	(b)	$000\,\bar{2}$	-2	–	
	(c)	$2\bar{2}00$	-2	–	

Figure 9[8] demonstrates the stereographic analysis of the slip plane for the dislocation shown in Fig. 6. The planes normal to the incident beam $\boldsymbol{B}_A$ or $\boldsymbol{B}_B$ are shown in the stereogram as great circles (A) or (B), respectively. The projected dislocation line directions on (A) or (B) are indicated by $\boldsymbol{d}_A$ or $\boldsymbol{d}_B$, respectively. Hence, the true dislocation line direction, $\boldsymbol{u}_d$, is determined as the intersection of two great circles; one of which straddles between $\boldsymbol{B}_A$ and $\boldsymbol{d}_A$, the other between $\boldsymbol{B}_B$ and $\boldsymbol{d}_B$. Consequently, the slip plane is given as a plane which contained both the Burgers vector, $\boldsymbol{b}$, and the true dislocation line direction, $\boldsymbol{u}_d$. The pole of this slip plane indicated by ◎ is very close to that of $(10\bar{1}0)$ prism plane. Therefore, it is confirmed that the dislocation shown in Fig. 6 is belong to the $\{10\bar{1}0\}[0001]$ prism slip system. Since $\boldsymbol{c}$ dislocations were the most frequently observed in deformed samples, the $\{10\bar{1}0\}[0001]$ prism system is considered to be the primary slip system in ß-Si_3N_4. This finding is in good agreement with that reported by Butler[1]. However, we have never observed the $\{11\bar{2}0\}[0001]$ slip system reported by Milhet *et al.*[4].

Figure 10[8] shows the stereogram illustrating the slip plane for the dislocation with the Burgers vector of $a/3[2\bar{1}\,\bar{1}0]$ shown in Fig. 7. From the trace analysis, the slip plane for the $\boldsymbol{a}$ dislocation was found to be $(01\bar{1}0)$ prism plane, so that the secondary slip system of $\{10\bar{1}0\}<1\bar{2}10>$ had been activated on the primary slip system during high temperature deformation. In this study, $\boldsymbol{a}$ dislocations lying on the (0001) basal plane have never been observed. This finding suggests that the Peierls' barrier against the motion of $\boldsymbol{a}$ dislocations on the (0001) basal plane is higher than that on the $\{10\bar{1}0\}$ prism plane because of the small c/a ratio of 0.38 in ß-Si_3N_4.

Figure 11[8] demonstrates the stereographic trace analysis of the slip plane for the $\boldsymbol{a}+\boldsymbol{c}$ dislocation, $a/3[\bar{2}110]+c[0001]$, shown in Fig. 8. The

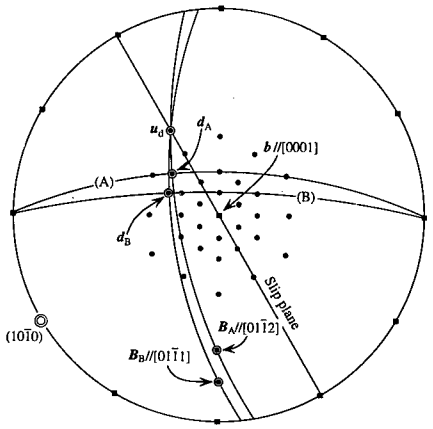

Fig. 9 Stereographic projection for the analysis of the slip plane for the dislocation in Fig. 6[8].

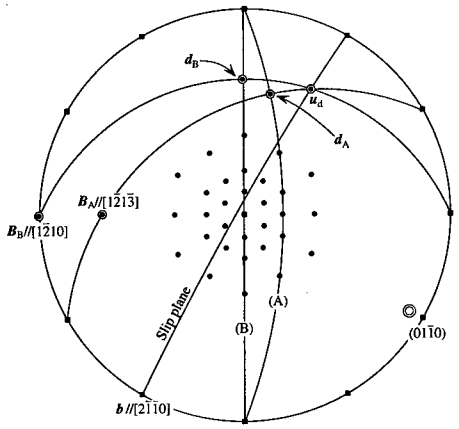

Fig. 10 Stereographic projection for the analysis of the slip plane for the dislocation in Fig. 7[8].

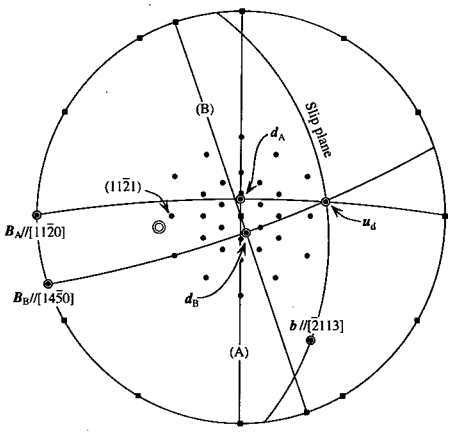

Fig. 11 Stereographic projection for the analysis of the slip plane for the dislocation in Fig. 8[8].

pole of the slip plane indicated by ◎ in Fig. 11 is close to the pole of (11$\bar{2}$1) pyramidal plane. Otherwise, there are not any other planes with low index except the (11$\bar{2}$1) pyramidal plane around it. Thus, if the experimental error is taken into account, we can conclude that the ***a+c*** dislocation shown in Fig. 8 lies on the (11$\bar{2}$1) pyramidal plane; *i.e.*, the {11$\bar{2}$1}<$\bar{2}$113> pyramidal slip system also can be activated during high temperature deformation. However, the density for ***a+c*** dislocations was very low and it was approximately 1/100 of that for ***c*** dislocations.

3. 3. Relation between high temperature deformation behavior and activated slip systems

The relation between the high temperature deformation behavior and the activated slip systems is summarized in Fig. 12[8]. The high temperature deformation behavior is seemed to be classified into two regions; one is the "Brittle" region where the cracks were observed after deformation, the other is the "Ductile" region where the good elongation of more than 10% was obtained without crack formation. The characters of dislocations observed are also shown in Fig. 12. Both the primary slip system of {10$\bar{1}$0}[0001] for ***c*** dislocations and the {10$\bar{1}$0}<1$\bar{2}$10> prism slip system for ***a*** dislocations operated during deformation under the all conditions conducted in this study. However, the {11$\bar{2}$1}<$\bar{2}$113> pyramidal slip for ***a+c*** dislocations was activated only under the limited conditions shown by "Ductile" in Fig. 12. In general, the primary slip system in a hexagonal structure such as ß-Si_3N_4 cannot satisfy the von Mises criterion[9], so that cracks are most likely to be initiated at grain boundaries in polycrystals unless a pyramidal slip contributes to the plastic strain besides the primary slip. The activation of the {10$\bar{1}$0}<1$\bar{2}$10> prism slip system on the primary prism slip cannot result in to satisfy the von Mises criterion. At "Brittle" region, the premature crack formation occurred. This is probably because that the von Mises criterion was not satisfied at this region. On the other hand, if the {11$\bar{2}$1}<$\bar{2}$113> pyramidal slip system operates, the von Mises criterion must be satisfied. In this study, however, since the density of ***a+c*** dislocations was very low ($\rho_c : \rho_a : \rho_{a+c} = 100 : 10 : 1$), it is hardly considered that the plastic strain obtained at the "Ductile" region was predominantly attributed to the dislocation motion of ***a+c*** dislo-

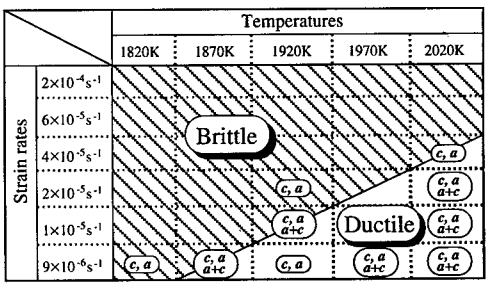

Fig. 12 Relation between deformation conditions conducted in this study and deformation behaviors. Characters of dislocations observed are also shown by ***c***, ***a*** and ***a+c***[8].

cations. Moreover, at the "Ductile" region, the stress exponent, n, was about 1 (see Fig. 4), indicating the grain boundary sliding was probably dominant deformation mechanism. Therefore, it is considered that the $\{11\bar{2}1\}<\bar{2}113>$ pyramidal slip system may operate as one of the accommodation processes for the stress concentration at triple points or ledges of grain boundaries caused by the grain boundary sliding. Therefore, the activity of the $\{11\bar{2}1\}<\bar{2}113>$ pyramidal slip system likely plays an important role for ductility of polycrystalline ß-Si_3N_4 at high temperatures.

4. CONCLUSIONS

High temperature deformation behavior of ß-Si_3N_4 was examined by compression and dislocation structures were observed by TEM. The weak-beam method was applied for the identification of activated slip systems during high temperature deformation. The results obtained are summarized as follows.

(1) High temperature deformation behavior of ß-Si_3N_4 depended strongly on deformation conditions. It was roughly classified into two regions; one is ductile region where a good elongation was obtained without crack formation, and the other is brittle region where the cracks initiated in slight deformation. The brittle to ductile transition resulted in change of the stress exponent from 3 to 1.

(2) The $\{10\bar{1}0\}<1\bar{2}10>$ prism slip for ***a*** dislocations and the $\{11\bar{2}1\}<\bar{2}113>$ pyramidal slip for ***a+c*** dislocations were found to be activated on the $\{10\bar{1}0\}[0001]$ primary slip for ***c*** dislocations during high temperature deformation. However, the activation of the pyramidal slip was limited in the ductile region. The ratio of the densities for ***c***, ***a*** and ***a+c*** dislocations was 100 : 10 : 1, respectively.

(3) The activity of the $\{11\bar{2}1\}<\bar{2}113>$ pyramidal slip system was of great importance for ductility of polycrystalline ß-Si_3N_4 at high temperatures.

ACKNOWLEDGMENT

The authors would like to thank Mr. T. Kudo, graduate student of Kyushu university, for his help of the experimental work and to Prof. Y. Ikuhara for supply of sintered material. We also acknowledge to Emeritus Prof. H. Yoshinaga (Kyushu university) for his fruitful advice and discussion.

REFERENCES

[1] E. Butler, Phil. Mag., **24**(1971), 829.
[2] A. G. Evans and J. V. Sharp, J. Mater. Sci., **6**(1971), 1292.
[3] W. E. Lee and G. E. Hilmas, J. Am. Ceram. Soc., **72**(1989), 1931.
[4] X. Milhet, J. L. Demenet and J. Rabier, Phil. Mag. Lett., **79**(1999), 19.
[5] H. Kurishita, K. Nakajima and H. Yoshinaga, Mater. Sci. Eng., **54**(1982), 177.
[6] Y. Ishida, H. Ishida, K. Kohra and H. Ichinose, Phil. Mag., **A42**(1980), 453.
[7] A. F. McLean, E. A. Fisher and R. J. Bratton, AMMRC. CTR 72-19, Interim Report on Contract DAAG 46-71-C-0162 (Sept. 1973).
[8] K. Kawahara, S. Tsurekawa and H. Nakashima, J. Japan Inst. Met., **60**(1996), 582.
[9] R. von Mises, Z. ang. Math. Mech, **8**(1928), 161.

Key Engineering Materials Vols. 171-174 (2000) pp. 833-840
© 2000 Trans Tech Publications, Switzerland

Transmission Electron Microscope Observation of Creep-Deformed Al_2O_3, SiC and Si_3N_4 Ceramics

T. Yano[1] and A.T. Yokobori Jr.[2]

[1] Research Laboratory for Nuclear Reactors, Tokyo Institute of Technology,
2-12-1, O-okayama, Meguro-ku, Tokyo 152-8550, Japan
Fax: +81-3-5734-2959, E-Mail: Tyano@nr.titech.ac.jp

[2] Department of Mechatronics and Precision Engineering, Tohoku University,
Aoba, Aramaki, Aoba-ku, Sendai 980-8579, Japan

Keywords: Transmission Electron Microscopy, Creep, SiC, Al_2O_3, Si_3N_4

Abstract

Microstructural observation using transmission electron microscope were conducted on creep-deformed SiC, Al_2O_3 and Si_3N_4 ceramics in order to analyze microscopic deformation mechanism in these ceramics directly. Thin foils were prepared from the tensile surface of the four-point bending bars after creep test at various conditions. In SiC ceramics crept at 1250°C, very sharp microcracks propagated relatively straight and transgranularly. Microcracks also branched and some of them extended along grain boundary. In SiC crept at 1480°C, grain boundary cavities and dislocations were also observed. In Si_3N_4 crept at around 1200°C, cavities along grain boundary were frequently observed. Dislocations were sometimes observed. No transgranular cracks were happened. In Al_2O_3 ceramics crept at 1000°C, sharp microcracks ran through both grain boundary and inside grains with small number of very tiny grain boundary cavities. Grain boundary glassy phase was partly crystallized. Based on the observed microstructure, creep mechanisms of these ceramics were discussed in relation with creep ductility.

Introduction

Ceramics are creep-deformed and finally ruptured under static stress at high temperatures. There are many studies to analyze creep deformation mechanisms up to now, and it has been shown that the deformation behavior changes material to material[1-10]. Diffusion mechanism, dislocation mechanism or subcritical crack growth mechanism are proposed for creep deformation of ceramics based on the number of stress exponent, n, in the empirical relation between steady state strain rate and applied stress at a given temperature. The values of 1, 2 or greater than 10 for n are reported to correspond with the diffusion mechanism, dislocation mechanism or subcritical crack growth mechanism, respectively.

Yokobori et al. reported that the creep deformation behavior of three typical high temperature structural ceramics such as alumina, SiC and Si_3N_4 at high temperatures, and mentioned that creep ductility increased in the order SiC<Al_2O_3<Si_3N_4[11-14]. To understand the creep mechanism more clearly, it is important to observe not only macroscopic deformation characteristics such as

creep rate and failure life measurement but also microstructure change during creep deformation. Grain size, grain size distribution, grain morphology, pore, amount and property of secondary phase(s) of ceramics always differ from material to material, so that deformation behavior should deeply depends on the microstructure. Therefore, deformation behavior of ceramics shows more complex feature than that of metals.

In this paper, microstructural investigation of creep-deformed alumina, SiC and Si_3N_4 ceramics are reported. The deformation mechanism is also discussed based on both microscopic observation and macroscopic mechanical properties.

Experimental Procedure

The following three ceramics were investigated. (1)Gas-pressure sintered Si_3N_4 containing Al_2O_3 and Y_2O_3 as sintering additives. The amount of sintering additives was about 8-10wt% in total. Sintering temperature was around 1800°C(NGK Spark Plug Co. Ltd, Japan). (2)Pressureless-sintered SiC containing about 2wt% in total B and C as sintering additives. Sintering temperature was 2100-2200°C(Hitachi Ltd, Japan). (3)Pressureless-sintered alumina containing 4wt% in total SiO_2, CaO and MgO (Hitachi Chemical Ltd, Japan).

Rectangular bending bars with dimensions of about 4mm(width)x3mm(depth)x36mm(length) were prepared. The tensile surface was lapped up to the surface roughness of less than 0.8s. The specimens were lorded in a four-point bending fixture with upper span of 10mm and lower span of 30mm in air using an universal testing machine[14].

Thin foils for transmission electron microscopy(TEM) were cut from the part where largest tensile stress was applied, i.e., the center part of lower spans. The thin section parallel to lower surface was cut using low-speed diamond cutter. Therefore, the tensile direction is included in the thin section. If the specimen was ruptured, the closest surface near broken surface was selected. After mechanical polishing, then the thin section was dimpled and finally ion-milled using Ar(Duo Mill or PIPS, Gatan Co. USA). Thin foils were observed using TEM(EM30, Philips, The Netherlands and H-9000, Hitachi Ltd., Japan). Un-deformed specimens were also observed as references.

Results

1. SiC

In the un-deformed SiC specimen, there was no detectable grain boundary phase. The average SiC grain size was about 3μm. Carbon grains were sometimes located at three grains junctions. In SiC grains, parallel stacking faults were frequently observed.

The specimen creep-deformed at 1250°C under an applied stress of 286MPa and ruptured after 30.4h was observed(relatively short life specimen). Fig.1 shows typical microstructure around crack path. Microcracks observed were very sharp and thin in thickness. They propagated mainly transgranular but sometimes intergranular in manner. The crack labeled as 'a' branched into two cracks, 'b' and 'c', at inner part of the grain. Two cracks crossed the grain boundary and into the adjoining grain, one went into the grain, 'd', but the other propagated through grain boundary, labeled as 'e'. In the other grain, as shown in Fig. 2, the crack 'a' twisted at inner grain portion of 'b', giving wavy contrast observed at 'c'. Branched cracks stopped at 'd' or produced dislocations at 'e'. The

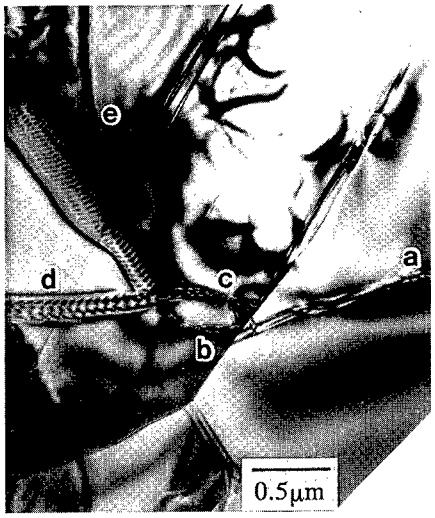

↑ Fig. 1 Microstructure of SiC crept at 1250°C under 286MPa.

→Fig. 2 Microstructure of SiC crept at 1250°C under 286MPa.

overall direction of the cracks was relatively uniform and straight, probably perpendicular to the maximum tensile stress direction. There was no detectable cavities along grain boundaries.

Figs. 3, 4 and 5 show microstructure of the specimen creep-deformed at 1480°C under an applied stress of 245MPa and did not ruptured until 490h(long life specimen). In this specimen, the formation of cavities along grain boundary was observed relatively frequently, as shown in Fig. 3. Cavities could be seen on a grain boundary of which direction should be perpendicular to the maximum tensile stress direction. The shape of cavities, lens-like or pyramidal or box-like, wasreflected the crystalline planes of adjoined grains. The size of cavities was less than 50nm in maximum length. Fig. 4 indicates high magnification photograph of a sharp crack. The crack

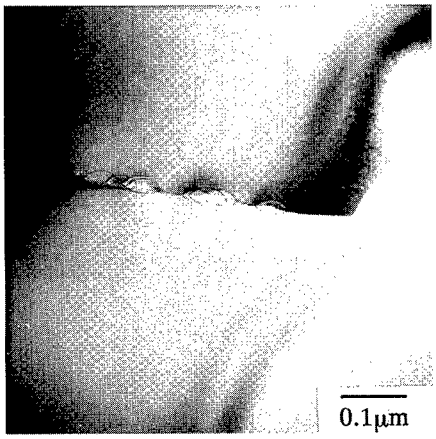

Fig. 3 Microstructure of SiC crept at 1480°C under 245MPa.

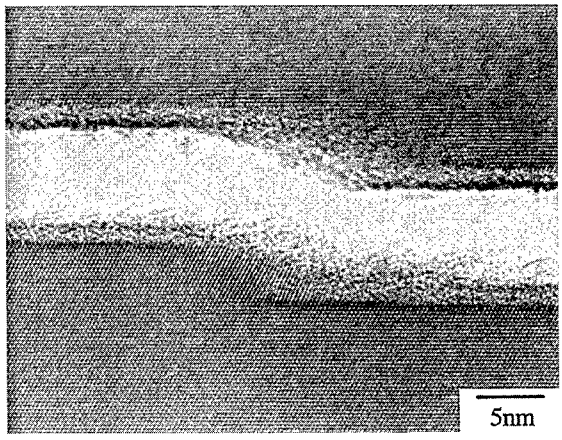

Fig. 4 Microstructure of SiC crept at 1480°C under 245MPa.

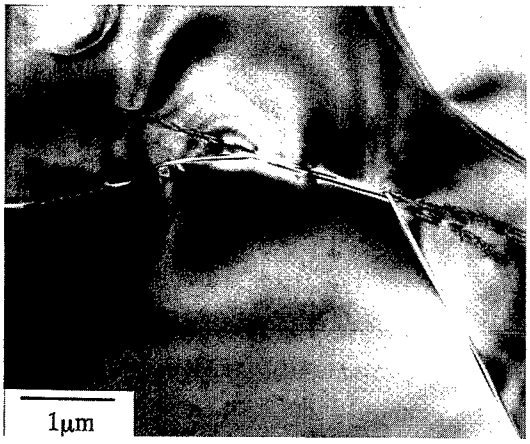

propagates mainly along the closest-packed crystal plane, but made steps with a constant interval. Fig. 5 shows the other cracks, which progressed along grain boundary. It is interesting that dislocations were initiated at the kink points of cracks. These dislocations directed the same direction and stopped after extension into a grain.

←Fig. 5 Microstructure of SiC crept at 1480°C under 245MPa.

2. Al_2O_3

The observation of reference alumina indicated that this alumina contained relatively large amount of grain boundary glassy phase. Most of Al_2O_3 grains were equiaxed and showed polyhedral-like crystal planes particularly along the grain boundary phase. The average grain size was observed to be 3-5μm. Small number of dislocations were presented before deformation.

The specimen creep-deformed at 1000°C under an applied stress of 54MPa and ruptured after 8.5h, relatively short life at lower temperature condition, was observed. Fig. 6 and 7 show typical microstructure around crack path. Many microcracks, very sharp, propagated along grain boundary and change direction at triple point glassy phase, as shown in Fig. 6. Not so frequent but some case, dislocation network was observed together with a crack, as shown in Fig. 7. Along some grain boundaries, very tiny cavities, less than 20nm in diameter, was observed. Grain boundary phase was partly crystallized as shown in Fig. 8. The crystallization of grain boundary phase was confirmed by X-ray diffraction in the specimen creep-deformed at 1100°C under 54MPa for 68h.

Fig. 6 Microstructure of Al_2O_3 crept at 1000°C under 54MPa.

Fig. 7 Microstructure of Al_2O_3 crept at 1000°C under 54MPa.

3. Si_3N_4

From the microstructure observation of reference Si_3N_4 specimen, it was clarified that the specimen contained relatively large amount of grain boundary glassy phase. It was existed between each grain boundaries without exception. The grains were mostly equiaxed with diameter of about 1 μm. The edges of each grains were rounded. There were some grains with plate-like or bar-like shape of which size was greater than equiaxed grains.

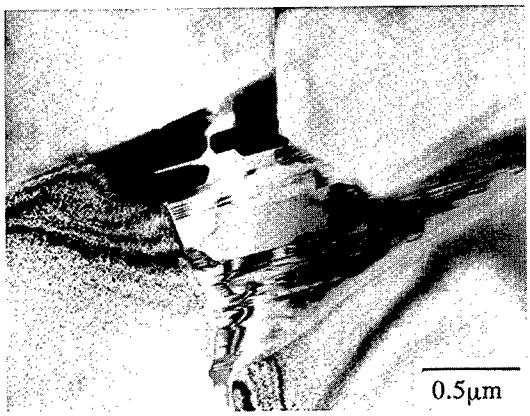

Fig. 8 Microstructure of Al_2O_3 crept at 1000°C under 54MPa.

Figs. 9 and 10 show microstructure of the specimen creep-deformed at 1150°C under an applied stress of 196MPa and did not ruptured until 300h(long life specimen). In the case of Si_3N_4, different from SiC and Al_2O_3, cracks or cavities were not so sharp. All cavities aligned along grain boundaries. These cavities were not continuous in the thin TEM specimen, but have tendency to lay in one direction macroscopically, probably perpendicular to the maximum tensile stress direction. The cavities were seemed to be expanded by viscous flow of grain boundary glassy phase under stress. No transgranular cracks was observed whereas some dislocations were observed. A part of grain boundary phase was crystallized, and it was also confirmed by X-ray diffrac-tion analysis.

After the creep test at 1215°C under an applied stress of 147MPa, and ruptured after 103h, the specimen showed almost resemble microstructure with that of the specimen crept at 1150°C. As shown in Figs. 11 and 12, grain boundary cavitation was frequently observed along one direction. The width of cavity was larger than the case of 1150°C specimen. Dislocation network was observed in some grains and also a part of grain boundary phase was crystallized.

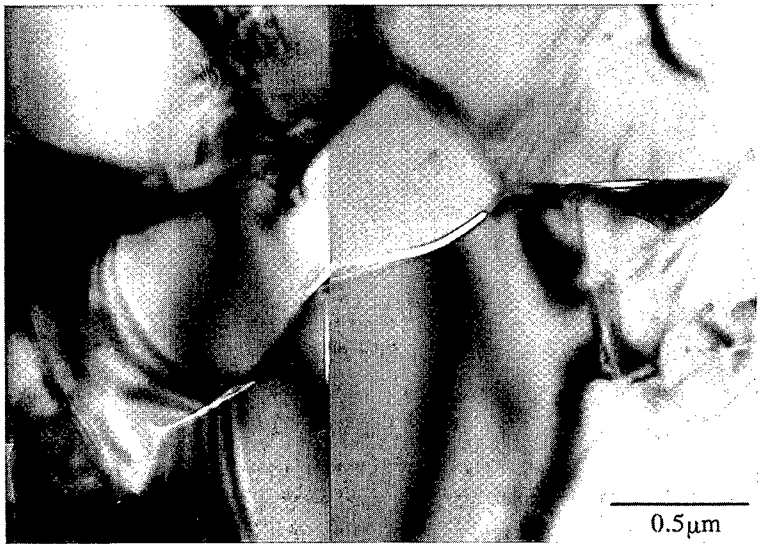

Fig. 9 Microstructure of Si_3N_4 crept at 1150°C under 196MPa.

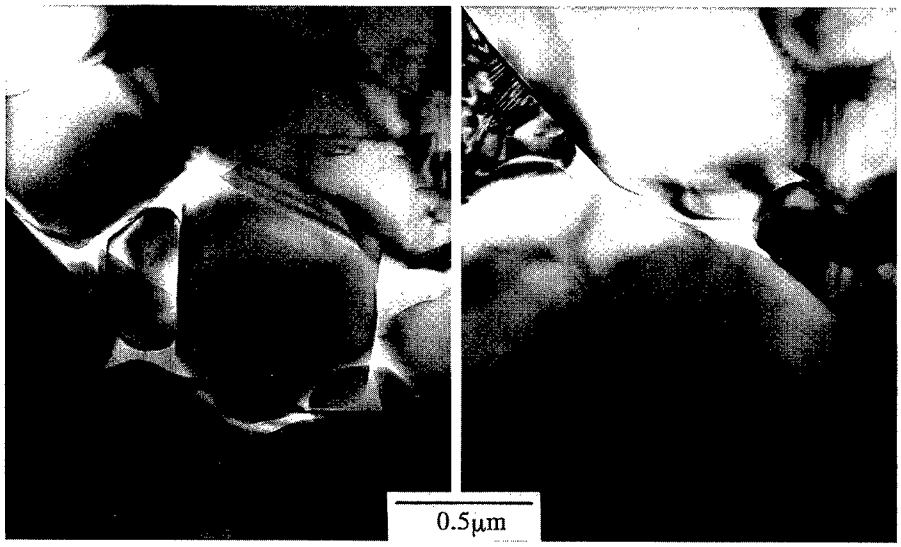

Fig. 10 Microstructure of Si_3N_4 crept at 1150°C under 196MPa.

Discussion

From the present microstructural observation, whereas the deformation conditions and materials were limited, deformation mechanism actually progressed in the materials was indicated and it showed variety depending on material and temperature.

In the case of SiC ceramics, deformation progressed mainly by the formation of microcracks which propagated mainly transgranularly without formation of grain boundary cavities at relatively low temperature under a high applied stress. High applied stress induced very complicated microcrack path through grains, sometimes it made steps and the other time was twisted or branched, probably due to high grain boundary strength of the present 'solid-state-sintered' SiC ceramics. This ceramics contains almost no grain boundary phase. At 1480°C, relatively high

Fig. 11 Microstructure of Si_3N_4 crept at 1215°C under 147MPa.

Fig. 12 Microstructure of Si_3N_4 crept at 1215°C under 147MPa.

deformation temperature, on the contrary, the formation of cavities along grain boundaries was observed, with concurrent microcrack propagation and formation of dislocations. It is expected that the creep behavior depends greatly on test temperature. From the recovery measurement of neutron-irradiated defects in SiC, it was reported that the temperature of irradiation-induced vacancy migration occurred significantly above about 1250°C[15,16]. Thus, the migration rate of vacancy changes around 1250°C or a little higher temperature. The relation between steady state creep rate and creep rupture time of the same SiC as the present study indicates that the data can be plotted as linear line in the log(steady state creep rate)-log(rupture life) diagram[5-7,13,14], but different lines depending on the test temperature. As test temperature increases, the line shifts to the direction of creep-ductile materials. It is supposed that cavity formation as a result of bulk and grain boundary diffusion causes this change. Besides cavity formation observed at relatively higher temperature, both subcritical crack growth and dislocation mechanisms are seemed to be contributed for the creep deformation in the present SiC ceramic. In other words, at relatively lower temperature, cavity formation may be suppressed. Change in apparent activation energy of stress-strain rate measurement of hot-pressed SiC containing small amount of Al was reported to be around 1500°C, smaller energy and higher stress exponent on strain rate value than 1 in the lower temperature than 1500°C[17]. Microstructure investigation of the deformed specimen in that study indicated brittle fracture with sharp microcracks without cavitation in the lower temperature region, which is roughly consistent with the present result.

Si_3N_4 ceramics observed in this study contained large amount of grain boundary phase. Grain boundary phase, which is mostly glassy phase before deformation, should be softened near its melting point of around 1500°C. Grain boundary phase is more easy to deform, rapid to diffuse at such a high deformation temperature. It was observed at all grain boundaries. Wiederhorn et al.[18] investigated creep and fracture behavior of a grassy phase containing alumina both with mechanically and microscopically. They concluded that the creep of the alumina dominated by the viscous flow and solute precipitation mechanism of grain boundary phase. In the case of 'liquid-phase-sintered' Si_3N_4 in the present study is also seemed to be dominated by the characteristics of grain boundary phase, i.e., viscous flow and solution precipitation of grain boundary phase. Cavitation or crack opening will be formed as a result of viscous flow of grassy phase. The log(steady state creep rate)-log(rupture time) plot was presented as one straight line independent of test temperature and more close to that of ductile materials such as Cr-Mo-V steel[13,14]. Before opening of continuous large cracks, formation of independent cavities should be observed. A part of grain boundary phase was crystallized. If plenty of glassy phase was crystallized during deformation, creep deformation rate should be lowered. The effect of dislocation on creep rate may be limited due to the small number of dislocations compared with the viscous flow. Thus the deformation of Si_3N_4 at observed narrow temperature range is mainly dominated by the deformation of grain boundary phase, and partial recrystallization and change in composition or dislocation lead not so significant effects on deformation. Tighe et al.[19] reported on MgO-doped and Y_2O_3-doped Si_3N_4 that stress exponent of 4.2 and presence of grain boundary cavitation.

In the case of alumina, the microstructure of deformed specimen showed intermediate feature between those of Si_3N_4 and SiC. It contained relatively large amount of grain boundary phase, but probably it is not ductile at around 1000°C. The grain boundary phase is weaker than alumina particle so that microcracks extended along mainly grain boundary. At lower temperature, the

deformation mechanism, i.e., mainly microcrack formation, is resemble with that of SiC. As test temperature increases, deformation of grain boundary phase and cavity formation will dominate creep deformation mechanism, as in the case of liquid phase sintered Si_3N_4, mentioned above and also of vitreous-bonded alumina discussed by Wiederhorn et al.[18], who measured the stress exponent of 4.8. In the latter case, crystallization of grain boundary phase may affect the deformation behavior. Then the log(steady state creep rate)-log(rupture time) plot was appeared between those of SiC and Si_3N_4[13,14], and may show slight temperature dependency[18].

Conclusions

Microstructural observation using TEM were conducted on creep-deformed SiC, Al_2O_3 and Si_3N_4 ceramics. In SiC ceramics crept at 1250°C, sharp microcracks propagated relatively straight and transgranularly. Microcracks were also branched and some of them extended along grain boundary. At 1480°C, grain boundary cavities and dislocations were also observed. In Si_3N_4 crept at around 1200°C, grain boundary cavities due to viscous flow were frequently observed with small number of dislocations. No transgranular cracks were observed. A part of grain boundary phase was crystallized. In Al_2O_3 ceramics crept at 1000°C, sharp microcracks ran through mainly grain boundary with small number of very tiny grain boundary cavities. Grain boundary phase was partly crystallized. Compared with microstructural deformation mechanisms of three ceramics, liquid-phase-sintered Si_3N_4 showed more creep-ductile and solid-state-sintered SiC more creep-brittle deformation. The results explain the estimation from log(steady state creep rate)-log(rupture life) diagram proposed by one of the authors. In every cases, creep deformation is not dominated by single simple micro-mechanism.

Acknowledgement

The work was supported by RF97R12101 program from JSPS.

References

[1] G. R. Telewilliger and F. F. Lange, J. Am. Ceram. Soc., 57 (1974) 25.
[2] F. F. Lange and B. I. Davis, J. Mater. Sci., 17 (1982) 3637.
[3] W. R. Cammon and T. Langdon, J. Mater. Sci., 18 (1983) 1.
[4] J. L. Chermant and F. Ostestorck, Mater. Sci. And Engng. 71 (1985) 147.
[5] Y. Okamoto, N. Michiura et. al., MRS Int'l Mtg. on Adv. Mater., 7 (1989) 233.
[6] M. Masuda and M. Matsui, J. Ceram. Soc. Jpn., 98 (1990) 83.
[7] L. J. Bowpn, R. J. Weston, T. G. Carruthers and R. J. Brook, J. Mater. Sci., 13 (1978) 341.
[8] F. F. Lange, D. R. Charke and B. I. Davis, J. Mater. Sci., 15 (1980) 611
[9] A. G. Evans and S. M. Wiederhorn, J. Mater. Sci., 9 (1974) 270.
[10] T. G. Wang and R. Raj, J. Am. Ceram. Soc., 67 (1984) 399.
[11] A. T. Yokobori, Jr., T. Yokobori, and T. Nishihara, Engng. Fracture Mech., 40 (1991) 737.
[12] A. T. Yokobori, Jr. et. al., Trans. Ann. Meeting of Jpn. Soc. Mech. Engineers, Vol. B, No. 920-978 (1992) 570.
[13] A. T. Yokobori, Jr., T. Yano and T. E. Mitchell, Mater. Sci. Forum, 233-234 (1997) 109.
[14] A. T. Yokobori, Jr., T. Yokobori and K. Yamazaki, J. Mater. Sci. Lett., 15 (1996) 2002.
[15] H. Miyazaki, T. Suzuki, T. Yano and T. Iseki, J. Nucl. Sci. Technol., 29 (1992) 656.
[16] K. Sasaki, T. Yano, T. Maruyama and T. Iseki, J. Nucl. Mater., 179-181 (1991) 407.
[17] R. Moussa, J. -L. Chermant and F. Osterstock, in Deformation of Ceramic Materials II, ed. by R. E. Tressler and R. C. Bradt, Plenum Press, New York (1984) pp.617.
[18] S. M. Wiederhorn, B. J. Hockey, R. F. Krause, Jr. And K. Jakus, J. Mater. Sci., 21 (1986) 810.
[19] N. J. Tighe, S. M. Wiederhorn, T. -J. Chuang and C. L. Mcdaniel, in Deformation of Ceramic Materials II, ed. by R. E. Tressler and R. C. Bradt, Plenum Press, New York (1984) pp.587.

Key Engineering Materials Vols. 171-174 (2000) pp. 841-846
© 2000 Trans Tech Publications, Switzerland

Lifetime Prediction and Confirmation of Long Term Creep Resistance in Advanced Silicon Nitride Ceramics

Y. Takigawa, J.-W. Cao, Y. Ikeda and H. Kawamoto

Japan Fine Ceramics Center, 2-4-1 Mutsuno, Atsuta-ku, Nagoya 456-8587, Japan

Keywords: Tensile Creep, Silicon Nitride, Time-to-Failure, Lifetime Prediction, Stress Exponent

Abstract

Tensile creep behavior is examined in advanced silicon nitride ceramics in order to reveal the lifetime controlling process and to confirm 10,000h creep resistance. From the creep rupture behavior under high stress level within short testing period less than 1,000h, the relationships between log-log plot of applied stress and time-to-failure exhibits a single straight line at each temperature examined. Then, the applied stress corresponding to time-to-failure of 10,000h is estimated from the extrapolation of straight lines, and 10,000h creep resistance was successfully confirmed under the predicted applied stress at relatively low temperatures. However, at 1300°C, the relationship is divided into two straight lines at the stress of 240MPa. Estimation of deformation parameters reveals that the slop of the log-log plot is nearly equal to the inverse of the stress exponent at the deformation condition. This result indicates that the change in the slope of creep lifetime dependence on applied stress can be predicted from the estimation of stress exponent in the creep tests for only a few hundred hours, which is very useful for lifetime prediction..

Introduction

Silicon nitride is one of the most promising materials for the application in advanced ceramic gas turbines with improved efficiency. For its high-temperature applications, however, many mechanical properties must be confirmed such as high levels of strength, oxidation and creep resistance and also high reliability of the lifetime at certain working conditions.

When the ceramic material is used as a high-temperature structural component, a durability more than 100,000h is expected in many case. However, it is practically difficult to perform a long-term tests of ceramic materials at high temperatures for more than 100,000h. Therefore, it is necessary to predict the long-term live from the result of short-term tests accurately. In order to estimate long-term durability, long-term creep rupture data is required. There are a few recent data of creep test more than several thousand hours [1, 2], but most of the creep tests conducted so far on ceramics have been at a level of several hundred hours, which is too short to estimated long-term durability. Collecting long-term creep rupture data is needed to raise reliability in the estimated durability.

In the present study, tensile creep behavior is examined in advanced silicon nitride ceramics to reveal the lifetime controlling process and to confirm the long term creep resistance more than 10,000h.

Experimental Procedure

Silicon nitride ceramics used in this study are SN88M produced by NGK Insulators, Ltd. (Nagoya, Japan), which is gas pressure sintered silicon nitride ceramics. The material was cut and ground to flat dog-bone specimens with rectangular cross section of 4x2.5mm^2 and a gage length of 20mm. Tensile creep tests were conducted in the temperature range of 1200 to 1300°C. The tests were made at a constant load. The displacement of the specimens was measured by two linear variable differential transducers (LVDT) located outside furnace and recorded by plotter. In some

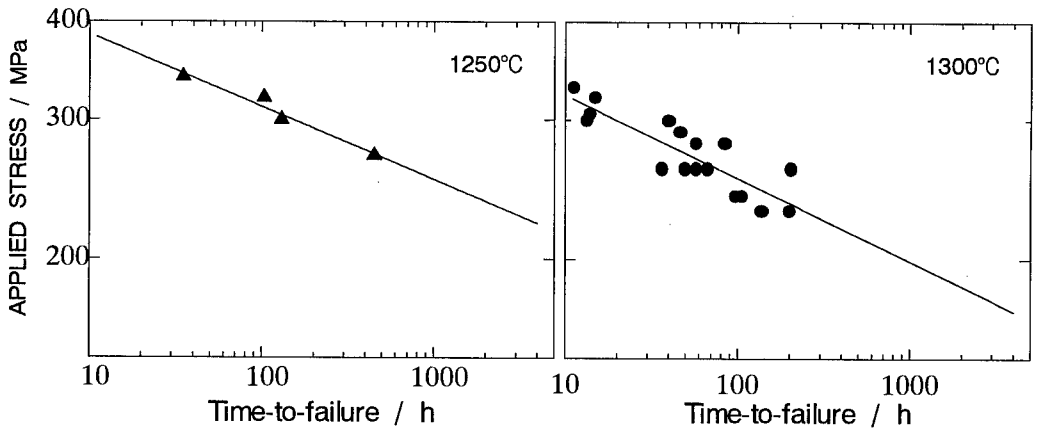

specimens, the displacement was measured *in situ* between two points in the gage section by an optical system and data were collected by a computer. The accuracy of the optical system is less than 10μm. In the tests, bending strain was minimized to less than 5% by adjustment at room temperature individually for each specimen. The bending strain was measured by 4 strain gauges on each surface of a specimen in the center of the gauge section. Detailed testing procedure has been reported elsewhere [3].

Testing program for the developed material is as follows. The first step is to evaluate creep rupture behavior within relatively short testing periods and under high stress level, typically less than 1,000h. The second step is to estimate the applied stress corresponding to time-to-failure of 10,000h, using log-log plots between applied stress and time-to-failure. The third step is to carry out confirmation tests of 10,000h in the estimated conditions.

Results and Discussion

At first, creep rupture behavior is evaluated within relatively short testing periods and under high stress level, typically less than 1,000h. Figure 1 shows the relationships between logarithm of applied stress and logarithm of time-to-failure in SN88M at 1250 and 1300°C. The relationship exhibits a single straight line at each temperature examined. From the extrapolation of straight lines, the applied stress corresponding to time-to-failure of 10,000h is estimated and confirmation tests of 10,000h creep resistance are conducted.

Figure 2 shows the results of confirmation tests of 10,000h creep resistance in SN88M at 1250°C and 1300°C. The creep resistance of 10,000h was confirmed under the predicted applied stress at 1250°C. The creep resistance of 10,000h has been confirmed in many materials at several conditions under the predicted applied stress from the extrapolation of straight lines obtained within relatively short testing periods [4].

In contrast to the results under the most of conditions, the creep resistance of 10,000h in SN88M at 1300°C is not confirmed under the predicted applied stress from the extrapolation of the straight line as shown in Fig. 2 (b). The time-to-failure is only about one or two thousand hours at the predicted stress for 10,000h.

Since the lifetime at the relatively low stress level is overestimated by the extrapolation of the straight line, a new function must be introduced. Assuming that the log-log plots of the applied stress vs. time-to-failure can be expressed as bimodal linear relationship, the slope changes at the

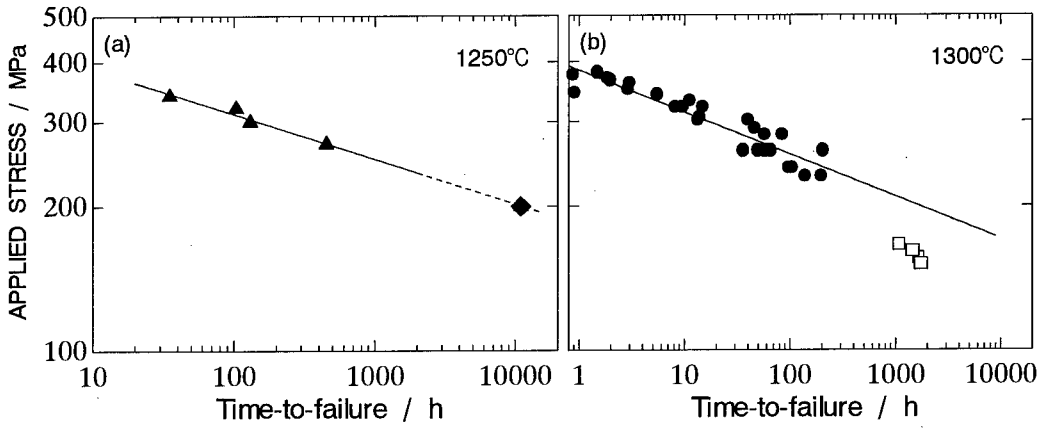

applied stress of about 240MPa. Figure 3 shows the result of the lifetime prediction from the extrapolation of log-log plots of relatively lower applied stress data. The lifetime of more than 10,000h is confirmed under the predicted condition.

In the case that the log-log plots of the applied stress (σ) vs. time-to-failure (t_r) is represented as straight lines, the relationship is described as,

$$\ln\sigma = -\frac{1}{N}\ln t_r + Const. \quad (1)$$

where N is a constant. As shown in Fig. 3, N is estimated to be about 4 at lower stress level than 240MPa and about 9 at higher stress level. It has been reported that the change in the slope of the stress vs. failure time curves represents the change in the kinetics of the crack growth mechanism depending on the applied stress, i.e., creep controlled failure occurs at low stress level, where failure is controlled by slow crack growth at higher stress level [5]. However, this is not the case in the present study because the slow crack growth region is obviously observed at the stress level higher than 400MPa in the present material. Creep controlled failure must occur in both region above and below the stress level of 240MPa. If it is the case, the change in some creep property is expected near the stress level of 240MPa. Then, the stress exponent n is estimated around the stress level of 240MPa.

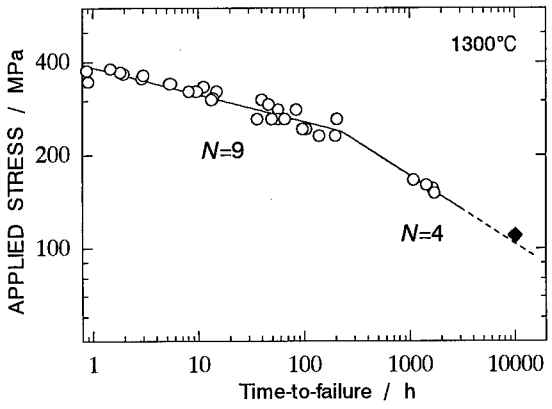

Figure 4 shows creep curves of SN88M at 1300°C under various applied stresses. At the lower stress level of 140 and 160MPa, transient creep and steady-state-

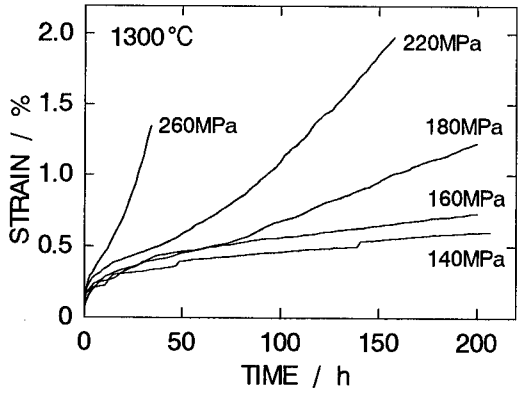

Fig. 4 Creep curves of SN88M at 1300°C under various applied stresses.

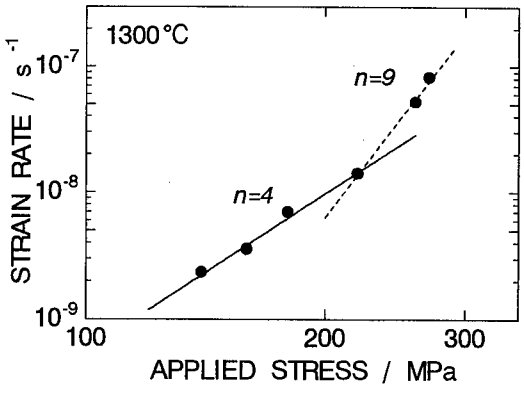

Fig. 5 Relationship between applied stress and strain rate in SN88M at 1300°C.

like creep regions are observed. On the other hand, tertiary creep region is also clearly observed at the stress level higher than 180MPa.

The previous reports reveals that the true steady-state creep is not clearly defined in silicon nitride [6]. The lack in steady-state may be caused by chemical or structural change due to oxidation during creep. The minimum creep strain rate is used in the previous studies, which is obtained at a creep time of several hundred hours. In the present study, the secondary creep strain rate is estimated from the strain rate at the time of 200h in the case that tertiary creep is not observed.

Figure 5 shows the relationship between applied stress and strain rate in SN88M at 1300°C. The results show that the creep rate strongly depends on the applied stress. It is explicitly shown that the relationship between log of applied stress and log of strain rate is bimodal, i.e., the slope is approximately 4 at the region under 220 MPa, and changed to about 9 at the region above 230 MPa.

There are some reports that the stress exponent increases with the increase of flow stress. A large increase of stress exponent with increasing applied stress has been attributed to failure at an early stage due to higher applied load in some cases [7]. However, this is not the case in the present study because tertiary creep region is clearly observed at the higher stress level. Another possible interpretation is due to creep damage or cavitation. There have been some reports that formation of cavity changes the stress exponent [8, 9]. In the present material, there is a report that the strain in compressive test, where effect of cavitation is limited, is much less than that in tensile test [10]. Detailed cavitation study will be conducted in future works.

As shown in Fig. 3, N is estimated to be about 4 at lower stress level than 240MPa and about 9 at higher stress level, while the stress exponents n estimated in Fig. 5 are approximately 4 at the region under 220 MPa, and changed to about 9 at the region above 220 MPa. Since the two plots have similar trend that the slope change from 4 to 9 at the stress level around 230MPa, it is expected that N and n have the same meaning. If it is the case, the change in the slope of creep lifetime dependence on applied stress can be predicted from the estimation of stress exponent in the creep tests for only a few hundred hours. It is very useful for lifetime prediction. Since the relationship between applied stress and strain rate ($\dot{\varepsilon}$) is represented as

$$\ln\sigma = \frac{1}{n}\ln\dot{\varepsilon} + Const. \tag{2}$$

the following relationship must be satisfied from Eq. 1 and Eq.2 when N and n have the same

meaning.

$$\dot{\varepsilon} \cdot t_r = Const. \quad (3)$$

As a lifetime prediction method developed and generally used in metallic materials, it is well known that the relationship between log of time-to-failure and log of the secondary creep strain rate exhibits single straight line in many materials. In that case, the relationship between secondary creep strain rate and time-to-failure is represented as,

$$\dot{\varepsilon}^m \cdot t_r = Const. \quad (4)$$

where m is the strain rate exponent. There are also some reports that silicon nitride ceramics also fits this linear relationship [1, 6, 11, 12]. When the strain rate exponent of 1, it has been reported that the time-to-failure is almost same with the time for the formation of facet size cavities [12], which is in good agreement with the present result that facet size cavities are observed but cracks are rarely observed in the failed specimens.

From these results, it is clarified that the change in the slope of creep lifetime dependence at 1300°C is originated from the change in stress exponent. This result indicates that the change in the slope of creep lifetime dependence on applied stress can be predicted from the estimation of stress exponent in the creep tests for only a few hundred hours, which is very useful for lifetime prediction.

Conclusion

Tensile creep behavior is examined in advanced silicon nitride ceramics in order to reveal the lifetime controlling process and to confirm the long term creep resistance more than 10,000h. The results obtained are as follows.

(1) The results of creep rupture behavior evaluated under high stress level within relatively short testing periods typically less than 1,000h reveals that the relationships between logarithm of applied stress and logarithm of time-to-failure exhibits a single straight line in each material examined. The creep resistance of 10,000h was confirmed in the most of materials under the predicted applied stress.

(2) The relationship between the logarithm of applied stress and the logarithm of time-to-failure is not represented by a single straight line in relatively long testing period, but is divided into two straight lines at the stress level of 240MPa at 1300°C. Estimation of deformation parameters reveals that the slop of the log-log plot between applied stress and time-to-failure is nearly equal to the inverse of the stress exponent at the deformation condition. This result indicates that the change in the slope of creep lifetime dependence on applied stress can be predicted from the estimation of stress exponent in the creep tests for only a few hundred hours, which is very useful for lifetime prediction.

Acknowledgement

This work is supported by NEDO Project "Research and Development on Ceramic Gas Turbine (300kW class)".

References

[1] B. J. Hockey, S. M. Wiederhorn, J. G. Baldoni and S. T. Buljan, J. Mater. Sci 26 (1991), p. 3931.

[2] T. Ohji and Y. Yamauchi, J. Am. Ceram. Soc. 75 (1992), p.2304.

[3] F. Lofaj, H. Usami, Y. Ikeda, Y. Mizuta and H. Kawamoto, in Proc. of the 1995 Yokohama Gas Turbine Congress, Yokohama, Oct. 22-27, 1995, Gas Turbine Soc. of JPN., Vol. 3 (1995),

pp.37.
[4] F. Lofaj, J-W. Cao, A. Okada and H. Kawamoto, in Proceeding of Sixth International Symposium on Ceramic Materials and Components for Engines, (1998), p. 713.
[5] M. K. Ferber, M. G. Jenkins, T. A. Nolan and R. L. Yeckley, J. Am. Ceram. Soc. 77 (1994), p.657.
[6] S. M. Wiederhorn, B. J. Hockey, D. C. Cranmer and R. L. Yeckley, J. Mater. Sci 28 (1993), p. 445.
[7] T. Ohji and Y. Yamauchi, J. Am. Ceram. Soc. 77 (1994), p. 678.
[8] D. F. Carroll and R. E. Tressler, J. Am. Ceram. Soc. 72 (1989), p. 49.
[9] S. M. Wiederhorn, D. E. Roberts, T. J. Chuang and L. Chuk, J. Am. Ceram. Soc. 71 (1988), p. 602.
[10] F. Lofaj, A. Okada and H. Kawamoto, J. Am. Ceram. Soc. 80 (1997), p. 1619.
[11] M. K. Ferber and M. G. Jenkins, J. Am. Ceram. Soc. 75 (1992), p. 2453.
[12] T. Ohji and Y. Yamauchi, J. Am. Ceram. Soc. 76 (1993), p. 3105.

Corresponding author:
Yorinobu TAKIGAWA
e-mail takigawa@jfcc.or.jp

Key Engineering Materials Vols. 171-174 (2000) pp. 847-854
© 2000 Trans Tech Publications, Switzerland

Creep Behavior of a Fine-Grained Tetragonal Zirconia

K. Morita, K. Hiraga and Y. Sakka

National Research Institute for Metals, 1-2-1, Sengen, Tsukuba-shi, Ibaraki 305-0047, Japan

Keywords: Primary Creep, Diffusional Creep, Dislocation Creep, Grain Growth, Stress Exponent, Grain Boundary Sliding (GBS), 3Y-TZP

Abstract: The high temperature deformation behavior of a high-purity yttria-stabilized tetragonal zirconia (3Y-TZP) was examined by constant load creep tests. By excluding the influence of grain growth during deformation, a sigmoidal relationship similar to superplastic metals appeared in the relationship between true stress and creep rate. At stresses lower than 10 MPa, a stress exponent of 1.6 appeared, suggesting the intervention of diffusional creep. At stresses higher than 15 MPa, a stress exponent of 2.7 appeared. In the high stress region, TEM observation revealed some intragranular dislocation activity. This result suggests that rate-controlling mechanism for the stress exponent of 2.7 is dislocation creep.

1. INTRODUCTION

The high temperature deformation of high-purity yttria-stabilized tetragonal zirconia (Y-TZP) has been characterized by a stress exponent of 2 at a high stress region and a stress exponent of ~3 at a low stress region [1-8]. Explanations for the origins of these deformation regions are inconsistent to each other. For example, Chokshi *et al.* [1-4] have proposed grain boundary sliding (GBS) and interface reaction processes for the high and low stress regions, respectively. Jimenez-Melendo *et al.* [5-8] have assumed the existence of a threshold stress for GBS, and attributed these regions to a single deformation process controlled by the lattice diffusion of cations.

High temperature deformation mechanism of high-purity Y-TZP has been analyzed by

$$\dot{\varepsilon} = A\sigma^n / d^p, \qquad (1)$$

where $\dot{\varepsilon}$ is the steady strain rate, σ is the stress, d is the grain size, n and p are the stress and the grain size exponents, respectively, A is a material constant. From this definition, n and p should be evaluated for the instantaneous relationship among stress, strain rate and grain size at strain ε in a steady state. Since the strict examination of this relationship is laborious and grain growth is sluggish in Y-TZP, however, most of earlier studies [1-8] examined the creep behavior without correcting the effect of grain growth on the stress-strain rate relationship. Furthermore, the studies measured overall strain rates that may include the effects of deformation in the grip region of tensile specimens or those of constrained deformation near both sides of compression specimens. There seems to be little assurance, however, that these situations did not influence the evaluation of the creep parameter. Indeed, a recent experiment [9] for a high-purity Y-TZP has shown that grain growth and deformation in the grip region strongly affect the shape of creep curves and the evaluation of n-value. Such a result indicate that strict examination in accordance with the definition of Eq. (1)

is necessary to obtain an essential understanding of the deformation behavior of Y-TZP.

The present study was undertaken to (1) examine the effects of grain growth on creep behavior, (2) to evaluate the stress exponent from creep strain-rate curves corrected for both instantaneous stress and strain, and (3) to assess the possible mechanisms of creep deformation in a high-purity 3Y-TZP on the basis of the evaluated stress exponent and the microstructural features in deformed specimens.

2. EXPERIMENTAL PROCEDURE

2-1. Material

High purity 3Y-TZP powder (Tosoh Co., Japan: <50 Al_2O_3, 50 SiO_2, <50 Fe_2O_3, 220 Na_2O in wt ppm) was cold-isostatically pressed at 100 MPa and then sintered at 1673 K for 3 h in air. The sintered material had a relative density higher than 98% and an average grain size of 0.35 μm. From the material, dog-bone-shaped flat tensile specimens with a gage portion of $'3\times{}''3\times{}'20$ mm were machined. In the present material, no intergranular glass phase was observed along grain boundaries.

2-2. Creep Test

Constant load creep tests were performed at 1673 K in air. In each test, the tensile stress was setted in a range of 3–80 MPa. True tensile displacement was measured with an electro-optical extensometor which can directly monitor the length between targets made at both ends of the gauge portion [9]. The monitored creep rate $\dot{\varepsilon}_m$ was corrected against the current values of both cross sectional area of the gauge portion and grain size follows [9].

Assuming constant volume and uniform deformation in the gauge portion, the instantaneous creep rate $\dot{\varepsilon}_\sigma$ at an arbitrary true strain ε_a can be written as

$$\dot{\varepsilon}_\sigma = \dot{\varepsilon}_m \exp(-n\varepsilon_a). \quad (2)$$

When the corrected creep rate decreases from $\dot{\varepsilon}_{\sigma 0}$ to $\dot{\varepsilon}_{\sigma 1}$ by grain growth, the grain size exponent can be expressed as

$$-p = \frac{\ln(\dot{\varepsilon}_{\sigma 1}/\dot{\varepsilon}_{\sigma 0})}{\ln(d/d_0)}, \quad (3)$$

where $\dot{\varepsilon}_{\sigma 0}$ and $\dot{\varepsilon}_{\sigma 1}$ are the creep rates corrected for the initial grain size d_0 and the instantaneous grain size d, respectively. Inserting Eq. (2) into Eq. (3) leads to the creep rate $\dot{\varepsilon}_{\sigma d}$ corrected against both instantaneous stress and grain size:

$$\dot{\varepsilon}_{\sigma d} = \dot{\varepsilon}_{\sigma 0}(d/d_0)^p = \dot{\varepsilon}_m \exp(-n\varepsilon_a)\cdot(d/d_0)^p. \quad (4)$$

For this correction, the stress exponent was evaluated from the monitored creep rate ε_m at a true strain of 0.03, where quasi-steady state was established and grain growth stayed less than 3% at 15-80 MPa and ~30 % at 3-10 MPa. The stress exponents used for the correction were 2.2 for ≤10 MPa and 2.6 for >10 MPa [9].

2-3. Microstructural Evaluation

Static grain growth was examined by annealing the sintered specimens at 1673 K in air. For the determination of average grain sizes in the annealed and the deformed specimens, scanning electron microscopy (SEM) was used. The specimens for SEM observation were mechanically polished and thermally etched at 1473 K for 30 min in air. The grain size was evaluated as $1.56L$, where L is the average intercept length of grains in SEM micrographs.

For TEM observation, the tensile specimens were deformed up to prescribed strains and

cooled at an initial rate of 5 Ks^{-1}. During the cooling, creep load was not removed to freeze-in the deformed structures. TEM specimens were cut from the deformed gauge portion, mechanically polished to a thickness of 100 μm and further thinned by Ar ion-milling.

3. EXPERIMENTAL RESULTS

3-1. Static and dynamic grain growths

The static grain growth of the present 3Y-TZP was examined by using the classical growth law:

$$d_S^r - d_0^r = k \cdot t, \qquad (5)$$

where r is the grain growth exponent, d_S is the grain size at annealing time t and k is the rate constant. Figure 1(a) confirms that the static grain growth follows the cubic law, *i.e.*, r=3. This is consistent with a previous result for a high-purity 3Y-TZP [10].

Grain growth during creep deformation, that is, dynamic grain growth was observed to proceed more rapidly than the prediction from Eq. (5). Such enhanced grain growth can be attributed to an additional strain-dependent component in the form [11]

$$\ln(d/d_S) = \alpha \cdot \varepsilon_a, \qquad (6)$$

where d is the instantaneous grain size at true strain ε_a, d_S is the grain size attained only by annealing for a duration of $[\exp(\varepsilon_a)-1]/\dot{\varepsilon}_0$ and α is the rate constant of dynamic grain growth. From the slope of the ε-$\ln(d/d_S)$ plot in Fig. 1(b), α is evaluated as 0.45. This value is close to α =0.6 reported for a high-purity 2.5Y-TZP [12]. Inserting Eq. (5) into Eq. (6), we can evaluate the instantaneous grain size in Eq. (4) as

$$d = \left(d_0^3 + kt\right)^{1/3} \exp(0.45\varepsilon_a). \qquad (7)$$

3-2. Creep behavior

Figure 2(a) shows the creep rate curves for 3Y-TZP deformed at 1673 K, at 5 MPa. The light solid line represents the creep rate curve, $\dot{\varepsilon}_m$, monitored along the gauge portion. In the $\dot{\varepsilon}_m$ -curve, a primary creep region appears up to ~0.02, where the creep rate decreases steeply with strain, and this region is followed by a quasi-steady state region, where the creep rate gradually decreases with increasing strain. The broken line represents the creep rate curve, $\dot{\varepsilon}_\sigma$, corrected only

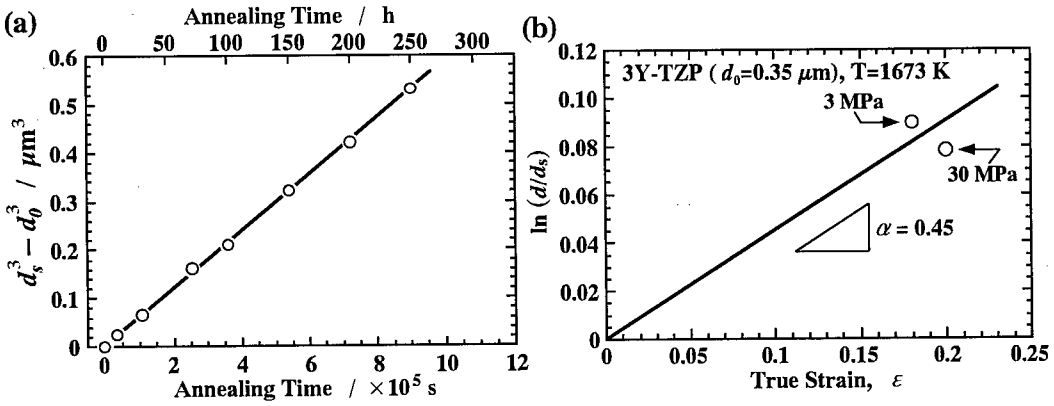

Fig. 1 (a) Static and (b) dynamic grain growth in 3Y-TZP at 1673 K.

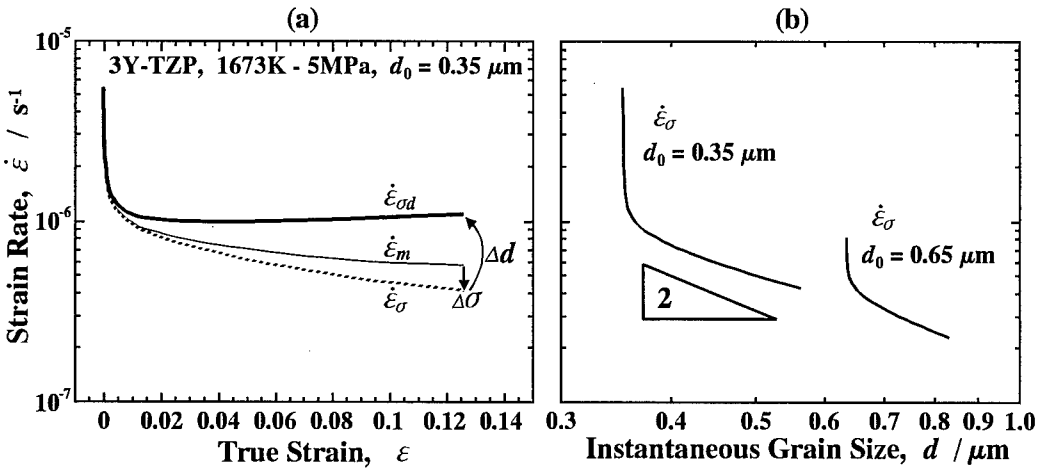

Fig. 2 Creep rate curves of 3Y-TZP at 1673 K, at 5 MPa; (a) the light solid, broken and heavy solid lines represent the creep rates monitored optically along the gauge portion ($\dot{\varepsilon}_m$), corrected only against the stress ($\dot{\varepsilon}_\sigma$) and corrected against both stress and grain size ($\dot{\varepsilon}_{\sigma d}$), respectively, and (b) $\dot{\varepsilon}_\sigma$-curves were shown as a function of the instantaneous grain size d.

against the instantaneous stress by using Eq. (2). Although the $\dot{\varepsilon}_\sigma$-curve has a similar feature to that of the $\dot{\varepsilon}_m$-curve, the quasi-steady state region shifts toward a lower creep rate region. Figure 2(b) shows $\dot{\varepsilon}_\sigma$ as a function of the instantaneous grain size evaluated by Eq. (7). The strain rate decreases almost linearly with increasing grain size and the slope of the trend line yields a grain size exponent of about 2.0. This means that the absence of steady-state is due to grain growth during deformation. The heavy solid line in Fig. 2(a) represents the creep rate curve, $\dot{\varepsilon}_{\sigma d}$, corrected against both stress and grain size by using Eqs. (4) and (7) for p=2.0. In contrast to the $\dot{\varepsilon}_m$ - and $\dot{\varepsilon}_\sigma$-curves, the $\dot{\varepsilon}_{\sigma d}$-curve exhibits a well-defined steady state region. It should be noted that the discrepancy in creep rate between the $\dot{\varepsilon}_\sigma$- and $\dot{\varepsilon}_{\sigma d}$-curves increase with strain.

Figure 3 illustrates the variation in the corrected creep rate with true stress in a double-logarithmic scale. The open circles represent the steady state creep rates, $\dot{\varepsilon}_{\sigma d}$, evaluated at ε =0.05~0.1. The open, filled and inverted triangles represent $\dot{\varepsilon}_\sigma$ evaluated at ε =0.03, 0.05 and 0.1, respectively. For comparison, earlier data obtained by Owen and Chokshi for a high-purity 3Y-TZP at 1673 K [3] are also shown with the thin solid line. Their data exhibit the typical feature of stress-strain rate relationship reported in earlier studies [1-8], where the stress exponent varies from 2.0 at >40 MPa to 3.0 at <40 MPa.

The present result is different from those of earlier studies [1-8]. The stress-strain rate relationship corrected against both instantaneous stress and grain size shows a sigmoidal feature similar to that of superplastic metals. The steady-state stress exponent takes a value of 2.7 at 15-80 MPa and 1.6 at stresses lower than 10 MPa. However, the transition of the stress exponent from 2 to 3 reported in the earlier studies [1-8] does not appear in the stress range of the present examination.

For $\dot{\varepsilon}_\sigma$, the stress exponent takes almost the same value as that for $\dot{\varepsilon}_{\sigma d}$, *i.e.*, n~2.7 at stresses higher than 15 MPa. There is also the lack of the transition from n~3 to n~2. At stresses lower than 10 MPa, the stress exponent tends to increase with an increase in strain. This trend is due to the effect of grain growth clearly seen in Fig. 2, that is, grain growth decreases $\dot{\varepsilon}_\sigma$ at larger strains and thereby results in spuriously large n-values. Thus, the correction against the instantaneous grain

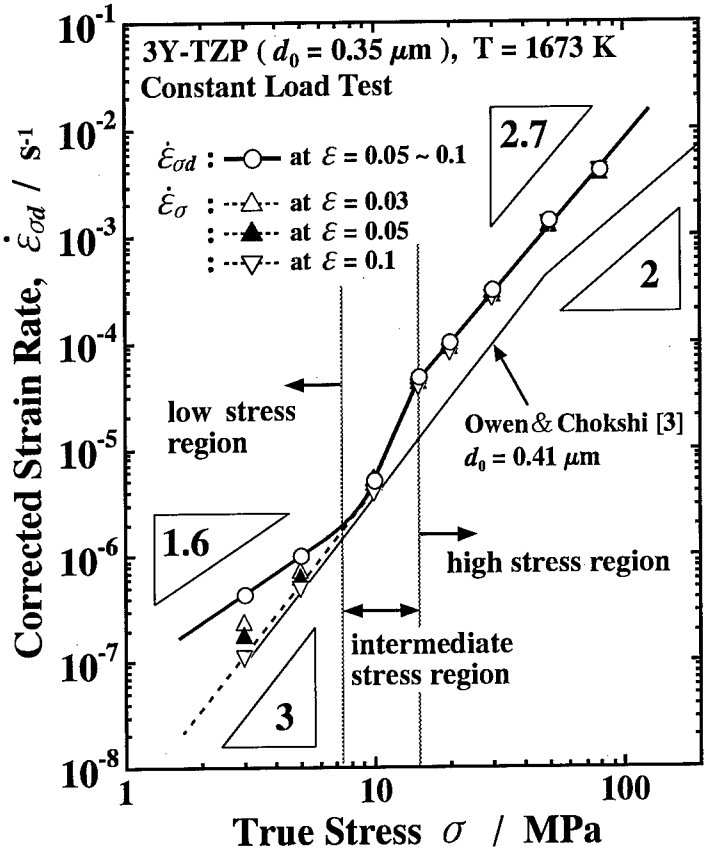

Fig. 3 Creep strain rates plotted against true stress for 3Y-TZP deformed at 1673 K.

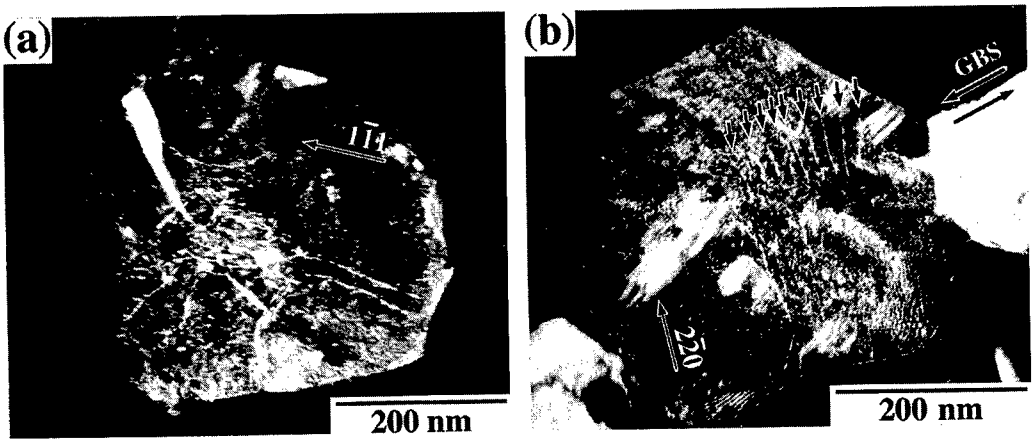

Fig. 4 Dark field TEM micrographs of 3Y-TZP deformed up to ε =0.18 at 1673 K, at 30 MPa; (a) tangled dislocations and (b) dislocations punched from multiple grain junction were observed.

size is indispensable for evaluating the stress exponent at low stresses. In Fig. 3, we should also note that the broken line for ε =0.1 parallels the earlier data and yields n~3.0, which is consistent with n-values obtained without considering the effect of grain growth at low stresses [1-8].

3-3. Deformed intragranular microstructure

Since dislocation structures are highly sensitive to the cooling procedure [13], the deformed specimens were cooled rapidly under loading at the respective initial stresses. As typically shown in Fig. 4, the present TEM observation revealed evidence of intragranular dislocation activities such as a tangle of dislocations and a dense alignment of dislocations, which were not found in undeformed specimens. The presence of tangled dislocations seen in Fig. 4(a) suggests that a few slip system can simultaneously be activated during deformation. As indicated with arrows in Fig. 4(b), dislocations were quite frequently observed near the multiple grain junctions. This is an indication that the dislocations were punched out from the grain junctions.

In contrast to the present observation, intragranular dislocation activities have not been reported in a fine-grained Y-TZP. A difference in specimen preparation seems to relate this situation. If the TEM samples are prepared from failed specimens or from interrupted specimens cooled without loading, a considerable part of intragranular dislocations introduced by deformation would be annealed out during cooling, as suggested by Messerschmidt *et al.* [13]. Furthermore, grain sizes smaller than about 0.5 μm may also make it difficult to observe intragranular dislocation under a two-beam condition.

4. Discussion

4.1 Absence of a region with n~2

A deformation region with n~2 reported in earlier studies [1-8] did not appear at stresses up to 80 MPa in the present examination. Such a difference cannot be connected with grain growth. This is because the effect of grain growth decreases with increasing stress and accordingly the data for $\dot{\varepsilon}_{od}$ and $\dot{\varepsilon}_{\sigma}$ almost overlap to each other as seen in Fig. 3. Earlier studies have noted that the transition stress tends to increase with decreasing grain size [1-8]. If this is true in the present material, there may be a possibility of n~2 for $\dot{\varepsilon}_{od}$ and $\dot{\varepsilon}_{\sigma}$ at stresses higher than 80 MPa, since the initial grain size of the present material is smaller than that used by Owen and Chokshi [3]. Interference from preferential deformation around the specimen grips in conventional experiments [9] may be also concerned with the difference, because the interference can be expected to enhanced at higher stresses owing to higher stress concentrations in the grip regions. To confirm the appearance of n=2, additional experiments using the present technique are desirable at stresses higher than 100 MPa.

4.2 High stress region with n=2.7

Although the stress exponent higher than 3.0 is usually correlated with dislocation creep for metals and some yttria-stabilized zirconia single crystals [5, 14], this has not been the case for fine-grained Y-TZP. This is because, in fine grained Y-TZP, intragranular dislocation activities have not confirmed in earlier studies [1-8] and the level of flow stress is much lower than the yield stress of the zirconia single crystals. Accordingly, n~3.0 in Y-TZP has been related with a interface-reaction-controlled process [1-4] or a diffusional process incorporated with a threshold stress for GBS [5-8]. According to the existent models [15, 16], however, n~3 does not seem to be consistent with such processes.

The present data seem to provide anther explanation for this deformation region. The present observation confirms that dislocations are activated itragranularlly as seen in Fig. 4, irrespective of the level of flow stress lower than the yield stress of single crystals as mentioned above. This

result indicates that stress concentrations occurring particularly around the multiple grain junctions are likely to activate the dislocation motion. Such dislocation motion can be assumed to relieve the strain concentrations due to GBS, and thereby contribute to the accommodation process during deformation. The stress exponent slightly smaller than 3.0 may be an indication of the intervention of some other processes noted in the earlier studies [1-8].

4.3 Low stress region with n=1.6

The comparison among $\dot{\varepsilon}_{od}$, $\dot{\varepsilon}_{\sigma}$ and the data by Owen and Chokshi [3] shown in Fig. 3 strongly suggests that n~3.0 in the low stress region of earlier studies is probably spurious at stresses lower than ~10 MPa. As described before, such a spurious region occurs from the use of large strains to attain the quasi-steady state sufficiently without correcting the effect of grain growth (Eqs. (4) and (7)). Instead of n~3.0, a n-value closing toward unity is essential at stresses lower than ~10 MPa.

Although stress exponents close to unity have been reported for coarse-grained Y-TZP with d_0 >~2 μm [17] and attributed to lattice diffusion creep, there has been little information available on the definite explanation of rate-controlling mechanisms in fine-grained Y-TZP at such low stresses. However, the stress exponent smaller than 2.0 incorporated with a grain size exponent of 2.0 suggests an intervention of diffusional creep in this stress region.

4.4 Intermediate region with n>5

For superplastic metallic alloys [18] and Y-TZP [5-8], the appearance of a large n-value in an intermediate deformation region is often related with the existence of a threshold stress, below which a rate-controlling mechanism working at higher stresses is suppressed. To examine this point, the steady strain rate compensated against the stress exponent for the high stress region as $\dot{\varepsilon}_{od}^{(1/2.7)}$ is plotted as a function of stress in Fig. 5. A liner relationship appears in the plot and the trend line intersects with the abscissa at ~1.0 MPa. This value is much smaller than 10-15 MPa at which the transition of the stress exponent occurs. Thus, the n-value larger than 5 in the intermediate region of Fig. 3 cannot be explained by such a threshold stress approach. The large n-value can be regarded as a transient one due to a change in rate-controlling mechanisms suggested in the former sections.

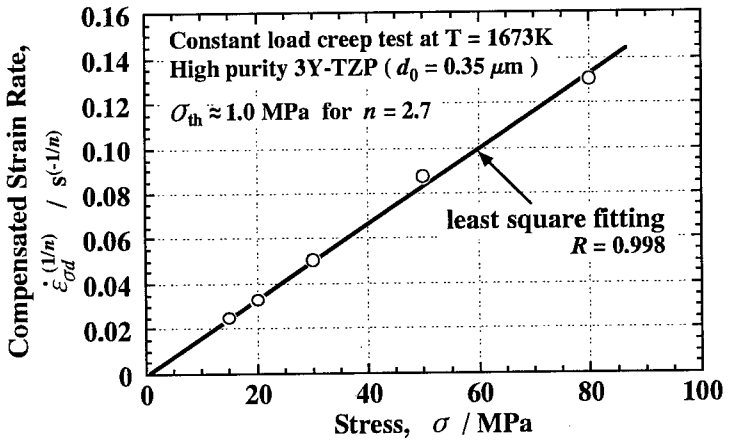

Fig. 5 Compensated creep rate $\dot{\varepsilon}_{od}^{(1/2.7)}$ plotted against the true stress for 3Y-TZP at 1673 K.

5. SUMMARY

The creep behavior of a high-purity yttria-stabilized tetragonal zirconia (3Y-TZP) at 1673 K is examined directly along the gauge portions of tensile specimens. Correction of creep rates against both instantaneous stress and grain size reveals a sigmoidal stress-strain rate relationship being different from that in earlier studies. In a high stress region lying at ≥15 MPa, the stress exponent takes a value of 2.7 and evidence of intragranular dislocation activities is found in deformed specimens. This result suggests that dislocation creep may pertain in this region. In a low stress region lying at <10 MPa, the stress exponent takes a value of 1.6, suggesting an intervention of diffusional creep. In an intermediate region connecting the former two regions, the stress exponents takes a value larger than 5. The large n-value can be regarded as a transient one accompanying the change in the rate-controlling mechanism between the high and the low stress regions.

Acknowledgements

The authors would like to express their thanks to Dr. H. Yoshinaga, emeritus professor of Kyushu Univ., for his useful discussion and advice on high temperature examination.

References

[1] A. H. Chokshi, Mat. Sci. Eng. **A166**, 119(1993).

[2] A. H. Chokshi, Mat. Sci. Eng. **A234-236**, 986(1997).

[3] D. M. Owen and A. H. Chokshi, Acta Mater. Mater. **46**, 667(1998).

[4] J. A. Hines, Y. Ikuhara, A. H. Chokshi and T. Sakuma, Acta Mater. Mater. **46**, 5557(1998).

[5] M. Jimenez-Melendo, A. Dominguez-Rodoriguez and A. Bravo-Leon, J. Am. Ceram. Soc. **81**, 2761(1998).

[6] A. Bravo-Leon, M. Jimenez-Melendo and A. Dominguez-Rodoriguez, Scripta Metall. **24**, 1459(1990).

[7] M. Jimenez-Melendo, A. Bravo-Leon and A. Dominguez-Rodoriguez, Mat. Sci. Forum **243-245**, 363(1997).

[8] A. Dominguez-Rodoriguez, A. Bravo-Leon, J. D. Ye and M. Jimenez-Melendo, Mat. Sci. Eng. **A247**, 97(1998).

[9] K. Morita and K. Hiraga, submitted to Scripta Metall.

[10] J. Zhao, Y. Ikuhara and T. Sakuma, J. Am. Ceram. Soc. **81**, 2087(1998).

[11] E. Sato and K. Kuribayashi, ISIJ Int. **33**, 825(1993).

[12] T. Kondo, Y. Takigawa and T. Sakuma, Mat. Sci. Eng. **A231**, 163(1997).

[13] U. Messerschmidt, D. Baither, B. Baufeld and M. Bartsch, Mat. Sci. Eng. **A233**, 61(1997).

[14] D. Gomez-Gracia, J. Martinez-Fernandez, A. Dominguez-Rodoriguez, P. Eveno and J. Castaing, Acta Mater. Mater. **44**, 991(1996).

[15] M. F. Ashby and R. A. Verrall, Acta Mater. Mater. **21**, 149(1973).

[16] E. Arzt, M. F. Ashby and R. A. Verrall, Acta Mater. Mater. **31**, 1977(1983).

[17] D. Dimos and D. L. Kohlstedt, J. Am. Ceram. Soc. **70**, 531(1987).

[18] F. A. Mohamed, J. Mat. Sci. **18**, 582(1983).

Corresponding author; Koji Morita, E-mail: morita@nrim.go.jp, Fax; +81-298-59-2501

Key Engineering Materials Vols. 171-174 (2000) pp. 855-862
© 2000 Trans Tech Publications, Switzerland

High-Temperature Deformation in Unidirectionally Solidified Eutectic Al_2O_3-YAG Single Crystal

H. Yoshida[1], K. Shimura[1], S. Suginohara[1], Y. Ikuhara[1], T. Sakuma[1], N. Nakagawa[2] and Y. Waku[2]

[1] Department of Material Science, Graduate School of Engineering, the University of Tokyo, 7-3-1 Hongo, Bunkyo-ku, Tokyo 113-8656, Japan

[2] Ube Research Laboratory, Corporate Research and Development, Ube Industries, Ltd., 1978-5 Kogushi, Ube City, Yamaguchi, Japan

Keywords: Unidirectionally Solidified Al_2O_3-YAG, Single Crystal

Abstract

Eutectic Al_2O_3–$Y_3Al_5O_{12}$ (YAG) single crystals were fabricated by unidirectional solidification. High-temperature deformation behaviour was examined by uniaxial compression testing in argon flow at temperatures between 1773K and 1973K under an initial strain rate in a range of $2.8 \times 10^{-6} \sim 1 \times 10^{-4}$ s^{-1}. High-temperature yield stress in Al_2O_3-YAG single crystal is much higher than that in sintered Al_2O_3-YAG composite with the same composition. The stress exponent n and the activation energy Q in the single crystal are estimated to be about 6 and about 730 kJ/mol, respectively. The activation energy is nearly the same with that in Al_2O_3 or YAG single crystal reported previously. In the deformed samples, tangled dislocations are observed in both Al_2O_3 and YAG single crystals. High-temperature deformation is likely to be controlled by dislocation motion.

1 Introduction

In recent years, considerable efforts have been made to develop high-performance materials with excellent high-temperature strength at above about 1800 K in an oxidized atmosphere in order to improve heat efficiency of gas generators or aerospace jet engines[1,2]. Oxide ceramics with high melting points must be useful for their high-temperature strength and oxidation resistance. However, high-temperature strength in sintered polycrystalline oxides is not so high because the strtength is reduced by an existence of grain boundaries[3].

More recently, unidirectionally solidified Al_2O_3 – YAG single crystals have been fabricated[4], whose flexural strength is as high as 400 MPa at 2000 K. This strength is about seven times higher than that in sintered Al_2O_3–50vol% YAG composite at the same temperature[5]. The present paper aims to examine the high-temperature flow behaviour in Al_2O_3–YAG single crystals at temperatures 1773 $\sim$ 1973K.

2 Experimental Procedure

The material used in this study is α-Al_2O_3–YAG single crystal. High-purity commercial powders of α-Al_2O_3 (AKP-30; Sumitomo Chemical Co. Ltd.) and Y_2O_3 (Y_2O_3-SU; Shin-etsu Chemical Co. Ltd.) were used for starting materials. These powders were ball-milled in ethanol with an α-Al_2O_3 and Y_2O_3 mole ratio of 82:18 to produce the composites with 50 vol% of each phase. The slurry obtained was dried, pressed into cylinder with a size of $\phi 10 \times 10$ mm^3, and then pre-melted by arc-melting to get initial ingots. The powders obtained by crushing the initial ingots were put into a Mo crucible heated by high-frequency induction at a pressure of 10^{-5} mmHg in an argon atmosphere. They were unidirectionally solidified using the advanced alloy crystalline structure controlling equipment at the Japan Ultra-high Temperature Materials Research Center. The unidirectional solidification was conducted at 2223K with a molybdenum crucible at a down-speed of 1.39×10^{-6} m/s to obtain the single crystal Al_2O_3–YAG composite.

High-tempereature compression tests were carried out using an Instron-type testing machine (MTS 808). The jigs were made of graphite rods, and the composite plates were set between rods and sample to protect the jigs. The size of the specimens was 4×4 mm^2 in cross section and 6 mm in height. Compression tests were carried out in argon flow at a constant cross-head speed with a resistance-heated furnace. The initial strain rate and temperatures

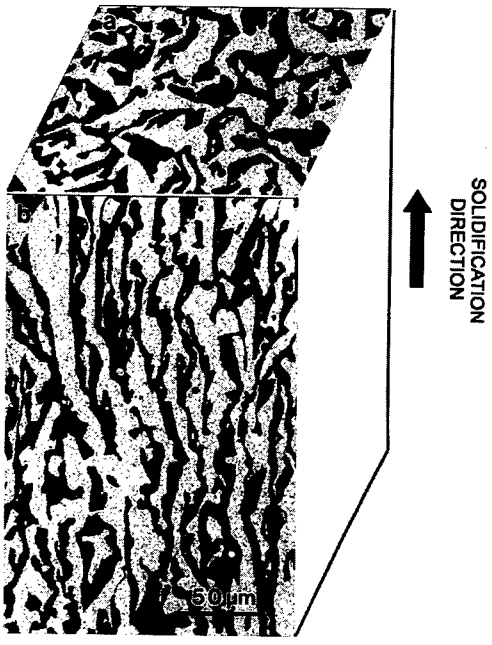

Figure 1. SEM micrographs of an unidirectionally solidified Al_2O_3–YAG single crystal on the cross-sectional plane (a) normal and (b) parallel to the solidificational direction.

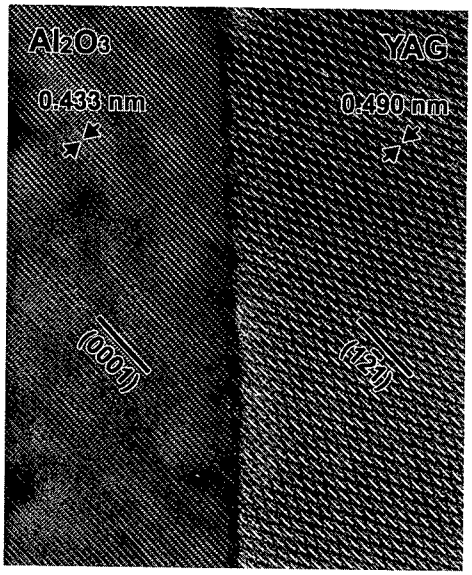

Figure 2. A high-resolution electron micrograph of an Al_2O_3/YAG interface.

examined were in a range of $2.8 \times 10^{-6} \sim 1.0 \times 10^{-4}$ s^{-1} and 1773 $\sim$ 1973 K, respectively.

Microstructures were examined with an optical microscope (Nikon AFX-II), scanning electron microscope (SEM; JSM-5200, JEOL, Japan) and transmission electron microscope(TEM; H-800, Hitachi, Japan). High-resolution transmission electron microscopy (HREM) was also performed to analyze the grain boundary structure using 300 keV high-resolution electron microscope (H-9000NAR, Hitachi, Japan).

3 Results and Discussion

The average bulk density of samples was about 99% of theorical density. Figure 1 shows SEM micrographs of the surface (a) normal and (b) parallel to the solidification direction in Al_2O_3–YAG single crystal. In this figure, bright and dark contrasts correspond to YAG and Al_2O_3 phases, respectively. The normal cross section shows an isotropic structure, but the parallel section seems to be elongated to the solidification direction. The Al_2O_3–YAG single crystal has a microstructure consisting of three dimensionally continuous and entangled Al_2O_3 and YAG single crystals.

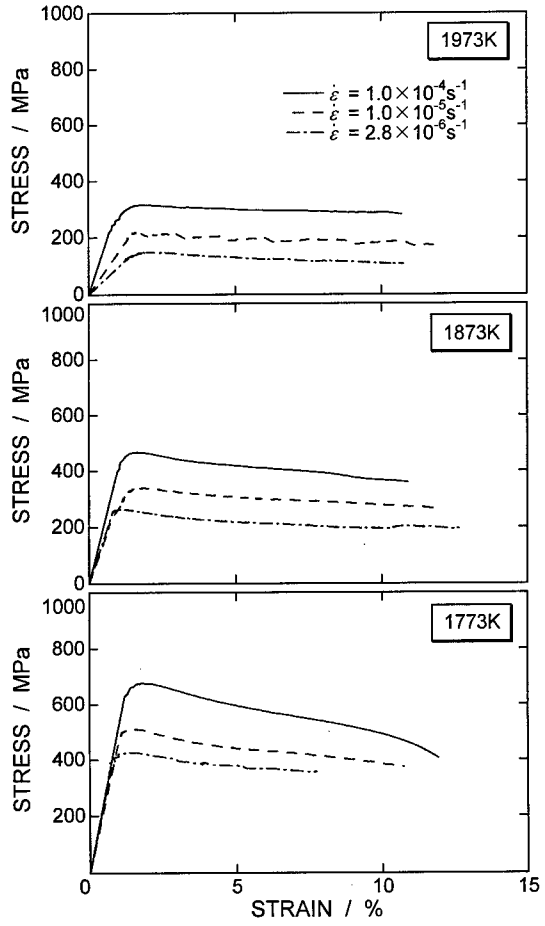

Figure 3. Strain-stress curves at temperatures between 1773K $\sim$ 1973K under an initial strain rate in a range of $2.8 \times 10^{-6} \sim 1.0 \times 10^{-4}$ s^{-1}.

Figure 2 shows the high-resolution transmission electron micrograph along an Al_2O_3 / YAG interface. No second phase is seen in Al_2O_3 and YAG phases with TEM examinations even in the interphase boundary. The growth directions of Al_2O_3 and YAG are determined to be $[11\bar{2}0]$ and [210], respectively. The (0001) lattice plane in Al_2O_3 is parallel to $(1\bar{2}1)$ in YAG lattice plane, but the interface between each phases seems not to be coherent, because the difference in the lattice parameters for each plane is more than 10%.

Figure 3 shows the strain-stress curves in the present material at temperatures between 1773K $\sim$ 1973K under an initial strain rate in a range of $2.8 \times 10^{-6} \sim 1.0 \times 10^{-4}$ s^{-1}. The stress-strain curves exhibit yield and flow behaviour at all temperatures.

In this study, we tentatively analyze the yield stress from the following equation,

$$\dot{\varepsilon} = A\sigma^n \exp\left(-\frac{Q}{RT}\right) \tag{1}$$

where A is the material constant, σ is the applied stress, R is the gas constant, T is the absolute temperature, Q is the activation energy for creep, and n is the constants termed the stress exponent. Figure 4 shows a log-log plot of initial strain rate against yield stress at three temperatures. The previous data of Al_2O_3[6] and YAG[7] single crystal and sintered Al_2O_3–YAG composite[4] are also shown in Fig. 4 for comparison. The compression axis of Al_2O_3 and YAG single crystal is [11$\bar{2}$0] and [111], respectively. The yield stress in Al_2O_3–YAG single crystal at 1873 K under the initial strain rate of 1.0×10^{-4} s^{-1} is 433 MPa, which is about 13 times higher than that in sintered Al_2O_3–YAG composite with the same composition, and twice as high as that in Al_2O_3 single crystal. However, the yield stress in YAG single crystal is much higher than that in Al_2O_3–YAG single crystal. The yield stress in YAG single crystal under the initial strain rate of 1.0×10^{-6} s^{-1} at 1803K is nearly the same with that in Al_2O_3–YAG single crystal at 1773K.

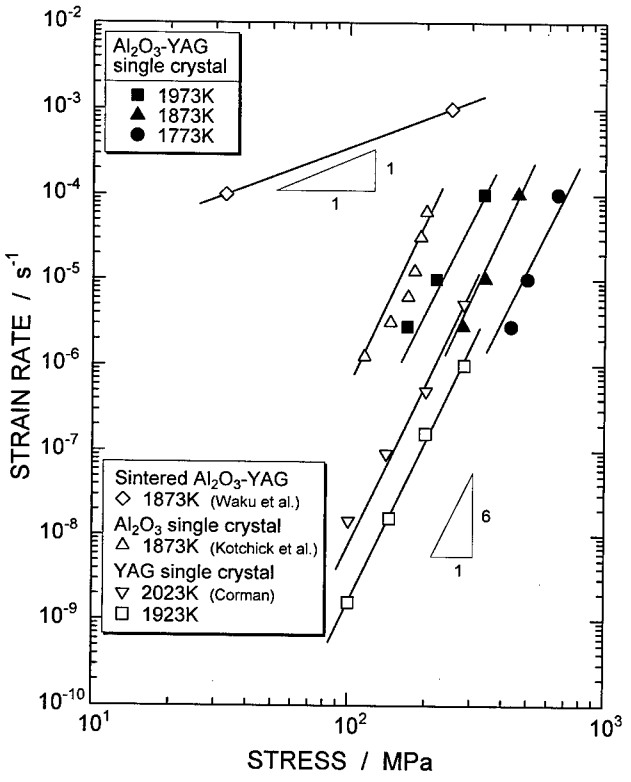

Figure 4. A log-log plot of initial strain rate against yield stress at three temperatures examined in Al_2O_3–YAG single crystal, accompanied with the previous data of Al_2O_3 and YAG single crystal and sintered Al_2O_3–YAG composite for compressive testing.

The log-log plot of initial strain rate against yield stress is approximately to be a single straight line at each temperature, and the stress exponent n is estimated to be about 6 for the present material. The stress exponent is nearly the same with that in Al_2O_3 or YAG single crystal, but is much larger than that in sintered Al_2O_3–YAG composite which is reported to be about 1. It has been reported that the high-temperature deformation in Al_2O_3 or YAG single crystal takes place by dislocation mechanism[6, 7], and that the creep deformation in sintered Al_2O_3–YAG composite occurs by diffusional process such as diffusional creep[8]. The large stress exponent in Al_2O_3–YAG single crystal indicates that the high-temperature deformation takes place mainly

by dislocation motion.

Figure 5 is a bright field image of (a) Al_2O_3 phase and (b) YAG phase of the present material after 10% deformation at 1873K under an initial strain rate of 1.0×10^{-4} s^{-1}. Many dislocations are seen in both phases. This result supports the dislocation motion as a rate-controlling mechanism for the high-temperature deformation in Al_2O_3–YAG single crystal.

Figure 6 shows an Arrhenius plot of initial strain rate against yield stress in Al_2O_3–YAG single crystal at temperatures in a range of 1773K $\sim$ 1973K. The activation energy for high-temperature deformation Q is estimated to be about 730 kJ/mol, which is not so different from the values estimated for high-temperature compressive tests in Al_2O_3 or YAG single cryatal; the activation energy for Al_2O_3 single crystal with a compression axis of $[11\bar{2}0]$ and YAG single crystal with an axis of [111] are reported to be 637kJ/mol[6] and 789 kJ/mol[7], respectively. This fact also suggests that the high-temperature deformation in Al_2O_3–YAG single crystal may be rate-controlled by a dislocation motion induced by lattice diffusion in Al_2O_3 or YAG single crystal.

Next, we will examine the high-temperature deformation of this composite from isostress and isostrain models[9]. On the assumption that the duplex microstructure can be simplified

Figure 5. A transmission electron micrograph of (a) Al_2O_3 and (b) YAG phase in the unidirectionally solidified Al_2O_3–YAG single crystal deformaed 10% in compression testing at 1873K under an initial strain rate of 1.0×10^{-4} s^{-1}.

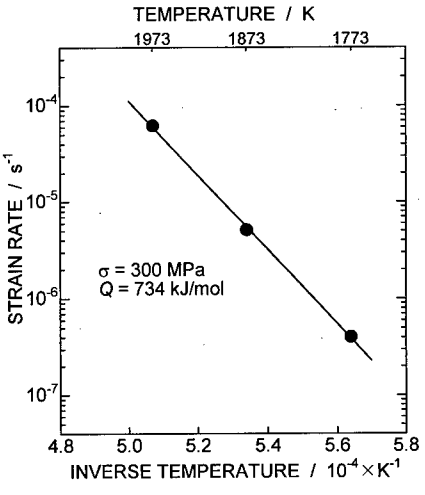

Figure 6. An Arrhenius plot of the initial strain rate against the flow stress at temperatures between 1773K $\sim$ 1973K.

such that the composite consists of the alternating plates of each phase as shown in Figure 7, the two models are the idealized isostress model of Fig.7(a), and the isostrain model of Fig.7(b). The composite strain rate $\dot{\varepsilon}$ and stress σ can be described by the following relations,

$$\text{isostress model}: \quad \dot{\varepsilon} = v_{Al_2O_3}\dot{\varepsilon}_{Al_2O_3} + v_{YAG}\dot{\varepsilon}_{YAG} \tag{2}$$

$$\text{isostrain model}: \quad \sigma = v_{Al_2O_3}\sigma_{Al_2O_3} + v_{YAG}\sigma_{YAG} \tag{3}$$

where v_X is the volume fraction, σ_X is the yield stress, $\dot{\varepsilon_X}$ is the initial strain rate and A_X is the materials constant of X single crystal (X: Al_2O_3, YAG). By using the activation energy Q_{YAG}[111] for YAG single crystal of 789 kJ/mol and v_{YAG} of 0.5, calculated $\dot{\varepsilon}$ against σ relationship at 1873K is shown in Figure 8. The isostrain model provides a better description of the experimental results. The result is consistent with the fact that dislocations are formed both in Al_2O_3 and YAG phases in deformed samples as shown in Fig.5.

4 Conclusion

High-temperature deformation in unidirectionally solidificated Al_2O_3–YAG single crystal was examined by uniaxial compression testing in argon flow at temperatures between 1773K and 1973K under an initial strain rate in a range of $2.8 \times 10^{-6} \sim 1 \times 10^{-4}$ s^{-1}. The strain-

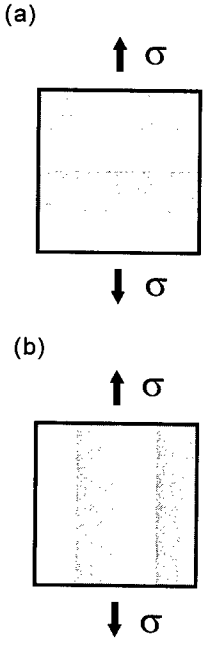

Figure 7. Idealized composite microstructures: (a) isostress and (b) isostrain orientations.

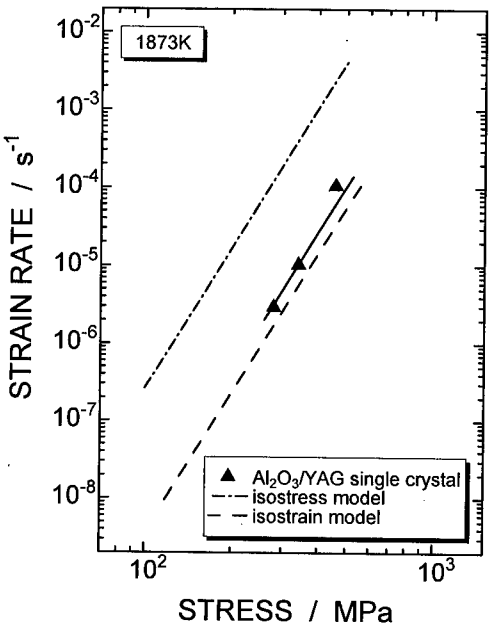

Figure 8. A mixing-rule predictions based on the isostress and isostrain models for the initial strain rate and yield stress together with the experimental data in Al_2O_3–YAG single crystal at 1873K.

stress curves in Al_2O_3–YAG single crystal exhibit yield and flow behaviour in this temperature range. High-temperature yield stress at 1873K under an initial strain rate of 1×10^{-4} s^{-1} in Al_2O_3-YAG single crystal is 433 MPa, which is much higher than that in sintered Al_2O_3–YAG composite with the same composition. The stress exponent n in the single crystal is estimated to be about 6, and the activation energy for deformation is about 730kJ/mol. The activation energy is nearly the same with that in Al_2O_3 single crystal deformed in compression in the $[11\bar{2}0]$ direction and YAG single crystal with a compression axis of [111] which are reported to be 637 kJ/mol and 789 kJ/mol, respectively. An analysis of high-resolution electron microscopy reveals that there is no amorphous phase at Al_2O_3–YAG interface. In the deformed samples, tangled dislocations are observed in both Al_2O_3 and YAG single crystals. Plastic flow must be induced by dislocation motion in the two phases. The initial strain rate against yield stress relationship in Al_2O_3–YAG single crystal can well be described by a simple isostrain model.

Acknowledgment

The authors wish to express their gratitude to the Ministry of Education, Science and Culture, Japan, for the financial support by a Grant-in-Aid for Developmental Scientific Research (2)–10450254 for Fundamental Scientific Research. A part of this study was supported by Kurata Science and Technology Foundation.

References

[1] R. Bowman and R. Noebe, *Adv. Mater. Process*, **8** (1989) 35–41.

[2] K. Nakakado, T. Machida, H. Miyata, T. Hisamatsu, N. Mori and I. Yuri, *J. Eng. for Gas Turbines and Power*, **177** (1995) 245–250.

[3] W.R. Cannon and T.G. Langdon, *J. Mater. Sci.*, **18** (1983) 1–50.

[4] Y. Waku, H. Ohtsubo, N. Nakagawa and Y. Kohtoku, *J. Mater. Sci.*, **31** (1995) 4663–4670.

[5] Y. Waku, N. Nakagawa, T. Wakamoto, H. Ohtsubo, K. Shimizu and Y. Kohtoku, *J. Mater. Sci.*, **33** (1998) 1217–1224.

[6] D.M. Kotchick and R.E. Tressler, *J. Am. Ceram. Soc.*, **63** (1980) 429–434.

[7] G.S. Corman, *J. Mater. Sci. Lett.*, **12**(1993) 379–382.

[8] Y. Waku, N. Nakagawa, H. Ohtsubo, Y. Ohsora and Y. Kohtoku, *J. Jpn. Inst. Metals*, **59** (1995) 71–78.

[9] M. McLean, *Directionally Solidified Materials for High Temperature Service*. The Metals Society, London, UK., 1983.

AUTHOR INDEX

Abe, F. 17, 395, 469, 483, 491, 505, 513, 521
Abe, T. 461
Akuzawa, T. 663
Ardakani, M. 545
Asai, T. 639
Aso, S. 161

Basoalto, H. 545
Besson, J.L. 817
Bhadeshia, H.K.D.H. 529
Bhanu Sankara Rao, K. 437, 537
Blum, W. 609
Brear, J.M. 35, 61

Cao, J.-W. 841
Carreño, F. 725
Carsi, M. 389
Cerjak, H. 453
Chaim, R. 787
Chokshi, A.H. 779
Choudhary, B.K. 437
Chuman, Y. 305
Church, J.M. 61

Dempers, R. 153
Dlouhý, A. 693
Domínguez-Rodríguez, A. 787

Eliasson, J. 277
Endo, T. 445

Fairman, A. 35
Fischer, B. 77
Foldyna, V. 419
Freund, D. 77
Frommeyer, G. 389
Fujitsuna, N. 469
Fukuzawa, T. 313
Futamura, Y. 411

Gencer, Y. 197
Geng, L. 369
Ghosh, R.N. 545
Glatzel, U. 253
Göcmen, A. 219
Gohlke, D. 77
Goloborodko, A. 355
Gong, J.-M. 51, 189
Goto, S. 161, 647
Granacher, J. 85
Granger, G.B. 817
Greenwood, G.W. 197
Gu, H. 741
Gu, Y. 625
Gu, Y.F. 669
Gülgün, M.A. 793
Gustafson, Å. 277
Gutiérrez-Mora, F. 787

Han, Y. 561
Harada, H. 625, 669, 677
Hasegawa, Y. 109, 131, 427, 499
Hayes, R.P. 69
Hidaka, K. 131
Higashi, K. 337, 363, 617
Hiraga, K. 763, 847
Hirata, S. 639
Hiroe, T. 305
Hofer, P. 453
Holdsworth, S.R. 1
Horkel, T. 693
Hsiung, L.M. 685
Humphrey, D.R. 61

Igarashi, M. 469, 491, 505
Ikeda, Y. 747, 841
Ikuhara, Y. 343, 375, 383, 809, 855
Imai, T. 369
Irie, H. 17, 513
Iseki, T. 771
Ishida, A. 741
Ishikawa, K. 337, 363
Ishiwari, Y. 553, 585
Itoh, G. 231, 291, 633
Iwanaga, K. 477
Iwasaki, H. 617

Jata, K.V. 147
Jiménez, J.A. 389
Jiménez-Melendo, M. 787

Kagawa, Y. 755
Kaibyshev, R. 213, 355
Karlsson, A. 169
Kawabata, K. 321
Kawaguchi, D. 577
Kawahara, K. 825
Kawamoto, H. 747, 841
Kazakulov, I. 213
Kim, W.J. 329
Kim, Y.-W. 147
Kimura, K. 461, 483
Kinugawa, J. 521
Klenk, A. 25, 85
Kohzu, M. 337
Komai, N. 99, 179
Komatsu, Y. 161
Kong, Q.P. 609
Kottada, R.S. 779
Kubo, K. 521
Kubobuchi, K. 771
Kubon, Z. 419
Kubota, K. 131
Kuchařová, K. 593, 693
Kunii, J. 663
Kuribayashi, K. 285, 321
Kushima, H. 461, 483
Kussmaul, A. 25

Langdon, T.G. 205, 593
Laurent, Y. 733
Lee, J.S. 43
Lenk, P. 25
Lin, D. 349
Ling, X. 189
Liu, C. 403
Lofaj, F. 747
Lupinc, V. 245

Mabuchi, M. 363, 617
MacKay, D.J.C. 529
Maile, K. 25, 85
Maldini, M. 245
Mannan, S.L. 437, 537
Mao, J. 369
Maruko, T. 625
Maruyama, K. 109, 601, 709, 717
Masuyama, F. 99, 179, 297, 445
Mathew, M.D. 537, 655
Matsui, M. 99
Matsuo, T. 553, 577, 585, 639
McCarthy, P.R. 9
McLean, M. 545
Middleton, C.J. 35
Mimura, H. 427
Mimurada, J. 343, 375, 383
Misra, A. 801
Mitchell, T.E. 801
Mitomo, M. 741
Miura, H. 269

Miyahara, K. 663
Miyazaki, H. 771
Miyazawa, H. 577
Mizoguchi, K. 717
Mizuno, M. 755
Montgomery, M. 169
Mori, T. 617
Morita, K. 847
Movva, S. 655
Mukai, T. 337, 363
Muneki, S. 491, 505
Muraki, T. 109, 427, 499
Murase, Y. 313
Murata, M. 513
Murty, K.L. 655
Muto, A. 647

Nagakawa, J. 115, 313
Nakagawa, N. 855
Nakano, K. 763
Nakano, M. 343
Nakashima, H. 261, 825
Nakazawa, S. 625
Nath, B. 121
Nieh, T.G. 685
Nikbin, K. 153
Nishimura, N. 297
Nishimura, T. 741
Nojima, A. 231, 291
Nomoto, A. 569
Northwood, D.O. 403

Ochi, Y. 755
Ogata, T. 569
Ohgami, M. 427, 499
Oikawa, H. 601
Okada, A. 747
Okanda, Y. 337, 363
Onodera, H. 461
Orr, J. 9
Ozaki, M. 297

Pahutová, M. 593
Paknikar, K. 537
Park, I. 445
Petrovic, J.J. 801
Phaniraj, C. 437
Polding, L. 35
Purmenský, J. 419

Rasmussen, F. 169
Ro, Y. 625, 669, 677
Robertson, D.G. 9
Rouxel, T. 733, 817
Ruano, O.A. 389
Rühle, M. 793

Saijo, K. 269
Sakai, T. 269, 355
Sakka, Y. 763, 847
Sakuma, T. 343, 375, 383, 809, 855
Sandström, R. 139, 277
Sanglebœuf, J.-C. 733
Sasaki, K. 343, 375, 383
Sato, E. 285, 321
Sato, H. 601
Sawada, K. 109
Schaffernak, B. 453
Schellenberg, G. 85
Seitisleam, F. 139
Shan, A. 349
Sharif, A.A. 801
Shiba, K. 115
Shimura, K. 343, 375, 855
Shiratori, N. 639
Shollock, B.A. 545

Siebörger, D. 253
Singh, R. 537
Sitdikov, O. 355
Sklenička, V. 593
Skrotzki, B. 701
Soboyejo, W.O. 69
Strang, A. 9
Suda, T. 709
Suginohara, S. 855
Suzuki, M. 601
Suzuki, T.S. 763
Svoboda, M. 593

Tabuchi, M. 521
Tagami, M. 647
Takahashi, S. 553
Takaki, S. 411, 477
Takaku, R. 577
Takeyama, M. 639
Takigawa, Y. 841
Takmori, S. 131
Tanabe, S. 337
Tanaka, H. 513
Tancret, F. 529
Terada, Y. 553, 577, 585
Testu, S. 817
Tochigi, I. 369
Tramer, M. 85
Tsuchiyama, T. 411, 477
Tsurekawa, S. 825
Tsutsui, H. 337
Tu, S.-T. 51, 189

Verdier, P. 733
Völkl, R. 77

Wade, N. 663
Waku, Y. 855
Watanabe, H. 337, 363
Watanabe, T. 237, 521
Watzinger, B. 609
Webster, G.A. 153
Wegmann, G. 709
Wilshire, B. 725
Wu, R. 139

Yagi, K. 17
Yaguchi, M. 569
Yamabe-Mitarai, Y. 625, 669, 677
Yamaguchi, K. 771
Yamamoto, N. 115, 313
Yamamoto, R. 717
Yamauchi, M. 305
Yano, T. 771, 833
Yeon, J.H. 329
Yokobori Jr., A.T. 131, 833
Yokobori, T. 131
Yoon, K.B. 43, 53
Yoshida, F. 261
Yoshida, H. 809, 855
Yu, X. 625
Yu, X.H. 677

Zhang, P. 609
Zhao, Z. 403
Zheng, Y. 561
Zhou, Q. 633
Zhu, S. 755

KEYWORD INDEX

ß-Si_3N_4 Whisker 369
σ Phase 513
ε-Cu Particle 411
½ Cr ½ Mo ¼ V 35
12%Cr Steel 99, 179
1CrMo 35
2 ¼ Cr1Mo 121
2 ¼ CrMo 35
2.25Cr-1Mo Steel 305
2124 Al Composite 329
3Y-TZP 847
9%Cr Steel 99, 179
9-12% Cr Steels 131
9Cr Steel 395
9Cr-1Mo Steel 437
9Cr-1Mo-V-Nb Steel 483

Accelerating Creep 427, 717
Acceleration of Creep Rate 395
Activation Energy 213, 329, 355, 655, 755
Ageing 537
Al-1%Si-0.5%Cu Alloy 633
Al_2O_3 ..... 809, 833
~ /TiC Composite 771
Al-Al_3Ni 161
Alloy 625 537
Alumina Short Fibres 593
Aluminum 601, 779, 793
~ Alloy 617
~ -Beryllium Alloy 261
~ -Manganese Alloy 261
Amorphous Phase 741
Anelasticity 197
Anisotropic
~ Creep 253
~ Deformation 545
ASME-P92 427
Atomic Pair 461
Austenitic
~ Stainless Steel 277
~ Steels 17

Back Stress 297, 701
Bainitic Steel 297
Bending Fatigue 161
Boilers 491
Brass 647
Brittle Particulate Composites 733
Burgers Vector 801

C^*-Integral 43
Carbide
~ Forming Element 477
~ Particle 477
Cast Superalloy 561
Cavitation 747
Cavity
~ Formation 25
~ ~ and Growth 763
~ Growth 25
~ Interlinkage 763
Central Atoms Model and Co-Segregation 461
Ceramic-Matrix Composites 725
Chemical Potential 291
Climb 277
~ Velocity 461
Coarsening Constant K_d 419
Coherent Precipitation 505
Commercial Magnesium Alloy 337
Component Geometry 61
Composition of Precipitate 513
Compression
~ Creep 609
~ Strength 625
Continuous Recrystallization 349
Continuum Damage Mechanics 35, 61, 545
Crack 43
~ Initiation Behavior 85
~ Propagation 763
Creep ... 43, 153, 189, 197, 395, 445, 513, 529, 537, 553, 577, 585, 639, 655, 685, 693, 725, 733, 755, 787, 817, 833
~ Acceleration Growth 219
~ Crack 131
~ ~ Growth 51, 85, 139, 147
~ Damage 25, 109, 245, 305
~ Deformation 77, 297, 483
~ ~ Curve 131
~ Embrittlement 121
~ Fatigue Crack Growth 85
~ Life 593
~ Mechanism 701
~ Modeling 219
~ Properties 521

Creep *(cont'd from prev. page)*
~ Rate 709
~ ~ Expression 231
~ Resistance 69, 419, 453, 709, 809
~ -Rupture 1
~ ~ Strength 17, 99, 179, 419
~ Strain 99, 179, 499
~ ~ Rate 427
~ Strength 477, 483, 663
~ Test Machine 77
~ Void 513
C_t 43
Cu-SiO_2 Bicrystal 269

Damage 219
~ Mechanics 189
Data
~ Assessment 1
~ Sheet 17
Deformation 213, 755
~ Mechanism 561
~ Twinning 685
Degradation 483
Delta-Phase 537
Denuded Zones 205
Diffusion 197
~ Creep 205, 231, 291, 779
~ Mechanism 231, 291
Diffusional Creep 847
Dislocation(s) 197, 253, 701
~ Climb 285
~ Creep 285, 337, 847
~ Pileup 685
~ Spacing 609
~ Strengthening 297
~ Substructure 297
Dispersion Strengthening 505
~ Alloy 321
Dissociation 801
Dopant 343, 383
Ductility 189, 343, 677
~ Exhaustion Method 305
Duplex
~ Microstructure 701
~ Stainless Steel 389
Dwell Times 85
Dynamic Recrystallization 553, 577, 585, 639, 701

EB Welded Joint 521
EDS 383
Effect of Composition on Properties .. 121
Einstein's Equation 231
Elongation-to-Failure 363
Energy Filtering TEM (EFTEM) 453
Erbium Oxide 801
Eutectic Alloy 161
Extensometry 9

Failure Mode 99
Fatigue 161
Fcc and $L1_2$ Two Phase Coherent Structure 625
Fe_2W Laves Phase 395
Fe_3Al 349
Fe-Ni-Co Martensite 491
FePd 505
Ferritic
~ -Martensitic Chromium Steels 453
~ Steels 17, 109, 121, 499
Fiber
~ Orientation 161
~ -Reinforced Composite 161
Fine Grain 647
Finite-Element
~ Analysis 153
~ Calculations 545
First Order Kinetics 437
Forged Niobium Aluminide Alloy 69
Fracture 593, 677, 725, 755
~ Behaviour 669
~ Control 237
~ Mechanics 85
~ Strain 77
Fully Lamellar Structure 709
Furnace Tube 189
Fusion Line 43

Gamma
~ Prime 569
~ Titanium Aluminide 147
Gas
~ Pressure Forming 337
~ Turbine Blade 569
Gaussian Processes 529
GB Embrittlement 115
Glass Industry 77
GPS Silicon Nitride 817
Grade 91 (9CrMoVNb) 35

Grain
~ Boundary 375, 383
~ ~ Character Distribution GBCD 237
~ ~ Design and Control 237
~ ~ Energy 269
~ ~ Fracture 269
~ ~ Segregation 121, 793, 809
~ ~ Sliding (GBS) 205, 269, 337, 363, 389, 647, 747, 847
~ ~ Structure 237
~ Growth 779, 793, 847
~ Shape 779
~ Size 337, 633
GTA Welded Joint 521

Hardness 35, 109, 513
Harper-Dorn Creep 205
Heat
~ Resistant Steel 297, 411, 477, 499
~ Resisting Materials 17
~ Treatment 403, 561
Helium
~ Embrittlement 115
~ Implantation 115
Heterogeneous Recovery 483
High
~ Strain Rate Superplasticity .. 363, 369
~ Strength
~ ~ Aluminum Alloy 355
~ ~ Low Alloy Steel 139
~ ~ Steel 403
~ Temperature ... 43, 77, 189, 277, 445, 709
~ ~ Creep 389, 717
~ ~ Deformation 269, 617, 647, 825
~ ~ Materials 625
~ -Cr Ferritic Steels 469
Homogeneous Deformation 491
Hot Deformation 355
Huddleston Equivalent Stress 305
Hydrostatic Stress 305

Ia3 801
In-Beam Experiment 313
Inelastic Strain 25
Interface 685
~ Sliding 685
~ Spacing 701
Interfacial Accommodation 321
Inter-Fiber Spacing 161
Intergranular Rupture 139
Intermediate Temperature Stress-Rupture . 561
Intermetallic(s) 153, 505, 693
~ Alloy 685
Ion Irradiation 115
Ir-Nb *fcc*-$L1_2$ Two-Phase Alloys 669
Ir-Nb-Ni-Al 677
Irradiation
~ Creep 313
~ Damage 313
Ir-Ta-Ni-Al 677
I-S Pair 445

Lamellar 639
~ Structure 717
Laminate 685
Large Scale Specimens 85
Lath 395
~ Structure 109, 411, 499
Lattice
~ -Diffusion Creep 231, 291
~ Misfit 505
Laves Phase 427, 469
Life
~ Assessment 189
~ Exhaustion 219
~ Extension 537
~ Prediction 179
Lifetime Prediction 841
Liquid Phase 617
Long Term Stability 491
Low
~ Alloy CrMo and CrMoV Steel 419
~ Alloys Steels 121
~ Temperature Superplasticity 349

$M_{23}C_6$ Carbide 395, 513
Magnesium Alloy 363, 593
Manganese 601
Martensite 411, 477
Martensitic Steel 85, 297
Master Creep Curve 437
Material Mismatch 51
Matrix 253
Maximum Principal Stress 305
MC Carbide 297
Mechanical
~ Property/-ies 115, 161

Mechanical *(cont'd from prev. page)*
~ Testing 61
~ Twinning 701
Metal Matrix Composites ... 285, 321, 593
Mg-Al-Alloy AZ91hp 609
Microalloying 663
Microchemistry 793
Microcracking 763
Microelectronic Circuit 633
Microstructural
~ Change 483
~ Evolution 693, 701
~ Investigations 453
~ Stability 453
Microstructure 17, 253, 553, 561, 585, 609, 663, 669, 677, 793, 817
Minimum Creep Rate 395, 601
Mises Equivalent Stress 305
Modelling 529
~ of Stress Relaxation 9
Molecular Orbital Calculations 809
Molybdenum 499
Multiaxial 61
~ Stress 153, 305
Multiaxiality 25, 189
m-Value 337
MX Carbonitride 297

Nanocrystals 787
Newtonian Viscous Flow 205
NF616 131
Nickel 253
~ Base Superalloys 529
~ Based Alloy 553, 577, 585
Nitrogen 445
Normalized Creep Rate 601
Notch 139
Notched Bars 153
Nuclear
~ Fusion Reactor 115
~ Transmutation 115

ODS 77
On Plant Test 169
Orientation 577, 709
Orowan
~ Mechanism 277
~ Stress 261
Ostwald
~ Growth 411
~ Ripening 419
Oxidation 237

Panel Wall 169
Particle
~ Coarsening 277
~ Dispersion Strengthening 297, 663
~ Size Distribution 277
~ Strengthening 277
Pinning Force 411
Plastic Accommodation 285, 321
Platinum 77
Point Defects 313
Post Assessment Tests (PATs) 1
Powder Metallurgy 363
Power-Law Regime 355
Precipitate(s) 609
~ Size 513
Precipitation 469, 537
~ Hardening 609, 625
~ Sequence 453
~ Strengthening 419, 499
Primary Creep 847
Prior Austenite Grain Boundary 483
PST Crystal 709
Pure Aluminum Composites 369

Quaternary 677

Rabotnov-Kachanov 219
Radiation Effect 115
Rafting 569
Rare-Earth 801
Recovery 411, 477
~ Creep 297
~ Rate 461
Reinforcement 593
Relative Strength 601
Remnant
~ Life 219
~ Strain 219
Rheological Model 771
Rheology 733
Rhodium 77
Room Temperature Creep 403
Rupture
~ Strain 99, 179
~ Strength 663

Schmid Factor 709

Segregation 375
Shear
~ Strength 801
~ Test 617
Si 469
Si_3N_4 833
SiC 833
SiC/SiC Composite 755
SiC_f/Al_2O_3 725
SiC_f/SiC 725
Silicon Nitride 747, 825, 841
Simulated Heat Affected Zone ... 139, 521
Simulation 313
Single Crystal 245, 253, 553, 577, 585, 639, 855
~ Superalloys 545
Sintering 793
Slip System 825
SMP14 Alloy 245
Sn-3.5Ag 655
Sn-5Sb 655
Sn-Pb Eutectic Alloy 663
Solder 655, 663
Solid Solution 253
~ Hardening 445
~ Strengthening 419, 461, 477, 499
Stainless Steel 445
Steady State Creep 69
~ Rate 419
Strain
~ Exhaustion 219
~ Measurement 77
~ Mismatch 321
~ Rate Sensitivity Exponent 363
Stress
~ Exponent 355, 617, 755, 779, 841, 847
~ Redistribution 219
~ Relaxation 17, 733, 817
~ Rupture 61
~ ~ Criterion 61
~ State 25, 61, 231
Subgrain 297, 633
Superalloy(s) 17, 253
Superplastic 329
Superplasticity 343, 375, 383, 787
SUS304 Steel 513

TAF650 131
TEM 453, 693
Tensile
~ Creep 747, 841
~ Ductility 763
Tertiary Creep 219
Test Data 9
Testing Standards 9, 51
Texture 389, 633
Thermal
~ Cycling 169
~ Fatigue Crack 169
Thermo-Calc 461
Thickness 633
Thin Foil 633
Third Elements (Ni, Mo, C, B) 669
Threshold
~ Behavior 213
~ Stress 213, 355
TiAl 693
Time
~ -Dependent Fracture 51
~ -to-Failure 841
Tin 655
Titanium Aluminides 639, 709, 717
Transient Creep 427, 437
Transition Joints 121
Transmission Electron Microscopy 833
Tungsten 131, 395, 499
Twinning 693, 709
Type
~ IIIa 35
~ IV 35
TZP 343, 383

Uniaxial Creep 139
Unidirectional Solidification 161
Unidirectionally Solidified Al_2O_3-YAG ... 855
USC 169
~ Plant 491

Vacancy 291
~ Concentration 231, 291
Viscosity 733
Viscous Flow 747
Void
~ Formation 647
~ -Hardening Stress 261

W Strengthened High Cr Ferritic Steel 521
Weak-Beam Method 825

Weld(s) 35, 43, 51
Welding 189
Weldment 99
Wetting 237
Work-Hardening 647
~ Coefficient 461

Y-α-Sialon 741
Yttrium 601, 793
~ Aluminum Garnet 741

Zener's Pinning Effect 771
Zirconia 375, 787
ZrO_2/TiC Composite 771

Key Engineering Materials

Specializing in Advanced Ceramics and Composites

Recent Volumes:
for complete tables of contents please visit http://www.ttp.net

Oxides: Phase Transitions, Non Stoichiometry, Superconductors, *Ed. C. Boulesteix*
Zirconia Engineering Ceramics: Old Challenges - New Ideas, *Ed. E. Kisi*
Solidification Processing of Reinforced Metals, *by R. Asthana*
Sol-Gel Production, *Ed. H. Schmidt*
Fracture and Strength of Solids, *Eds. P. Tong, T.Y. Zhang and J.K. Kim*
Experimental Techniques and Design in Composite Materials, *Ed. Pierluigi Priolo*
Impact Response and Dynamic Failure of Composites and Laminate Materials, *Eds. J.K. Kim and T.X. Yu*
Advanced Ceramic Tools for Machining Application - III, *Ed. I.M. Low*
Polymer Blends and Polymer Composites, *L. Ye and Y.-W. Mai*
Euro Ceramics V, *Eds. P. Abelard, J. Baxter, D. Bortzmeyer et al.*
Ceramic and Metal Matrix Composites, *Eds. M. Fuentes, J.M. Martínez-Esnaola, A.M. Daniel*
Electrical Properties of Oxide Materials, *J. Nowotny and C.C. Sorrell*
Advanced Ceramic Materials, *Hamid Mostaghaci*
Fracture of Composites, *Ed. E.A. Armanios*
Metal Matrix Composites, *Ed. G.M. Newaz*
Ceramic Matrix Composites, *Ed. G.M. Newaz*
Porous Ceramic Materials, *D.M. Liu*
Sol-Gel Production, *Eds. H. Schmidt, Germany, & R. Uhlmann*
Zirconia Engineering Ceramics, *Ed. E. Kisi, Australia*
Glass Ceramics: Preparation, Properties & Applications, *Ed. C. Ruessel, Germany*
Solidification of Composites, *Ed. R. Asthana*
Structural Ceramics Powders, *Ed. S.G. Malghan*
Advanced Ceramic Tools, *Eds. I.-M. Low & X.S. Li*
Joining of Metal Matrix Composites, *Eds. N.B. Dahotre et al.*
Corrosion of Advanced Ceramics, *Eds. R.J. Fordham et al.*
Nonequilibrium Materials, *Ed. J. Lendvai*
Interfaces of Ceramic Materials, *Ed. K. Uematsu & J. Nowotny*

***Key Engineering Materials** presents 18 volumes per year, each centering on a special topic of current interest in the fields of advanced ceramics and composites. The yearly subscription rate is US $ 1404.00.*

Please place your trial subscription with complete return rights:

Trans Tech Publications Ltd • Brandrain 6 • CH-8707 Zuerich-Uetikon • Switzerland
Fax: (++41) 1 922 10 33 • E-Mail: ttp@ttp.net • Web Site: http://www.ttp.net